April 2015

Design of a Nozzle for Semi-Solid Metal Printing

Michael James Wight
Worcester Polytechnic Institute

April 22, 2015

Design of a Nozzle for SSM Printing

A Major Qualifying Project Submitted to the Faculty of

Worcester Polytechnic Institute

In partial fulfillment of the requirements for the

Degree in Bachelors of Science

By:

Michael Wight

Date:

April 22, 2015

Approved By:

Professor Diran Apelian

Abstract

Additive manufacturing (AM) is a burgeoning industry. Direct metal writing (DMW) is a metal AM technique where semi-solid metal (SSM) slurries are deposited layer-by-layer similar to how thermoplastics are deposited for fused deposition modelling (FDM) 3D printers. SSM slurries are processed between an alloy's solidus and liquidus line, demonstrate shear thinning behavior, and have viscosities similar to toothpaste or motor oil. Bismuth-tin, a low temperature alloy system, was selected for the preliminary tests. An oscillatory shear rheometer was used to confirm the shear thinning behavior of SSM slurries and develop a processing range for bismuth-tin. Computer simulations for the flow of SSM slurries through a nozzle demonstrated that precise thermal control at the nozzle's tip was necessary to avoid clogging and large pressure drops, especially for nozzles with outlet diameters smaller than 300 microns. The collected data had applications for a physical DMW apparatus being tested at the Lawrence Livermore National Laboratory.

Acknowledgements

First and foremost, I would like to thank my advisor, Professor Diran Apelian, for his feedback and guidance during the project. I would also like to thank the Lawrence Livermore National Lab (LLNL) and specifically the Direct Metal Writing team for the opportunity to be involved in the project. My involvement began with a summer internship in the summer before my senior year. This work was performed under the auspices of the U.S. Department of Energy by Lawrence Livermore National Laboratory under Contract DE-AC52-07NA27344. LLNL-POST-669580. I am appreciative of the support and guidance provided by lab employees, and would like to commend the efforts of my mentor, Dr. Andrew Pascall, and employees Dr. Eric Duoss, Dr. Ryan Hunt, Dr. Joshua Kuntz, Dr. Christopher Spadaccini and Mr. John Vericella.

I would also like to thank a colleague, Michael Perrone, for his interest and collaboration in the project. I would like to thank Professor Andreas Alexandrou at the University of Cyprus for his assistance interpreting the collected rheological data. I would like to thank Dr. Libo Wang for his assistance preparing and casting the second batch of alloys prepared from ingots. I would also like to thank the team at Sigma, especially Mr. Kaushik Manek, for training me on *SIGMASOFT* and troubleshooting my simulations. Finally, I would like to thank Mr. Siamek Najafi for his technical support throughout the project.

Table of Contents

1. Introduction

Additive manufacturing (AM) is a burgeoning industry and can revolutionize how products are made. In 2013, the AM industry had profits in excess of $3 billion and by 2020, the annual revenue for AM and 3D printers is expected to exceed $21 billion (Wohlers Associates, 2014). Most commercial applications for AM have been using thermoplastics, but metallic parts are desirable because of their improved strength and conductive properties. Laser powder-bed fusion and casting are two common metal AM methods. Casted parts suffer from porosity while powder-bed fusion necessitates the use of high cost and energy lasers (Wimmer & Kline, 1996).

Direct metal writing (DMW) is an alternate AM technique. DMW is 3D printing with semi-solid metal (SSM) slurries. SSMs are composed of solid and liquid particles and are formed when alloys are processed between the freezing and melting points. SSM alloys exhibit thixotropic and non-Newtonian behavior at certain temperatures and compositions when sheared, which results in a viscous mixture similar to that of motor oil (Rice et al., 2000). SSM processing is superior to traditional die casting due to the non-turbulent flow of highly viscous metals leading to less entrapped air and less shrinkage porosity (de Figueredo & Apelian, 2001).

A major obstacle for DMW is the print nozzle. Crude direct metal writers have been created, but they suffer from non-uniform temperature distributions, clogging, and erosion of the nozzle itself (Krassenstein, 2014). The behavior of the SSM slurry during the extrusion process is complex and relatively unknown. This project investigates this behavior by gathering rheological data for bismuth-tin with a rotational shear rheometer. Rheological data is then used to model the flow of SSM slurries through nozzles of varying geometries using *SIGMASOFT*. By understanding how SSM slurries behave during the extrusion process, a reliable nozzle can be created that would allow DMW to form strong and accurate parts with metal alloys.

2. Background

2.1. SSM Processing

Semi-solid metals (SSM) exist between the solidus (freezing) and liquidus (melting) lines for alloys, as seen in Figure 1. When the alloy reaches thermal equilibrium, it exists in a two-phase state with solid and liquid particles. The eutectic point is the location where the solid phase transforms directly into the liquid state and vice-versa without forming a SSM slurry. SSM processing was discovered by Spencer at al. in the early 1970s at MIT while conducting tearing tests on tin-lead alloys (Spencer et al., 1972). During solidification, they discovered that shearing the alloy and breaking up its dendritic network caused the alloy to enter a mushy state with a lower viscosity similar to that of motor oil. This semi-solid alloy has non-turbulent flow, which minimizes the entrapped air and shrinkage porosity (de Figueredo & Apelian, 2001).

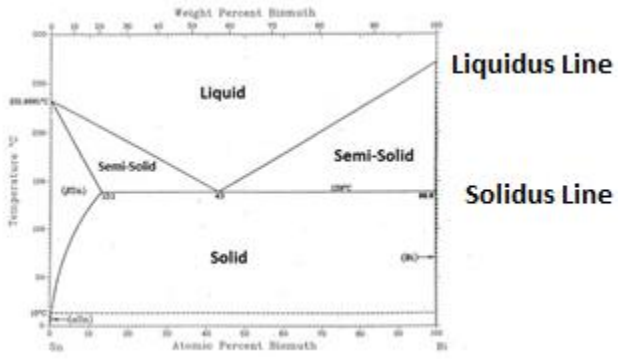

Figure 1- Phase Diagram (Smithells et al., 2004)

This mushy region is characterized by thixotropic and non-Newtonian behavior (Rice et al., 2000). Viscosity is a measure of fluidity and is a function of shear stress and strain rate, as seen in Equation 1. As the viscosity decreases, materials flow more easily. Thixotropic behavior is a shear thinning property where materials become less viscous over time. Newtonian fluids such as water have the same viscosity regardless of the shear rate while non-Newtonian fluids such as SSM slurries have viscosities highly dependent upon the shear rate.

$$Viscosity = \eta = \frac{Shear\ Stress}{Strain\ Rate} = \frac{\tau}{\dot{\gamma}}$$

Equation 1- True Viscosity

SSM processing is highly dependent upon three parameters: fraction solid, particle size and distribution, and pouring temperature (Lashkari & Ghomashchi, 2007). Viscosity increases progressively with fraction solid until reaching the dendrite coherency point (Chai et al., 1992). Once this point is reached, the viscosity increases abruptly, as seen in Figure 2. SSMs with equiaxed structures have viscosities several orders of magnitude below those of SSMs with dendritic structures (Lashkari & Ghomashchi, 2007). Globular equiaxed particles are able to flow more freely while dendritic structures become interlocked and impede flow. Finer particles also demonstrate lower viscosities than larger particles (Flemings, 1991). Adding solute elements to the SSM slurry is one method to reduce grain size and subsequently lower its viscosity (Kissling & Wallace, 1963). Regulating the pouring temperature through a shallow temperature gradient can prevent the formation of the dendritic network by removing directional heat extraction, which eliminates the need to agitate the SSM slurry (Flemings, 1974).

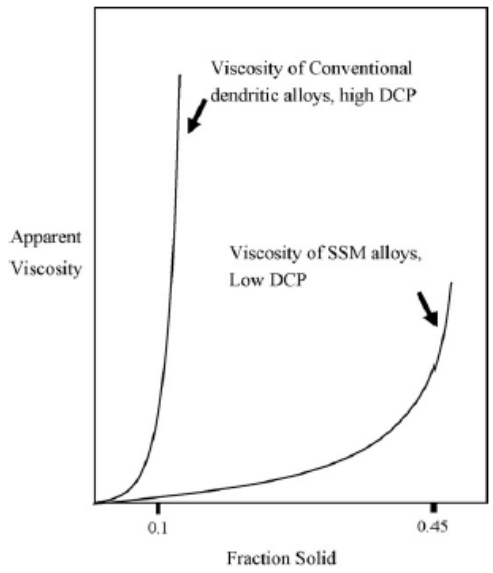

Figure 2- Viscosity vs. Fraction Solid (Chai et al., 1992)

There are four major steps in the preparation of SSM slurries: nucleation and growth, globularization of equiaxed particles, coarsening and coalescing of globules, and agglomeration of globules during flow (de Figueredo & Apelian, 2001). Each step of the process aims to eliminate dendrites, as true SSM slurries are free of dendrites. Preparation methods depend whether the metal will be cast in the liquid (rheocasting) or the semi-solid state (thixoforming). Appendix A describes specific rheocasting and thixoforming methods in detail.

2.2. Rheology

Rheology is the "study of the flow of matter; but, more specifically, the influence of the structural details of the material on its rheological response" (Shaw, 2001). Rheological experiments reveal how materials flow under different conditions such as temperature, shear stress, and shear rate. Viscosity tends to increase with fraction solid and decrease with an increase in temperature (Alexandrou, 2006). Since SSM structures break down at a rate faster than the rate at which they build up, one must capture and analyze the early behavior before steady-state properties are reached. Figure 3 shows the existing rheological models (Atkinson, 2005). Metals and SSM slurries exhibit the non-Newtonian, shear thinning behavior.

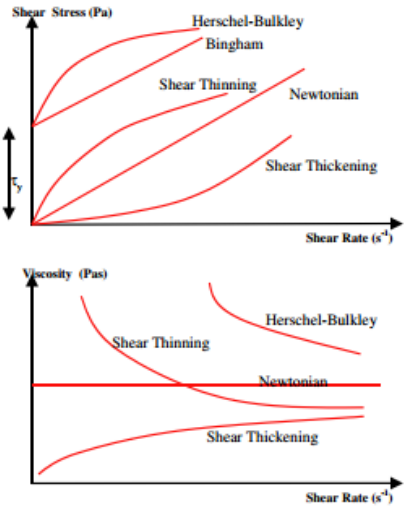

Figure 3- Rheology Models (Atkinson, 2005)

Rheological experiments are typically conducted on liquids or semi-solids since these states demonstrate a measurable viscoelastic response. In oscillatory shear rheology experiments, a sinusoidal shear stress is induced in the sample. The stress response in the sample is then studied by comparing the phase shift (φ or δ) between the shear stress and strain rate, as seen in Figure 4 (Biolin Scientific, 2014). Solids have matching stress-strain curves with a phase shift of 0 (φ = δ = 0), pure liquids have stress-strain curves with a phase shift of π/2 (φ = δ = π/2), and viscoelastic materials have stress-strain curves with a phase shift between 0 and π/2 (Wyss et al., 2007). Figure 5 conveys the response of these three states graphically (Wyss et al., 2007). Rotational rheological tests calculate the true viscosity, as seen in Equation 1, while oscillatory rheological tests calculate the complex viscosity because of the phase shift.

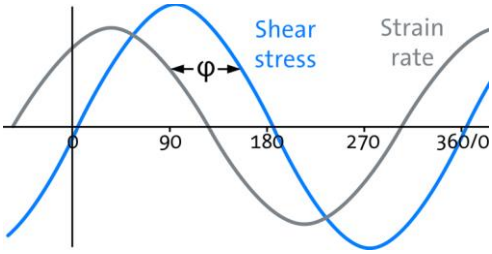

Figure 4- Rheology Phase Shift (Biolin Scientific, 2014)

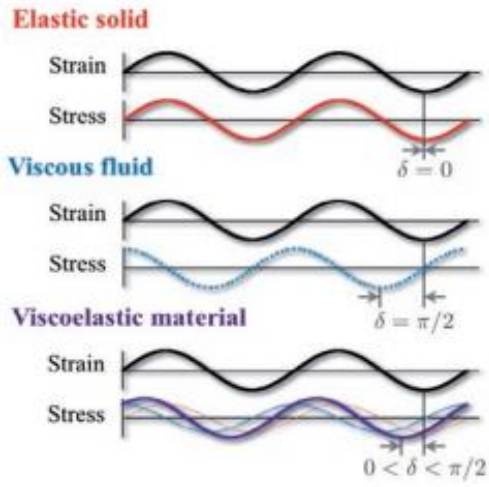

Figure 5- Solid, Liquid, & Viscoelastic Material Phase Shifts (Wyss et al., 2007)

When a shear stress is applied, materials demonstrate an elastic and viscoelastic response. These responses can be broken down into the storage and loss moduli (Meyers & Chawla, 2009). The storage modulus (G') measures the material's solid properties using its elasticity and ability to retain its initial shape when the stress is removed, which can be seen in Equation 2. The loss modulus (G'') measures the material's liquid properties using its viscosity, which can be seen in Equation 3. When the storage modulus is greater than the loss modulus, the material demonstrates solid-like behavior. Alternatively, when the loss modulus is greater than the storage modulus, the material demonstrates liquid-like behavior. Both the storage and loss moduli are dependent upon the viscosity and phase shift. The ratio between the two moduli can be seen in Equation 4.

$$Storage\ Modulus = G' = \frac{\tau}{\gamma}\cos(\varphi) = \eta\cos(\varphi)$$

Equation 2- Storage Modulus

$$Loss\ Modulus = G'' = \frac{\tau}{\gamma}\sin(\varphi) = \eta\sin(\varphi)$$

Equation 3- Loss Modulus

$$\tan(\varphi) = \frac{G''}{G'}$$

Equation 4- Loss to Storage Modulus

2.2.1. Non-Newtonian Models

Two common non-Newtonian rheology models are the Ostwald-de-Waele and the Herschel-Bulkley models. Both models use power laws. The Ostwald-de-Waele (Equation 5) model shows the power law relationship between the shear stress (τ) and the shear rate ($\dot{\gamma}$) using a flow consistency index (K) and a power law exponent (n) (Atkinson, 2005). Equation 6 is derived from Equation 5 and relates the viscosity to the shear stress with a structural parameter (κ) and a power law exponent (n). If n is equal to 1, the equation models a Newtonian fluid and

K is equivalent to the viscosity. If n is greater than 1, the fluid exhibits shear thickening or dilatant behavior. If n is less than 1, as with semi-solid metals, the fluid exhibits shear thinning or pseudoplastic behavior. Additional rheological flow models are covered in Appendix B.

$$\tau = K\dot{\gamma}^n$$

Equation 5- Ostwald-de-Waele Model Shear Stress (Atkinson, 2005)

$$\eta = nK\dot{\gamma}^{n-1} = \kappa\dot{\gamma}^{n-1}$$

Equation 6- Ostwald-de-Waele and Herschel-Bulkley Model Viscosity (Atkinson, 2005)

The Herschel-Bulkley model is similar to the Ostwald-de-Waele model except the Herschel-Bulkley model applies to Bingham fluids (Atkinson, 2005). Bingham fluids require a minimum shear stress to induce flow. Equation 7 shows the Herschel-Bulkley shear stress, which is the Ostwald-de-Waele shear stress plus the fluid's yield stress (τ_y). Both models share the same viscosity equation since the yield stress is a constant. Semi-solid metals have finite yield stresses, or exhibit Bingham fluid behavior, at low shear rates, but this yield stress is difficult to measure since rheometers have a low shear rate limit (Pan et al., 2004).

$$\tau = \tau_y + K\dot{\gamma}^n$$

Equation 7- Herschel-Bulkley Model Shear Stress (Atkinson, 2005)

Couette flow, or annular flow, has four assumptions: the inner radius (R_1) is smaller than that of the outer radius (R_2), the flow is isothermal and laminar, the flow is asymmetric and end effects are negligible, and gravity is negligible (Chatzimina et al., 2009). To avoid wall friction, the gap between the inner and outer cylinder walls must be at least ten times larger than the largest particle in the test material (Boger, 1999). The Herschel-Bulkley model is often incorrectly used for Couette flow. Rotational shear rheometers often report the apparent strain rate instead of the true strain rate, and the latter is the quantity that must be used in the power law

equation (Alexandrou, 2006). The yield stress determines the rheometer's effective gap and can alter the shear rate by orders of magnitude. Therefore, a correction factor must be applied between the apparent and true strain rates to interpret the data.

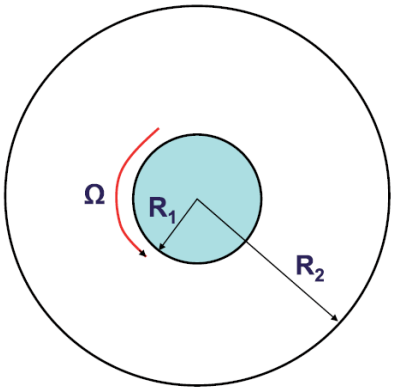

Figure 6- Couette Flow (Chatzimina et al., 2009)

Cone and plate rheometers use the low angle cone geometry to eliminate the radial dependence of the shear rate (Morrison, 2001). No correction factor is necessary in the power law equations for a cone and plate rheometer since the shear rate, shear stress, and viscosity are constant throughout the entire domain. Special care must be taken that material is not ejected during experiments and that edge distortions do not occur at high shear rates (Morrison, 2001).

2.2.2. Cox-Merz Rule

In 1958, Cox and Merz discovered that the shear rate dependence of the steady shear viscosity ($\eta(\dot{\gamma})$) and the angular frequency dependence of the complex viscosity ($\eta^*(\omega)$) of melted polymers are nearly identical (Cox & Merz, 1958). Thus, the Cox-Merz relation can relate rotational and oscillatory viscosity data. The steady shear flow ($\tau(\dot{\gamma})$) has also been observed to be equivalent to the complex modulus value ($G^*(\omega) = \sqrt{G'^2 + G''^2}$) for small amplitude oscillatory shear when rearranging the Cox-Merz relation (Winter, 2009). This relation's validity for metals and SSMs needs to be investigated.

3. Methodology

Direct metal writing (DMW) is heavily reliant upon viscosity. In order to model the behavior of the SSM slurry through the nozzle, it is important to conduct rheological tests to quantitatively understand how the viscosity relates to fraction solid, temperature, shear stress, and shear rate. A bismuth-tin system was used for rheological testing because of its low melting range. These samples were prepared in a tube furnace from metal powders or by diluting a commercially available bismuth-tin alloy with the required amount of bismuth or tin. The first rheological tests were conducted on a low-temperature cone and plate rheometer, but future tests were conducted on a high-temperature oscillatory shear rheometer with a cup and bob geometry.

The *SIGMASOFT Thixo* software was used to model the flow of the SSM slurry through the nozzle. Most commercially available flow modeling software is designed for liquids with a constant viscosity independent of the shear rate and time. This software is applicable for traditional liquid metal die casting, but the rules for die casting are not transferrable to rheocasting or thixoforming. *SIGMASOFT Thixo* is designed specifically for the thixotropic, non-Newtonian flow of SSM slurries. Atkinson summarizes the three different methods for modeling SSM flow: Kumar, Martin, and Brown's model, finite difference modeling, and finite element modeling (Atkinson, 2005). *SIGMASOFT Thixo* numerically simulates fluid flow by generating a mesh and solving the Navier Stokes partial differential equations with the finite difference model (Lipinski & Flender, 1998).

3.1. Alloy Creation

Bismuth-tin alloys were used because of their low melting points. Compositions tested on the cone and plate rheometer had to have the entire semi-solid region below 200 °C since that was the maximum operating temperature of the device. Using a bismuth-tin phase diagram

(Figure 7), bismuth-tin samples ranging from 10% tin to 86.9% tin were created using powder or ingots (Smithells et al., 2004).

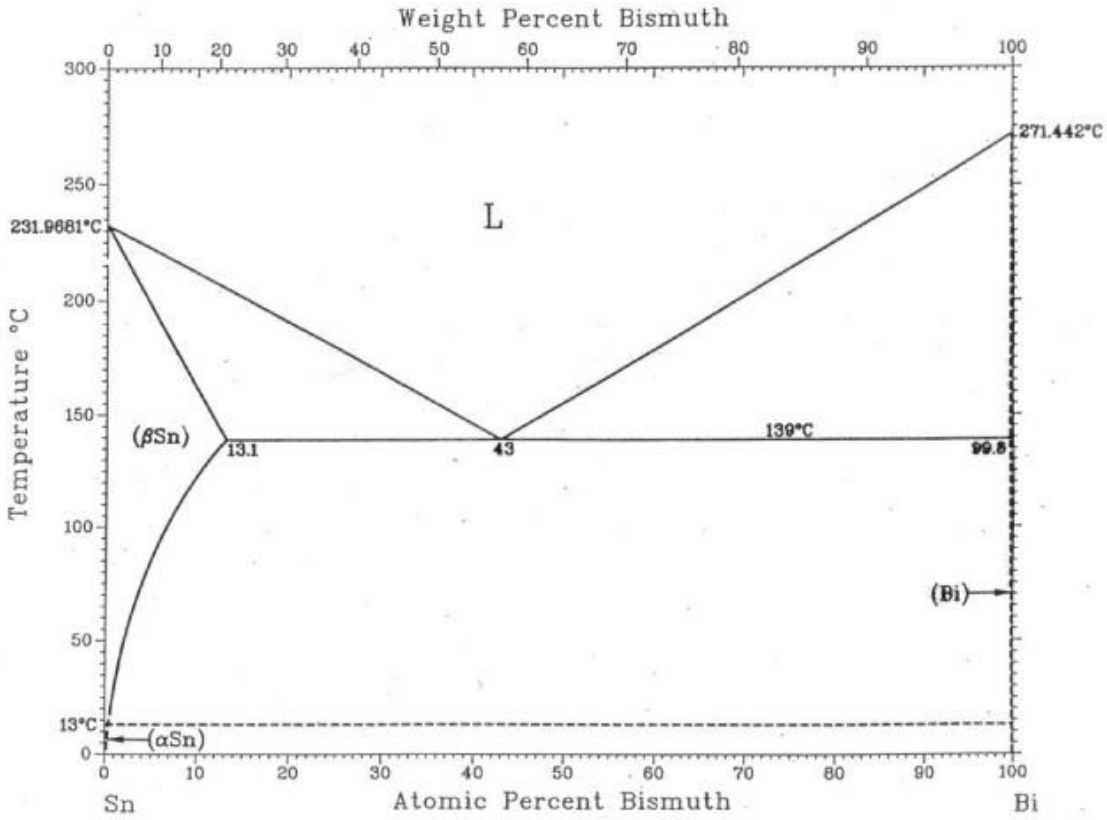

Figure 7- Bismuth-Tin Phase Diagram (Smithells et al., 2004)

The bismuth-tin alloys created for the cone and plate rheometer were formed from bismuth and tin powders. These powders were melted and reformed in a tube furnace with a hydrogen atmosphere to reduce the oxides present in the metal powders. Alloys created for the high-temperature rotational rheometer were created by diluting a bismuth-tin ingot with the appropriate amount of bismuth or tin to mitigate the oxidation issues with powder processing.

3.1.1. From Powders

325 mesh bismuth and tin powders were used to ensure more even mixing. The bismuth powder was certified as 99.5% pure, and the tin powder was certified as 99.8% pure by Alfa Aesar, the supplier. Twelve different samples were measured and massed with the desired

atomic percentages, as seen in Table 1. These powders were then thoroughly mixed in an acoustic energy mixer that applies a uniform shear field at the material's resonant frequency. When loaded into the mixer, the powders were placed in non-static plastic bags. The powders were exposed to a maximum of 30 Gs during mixing to avoid overheating.

Bismuth-Tin Alloy Composition				
Tin (Atomic %)	**Bismuth (Atomic %)**	**Tin/Bismuth (Weight Ratio)**	**Solidus Temperature (°C)**	**Liquidus Temperature (°C)**
10	90	0.063	139	248.2
15	85	0.100	139	236.6
20	80	0.142	139	225.0
35	65	0.306	139	190.1
40	60	0.379	139	178.5
45	55	0.465	139	166.9
50	50	0.568	139	147.1
55	45	0.694	139	141.3
60	40	0.852	139	145.5
62.5	37.5	0.947	139	150.9
65	35	1.055	139	156.3
70	30	1.325	139	167.1
75	25	1.704	139	177.9
80	20	2.272	139	188.7
85	15	3.219	139	199.5
86.9	13.1	3.768	139	203.6

Table 1- Bismuth-Tin Alloy Composition

Samples were created from the bismuth-tin powder mixtures in a tube furnace. Forming gas (argon) purged the system of air before increasing the temperature. During the melting and solidification process, hydrogen gas was flowing through the tube furnace to reduce the oxides present in the metallic powders. The powders were heated to approximately 600 °C and held for at least a half hour to ensure the powders were fully molten inside the crucible. For the bismuth rich samples, the powders had to be heated to almost 700 °C since the bismuth was more resistant to melting. The samples were slightly shaken during melting and freezing to help ensure even dispersion and solidification of the bismuth and tin particles.

3.1.2. From Ingots

To avoid the oxidation present in powder formation and the need for a reducing atmosphere, alloys for the high temperature rheometer were created from metal ingots and cast to the required volume. A commercially available 58% bismuth-42% tin alloy was purchased to serve as a master alloy. This master alloy was then diluted with the appropriate amount of 99.9% pure bismuth or 99.9% pure tin, which were cut from larger pieces of stock material. The metals were heated in a box furnace 30° C above the liquidus temperature to ensure the entire mixture was fully molten while also preventing excessive oxidation that would occur at higher temperatures. The mixture was periodically removed from the oven and stirred during melting. Some oxides were present on the metal's surface after heating, but these were removed with a spoon before pouring. The molten metal was then poured into approximately one inch diameter, tapered dies, as seen in Figure 8. These dies were lined with white silk boron nitride to assist in the removal of the casting.

Figure 8- Casting the Bismuth-Tin Alloys

3.2. Alloy Verification

The bismuth-tin alloys created in the tube furnace were subjected to glow discharge mass spectroscopy (GDMS), inductively coupled plasma mass spectroscopy (ICP-MS), and differential scanning calorimetry (DSC) tests to determine the presence of impurities, the exact ratio of tin to bismuth, and the melting behavior of the samples respectively.

3.2.1. Glow Discharge Mass Spectroscopy (GDMS)

Glow discharge mass spectrometry (GDMS) is an analytical technique that determines trace elemental impurities present in samples. The sample's surface is atomized and ionized by a glow discharge and serves as a mass spectrometer when coupled with a quadrupole mass filter (Harrison et al., 1986). Thin samples of the bismuth-tin alloys were prepared and sent offsite for testing. GDMS detected the impurities present in the tube furnace environment and the bismuth and tin powders. This was critical to ensure that the bismuth-tin alloys were thoroughly pure so that the bismuth-tin phase diagram was applicable for the rheological testing.

3.2.2. Inductively Coupled Plasma Mass Spectroscopy (ICP-MS)

Inductively coupled plasma mass spectroscopy (ICP-MS) is an analytical technique that determines the ratio of major elements relative to each other in a sample. The sample's surface is ionized with a plasma and then quantified using a mass spectrometer (Montaser et al., 1998). Approximately one gram samples for each alloy were prepared. ICP-MS provided the exact ratio of tin to bismuth so the correct solidus and liquidus temperatures could be used for testing.

3.2.3. Differential Scanning Calorimetry (DSC)

Differential scanning calorimetry (DSC) measures "the change of the difference in the heat flow rate to the sample and to a reference sample while they are subjected to a controlled temperature program" (Höhne et al., 2003). Samples of the bismuth-tin alloys were massed and

placed in a sample crucible and compared to an empty reference crucible. The heat flow can be used to signal phase changes and determine the location of the solidus and liquidus lines for each composition. These results were juxtaposed to the theoretical bismuth-tin phase diagram to establish the upper and lower bounds during experiments on the rheometer and also to determine the sample's expected tin to bismuth ratio.

Metals change from a solid to a semi-solid at the solidus line when heated. For pure bismuth-tin alloys, the solidus line is at 139 ℃. After the metal is heated further, it transforms from a semi-solid to a liquid at the liquidus line. The exception is the eutectic point, where the solidus and liquidus lines overlap, and the metal has its lowest melting point, transforming directly from a solid to a liquid. When cooled, metals can experience a phenomenon known as supercooling where molten metal solidifies below the melting point, as nucleation is postponed until the metal reaches a lower temperature. Once this lower temperature is reached, rapid solidification known as recalescence occurs (Wei & Ohsasa, 2010).

This study used a differential scanning calorimeter able to measure mass and thermal variations between -150℃ and 2400 ℃. Samples were contained in an inert argon environment to prevent the oxidation of the metallic samples. Data for the temperature, time, and heat flow were collected in increments smaller than 30 seconds.

Derivatives for the heat flow with respect to temperature were computed. In regions where the phase changes were expected, the temperature was increased by 1.50 ℃ per minute, which resulted in 0.75 ℃ between data measurements. Because of the relatively small changes in temperature between data points, the average rate of change is approximately equal to the instantaneous rate of change, as seen in Equation 8.

$$\frac{d(Heat\ Flow)}{d(Temperature)} = \frac{dQ}{dT} = \frac{Heat\ Flow\ 2 - Heat\ Flow\ 1}{Temperature\ 2 - Temperature\ 1} = \frac{Q_2 - Q_1}{T_2 - T_1}$$

Equation 8- DSC Derivatives

Solidus and liquidus line temperatures were extracted from the heating curve as opposed to the cooling curve due to the latter having supercooling. Figure 9 shows heating curves for two separate silver-copper alloys (Boettinger et al., 2006). During the heating curve, the beginning of the first peak signifies the approximate location of the solidus line. The maximum of the second peak occurs near the liquidus line. Discerning the liquidus temperatures for alloys near the eutectic point is more challenging. Because of the close proximity of the solidus and liquidus lines, there is just one peak for the heat flow, and the liquidus line is instead signified by a minor bump or bulge after the main peak, as seen in Figure 10 (Boettinger et al., 2006).

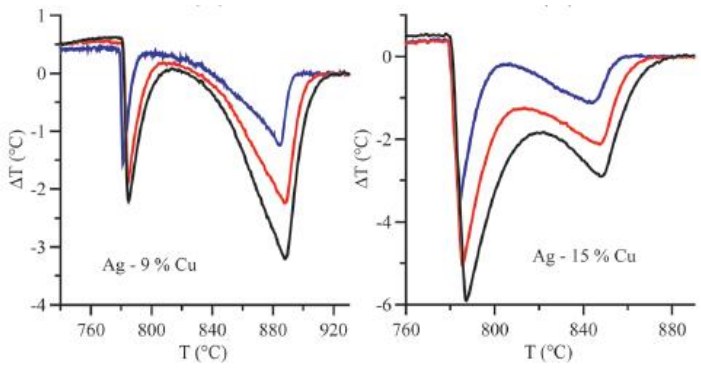

Figure 9- Two Peak Heating Curve

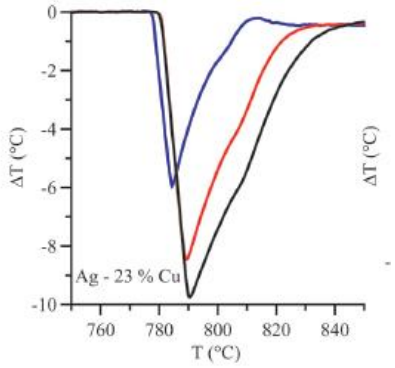

Figure 10- One Peak Heating Curve

3.3. Rheological Data

The initial rheological tests were conducted on a cone and plate rheometer that could operate up to 200 °C. The latter rheological tests were conducted on an oscillatory shear rheometer with a cup and bob geometry. The early tests suffered from oxidation and ejected material during high stresses. The oscillatory shear rheometer operated inside an inert nitrogen atmosphere to prevent oxidation and the outer walls prevented material ejection during shearing.

Stress sweeps were conducted to determine the plateau stresses and crossover points. The plateau stresses are the stress values for the storage (G') and loss moduli (G'') before the sharp decline in shear stress occurs. A visual example of the plateau and crossover stresses can be seen in Figure 11. These stresses are important for determining the force necessary to extrude the semi-solid metal from the nozzle. The crossover strain, stress, and viscosity are particularly important because the crossover point signifies the start of liquid dominant behavior where the extruded metal fails to retain its shape during extrusion.

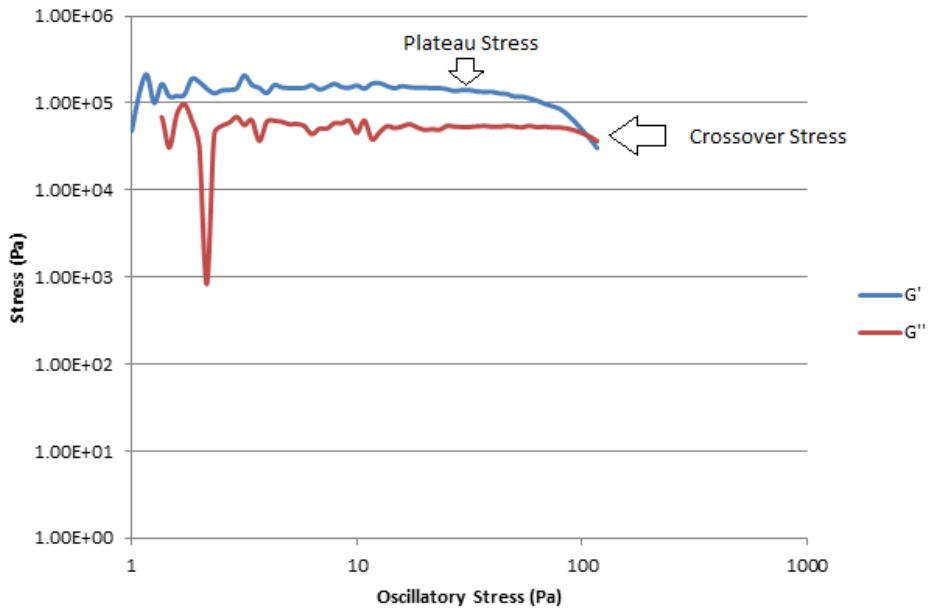

Figure 11- Plateau and Crossover Stress Example

3.3.1. Cone and Plate Rheometer

The initial rheological tests were conducted on a TA Instruments AR1500ex cone and plate, oscillatory shear rheometer. The Teflon-coated Peltier stage could heat samples up to 200 °C. All experiments on the cone and plate rheometer used a stainless steel cone geometry with a diameter of 40 mm and an angle of inclination of 2 degrees. One alloy was tested at a time. For most alloys, stress sweeps were conducted in 5 degree Celsius increments. For alloys near the eutectic point, stress sweeps were conducted in 1-2.5 degree Celsius increments due to the smaller semi-solid region. Before each stress sweep, a pre-shear conditioning step was run to break up the pre-existing surface oxides.

The cone's frequency was held constant at 1 Hz while the oscillatory stress was increased from 1 Pa until the value when the loss modulus (G'') became greater than the storage modulus (G'), or the alloy's liquid properties dominated the solid properties. Stress, strain rate, angle, displacement, and viscosity data were collected at specified oscillatory stress values. The stress was plotted against the shear rate and power law equations of the form $\tau = K\dot{\gamma}^n$ were developed using a least squares fitting equation in Equation 9 and Equation 10 (Weisstein, 1996). K is the consistency index and n is the power law index.

$$n = \frac{N\sum(\ln\dot{\gamma}\ln\tau) - \sum(\ln\dot{\gamma})\sum(\ln\tau)}{N\sum[(\ln\dot{\gamma})^2] - (\sum\ln\dot{\gamma})^2}, \qquad N = number\ of\ data\ points$$

Equation 9- Power Law Exponent

$$K = \exp\left(\frac{\sum(\ln\tau) - n\sum(ln\,\dot{\gamma})}{N}\right)$$

Equation 10- Power Law Consistency Index

3.3.2. Oscillatory Shear (Couette Flow) Rheometer

The cone and plate rheometer had three issues: a low heating temperature, edge distortion, and the ejection of material. An Anton-Paar MCR 502 oscillatory shear rheometer

with a cup and bob geometry was used for experiments after an initial series of tests was conducted on the cone and plate rheometer. The double wall set-up results in Couette flow which prevents edge distortion and the ejection of material. A convection temperature device was added to the rheometer to create accurate and gradient-free temperature control. This rheometer was able to heat samples up to 1000 °C, which allowed rheology data to be collected for the entire bismuth-tin system. The rheometer was also housed within a glove box with an inert nitrogen atmosphere to prevent the oxidation at high temperatures and shear rates.

The Anton-Paar MCR 502's geometries are disposable. A 26 mm diameter, 39.7 mm tall carbon cup serves as the outer cylinder. The bob serves as the inner cylinder. Two bobs were used: a 20 mm and a 24 mm bob. Both bobs were 23.122 mm tall and had 2 degree angles of inclination. The larger bob was the preferred geometry since the smaller wall gap was able to effectively measure the low strain regions ($\gamma < 1\%$) while the smaller bob was plagued with noise in the same region. For the 20 mm bob, 10.2 mL of material was necessary and for the 24 mm bob, 7.25 mL of material was necessary. The sample volumes are taken at the experiment's temperature, so the metal's coefficient of thermal expansion must be taken into consideration.

3.4. SIGMASOFT Thixo Software

SIGMASOFT Thixo is a computational flow modeling software designed specifically for thixotropic, non-Newtonian SSM slurries (*SIGMASOFT*, 2014). Melt viscosities are shear rate and temperature dependent, which allows for the detection and optimization of viscosity during flow. The software can analyze melt flow for fraction solids ranging from 0 to 99.4% and velocities up to 35 m/s. The program can also find the optimal process window for the extrusion process.

The *Thixo* extension is designed for die casting. A direct metal writer operates by extruding the metal slurry through a nozzle and printing structures layer-by-layer onto a substrate much like fused deposition modeling (FDM) 3D printers for thermoplastics. *SIGMASOFT* is unable to model the deposition and adhesion behavior on the substrate, as the program requires that the metal be extruded into a mold. The program can still be used to simulate flow through the nozzle by designing the die to include the nozzle and an additional geometry beginning at the nozzle's outlet. The system's inlet is coincident to the start of the nozzle and equal in diameter. Cooling, fraction solid, shear rate, shear stress, temperature, velocity, and viscosity data versus time and position can be generated as the metal flows through the nozzle. This information can be utilized to design more efficient nozzles and adjust the operational parameters of the DMW writing apparatus to produce a uniform, viscous slurry during printing. The metal's behavior after passing through the nozzle is not considered for this application.

Complex nozzle geometries could be formed within *SIGMASOFT* or imported from computer-aided design (CAD) programs as .step files. If CAD nozzles are imported, the nozzle's interior cavity must be made into a solid since *SIGMASOFT* treats the nozzle as a die. Figure 12 compares a standard CAD nozzle (left) with a nozzle that has had its interior cavity converted to a solid (right).

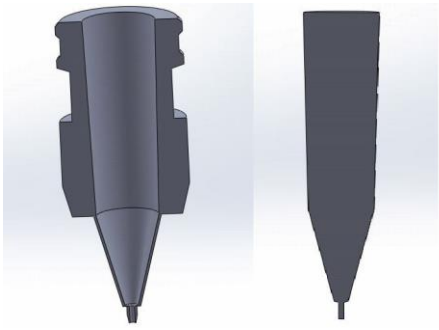

Figure 12- Typical CAD Nozzle (Left), SIGMASOFT Nozzle (Right)

SIGMASOFT converts the solid geometries into a 3D finite element mesh, as seen in Figure 13. The minimum element size in each direction can be specified by dividing the minimum wall thickness by the desired accuracy, or the minimum number of subdivisions per layer, as seen in Equation 11. An accuracy level of 3 produces a useful filling pattern, but the shear and pressure calculations are less than optimal. The program's maximum accuracy level is 5, and this produces highly accurate filling, shear, and pressure results. This maximum accuracy level was used for all simulations except those with a minimum wall thickness below 100 microns, as the available servers did not have enough computational power to handle the meshes.

$$Minimum\ Element\ Size = {Minimum\ Wall\ Thickness}/{Accuracy}$$

Equation 11- Mesh Minimum Element Size

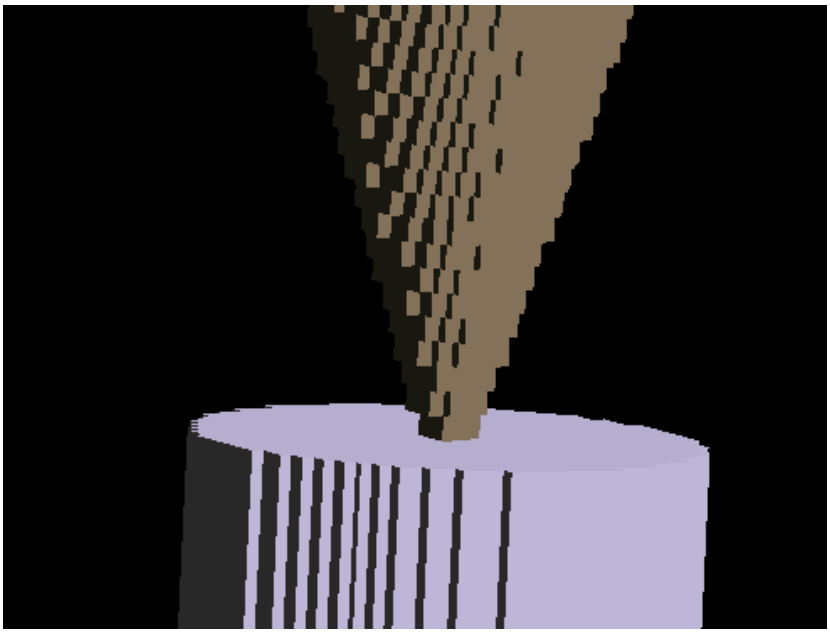

Figure 13- Finite Element Mesh

A combination of commercial and custom nozzles were modeled and tested. Dimensions and drawings for the commercial nozzles were obtained from manufacturers. Custom nozzles were designed to study how geometric parameters impacted the flow and temperature data. The

inlet and outlet diameters, nozzle height, and angle of inclination were adjusted by 25% between runs while holding all other geometric parameters constant.

The process parameters were also adjusted. Filling could be defined by the fill time, a pressure curve, or a flow curve. The physical DMW apparatus operates between 15-100 psi (1.03-6.89 bars), so this operational range was targeted during simulations. The nozzle's heating profile versus position could be studied. The impact of heaters could be studied by varying the heat transfer coefficients between the nozzle geometry and the ambient air. Most simulations were 1-3 seconds in length and collected data points in 0.1% fill increments.

Filling data is calculated using the finite difference approach. The Ostwald-de-Waele rheological model is used to calculate the shear rate, shear stress, and viscosity at each control volume in the mesh. Material specific fraction solid, thermal conductivity, specific heat, latent heat, Young's moduli, Poisson ratio, and coefficient of thermal expansion data are also used in conjunction with the rheology data to generate filling and flow data.

The *SIGMASOFT* thixotropic metals database contained four metals: AM50, AM60, AZ91, and thixoalloy-540. Their composition and thermal data can be seen in Table 2. Early simulations were conducted on the thixoalloy-540 system because of aluminum's diverse and widespread applications. Additional alloys can be added into the database by providing the material composition, solidus temperature, liquidus temperature, initial process temperature, Young's modulus, and Poisson ratio along with the density, thermal conductivity, specific heat, latent heat, fraction solid, coefficient of thermal expansion, and rheology versus temperature. Rheological data was collected for the low-temperature bismuth-tin system with the oscillatory shear rheometer to add bismuth-tin to the *SIGMASOFT* database in order to model the physical direct metal writer's flow behavior.

***SIGMASOFT Thixo* Materials Database**			
	Composition	**Solidus Temperature**	**Liquidus Temperature**
AM50	93.78 - 95.12% Mg 4.4 - 5.4% Al 0.26 - 0.6% Mn 0.22% Zn	435 °C	620 °C
AM60	93.1 - 94.14% Mg 5.6 - 6.4% Al 0.26 - 0.5% Mn	433 °C	619 °C
AZ91	90.8% Mg 8.25% Al 0.63% Zn 0.22% Mn 0.04% Si 0.01% Fe	425 °C	601 °C
Thixoalloy-540	91.54% Al 5.7% Mg 2.5% Si 0.15% Mn 0.11% Fe	588 °C	620 °C

Table 2- SIGMASOFT Thixo Materials Database

4. Results and Discussion

4.1. Alloy Creation

Both powder and ingot preparation methods were used during the project. The ingot preparation method was faster and more convenient. The high-surface area of the powders encourages oxidation. Therefore, the powders must be processed in a reducing atmosphere such as hydrogen. The powders also needed to be heated to 600-700 °C to fully melt while all of the compositions created with the ingot method could be formed at temperatures below 300 °C.

The structure of the metals varied between compositions. Tin is extremely ductile while bismuth is brittle. Therefore, tin rich oxides were more ductile and difficult to fracture while bismuth rich oxides exhibited the opposite properties. Tin rich alloys (Figure 14) had a smooth interior structure while bismuth rich alloys (Figure 16) had an interior composed of fine chunks akin to sand. The alloys near the eutectic point (Figure 15) blended these two structures together, as the interior was fairly smooth with coarse lines scattered throughout.

Figure 14- Tin Rich Alloy

Figure 15- Eutectic Alloy

Figure 16- Bismuth Rich Alloy

4.2. Alloy Verification

Glow discharge mass spectroscopy (GDMS) and inductively coupled plasma mass spectroscopy (ICP-MS) determined that the bismuth-tin alloys created in the laboratory with the powder method had purity levels on par with purchased alloys. These tests must be repeated for samples prepared from ingots. Differential scanning calorimetry was used to determine the operating range for the rheometer during testing for alloys prepared using both methods.

4.2.1. Glow Discharge Mass Spectroscopy (GDMS)

Two samples were tested with GDMS: a 50-50 bismuth-tin alloy created from powders and a 50-50 bismuth-tin alloy purchased commercially. The created alloy had over 100 ppmw for three impurities (copper, arsenic, lead) while the purchased alloy's impurities were all below the 100 ppmw. While the purchased alloy was cleaner, both samples had similar impurities and neither sample contained quantities that would significantly alter the expected composition. These tests must be conducted on additional compositions, including some prepared from ingots.

4.2.2. Inductively Coupled Plasma Mass Spectroscopy (ICP-MS)

Five samples were analyzed with ICP-MS. Three 50% Sn 50% Bi samples were analyzed. Two of these 50-50 samples were created with the powder method. The third 50-50 sample was purchased commercially and produced using vacuum induction melting. The other two samples analyzed were a 70% Sn 30% Bi sample and an 80% Sn 20% Bi sample, both of which were created in the laboratory using the powder method.

The two laboratory 50-50 alloys had a composition closer to the expected composition than the purchased alloy. Since the tube furnace samples were closer to the target composition, this validated the powder processing method and verified that the alloy's purity was within acceptable limits. Table 3 details the ICP-MS results for the five different samples.

Inductively Coupled Plasma Mass Spectroscopy Results					
Sample Creator	**Expected Composition**	**Actual Composition**	**Tin Gain (Atomic %)**	**Expected Liquidus Line (°C)**	**Actual Liquidus Line (°C)**
Lab	50% Sn 50% Bi	51.95% Sn 48.05% Bi	1.95	166.6	162.5
Lab	50% Sn 50% Bi	52.78% Sn 47.22% Bi	2.78	166.6	160.8
Sophisticated Alloys	50% Sn 50% Bi	52.94% Sn 47.06% Bi	2.94	166.6	160.5
Lab	70% Sn 30% Bi	71.83% Sn 28.17% Bi	1.83	158.8	163.3
Lab	80% Sn 20% Bi	81.57% Sn 18.43% Bi	1.57	183.2	187.0

Table 3- Inductively Coupled Plasma Mass Spectroscopy Results

On average, the four laboratory samples had 2% more tin by atomic percent than expected. Any of the created alloys that did not receive ICP-MS testing was assumed to have 2% more tin than expected. Two observations during the alloy creation process support the notion that some bismuth was lost. First, the bismuth powder was more difficult to transfer. The black bismuth powders would cling to the sides of the storage container. Second, the bismuth powder was more resistant to melting. While inside the tube furnace, the gray tin powders would melt at lower temperatures in less time than the bismuth powders. After solidifying the ingot, there was often a very thin dusting of black powder, which was likely bismuth powder that did not melt.

Samples created with the ingot preparation method must also be verified with ICP-MS. Because of the DSC results that will be discussed in the following section, samples created with the ingot preparation method were also assumed to have 2% more tin by atomic percent.

4.2.3. Differential Scanning Calorimetry (DSC)

Figure 17 juxtaposes the actual and experimental phase diagrams for bismuth-tin alloys. The actual phase diagram can be seen in Figure 7 and was obtained from the Smithells Metals Reference Book (Smithells et al., 2004). For compositions without ICP-MS data, the theoretical

composition was found by adding 2% tin by atomic percent to the composition since that was the average tin gain from ICP-MS tests, and this percentage was used for the temperature error. All but one of the solidus temperatures were within 2% of the expected values, and all but three of liquidus temperatures were as well. A full list of DSC results can be found in Appendix C.

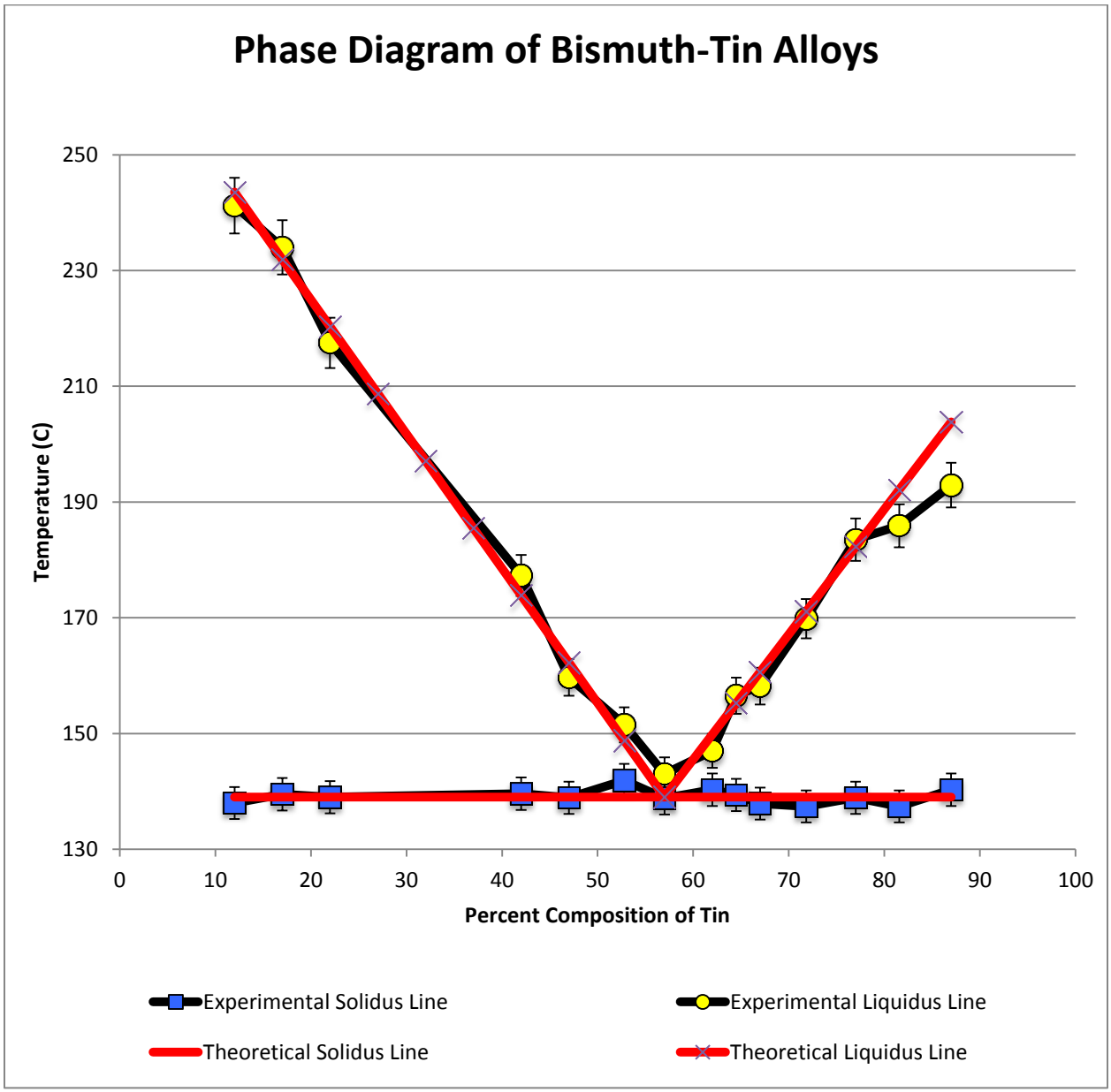

Figure 17- Phase Diagram of Bismuth-Tin Alloys with DSC Results (Error Bars- 2%)

Figure 18 shows the error for the solidus and liquidus lines for the fourteen bismuth-tin alloys. Thirteen of the solidus temperature errors and eleven of the liquidus temperature errors

were within 2% of the DSC's tolerance and the theoretical temperatures. The liquidus temperature errors were larger than the solidus temperature errors. This is because the transition from a solid to a semi-solid occurs over a longer time span and produces a larger heat flow on an order of magnitude than the transition from a semi-solid to a liquid. The largest errors for both the solidus and liquidus lines occurred for the tin rich alloys. While the solidus line temperatures were within tolerance, the liquidus line temperatures were up to 5.37% less than the theoretical temperatures. The next largest errors were concentrated towards the eutectic point (57% Sn 43% Bi). Since the semi-solid region near the eutectic point is small and the properties of SSMs are highly dependent on fraction solid, a small deviation in fraction solid has a large impact. The DSC results comparing the theoretical and experimental solidus and liquidus lines can be seen in Table 4 and Table 5 respectively.

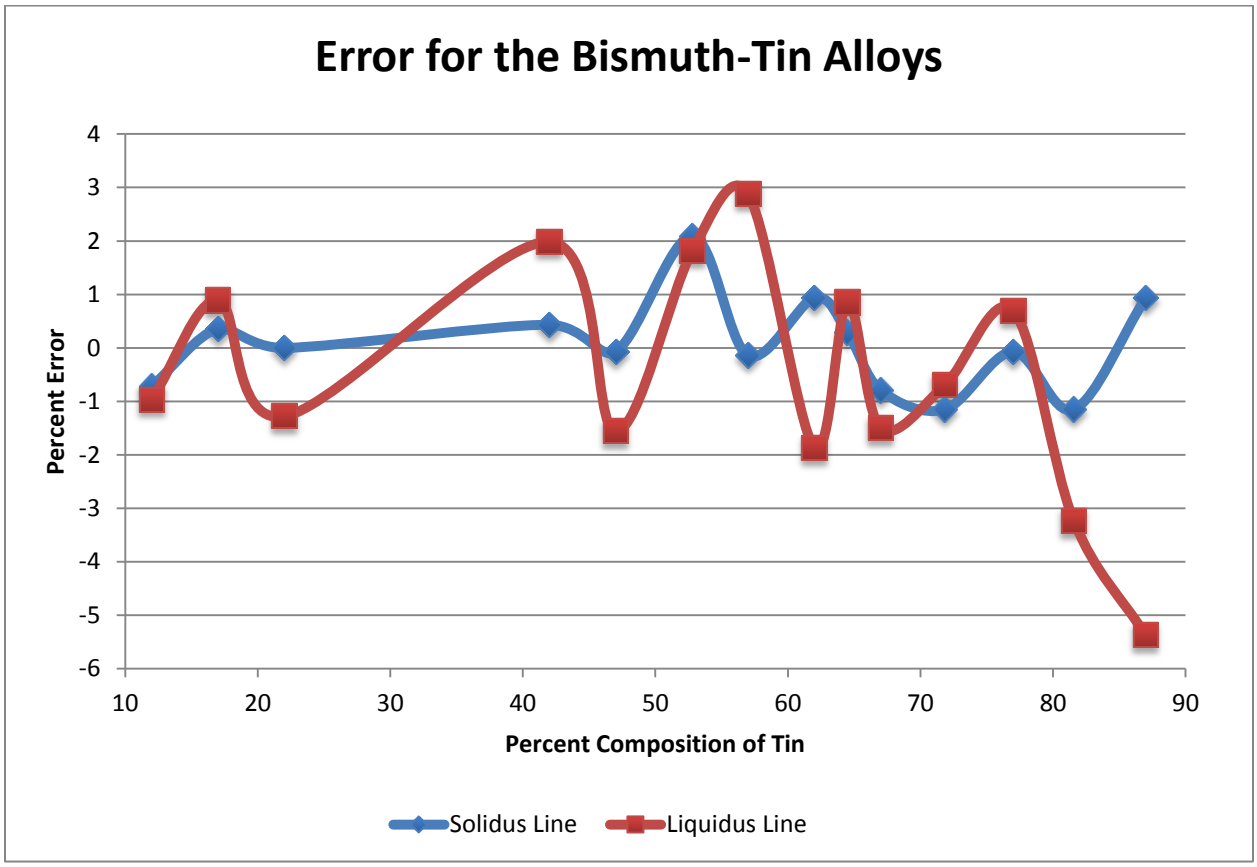

Figure 18- Error for the Bismuth-Tin Alloys

Differential Scanning Calorimetry Solidus Line				
Desired Composition	**Theoretical Composition[1,2]**	**Theoretical Solidus Line (°C)**	**Experimental Solidus Line (°C)**	**Percent Error (%)**
10% Tin 90% Bismuth	12% Tin 88% Bismuth	139	138.0	- 0.72
15% Tin 85% Bismuth	17% Tin 83% Bismuth	139	139.5	+ 0.36
20% Tin 80% Bismuth	22% Tin 78% Bismuth	139	139.0	0
40% Tin 60% Bismuth	42% Tin 58% Bismuth	139	139.6	+ 0.43
45% Tin 55% Bismuth	47% Tin 53% Bismuth	139	138.9	- 0.07
50% Tin 50% Bismuth	52.78% Tin 47.22% Bismuth	139	141.9	+ 2.09
55% Tin 45% Bismuth	57% Tin 43% Bismuth	139	138.8	- 0.14
60% Tin 40% Bismuth	62% Tin 38% Bismuth	139	140.3	+ 0.94
62.5% Tin 37.5% Bismuth	64.5% Tin 35.5% Bismuth	139	139.4	+ 0.29
65% Tin 35% Bismuth	67% Tin 33% Bismuth	139	137.9	- 0.79
70% Tin 30% Bismuth	71.83% Tin 29.17% Bismuth	139	137.4	- 1.15
75% Tin 25% Bismuth	77% Tin 23% Bismuth	139	138.9	- 0.07
80% Tin 20% Bismuth	81.57% Tin 18.43% Bismuth	139	137.4	- 1.15
85% Tin 15% Bismuth	87% Tin 13% Bismuth	139	140.3	+ 0.94

Table 4- Differential Scanning Calorimetry Solidus Line

[1] If the cell is shaded green, the theoretical composition is exact and was verified with ICP-MS. 2% tin (the average tin increase from ICP-MS results) was added to compositions that were not verified by ICP-MS.
[2] If the row is gray, the sample was prepared with the ingot method. If the row is unshaded, the sample was prepared with the powder method.

Differential Scanning Calorimetry Liquidus Line				
Desired Composition	**Theoretical Composition[3,4]**	**Theoretical Liquidus Line (°C)**	**Experimental Liquidus Line (°C)**	**Percent Error (%)**
10% Tin 90% Bismuth	12% Tin 88% Bismuth	243.6	241.2	- 0.97
15% Tin 85% Bismuth	17% Tin 83% Bismuth	231.9	234.0	+ 0.89
20% Tin 80% Bismuth	22% Tin 78% Bismuth	220.3	217.5	- 1.28
40% Tin 60% Bismuth	42% Tin 58% Bismuth	173.9	177.3	+ 1.98
45% Tin 55% Bismuth	47% Tin 53% Bismuth	162.2	159.7	- 1.56
50% Tin 50% Bismuth	52.78% Tin 47.22% Bismuth	148.8	151.5	+ 1.81
55% Tin 45% Bismuth	57% Tin 43% Bismuth	139.0	143.0	+ 2.88
60% Tin 40% Bismuth	62% Tin 38% Bismuth	149.8	147.0	- 1.87
62.5% Tin 37.5% Bismuth	64.5% Tin 35.5% Bismuth	155.2	156.5	+ 0.85
65% Tin 35% Bismuth	67% Tin 33% Bismuth	160.6	158.2	- 1.50
70% Tin 30% Bismuth	71.83% Tin 29.17% Bismuth	171.1	169.9	- 0.70
75% Tin 25% Bismuth	77% Tin 23% Bismuth	182.2	183.5	+ 0.69
80% Tin 20% Bismuth	81.57% Tin 18.43% Bismuth	192.1	185.9	- 3.23
85% Tin 15% Bismuth	87% Tin 13% Bismuth	203.9	192.9	- 5.37

Table 5- Differential Scanning Calorimetry Liquidus Line

[3] If the cell is shaded green, the theoretical composition is exact and was verified with ICP-MS. 2% tin (the average tin increase from ICP-MS results) was added to compositions that were not verified by ICP-MS.
[4] If the row is gray, the sample was prepared with the ingot method. If the row is unshaded, the sample was prepared with the powder method.

4.3. Rheological Testing

Rheological tests were conducted on bismuth-tin alloys. Determining the viscosity of the alloys while varying the fraction solid, temperature, shear stress, and strain rate were important before attempting to extrude metal through the printing apparatus. Early tests were conducted on a cone and plate rheometer in air. Later tests were conducted on an oscillatory shear rheometer in an inert nitrogen environment. Oxidation in earlier experiments impeded experimental repeatability, changed the metal's composition, and generated storage and loss moduli orders of magnitude greater than those obtained in the nitrogen environment.

4.3.1. Cone and Plate Rheometer

Once the light gray samples were melted on the stage, darker gray compounds formed on the surface of the molten metal. These dark gray compounds were likely oxides, as molten metal readily reacts with oxygen. The pre-shear step was intended to break up the pre-existing oxides. While this step may have broken up surface oxides, it agitated and rearranged the sample, which could have exposed more molten metal to be oxidized. Oxidized metal is more viscous than pure metal, and the non-controlled oxidation impeded the experimental repeatability of the sweeps.

A complete list of cone and plate rheological data can be seen in Appendix D. Different compositions had general viscosity and plateau stress trends, but the exact numerical values were unreliable due to the aforementioned oxidation. As the solid fraction increased within a composition, the storage and loss moduli also increased, as long as material had not been ejected during a previous stress sweep. Within composition, the storage and loss moduli increased by an order of magnitude from the processing temperatures near the liquidus line to those near the solidus line due to increasing fraction solid. The difference in storage and loss moduli values within composition were more pronounced for the oscillatory shear rheometer since the nitrogen

environment prevented the formation of oxides. Meanwhile, the cone and plate tests saw the pure metal's viscosity properties get dominated by the viscosity properties of the oxides.

Figure 19 shows the storage modulus plateau stresses and Figure 20 shows the loss modulus plateau stresses. As the fraction solid increased, the plateau stresses for both the storage and loss moduli tended to increase as well. As the temperature increased, the plateau stresses for both the storage and loss moduli decreased, as semi-solid metals at higher temperatures have lower solid fractions. The storage modulus plateau was also higher than the loss modulus plateau for all compositions. The stress of the storage modulus was at least twice that of the loss modulus, and this differential increased with fraction solid.

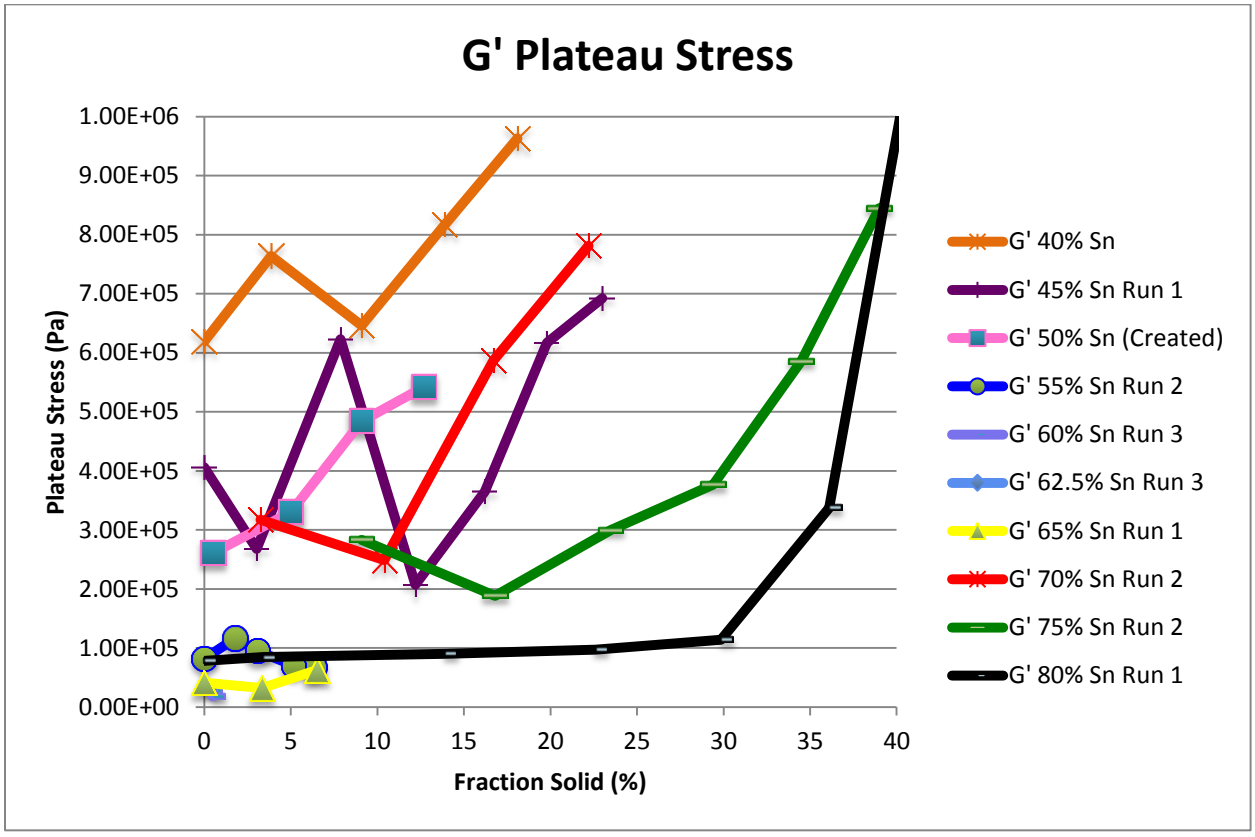

Figure 19- Cone and Plate Storage Modulus Plateau Stresses

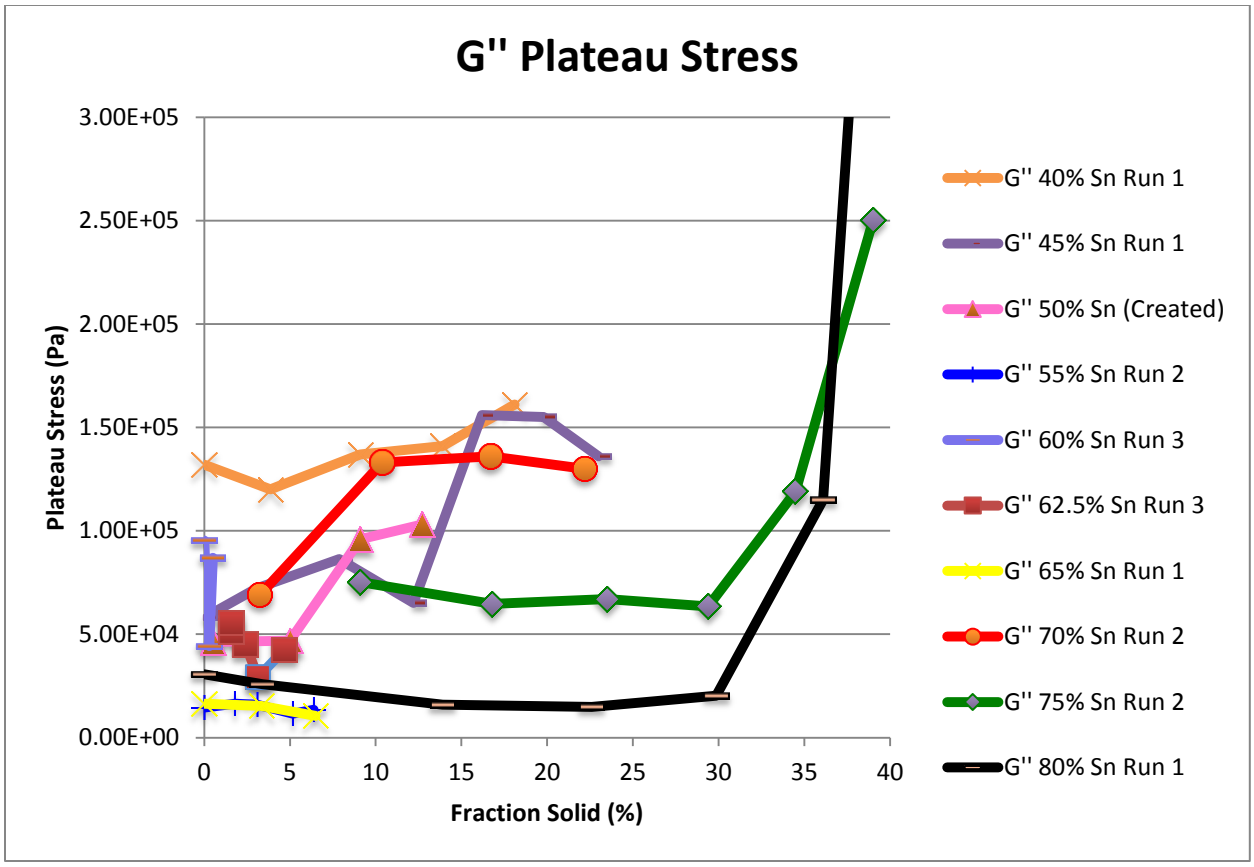

Figure 20- Cone and Plate Loss Modulus Plateau Stresses

Figure 21 shows the crossover stress data for bismuth-tin alloys ranging from 40% tin to 80% tin versus fraction solid. The oxidation prevented a clear crossover stress trend from forming. At the low solid fraction regions, the crossover stress tended to decrease across most bismuth-tin compositions. No distinguishable pattern for the maximum crossover stress versus both fraction solid, temperature, or experimental order could be found. This can be attributed to the uncontrolled oxidation during the experiments. There was no way to measure the exact composition of the sample while it was being sheared under the rheometer since the sample would continue to oxidize between the end of the stress sweeps and solidification.

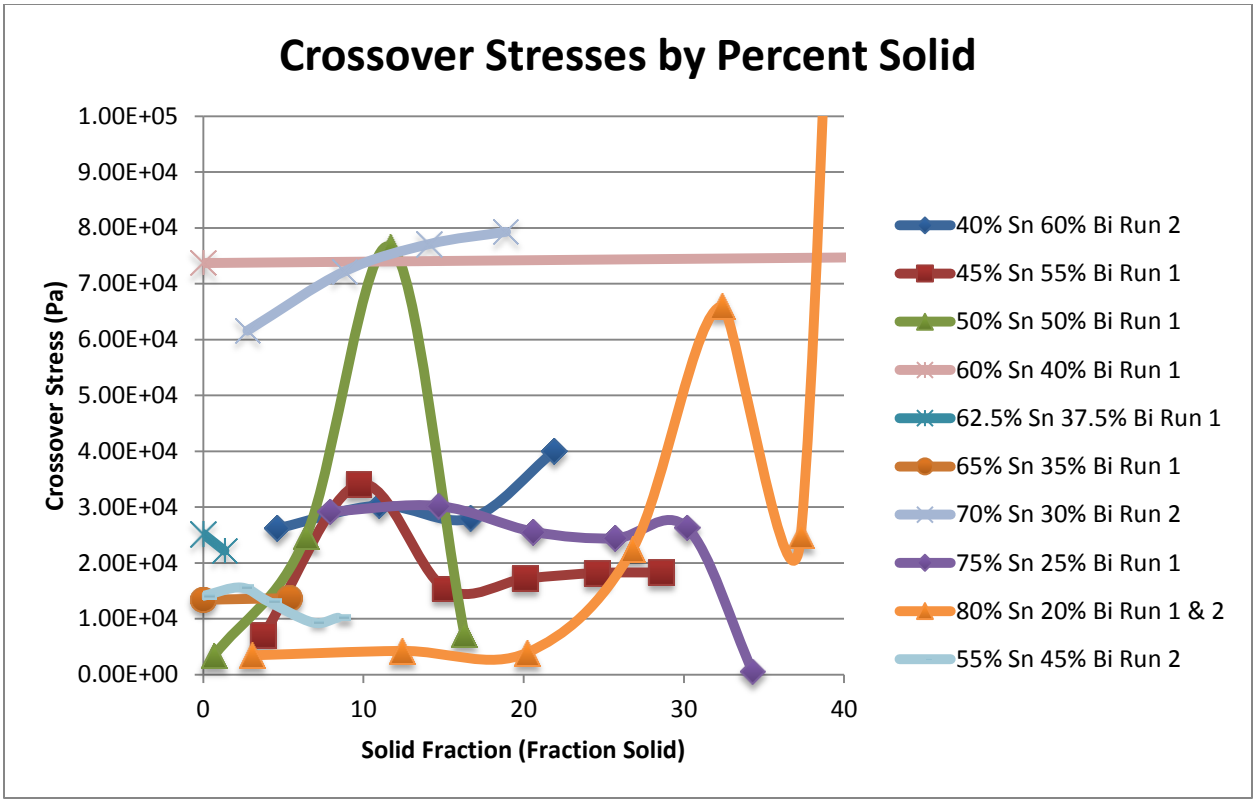

Figure 21- Cone and Plate Crossover Stresses

There were also concerns that the bismuth-tin samples were improperly heated. Before each sweep, there was a five minute hold time to allow the stage, cone, and sample to ideally reach the same temperature. The temperature distribution on the stage and cone were measured using a thermocouple for two different temperatures: 50°C (Figure 22) and 200°C (Figure 23). Unfortunately, a perfect temperature distribution was never reached. The cone and stage both had temperature values less than the input temperature due to the ambient air, and this difference was greater at higher temperatures. The error increased radially outwards from the stage. The cone was also at lower temperatures than the stage since it was not directly in contact with the heating element. These temperature inaccuracies could have caused the metal to transition to a solid for the lower temperature sweeps, which would result in higher viscosities since solids do not demonstrate shear thinning behavior. The oscillatory shear rheometer's convection furnace engulfed the samples on all sides to more uniformly heat the sample.

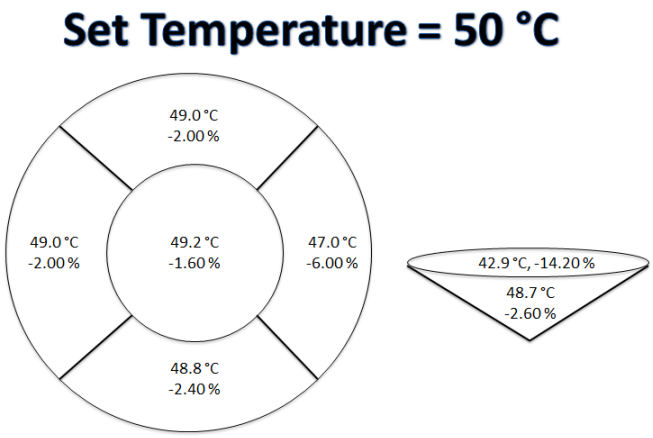

Figure 22- 50°C Cone and Plate Temperature Distribution

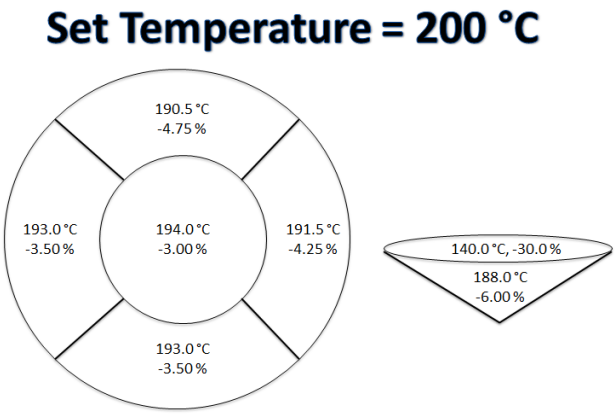

Figure 23- 200°C Cone and Plate Temperature Distribution

Material ejection was also an issue. As the oscillatory shear stress and strain rate increased, the metal's viscosity sharply decreased. This shear thinning behavior would cause the cone to have less resistance during the stress sweep, and the cone's increased rotation speed would eject some material. After the material was ejected, the data's accuracy became invalid as the cone's surface area was no longer completely covered entirely by the alloy. The material ejection would often occur near the crossover stresses. The oscillatory shear rheometer's double cylinder design prevented this issue from reoccurring.

4.3.2. Oscillatory Shear (Couette Flow) Rheometer

Preliminary tests determined the bismuth-tin system has low viscosities. Because the oscillatory shear rheology tests were conducted inside an inert atmosphere, oxides did not form. Without the viscous oxides, the resulting viscosities, storage moduli, loss moduli, and shear stresses were at least an order of magnitude lower than those from the cone and plate rheometer.

Because of the bismuth-tin's low viscosities, the 24 mm bob was selected over the 20 mm bob. The carbon cups were 26 mm in diameter. The smaller bob increased the cross-sectional annulus gap area by a factor of approximately 2.76. The smaller area produced superior data for low viscosity systems. The smaller gap also needed 40.7% less bismuth-tin per test. The rheometer was not able to consistently collect data for fraction solids in excess of 25-30%. As the solid particles increased, the necessary torque to produce the 10 rad/s angular velocity exceeded the rheometer's limit. This problem manifested itself in bismuth and tin rich systems with large semi-solid regions and high fraction solids. Compositions near the eutectic point had fraction solids below the rheometer's limit, which prevented solids from jamming the bob.

Complex viscosity (Pa*s) was plotted against strain. A complete list of results for each composition can be seen in Appendix E. For the oscillatory tests, the strain was increased from 0.01% to 200% for each temperature, and the sample demonstrated shear-thinning behavior. The crossover stress, crossover moduli, crossover viscosities, final viscosities, and plateau stresses were specifically studied across the bismuth-tin compounds with respect to fraction solid.

The crossover stress and final complex viscosity's behavior versus fraction solid was nearly identical, as seen in Figure 24 and Figure 25. As the fraction solid increased, the crossover stress and final complex viscosity also increased. After the crossover stress was achieved, the liquid properties dominated and the complex viscosity decreased. Alloys requiring

greater stresses to flow, primarily the bismuth rich alloys, had larger final complex viscosities. True viscosity is directly proportional to shear stress, and since complex viscosity is related to true viscosity, the complex viscosity and crossover stress should also be proportional. The crossover stresses were an order of magnitude greater than the final complex viscosities, which were taken at the maximum strain value (200%), as the samples approached steady state.

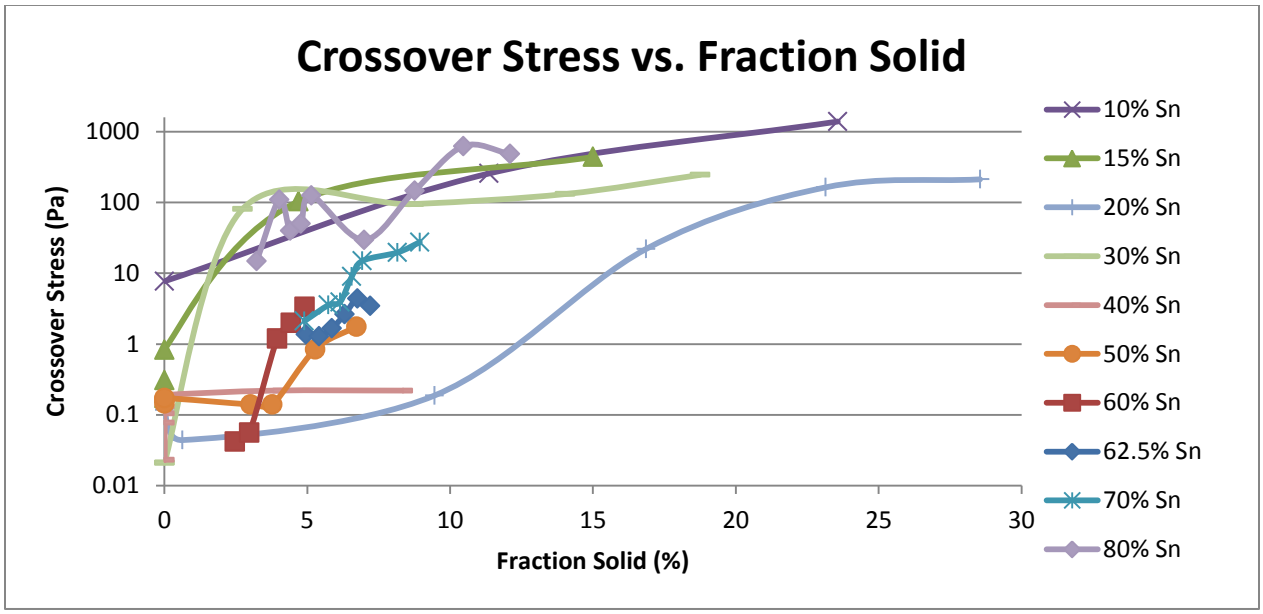

Figure 24- Crossover Stress vs. Fraction Solid, Oscillatory Shear Rheometer

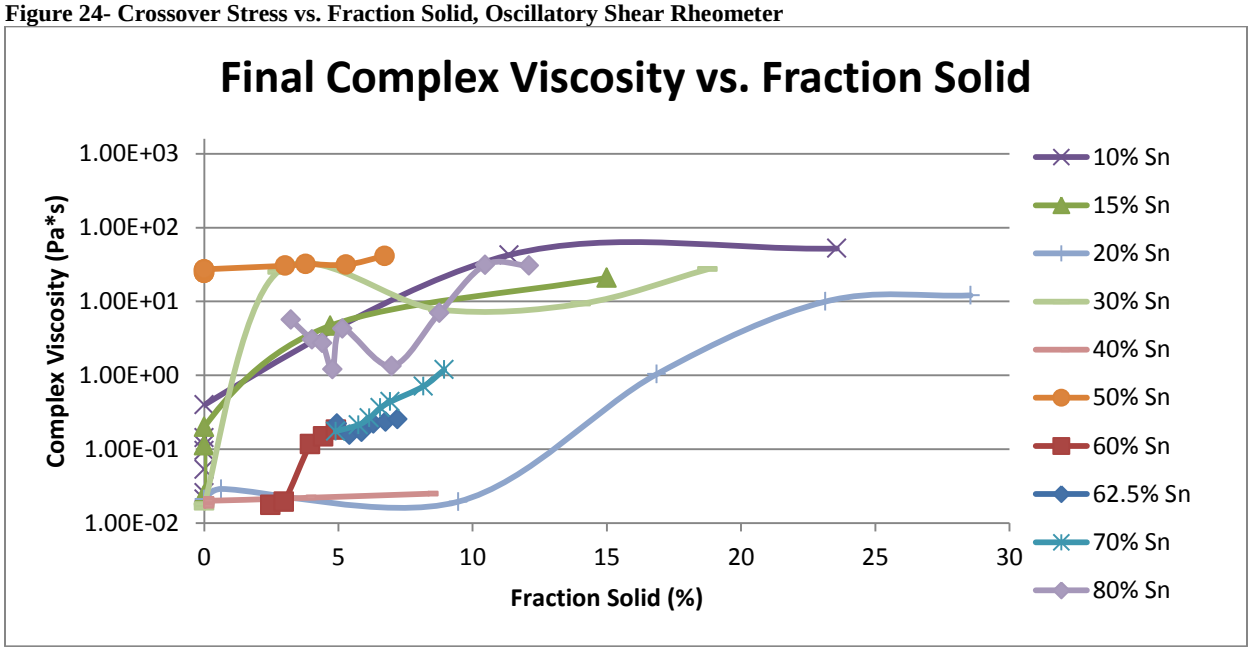

Figure 25- Final Complex Viscosity vs. Fraction Solid, Oscillatory Shear Rheometer

The crossover complex viscosity and crossover modulus versus fraction solid exhibited similar behavior across the tested compositions of bismuth-tin, as seen in Figure 26 and Figure 27. Bismuth rich alloys tended to demonstrate a gradual increase in these two parameters versus fraction solid while the tin rich compositions tended to demonstrate a sharp increase in these two parameters. Alloys near the eutectic point exhibited similar behavior to the tin rich behavior. Tin rich alloys tended to be more viscous and have higher modulus values at the crossover point than bismuth rich alloys. While the crossover complex viscosity and crossover modulus versus fraction solid demonstrated similar behavior, the crossover complex viscosity was approximately an order of magnitude smaller.

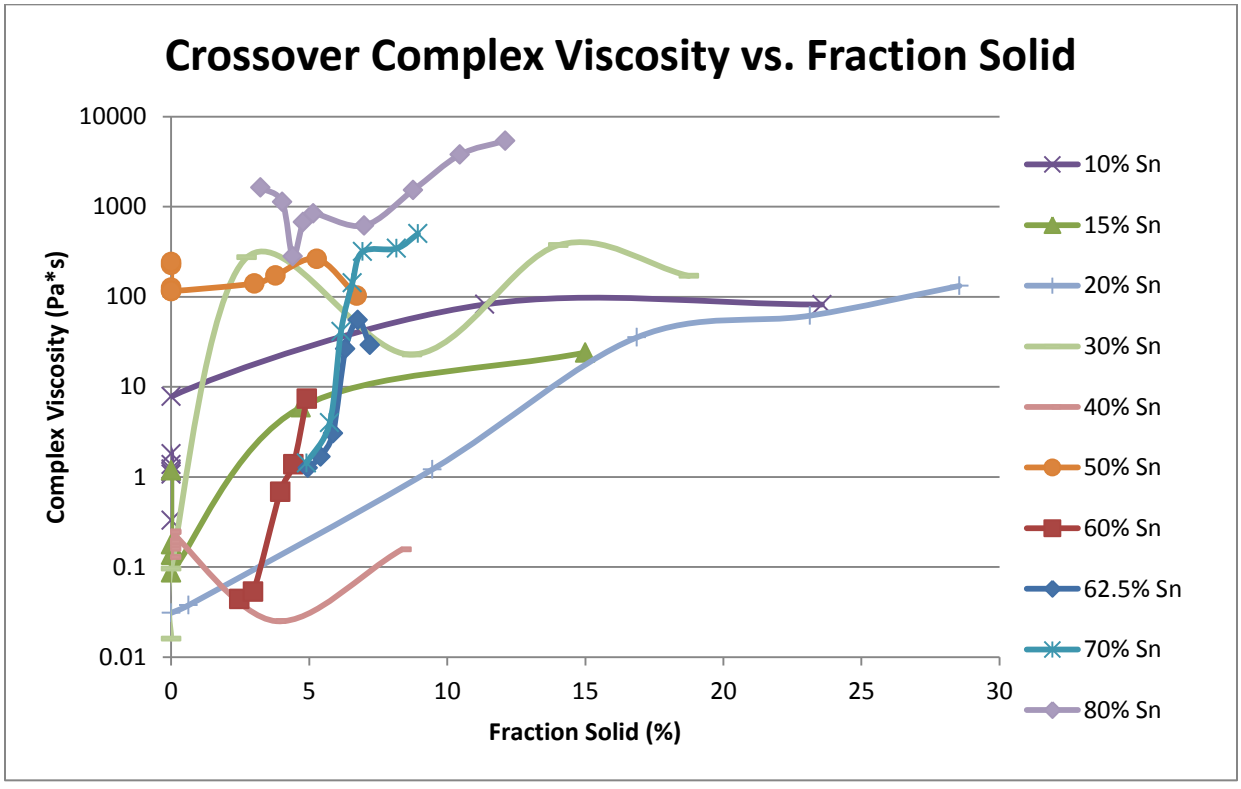

Figure 26- Crossover Complex Viscosity vs. Fraction Solid, Oscillatory Shear Rheometer

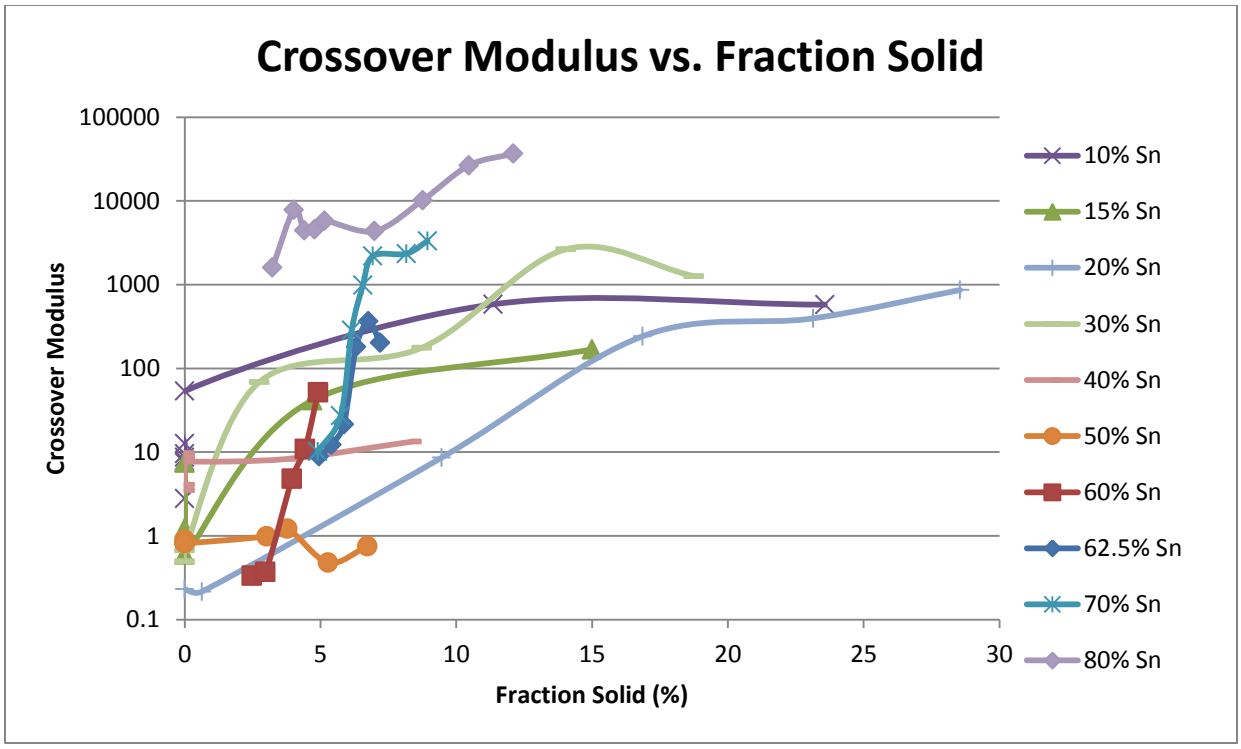

Figure 27- Crossover Modulus vs. Fraction Solid, Oscillatory Shear Rheometer

Before the crossover point, the storage modulus was greater than the loss modulus, or the solid properties were dominant over the liquid properties, which can be seen in Figure 28 and Figure 29. As a result, the storage modulus was about an order of magnitude greater than that of the loss modulus. Both the storage and loss moduli before the crossover point were shaped identically versus fraction solid. Following the crossover point, the storage modulus sharply dropped. The storage modulus drops by 5-7 orders of magnitude for the tin rich and near eutectic alloys while the drop is only about an order of magnitude for the bismuth rich alloys, as seen in Figure 30. The difference between the loss moduli before and after the crossover point is less pronounced, as seen in Figure 31. This difference is a maximum of about 1 order of magnitude, as the driving force in the transfer from solid to liquid dominant behavior is the sharp fall of the storage modulus.

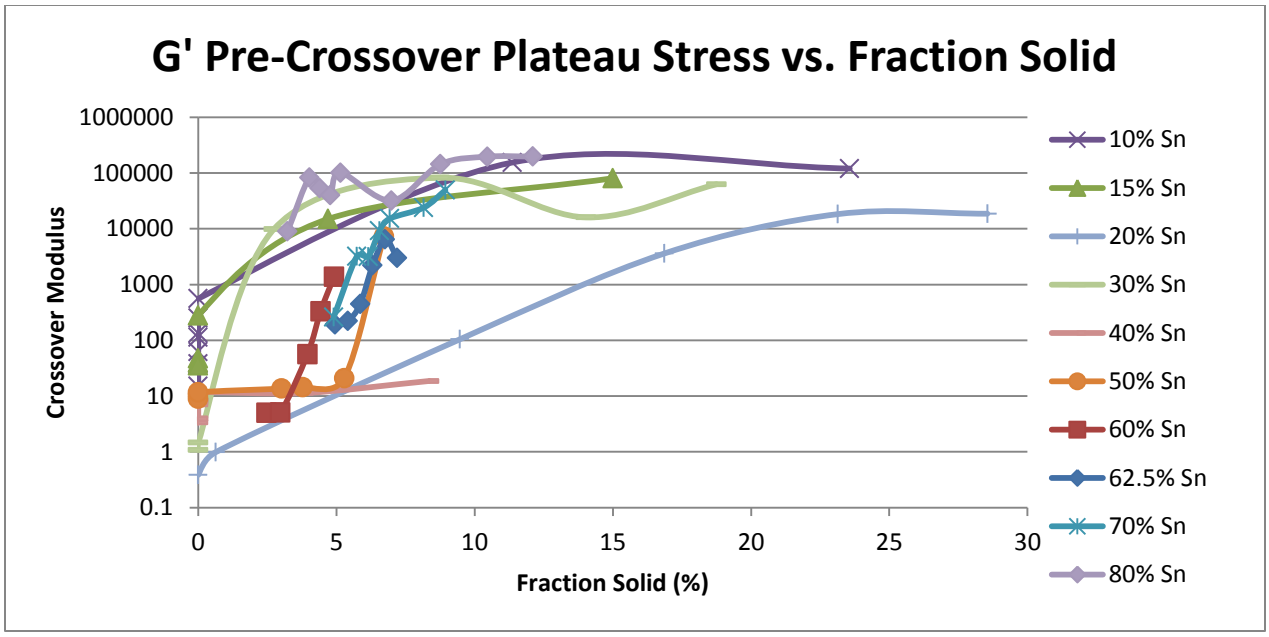

Figure 28- G' Pre-Crossover Plateau Stress vs. Fraction Solid, Oscillatory Shear Rheometer

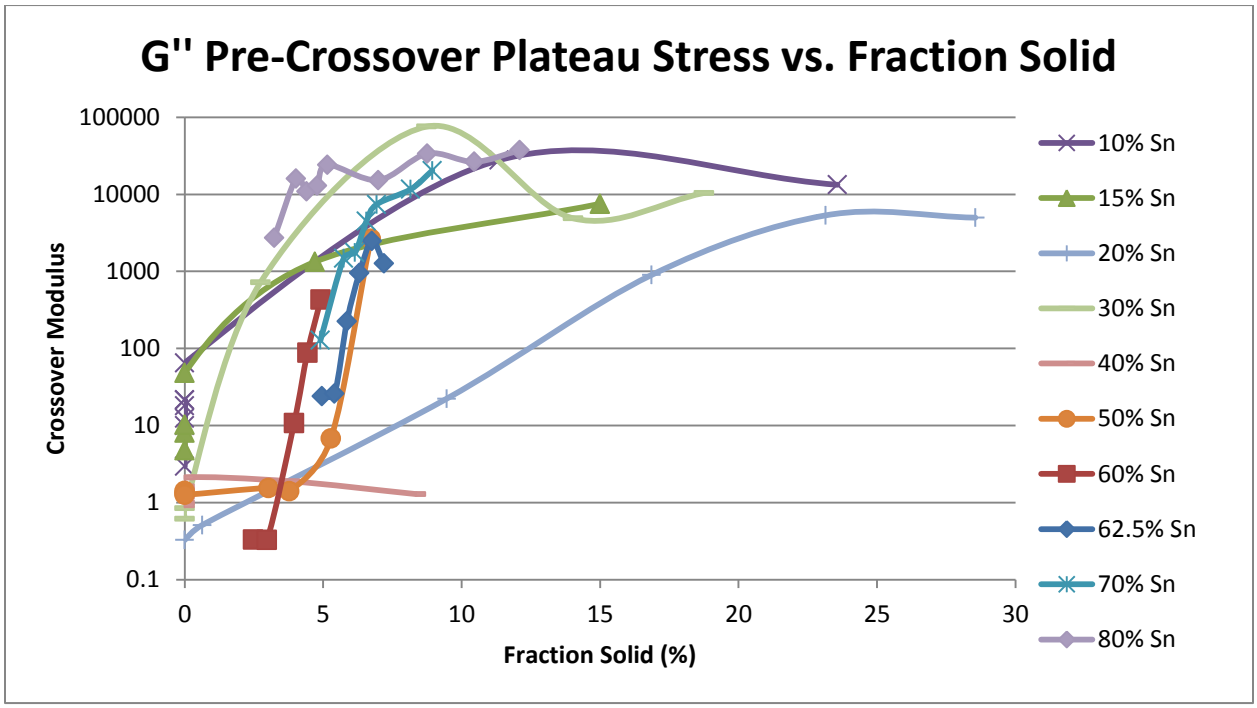

Figure 29- G'' Pre-Crossover Plateau Stress vs. Fraction Solid, Oscillatory Shear Rheometer

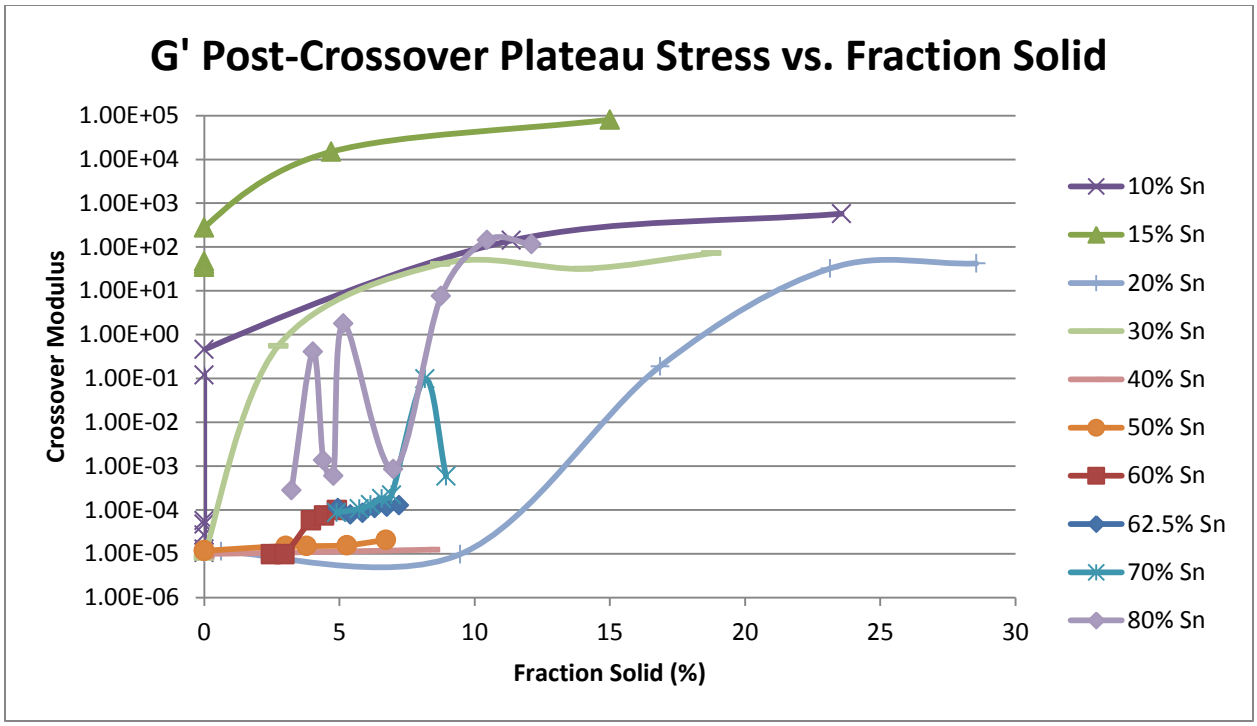

Figure 30- G' Post-Crossover Plateau Stress vs. Fraction Solid

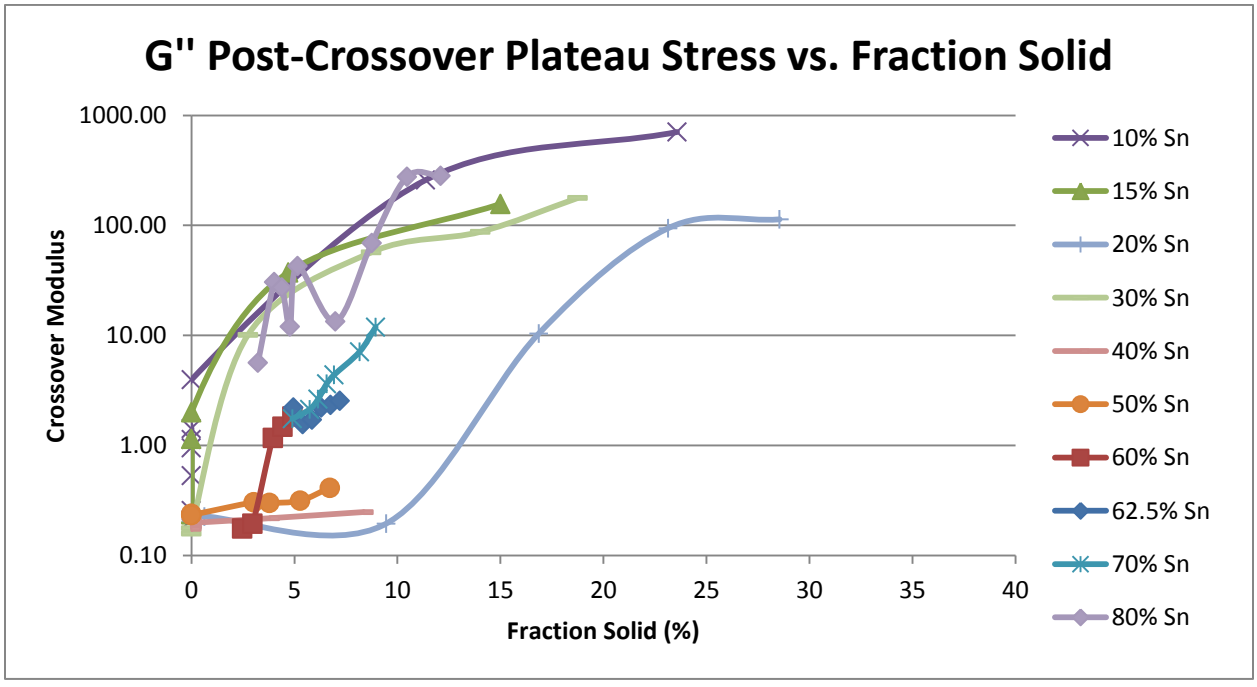

Figure 31- G'' Post-Crossover Plateau Stress vs. Fraction Solid, Oscillatory Shear Rheometer

The crossover strain versus the fraction solid exhibited the most unique trend. As seen in Figure 32, the crossover strain was highly dependent upon the bismuth concentration. The

bismuth rich alloys had crossover strain values increase with fraction solid while the tin rich and near eutectic alloys had the crossover strain decrease with increasing fraction solid for some compositions (60% Sn, 62.5% Sn, and 70% Sn). However, 80% tin saw the crossover strain increase with fraction solid, so these tests should be repeated. The bismuth rich alloys also tended to have a crossover strain 2-3 orders of magnitude greater than the near eutectic or tin rich alloys, which conflicted with the test's hypothesis. Tin is far more ductile than bismuth. Bismuth has a base centered monoclinic crystal structure while tin has a centered tetragonal crystal structure (Askeland et al., 2011). Since tin's crystal structure contains more slip planes than that of bismuth, tin is more ductile than bismuth, and it was expected that the crossover strain would increase with the tin concentration. However, the inverse was true and must be investigated further.

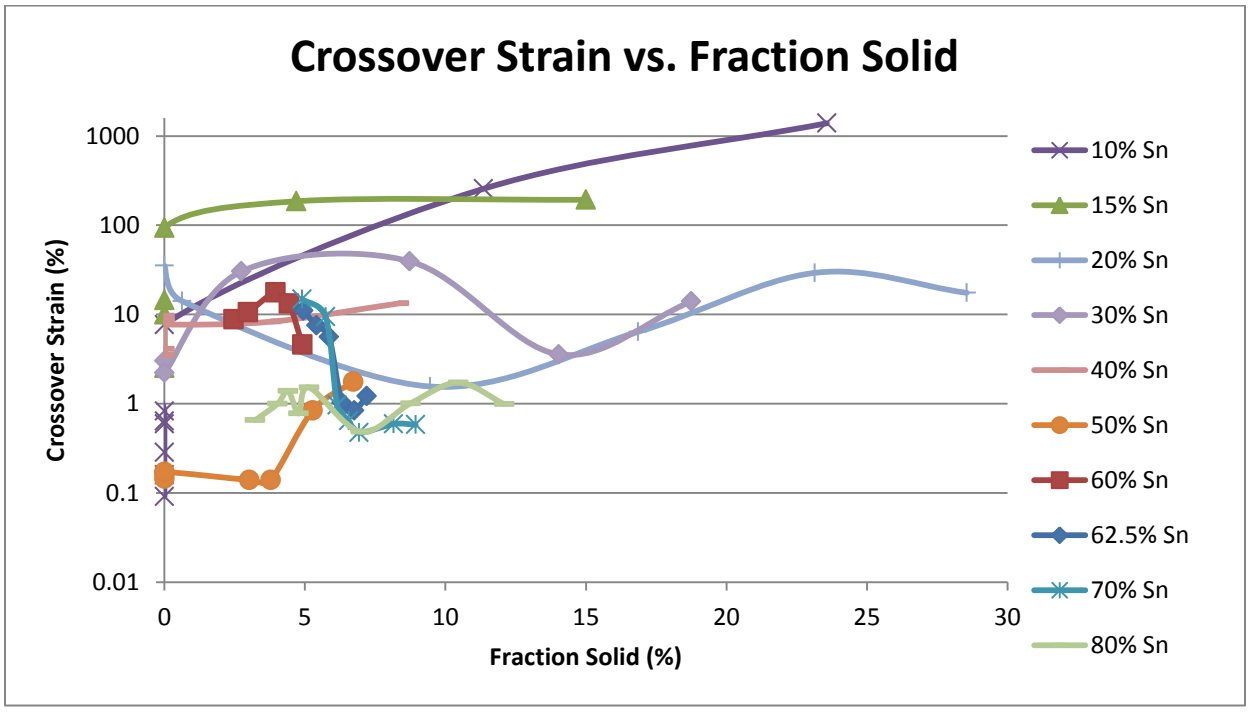

Figure 32- Crossover Strain vs. Fraction Solid, Oscillatory Shear Rheometer

Based upon the rheological properties for the bismuth-tin system, the bismuth rich alloys are the most advisable choice for direct metal writing. The bismuth rich alloys have the largest

semi-solid region on the bismuth-tin phase diagram, ranging from 139°C up to 271°C. The large semi-solid range offers some error if the thermal control in the apparatus is not perfectly uniform. Materials used for direct-deposition 3D printing methods should have viscosities similar to that of toothpaste, which is around 50-100 Pa*s (Rice, 1995). While the bismuth rich alloys required higher stresses to induce flow, their viscosities approaching the crossover point and at the crossover point were in the desired viscosity range. Also, the liquid dominant region for bismuth rich alloys maintained a viscosity in this processing range while the other bismuth-tin compositions were at least 1-2 orders of magnitude below the desired threshold. Printing can be achieved with tin rich alloys, but caution must be exercised near the liquid dominant region due to the low viscosities. The near eutectic alloys are not advisable since their parameters can change by an order of magnitude over just 1°C.

The complex viscosity as a function oscillation frequency is analogous to the true viscosity as a function of shear rate according to the Cox-Merz Rule. This relation worked for several polymers, but there were various exceptions. This study investigated the Cox-Merz relation for the bismuth-tin system, which would have applications for other SSMs as well if it were valid. Steady rotational tests were conducted on the 20%, 30%, 40%, and 80% tin samples and the true viscosity data can be seen in Appendix F. These steady rotational tests increased the shear rate from 1 to 100 s^{-1}. After comparing the data from the oscillatory and steady rotational tests in Table 6, it was determined that the Cox-Merz relation was not valid for the bismuth-tin system. The true viscosity was at least 2-3 times greater than the complex viscosity for several compositions and temperatures of SSM bismuth-tin. Alternatively, the complex viscosity tended to be greater than the true viscosity for the liquid samples of bismuth-tin. The Cox-Merz relation could be applicable for the semi-solid region of other alloys and should be investigated.

Cox-Merz Analysis for Bismuth-Tin				
Composition	**Fraction Solid (%)**	**Temperature (C)**	**Final Complex Viscosity (Pa·s)**	**True Viscosity (Pa·s)**
20% Sn 80% Bi	0	229	0.025	0.019
20% Sn 80% Bi	0	225	0.021	0.025
20% Sn 80% Bi	0.63	220	0.029	0.022
20% Sn 80% Bi	9.46	215	0.020	0.141
20% Sn 80% Bi	16.9	210	1.04	2.92
20% Sn 80% Bi	23.1	205	9.97	11.5
20% Sn 80% Bi	28.6	200	12.1	18.1
30% Sn 70% Bi	0	210	0.017	0.002
30% Sn 70% Bi	0	205	0.016	0.002
30% Sn 70% Bi	0	200	0.018	0.436
40% Sn 60% Bi	0	190	0.019	0.005
40% Sn 60% Bi	0	185	0.019	0.012
40% Sn 60% Bi	0	180	0.021	0.013
40% Sn 60% Bi	0	175	0.020	0.014
40% Sn 60% Bi	3.81	170	0.022	0.016
40% Sn 60% Bi	8.35	165	0.025	0.014
80% Sn 20% Bi	3.23	185	5.66	6.46
80% Sn 20% Bi	4.02	183	3.06	6.14
80% Sn 20% Bi	4.40	182	2.73	7.98
80% Sn 20% Bi	4.78	181	1.21	9.57
80% Sn 20% Bi	5.15	180	4.28	11.07
80% Sn 20% Bi	6.99	175	1.34	16.45
80% Sn 20% Bi	8.76	170	6.97	13.76
80% Sn 20% Bi	10.5	165	31.2	69.69
80% Sn 20% Bi	12.1	160	30.5	101.5

Table 6- Cox Merz Analysis for Bismuth-Tin

4.4. Modeling

The Lawrence Livermore National Laboratory tested their physical DMW apparatus and was able to print some basic parts with a 50% tin 50% bismuth alloy in Figure 33 and Figure 34. The printer's temperature was set to 180°C, which was well above the liquidus temperature of 147.1°C. The system's heaters were located well above the nozzle, so the actual printing temperature was well below 180°C somewhere in the SSM range. Both parts were printed with a 500 micron nozzle. Figure 33 is especially important since it shows that the SSM layers are able to adhere to previously extruded layers. While these two simple prints were created, the machine's thermal control was problematic and simulations were conducted to determine whether or not the printer's nozzle should have its own heater to compliment the tank's heater.

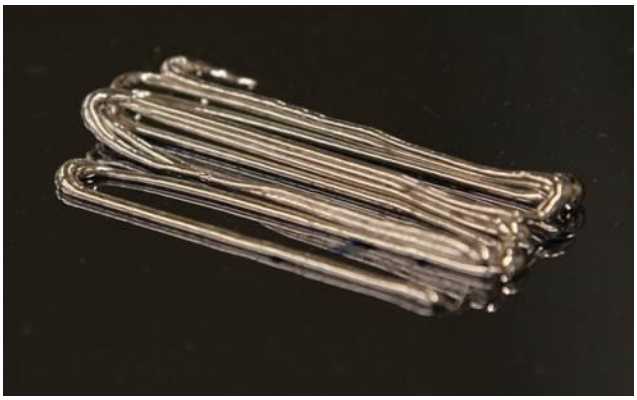

Figure 33- LLNL Print 1

Figure 34- LLNL Print 2

Physical rheological tests were coupled with flow simulations to test how the viscosity and pressure drop varied with the nozzle geometry and flow rate. Different thermal constraints were added to test the importance and location of heaters on a physical apparatus. Thixoalloy-540 (91.54% Al, 5.7% Mg, 2.5% Si, 0.15% Mn, 0.11% Fe) was selected for the simulations since bismuth-tin was not an option and the future goal is to print with aluminum alloys.

A list of simulations can be seen in Table 7. Appendix G contains the list of parameters and results. The simulations were separated into two groups. The first group (Simulations 1-9) started with a conic nozzle, and the dimensional and flow parameters were adjusted in 25% increments while holding the other parameters constant. The second group (Simulations 13-27) tested a commercially available nozzle that was purchased for Lawrence Livermore National Laboratory's direct metal writer. Additional nozzle designs were tested sporadically as well.

Initial simulations began with a 15 mm tall conic nozzle with a 10 mm inlet diameter and 500 micron outlet diameter, as seen in Figure 35. The inlet, outlet, height, and flow rate were varied. No heaters were added to the nozzle, as the material was heated in the tank before entering the nozzle, which was surrounded by ambient air. Increasing or decreasing the outlet diameter was the most influential parameter. A 25% decrease in the outlet diameter from 500 to 375 microns increased the exit velocity by 34.7% and the pressure drop by 73.7%. A 25% increase in the outlet diameter had the opposite effect. Increasing the flow rate by 25% increased the exit velocity and pressure drop similarly to decreasing the outlet diameter. However, decreasing the flow rate 25% only reduced the pressure drop and exit velocity by about 35%. Adjusting the nozzle geometry and flow rate had a negligible effect on the viscosity, as it was found to be almost entirely a function of fraction solid and temperature in future simulations.

Nozzle Simulations				
	Exit Velocity (cm/s)	**Exit Viscosity (Pa*s)**	**Pressure Drop (bar)**	**Pressure Drop (PSI)**
1- 500 Microns	1257	0.265	2.81	40.76
2- 500 Microns (Slower)	1026	0.265	2.01	29.15
3- 500 Microns (Faster)	1636	0.264	4.37	63.38
4- 375 Microns	1693	0.265	4.88	70.78
5- 500 Microns (Longer)	1470	0.265	3.77	54.68
6- 500 Microns (Shorter)	906.7	0.265	1.653	23.97
7- 500 Microns (Smaller Inlet)	1097	0.265	2.626	38.09
8- 625 Microns	726.3	0.281	1.333	19.33
9- 500 Microns (Larger Inlet)	1372	0.264	3.247	47.09
10- Cylindrical Nozzle	2537	0.282	42.049	609.9
11- Cylindrical Nozzle (Faster)	2621	0.271	58.628	850.2
12- Dual Cylinder Nozzle	4074.9	0.270	83.08	1205
13- LLNL 30 Micron	4457.8	1.131	2377.25	34479
14- LLNL 500 Micron	628	0.291	2.613	37.90
15- LLNL 400 Micron	817	0.338	4.654	67.50
16- LLNL 300 Micron	1200	0.299	7.376	107.0
17- LLNL 200 Micron (0.25 s)	3814	0.273	60.489	877.3
18- LLNL 100 Micron	8792	0.278	617.89	8962
19- LLNL 50 Micron (0.25 s)	99.3	0.804	0.749	10.86
20- LLNL 50 Micron (0.3125 s)	76.1	2.201	0.804	11.66
21- LLNL 50 Micron (1 s)	23.3	8.490	1.596	23.15
22- LLNL 200 Micron (1 s)	851.6	0.488	53.98	782.9
23- LLNL 200 Micron (1.5 s)	1128.5	1.305	299.83	4349
24- LLNL 300 Micron (TC, 3 s)	70.65	0.271	0.719	10.43
25- LLNL 300 Micron (TC, 2.5 s)	73.13	0.272	0.723	10.50
26- LLNL 300 Micron (2 s)	91.49	0.479	2.111	30.62
27- LLNL 300 Micron (TC, 2 s)	25.11	36.626	7.013	101.7

Table 7- Nozzle Simulations

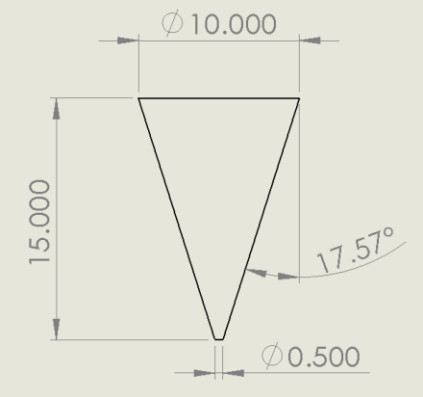

Figure 35- Simple Nozzle Drawing

The commercially available nozzles featured a more intricate design with multiple tapers and grooves. Nozzles could be purchased with the following exit diameters: 30 micron, 50 micron, 100 micron, 200 micron, 300 micron, 400 micron, and 500 micron. The inlet diameter and chamber widths were adjusted to predetermined values depending on the exit diameter. The first series of tests on the commercial nozzles did not include heaters.

The program had difficulties creating accurate mesh for the 30 and 50 micron nozzles. The meshes that were generated for Simulations 13 (30 micron) and 19-21 (50 micron) included one and two layer elements, which was less than the five layers recommended by *SIGMASOFT* for accurate shearing and stress data. Prior to conducting the simulations, there were concerns that extruding semi-solid metal out of a nozzle below 100 microns would be infeasible. The 50 micron nozzle produced inconclusive results due to meshing difficulties, but the 30 micron nozzle supported this notion. While the physical apparatus is capable of exerting up to 100 psi, the 30 micron nozzle required over 23 times that pressure to successfully extrude the alloy. The exit velocity was around 4457.8 cm/s, or almost 100 MPH. This exit velocity would cause significant splattering during extrusion and inhibit the creation of fine features.

Nozzles in excess of 100 microns could readily be modeled on the available computers. In the absence of heaters, nozzles larger than 300 microns were feasible. The absence of heaters resulted in the fraction solid increasing radially outwards, as seen in Figure 36. While the center of the nozzle maintained the desired temperature, the outer walls cooled adjacent metal, which could cause the nozzle to clog over time. The increase in fraction solid also caused the viscosity to increase radially outwards. Meanwhile, the velocity increased radially inwards. At the nozzle's tip, the maximum shearing occurred, as seen in Figure 37, which dramatically reduced the metal's viscosity and increased the velocity, as seen in Figure 38 and Figure 39 respectively.

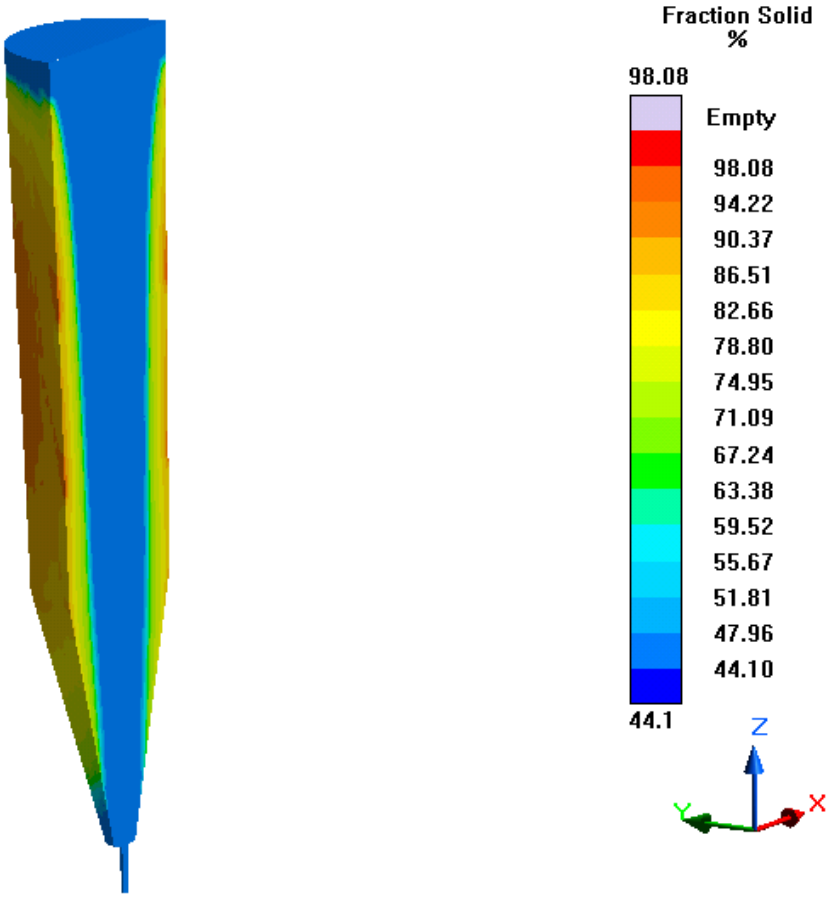

Figure 36- Fraction Solid for Simulations without Heaters

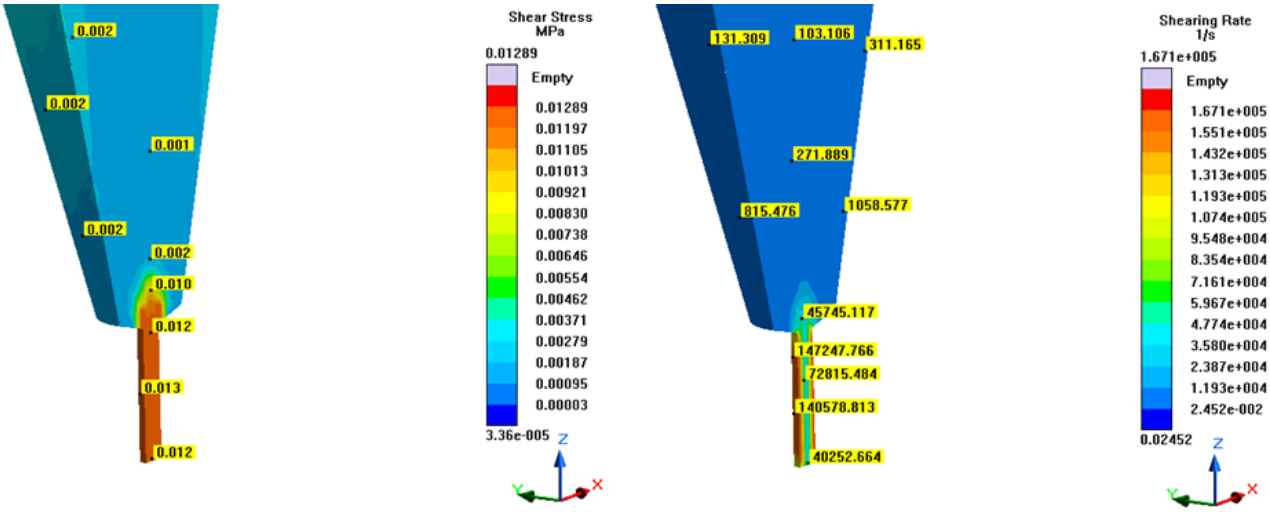

Figure 37- Shearing for Simulations without Heaters

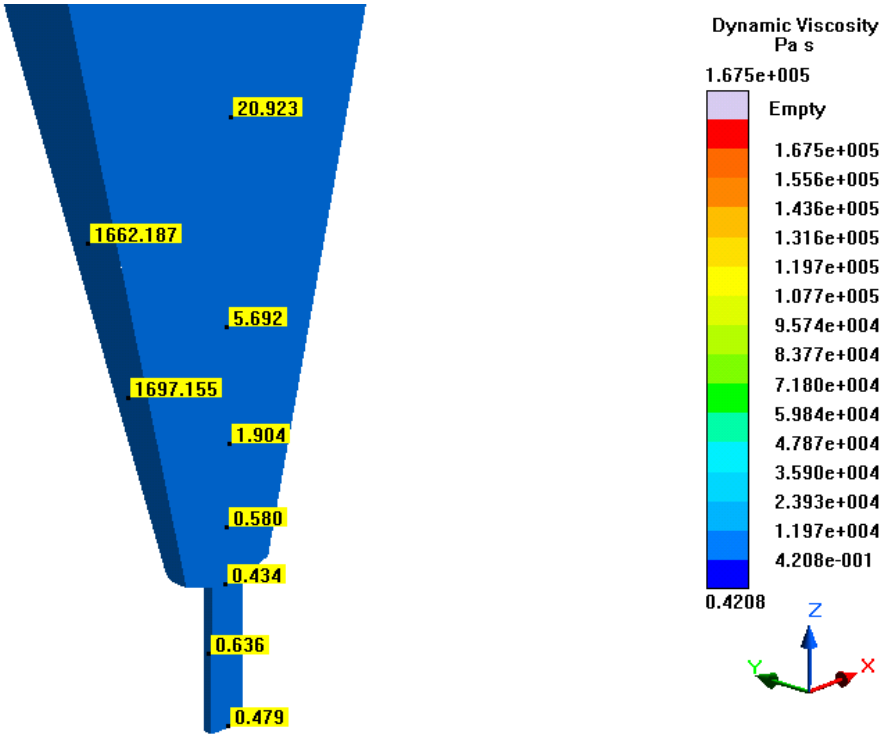

Figure 38- Viscosity for Simulations without Heaters

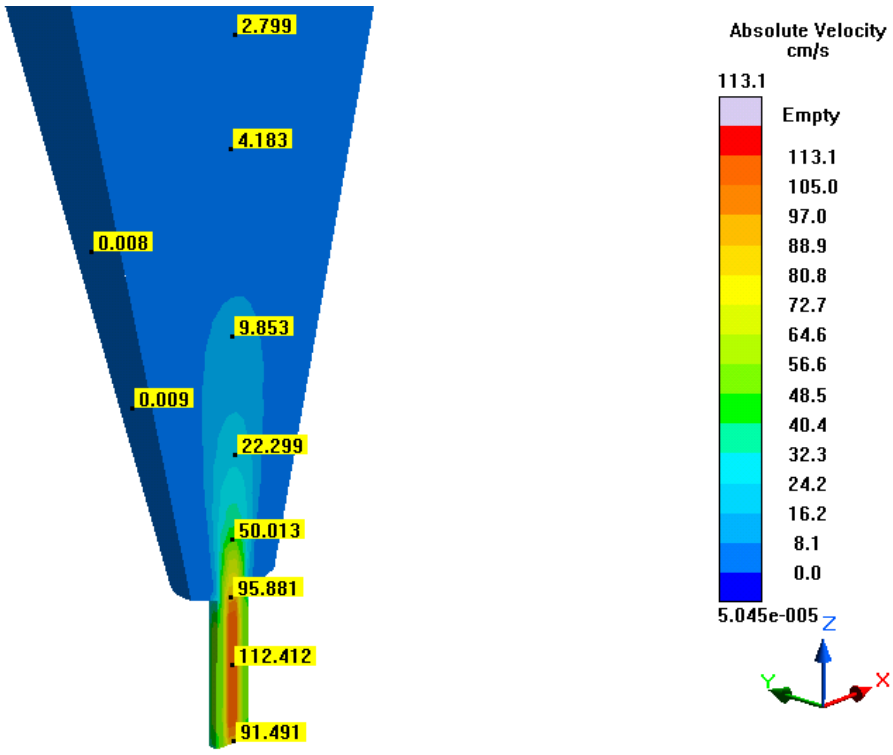

Figure 39- Velocity for Simulations without Heaters

The 300 micron nozzle just slightly exceeded the 100 psi limit of the apparatus, but some minor modifications to the flow rate and geometry or the addition of heating could make this nozzle size compatible. Both the nozzle velocity (Figure 40) and pressure drop (Figure 41) increased exponentially as the outlet diameter decreased. As with the simple conic nozzle simulations, the exit viscosity did not vary significantly for the 100-500 micron nozzles, which can be seen in Figure 42.

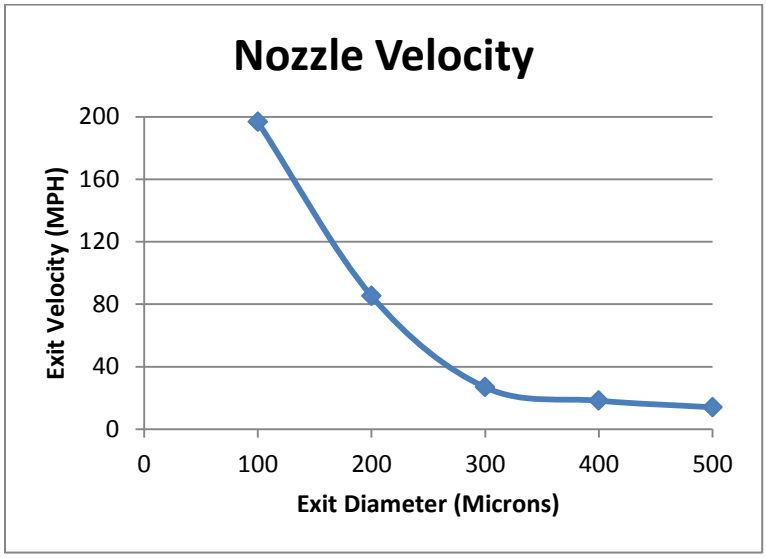

Figure 40- Nozzle Velocity without Heaters

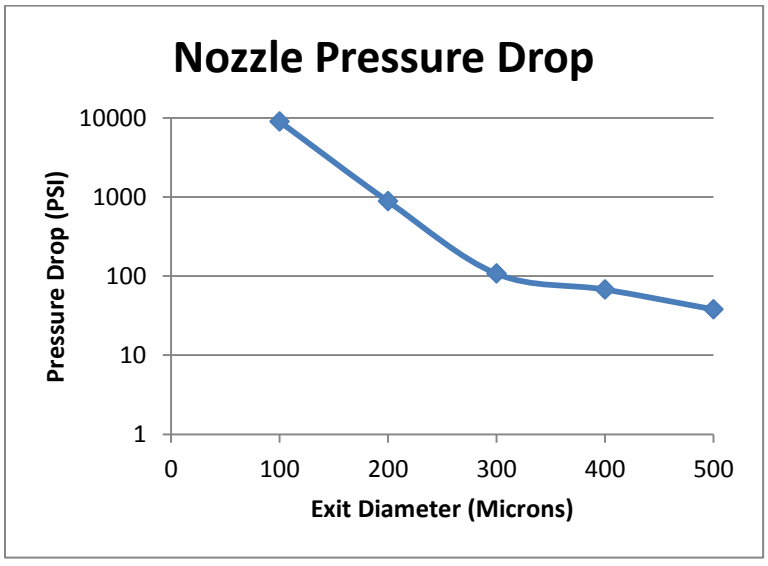

Figure 41- Nozzle Pressure Drop without Heaters

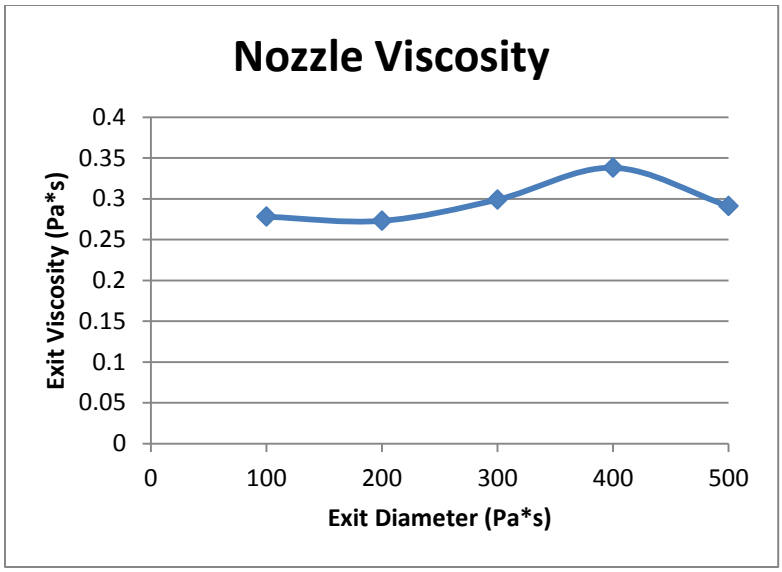

Figure 42- Nozzle Viscosity without Heaters

The final group of simulations conducted on the commercially available nozzles included heaters. These simulations are denoted with a TC in Table 7 and Appendix G. The heater encompassed the entire nozzle, and this alleviated the clogging at the outer walls. Figure 43 demonstrates a uniform fraction solid profile. The uniform temperature and fraction solid profile is most advantageous with regards to the pressure drop. As seen in Figure 44, the pressure drop decreased by a factor of 10 for the 300 micron nozzle when heaters were added.

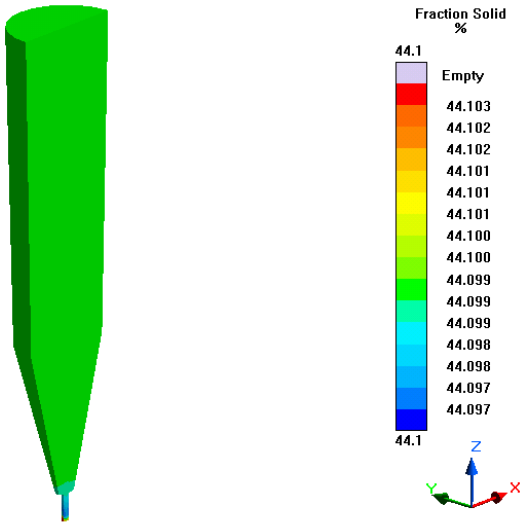

Figure 43- Fraction Solid with Heaters

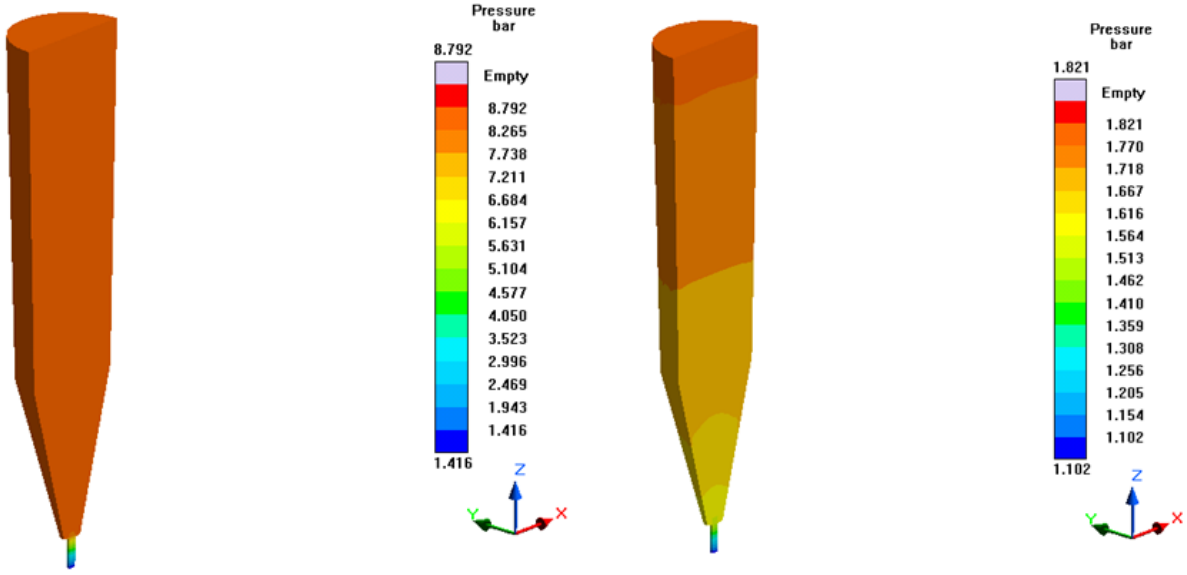

Figure 44- Comparing the Pressure Drop of a 300 Micron Nozzle without (Left) and With (Right) Heaters

The simulations reinforced the importance of heating the nozzle. This becomes especially important for alloys with small semi-solid regions since the impact of solid particles agglomerating at the walls would become more pronounced. Initial versions of the physical direct metal writer did not include a nozzle heater. The metal's measured temperature was below the set value, which was partially responsible for clogging the nozzle and impeding flow.

Some of the printing difficulties can also be attributed to insufficient shearing of the metal's dendritic structure. Dendrites form during cooling and solidification, so mechanical, magnetic, or ultrasonic agitation is necessary to break up the metal's dendritic network. Uniform cooling could significantly stunt the formation of dendrites while also keeping the alloy's solid fraction and viscosity below values that would clog the apparatus. Future simulations should model bismuth-tin to assist the design of Lawrence Livermore National Laboratory's physical apparatus. While the study's simulations did not use bismuth-tin, many of the design considerations for the Thixoalloy-540 would likely hold true for another metallic system since both metals have thixotropic behavior.

5. Conclusions

Direct metal writing (DMW) with semi-solid metal (SSM) alloys has a promising future. DMW is a novel approach similar to the fused deposition modeling 3D printers for thermoplastics. Advancements in the understanding of SSM rheology and nozzle designs will accelerate the feasibility and usefulness of DMW.

Molten and semi-solid metals readily oxidize, especially when they are allowed to rest without agitation. This behavior plagued the early cone and plate experiments. While the data collected from these experiments was unreproducible, the cone and plate experiments were important to develop test conditions for future experiments. First, metal rheological tests should be conducted in an inert environment such as nitrogen to prevent unwanted oxidation. This oxidation increases the shear stress necessary to achieve liquid properties and alters the metal's composition. Second, metal rheological tests should be conducted in an oscillatory shear rheometer that minimizes the gap between cylinders. Minimizing the gap maximizes the uniformity of the SSM slurry. Metal has a low viscosity, so high shear rates or stresses with the cone and plate rheometer can cause edge fracture and eject material, which compromises the accuracy of the experiments. Oscillatory shear rheometers solve these two issues.

The bismuth-tin system was used for the first generation DMW apparatus. Bismuth-tin's low melting point made it easier to create in the laboratory, and the samples could be tested with the low temperature cone and plate rheometer until the high temperature oscillatory shear rheometer arrived. The oscillatory shear measurements were all conducted with the angular velocity held constant, so future experiments should vary the angular velocity. Rotational tests were compared with oscillatory shear tests and determined the Cox-Merz rule did not work for the bismuth-tin system, and this relation should be investigated for additional SSM alloys too.

Computer simulations for SSM flow were valuable in the design of the DMW system's nozzle. The nozzle's outlet size was the driving factor in determining the system's pressure drop and exit velocity. Varying the nozzle size from 100 microns to 500 microns had a negligible effect on the metal's exit viscosity. Nozzles larger than 300 microns are recommended. Smaller nozzles produce massive pressure drops well in excess of 100 psi, velocities greater than 100 MPH, and clogging if the nozzle is not heated. If uniform thermal control can be achieved and maintained using heaters at the nozzle tip, smaller outlet diameters can be used.

All alloys were created in the laboratory from powders or ingots. Powder processing was more problematic, as it required a reducing atmosphere and the powders' greater surface area readily oxidized. Inductively coupled plasma mass spectroscopy (ICP-MS) determined that the samples made from powders had 2% more tin than expected, and glow discharge mass spectroscopy (GDMS) determined these samples were free of major impurities. Samples created with the ingot method need to be verified with ICP-MS and GDMS. Direct scanning calorimetry (DSC) was used for both the powder and ingot preparation methods to determine the solidus and liquidus lines. Both methods produced similar heat flow data, and the resulting phase diagram was within 2% of the actual phase diagram for bismuth-tin at most compositions.

The bismuth-tin rheology and simulation work has improved the DMW apparatus. The ultimate goal of the DMW project is to print with high temperature, functional alloys such as aluminum. After controlled and repeatable printing is achieved for the DMW apparatus with bismuth-tin, the design can be adapted for these high temperature alloys. This necessitates the collection of rheological data for the high temperature alloys and the creation of new simulations to verify their feasibility with several different nozzle designs. Continued research into the rheology of SSM alloys will improve DMW's feasibility and reliability.

References

Abramov, V., Abramov, O., Bulgakov, V., & Sommer, F. (1998). Solidification of Aluminum Alloys Under Ultrasonic Irradiation Using Water-Cooled Resonator. *Materials Letters, 37*(1-2). 27-34.

Alexandrou, A., Le Menn, P., Georgiou, G., & Entov, V. (2003). Flow Instabilities of Herschel-Bulkley Fluids. *Journal of Non-Newtonian Fluid Mechanics, 116,* 19-32.

Alexandrou, A. (2006). Parameter Estimation for Semi-Solid Aluminum Alloys using Transient Experiments. *Solid State Phenomena, 116-117,* 429-432.

Askeland, D., Fulay, P., & Wright, W. (2011). The Science and Engineering of Materials (6th Edition). *CENGAGE Learning*: Stamford, CT.

Atkinson, H. (2005). Modelling the Semisolid Processing of Metallic Alloys. *Progress in Materials Science, 50,* 341-412.

Behrens, B., & Frischkorn, C. (2014). Thixoforging of Particle-Reinforced Steel Materials. *Prod. Eng. Res. Devel., 8*, 335-343.

Boettinger, W., Kattner, U., & Moon, K. (2006). DTA and Heat-Flux DSC Measurements of Alloy Melting and Freezing. *National Institute of Standards and Technology*.

Boger, D. (1999). Rheology and the Minerals Industry. *Mineral Processing and Extractive Metallurgy Review, 20,* 1-25.

Chai, G., Roland, T., Arnberg, L., & Backerud, L. (1992). Studies of Dendrite Coherency in Solidifying Aluminum Alloy Melts by Rheological Measurements. *2nd International Conference of Semisolid Material Processing,* 193-201.

Chatzimina, M., Georgiou, G., & Alexandrou, A. (2009). Wall Shear Rates in Circular Couette Flow of a Herschel-Bulkley Fluid. *University of Cyprus*.

Cox, W., & Merz, E. (1958). Correlation of Dynamic and Steady-Flow Viscosities. *Journal of Polymer Science, 28,* 619-622.

Cross, M. (1965). Rheology of Non-Newtonian Fluids: A New Flow Equation for Pseudoplastic Systems. *Journal of Colloidal Science, 20*(5), 417-437.

de Figueredo, A., & Apelian, D. (2001). Science and Technology of Semi-Solid Metal Processing. *North American Die Cast Association*: Rosemont, IL.

Fan, Z. (2002). Semisolid Metal Processing. *International Materials Reviews, 47*(2), 49-86.

Fan, Z., Bevis, M., Ji, S. (2004). Method and Apparatus for Producing Semisolid Method Slurries and Shaped Components. *US Patent 6745818 B1*.

Ferrante, M., & De Freitas, E. (1999). Rheology and Microstructural Development of a Al-4wt%Cu Alloy in the Semi-Solid State. *Materials Science and Engineering A, 271*(1-2), 172-180.

Flemings, M. (1974). Solidification Processing. *McGraw Hill Publication*.

Flemings, M. (1991). Behavior of Metal Alloys in the Semi-Solid State. *Metall. Trans., 22A*, 952-981.

Haller, B. (2006). Influence of Process Parameters in Thixoforging of Steel C60. *Leibniz University*.

Harrison, W., Hess K., Marcus, R., & King, F. (1986). Glow Discharge Mass Spectroscopy. *Analytical Chemistry*, 341.

Hirt, G., Bleck, W., Bührig-Polaczek, A., Shimahara, H., Püttgen, W., & Afrath, C. (2006). Semi-Solid Casting and Forging of Steel. *Diffusion and Defect Data B, 116-117*, 34-43.

Höhne, G., Hemminger, W., & Flammersheim, H. (2003). Differential Scanning Calorimetry (2nd Edition). *Springer Science and Business Media*: Berlin.

Kapranos, P., Kirkwood, D., & Sellars, C. (1993). Semi-Solid Processing of Aluminum and High Melting Point Alloys. *Proceedings of the Institiution of Mechanical Engineers, 207*(1), 1-8.

Kenney, M., Courtois, R., Evans, G., Farrior, C., Koch, A., & Young, K. (1998). Semi Solid Metal Casting and Forging. *Metals Handbook, 15*, 327-338.

Kirkwood, D. (1994). Semisolid Metal Processing. *Int. Mat. Rev., 3*, 173-189.

Kirkwood, D., & Kapranos, P. (1989). Semi-Solid Processing of Alloys. *Metals and Materials Bury St Edmunds, 5*(1). 16-19.

Kirkwood, D., Sellars, C., & Boyed, L. (1992). Thixotropic Materials. *European Patent 0305 375 B1*.

Kissling, R., & Wallace, J. (1963). Grain Refinement of Aluminum Castings, *Foundry*. 78-82.

Kumar, P., Martin, C., & Brown, S. (1994). Constitutive Modeling and Characterization of the Flow Behavior of Semi-Solid Metal Alloys Slurries. *Acta Metallurgica Et Materialia (0956-7151), 42*(11), 3595-3602.

Krassenstein, E. (2014, June 11). 17-Year-Old Creates Affordable 3D Metal Printer – Hopes to Launch Kickstarter Campaign. *3DPrint.com*.

Lashkari, O., & Ghomashchi, R. (2007). The Implication of Rheology in Semi-Solid Metal Processes: An Overview. *Journal of Materials Processing Technology, 182*, 229-240.

Lee, S., Han, S., & Kang, C. (2007). Thixo Forging Process of Wrought Aluminum Alloy Fabricated by Rotational Helical Shape Stirrer. *Journal of Mechanical Science and Technology, 21*, 1656-1662.

Lipinski, D., & Flender, E. (1998). Numerical Simulation of Fluid Flow and Heat Transfer Phenomena for Semi-Solid Processing of Complex Casings. *Proceedings of the Fifth International Conference on Semi-Solid Processing of Alloys and Composites*, 273-280.

Martinez, V., & Valencia, M. (2012). Recent Researches in Metallurgical Engineering- From Extraction to Forming. Intech: Croatia. 125-142.

Meyers, M., & Chawla, K. (2009). Mechanical Behavior of Materials. *Cambridge UP*.

Modigell M., & Koke J. (1999). Time-Dependent Rheological Properties of Semi-Solid Metal Alloys. *Mechanics of Time-Dependent Materials, 3*, 15-30.

Mohammed, M., Omar, M., Salleh, M., Alhawari, K., & Kapranos, P. (2013). Semisolid Metal Processing Techniques for Nondendritic Feedstock Production. *The Scientific World Journal, 2013*, 1-16.

Montaser, A., McLean, J., & Liu, H. (1998). Inductively Coupled Plasma Mass Spectroscopy. *Wiley-VCH*: New York. 1-6.

Morrison, F. (2001). Understanding Rheology. *Oxford University Press*: New York.

Morton, K., & Mayers, D. (). Numerical Solution of Partial Differential Equations (2nd Edition). *Cambridge University Press*: Cambridge.

Niedick, I. (2000). Suitability Evaluation and Optimization of Material for Thixoforming. *RWTH Aachen University*: Germany.

Pan, Q., Apelian, D., & Alexandrou, A. (2004). *Metallurgical and Materials Transactions B, 35*(6), 1187-1202.

Rice, C. (1995). Solid Freeform Fabrication Using Semi-Solid Processing. *Massachusetts Institute of Technology*.

Rice, C., Mendez, P., & Brown, S. (2000). Metal Solid Freeform Fabrication Using Semi-Solid Metal Processing. *JOM, 52*(12), 31-33.

Shaw, M. (2001). Rheology as a Tool for the Polymer Scientist. *SPE/ANTEC 2001 Proceedings*, 1906-1907.

Smithells, C., Gale, W., & Totemeier, T. (2004). Smithells Metals Reference Book. *Elsevier Butterworth-Heinemann*: Amsterdam. Print.

Song, Y., Park, K., & Hong, C. (2006). Recrystallization Behavior of 7175 Al Alloy During Modified Strain-Induced Melt-Activated (SIMA) Process. *Materials Transactions, 47*(4). 1250-1256.

Spencer, D., Mehrabian, R., & Flemings, M. (1972). Rheological Behavior of Sn- 15Pct Pb in the Crystallization Range. *Metall. Trans., 3*, 1925-1932.

Terrel A. (2010). Finite Element Method Automation for Non-Newtonian Fluid Models. *University of Chicago*.

Wei, L., & Ohsasa, K. (2010). Supercooling and Solidification Behavior of Phase Change Material. *ISIJ International, 50*, 1265-1269.

Weisstein, E. (1999). CRC Concise Encyclopedia of Mathematics. *Chapman and Hall/CRC*: Boca Raton.

Wimmer P., & Klein, F. (1996). Porosity in Zinc Die Castings. *Giesserei-Praxis*, 6, 112-119.

Winter, H. (2009). Three Views of Viscoelasticity for Cox-Merz Materials. *Rheologica Acta*, *48*, 241-243.

Wohlers Associates (2014). "Wohlers Report 2014."

Wyss, H., Larsen, R., & Weitz, D. (2007). Oscillatory Rheology. *G.I.T. Laboratory Journal, 3-4/2007*, 68-70.

Zhang, Y., Liu, Y., & Cao, Z. (2009). Mechanical Properties of Thixomolded AZ91D Magnesium Alloy. *Journal of Processing Technology, 209*(3), 1375-1384.

Zhang, Z., Le, Q., & Cui, J. (2008). Microstructures and Mechanical Properties of AZ80 Alloy Treated by Pulsed Ultrasonic Vibration. *Transactions of Nonferrous Metals Society of China, 18*(1). s-113-s116.

(2014). Interfacial Shear Rheometry. *Biolin Scientific*.

(2014). SIGMASOFT Thixo. *SIGMASOFT*.

Appendix A- Semi-Solid Processing Techniques

Semi-solid metal (SSM) processing has two main routes dictated by the metal's starting phase: solid or liquid. Rheocasting begins with the alloy in the liquid state. The liquid is then shaped using a die or a mold (de Figueredo & Apelian, 2001). Thixoforming reheats solid alloys to form non-dendritic, globular SSM slurries (de Figueredo & Apelian, 2001). The semi-solid nature of the metal results in non-turbulent flow that minimizes the porosity compared to traditional liquid metal casting, and this can be seen in Figure 45 (Hirt et al., 2006). Casting is troubled by porosity. Non-agitated liquid metal is littered with dendritic arms that create gaps between metal particles (the black portions represent gaps) and result in a high porosity. This porosity compromises the metal's strength. In the semi-solid region, particles can be tightly packed to minimize porosity and maximize strength due to their uniform, spheroid geometry.

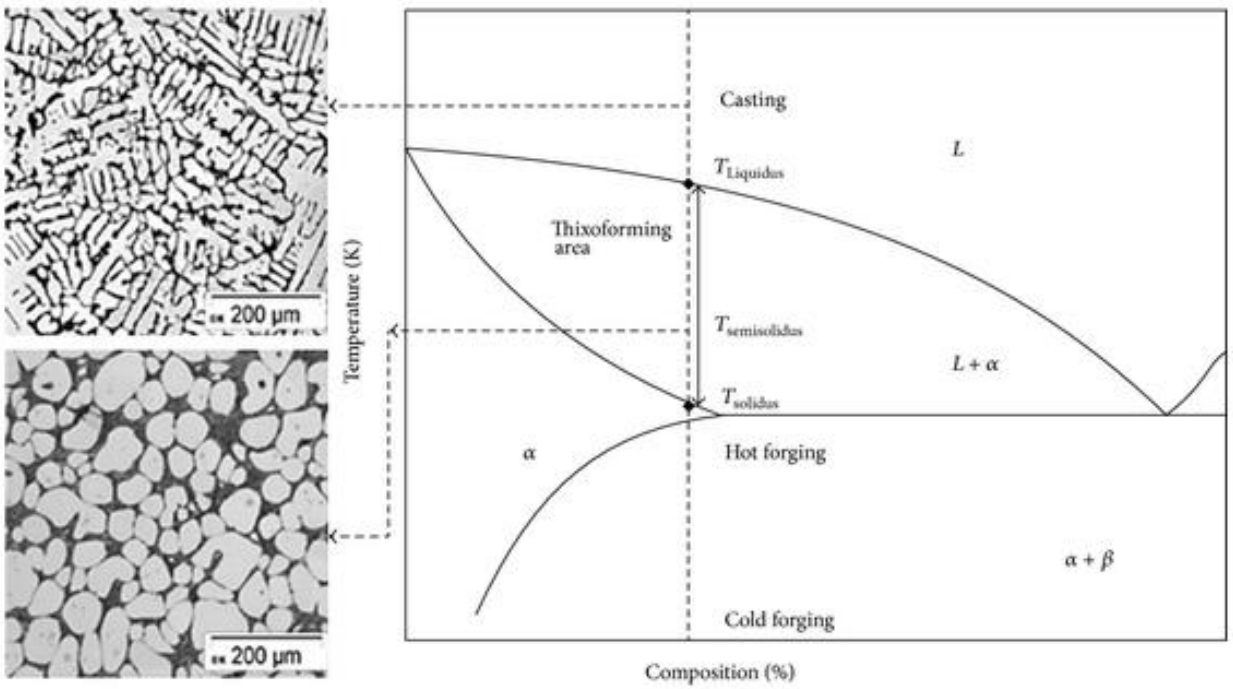

Figure 45- SSM Slurry Morphology (Hirt et al., 2006)

Rheocasting

Rheocasting can be further divided into agitation and non-agitation routes. Agitation routes break up the alloy's dendritic network and produce globular, equiaxed particles through either direct or indirect agitation. Non-agitation routes rely on precise thermal or chemical control to obtain a uniform SSM slurry.

Mechanical Stirring

Mechanical stirring is an agitation based SSM slurry preparation route. Blades or augers mechanically agitate the sample to break up the dendritic network and produce globular particles. Figure 46 shows an example of a stirrer agitation system and how different geometries can result in different shear rates and sample viscosities (Martinez & Valencia, 2012). Traditional stirrer based systems have four major drawbacks: erosion of the stirrer, gas entrapment, oxidation, and difficulty controlling the process on an industrial level (de Figueredo & Apelian, 2001). Newer mechanical agitation systems have used helical screws to improve production rates, as in Figure 47 (Fan et al., 2004). Indirect stirring methods such as magnetohydrodynamic (MHD) and ultrasonic stirring are used more frequently than mechanical agitation.

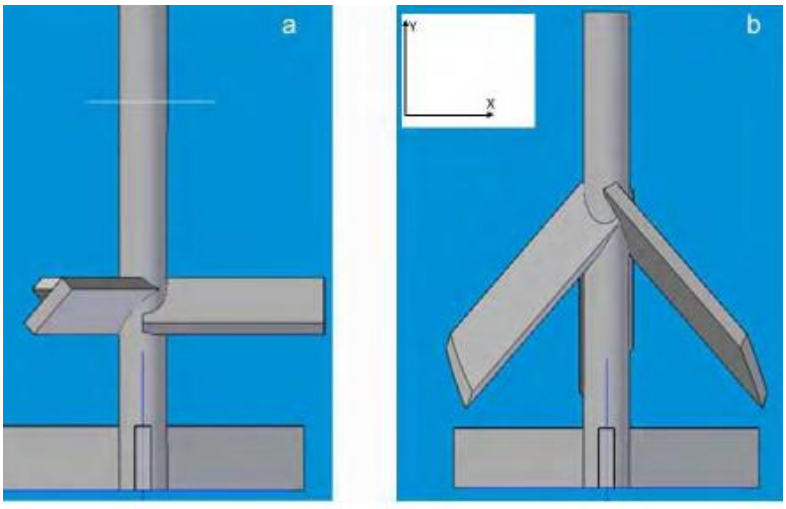

Two configurations of upper trowels: (a) 45°-x, (b) 45°-x/45°-y.

Figure 46- Mechanical Stirrer Geometries (Martinez & Valencia, 2012)

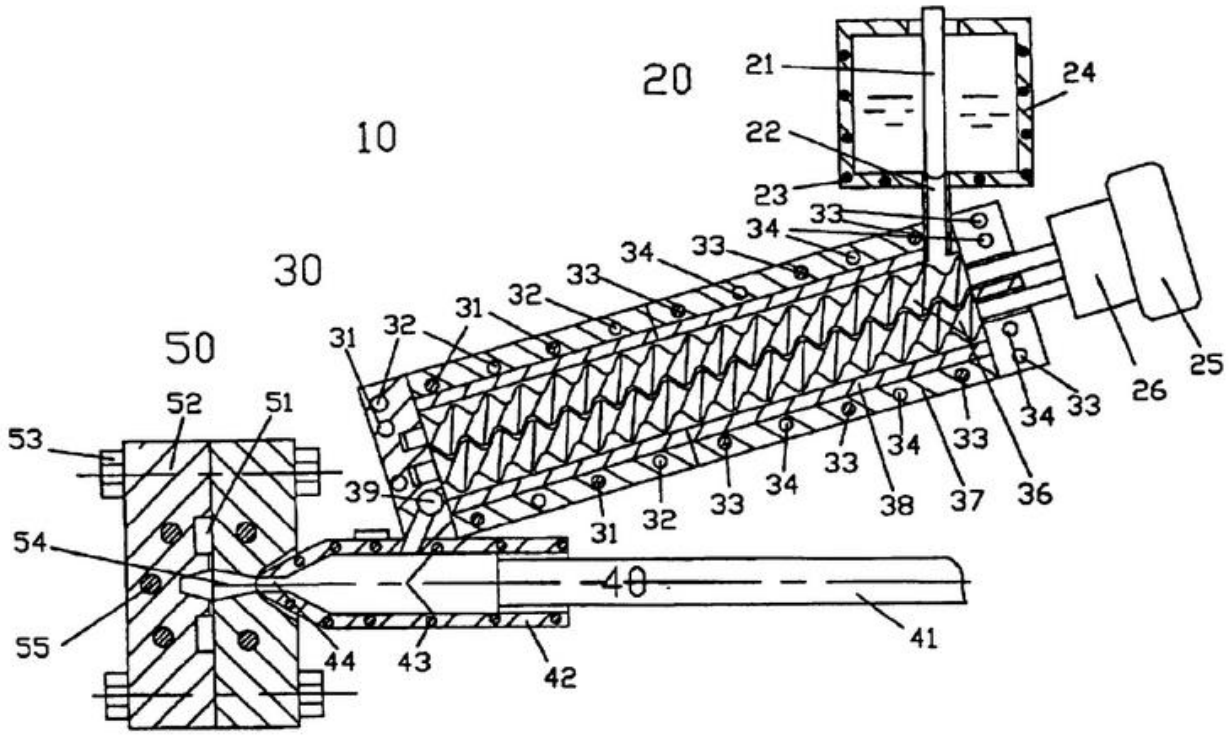

Figure 47- Helical Screw Mechanical Agitator (Fan et al., 2004)

Magnetohydrodynamic (MHD) Stirring

Magnetohydrodynamic (MHD) stirring is an indirect agitation method. Rotating magnetic fields are applied to the semi-solid metal to break up the dendritic network. MHD stirring is the most common SSM slurry agitation method because of its speed, large capacity, and repeatability (Kenney et al., 1998). The process is not without flaws, as the resulting microstructure is non-uniform and the solid particles cluster and form rosettes, so additional treatment steps are necessary to create the uniform, globular particles (Mohammed et al., 2013). Figure 48 shows three MHD stirring patterns (Niedick, 2000). The left image shows horizontal mixing, which keeps the metal in one plane and mechanically shears the particles. The center image shows vertical mixing, which uses convection currents to thermally shear the particles. The right image shows helical mixing, which combines the mechanical shearing of horizontal mixing with the thermal shearing of vertical mixing.

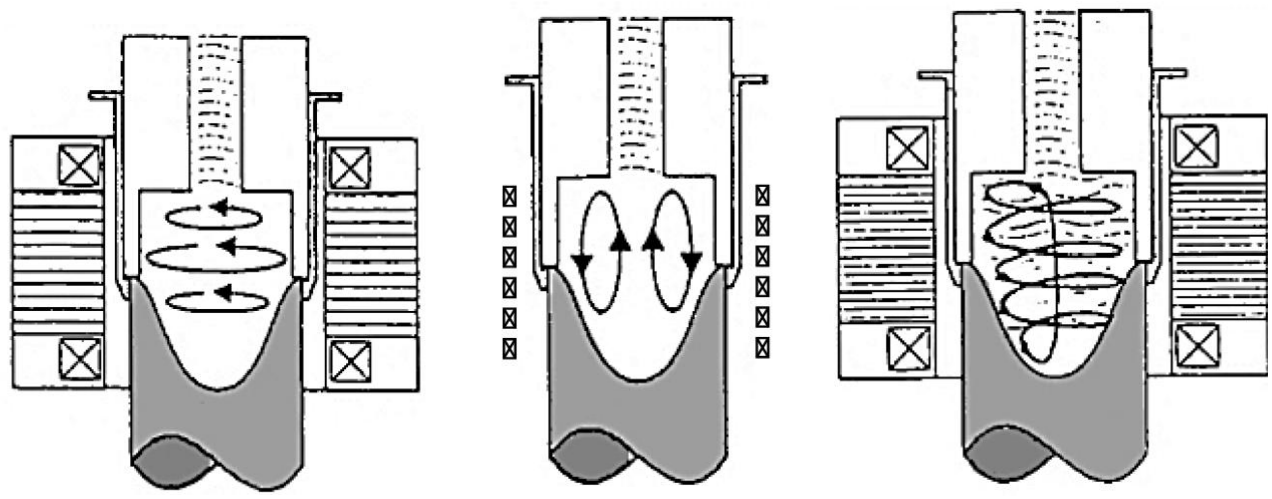

Figure 48- MHD Stirring (Niedick, 2000)

Ultrasonic Vibrations

Ultrasonic vibrations are another indirect stirring method. High frequency mechanical waves, or ultrasonic vibrations, increase nucleation amongst particles and the waves cause cavitation, or the oscillation of the slurry's temperature and pressure, to produce uniform, globular microstructures (Abramov et al., 1998). The slurry's cavitation causes high compression rates for unsteady states that can cause the particles to collapse, and the waves of hydraulic shock separate the primary particles and produce artificial nucleation sites (Mohammed et al., 2013). Figure 49 shows the set-up for this process (Zhang et al., 2008). The vigorous mixing produces strong slurry homogeneity, low porosity, and high overall part strength. Ultrasonic vibrations can also be applied during the metal's solidification, and this causes a decrease in the average grain size, controls segregation, and improves homogeneity (Zhang et al., 2008).

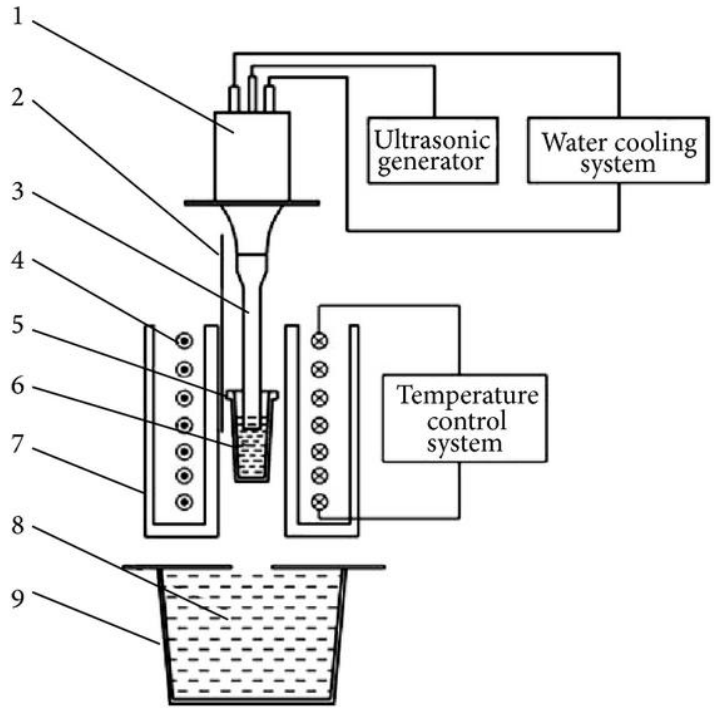

Schematic diagrams of the ultrasonic vibration device: (1) ultrasonic transducer; (2) thermocouple; (3) ultrasonic radiator; (4) resistance heater; (5) iron crucible; (6) Mg-9.0Al%; (7) ceramic tube; (8) water; (9) tank [52].

Figure 49- Ultrasonic Vibration Mixing (Zhang et al., 2008)

New MIT Process

The new MIT process, or the semisolid rheocasting (SSR) process, was developed in 2000 at MIT and is an agitation and thermal based preparation method (Mohammed et al., 2013). Figure 50 shows an overview of the new MIT process and the three steps (de Figueredo & Apelian, 2001). First, the metal is held just above the liquidus temperature to melt the metal uniformly. Second, the metal is simultaneously cooled and stirred by a rod until solidification begins in the semi-solid region. By having a high solidification temperature, the dendrites cluster on the stirrer and are subsequently fragmented and dispersed to produce a uniform SSM slurry. Third, the stirrer is removed and the slurry, which has uniform, globular particles, is further cooled to produce the desired solid fraction before being poured into a casting device.

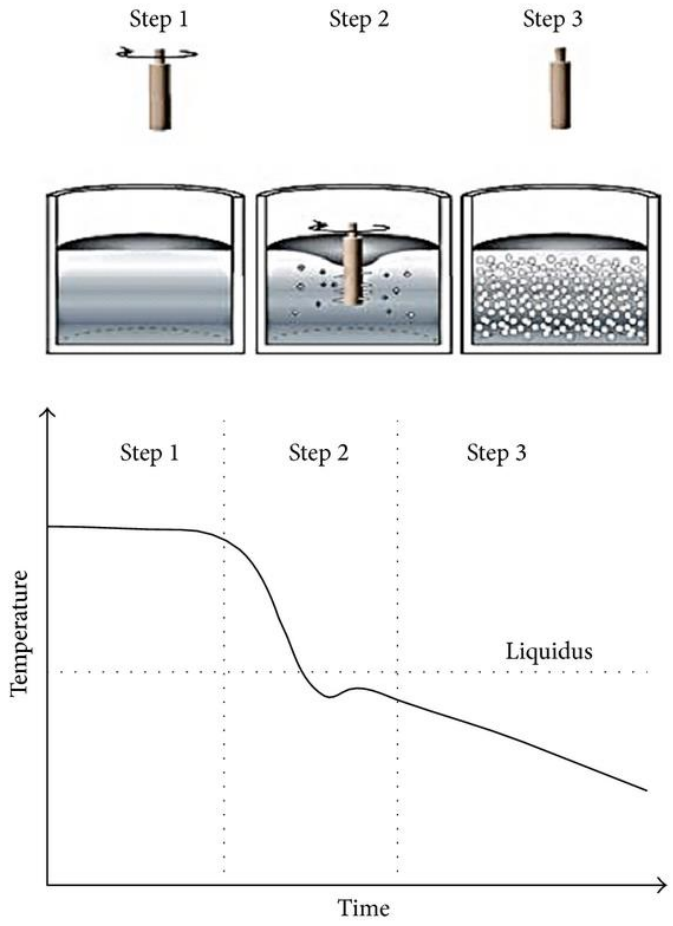

Figure 50- New MIT Process (de Figueredo & Apelian, 2001)

Spray Casting

Spray casting is a unique non-agitation process that can produce particles with a grain size below 20μm (Mohammed et al., 2013). Liquid metal is atomized by a gas jet, and the metal particles are shot onto a cool deposition site at high velocities. This process can be seen in Figure 51 (Kapranos, et al, 1993). The high velocities fragment the dendritic arms and produce globular particles. While this method produces a uniform SSM slurry, it is rarely used due to the cost and the larger than ideal bullets (60 mm or greater). This process is mostly used for high melting point alloys (Mohammed et al., 2013).

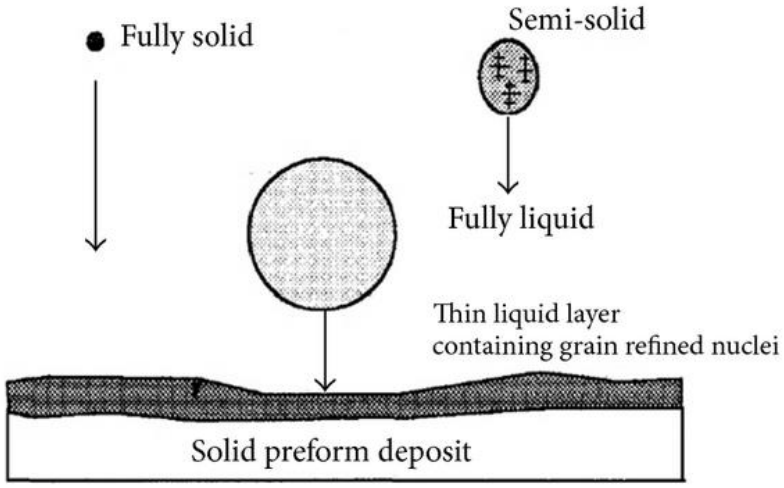

Figure 51- Spray Casting (Kapranos et al., 1993)

Chemical Grain Refining

Chemical grain refining is a non-agitation process. A heterogeneous nucleation agent is added to the alloys that suppresses dendrite formation and produces globular, equiaxed particles (Ferrante & De Freitas, 1999). This method is not a standalone process, as it needs to be combined with another SSM slurry preparation method such as mechanical or MHD stirring. Chemical grain refining is only compatible with alloy systems with a large liquid fraction and irregular spheroidal grain size, which limits its adoption (Fan, 2002).

New Rheocasting (NRC)

New rheocasting (NRC), or liquidus casting, is a non-agitation process. NRC is a three stage process, as seen in Figure 52 (de Figueredo & Apelian, 2001). The alloy is first heated to a temperature near the liquidus line and poured into a holding vessel. The high temperature of the metal heats and fragments the dendrites while promoting nucleation. The metal is then transferred to a holding mold until the slurry has globular, equiaxed particles. Finally, the alloy is transferred into the shot sleeve of a casting machine. Figure 53 shows the microstructure for an A356 alloy formed using the NRC process (Robert et al., 2007).

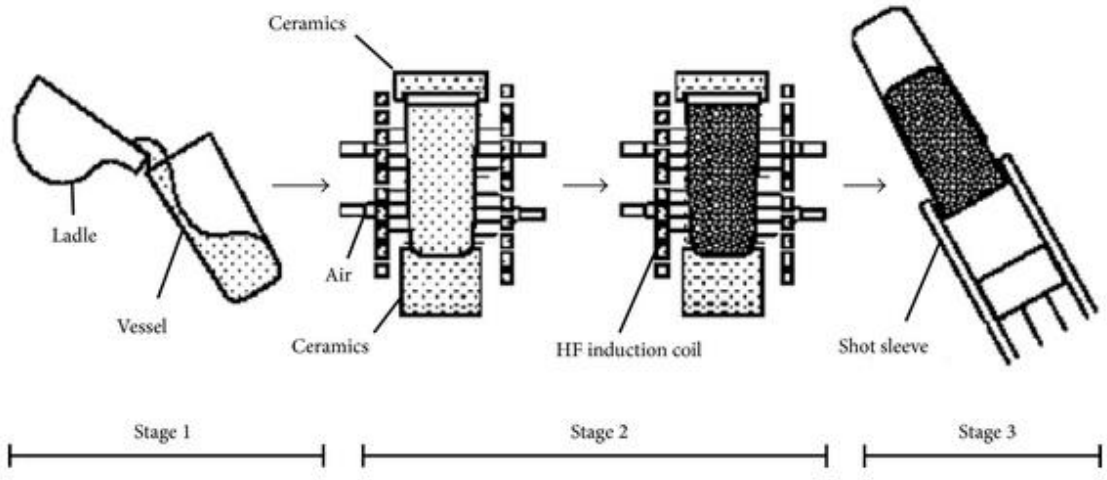

Figure 52- New Rheocasting (de Figueredo & Apelian, 2001)

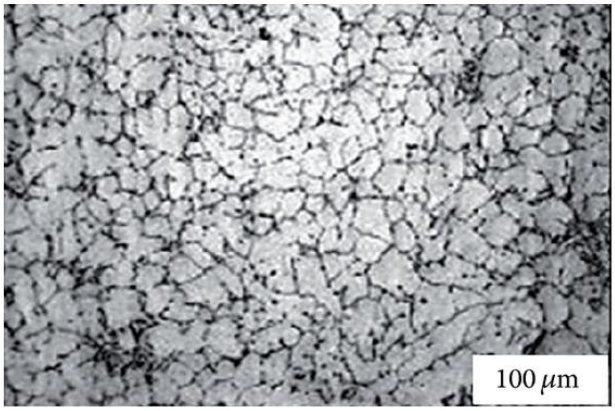

Figure 53- New Rheocasting Microstructure for an A356 Alloy (Robert et al., 2007)

Thixoforming

Thixoforming begins with the metal in the solid state, but it is reheated to the semisolid region. When agitated, the dendritic network is broken up and non-dendritic, globular particles are formed. Thixoforming processes are near-net shape processes, and include thixomolding, thixoforging, the strain induced melt activated (SIMA) process, and the recrystallization and partial melting (RAP) process (Mohammad et al., 2013).

Thixomolding

Thixomolding, which is also known as thixocasting, is the metal equivalent of polymer injection molding. Figure 54 demonstrates the thixomolding process with the JSW JLM220-MG Thixomolder® (Zhang et al., 2009). Metal chips are loaded into the feeder and heated in an inert atmosphere. Higher temperatures are preferable because they have a lower solid fraction and can be more densely packed into a mold. Once in the semi-solid state, the metal is sheared with a reciprocating screw. Lower screw rotation speeds minimize porosity and improve the metal's strength and ductility. The SSM is then then injected into a mold. Increasing the shot velocity reduces part porosity as well by refining the α eutectic.

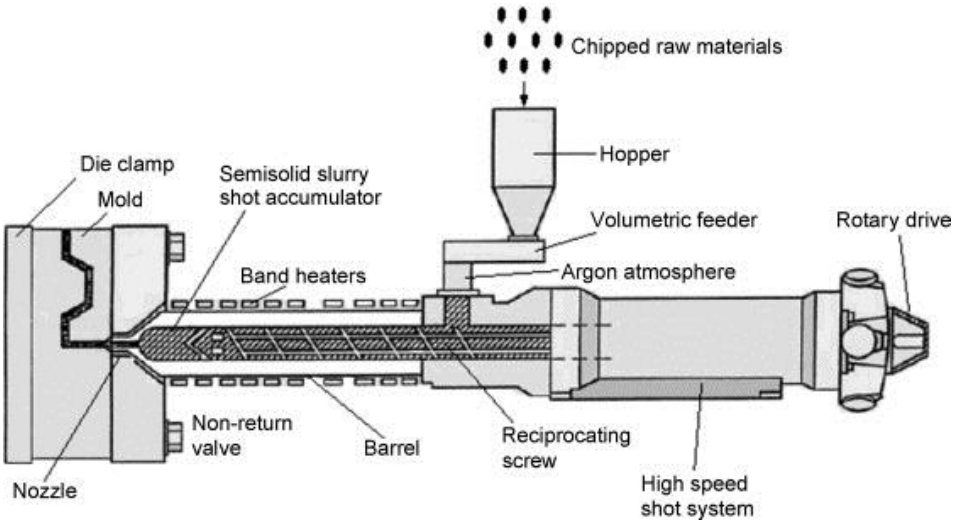

Figure 54- JSW JLM220-MG Thixomolder® (Zhang et al., 2009)

Thixoforging

Thixoforging reheats solid metal to the semi-solid state and shapes it between dies, as seen in Figure 55 (Lee et al., 2007). Thixoforging is superior to standard forging because it can create more complex geometries, reduce stress on the forging tools, and reduce overall part shrinkage while maintaining the mechanical properties of traditional forging (Behrens & Frischkorn, 2014). Thixoforging is also distinguished from thixomolding by the required liquid

fraction. Thixomolding needs a higher liquid fraction around 40-70% while thixoforging needs a liquid fraction of just 10-40% (Haller, 2006). This allows thixoforging to be done at lower temperatures.

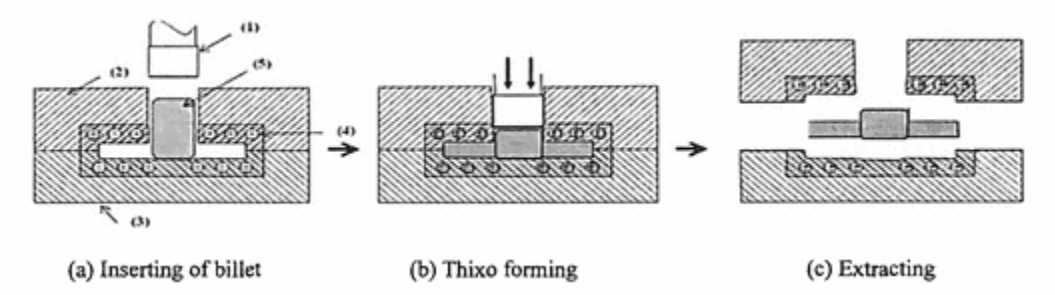

Figure 55- Thixoforging (Lee et al., 2007)

Strain Induced Melt Activated (SIMA) Process

The strain induced melt activated (SIMA) process was developed in the 1990's (Kirkwood, 1994). As the temperature increases to the semi-solid state, the liquid component penetrates high-angle grain boundaries. Figure 56 illustrates the SIMA process (Song et al., 2006). Hot rolling above the crystallization temperature (RT) strains and breaks the grain boundaries. The metal can then be reheated and a uniform, global slurry is formed. A cold working step can also be added between the hot rolling and melting stages to further refine the alloy's particles.

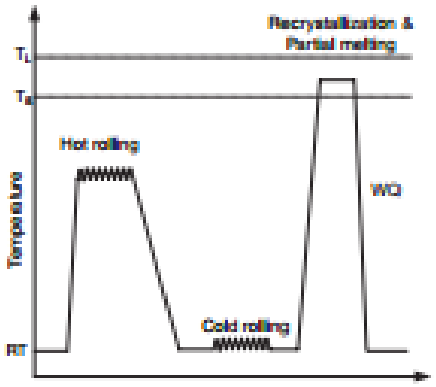

Figure 56- Strain Induced Melt Activated (SIMA) Process Graph (Song et al., 2006)

Recrystallization and Partial Melting (RAP)

The crystallization and partial melting (RAP) process is very similar to the SIMA process. While the SIMA process always includes hot rolling, the cold rolling step is optional. For the RAP process, the hot rolling step is eliminated and replaced with a mandatory cold rolling step that occurs below the recrystallization temperature to have optimal strain hardening behavior (Kirkwood & Kapranos, 1989). Figure 57 illustrates this process (Kirkwood et al., 1992). The cold-working step occurs at the warm extrude, which is above room temperature but below the recrystallization temperature as specified. This process also breaks the high-angle grain boundaries using the flow of liquid metal and involves a final heating step.

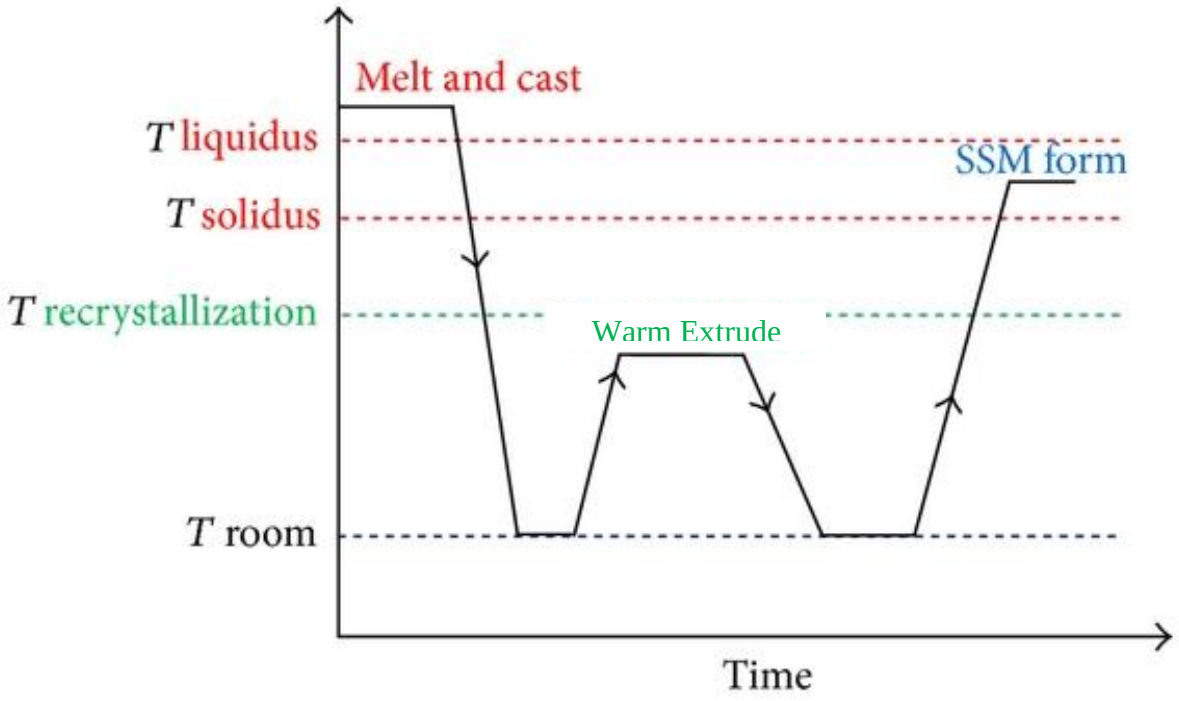

Figure 57- Recrystallization and Partial Melting (RAP) Process Graph (Kirkwood et al., 1992)

Appendix B- Semi-Solid Modeling

The rules for traditional die casting are not transferrable to rheocasting or thixoforming due to the thixotropic behavior of the SSM slurry. Most commercially available fluid modeling software is designed for liquids with constant viscosities independent of shear rate and time while SSM slurries are thixotropic and non-Newtonian. Therefore, alternative fluid flow modeling techniques are necessary. Atkinson summarizes the three different methods for modeling SSM flow: model of Kumar, Martin, and Brown, finite difference modeling, and finite element modeling (Atkinson, 2005).

Kumar, Martin, Brown Model

The Kumar et al. model is based upon the "single internal variable" concept and the structural parameter (λ), which represents if the structure is completely built up ($\lambda = 1$) or broken down ($\lambda = 0$) (Kumar et al., 1994). This model can be applied to both finite difference and finite element methods (Atkinson, 2005). Thixotropic behavior can be explained by the time derivative of the structural parameter ($d\lambda/dt$), as seen in Equation 12 (Kumar et al., 1994). A negative derivative denotes that the structure is being broken down while a positive derivative denotes that the structure is being built up. Flow resistance is assumed to be a result of the hydrodynamic flow of agglomerates and the deformation of solid particles within the agglomerates. The structural parameter is then related to the shear stress (τ) or viscosity (η) in another flow equation such as a power law Bingham equation (Equation 13, Atkinson, 2005). At very high and low shear rates, thixotropic metals exhibit Newtonian behavior, which can be seen in the Cross model (Equation 14, Cross, 1965). The Kumar et al. model predicts that between a fraction solid of 50-60%, the deformation resistance rapidly increases, and fraction solids beyond this increase cannot be analyzed accurately with this model.

$$\frac{d\lambda}{dt} = a(1-\lambda)^{\mathrm{b}} - c\lambda\dot{\gamma}^{d}$$

$$a, b, c, d = constants\ of\ the\ system$$

Equation 12- Thixotropic Behavior for SSM Slurries (Kumar et al., 1994)

$$\tau = \tau_y + K\dot{\gamma}^{n}$$

Equation 13- Power Law Equation (Atkinson, 2005)

$$\eta = \eta_\infty + \left[\frac{\eta_0 - \eta_\infty}{1 + k\dot{\gamma}^{n}}\right]$$

Equation 14- Cross Model (Cross, 1965)

Finite Difference Modeling

In finite difference modeling, derivatives are approximated and replaced with difference quotients (Morton & Mayers, 2005). *MAGMASOF*T and *FLOW3D* are two of the most well-known finite difference modeling programs for flow simulation. Modigell and Koke created a steady state flow curve from a Herschel-Bulkley model for FLOW3D in Equation 15-Equation 18 that replaced Kumar et al.'s structural parameter (λ) with a structural parameter (κ) that varies from 0 (completely broken down) to infinity (completely built up) (Modigell & Koke, 1999). *MAGMASOFT* developed *SIGMASOFT Thixo* software for thixotropic, non-Newtonian SSM slurries and this can be seen in Section 3.1.

$$\tau = \tau_y(f_s) + \exp(Bf_s)\, k^{*}\kappa\dot{\gamma}^{m}$$

$$B = rheological\ parameter\ [1/s]$$

$$m = exponent$$

Equation 15- FLOW3D Stress (Modigell & Koke, 1999)

$$\frac{\partial \kappa}{\partial t} = a \exp(b\dot{\gamma})(\kappa_e - \kappa)$$

$$a = rheological\ parameter\ [1/s]$$

$$b = rheological\ parameter$$

Equation 16- FLOW3D Structural Parameter (Modigell & Koke, 1999)

$$\kappa_e = \frac{1}{(\alpha\dot{\gamma})^{m-n}}$$

$$\alpha = rheological\ parameter\ [1/s]$$

$$m, n = exponent$$

Equation 17- FLOW3D Equilibrium Condition (Modigell & Koke, 1999)

$$\tau = \tau_y(f_s) + \exp(Bf_s)\, k\dot{\gamma}^m$$

$$B = rheological\ parameter\ [1/s]$$

$$k, k^* = k^*\alpha^{n-m} = rheological\ parameter\ [Ns^m/m^2]$$

$$\alpha = rheological\ parameter\ [1/s]$$

$$m, n = exponent$$

Equation 18- FLOW3D Stress at Equilibrium (Modigell & Koke, 1999)

Finite Element Modeling

Finite element models discretize partial differential equations into an algebra problem (Terrel, 2010). One-phase and two-phase finite element calculations can be conducted. Finite element models expand upon the Kumar, Martin, and Brown models and include popular models such as the power law and Herschel-Bulkley methods. Depending upon the properties that are emphasized, different assumptions impact the weighting of elements such as friction, deformation, and local strain.

Appendix C- Differential Scanning Calorimeter (DSC) Data

10% Tin 90% Bismuth

Predicted Composition: 12% Sn 88% Bi

Theoretical Solidus Line: 139 C
Theoretical Liquidus Line: 243.6 C

Experimental Solidus Line: 138 C
Experimental Liquidus Line: 241.2 C

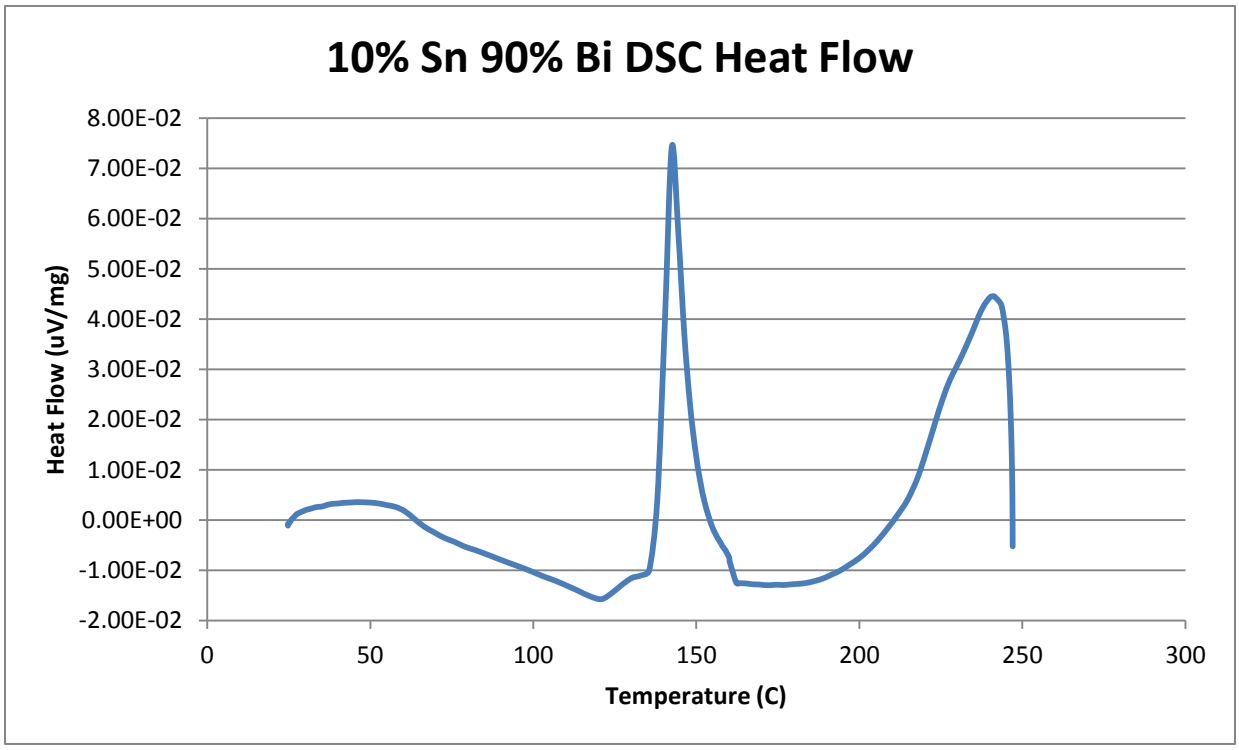

Figure 58- 10% Tin 90% Bismuth DSC Heat Flow

15% Tin 85% Bismuth

Predicted Composition: 17% Sn 83% Bi

Theoretical Solidus Line: 139 C
Theoretical Liquidus Line: 231.9 C

Experimental Solidus Line: 139.5 C
Experimental Liquidus Line: 234 C

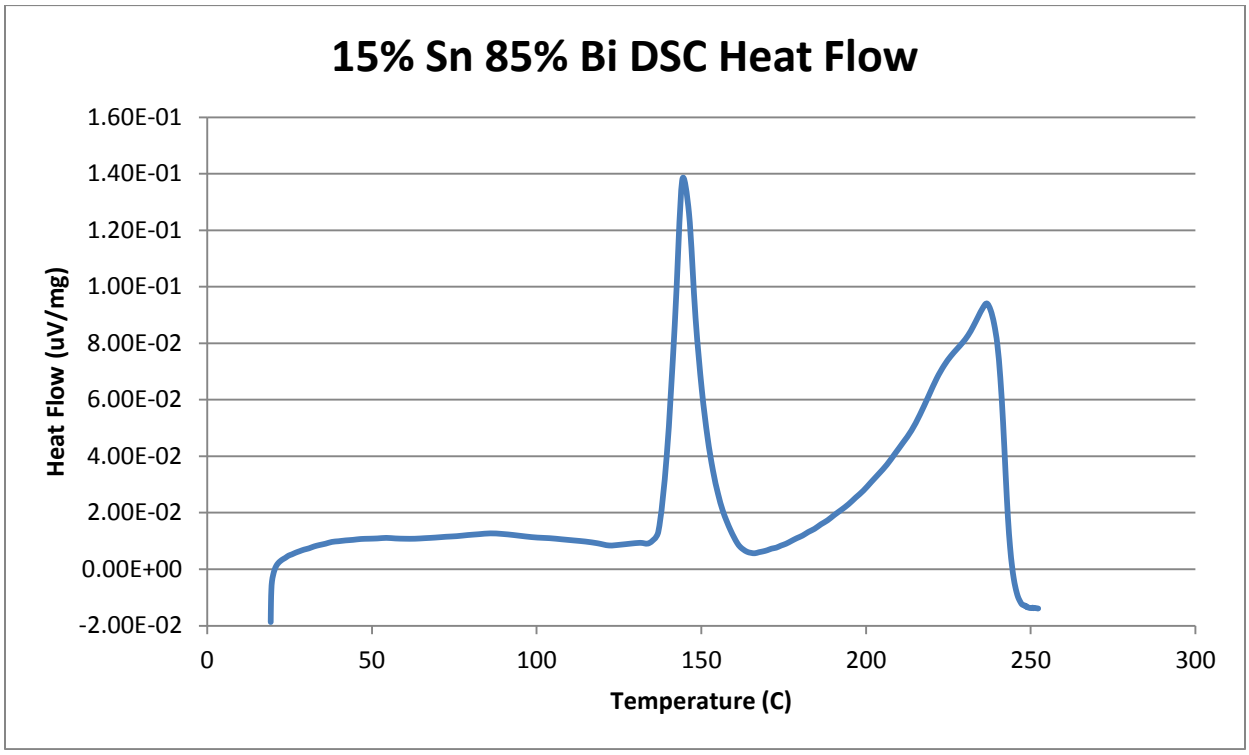

Figure 59- 15% Tin 85% Bismuth DSC Heat Flow

20% Tin 80% Bismuth

Predicted Composition: 22% Sn 78% Bi

Theoretical Solidus Line: 139 C
Theoretical Liquidus Line: 220.3 C

Experimental Solidus Line: 139 C
Experimental Liquidus Line: 217.5 C

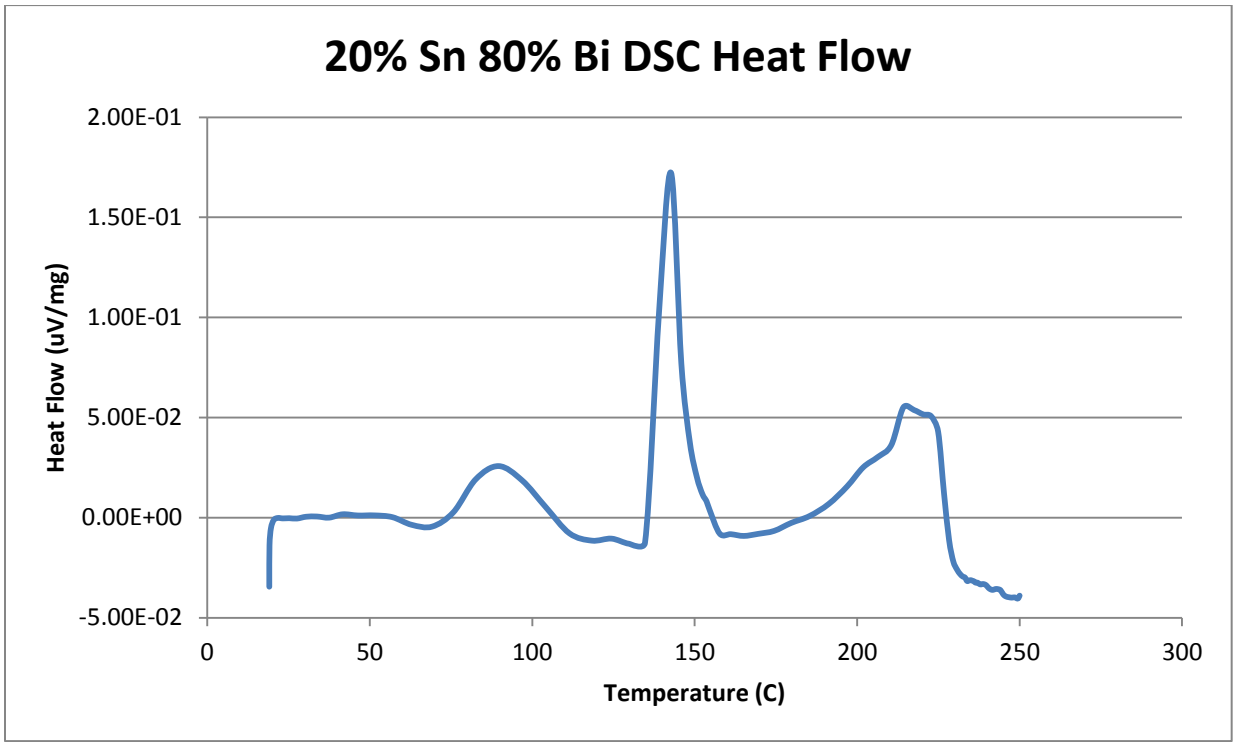

Figure 60- 20% Tin 80% Bismuth DSC Heat Flow

40% Tin 60% Bismuth

Predicted Composition: 42 % Sn, 58 % Bi

Theoretical Solidus Line: 139 C
Theoretical Liquidus Line: 173.9 C

Experimental Solidus Line: 139.6 C
Experimental Liquidus Line: 177.3 C

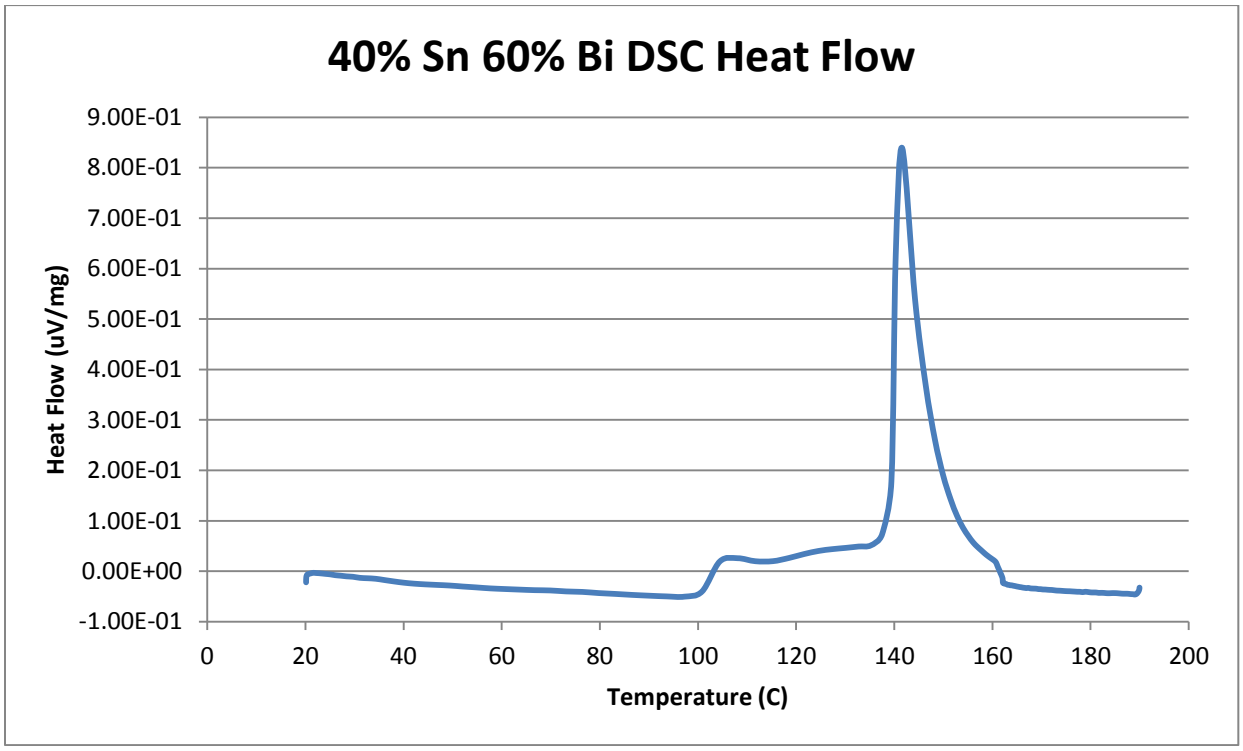

Figure 61- 40% Tin 60% Bismuth DSC Heat Flow

45% Tin 55% Bismuth

Expected Composition: 47% Tin, 53% Bismuth

Theoretical Solidus Line: 139 C
Theoretical Liquidus Line: 159.7 C

Experimental Solidus Line: 138.9 C
Experimental Liquidus Line: 162.2 C

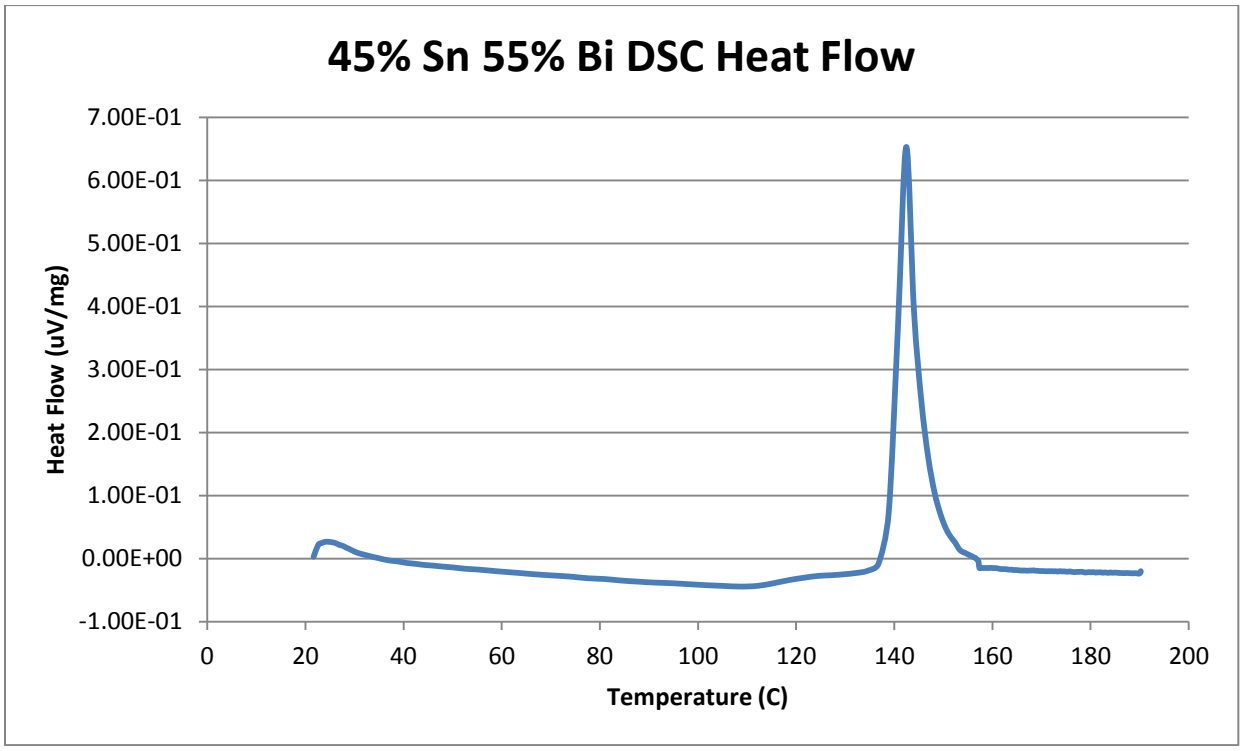

Figure 62- 45% Tin 55% Bismuth DSC Heat Flow

50% Tin 50% Bismuth

Actual Composition: 52.94% Sn, 47.06% Bi

Theoretical Solidus Line: 139 C
Theoretical Liquidus Line: 148.8 C

Experimental Solidus Line: 141.9 C
Experimental Liquidus Line: 151.5 C

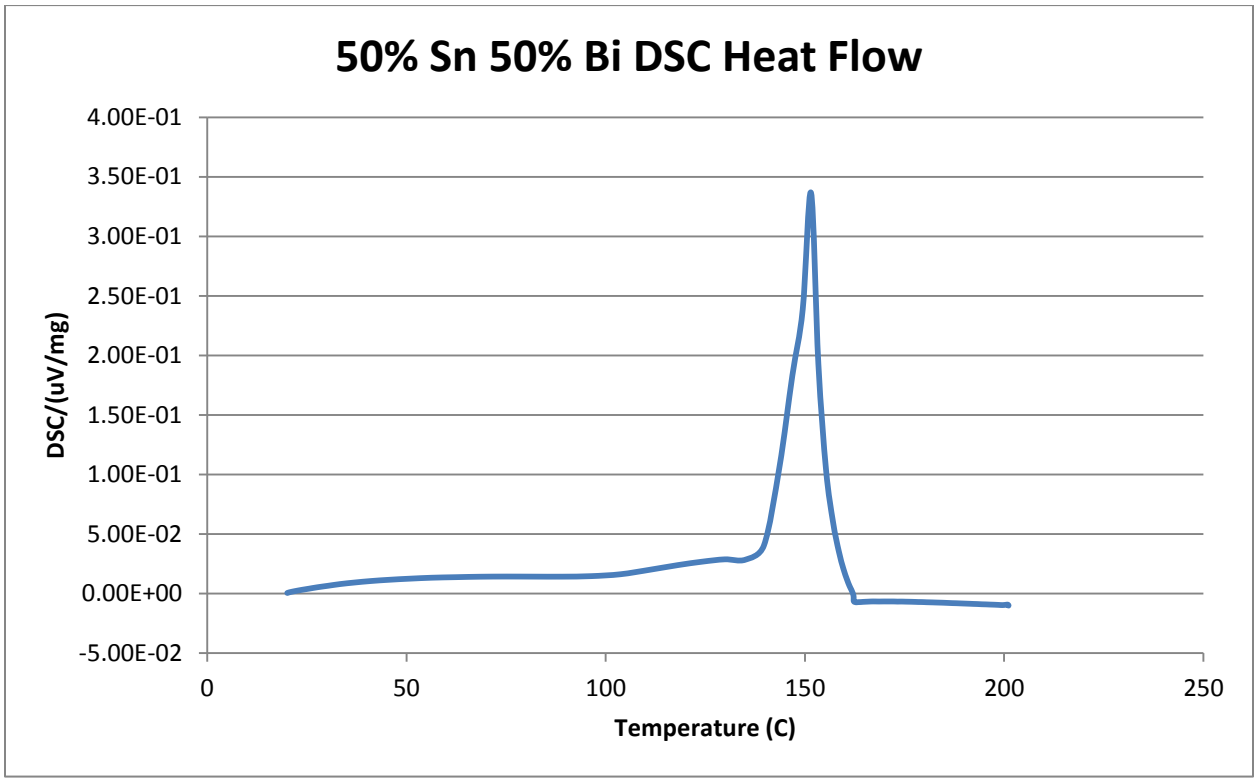

Figure 63- 50% Tin 50% Bismuth DSC Heat Flow

55% Tin 45% Bismuth

Expected Composition: 57% Sn, 43% Bi

Theoretical Solidus Line: 139 C
Theoretical Liquidus Line: 139 C

Experimental Solidus Line: 138.8 C
Experimental Liquidus Line: 143 C

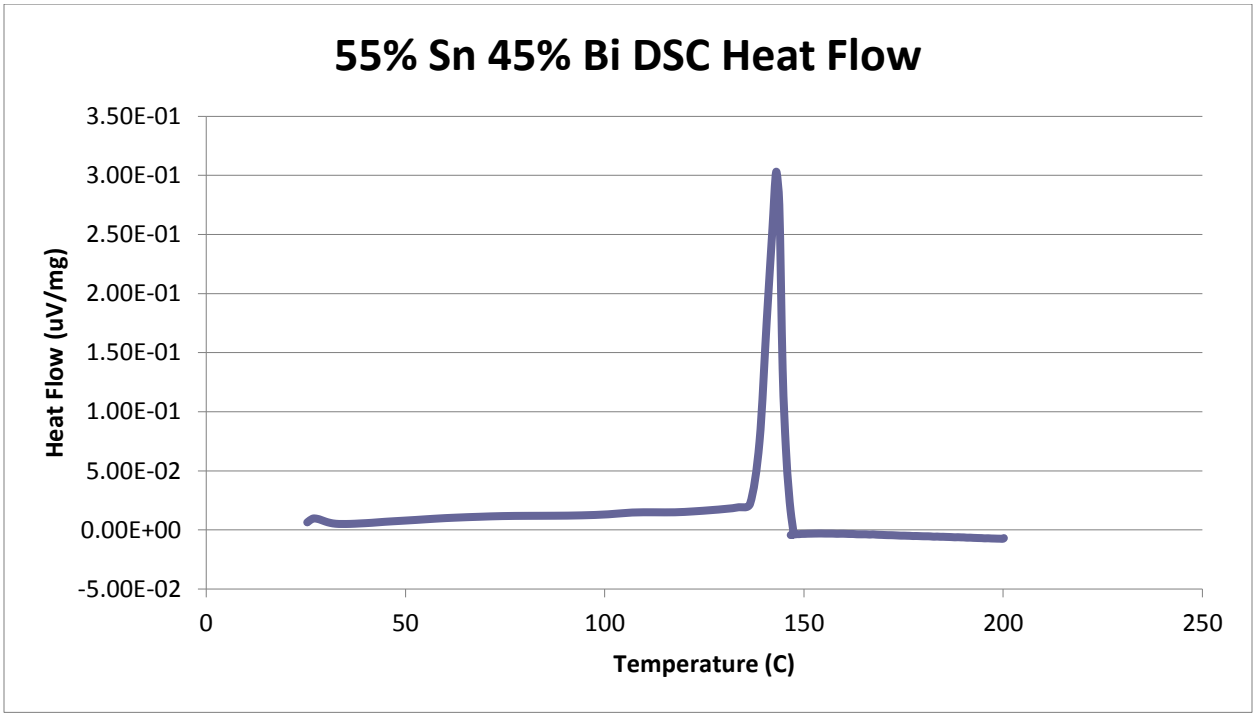

Figure 64- 55% Tin 45% Bismuth DSC Heat Flow

60% Tin 40% Bismuth

Expected Composition: 62.00% Sn, 38.00% Bi

Theoretical Solidus Line: 139 C
Theoretical Liquidus Line: 149.8 C

Experimental Solidus Line: 140.3 C
Experimental Liquidus Line: 147.0 C

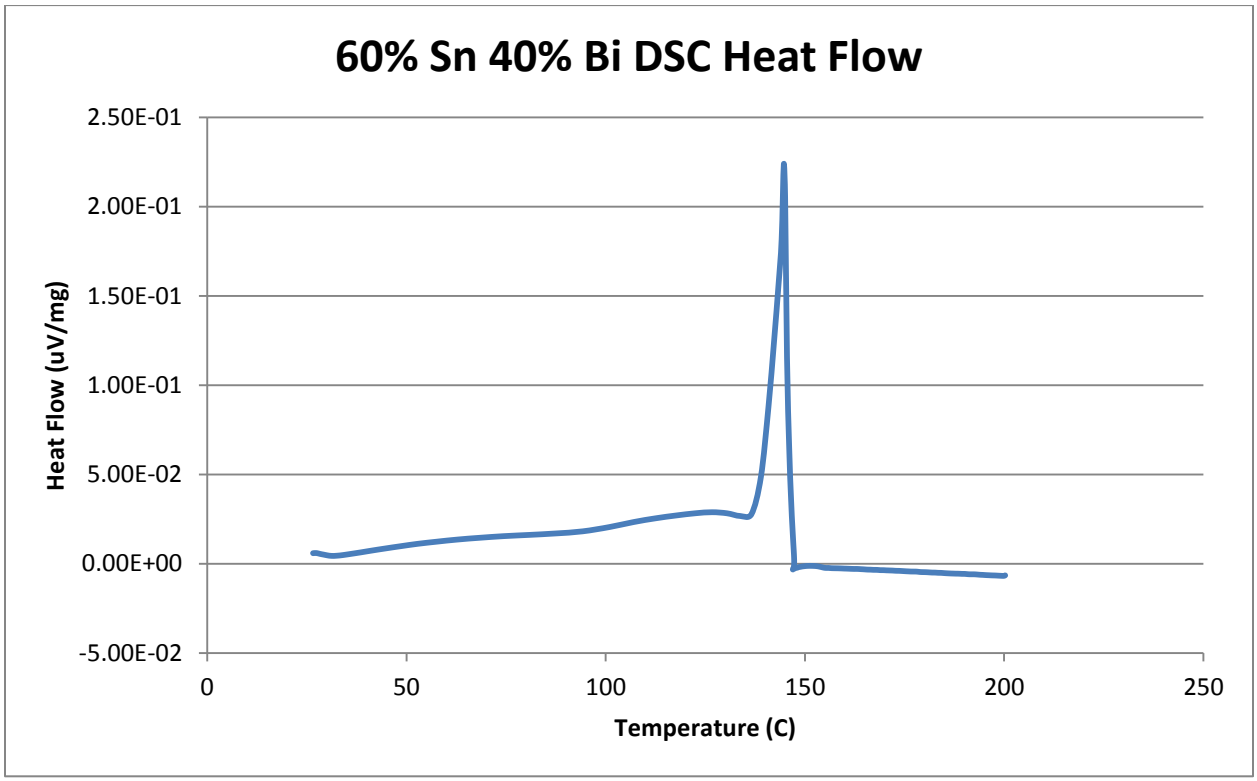

Figure 65- 60% Tin 40% Bismuth DSC Heat Flow

62.5% Tin 37.5% Bismuth

Expected Composition: 64.50% Sn, 35.50% Bi

Theoretical Solidus Line: 139 C
Theoretical Liquidus Line: 155.2 C

Experimental Solidus Line: 139.4 C
Experimental Liquidus Line: 156.5 C

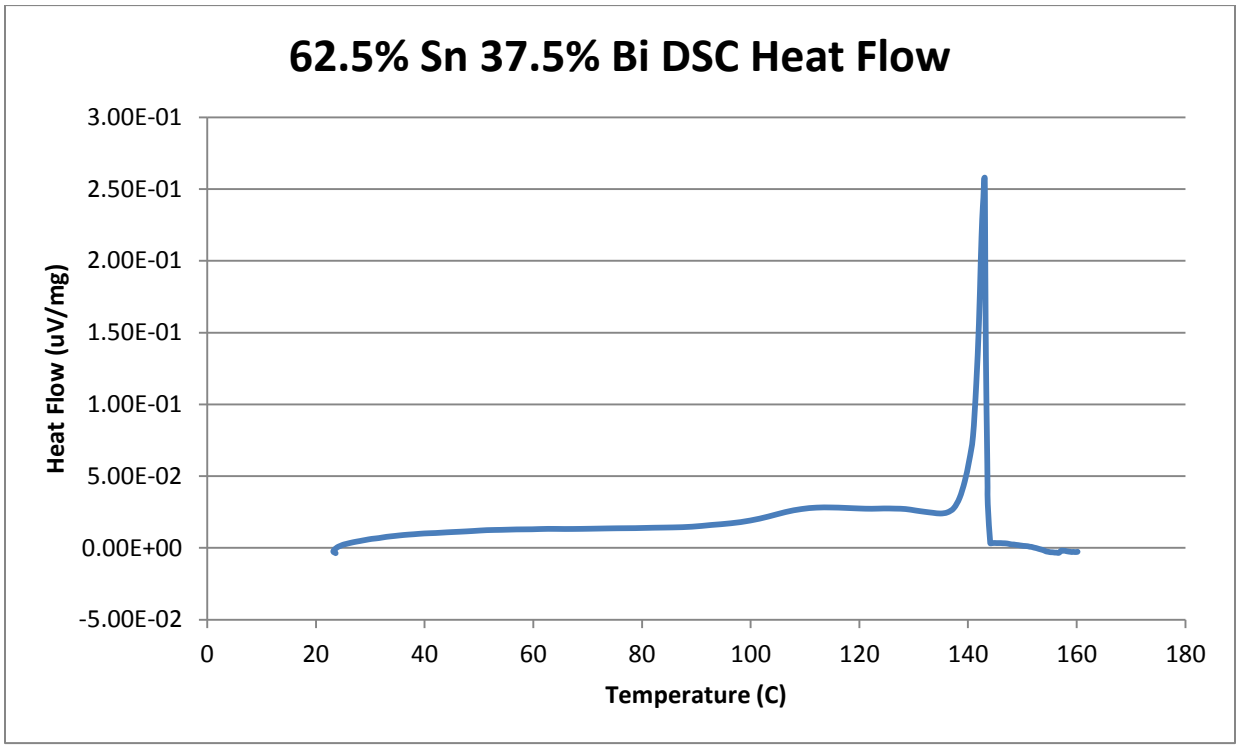

Figure 66- 62.5% Tin 37.5% Bismuth DSC Heat Flow

65% Tin 35% Bismuth

Predicted Composition: 67.00% Sn, 33.00% Bi

Theoretical Solidus Line: 139 C
Theoretical Liquidus Line: 160.6 C

Experimental Solidus Line: 137.9 C
Experimental Liquidus Line: 158.2 C

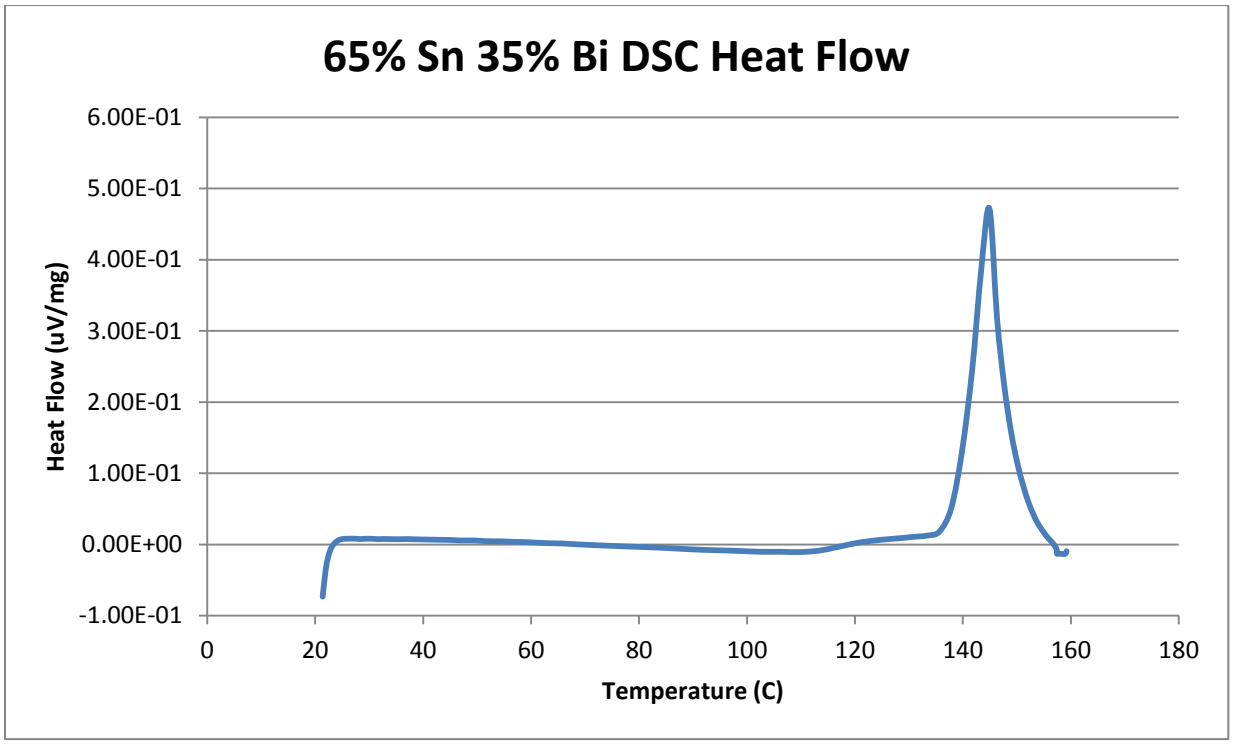

Figure 67- 65% Tin 35% Bismuth DSC Heat Flow

70% Tin 30% Bismuth

Actual Composition: 71.83% Sn, 28.17% Bi

Theoretical Solidus Line: 139 C
Theoretical Liquidus Line: 171.1 C

Experimental Solidus Line: 137.4 C
Experimental Liquidus Line: 169.9 C

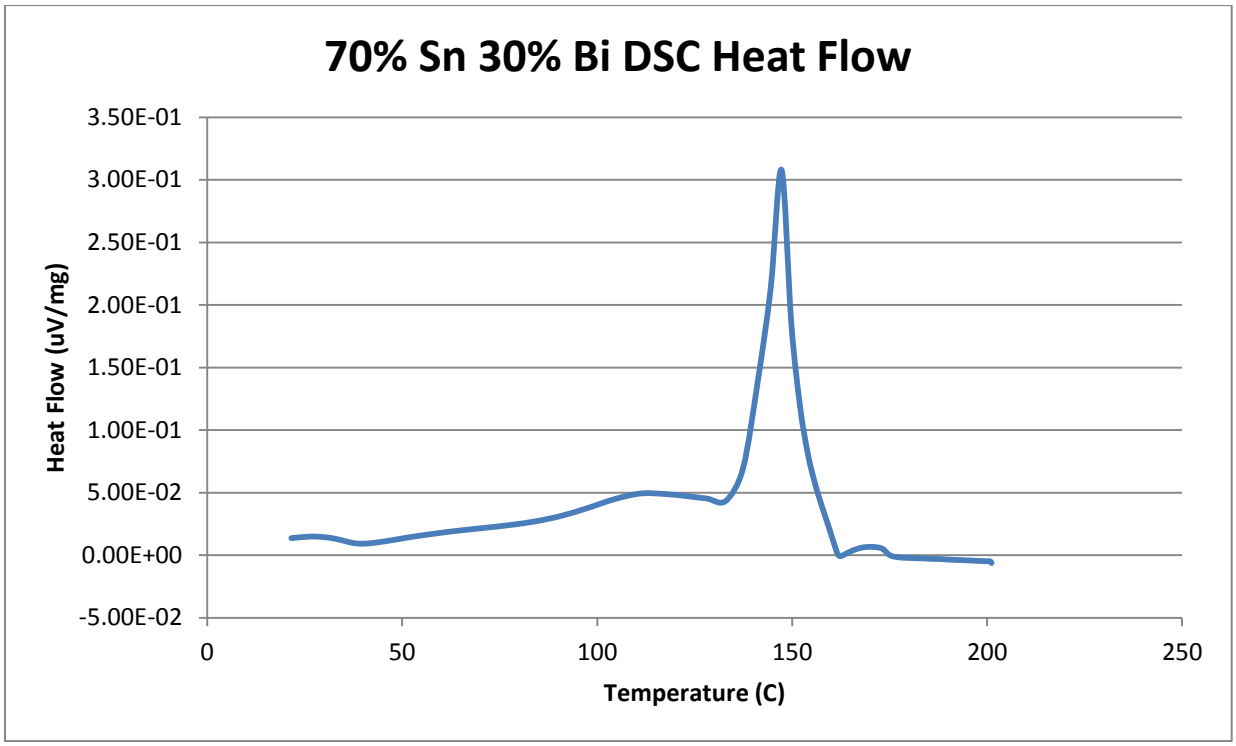

Figure 68- 70% Tin 30% Bismuth DSC Heat Flow

75% Tin 25% Bismuth

Predicted Composition: 75% Tin, 25% Bismuth

Theoretical Solidus Line: 139 C
Theoretical Liquidus Line: 182.2 C

Experimental Solidus Line: 138.9 C
Experimental Liquidus Line: 183.5 C

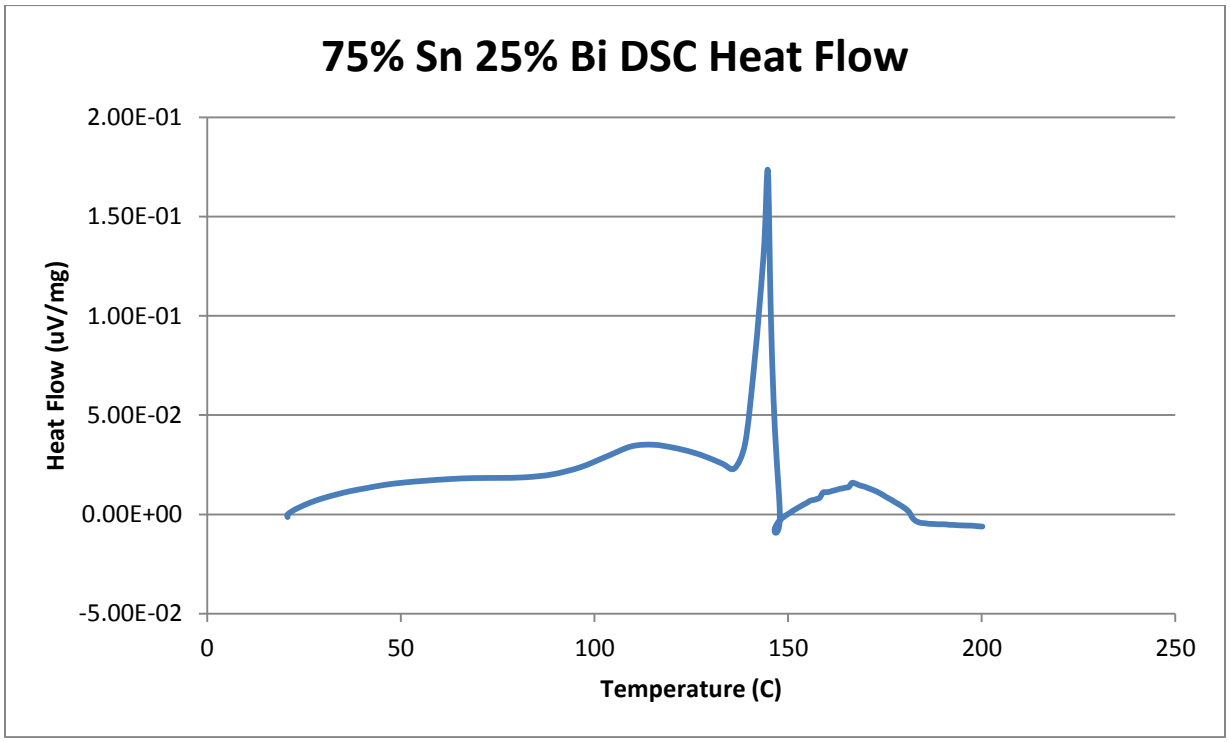

Figure 69- 75% Tin 25% Bismuth DSC Heat Flow

80% Tin 20% Bismuth

Actual Composition: 81.57% Sn, 18.43% Bi

Theoretical Solidus Line: 139 C
Theoretical Liquidus Line: 192.1 C

Experimental Solidus Line: 137.4 C
Experimental Liquidus Line: 185.9 C

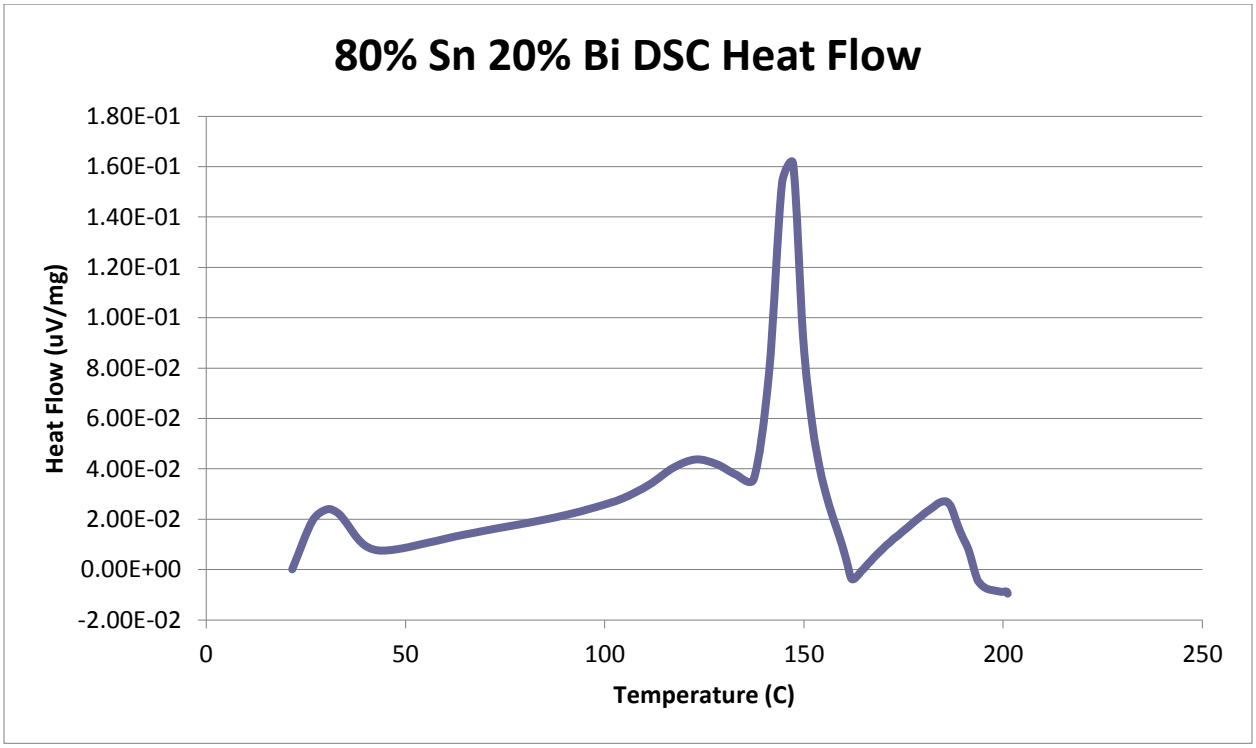

85% Tin 15% Bismuth

Predicted Composition: 87% Sn, 13% Bi

Theoretical Solidus Line: 139 C
Theoretical Liquidus Line: 203.9 C

Experimental Solidus Line: 140.3 C
Experimental Liquidus Line: 192.9 C

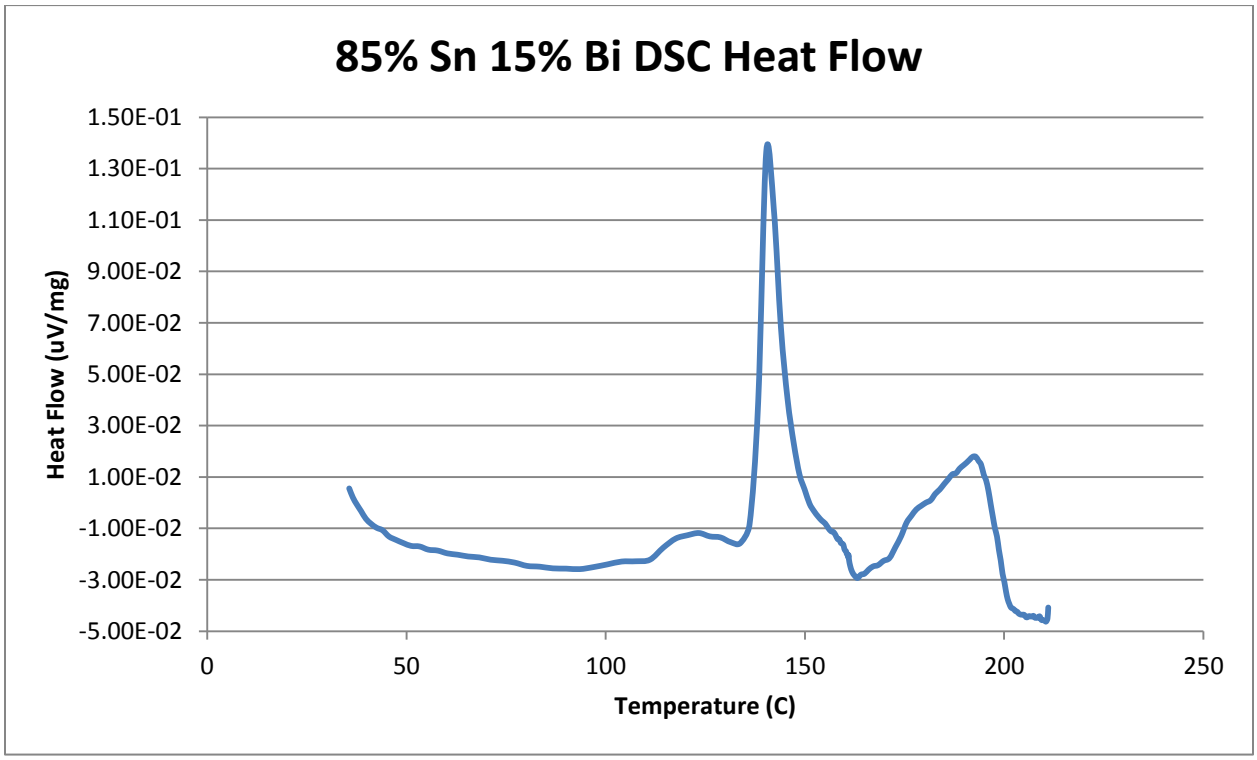

Figure 70- 85% Tin 15% Bismuth DSC Heat Flow

Appendix D- Cone and Plate Rheometer Data

Rheometer Notes

Rheometer: TA Instruments Cone and Plate Oscillatory Rheometer
Geometry: 40 mm diameter, 2 degree angle, steel
Analysis Software: Rheology Advantage

Material: Bismuth-Tin alloys

Note- ICP-MS tests were conducted on 5 of the bismuth-tin alloys. For the alloys that we tested, they on average had 2% more tin than we expected. Therefore, for any alloy without the ICP-MS test results, the expected composition was increased by 2% tin.

Forming the Ingots

- Atomic percents were used.
- Bismuth-tin samples were prepared from 325 mesh powders in a tube furnace with hydrogen gas flowing through it. No mechanical agitation was provided during the cooling process, so dendrites likely formed.
- The ratio of bismuth to tin was verified for some samples with ICP-MS and trace impurity analyses were conducted on some samples as well using GDMS.

Rheometer

- Rheometer was not in an inert environment, so oxidation was likely.
- The geometry gap was 55 μm above the Peltier stage. The cone was left at this distance for at least 5 minutes so that it would have the same temperature as the stage to prevent cooling the metal. The cone was then raised slightly so the material could be slid under.
- Oscillatory shear experiments were conducted from 1-5000 Pa. The experiment was stopped after the G'-G'' crossover point was reached to prevent liquid material from being ejected.
- A brief pre-shear step was conducted before each stress sweep to break the surface oxide layer.
- Before starting a stress sweep, the temperature was set and held for a minimum of 2 minutes.

Data Notes

- The crossover stress is the stress at which the storage and loss moduli intersect.
- The plateau stress is the flat portion of the curve for the storage and loss moduli.
- Red cells in the data tables denote a poor fit on the viscosity curves.

40% Tin 60% Bismuth

Predicted Composition: 42.00% Sn, 58.00% Bi

Theoretical Solidus Line: 139 C
Theoretical Liquidus Line: 173.9 C

Experimental Solidus Line: 139.6 C
Experimental Liquidus Line: 177.3 C

Set-Up Notes

- For temperatures from 165-185 C, the stage was heated to 165 Celsius and the metal pieces were melted underneath the cone. The cone was then lowered to the geometry gap. Then the temperature was increased in 5 C increments.

- For temperatures from 145-160 C, the stage was lowered to 160 Celsius and the metal pieces were melted underneath the cone. The cone was then lowered to the geometry gap. Then the temperature was decreased in 5 C increments.

Plots

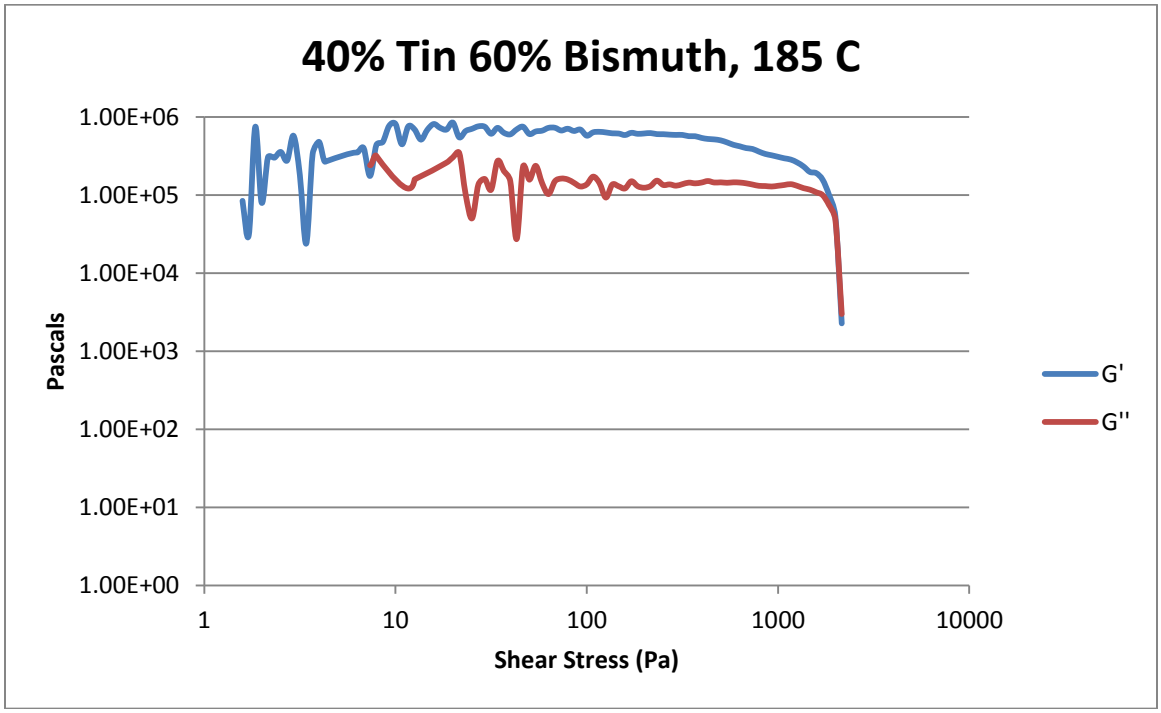

Figure 71- 40% Sn 60% Bi, 185 C, Cone and Plate Stress Sweep

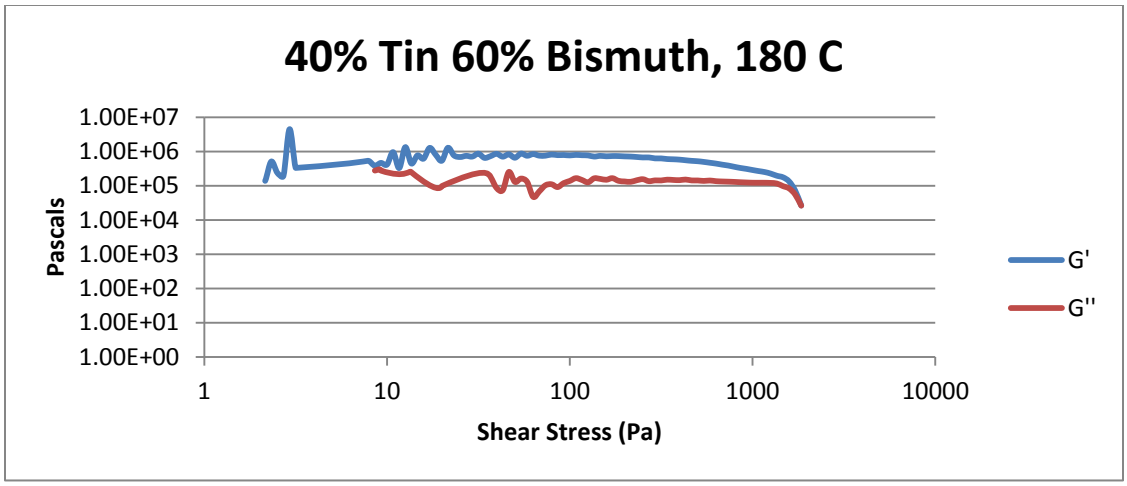

Figure 72- 40% Sn 60% Bi, 180 C, Cone and Plate Stress Sweep

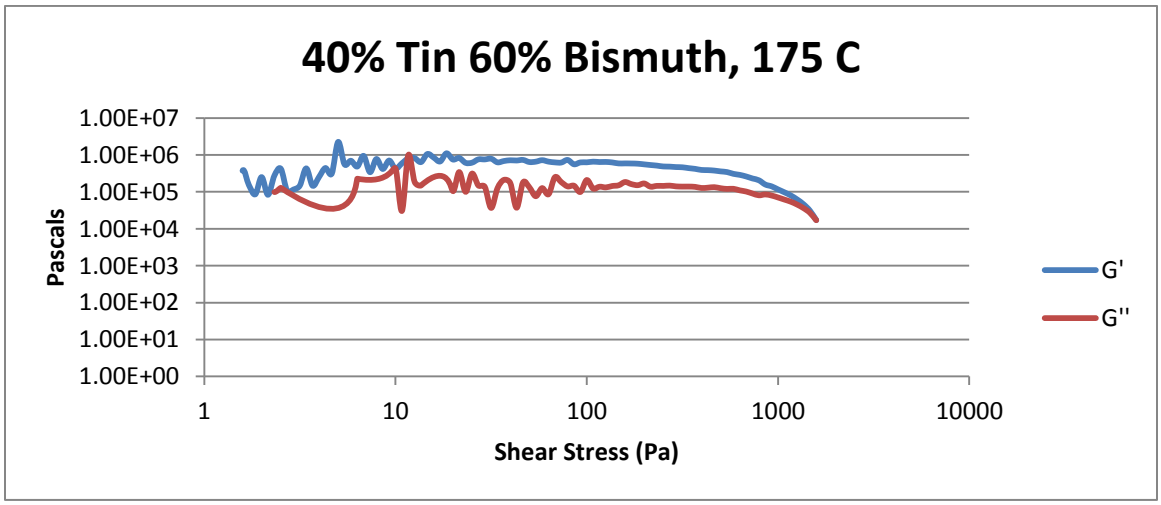

Figure 73- 40% Sn 60% Bi, 175 C, Cone and Plate Stress Sweep

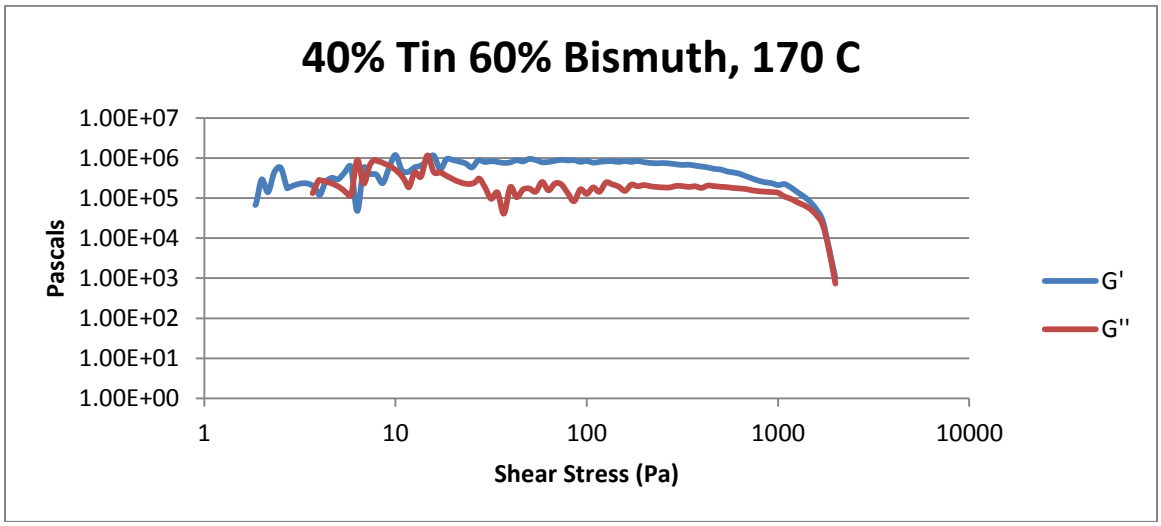

Figure 74- 40% Sn 60% Bi, 170 C, Cone and Plate Stress Sweep

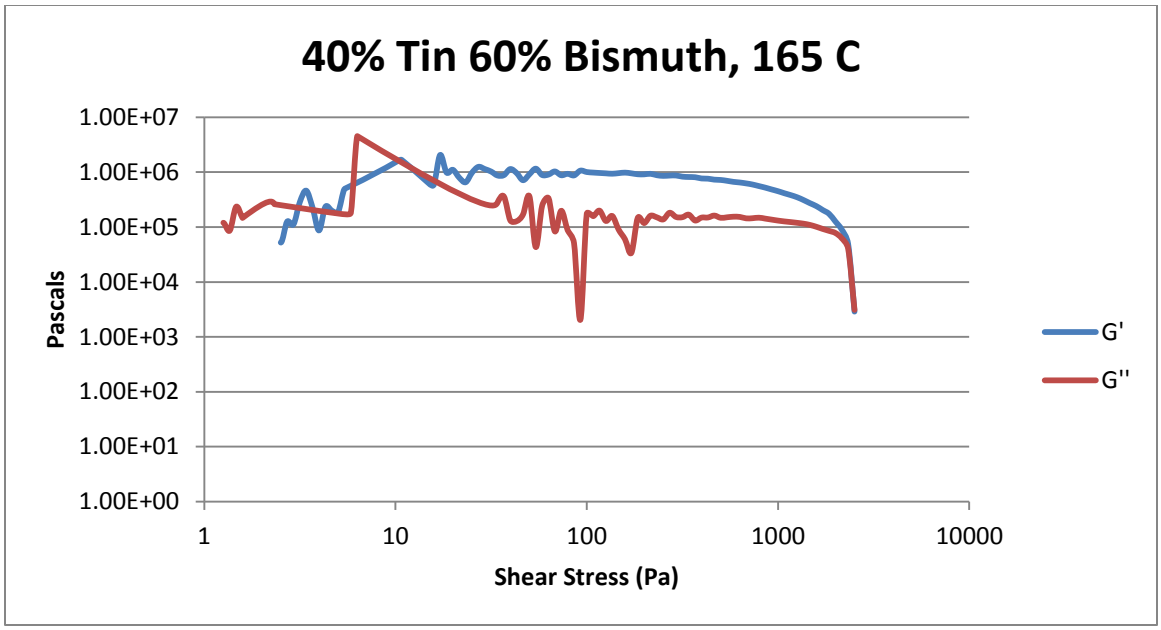

Figure 75- 40% Sn 60% Bi, 165 C, Cone and Plate Stress Sweep

Temperature	Crossover Stress (Pa)	Crossover Stress (PSI)
165 C	$4.00 * 10^4$	5.80
170 C	$2.80 * 10^4$	4.06
175 C	$3.03 * 10^4$	4.39
180 C	$2.62 * 10^4$	3.80
185 C	$8.17 * 10^3$	1.18

Table 8- 40% Sn 60% Bi, Cone and Plate Crossover Stresses

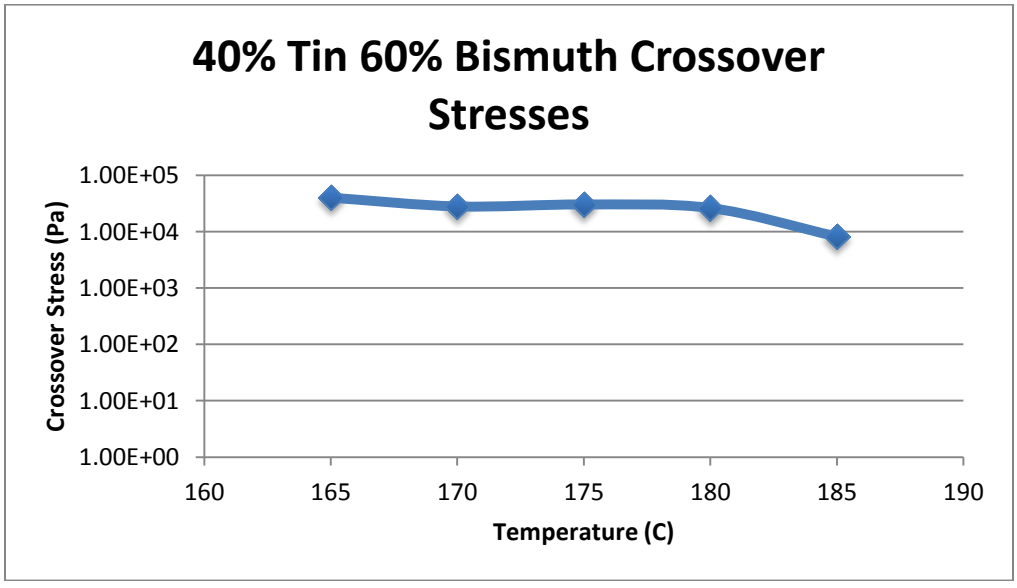

Table 9- 40% Sn 60% Bi, Cone and Plate Crossover Stresses

Temperature	Fraction Solid (At %)	G' Plateau (Pa)	G'' Plateau (Pa)
165 C	18.1	$9.63 * 10^5$	$1.48 * 10^5$
170 C	13.9	$8.17 * 10^5$	$1.94 * 10^5$
175 C	9.10	$6.46 * 10^5$	$1.44 * 10^5$
180 C	3.86	$7.64 * 10^5$	$1.42 * 10^5$
185 C	2.41	$6.19 * 10^5$	$1.37 * 10^5$

Table 10- 40% Sn 60% Bi, Cone and Plate Plateau Stresses

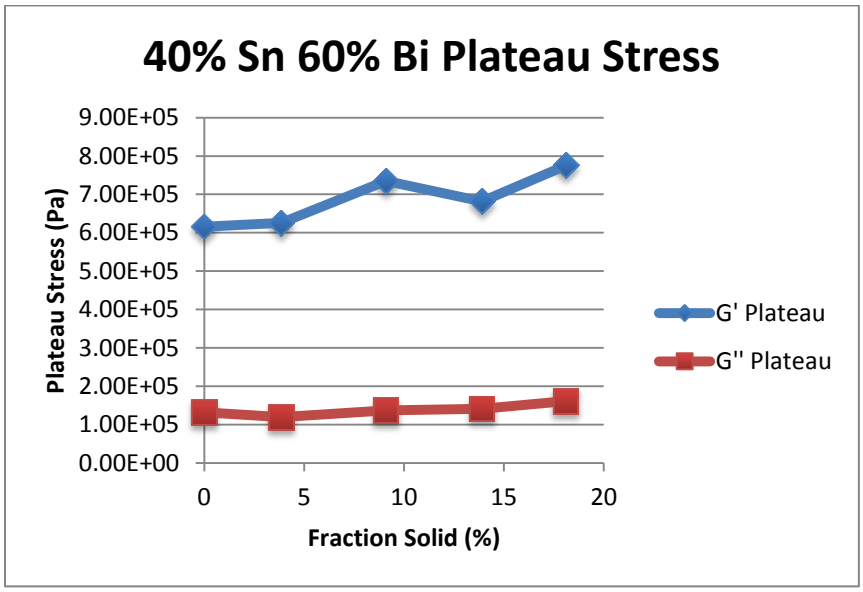

Figure 76- 40% Sn 60% Bi, Cone and Plate Plateau Stresses vs. Fraction Solid

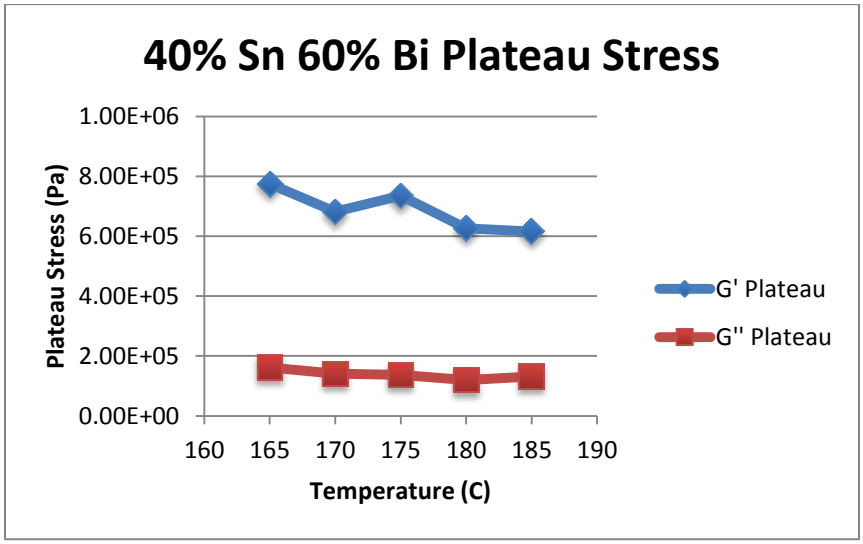

Figure 77- 40% Sn 60% Bi, Cone and Plate Plateau Stresses vs. Temperature

40% Sn 60% Bi Viscosity					
Temperature	**Fraction Solid**	**Power Law**	**K**	**n**	**R^2**
165 C	18.1 %	$\tau = 7.55 * 10^{-4} * \dot{\gamma}^{0.2718}$ $\mu = 2.05 * 10^{-4} * \dot{\gamma}^{-0.7282}$	$7.55 * 10^{-4}$	0.2718	98.62 %
170 C	13.9 %	$\tau = 4.53 * 10^{-4} * \dot{\gamma}^{0.3016}$ $\mu = 1.37 * 10^{-4} * \dot{\gamma}^{-0.6984}$	$4.53 * 10^{-4}$ Pa*s	0.3016	97.45 %
175 C	9.1 %	$\tau = 3.56 * 10^{-4} * \dot{\gamma}^{0.2868}$ $\mu = 1.02 * 10^{-4} * \dot{\gamma}^{-0.7132}$	$3.56 * 10^{-4}$ Pa*s	0.2868	96.39 %
180 C	3.86 %	$\tau = 7.25 * 10^{-4} * \dot{\gamma}^{0.3115}$ $\mu = 2.26 * 10^{-4} * \dot{\gamma}^{-0.6885}$	$7.25 * 10^{-4}$ Pa*s	0.3115	98.27 %
185 C	2.41 %	$\tau = 1.22 * 10^{-3} * \dot{\gamma}^{0.3954}$ $\mu = 4.82 * 10^{-4} * \dot{\gamma}^{-0.6046}$	$1.22 * 10^{-3}$ Pa*s	0.3954	95.14 %

Table 11- 40% Sn 60% Bi, Cone and Plate Viscosity

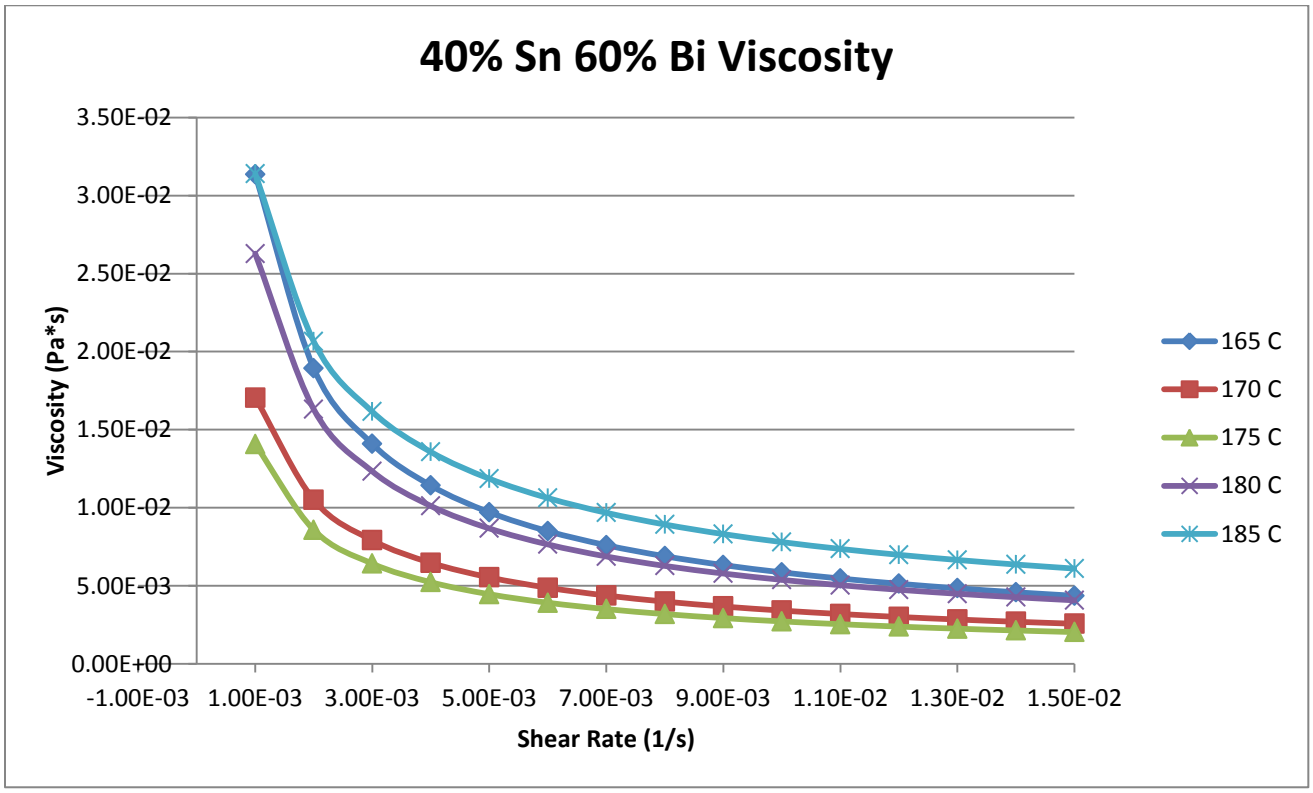

Figure 78- 40% Sn 60% Bi, Cone and Plate Viscosity

165 C

Fraction Solid	18.1%
Power Law	$\tau = 7.55 * 10^{-4} * \dot{\gamma}^{0.2718}$
	$\mu = 2.05 * 10^{-4} * \dot{\gamma}^{-0.7282}$
R^2	98.62 %

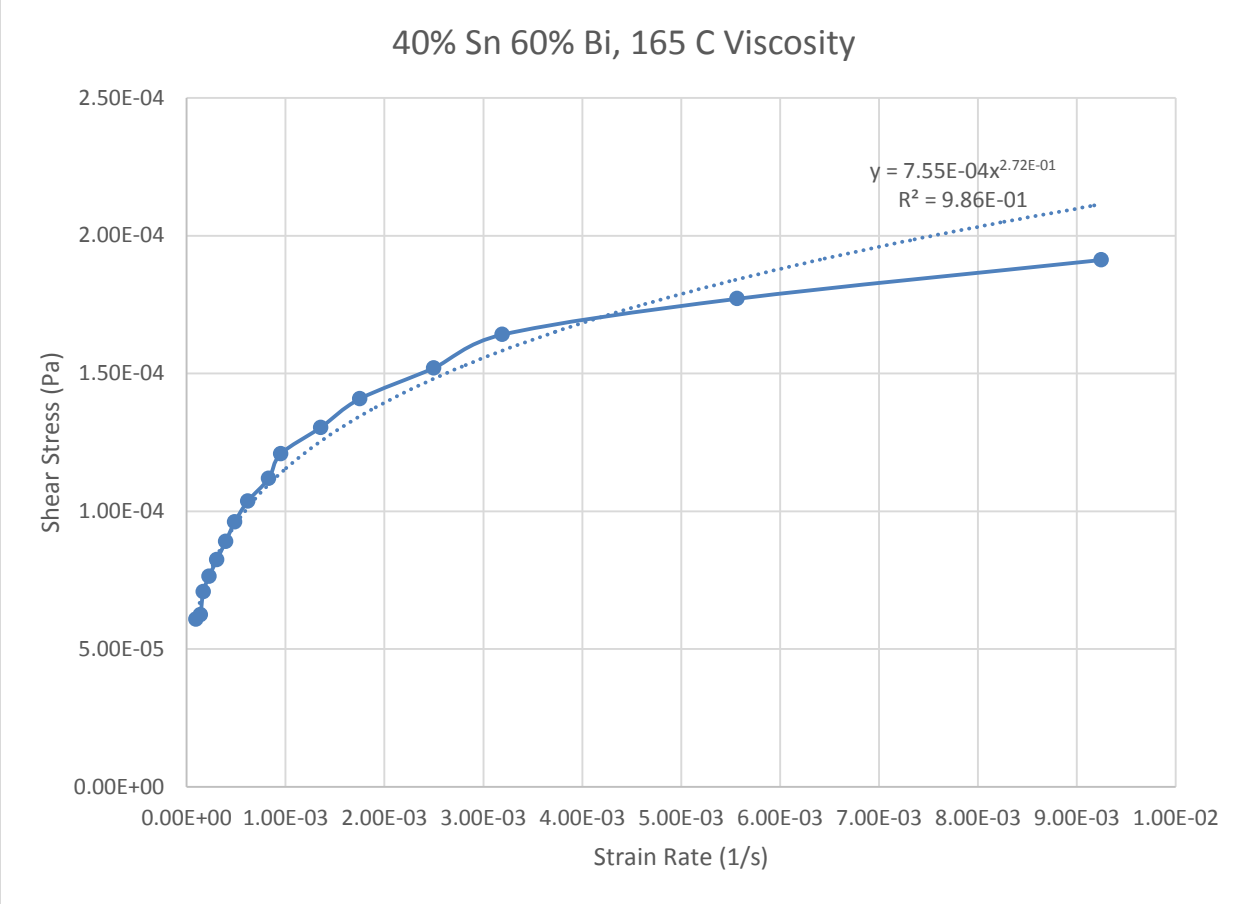

Figure 79- 40% Sn 60% Bi, 165 C, Cone and Plate Viscosity

170 C

Fraction Solid	13.9 %
Power Law	$\tau = 4.53 * 10^{-4} * \dot{\gamma}^{0.3016}$
	$\mu = 1.37 * 10^{-4} * \dot{\gamma}^{-0.6984}$
R^2	97.45 %

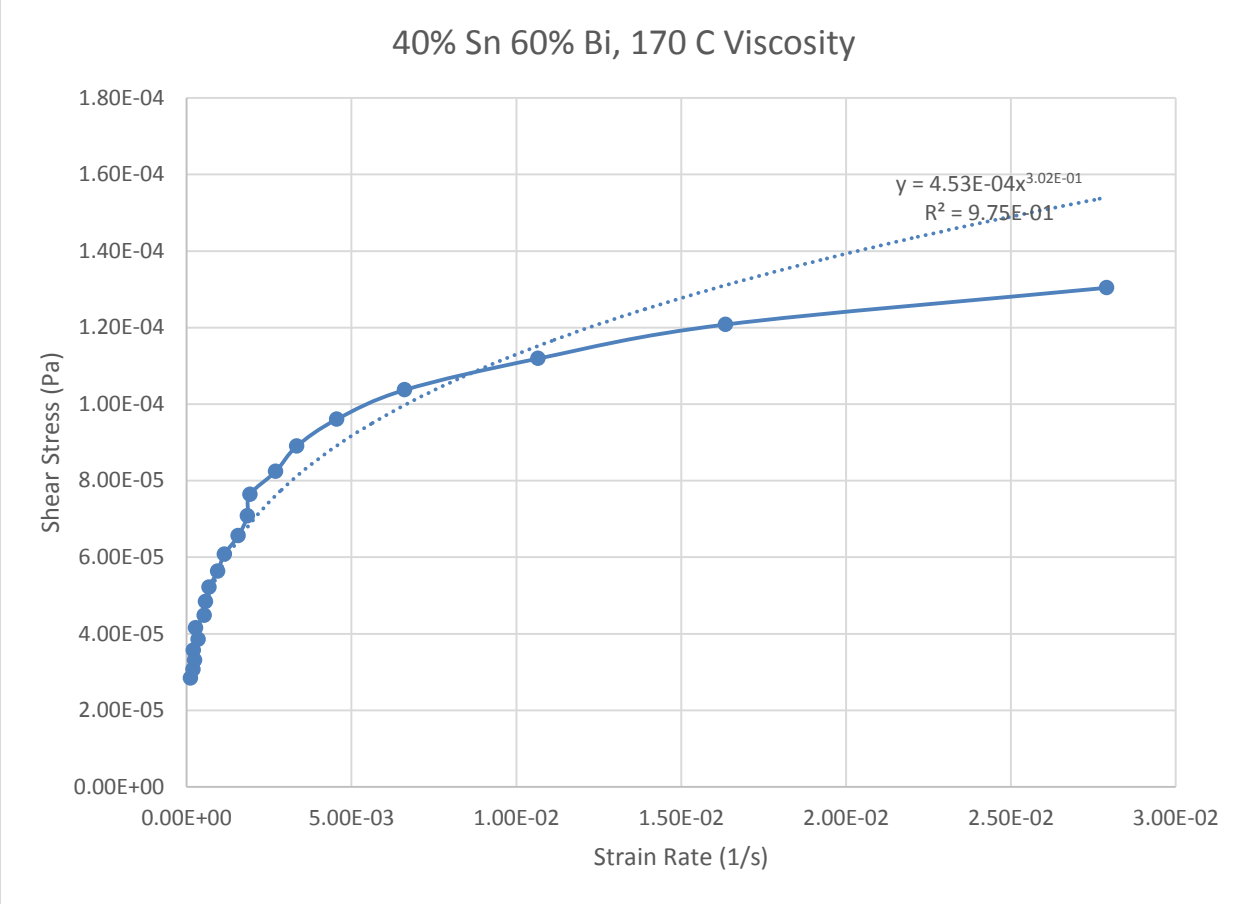

Figure 80- 40% Sn 60% Bi, 170 C, Cone and Plate Viscosity

175 C

Fraction Solid	9.1 %
Power Law	$\tau = 3.56 * 10^{-4} * \dot{\gamma}^{0.2868}$
	$\mu = 1.02 * 10^{-4} * \dot{\gamma}^{-0.7132}$
R^2	96.39 %

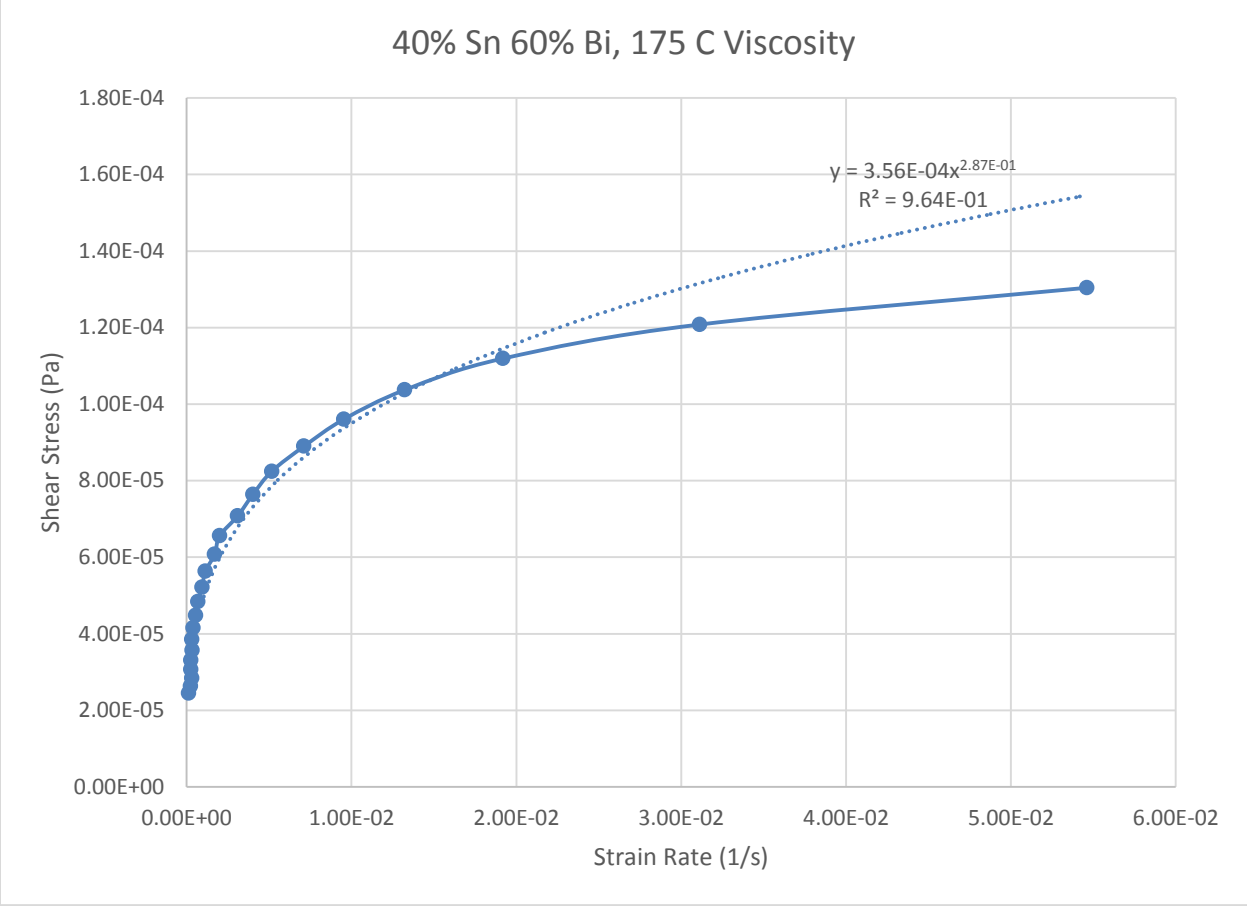

Figure 81- 40% Sn 60% Bi, 175 C, Cone and Plate Viscosity

180 C

Fraction Solid	3.86 %
Power Law	$\tau = 7.25 * 10^{-4} * \dot{\gamma}^{0.3115}$
	$\mu = 2.26 * 10^{-4} * \dot{\gamma}^{-0.6885}$
R^2	98.27 %

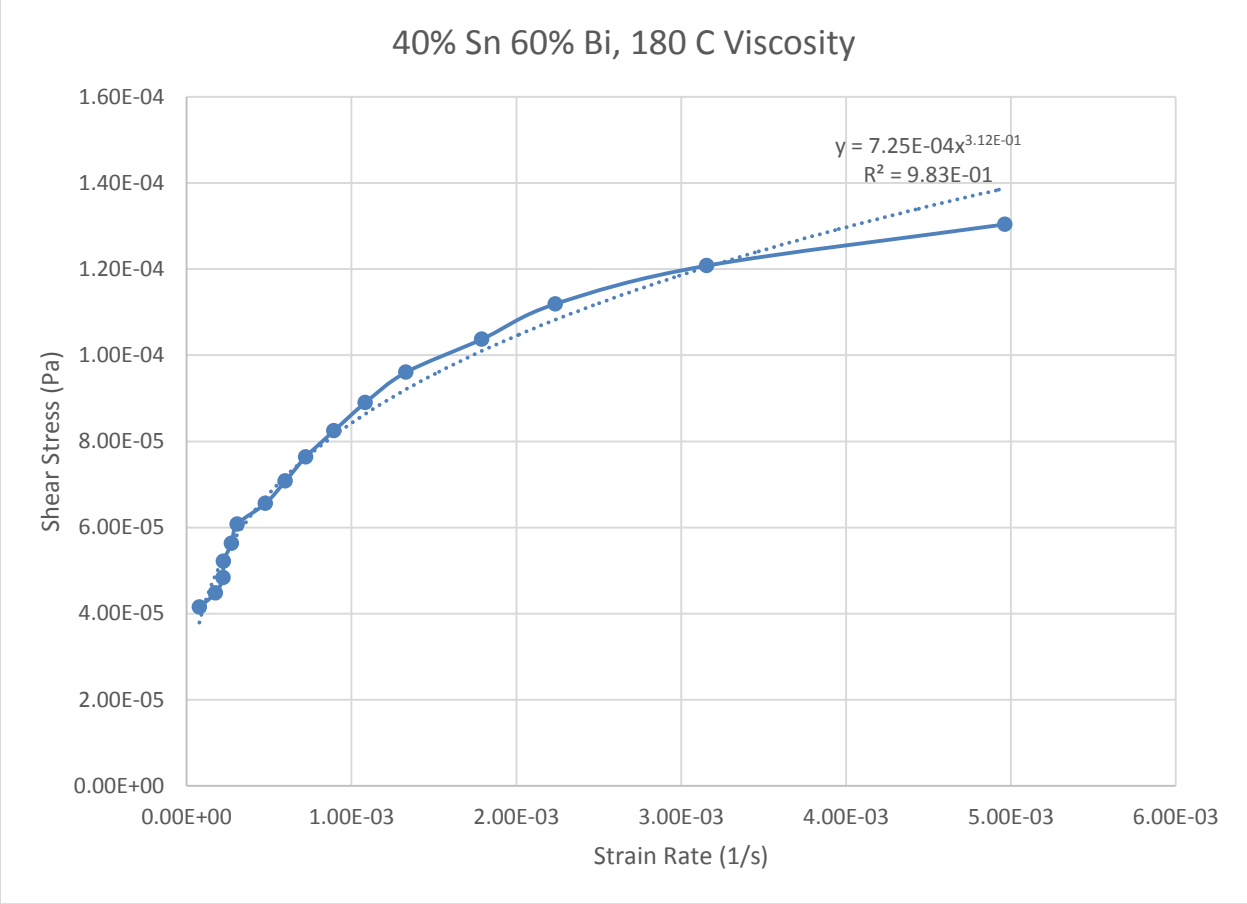

Figure 82- 40% Sn 60% Bi, 180 C, Cone and Plate Viscosity

185 C

Fraction Solid	2.41 %
Power Law	$\tau = 1.22 * 10^{-3} * \dot{\gamma}^{0.3954}$
	$\mu = 4.82 * 10^{-4} * \dot{\gamma}^{-0.6046}$
R^2	*95.14 %*

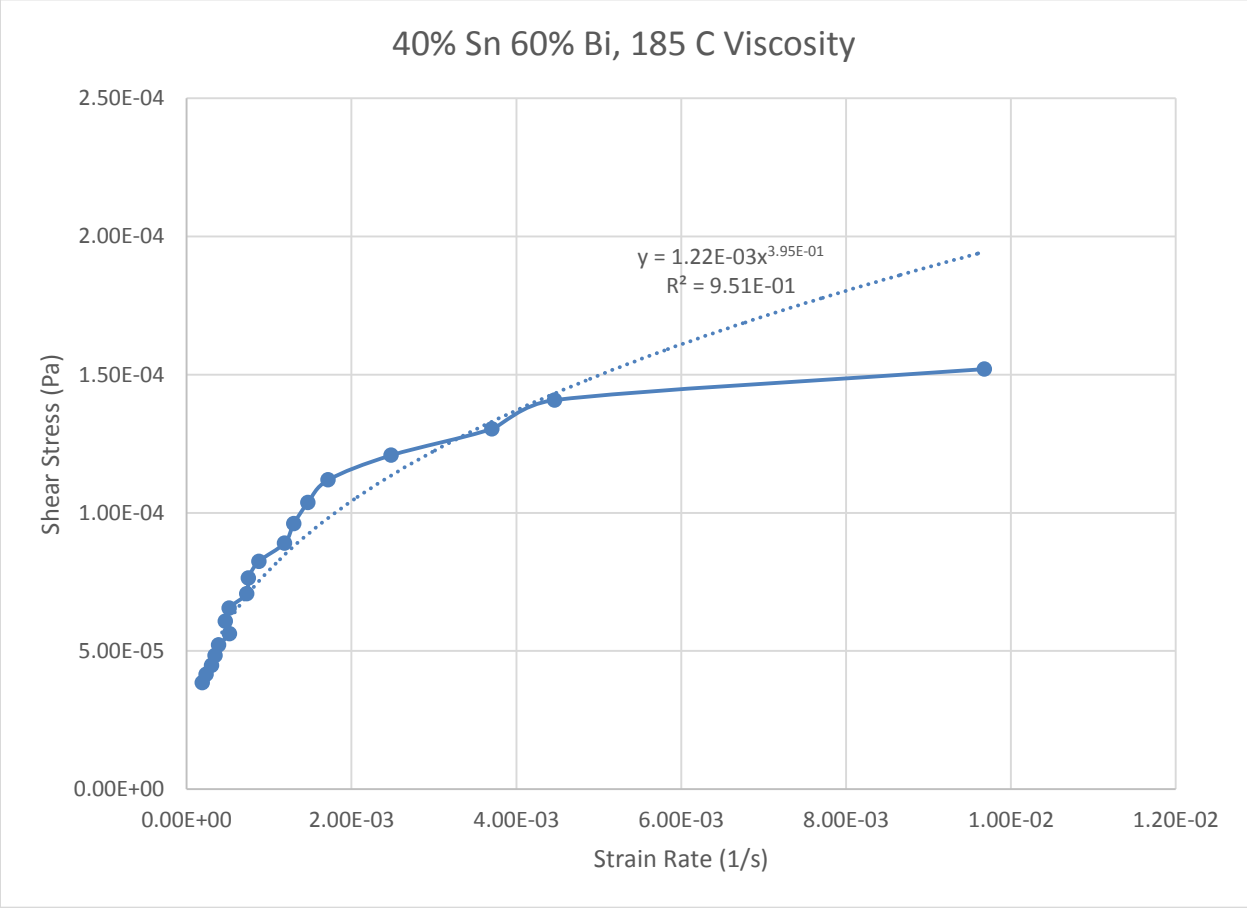

Figure 83- 40% Sn 60% Bi, 185 C, Cone and Plate Viscosity

45% Tin 55% Bismuth (Run 1)

Expected Composition: 47% Tin, 53% Bismuth

Theoretical Solidus Line: 139 C
Theoretical Liquidus Line: 159.7 C

Experimental Solidus Line: 138.9 C
Experimental Liquidus Line: 162.2 C

Set-Up Notes

- Semi-solid was difficult to get to stay under cone
- Zeroed gap at 160 C. Stress sweeps were conducted from 160 C to 145 C with temperature decreasing by 5 C after each run. Then the temperature was raised to 165 C and a stress sweep was conducted. The temperature was then raised in 5 C increments.
- Black powder remained on the stage (bismuth?)
- Black spots seemed to solidify at a much slower rate than the tin

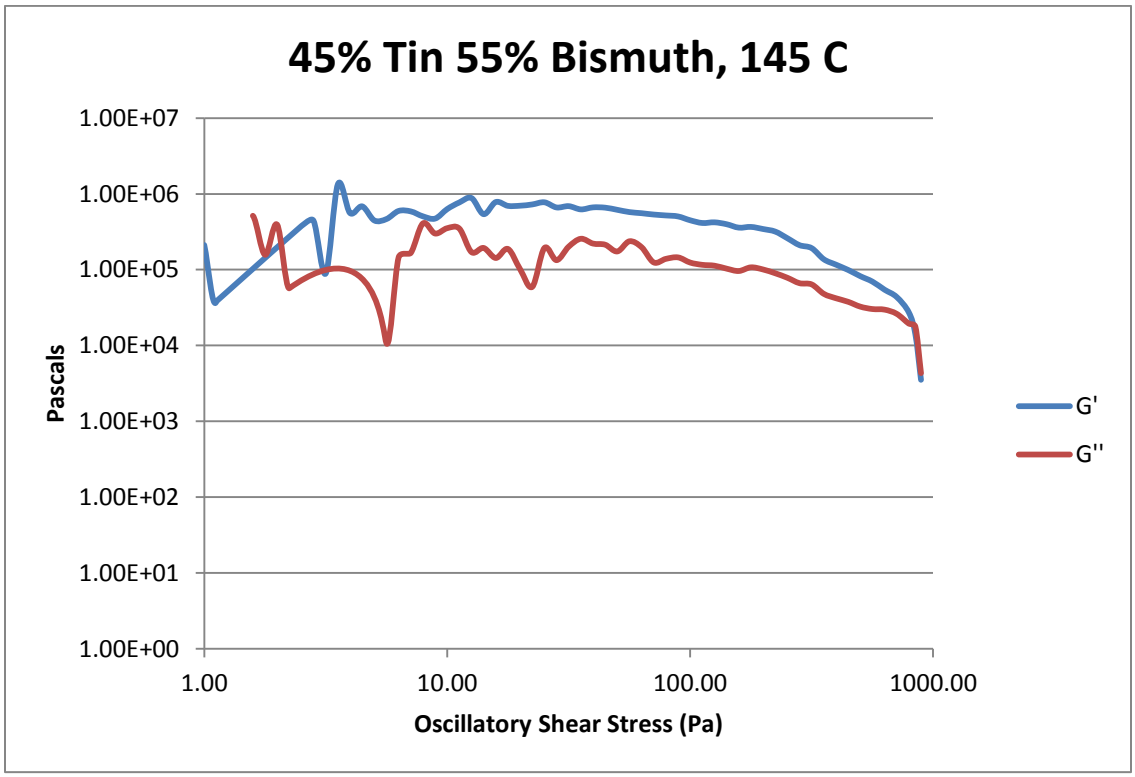

Figure 84- 45% Sn 55% Bi (Run 1), 145 C, Cone and Plate Stress Sweep

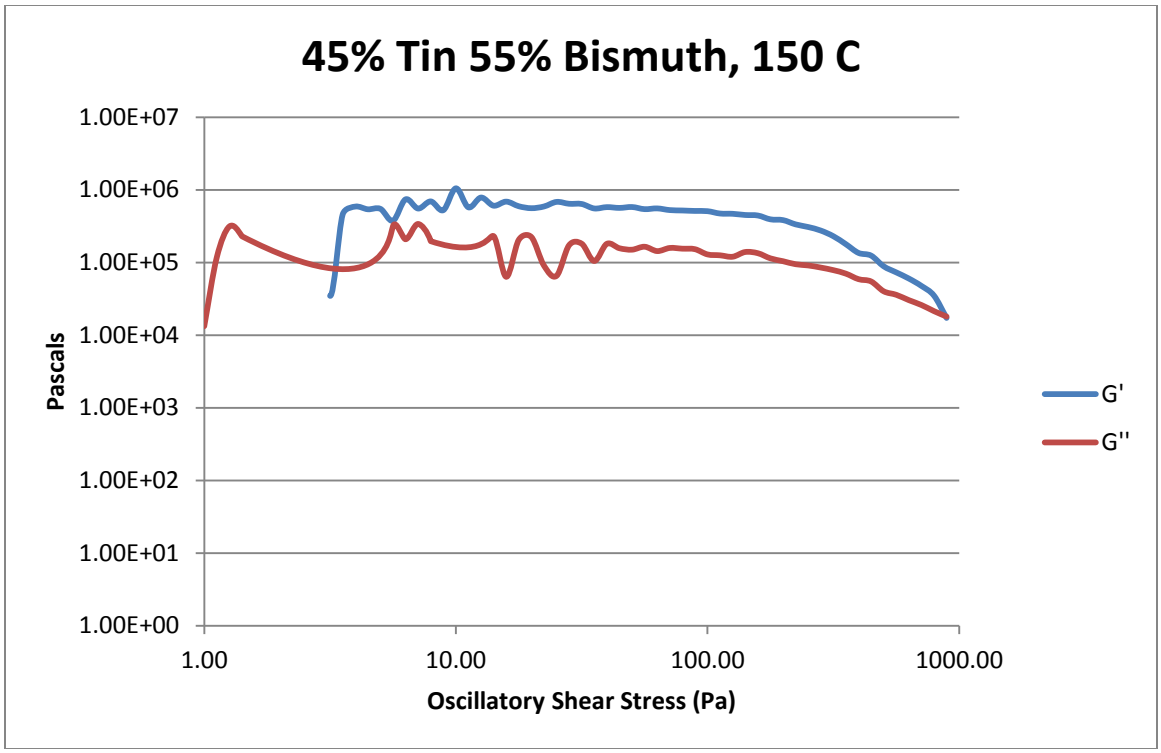

Figure 85- 45% Sn 55% Bi (Run 1), 150 C, Cone and Plate Stress Sweep

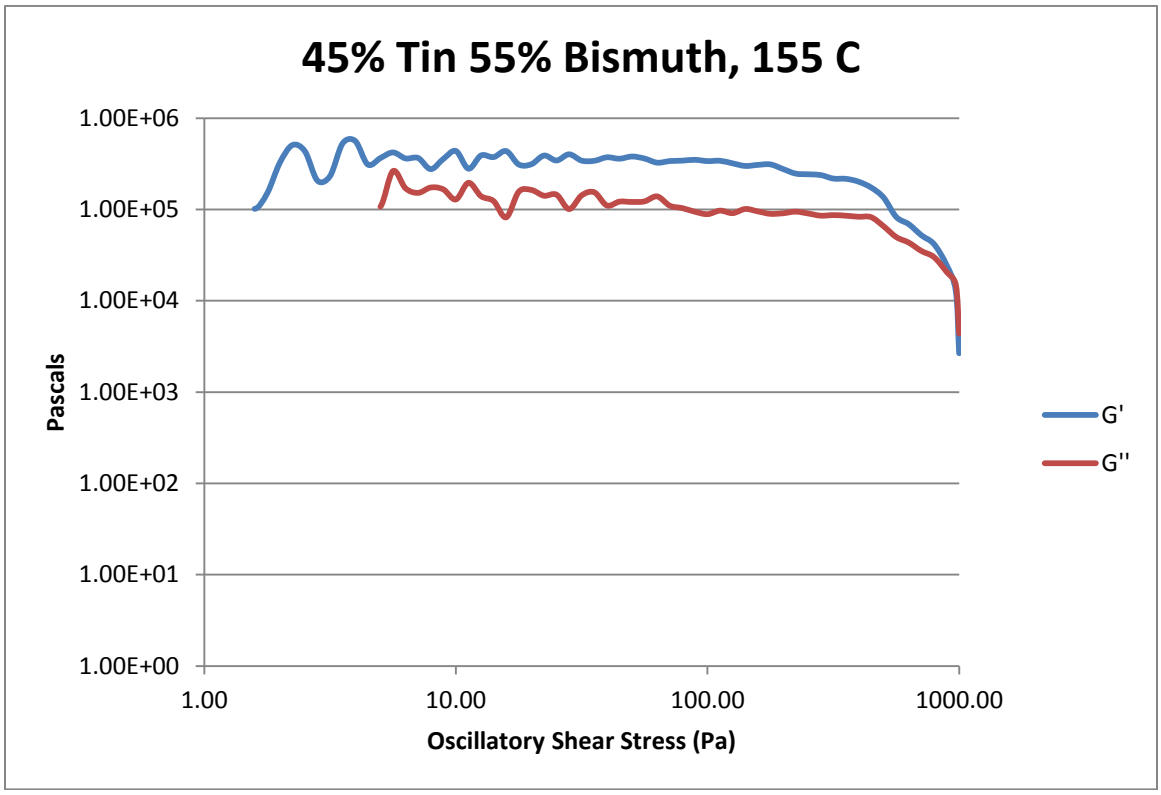

Figure 86- 45% Sn 55% Bi (Run 1), 155 C, Cone and Plate Stress Sweep

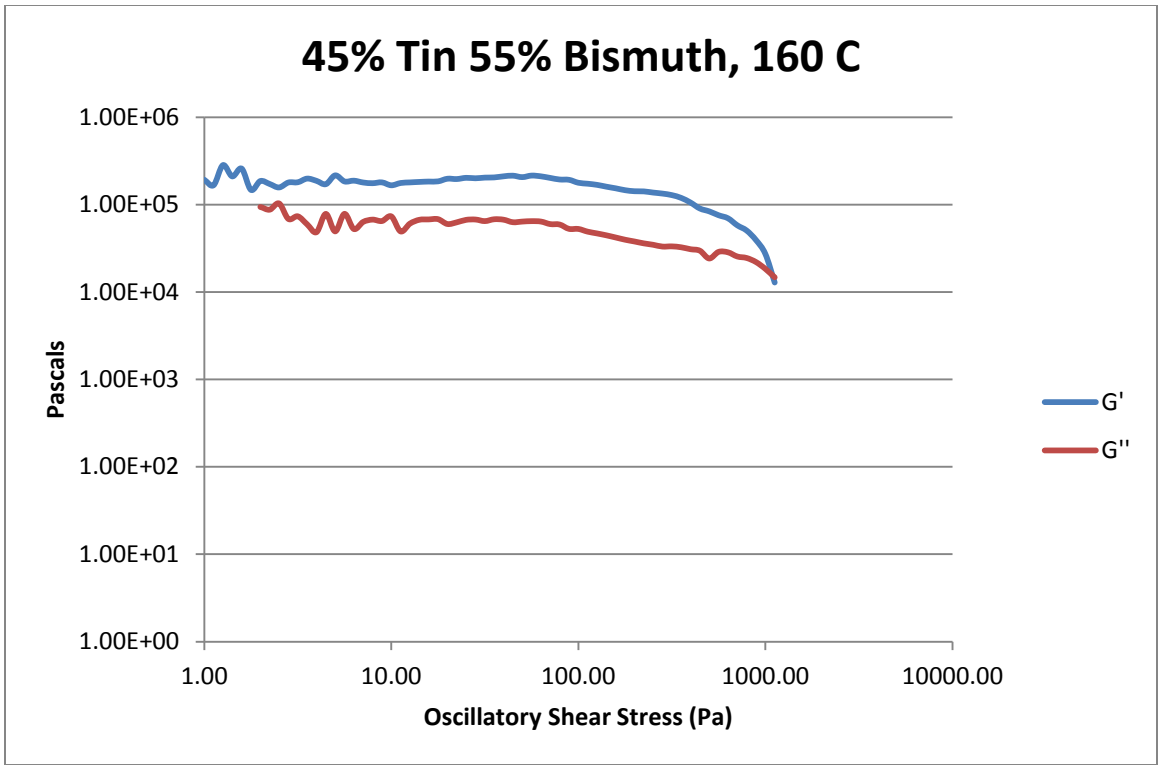

Figure 87- 45% Sn 55% Bi (Run 1), 160 C, Cone and Plate Stress Sweep

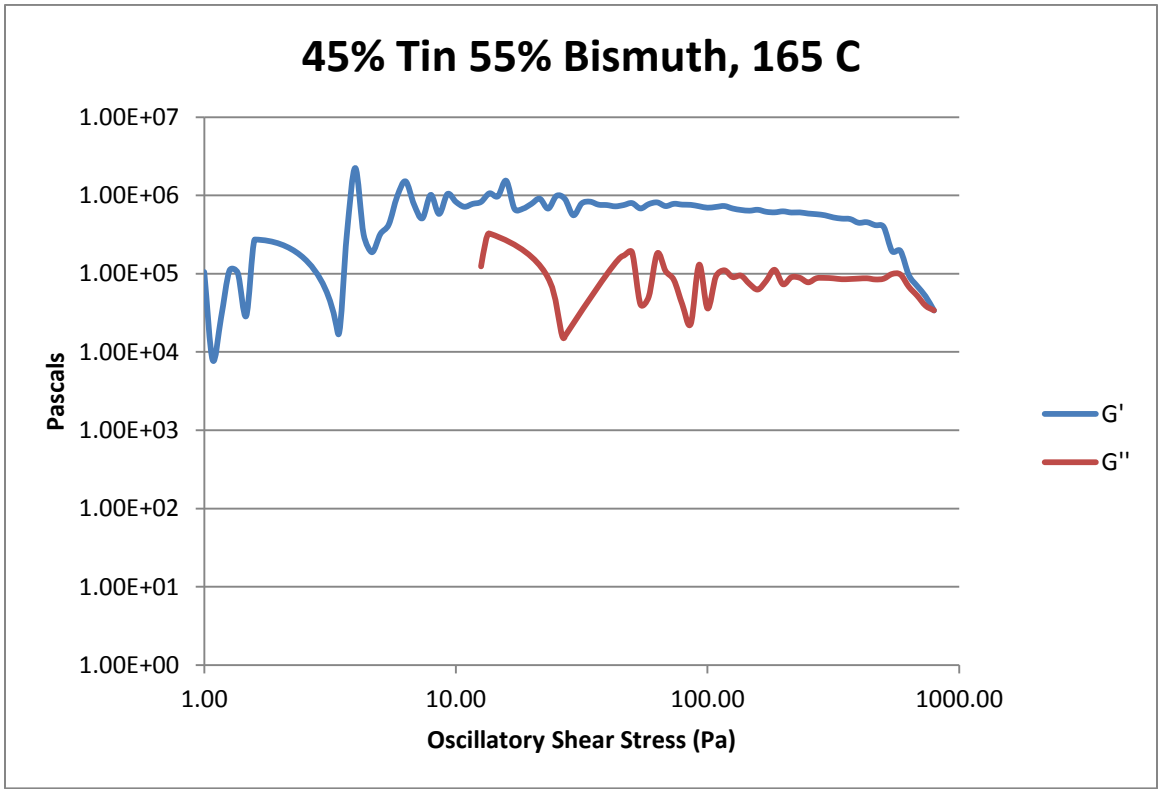

Figure 88- 45% Sn 55% Bi (Run 1), 165 C, Cone and Plate Stress Sweep

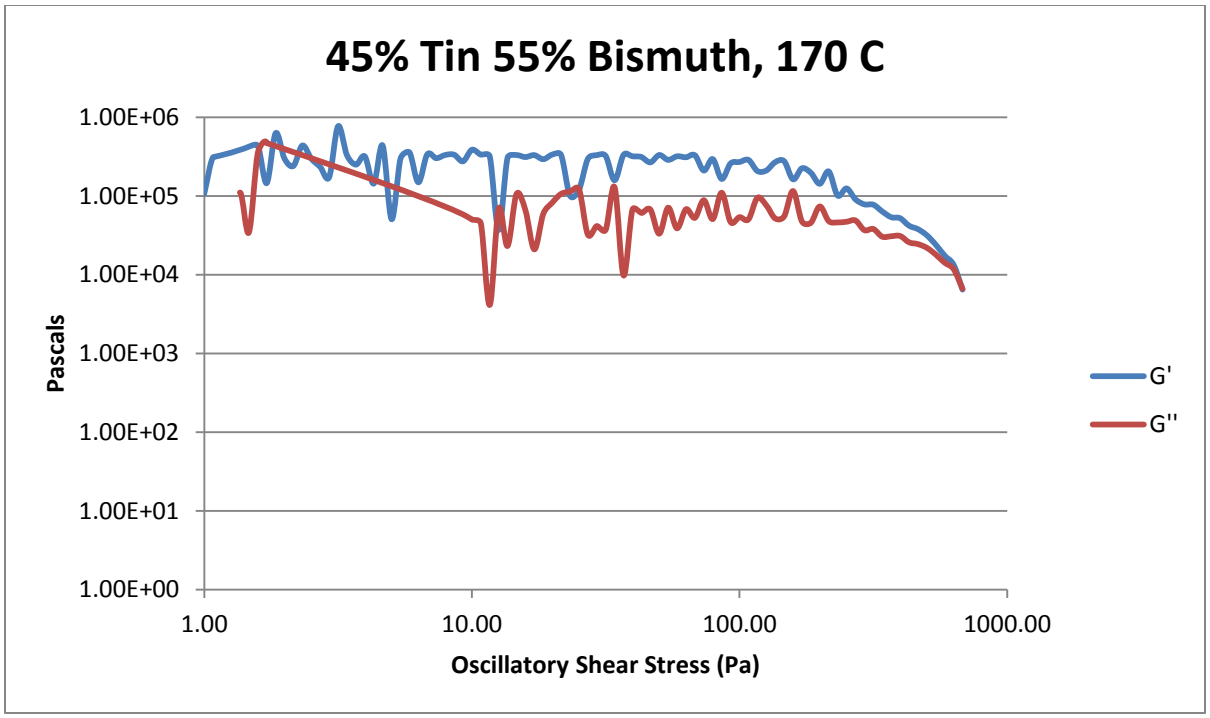

Figure 89- 45% Sn 55% Bi (Run 1), 170 C, Cone and Plate Stress Sweep

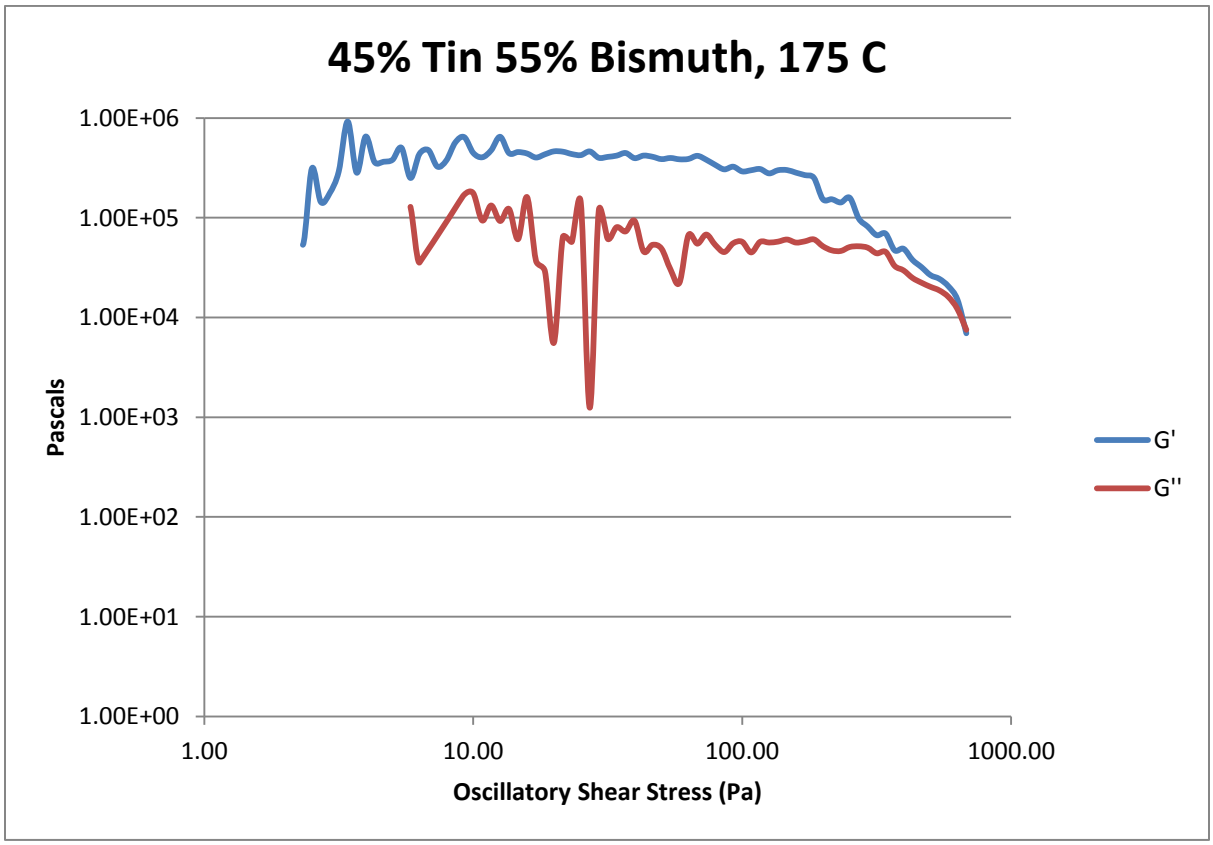

Figure 90- 45% Sn 55% Bi (Run 1), 175 C, Cone and Plate Stress Sweep

Temperature	Crossover Stress (Pa)	Crossover Stress (PSI)
145 C	$1.83 * 10^4$	2.65
150 C	$1.82 * 10^4$	2.64
155 C	$1.72 * 10^4$	2.49
160 C	$1.54 * 10^4$	2.23
165 C	$3.41 * 10^4$	4.95
170 C	$7.09 * 10^3$	1.03
175 C	$8.28 * 10^3$	1.20

Table 12- 45% Sn 55% Bi (Run 1), Cone and Plate Crossover Stresses

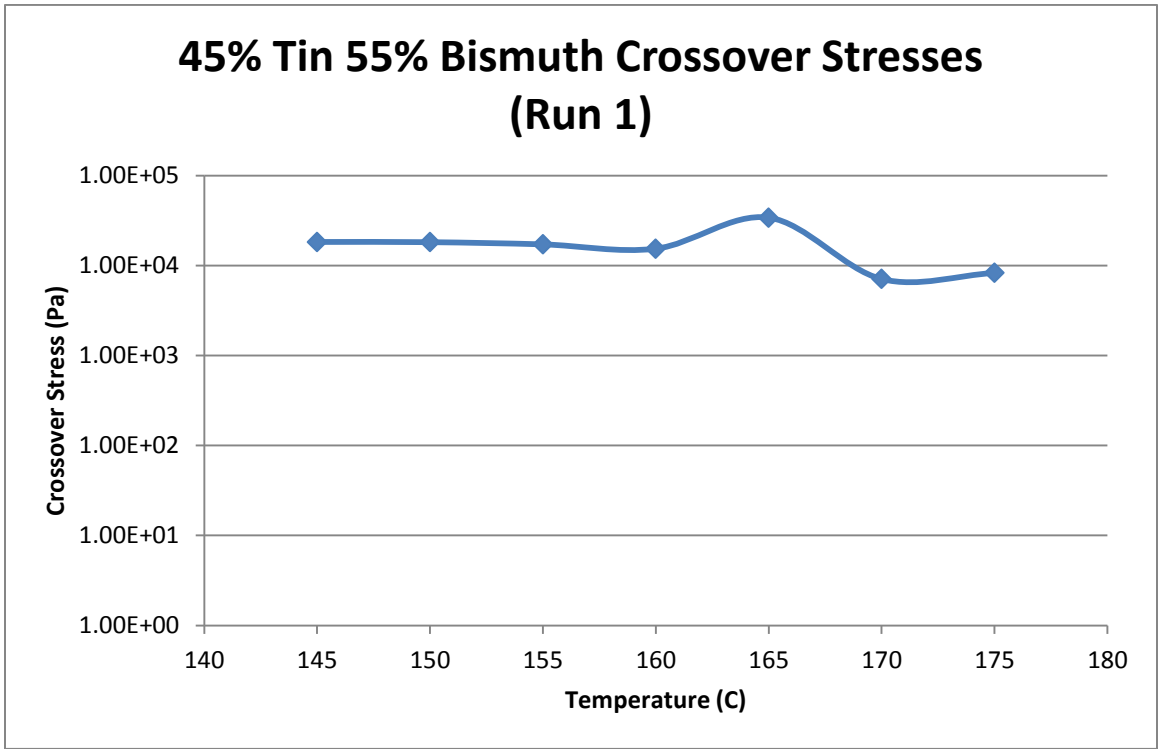

Figure 91- 45% Sn 55% Bi (Run 1), Cone and Plate Crossover Stresses

Temperature	Fraction Solid (At %)	G' Plateau (Pa)	G'' Plateau (Pa)
145 C	23.0	$6.92 * 10^5$	$1.36 * 10^5$
150 C	19.8	$6.17 * 10^5$	$1.55 * 10^5$
155 C	16.2	$3.65 * 10^5$	$1.56 * 10^5$
160 C	12.2	$2.07 * 10^5$	$6.51 * 10^4$
165 C	7.88	$6.23 * 10^5$	$8.64 * 10^4$
170 C	3.03	$2.68 * 10^5$	$7.21 * 10^4$
175 C	0	$4.06 * 10^5$	$5.81 * 10^4$

Table 13- 45% Sn 55% Bi (Run 1), Cone and Plate Plateau Stresses

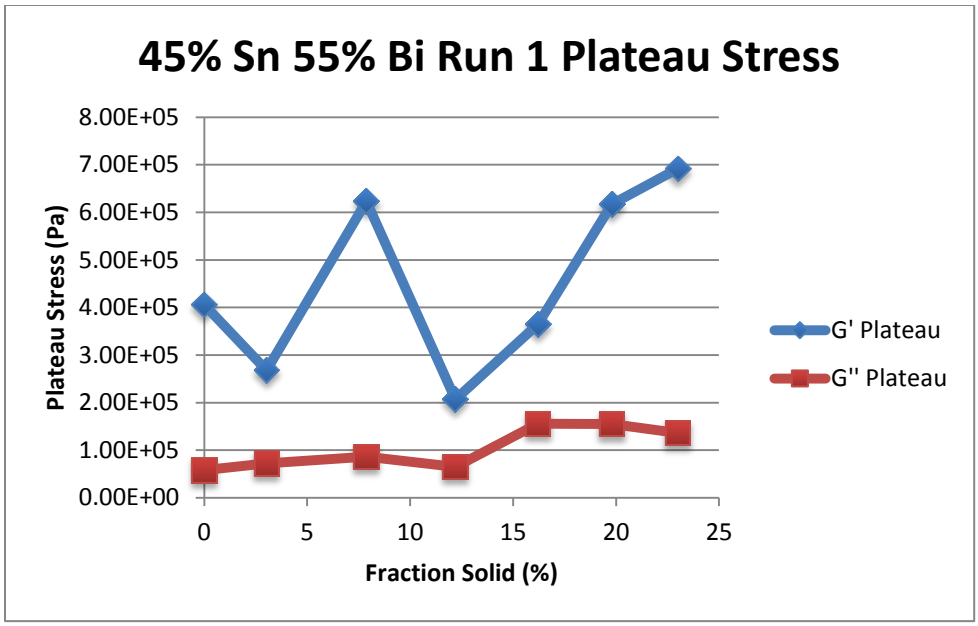

Figure 92- 45% Sn 55% Bi (Run 1), Cone and Plate Plateau Stresses vs. Fraction Solid

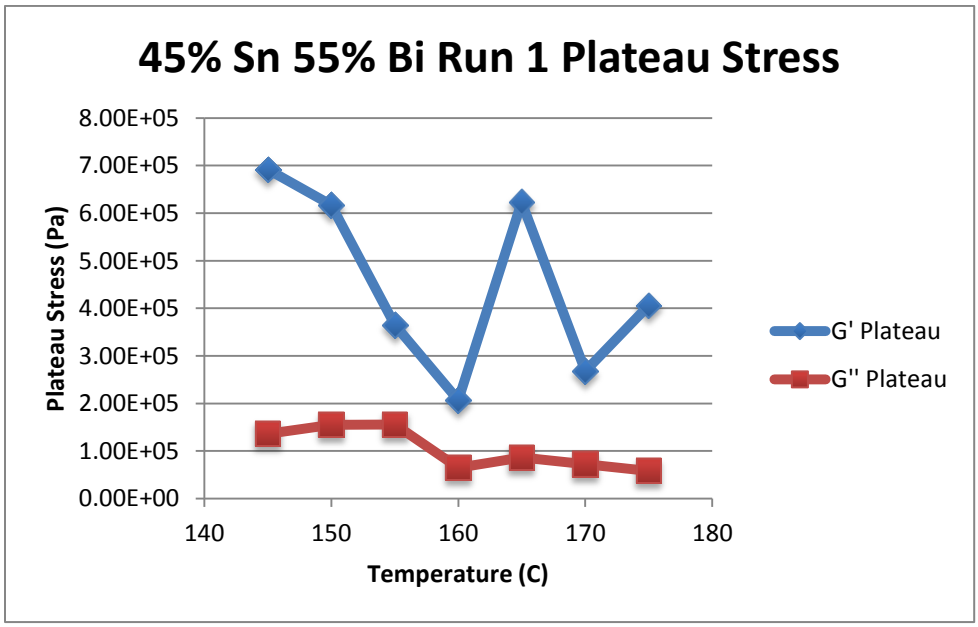

Figure 93- 45% Sn 55% Bi (Run 1), Cone and Plate Plateau Stresses vs. Temperature

45% Sn 55% Bi (Run 1) Viscosity					
Temperature	**Fraction Solid**	**Power Law**	**K**	**n**	**R^2**
145 C	23.0 %	$\tau = 1.97 * 10^{-4} * \dot{\gamma}^{0.2346}$ $\mu = 4.62 * 10^{-5} * \dot{\gamma}^{-0.7654}$	$1.97 * 10^{-4}$ Pa*s	0.2346	96.30 %
150 C	19.8 %	$\tau = 4.35 * 10^{-4} * \dot{\gamma}^{0.2868}$ $\mu = 1.25 * 10^{-4} * \dot{\gamma}^{-0.7132}$	$4.35 * 10^{-4}$ Pa*s	0.2868	71.68 %
155 C	16.2 %	$\tau = 2.32 * 10^{-4} * \dot{\gamma}^{0.2866}$ $\mu = 6.65 * 10^{-5} * \dot{\gamma}^{-0.7134}$	$2.32 * 10^{-4}$ Pa*s	0.2866	96.92 %
160 C	12.2 %	$\tau = 4.12 * 10^{-4} * \dot{\gamma}^{0.3914}$ $\mu = 1.61 * 10^{-4} * \dot{\gamma}^{-0.6086}$	$4.12 * 10^{-4}$ Pa*s	0.3914	93.81 %
165 C	7.88 %	$\tau = 1.37 * 10^{-4} * \dot{\gamma}^{0.1612}$ $\mu = 2.21 * 10^{-5} * \dot{\gamma}^{-0.8388}$	$1.37 * 10^{-4}$ Pa*s	0.1612	57.11 %
170 C	3.03 %	$\tau = 1.38 * 10^{-4} * \dot{\gamma}^{0.2570}$ $\mu = 3.55 * 10^{-5} * \dot{\gamma}^{-0.7430}$	$1.38 * 10^{-4}$ Pa*s	0.2570	93.29 %

Table 14- 45% Sn 55% Bi (Run 1), Cone and Plate Viscosity

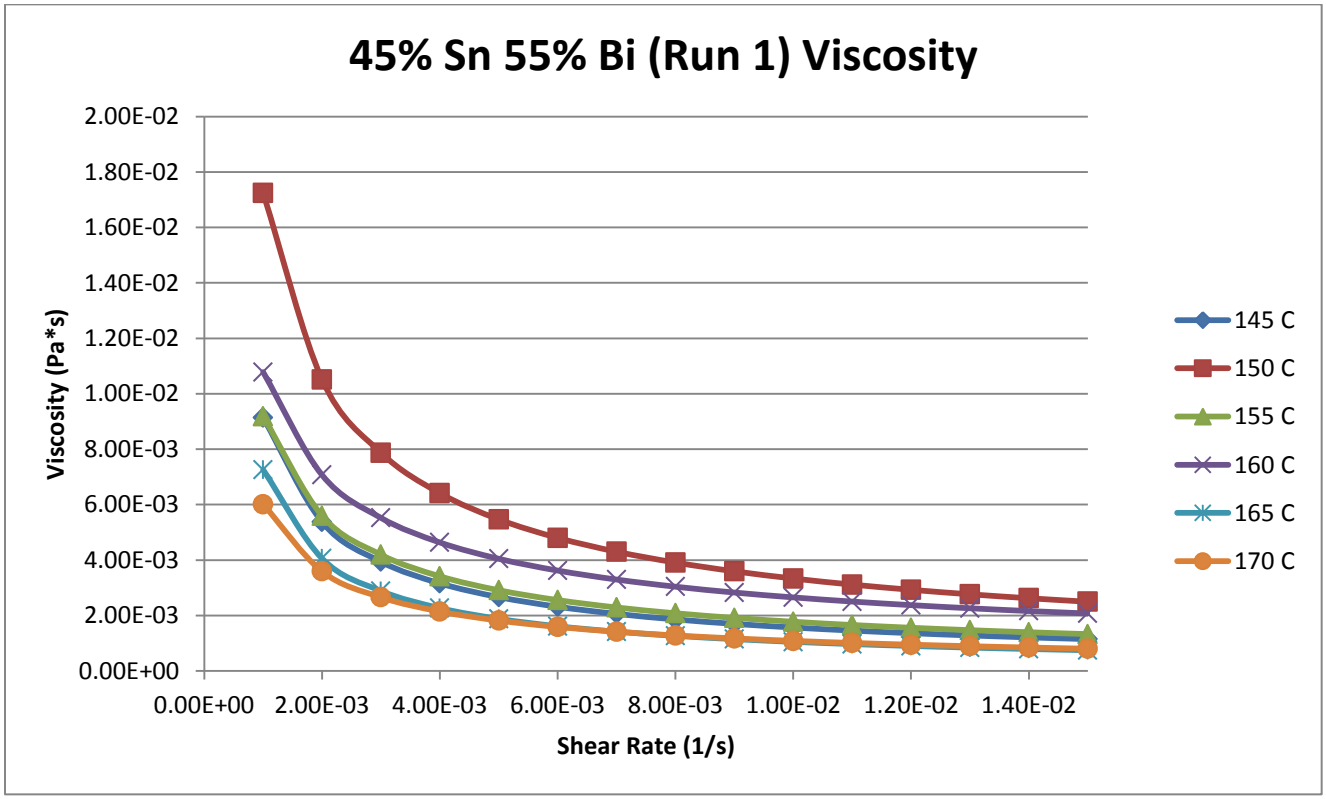

Figure 94- 45% Sn 55% Bi (Run 1), Cone and Plate Viscosity

145 C

Fraction Solid	23.0 %
Power Law	$\tau = 1.97 * 10^{-4} * \dot{\gamma}^{0.2346}$
	$\mu = 4.62 * 10^{-5} * \dot{\gamma}^{-0.7654}$
R^2	96.30 %

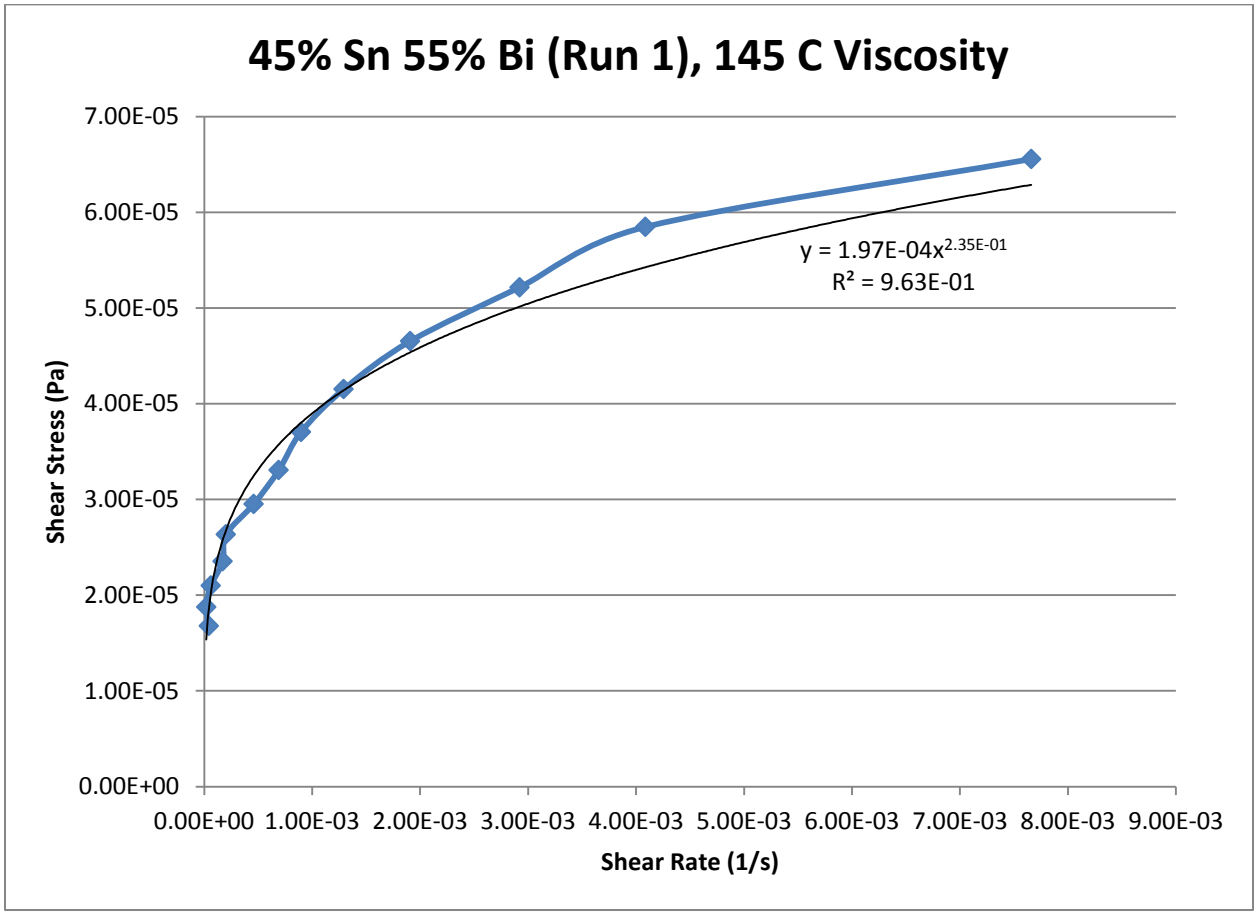

Figure 95- 45% Sn 55% Bi (Run 1), 145 C, Cone and Plate Viscosity

150 C

Fraction Solid	19.8 %
Power Law	$\tau = 4.35 * 10^{-4} * \dot{\gamma}^{0.2868}$
	$\mu = 1.25 * 10^{-4} * \dot{\gamma}^{-0.7132}$
R^2	71.66 %

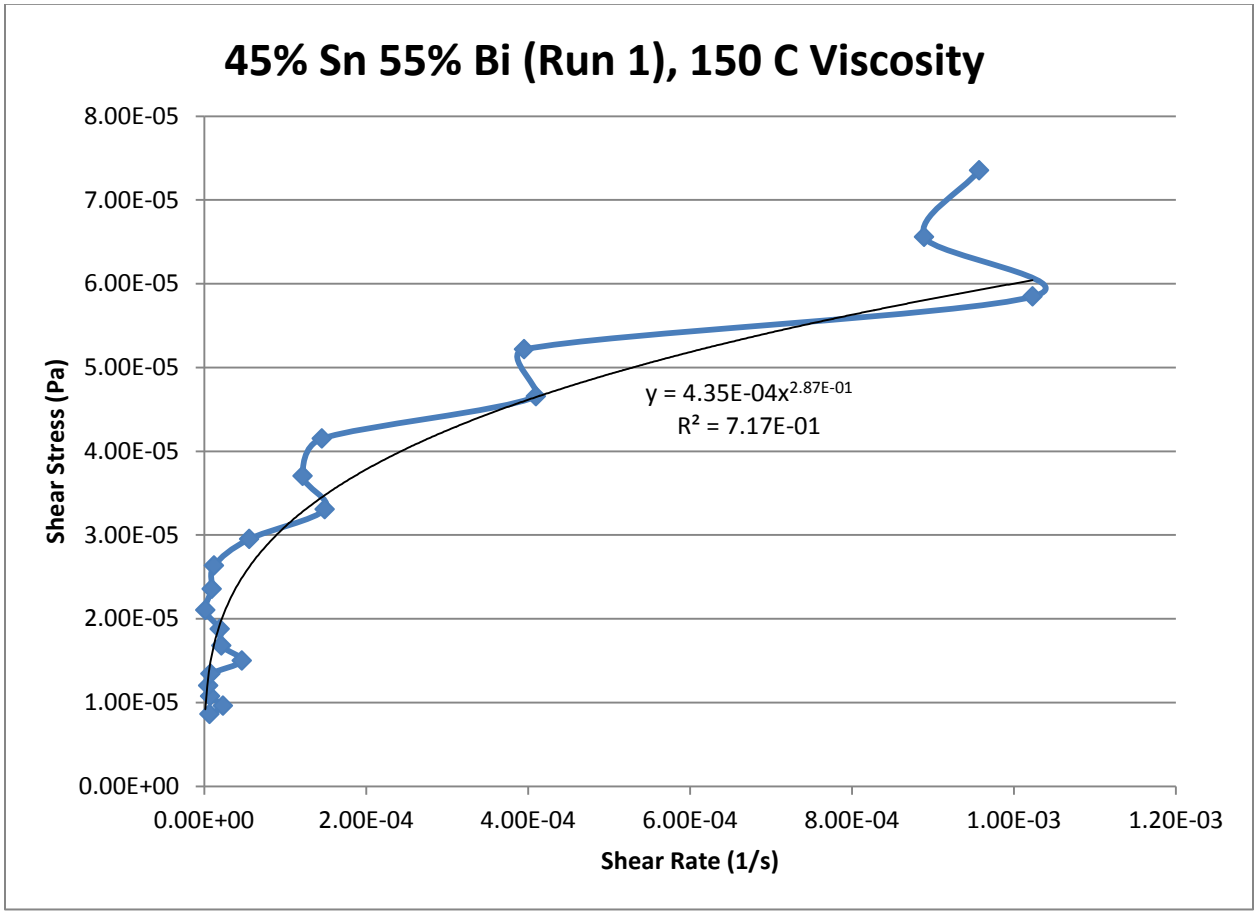

Figure 96- 45% Sn 55% Bi (Run 1), 150 C, Cone and Plate Viscosity

155 C

Fraction Solid	16.8 %
Power Law	$\tau = 2.32 * 10^{-4} * \dot{\gamma}^{0.2866}$
	$\mu = 6.65 * 10^{-5} * \dot{\gamma}^{-0.7134}$
R^2	96.92 %

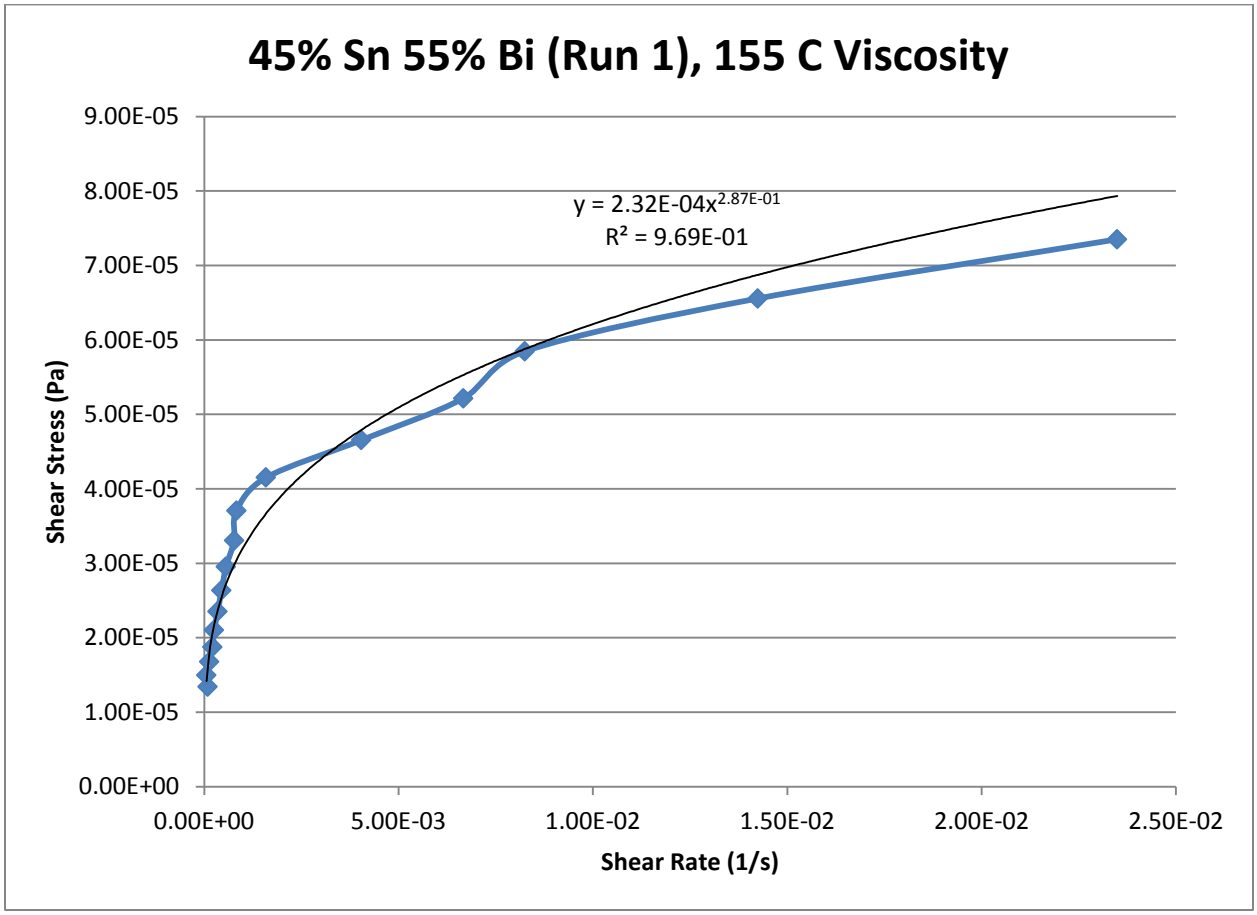

Figure 97- 45% Sn 55% Bi (Run 1), 155 C, Cone and Plate Viscosity

160 C

Fraction Solid	12.2 %
Power Law	$\tau = 4.12 * 10^{-4} * \dot{\gamma}^{0.3914}$
	$\mu = 1.61 * 10^{-4} * \dot{\gamma}^{-0.6086}$
R^2	93.81 %

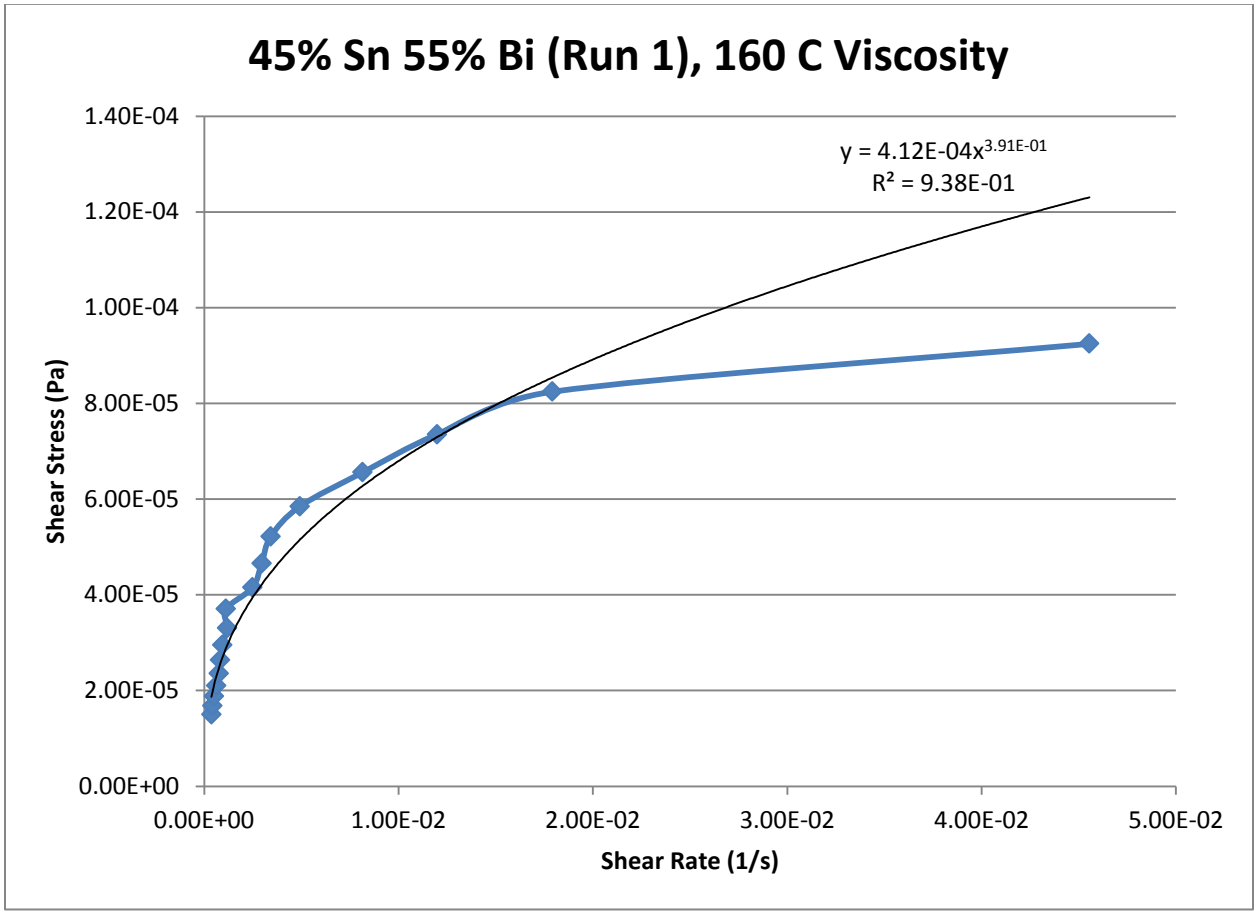

Figure 98- 45% Sn 55% Bi (Run 1), 160 C, Cone and Plate Viscosity

165 C

Fraction Solid	7.88 %
Power Law	$\tau = 1.37 * 10^{-4} * \dot{\gamma}^{0.1612}$
	$\mu = 2.21 * 10^{-5} * \dot{\gamma}^{-0.8388}$
R^2	57.11 %

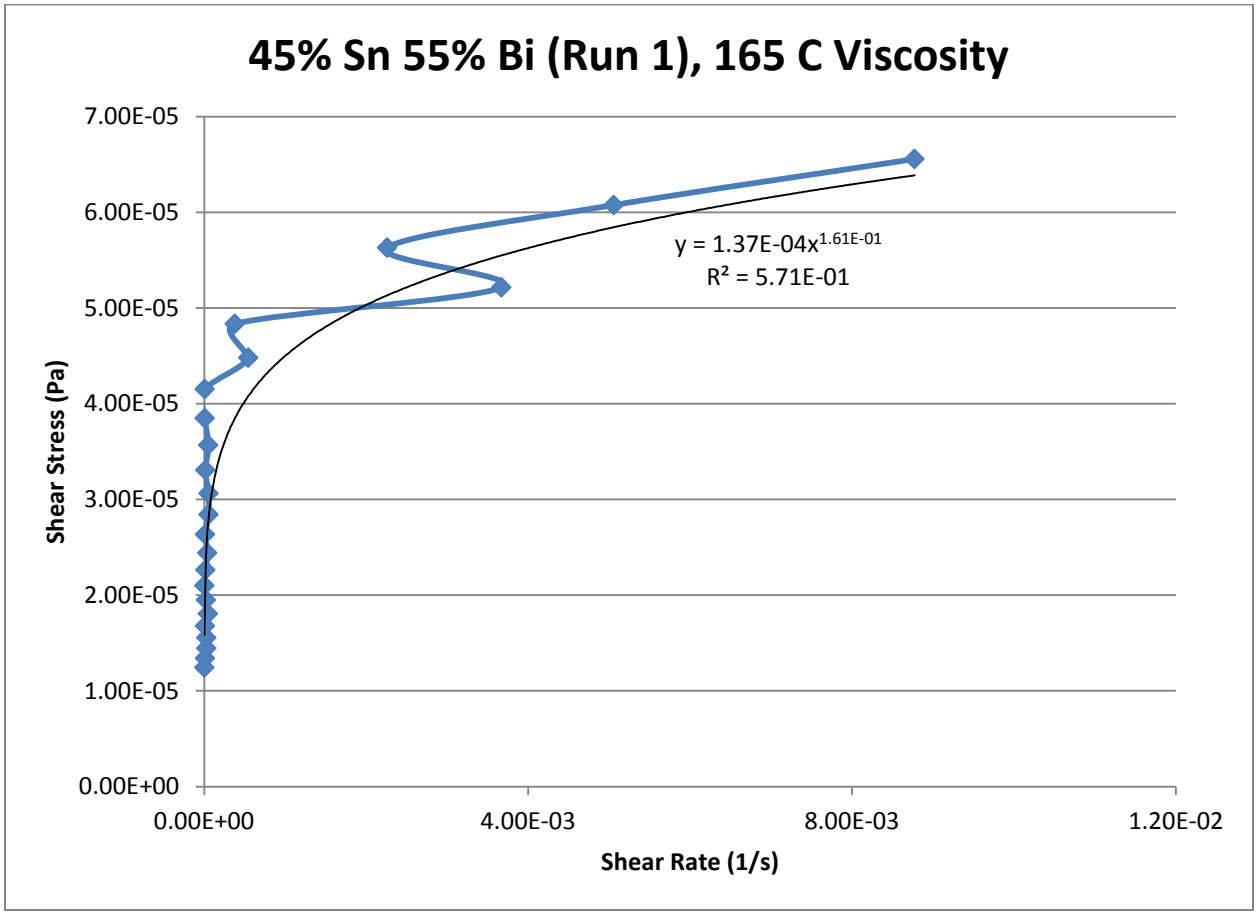

Figure 99- 45% Sn 55% Bi (Run 1), 165 C, Cone and Plate Viscosity

170 C

Fraction Solid	3.03 %
Power Law	$\tau = 1.38 * 10^{-4} * \dot{\gamma}^{0.2570}$
	$\mu = 3.55 * 10^{-4} * \dot{\gamma}^{-0.7430}$
R^2	93.29 %

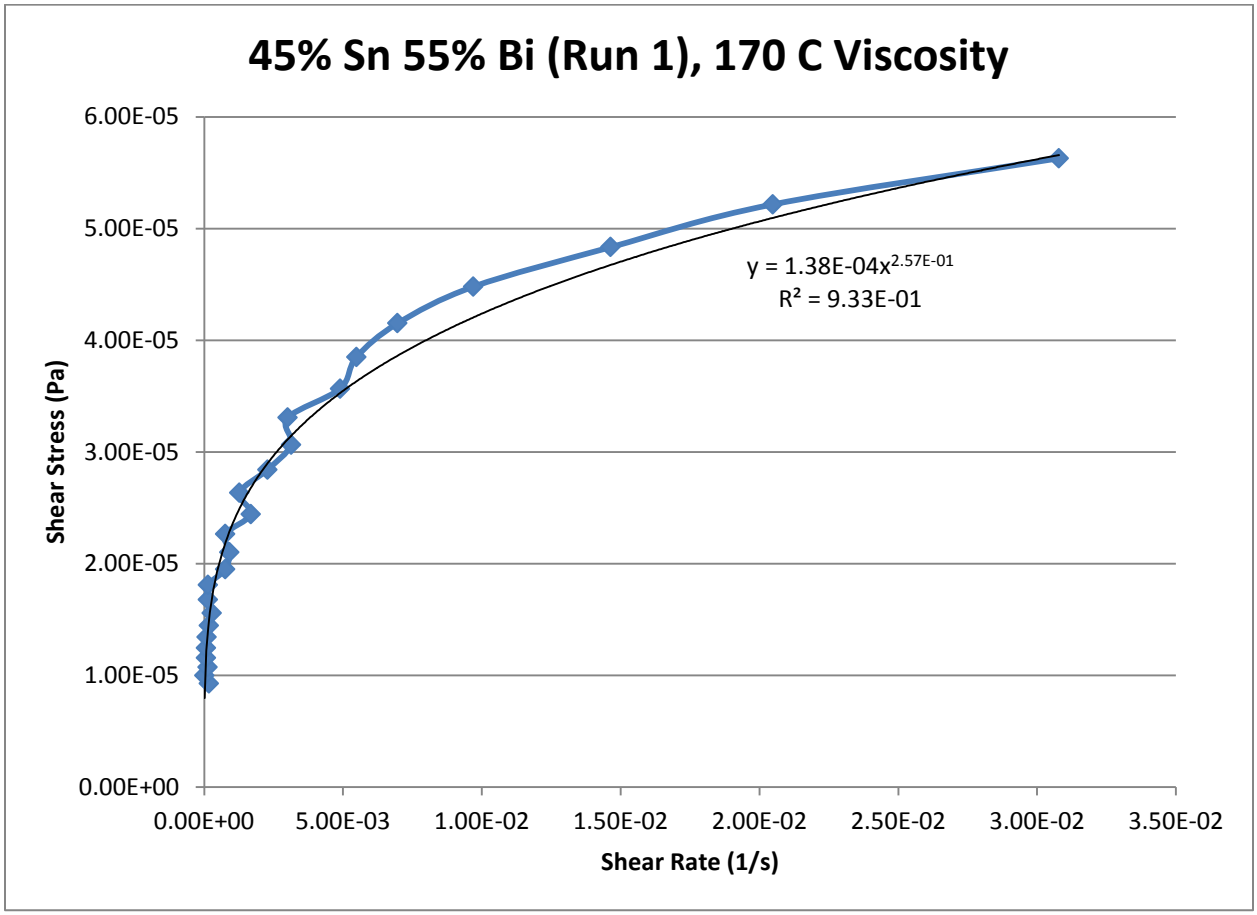

Figure 100- 45% Sn 55% Bi (Run 1), 170 C, Cone and Plate Viscosity

45% Tin 55% Bismuth (Run 2)

Expected Composition: 47% Tin, 53% Bismuth

Theoretical Solidus Line: 139 C
Theoretical Liquidus Line: 159.7 C

Experimental Solidus Line: 138.9 C
Experimental Liquidus Line: 162.2 C

Set-Up Notes

- Semi-solid was difficult to get to stay under cone
- Zeroed gap at 165 C. Stress sweeps were conducted from 165 C to 150 C with temperature decreasing by 5 C after each run.
- A 5000 Pascal oscillatory shear stress was insufficient to induce a G'-G'' crossover.
- The semi-solid was very chunky and appeared to be heavily oxidized.

Plots

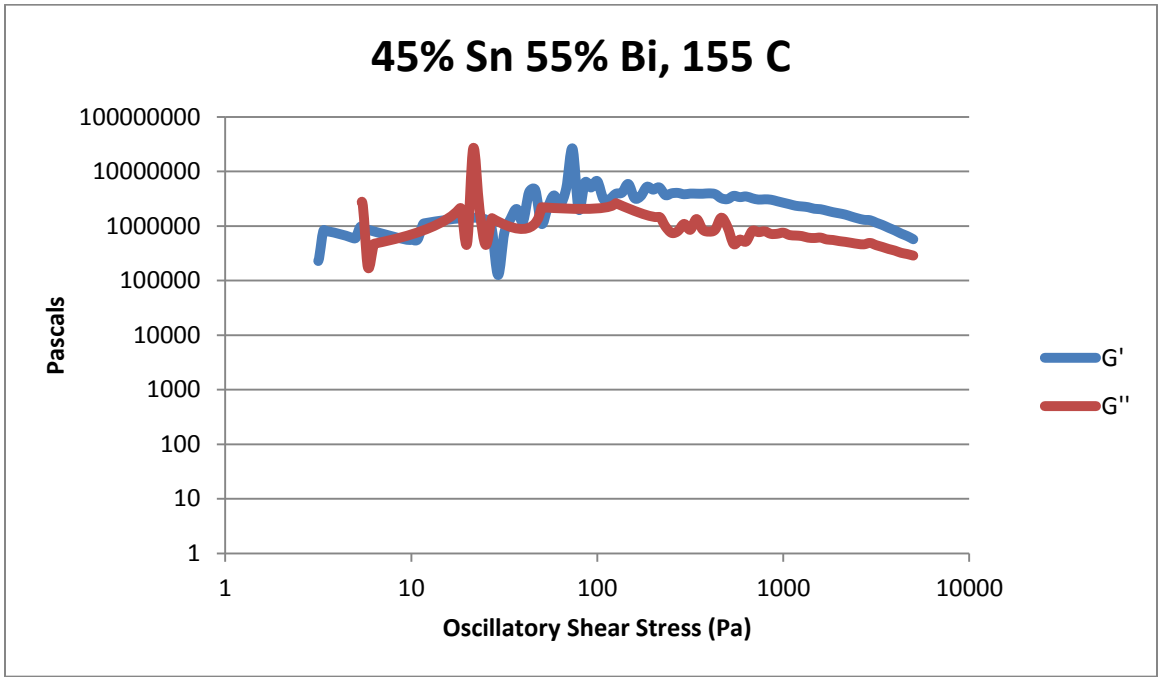

Figure 101- 45% Sn 55% Bi (Run 2), 155 C, Cone and Plate Stress Sweep

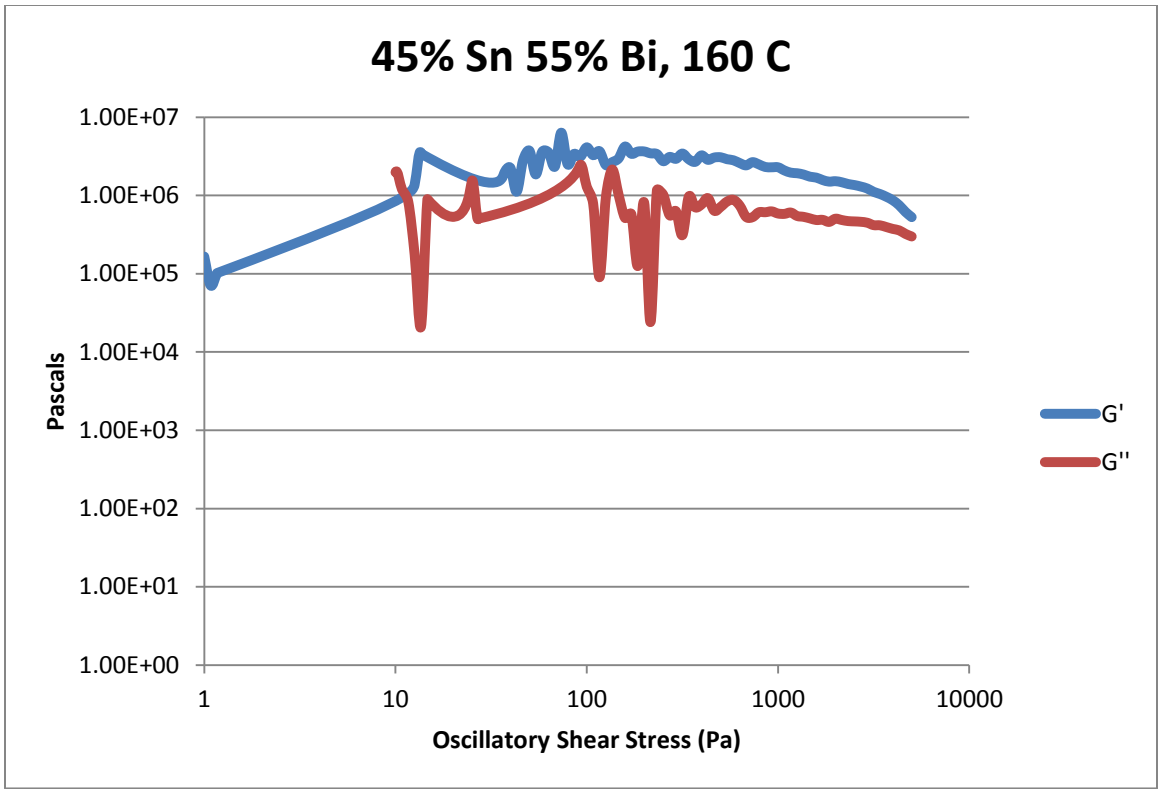

Figure 102- 45% Sn 55% Bi (Run 2), 160 C, Cone and Plate Stress Sweep

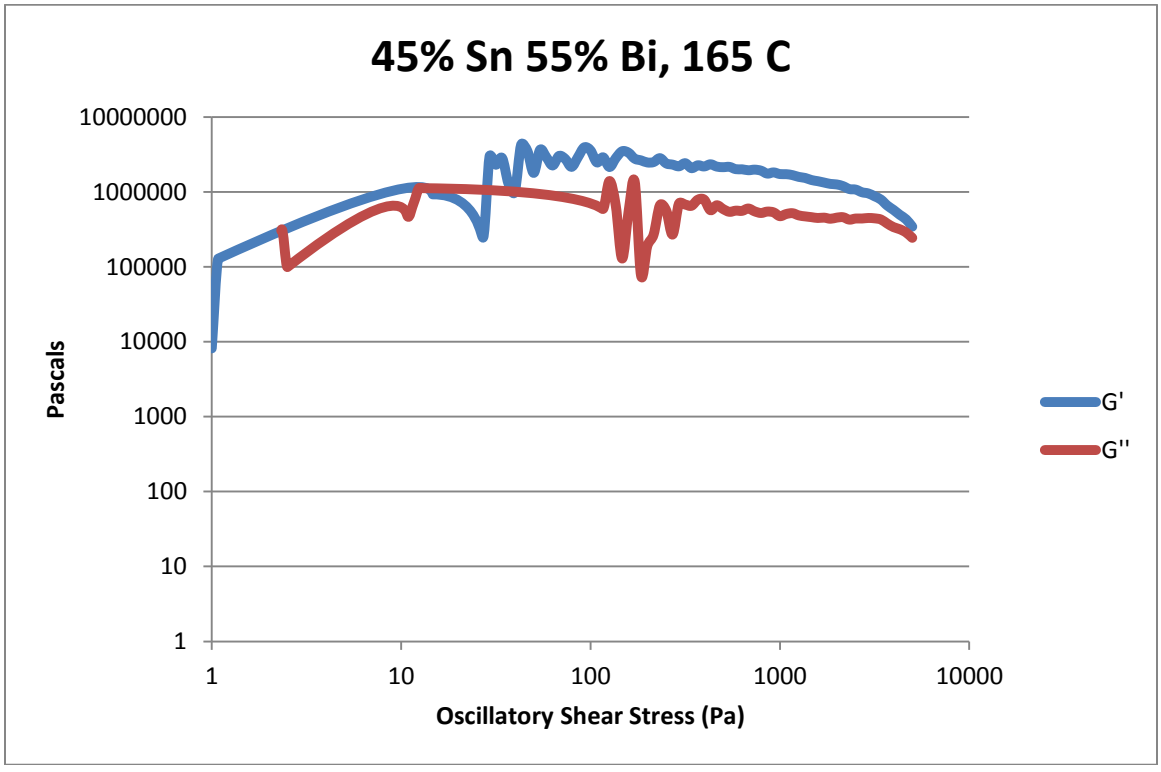

Figure 103- 45% Sn 55% Bi (Run 2), 165 C, Cone and Plate Stress Sweep

Temperature	Fraction Solid (At %)	G' Plateau (Pa)	G'' Plateau (Pa)
155 C	20.1	$3.92 * 10^6$	$6.03 * 10^5$
160 C	15.1	$2.90 * 10^6$	$4.89 * 10^5$
165 C	9.73	$2.10 * 10^6$	$4.45 * 10^5$

Table 15- 45% Sn 55% Bi (Run 2), Cone and Plate Plateau Stresses

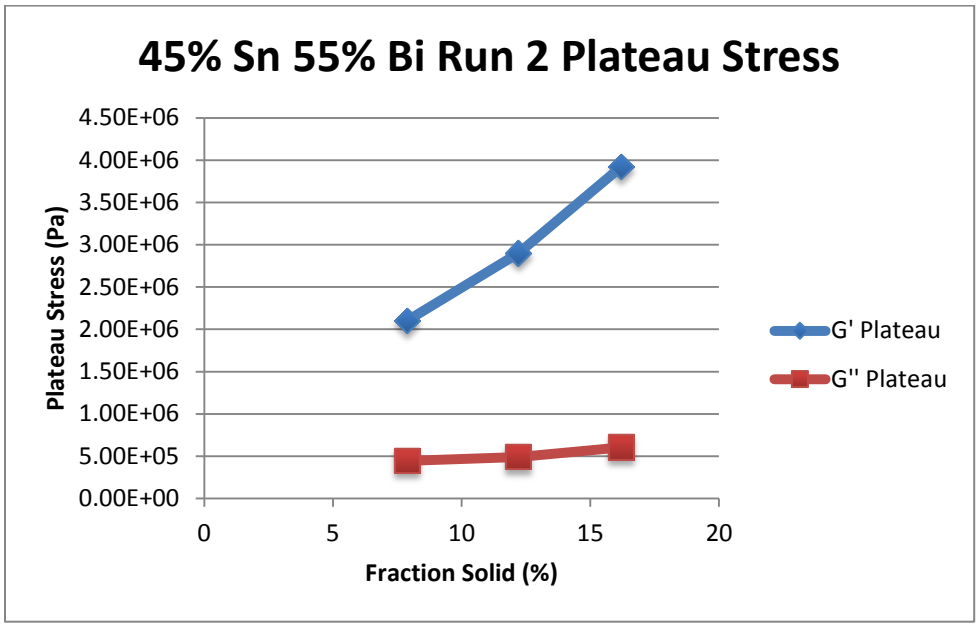

Figure 104- 45% Sn 55% Bi (Run 2), Cone and Plate Plateau Stresses vs. Fraction Solid

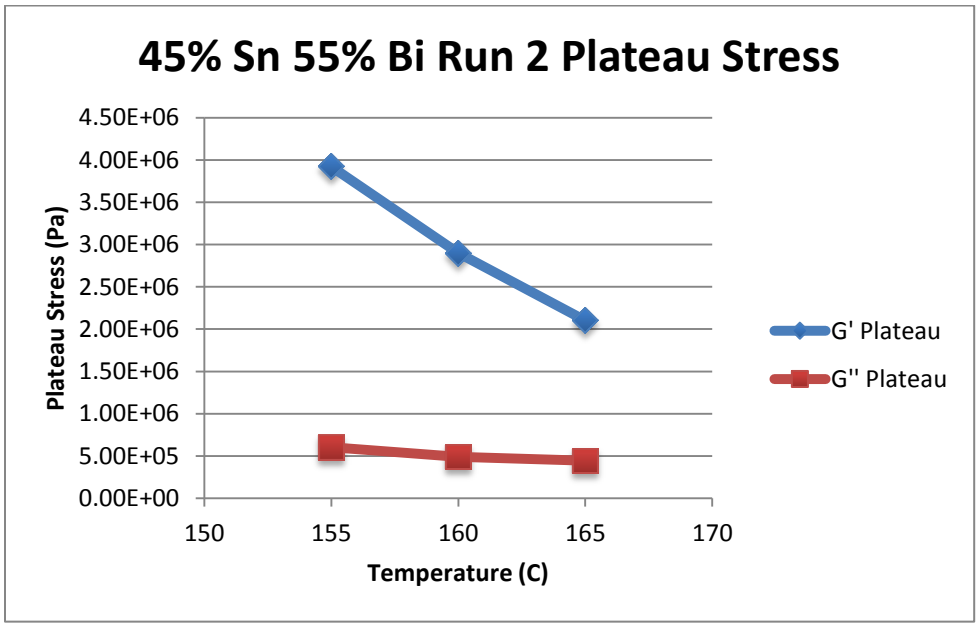

Figure 105- 45% Sn 55% Bi (Run 2), Cone and Plate Plateau Stresses vs. Temperature

45% Sn 55% Bi (Run 2) Viscosity					
Temperature	**Fraction Solid**	**Power Law**	**K**	**n**	**R^2**
150 C	19.8 %	$\tau = 3.85 * 10^{-6} * \dot{\gamma}^{0.0079}$ $\mu = 3.04 * 10^{-8} * \dot{\gamma}^{-0.9921}$	$3.85 * 10^{-6}$ Pa*s	0.0079	0.05 %
155 C	16.2 %	$\tau = 1.31 * 10^{-3} * \dot{\gamma}^{0.1836}$ $\mu = 2.41 * 10^{-4} * \dot{\gamma}^{-0.8164}$	$1.31 * 10^{-3}$ Pa*s	0.1836	79.28 %
160 C	12.2 %	$\tau = 8.10 * 10^{-4} * \dot{\gamma}^{0.1216}$ $\mu = 9.85 * 10^{-5} * \dot{\gamma}^{-0.8784}$	$8.10 * 10^{-4}$ Pa*s	0.1216	69.86 %
165 C	7.88 %	$\tau = 2.00 * 10^{-3} * \dot{\gamma}^{0.2721}$ $\mu = 5.44 * 10^{-4} * \dot{\gamma}^{-0.7279}$	$2.00 * 10^{-3}$ Pa*s	0.2721	63.28 %

Table 16- 45% Sn 55% Bi (Run 2), Cone and Plate Viscosity

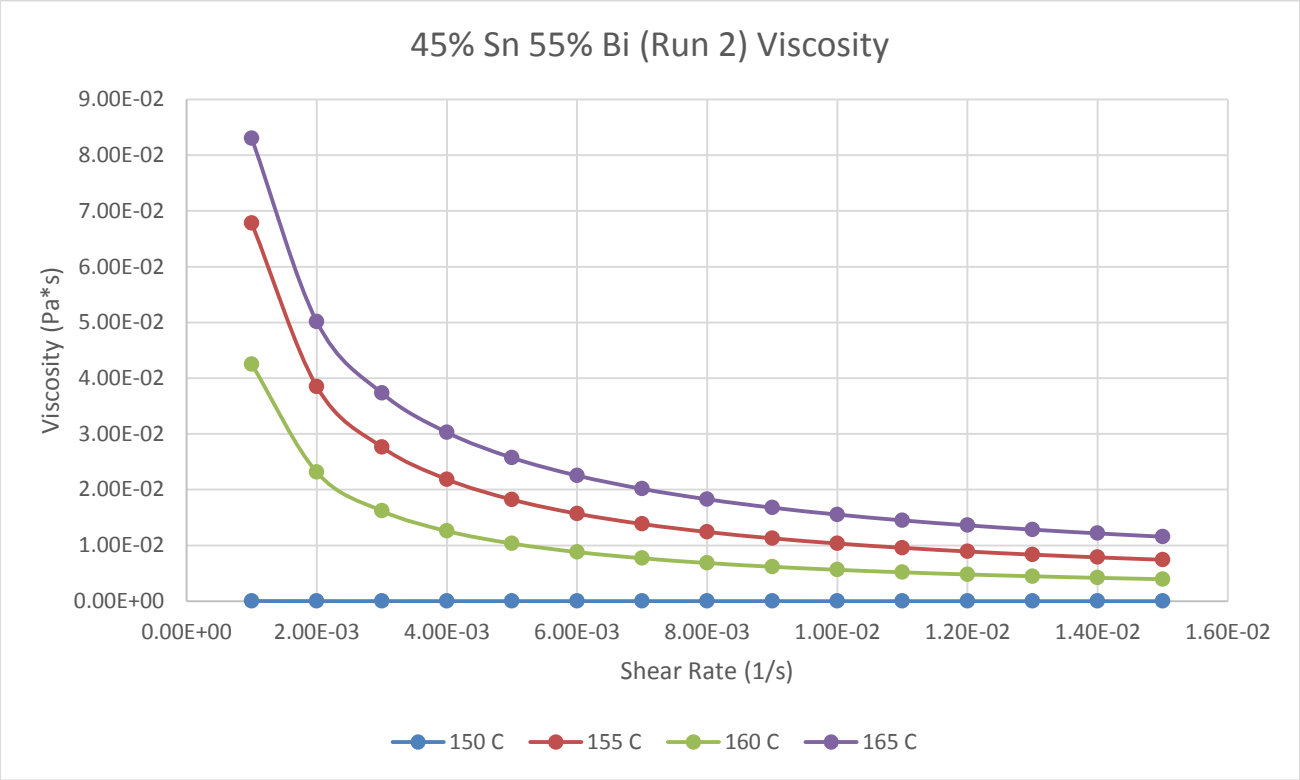

Figure 106- 45% Sn 55% Bi (Run 2), Cone and Plate Viscosity

150 C

Fraction Solid	19.8 %
Power Law	$\tau = 3.85 * 10^{-6} * \dot{\gamma}^{0.0079}$
	$\mu = 3.04 * 10^{-8} * \dot{\gamma}^{-0.9921}$
R^2	0.05 %

Very poor fit

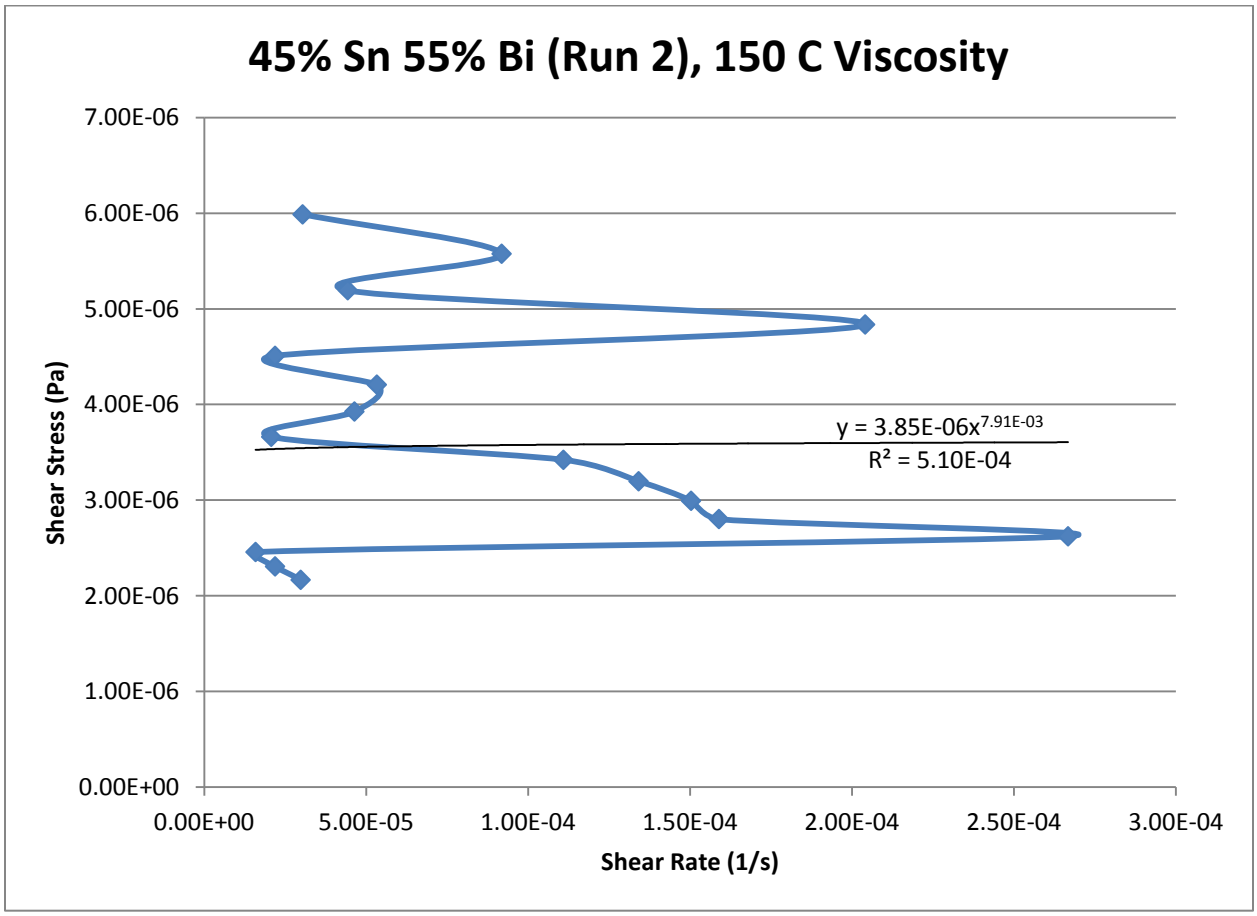

Figure 107- 45% Sn 55% Bi (Run 2), 150 C, Cone and Plate Viscosity

155 C

Fraction Solid	16.8 %
Power Law	$\tau = 1.31 * 10^{-3} * \dot{\gamma}^{0.1836}$
	$\mu = 2.41 * 10^{-4} * \dot{\gamma}^{-0.8164}$
R^2	79.28 %

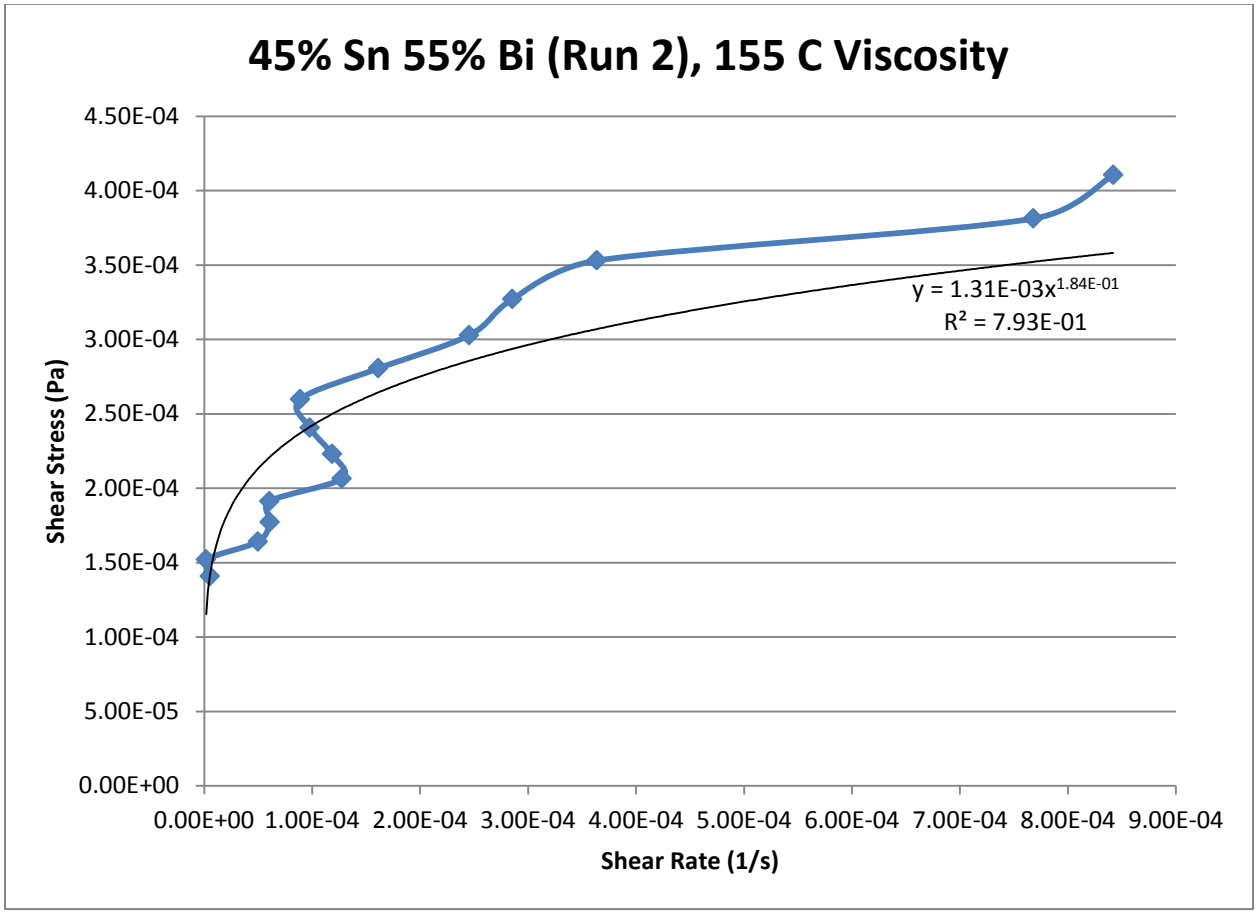

Figure 108- 45% Sn 55% Bi (Run 2), 155 C, Cone and Plate Viscosity

160 C

Fraction Solid	12.2 %
Power Law	$\tau = 8.10 * 10^{-4} * \dot{\gamma}^{0.1216}$
	$\mu = 9.85 * 10^{-5} * \dot{\gamma}^{-0.8784}$
R^2	69.86 %

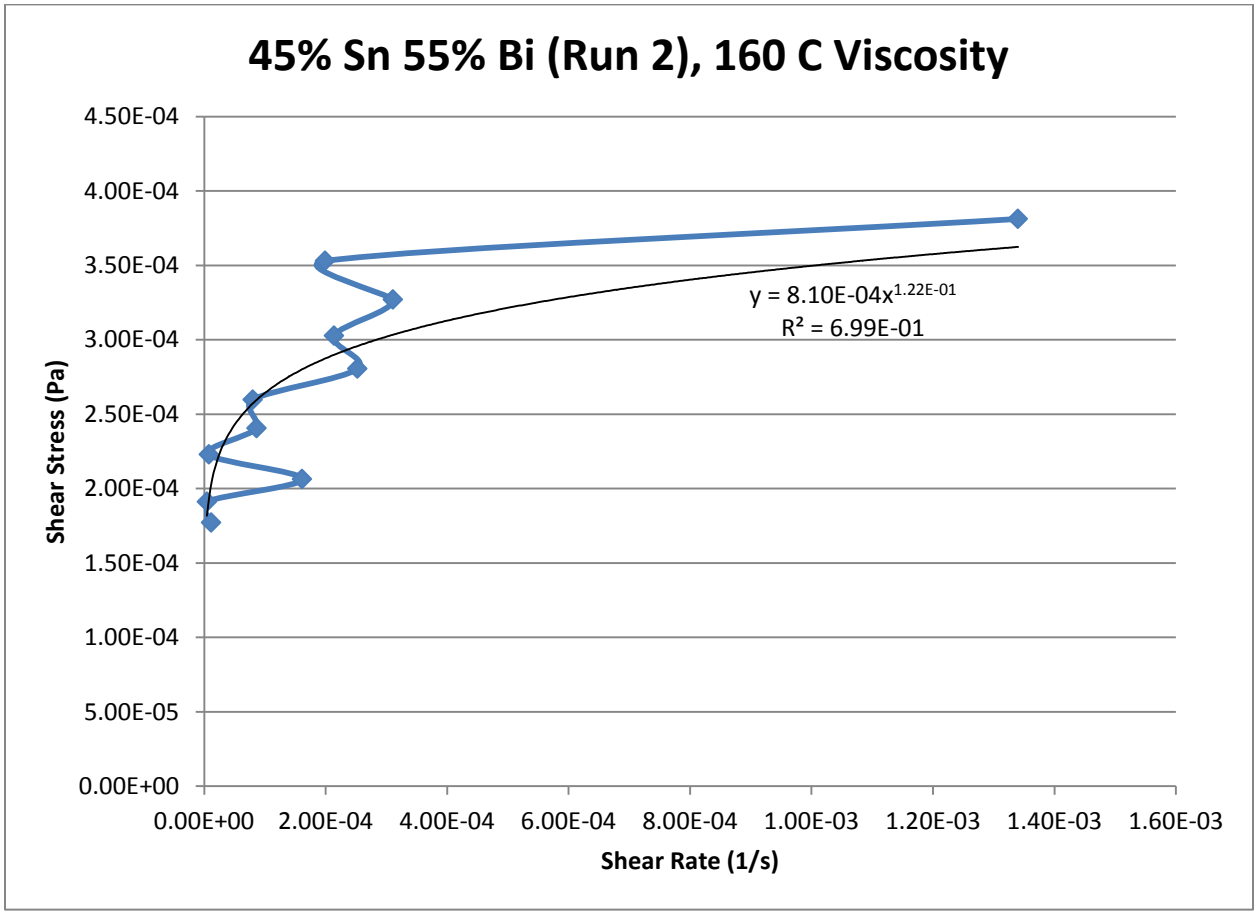

Figure 109- 45% Sn 55% Bi (Run 2), 160 C, Cone and Plate Viscosity

165 C

Fraction Solid	7.88 %
Power Law	$\tau = 2.00 * 10^{-3} * \dot{\gamma}^{0.2721}$
	$\mu = 5.44 * 10^{-4} * \dot{\gamma}^{-0.7279}$
R^2	63.28 %

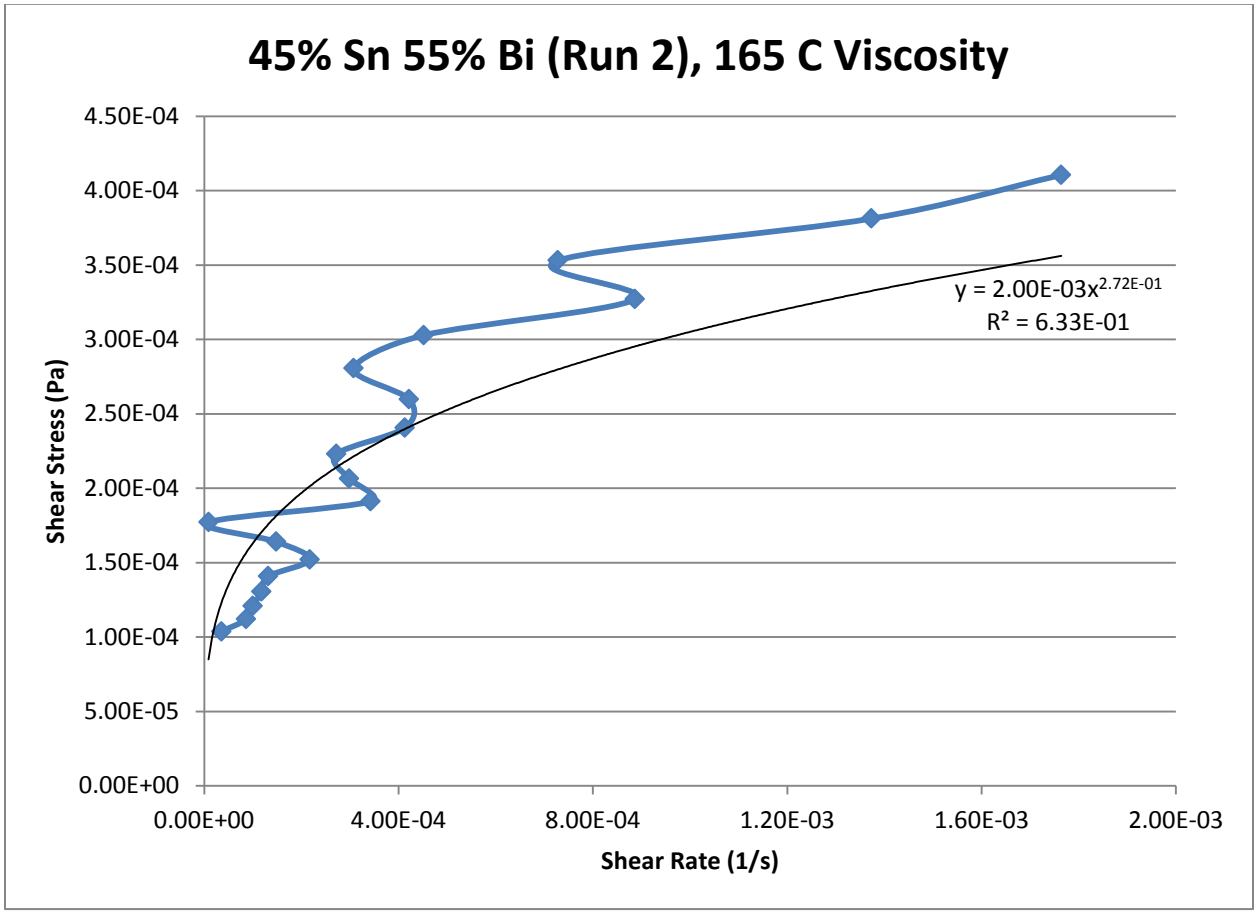

Figure 110- 45% Sn 55% Bi (Run 2), 165 C, Cone and Plate Viscosity

50% Tin 50% Bismuth (Run 1)

Actual Composition: 52.94% Sn, 47.06% Bi

Theoretical Solidus Line: 139 C
Theoretical Liquidus Line: 148.8 C

Experimental Solidus Line: 141.9 C
Experimental Liquidus Line: 151.5 C

Set-Up Notes

- Two pieces of the bismuth-tin alloy were used (~ 15-20 grams).
- Low number of points per decade since this run was done towards the end of the workday and I had to catch the bus.
- The stage was heated to 200 Celsius and the metal pieces were melted underneath the cone. The cone was then lowered to the geometry gap.
- During the experiment, I started with 145 C. Then the temperature was increased in 5 C increments.

Plots

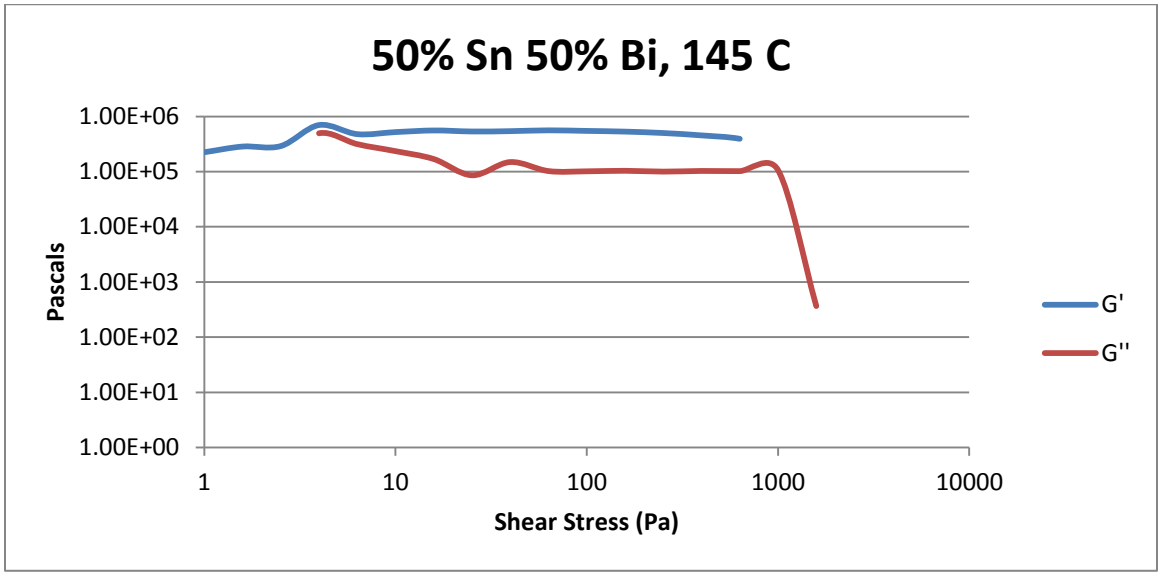

Figure 111- 50% Sn 50% Bi (Created), 145 C, Cone and Plate Stress Sweep

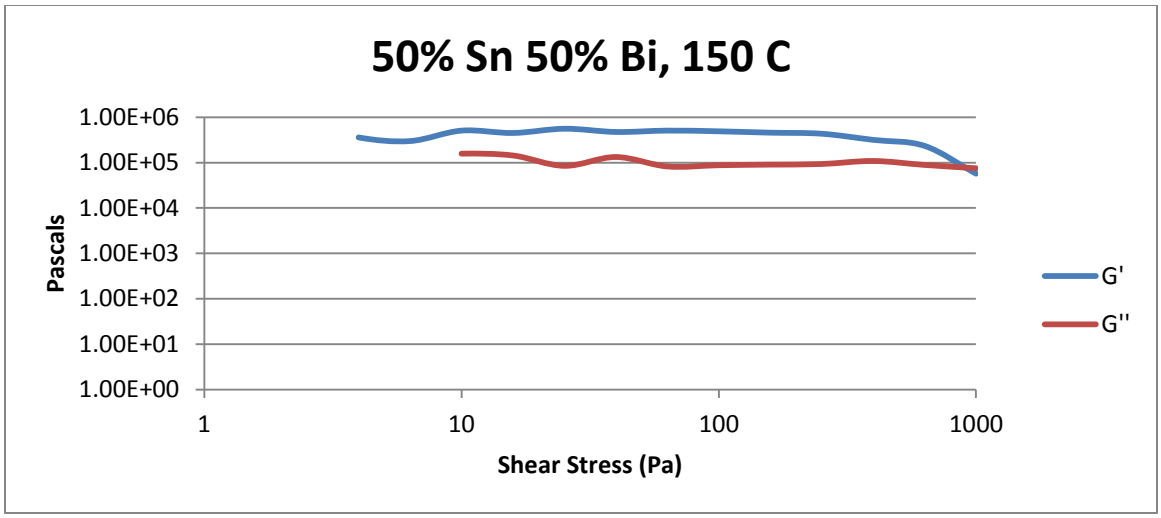

Figure 112- 50% Sn 50% Bi (Created), 150 C, Cone and Plate Stress Sweep

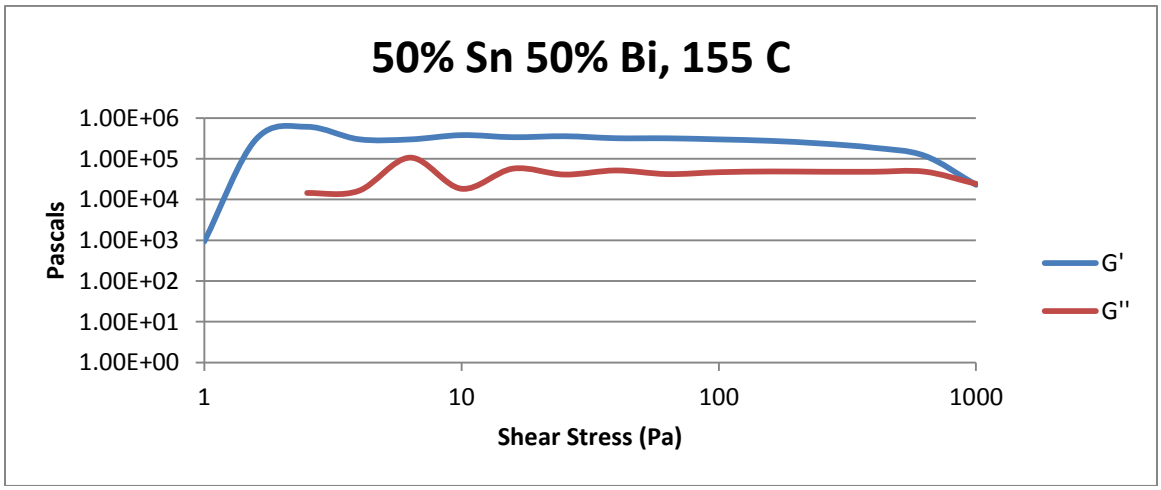

Figure 113- 50% Sn 50% Bi (Created), 155 C, Cone and Plate Stress Sweep

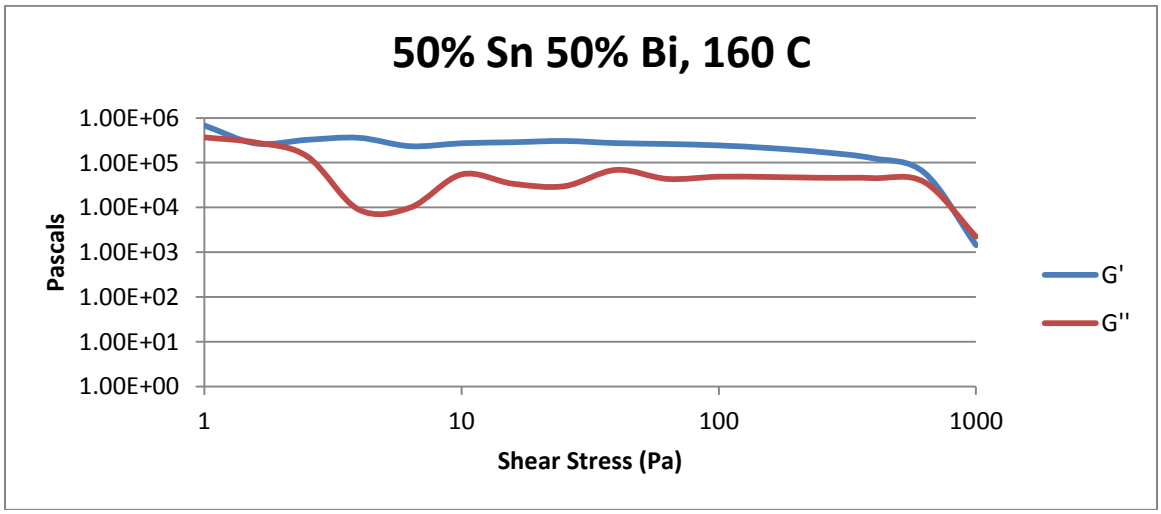

Figure 114- 50% Sn 50% Bi (Created), 160 C, Cone and Plate Stress Sweep

Temperature	Crossover Stress (Pa)	Crossover Stress (PSI)
145 C	$7.23 * 10^3$	0.105
150 C	$7.66 * 10^4$	11.1
155 C	$2.47 * 10^4$	3.58
160 C	$3.38 * 10^3$	0.490

Table 17- 50% Sn 50% Bi (Created), Cone and Plate Crossover Stresses

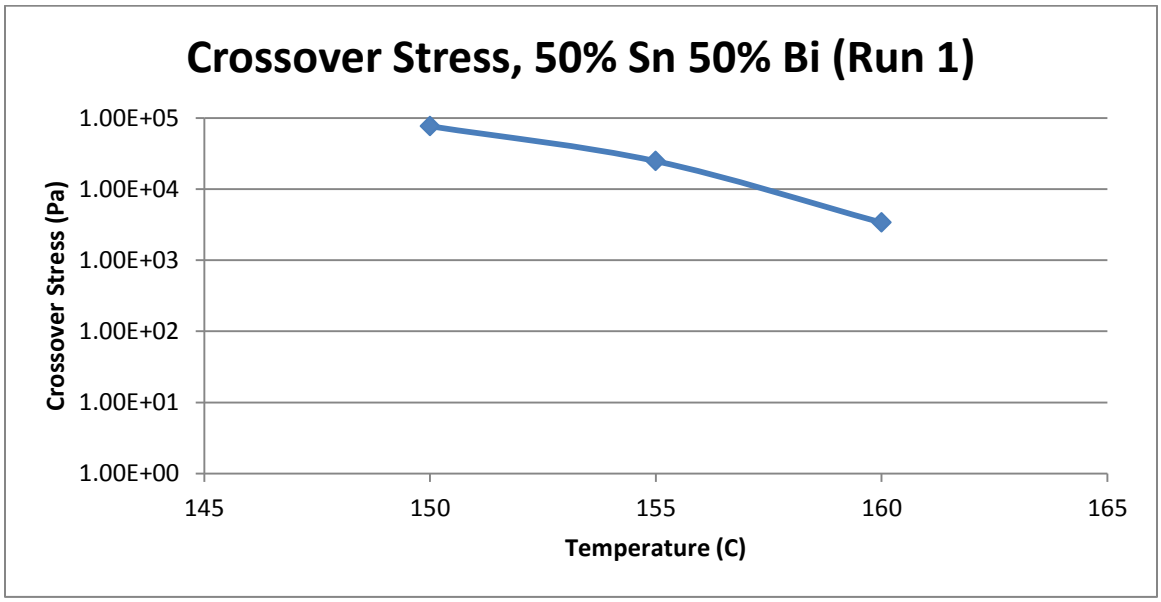

Figure 115- 50% Sn 50% Bi (Created), Cone and Plate Crossover Stresses

Temperature	Fraction Solid (At %)	G' Plateau (Pa)	G'' Plateau (Pa)
145 C	12.7	$5.42 * 10^5$	$1.03 * 10^5$
150 C	9.10	$4.84 * 10^5$	$9.60 * 10^4$
155 C	5.00	$3.30 * 10^5$	$4.69 * 10^4$
160 C	0.51	$2.61 * 10^5$	$4.63 * 10^4$

Table 18- 50% Sn 50% Bi (Created), Cone and Plate Plateau Stresses

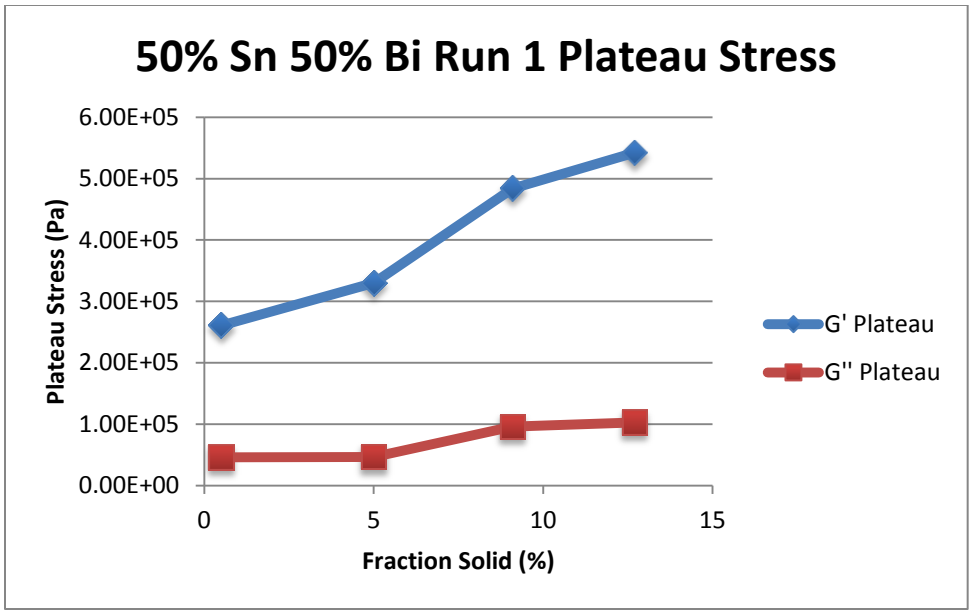

Figure 116- 50% Sn 50% Bi (Created), Cone and Plate Plateau Stresses vs. Fraction Solid

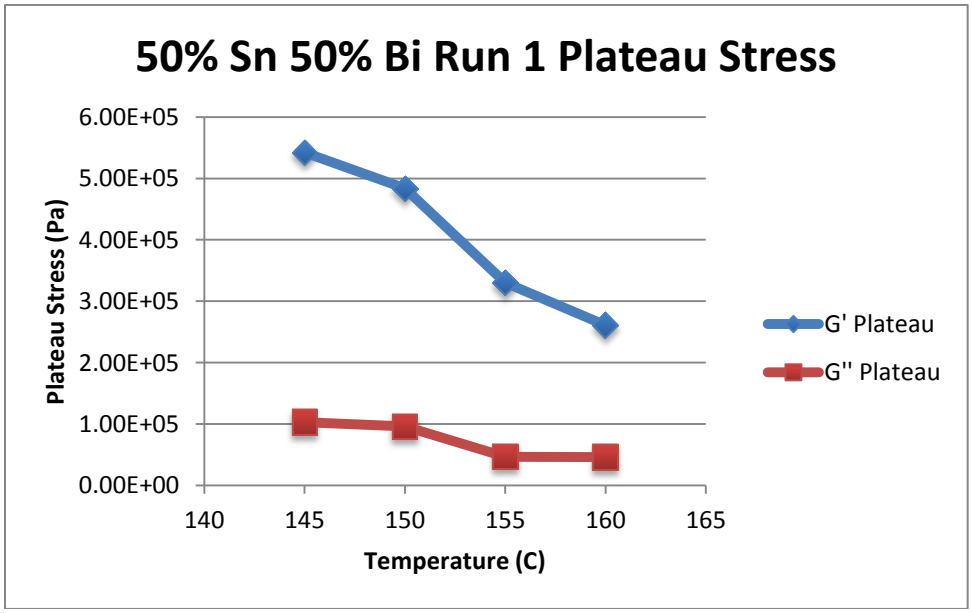

Figure 117- 50% Sn 50% Bi (Created), Cone and Plate Plateau Stresses vs. Temperature

50% Sn 50% Bi Viscosity					
Temperature	**Fraction Solid**	**Power Law**	**K**	**n**	**R^2**
145 C	12.7 %	$\tau = 3.60 * 10^{-3} * \dot{\gamma}^{0.5101}$ $\mu = 1.84 * 10^{-3} * \dot{\gamma}^{-0.4899}$	$3.60 * 10^{-3}$ Pa*s	0.5101	93.94 %
150 C	9.10 %	$\tau = 6.33 * 10^{-4} * \dot{\gamma}^{0.3782}$ $\mu = 2.39 * 10^{-4} * \dot{\gamma}^{-0.6218}$	$6.33 * 10^{-4}$ Pa*s	0.3782	89.48 %
155 C	5.00 %	$\tau = 2.26 * 10^{-3} * \dot{\gamma}^{0.5527}$ $\mu = 1.25 * 10^{-3} * \dot{\gamma}^{-0.4473}$	$2.26 * 10^{-3}$ Pa*s	0.5527	95.16 %
160 C	0.51 %	$\tau = 2.31 * 10^{-4} * \dot{\gamma}^{0.2735}$ $\mu = 6.32 * 10^{-5} * \dot{\gamma}^{-0.7265}$	$2.31 * 10^{-4}$ Pa*s	0.2735	99.24 %

Table 19- 50% Sn 50% Bi (Created), Cone and Plate Viscosity

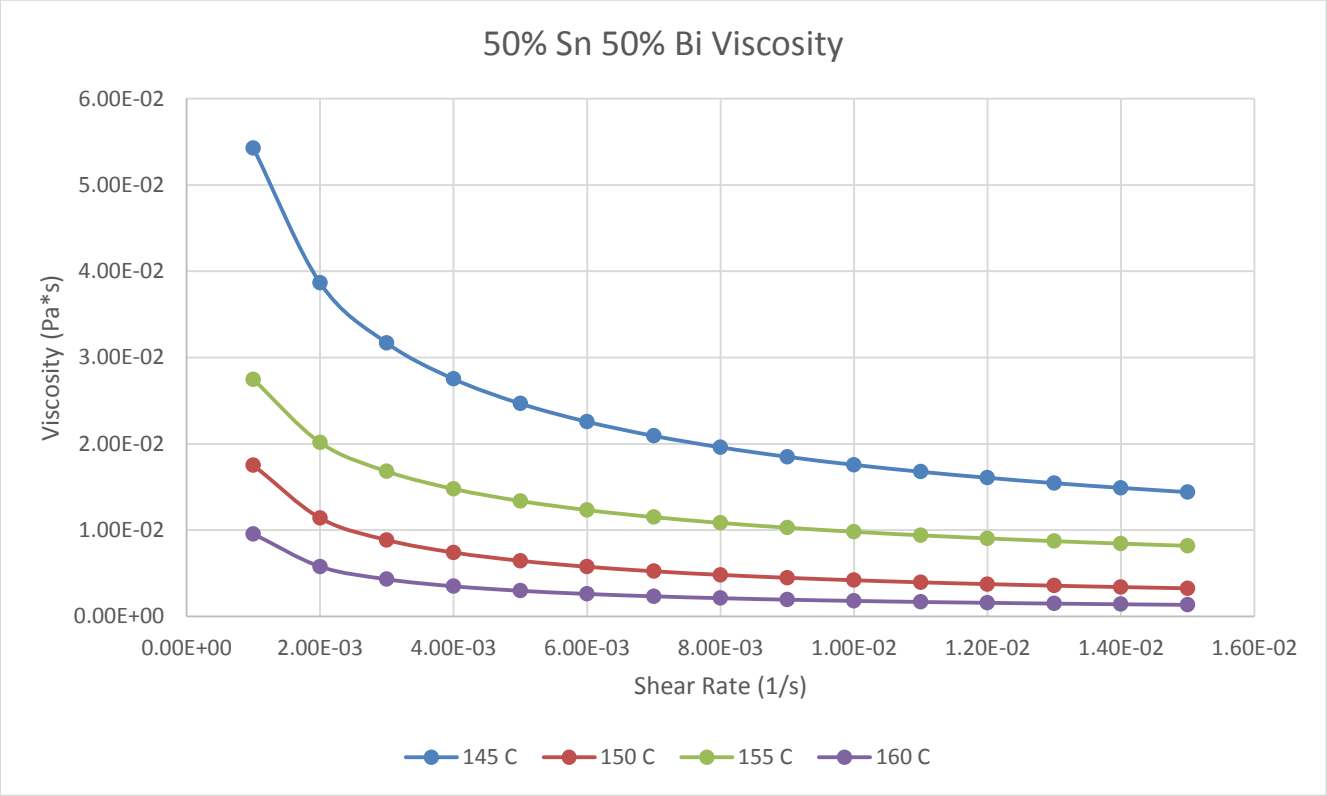

Figure 118- 50% Sn 50% Bi (Created), Cone and Plate Viscosity

145 C

Fraction Solid	12.7 %
Power Law	$\tau = 3.60 * 10^{-3} * \dot{\gamma}^{0.5101}$
	$\mu = 1.84 * 10^{-3} * \dot{\gamma}^{-0.4899}$
R^2	93.94 %

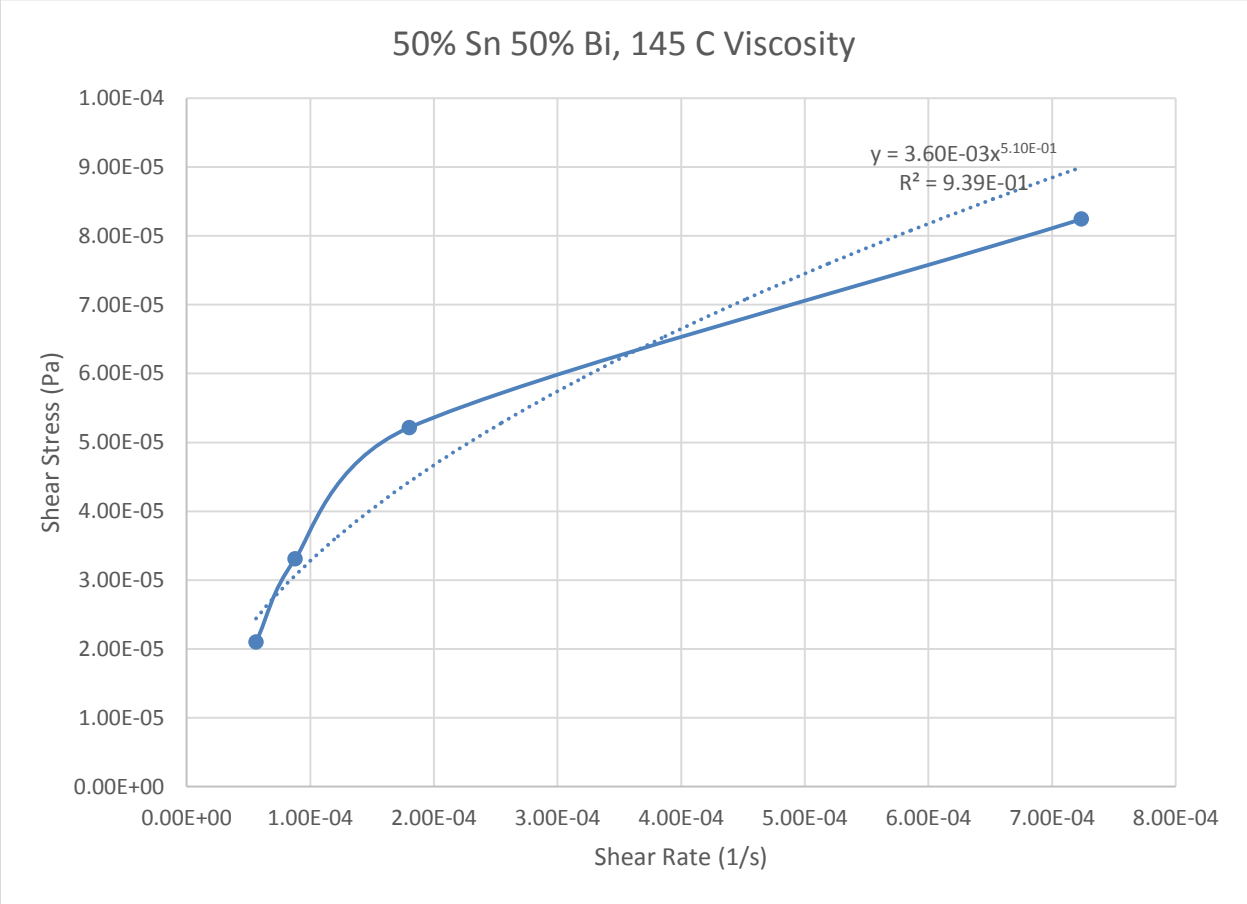

Figure 119- 50% Sn 50% Bi (Created), 145 C, Cone and Plate Viscosity

150 C

Fraction Solid	9.10 %
Power Law	$\tau = 6.33 * 10^{-4} * \dot{\gamma}^{0.3782}$
	$\mu = 2.39 * 10^{-4} * \dot{\gamma}^{-0.6218}$
R^2	89.48 %

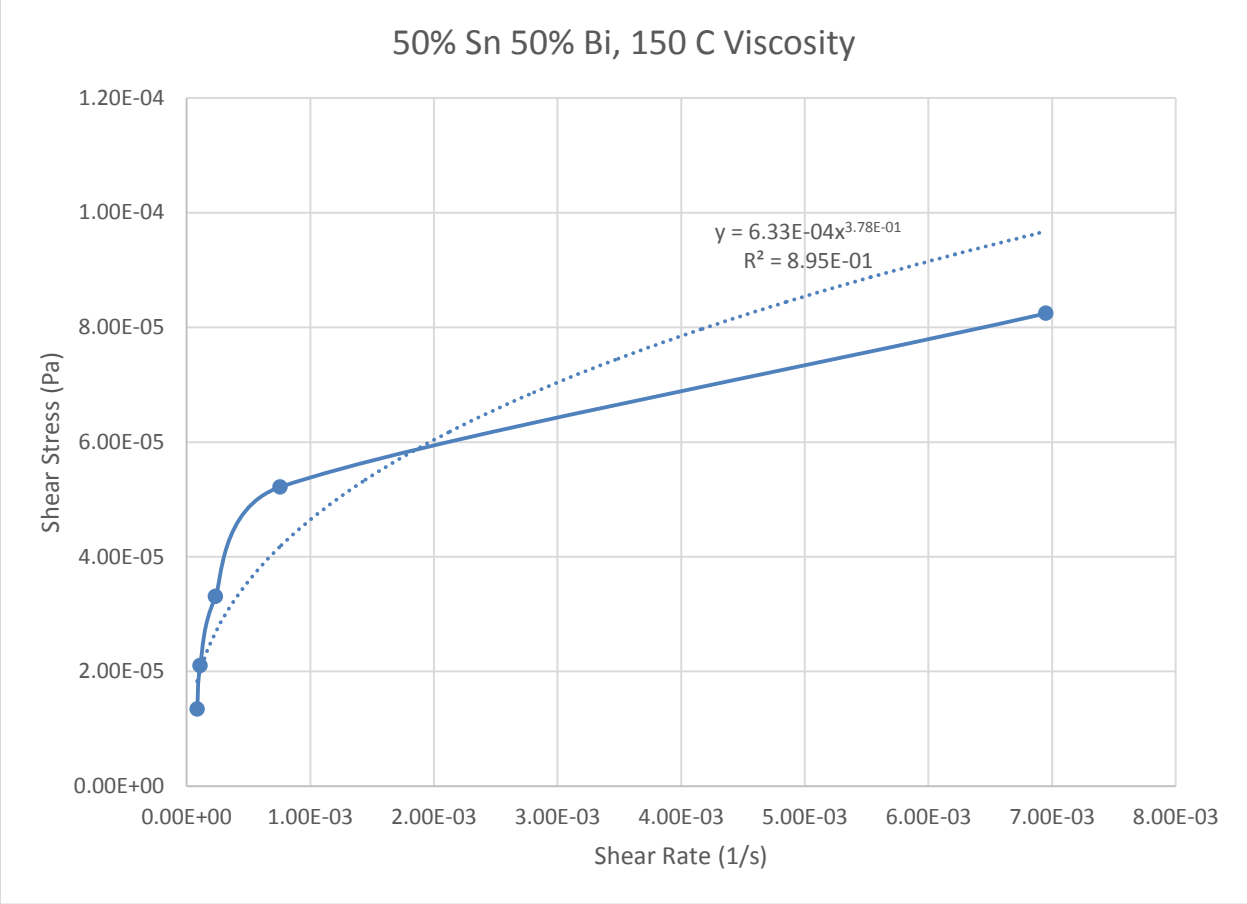

Figure 120- 50% Sn 50% Bi (Created), 150 C, Cone and Plate Viscosity

155 C

Fraction Solid	5.96 %
Power Law	$\tau = 2.26 * 10^{-3} * \dot{\gamma}^{0.5527}$
	$\mu = 1.25 * 10^{-3} * \dot{\gamma}^{-0.4473}$
R^2	95.16 %

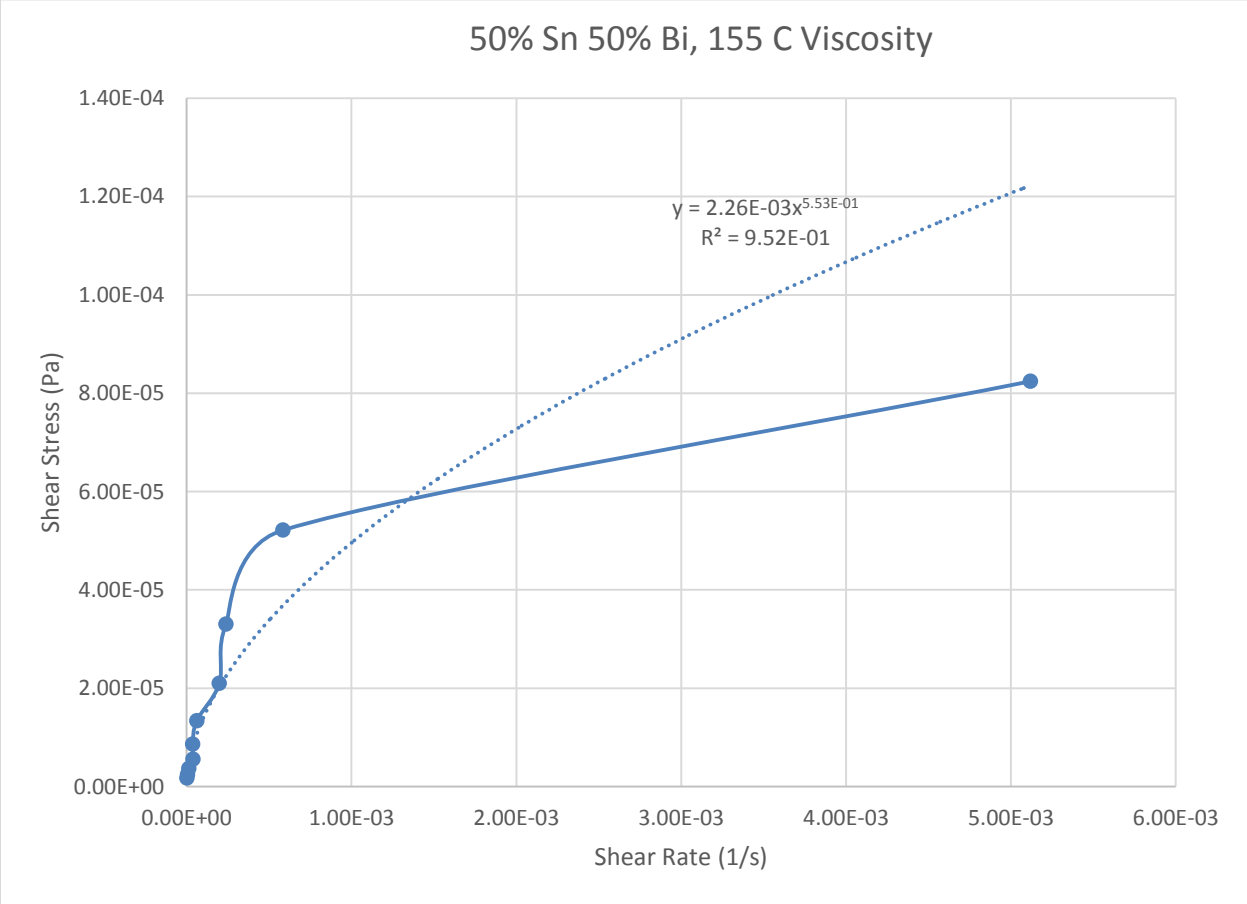

Figure 121- 50% Sn 50% Bi (Created), 155 C, Cone and Plate Viscosity

160 C

Fraction Solid	2.35 %
Power Law	$\tau = 2.31 * 10^{-4} * \dot{\gamma}^{0.2735}$
	$\mu = 6.32 * 10^{-5} * \dot{\gamma}^{-0.7265}$
R^2	99.24 %

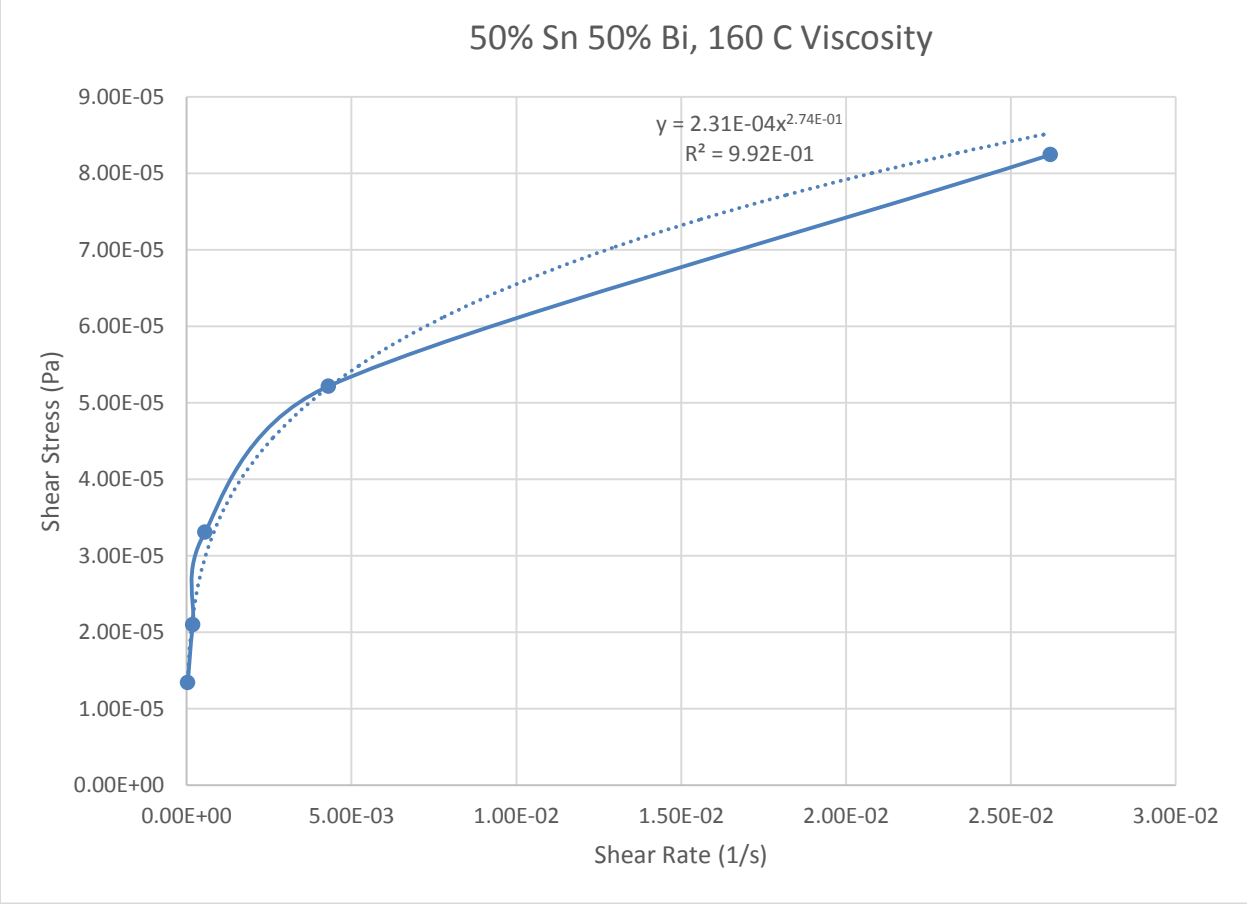

Figure 122- 50% Sn 50% Bi (Created), 160 C, Cone and Plate Viscosity

50% Tin 50% Bismuth (Sophisticated Alloys)

Actual Composition: 52.78% Sn, 47.22% Bi

Theoretical Solidus Line: 139 C
Theoretical Liquidus Line: 148.8 C

Experimental Solidus Line: 141.9 C
Experimental Liquidus Line: 151.5 C

Set-Up Notes

- Zeroed gap at 155 C. The temperature was then decreased by 5 C for each stress sweep. After this, the temperature was increased to 160 C for a final stress sweep.

- All liquid even in the SSM region, as opposed to my samples which were more likely to be SSM even in the liquid region

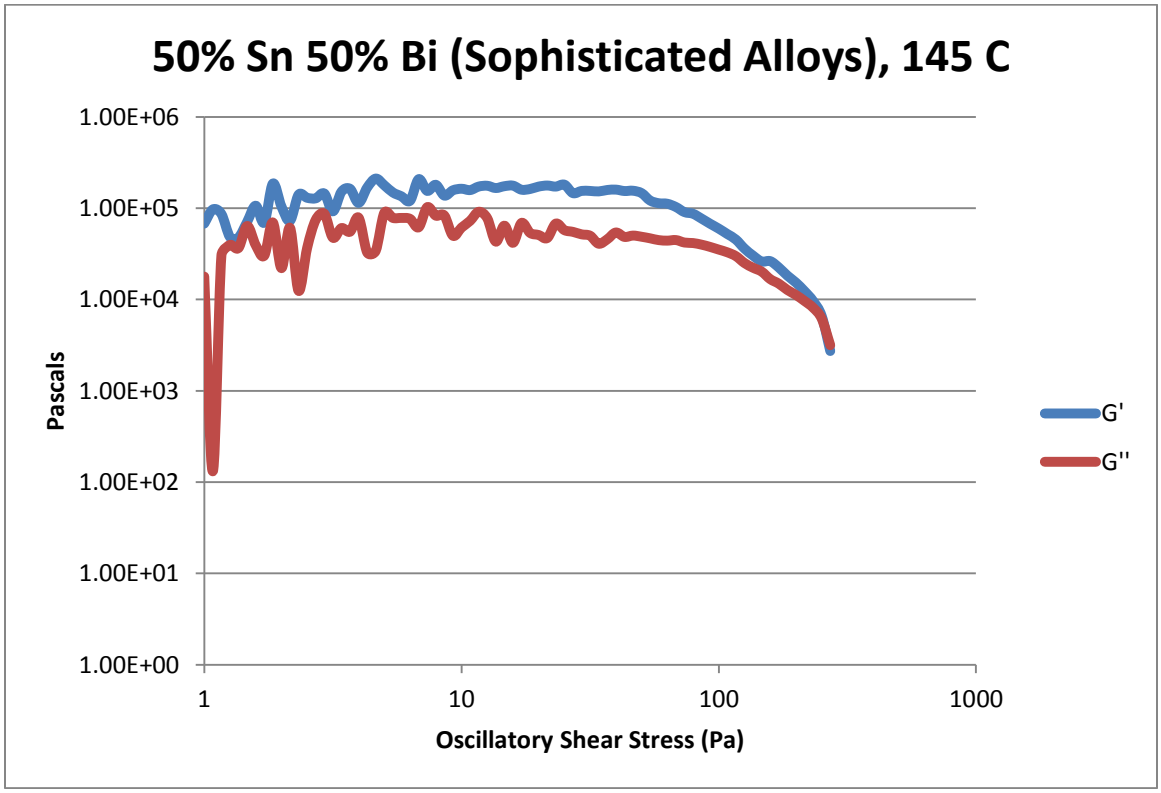

Figure 123- 50% Sn 50% Bi (Sophisticated Alloys), 145 C, Cone and Plate Stress Sweep

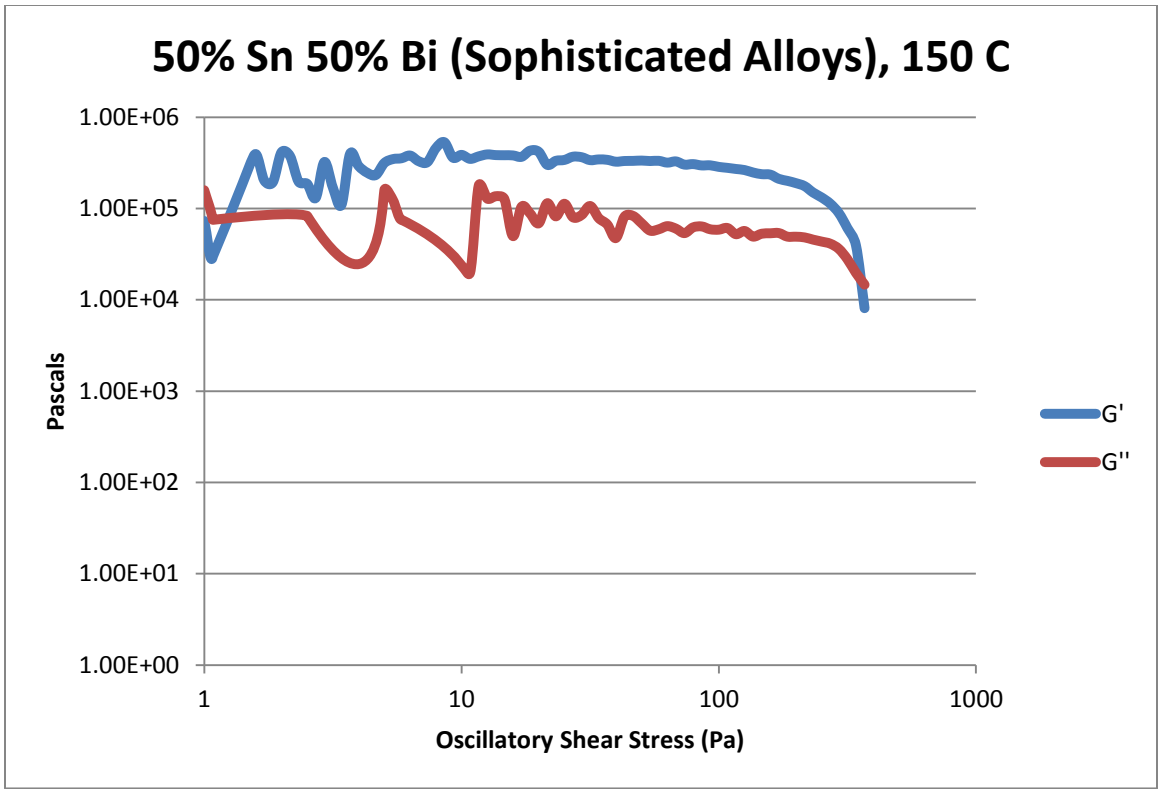

Figure 124- 50% Sn 50% Bi (Sophisticated Alloys), 150 C, Cone and Plate Stress Sweep

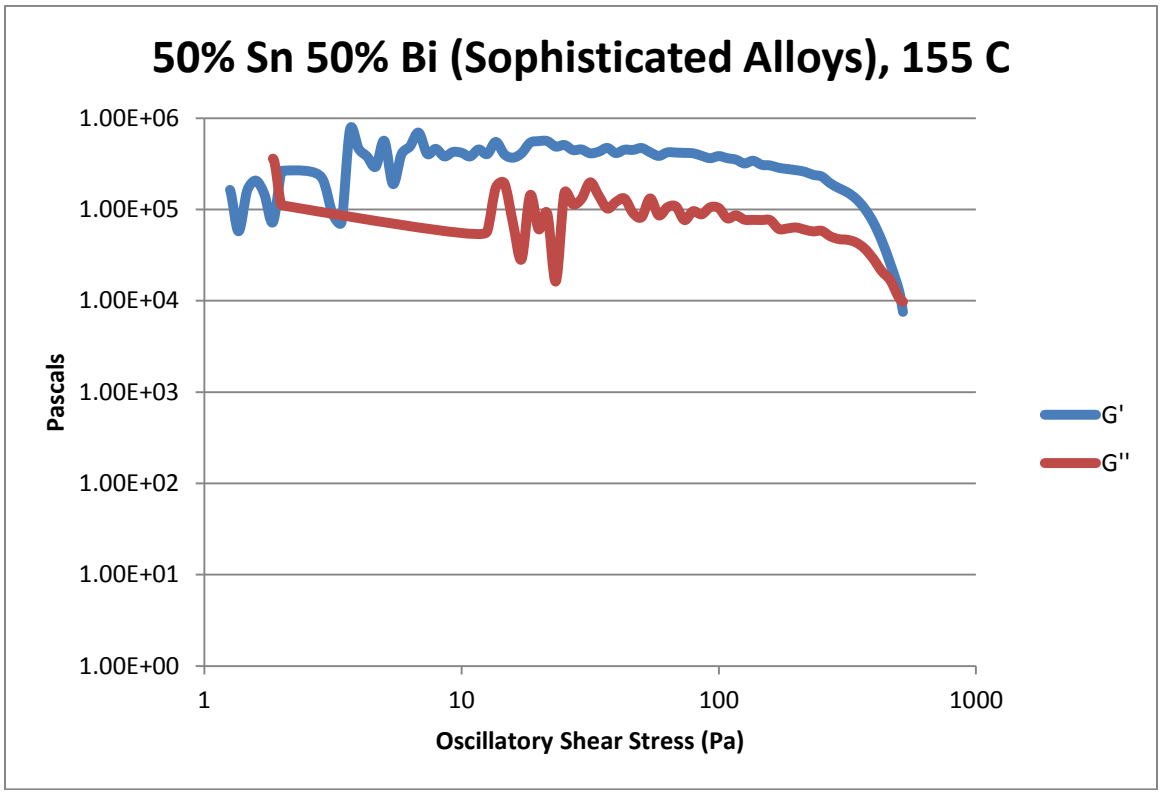

Figure 125- 50% Sn 50% Bi (Sophisticated Alloys), 155 C, Cone and Plate Stress Sweep

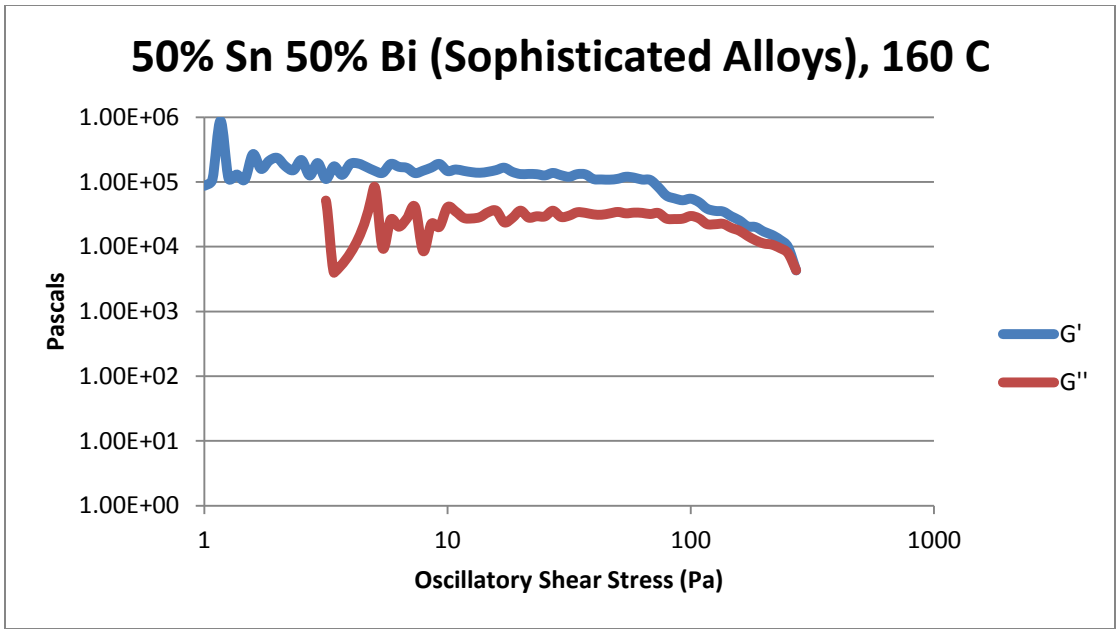

Figure 126- 50% Sn 50% Bi (Sophisticated Alloys), 160 C, Cone and Plate Stress Sweep

Temperature	Crossover Stress (Pa)	Crossover Stress (PSI)
145 C	$4.65 * 10^3$	0.674
150 C	$1.59 * 10^4$	2.31
155 C	$1.03 * 10^4$	1.49
160 C	$4.40 * 10^3$	0.638

Table 20- 50% Sn 50% Bi (Sophisticated Alloys), Cone and Plate Crossover Stresses

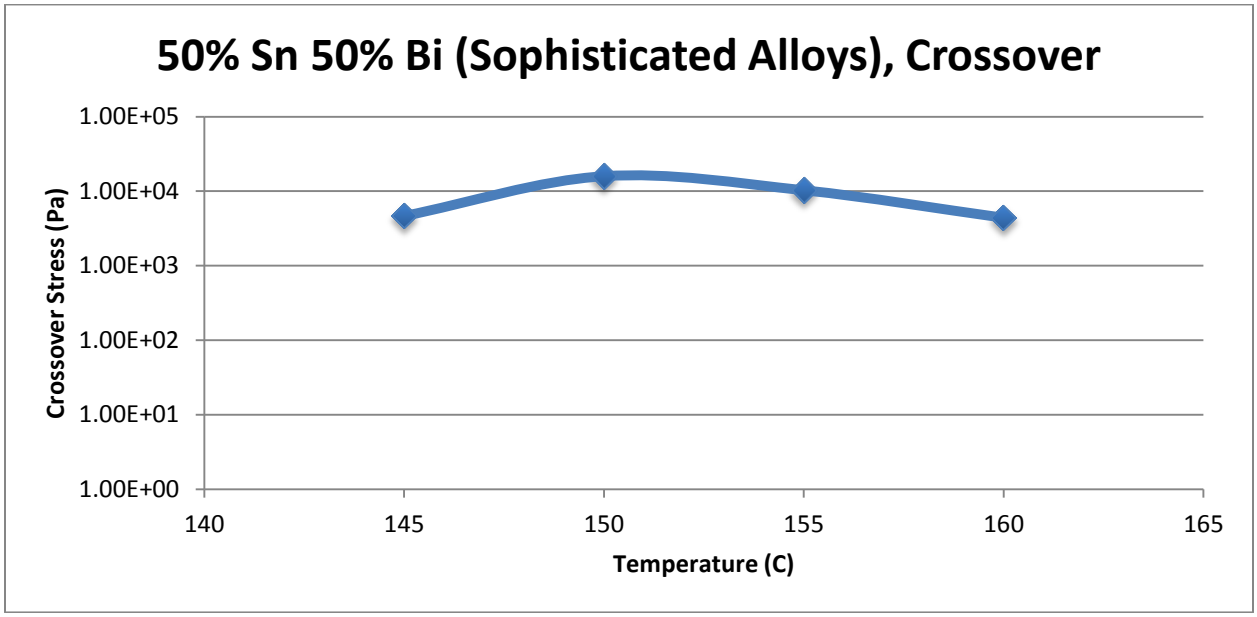

Figure 127- 50% Sn 50% Bi (Sophisticated Alloys), Cone and Plate Crossover Stresses

Temperature	Fraction Solid (At %)	G' Plateau (Pa)	G'' Plateau (Pa)
145 C	12.7	$1.55 * 10^5$	$4.87 * 10^4$
150 C	9.10	$3.33 * 10^5$	$6.22 * 10^4$
155 C	5.00	$4.54 * 10^5$	$1.32 * 10^5$
160 C	0.51	$1.42 * 10^5$	$3.35 * 10^4$

Table 21- 50% Sn 50% Bi (Sophisticated Alloys), Cone and Plate Plateau Stresses

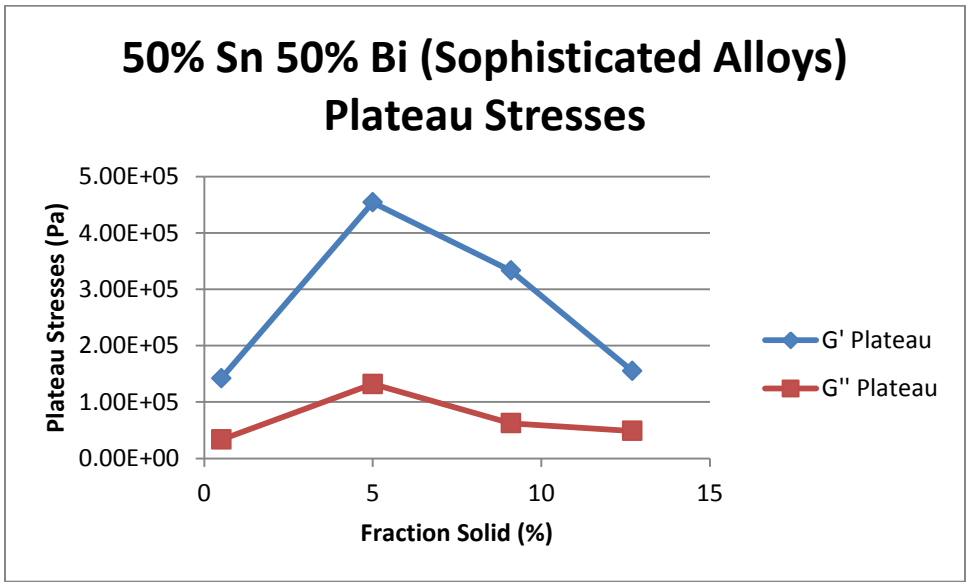

Figure 128- 50% Sn 50% Bi (Sophisticated Alloys), Cone and Plate Plateau Stresses vs. Fraction Solid

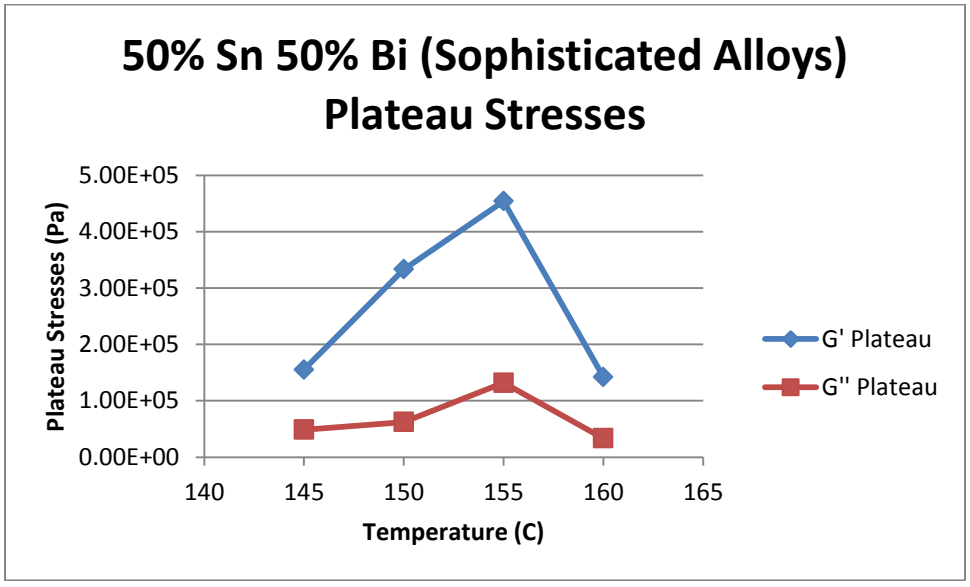

Figure 129- 50% Sn 50% Bi (Sophisticated Alloys), Cone and Plate Plateau Stresses vs. Temperature

50% Sn 50% Bi (Sophisticated Alloys) Viscosity					
Temperature	**Fraction Solid**	**Power Law**	**K**	**n**	**R^2**
145 C	12.7 %	$\tau = 6.05 * 10^{-5} * \dot{\gamma}^{0.2725}$ $\mu = 1.65 * 10^{-5} * \dot{\gamma}^{-0.7275}$	$6.05 * 10^{-5}$ Pa*s	0.2725	98.90 %
150 C	9.10 %	$\tau = 5.05 * 10^{-5} * \dot{\gamma}^{0.0961}$ $\mu = 4.85 * 10^{-6} * \dot{\gamma}^{-0.9039}$	$5.05 * 10^{-5}$ Pa*s	0.0961	21.23 %
155 C	5.00 %	$\tau = 7.58 * 10^{-5} * \dot{\gamma}^{0.1303}$ $\mu = 9.88 * 10^{-6} * \dot{\gamma}^{-0.8697}$	$7.58 * 10^{-5}$ Pa*s	0.1303	93.46 %
160 C	0.51 %	$\tau = 7.86 * 10^{-5} * \dot{\gamma}^{0.2919}$ $\mu = 2.29 * 10^{-6} * \dot{\gamma}^{-0.7081}$	$7.86 * 10^{-5}$ Pa*s	0.2919	93.89 %

Table 22- 50% Sn 50% Bi (Sophisticated Alloys), Cone and Plate Viscosity

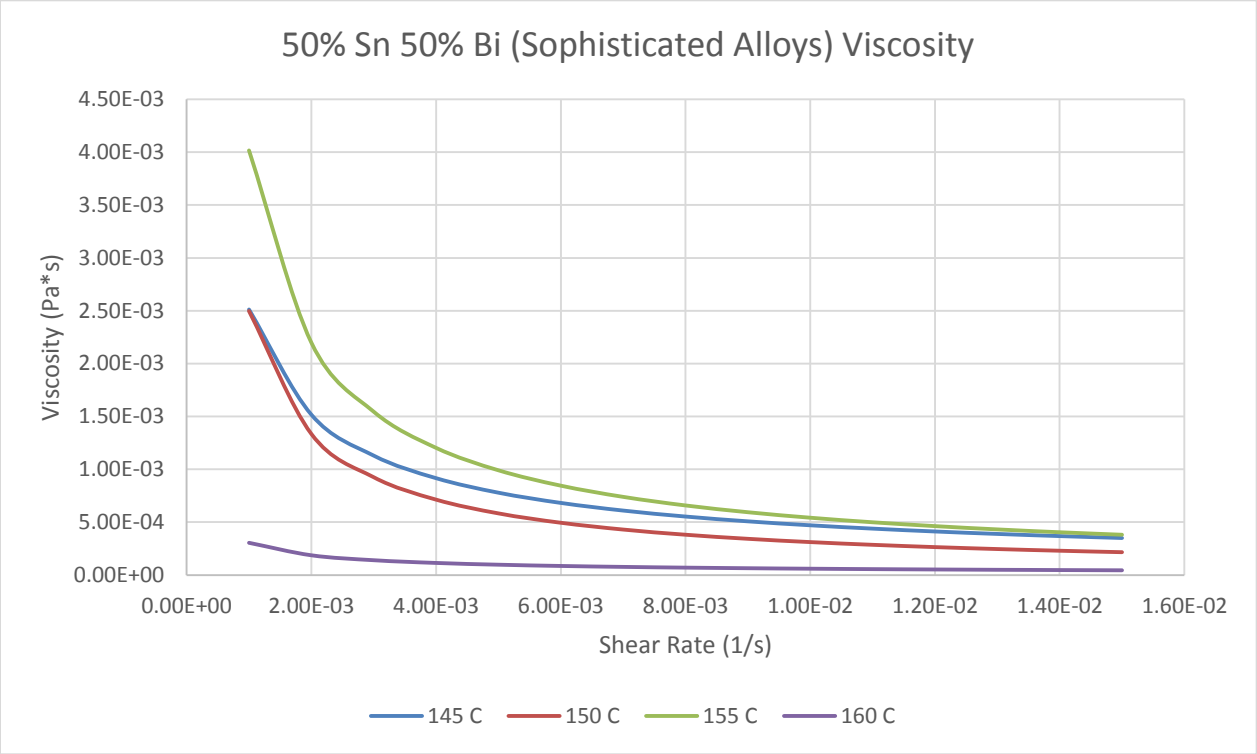

Figure 130- 50% Sn 50% Bi (Sophisticated Alloys), Cone and Plate Viscosity

145 C

Fraction Solid	13.9 %
Power Law	$\tau = 6.05 * 10^{-5} * \dot{\gamma}^{0.2725}$
	$\mu = 1.65 * 10^{-5} * \dot{\gamma}^{-0.7275}$
R^2	98.90 %

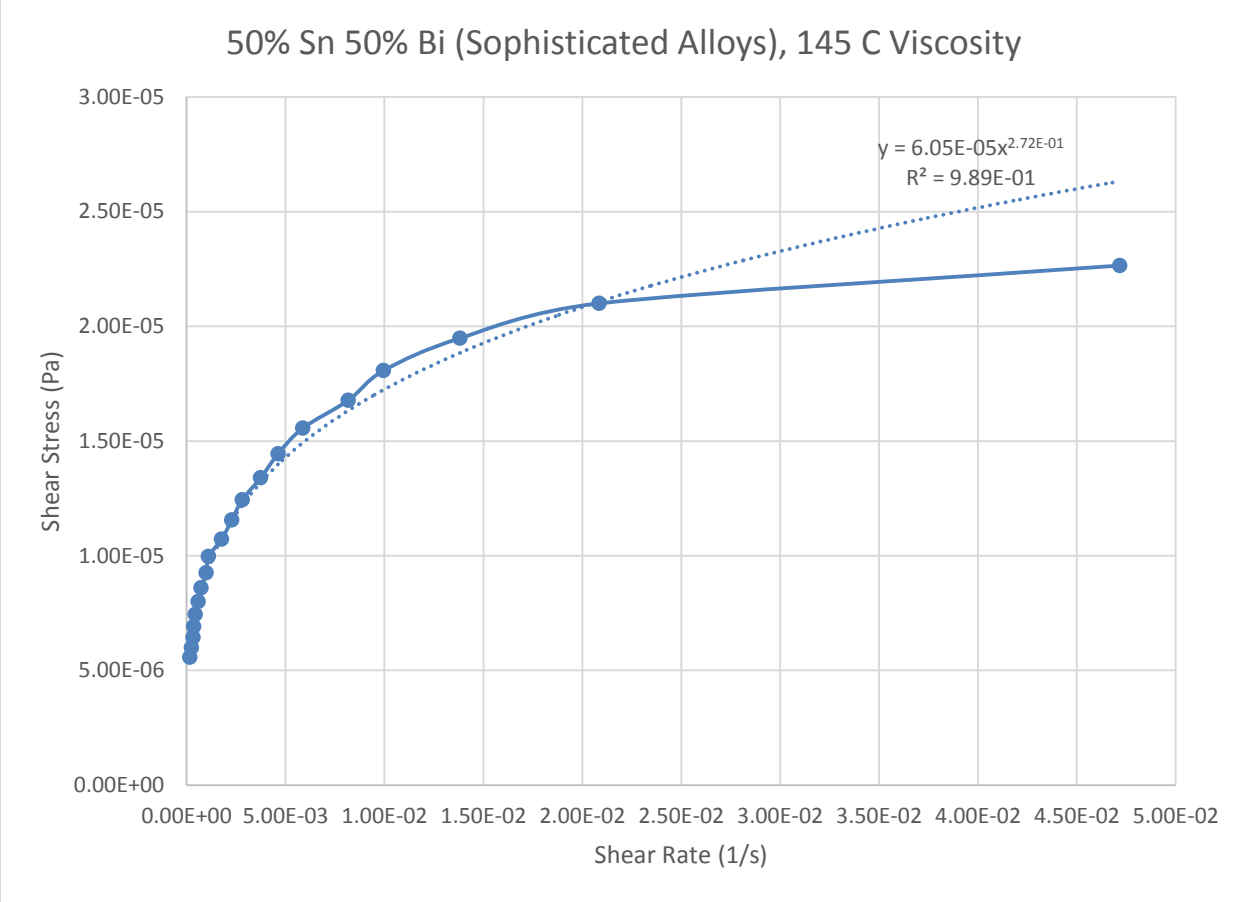

Figure 131- 50% Sn 50% Bi (Sophisticated Alloys), 145 C, Cone and Plate Viscosity

150 C

Fraction Solid	9.32 %
Power Law	$\tau = 5.05 * 10^{-5} * \dot{\gamma}^{0.0961}$
	$\mu = 4.85 * 10^{-6} * \dot{\gamma}^{-0.9039}$
R^2	21.23%

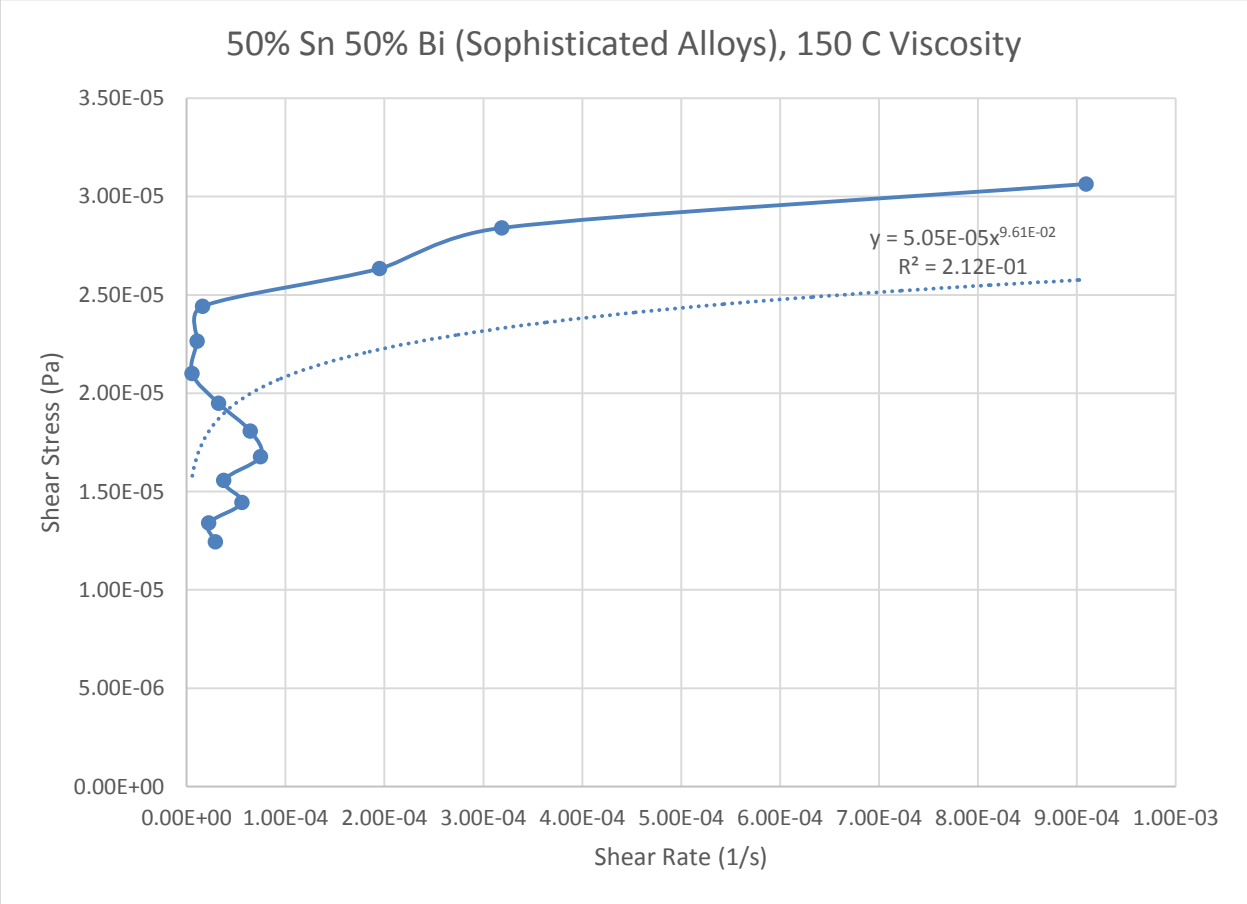

Figure 132- 50% Sn 50% Bi (Sophisticated Alloys), 150 C, Cone and Plate Viscosity

155 C

Fraction Solid	5.96 %
Power Law	$\tau = 7.58 * 10^{-5} * \dot{\gamma}^{0.1303}$
	$\mu = 9.88 * 10^{-6} * \dot{\gamma}^{-0.8697}$
R^2	93.46 %

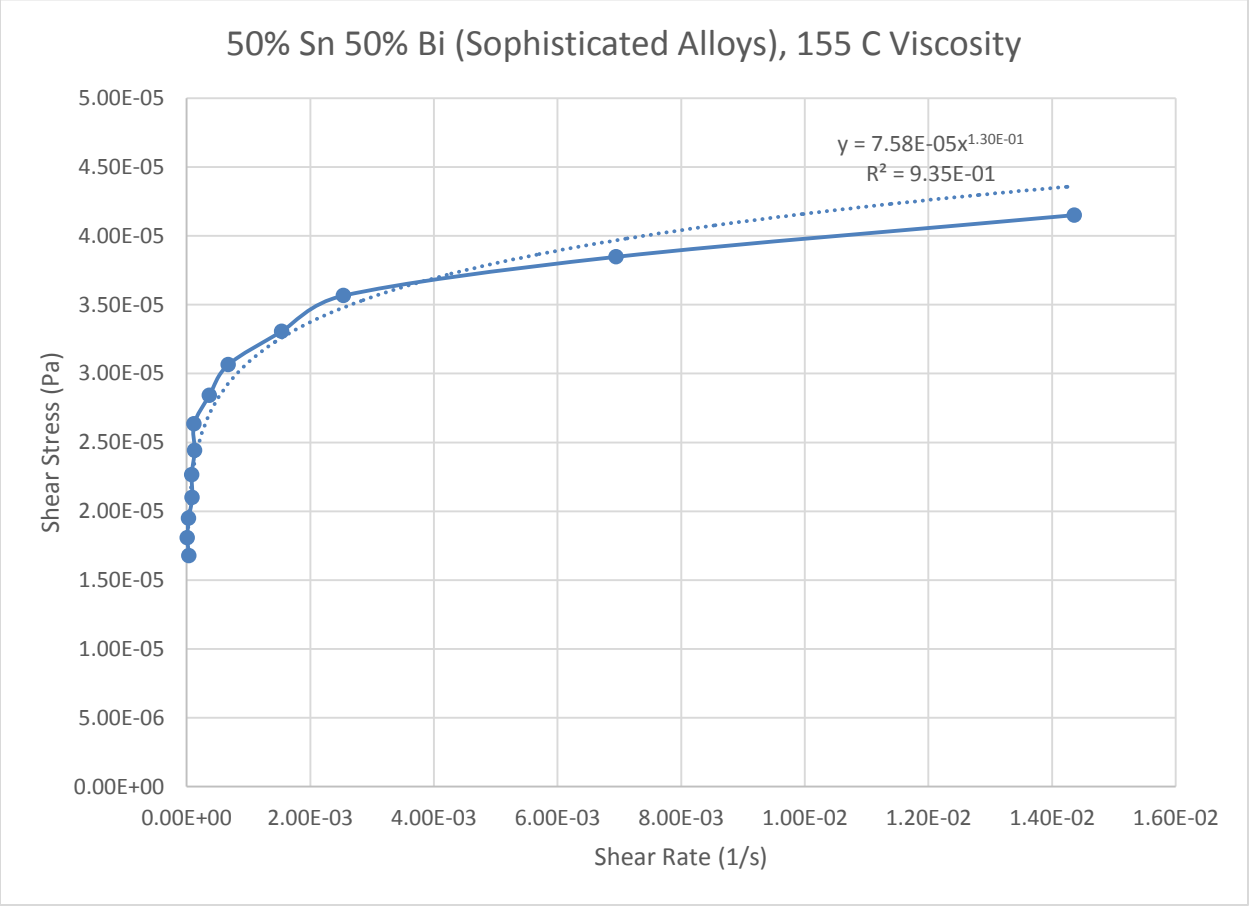

Figure 133- 50% Sn 50% Bi (Sophisticated Alloys), 155 C, Cone and Plate Viscosity

160 C

Fraction Solid	2.35 %
Power Law	$\tau = 7.86 * 10^{-5} * \dot{\gamma}^{0.2919}$
	$\mu = 2.29 * 10^{-6} * \dot{\gamma}^{-0.7081}$
R^2	93.89%

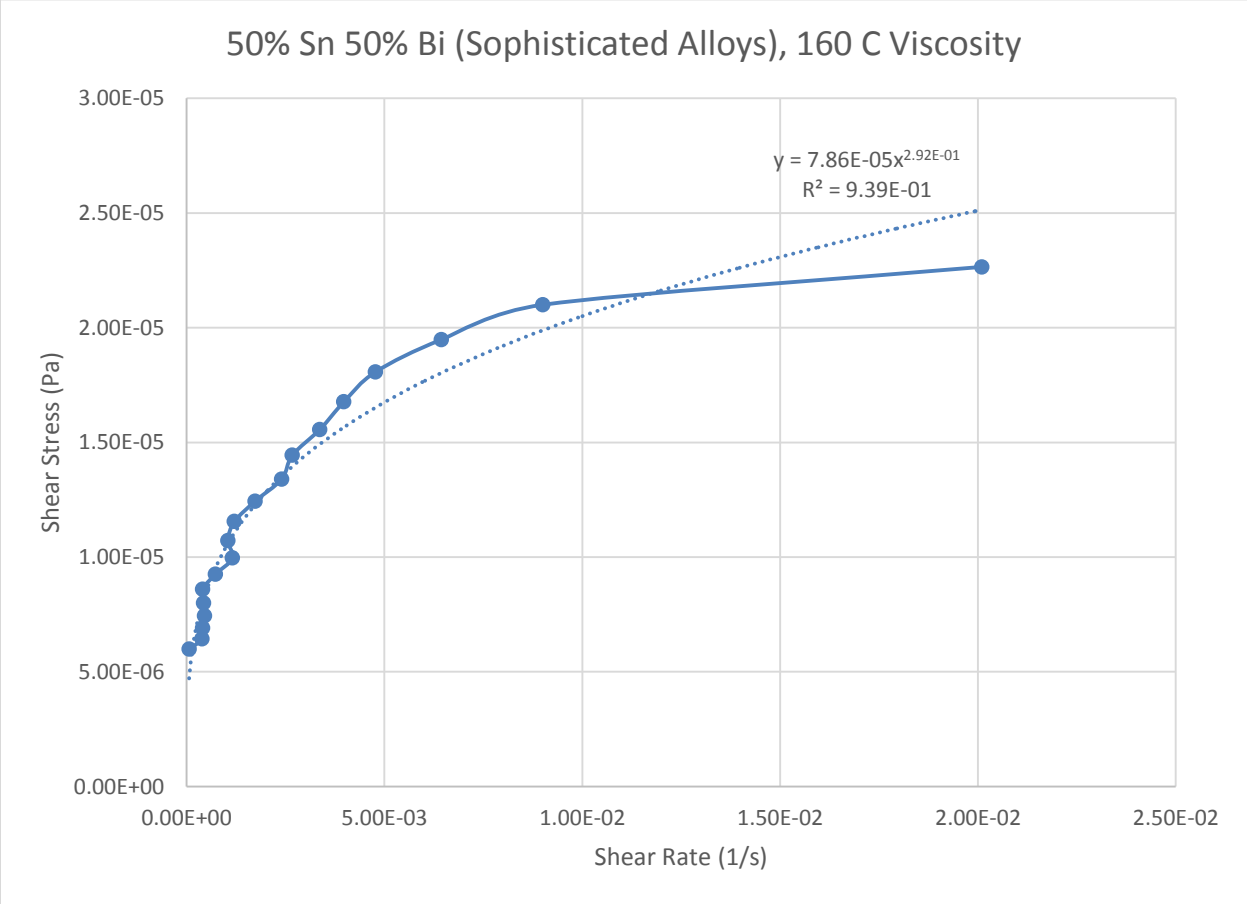

Figure 134- 50% Sn 50% Bi (Sophisticated Alloys), 160 C, Cone and Plate Viscosity

55% Tin 45% Bismuth (Run 1)

Expected Composition: 57.00% Sn, 43.00% Bi

Theoretical Solidus Line: 139 C
Theoretical Liquidus Line: 139 C

Experimental Solidus Line: 138.8 C
Experimental Liquidus Line: 143 C

Set-Up Notes

- Zeroed the gap at 150 C. This stress sweep was conducted and followed by a stress sweep at 145 C. The temperature was then raised to 155 C and 160 C for the two final stress sweeps.

- Data had a weird double-dip instead of a clean drop-off, which leads me to question the accuracy of the data.

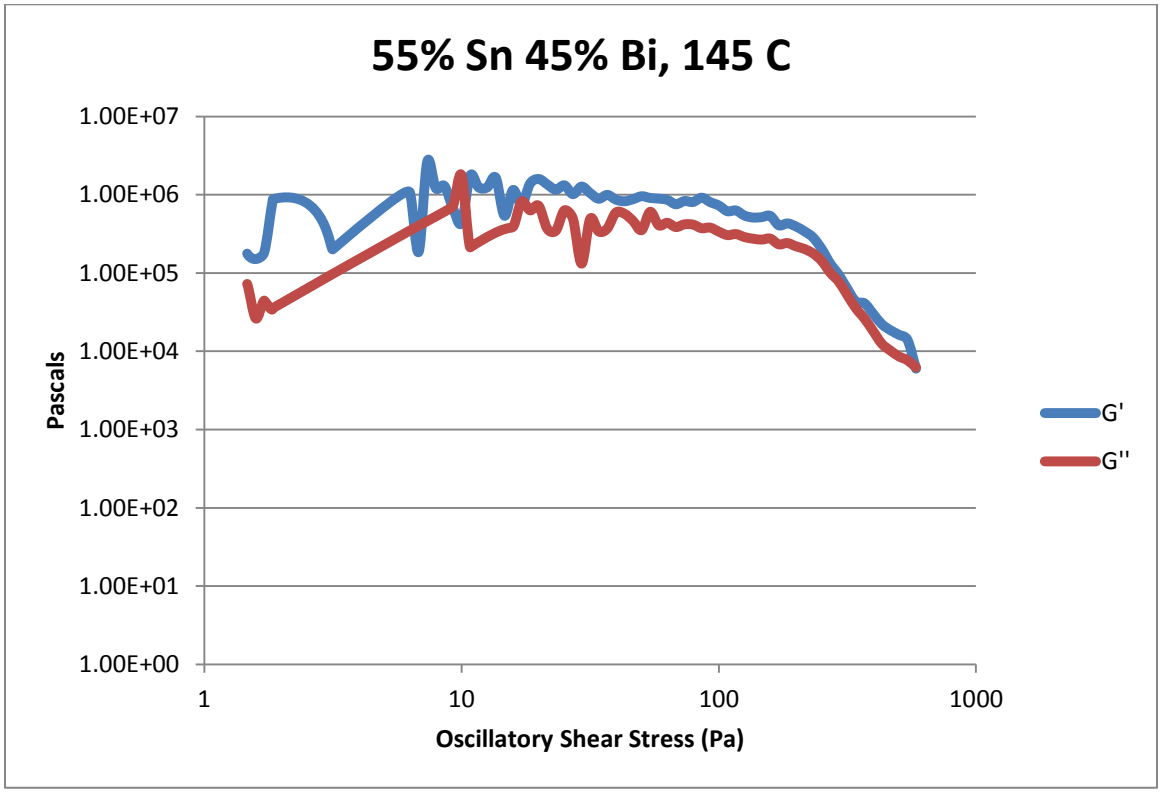

Figure 135- 55% Sn 45% Bi (Run 1), 145 C, Cone and Plate Stress Sweep

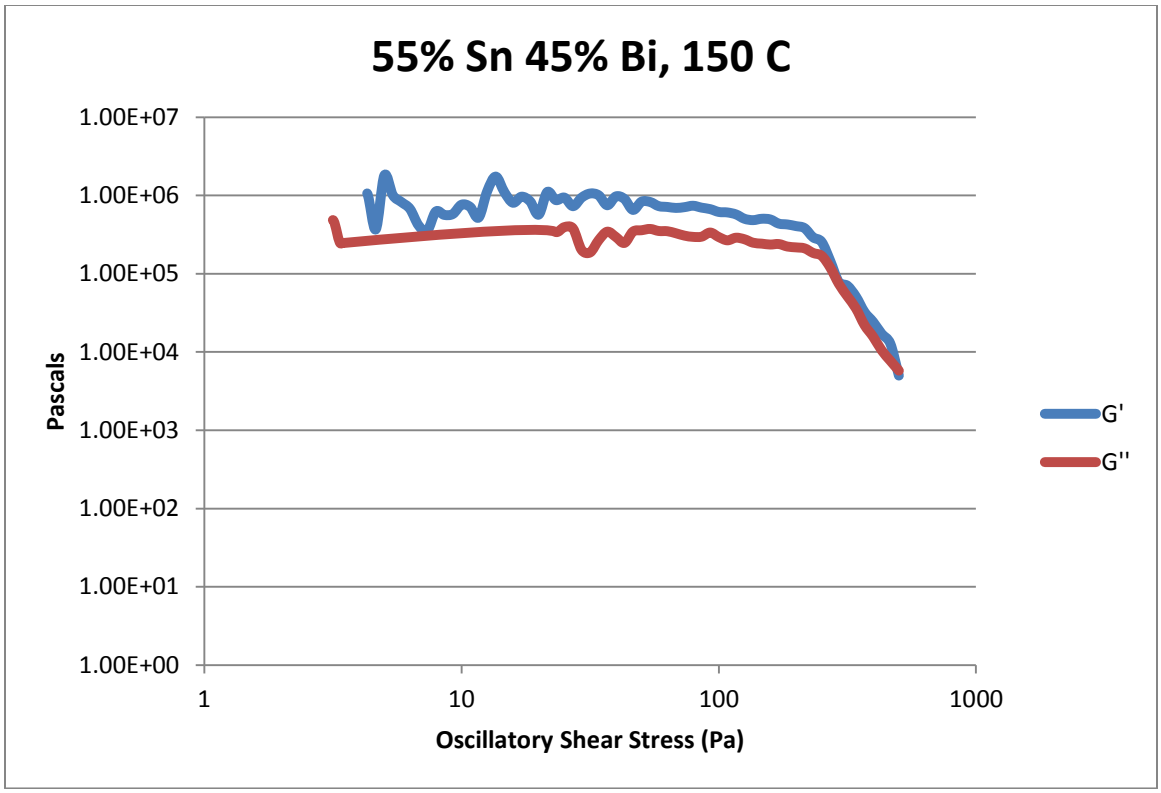

Figure 136- 55% Sn 45% Bi (Run 1), 150 C, Cone and Plate Stress Sweep

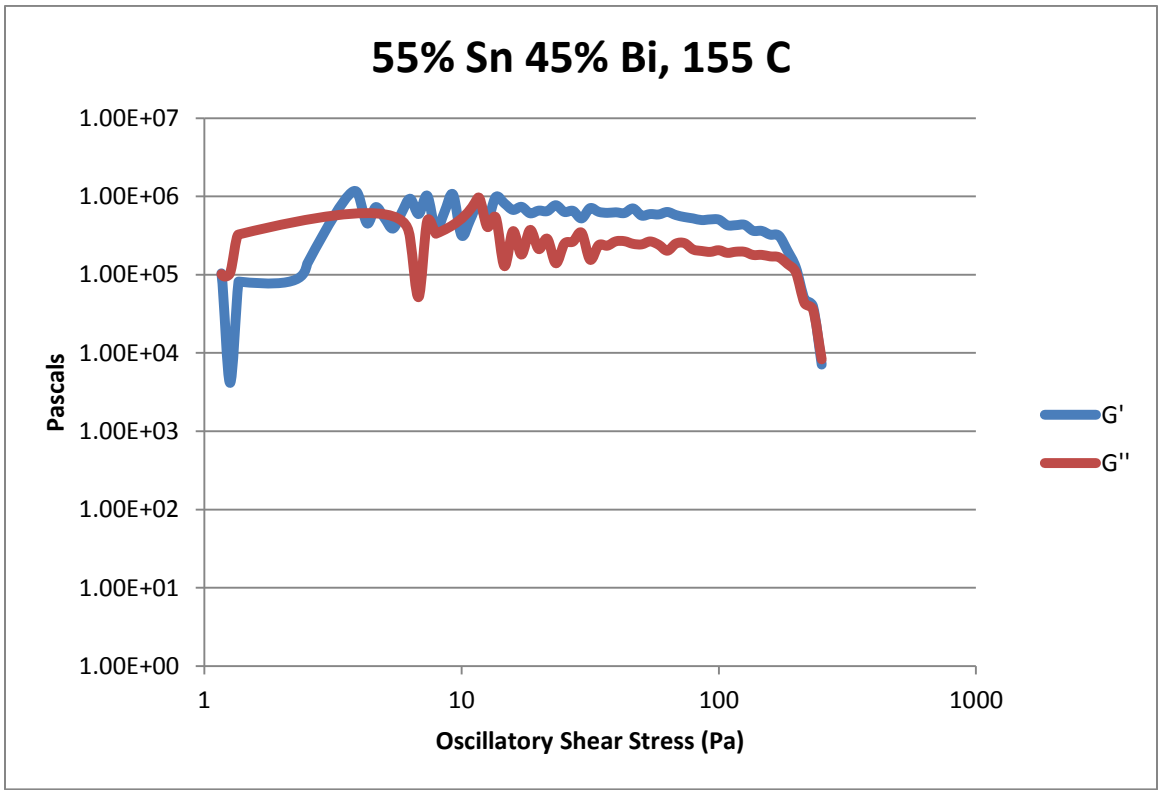

Figure 137- 55% Sn 45% Bi (Run 1), 155 C, Cone and Plate Stress Sweep

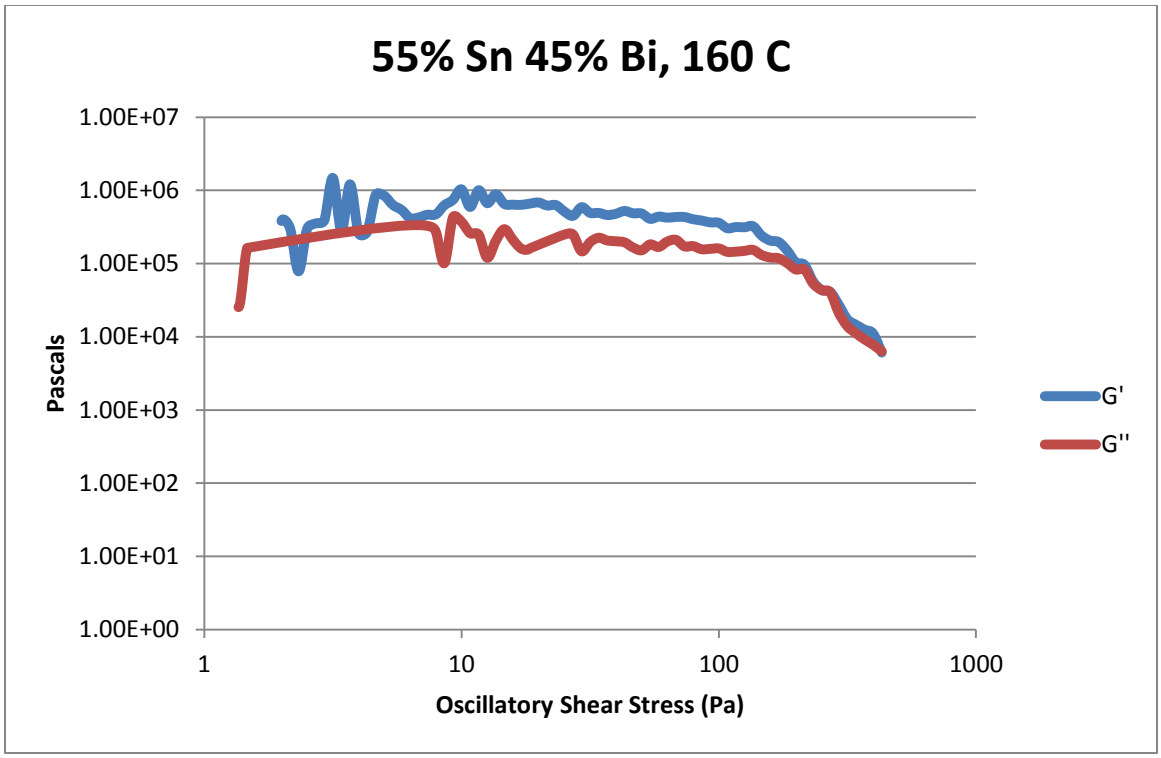

Figure 138- 55% Sn 45% Bi (Run 1), 160 C, Cone and Plate Stress Sweep

Temperature	Crossover Stress (Pa)	Crossover Stress (PSI)
145 C	$6.05 * 10^3$	0.88
150 C	$6.28 * 10^3$	0.91
155 C	$7.24 * 10^3$	1.05
160 C	$6.46 * 10^3$	0.94

Table 23- 55% Sn 45% Bi (Run 1), Cone and Plate Crossover Stresses

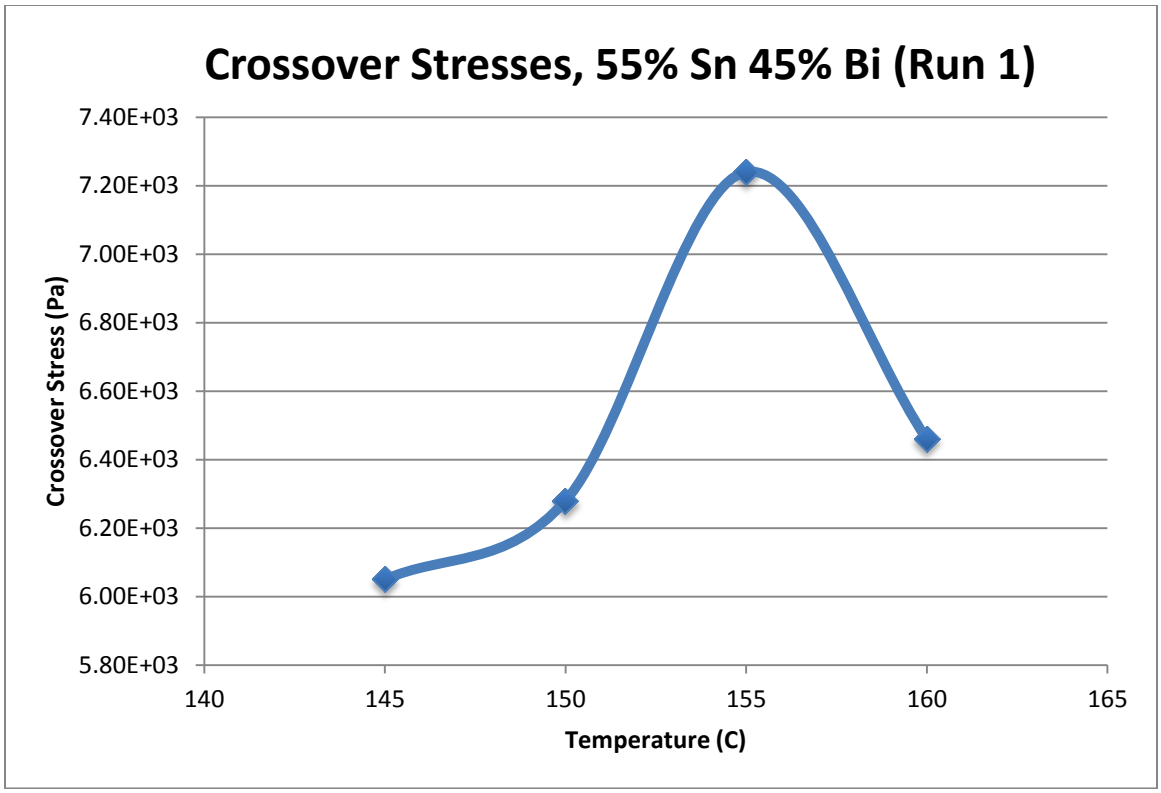

Figure 139- 55% Sn 45% Bi (Run 1), Cone and Plate Crossover Stresses

Temperature	Fraction Solid (At %)	G' Plateau (Pa)	G'' Plateau (Pa)
145 C	5.17	$8.68 * 10^5$	$3.95 * 10^5$
150 C	1.79	$7.14 * 10^5$	$3.22 * 10^5$
155 C	0	$6.54 * 10^5$	$2.52 * 10^5$

Table 24- 55% Sn 45% Bi (Run 1), Cone and Plate Plateau Stresses

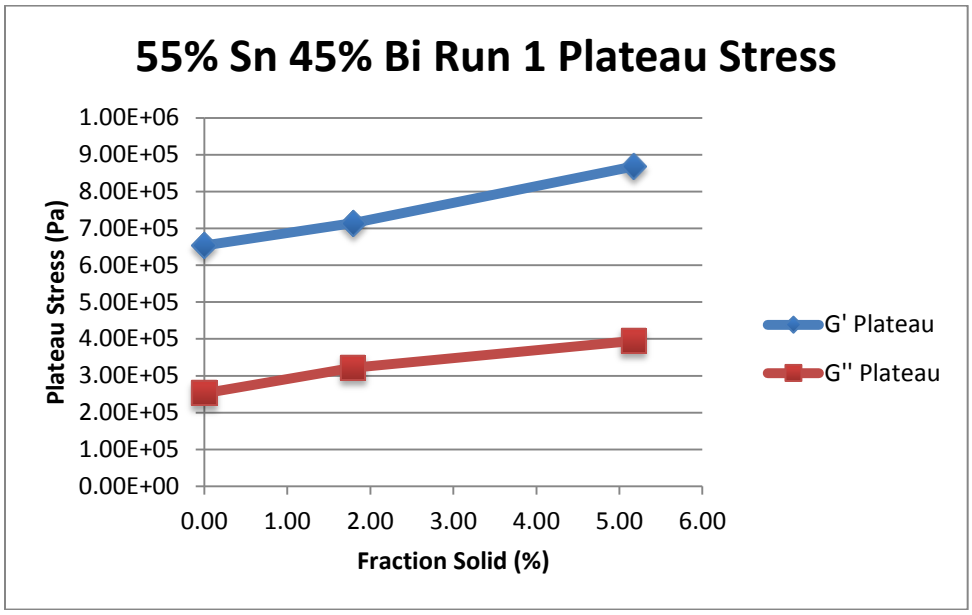

Figure 140- 55% Sn 45% Bi (Run 1), Cone and Plate Plateau Stresses vs. Fraction Solid

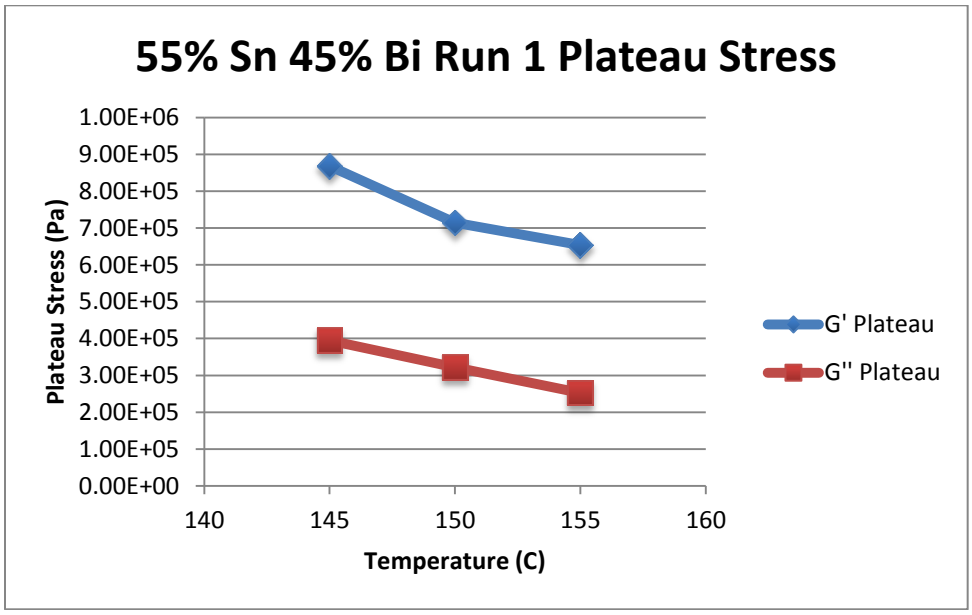

Figure 141- 55% Sn 45% Bi (Run 1), Cone and Plate Plateau Stresses vs. Temperature

55% Sn 45%% Bi (Run 1) Viscosity					
Temperature	**Fraction Solid**	**Power Law**	**K**	**n**	**R^2**
145 C	5.17 %	$\tau = 7.66 * 10^{-5} * \dot{\gamma}^{0.1576}$ $\mu = 1.21 * 10^{-5} * \dot{\gamma}^{-0.8424}$	$7.66 * 10^{-5}$ Pa*s	0.1576	84.97 %
150 C	1.79 %	$\tau = 7.69 * 10^{-5} * \dot{\gamma}^{0.1796}$ $\mu = 1.38 * 10^{-5} * \dot{\gamma}^{-0.8204}$	$7.69 * 10^{-5}$ Pa*s	0.1796	90.03 %
155 C	0 %	$\tau = 3.93 * 10^{-5} * \dot{\gamma}^{0.1245}$ $\mu = 4.83 * 10^{-6} * \dot{\gamma}^{-0.8755}$	$3.93 * 10^{-5}$ Pa*s	0.1245	62.71 %

Table 25- 55% Sn 45% Bi (Run 1), Cone and Plate Viscosity

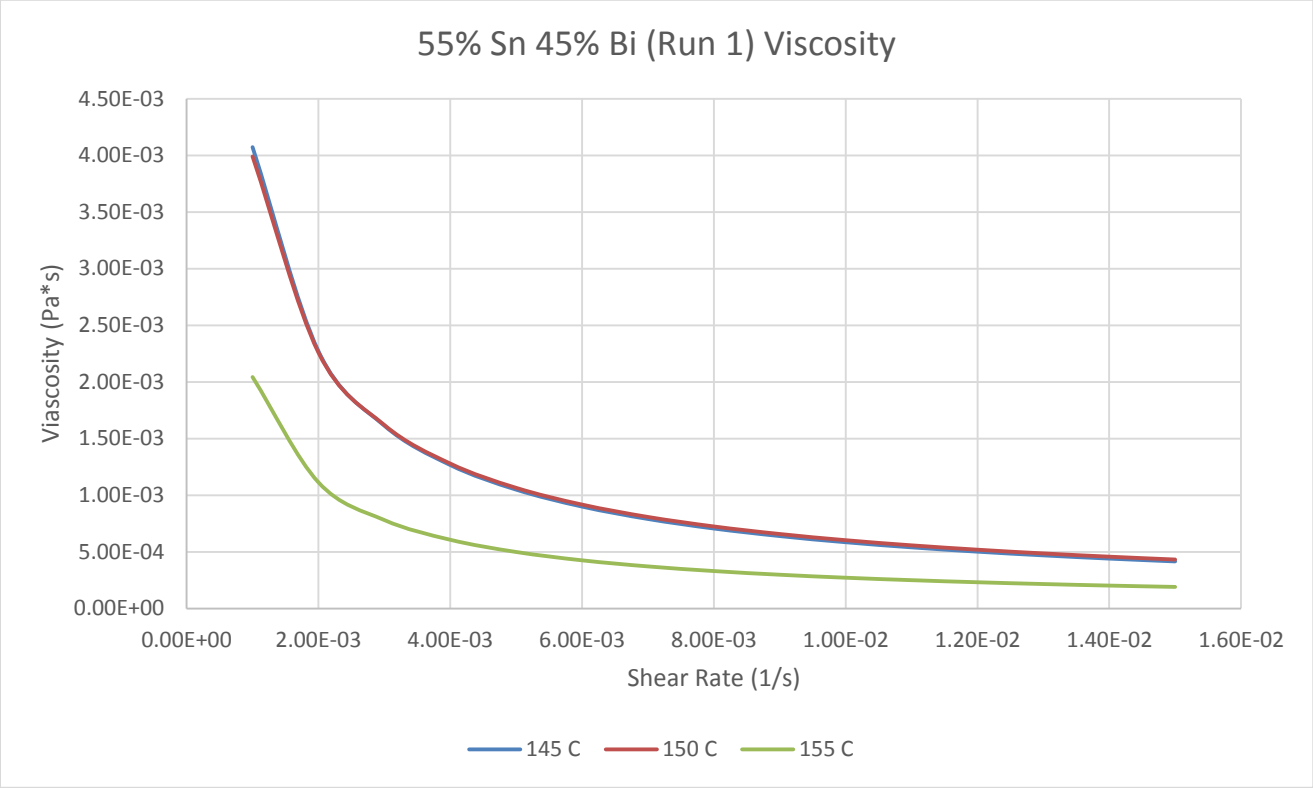

Figure 142- 55% Sn 45% Bi (Run 1), Cone and Plate Viscosity

145 C

Fraction Solid	5.17 %
Power Law	$\tau = 7.66 * 10^{-5} * \dot{\gamma}^{0.1576}$
	$\mu = 1.21 * 10^{-5} * \dot{\gamma}^{-0.8424}$
R^2	84.97 %

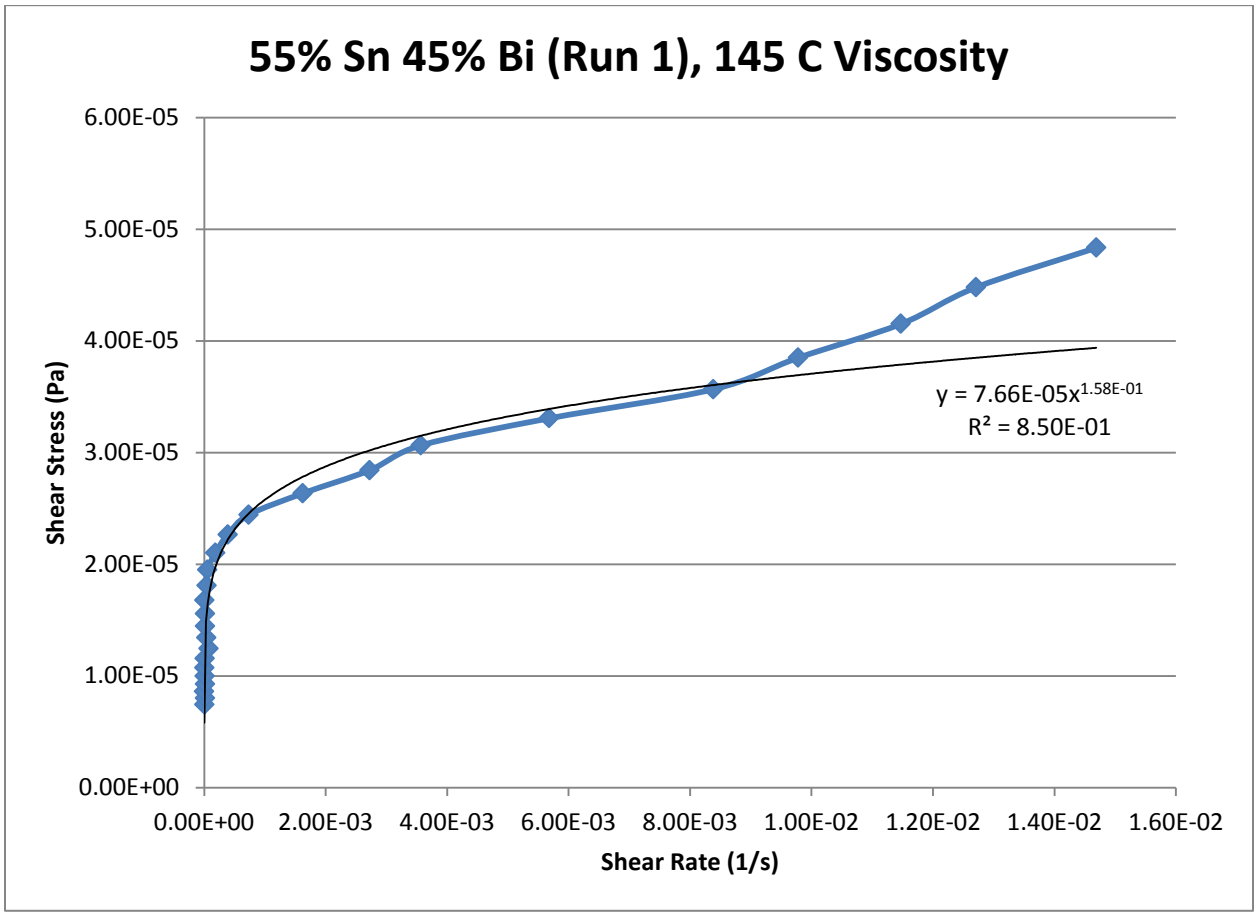

Figure 143- 55% Sn 45% Bi (Run 1), 145 C, Cone and Plate Viscosity

150 C

Fraction Solid	1.79 %
Power Law	$\tau = 7.69 * 10^{-5} * \dot{\gamma}^{0.1796}$
	$\mu = 1.38 * 10^{-5} * \dot{\gamma}^{-0.8204}$
R^2	90.03 %

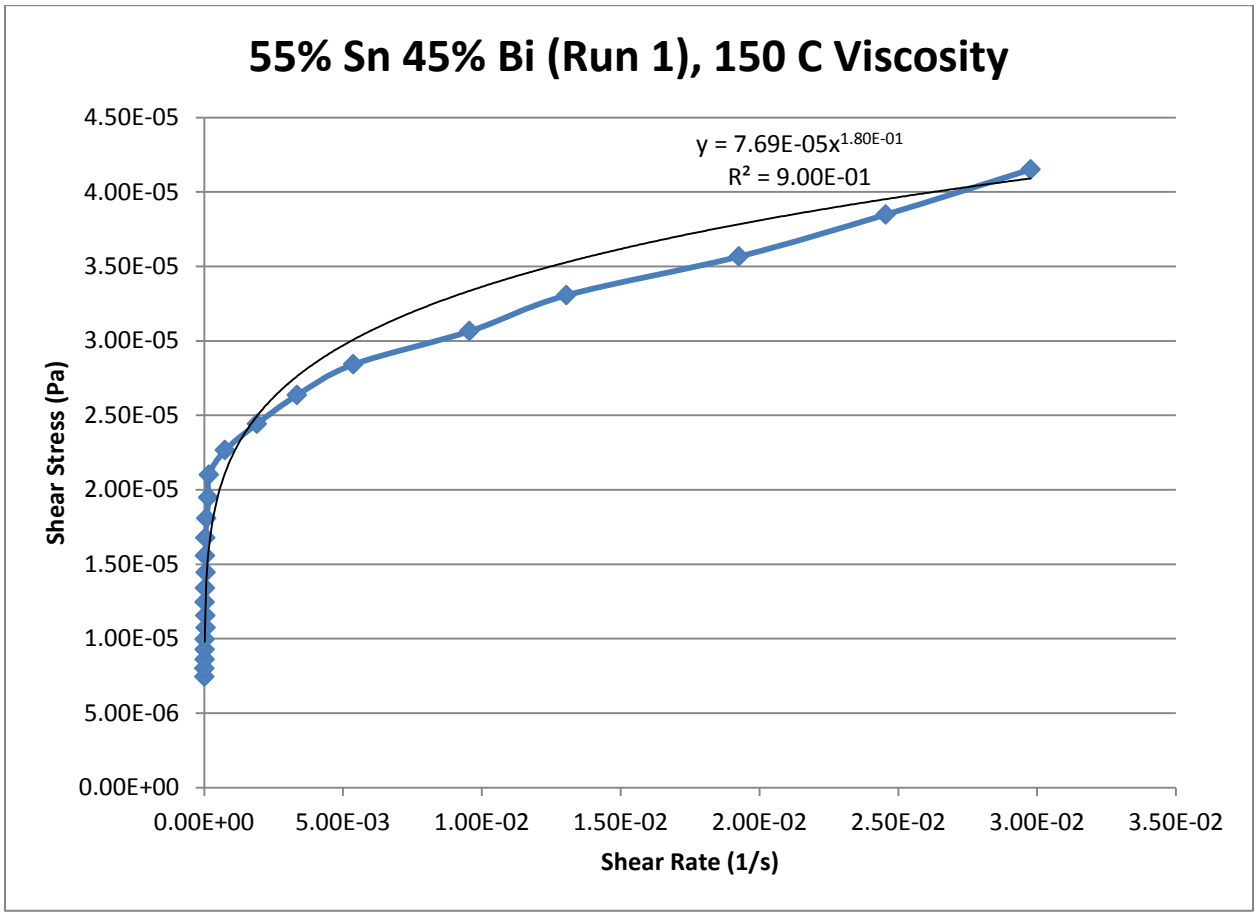

Figure 144- 55% Sn 45% Bi (Run 1), 150 C, Cone and Plate Viscosity

155 C

Fraction Solid	0 %
Power Law	$\tau = 3.93 * 10^{-5} * \dot{\gamma}^{0.1245}$
	$\mu = 4.83 * 10^{-6} * \dot{\gamma}^{-0.8755}$
R^2	62.71 %

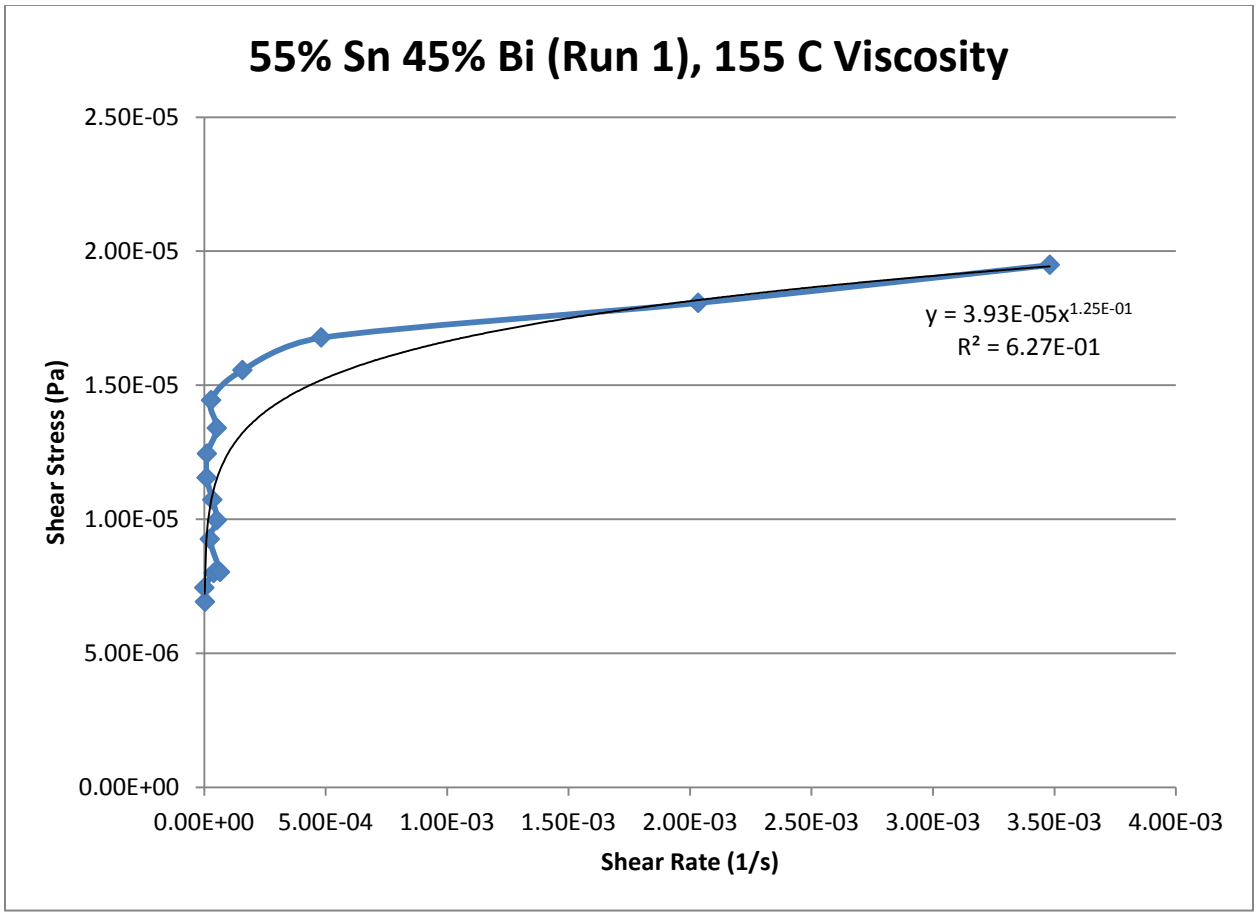

Figure 145- 55% Sn 45% Bi (Run 1), 155 C, Cone and Plate Viscosity

55% Tin 45% Bismuth (Run 2)

Expected Composition: 57.00% Sn, 43.00% Bi

Theoretical Solidus Line: 139 C
Theoretical Liquidus Line: 139 C

Experimental Solidus Line: 138.8 C
Experimental Liquidus Line: 143 C

Set-Up Notes

- Zeroed the gap at 150 C. This stress sweep was then followed by stress sweeps in decreasing intervals of 2.5 C. The temperature was then raised to 152.5 C and 155 C for the final two stress sweeps.

- The sample had a very low viscosity and appeared to be liquid like at most of the temperatures even without agitation.

- Hard to get the material to settle underneath the cone since it flowed out when the cone approached the geometry gap.

Plots

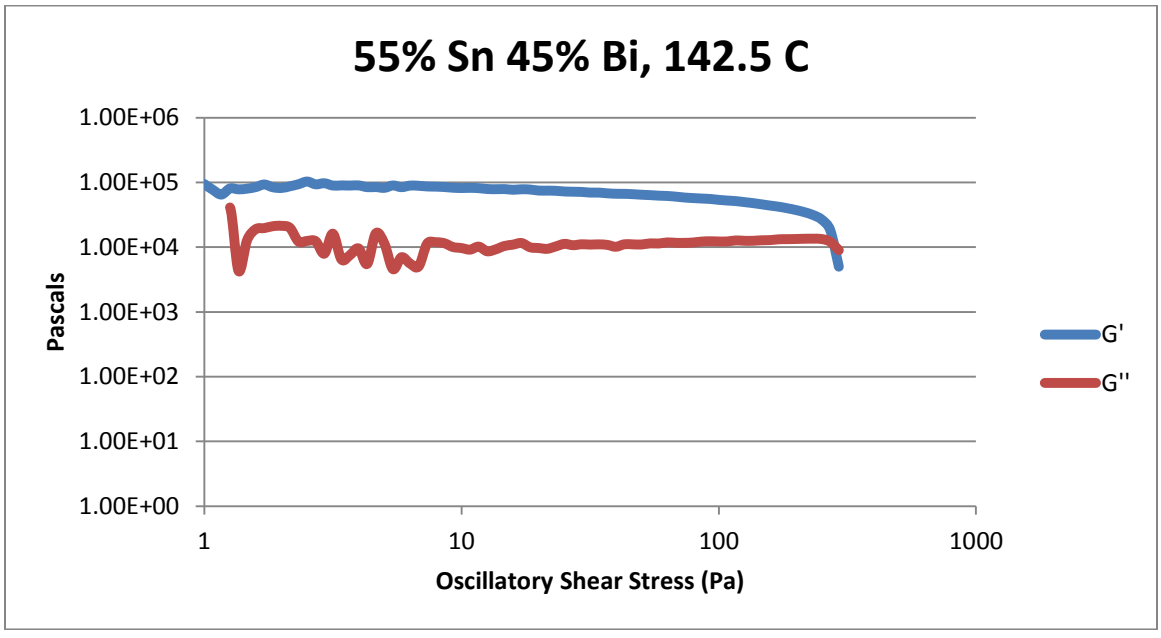

Figure 146- 55% Sn 45% Bi (Run 2), 142.5 C, Cone and Plate Stress Sweep

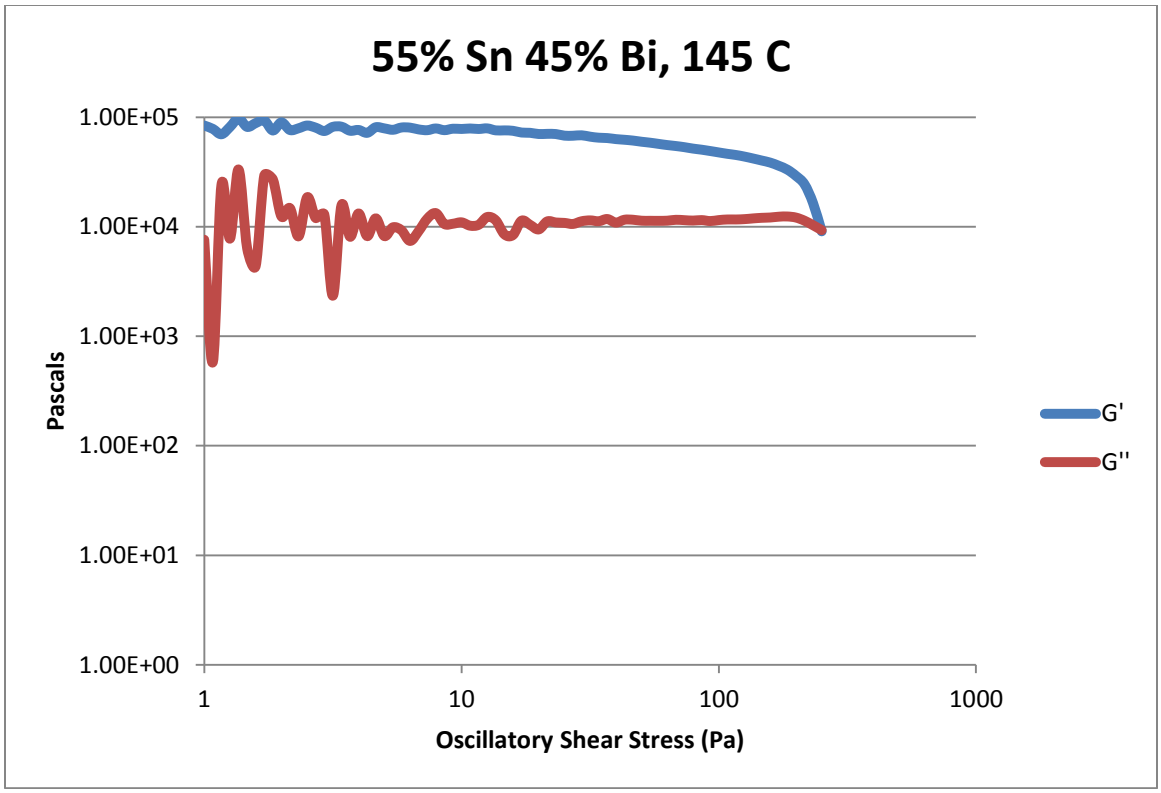

Figure 147- 55% Sn 45% Bi (Run 2), 145 C, Cone and Plate Stress Sweep

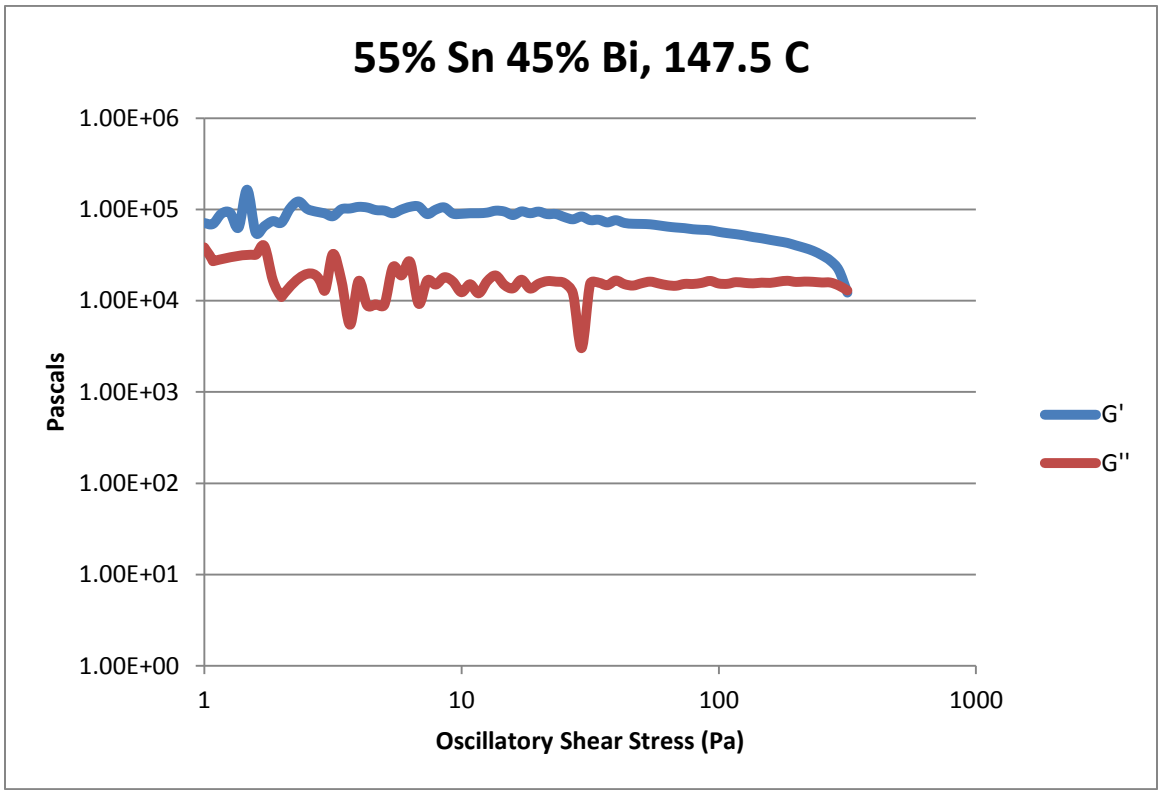

Figure 148- 55% Sn 45% Bi (Run 2), 147.5 C, Cone and Plate Stress Sweep

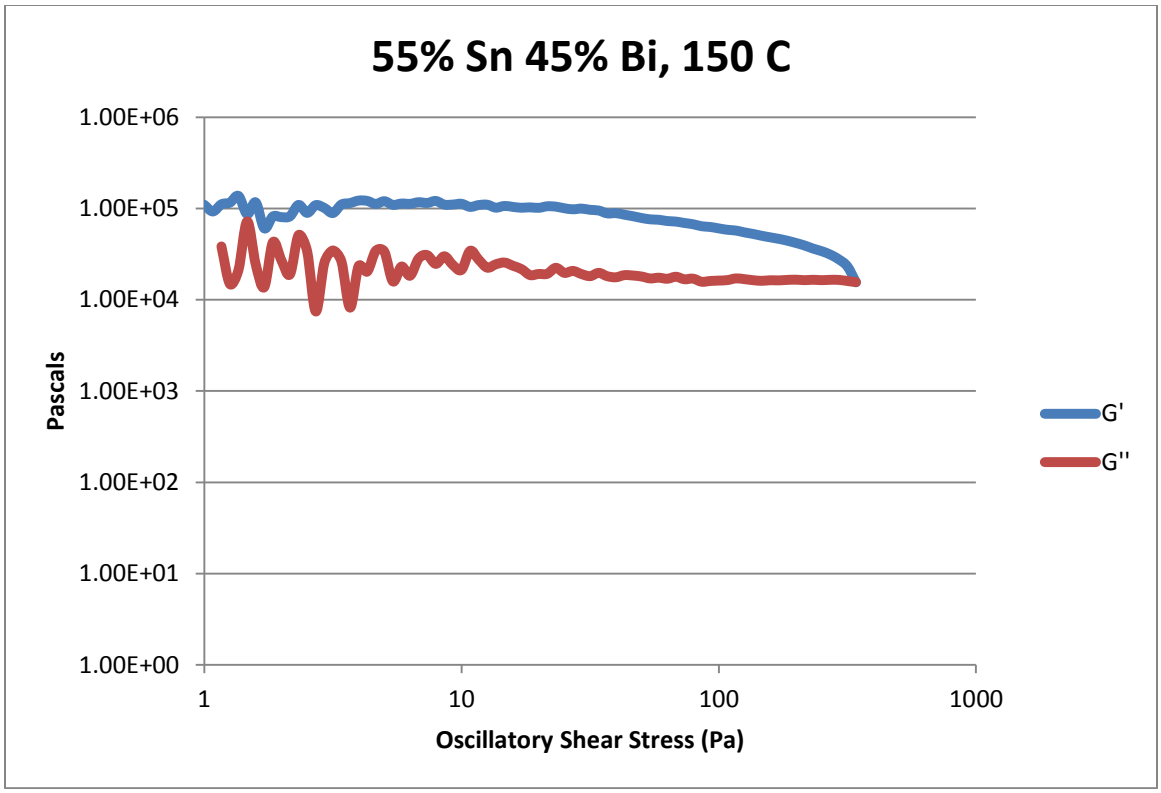

Figure 149- 55% Sn 45% Bi (Run 2), 150 C, Cone and Plate Stress Sweep

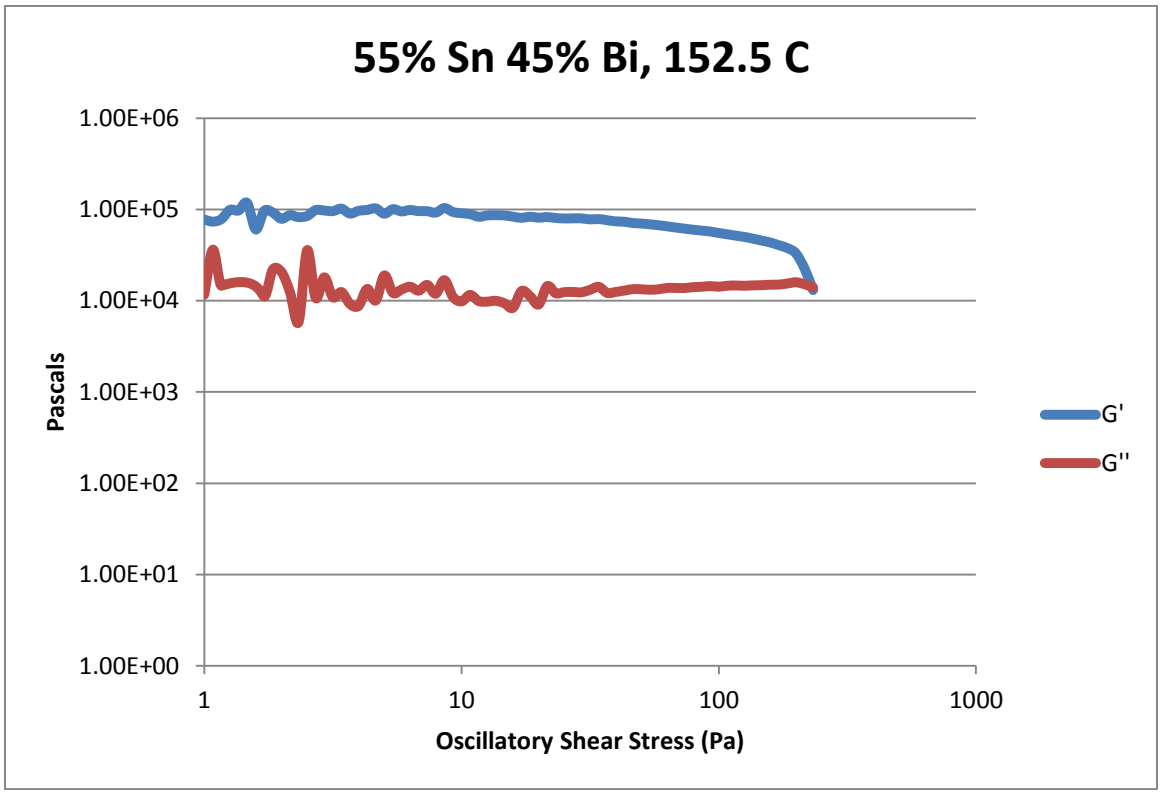

Figure 150- 55% Sn 45% Bi (Run 2), 152.5 C, Cone and Plate Stress Sweep

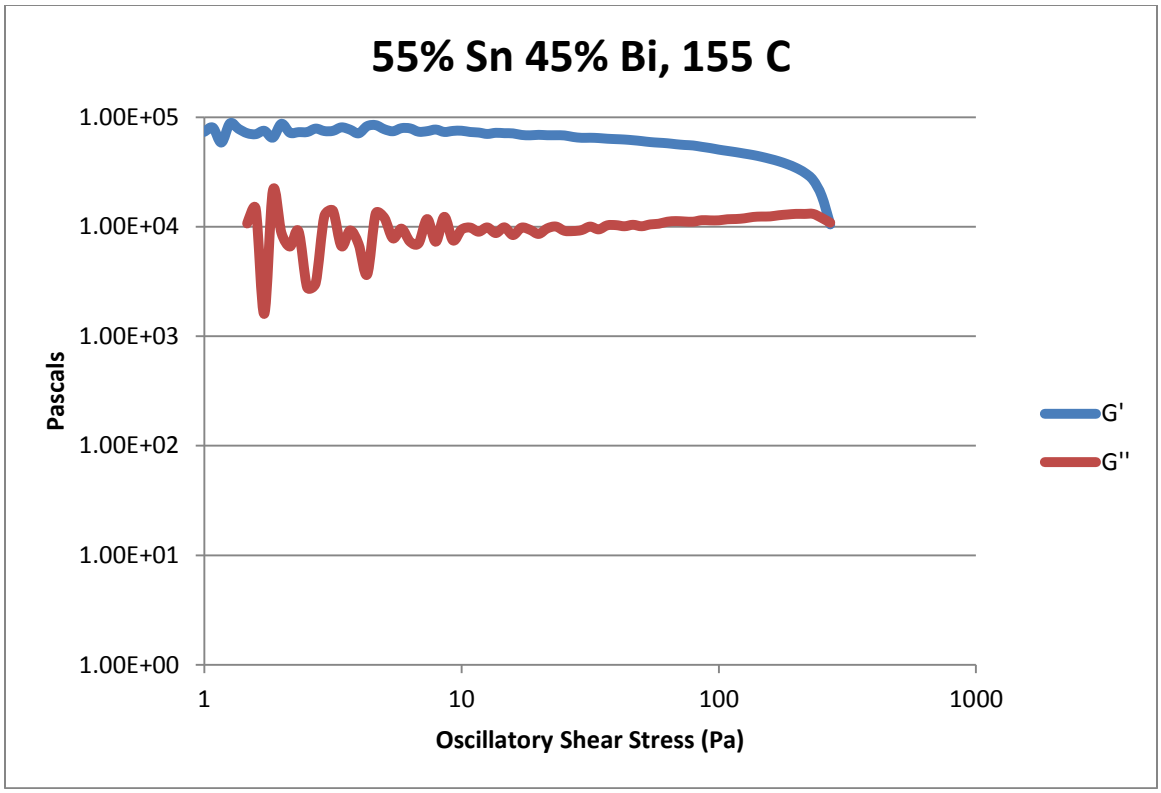

Figure 151- 55% Sn 45% Bi (Run 2), 155 C, Cone and Plate Stress Sweep

Temperature	Crossover Stress (Pa)	Crossover Stress (PSI)
142.5 C	$1.02 * 10^4$	1.48
145 C	$9.35 * 10^3$	1.36
147.5 C	$1.31 * 10^4$	1.90
150 C	$1.56 * 10^4$	2.26
152.5 C	$1.41 * 10^4$	2.05
155 C	$1.09 * 10^4$	1.58

Table 26- 55% Sn 45% Bi (Run 2), Cone and Plate Crossover Stresses

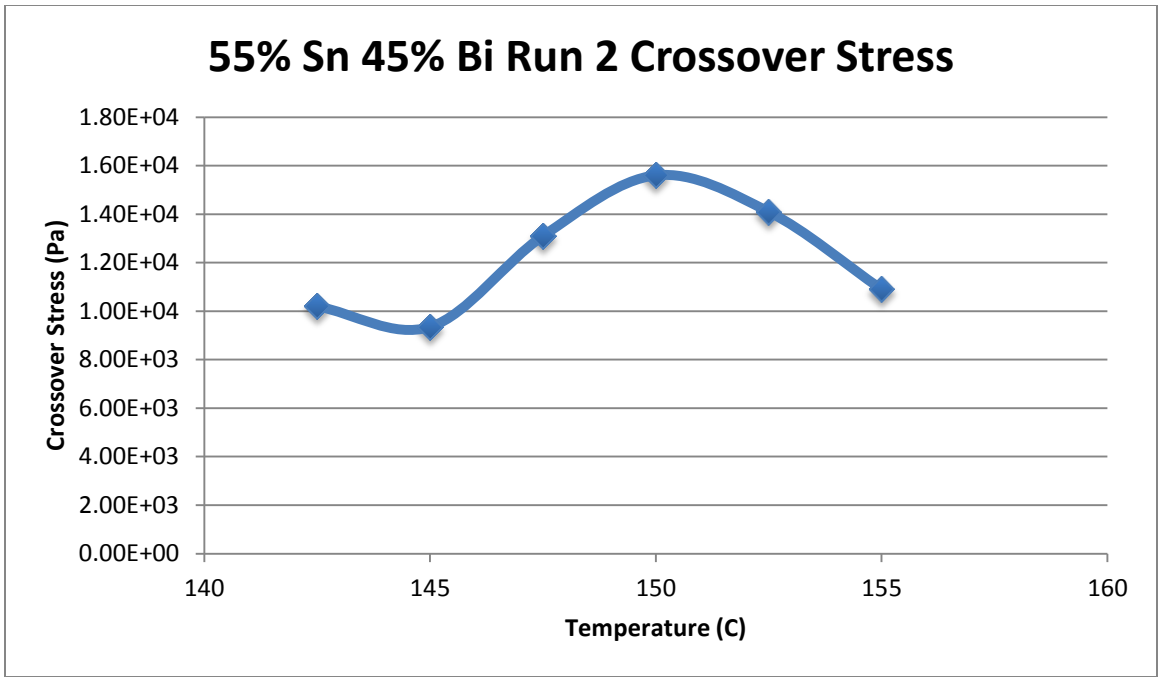

Figure 152- 55% Sn 45% Bi (Run 2), Cone and Plate Crossover Stresses vs. Temperature

Temperature	Fraction Solid (At %)	G' Plateau (Pa)	G'' Plateau (Pa)
142.5 C	8.41	$6.66 * 10^4$	$1.35 * 10^4$
145 C	6.82	$7.03 * 10^4$	$1.16 * 10^4$
147.5 C	4.06	$9.51 * 10^4$	$1.59 * 10^4$
150 C	2.36	$1.16 * 10^5$	$1.64 * 10^4$
152.5 C	0	$8.20 * 10^4$	$1.46 * 10^4$

Table 27- 55% Sn 45% Bi (Run 2), Cone and Plate Plateau Stresses

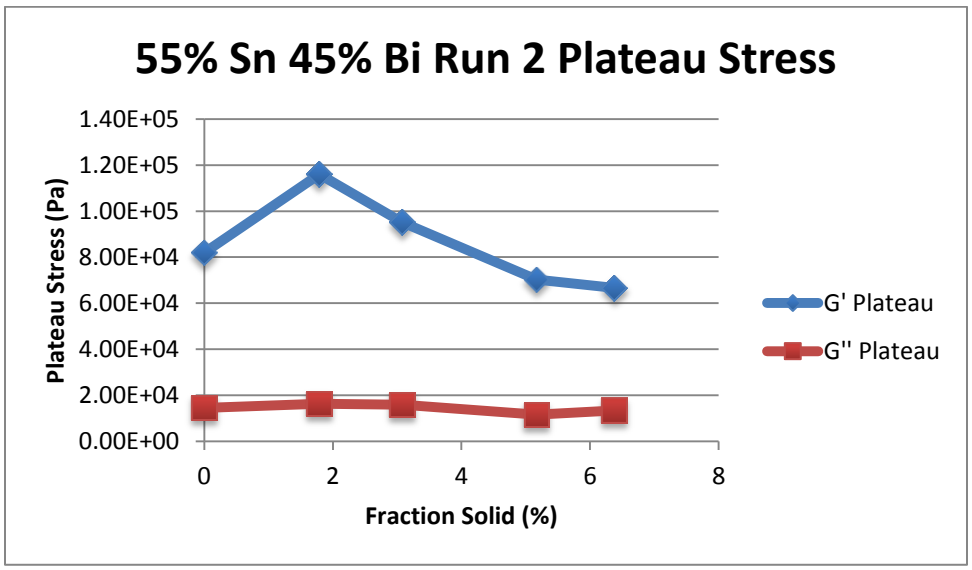

Figure 153- 55% Sn 45% Bi (Run 2), Cone and Plate Plateau Stresses vs. Fraction Solid

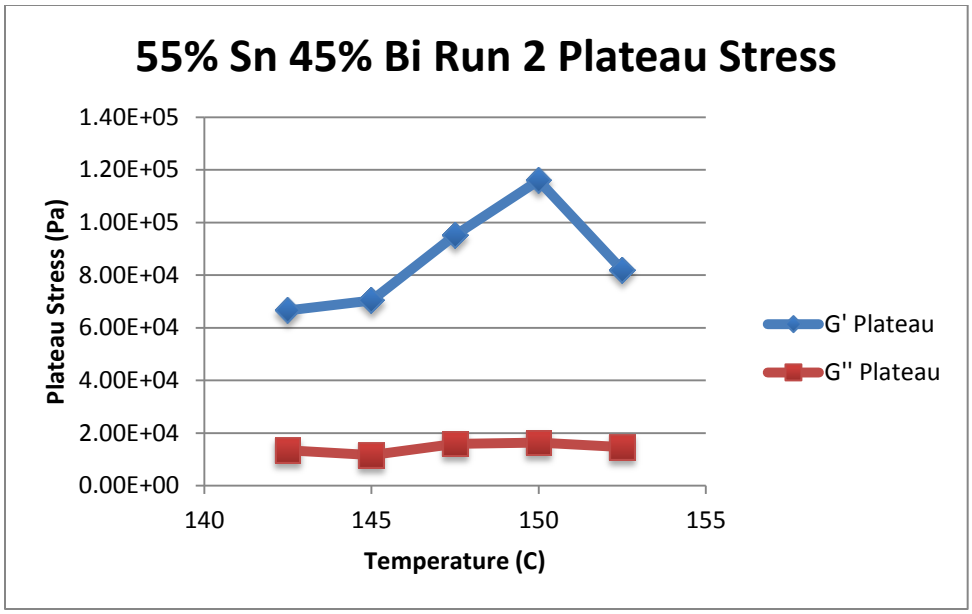

Figure 154- 55% Sn 45% Bi (Run 2), Cone and Plate Plateau Stresses vs. Temperature

55% Sn 45% Bi (Run 2) Viscosity					
Temperature	**Fraction Solid**	**Power Law**	**K**	**n**	**R^2**
142.5 C	6.38 %	$\tau = 2.92 * 10^{-4} * \dot{\gamma}^{0.3074}$ $\mu = 8.98 * 10^{-5} * \dot{\gamma}^{-0.6926}$	$2.92 * 10^{-4}$ Pa*s	0.3074	52.76 %
145 C	5.17 %	$\tau = 9.98 * 10^{-5} * \dot{\gamma}^{0.2797}$ $\mu = 2.79 * 10^{-5} * \dot{\gamma}^{-0.7203}$	$9.98 * 10^{-5}$ Pa*s	0.2797	87.26 %
147.5 C	3.08 %	$\tau = 5.20 * 10^{-4} * \dot{\gamma}^{0.4524}$ $\mu = 2.35 * 10^{-4} * \dot{\gamma}^{-0.5476}$	$5.20 * 10^{-4}$ Pa*s	0.4524	94.71 %
150 C	1.79 %	$\tau = 4.99 * 10^{-4} * \dot{\gamma}^{0.4816}$ $\mu = 2.40 * 10^{-4} * \dot{\gamma}^{-0.5184}$	$4.99 * 10^{-4}$ Pa*s	0.4816	95.45 %
152.5 C	0 %	$\tau = 4.55 * 10^{-5} * \dot{\gamma}^{0.1437}$ $\mu = 6.54 * 10^{-6} * \dot{\gamma}^{-0.8563}$	$4.55 * 10^{-5}$ Pa*s	0.1437	80.90 %

Table 28- 55% Sn 45% Bi (Run 2), Cone and Plate Viscosity

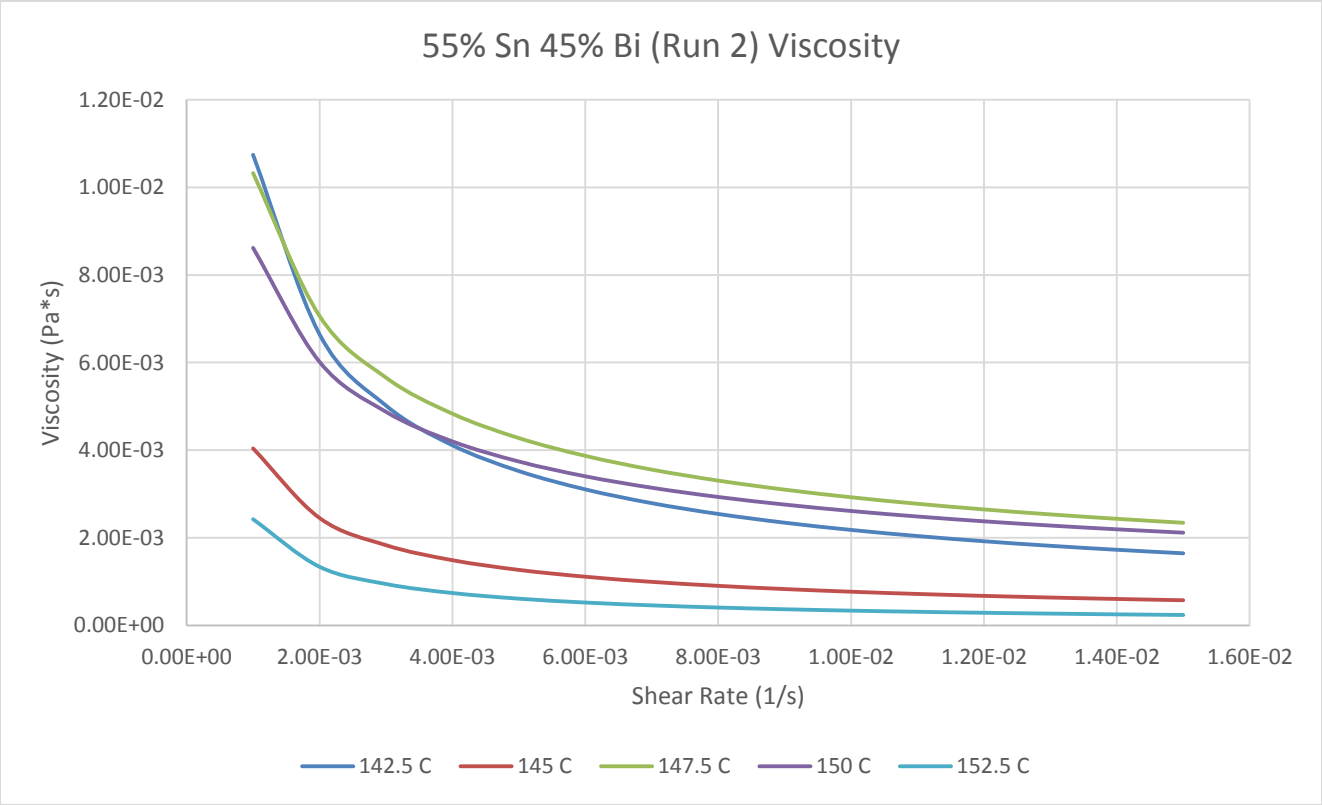

Figure 155- 55% Sn 45% Bi (Run 2), Cone and Plate Viscosity

142.5 C

Fraction Solid	6.38 %
Power Law	$\tau = 2.92 * 10^{-4} * \dot{\gamma}^{0.3074}$
	$\mu = 8.98 * 10^{-5} * \dot{\gamma}^{-0.6926}$
R^2	52.76 %

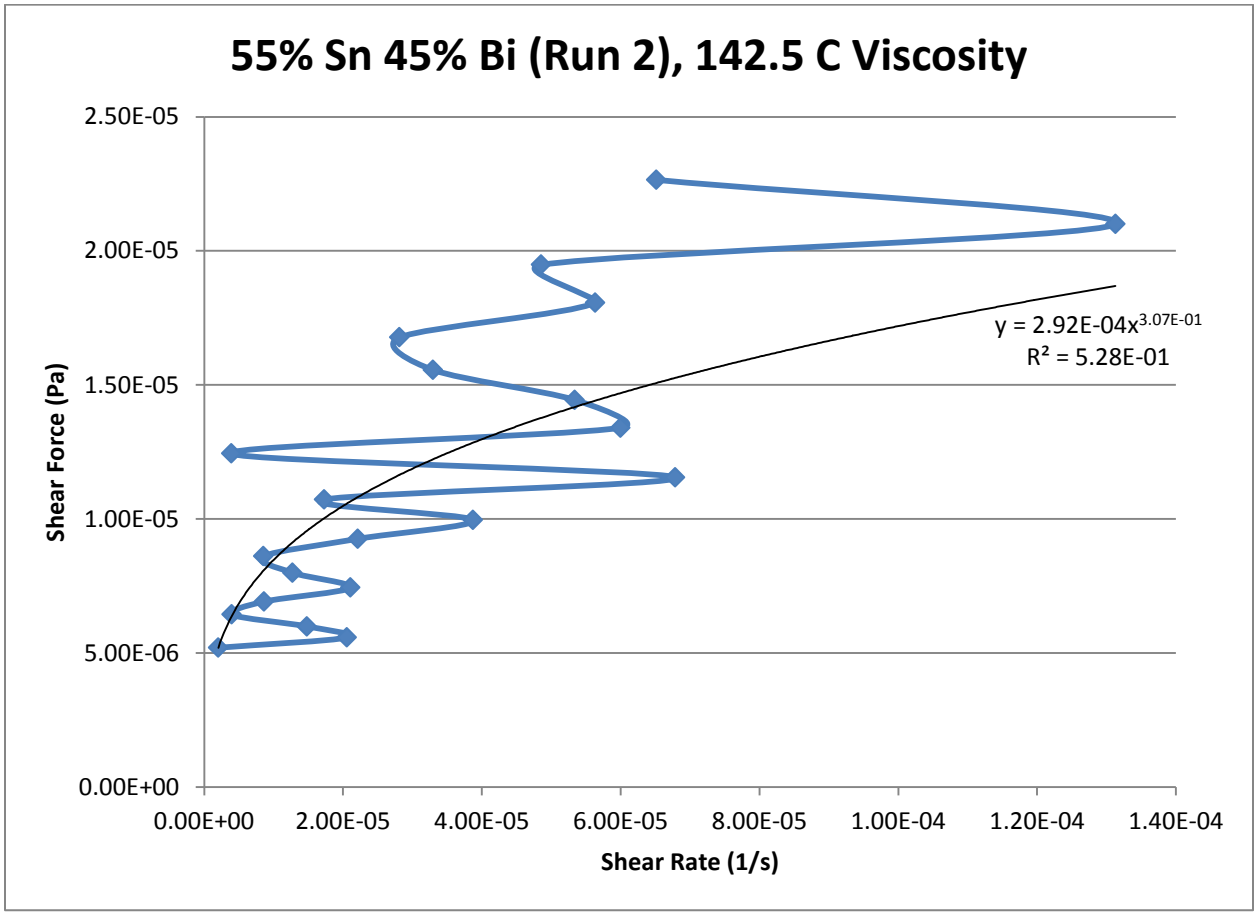

Figure 156- 55% Sn 45% Bi (Run 2), 142.5 C, Cone and Plate Viscosity

145 C

Fraction Solid	5.17 %
Power Law	$\tau = 9.98 * 10^{-5} * \dot{\gamma}^{0.2797}$
	$\mu = 2.79 * 10^{-5} * \dot{\gamma}^{-0.7203}$
R^2	87.26 %

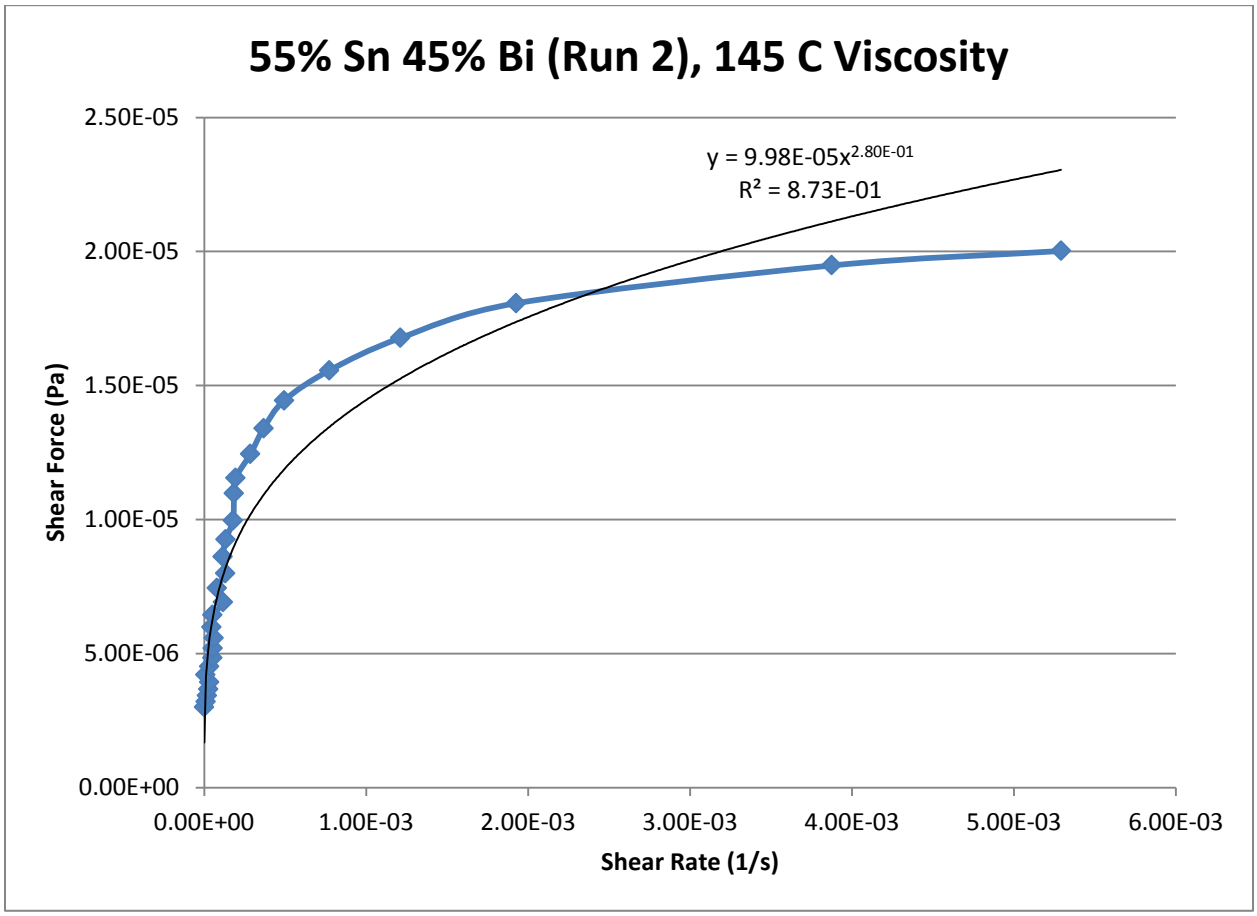

Figure 157- 55% Sn 45% Bi (Run 2), 145 C, Cone and Plate Viscosity

147.5 C

Fraction Solid	3.08 %
Power Law	$\tau = 5.20 * 10^{-4} * \dot{\gamma}^{0.4524}$
	$\mu = 2.35 * 10^{-4} * \dot{\gamma}^{-0.5476}$
R^2	94.71 %

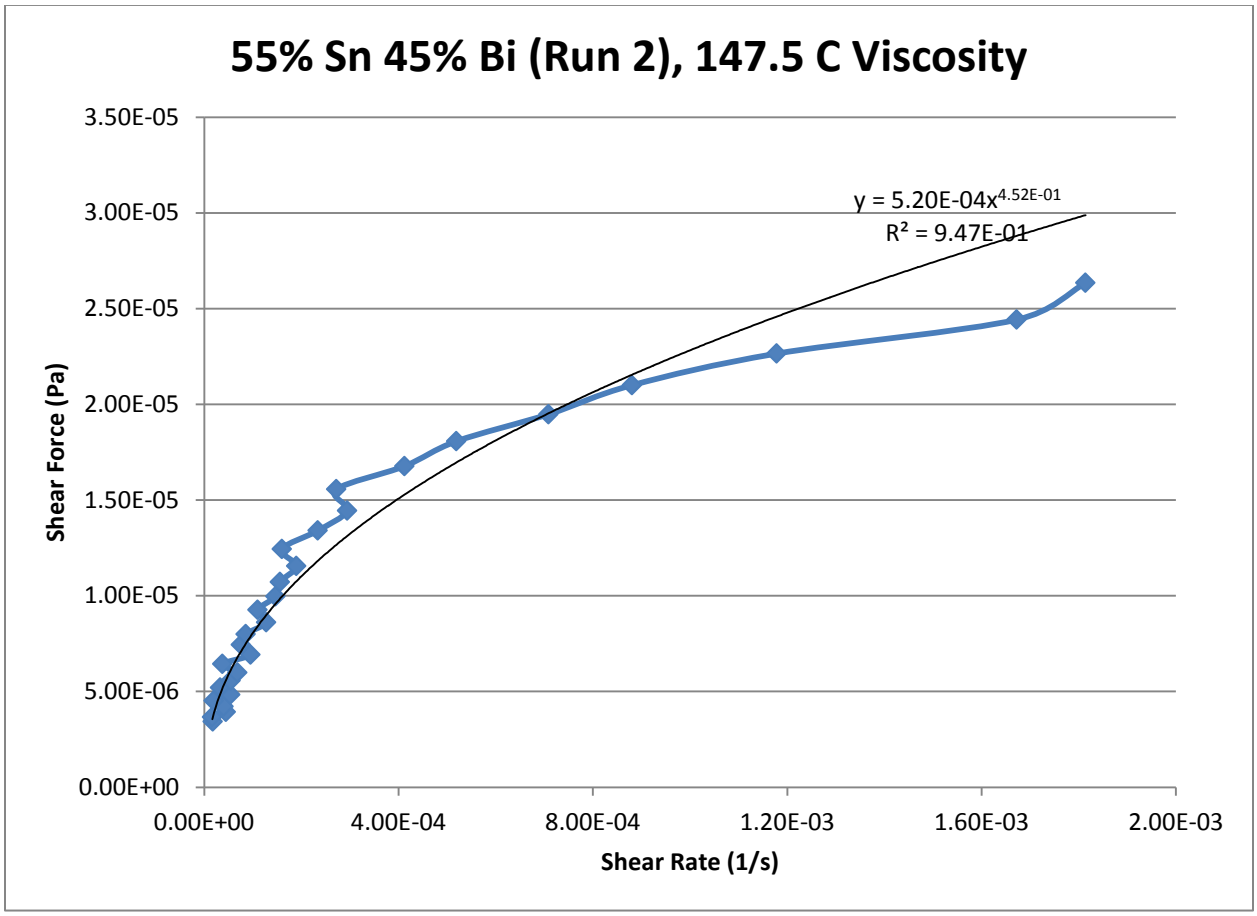

Figure 158- 55% Sn 45% Bi (Run 2), 147.5 C, Cone and Plate Viscosity

150 C

Fraction Solid	1.79 %
Power Law	$\tau = 4.99 * 10^{-4} * \dot{\gamma}^{0.4816}$
	$\mu = 2.40 * 10^{-4} * \dot{\gamma}^{-0.5184}$
R^2	95.45 %

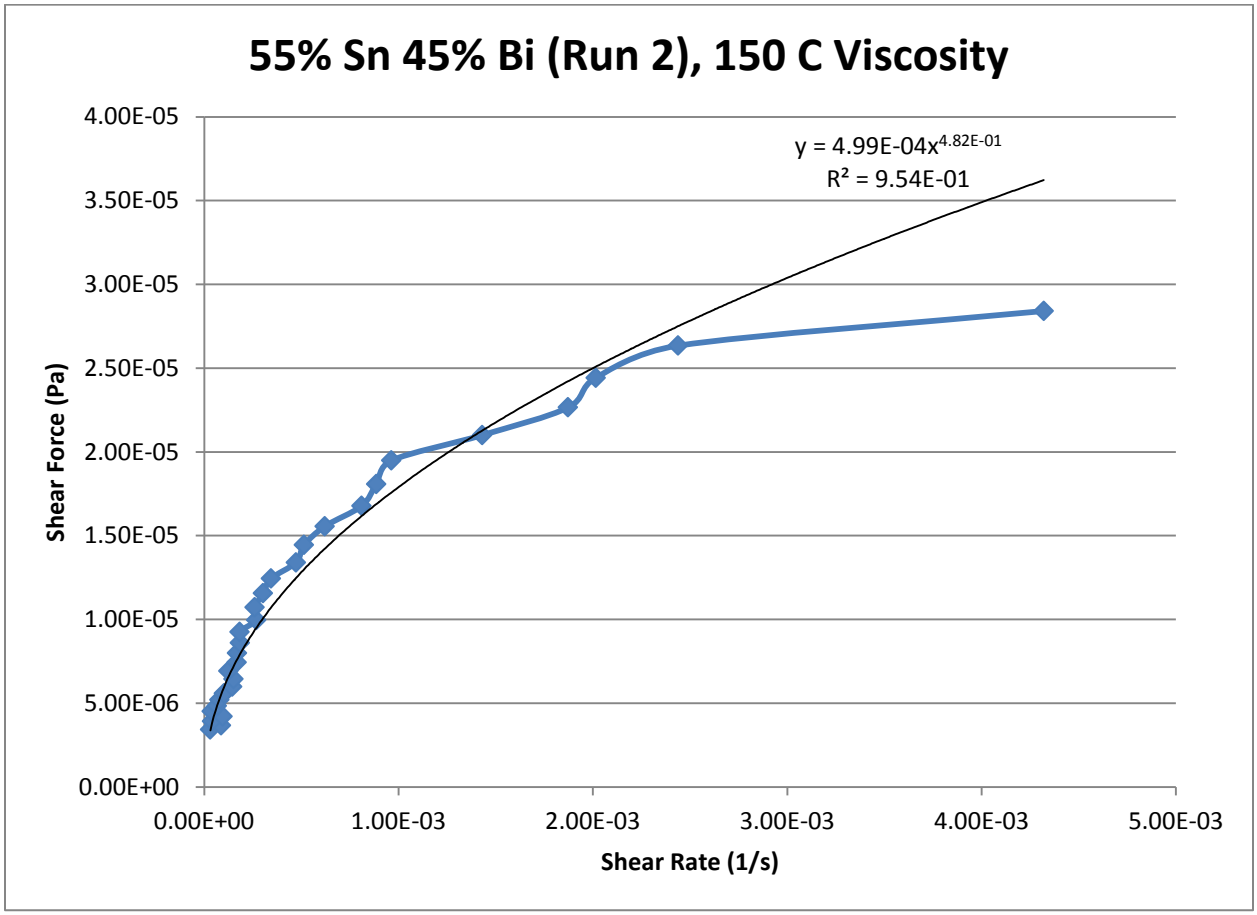

Figure 159- 55% Sn 45% Bi (Run 2), 150 C, Cone and Plate Viscosity

152.5 C

Fraction Solid	0 %
Power Law	$\tau = 4.55 * 10^{-5} * \dot{\gamma}^{0.1437}$
	$\mu = 6.54 * 10^{-6} * \dot{\gamma}^{-0.8563}$
R^2	87.65 %

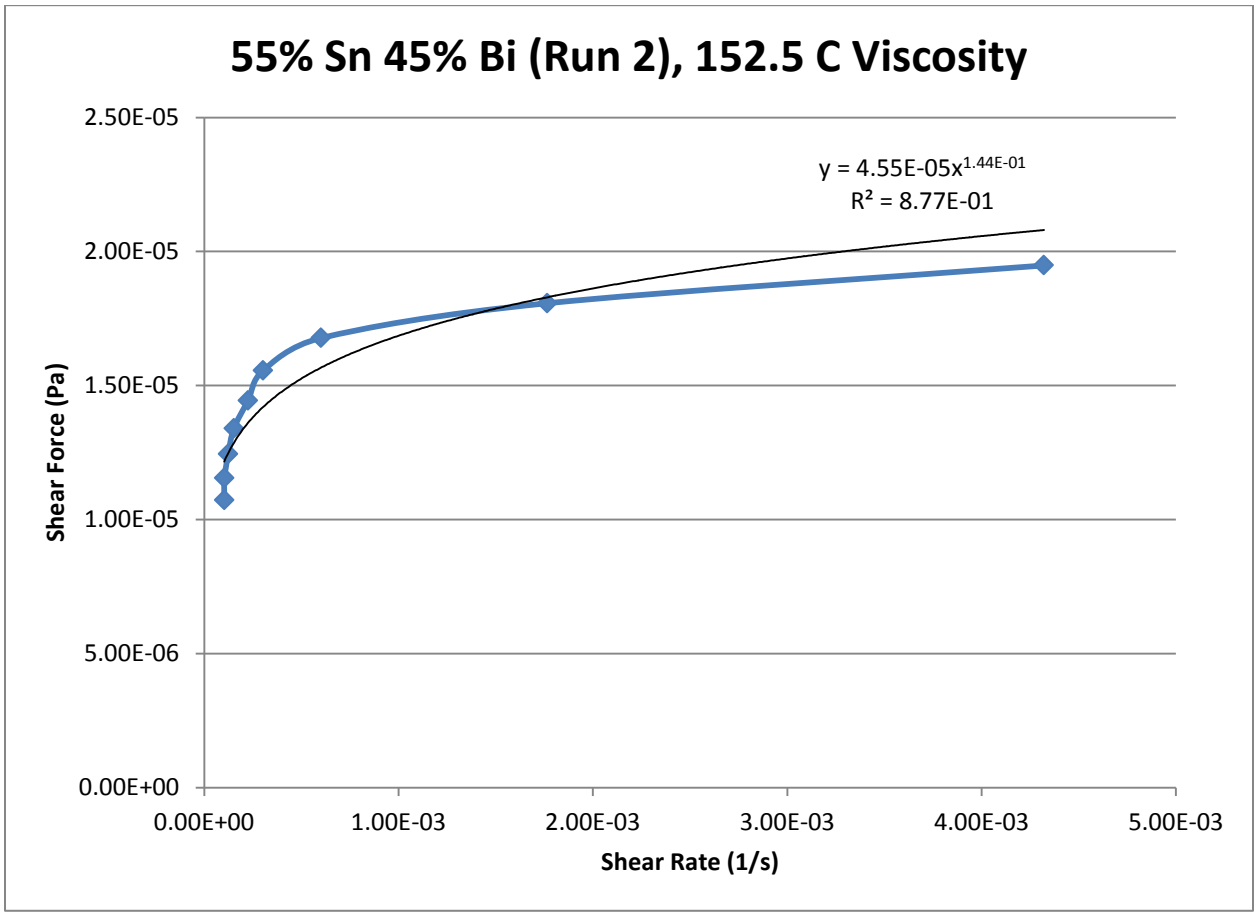

Figure 160- 55% Sn 45% Bi (Run 2), 152.5 C, Cone and Plate Viscosity

55% Tin 45% Bismuth (Run 3)

Expected Composition: 57.00% Sn, 43.00% Bi

Theoretical Solidus Line: 139 C
Theoretical Liquidus Line: 139 C

Experimental Solidus Line: 138.8 C
Experimental Liquidus Line: 143 C

Set-Up Notes

- Zeroed the gap at 147.5 C. This stress sweep was then followed by stress sweeps in decreasing intervals of 2.5 C. The temperature was then raised to 150 C and 152.5 C for the final two stress sweeps.

Plots

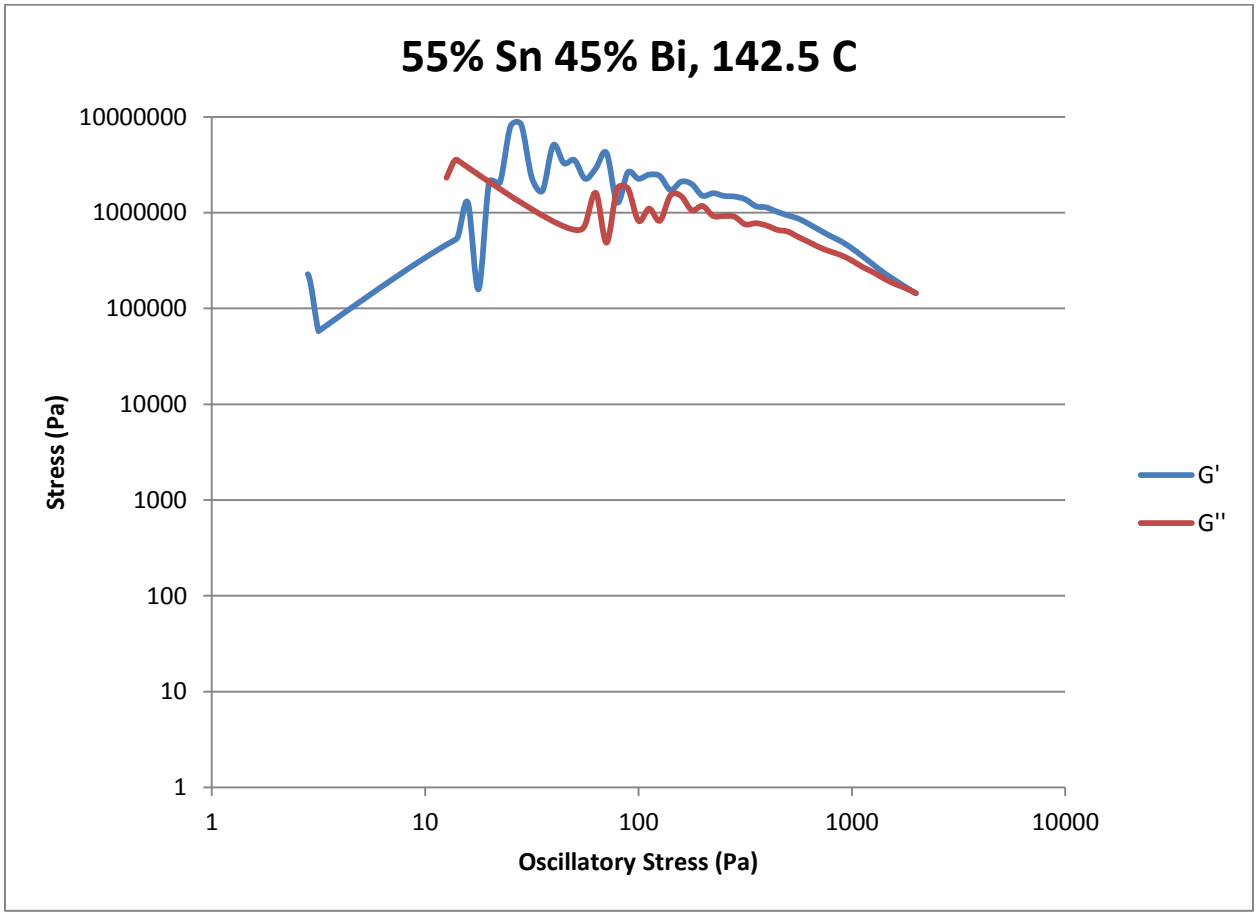

Figure 161- 55% Sn 45% Bi (Run 3), 142.5 C, Cone and Plate Stress Sweep

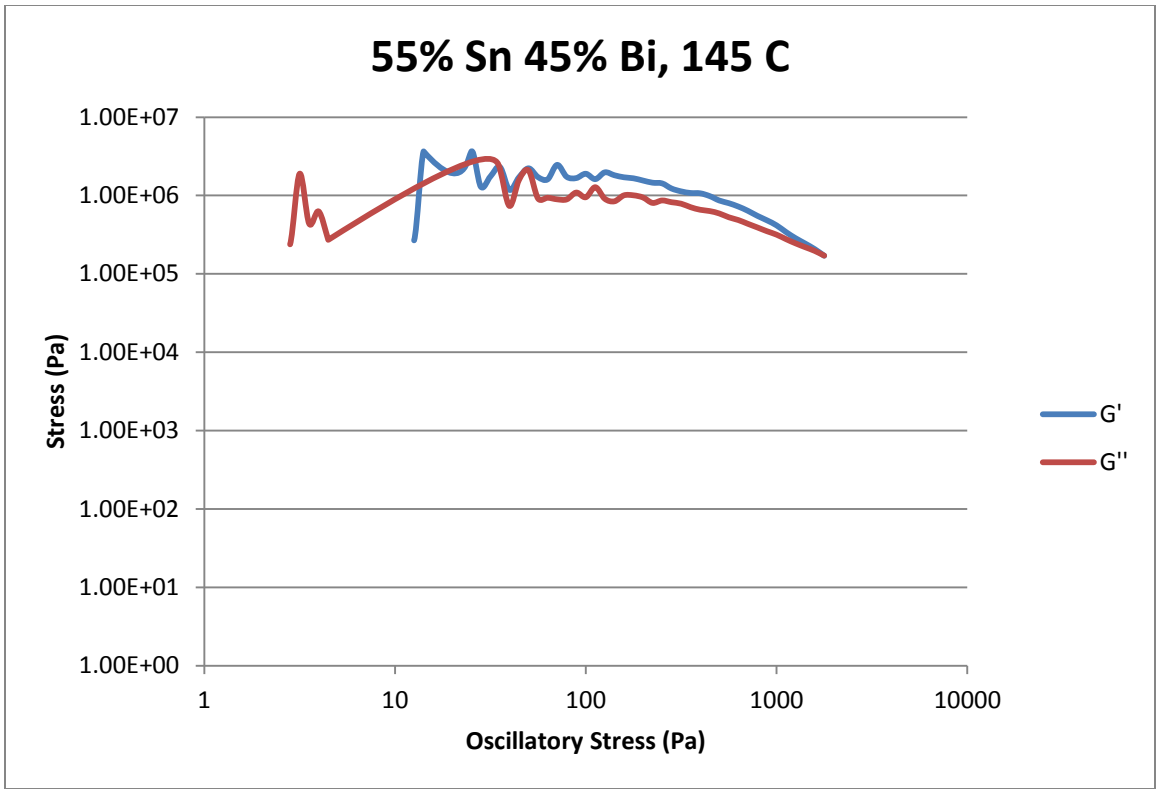

Figure 162- 55% Sn 45% Bi (Run 3), 145 C, Cone and Plate Stress Sweep

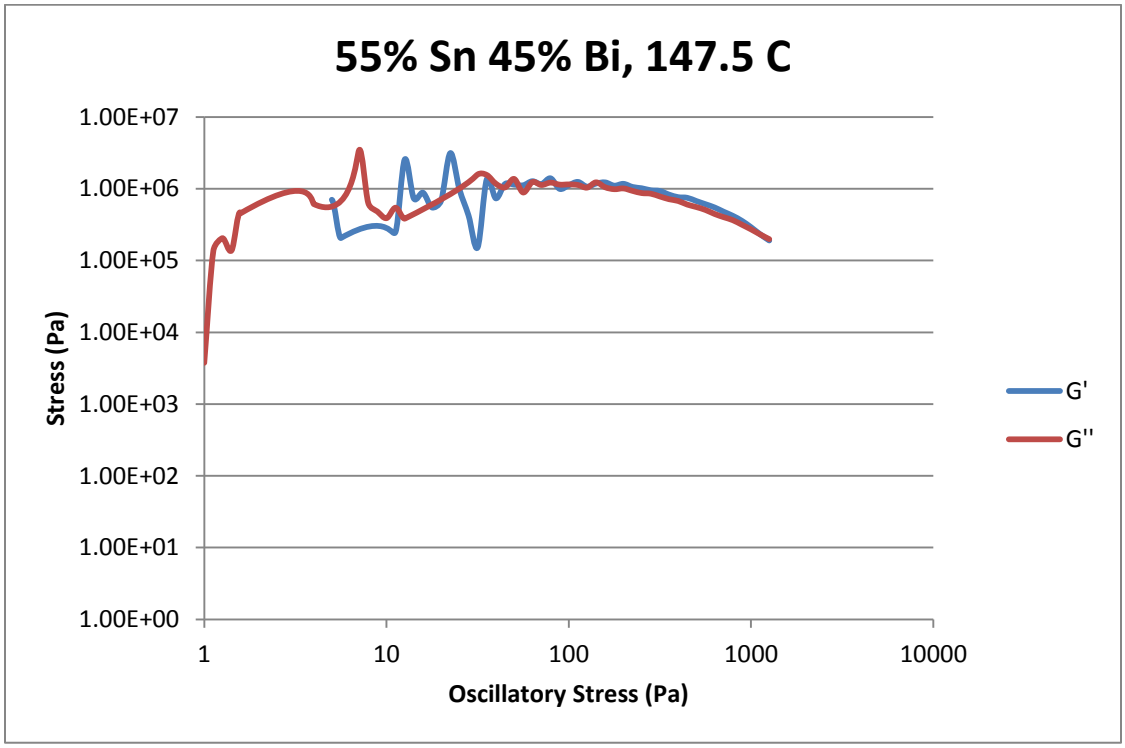

Figure 163- 55% Sn 45% Bi (Run 3), 147.5 C, Cone and Plate Stress Sweep

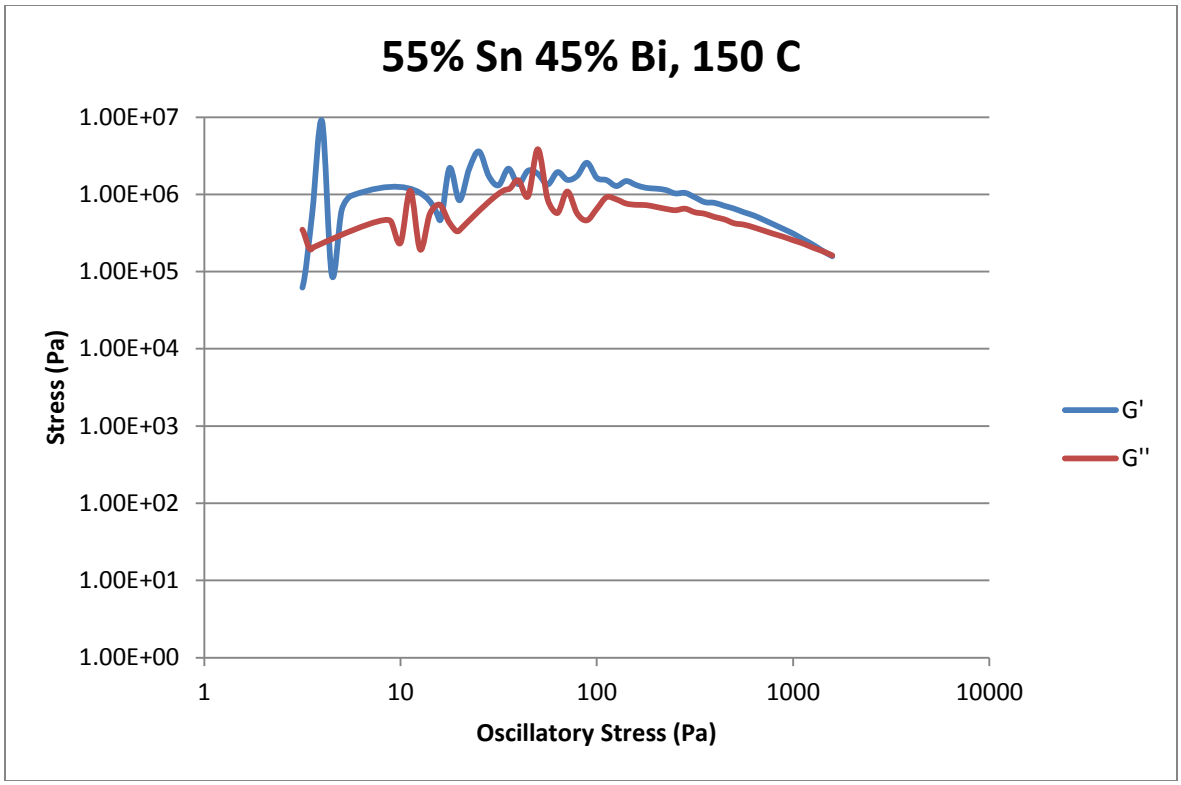

Figure 164- 55% Sn 45% Bi (Run 3), 150 C, Cone and Plate Stress Sweep

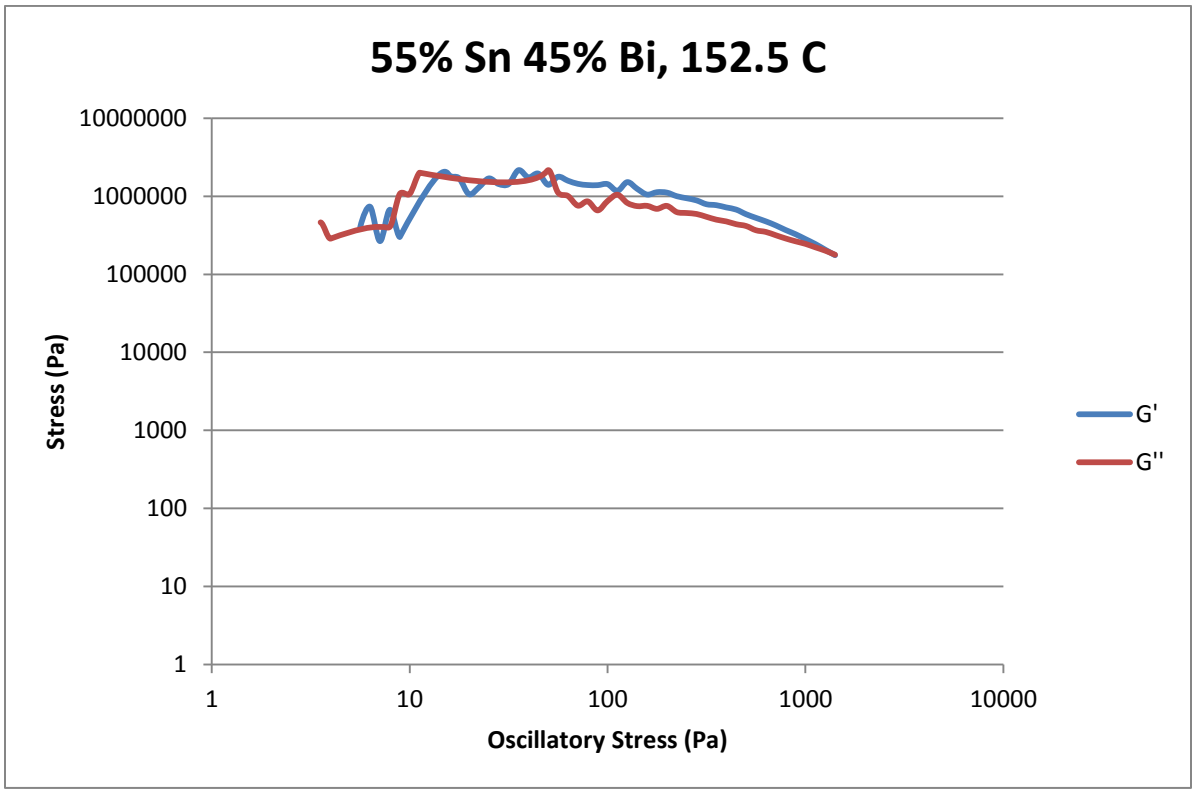

Figure 165- 55% Sn 45% Bi (Run 3), 152.5 C, Cone and Plate Stress Sweep

Temperature	Fraction Solid (At %)	Crossover Stress (Pa)	G' Plateau Stress (Pa)	G'' Plateau Stress (Pa)
142.5 C	8.41	$1.49 * 10^5$	$2.47 * 10^6$	$1.45 * 10^6$
145 C	6.82	$1.71 * 10^5$	$1.84 * 10^6$	$9.95 * 10^5$
147.5 C	4.06	$2.28 * 10^5$	$1.30 * 10^6$	$1.26 * 10^6$
150 C	2.36	$1.68 * 10^5$	$1.75 * 10^6$	$1.12 * 10^6$
152.5 C	0	$1.80 * 10^5$	$1.48 * 10^6$	$9.74 * 10^5$

Table 29- 55% Sn 45% Bi (Run 3), Cone and Plate Crossover and Plateau Stresses

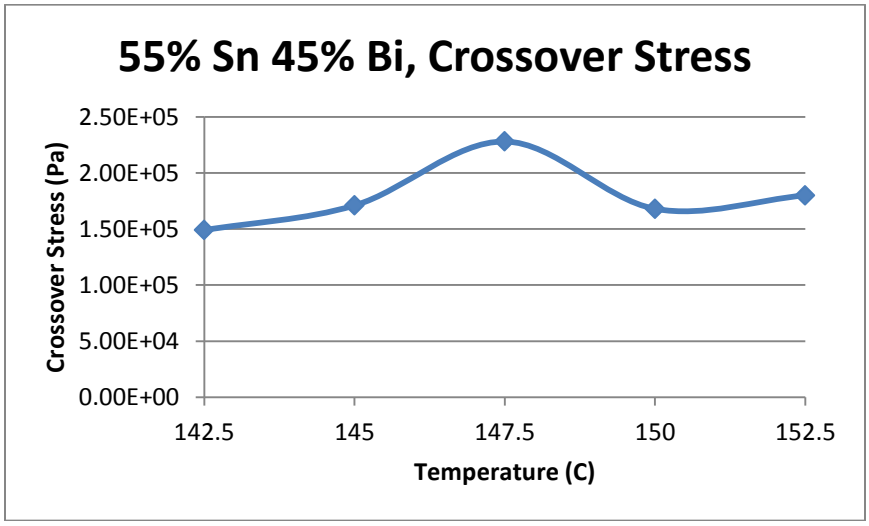

Figure 166- 55% Sn 45% Bi (Run 3), Cone and Plate Crossover Stresses

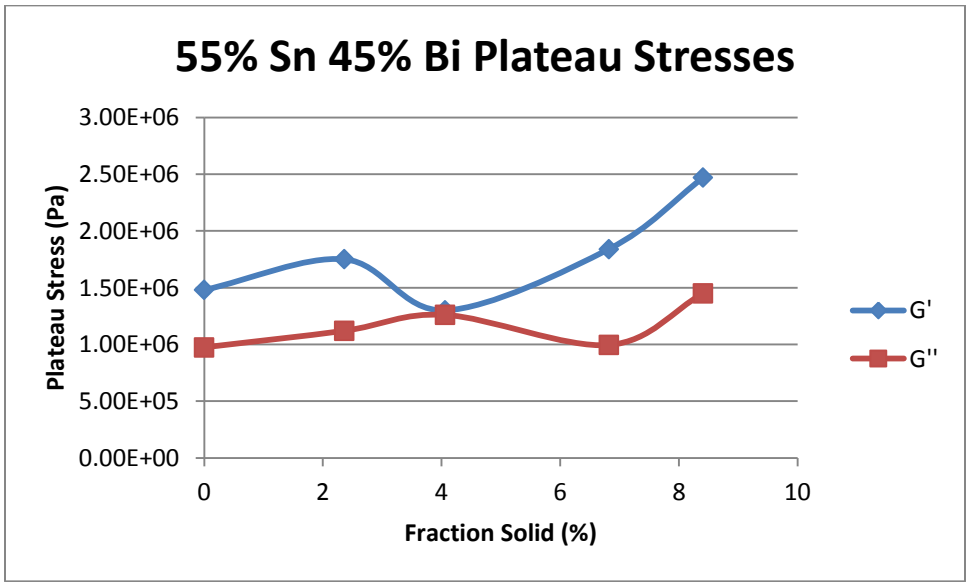

Figure 167- 55% Sn 45% Bi (Run 3), Cone and Plate Plateau Stresses

55% Sn 45% Bi (Run 3) Viscosity					
Temperature	**Fraction Solid**	**Power Law**	**K**	**n**	**R^2**
142.5 C	6.38 %	$\tau = 2.16 * 10^{-3} * \dot{\gamma}^{0.4407}$ $\mu = 9.52 * 10^{-4} * \dot{\gamma}^{-0.5593}$	$2.16 * 10^{-3}$ Pa*s	0.4407	89.64 %
145 C	5.17 %	$\tau = 1.12 * 10^{-3} * \dot{\gamma}^{0.358}$ $\mu = 4.00 * 10^{-4} * \dot{\gamma}^{-0.642}$	$1.12 * 10^{-3}$ Pa*s	0.358	94.08 %
147.5 C	3.08 %	$\tau = 7.97 * 10^{-3} * \dot{\gamma}^{0.6425}$ $\mu = 5.12 * 10^{-3} * \dot{\gamma}^{-0.3575}$	$7.97 * 10^{-3}$ Pa*s	0.6425	90.13 %
150 C	1.79 %	$\tau = 1.86 * 10^{-3} * \dot{\gamma}^{0.4409}$ $\mu = 8.20 * 10^{-4} * \dot{\gamma}^{-0.5591}$	$1.86 * 10^{-3}$ Pa*s	0.4409	91.13 %
152.5 C	0 %	$\tau = 5.49 * 10^{-4} * \dot{\gamma}^{0.2737}$ $\mu = 1.50 * 10^{-4} * \dot{\gamma}^{-0.5184}$	$5.49 * 10^{-4}$ Pa*s	0.2737	80.90 %

Table 30- 55% Sn 45% Bi (Run 3), Cone and Plate Viscosity

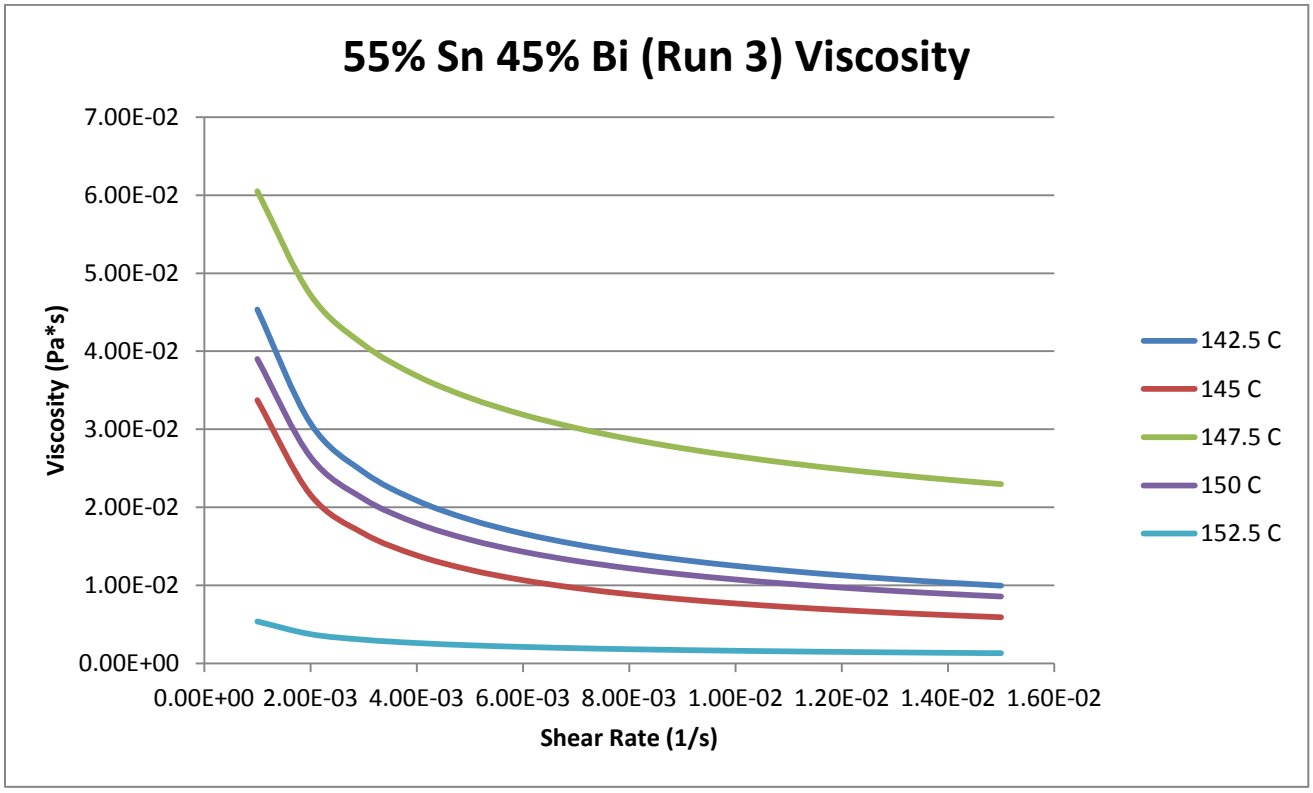

Figure 168- 55% Sn 45% Bi (Run 3), Cone and Plate Viscosity

142.5 C

Fraction Solid	6.38 %
Power Law	$\tau = 2.16 * 10^{-3} * \dot{\gamma}^{0.4407}$
	$\mu = 9.52 * 10^{-4} * \dot{\gamma}^{-0.5593}$
R^2	89.64 %

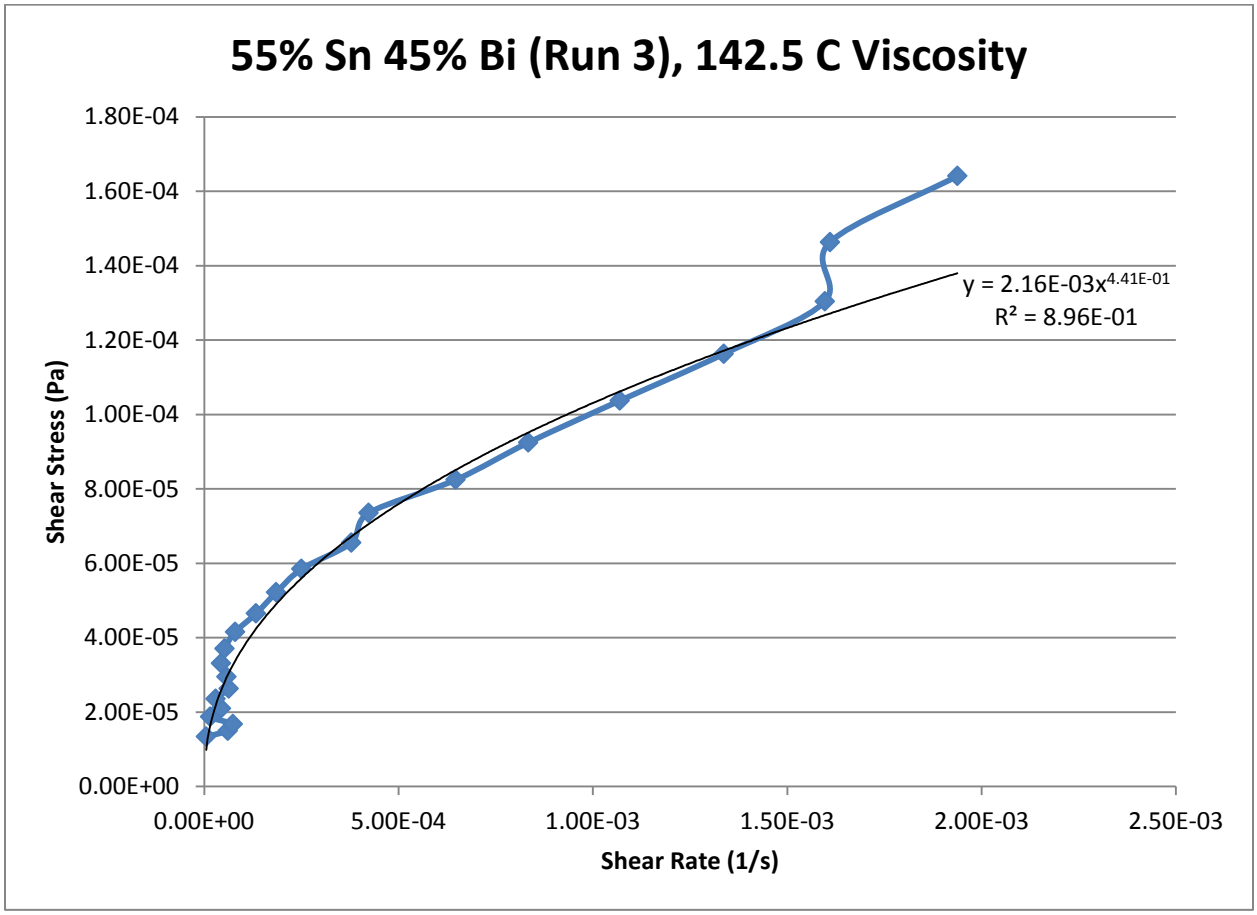

Figure 169- 55% Sn 45% Bi (Run 3), 142.5 C, Cone and Plate Viscosity

145 C

Fraction Solid	5.17 %
Power Law	$\tau = 1.12 * 10^{-3} * \dot{\gamma}^{0.358}$
	$\mu = 4.00 * 10^{-4} * \dot{\gamma}^{-0.642}$
R^2	94.08 %

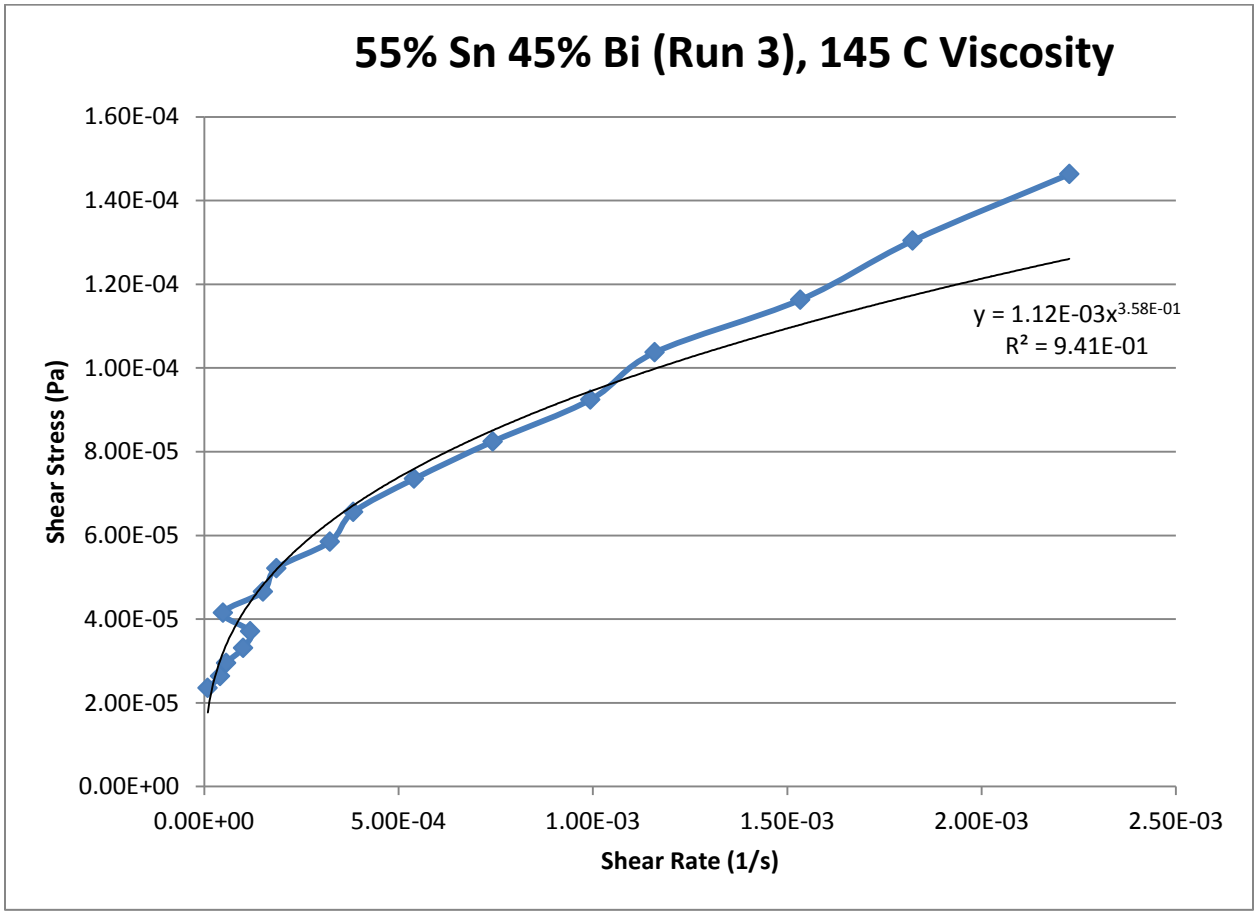

Figure 170- 55% Sn 45% Bi (Run 3), 145 C, Cone and Plate Viscosity

147.5 C

Fraction Solid	3.08 %
Power Law	$\tau = 7.97 * 10^{-3} * \dot{\gamma}^{0.6425}$
	$\mu = 5.12 * 10^{-3} * \dot{\gamma}^{-0.3575}$
R^2	90.13 %

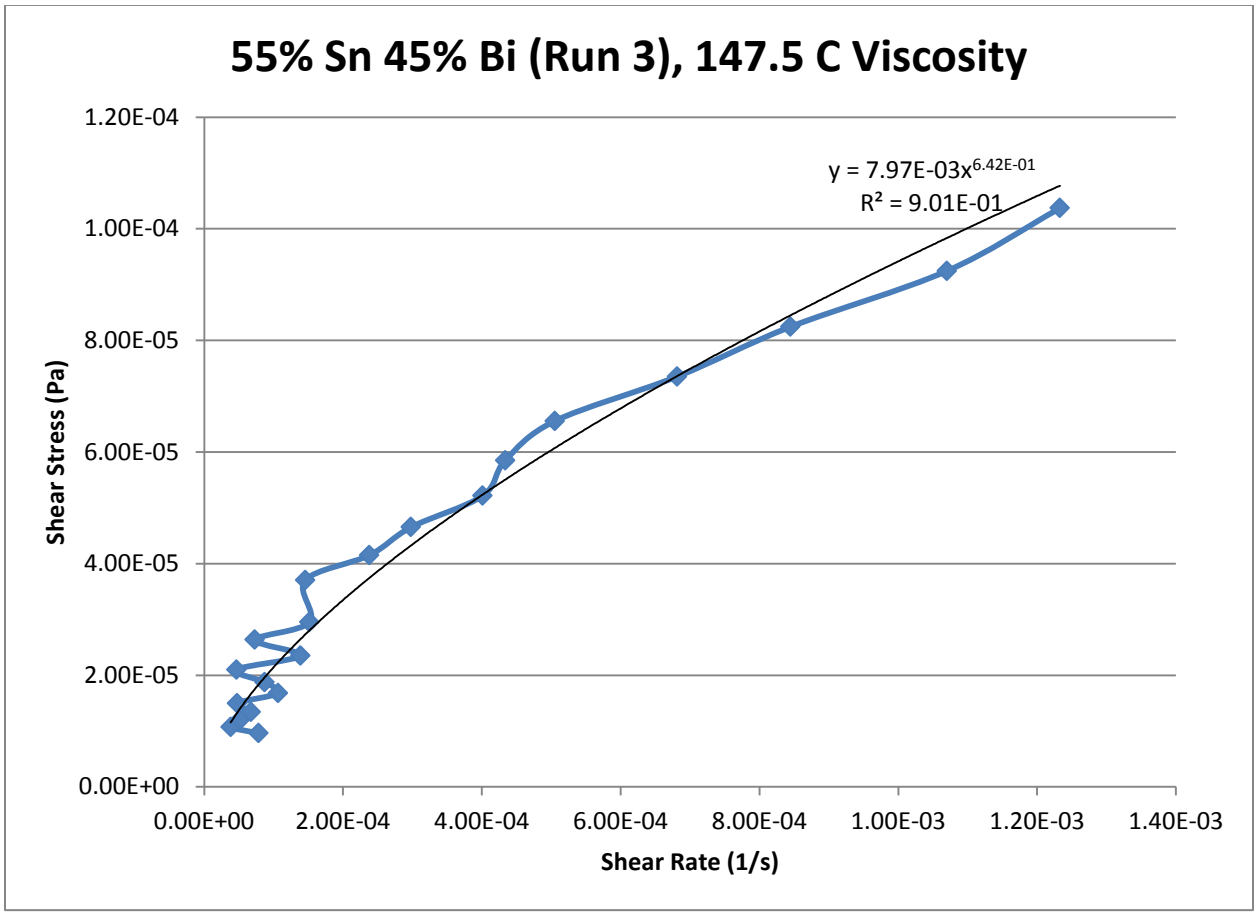

Figure 171- 55% Sn 45% Bi (Run 3), 147.5 C, Cone and Plate Viscosity

150 C

Fraction Solid	1.79 %
Power Law	$\tau = 1.86 * 10^{-3} * \dot{\gamma}^{0.4409}$
	$\mu = 8.20 * 10^{-4} * \dot{\gamma}^{-0.5591}$
R^2	91.13 %

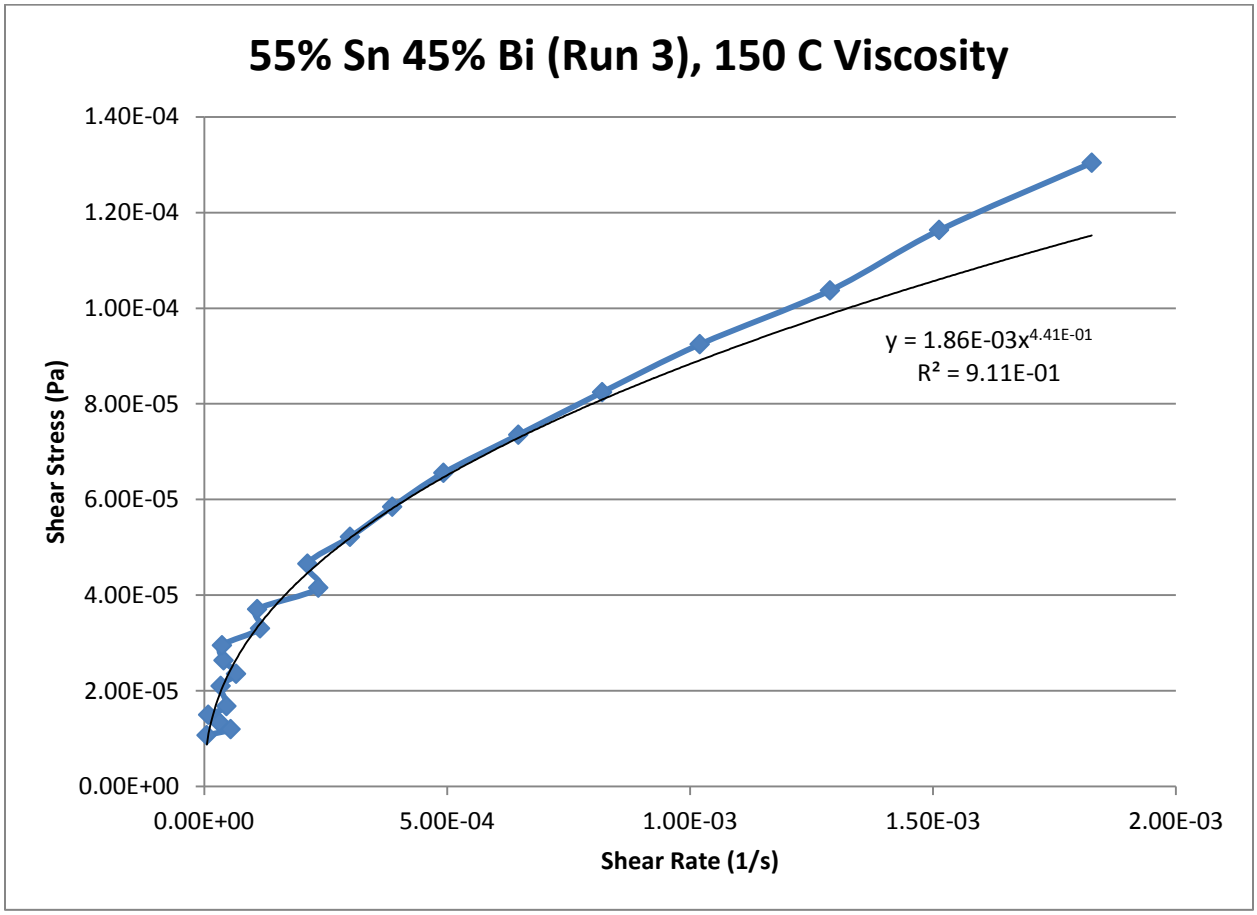

Figure 172- 55% Sn 45% Bi (Run 3), 150 C, Cone and Plate Viscosity

152.5 C

Fraction Solid	0 %
Power Law	$\tau = 5.49 * 10^{-4} * \dot{\gamma}^{0.2737}$
	$\mu = 1.50 * 10^{-4} * \dot{\gamma}^{-0.5184}$
R^2	80.90 %

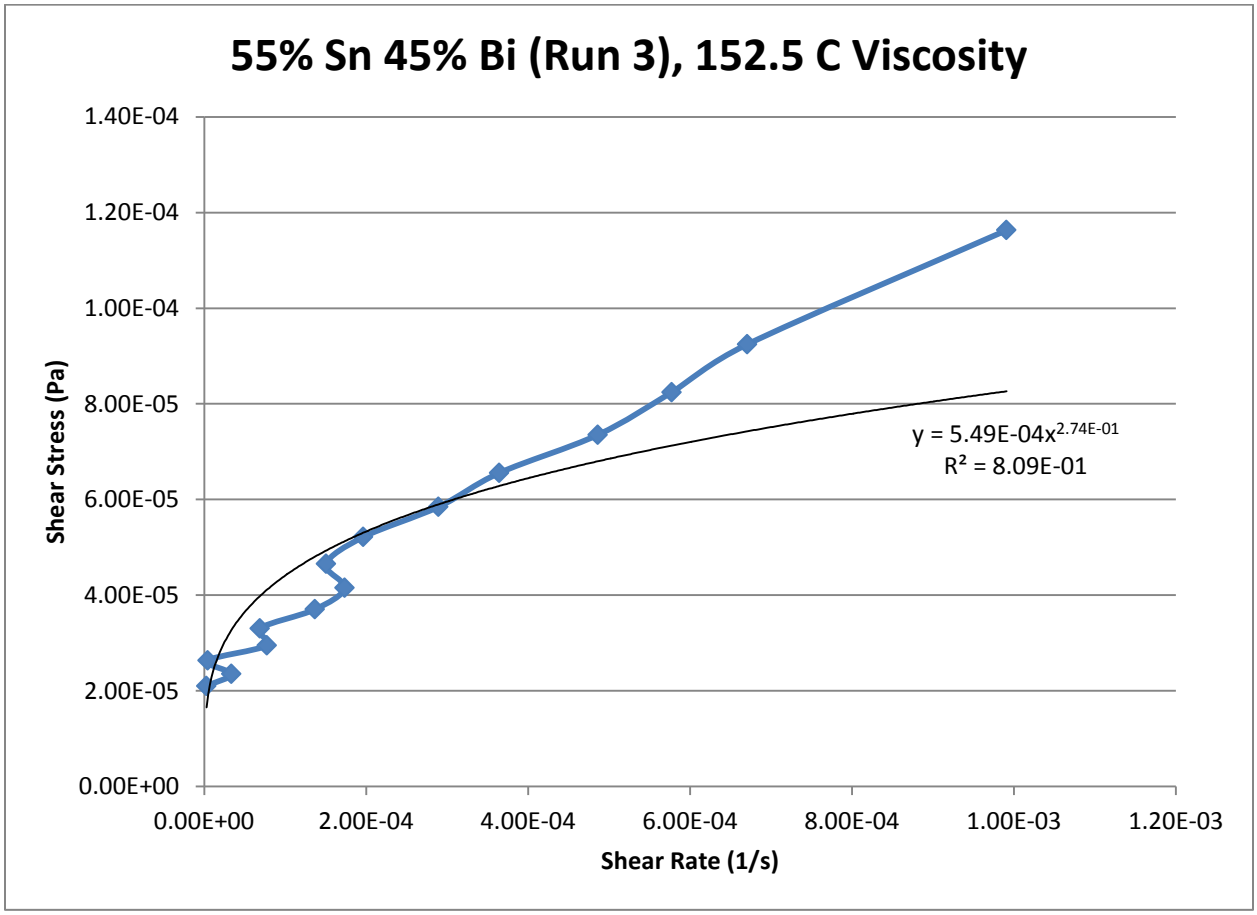

Figure 173- 55% Sn 45% Bi (Run 3), 152.5 C, Cone and Plate Viscosity

60% Tin 40% Bismuth (Run 1)

Expected Composition: 62.00% Sn, 38.00% Bi

Theoretical Solidus Line: 139 C
Theoretical Liquidus Line: 149.8 C

Experimental Solidus Line: 140.3 C
Experimental Liquidus Line: 147.0 C

Set-Up Notes

- The stage was heated to 145 Celsius and the metal pieces were melted underneath the cone. The cone was then lowered to the geometry gap. Stress sweeps at 145 C, 140 C, and 150 C were conducted in that order.

- Sample appeared to still be a semi-solid above 150 C.

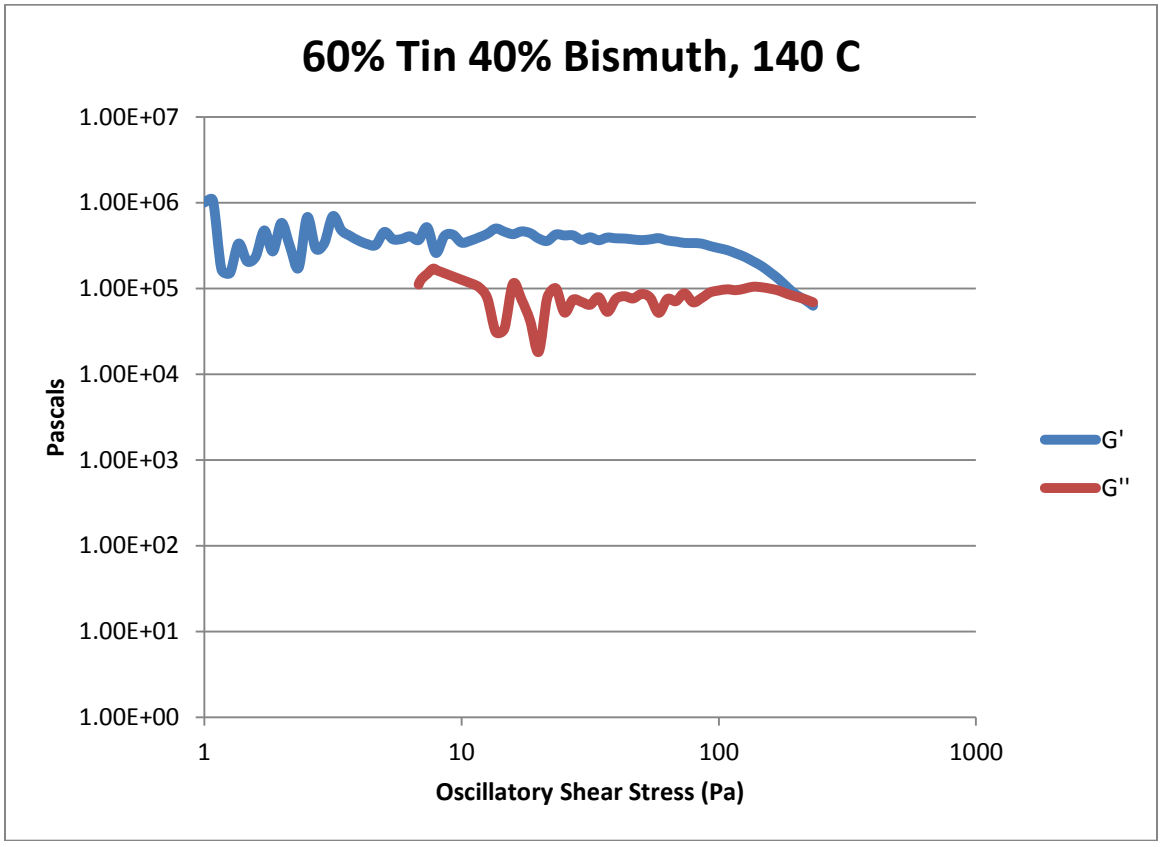

Figure 174- 60% Sn 40% Bi (Run 1), 140 C, Cone and Plate Stress Sweep

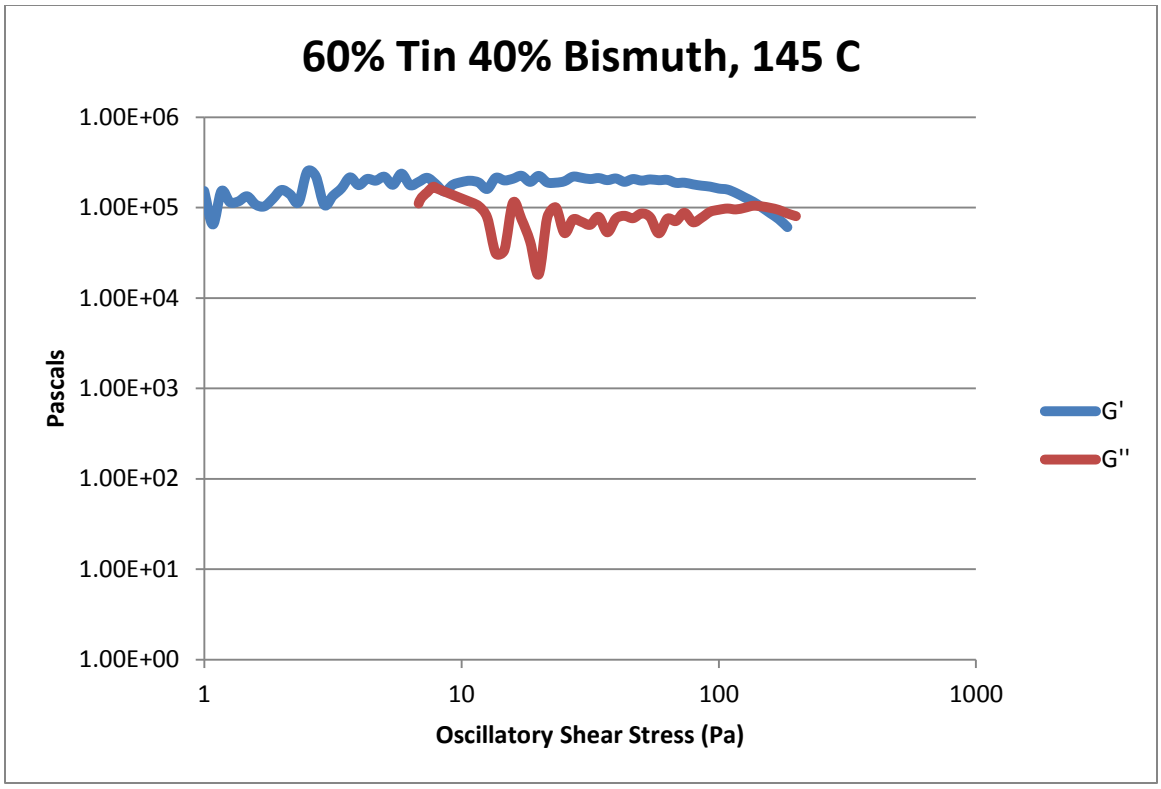

Figure 175- 60% Sn 40% Bi (Run 1), 145 C, Cone and Plate Stress Sweep

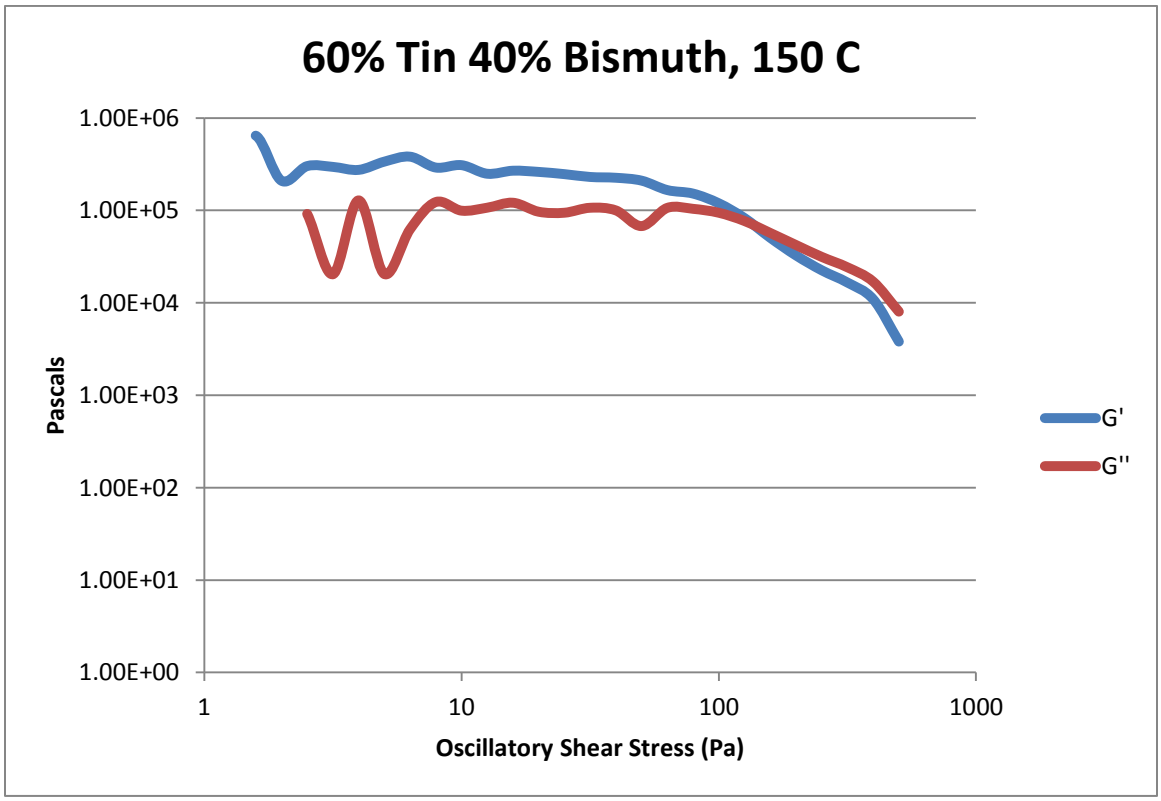

Figure 176- 60% Sn 40% Bi (Run 1), 150 C, Cone and Plate Stress Sweep

Temperature	Crossover Stress (Pa)	Crossover Stress (PSI)
140 C	$7.62 * 10^4$	11.1
145 C	$7.37 * 10^4$	10.7
150 C	$6.74 * 10^4$	9.78

Table 31- 60% Sn 40% Bi (Run 1), Cone and Plate Crossover Stresses

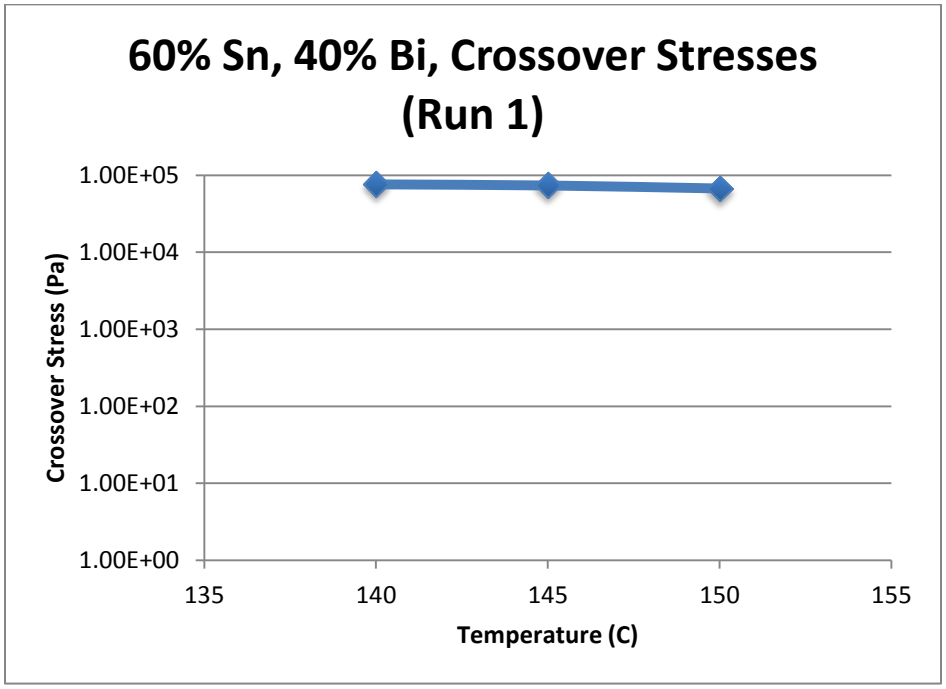

Figure 177- 60% Sn 40% Bi (Run 1), Cone and Plate Crossover Stresses

Temperature	Fraction Solid (At %)	G' Plateau (Pa)	G'' Plateau (Pa)
140 C	100	$3.77 * 10^5$	$7.20 * 10^4$
145 C	0	$2.05 * 10^5$	$1.15* 10^5$

Table 32- 60% Sn 40% Bi (Run 1), Cone and Plate Crossover Stresses

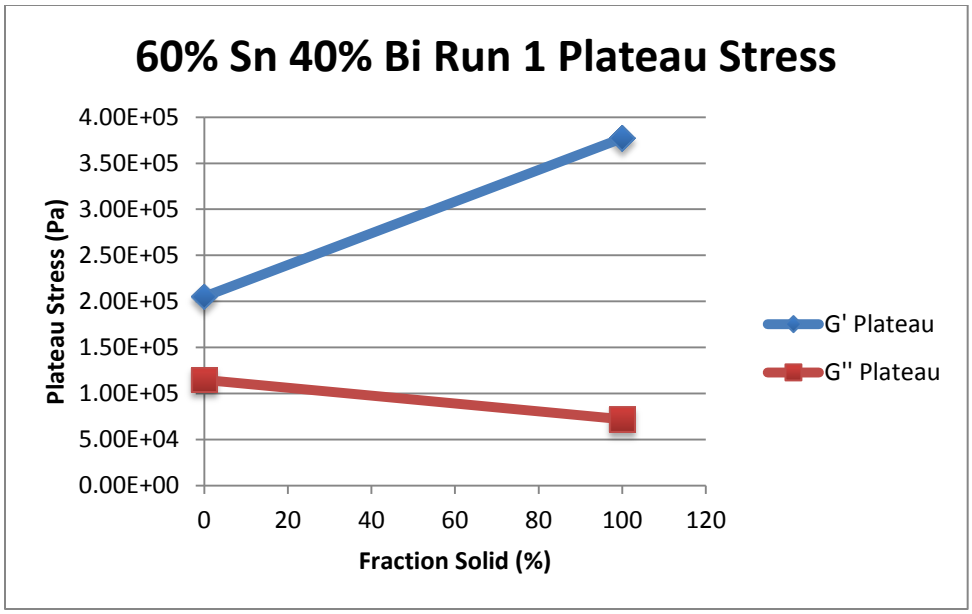

Figure 178- 60% Sn 40% Bi (Run 1), Cone and Plate Crossover Stresses vs. Fraction Solid

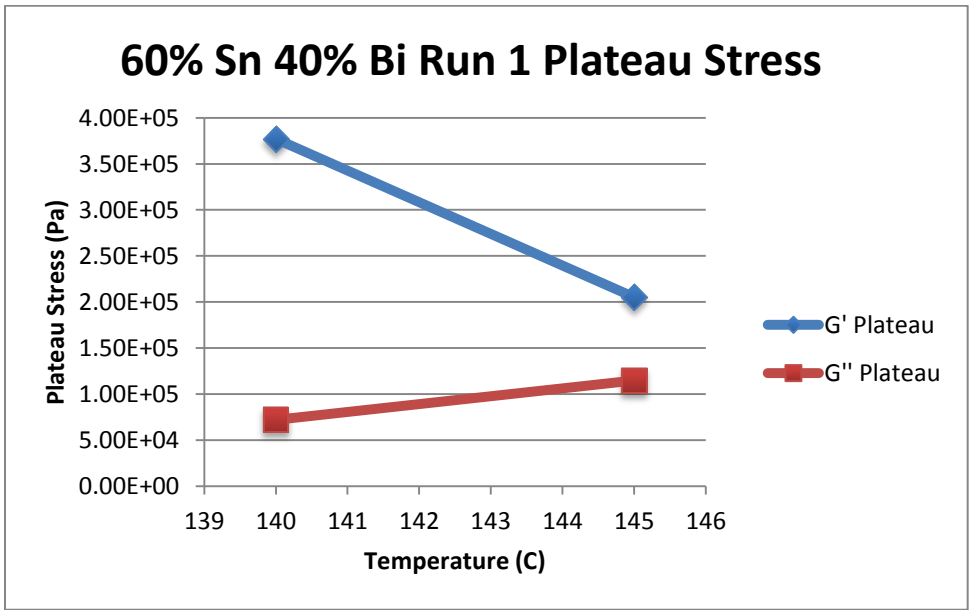

Figure 179- 60% Sn 40% Bi (Run 1), Cone and Plate Crossover Stresses vs. Temperature

60% Sn 40% Bi (Run 1) Viscosity					
Temperature	**Fraction Solid**	**Power Law**	**K**	**n**	**R^2**
140 C	100 %	$\tau = 7.82 * 10^{-5} * \dot{\gamma}^{0.1794}$ $\mu = 1.40 * 10^{-5} * \dot{\gamma}^{-0.8206}$	$7.82 * 10^{-5}$ Pa*s	0.1794	70.91 %
145 C	0 %	$\tau = 1.29 * 10^{-4} * \dot{\gamma}^{0.263}$ $\mu = 3.39 * 10^{-5} * \dot{\gamma}^{-0.737}$	$1.29 * 10^{-4}$ Pa*s	0.0993	52.10 %
150 C	0 %	$\tau = 8.46 * 10^{-4} * \dot{\gamma}^{0.5138}$ $\mu = 4.35 * 10^{-4} * \dot{\gamma}^{-0.4862}$	$8.46 * 10^{-4}$ Pa*s	0.5138	89.68 %

Table 33- 60% Sn 40% Bi (Run 1), Cone and Plate Viscosity

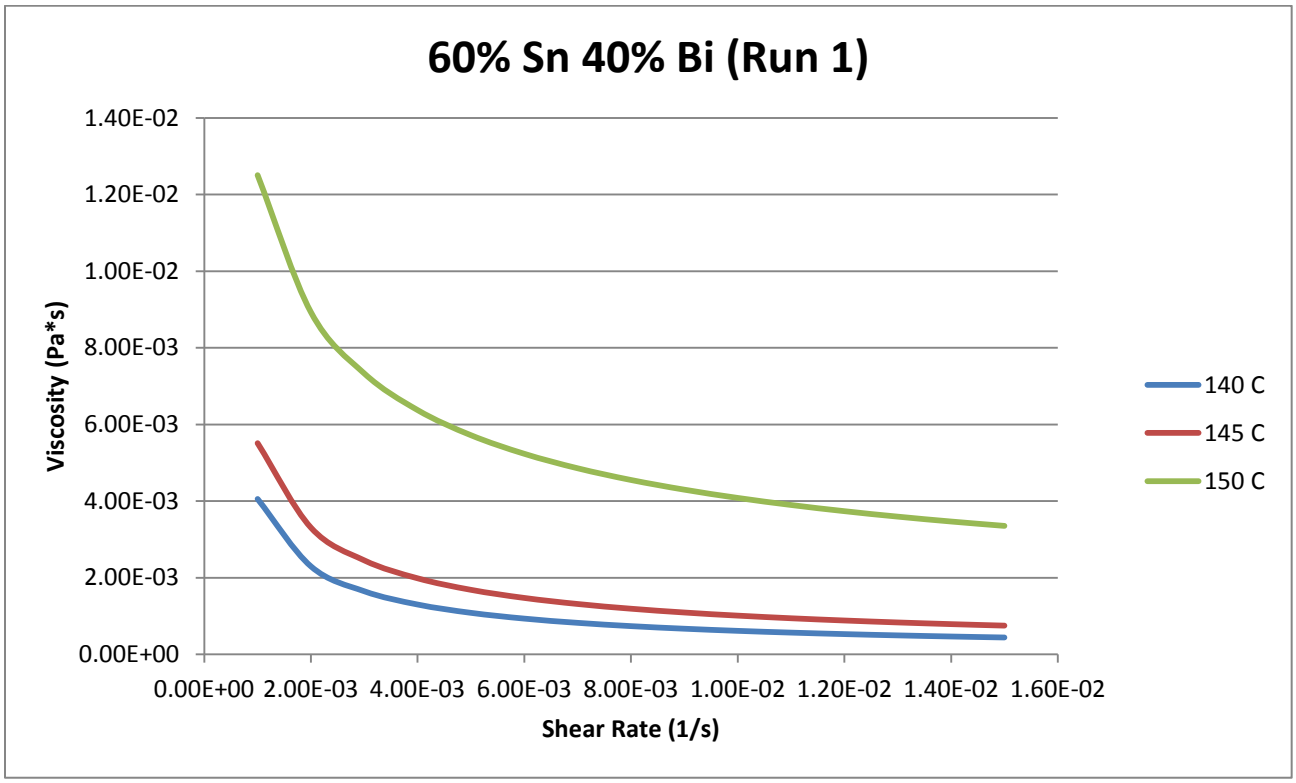

Figure 180- 60% Sn 40% Bi (Run 1), Cone and Plate Viscosity

140 C

Fraction Solid	100 %
Power Law	$\tau = 7.82 * 10^{-5} * \dot{\gamma}^{0.1794}$
	$\mu = 1.40 * 10^{-5} * \dot{\gamma}^{-0.8206}$
R^2	70.91 %

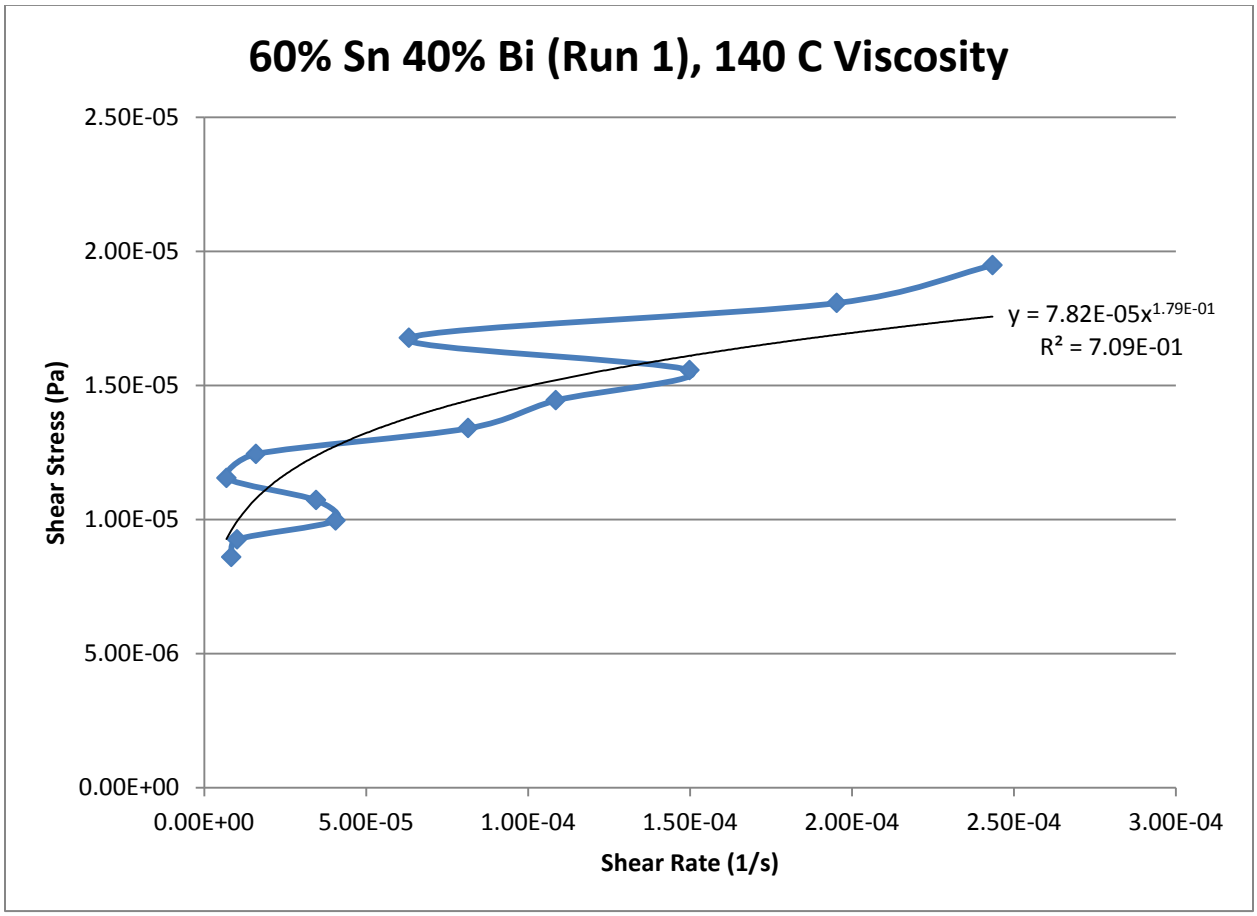

Figure 181- 60% Sn 40% Bi (Run 1), 140 C, Cone and Plate Viscosity

145 C

Fraction Solid	0 %
Power Law	$\tau = 1.29 * 10^{-4} * \dot{\gamma}^{0.263}$
	$\mu = 3.39 * 10^{-5} * \dot{\gamma}^{-0.737}$
R^2	52.10 %

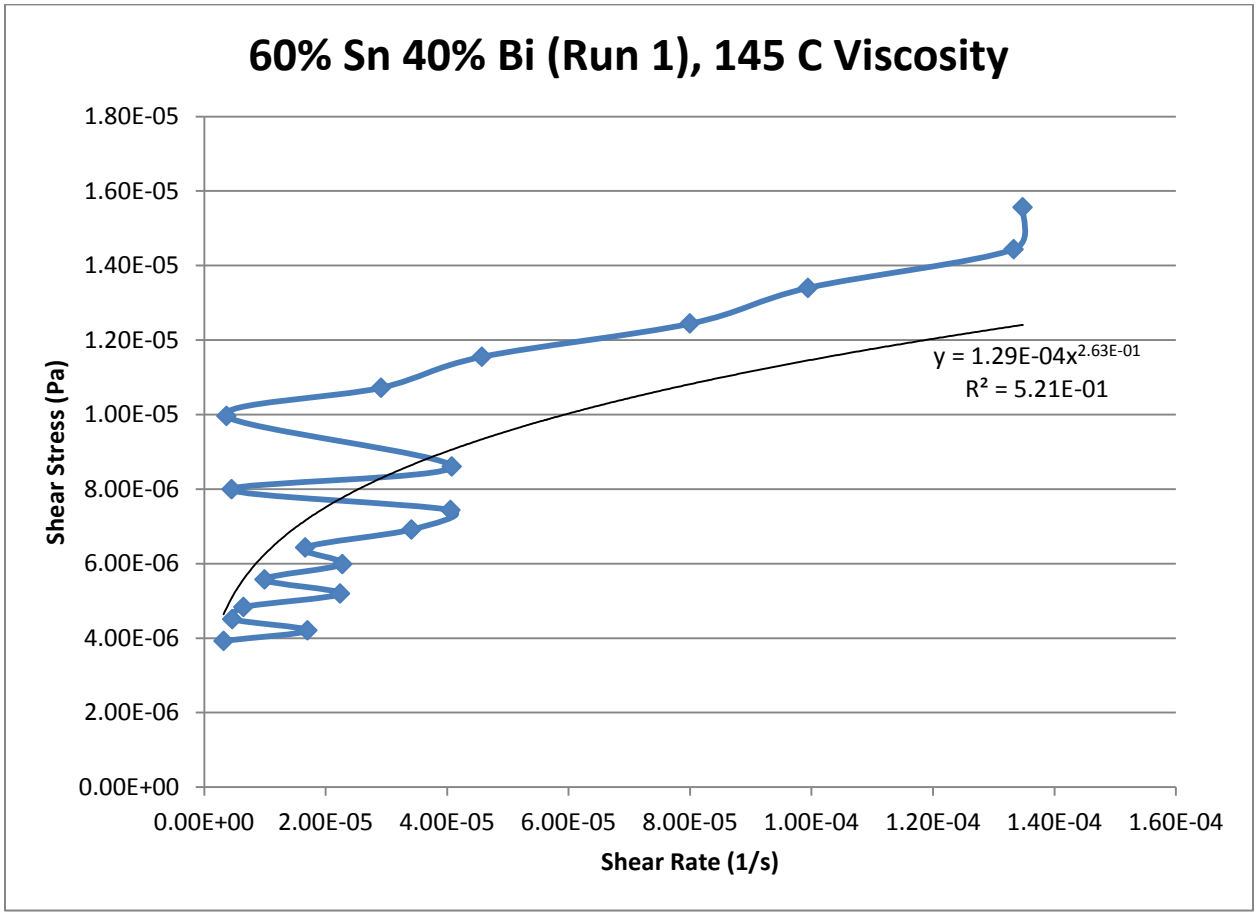

Figure 182- 60% Sn 40% Bi (Run 1), 145 C, Cone and Plate Viscosity

150 C

Fraction Solid	0 %
Power Law	$\tau = 8.46 * 10^{-4} * \dot{\gamma}^{0.5138}$
	$\mu = 4.35 * 10^{-4} * \dot{\gamma}^{-0.4862}$
R^2	89.68 %

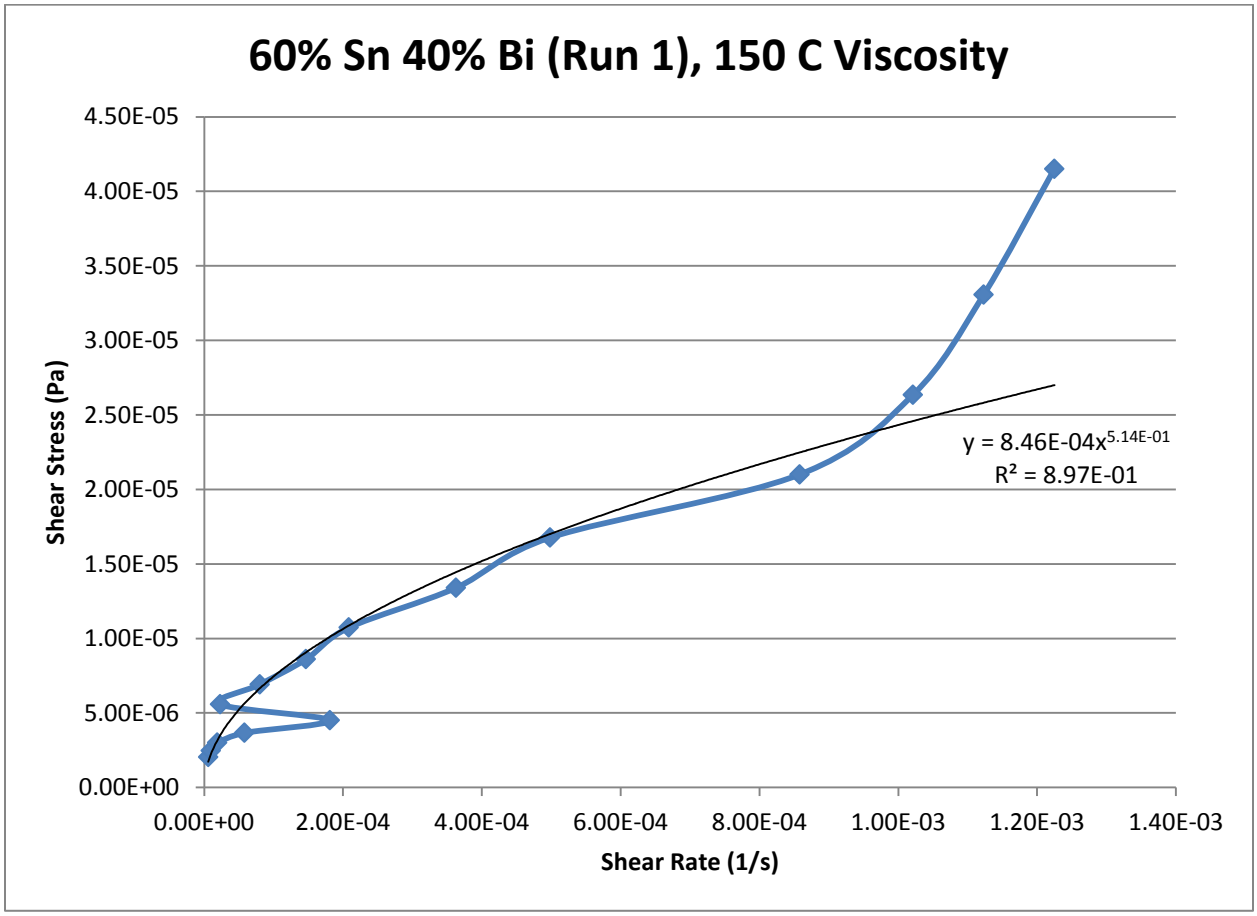

Figure 183- 60% Sn 40% Bi (Run 1), 150 C, Cone and Plate Viscosity

60% Tin 40% Bismuth (Run 2)

Expected Composition: 62.00% Sn, 38.00% Bi

Theoretical Solidus Line: 139 C
Theoretical Liquidus Line: 149.8 C

Experimental Solidus Line: 140.3 C
Experimental Liquidus Line: 147.0 C

Set-Up Notes

- The stage was heated to 142 Celsius and the metal pieces were melted underneath the cone. The cone was then lowered to the geometry gap. Stress sweeps at 141 C, 143 C, 144 C, 145 C, 150 C, and 155 C were conducted, in that order.

Plots

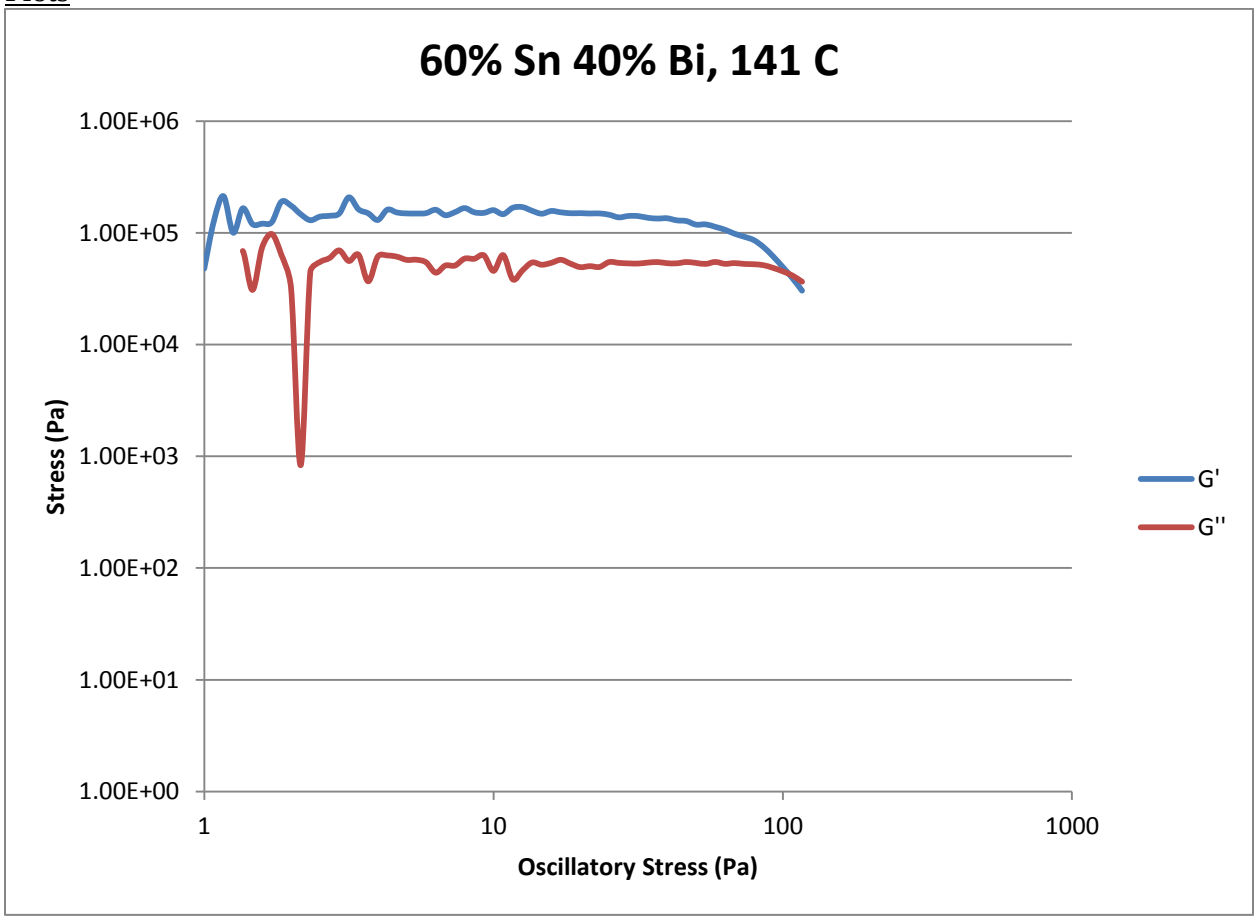

Figure 184- 60% Sn 40% Bi (Run 2), 141 C, Cone and Plate Stress Sweep

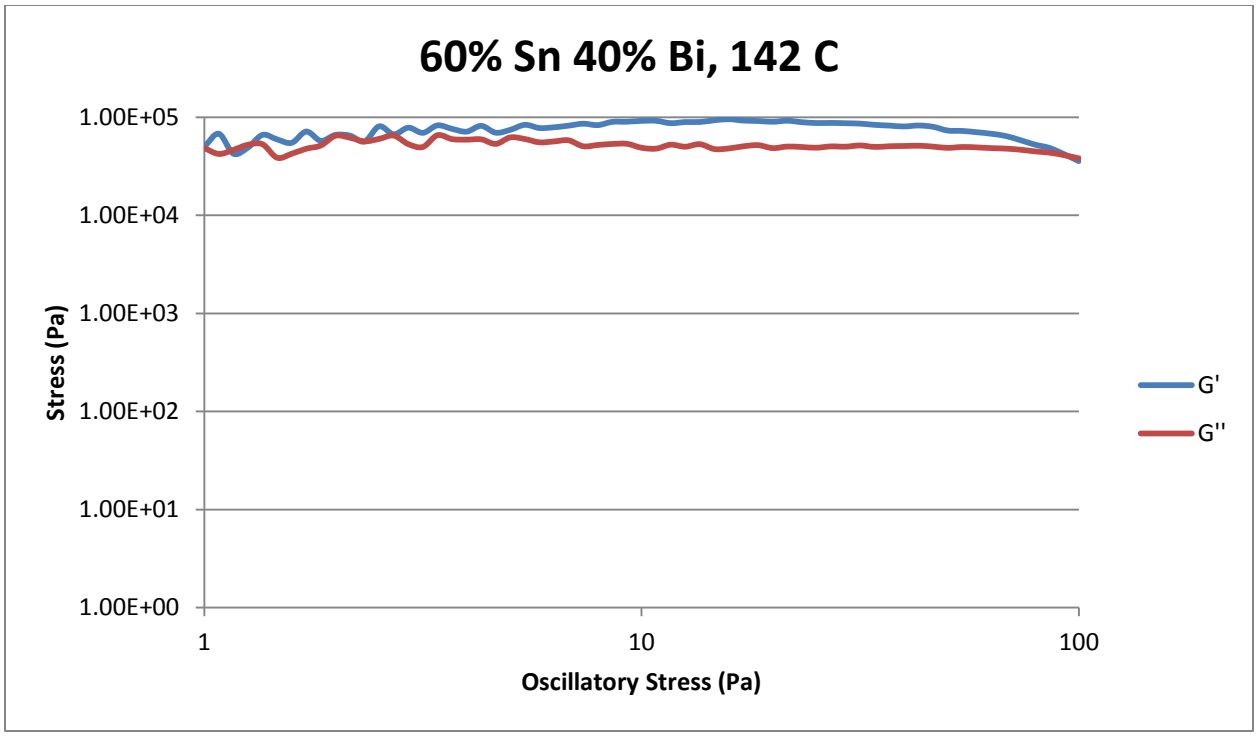

Figure 185- 60% Sn 40% Bi (Run 2), 142 C, Cone and Plate Stress Sweep

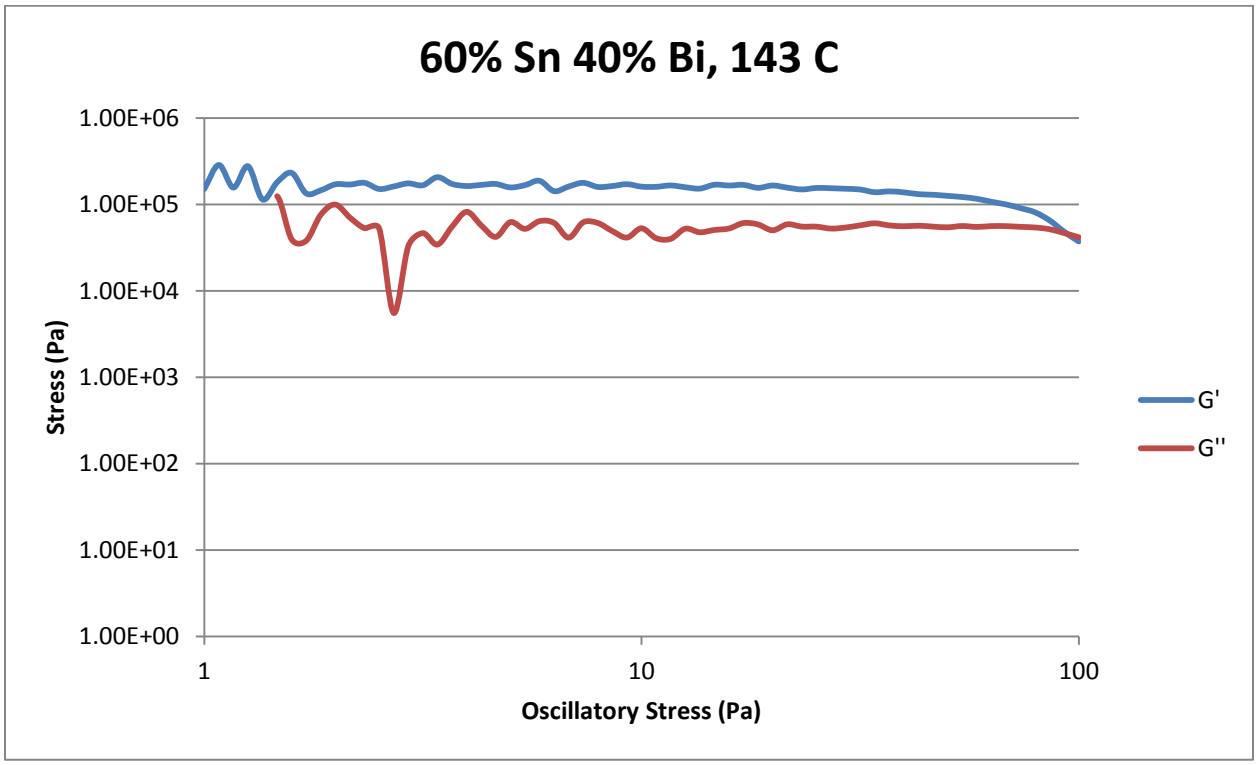

Figure 186- 60% Sn 40% Bi (Run 2), 143 C, Cone and Plate Stress Sweep

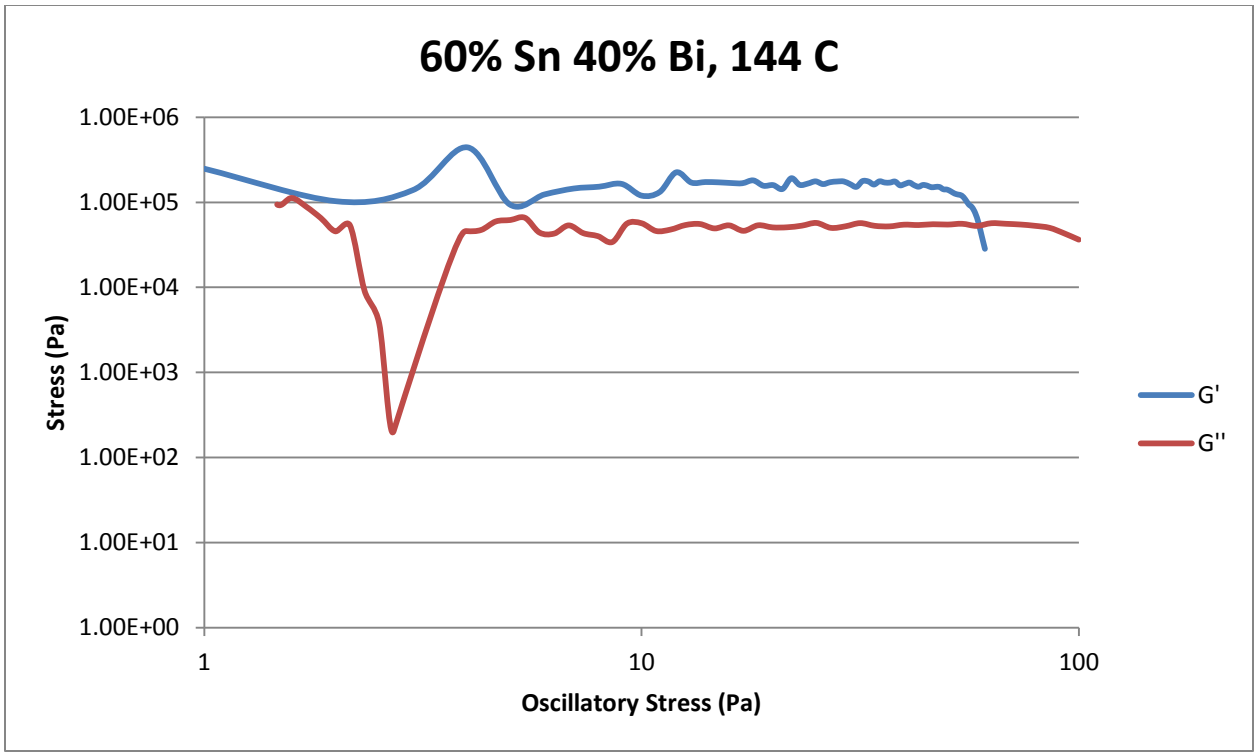

Figure 187- 60% Sn 40% Bi (Run 2), 144 C, Cone and Plate Stress Sweep

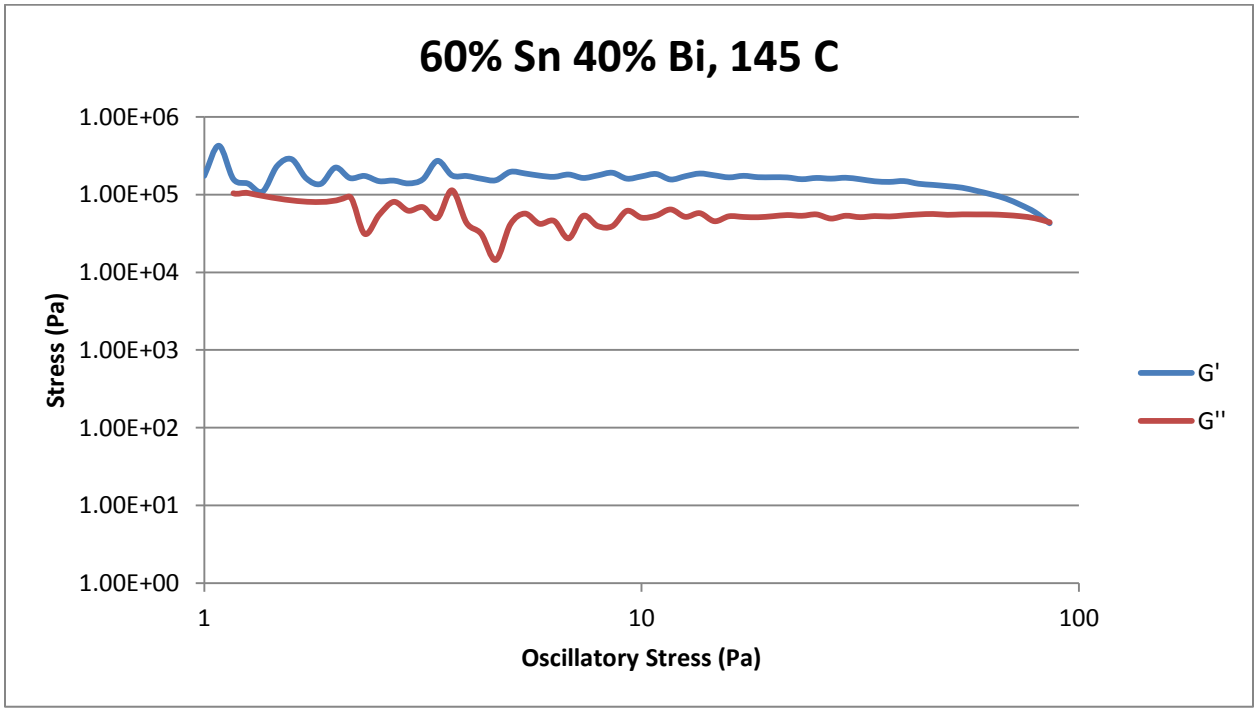

Figure 188- 60% Sn 40% Bi (Run 2), 145 C, Cone and Plate Stress Sweep

Temperature	Fraction Solid (At %)	Crossover Stress (Pa)	G' Plateau (Pa)	G'' Plateau (Pa)
141 C	0.50	$4.39 * 10^4$	$1.55 * 10^5$	$5.38 * 10^4$
142 C	0.30	$3.90 * 10^4$	$9.13 * 10^4$	$5.03 * 10^4$
143 C	0	$4.42 * 10^4$	$1.62 * 10^5$	$5.71 * 10^4$
144 C	0	$4.66 * 10^4$	$1.60 * 10^5$	$5.44 * 10^4$
145 C	0	$4.60 * 10^4$	$1.62 * 10^5$	$5.41 * 10^4$

Table 34- 60% Sn 40% Bi (Run 2), Cone and Plate Crossover and Plateau

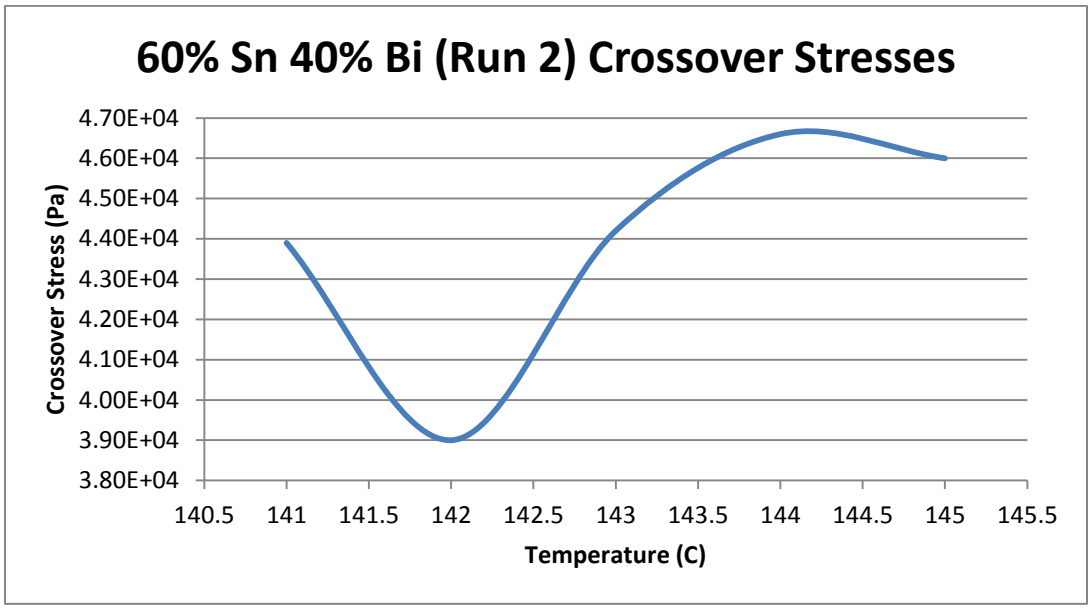

Figure 189- 60% Sn 40% Bi (Run 2), Cone and Plate Crossover Stresses

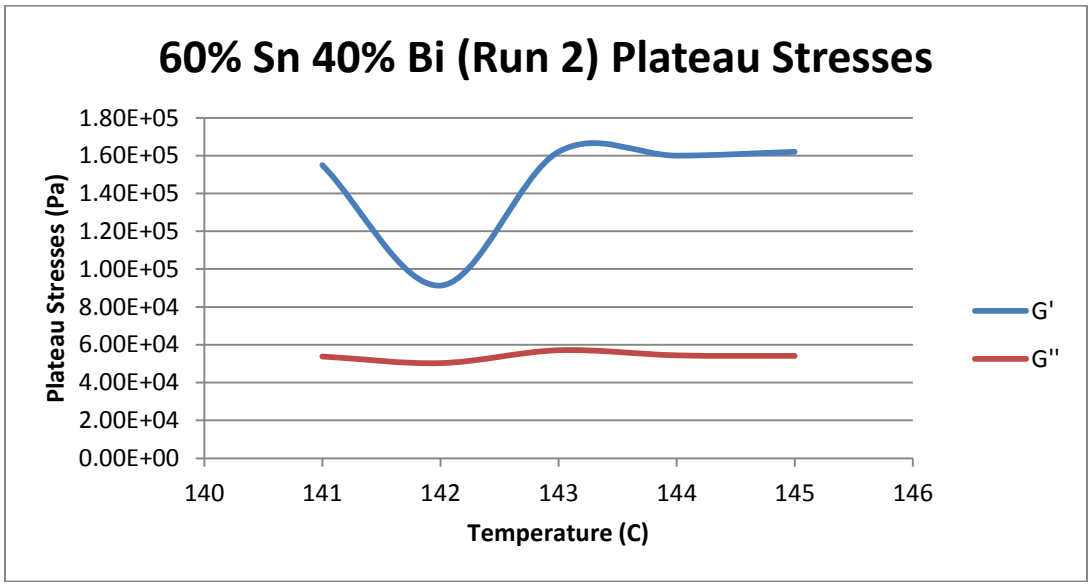

Figure 190- 60% Sn 40% Bi (Run 2), Cone and Plate Plateau Stresses

60% Sn 40% Bi (Run 2) Viscosity					
Temperature	**Fraction Solid**	**Power Law**	**K**	**n**	**R^2**
141 C	0.50 %	$\tau = 2.77 * 10^{-5} * \dot{\gamma}^{0.1207}$ $\mu = 3.34 * 10^{-6} * \dot{\gamma}^{-0.8793}$	$2.77 * 10^{-5}$ Pa*s	0.1207	41.92 %
142 C	0.30 %	$\tau = 5.86 * 10^{-5} * \dot{\gamma}^{0.0993}$ $\mu = 5.82 * 10^{-6} * \dot{\gamma}^{-0.9007}$	$5.86 * 10^{-5}$ Pa*s	0.0993	67.04 %
143 C	0 %	$\tau = 8.78 * 10^{-6} * \dot{\gamma}^{0.0507}$ $\mu = 4.45 * 10^{-7} * \dot{\gamma}^{-0.9493}$	$8.78 * 10^{-6}$ Pa*s	0.0507	2.56 %

Table 35- 60% Sn 40% Bi (Run 2), Cone and Plate Viscosity

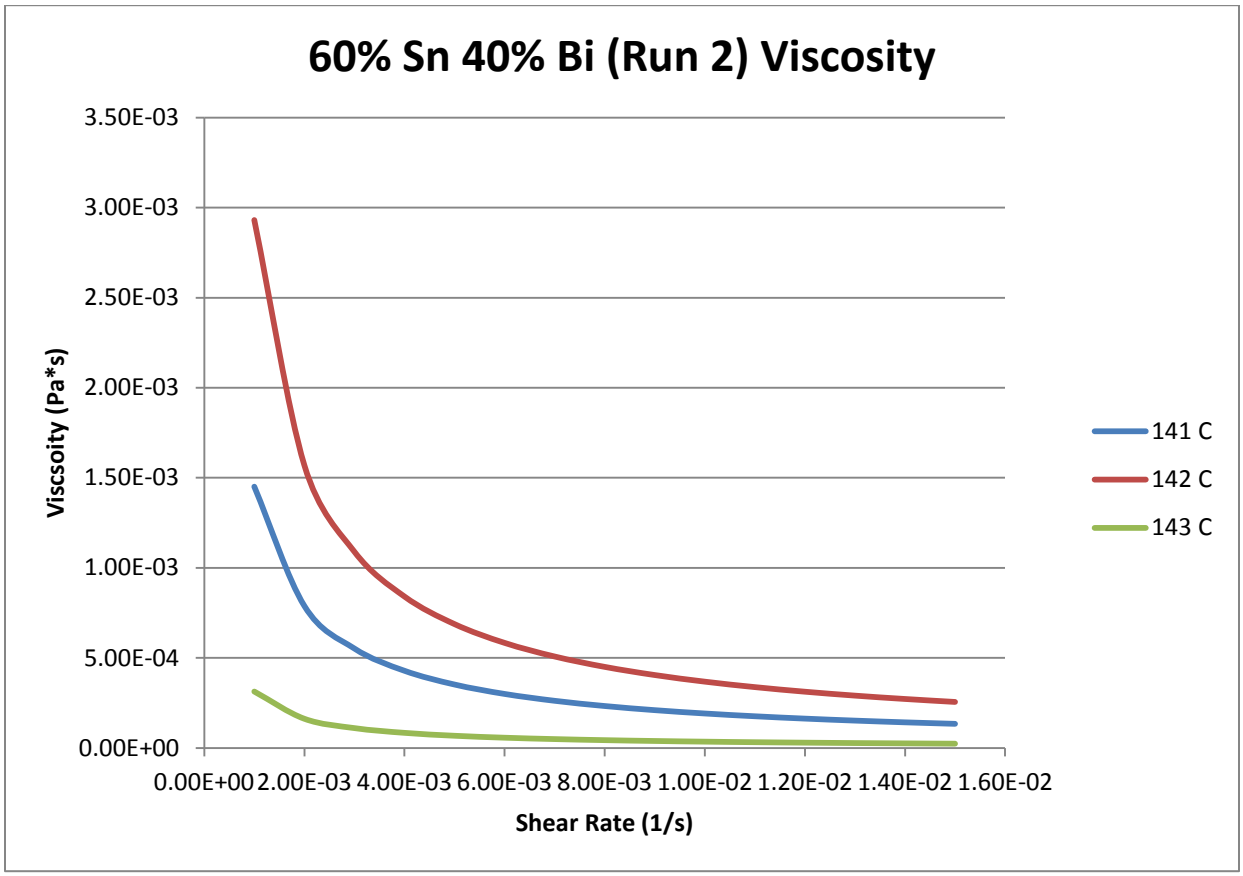

Figure 191- 60% Sn 40% Bi (Run 2), Cone and Plate Viscosity

141 C

Fraction Solid	0.50 %
Power Law	$\tau = 2.77 * 10^{-5} * \dot{\gamma}^{0.1207}$
	$\mu = 3.34 * 10^{-6} * \dot{\gamma}^{-0.8793}$
R^2	41.92 %

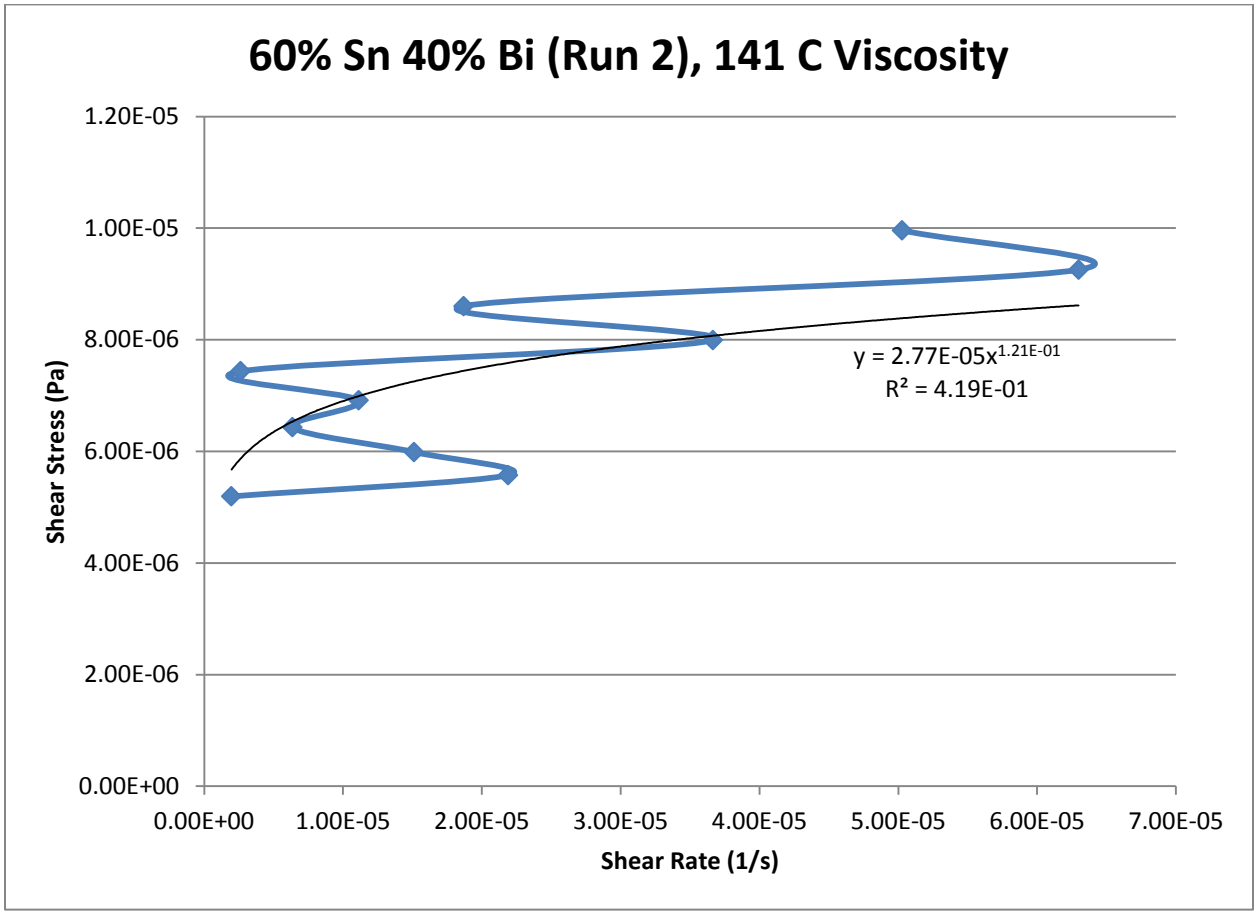

Figure 192- 60% Sn 40% Bi (Run 2), 141 C, Cone and Plate Viscosity

142 C

Fraction Solid	0.30 %
Power Law	$\tau = 5.86 * 10^{-5} * \dot{\gamma}^{0.0993}$
	$\mu = 5.82 * 10^{-6} * \dot{\gamma}^{-0.9007}$
R^2	67.04 %

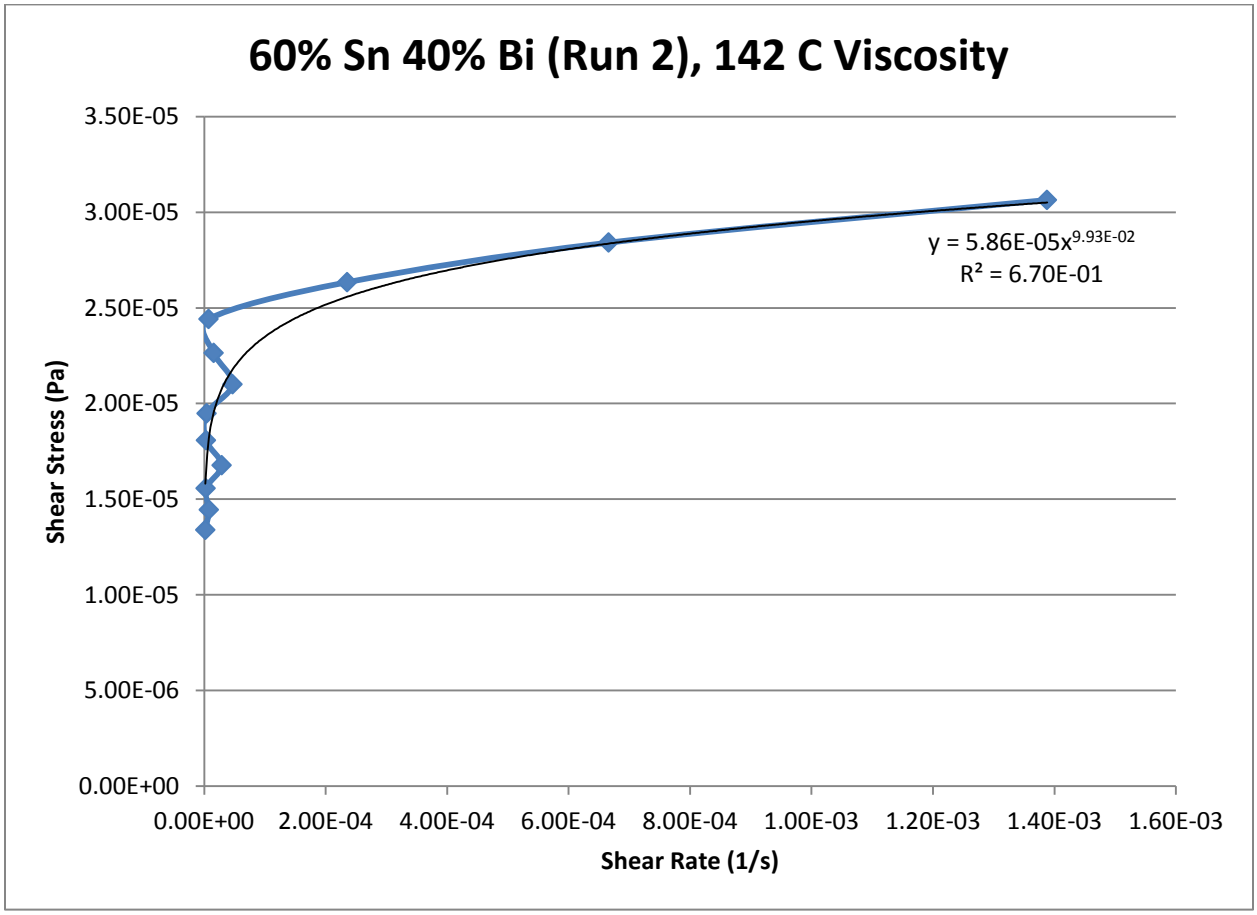

Figure 193- 60% Sn 40% Bi (Run 2), 142 C, Cone and Plate Viscosity

143 C

Fraction Solid	0 %
Power Law	$\tau = 8.78 * 10^{-6} * \dot{\gamma}^{0.0507}$
	$\mu = 4.45 * 10^{-7} * \dot{\gamma}^{-0.9493}$
R^2	2.56 %

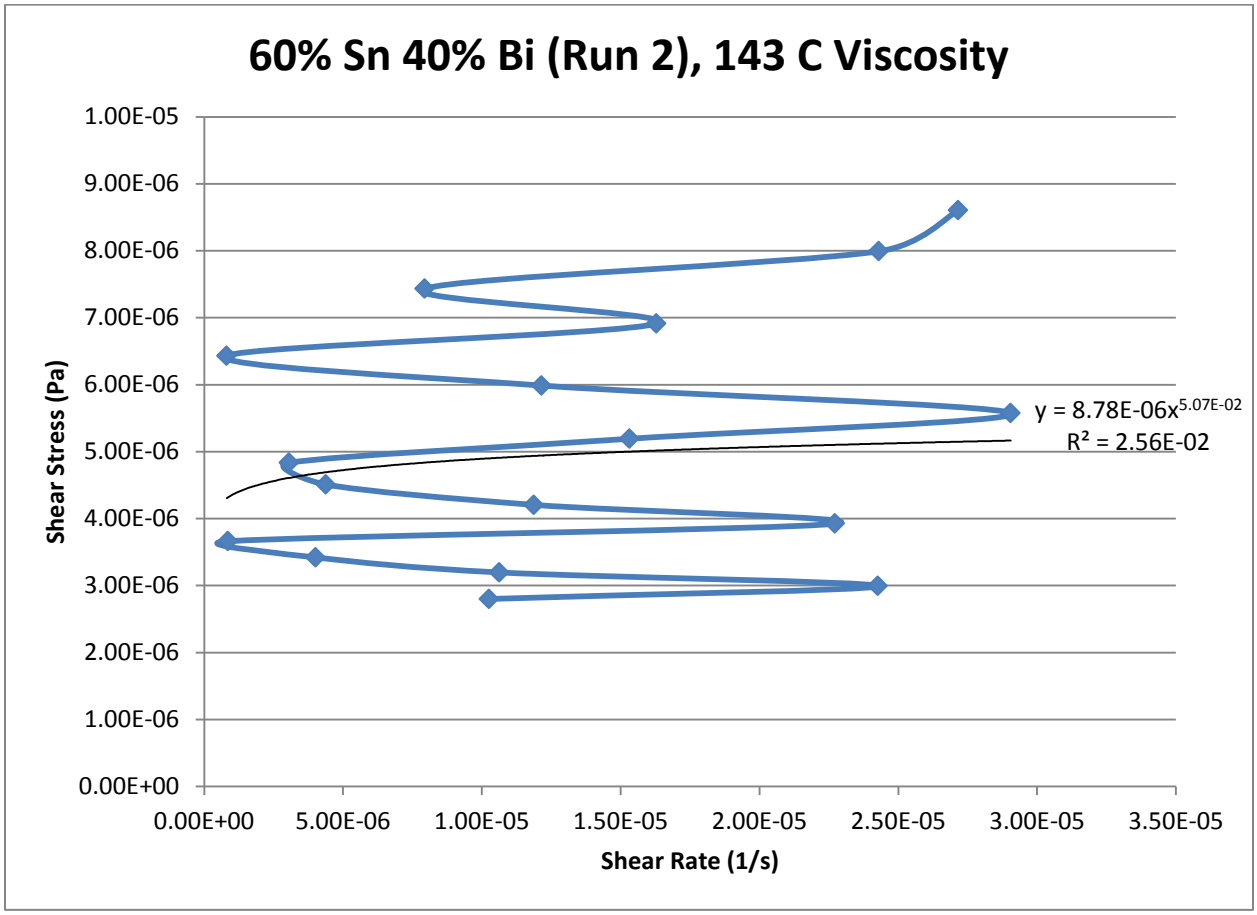

Figure 194- 60% Sn 40% Bi (Run 2), 143 C, Cone and Plate Viscosity

60% Tin 40% Bismuth (Run 3)

Expected Composition: 62.00% Sn, 38.00% Bi

Theoretical Solidus Line: 139 C
Theoretical Liquidus Line: 149.8 C

Experimental Solidus Line: 140.3 C
Experimental Liquidus Line: 147.0 C

Set-Up Notes

- The stage was heated to 142 Celsius and the metal pieces were melted underneath the cone. The cone was then lowered to the geometry gap. Stress sweeps at 141 C, 143 C, 144 C, 145 C, 150 C, and 155 C were conducted, in that order.

Plots

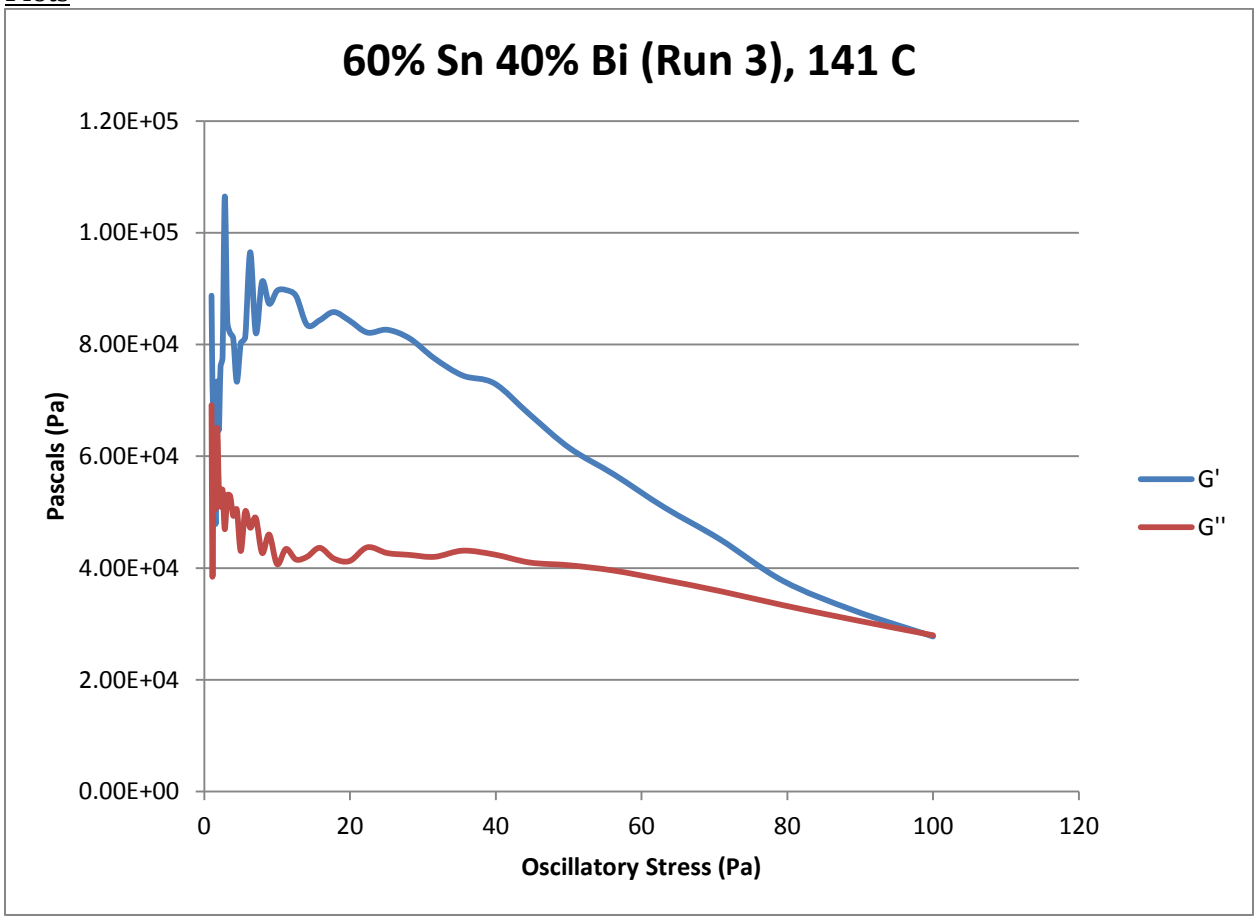

Figure 195- 60% Sn 40% Bi (Run 3), 141 C, Cone and Plate Stress Sweep

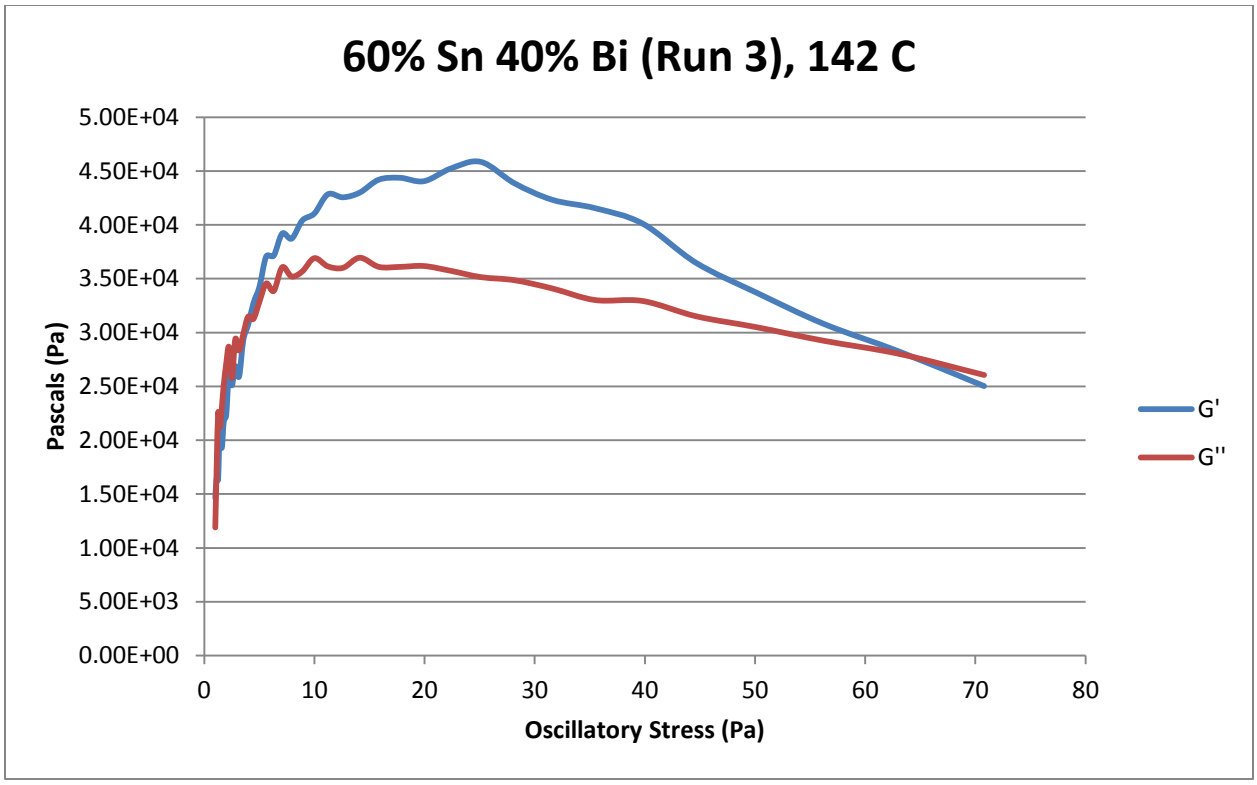

Figure 196- 60% Sn 40% Bi (Run 3), 142 C, Cone and Plate Stress Sweep

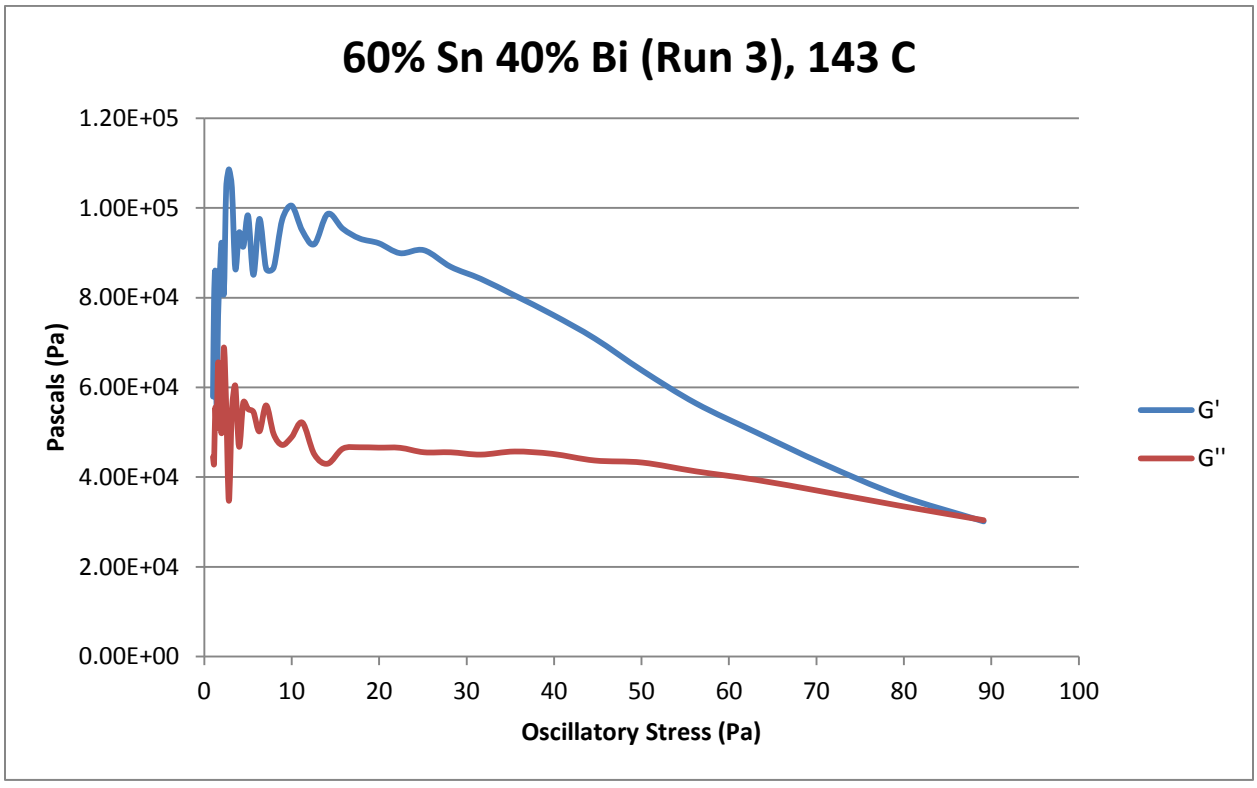

Figure 197- 60% Sn 40% Bi (Run 3), 143 C, Cone and Plate Stress Sweep

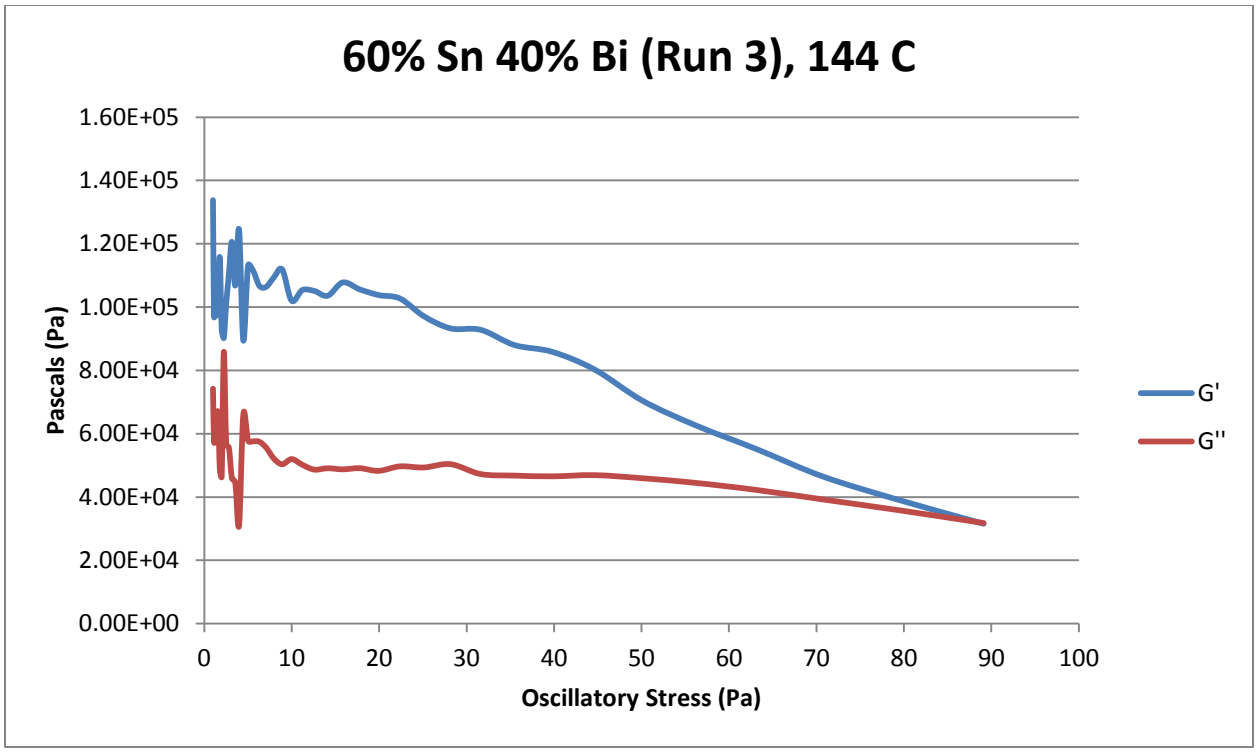

Figure 198- 60% Sn 40% Bi (Run 3), 144 C, Cone and Plate Stress Sweep

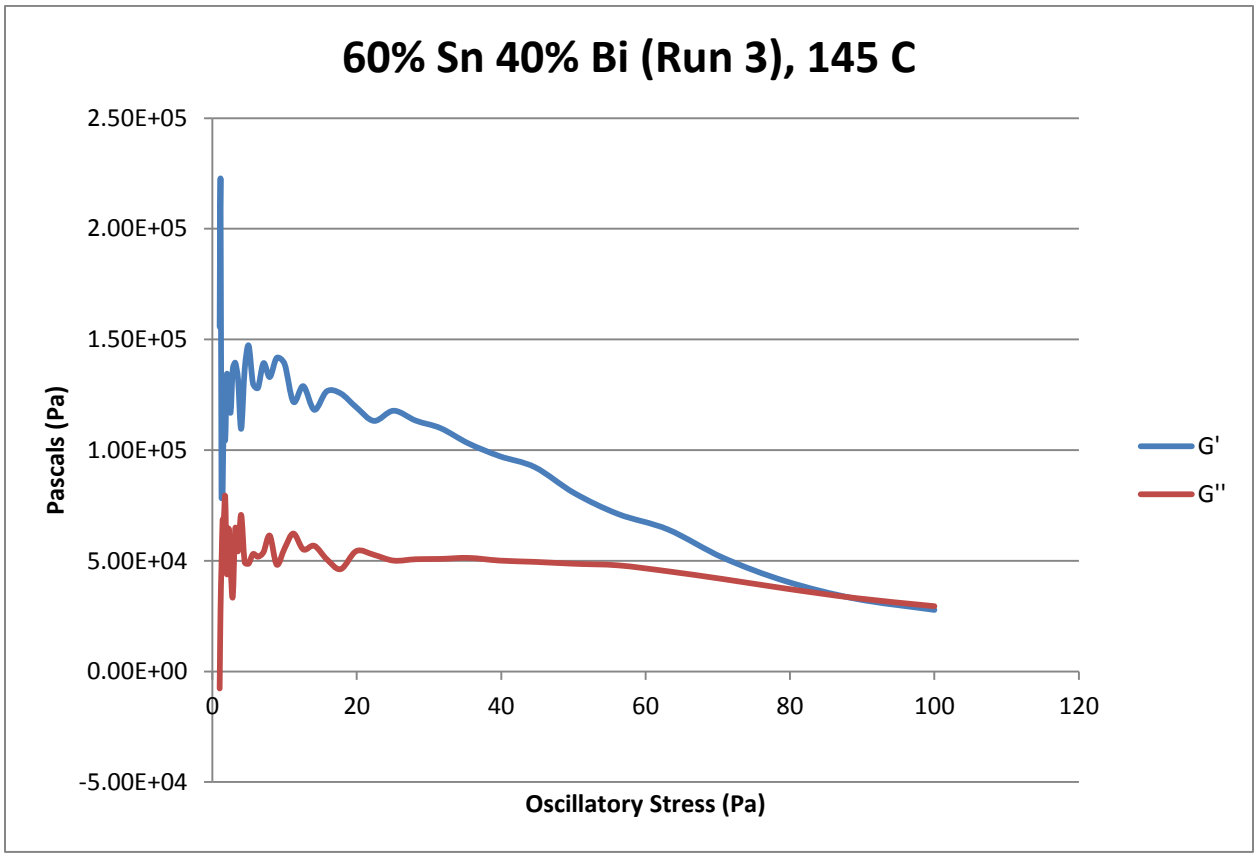

Figure 199- 60% Sn 40% Bi (Run 3), 145 C, Cone and Plate Stress Sweep

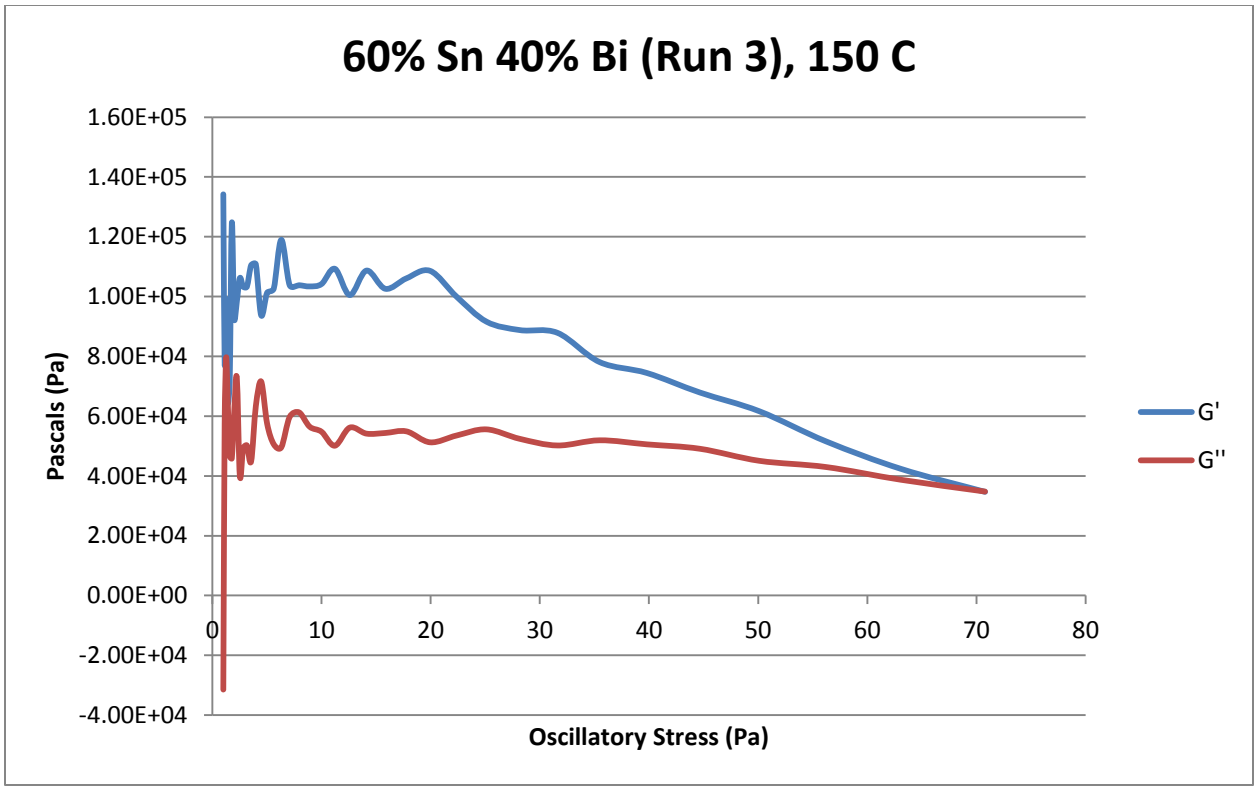

Figure 200- 60% Sn 40% Bi (Run 3), 150 C, Cone and Plate Stress Sweep

Temperature	Fraction Solid (At %)	Crossover Stress (Pa)	G' Plateau (Pa)	G'' Plateau (Pa)
141 C	0.50	$1.82 * 10^4$	$8.70 * 10^4$	$4.30 * 10^4$
142 C	0.30	$2.76 * 10^4$	$4.42 * 10^4$	$3.61 * 10^4$
143 C	0	$3.08 * 10^4$	$9.53 * 10^4$	$4.62 * 10^4$
144 C	0	$3.21 * 10^4$	$1.12 * 10^5$	$5.01 * 10^4$
145 C	0	$3.37 * 10^4$	$1.26 * 10^5$	$5.05 * 10^4$
150 C	0	$3.49 * 10^4$	$1.08 * 10^5$	$5.35 * 10^4$

Table 36- 60% Sn 40% Bi (Run 3), Cone and Plate Crossover and Plateau Stresses

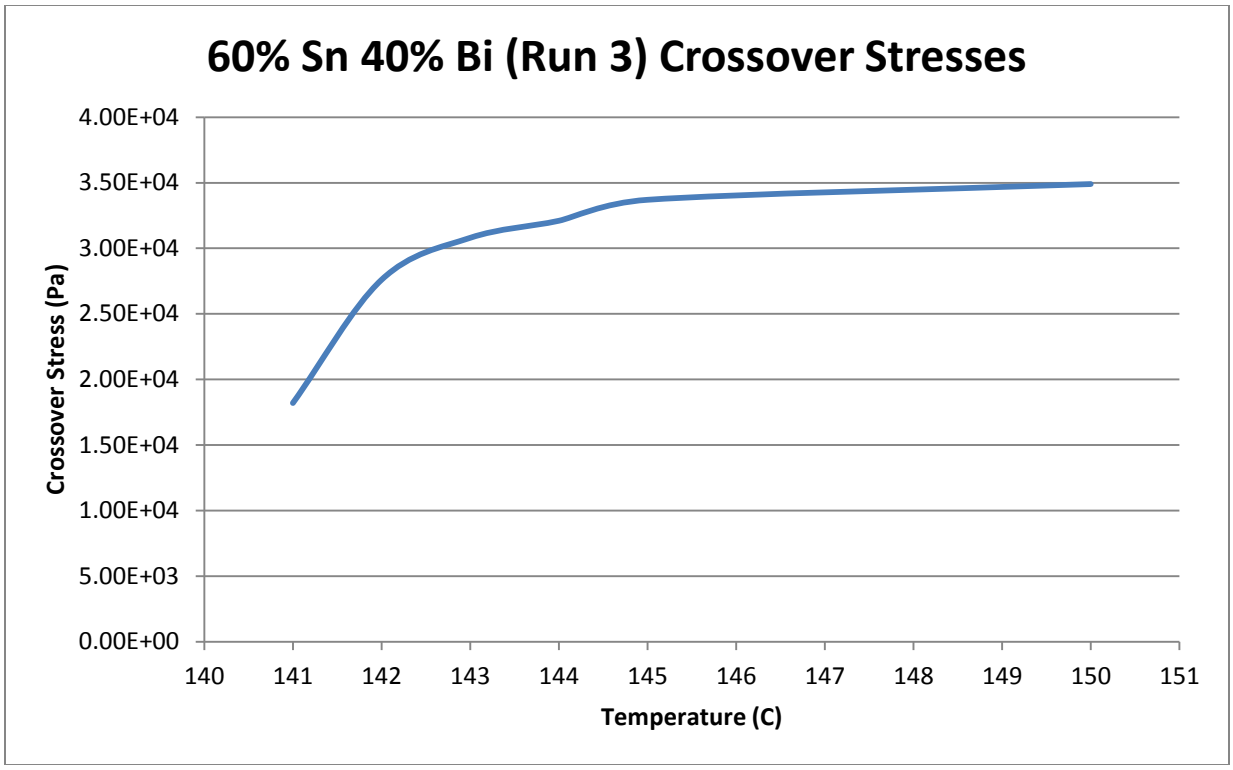

Figure 201- 60% Sn 40% Bi (Run 3), Cone and Plate Crossover Stresses

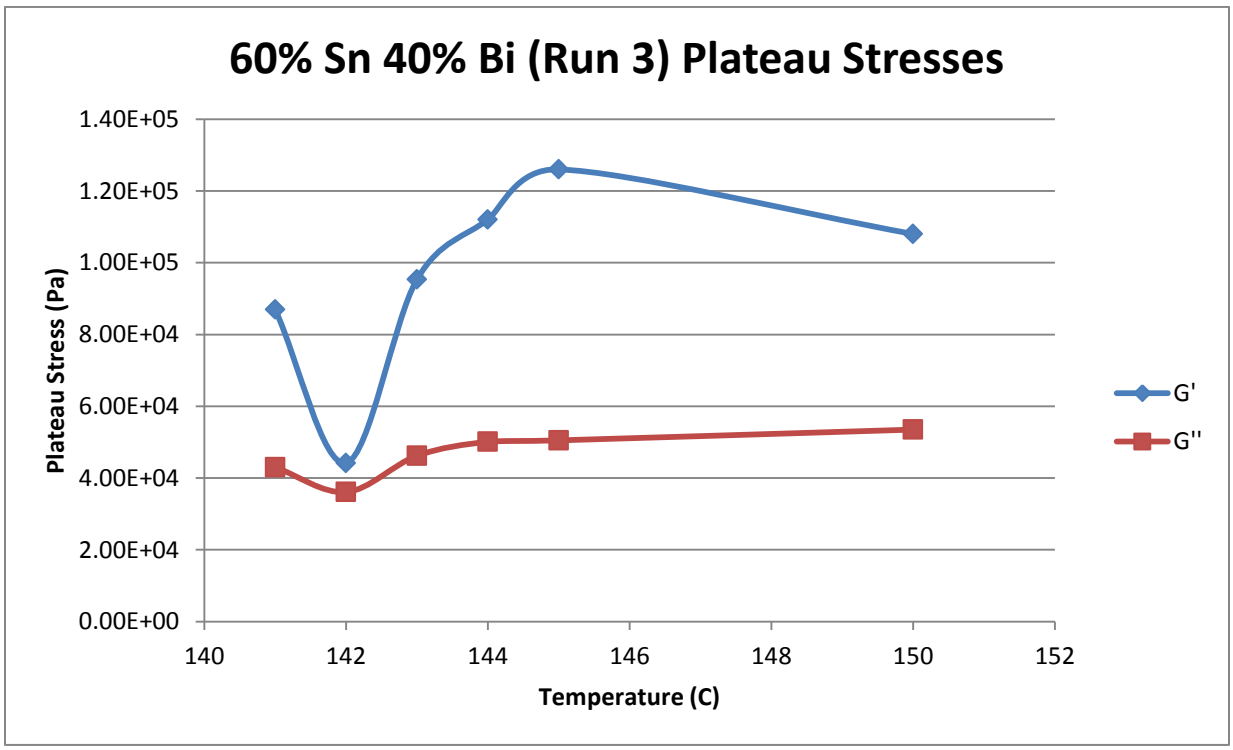

Figure 202- 60% Sn 40% Bi (Run 3), Cone and Plate Plateau Stresses

60% Sn 40% Bi (Run 3) Viscosity					
Temperature	**Fraction Solid**	**Power Law**	**K**	**n**	**R^2**
141 C	0.50 %	$\tau = 6.68 * 10^{-4} * \dot{\gamma}^{0.4951}$ $\mu = 3.31 * 10^{-4} * \dot{\gamma}^{-0.5049}$	$6.68 * 10^{-4}$ Pa*s	0.4951	62.11 %
142 C	0.30 %	$\tau = 2.88 * 10^{-5} * \dot{\gamma}^{0.1793}$ $\mu = 5.16 * 10^{-6} * \dot{\gamma}^{-0.8207}$	$2.88 * 10^{-5}$ Pa*s	0.1793	65.87 %
143 C	0 %	$\tau = 1.37 * 10^{-5} * \dot{\gamma}^{0.1189}$ $\mu = 1.63 * 10^{-6} * \dot{\gamma}^{-0.8811}$	$1.37 * 10^{-5}$ Pa*s	0.1189	23.46 %

Table 37- 60% Sn 40% Bi (Run 3), Cone and Plate Viscosity

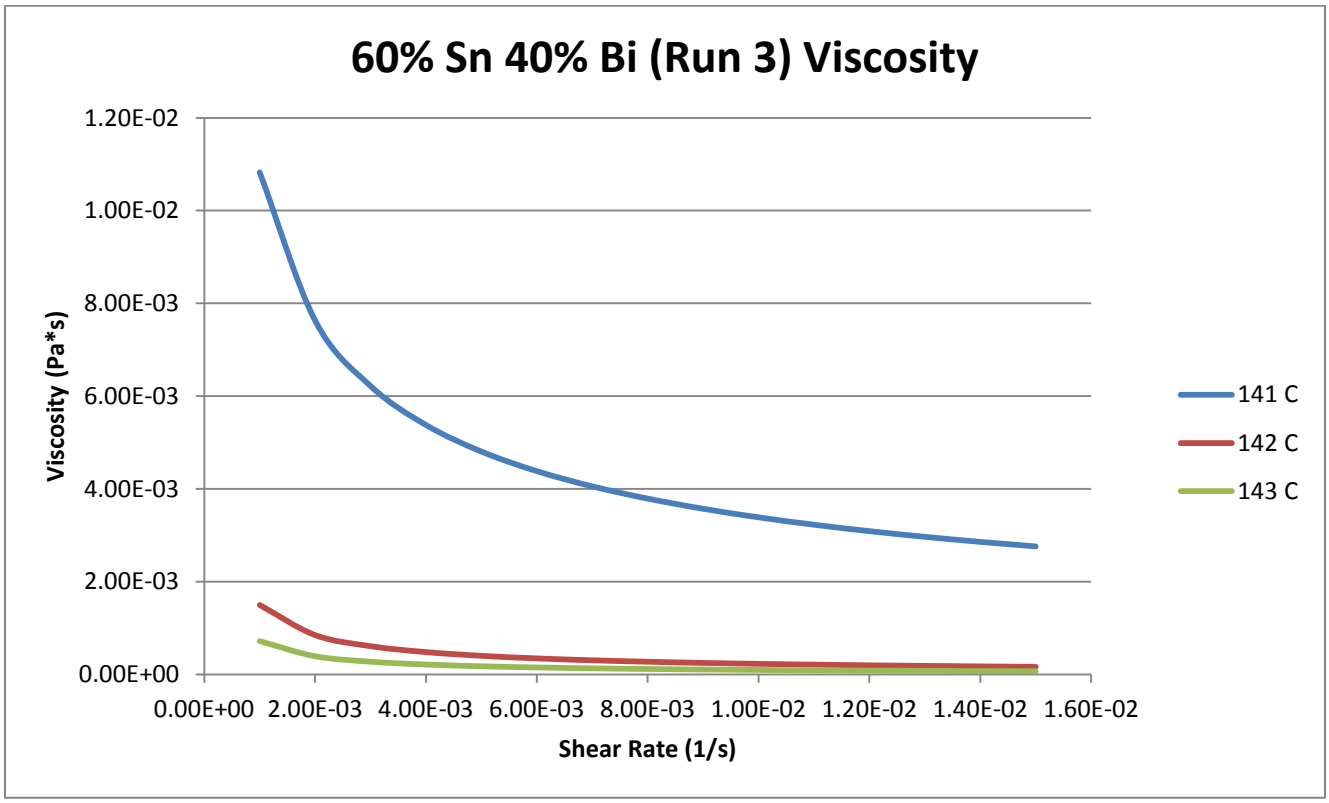

Figure 203- 60% Sn 40% Bi (Run 3), Cone and Plate Viscosity

141 C

Fraction Solid	0.50 %
Power Law	$\tau = 6.68 * 10^{-4} * \dot{\gamma}^{0.4951}$
	$\mu = 3.31 * 10^{-4} * \dot{\gamma}^{-0.5049}$
R^2	62.11 %

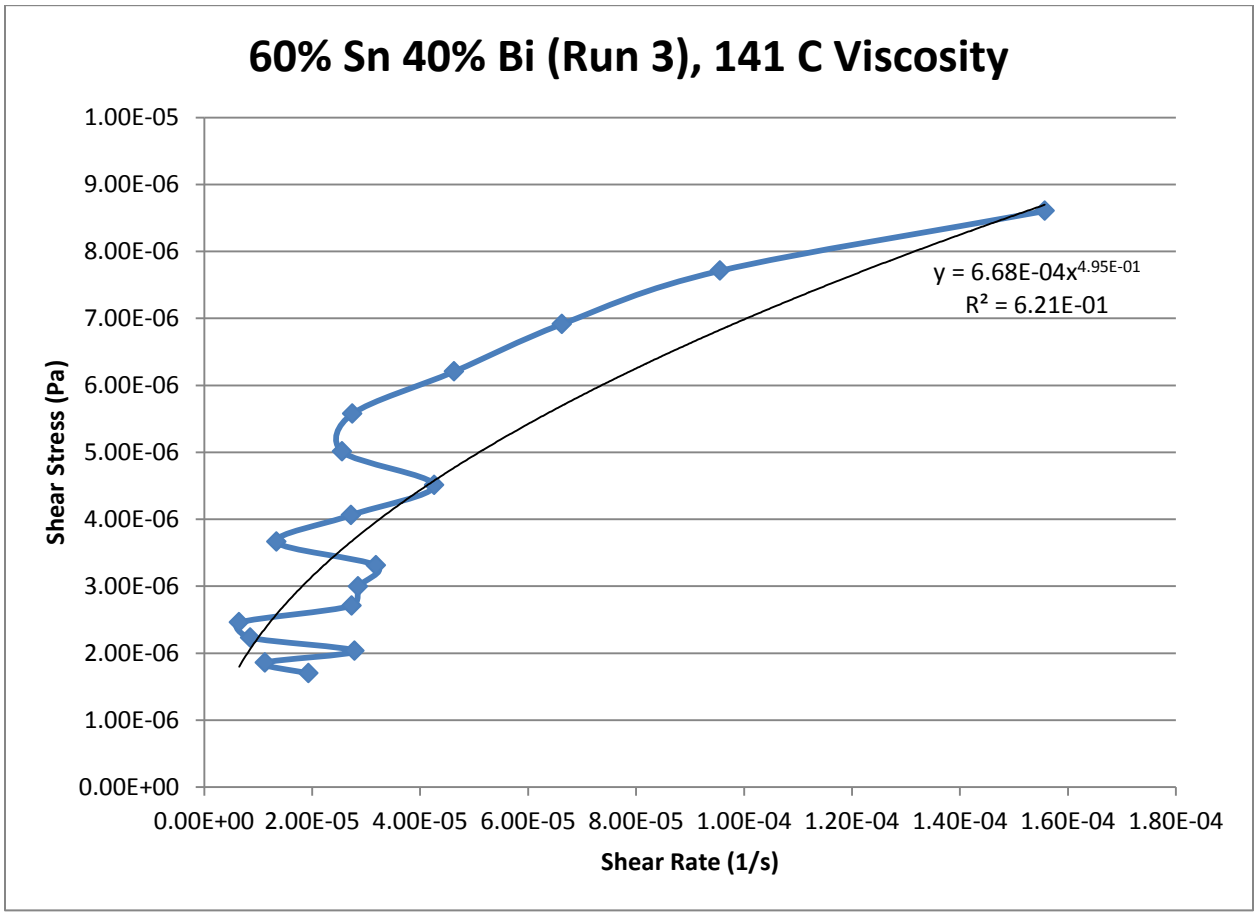

Figure 204 - 60% Sn 40% Bi (Run 3), 141 C, Cone and Plate Viscosity

142 C

Fraction Solid	0.30 %
Power Law	$\tau = 2.88 * 10^{-5} * \dot{\gamma}^{0.1793}$
	$\mu = 5.16 * 10^{-6} * \dot{\gamma}^{-0.8207}$
R^2	65.87 %

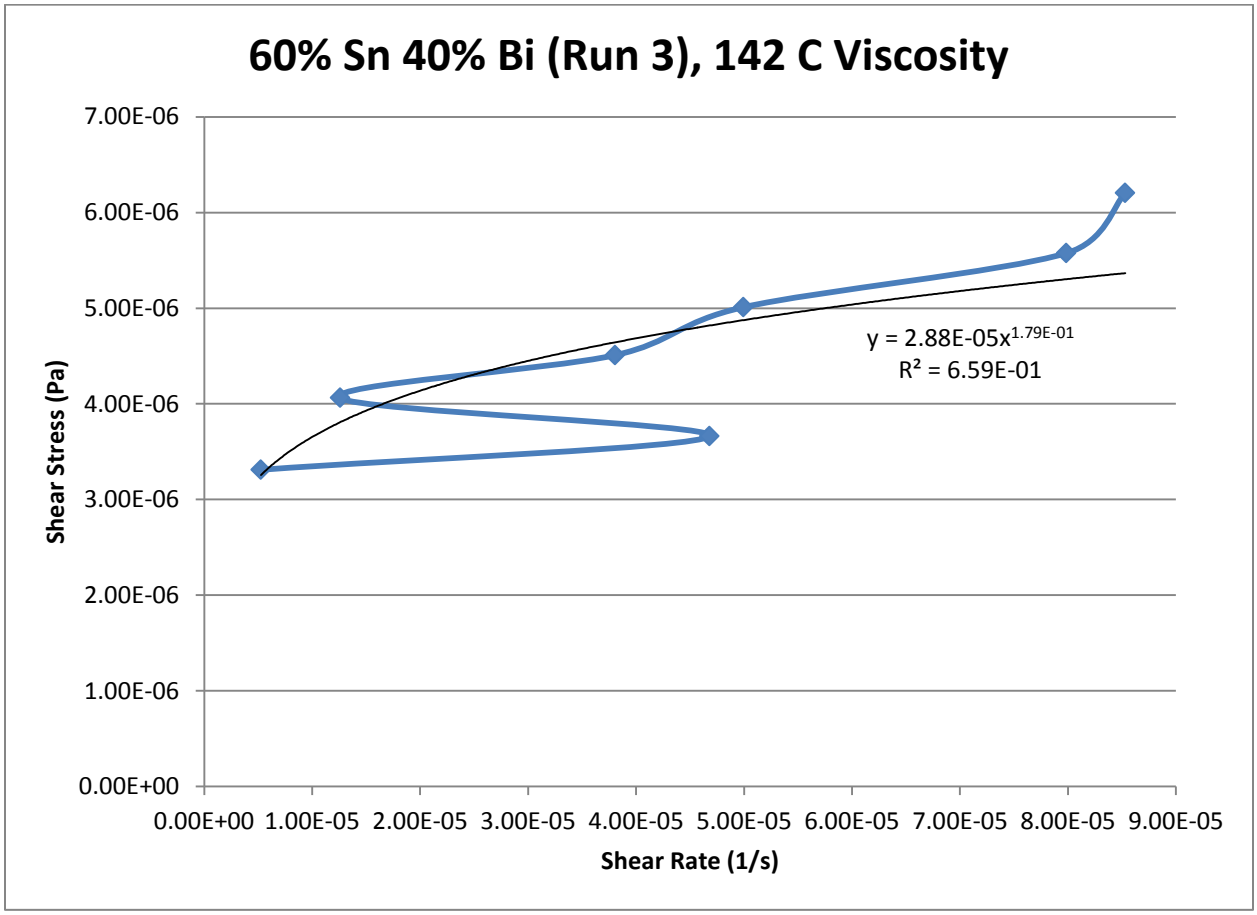

Figure 205- 60% Sn 40% Bi (Run 3), 142 C, Cone and Plate Viscosity

143 C

Fraction Solid	0 %
Power Law	$\tau = 1.37 * 10^{-5} * \dot{\gamma}^{0.1189}$
	$\mu = 1.63 * 10^{-6} * \dot{\gamma}^{-0.8811}$
R^2	23.46 %

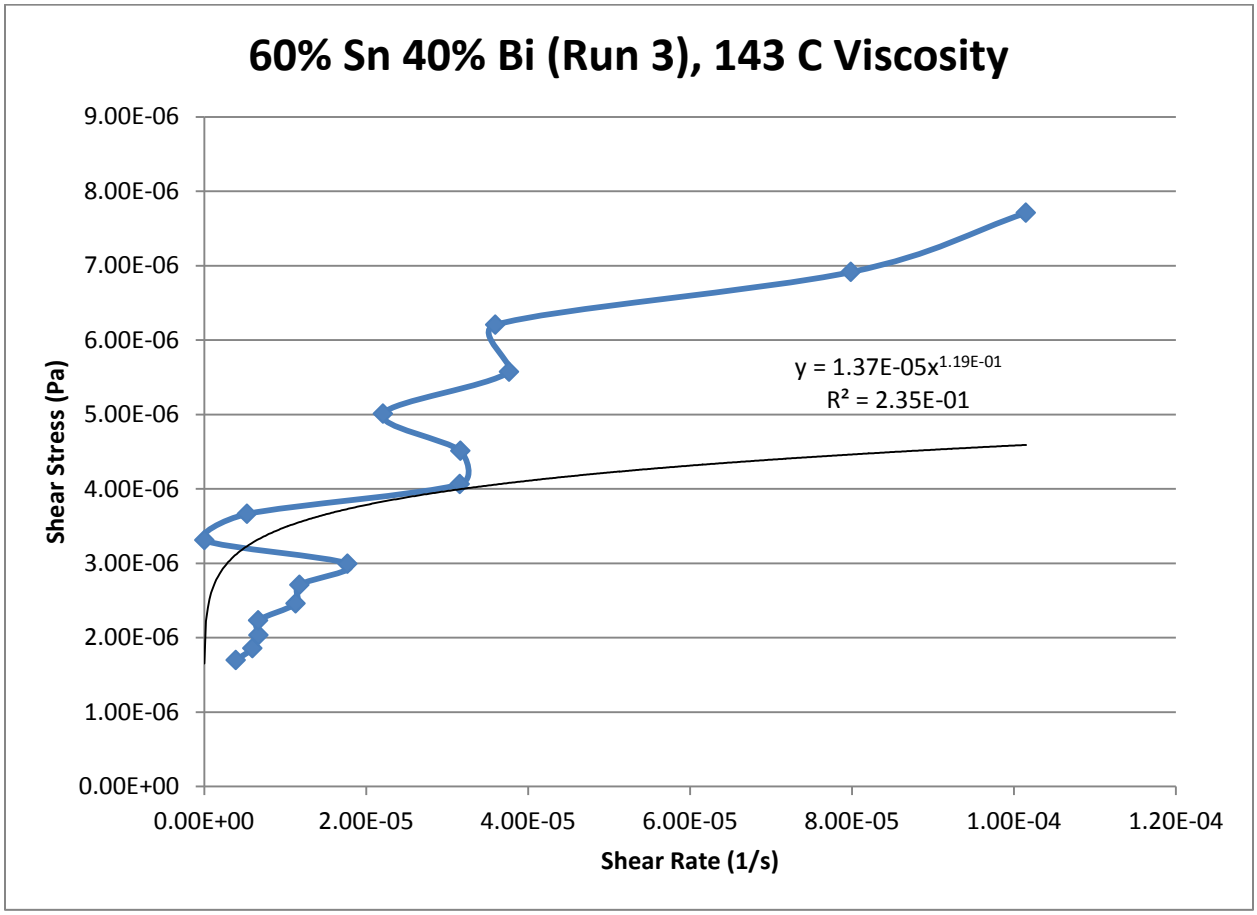

Figure 206- 60% Sn 40% Bi (Run 3), 143 C, Cone and Plate Viscosity

62.5% Tin 37.5% Bismuth (Run 1)

Expected Composition: 64.50% Sn, 35.50% Bi

Theoretical Solidus Line: 139 C
Theoretical Liquidus Line: 155.2 C

Experimental Solidus Line: 139.4 C
Experimental Liquidus Line: 156.5 C

Set-Up Notes

- The stage was heated to 142.5 Celsius and the metal pieces were melted underneath the cone. The cone was then lowered to the geometry gap. Stress sweeps at 142.5 C, 140 C, and 145 C were then conducted in that order.

- During the experiment, I started with the higher temperatures.

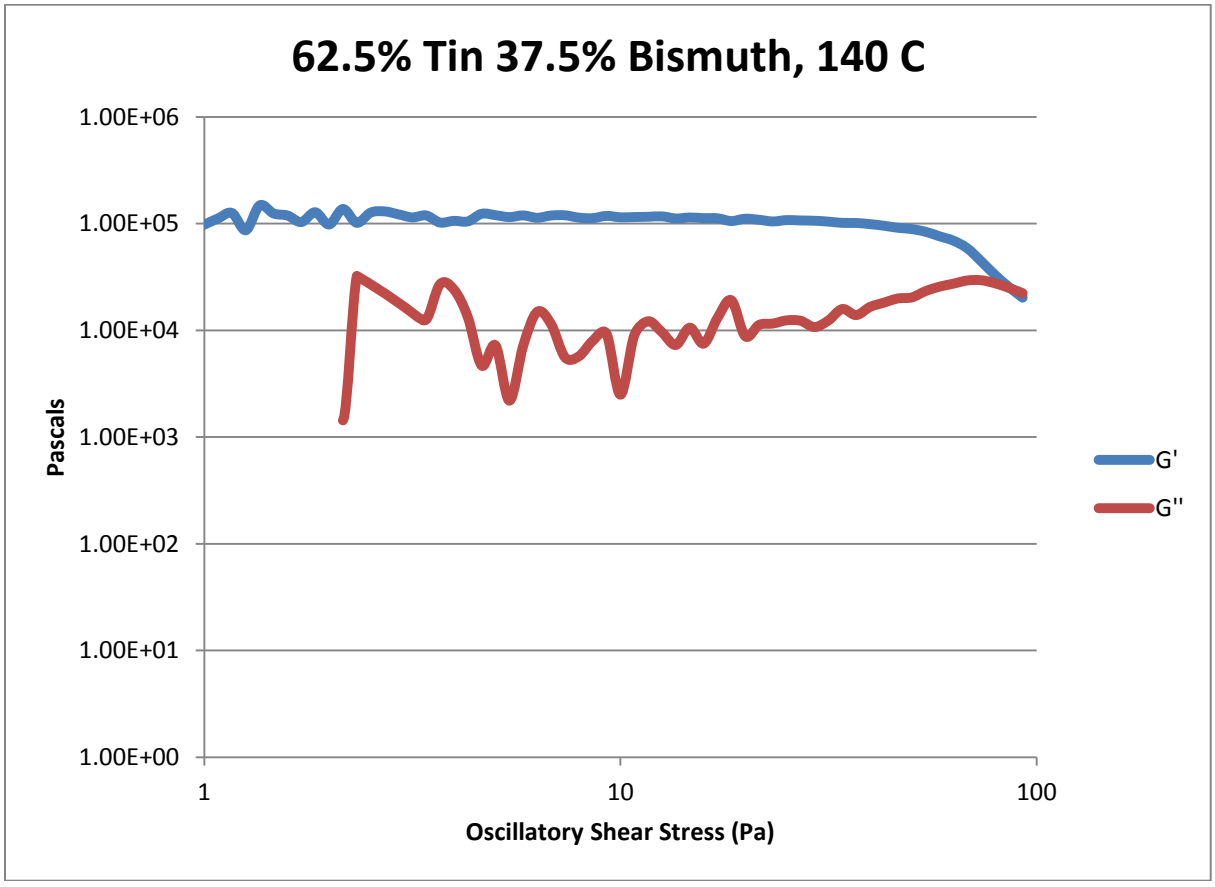

Figure 207- 62.5% Sn 37.5 Bi (Run 1), 140 C, Cone and Plate Stress Sweep

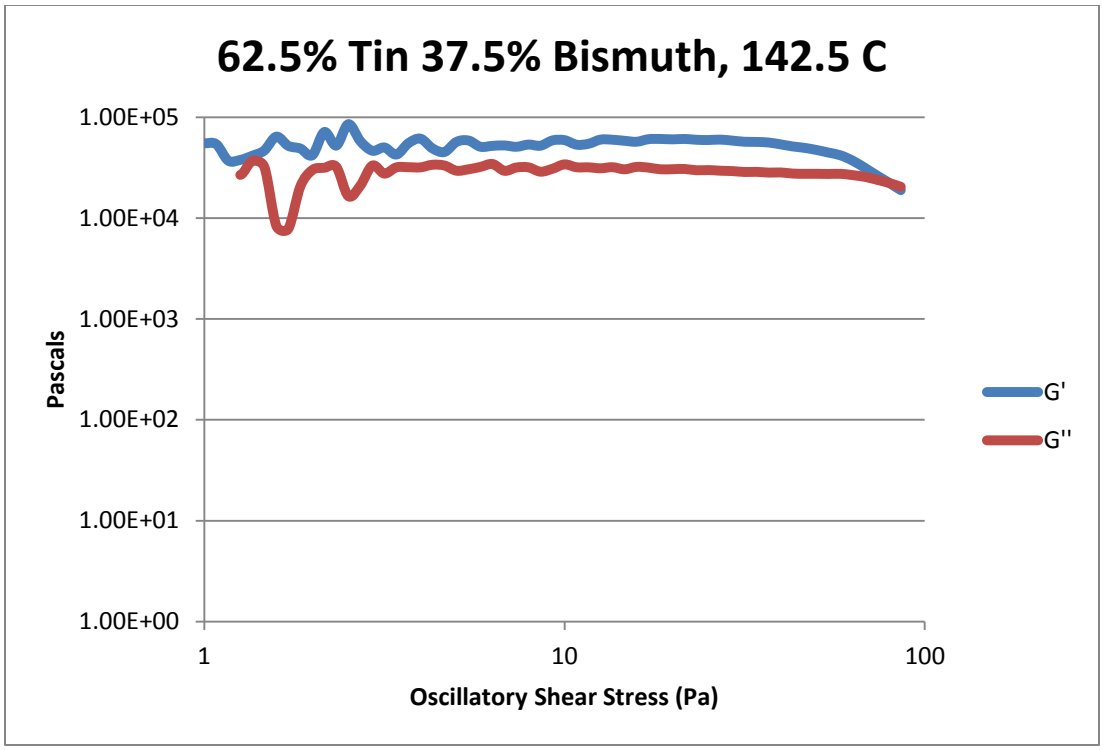

Figure 208- 62.5% Sn 37.5 Bi (Run 1), 142.5 C, Cone and Plate Stress Sweep

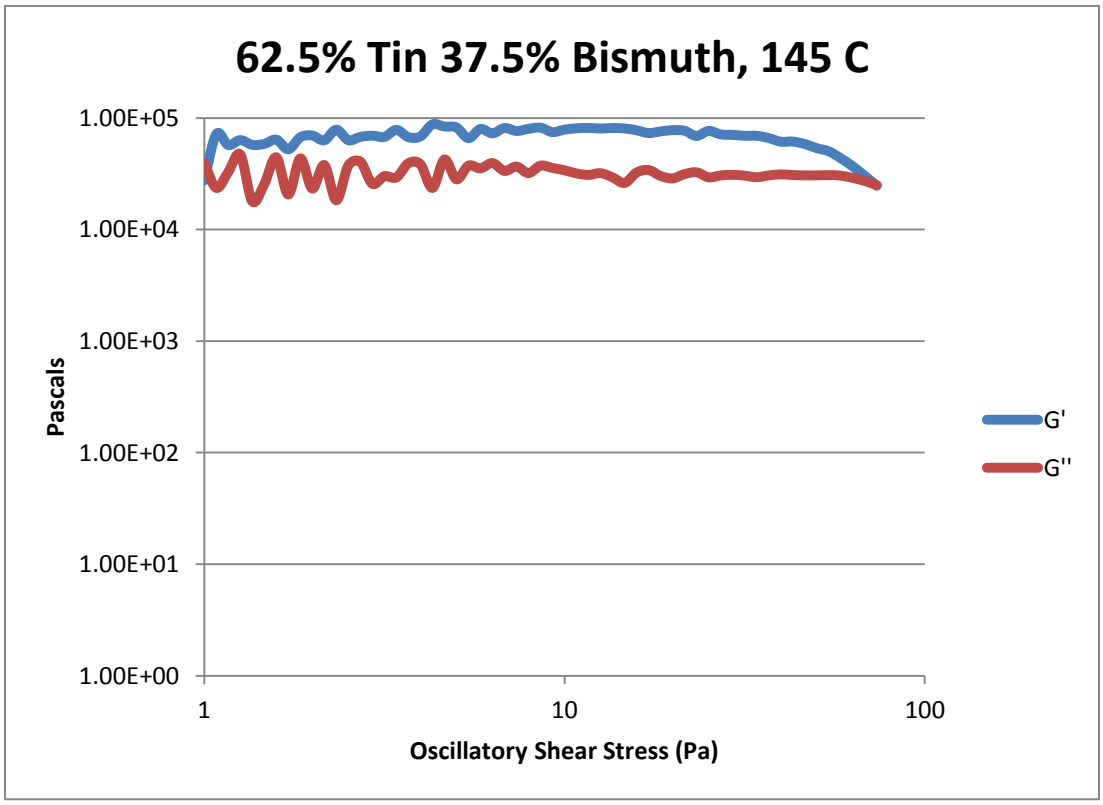

Figure 209- 62.5% Sn 37.5 Bi (Run 1), 145 C, Cone and Plate Stress Sweep

Temperature	Crossover Stress (Pa)	Crossover Stress (PSI)
140 C	$2.45 * 10^4$	3.55
142.5 C	$2.22 * 10^4$	3.21
145 C	$2.52 * 10^4$	3.65

Table 38- 62.5% Sn 37.5% Bi (Run 1), Cone and Plate Crossover Stresses

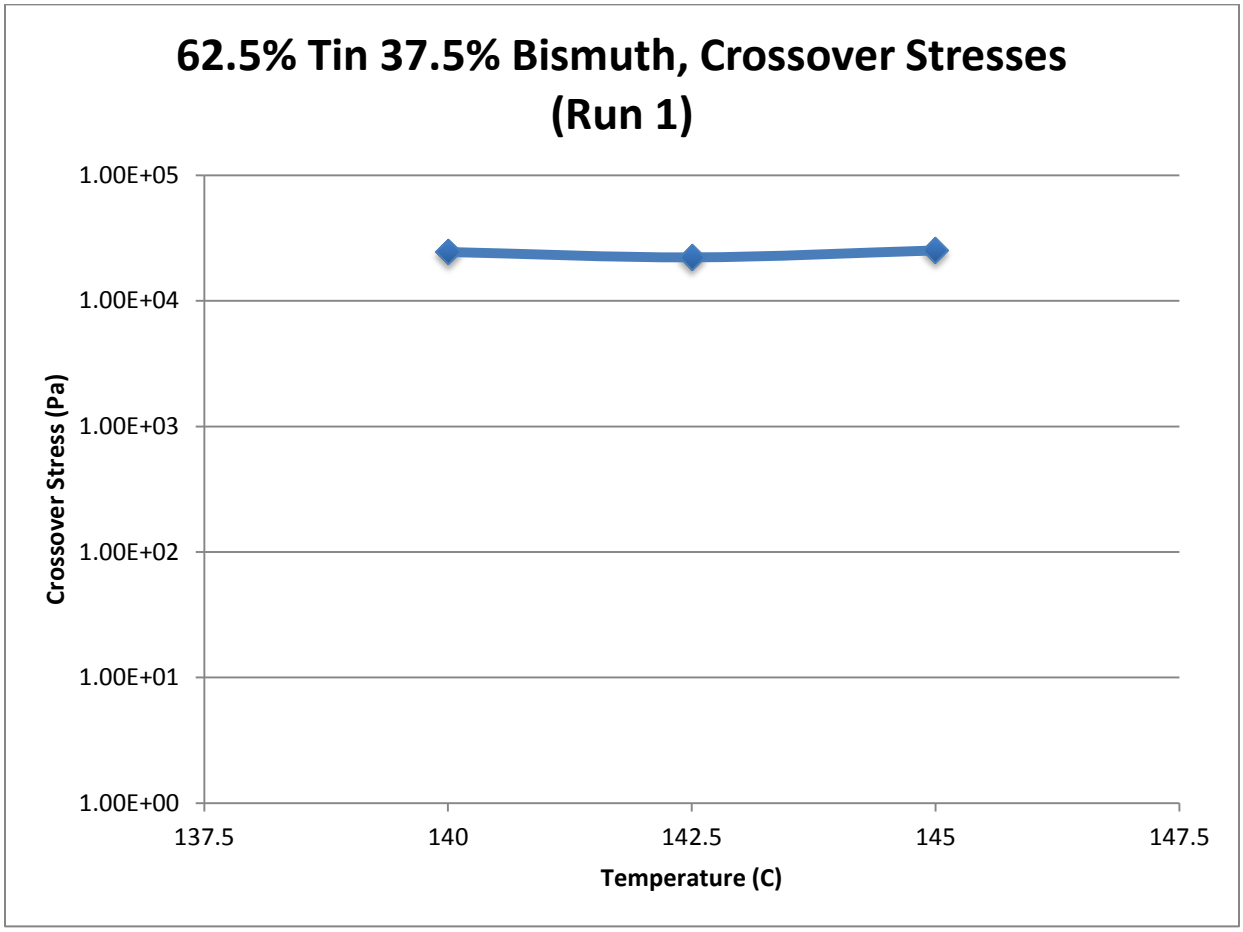

Figure 210- 62.5% Sn 37.5% Bi (Run 1), Cone and Plate Crossover Stresses

Temperature	Fraction Solid (At %)	G' Plateau (Pa)	G'' Plateau (Pa)
140 C	100	$1.14 * 10^5$	$1.18 * 10^4$
142.5 C	3.11	$5.97 * 10^4$	$3.14 * 10^4$
145 C	1.57	$7.98 * 10^4$	$3.06* 10^4$

Table 39- 62.5% Sn 37.5% Bi (Run 1), Cone and Plate Plateau Stresses

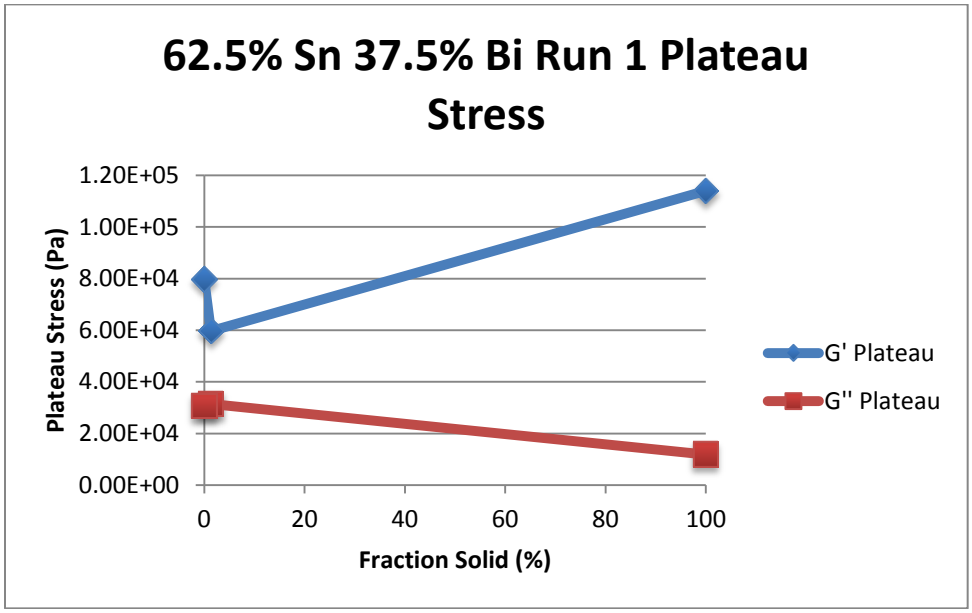

Figure 211- 62.5% Sn 37.5% Bi (Run 1), Cone and Plate Plateau Stresses vs. Fraction Solid

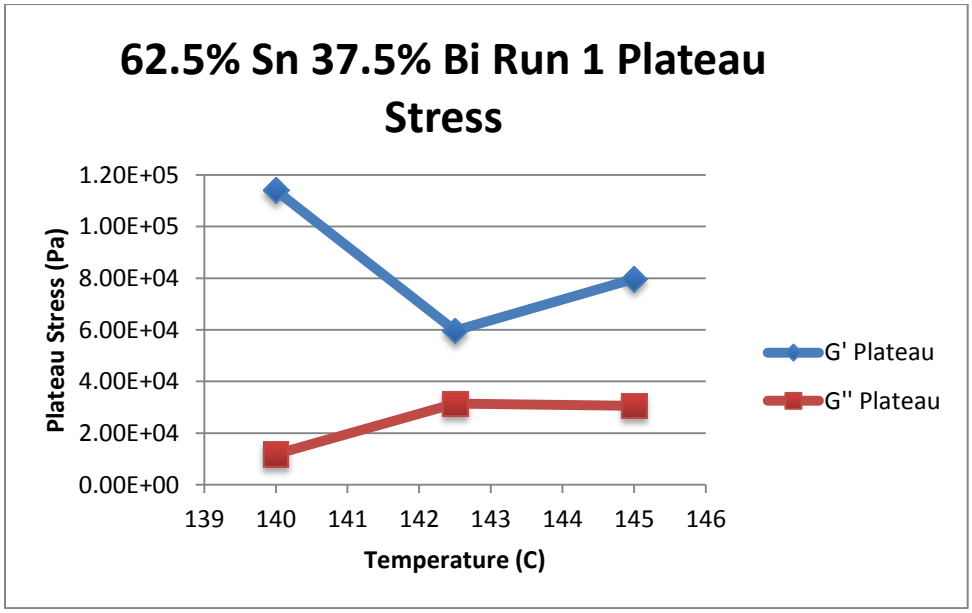

Figure 212- 62.5% Sn 37.5% Bi (Run 1), Cone and Plate Plateau Stresses vs. Temperature

62.5% Sn 37.5% Bi (Run 1) Viscosity					
Temperature	**Fraction Solid**	**Power Law**	**K**	**n**	**R^2**
140 C	100 %	$\tau = 1.30 * 10^{-4} * \dot{\gamma}^{0.2958}$ $\mu = 3.85 * 10^{-5} * \dot{\gamma}^{-0.7042}$	$1.30 * 10^{-4}$ Pa*s	0.2958	63.08 %
142.5 C	3.11 %	$\tau = 3.51 * 10^{-5} * \dot{\gamma}^{0.1799}$ $\mu = 6.31 * 10^{-6} * \dot{\gamma}^{-0.8201}$	$3.51 * 10^{-5}$ Pa*s	0.1799	37.33 %
145 C	1.57 %	$\tau = 8.46 * 10^{-5} * \dot{\gamma}^{0.2811}$ $\mu = 2.38 * 10^{-5} * \dot{\gamma}^{-0.7189}$	$8.46 * 10^{-5}$ Pa*s	0.2811	47.82 %

Table 40- 62.5% Sn 37.5% Bi (Run 1), Cone and Plate Viscosity

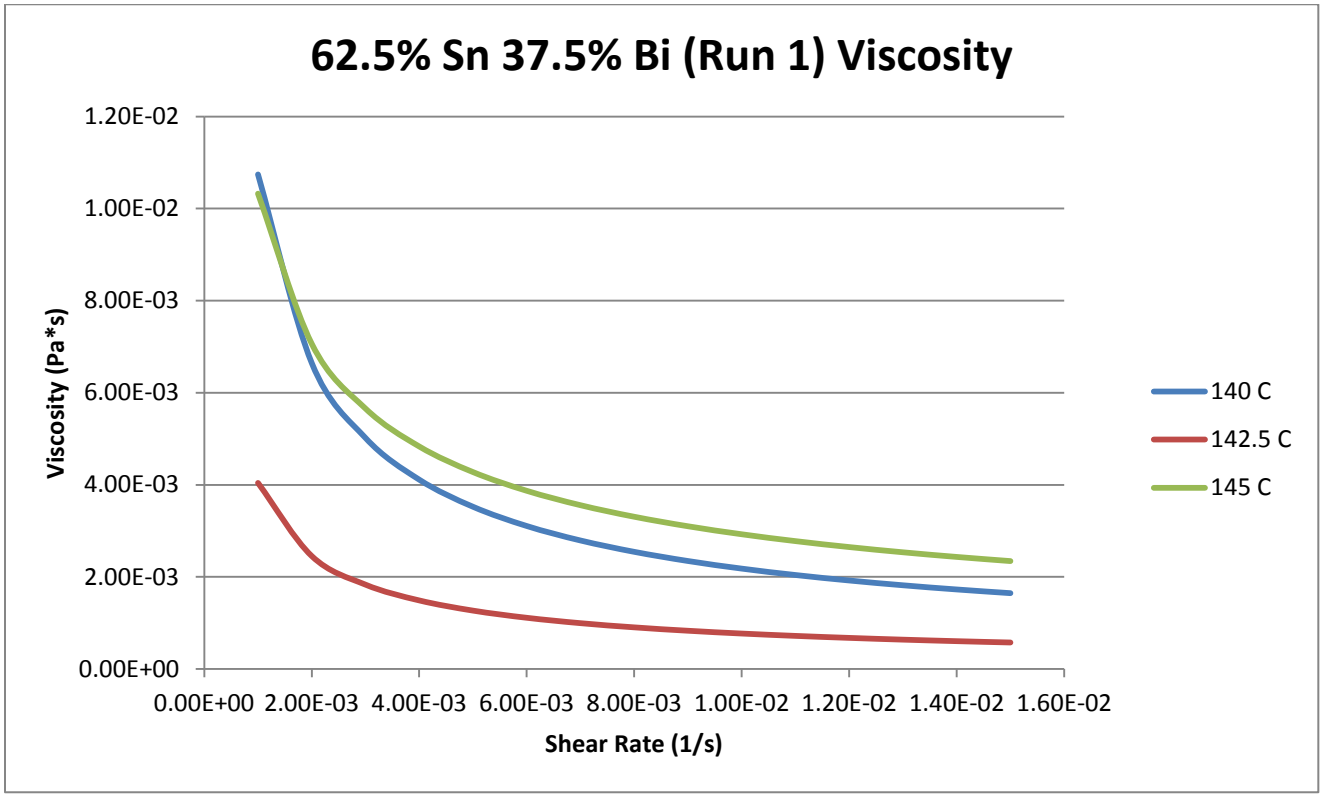

Figure 213- 62.5% Sn 37.5% Bi (Run 1), Cone and Plate Viscosity

140 C

Fraction Solid	100 %
Power Law	$\tau = 1.30 * 10^{-4} * \dot{\gamma}^{0.2958}$
	$\mu = 3.85 * 10^{-5} * \dot{\gamma}^{-0.7042}$
R^2	63.08 %

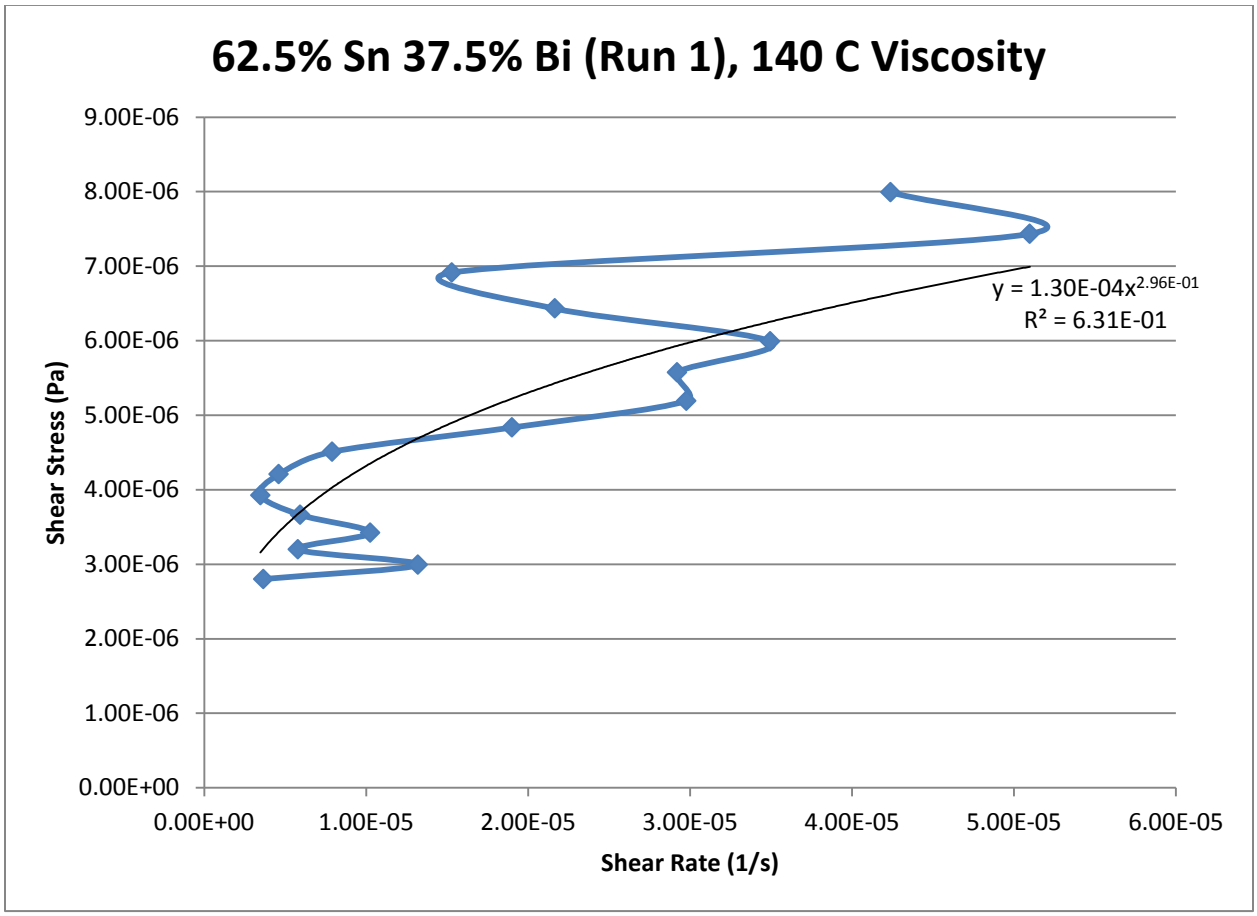

Figure 214- 62.5% Sn 37.5% Bi (Run 1), 140 C, Cone and Plate Viscosity

142.5 C

Fraction Solid	3.11 %
Power Law	$\tau = 3.51 * 10^{-5} * \dot{\gamma}^{0.1799}$
	$\mu = 6.31 * 10^{-6} * \dot{\gamma}^{-0.8201}$
R^2	37.33 %

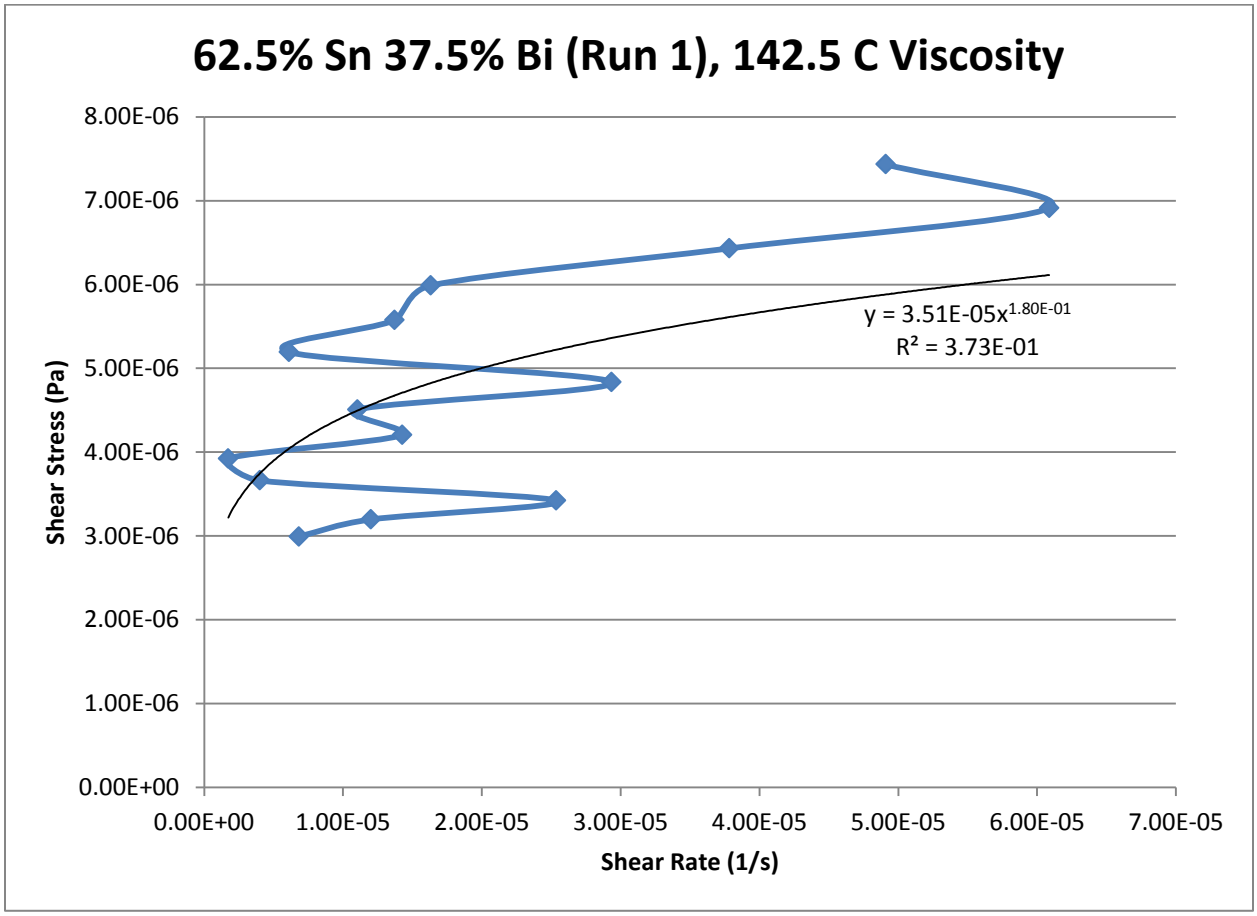

Figure 215- 62.5% Sn 37.5% Bi (Run 1), 142.5 C, Cone and Plate Viscosity

145 C

Fraction Solid	1.57 %
Power Law	$\tau = 8.46 * 10^{-5} * \dot{\gamma}^{0.2811}$
	$\mu = 2.38 * 10^{-5} * \dot{\gamma}^{-0.7189}$
R^2	47.82 %

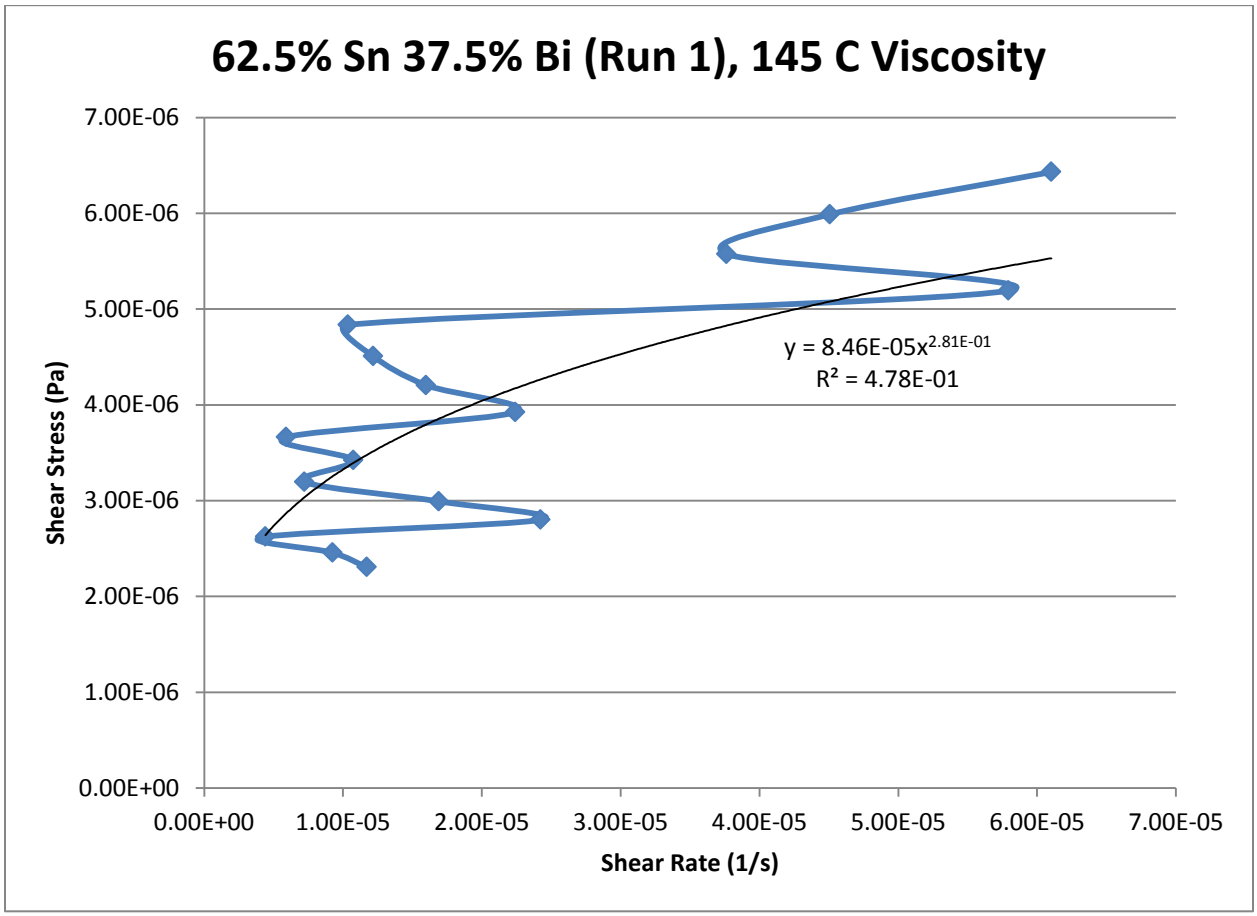

Figure 216- 62.5% Sn 37.5% Bi (Run 1), 145 C, Cone and Plate Viscosity

62.5% Tin 37.5% Bismuth (Run 2)

Predicted Composition: 64.50% Sn, 35.50% Bi

Theoretical Solidus Line: 139 C
Theoretical Liquidus Line: 155.2 C

Experimental Solidus Line: 139.4 C
Experimental Liquidus Line: 156.5 C

Set-Up Notes

- The stage was heated to 144 C and subsequently zeroed. Stress sweeps were then run in decreasing increments of 1 C before increasing to 145 C for a final stress sweep.

- Very clean sample with no residue

Plots

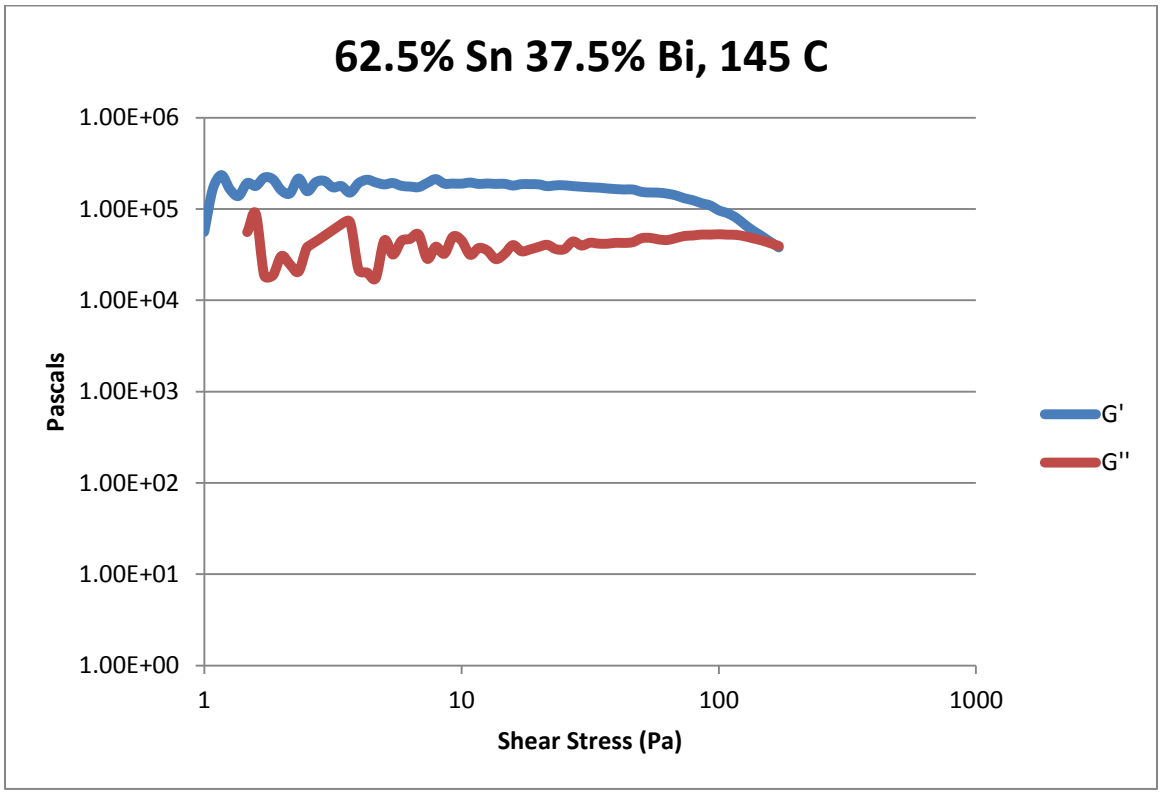

Figure 217- 62.5% Sn 37.5% Bi (Run 2), 145 C, Cone and Plate Stress Sweep

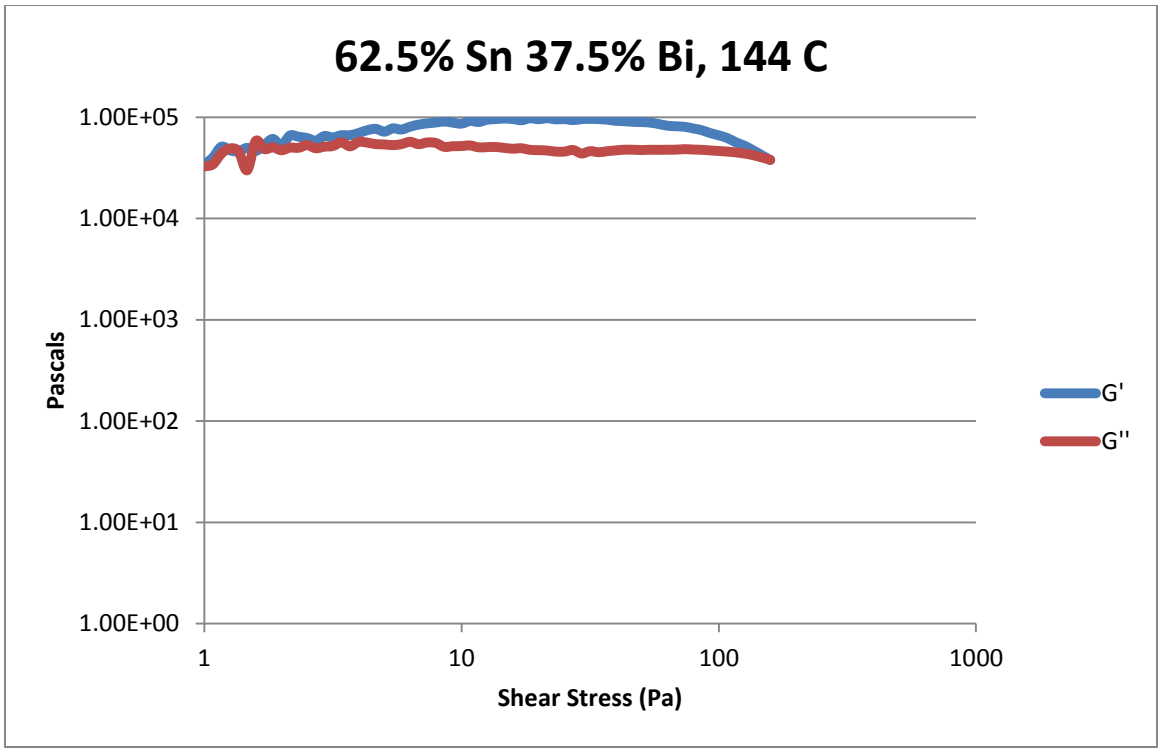

Figure 218- 62.5% Sn 37.5% Bi (Run 2), 144 C, Cone and Plate Stress Sweep

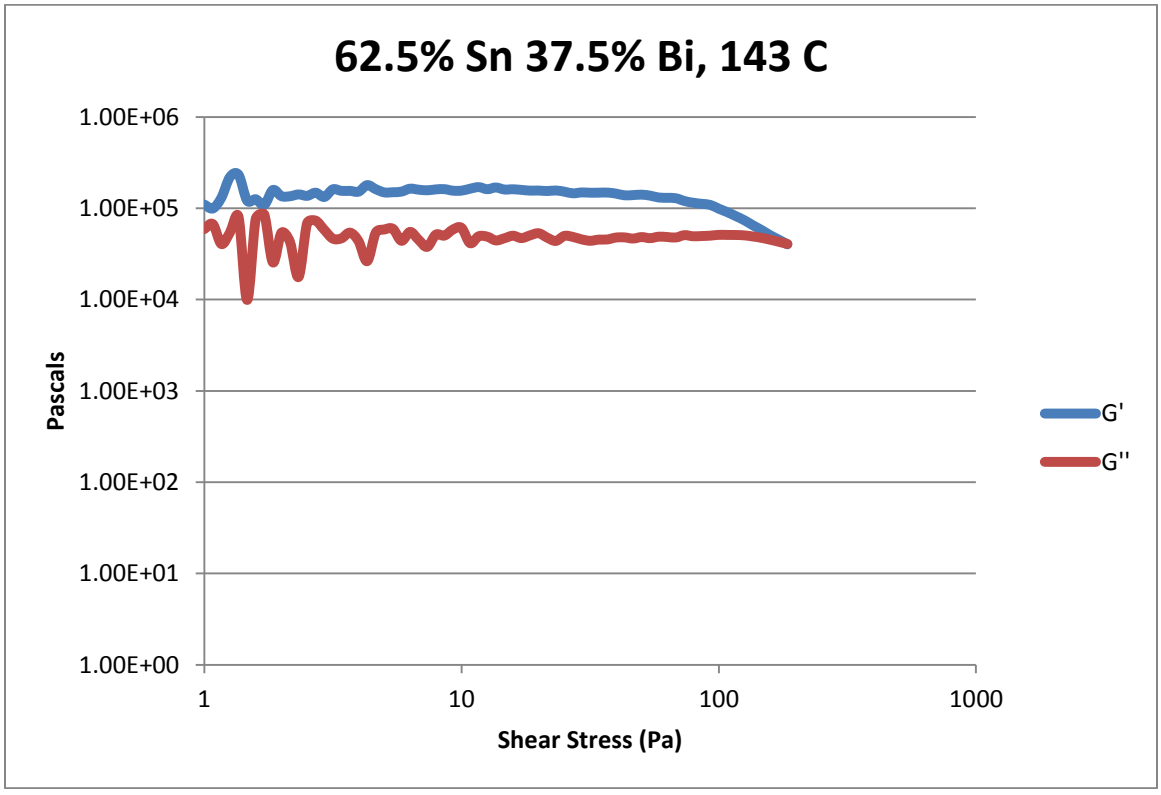

Figure 219- 62.5% Sn 37.5% Bi (Run 2), 143 C, Cone and Plate Stress Sweep

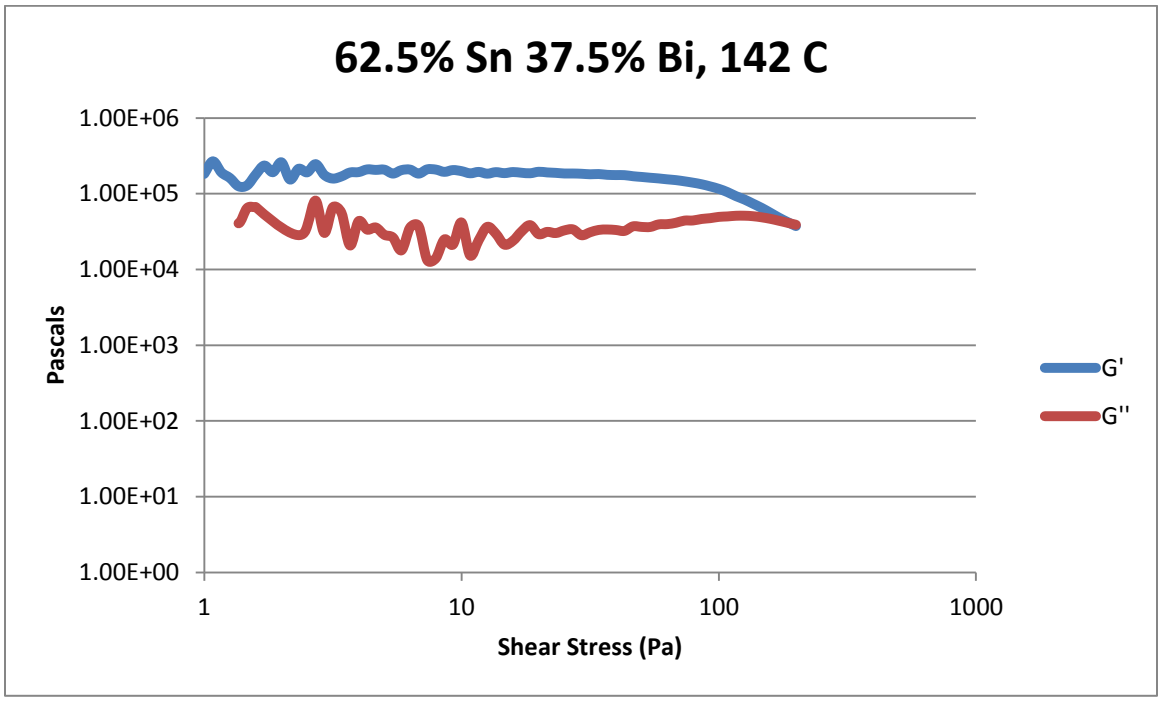

Figure 220- 62.5% Sn 37.5% Bi (Run 2), 142 C, Cone and Plate Stress Sweep

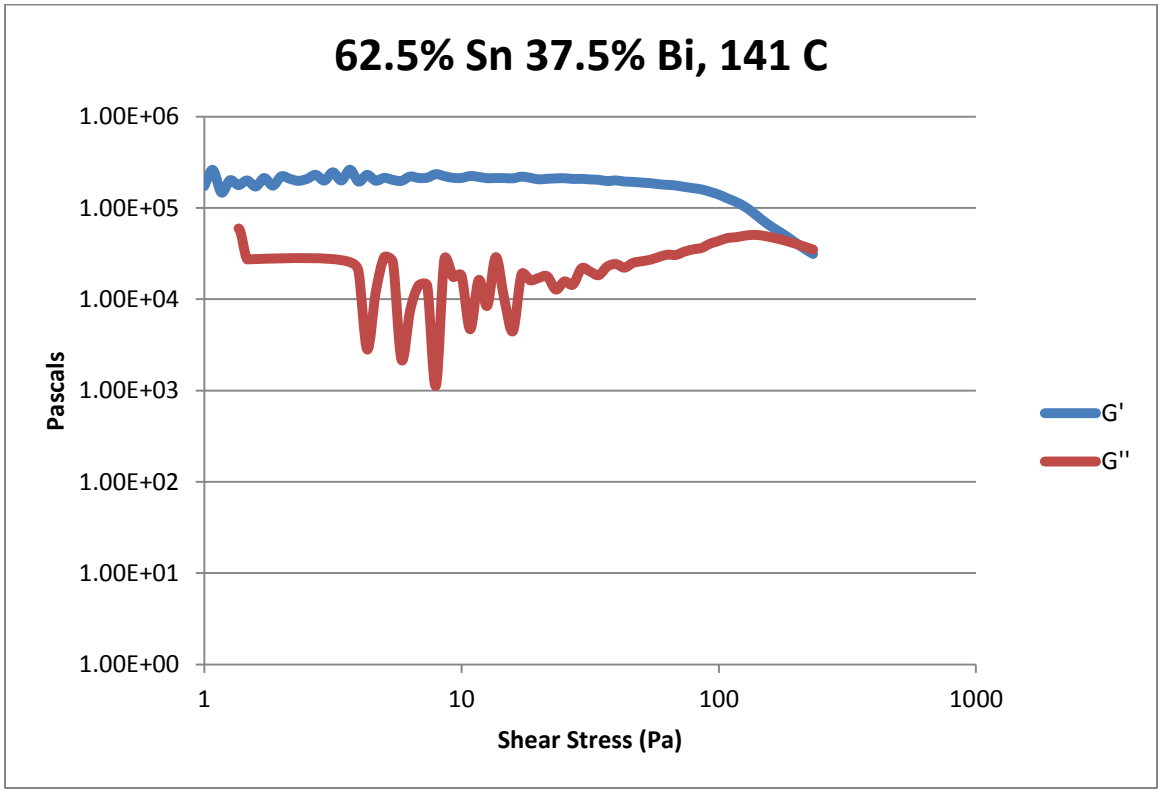

Figure 221- 62.5% Sn 37.5% Bi (Run 2), 141 C, Cone and Plate Stress Sweep

Temperature	Fraction Solid (At %)	Crossover Stress (Pa)	G' Plateau (Pa)	G'' Plateau (Pa)
145 C	1.57	$4.08 * 10^4$	$1.87 * 10^5$	$4.50 * 10^4$
144 C	1.59	$3.82 * 10^4$	$9.57 * 10^4$	$4.70 * 10^4$
143 C	2.40	$4.10 * 10^4$	$1.62 * 10^5$	$4.84 * 10^4$
142 C	3.13	$4.05 * 10^4$	$1.96 * 10^5$	$4.99 * 10^4$
141 C	4.69	$3.95 * 10^4$	$2.13 * 10^5$	$4.92 * 10^4$

Table 41- 62.5% Sn 37.5% Bi (Run 2), Cone and Plate Crossover and Plateau Stresses

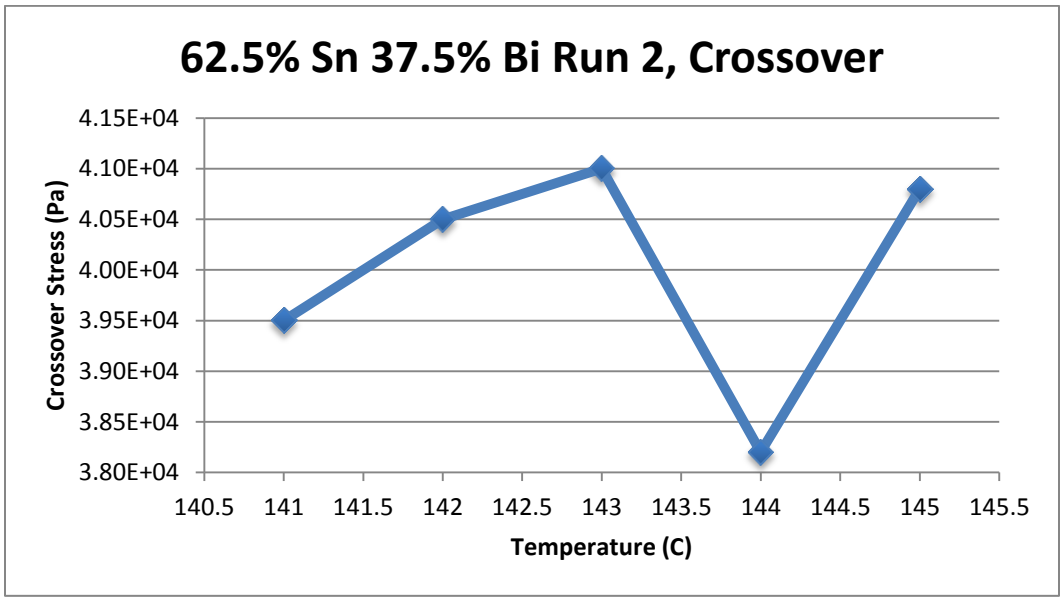

Figure 222- 62.5% Sn 37.5% Bi (Run 2), Cone and Plate Crossover Stresses

Figure 223- 62.5% Sn 37.5% Bi (Run 2), Cone and Plate Plateau Stresses vs. Fraction Solid

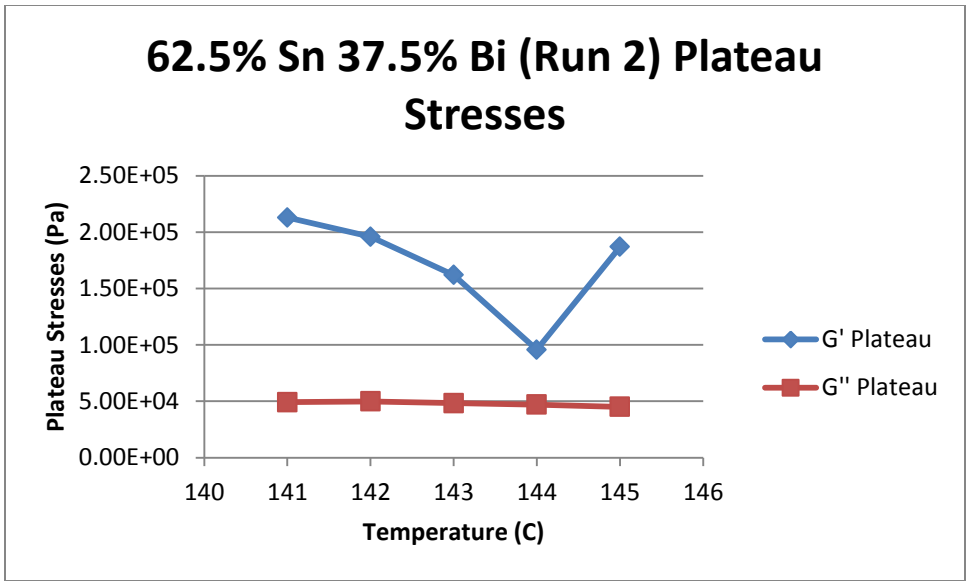

Figure 224- 62.5% Sn 37.5% Bi (Run 2), Cone and Plate Plateau Stresses vs. Temperature

62.5% Sn 37.5% Bi (Run 2) Viscosity					
Temperature	**Fraction Solid**	**Power Law**	**K**	**n**	**R^2**
141 C	4.69 %	$\tau = 5.29 * 10^{-4} * \dot{\gamma}^{0.3399}$ $\mu = 1.80 * 10^{-4} * \dot{\gamma}^{-0..6601}$	$5.29 * 10^{-4}$ Pa*s	0.3399	53.78 %
142 C	3.13 %	$\tau = 5.63 * 10^{-5} * \dot{\gamma}^{0.1423}$ $\mu = 8.01 * 10^{-6} * \dot{\gamma}^{-0.8577}$	$5.63 * 10^{-5}$ Pa*s	0.1423	25.98 %
143 C	2.40 %	$\tau = 1.68 * 10^{-5} * \dot{\gamma}^{0.0674}$ $\mu = 1.13 * 10^{-6} * \dot{\gamma}^{-0.9326}$	$1.68 * 10^{-5}$ Pa*s	0.0674	7.67 %
144 C	1.59 %	$\tau = 2.51 * 10^{-5} * \dot{\gamma}^{0.1141}$ $\mu = 2.86 * 10^{-6} * \dot{\gamma}^{-0.8859}$	$2.51 * 10^{-5}$ Pa*s	0.1141	6.43 %
145 C	1.57 %	$\tau = 1.39 * 10^{-4} * \dot{\gamma}^{0.2422}$ $\mu = 3.37 * 10^{-5} * \dot{\gamma}^{-0.7578}$	$1.39 * 10^{-4}$ Pa*s	0.2422	61.72 %

Table 42- 62.5% Sn 37.5% Bi (Run 2), Cone and Plate Viscosity

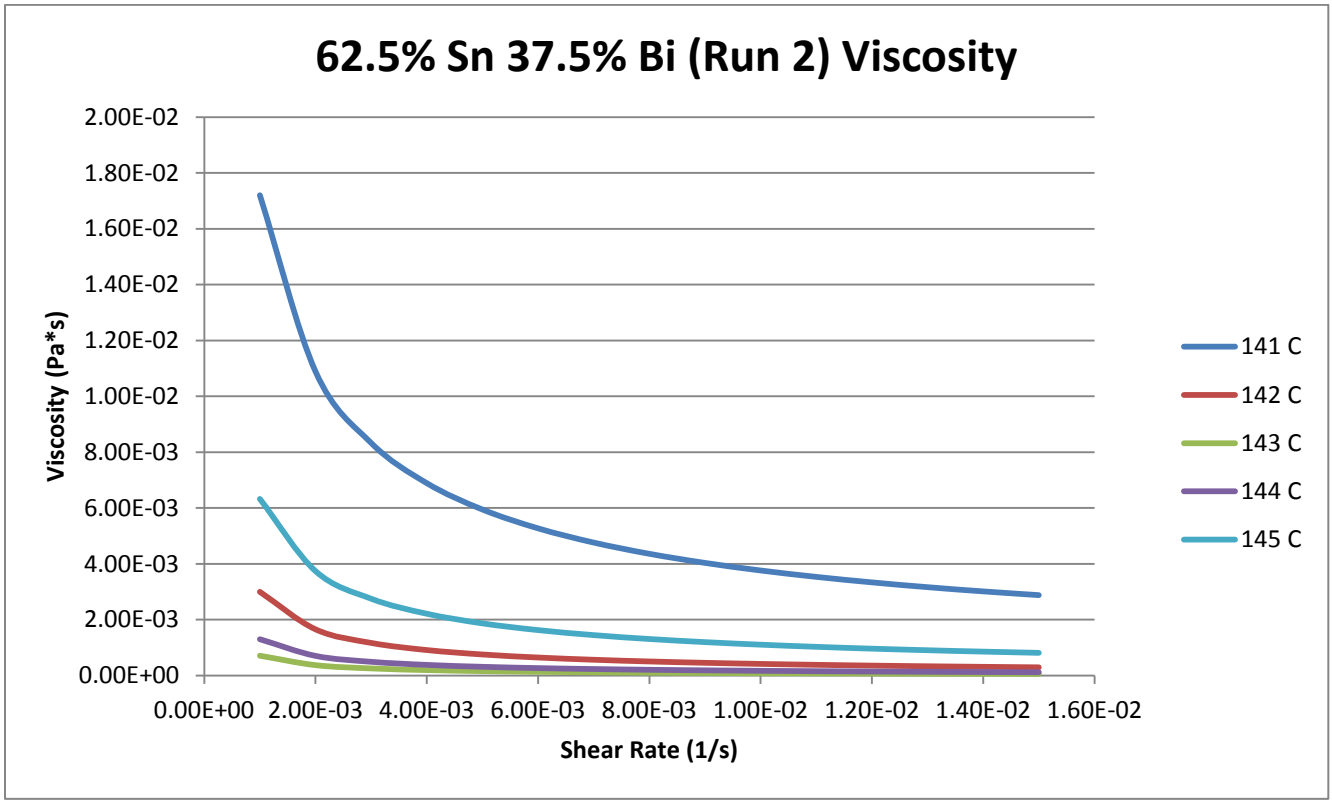

Figure 225- 62.5% Sn 37.5% Bi (Run 2), Cone and Plate Viscosity

141 C

Fraction Solid	4.69 %
Power Law	$\tau = 5.29 * 10^{-4} * \dot{\gamma}^{0.3399}$
	$\mu = 1.80 * 10^{-4} * \dot{\gamma}^{-0..6601}$
R^2	53.78 %

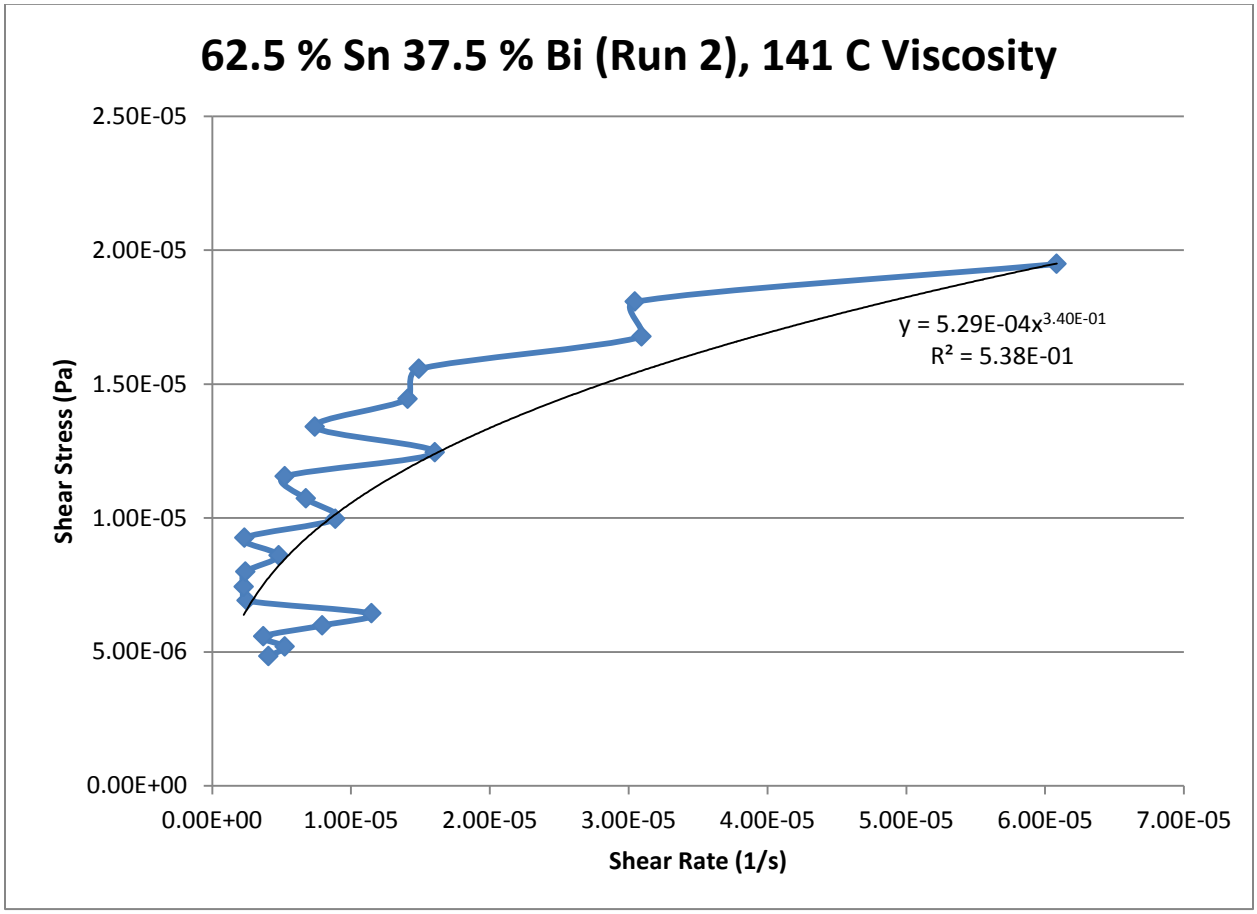

Figure 226- 62.5% Sn 37.5% Bi (Run 2), 141 C, Cone and Plate Viscosity

142 C

Fraction Solid	3.13 %
Power Law	$\tau = 5.63 * 10^{-5} * \dot{\gamma}^{0.1423}$
	$\mu = 8.01 * 10^{-6} * \dot{\gamma}^{-0.8577}$
R^2	25.98 %

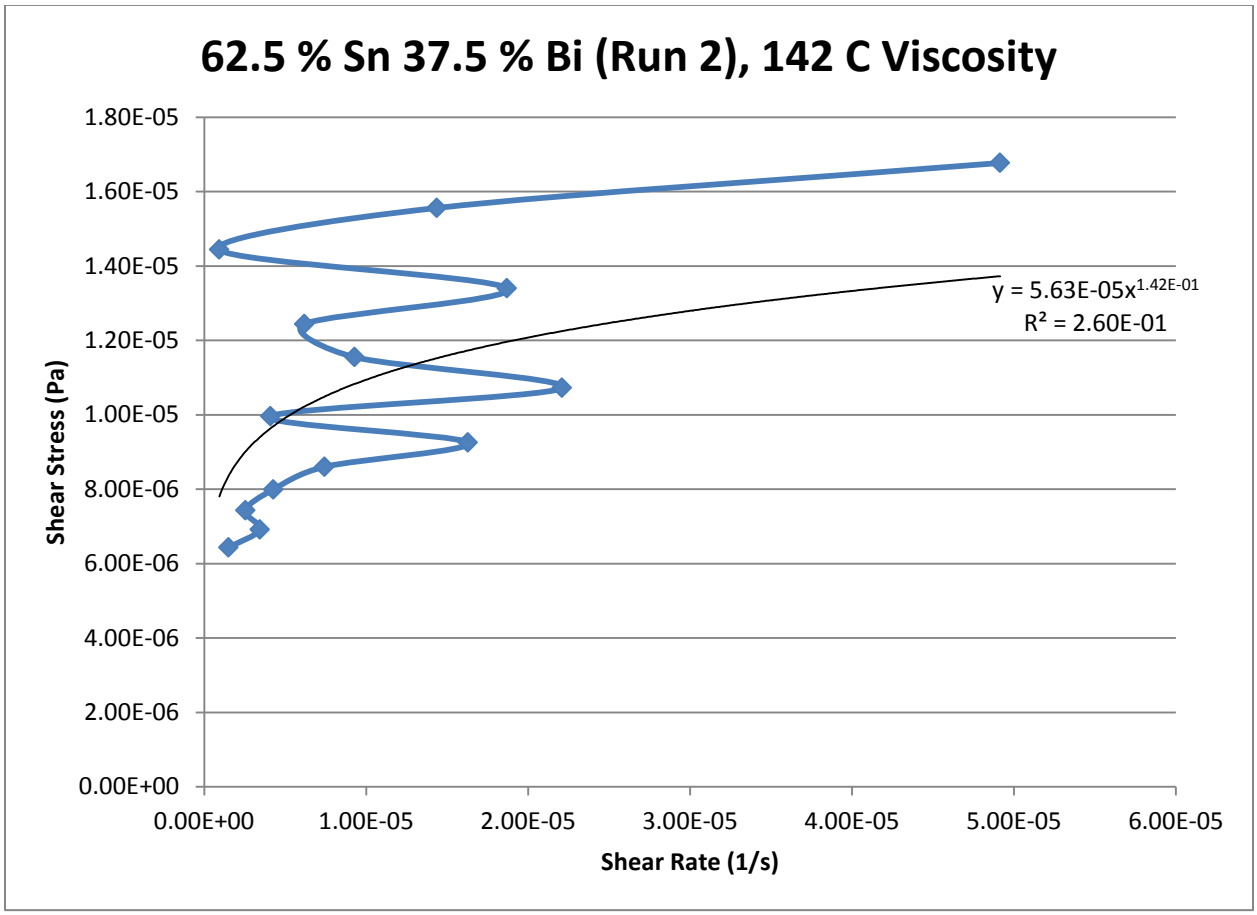

Figure 227- 62.5% Sn 37.5% Bi (Run 2), 142 C, Cone and Plate Viscosity

143 C

Fraction Solid	2.40 %
Power Law	$\tau = 1.68 * 10^{-5} * \dot{\gamma}^{0.0674}$
	$\mu = 1.13 * 10^{-6} * \dot{\gamma}^{-0.9326}$
R^2	7.67 %

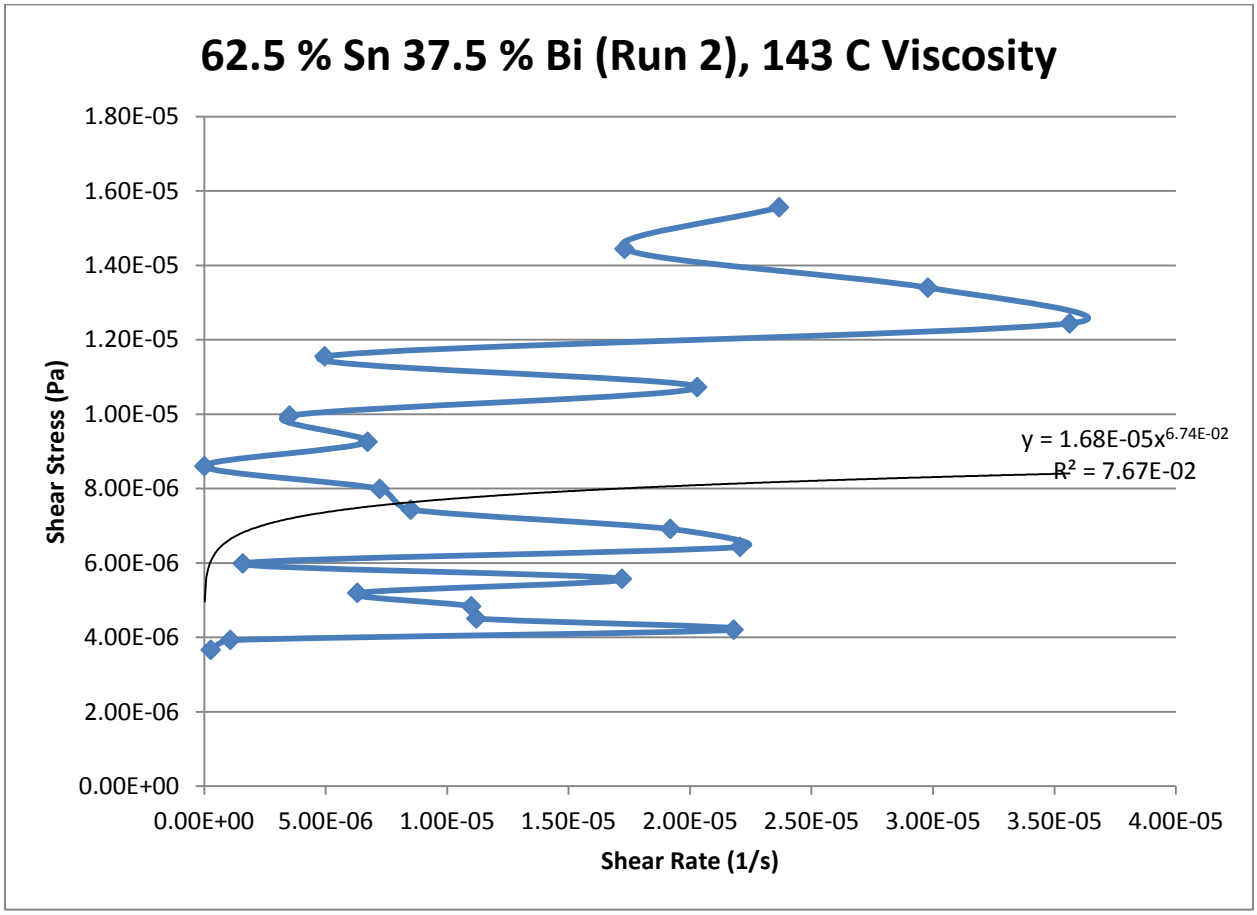

Figure 228- 62.5% Sn 37.5% Bi (Run 2), 143 C, Cone and Plate Viscosity

144 C

Fraction Solid	1.59 %
Power Law	$\tau = 2.51 * 10^{-5} * \dot{\gamma}^{0.1141}$
	$\mu = 2.86 * 10^{-6} * \dot{\gamma}^{-0.8859}$
R^2	6.43 %

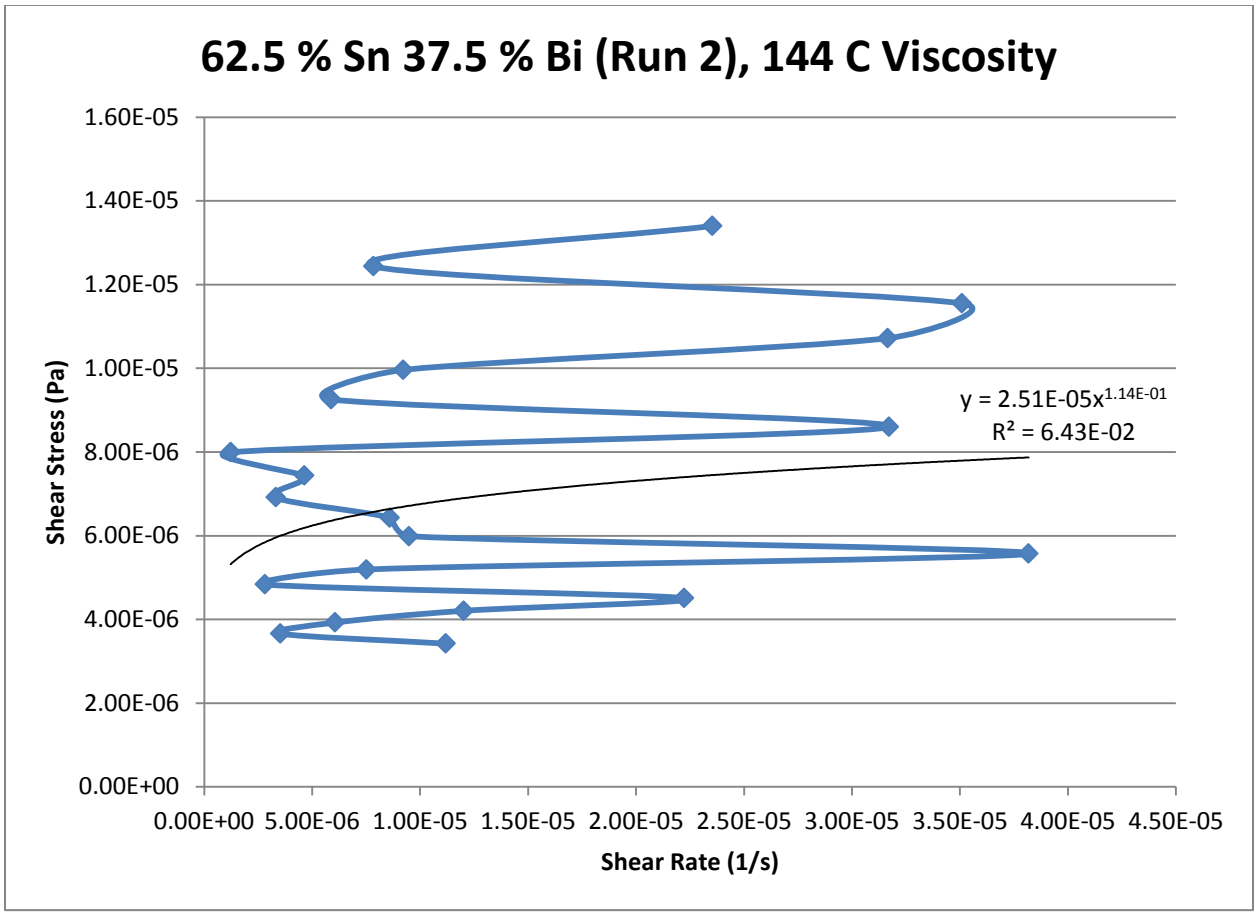

Figure 229- 62.5% Sn 37.5% Bi (Run 2), 144 C, Cone and Plate Viscosity

145 C

Fraction Solid	1.57 %
Power Law	$\tau = 1.39 * 10^{-4} * \dot{\gamma}^{0.2422}$
	$\mu = 3.37 * 10^{-5} * \dot{\gamma}^{-0.7578}$
R^2	61.72 %

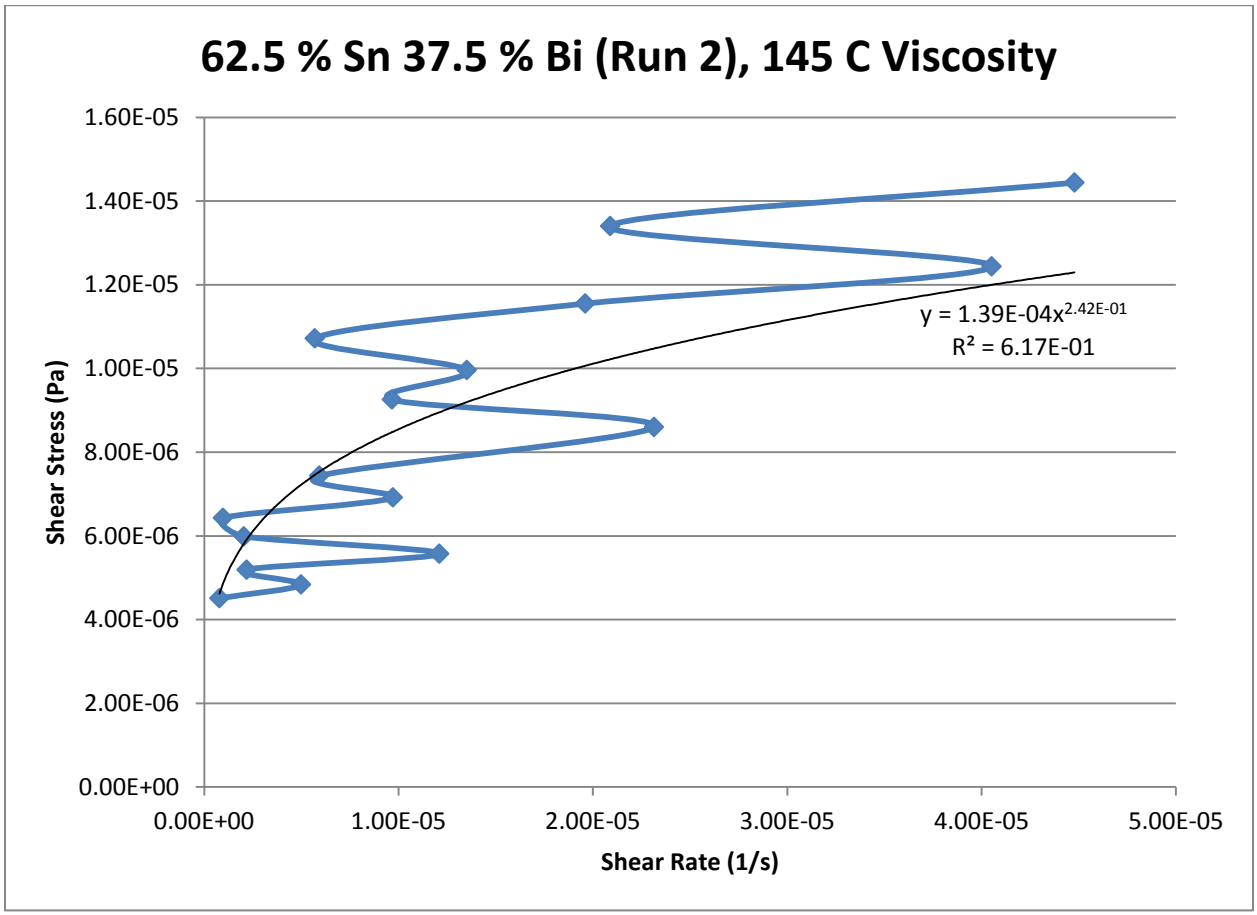

Figure 230- 62.5% Sn 37.5% Bi (Run 2), 145 C, Cone and Plate Viscosity

62.5% Tin 37.5% Bismuth (Run 3)

Predicted Composition: 64.50% Sn, 35.50% Bi

Theoretical Solidus Line: 139 C
Theoretical Liquidus Line: 155.2 C

Experimental Solidus Line: 139.4 C
Experimental Liquidus Line: 156.5 C

Set-Up Notes

- The stage was heated to 144 C and subsequently zeroed. Stress sweeps were then run in decreasing increments of 1 C before increasing to 145 C for a final stress sweep.

- G' and G'' values appeared to be very low.

Plots

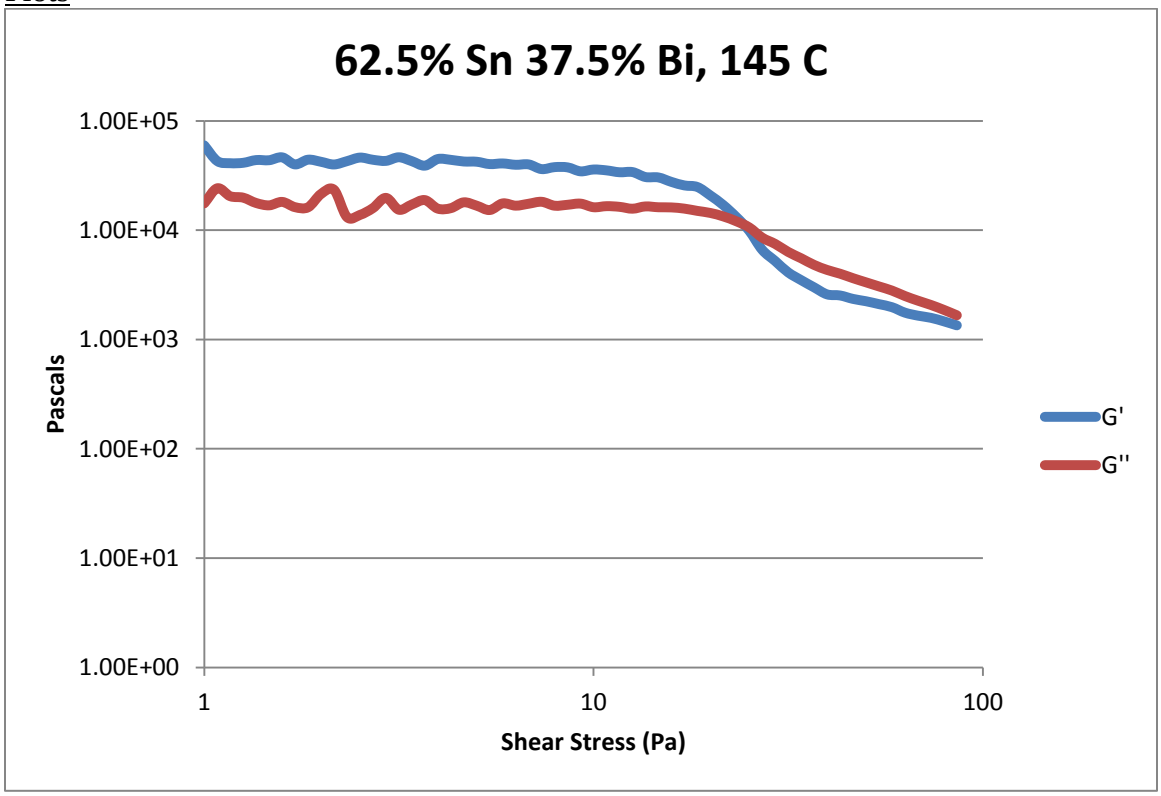

Figure 231- 62.5% Sn 37.5% Bi, 145 C, Cone and Plate Stress Sweep

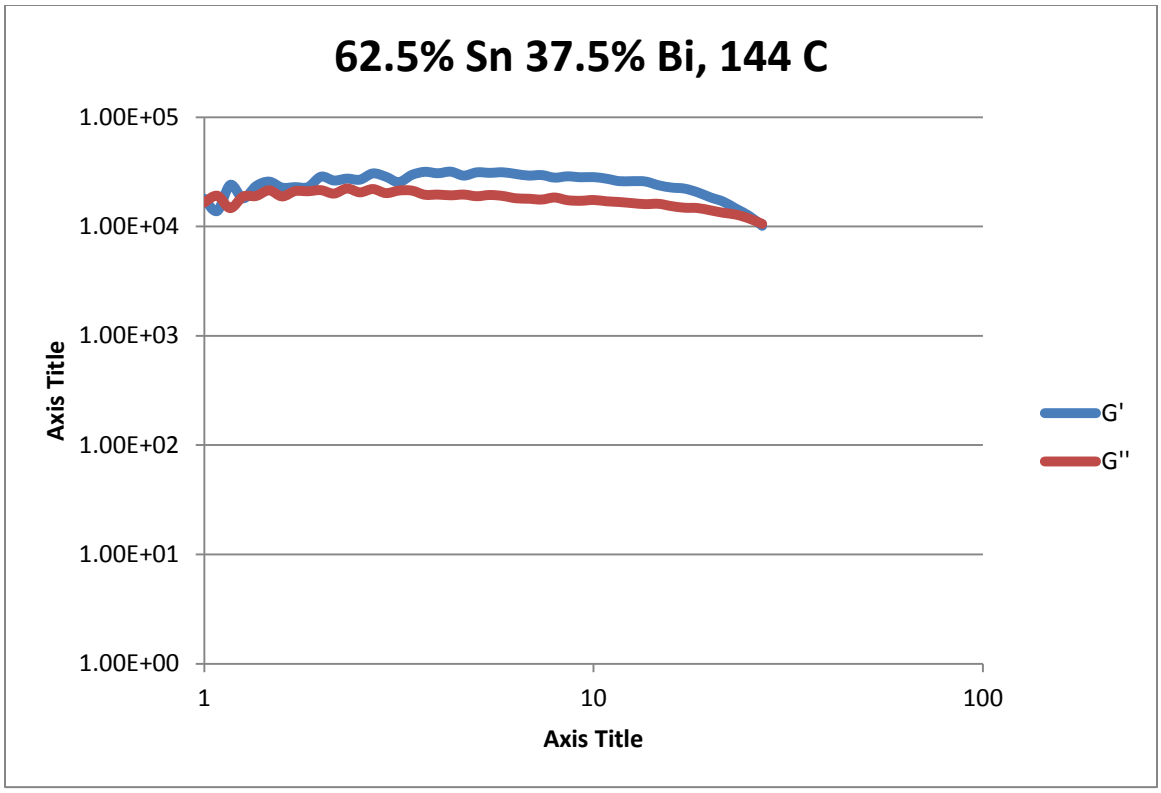

Figure 232- 62.5% Sn 37.5% Bi, 144 C, Cone and Plate Stress Sweep

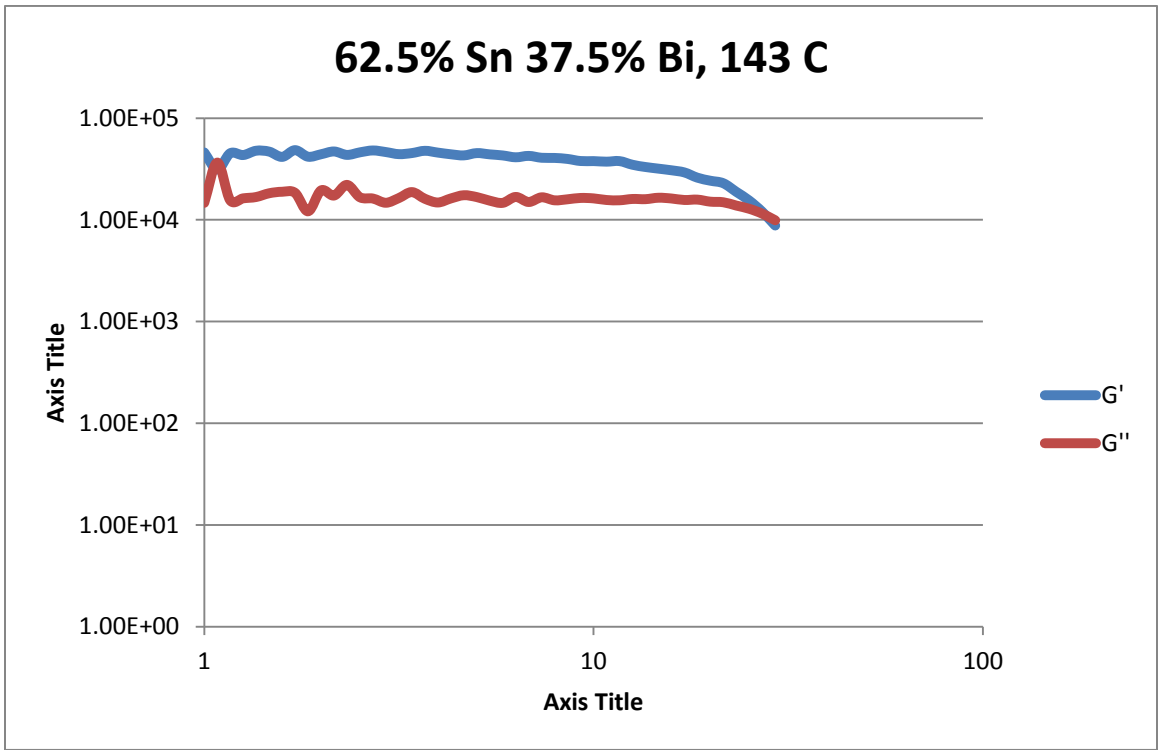

Figure 233- 62.5% Sn 37.5% Bi, 143 C, Cone and Plate Stress Sweep

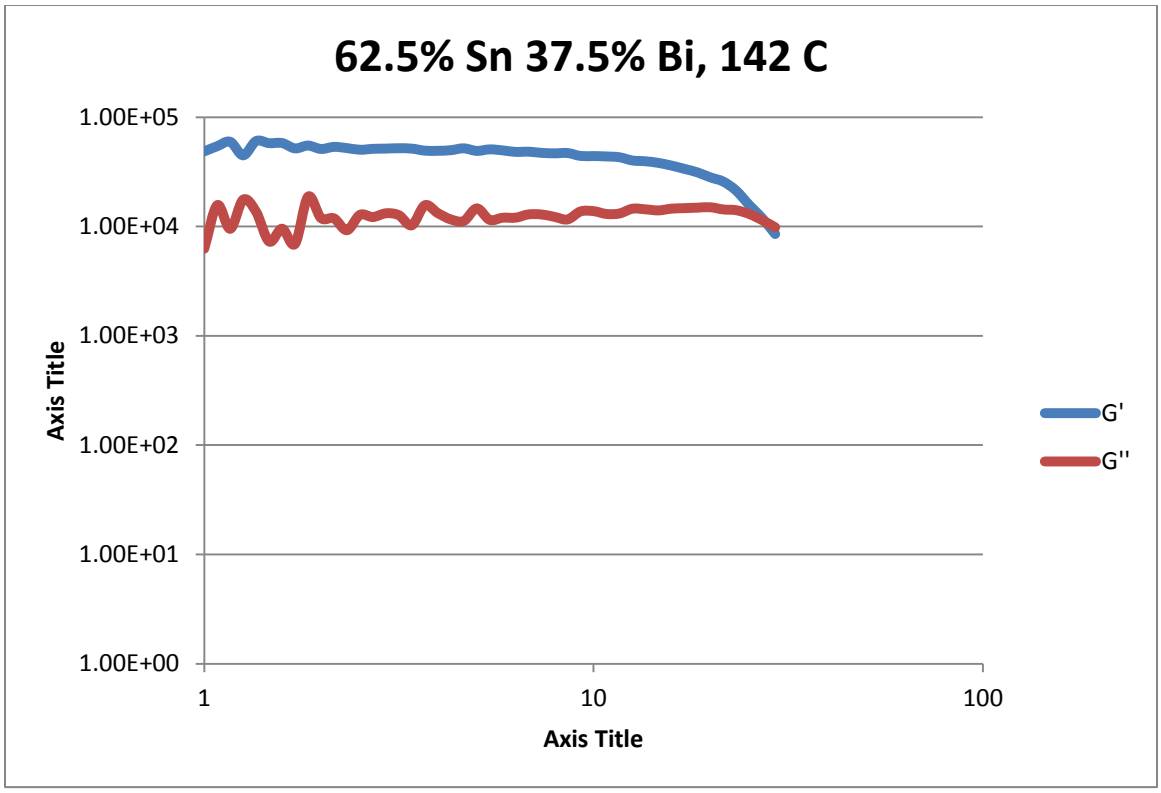

Figure 234- 62.5% Sn 37.5% Bi, 142 C, Cone and Plate Stress Sweep

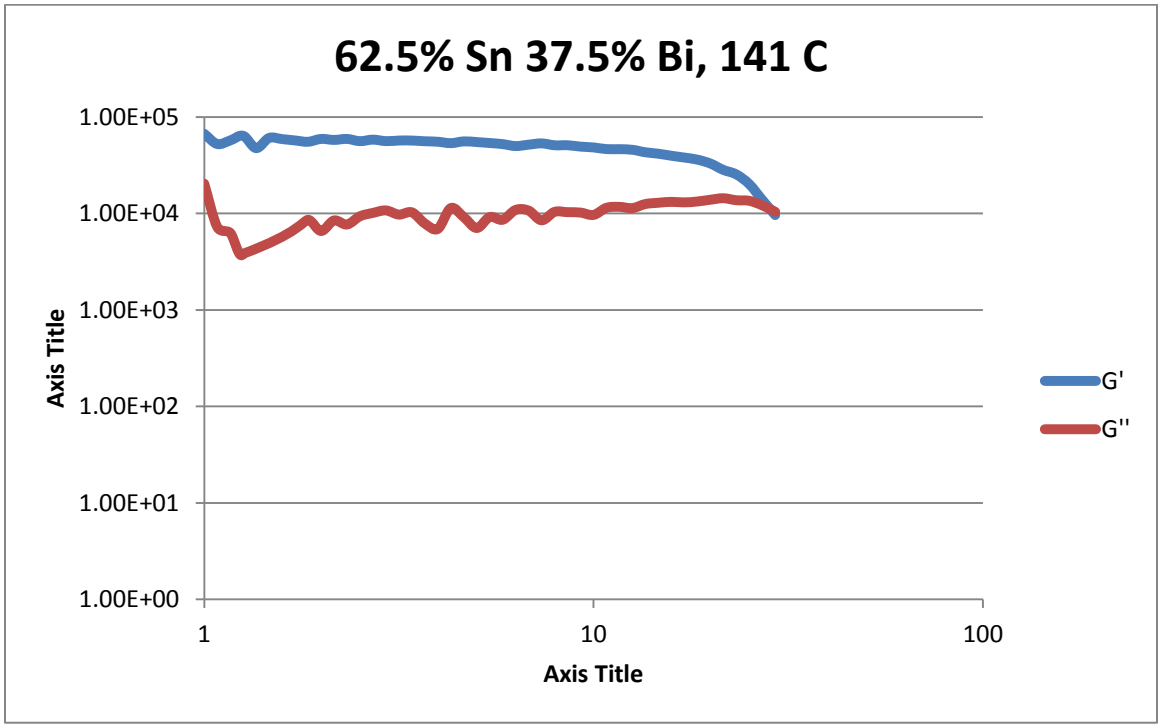

Figure 235- 62.5% Sn 37.5% Bi, 141 C, Cone and Plate Stress Sweep

Temperature	Fraction Solid (At %)	Crossover Stress (Pa)	G' Plateau (Pa)	G'' Plateau (Pa)
145 C	1.57	$1.12 * 10^4$	$4.25 * 10^4$	$1.67 * 10^4$
144 C	1.59	$1.11 * 10^4$	$2.93 * 10^4$	$2.02 * 10^4$
143 C	2.40	$1.10 * 10^4$	$4.50 * 10^4$	$1.61 * 10^4$
142 C	3.13	$1.10 * 10^4$	$5.13 * 10^4$	$1.35 * 10^4$
141 C	4.69	$1.09 * 10^4$	$5.55 * 10^4$	$1.33 * 10^4$

Table 43- 62.5% Sn 37.5% Bi (Run 3), Cone and Plate Crossover and Plateau Stresses

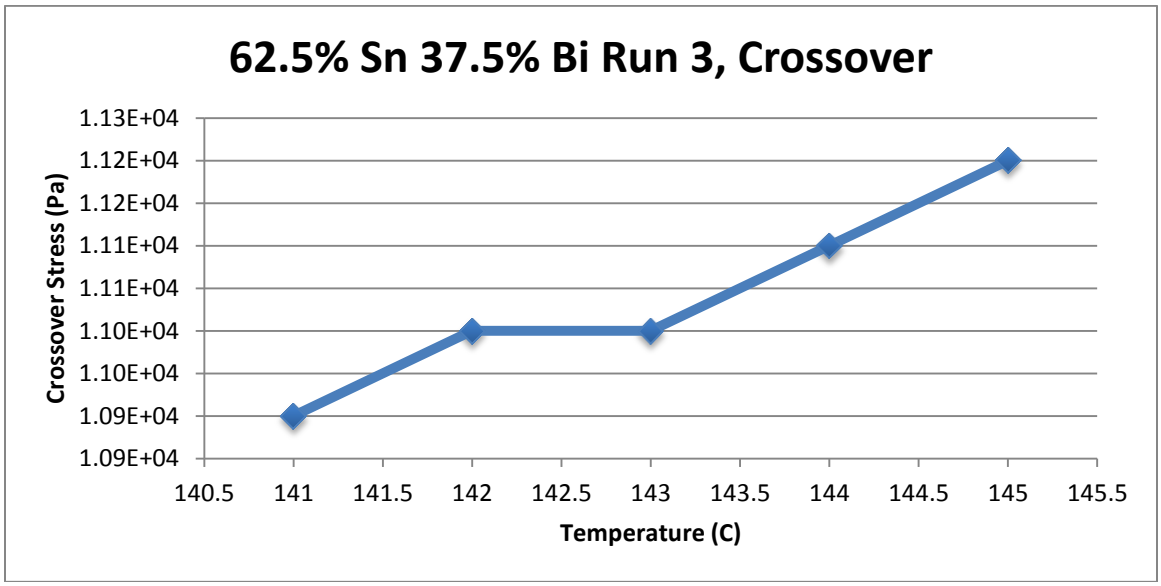

Figure 236- 62.5% Sn 37.5% Bi (Run 3), Cone and Plate Crossover Stresses

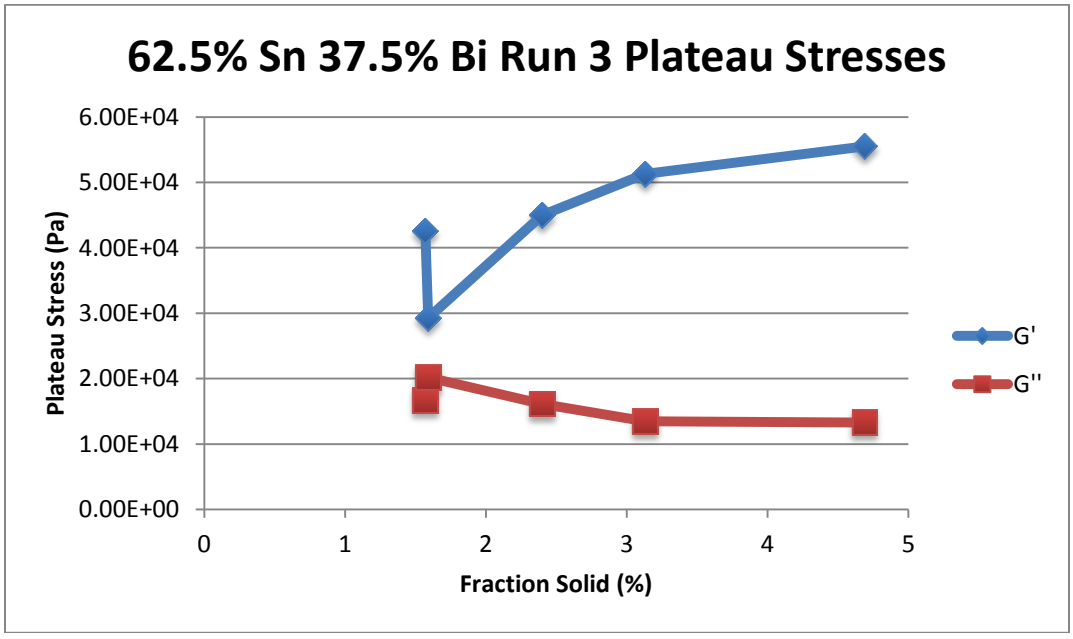

Figure 237- 62.5% Sn 37.5% Bi (Run 3), Cone and Plate Plateau Stresses vs. Fraction Solid

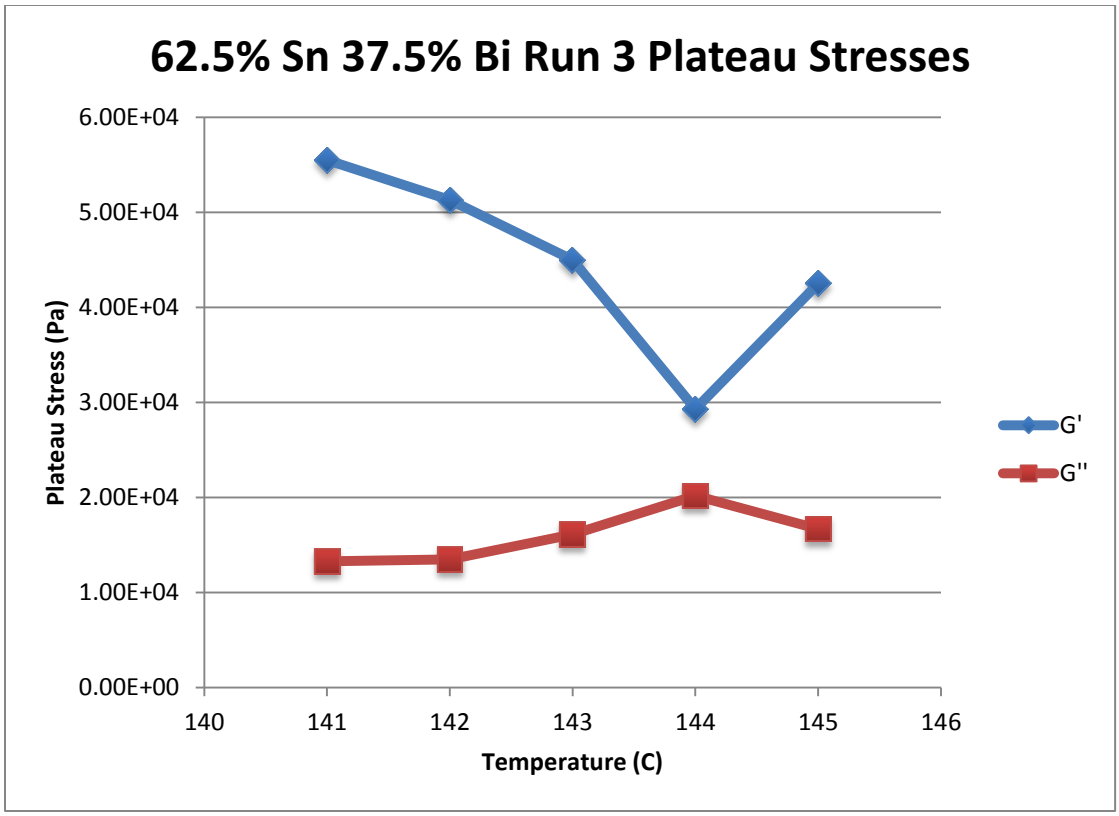

Figure 238- 62.5% Sn 37.5% Bi (Run 3), Cone and Plate Plateau Stresses vs. Temperature

62.5% Sn 37.5% Bi (Run 3) Viscosity					
Temperature	**Fraction Solid**	**Power Law**	**K**	**n**	**R^2**
141 C	4.69 %	$\tau = 1.16 * 10^{-5} * \dot{\gamma}^{0.1572}$ $\mu = 1.82 * 10^{-6} * \dot{\gamma}^{-0.8428}$	$1.16 * 10^{-5}$ Pa*s	0.1572	68.61 %
142 C	3.13 %	$\tau = 7.70 * 10^{-6} * \dot{\gamma}^{0.1190}$ $\mu = 9.16 * 10^{-7} * \dot{\gamma}^{-0.8810}$	$7.70 * 10^{-6}$ Pa*s	0.1190	65.91 %
143 C	2.40 %	$\tau = 9.36 * 10^{-6} * \dot{\gamma}^{0.1517}$ $\mu = 1.42 * 10^{-6} * \dot{\gamma}^{-0.8483}$	$9.36 * 10^{-6}$ Pa*s	0.1517	28.13 %
144 C	1.59 %	$\tau = 5.62 * 10^{-5} * \dot{\gamma}^{0.3565}$ $\mu = 2.00 * 10^{-5} * \dot{\gamma}^{-0.6435}$	$5.62 * 10^{-5}$ Pa*s	0.3565	25.22 %
145 C	1.57 %	$\tau = 2.26 * 10^{-5} * \dot{\gamma}^{0.2400}$ $\mu = 5.42 * 10^{-6} * \dot{\gamma}^{-0.7600}$	$2.26 * 10^{-5}$ Pa*s	0.2400	97.48 %

Table 44- 62.5% Sn 37.5% Bi (Run 3), Cone and Plate Viscosity

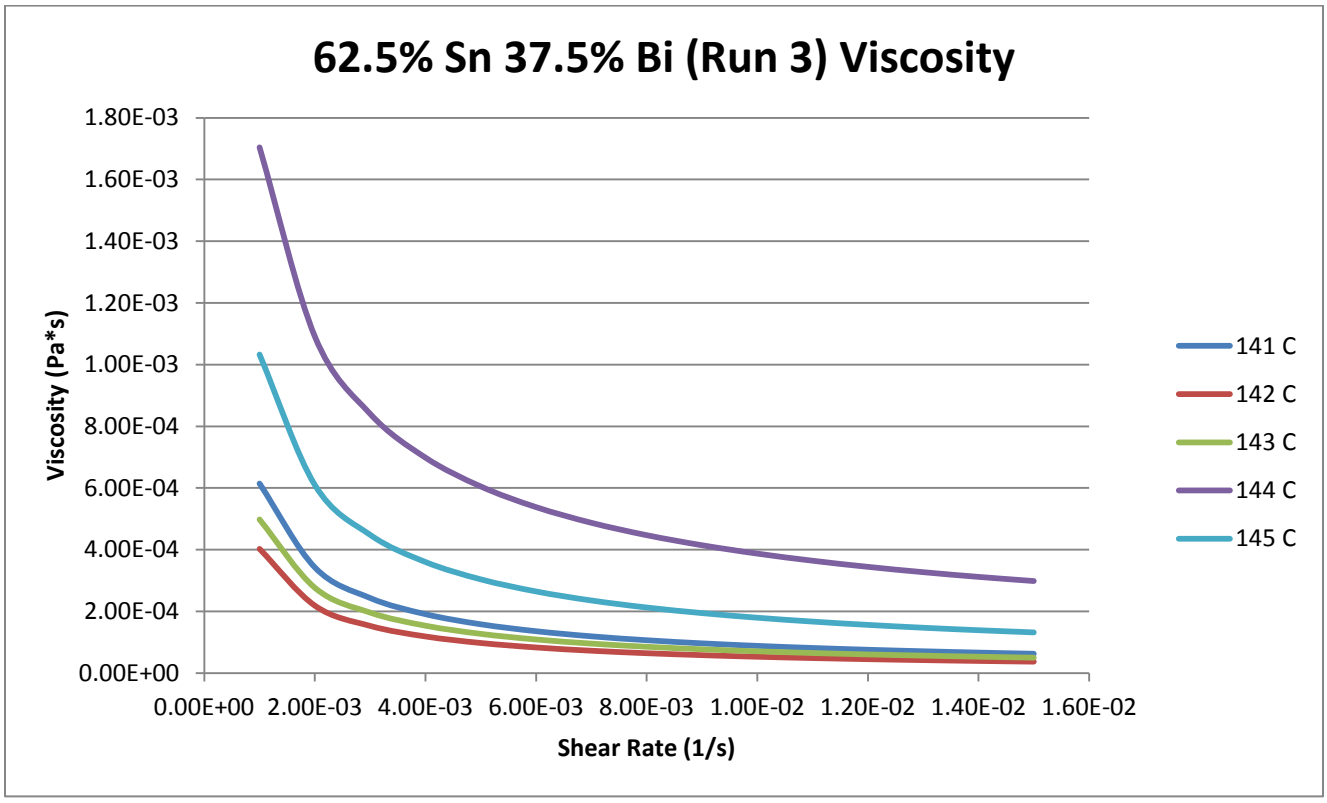

Figure 239- 62.5% Sn 37.5% Bi (Run 3), Cone and Plate Viscosity

141 C

Fraction Solid	4.69 %
Power Law	$\tau = 1.16 * 10^{-5} * \dot{\gamma}^{0.1572}$
	$\mu = 1.82 * 10^{-6} * \dot{\gamma}^{-0.8428}$
R^2	68.61 %

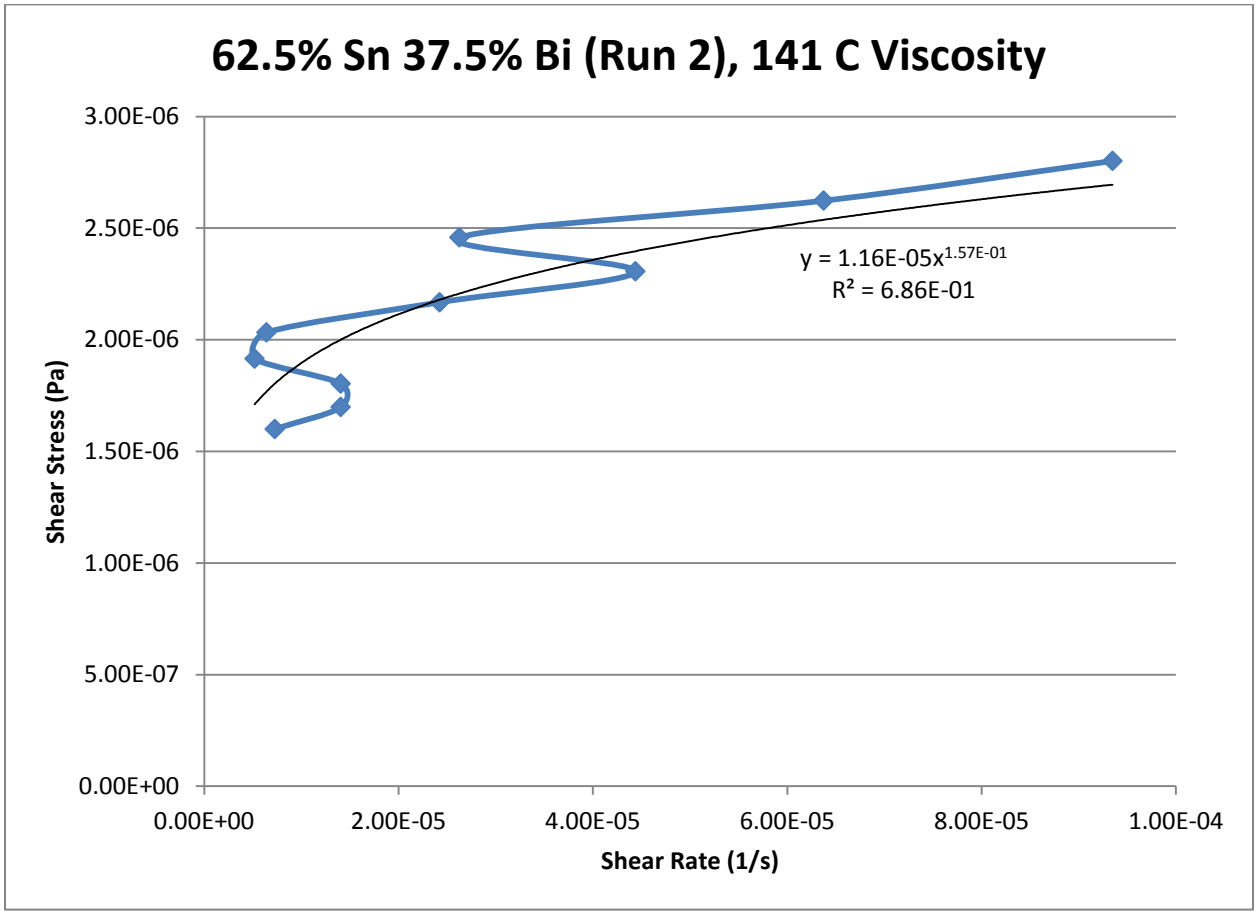

Figure 240- 62.5% Sn 37.5% Bi (Run 3), 141 C, Cone and Plate Viscosity

142 C

Fraction Solid	3.13 %
Power Law	$\tau = 7.70 * 10^{-6} * \dot{\gamma}^{0.1190}$
	$\mu = 9.16 * 10^{-7} * \dot{\gamma}^{-0.8810}$
R^2	65.91 %

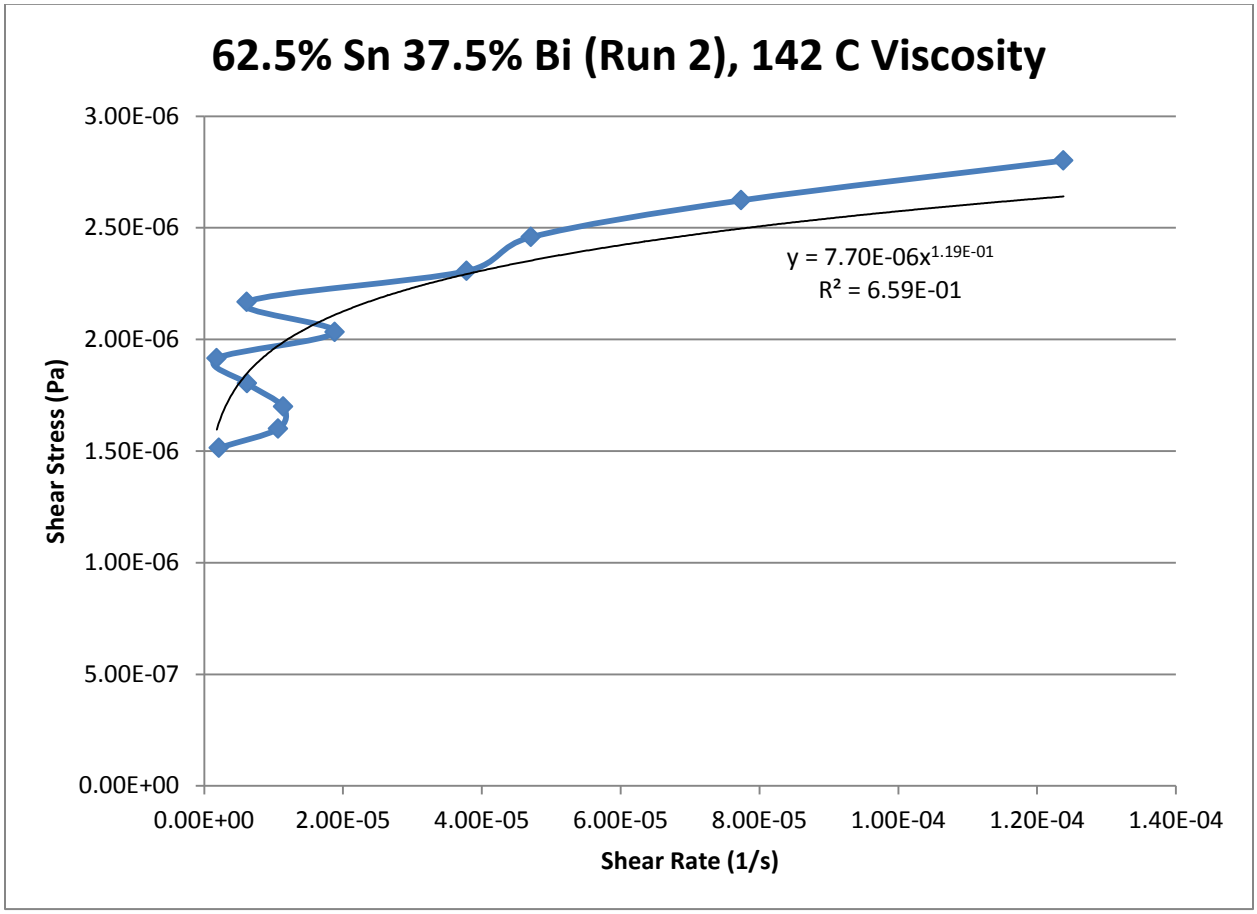

Figure 241- 62.5% Sn 37.5% Bi (Run 3), 142 C, Cone and Plate Viscosity

143 C

Fraction Solid	2.40 %
Power Law	$\tau = 9.36 * 10^{-6} * \dot{\gamma}^{0.1517}$
	$\mu = 1.42 * 10^{-6} * \dot{\gamma}^{-0.8483}$
R^2	28.13 %

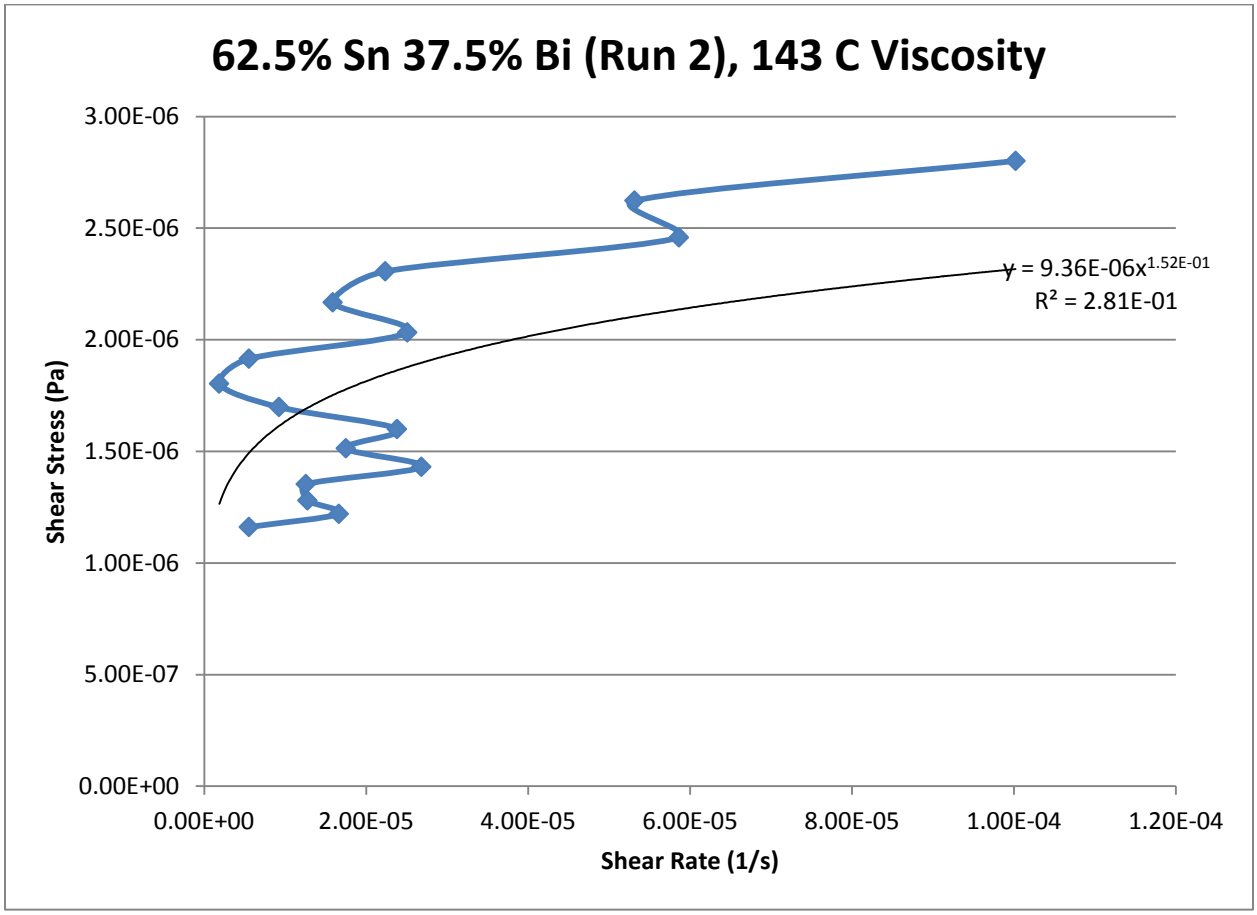

Figure 242- 62.5% Sn 37.5% Bi (Run 3), 143 C, Cone and Plate Viscosity

144 C

Fraction Solid	1.59 %
Power Law	$\tau = 5.62 * 10^{-5} * \dot{\gamma}^{0.3565}$
	$\mu = 2.00 * 10^{-5} * \dot{\gamma}^{-0.6435}$
R^2	25.22 %

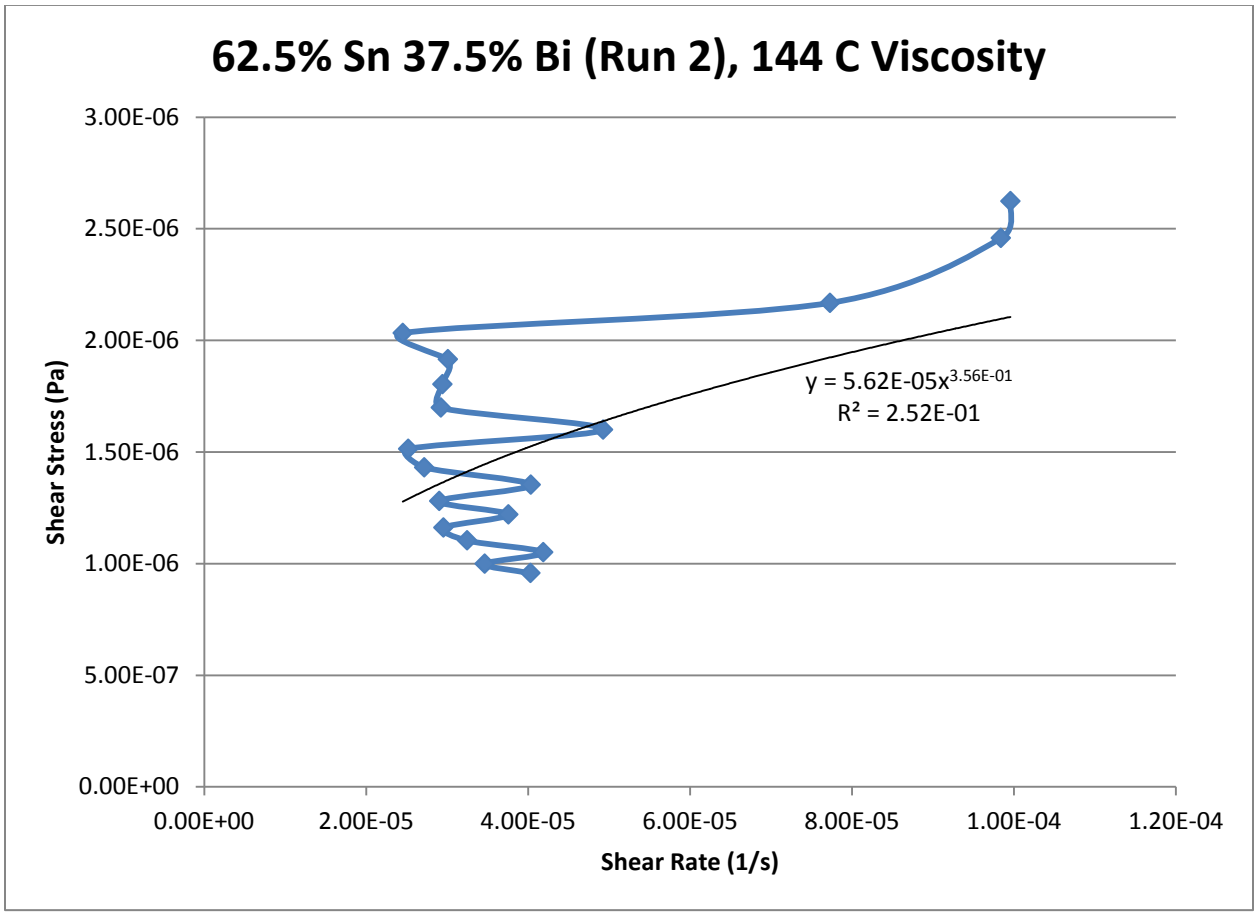

Figure 243- 62.5% Sn 37.5% Bi (Run 3), 144 C, Cone and Plate Viscosity

145 C

Fraction Solid	1.57 %
Power Law	$\tau = 2.26 * 10^{-5} * \dot{\gamma}^{0.2400}$
	$\mu = 5.42 * 10^{-6} * \dot{\gamma}^{-0.7600}$
R^2	97.48 %

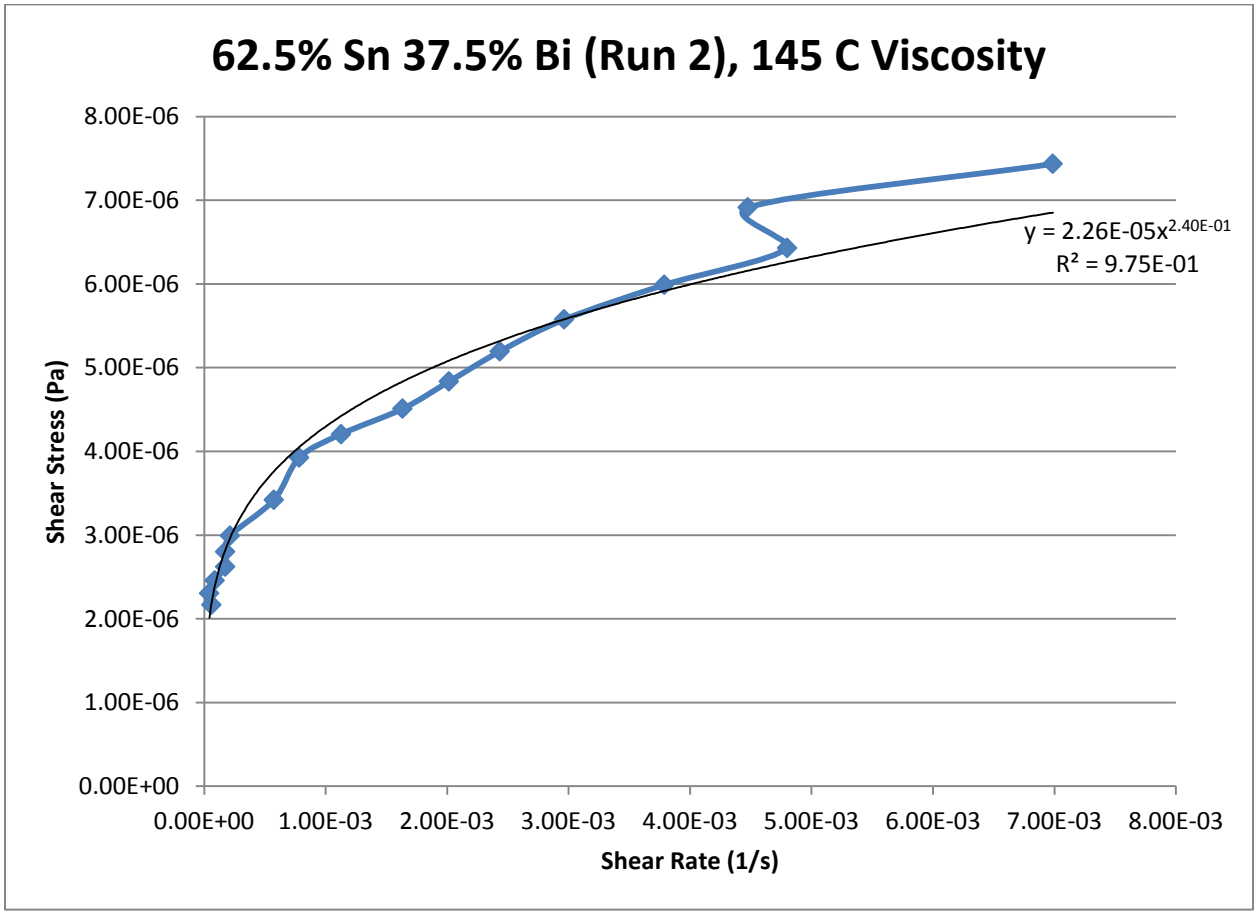

Figure 244- 62.5% Sn 37.5% Bi (Run 3), 145 C, Cone and Plate Viscosity

65% Tin 35% Bismuth (Run 1)

Predicted Composition: 67.00% Sn, 33.00% Bi

Theoretical Solidus Line: 139 C
Theoretical Liquidus Line: 160.6 C

Experimental Solidus Line: 137.9 C
Experimental Liquidus Line: 158.2 C

Set-Up Notes

- The stage was heated to 150 Celsius and the metal pieces were melted underneath the cone. The cone was then lowered to the geometry gap. Stress sweeps were then conducted in decreasing increments of 5 C.

- The stage's temperature at the bottom was 147.1 C, the bottom of the cone's temperature was 145.2 C, and the top of the cone's temperature was 103.4 C.

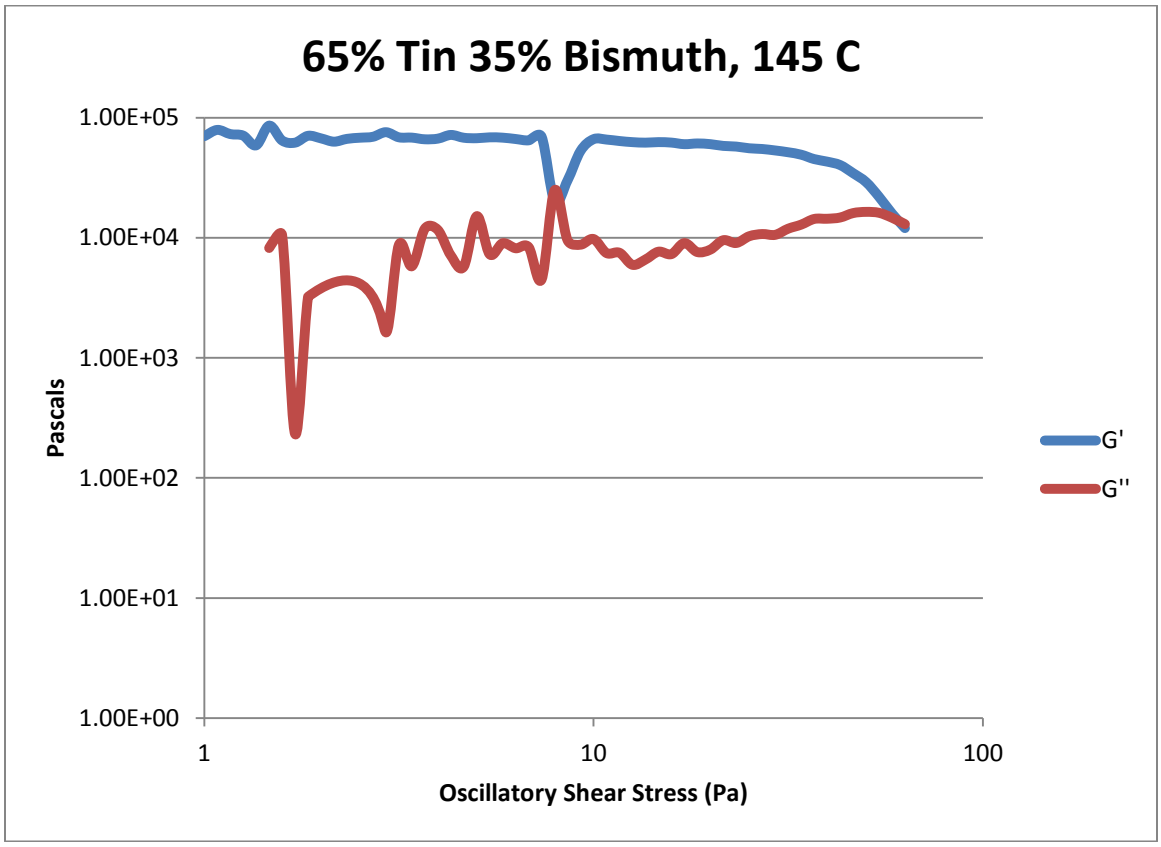

Figure 245- 65% Sn 35% Bi (Run 1), 145 C, Cone and Plate Stress Sweep

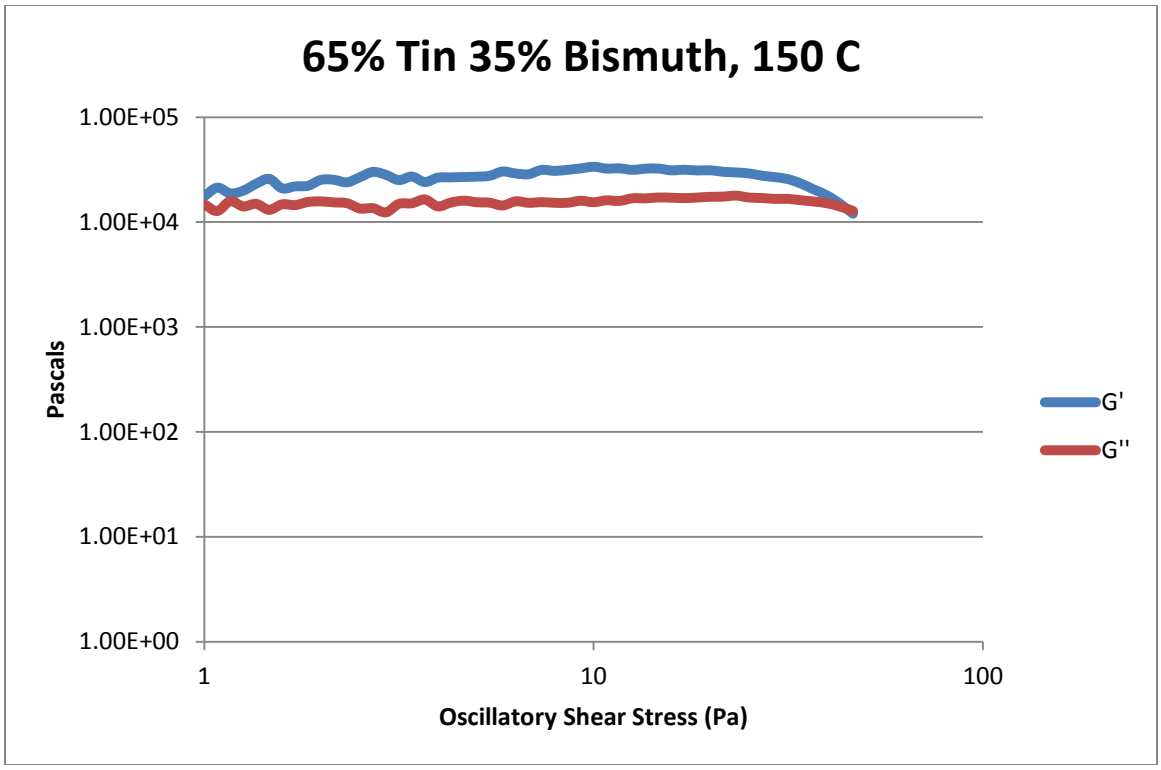

Figure 246- 65% Sn 35% Bi (Run 1), 150 C, Cone and Plate Stress Sweep

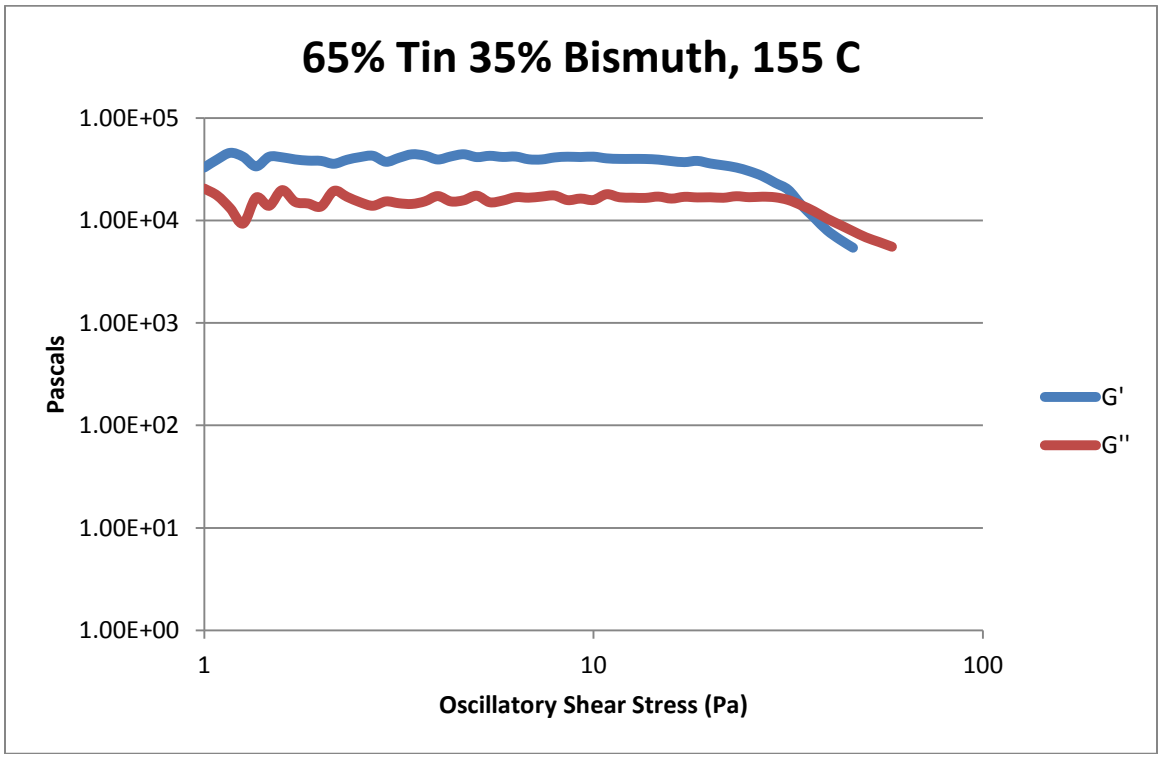

Figure 247- 65% Sn 35% Bi (Run 1), 155 C, Cone and Plate Stress Sweep

Temperature	Crossover Stress (Pa)	Crossover Stress (PSI)
145 C	$1.39 * 10^4$	2.02
150 C	$1.34 * 10^4$	1.94
155 C	$1.37 * 10^4$	1.99

Table 45- 65% Sn 35% Bi (Run 1), Cone and Plate Crossover Stresses

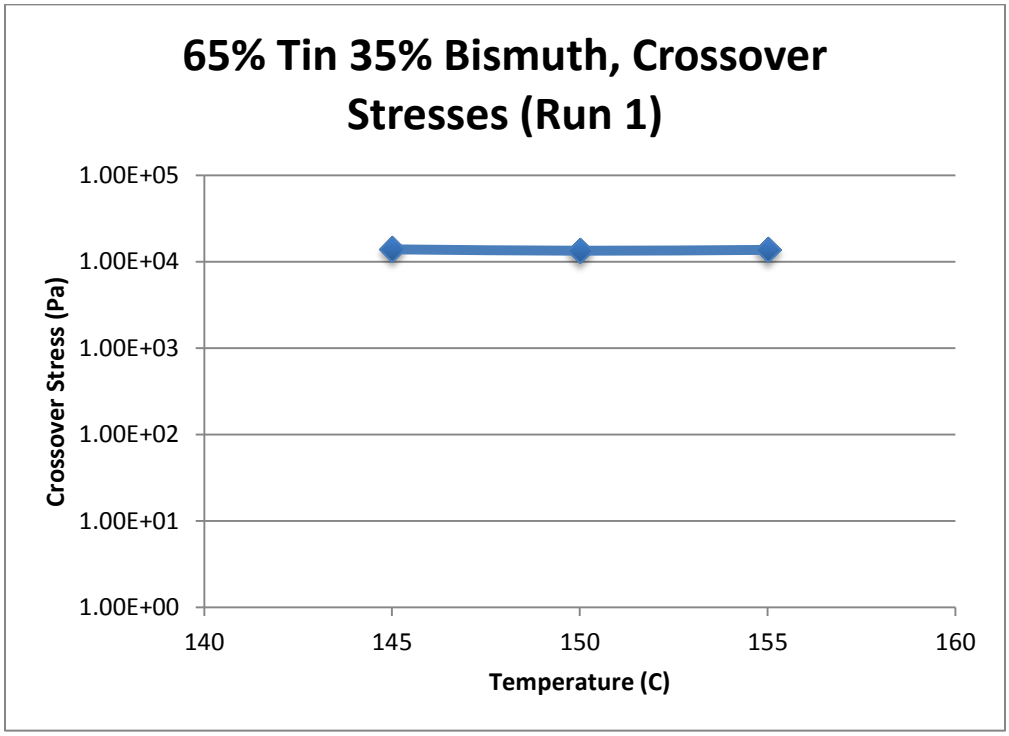

Figure 248- 65% Sn 35% Bi (Run 1), Cone and Plate Crossover Stresses

Temperature	Fraction Solid (At %)	G' Plateau (Pa)	G'' Plateau (Pa)
145 C	6.50	$6.23 * 10^4$	$1.05 * 10^4$
150 C	3.33	$3.19 * 10^4$	$1.53 * 10^4$
155 C	0	$4.12 * 10^4$	$1.64 * 10^4$

Table 46- 65% Sn 35% Bi (Run 1), Cone and Plate Plateau Stresses

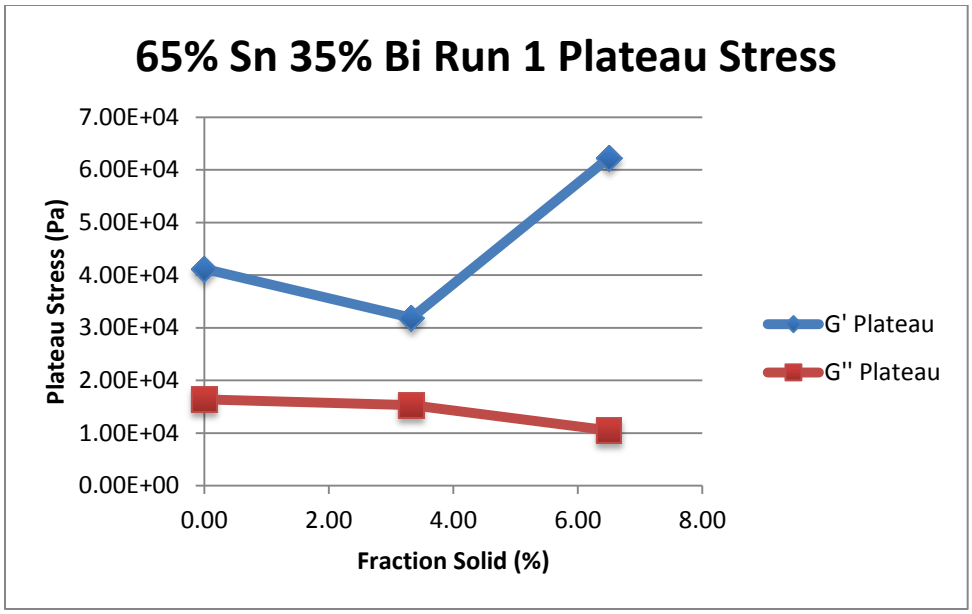

Figure 249- 65% Sn 35% Bi (Run 1), Cone and Plate Plateau Stresses vs. Fraction Solid

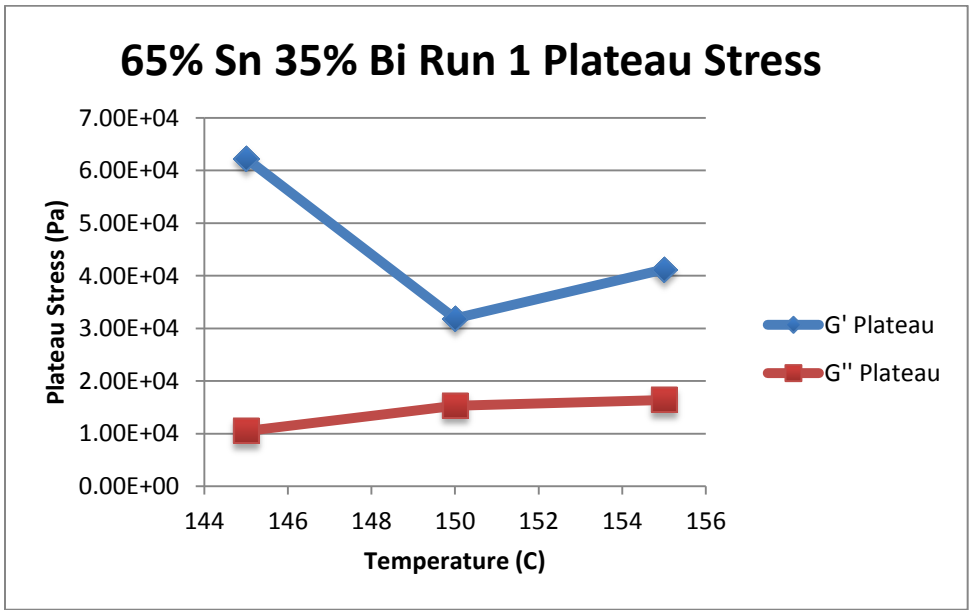

Figure 250- 65% Sn 35% Bi (Run 1), Cone and Plate Plateau Stresses vs. Temperature

65% Sn 35% Bi (Run 1) Viscosity					
Temperature	**Fraction Solid**	**Power Law**	**K**	**n**	**R^2**
145 C	6.50 %	$\tau = 3.59 * 10^{-5} * \dot{\gamma}^{0.2361}$ $\mu = 8.48 * 10^{-6} * \dot{\gamma}^{-0.7639}$	$3.59 * 10^{-5}$ Pa*s	0.2361	54.58 %
150 C	3.33 %	$\tau = 5.02 * 10^{-6} * \dot{\gamma}^{0.0439}$ $\mu = 2.20 * 10^{-7} * \dot{\gamma}^{-0.9561}$	$5.02 * 10^{-6}$ Pa*s	0.0439	16.78 %
155 C	0 %	$\tau = 1.03 * 10^{-5} * \dot{\gamma}^{0.1201}$ $\mu = 1.24 * 10^{-6} * \dot{\gamma}^{-0.8799}$	$1.03 * 10^{-5}$ Pa*s	0.2811	80.76 %

Table 47- 65% Sn 35% Bi (Run 1), Cone and Plate Viscosity

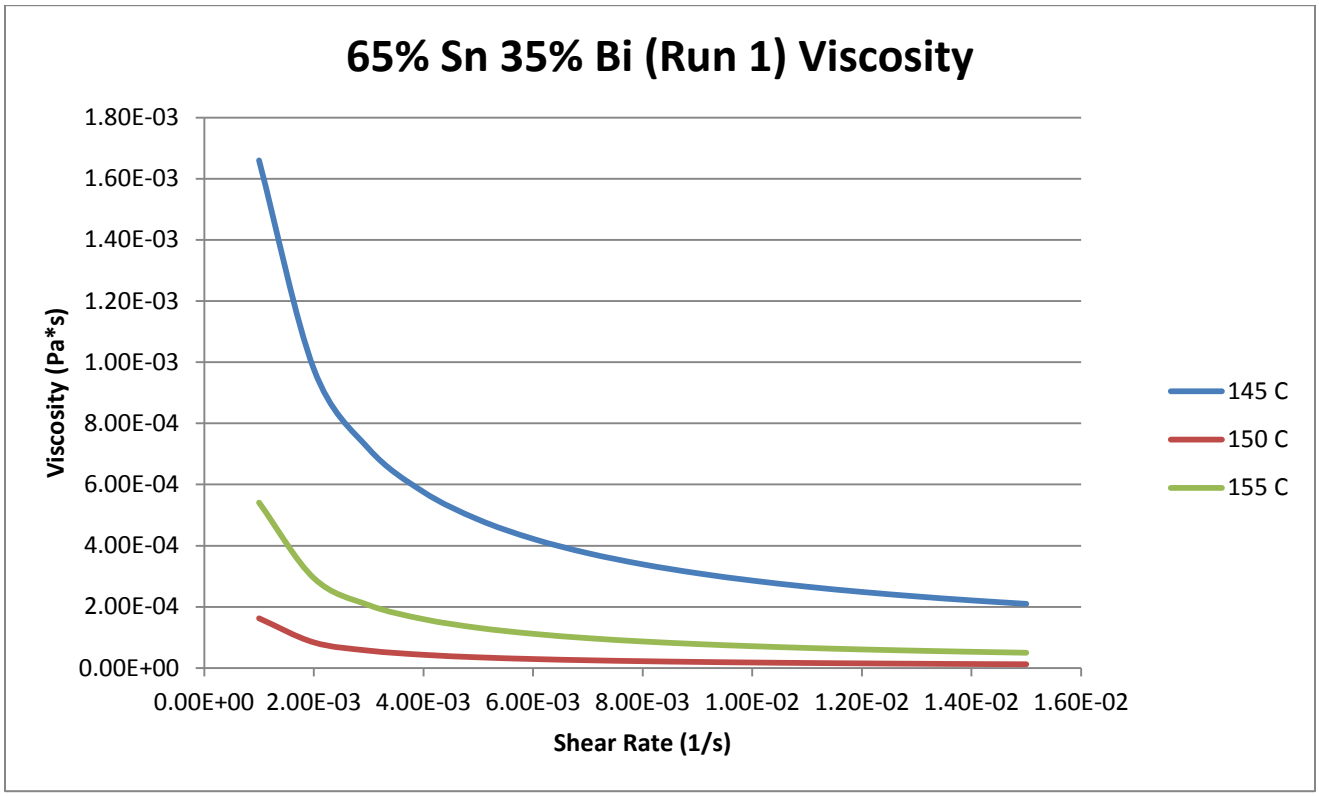

Figure 251- 65% Sn 35% Bi (Run 1), Cone and Plate Viscosity

145 C

Fraction Solid	6.50 %
Power Law	$\tau = 3.59 * 10^{-5} * \dot{\gamma}^{0.2361}$
	$\mu = 8.48 * 10^{-6} * \dot{\gamma}^{-0.7639}$
R^2	54.58 %

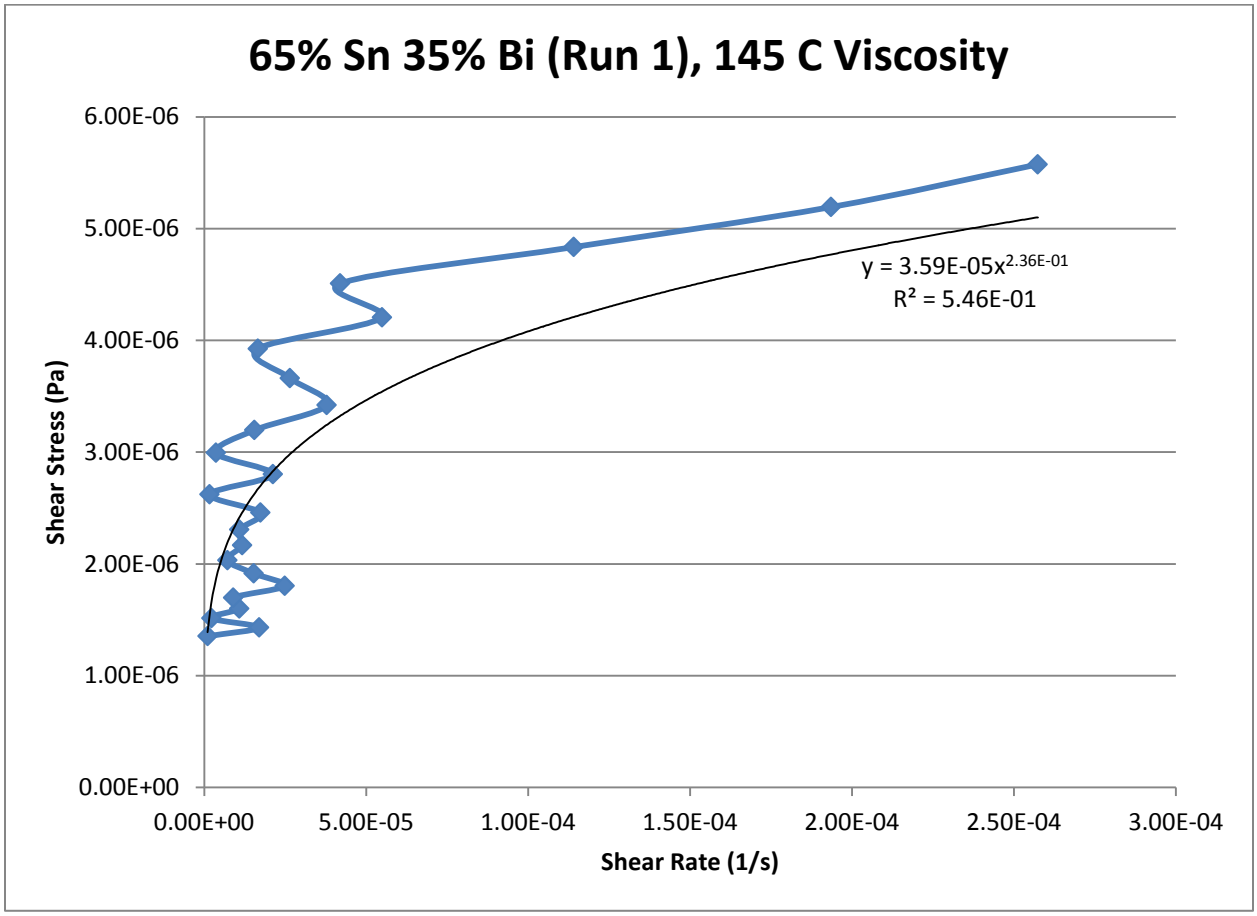

Figure 252- 65% Sn 35% Bi (Run 1), 145 C, Cone and Plate Viscosity

150 C

Fraction Solid	3.33 %
Power Law	$\tau = 5.02 * 10^{-6} * \dot{\gamma}^{0.0439}$
	$\mu = 2.20 * 10^{-7} * \dot{\gamma}^{-0.9561}$
R^2	16.78 %

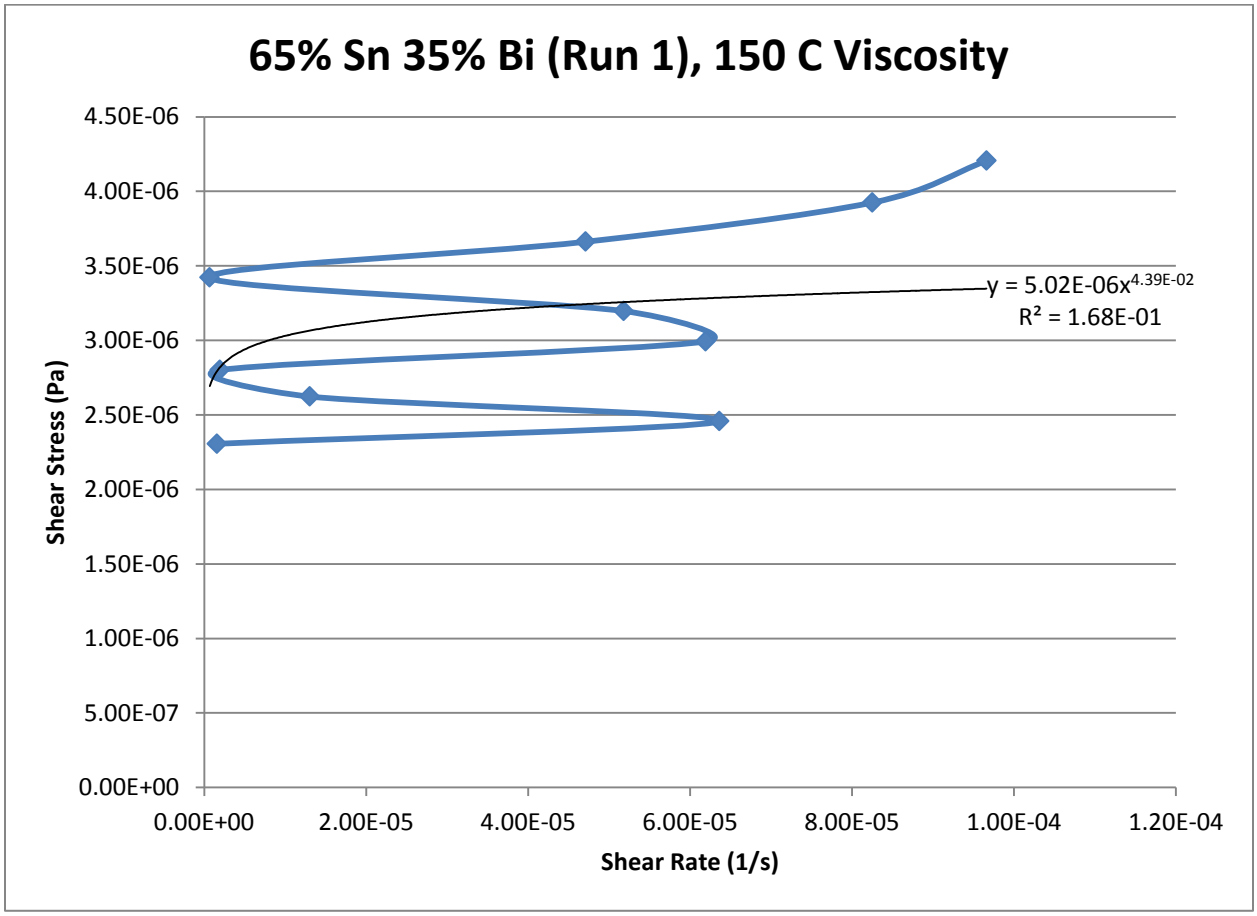

Figure 253- 65% Sn 35% Bi (Run 1), 150 C, Cone and Plate Viscosity

155 C

Fraction Solid	0 %
Power Law	$\tau = 1.03 * 10^{-5} * \dot{\gamma}^{0.1201}$
	$\mu = 1.24 * 10^{-6} * \dot{\gamma}^{-0.8799}$
R^2	80.76 %

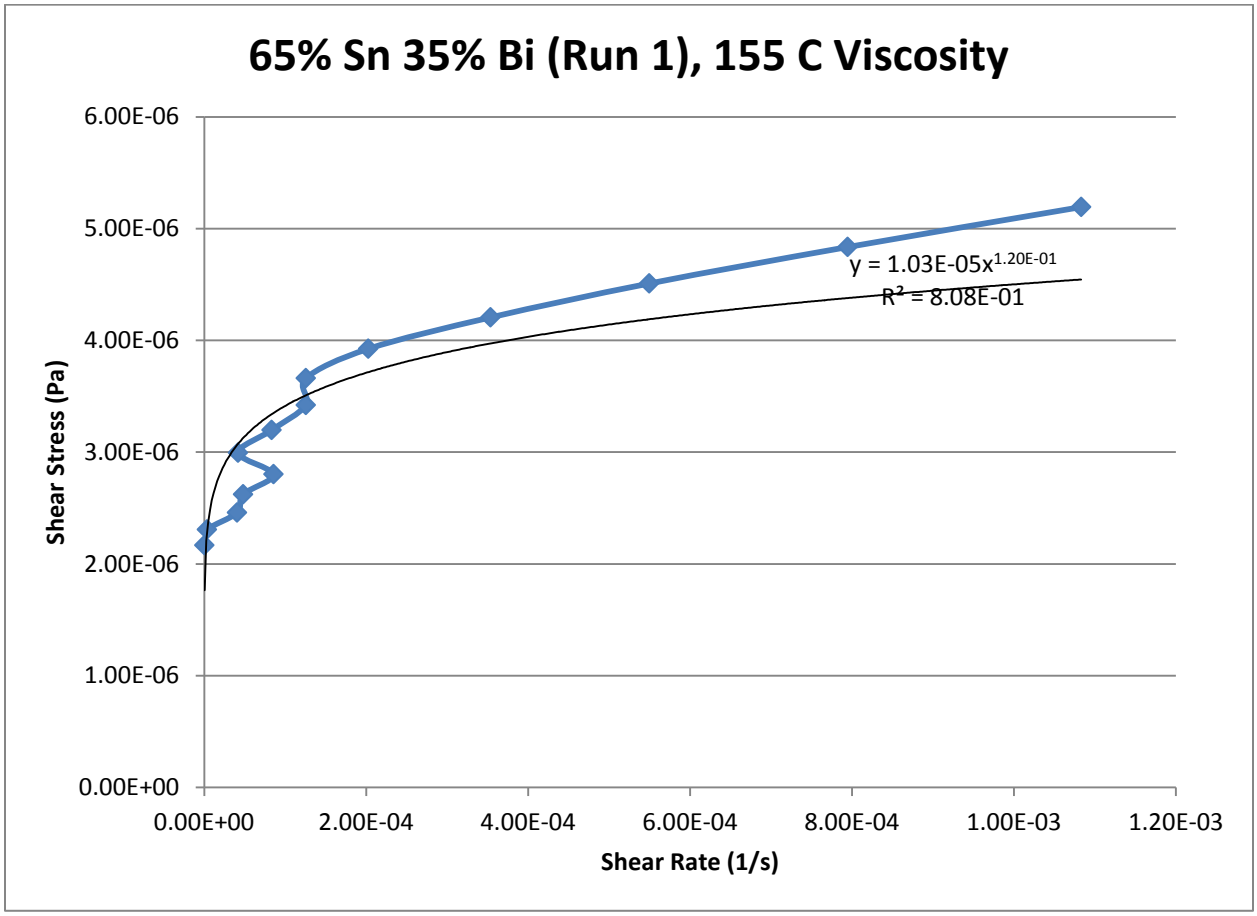

Figure 254- 65% Sn 35% Bi (Run 1), 155 C, Cone and Plate Viscosity

65% Tin 35% Bismuth (Run 2)

Predicted Composition: 67.00% Sn, 33.00% Bi

Theoretical Solidus Line: 139 C
Theoretical Liquidus Line: 160.6 C

Experimental Solidus Line: 137.9 C
Experimental Liquidus Line: 158.2 C

Set-Up Notes

- The stage was heated to 150 Celsius and the metal pieces were melted underneath the cone. The cone was then lowered to the geometry gap. Stress sweeps were then conducted in decreasing increments of 2.5 C before increasing to 155 C for a final stress sweep.

Plots

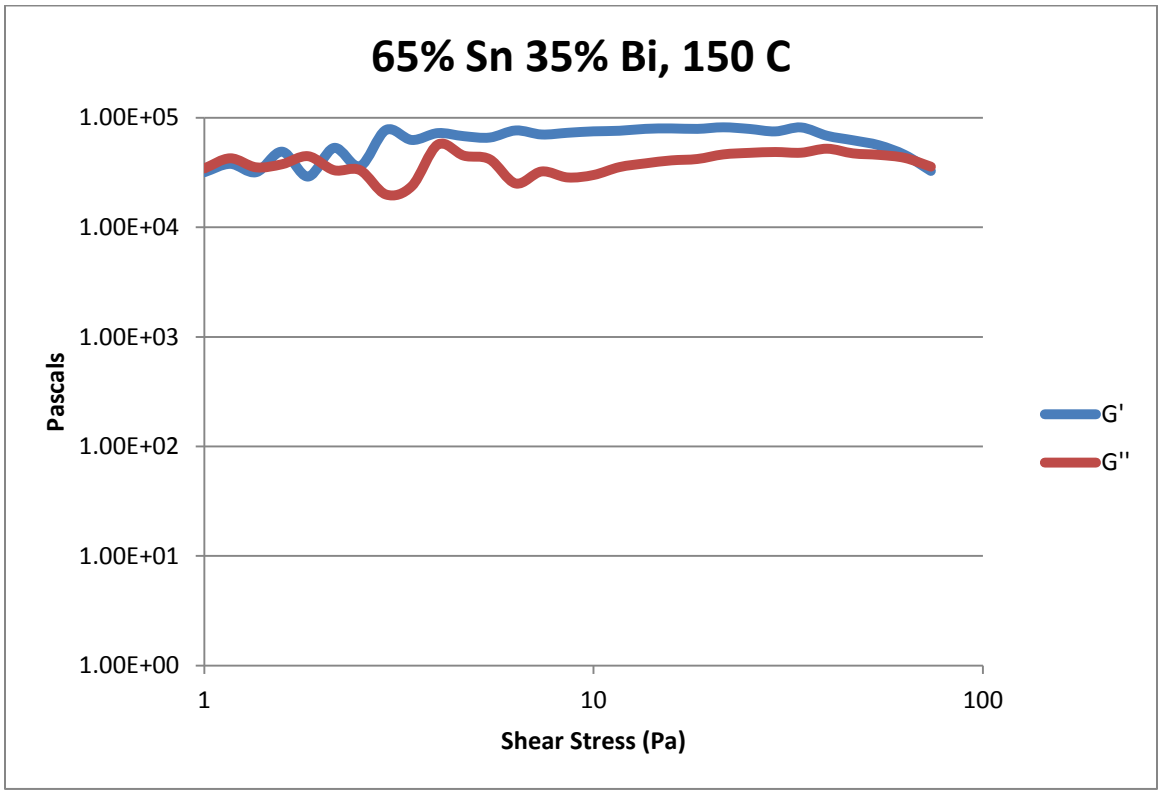

Figure 255- 65% Sn 35% Bi (Run 2), 150 C, Cone and Plate Stress Sweep

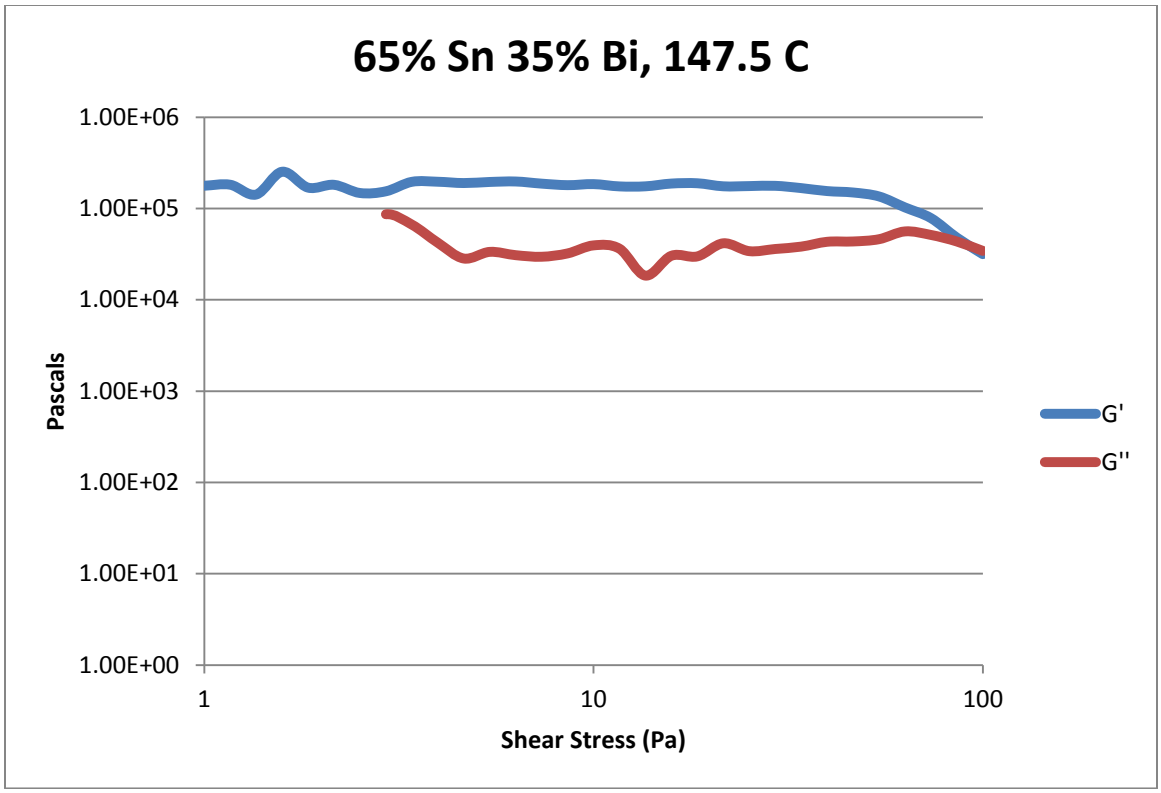

Figure 256- 65% Sn 35% Bi (Run 2), 147.5 C, Cone and Plate Stress Sweep

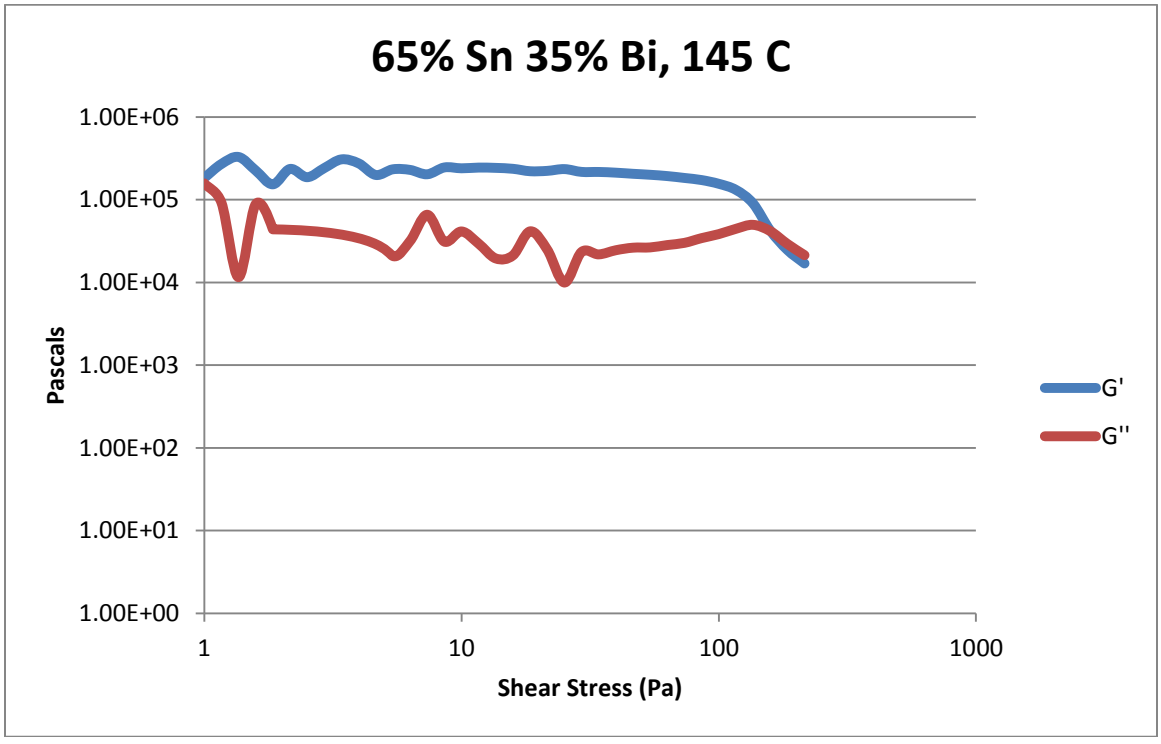

Figure 257- 65% Sn 35% Bi (Run 2), 145 C, Cone and Plate Stress Sweep

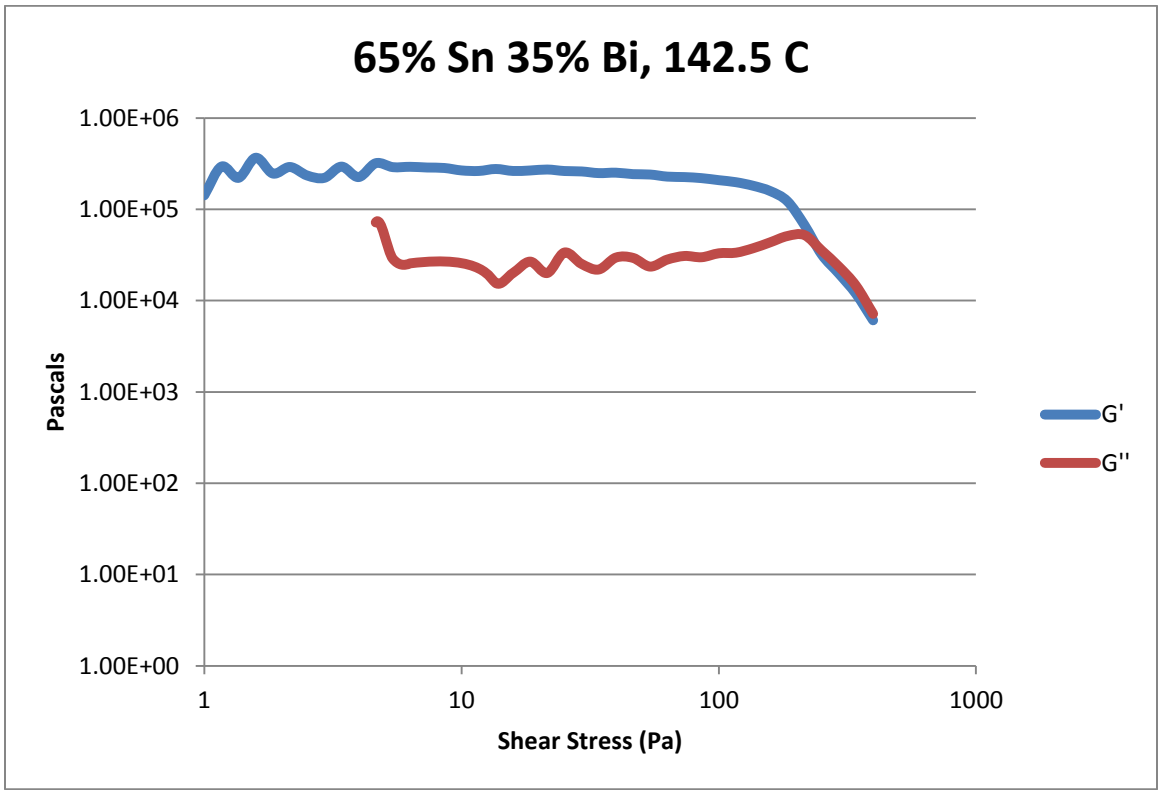

Figure 258- 65% Sn 35% Bi (Run 2), 142.5 C, Cone and Plate Stress Sweep

Temperature	Fraction Solid (At %)	Crossover Stress (Pa)	G' Plateau (Pa)	G'' Plateau (Pa)
150 C	3.33	$7.48 * 10^4$	$4.79 * 10^4$	$3.95 * 10^4$
147.5 C	4.92	$1.80 * 10^5$	$4.73 * 10^4$	$3.78 * 10^4$
145 C	6.50	$2.83 * 10^5$	$4.53 * 10^4$	$4.00 * 10^4$
142.5 C	9.09	$2.65 * 10^5$	$4.89 * 10^4$	$3.84 * 10^4$

Table 48- 65% Sn 35% Bi (Run 2), Cone and Plate Crossover and Plateau Stresses

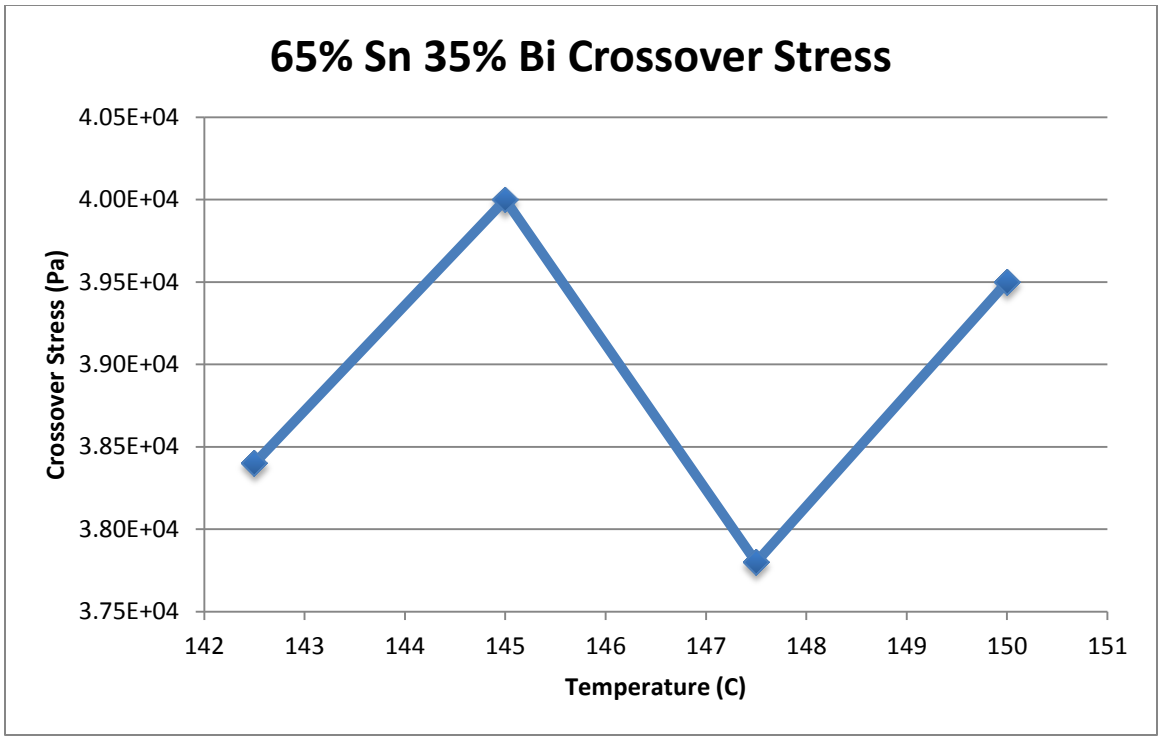

Figure 259- 65% Sn 35% Bi (Run 2), Cone and Plate Crossover Stresses

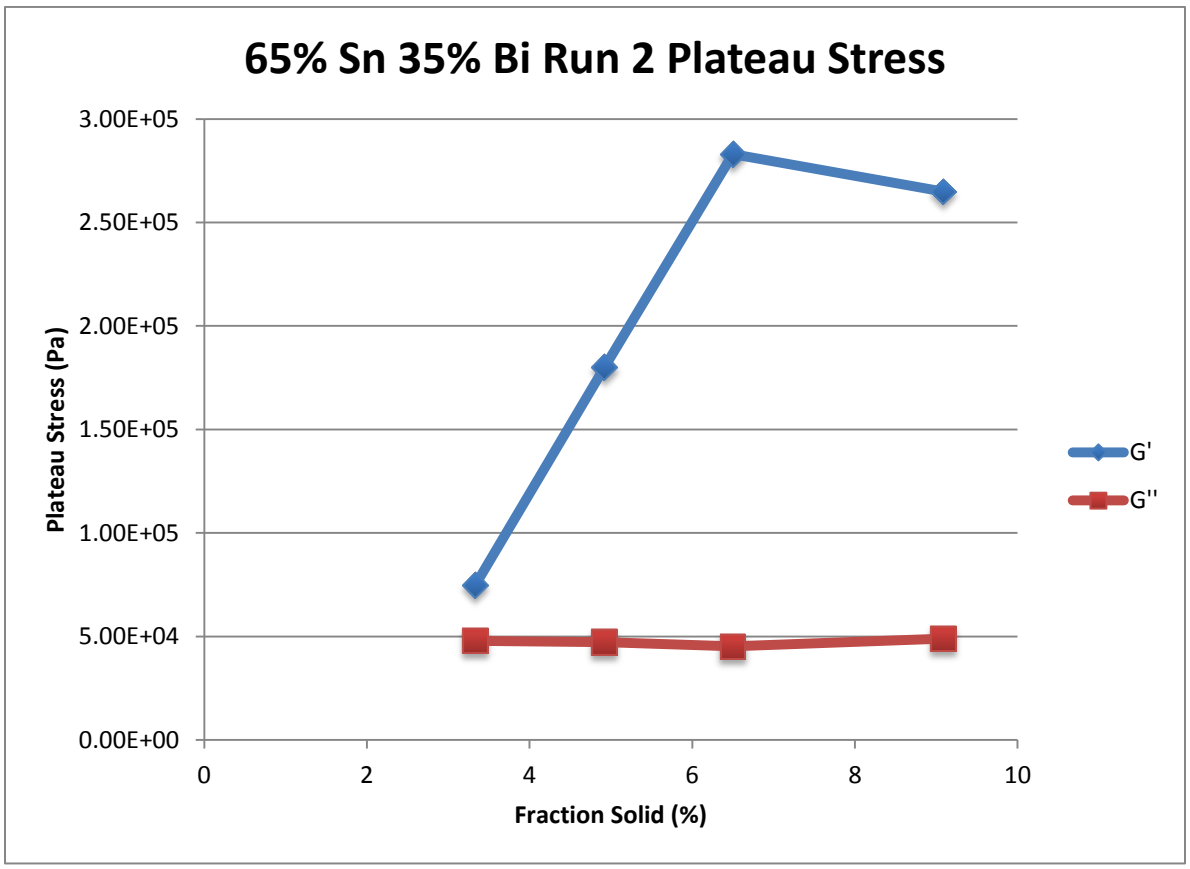

Figure 260- 65% Sn 35% Bi (Run 2), Cone and Plate Plateau Stresses vs. Fraction Solid (%)

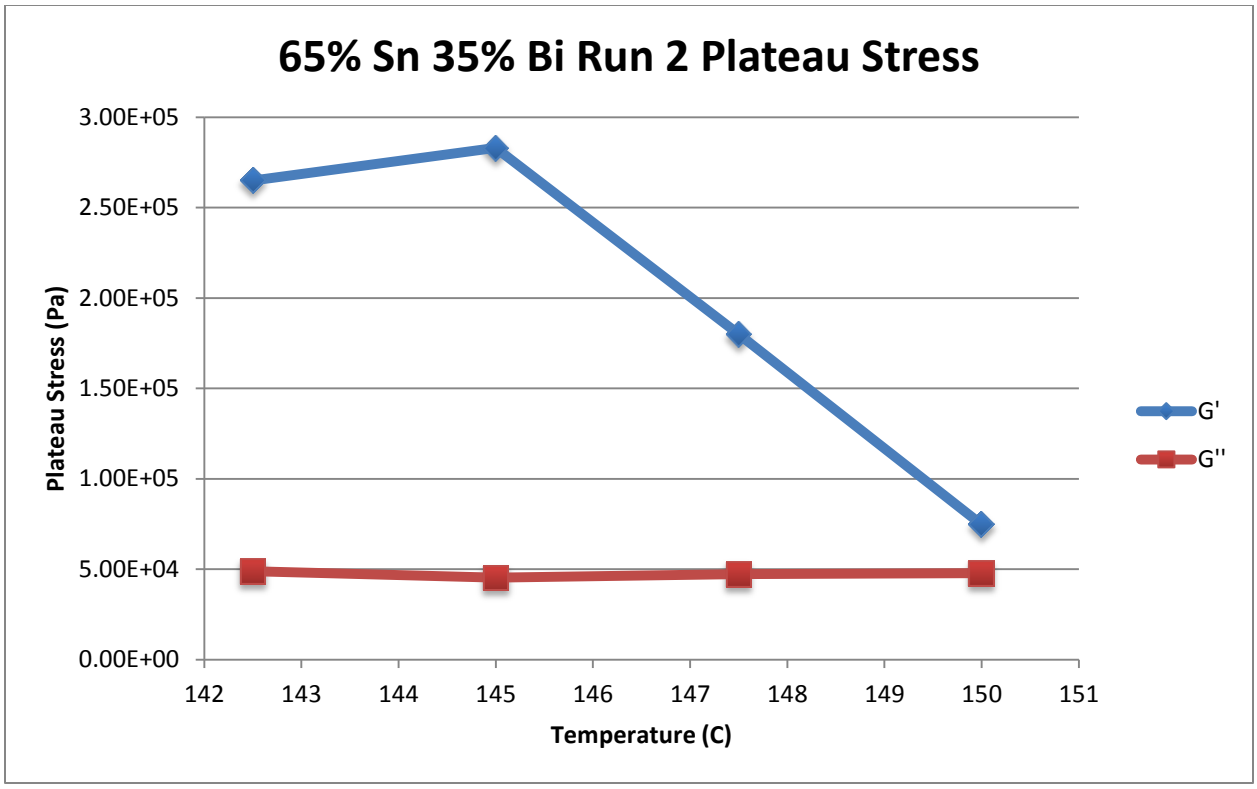

Figure 261- 65% Sn 35% Bi (Run 2), Cone and Plate Plateau Stresses vs. Temperature

65% Sn 35% Bi (Run 2) Viscosity					
Temperature	**Fraction Solid**	**Power Law**	**K**	**n**	**R^2**
142.5 C	9.09 %	$\tau = 6.29 * 10^{-5} * \dot{\gamma}^{0.1037}$ $\mu = 6.52 * 10^{-6} * \dot{\gamma}^{-0..8963}$	$6.29 * 10^{-5}$ Pa*s	0.1037	92.15 %
145 C	6.50 %	$\tau = 3.39 * 10^{-5} * \dot{\gamma}^{0.1309}$ $\mu = 4.44 * 10^{-6} * \dot{\gamma}^{-0.8691}$	$3.39 * 10^{-5}$ Pa*s	0.1309	12.73 %
147.5 C	4.92 %	$\tau = 3.44 * 10^{-4} * \dot{\gamma}^{0.3810}$ $\mu = 1.31 * 10^{-4} * \dot{\gamma}^{-0.6190}$	$3.44 * 10^{-4}$ Pa*s	0.3810	48.50 %
150 C	3.33 %	$\tau = 8.42 * 10^{-6} * \dot{\gamma}^{0.1176}$ $\mu = 9.90 * 10^{-7} * \dot{\gamma}^{-0.8824}$	$8.42 * 10^{-6}$ Pa*s	0.1176	1.69 %

Table 49- 65% Sn 35% Bi (Run 2), Cone and Plate Viscosity

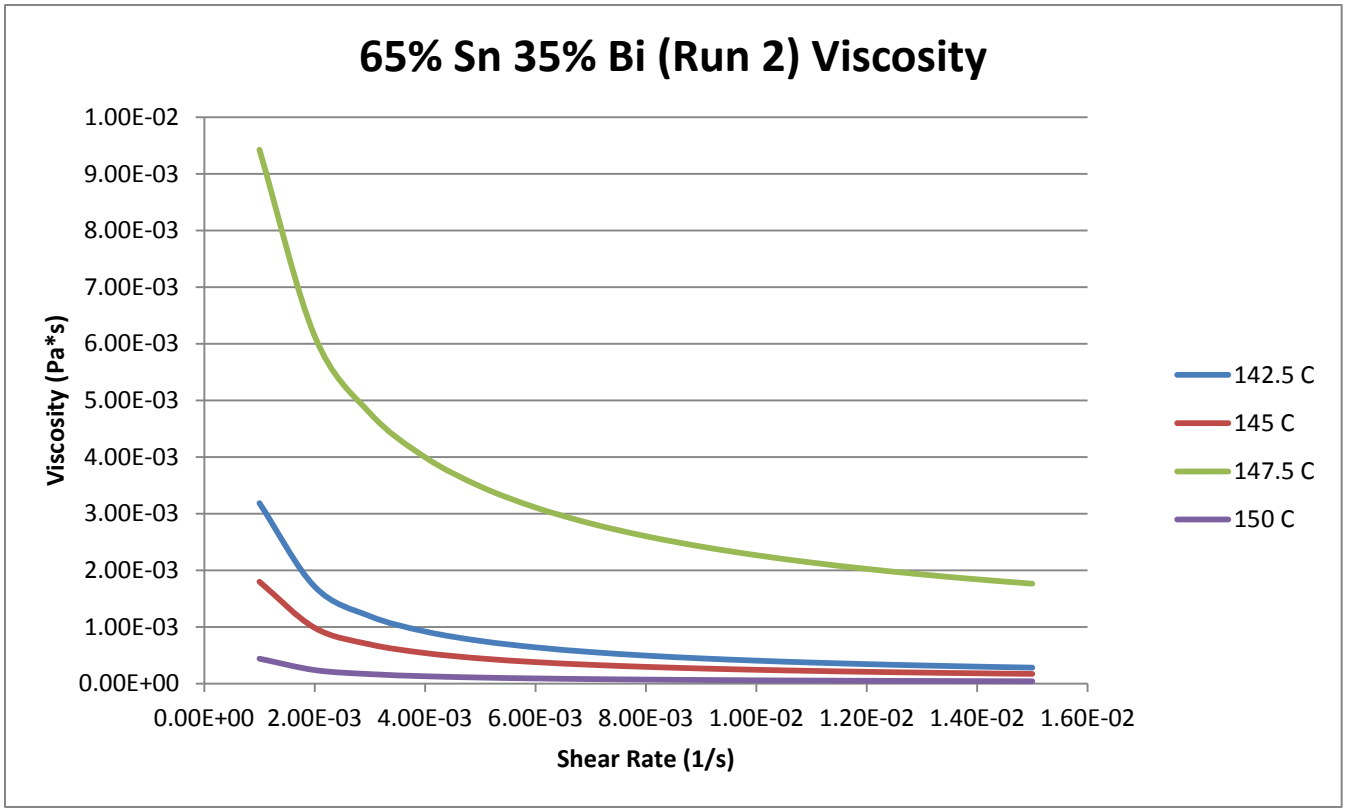

Figure 262- 65% Sn 35% Bi (Run 2), Cone and Plate Viscosity

142.5 C

Fraction Solid	9.09 %
Power Law	$\tau = 6.29 * 10^{-5} * \dot{\gamma}^{0.1037}$
	$\mu = 6.52 * 10^{-6} * \dot{\gamma}^{-0..8963}$
R^2	92.15 %

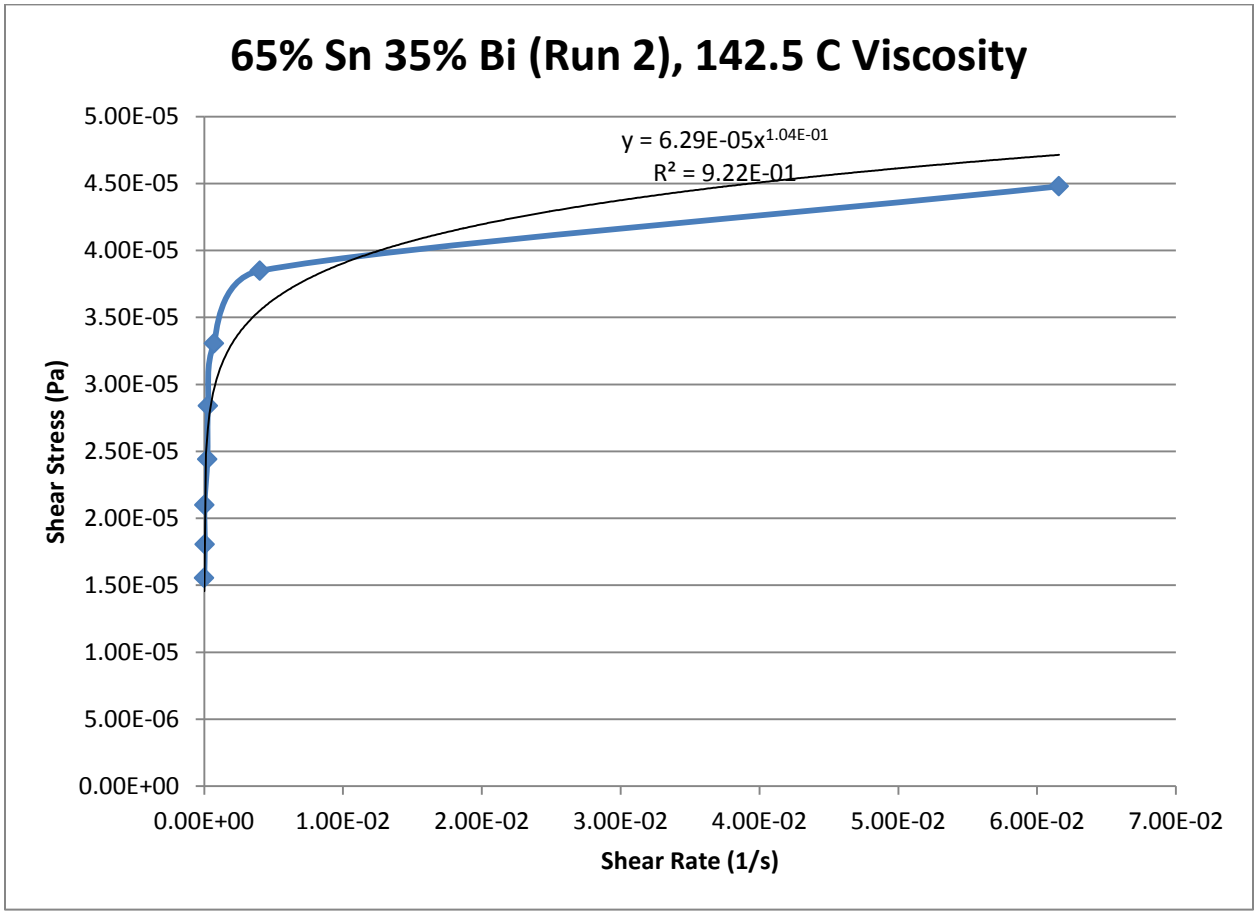

Figure 263- 65% Sn 35% Bi (Run 2), 142.5 C, Cone and Plate Viscosity

145 C

Fraction Solid	6.50 %
Power Law	$\tau = 3.39 * 10^{-5} * \dot{\gamma}^{0.1309}$
	$\mu = 4.44 * 10^{-6} * \dot{\gamma}^{-0.8691}$
R^2	12.73 %

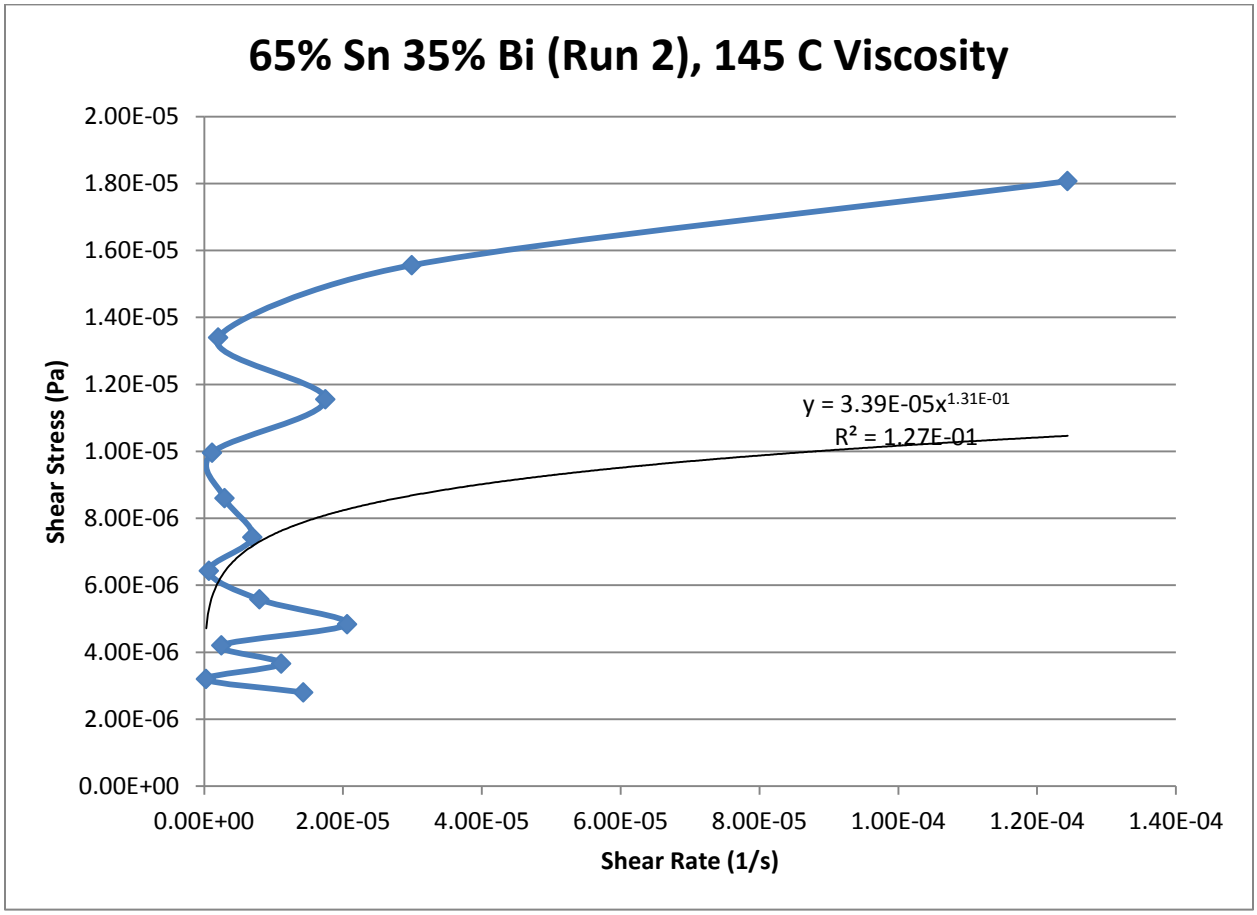

Figure 264- 65% Sn 35% Bi (Run 2), 145 C, Cone and Plate Viscosity

147.5 C

Fraction Solid	4.92 %
Power Law	$\tau = 3.44 * 10^{-4} * \dot{\gamma}^{0.3810}$
	$\mu = 1.31 * 10^{-4} * \dot{\gamma}^{-0.6190}$
R^2	48.50 %

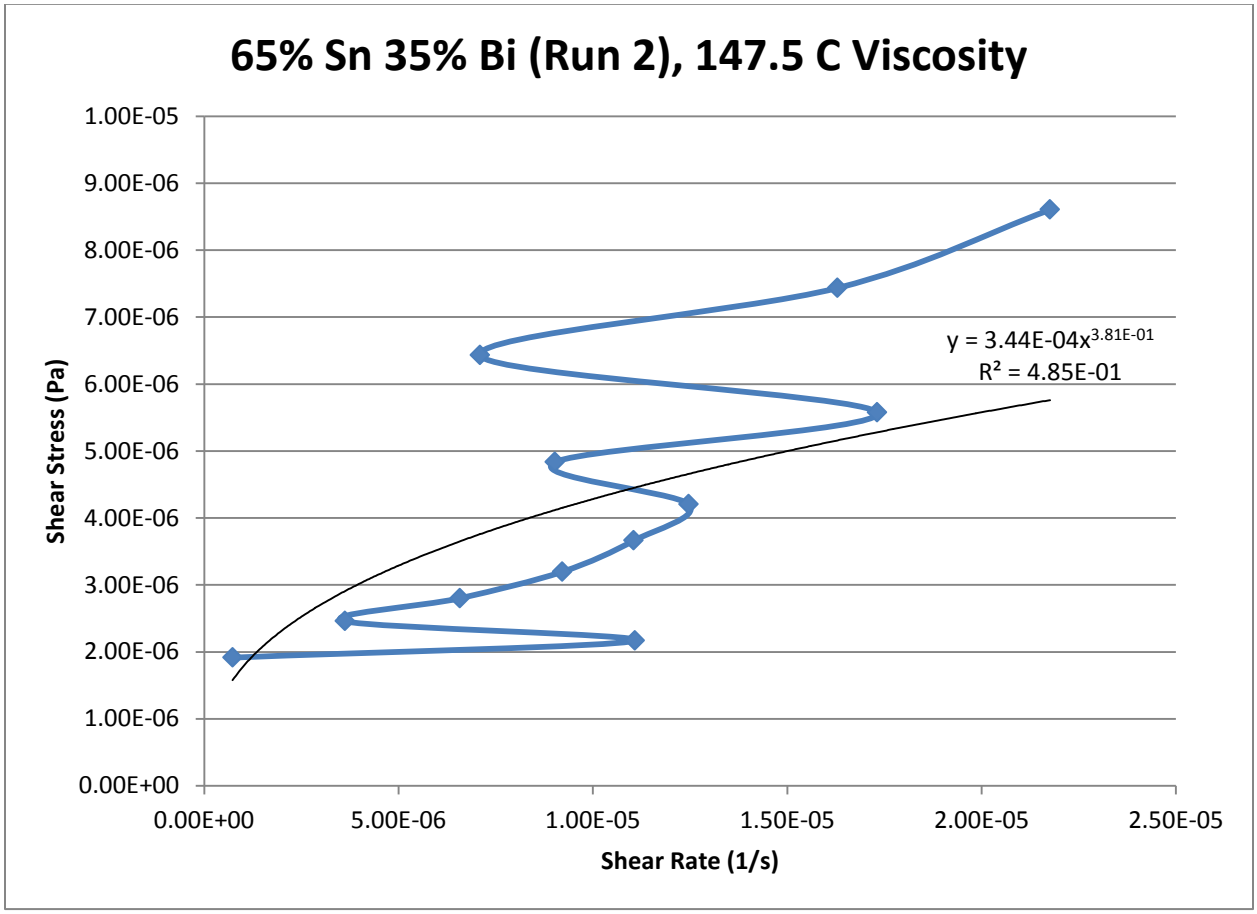

Figure 265- 65% Sn 35% Bi (Run 2), 147.5 C, Cone and Plate Viscosity

150 C

Fraction Solid	3.33 %
Power Law	$\tau = 8.42 * 10^{-6} * \dot{\gamma}^{0.1176}$
	$\mu = 9.90 * 10^{-7} * \dot{\gamma}^{-0.8824}$
R^2	1.69 %

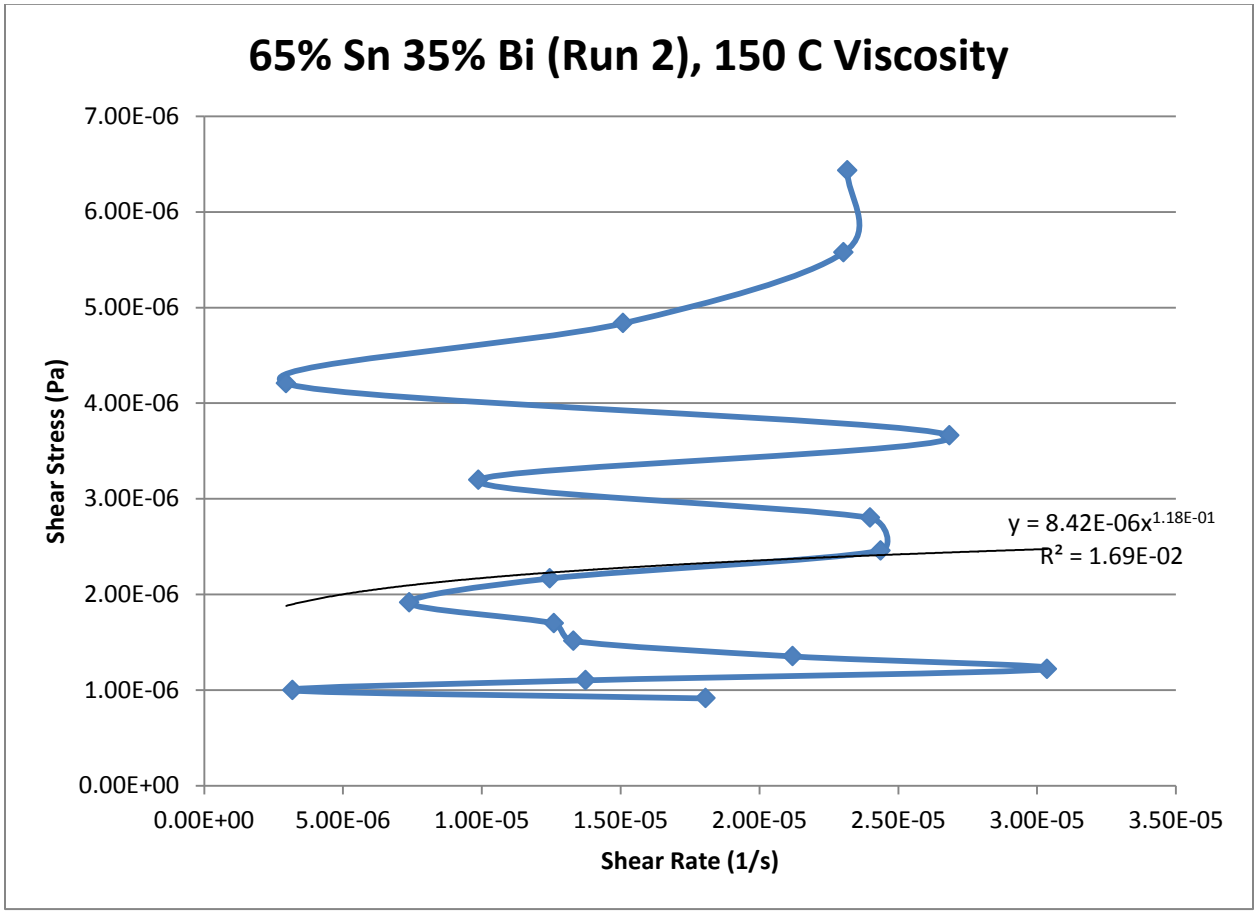

Figure 266- 65% Sn 35% Bi (Run 2), 150 C, Cone and Plate Viscosity

70% Tin 30% Bismuth (Run 1)

Actual Composition: 71.83% Sn, 28.17% Bi

Theoretical Solidus Line: 139 C
Theoretical Liquidus Line: 171.1 C

Experimental Solidus Line: 137.4 C
Experimental Liquidus Line: 169.9 C

Set-Up Notes

- The stage was heated to 200 Celsius and the metal pieces were melted underneath the cone. The cone was then lowered to the geometry gap.

- During the experiment, I started with the lower temperatures because of past runs where a small amount of material slipped from underneath the cone at higher temperatures. The first stress sweep was run at 145 C and each subsequent sweep was at 5 C more than its predecessor.

Plots

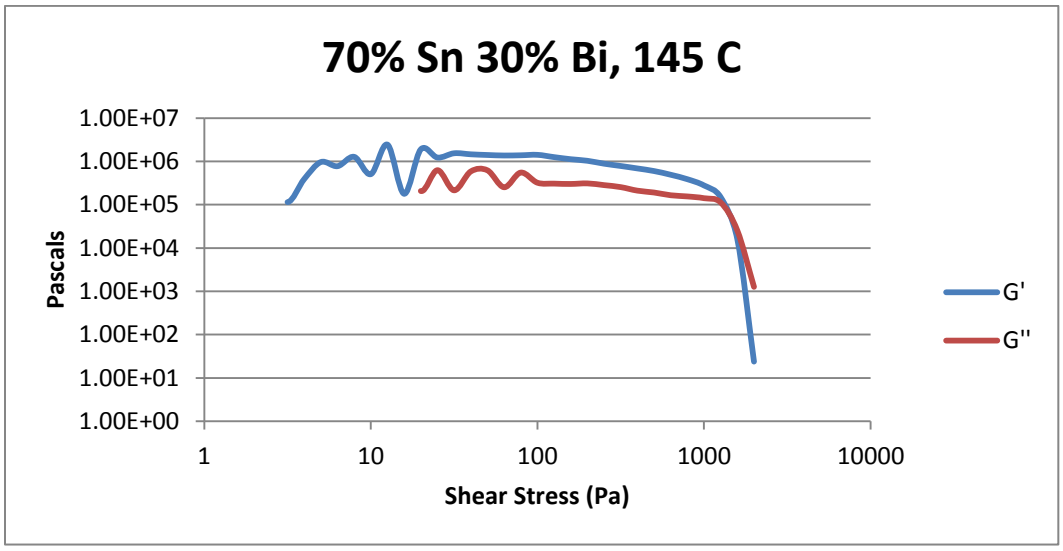

Figure 267- 70% Sn 30% Bi (Run 1), 145 C, Cone and Plate Stress Sweep

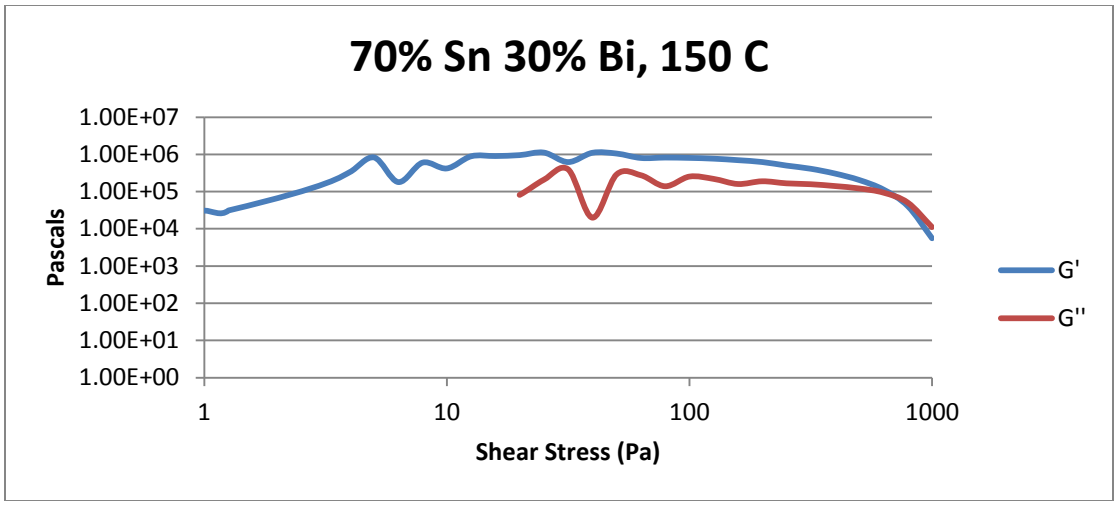

Figure 268- 70% Sn 30% Bi (Run 1), 150 C, Cone and Plate Stress Sweep

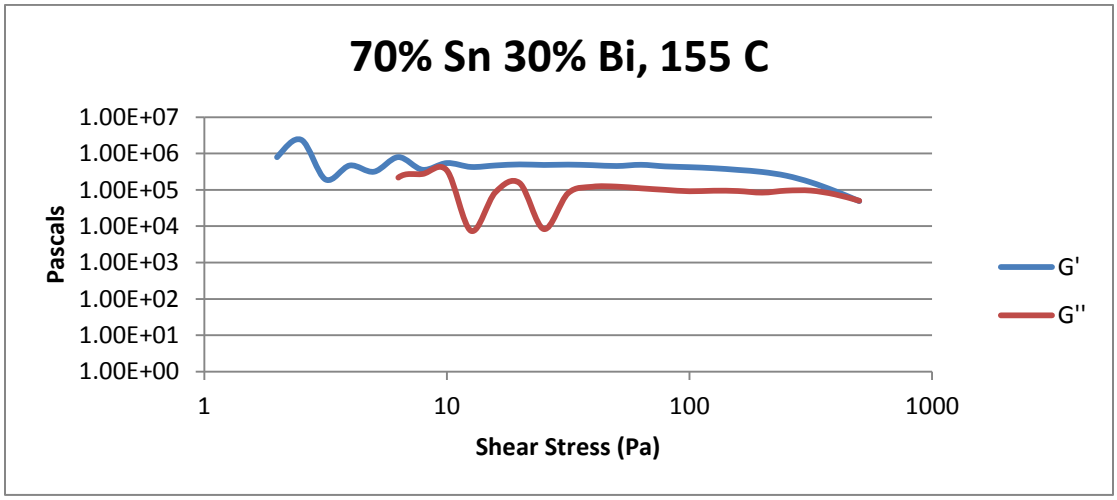

Figure 269- 70% Sn 30% Bi (Run 1), 155 C, Cone and Plate Stress Sweep

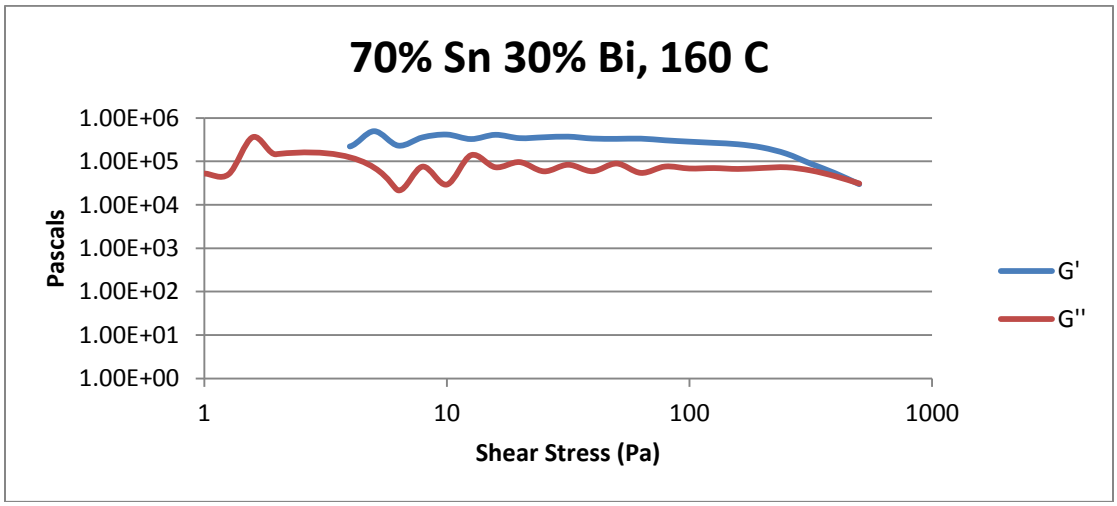

Figure 270- 70% Sn 30% Bi (Run 1), 160 C, Cone and Plate Stress Sweep

Temperature	Crossover Stress (Pa)	Crossover Stress (PSI)
145 C	$9.34 * 10^4$	13.5
150 C	$8.03 * 10^4$	11.6
155 C	$6.25 * 10^4$	9.06
160 C	$4.08 * 10^4$	5.92

Table 50- 70% Sn 30% Bi (Run 1), Cone and Plate Crossover Stresses

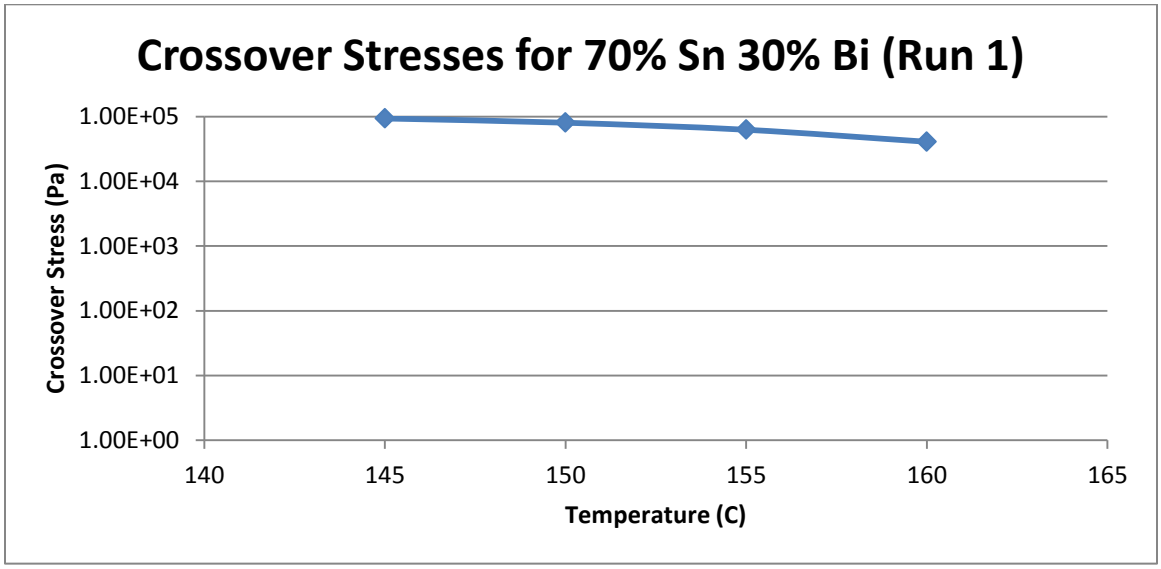

Figure 271- 70% Sn 30% Bi (Run 1), Cone and Plate Crossover Stresses

Temperature	Fraction Solid (At %)	G' Plateau (Pa)	G'' Plateau (Pa)
145 C	22.2	$1.40 * 10^6$	$2.90 * 10^5$
150 C	16.7	$9.19 * 10^5$	$1.90* 10^5$
155 C	10.4	$4.81 * 10^5$	$9.34 * 10^4$
160 C	3.25	$3.46 * 10^5$	$6.90 * 10^4$
165 C	0	$2.60 * 10^5$	$5.70 * 10^4$

Table 51- 70% Sn 30% Bi (Run 1), Cone and Plate Plateau Stresses

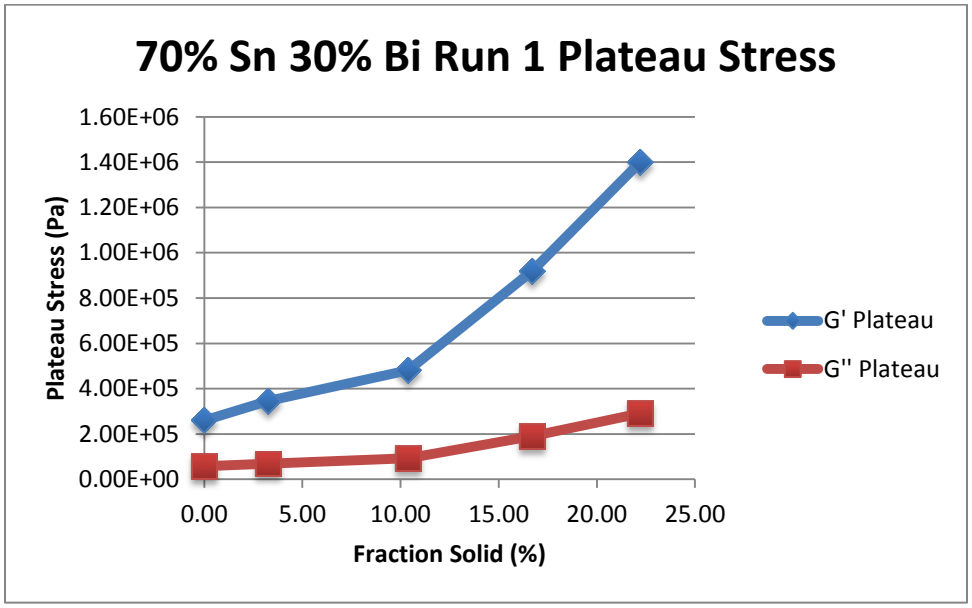

Figure 272- 70% Sn 30% Bi (Run 1), Cone and Plate Plateau Stresses vs. Fraction Solid

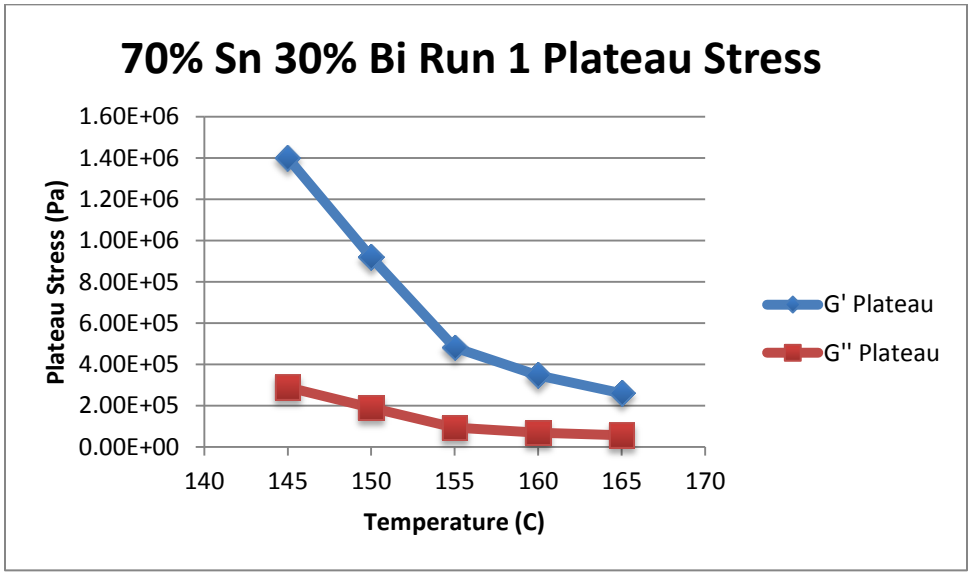

Figure 273- 70% Sn 30% Bi (Run 1), Cone and Plate Plateau Stresses vs. Temperature

70% Sn 30% Bi (Run 1) Viscosity					
Temperature	**Fraction Solid**	**Power Law**	**K**	**n**	**R^2**
145 C	22.2 %	$\tau = 7.95 * 10^{-4} * \dot{\gamma}^{0.2504}$ $\mu = 1.99 * 10^{-4} * \dot{\gamma}^{-0.7496}$	$7.95 * 10^{-4}$ Pa*s	0.2504	53.6 %
150 C	16.7 %	$\tau = 3.01 * 10^{-4} * \dot{\gamma}^{0.213}$ $\mu = 6.41 * 10^{-5} * \dot{\gamma}^{-0.7870}$	$3.01 * 10^{-4}$ Pa*s	0.213	73.87 %
155 C	10.4 %	$\tau = 4.30 * 10^{-4} * \dot{\gamma}^{0.3099}$ $\mu = 1.33 * 10^{-4} * \dot{\gamma}^{-0.6901}$	$4.30 * 10^{-4}$ Pa*s	0.3099	84.88 %
160 C	3.25 %	$\tau = 4.58 * 10^{-4} * \dot{\gamma}^{0.3567}$ $\mu = 1.63 * 10^{-4} * \dot{\gamma}^{-0.6433}$	$4.58 * 10^{-4}$ Pa*s	0.3567	83.67 %

Table 52- 70% Sn 30% Bi (Run 1), Cone and Plate Viscosity

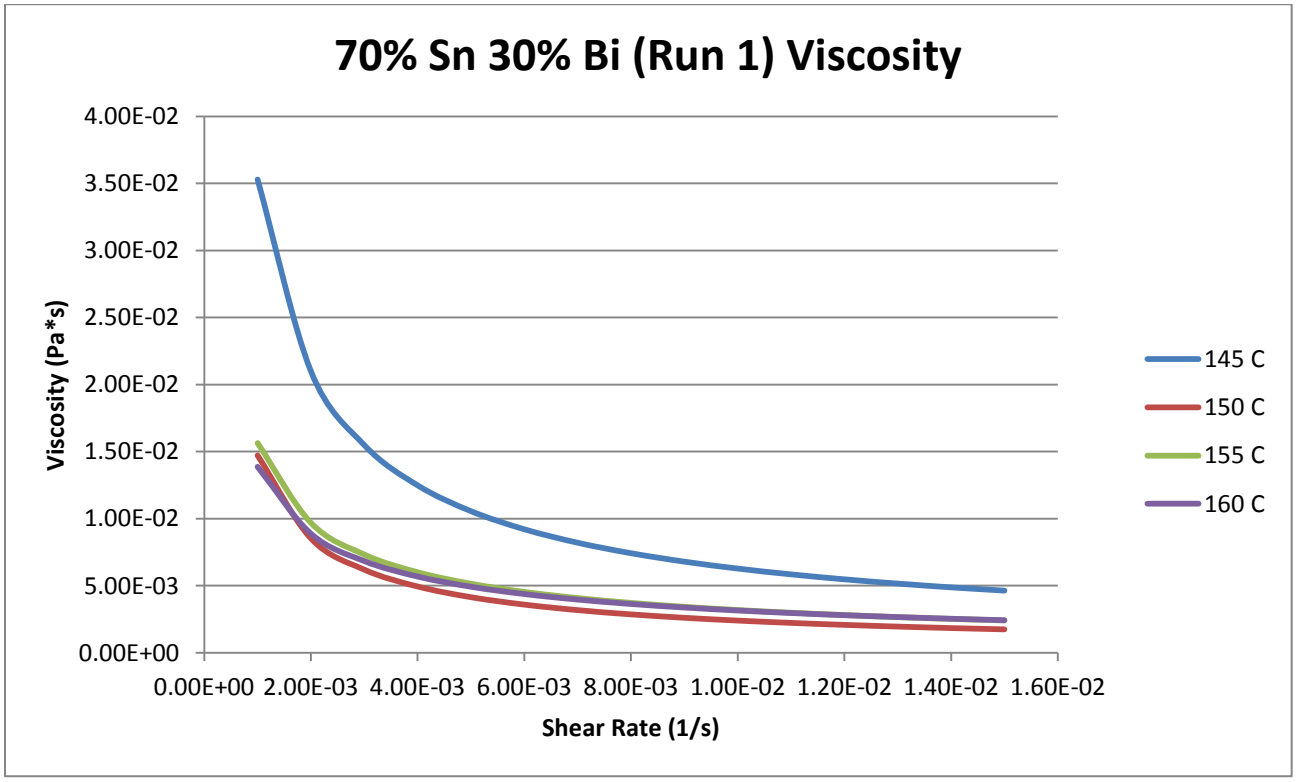

Figure 274- 70% Sn 30% Bi (Run 1), Cone and Plate Viscosity

145 C

Fraction Solid	22.2 %
Power Law	$\tau = 7.95 * 10^{-4} * \dot{\gamma}^{0.2504}$
	$\mu = 1.99 * 10^{-4} * \dot{\gamma}^{-0.7496}$
R^2	53.6 %

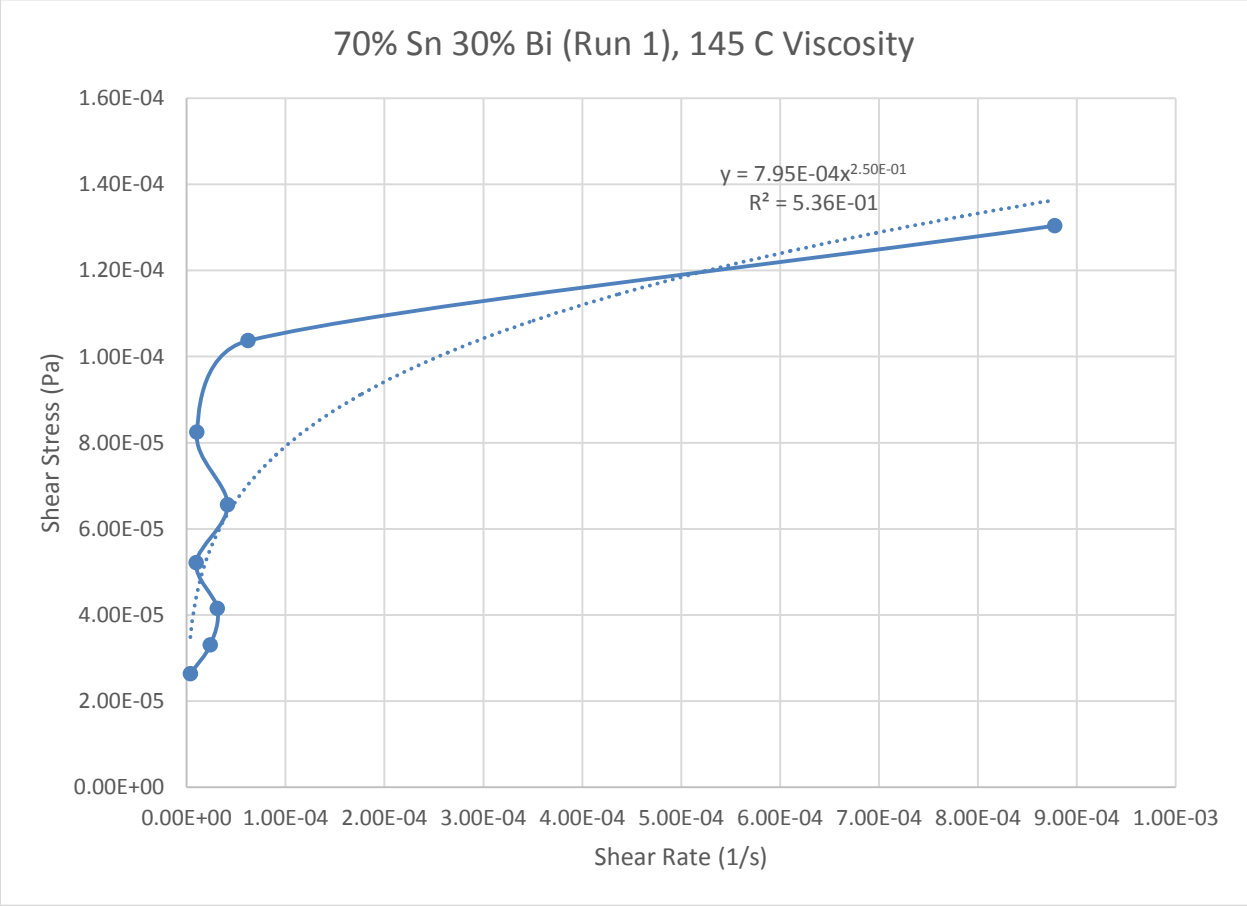

Figure 275- 70% Sn 30% Bi (Run 1), 145 C, Cone and Plate Viscosity

150 C

Fraction Solid	16.7 %
Power Law	$\tau = 3.01 * 10^{-4} * \dot{\gamma}^{0.213}$
	$\mu = 6.41 * 10^{-5} * \dot{\gamma}^{-0.7870}$
R^2	73.87 %

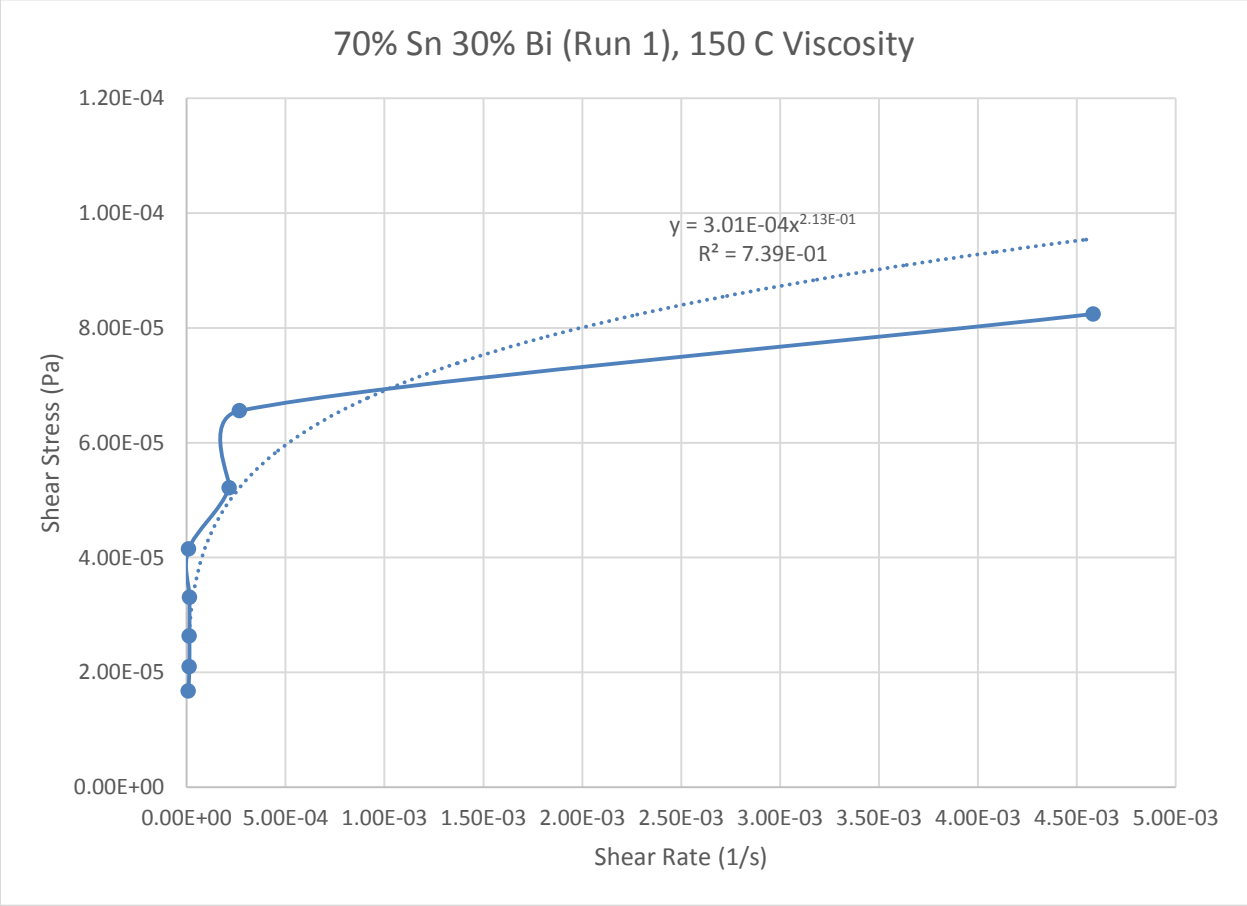

Figure 276- 70% Sn 30% Bi (Run 1), 150 C, Cone and Plate Viscosity

155 C

Fraction Solid	10.4 %
Power Law	$\tau = 4.30 * 10^{-4} * \dot{\gamma}^{0.3099}$
	$\mu = 1.33 * 10^{-4} * \dot{\gamma}^{-0.6901}$
R^2	84.88 %

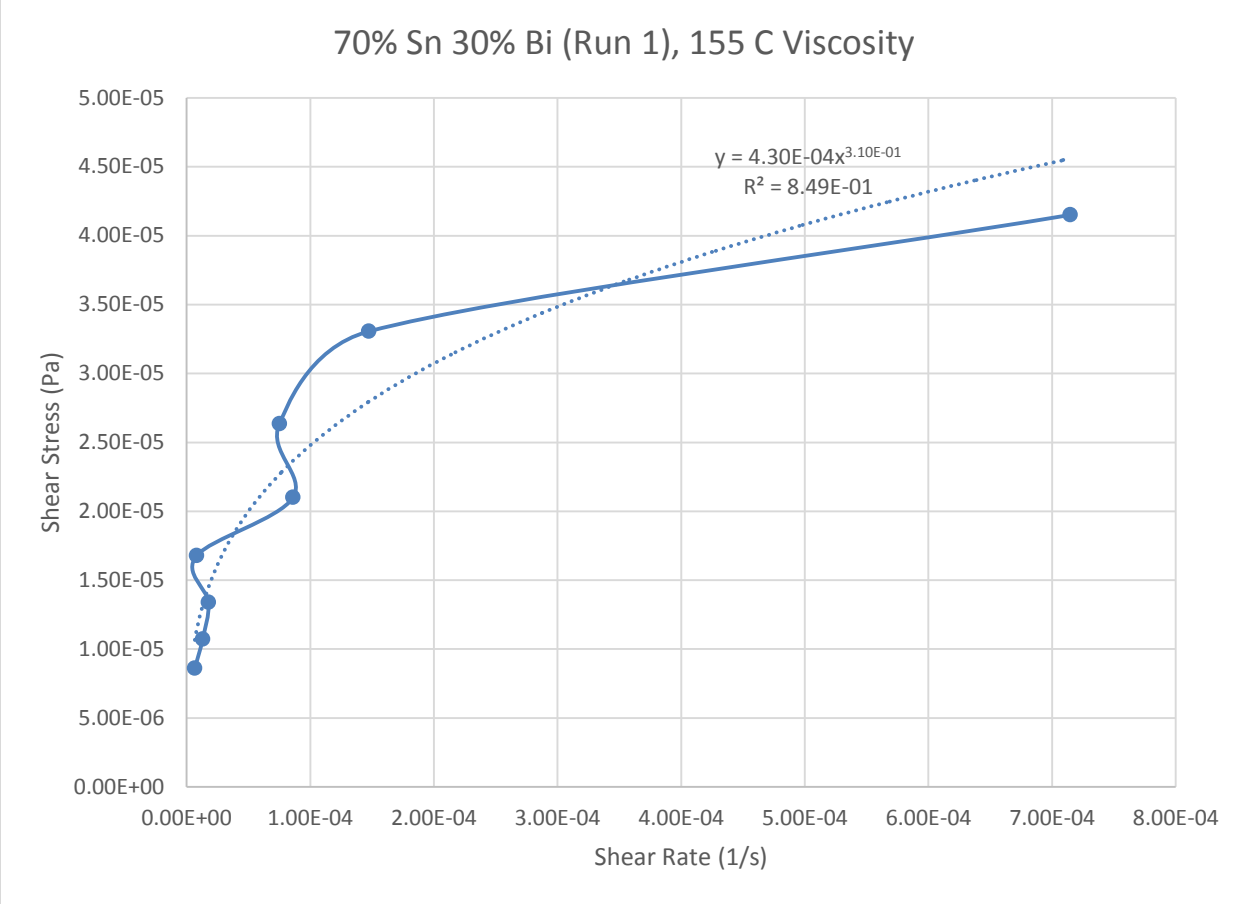

Figure 277- 70% Sn 30% Bi (Run 1), 155 C, Cone and Plate Viscosity

160 C

Fraction Solid	3.25 %
Power Law	$\tau = 4.58 * 10^{-4} * \dot{\gamma}^{0.3567}$
	$\mu = 1.63 * 10^{-4} * \dot{\gamma}^{-0.6433}$
R^2	83.67 %

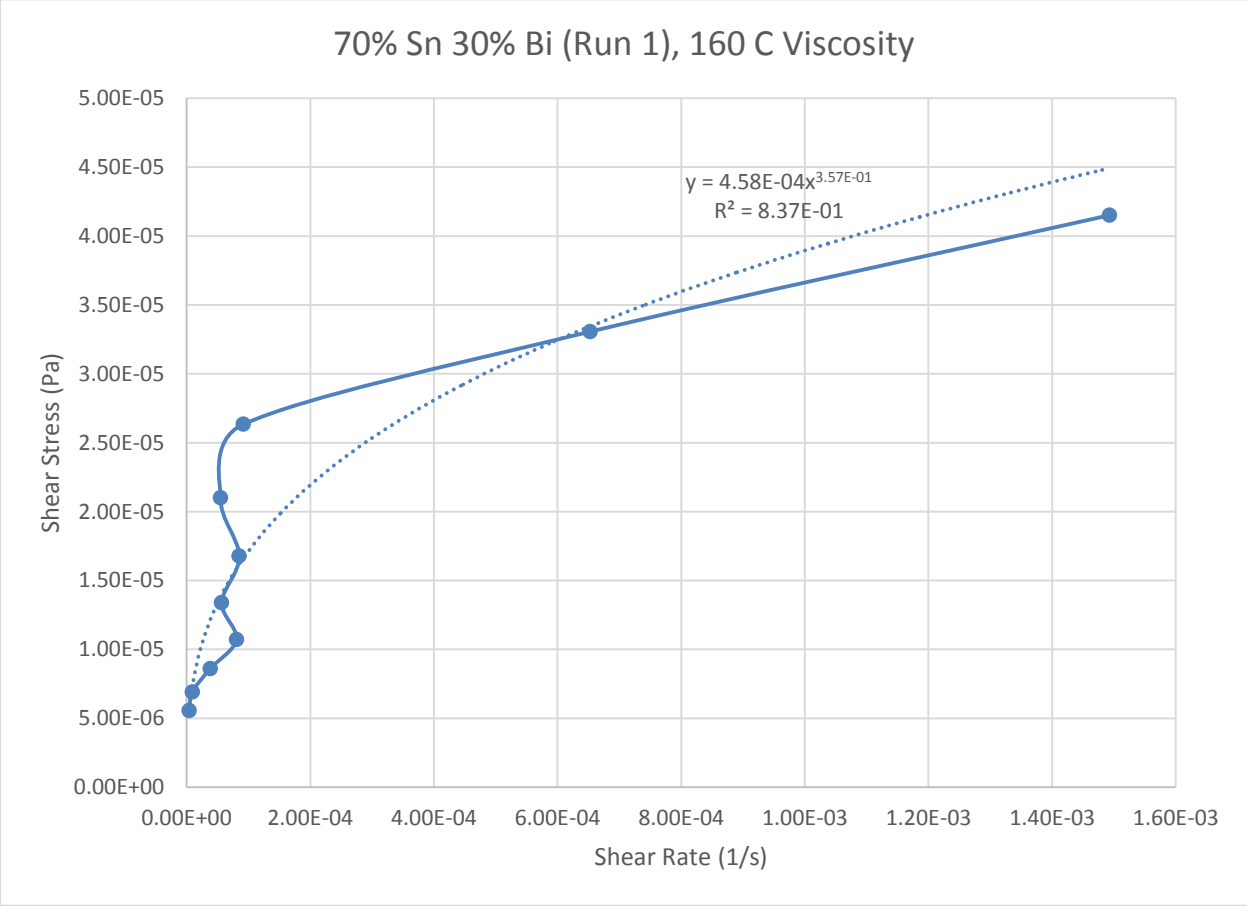

Figure 278- 70% Sn 30% Bi (Run 1), 160 C, Cone and Plate Viscosity

70% Tin 30% Bismuth (Run 2)

Actual Composition: 71.83% Sn, 28.17% Bi

Theoretical Solidus Line: 139 C
Theoretical Liquidus Line: 171.1 C

Experimental Solidus Line: 137.4 C
Experimental Liquidus Line: 169.9 C

Set-Up Notes

- Zeroed gap at 155 C. Stress sweeps were conducted from 155 C in decreasing increments of 5 C. Then a final stress sweep was conducted at 160 C.

- Exhibited same behavior as the previous 70% Sn 30% Bi run.

Plots

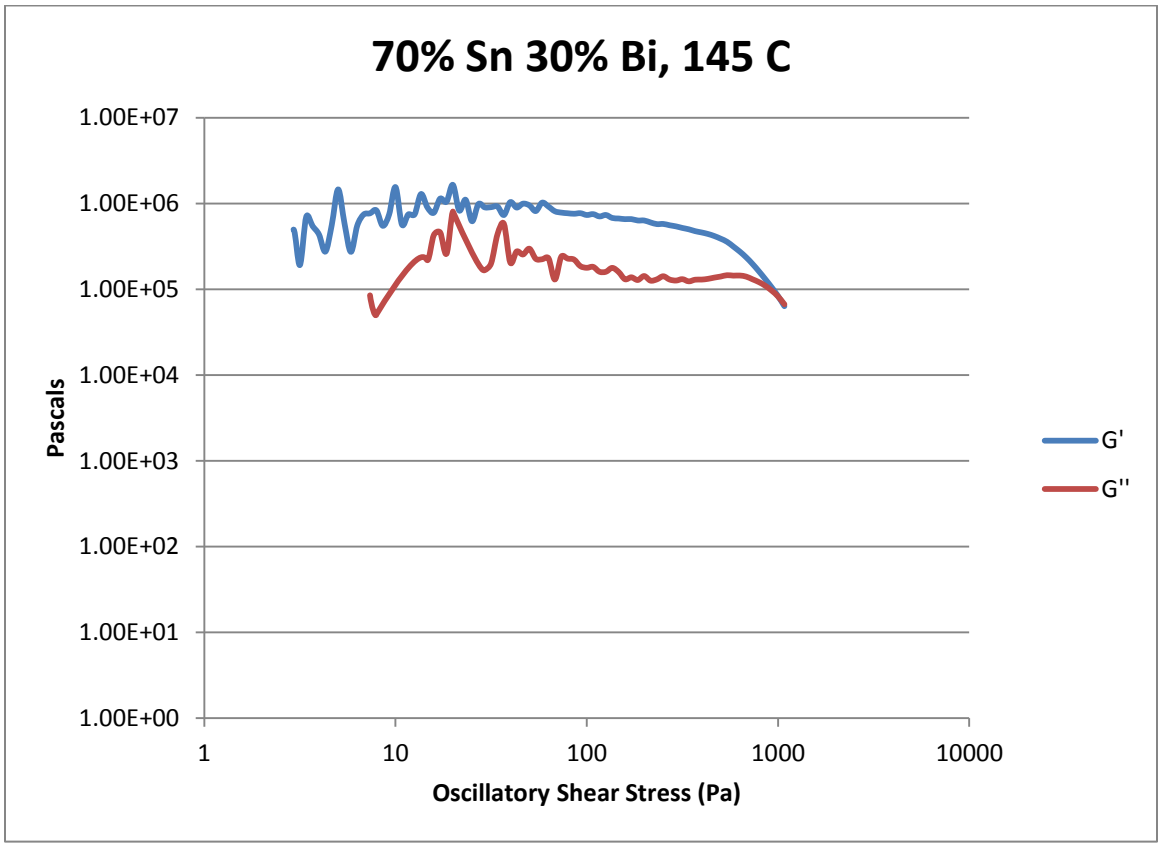

Figure 279- 70% Sn 30% Bi (Run 2), 145 C, Cone and Plate Stress Sweep

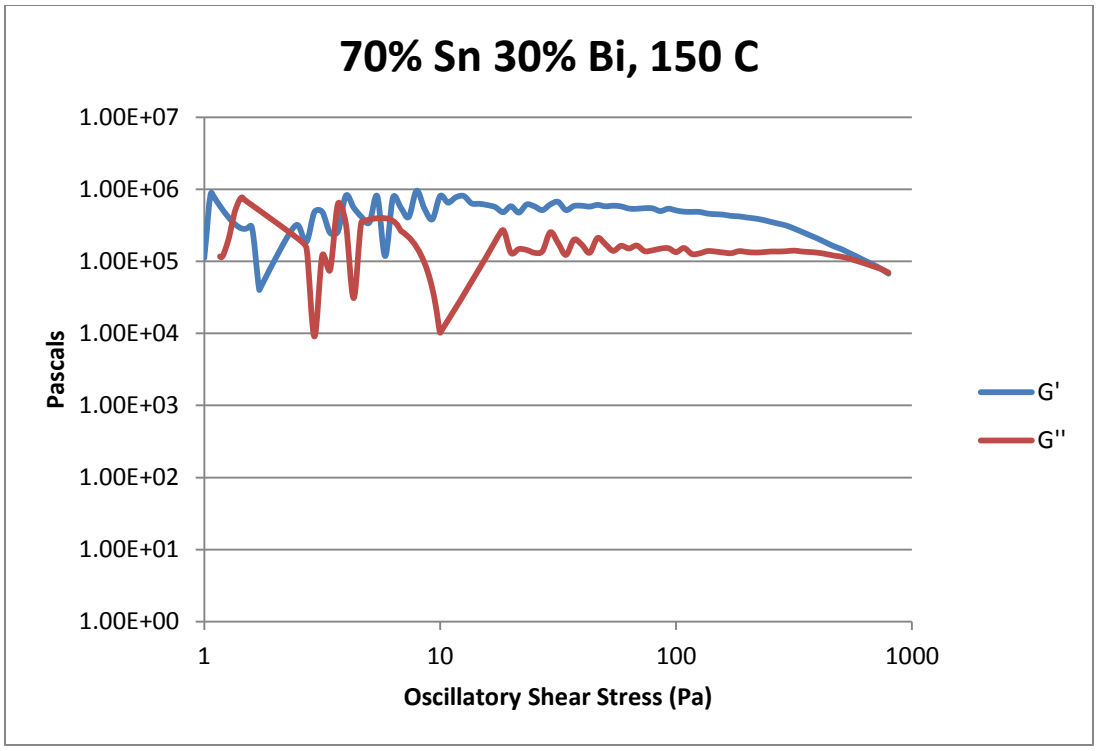

Figure 280- 70% Sn 30% Bi (Run 2), 150 C, Cone and Plate Stress Sweep

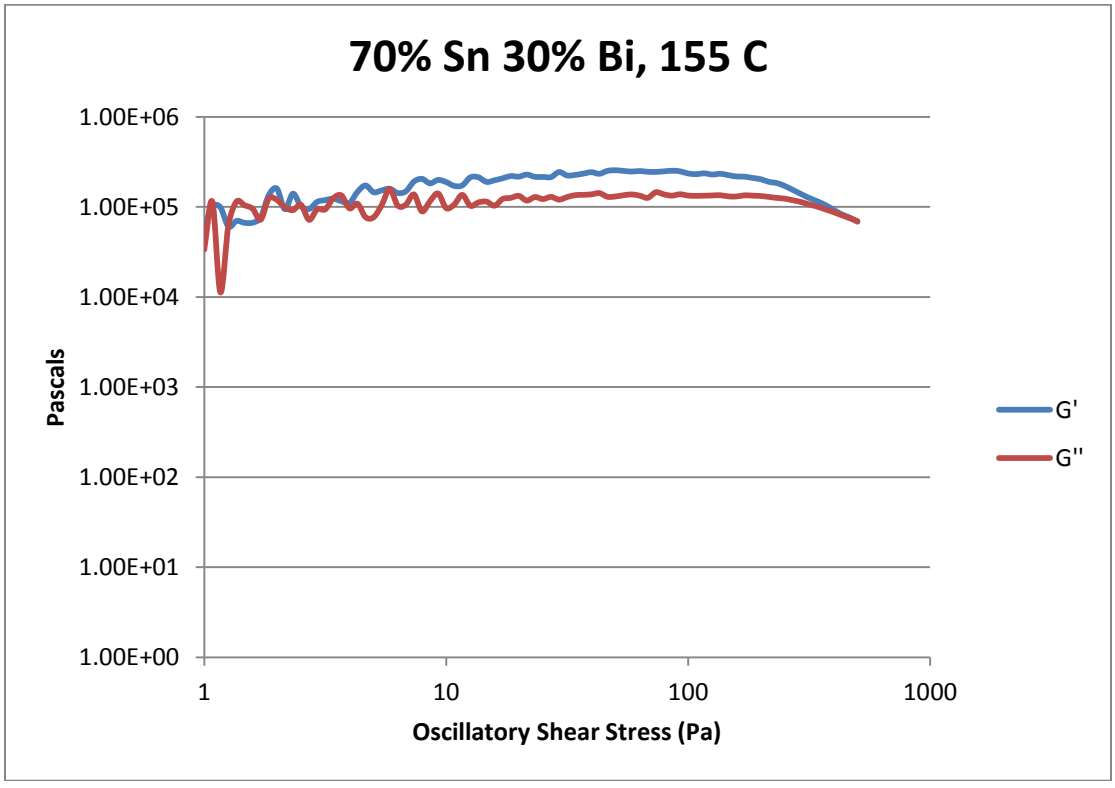

Figure 281- 70% Sn 30% Bi (Run 2), 155 C, Cone and Plate Stress Sweep

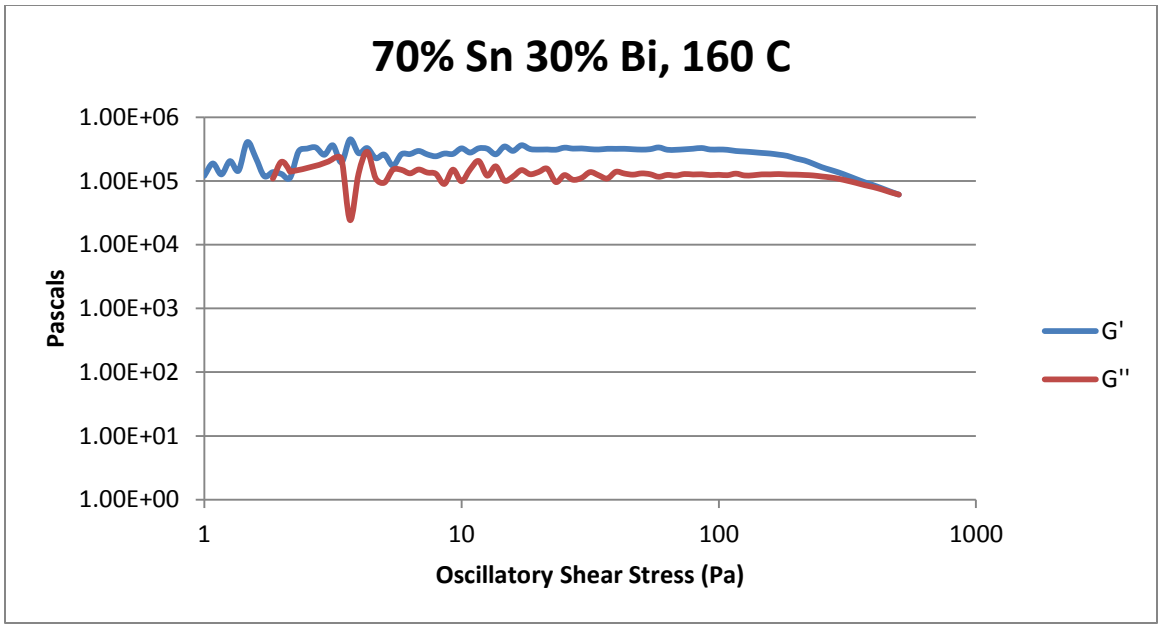

Figure 282- 70% Sn 30% Bi (Run 2), 160 C, Cone and Plate Stress Sweep

Temperature	Crossover Stress (Pa)	Crossover Stress (PSI)
145 C	$7.93 * 10^4$	11.5
150 C	$7.71 * 10^4$	11.2
155 C	$7.22 * 10^4$	10.5
160 C	$6.16 * 10^4$	8.93

Table 53- 70% Sn 30% Bi (Run 2), Cone and Plate Crossover Stresses

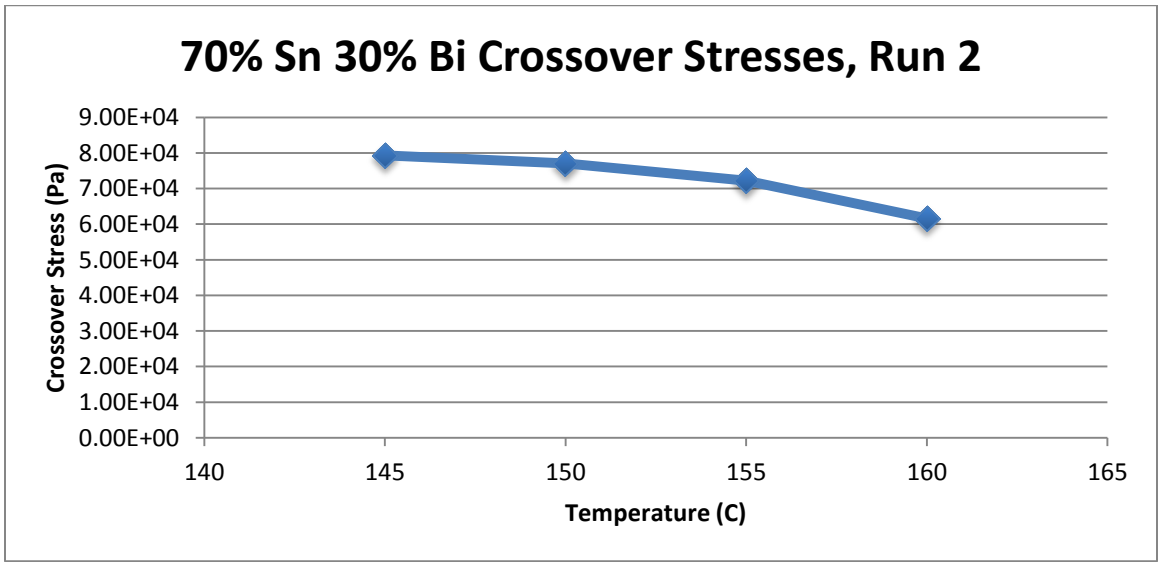

Figure 283- 70% Sn 30% Bi (Run 2), Cone and Plate Crossover Stresses

Temperature	Fraction Solid (At %)	G' Plateau (Pa)	G'' Plateau (Pa)
145 C	22.2	$7.81 * 10^5$	$1.30 * 10^5$
150 C	16.7	$5.87 * 10^5$	$1.36* 10^5$
155 C	10.4	$2.49 * 10^5$	$1.33 * 10^5$
160 C	3.25	$3.17 * 10^5$	$1.25 * 10^5$

Table 54- 70% Sn 30% Bi (Run 2), Cone and Plate Plateau Stresses

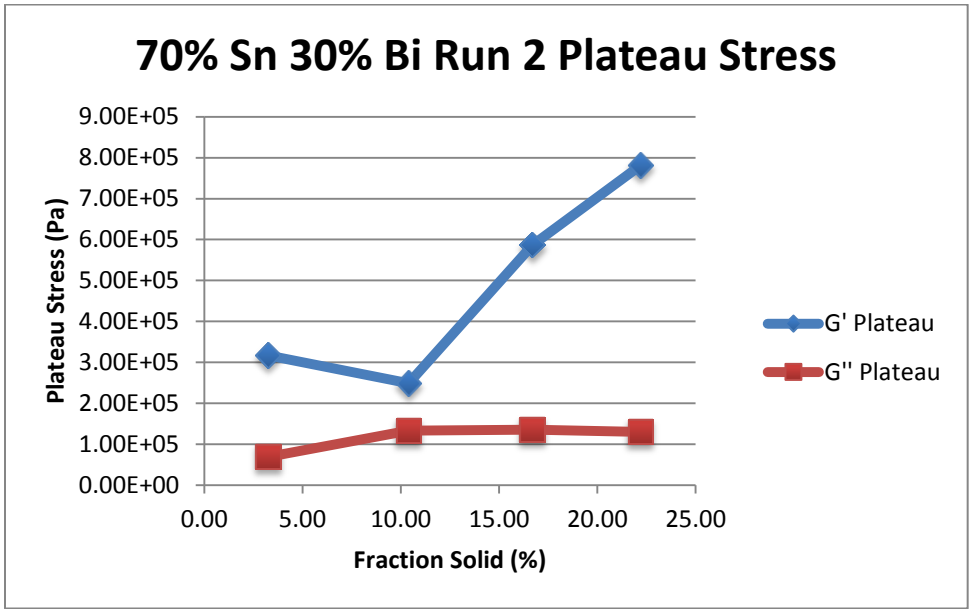

Figure 284- 70% Sn 30% Bi (Run 2), Cone and Plate Plateau Stresses vs. Fraction Solid

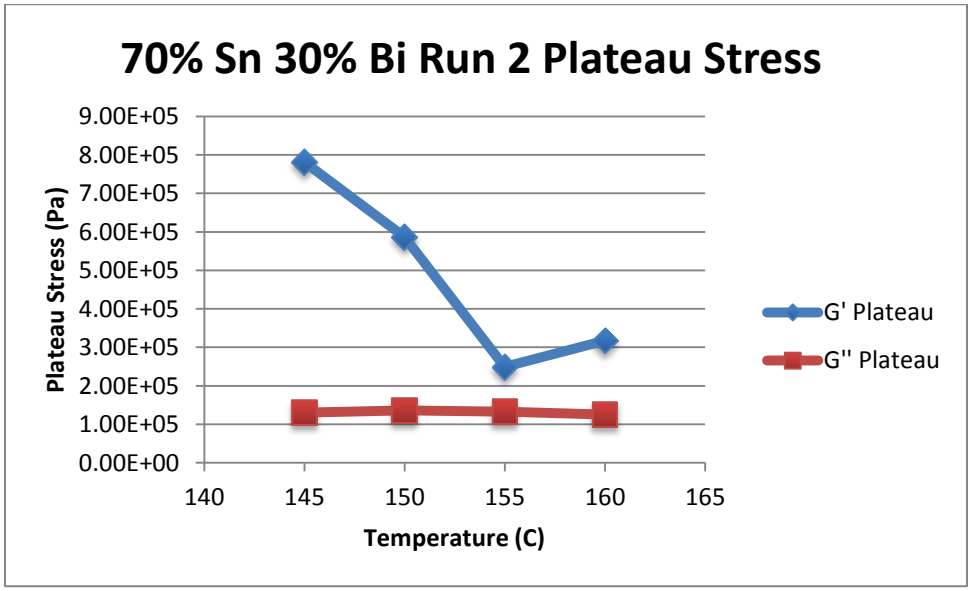

Figure 285- 70% Sn 30% Bi (Run 2), Cone and Plate Plateau Stresses vs. Temperature

70% Sn 30% Bi (Run 2) Viscosity					
Temperature	**Fraction Solid**	**Power Law**	**K**	**n**	**R^2**
145 C	22.2 %	$\tau = 3.82 * 10^{-4} * \dot{\gamma}^{0.2333}$ $\mu = 8.91 * 10^{-5} * \dot{\gamma}^{-0.7667}$	$3.82 * 10^{-4}$ Pa*s	0.2333	90.63 %
150 C	16.7 %	$\tau = 6.65 * 10^{-4} * \dot{\gamma}^{0.3497}$ $\mu = 2.33 * 10^{-4} * \dot{\gamma}^{-0.6503}$	$6.65 * 10^{-4}$ Pa*s	0.3497	98.29 %
155 C	10.4 %	$\tau = 3.32 * 10^{-3} * \dot{\gamma}^{0.6145}$ $\mu = 2.04 * 10^{-3} * \dot{\gamma}^{-0.3855}$	$3.32 * 10^{-3}$ Pa*s	0.6145	95.27 %
160 C	3.25 %	$\tau = 4.30 * 10^{-4} * \dot{\gamma}^{0.3283}$ $\mu = 1.41 * 10^{-4} * \dot{\gamma}^{-0.6717}$	$4.30 * 10^{-4}$ Pa*s	0.3283	96.13 %

Table 55- 70% Sn 30% Bi (Run 2), Cone and Plate Viscosity

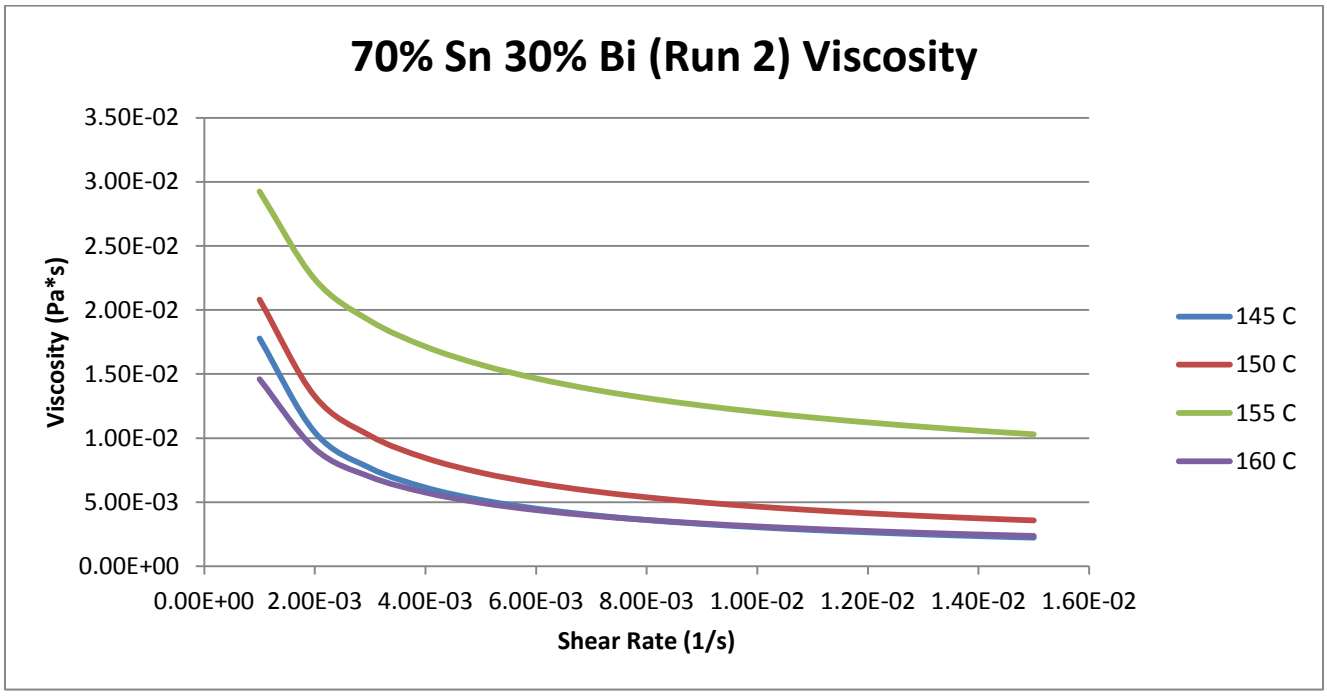

Figure 286- 70% Sn 30% Bi (Run 2), Cone and Plate Viscosity

145 C

Fraction Solid	22.2 %
Power Law	$\tau = 3.82 * 10^{-4} * \dot{\gamma}^{0.2333}$
	$\mu = 8.91 * 10^{-5} * \dot{\gamma}^{-0.7667}$
R^2	90.63 %

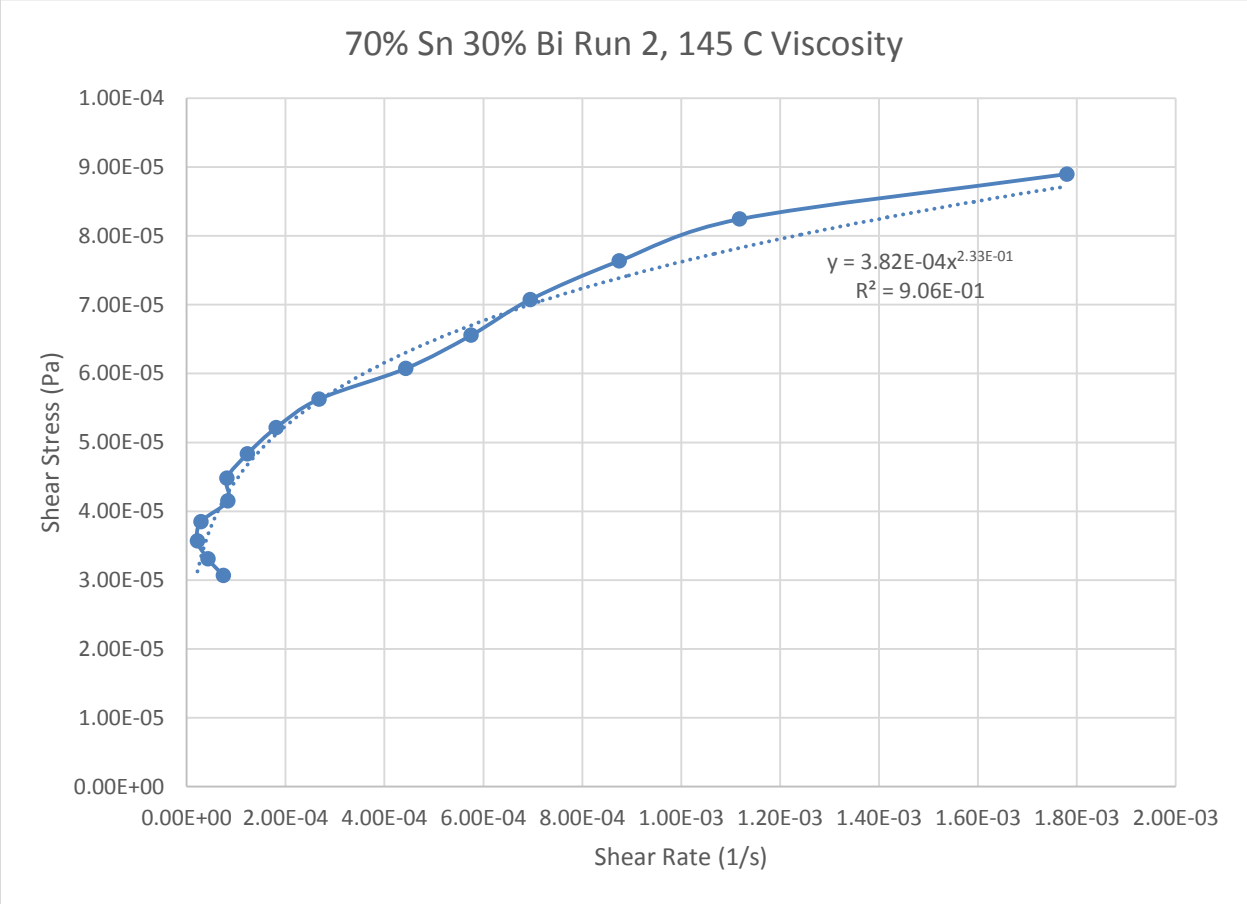

Figure 287- 70% Sn 30% Bi (Run 2), 145 C, Cone and Plate Viscosity

150 C

Fraction Solid	16.7 %
Power Law	$\tau = 6.65 * 10^{-4} * \dot{\gamma}^{0.3497}$
	$\mu = 2.33 * 10^{-4} * \dot{\gamma}^{-0.6503}$
R^2	98.29 %

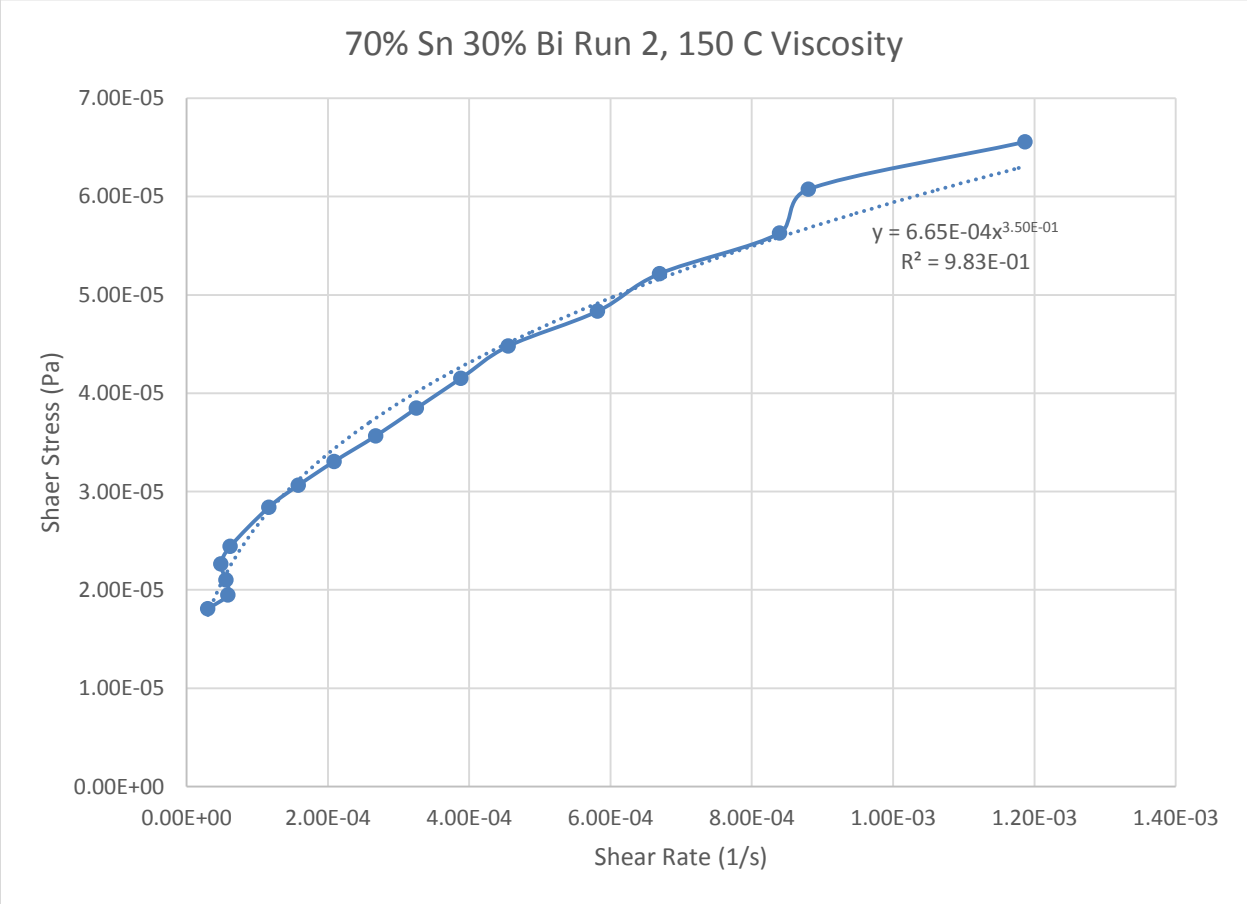

Figure 288- 70% Sn 30% Bi (Run 2), 150 C, Cone and Plate Viscosity

155 C

Fraction Solid	10.4 %
Power Law	$\tau = 3.32 * 10^{-3} * \dot{\gamma}^{0.6145}$
	$\mu = 2.04 * 10^{-3} * \dot{\gamma}^{-0.3855}$
R^2	95.27 %

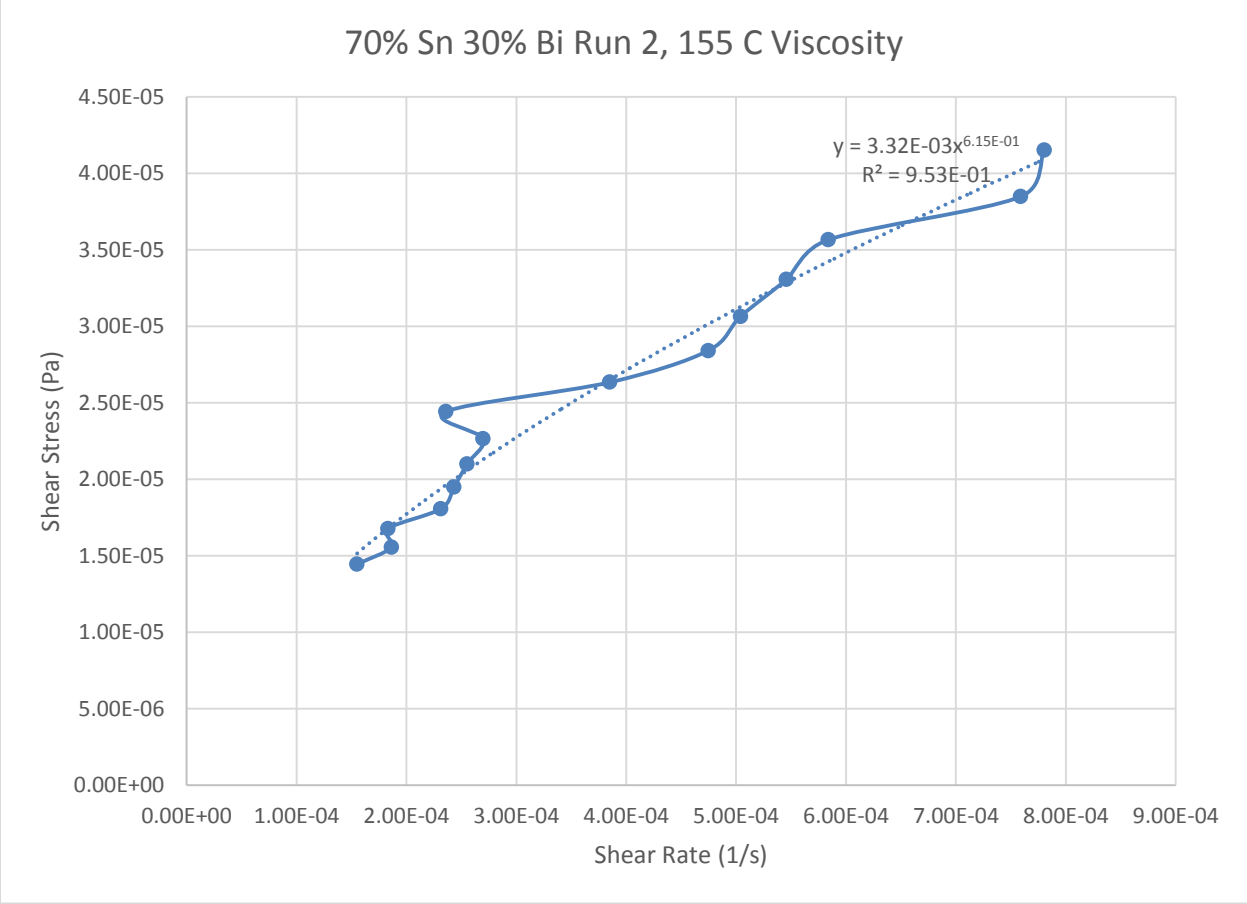

Figure 289- 70% Sn 30% Bi (Run 2), 155 C, Cone and Plate Viscosity

160 C

Fraction Solid	3.25 %
Power Law	$\tau = 4.30 * 10^{-4} * \dot{\gamma}^{0.3283}$
	$\mu = 1.41 * 10^{-4} * \dot{\gamma}^{-0.6717}$
R^2	96.13 %

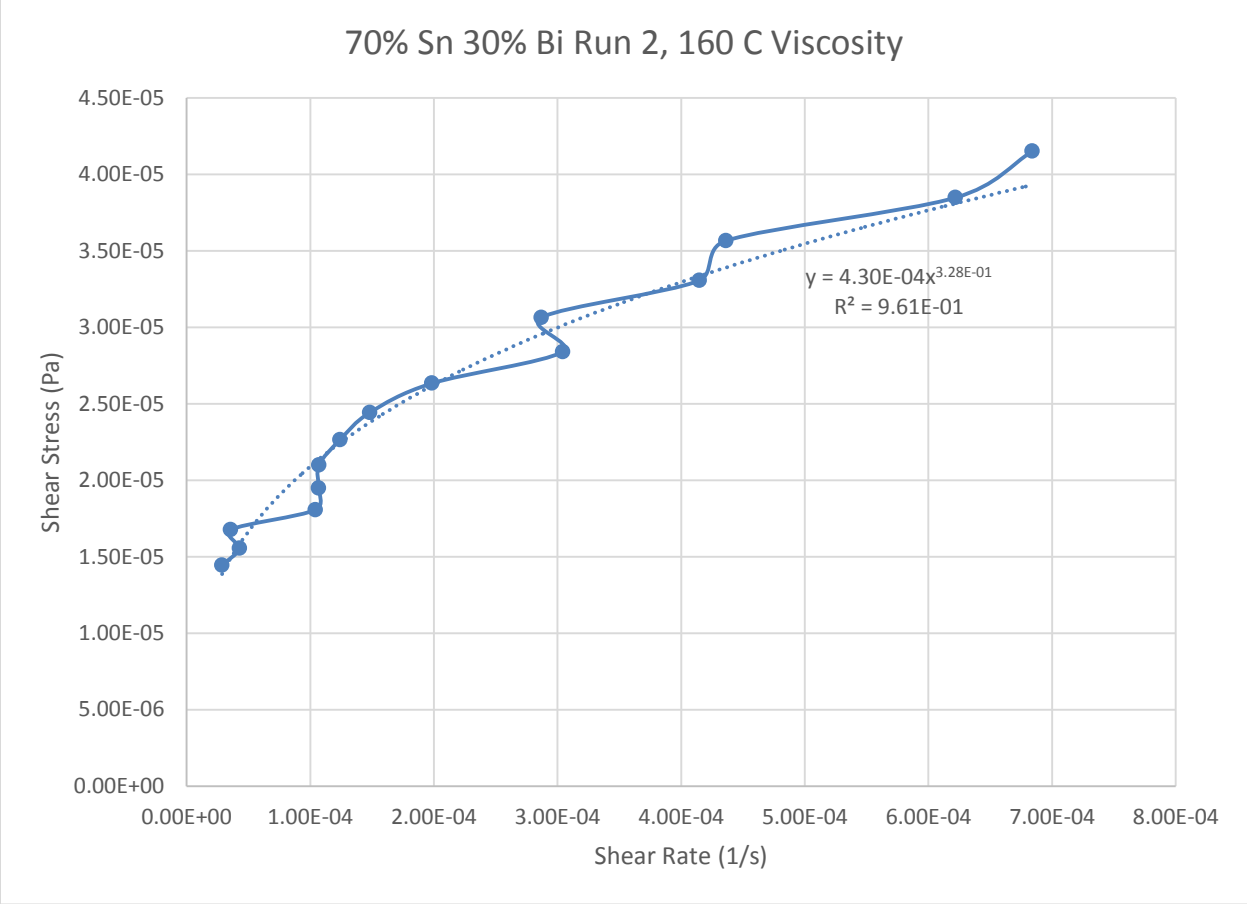

Figure 290- 70% Sn 30% Bi (Run 2), 160 C, Cone and Plate Viscosity

75% Tin 25% Bismuth (Run 1)

Predicted Composition: 75% Tin, 25% Bismuth

Theoretical Solidus Line: 139 C
Theoretical Liquidus Line: 182.2 C

Experimental Solidus Line: 138.9 C
Experimental Liquidus Line: 183.5 C

Set-Up Notes

- Zeroed gap at 160 C. Ran stress sweeps from 160 C to 145 C in decreasing intervals of 5 C. The temperature was then raised to 165 C and 170 C for the final two stress sweeps.

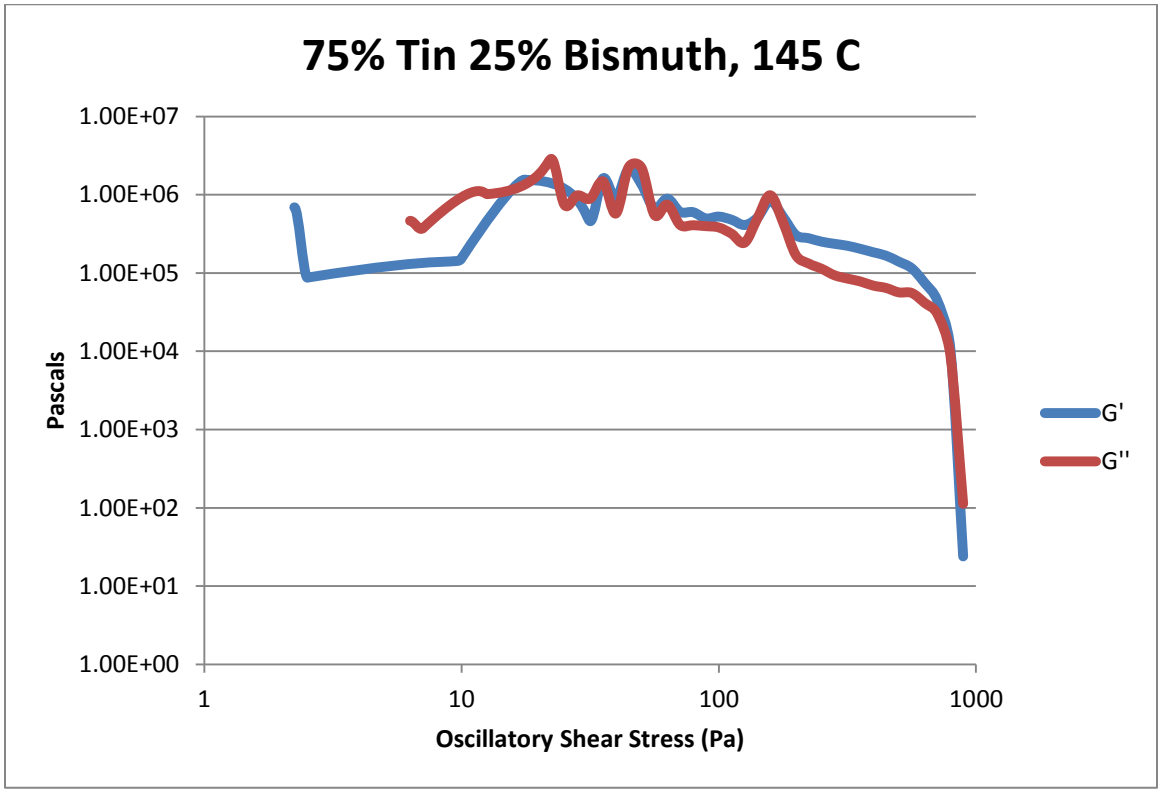

Figure 291- 75% Sn 25% Bi (Run 1), 145 C, Cone and Plate Stress Sweep

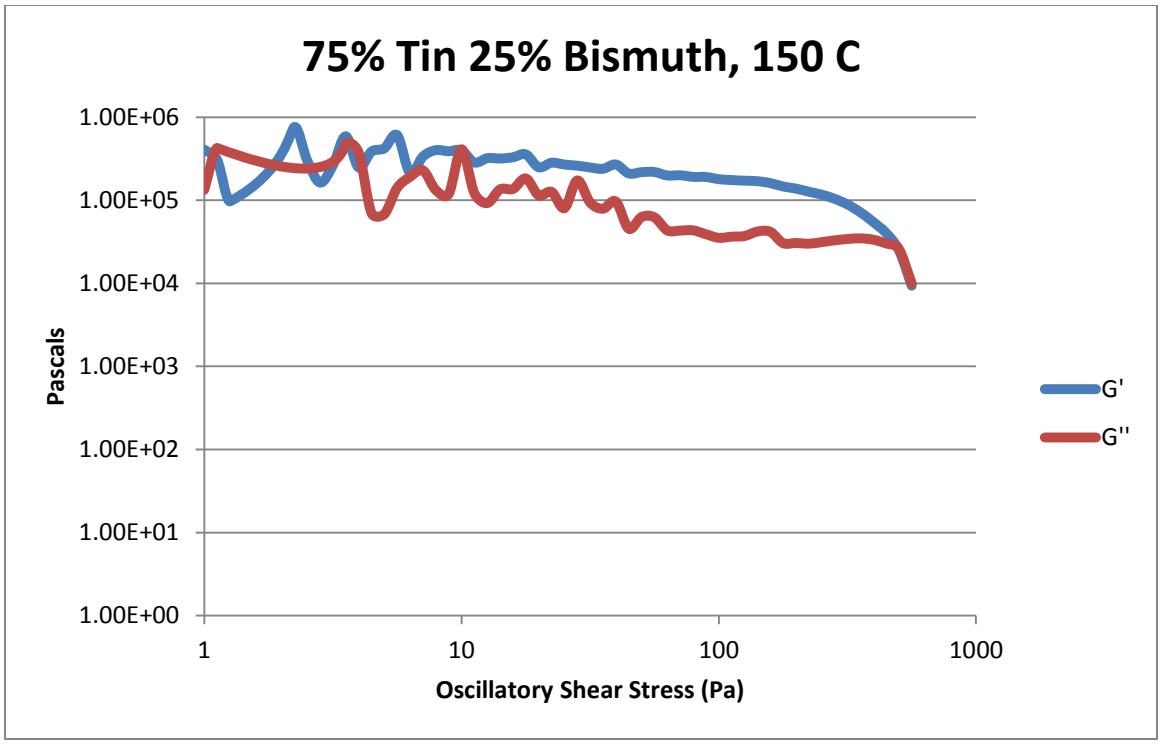

Figure 292- 75% Sn 25% Bi (Run 1), 150 C, Cone and Plate Stress Sweep

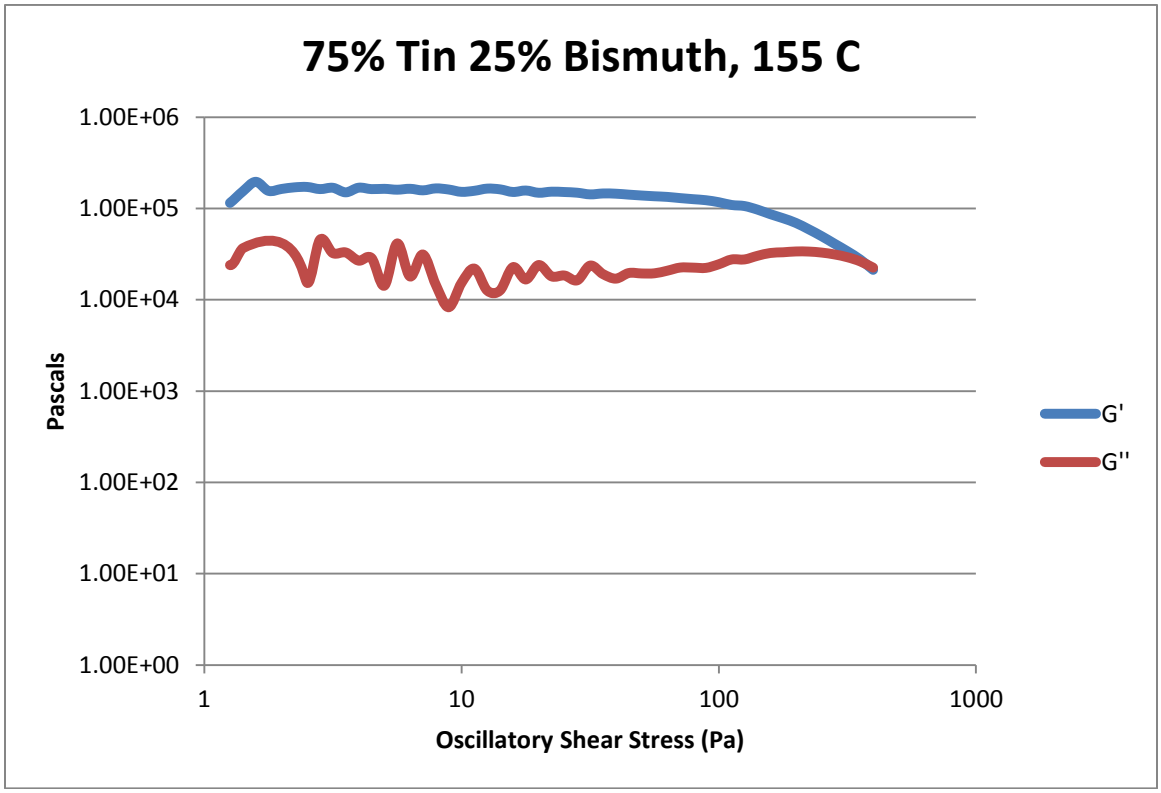

Figure 293- 75% Sn 25% Bi (Run 1), 155 C, Cone and Plate Stress Sweep

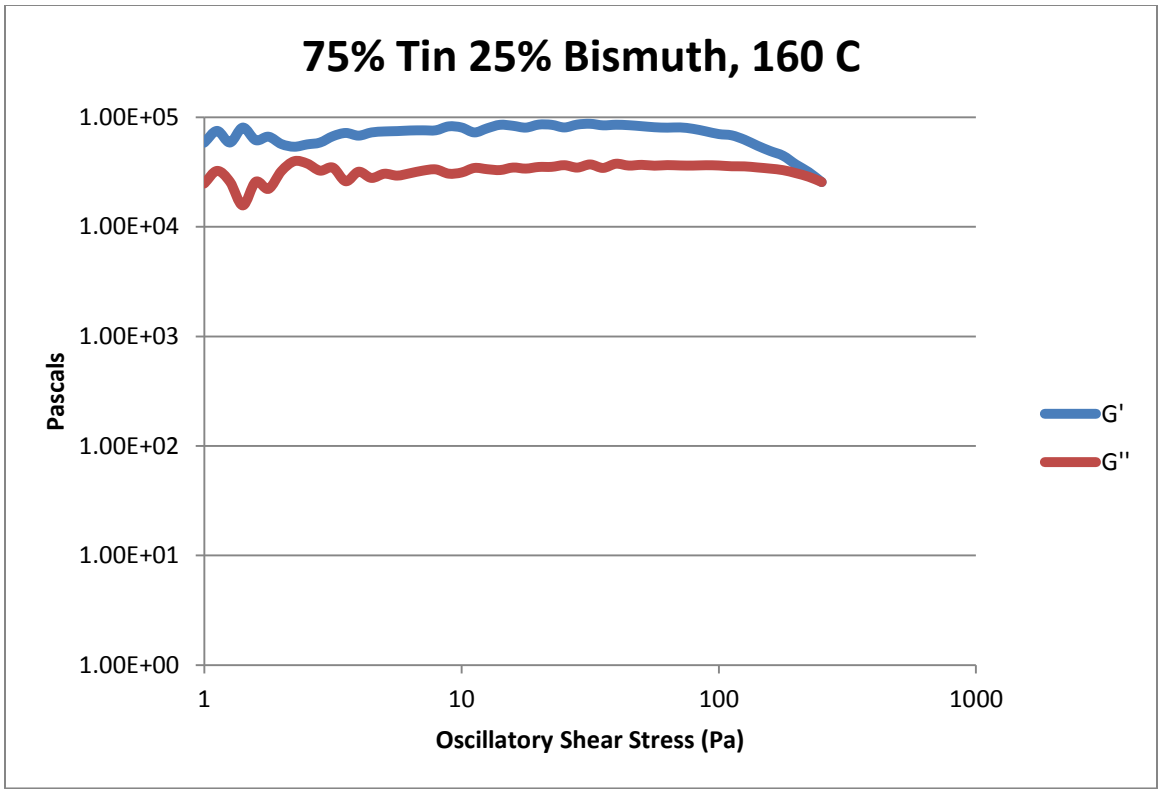

Figure 294- 75% Sn 25% Bi (Run 1), 160 C, Cone and Plate Stress Sweep

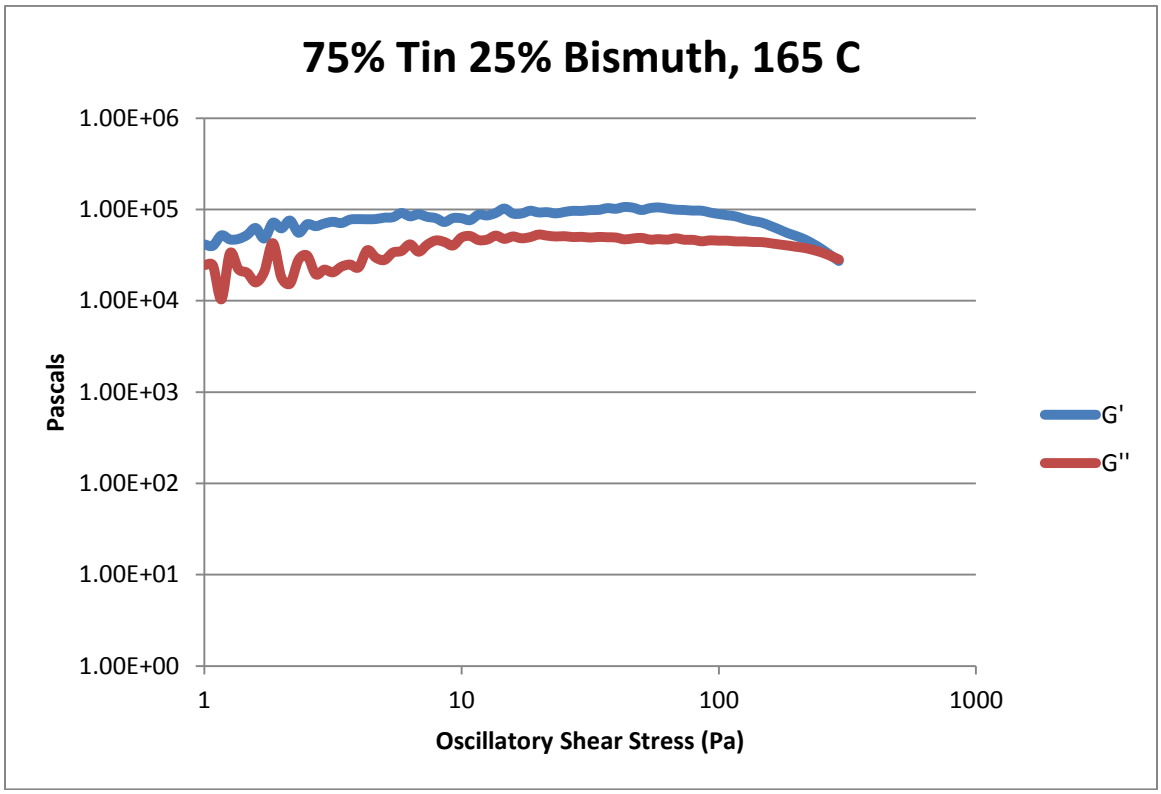

Figure 295- 75% Sn 25% Bi (Run 1), 165 C, Cone and Plate Stress Sweep

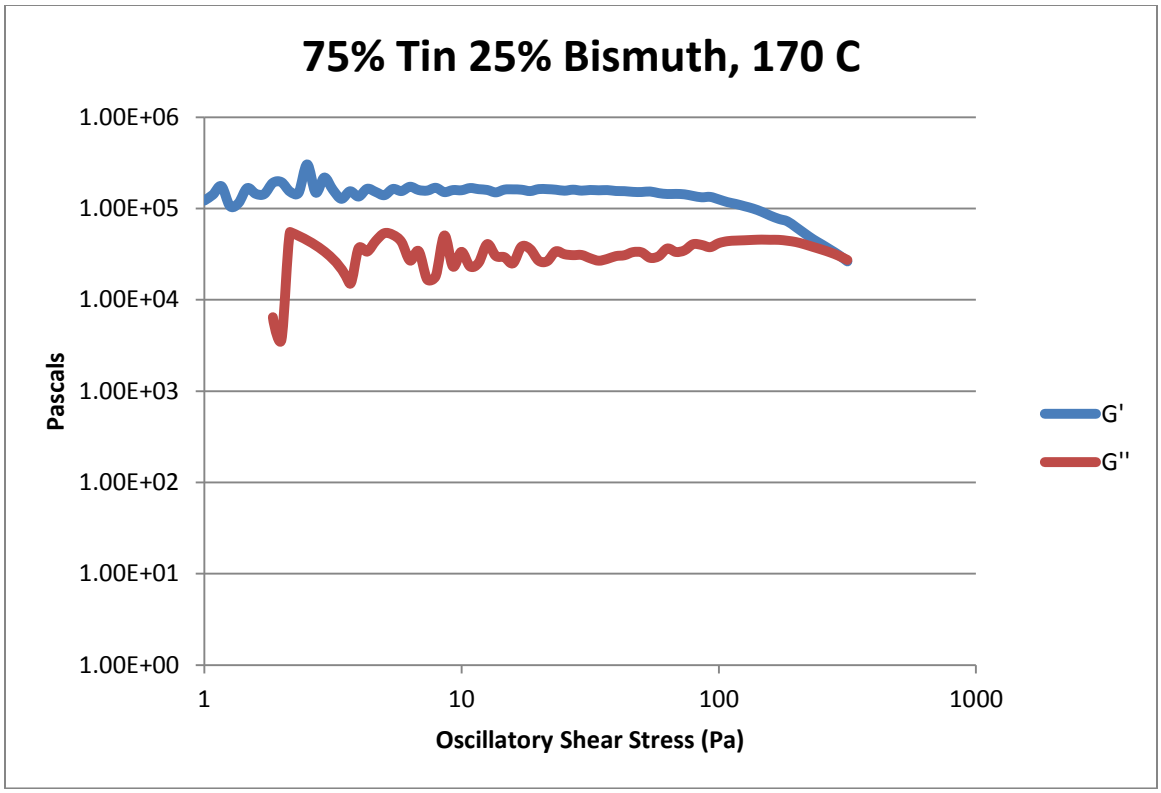

Figure 296- 75% Sn 25% Bi (Run 1), 170 C, Cone and Plate Stress Sweep

Temperature	Crossover Stress (Pa)	Crossover Stress (PSI)
145 C	$5.05 * 10^2$	0.073
150 C	$2.63 * 10^4$	3.81
155 C	$2.44 * 10^4$	3.54
160 C	$2.56 * 10^4$	3.71
165 C	$3.02 * 10^4$	4.38
170 C	$2.92 * 10^4$	4.23

Table 56- 75% Sn 25% Bi (Run 1), Cone and Plate Crossover Stresses

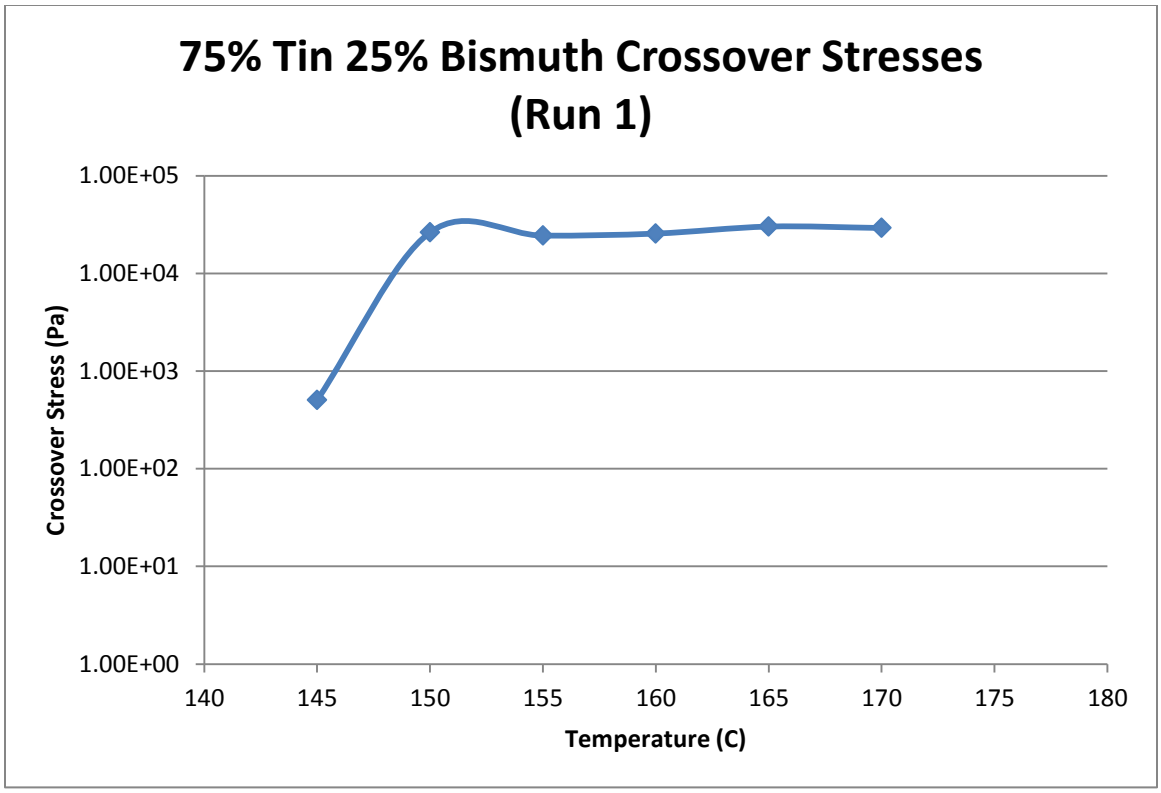

Figure 297- 75% Sn 25% Bi (Run 1), Cone and Plate Crossover Stresses

Temperature	Fraction Solid (At %)	G' Plateau (Pa)	G'' Plateau (Pa)
145 C	39.0	$5.95 * 10^5$	$8.00 * 10^4$
150 C	34.5	$2.86 * 10^5$	$4.02 * 10^4$
155 C	29.4	$1.62 * 10^5$	$3.34 * 10^4$
160 C	23.5	$8.43 * 10^4$	$3.62 * 10^4$
165 C	16.8	$1.02 * 10^5$	$4.74 * 10^4$
170 C	9.10	$1.58 * 10^5$	$4.47 * 10^4$

Table 57- 75% Sn 25% Bi (Run 1), Cone and Plate Plateau Stresses

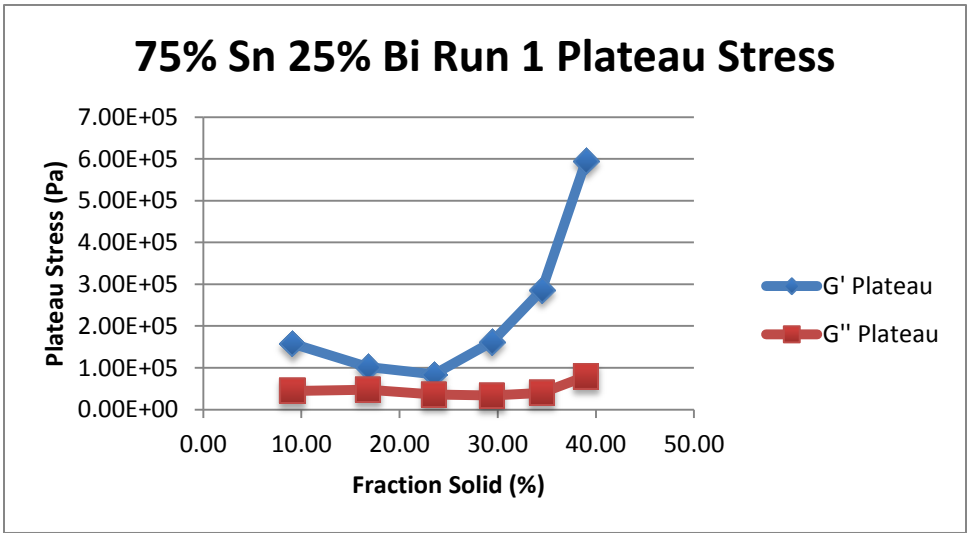

Figure 298- 75% Sn 25% Bi (Run 1), Cone and Plate Plateau Stresses vs. Fraction Solid

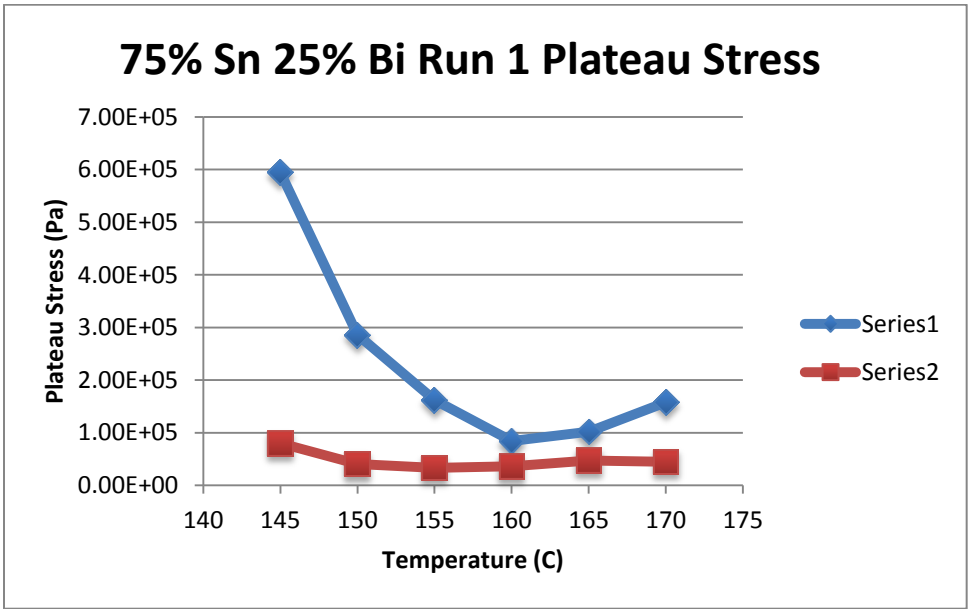

Figure 299- 75% Sn 25% Bi (Run 1), Cone and Plate Plateau Stresses vs. Temperature

75% Sn 25% Bi (Run 1) Viscosity					
Temperature	**Fraction Solid**	**Power Law**	**K**	**n**	**R^2**
145 C	39.0 %	$\tau = 1.10 * 10^{-4} * \dot{\gamma}^{0.1149}$ $\mu = 1.26 * 10^{-5} * \dot{\gamma}^{-0.8851}$	$1.10 * 10^{-4}$ Pa*s	0.1149	64.2 %
150 C	34.5 %	$\tau = 1.80 * 10^{-4} * \dot{\gamma}^{0.2054}$ $\mu = 3.70 * 10^{-5} * \dot{\gamma}^{-0.7946}$	$1.80 * 10^{-4}$ Pa*s	0.2054	34.5 %
155 C	29.4 %	$\tau = 3.99 * 10^{-4} * \dot{\gamma}^{0.3139}$ $\mu = 1.25 * 10^{-4} * \dot{\gamma}^{-0.6861}$	$3.99 * 10^{-4}$ Pa*s	0.3139	61.09 %
160 C	23.5 %	$\tau = 1.98 * 10^{-4} * \dot{\gamma}^{0.2829}$ $\mu = 5.60 * 10^{-5} * \dot{\gamma}^{-0.7171}$	$1.98 * 10^{-4}$ Pa*s	0.2829	74.88 %
165 C	16.8 %	$\tau = 3.99 * 10^{-4} * \dot{\gamma}^{0.3998}$ $\mu = 1.60 * 10^{-4} * \dot{\gamma}^{-0.6002}$	$3.99 * 10^{-4}$ Pa*s	0.3998	96.08 %
170 C	9.10 %	$\tau = 2.53 * 10^{-4} * \dot{\gamma}^{0.3163}$ $\mu = 8.00 * 10^{-5} * \dot{\gamma}^{-0.6837}$	$2.53 * 10^{-4}$ Pa*s	0.3163	95.12 %

Table 58- 75% Sn 25% Bi (Run 1), Cone and Plate Viscosity

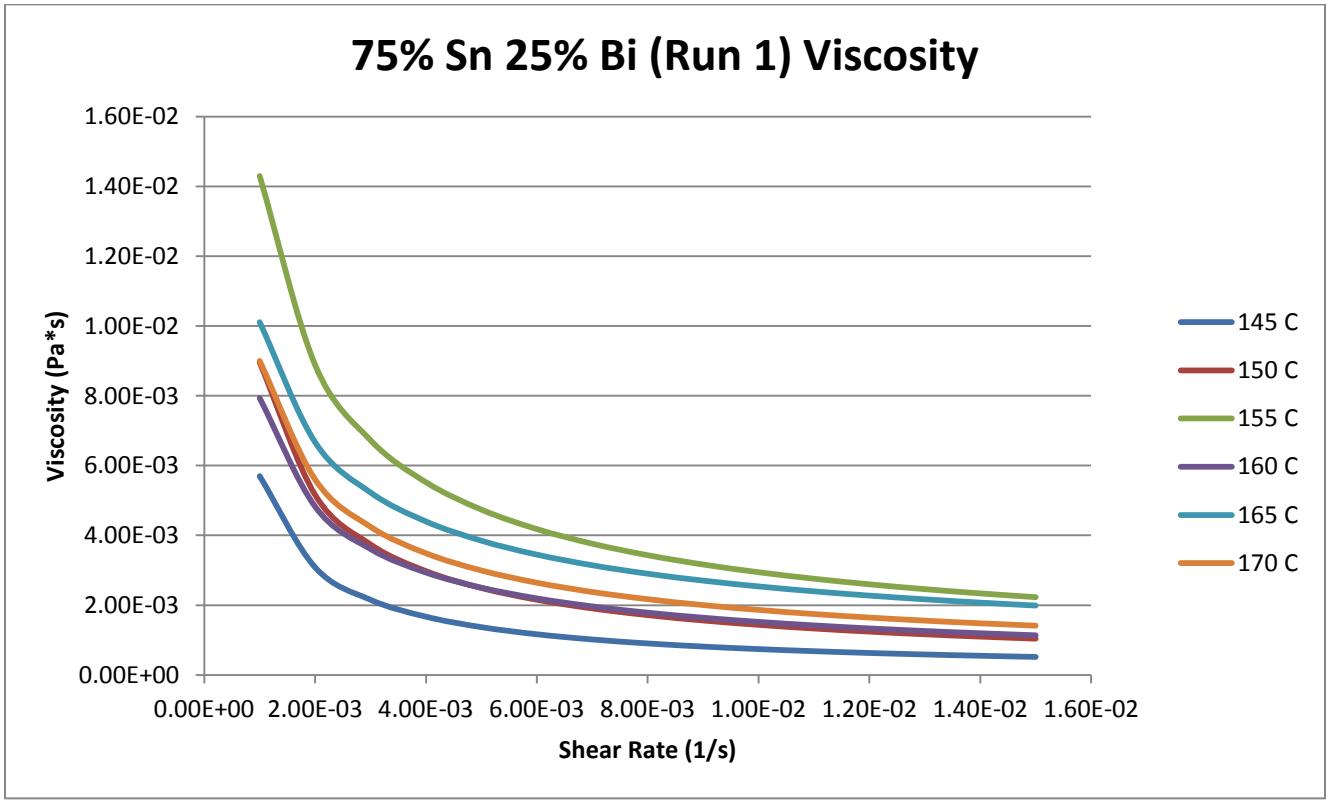

Figure 300- 75% Sn 25% Bi (Run 1), Cone and Plate Viscosity

145 C

Fraction Solid	39.0 %
Power Law	$\tau = 1.10 * 10^{-4} * \dot{\gamma}^{0.1149}$
	$\mu = 1.26 * 10^{-5} * \dot{\gamma}^{-0.8851}$
R^2	64.2 %

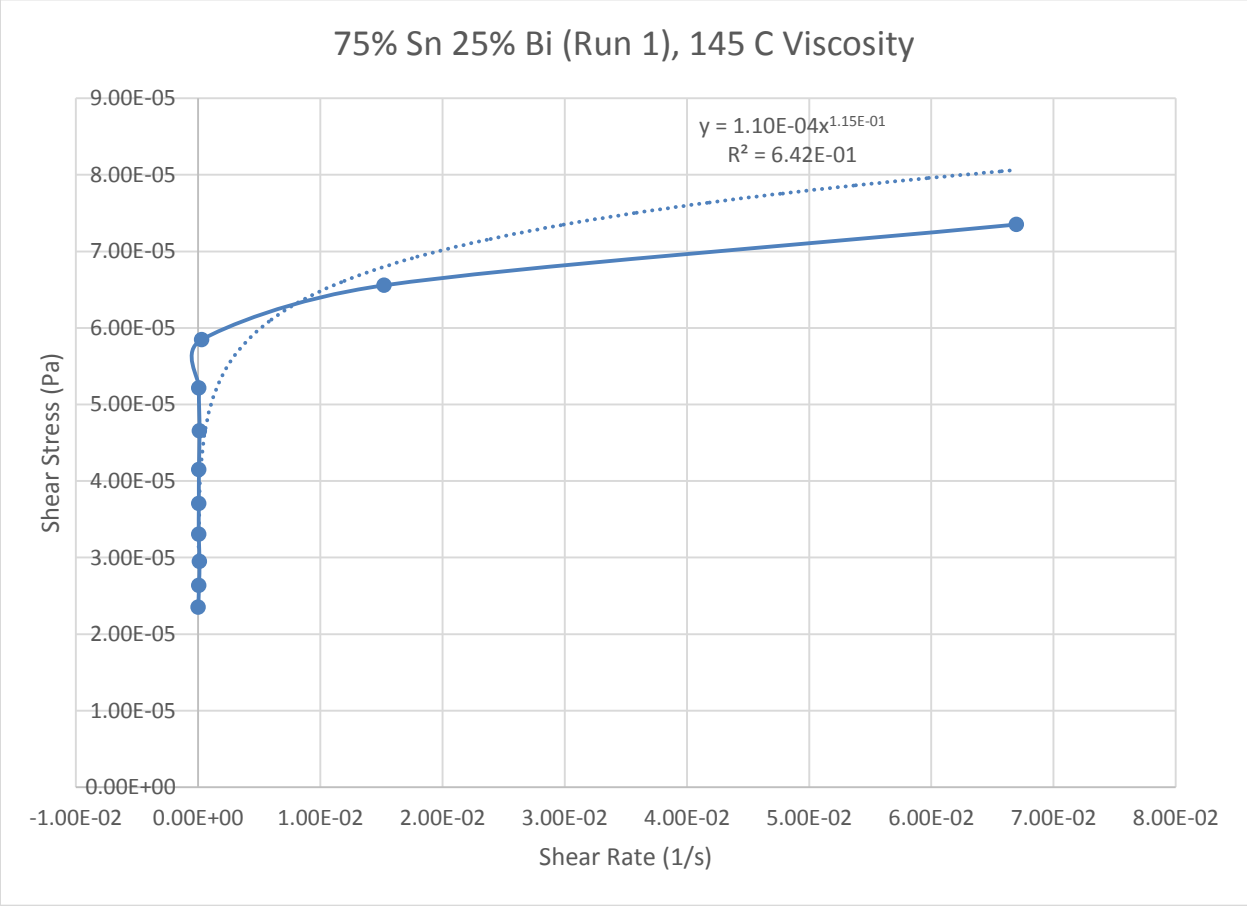

Figure 301- 75% Sn 25% Bi (Run 1), 145 C, Cone and Plate Viscosity

150 C

Fraction Solid	34.5 %
Power Law	$\tau = 1.80 * 10^{-4} * \dot{\gamma}^{0.2054}$
	$\mu = 3.70 * 10^{-5} * \dot{\gamma}^{-0.7946}$
R^2	86.37 %

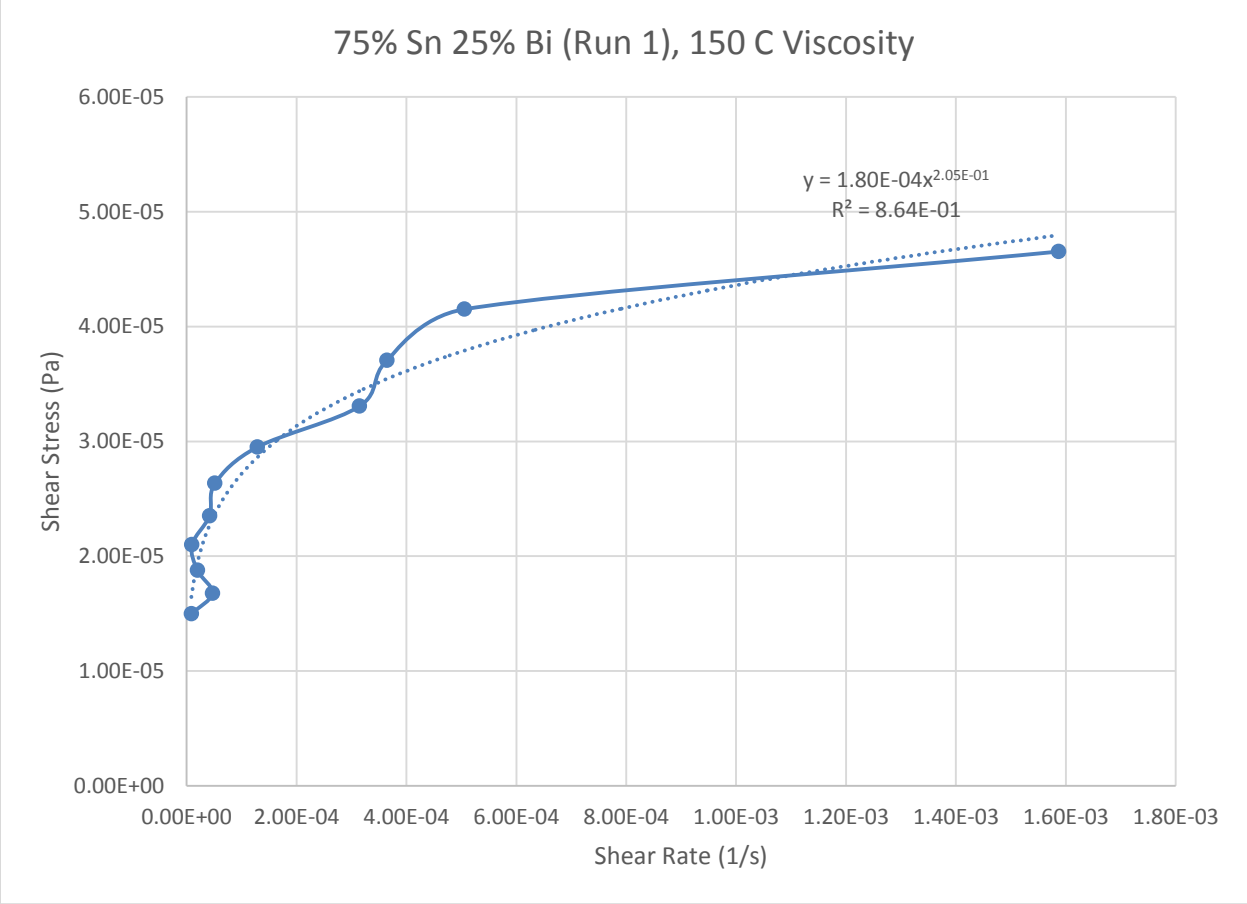

Figure 302- 75% Sn 25% Bi (Run 1), 150 C, Cone and Plate Viscosity

155 C

Fraction Solid	29.40 %
Power Law	$\tau = 3.99 * 10^{-4} * \dot{\gamma}^{0.3139}$
	$\mu = 1.25 * 10^{-4} * \dot{\gamma}^{-0.6861}$
R^2	61.09 %

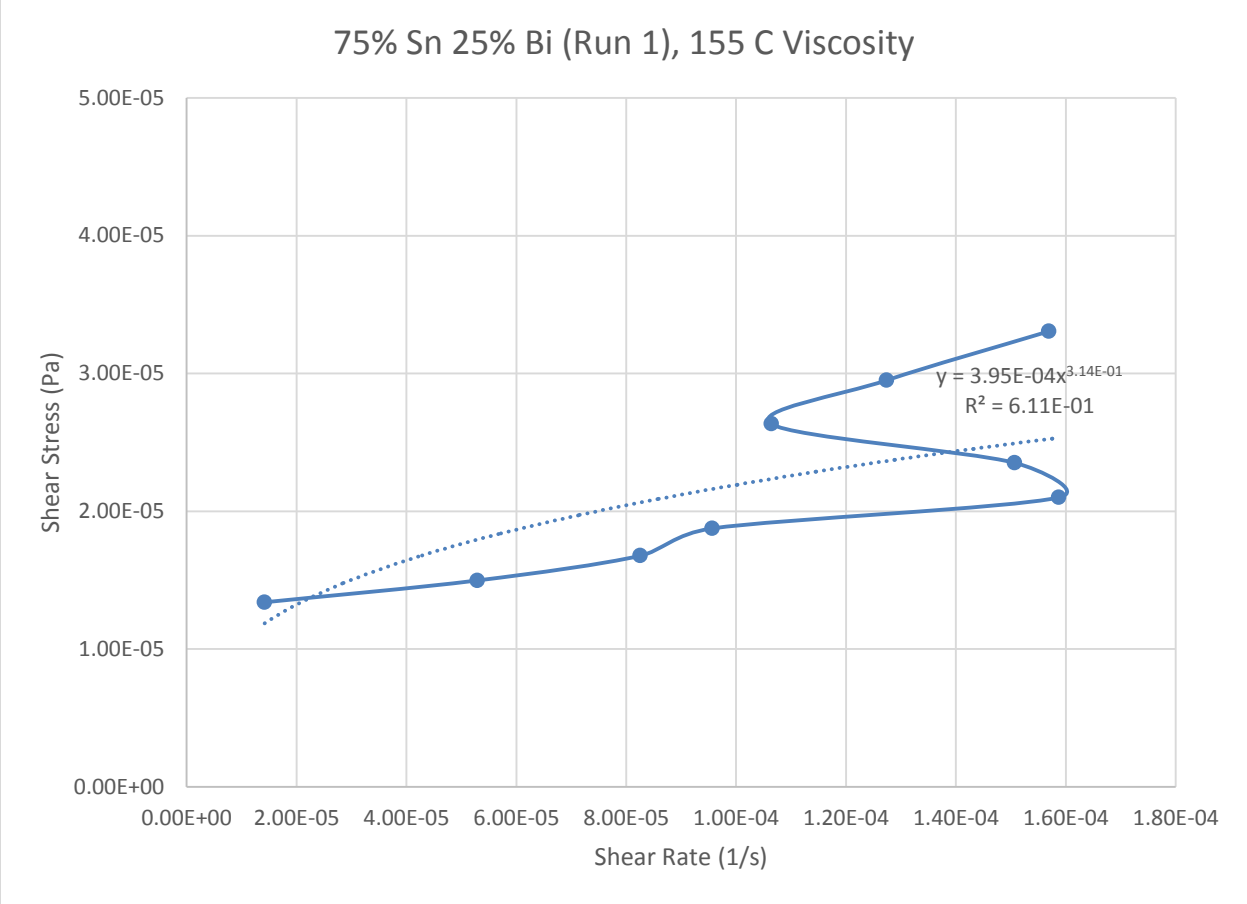

Figure 303- 75% Sn 25% Bi (Run 1), 155 C, Cone and Plate Viscosity

160 C

Fraction Solid	23.50 %
Power Law	$\tau = 1.98 * 10^{-4} * \dot{\gamma}^{0.2829}$
	$\mu = 5.60 * 10^{-5} * \dot{\gamma}^{-0.7171}$
R^2	74.88 %

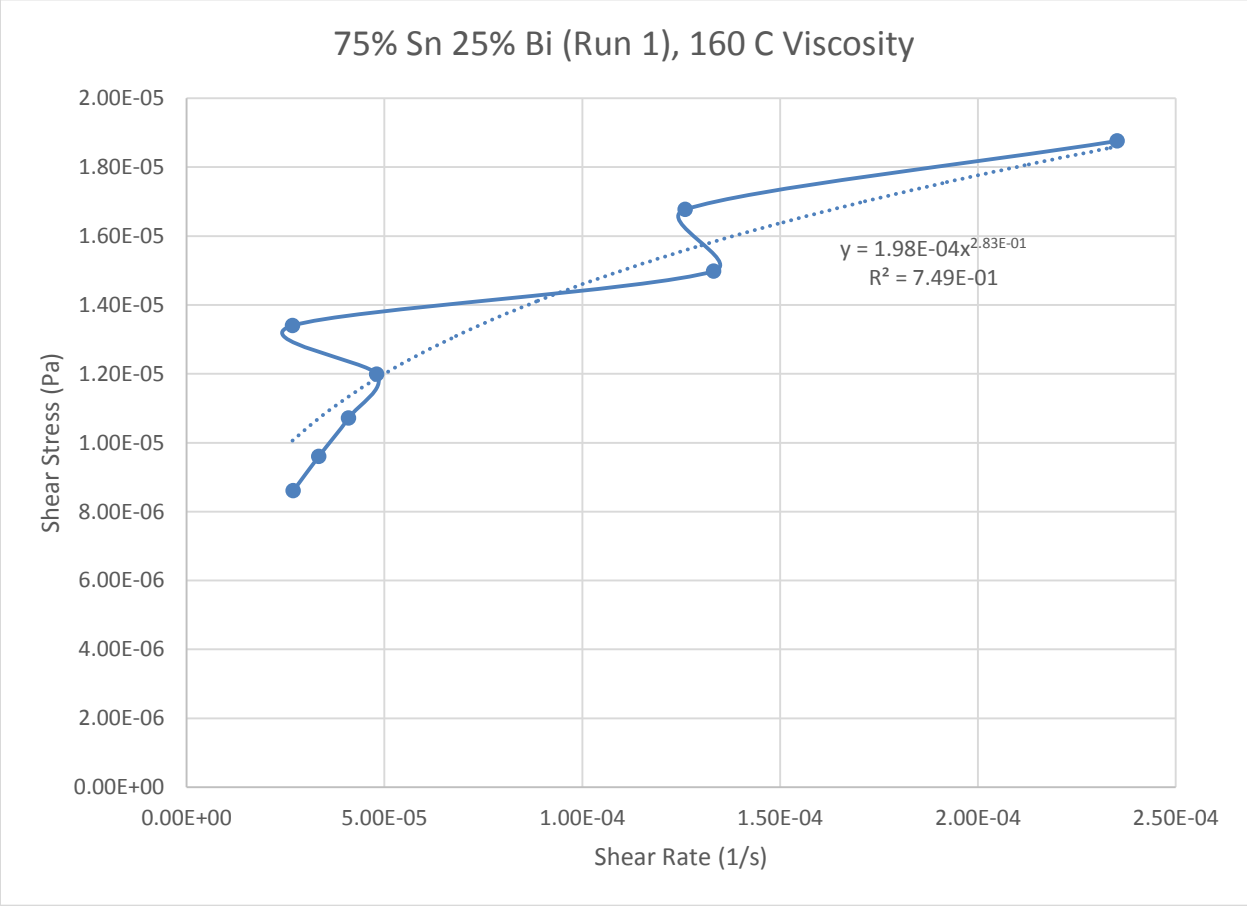

Figure 304- 75% Sn 25% Bi (Run 1), 160 C, Cone and Plate Viscosity

165 C

Fraction Solid	16.80 %
Power Law	$\tau = 3.99 * 10^{-4} * \dot{\gamma}^{0.3998}$
	$\mu = 1.60 * 10^{-4} * \dot{\gamma}^{-0.6002}$
R^2	96.08 %

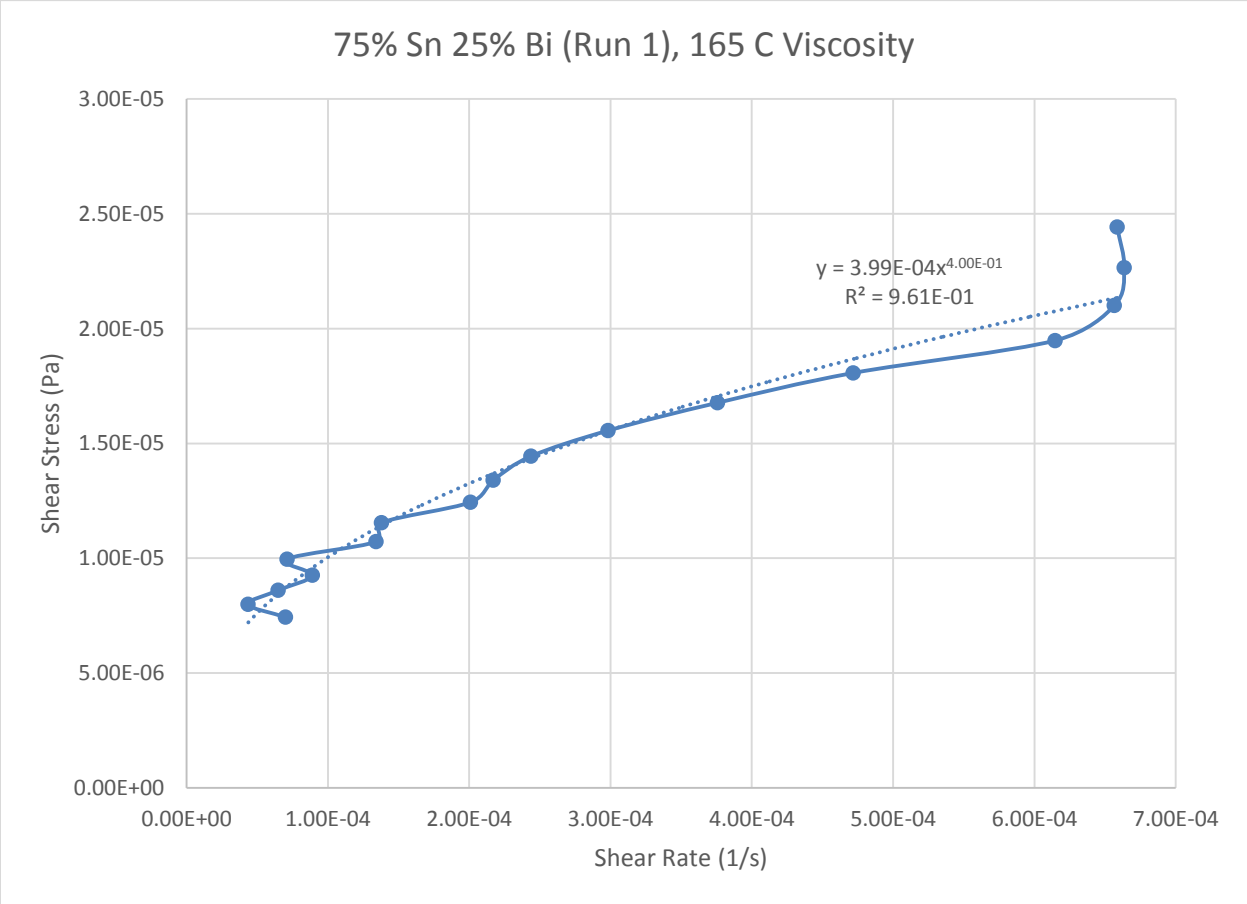

Figure 305- 75% Sn 25% Bi (Run 1), 165 C, Cone and Plate Viscosity

170 C

Fraction Solid	9.10 %
Power Law	$\tau = 2.53 * 10^{-4} * \dot{\gamma}^{0.3163}$
	$\mu = 8.00 * 10^{-5} * \dot{\gamma}^{-0.6837}$
R^2	95.12 %

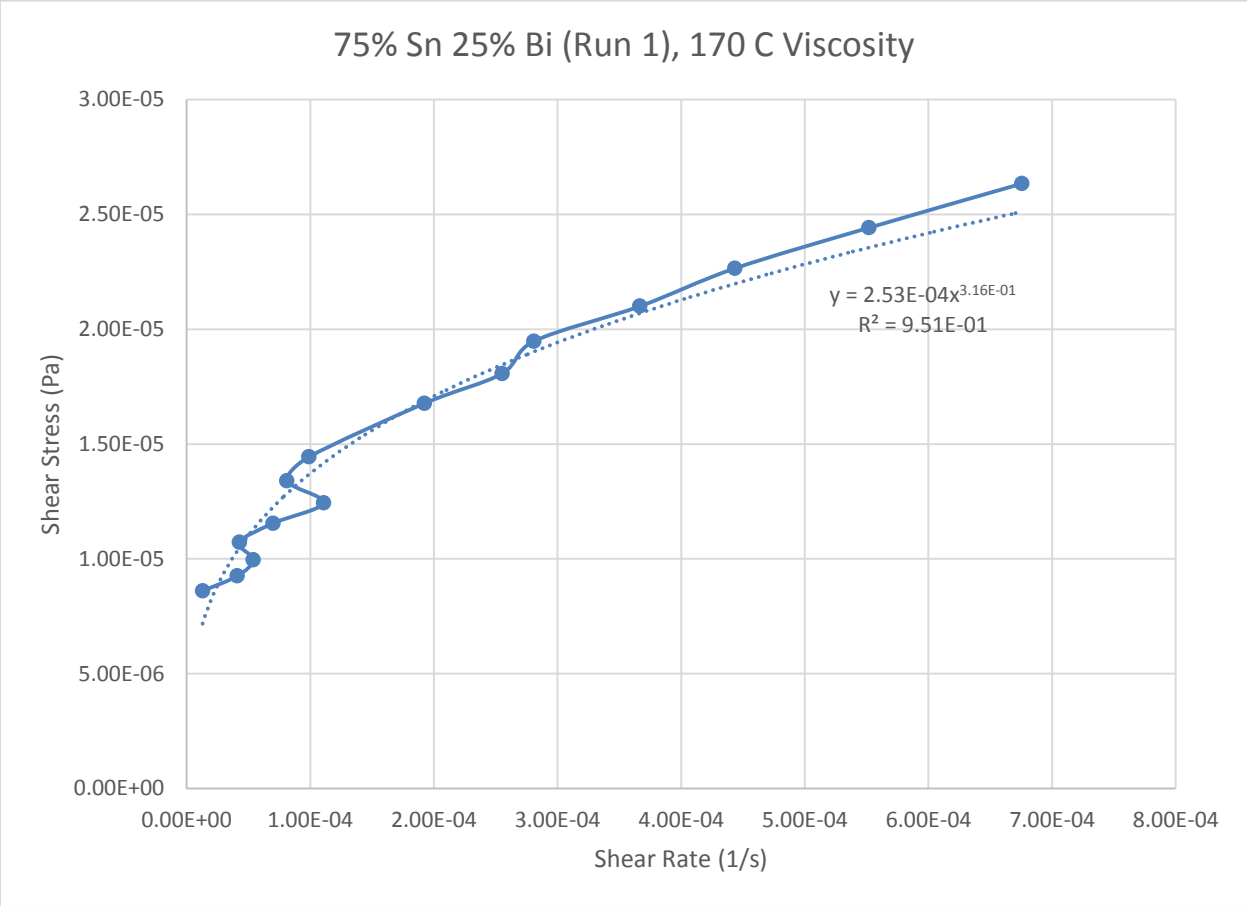

Figure 306- 75% Sn 25% Bi (Run 1), 170 C, Cone and Plate Viscosity

75% Tin 25% Bismuth (Run 2)

Predicted Composition: 75% Tin, 25% Bismuth

Theoretical Solidus Line: 139 C
Theoretical Liquidus Line: 182.2 C

Experimental Solidus Line: 138.9 C
Experimental Liquidus Line: 183.5 C

Set-Up Notes

- Zeroed gap at 165 C. Stress sweeps were then conducted in decreasing intervals of 5 C. The final stress sweep was conducted at 170 C.

- Crossover stress didn't fall after 165 C like the first 75% tin 25% bismuth run; it actually increased, but the minimum was still at 145 C.

Plots

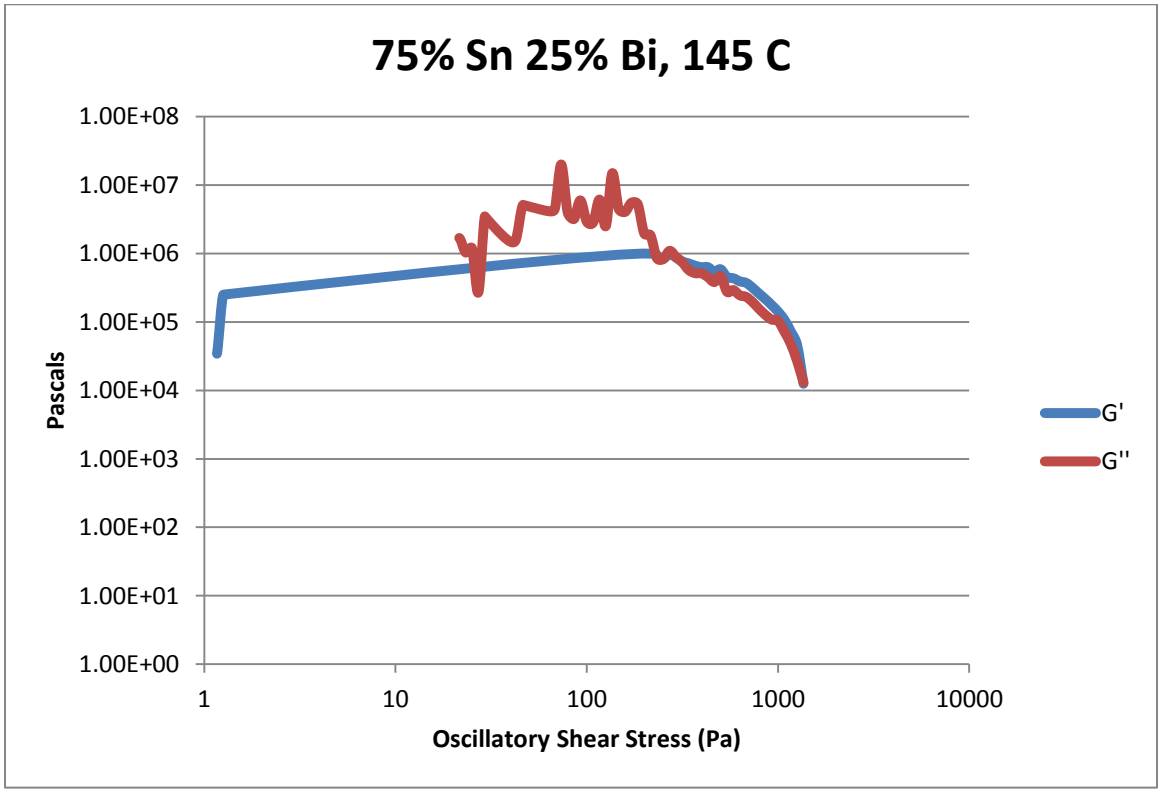

Figure 307- 75% Sn 25% Bi (Run 2), 145 C, Cone and Plate Stress Sweep

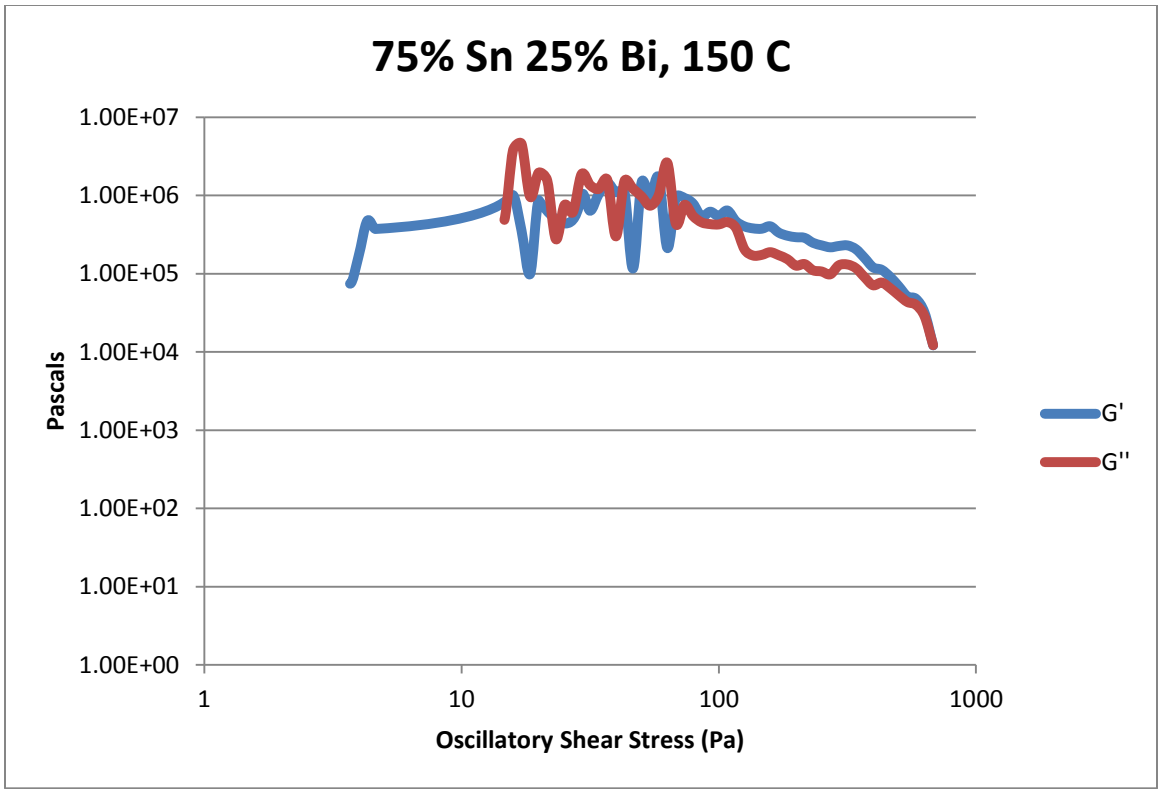

Figure 308- 75% Sn 25% Bi (Run 2), 150 C, Cone and Plate Stress Sweep

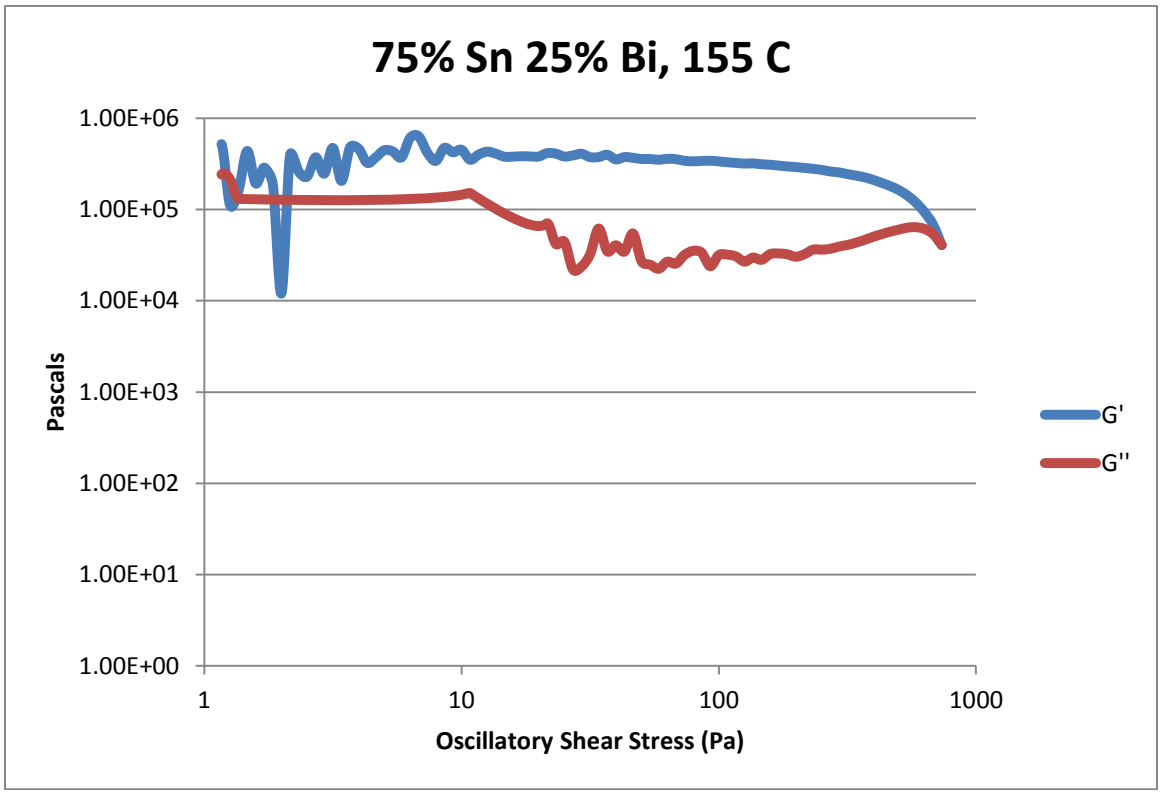

Figure 309- 75% Sn 25% Bi (Run 2), 155 C, Cone and Plate Stress Sweep

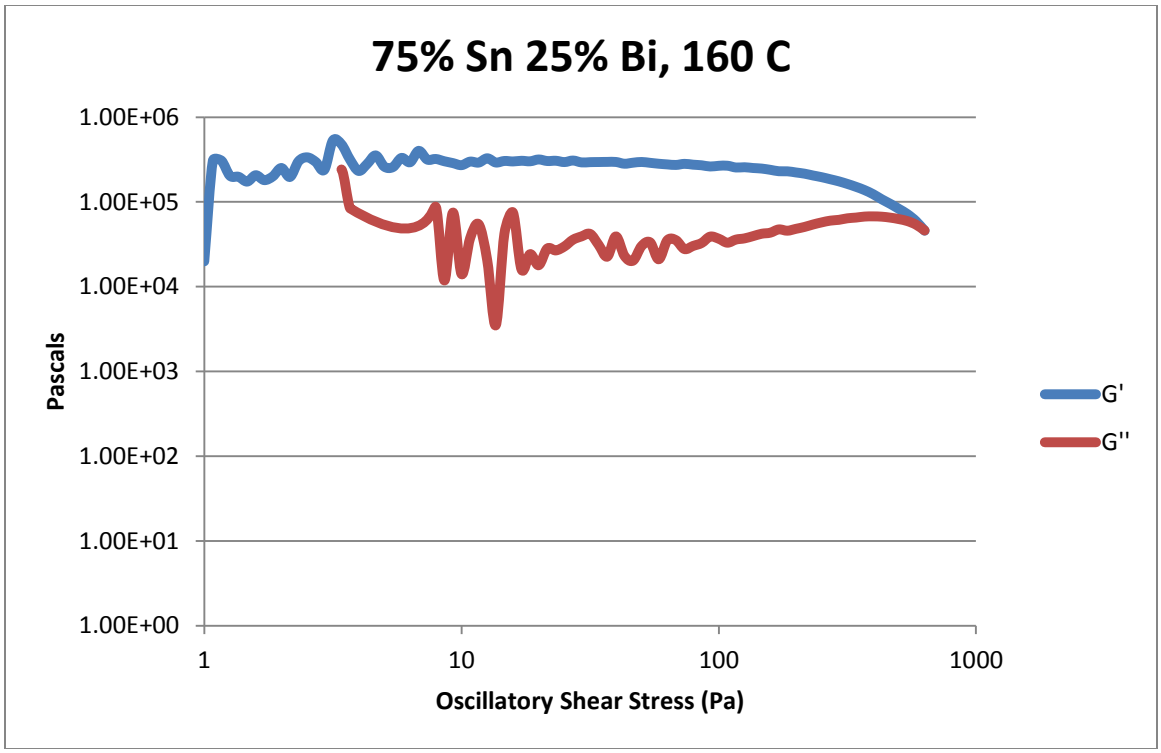

Figure 310- 75% Sn 25% Bi (Run 2), 160 C, Cone and Plate Stress Sweep

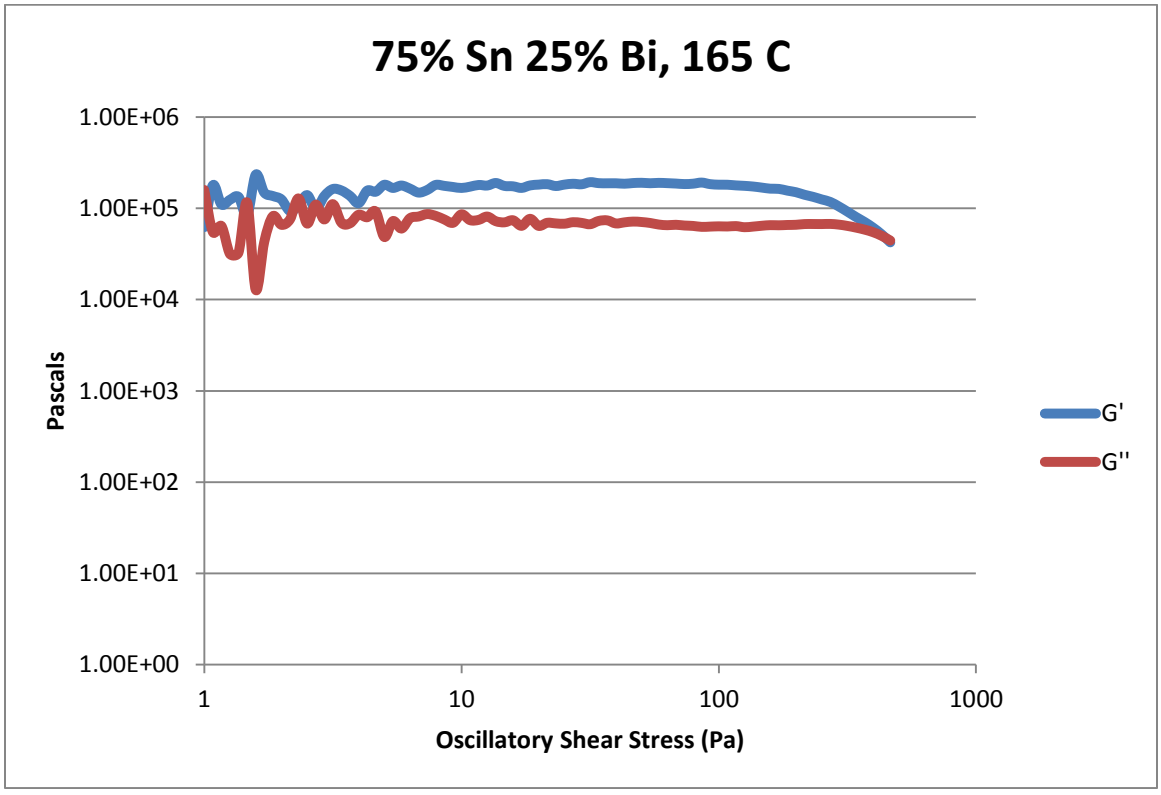

Figure 311- 75% Sn 25% Bi (Run 2), 165 C, Cone and Plate Stress Sweep

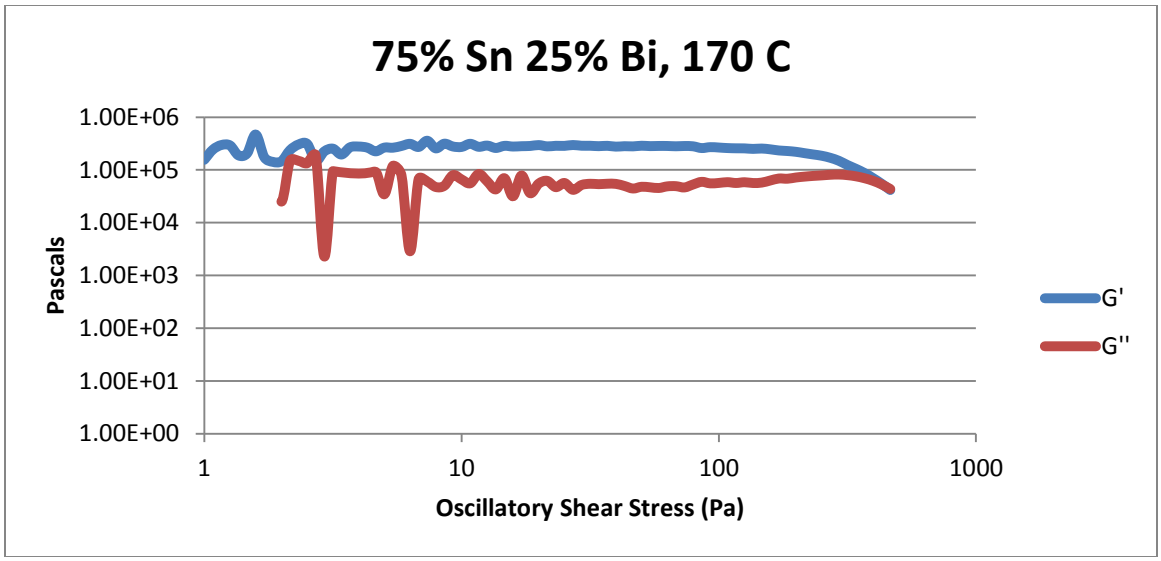

Figure 312- 75% Sn 25% Bi (Run 2), 170 C, Cone and Plate Stress Sweep

Temperature	Crossover Stress (Pa)	Crossover Stress (PSI)
145 C	$1.35 * 10^4$	1.96
150 C	$1.25 * 10^4$	1.81
155 C	$4.09 * 10^4$	5.93
160 C	$4.65 * 10^4$	6.74
165 C	$4.72 * 10^4$	6.85
170 C	$4.86 * 10^4$	7.05

Table 59- 75% Sn 25% Bi (Run 2), Cone and Plate Crossover Stresses

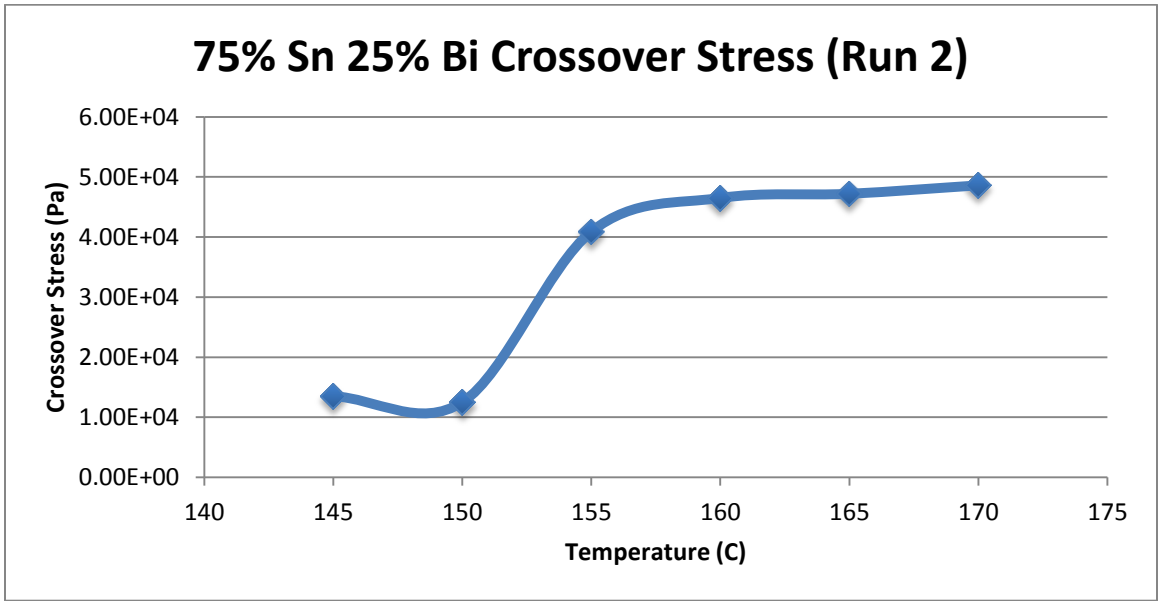

Figure 313- 75% Sn 25% Bi (Run 2), Cone and Plate Crossover Stresses

Temperature	Fraction Solid (At %)	G' Plateau (Pa)	G'' Plateau (Pa)
145 C	39.0	$8.45 * 10^5$	$2.50 * 10^5$
150 C	34.5	$5.86 * 10^5$	$1.19 * 10^5$
155 C	29.4	$3.77 * 10^5$	$6.35 * 10^4$
160 C	23.5	$3.00 * 10^5$	$6.70 * 10^4$
165 C	16.8	$1.88 * 10^5$	$6.47 * 10^4$
170 C	9.10	$2.83 * 10^5$	$7.52 * 10^4$

Table 60- 75% Sn 25% Bi (Run 2), Cone and Plate Plateau Stresses

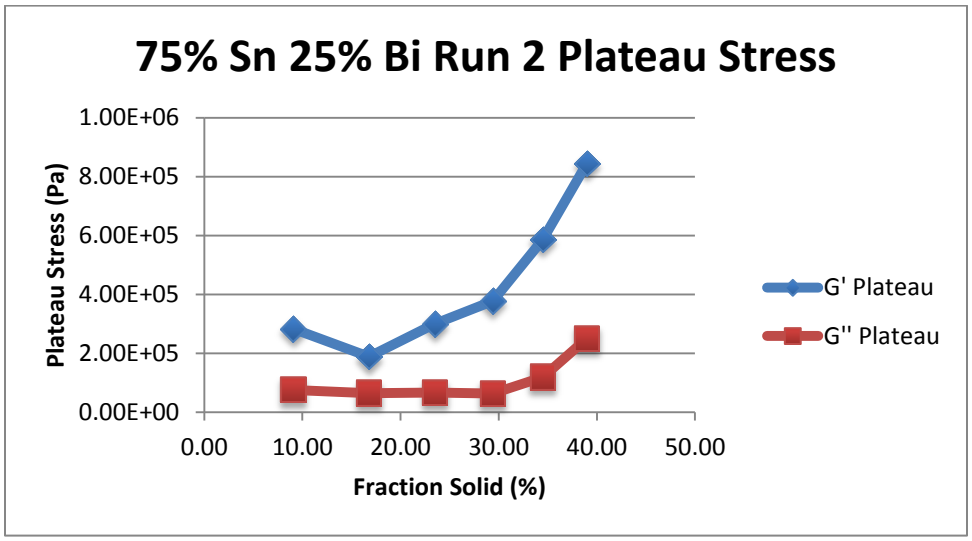

Figure 314- 75% Sn 25% Bi (Run 2), Cone and Plate Plateau Stresses vs. Fraction Solid

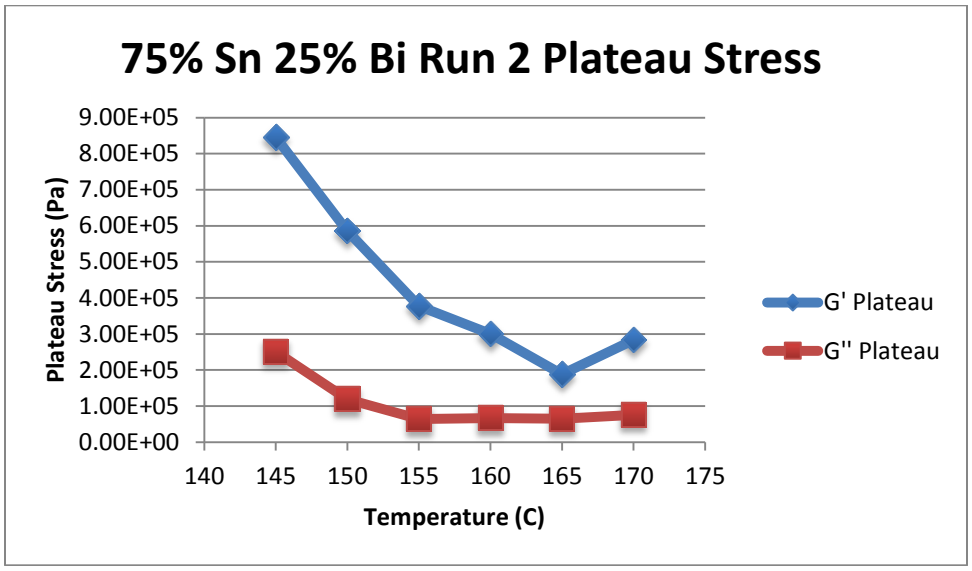

Figure 315- 75% Sn 25% Bi (Run 2), Cone and Plate Plateau Stresses vs. Temperature

75% Sn 25% Bi (Run 2) Viscosity					
Temperature	**Fraction Solid**	**Power Law**	**K**	**n**	**R^2**
145 C	39.0 %	$\tau = 2.41 * 10^{-4} * \dot{\gamma}^{0.1627}$ $\mu = 3.92 * 10^{-5} * \dot{\gamma}^{-0.8373}$	$2.41 * 10^{-4}$ Pa*s	0.1627	93.27 %
150 C	34.5 %	$\tau = 1.11 * 10^{-4} * \dot{\gamma}^{0.1612}$ $\mu = 1.79 * 10^{-5} * \dot{\gamma}^{-0.8388}$	$1.11 * 10^{-4}$ Pa*s	0.1612	95.35 %
155 C	29.4 %	$\tau = 2.19 * 10^{-4} * \dot{\gamma}^{0.1761}$ $\mu = 3.86 * 10^{-5} * \dot{\gamma}^{-0.8239}$	$2.19 * 10^{-4}$ Pa*s	0.1761	86.62 %
160 C	23.5 %	$\tau = 2.09 * 10^{-4} * \dot{\gamma}^{0.1844}$ $\mu = 3.85 * 10^{-5} * \dot{\gamma}^{-0.8156}$	$2.09 * 10^{-4}$ Pa*s	0.1844	81.59 %
165 C	16.8 %	$\tau = 1.63 * 10^{-4} * \dot{\gamma}^{0.1958}$ $\mu = 3.19 * 10^{-5} * \dot{\gamma}^{-0.8042}$	$1.63 * 10^{-4}$ Pa*s	0.1958	73.70 %
170 C	9.10 %	$\tau = 8.36 * 10^{-5} * \dot{\gamma}^{0.1136}$ $\mu = 9.50 * 10^{-6} * \dot{\gamma}^{-0.8864}$	$8.36 * 10^{-5}$ Pa*s	0.1136	80.28 %

Table 61- 75% Sn 25% Bi (Run 2), Cone and Plate Viscosity

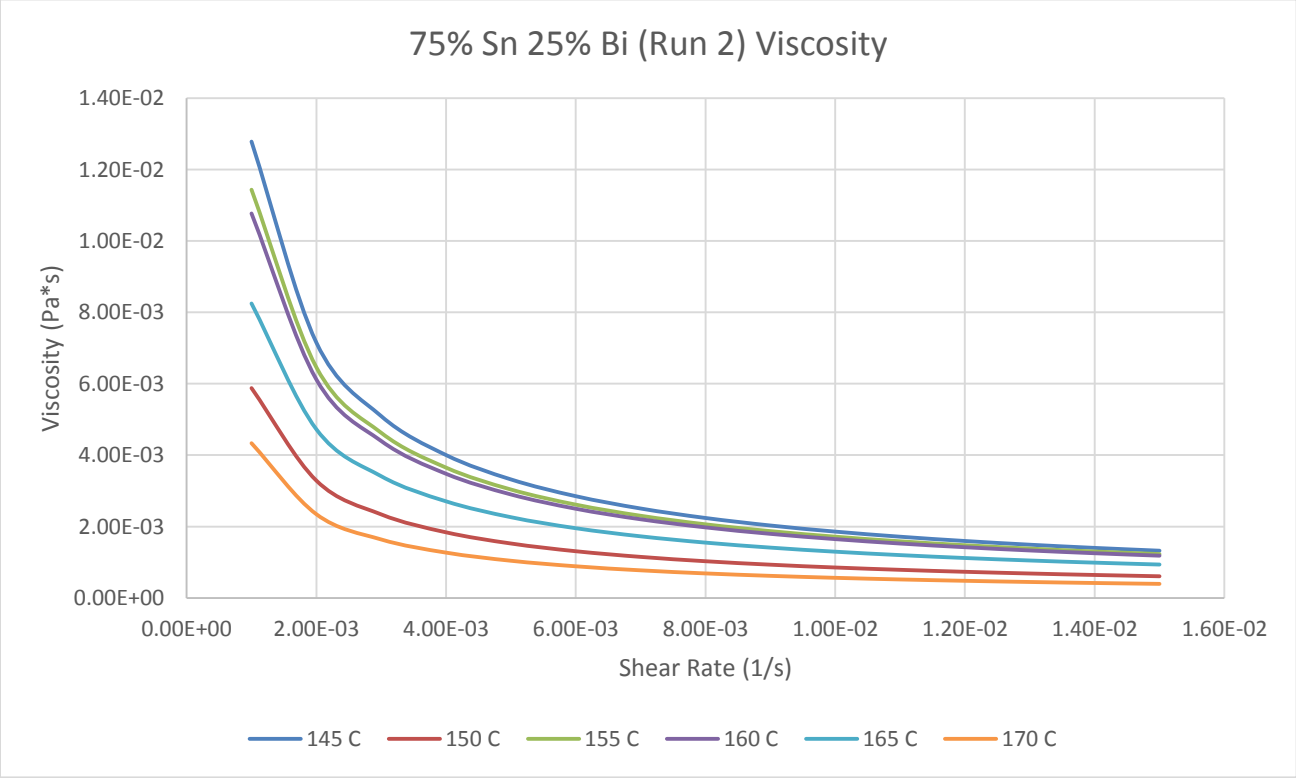

Figure 316- 75% Sn 25% Bi (Run 2), Cone and Plate Viscosity

145 C

Fraction Solid	39.0 %
Power Law	$\tau = 2.41 * 10^{-4} * \dot{\gamma}^{0.1627}$
	$\mu = 3.92 * 10^{-5} * \dot{\gamma}^{-0.8373}$
R^2	93.27 %

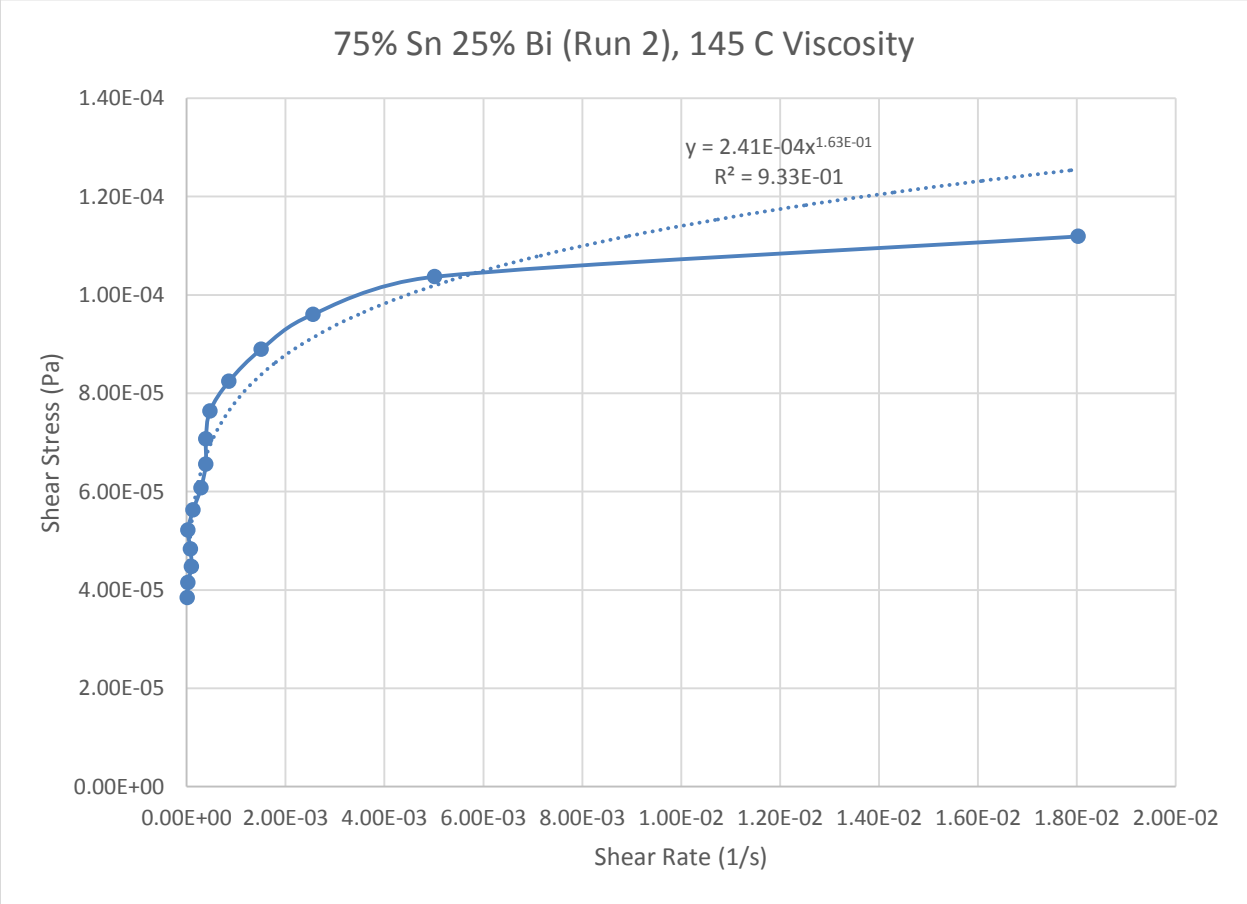

Figure 317- 75% Sn 25% Bi (Run 2), 145 C, Cone and Plate Viscosity

150 C

Fraction Solid	34.5 %
Power Law	$\tau = 1.11 * 10^{-4} * \dot{\gamma}^{0.1612}$
	$\mu = 1.79 * 10^{-5} * \dot{\gamma}^{-0.8388}$
R^2	95.35 %

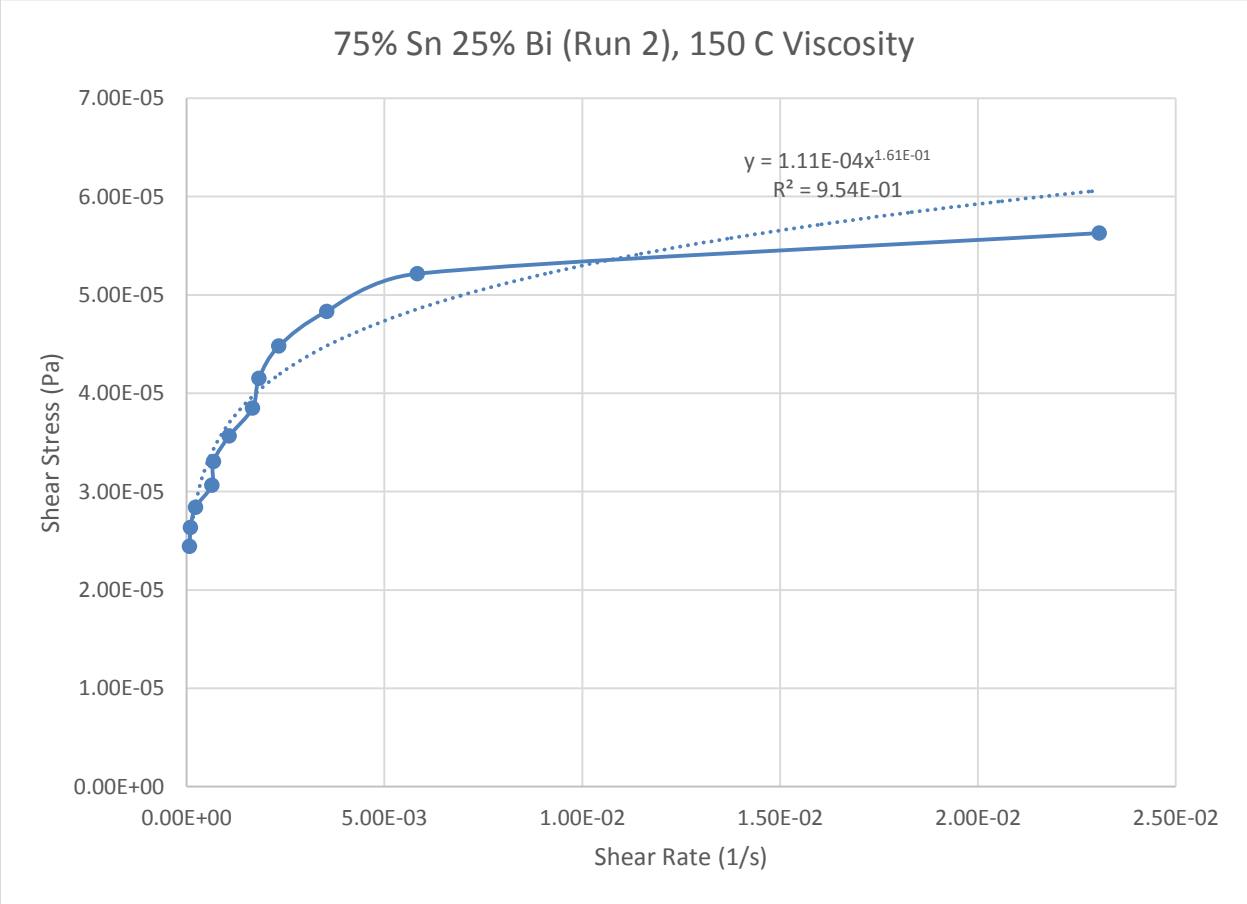

Figure 318- 75% Sn 25% Bi (Run 2), 150 C, Cone and Plate Viscosity

155 C

Fraction Solid	29.40 %
Power Law	$\tau = 2.19 * 10^{-4} * \dot{\gamma}^{0.1761}$
	$\mu = 3.86 * 10^{-5} * \dot{\gamma}^{-0.8239}$
R^2	86.62 %

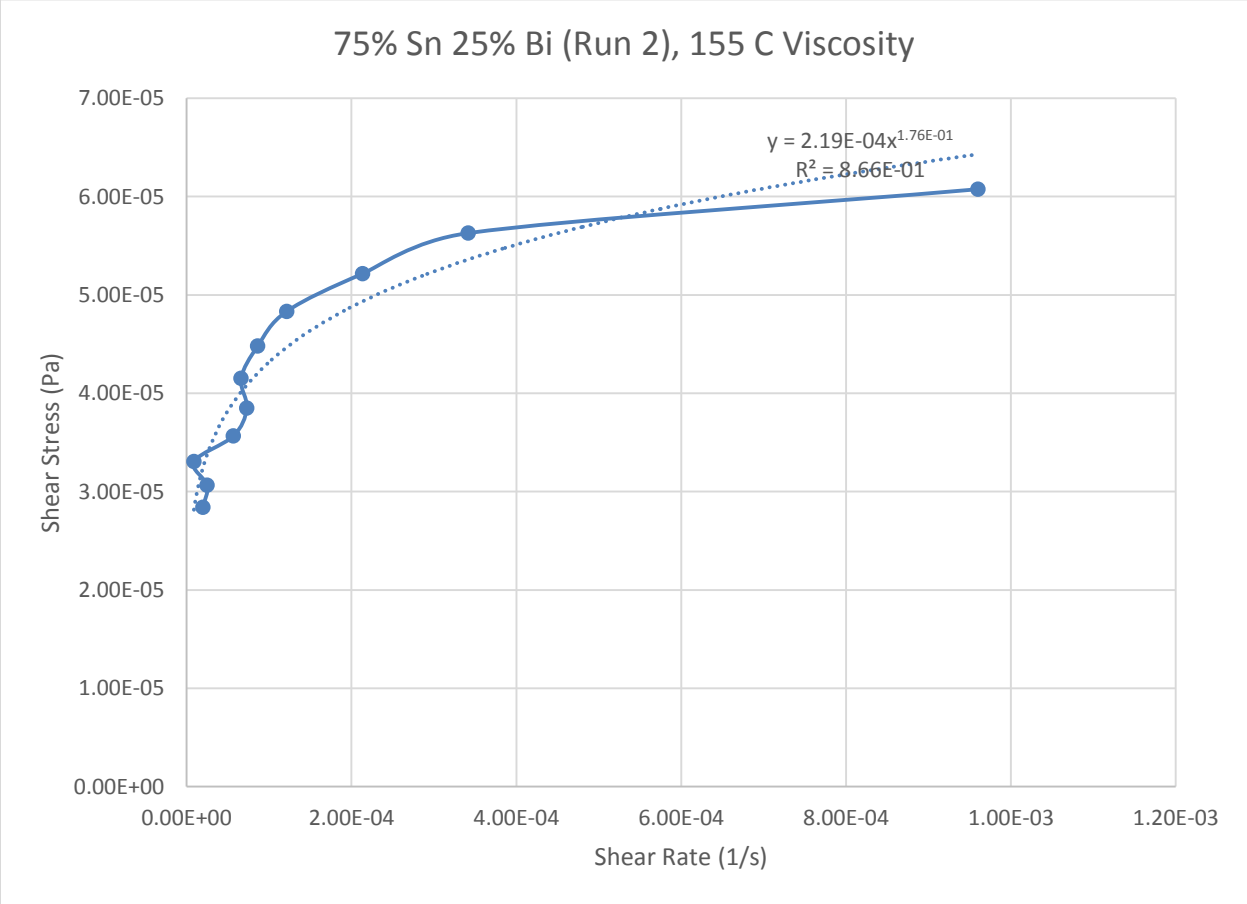

Figure 319- 75% Sn 25% Bi (Run 2), 155 C, Cone and Plate Viscosity

160 C

Fraction Solid	23.50 %
Power Law	$\tau = 2.09 * 10^{-4} * \dot{\gamma}^{0.1844}$
	$\mu = 3.85 * 10^{-5} * \dot{\gamma}^{-0.8156}$
R^2	81.59 %

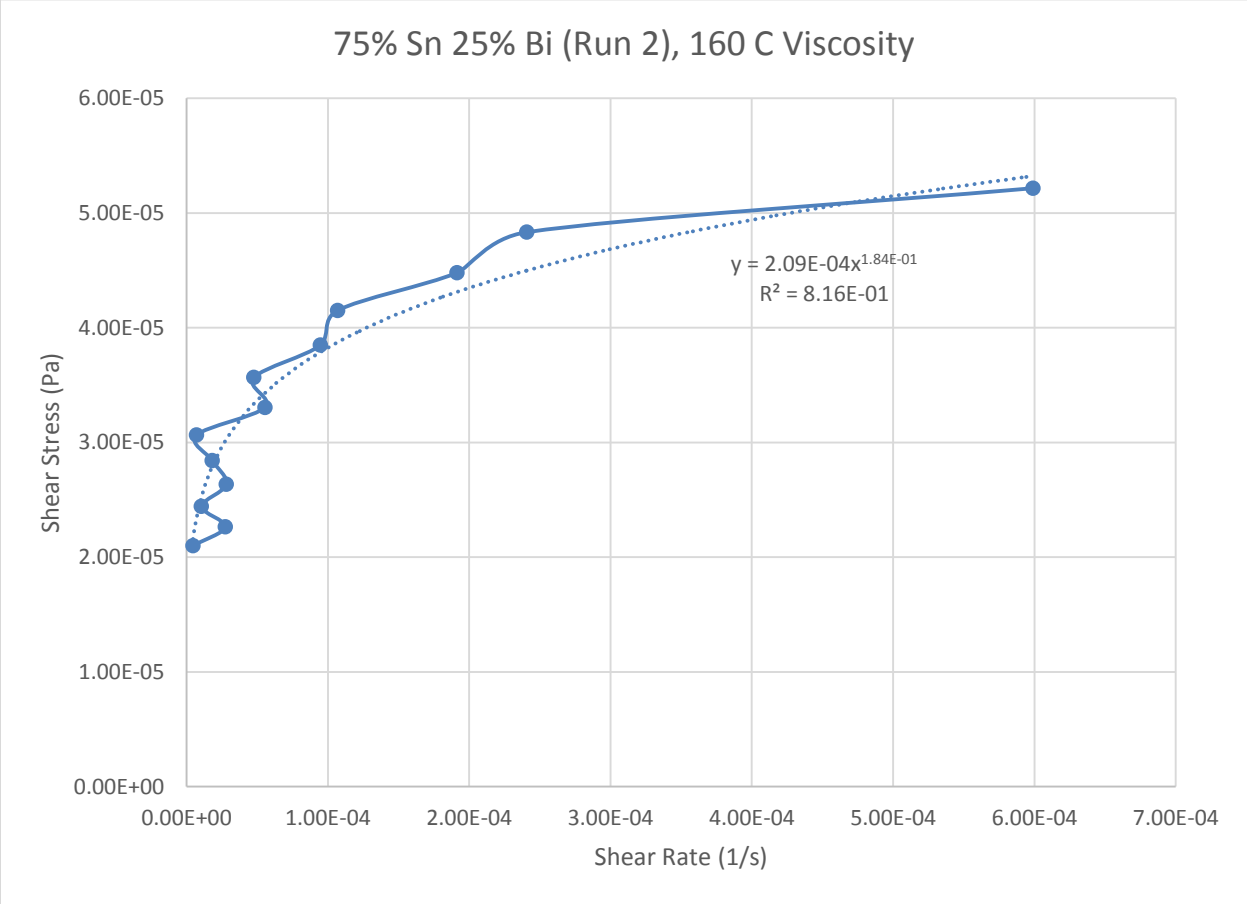

Figure 320- 75% Sn 25% Bi (Run 2), 160 C, Cone and Plate Viscosity

165 C

Fraction Solid	16.80 %
Power Law	$\tau = 1.63 * 10^{-4} * \dot{\gamma}^{0.1958}$
	$\mu = 3.19 * 10^{-5} * \dot{\gamma}^{-0.8042}$
R^2	73.70 %

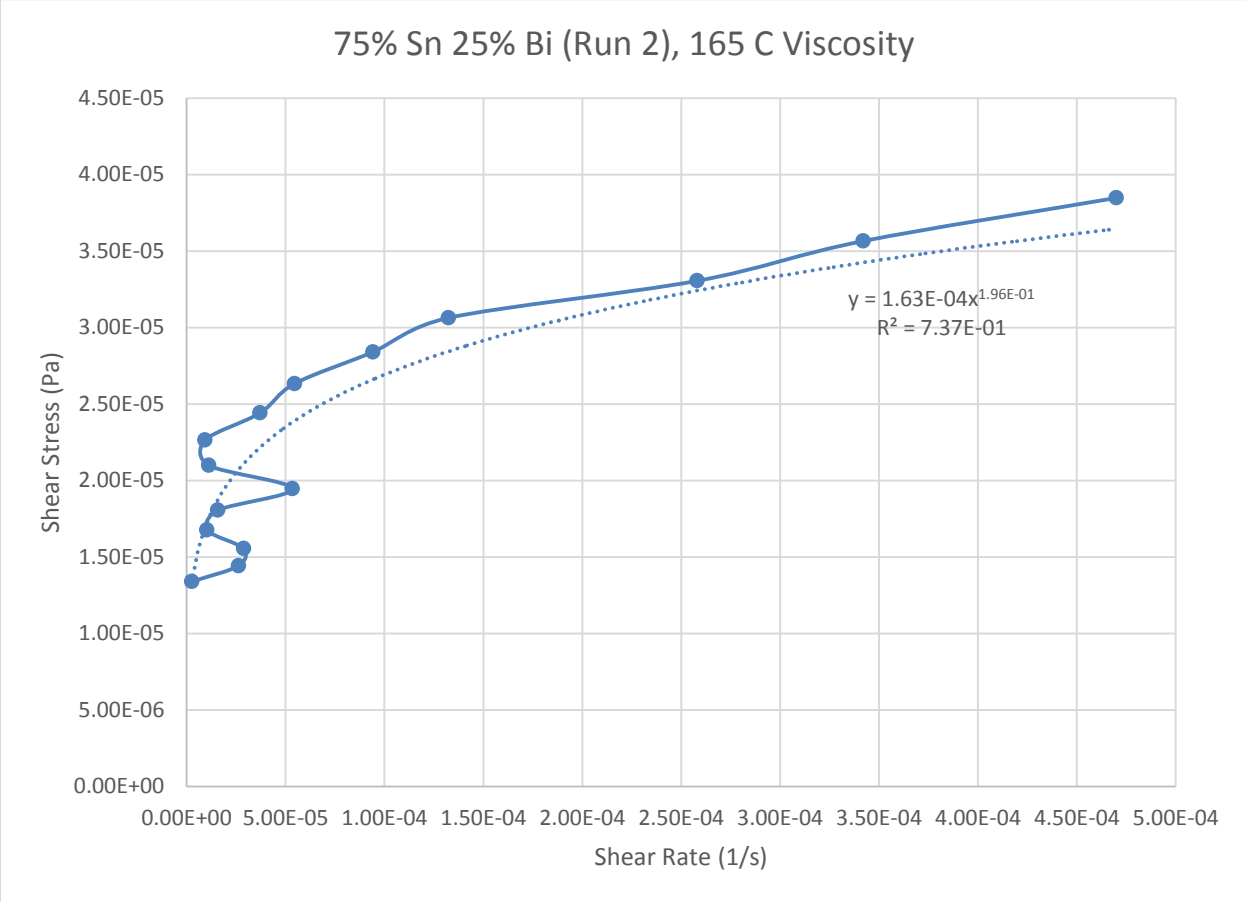

Figure 321- 75% Sn 25% Bi (Run 2), 165 C, Cone and Plate Viscosity

170 C

Fraction Solid	9.10 %
Power Law	$\tau = 8.36 * 10^{-5} * \dot{\gamma}^{0.1136}$
	$\mu = 9.50 * 10^{-6} * \dot{\gamma}^{-0.8864}$
R^2	80.28 %

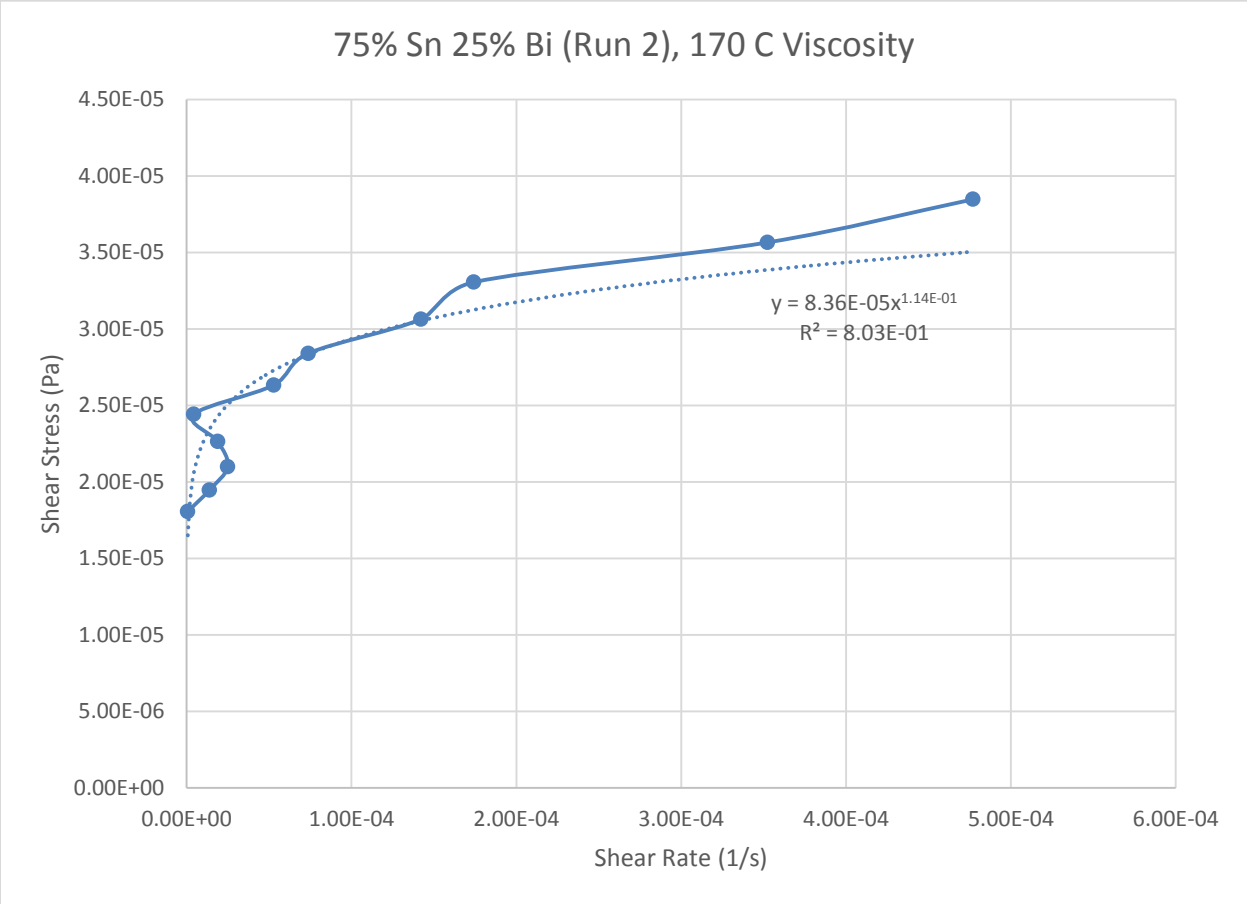

Figure 322- 75% Sn 25% Bi (Run 2), 170 C, Cone and Plate Viscosity

75% Tin 25% Bismuth (Run 3)

Predicted Composition: 75% Tin, 25% Bismuth

Theoretical Solidus Line: 139 C
Theoretical Liquidus Line: 182.2 C

Experimental Solidus Line: 138.9 C
Experimental Liquidus Line: 183.5 C

Set-Up Notes

- Zeroed gap at 165 C. Stress sweeps were then conducted in decreasing intervals of 5 C. The final stress sweep was conducted at 170 C.

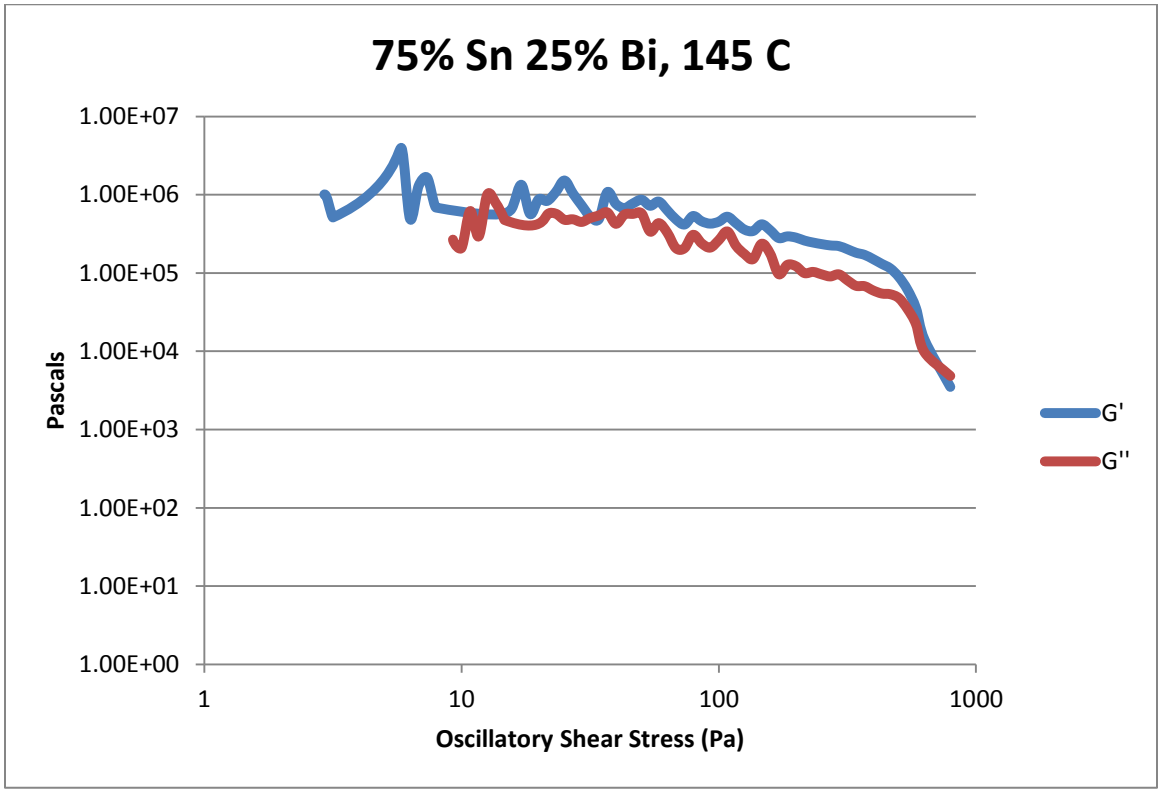

Figure 323- 75% Sn 25% Bi (Run 3), 145 C, Cone and Plate Stress Sweep

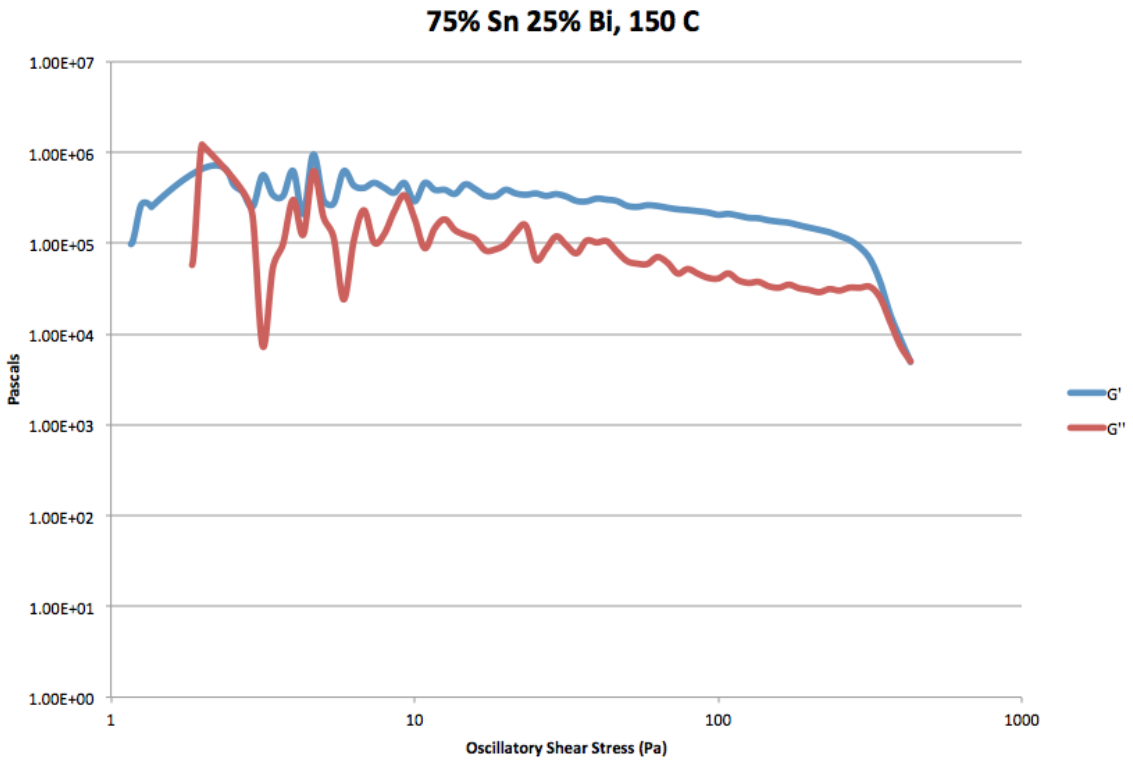

Figure 324- 75% Sn 25% Bi (Run 3), 150 C, Cone and Plate Stress Sweep

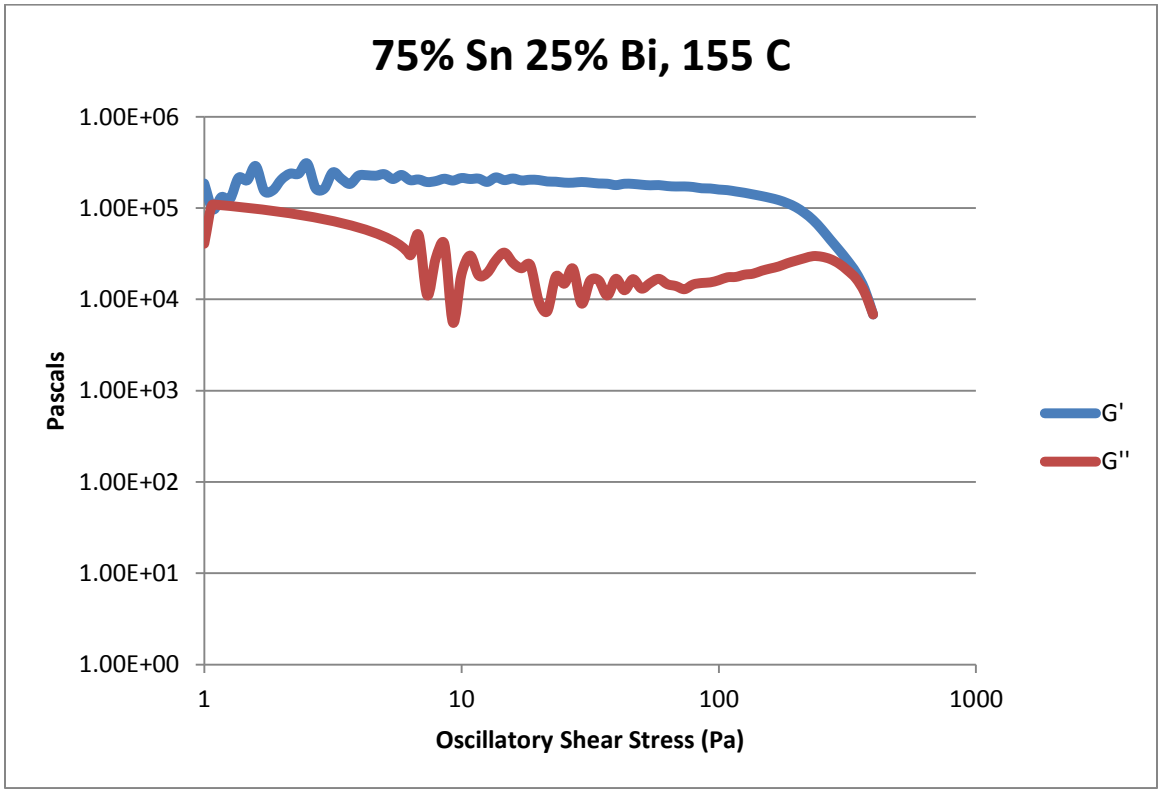

Figure 325- 75% Sn 25% Bi (Run 3), 155 C, Cone and Plate Stress Sweep

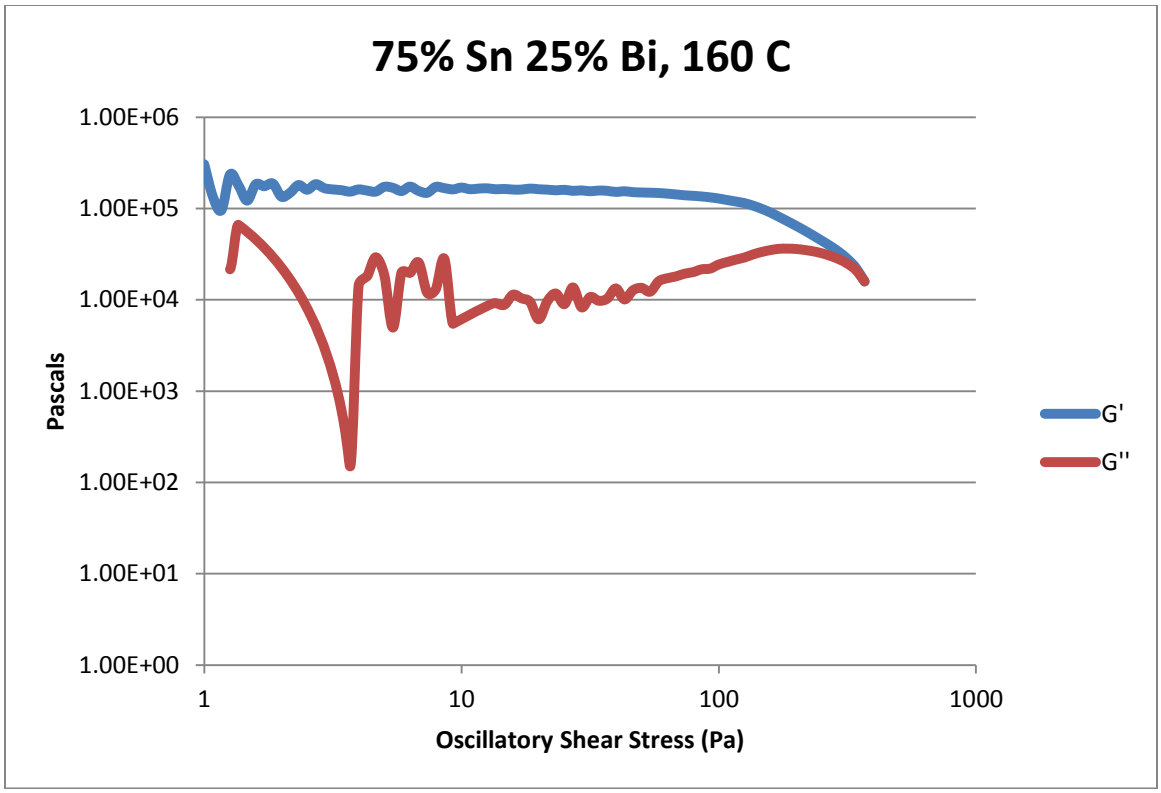

Figure 326- 75% Sn 25% Bi (Run 3), 160 C, Cone and Plate Stress Sweep

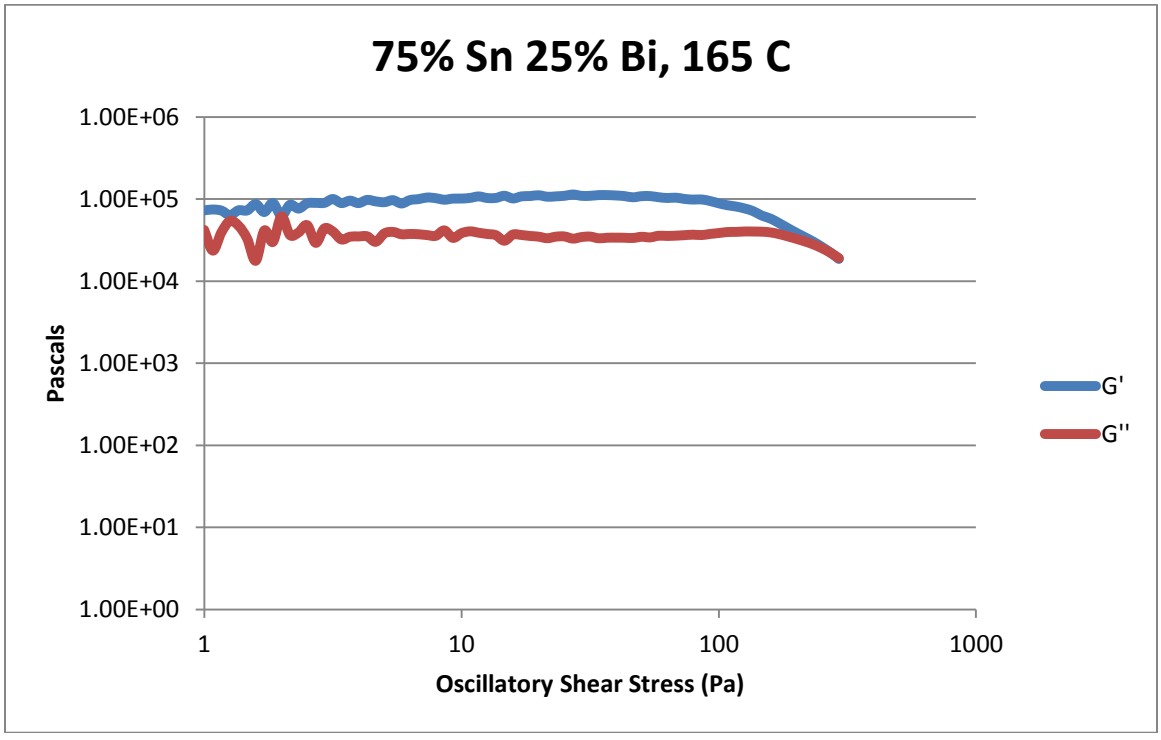

Figure 327- 75% Sn 25% Bi (Run 3), 165 C, Cone and Plate Stress Sweep

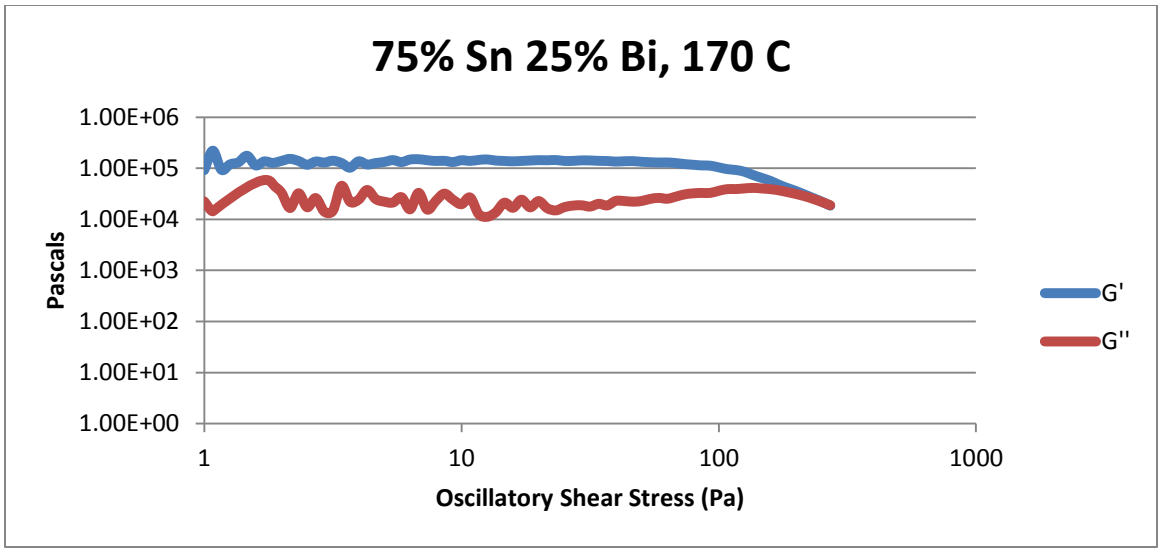

Figure 328- 75% Sn 25% Bi (Run 3), 170 C, Cone and Plate Stress Sweep

Temperature	Crossover Stress (Pa)	Crossover Stress (PSI)
145 C	$5.99 * 10^3$	0.869
150 C	$5.11 * 10^3$	0.741
155 C	$6.95 * 10^3$	1.01
160 C	$1.63 * 10^4$	2.36
165 C	$2.16 * 10^4$	3.13
170 C	$2.06 * 10^4$	2.99

Table 62- 75% Sn 25% Bi (Run 3), Cone and Plate Crossover Stresses

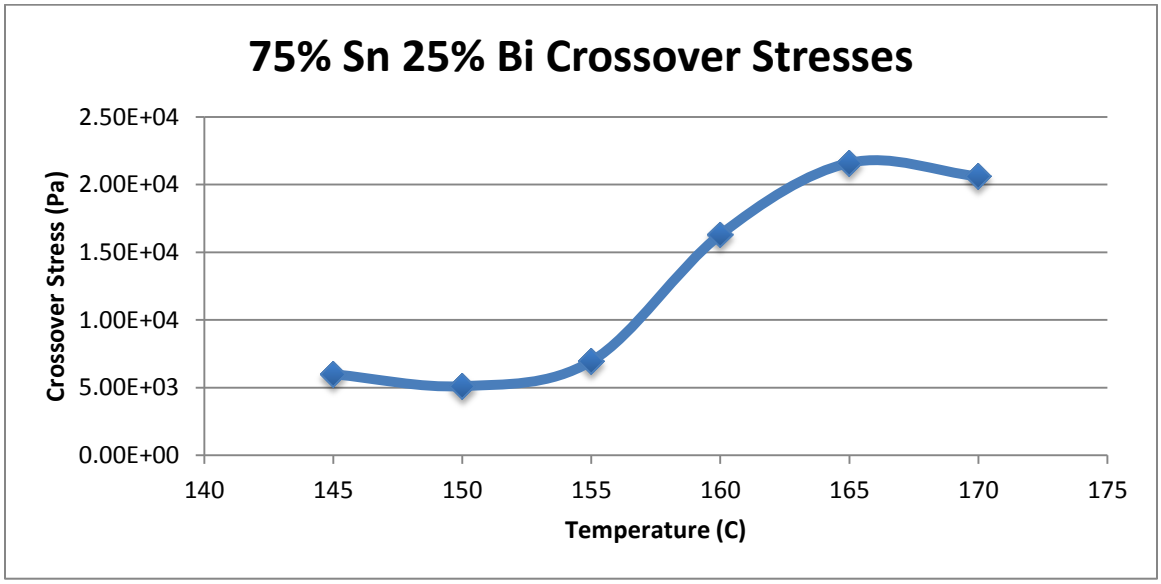

Figure 329- 75% Sn 25% Bi (Run 3), Cone and Plate Crossover Stresses

Temperature	Fraction Solid (At %)	G' Plateau (Pa)	G'' Plateau (Pa)
145 C	39.0	$3.50 * 10^5$	$8.05 * 10^4$
150 C	34.5	$2.98 * 10^5$	$3.05 * 10^4$
155 C	29.4	$1.92 * 10^5$	$2.98 * 10^4$
160 C	23.5	$1.62 * 10^5$	$3.35 * 10^4$
165 C	16.8	$1.09 * 10^5$	$4.02 * 10^4$
170 C	9.10	$1.41 * 10^5$	$3.99 * 10^4$

Table 63- 75% Sn 25% Bi (Run 3), Cone and Plate Plateau Stresses

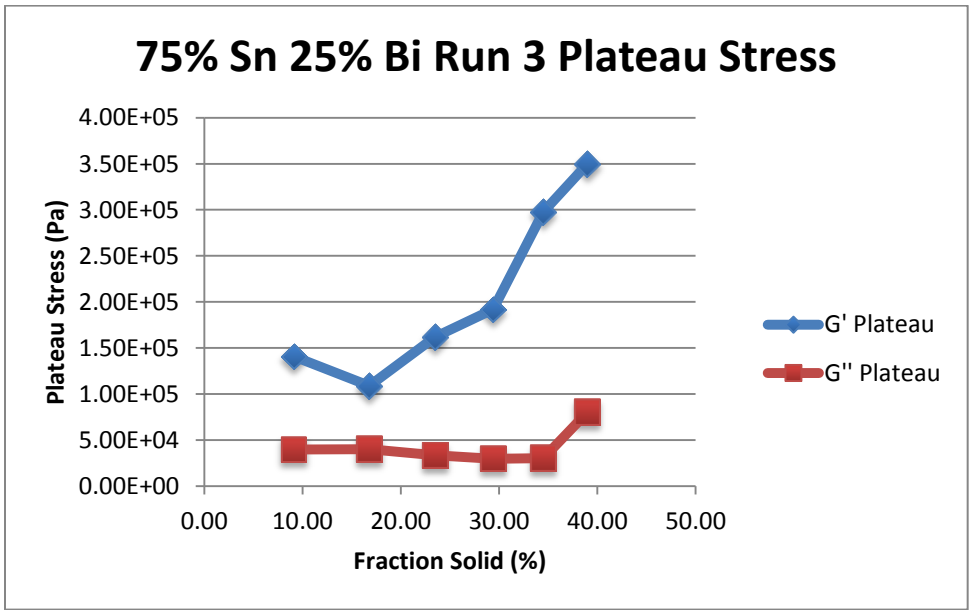

Figure 330- 75% Sn 25% Bi (Run 3), Cone and Plate Plateau Stresses vs. Fraction Solid

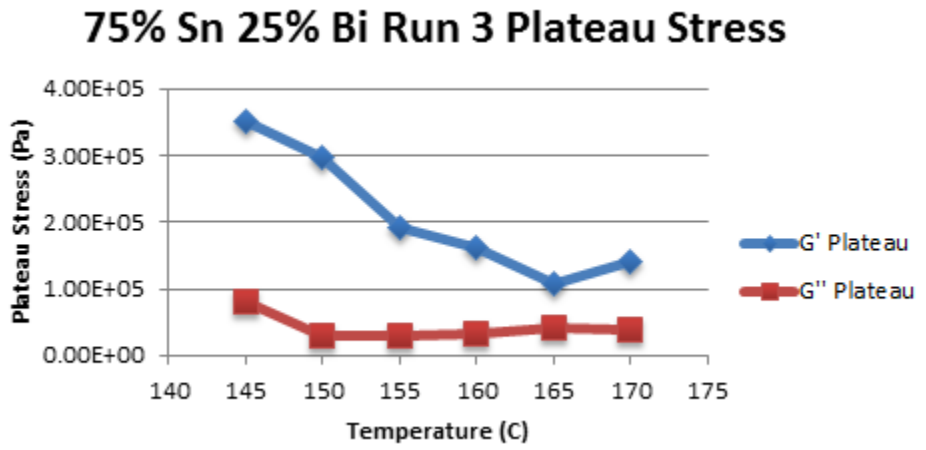

Figure 331- 75% Sn 25% Bi (Run 3), Cone and Plate Plateau Stresses vs. Temperature

75% Sn 25% Bi (Run 3) Viscosity					
Temperature	**Fraction Solid**	**Power Law**	**K**	**n**	**R^2**
145 C	39.0 %	$\tau = 1.18 * 10^{-4} * \dot{\gamma}^{0.1627}$ $\mu = 1.92 * 10^{-5} * \dot{\gamma}^{-0.8373}$	$1.18 * 10^{-4}$ Pa*s	0.1627	93.27 %
150 C	34.5 %	$\tau = 7.32 * 10^{-5} * \dot{\gamma}^{0.1612}$ $\mu = 1.18 * 10^{-5} * \dot{\gamma}^{-0.8388}$	$7.32 * 10^{-5}$ Pa*s	0.1612	95.35 %
155 C	29.4 %	$\tau = 1.93 * 10^{-4} * \dot{\gamma}^{0.2854}$ $\mu = 5.51 * 10^{-5} * \dot{\gamma}^{-0.7146}$	$1.93 * 10^{-4}$ Pa*s	0.2854	69.93 %
160 C	23.5 %	$\tau = 2.44 * 10^{-4} * \dot{\gamma}^{0.2978}$ $\mu = 7.27 * 10^{-5} * \dot{\gamma}^{-0.7022}$	$2.44 * 10^{-4}$ Pa*s	0.2978	86.42 %
165 C	16.8 %	$\tau = 1.59 * 10^{-4} * \dot{\gamma}^{0.2610}$ $\mu = 4.15 * 10^{-5} * \dot{\gamma}^{-0.7390}$	$1.59 * 10^{-4}$ Pa*s	0.2610	79.69 %
170 C	9.10 %	$\tau = 1.81 * 10^{-4} * \dot{\gamma}^{0.2810}$ $\mu = 5.09 * 10^{-5} * \dot{\gamma}^{-0.7190}$	$1.81 * 10^{-4}$ Pa*s	0.2810	75.79 %

Table 64- 75% Sn 25% Bi (Run 3), Cone and Plate Viscosity

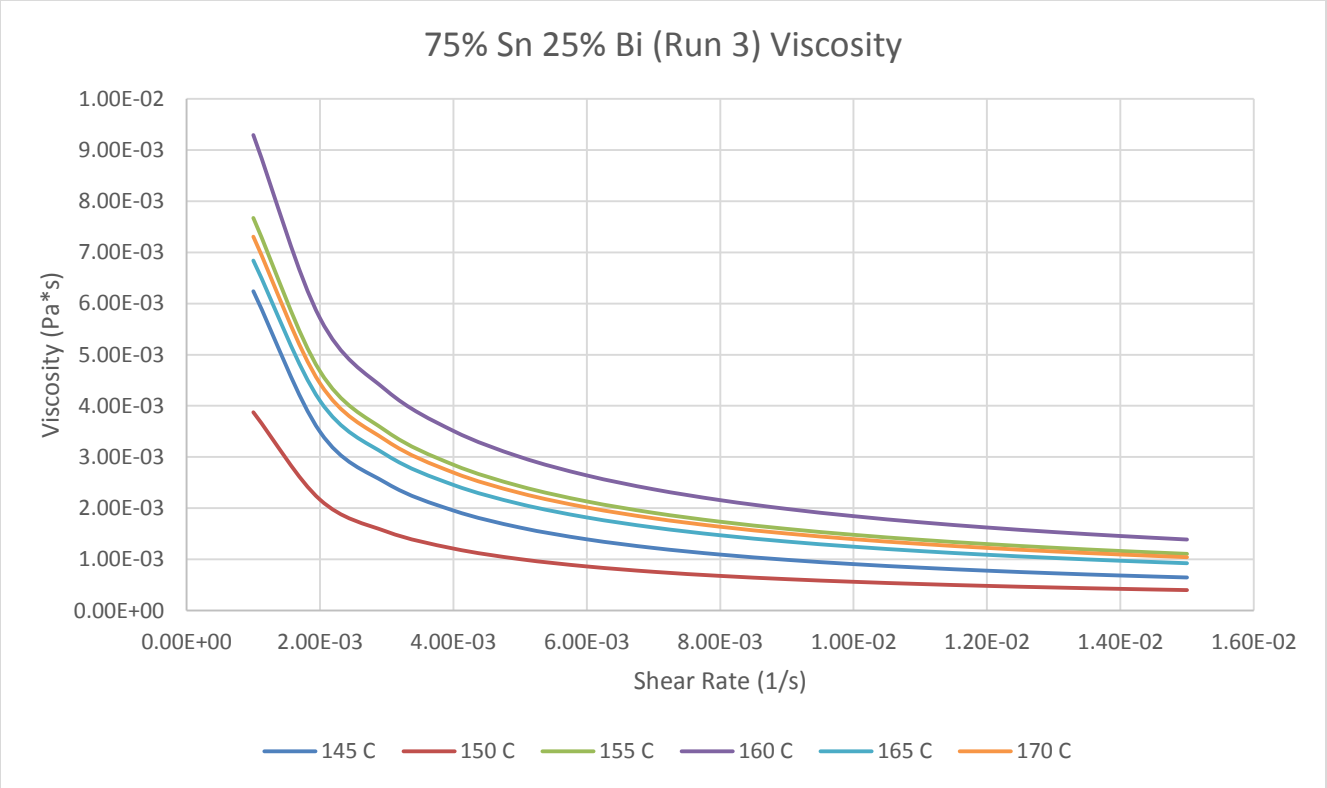

Figure 332- 75% Sn 25% Bi (Run 3), Cone and Plate Viscosity

145 C

Fraction Solid	39.0 %
Power Law	$\tau = 1.18 * 10^{-4} * \dot{\gamma}^{0.1627}$
	$\mu = 1.92 * 10^{-5} * \dot{\gamma}^{-0.8373}$
R^2	93.27 %

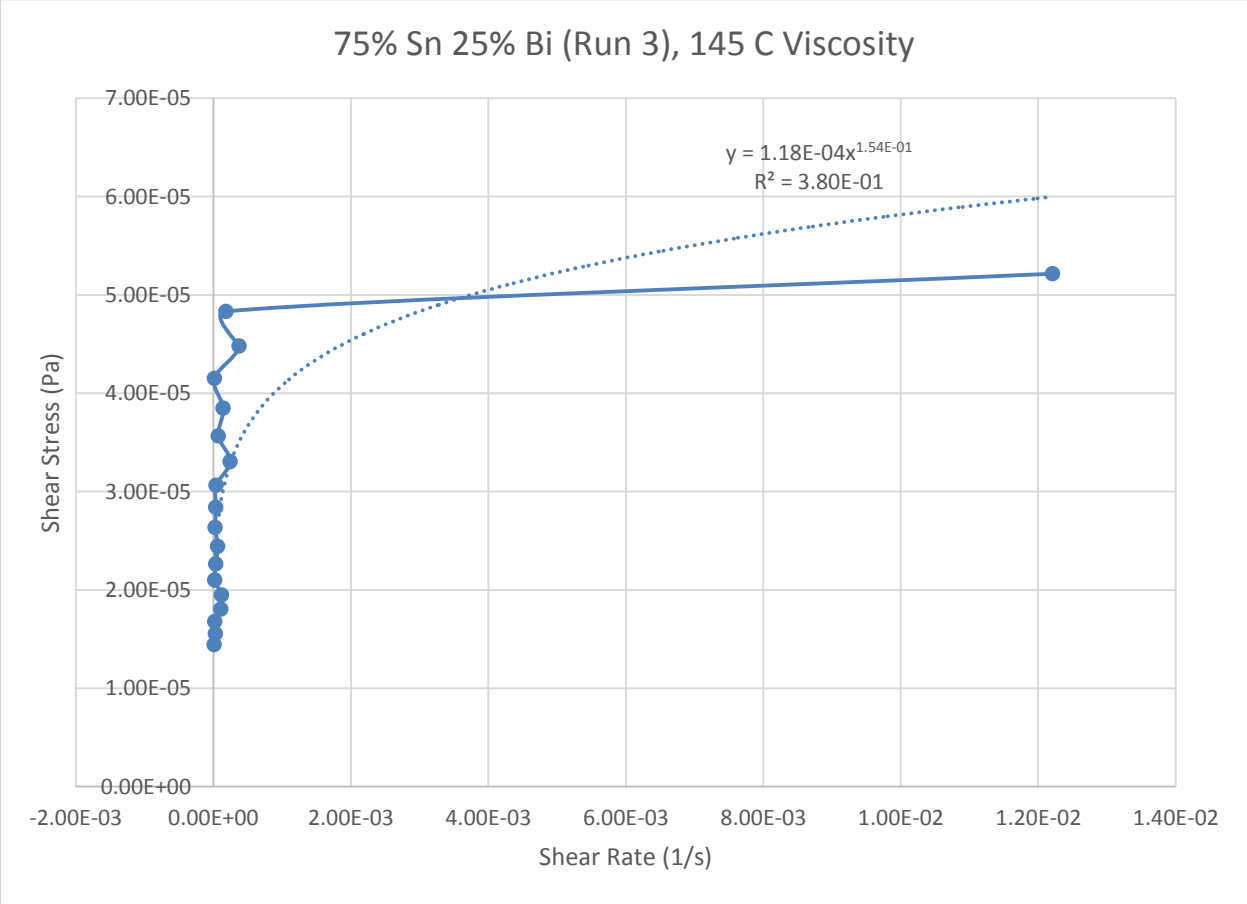

Figure 333- 75% Sn 25% Bi (Run 3), 145 C, Cone and Plate Viscosity

150 C

Fraction Solid	34.5 %
Power Law	$\tau = 7.32 * 10^{-5} * \dot{\gamma}^{0.1612}$
	$\mu = 1.18 * 10^{-5} * \dot{\gamma}^{-0.8388}$
R^2	95.35 %

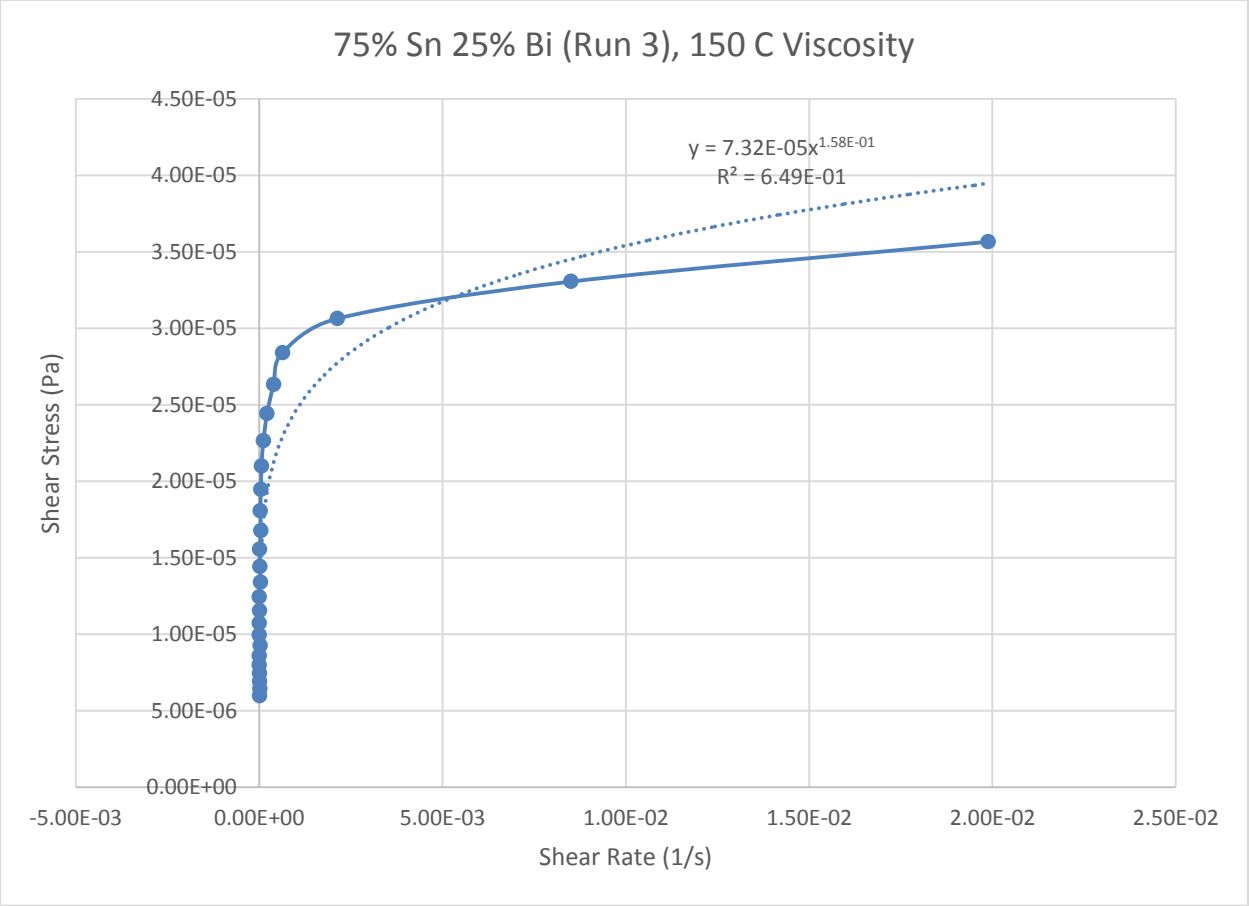

Figure 334- 75% Sn 25% Bi (Run 3), 150 C, Cone and Plate Viscosity

155 C

Fraction Solid	29.40 %
Power Law	$\tau = 1.93 * 10^{-4} * \dot{\gamma}^{0.2854}$
	$\mu = 5.51 * 10^{-5} * \dot{\gamma}^{-0.7146}$
R^2	69.93 %

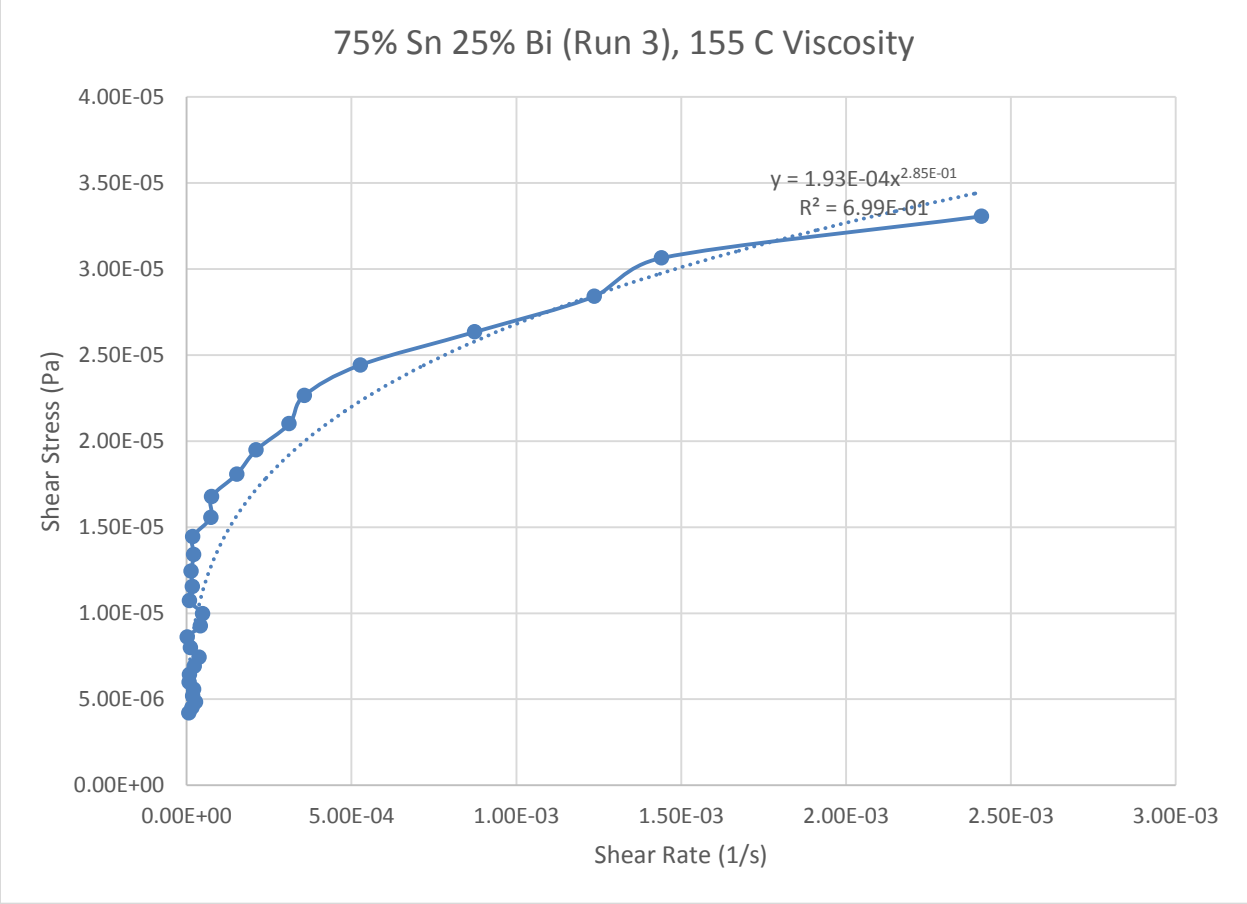

Figure 335- Figure 266- 75% Sn 25% Bi (Run 3), 155 C, Cone and Plate Viscosity

160 C

Fraction Solid	23.50 %
Power Law	$\tau = 2.44 * 10^{-4} * \dot{\gamma}^{0.2978}$
	$\mu = 7.27 * 10^{-5} * \dot{\gamma}^{-0.7022}$
R^2	86.42 %

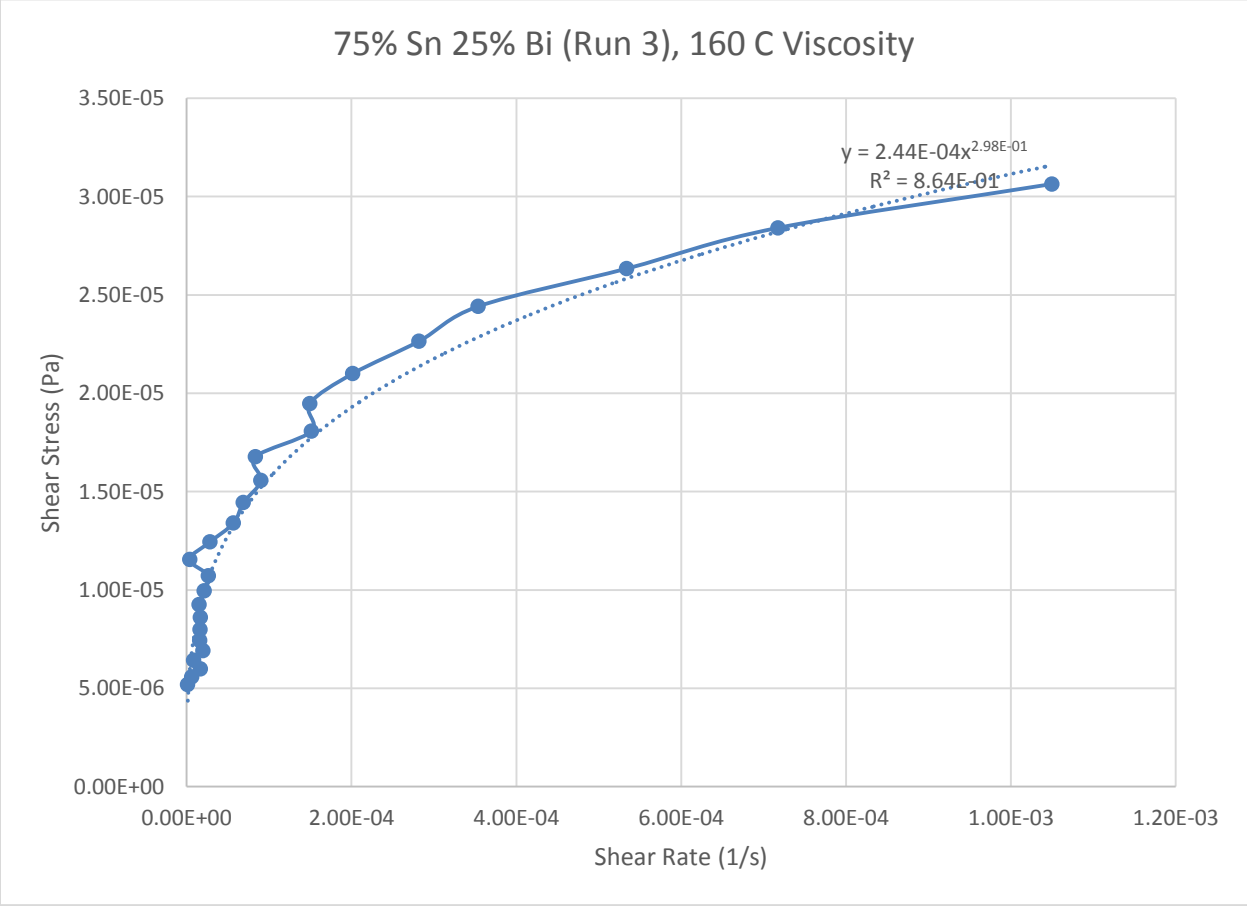

Figure 336- Figure 266- 75% Sn 25% Bi (Run 3), 160 C, Cone and Plate Viscosity

165 C

Fraction Solid	16.80 %
Power Law	$\tau = 1.59 * 10^{-4} * \dot{\gamma}^{0.261}$
	$\mu = 4.15 * 10^{-5} * \dot{\gamma}^{-0.7390}$
R^2	79.69 %

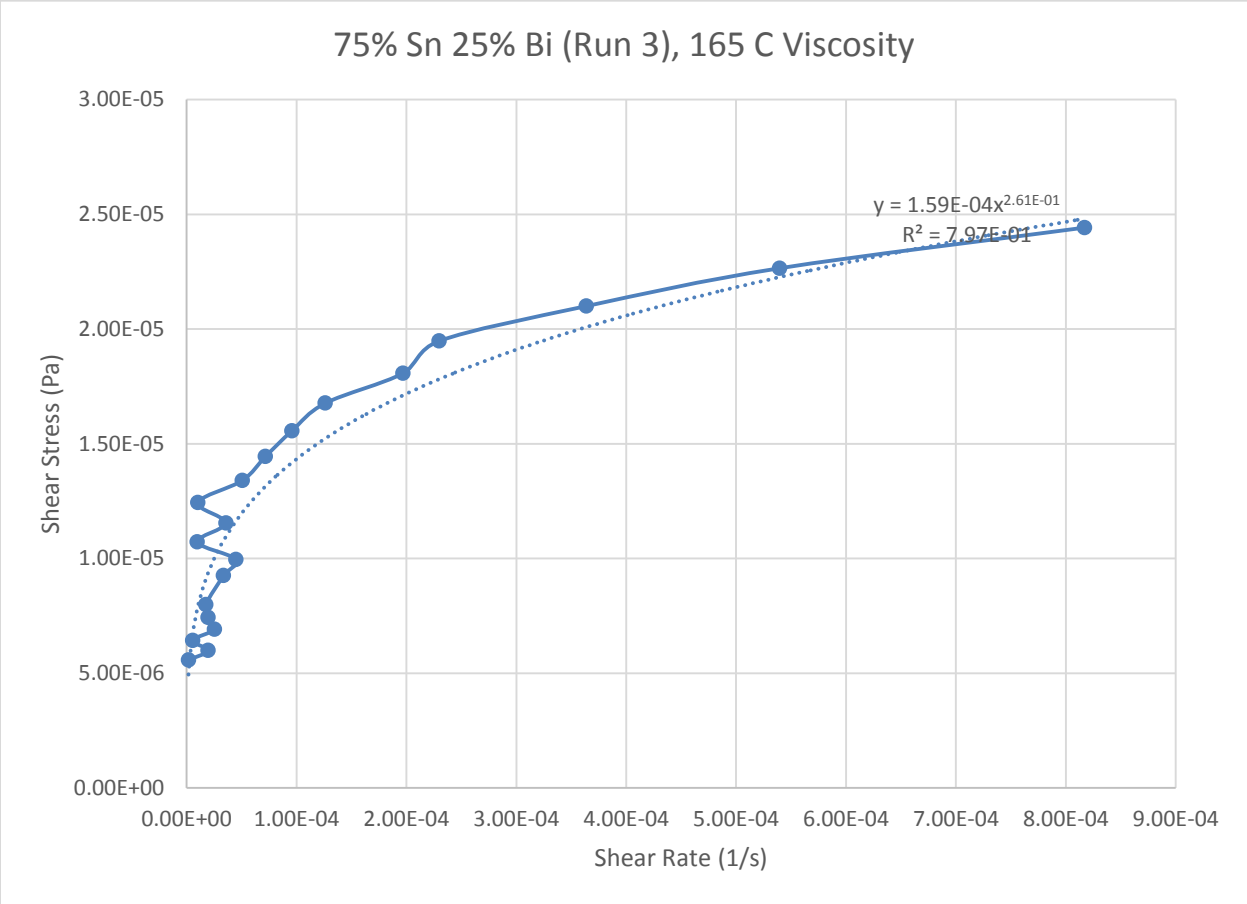

Figure 337- Figure 266- 75% Sn 25% Bi (Run 3), 165 C, Cone and Plate Viscosity

170 C

Fraction Solid	9.10 %
Power Law	$\tau = 1.81 * 10^{-4} * \dot{\gamma}^{0.281}$
	$\mu = 5.09 * 10^{-5} * \dot{\gamma}^{-0.7190}$
R^2	75.79 %

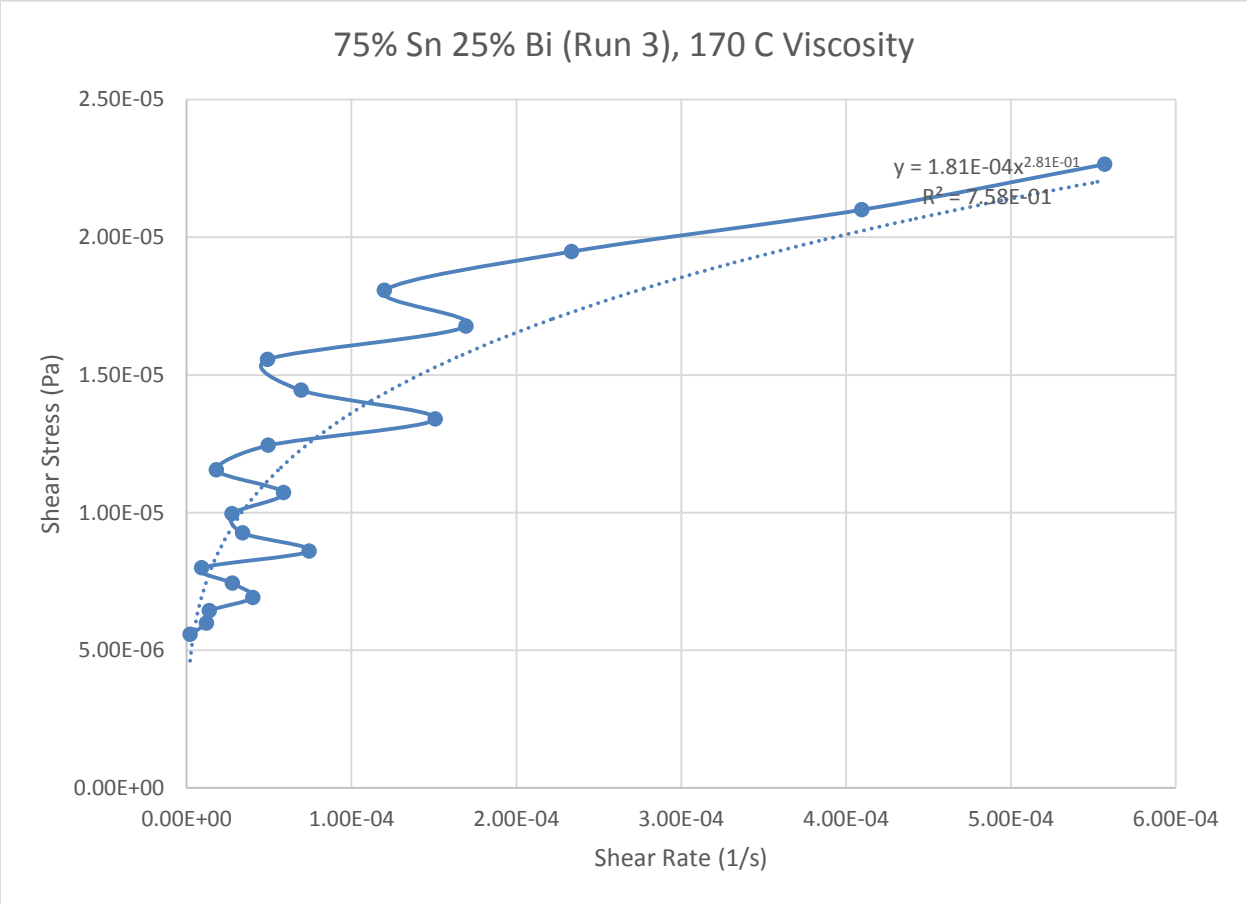

Figure 338- Figure 266- 75% Sn 25% Bi (Run 3), 170 C, Cone and Plate Viscosity

80% Tin 20% Bismuth (Run 1)

Actual Composition: 81.57% Sn, 18.43% Bi

Theoretical Solidus Line: 139 C
Theoretical Liquidus Line: 192.1 C

Experimental Solidus Line: 137.4 C
Experimental Liquidus Line: 185.9 C

Run 1 Set Up Notes

- The stage was heated to 200 Celsius and the gap was zeroed. During the experiment, the temperature was lowered to 145 C and then increased in increments of 5 C to 190 C. 170 C to 190 C gave usable data.

- The lower temperatures had excessive noise (which resulted in multiple crossover points) or too many negative values (which is why some of the logarithmic plots below appear to be missing data).

Plots

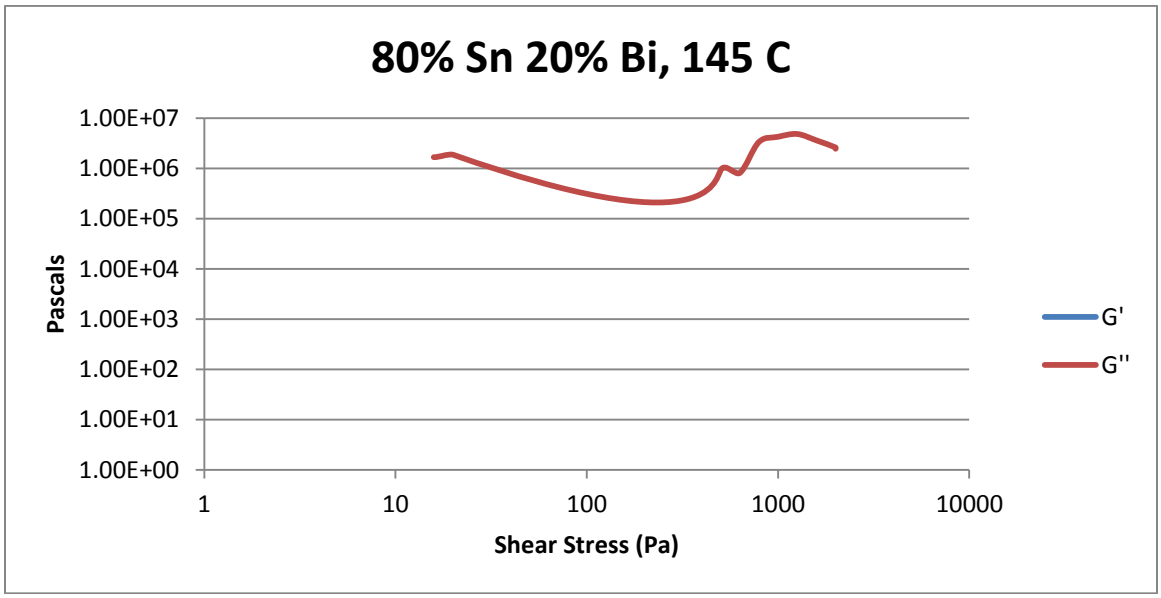

Figure 339- 80% Sn 20% Bi (Run 1), 145 C, Cone and Plate Stress Sweep

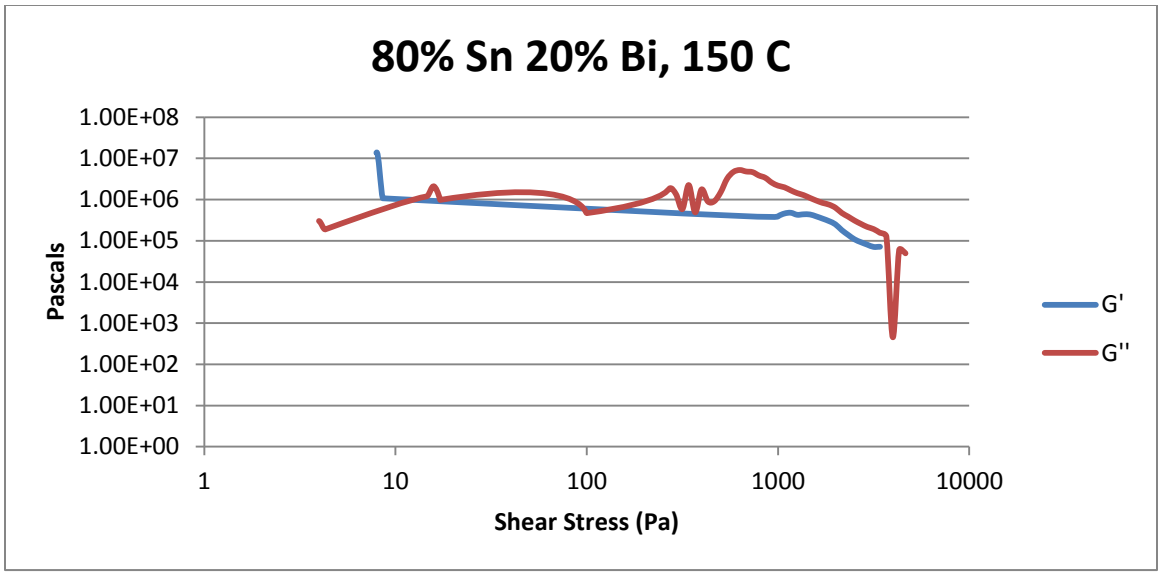

Figure 340- 80% Sn 20% Bi (Run 1), 150 C, Cone and Plate Stress Sweep

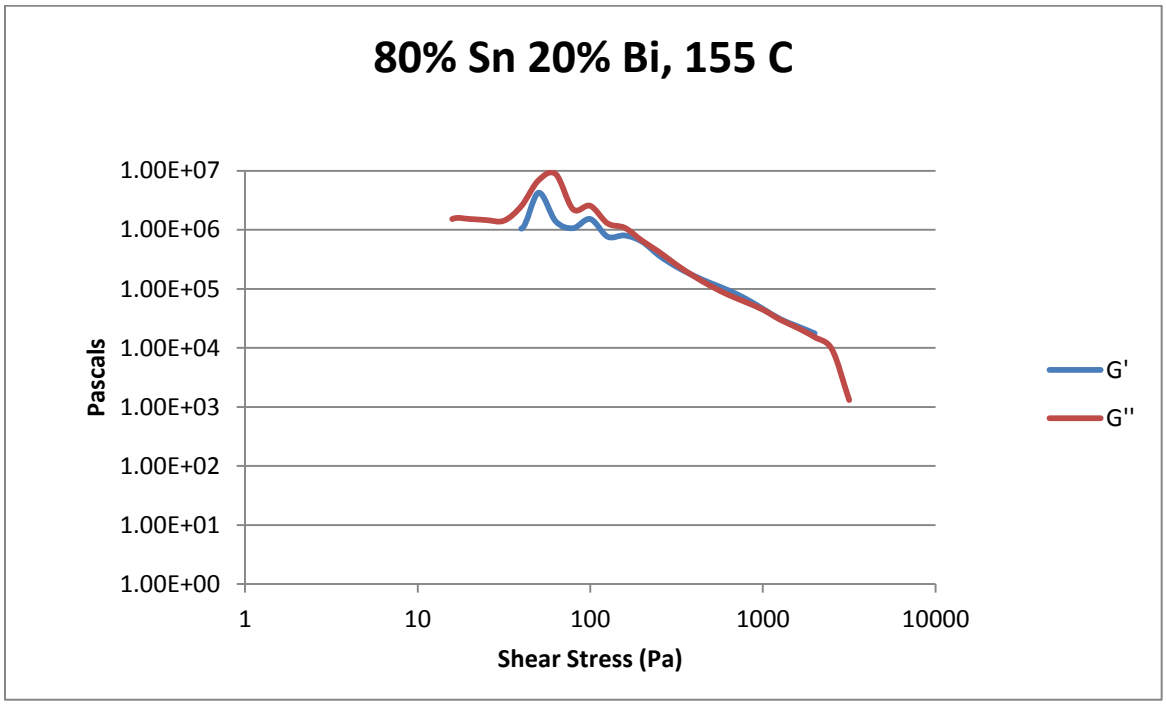

Figure 341- 80% Sn 20% Bi (Run 1), 155 C, Cone and Plate Stress Sweep

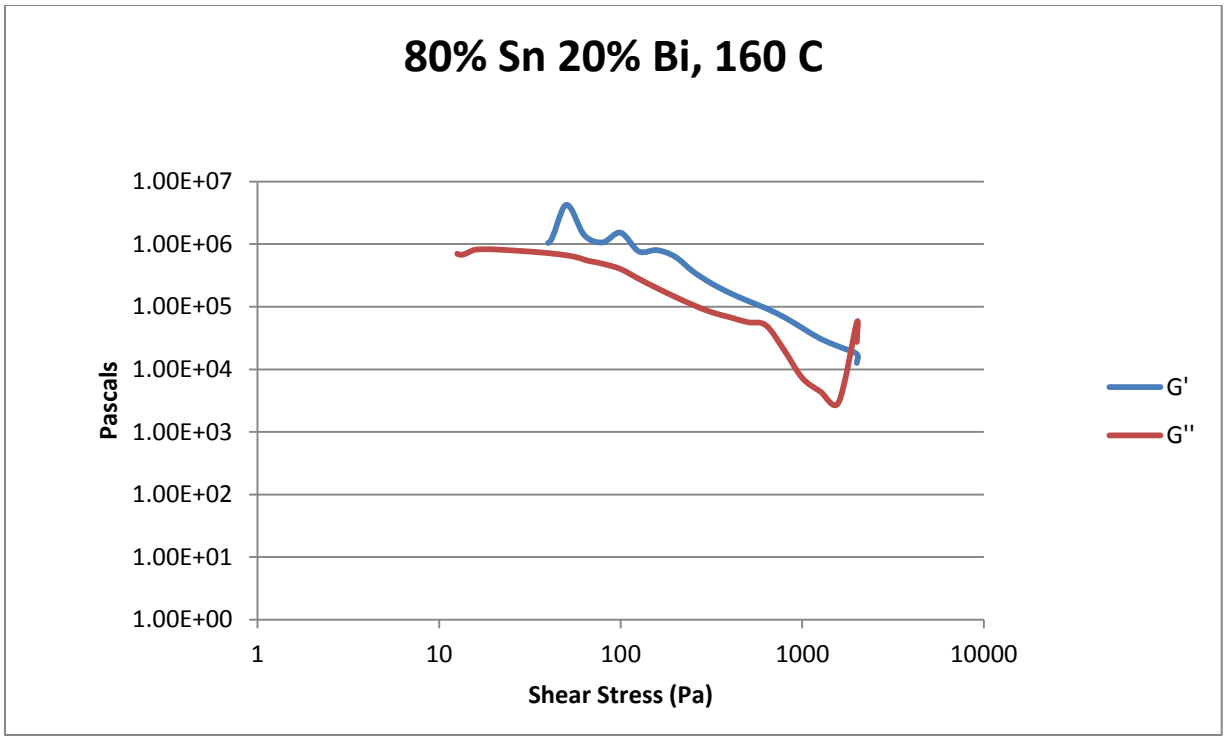

Figure 342- 80% Sn 20% Bi (Run 1), 160 C, Cone and Plate Stress Sweep

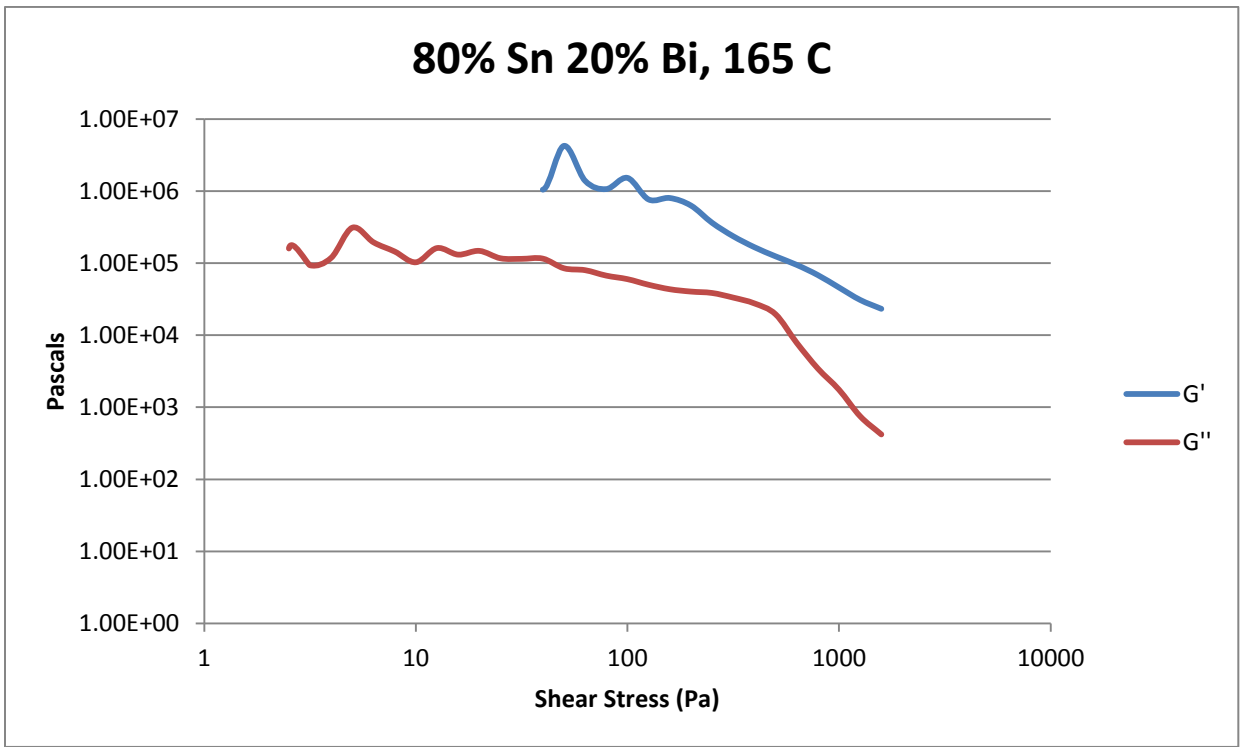

Figure 343- 80% Sn 20% Bi (Run 1), 165 C, Cone and Plate Stress Sweep

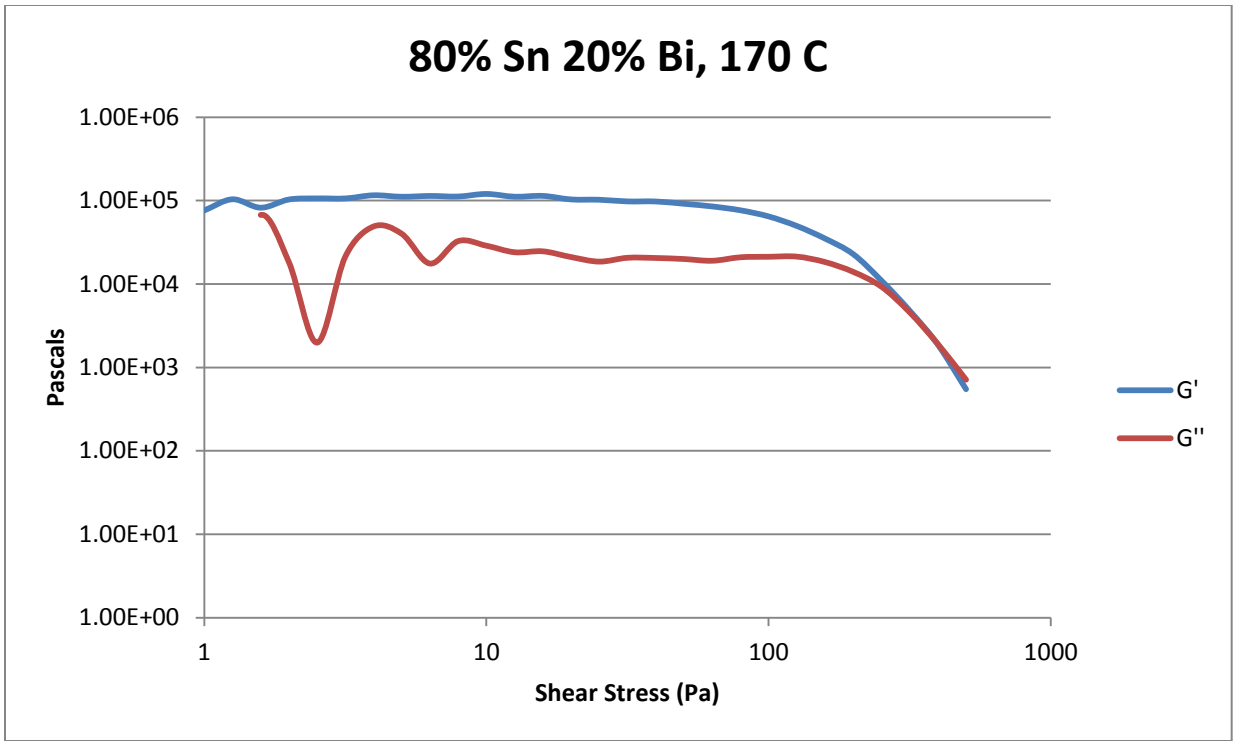

Figure 344- 80% Sn 20% Bi (Run 1), 170 C, Cone and Plate Stress Sweep

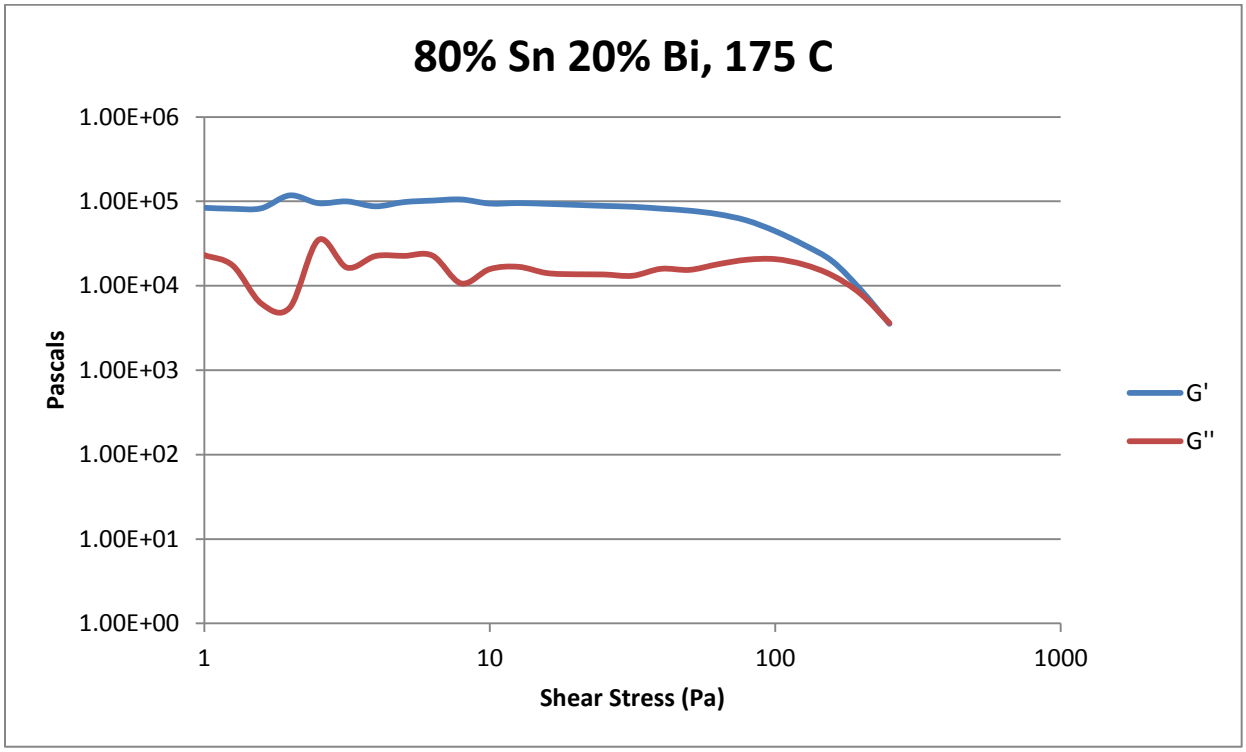

Figure 345- 80% Sn 20% Bi (Run 1), 175 C, Cone and Plate Stress Sweep

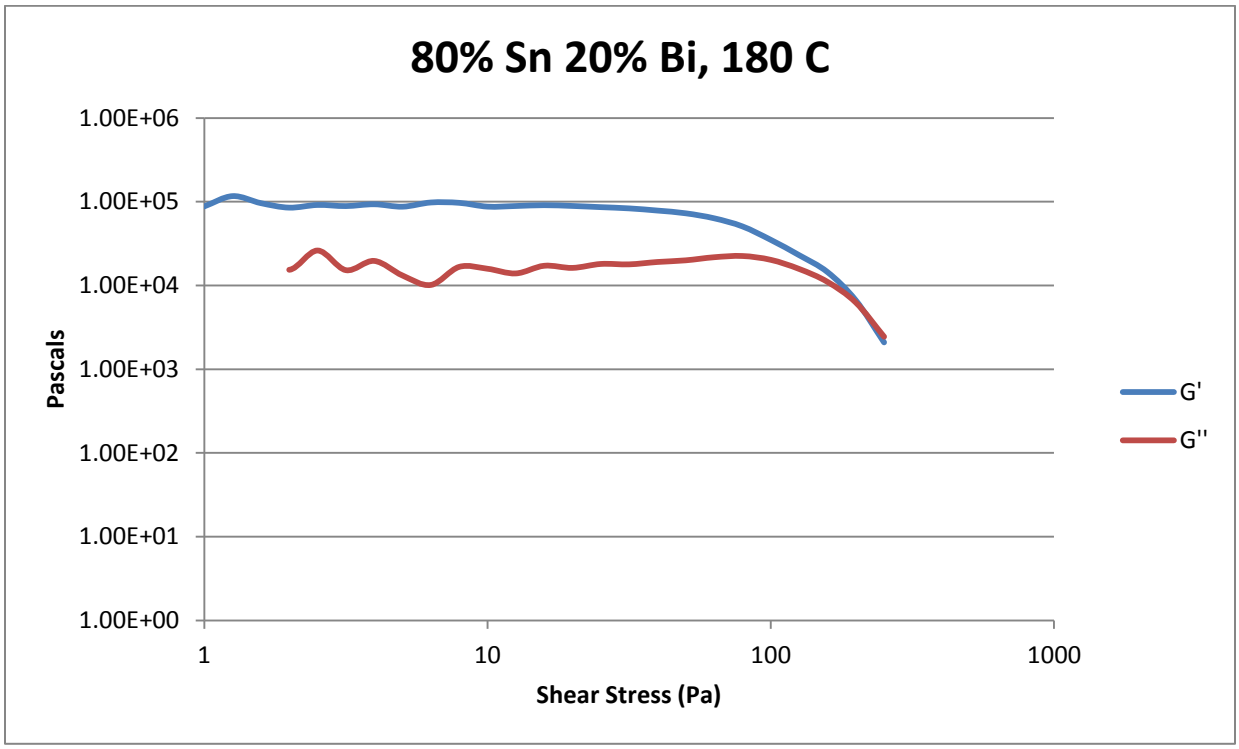

Figure 346- 80% Sn 20% Bi (Run 1), 180 C, Cone and Plate Stress Sweep

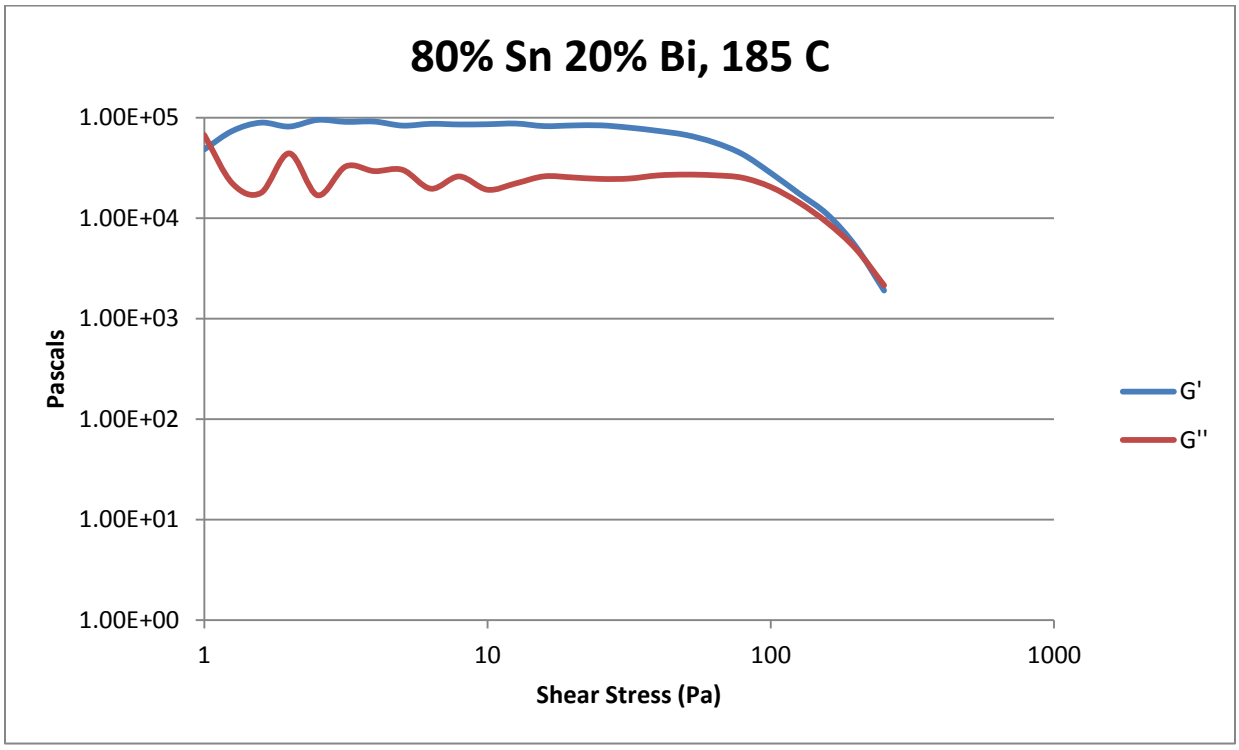

Figure 347- 80% Sn 20% Bi (Run 1), 185 C, Cone and Plate Stress Sweep

Temperature	Crossover Stress (Pa)	Crossover Stress (PSI)
155 C	$4.47 * 10^3$ *	0.648
160 C	$4.93 * 10^3$	0.715
165 C	$7.94 * 10^2$ *	0.115
170 C	$2.25 * 10^3$	0.326
175 C	$3.91 * 10^3$	0.567
180 C	$4.25 * 10^3$	0.616
185 C	$3.46 * 10^3$	0.502

Table 65- 80% Sn 20% Bi (Run 1), Cone and Plate Crossover Stresses

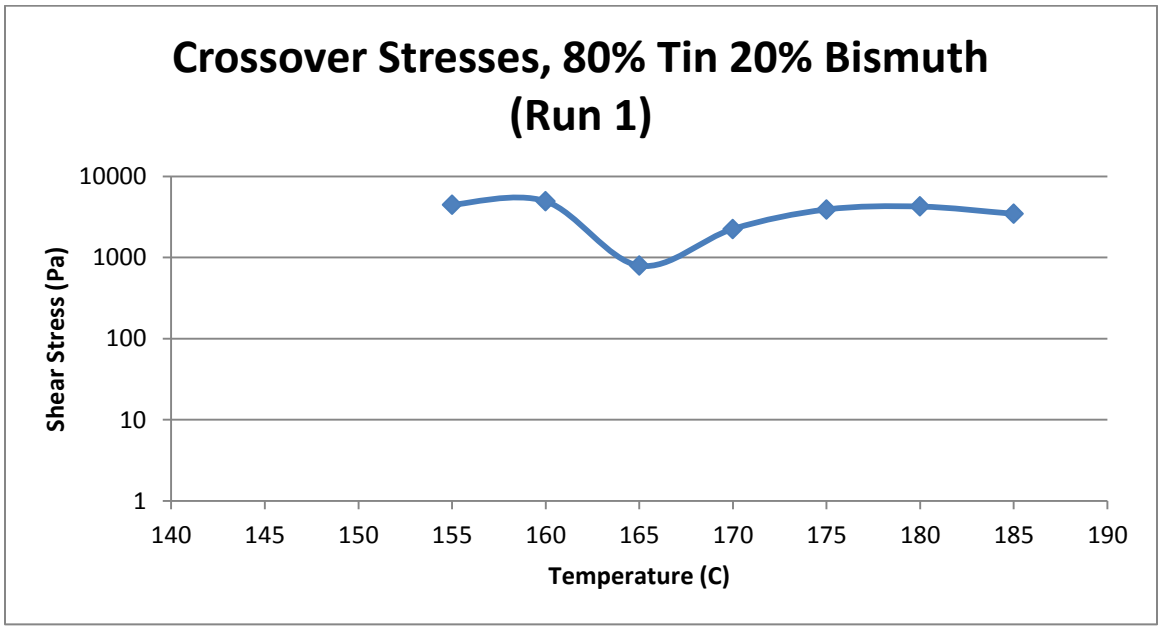

Figure 348- 80% Sn 20% Bi (Run 1), Cone and Plate Crossover Stresses

Temperature	Fraction Solid (At %)	G' Plateau (Pa)	G'' Plateau (Pa)
145 C	62.0	$9.56 * 10^5$	$5.39 * 10^6$
150 C	54.5	$2.37 * 10^6$	$3.00 * 10^6$
155 C	47.5	$1.52 * 10^6$	$2.11 * 10^6$
160 C	41.5	$1.21 * 10^6$	$7.84 * 10^5$
165 C	36.1	$3.37 * 10^5$	$1.15 * 10^5$
170 C	29.9	$1.14 * 10^5$	$2.03 * 10^4$
175 C	22.6	$9.72 * 10^4$	$1.48 * 10^4$
180 C	13.9	$9.03 * 10^4$	$1.60 * 10^4$
185 C	3.40	$8.48 * 10^4$	$2.58 * 10^4$
190 C	0	$7.81 * 10^4$	$3.07 * 10^4$

Table 66- 80% Sn 20% Bi (Run 1), Cone and Plate Plateau Stresses

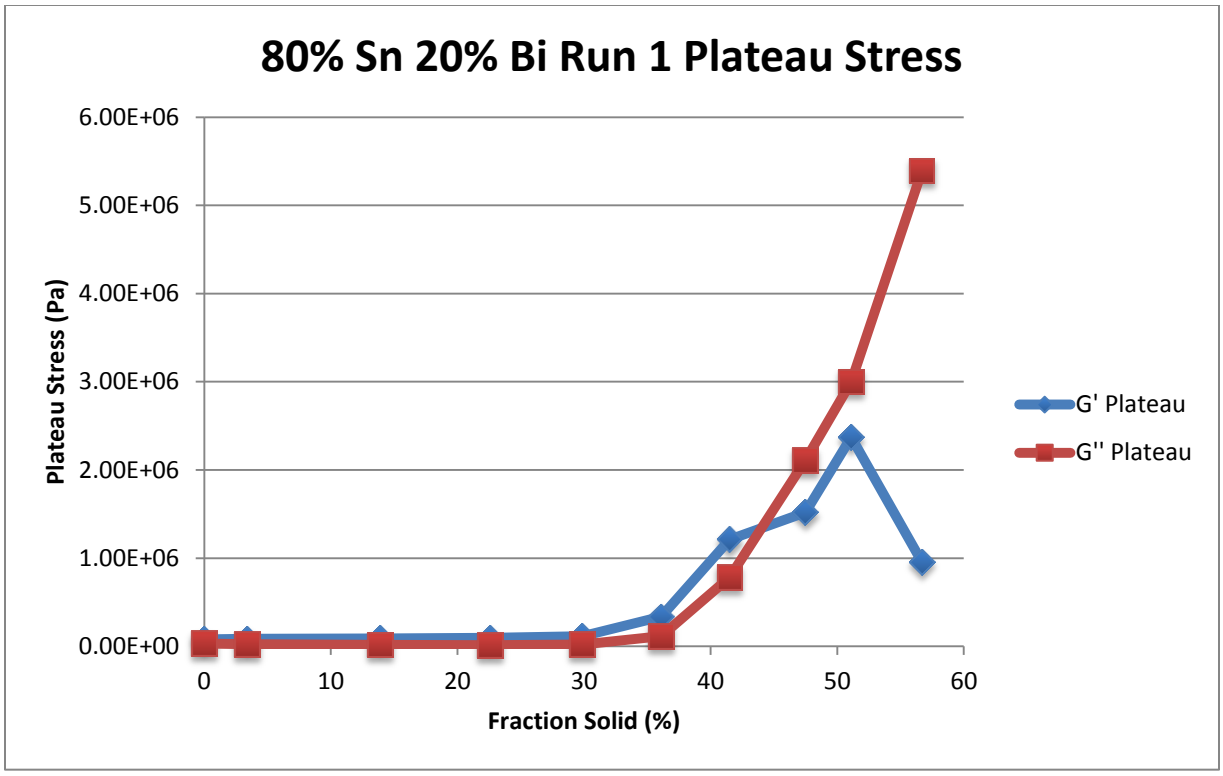

Figure 349- 80% Sn 20% Bi (Run 1), Cone and Plate Plateau Stresses vs. Fraction Solid

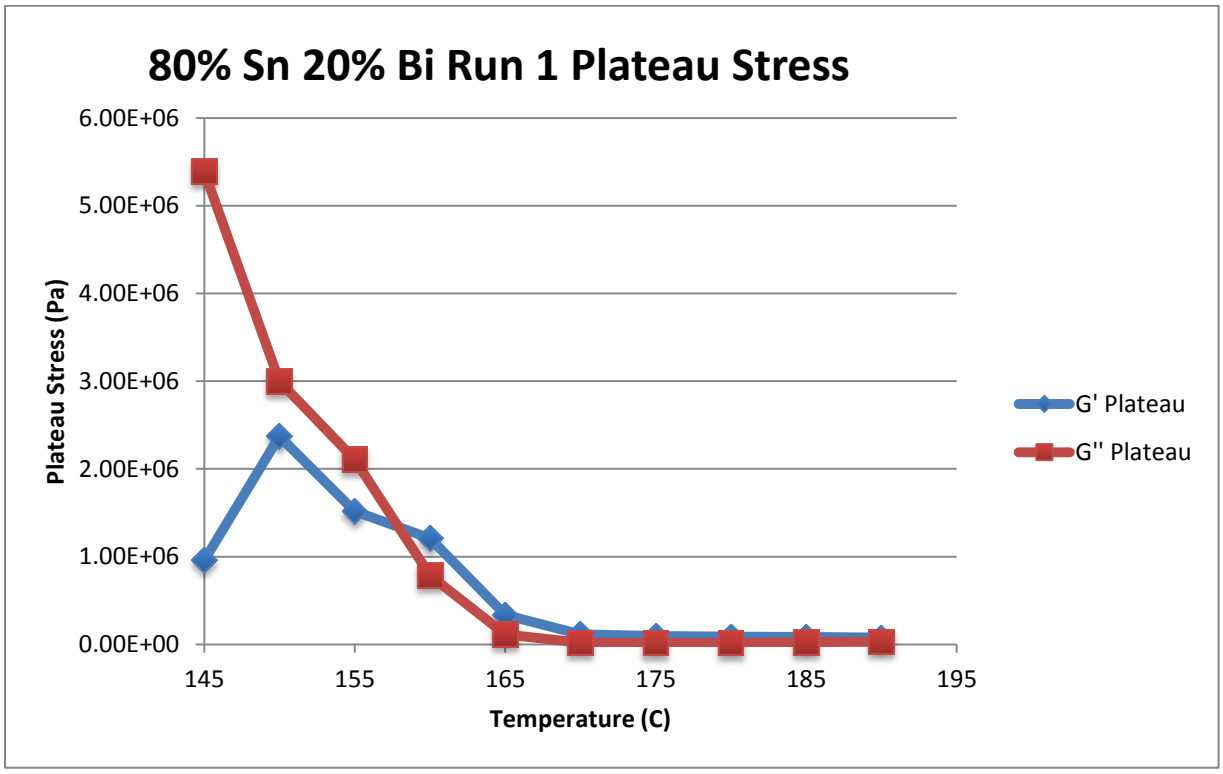

Figure 350- 80% Sn 20% Bi (Run 1), Cone and Plate Plateau Stresses vs. Temperature

80% Sn 20% Bi (Run 1) Viscosity					
Temperature	**Fraction Solid**	**Power Law**	**K**	**n**	**R^2**
145 C	56.68 %	$\tau = 1.73 * 10^{-5} * \dot{\gamma}^{0.0115}$ $\mu = 1.99 * 10^{-7} * \dot{\gamma}^{-0.9885}$	$1.73 * 10^{-5}$ Pa*s	0.0115	0.03 %
150 C	51.08 %	$\tau = 4.54 * 10^{-4} * \dot{\gamma}^{0.1785}$ $\mu = 8.10 * 10^{-5} * \dot{\gamma}^{-0.8215}$	$4.54 * 10^{-4}$ Pa*s	0.1785	46.18 %
155 C	47.50 %	$\tau = 7.98 * 10^{-4} * \dot{\gamma}^{0.3105}$ $\mu = 2.48 * 10^{-5} * \dot{\gamma}^{-0.6895}$	$7.98 * 10^{-4}$ Pa*s	0.3105	78.93 %
160 C	41.50 %	$\tau = 8.75 * 10^{-4} * \dot{\gamma}^{0.3600}$ $\mu = 3.15 * 10^{-4} * \dot{\gamma}^{-0.6400}$	$8.75 * 10^{-4}$ Pa*s	0.3600	86.71 %
165 C	36.10 %	$\tau = 1.63 * 10^{-4} * \dot{\gamma}^{0.2146}$ $\mu = 3.50 * 10^{-5} * \dot{\gamma}^{-0.7854}$	$1.63 * 10^{-4}$ Pa*s	0.2146	88.37 %
170 C	29.86 %	$\tau = 1.63 * 10^{-4} * \dot{\gamma}^{0.3566}$ $\mu = 5.81 * 10^{-5} * \dot{\gamma}^{-0.6434}$	$1.63 * 10^{-4}$ Pa*s	0.3566	79.90 %
175 C	22.60 %	$\tau = 6.03 * 10^{-5} * \dot{\gamma}^{0.2355}$ $\mu = 1.42 * 10^{-5} * \dot{\gamma}^{-0.7645}$	$6.03 * 10^{-5}$ Pa*s	0.2355	99.16 %
180 C	13.90 %	$\tau = 5.97 * 10^{-5} * \dot{\gamma}^{0.2461}$ $\mu = 1.47 * 10^{-5} * \dot{\gamma}^{-0.7539}$	$5.97 * 10^{-5}$ Pa*s	0.2461	98.19 %
185 C	3.40 %	$\tau = 6.25 * 10^{-5} * \dot{\gamma}^{0.2573}$ $\mu = 1.61 * 10^{-5} * \dot{\gamma}^{-0.7427}$	$6.25 * 10^{-5}$ Pa*s	0.2573	96.73 %
190 C	0 %	$\tau = 6.35 * 10^{-3} * \dot{\gamma}^{0.8213}$ $\mu = 5.21 * 10^{-3} * \dot{\gamma}^{-0.1787}$	$6.35 * 10^{-3}$ Pa*s	0.8213	77.03 %

Table 67- 80% Sn 20% Bi (Run 1), Cone and Plate Viscosity

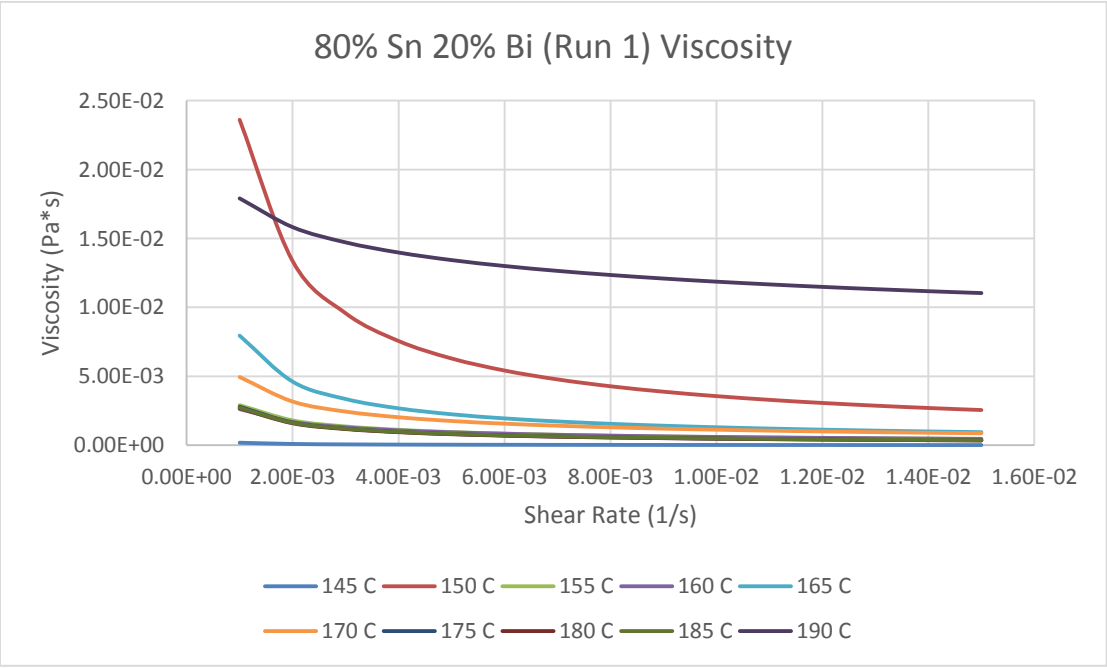

Figure 351- 80% Sn 20% Bi (Run 1), Cone and Plate Viscosity

145 C

Fraction Solid	56.68 %
Power Law	$\tau = 1.73 * 10^{-5} * \dot{\gamma}^{0.0115}$
	$\mu = 1.99 * 10^{-7} * \dot{\gamma}^{-0.9885}$
R^2	0.03 %

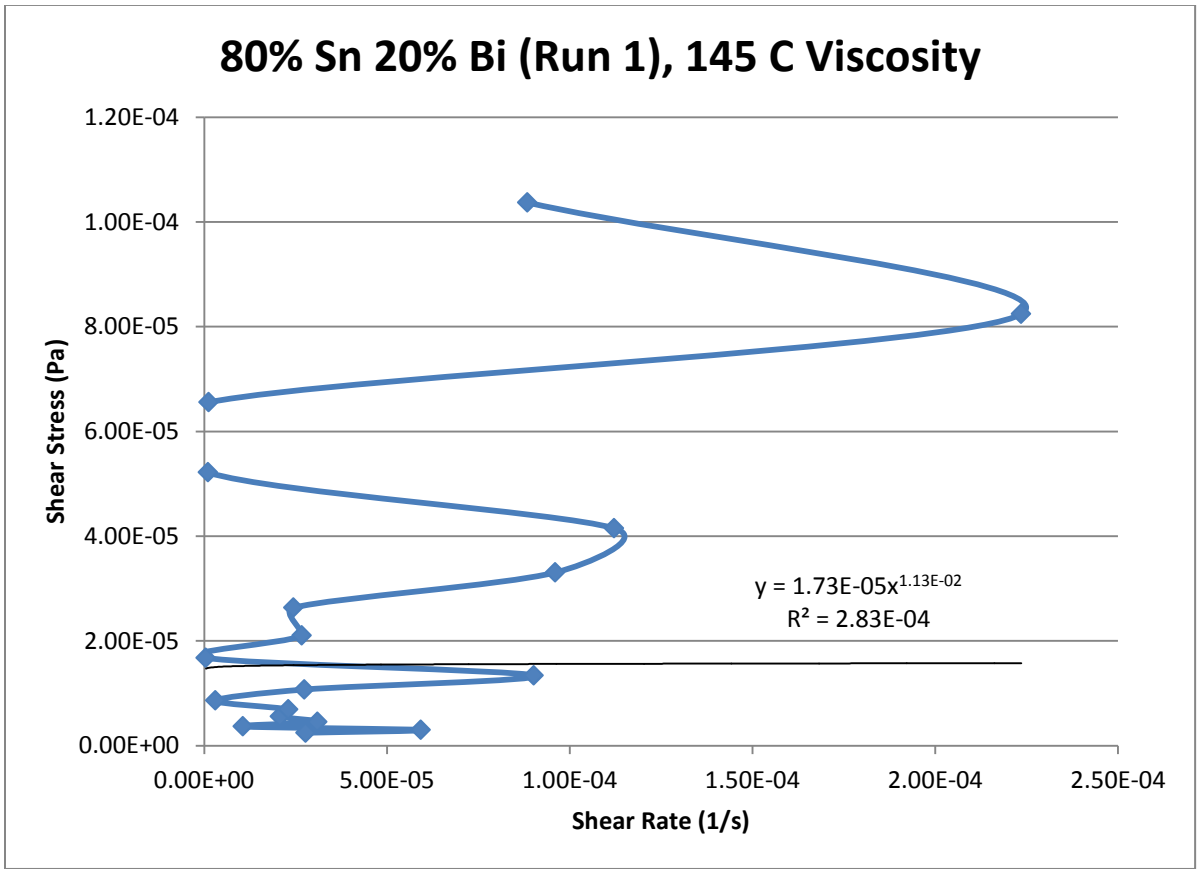

Figure 352- 80% Sn 20% Bi (Run 1), 145 C, Cone and Plate Viscosity

150 C

Fraction Solid	51.08 %
Power Law	$\tau = 4.54 * 10^{-4} * \dot{\gamma}^{0.1785}$
	$\mu = 8.10 * 10^{-5} * \dot{\gamma}^{-0.8215}$
R^2	46.18 %

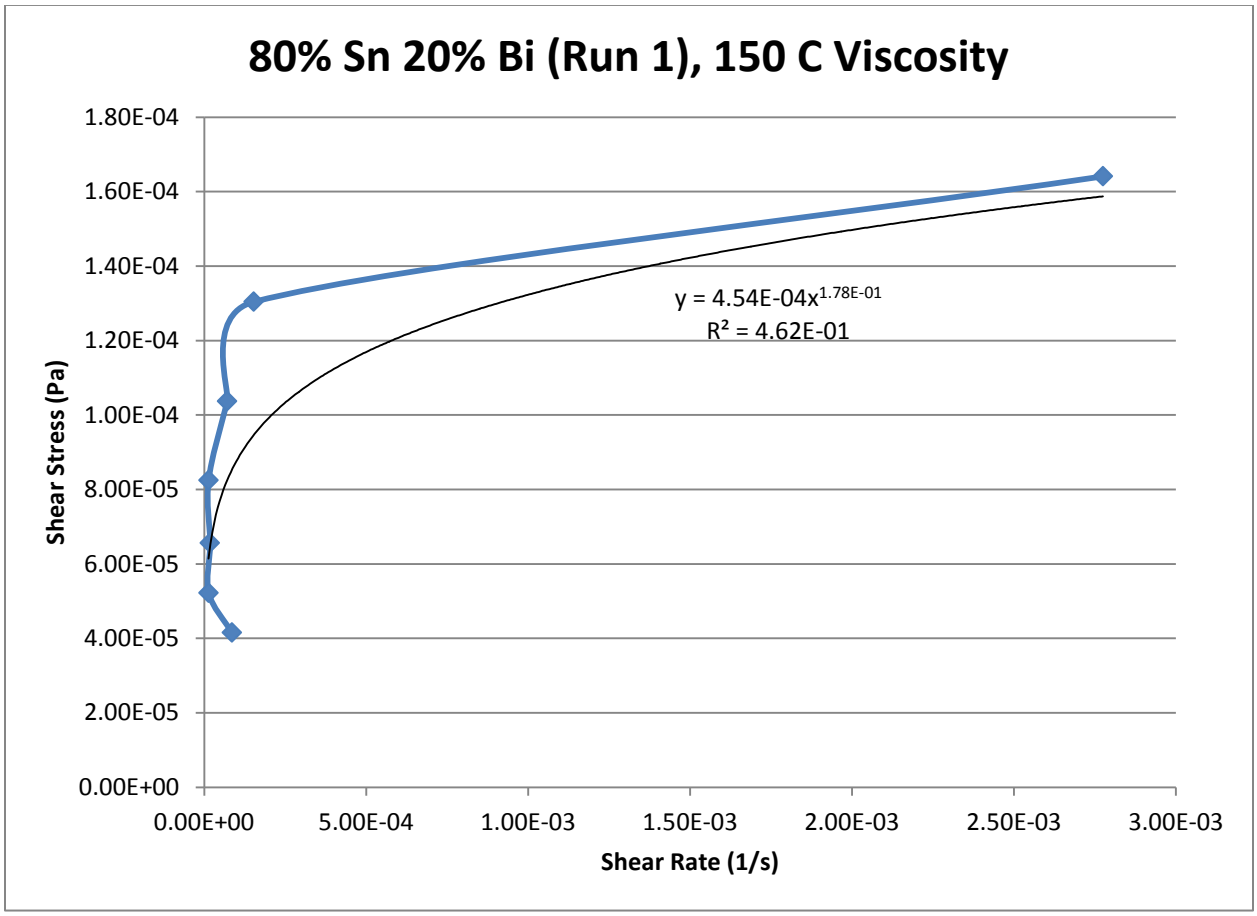

Figure 353- 80% Sn 20% Bi (Run 1), 150 C, Cone and Plate Viscosity

155 C

Fraction Solid	47.50 %
Power Law	$\tau = 7.98 * 10^{-4} * \dot{\gamma}^{0.3105}$
	$\mu = 2.48 * 10^{-5} * \dot{\gamma}^{-0.6895}$
R^2	78.93 %

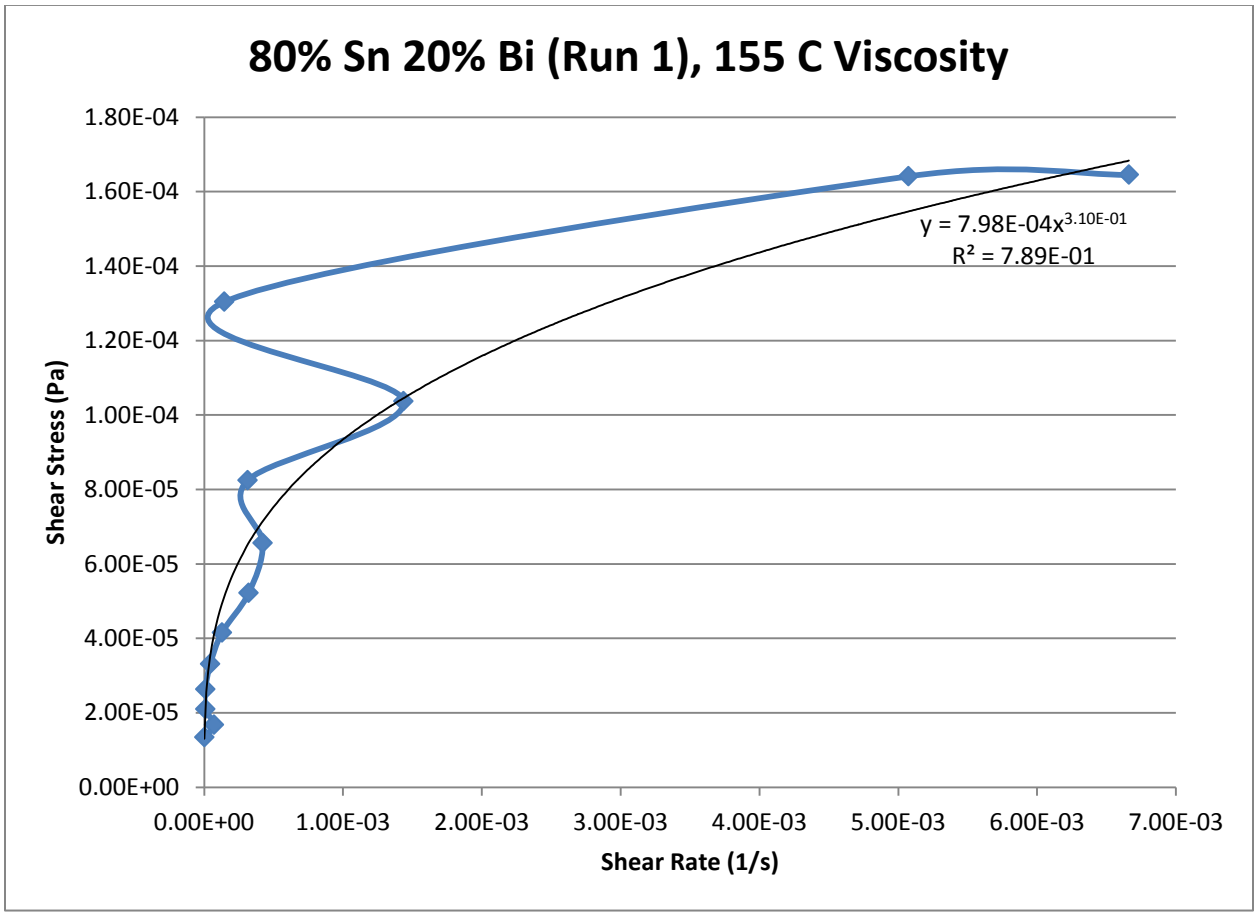

Figure 354- 80% Sn 20% Bi (Run 1), 155 C, Cone and Plate Viscosity

160 C

Fraction Solid	41.50 %
Power Law	$\tau = 8.75 * 10^{-4} * \dot{\gamma}^{0.3600}$
	$\mu = 3.15 * 10^{-4} * \dot{\gamma}^{-0.6400}$
R^2	86.71 %

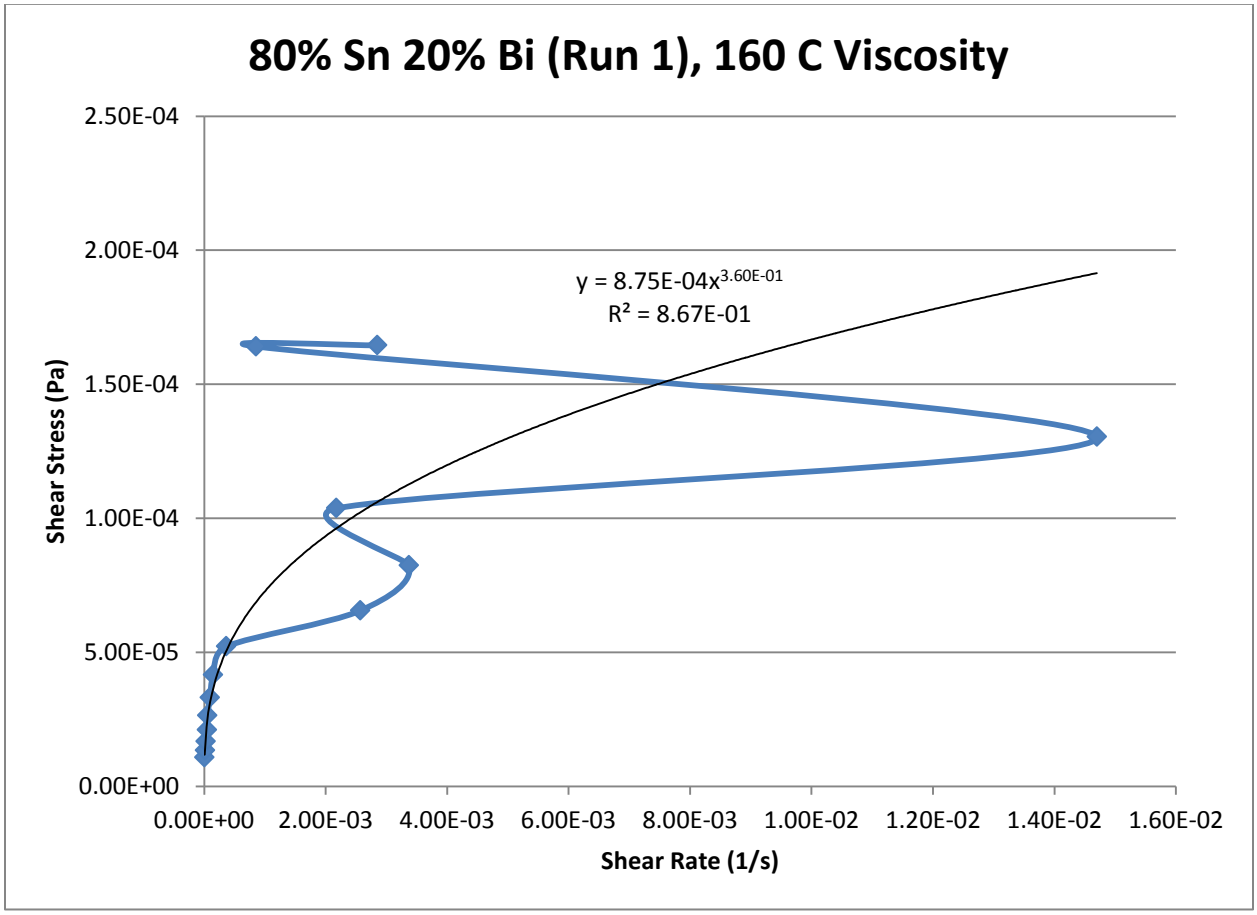

Figure 355- 80% Sn 20% Bi (Run 1), 160 C, Cone and Plate Viscosity

165 C

Fraction Solid	36.10 %
Power Law	$\tau = 1.63 * 10^{-4} * \dot{\gamma}^{0.2146}$
	$\mu = 3.50 * 10^{-5} * \dot{\gamma}^{-0.7854}$
R^2	88.37 %

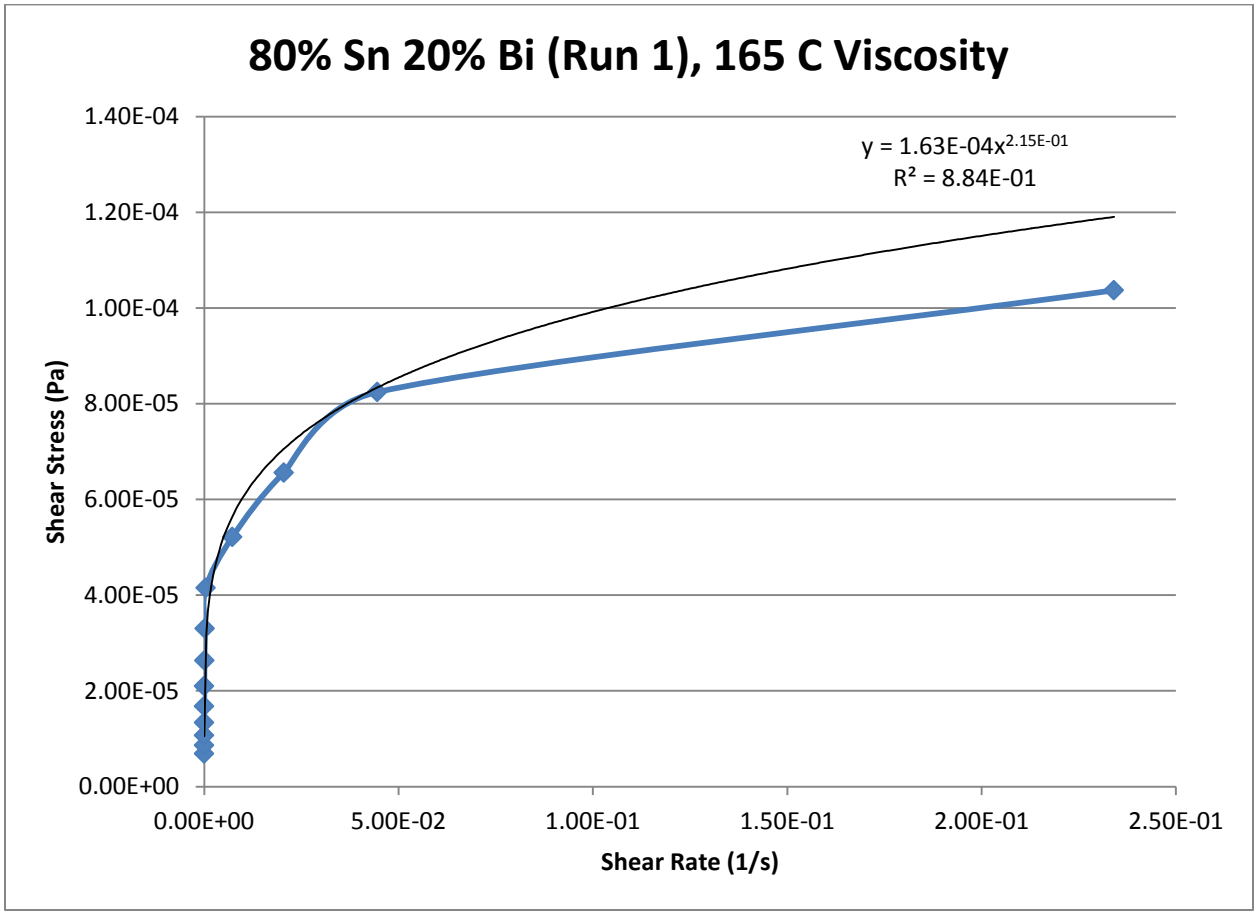

Figure 356- 80% Sn 20% Bi (Run 1), 165 C, Cone and Plate Viscosity

170 C

Fraction Solid	29.86 %
Power Law	$\tau = 1.63 * 10^{-4} * \dot{\gamma}^{0.3566}$
	$\mu = 5.81 * 10^{-5} * \dot{\gamma}^{-0.6434}$
R^2	79.90 %

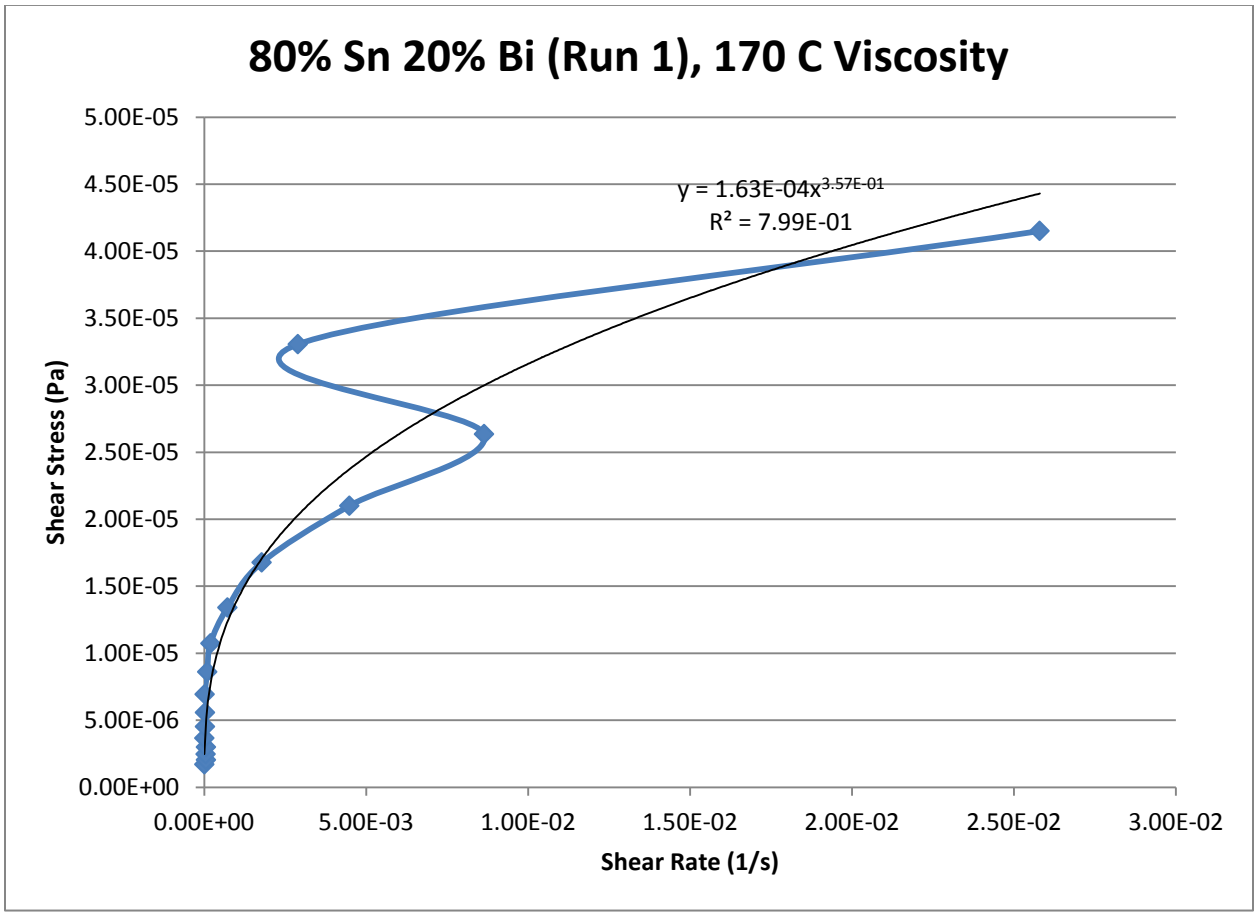

Figure 357- 80% Sn 20% Bi (Run 1), 170 C, Cone and Plate Viscosity

175 C

Fraction Solid	22.60 %
Power Law	$\tau = 6.03 * 10^{-5} * \dot{\gamma}^{0.2355}$
	$\mu = 1.42 * 10^{-5} * \dot{\gamma}^{-0.7645}$
R^2	99.16 %

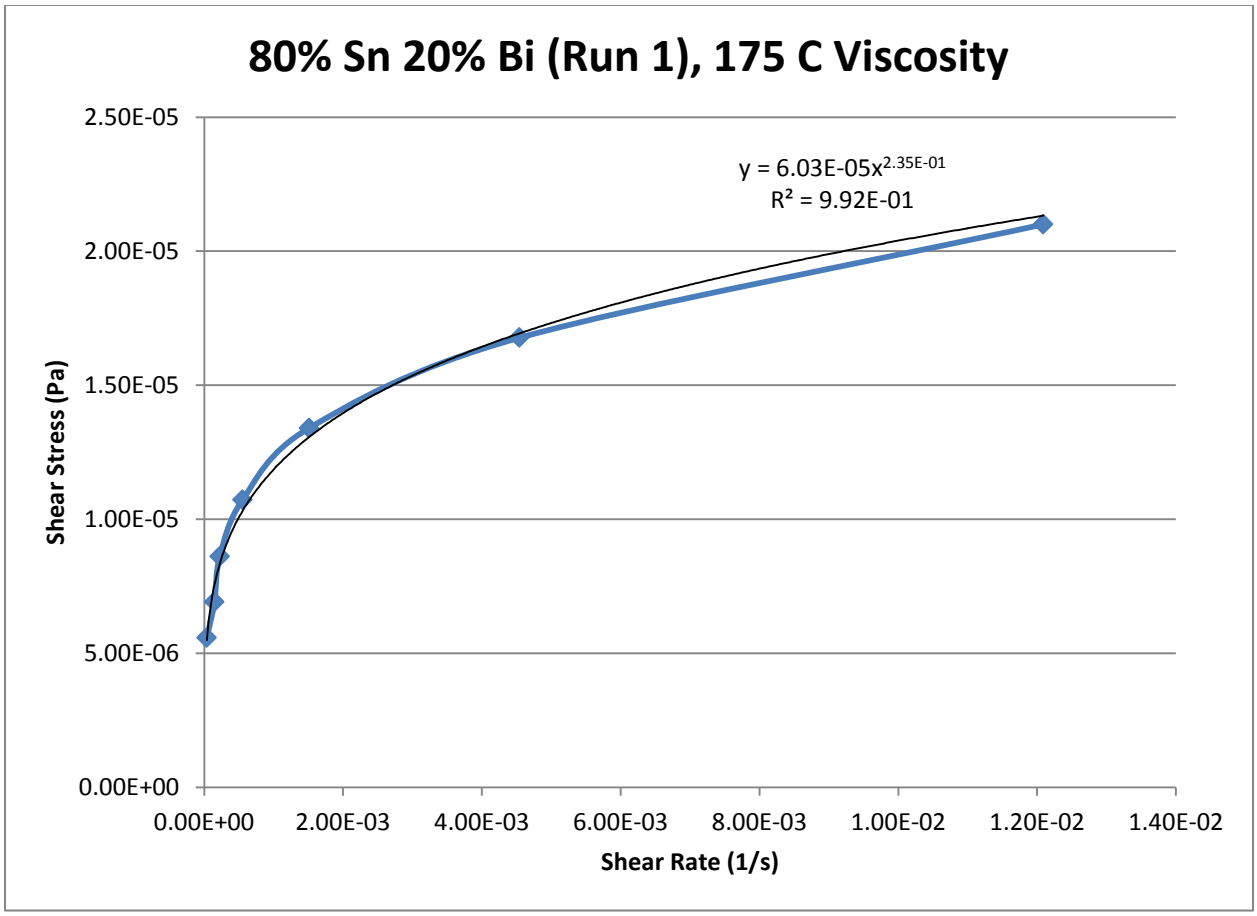

Figure 358- 80% Sn 20% Bi (Run 1), 175 C, Cone and Plate Viscosity

180 C

Fraction Solid	13.90 %
Power Law	$\tau = 5.97 * 10^{-5} * \dot{\gamma}^{0.2461}$
	$\mu = 1.47 * 10^{-5} * \dot{\gamma}^{-0.7539}$
R^2	98.19 %

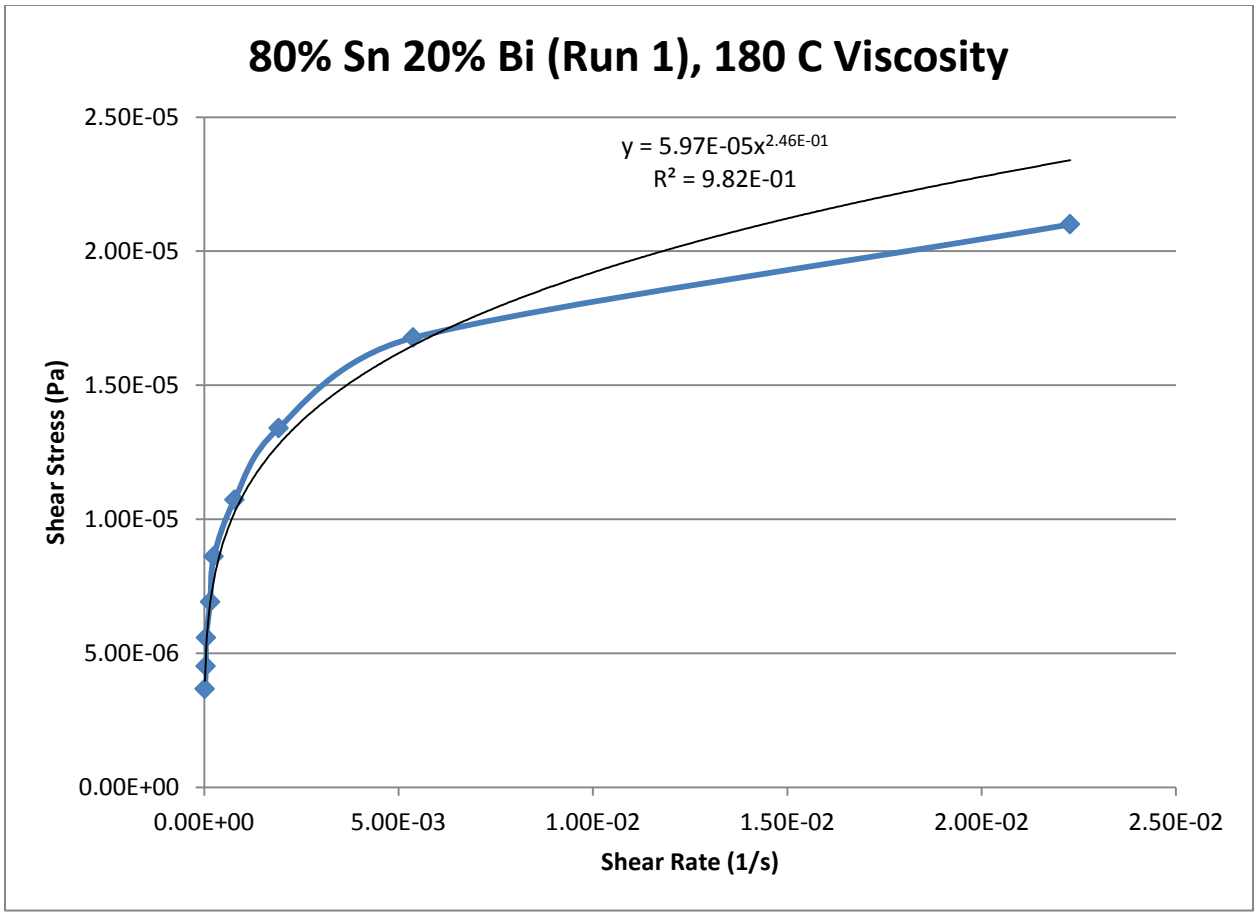

Figure 359- 80% Sn 20% Bi (Run 1), 180 C, Cone and Plate Viscosity

185 C

Fraction Solid	3.40 %
Power Law	$\tau = 6.25 * 10^{-5} * \dot{\gamma}^{0.2573}$
	$\mu = 1.61 * 10^{-5} * \dot{\gamma}^{-0.7427}$
R^2	96.73 %

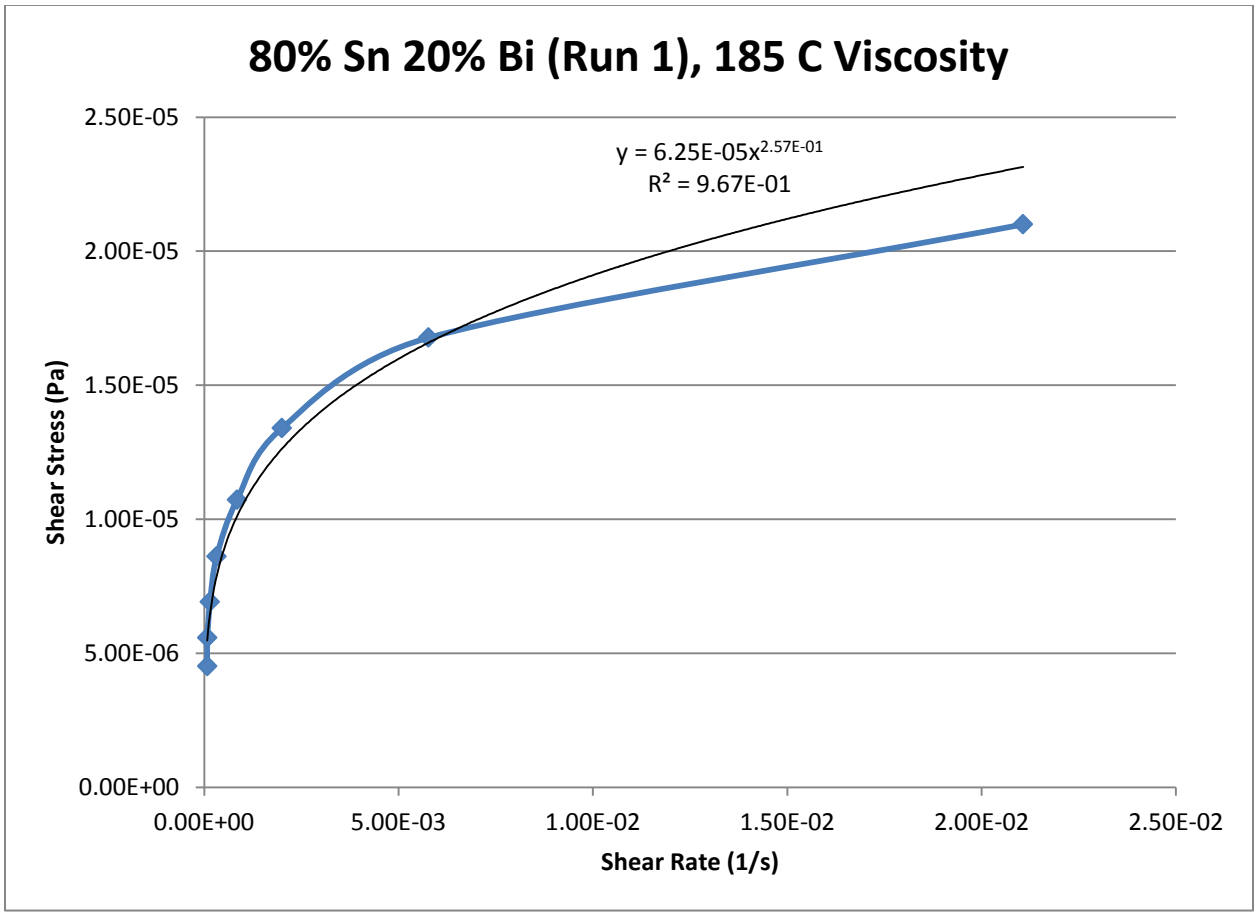

Figure 360- 80% Sn 20% Bi (Run 1), 185 C, Cone and Plate Viscosity

190 C

Fraction Solid	0 %
Power Law	$\tau = 6.35 * 10^{-3} * \dot{\gamma}^{0.8213}$
	$\mu = 5.21 * 10^{-3} * \dot{\gamma}^{-0.1787}$
R^2	77.03 %

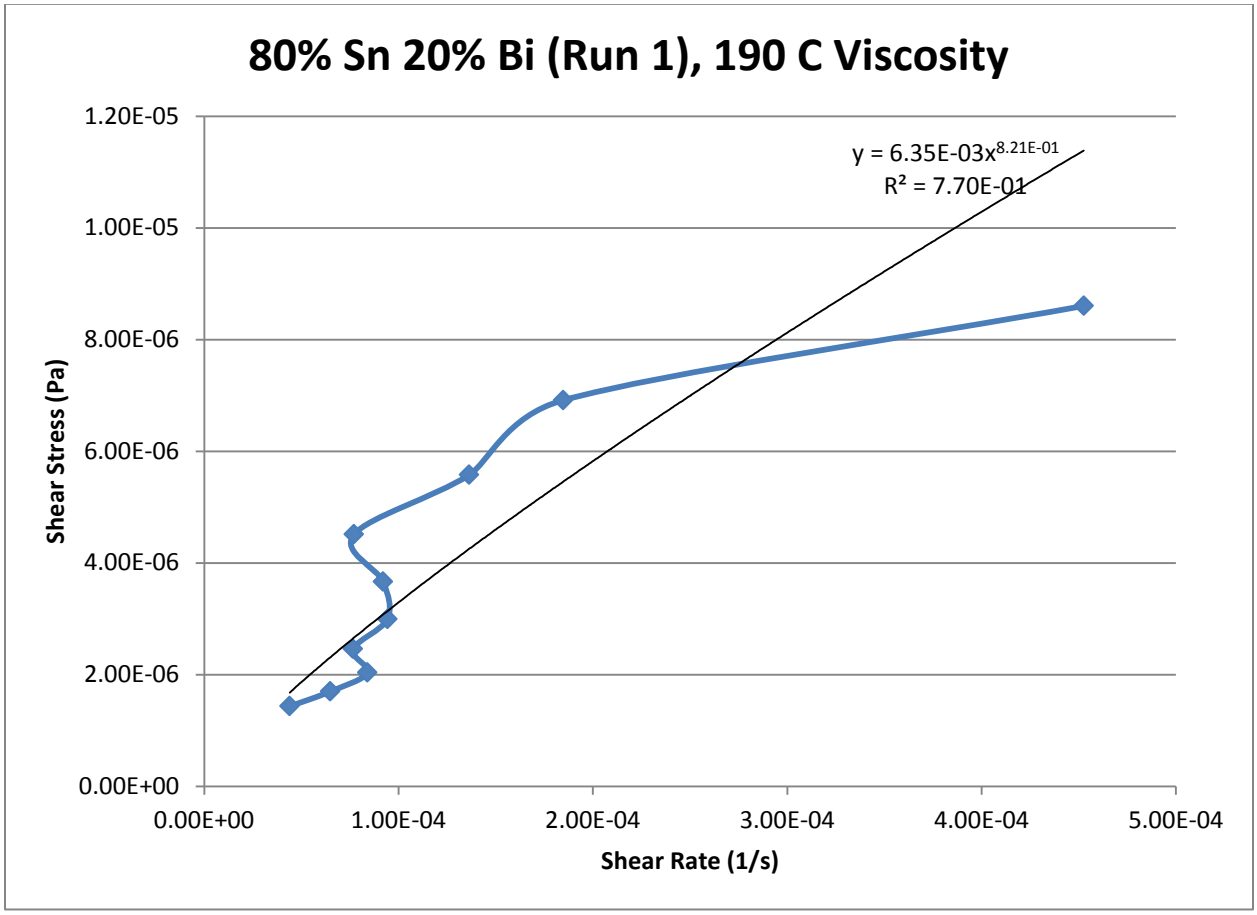

Figure 361- 80% Sn 20% Bi (Run 1), 190 C, Cone and Plate Viscosity

80% Tin 20% Bismuth (Run 2)

Actual Composition: 81.57% Sn, 18.43% Bi

Theoretical Solidus Line: 139 C
Theoretical Liquidus Line: 192.1 C

Experimental Solidus Line: 137.4 C
Experimental Liquidus Line: 185.9 C

Set Up Notes

- The stage was heated to 165 C and the gap was zeroed. The temperature was then lowered in increments of 5 C.

- Sweeps at temperatures at 150 C or below appeared to be too solid to be broken down by the rheometer. After the experiment, there was a thin, gray, solid ring of the alloy on the cone (oxidation).

- The lower temperatures were selected to fill in the gaps from Run 1.

Plots

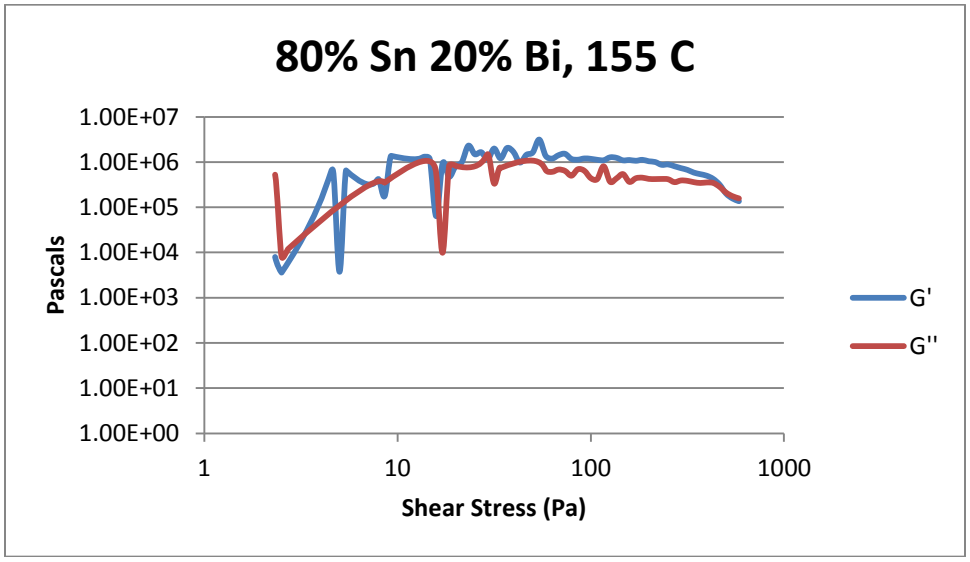

Figure 362- 80% Sn 20% Bi (Run 2), 155 C, Cone and Plate Stress Sweep

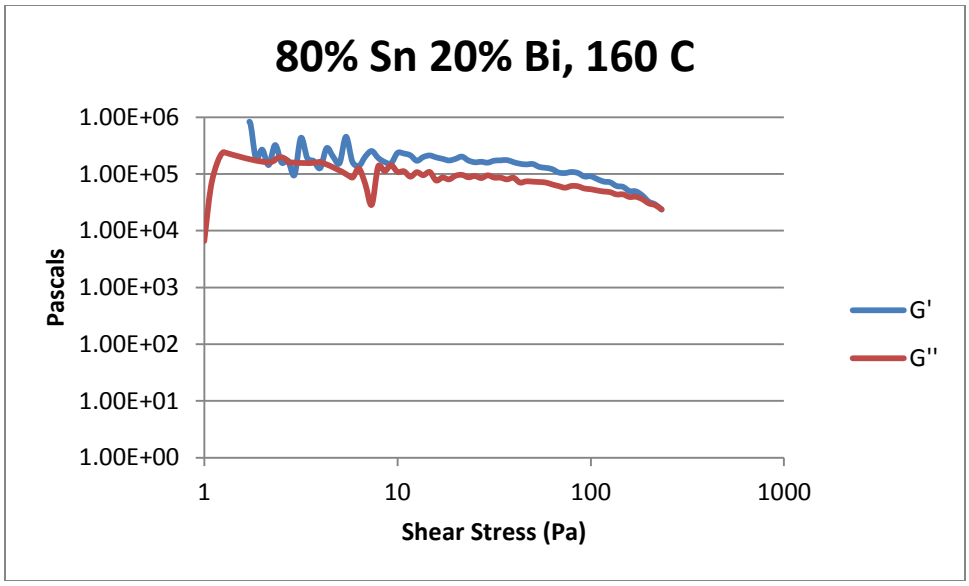

Figure 363- 80% Sn 20% Bi (Run 2), 160 C, Cone and Plate Stress Sweep

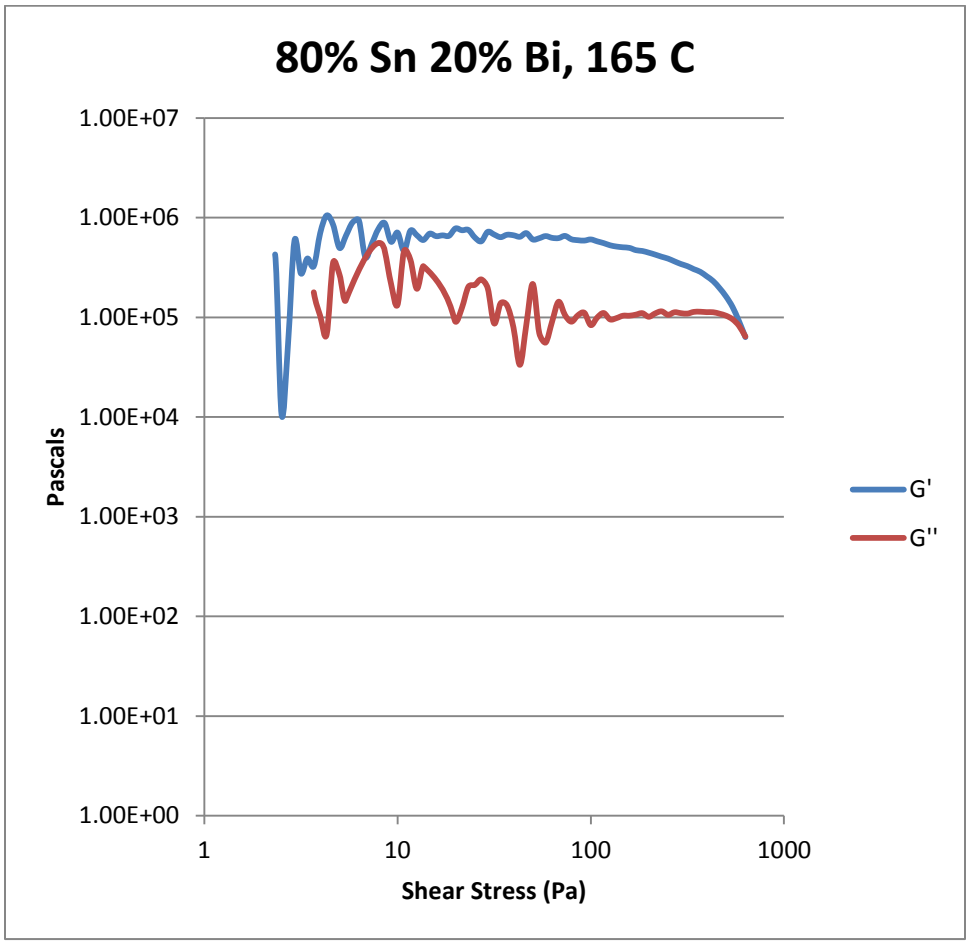

Figure 364- 80% Sn 20% Bi (Run 2), 165 C, Cone and Plate Stress Sweep

Temperature	Crossover Stress (Pa)	Crossover Stress (PSI)
155 C	$3.63 * 10^5$	52.7
160 C	$2.49 * 10^4$	3.62
165 C	$6.60 * 10^4$	9.58

Table 68- 80% Sn 20% Bi (Run 2), Cone and Plate Crossover Stresses

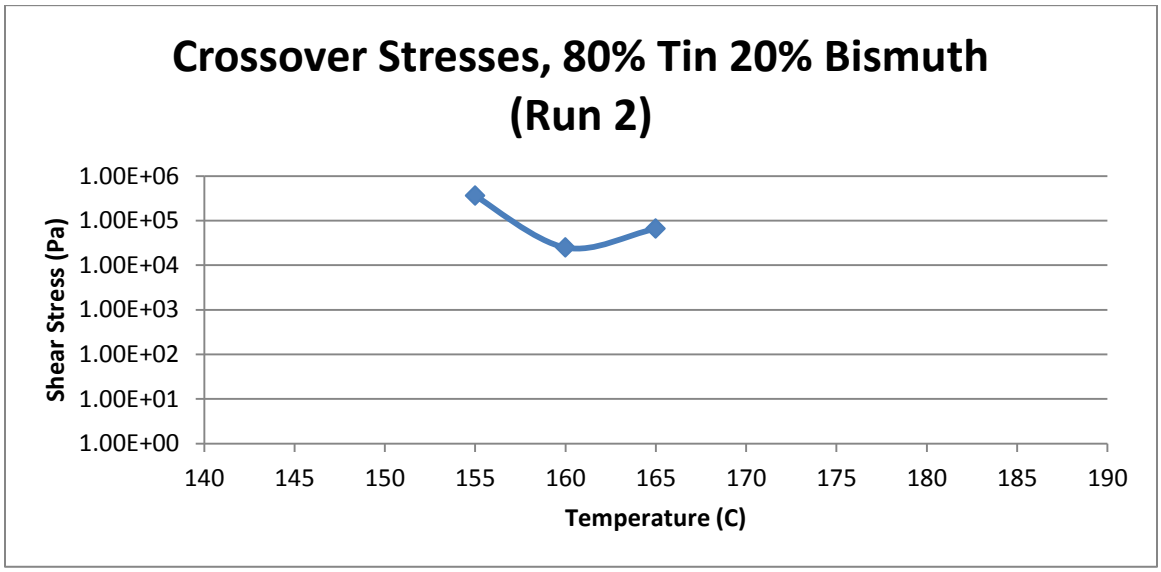

Figure 365- 80% Sn 20% Bi (Run 2), Cone and Plate Crossover Stresses

Temperature	Fraction Solid (At %)	G' Plateau Stress (Pa)	G'' Plateau Stress (PSI)
155 C	47.5	$1.15 * 10^6$	$4.04 * 10^5$
160 C	41.5	$1.67 * 10^5$	$8.77 * 10^4$
165 C	36.1	$6.14 * 10^5$	$1.09 * 10^5$

Table 69- 80% Sn 20% Bi (Run 2), Cone and Plate Plateau Stresses

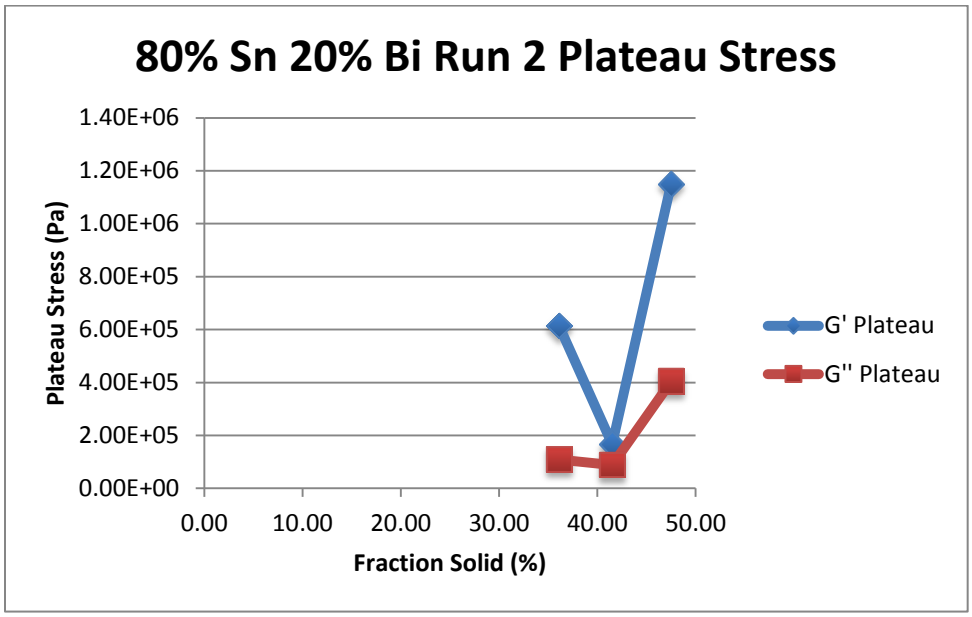

Figure 366- 80% Sn 20% Bi (Run 2), Cone and Plate Plateau Stresses vs. Fraction Solid

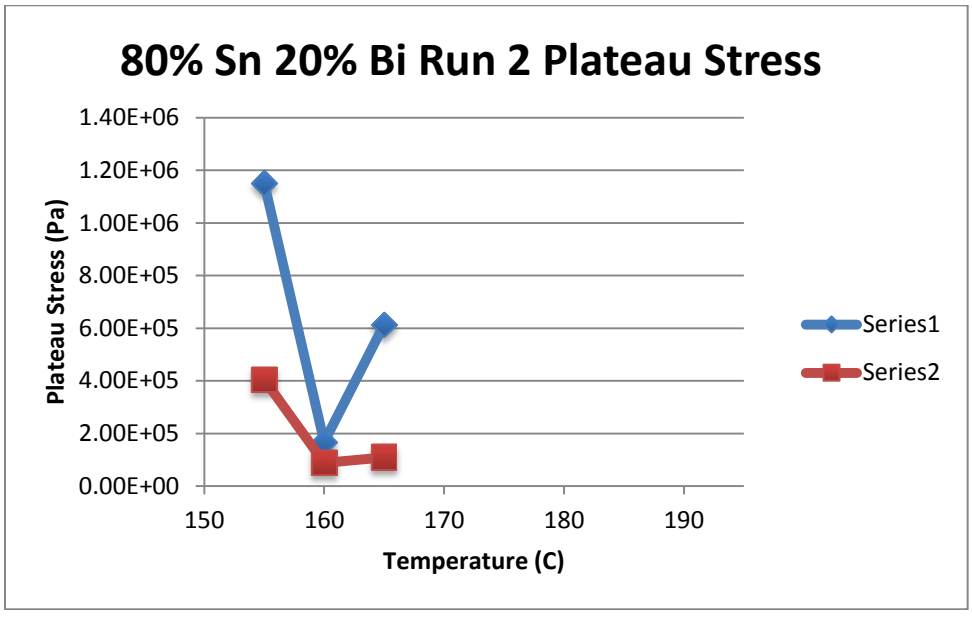

Figure 367- 80% Sn 20% Bi (Run 2), Cone and Plate Plateau Stresses vs. Temperature

80% Sn 20% Bi (Run 2) Viscosity					
Temperature	**Fraction Solid**	**Power Law**	**K**	**n**	**R^2**
170 C	29.86 %	$\tau = 1.79 * 10^{-4} * \dot{\gamma}^{0.2143}$ $\mu = 3.84 * 10^{-5} * \dot{\gamma}^{-0.7857}$	$1.79 * 10^{-4}$ Pa*s	0.2143	65.80 %
175 C	22.60 %	$\tau = 1.51 * 10^{-4} * \dot{\gamma}^{0.2210}$ $\mu = 3.34 * 10^{-5} * \dot{\gamma}^{-0.7790}$	$1.51 * 10^{-4}$ Pa*s	0.2210	50.13 %
180 C	13.90 %	$\tau = 1.58 * 10^{-5} * \dot{\gamma}^{0.0373}$ $\mu = 5.89 * 10^{-7} * \dot{\gamma}^{-0.9627}$	$1.58 * 10^{-5}$ Pa*s	0.0373	1.58 %
185 C	3.40 %	$\tau = 3.33 * 10^{-5} * \dot{\gamma}^{0.0973}$ $\mu = 3.24 * 10^{-6} * \dot{\gamma}^{-0.9027}$	$3.33 * 10^{-5}$ Pa*s	0.0973	29.77 %
190 C	0 %	$\tau = 1.31 * 10^{-5} * \dot{\gamma}^{0.0707}$ $\mu = 9.26 * 10^{-7} * \dot{\gamma}^{-0.9293}$	$1.31 * 10^{-5}$ Pa*s	0.0707	3.78 %

Table 70- 80% Sn 20% Bi (Run 2), Cone and Plate Viscosity

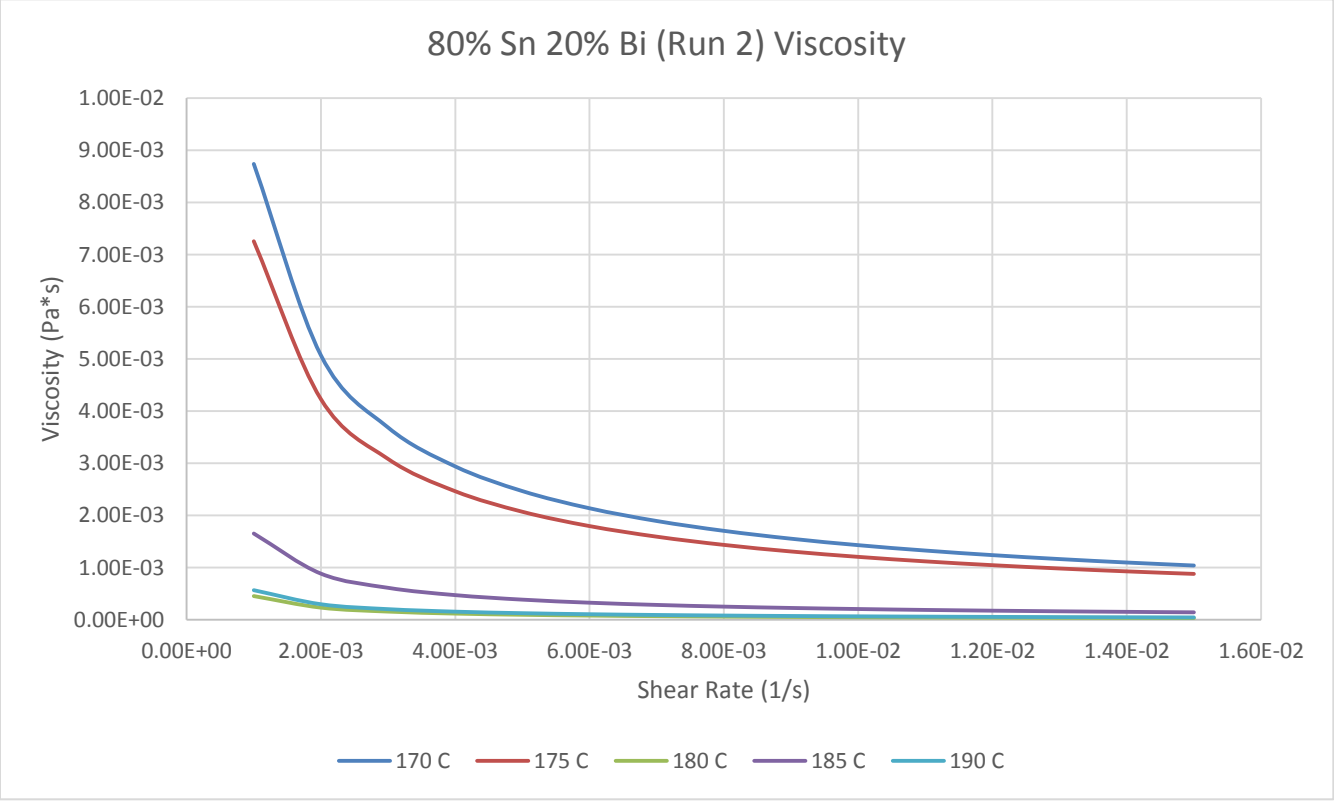

Figure 368- 80% Sn 20% Bi (Run 2), Cone and Plate Viscosity

170 C

Fraction Solid	29.86 %
Power Law	$\tau = 1.79 * 10^{-4} * \dot{\gamma}^{0.2143}$
	$\mu = 3.84 * 10^{-5} * \dot{\gamma}^{-0.7857}$
R^2	65.80 %

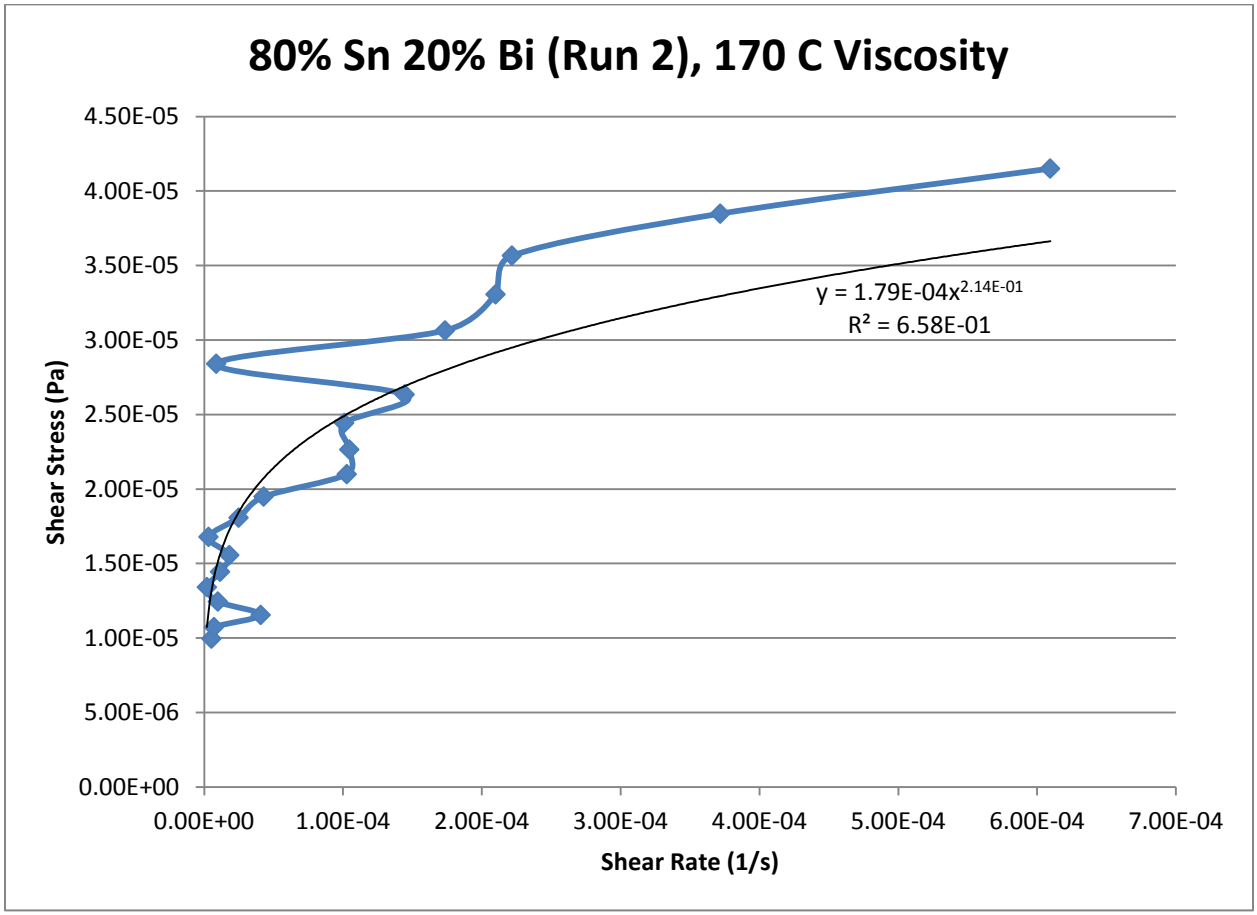

Figure 369- 80% Sn 20% Bi (Run 2), 170 C, Cone and Plate Viscosity

175 C

Fraction Solid	22.60 %
Power Law	$\tau = 1.51 * 10^{-4} * \dot{\gamma}^{0.2210}$
	$\mu = 3.34 * 10^{-5} * \dot{\gamma}^{-0.7790}$
R^2	50.13 %

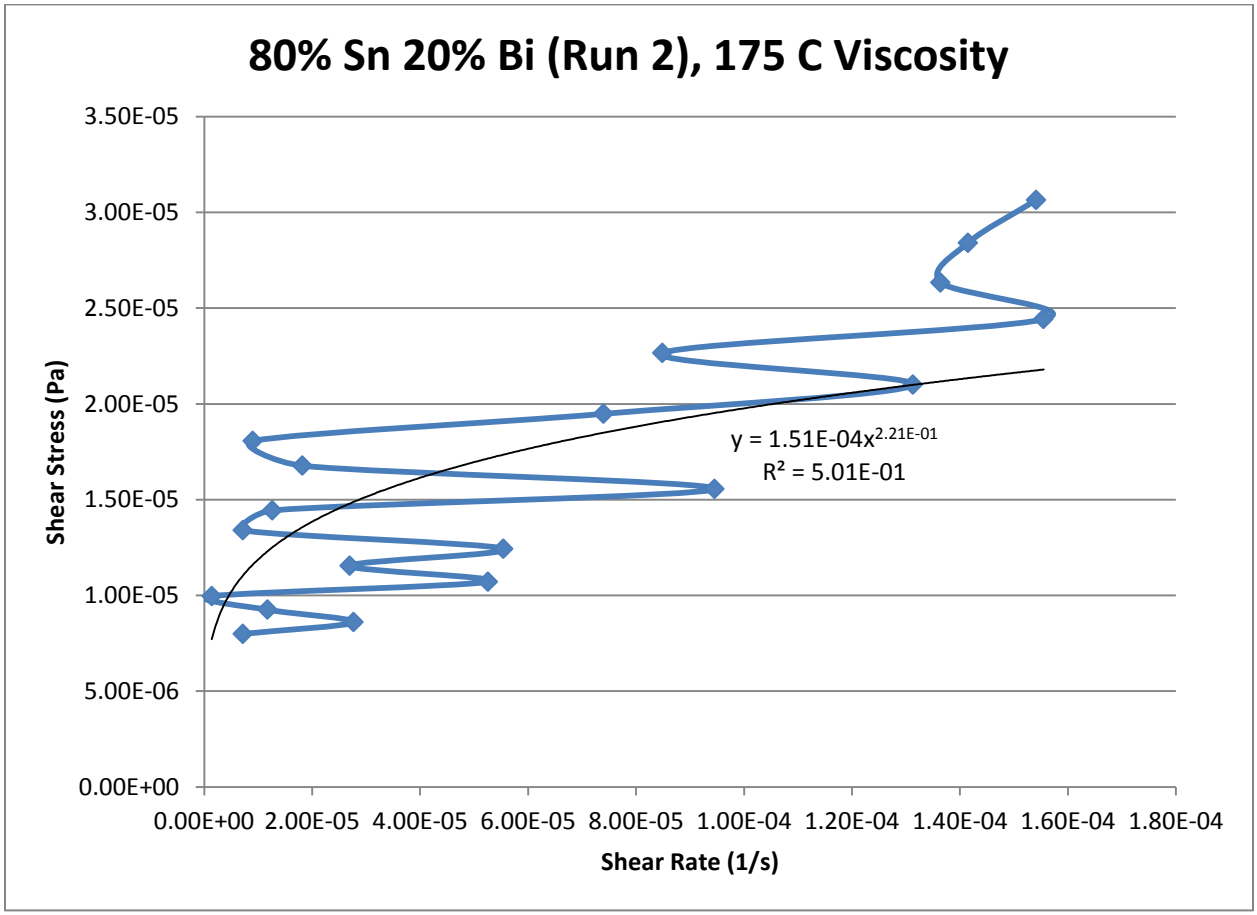

Figure 370- 80% Sn 20% Bi (Run 2), 175 C, Cone and Plate Viscosity

180 C

Fraction Solid	13.90 %
Power Law	$\tau = 1.58 * 10^{-5} * \dot{\gamma}^{0.0373}$
	$\mu = 5.89 * 10^{-7} * \dot{\gamma}^{-0.9627}$
R^2	1.58 %

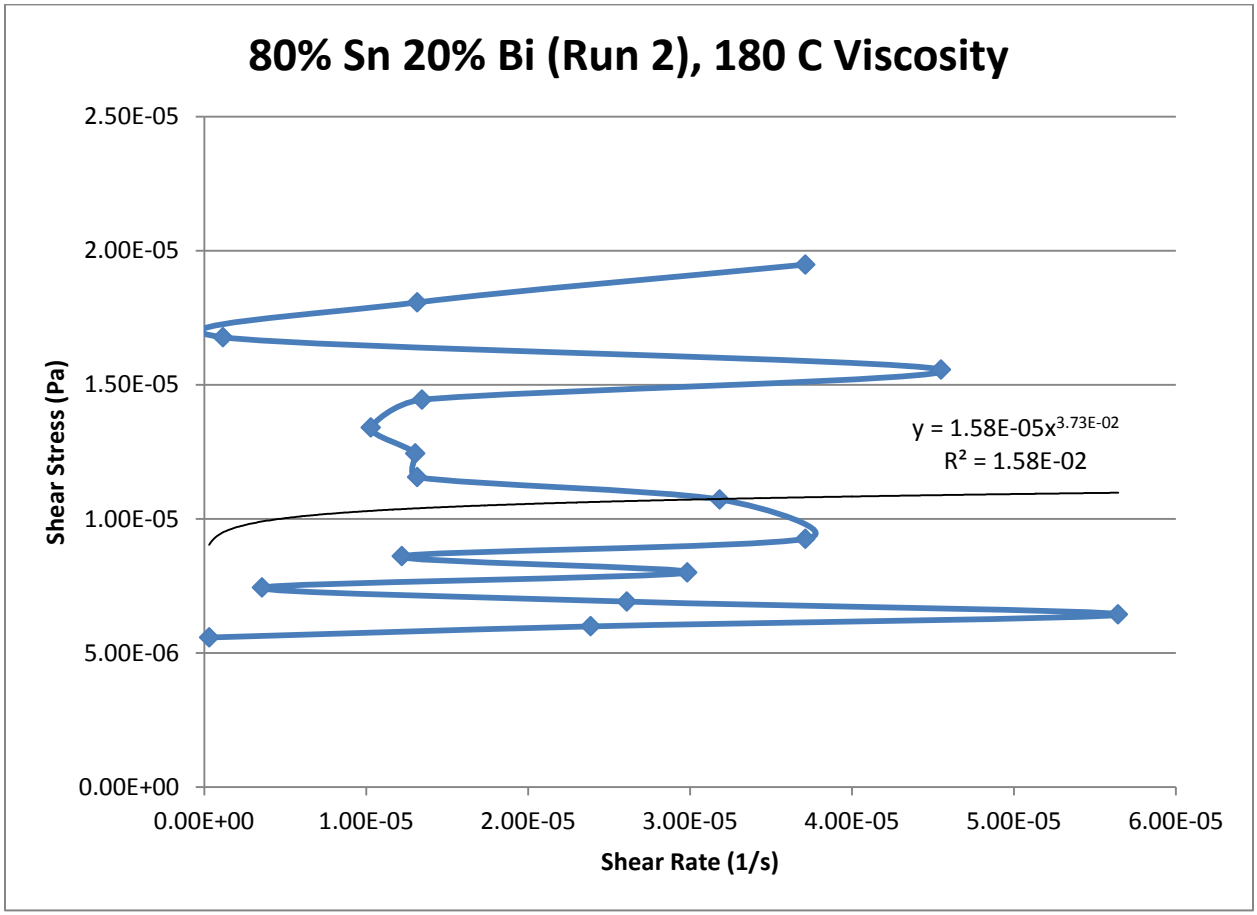

Figure 371- 80% Sn 20% Bi (Run 2), 180 C, Cone and Plate Viscosity

185 C

Fraction Solid	3.40 %
Power Law	$\tau = 3.33 * 10^{-5} * \dot{\gamma}^{0.0973}$
	$\mu = 3.24 * 10^{-6} * \dot{\gamma}^{-0.9027}$
R^2	29.77 %

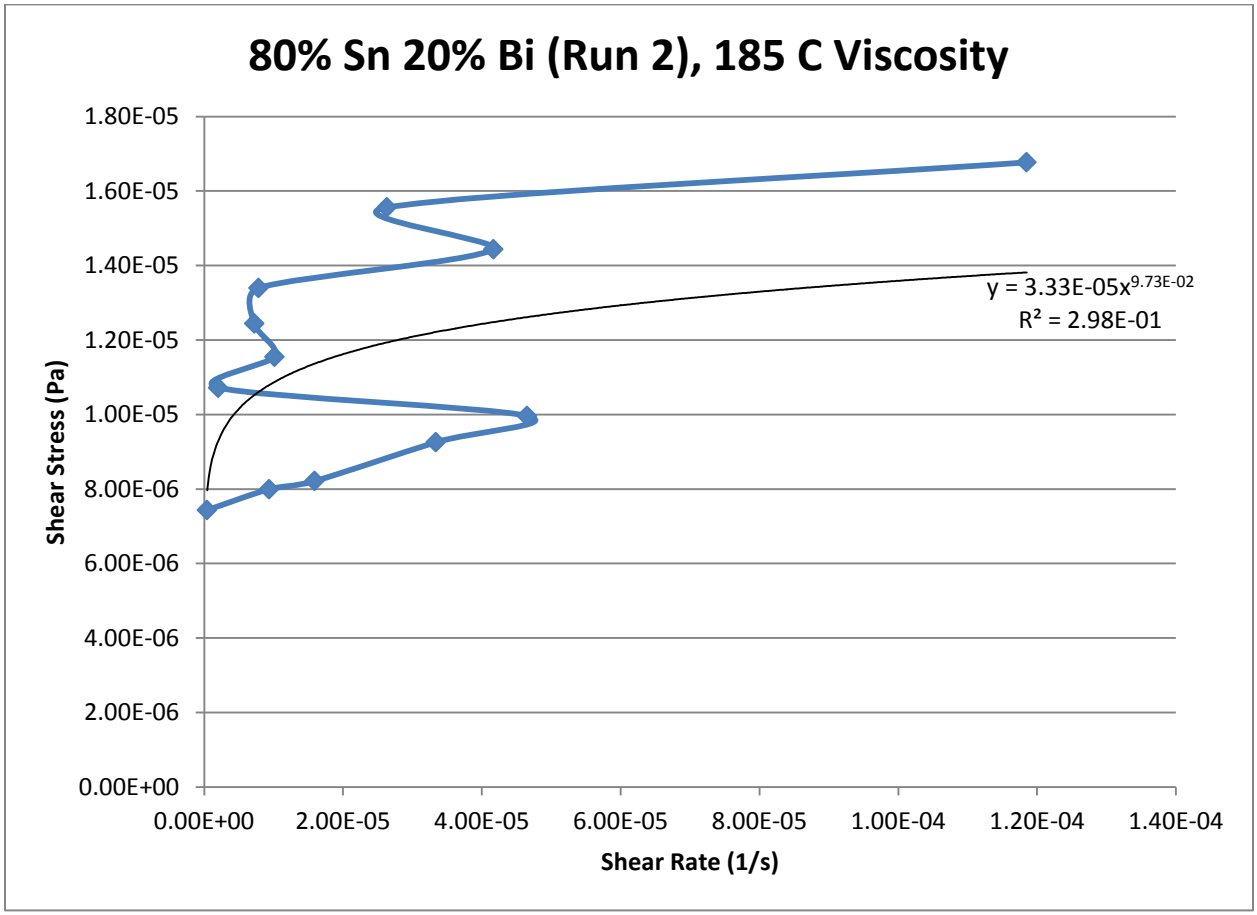

Figure 372- 80% Sn 20% Bi (Run 2), 185 C, Cone and Plate Viscosity

190 C

Fraction Solid	0 %
Power Law	$\tau = 1.31 * 10^{-5} * \dot{\gamma}^{0.0707}$
	$\mu = 9.26 * 10^{-7} * \dot{\gamma}^{-0.9293}$
R^2	3.78 %

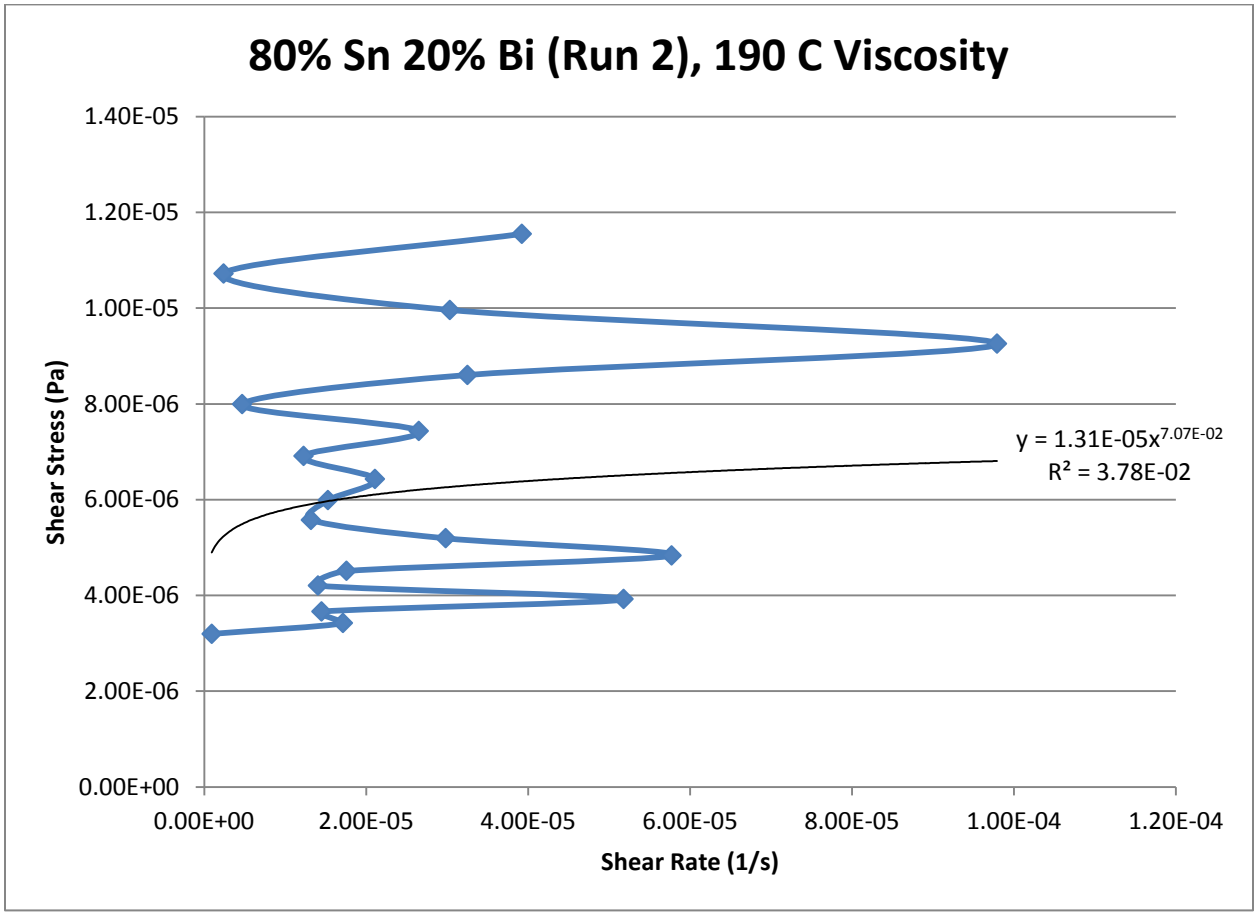

Figure 373- 80% Sn 20% Bi (Run 2), 190 C, Cone and Plate Viscosity

80% Tin 20% Bismuth (Run 3)

Actual Composition: 81.57% Sn, 18.43% Bi

Theoretical Solidus Line: 139 C
Theoretical Liquidus Line: 192.1 C

Experimental Solidus Line: 137.4 C
Experimental Liquidus Line: 185.9 C

Set Up Notes

- The stage was heated to 180 C. The metal pieces were then placed on the stage and melted underneath the cone. The cone was then lowered to the geometry gap. After each sweep, the temperature was decreased 5 C.

- Material was likely ejected during the 160 C stress sweep since the subsequent 155 C stress sweep had far too many negative values and the 160 C stress sweep did not have a clear drop off like the previous temperatures.

Plots

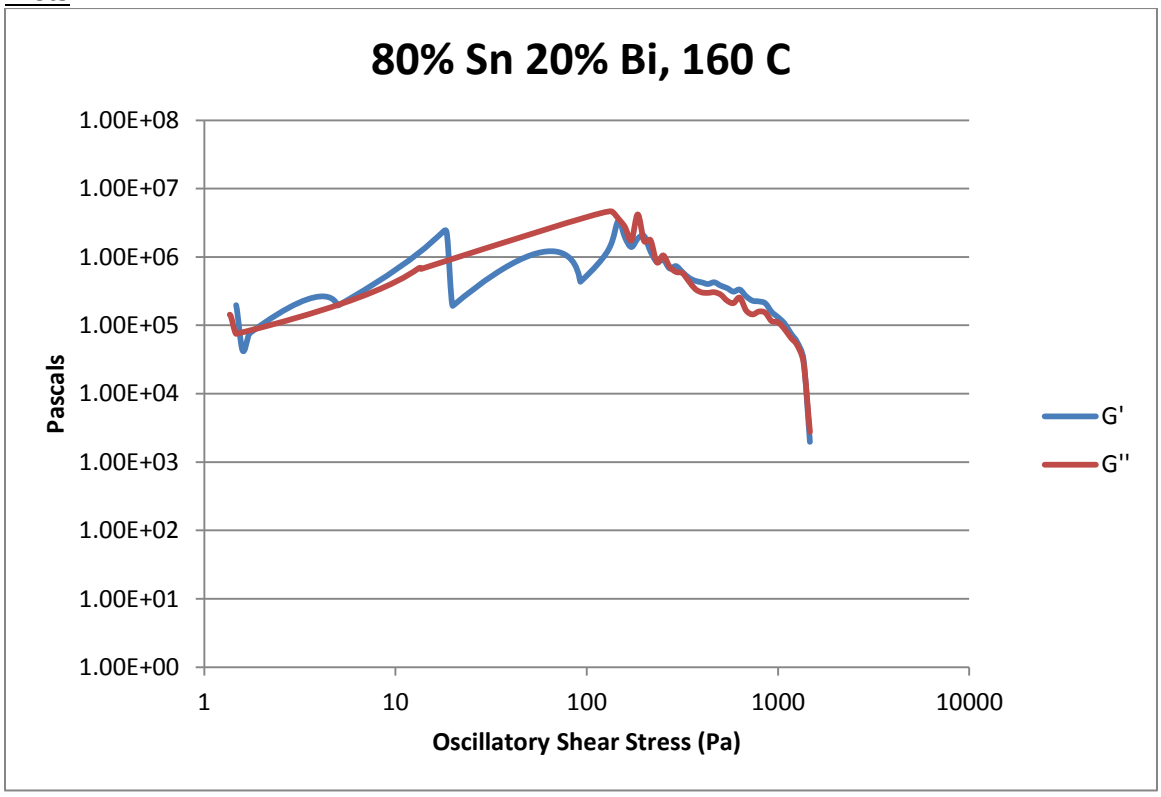

Figure 374- 80% Sn 20% Bi (Run 3), 160 C, Cone and Plate Stress Sweep

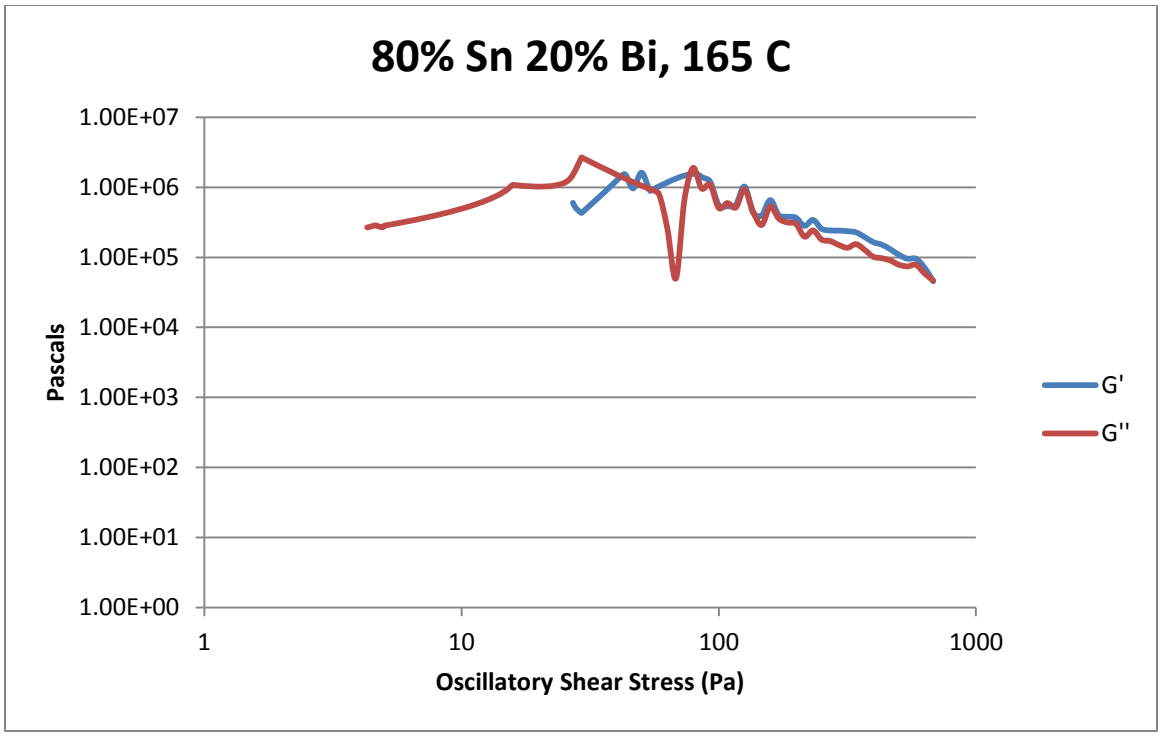

Figure 375- 80% Sn 20% Bi (Run 3), 165 C, Cone and Plate Stress Sweep

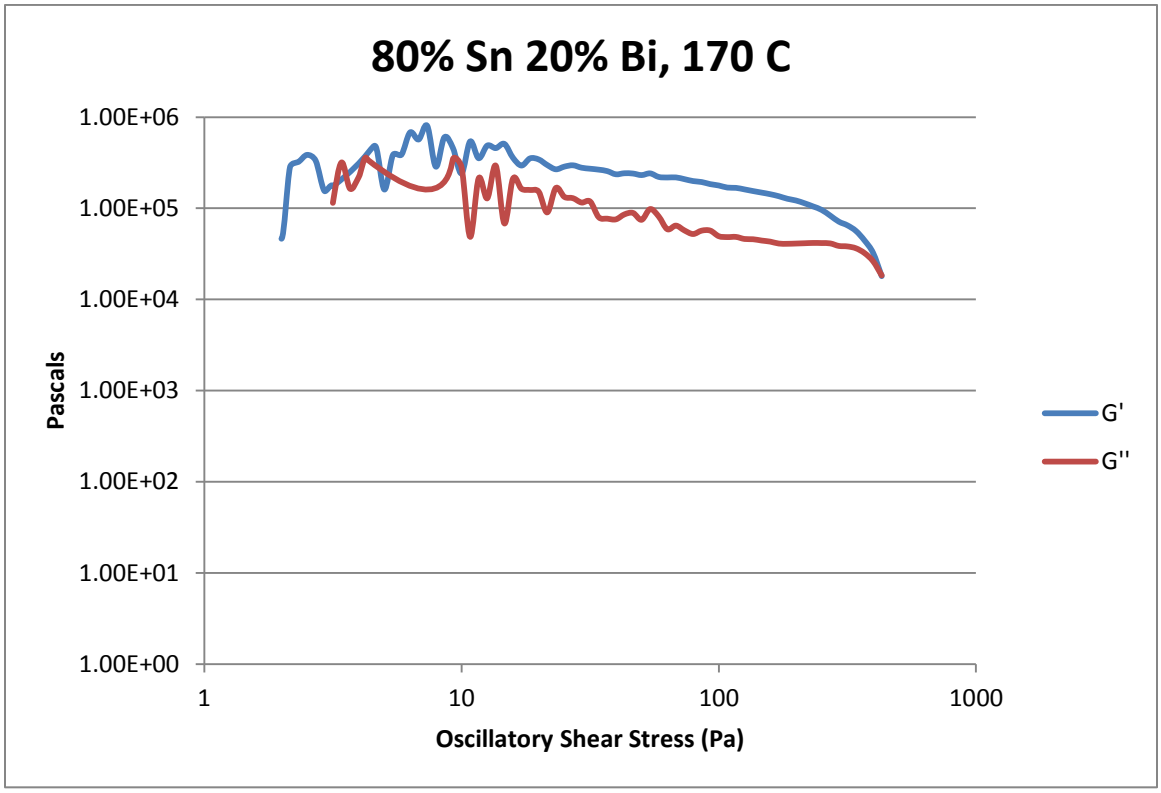

Figure 376- 80% Sn 20% Bi (Run 3), 170 C, Cone and Plate Stress Sweep

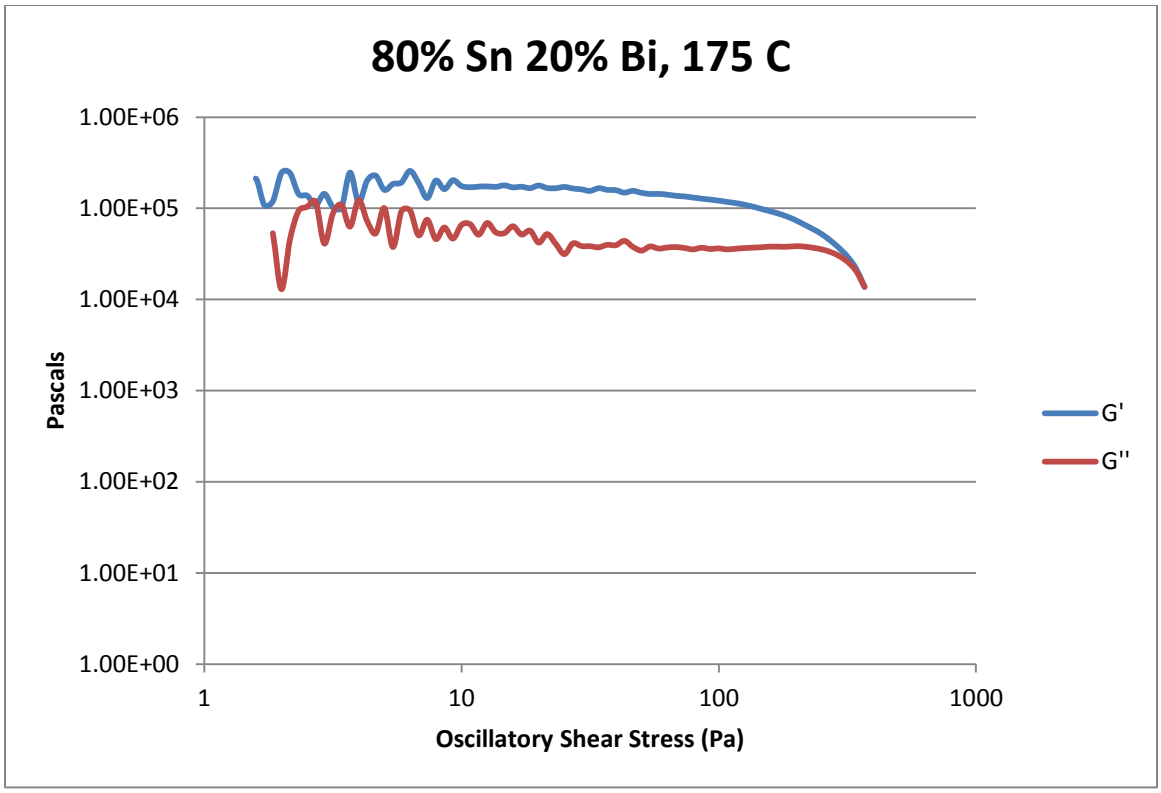

Figure 377- 80% Sn 20% Bi (Run 3), 175 C, Cone and Plate Stress Sweep

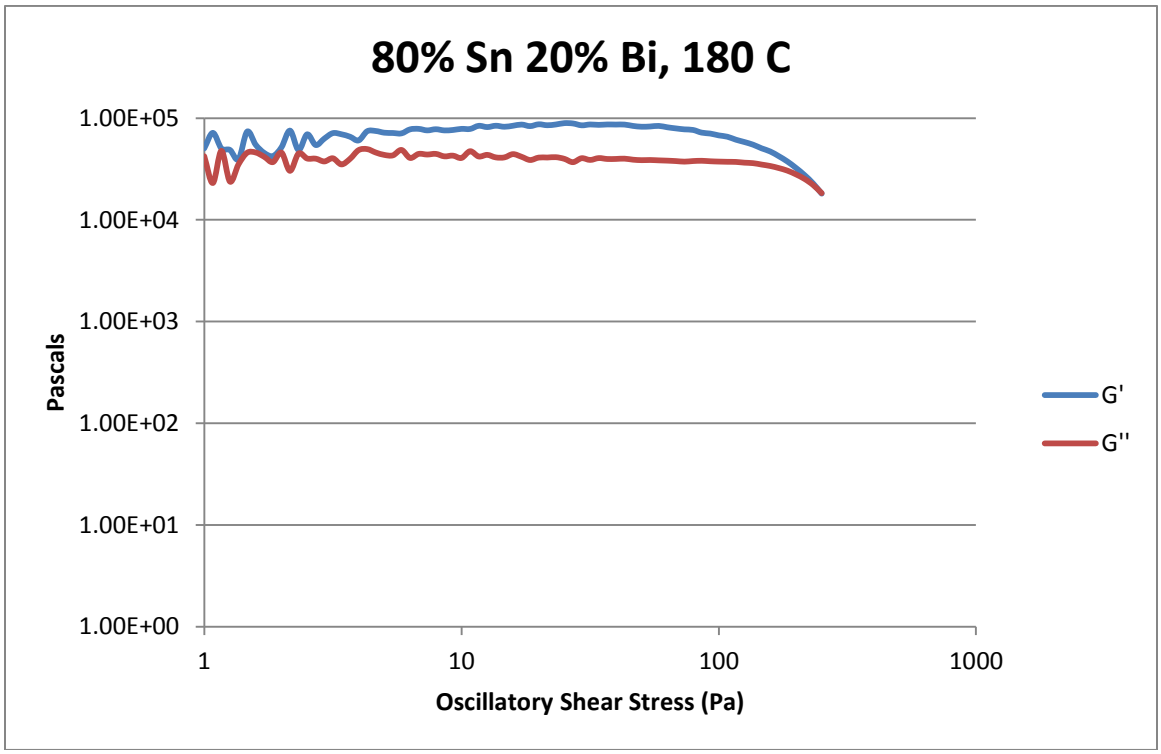

Figure 378- 80% Sn 20% Bi (Run 3), 180 C, Cone and Plate Stress Sweep

Temperature	Crossover Stress (Pa)	Crossover Stress (PSI)
160 C	$8.03 * 10^3$	1.16
165 C	$4.80 * 10^4$	6.96
170 C	$1.88 * 10^4$	2.73
175 C	$1.38 * 10^4$	2.00
180 C	$1.91 * 10^4$	2.77

Table 71- 80% Sn 20% Bi (Run 3), Cone and Plate Crossover Stresses

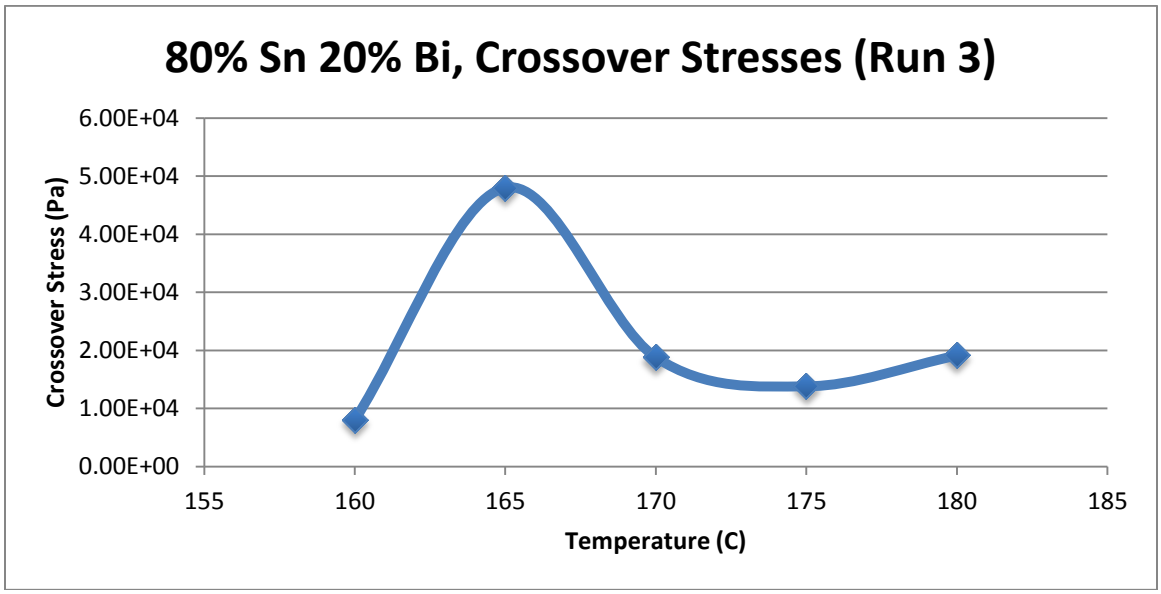

Figure 379- 80% Sn 20% Bi (Run 3), Cone and Plate Crossover Stresses

Temperature	Fraction Solid (At %)	G' Plateau (Pa)	G'' Plateau (Pa)
160 C	41.5	$4.75 * 10^5$	$2.44 * 10^5$
165 C	36.1	$4.39 * 10^5$	$1.47 * 10^5$
170 C	29.9	$2.40 * 10^5$	$4.13 * 10^4$
175 C	22.6	$1.73 * 10^5$	$3.75 * 10^4$
180 C	13.9	$8.65 * 10^4$	$3.99 * 10^4$

Table 72- 80% Sn 20% Bi (Run 3), Cone and Plate Plateau Stresses

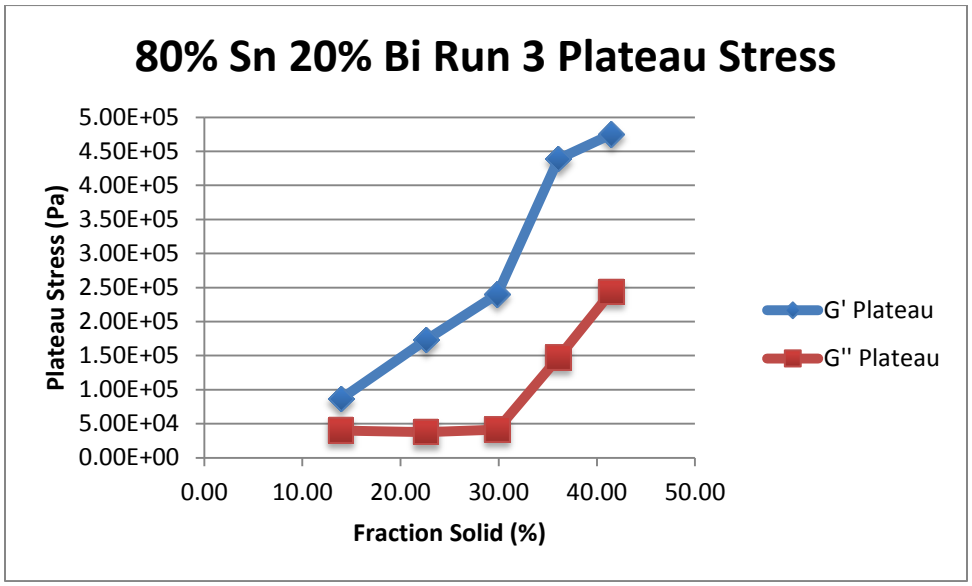

Figure 380- 80% Sn 20% Bi (Run 3), Cone and Plate Plateau Stresses vs. Fraction Solid

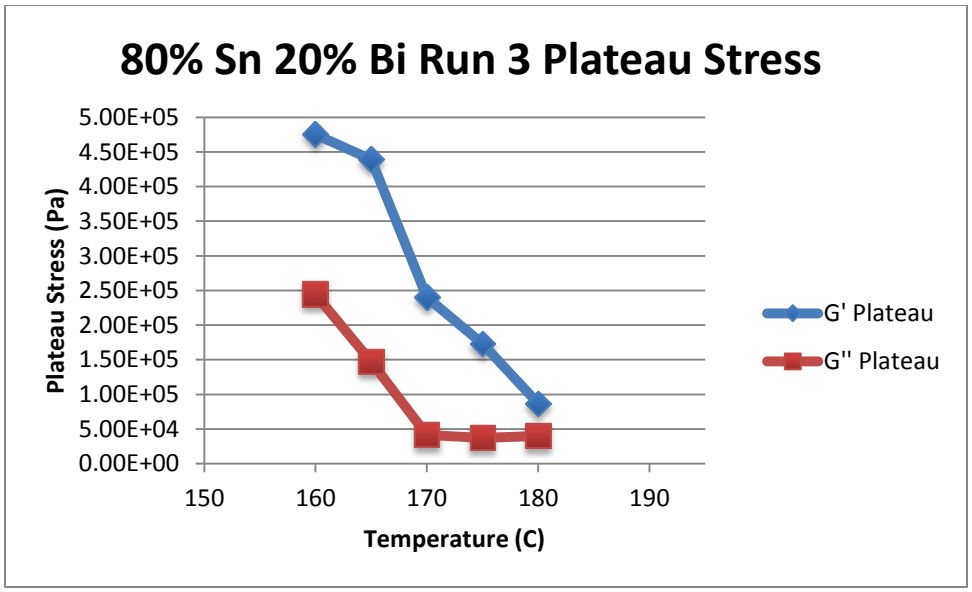

Figure 381- 80% Sn 20% Bi (Run 3), Cone and Plate Plateau Stresses vs. Temperature

80% Sn 20% Bi (Run 3) Viscosity					
Temperature	**Fraction Solid**	**Power Law**	**K**	**n**	**R^2**
155 C	47.50 %	$\tau = 9.52 * 10^{-6} * \dot{\gamma}^{0.0387}$ $\mu = 3.68 * 10^{-7} * \dot{\gamma}^{-0.9613}$	$9.52 * 10^{-6}$ Pa*s	0.0387	4.0 %
160 C	41.50 %	$\tau = 8.58 * 10^{-4} * \dot{\gamma}^{0.3527}$ $\mu = 3.03 * 10^{-4} * \dot{\gamma}^{-0.6473}$	$8.58 * 10^{-4}$ Pa*s	0.3527	88.99 %
165 C	36.10 %	$\tau = 3.66 * 10^{-4} * \dot{\gamma}^{0.3406}$ $\mu = 1.25 * 10^{-4} * \dot{\gamma}^{-0.6594}$	$3.66 * 10^{-4}$ Pa*s	0.3406	94.24 %
170 C	29.86 %	$\tau = 1.76 * 10^{-4} * \dot{\gamma}^{0.2270}$ $\mu = 4.00 * 10^{-5} * \dot{\gamma}^{-0.7730}$	$1.76 * 10^{-4}$ Pa*s	0.2270	84.03 %
175 C	22.60 %	$\tau = 1.04 * 10^{-4} * \dot{\gamma}^{0.1992}$ $\mu = 2.07 * 10^{-5} * \dot{\gamma}^{-0.8008}$	$1.04 * 10^{-4}$ Pa*s	0.1992	84.08 %
180 C	13.90 %	$\tau = 6.19 * 10^{-5} * \dot{\gamma}^{0.2461}$ $\mu = 1.01 * 10^{-5} * \dot{\gamma}^{-0.8373}$	$6.19 * 10^{-5}$ Pa*s	0.2461	98.19 %

Table 73- 80% Sn 20% Bi (Run 3), Cone and Plate Viscosity

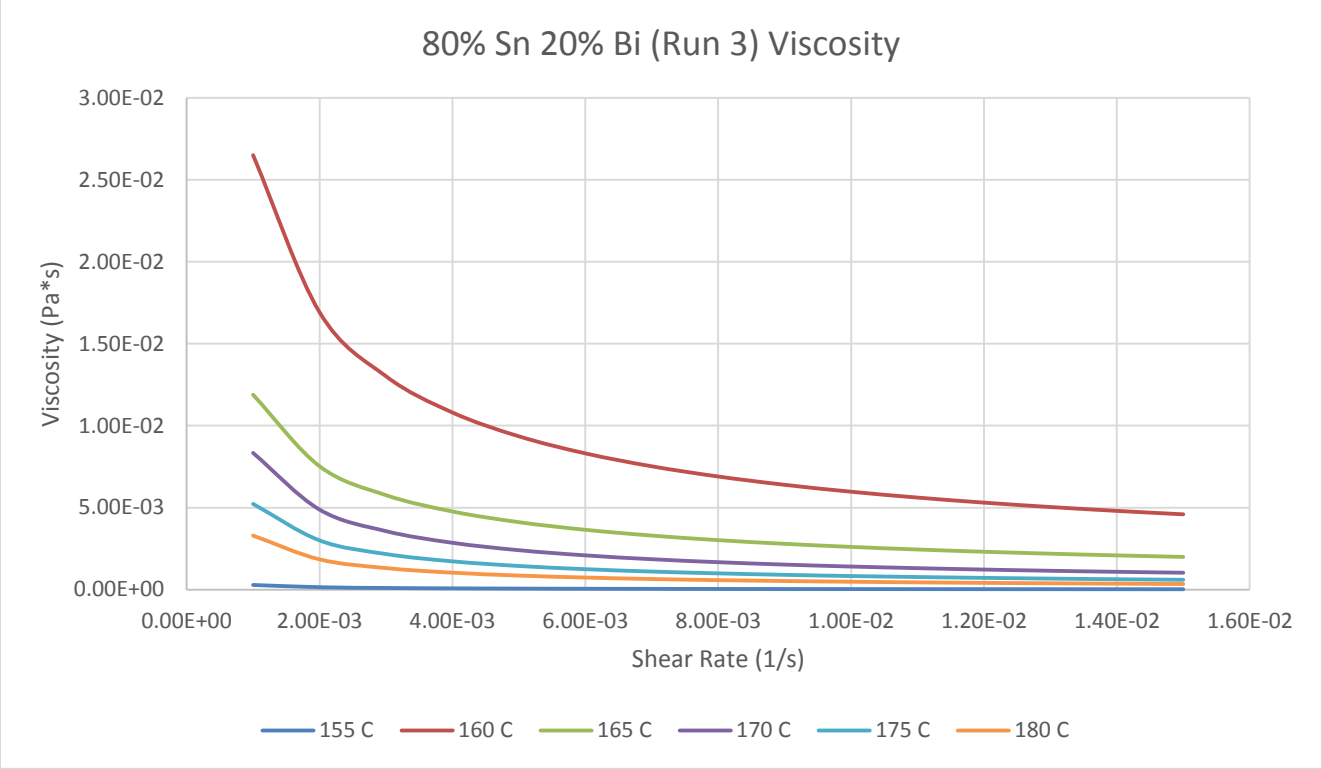

Figure 382- 80% Sn 20% Bi (Run 3), Cone and Plate Viscosity

155 C

Fraction Solid	47.50 %
Power Law	$\tau = 9.52 * 10^{-6} * \dot{\gamma}^{0.0387}$
	$\mu = 3.68 * 10^{-7} * \dot{\gamma}^{-0.9613}$
R^2	4.0 %

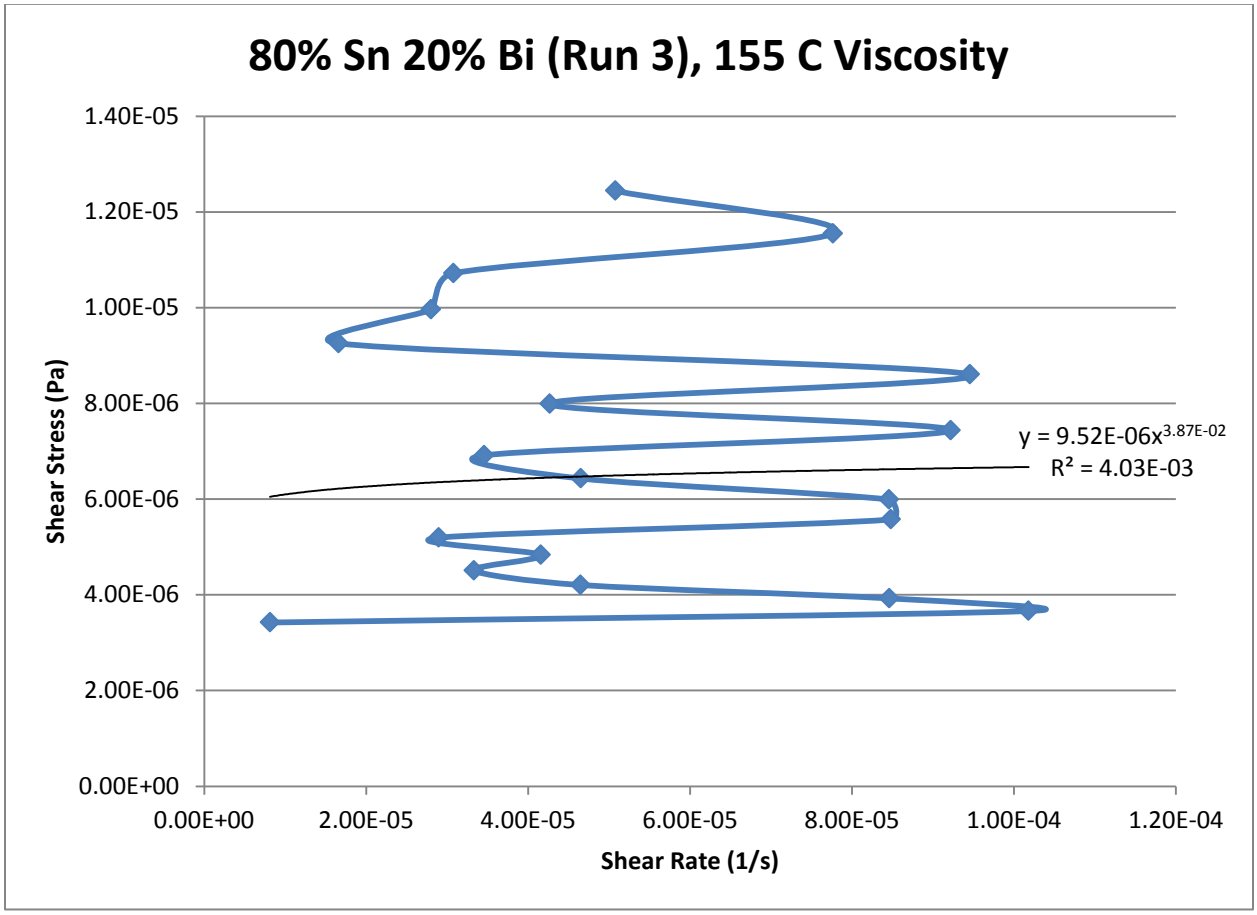

Figure 383- 80% Sn 20% Bi (Run 3), 155 C, Cone and Plate Viscosity

160 C

Fraction Solid	41.50 %
Power Law	$\tau = 8.58 * 10^{-4} * \dot{\gamma}^{0.3527}$
	$\mu = 3.03 * 10^{-4} * \dot{\gamma}^{-0.6473}$
R^2	88.99 %

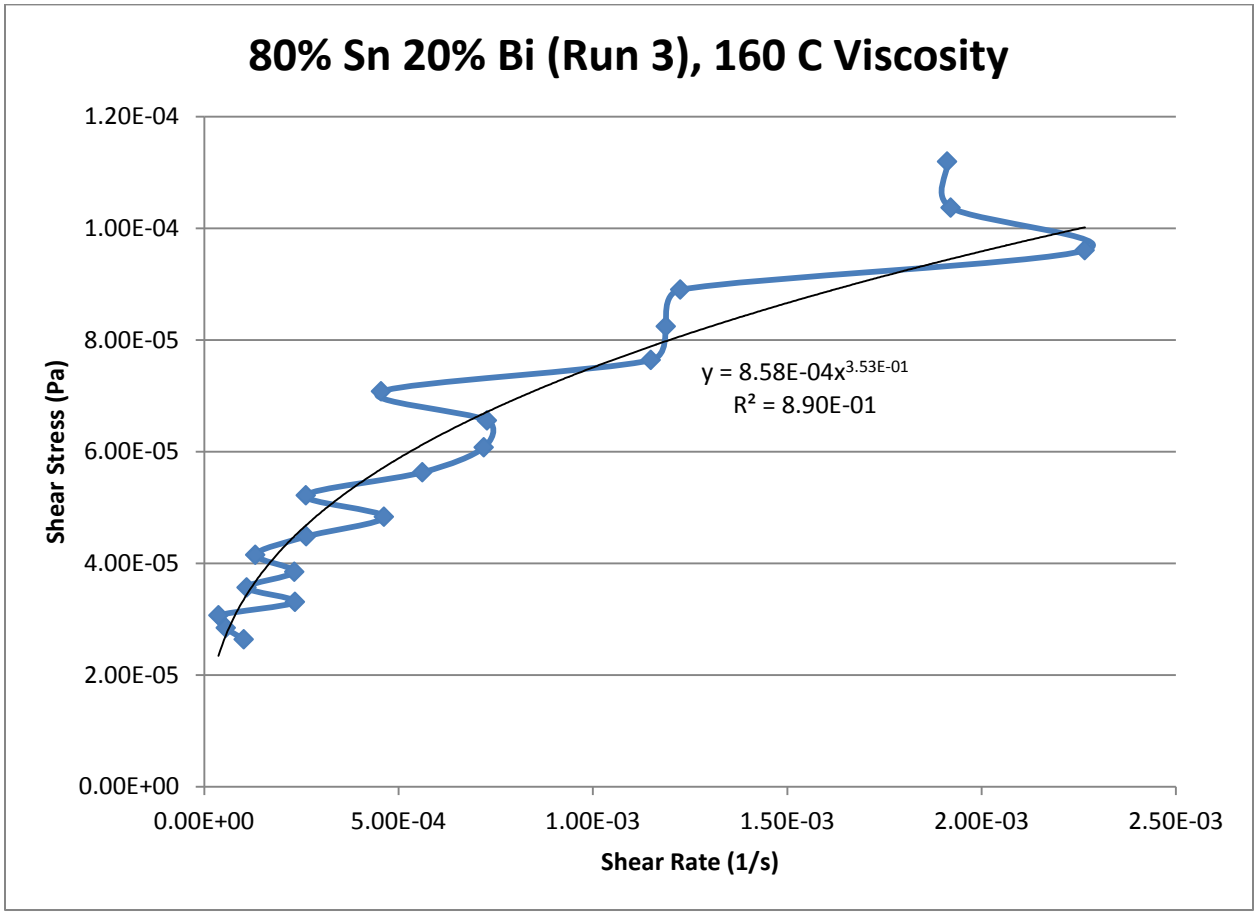

Figure 384- 80% Sn 20% Bi (Run 3), 160 C, Cone and Plate Viscosity

165 C

Fraction Solid	36.10 %
Power Law	$\tau = 3.66 * 10^{-4} * \dot{\gamma}^{0.3406}$
	$\mu = 1.25 * 10^{-4} * \dot{\gamma}^{-0.6594}$
R^2	94.24%

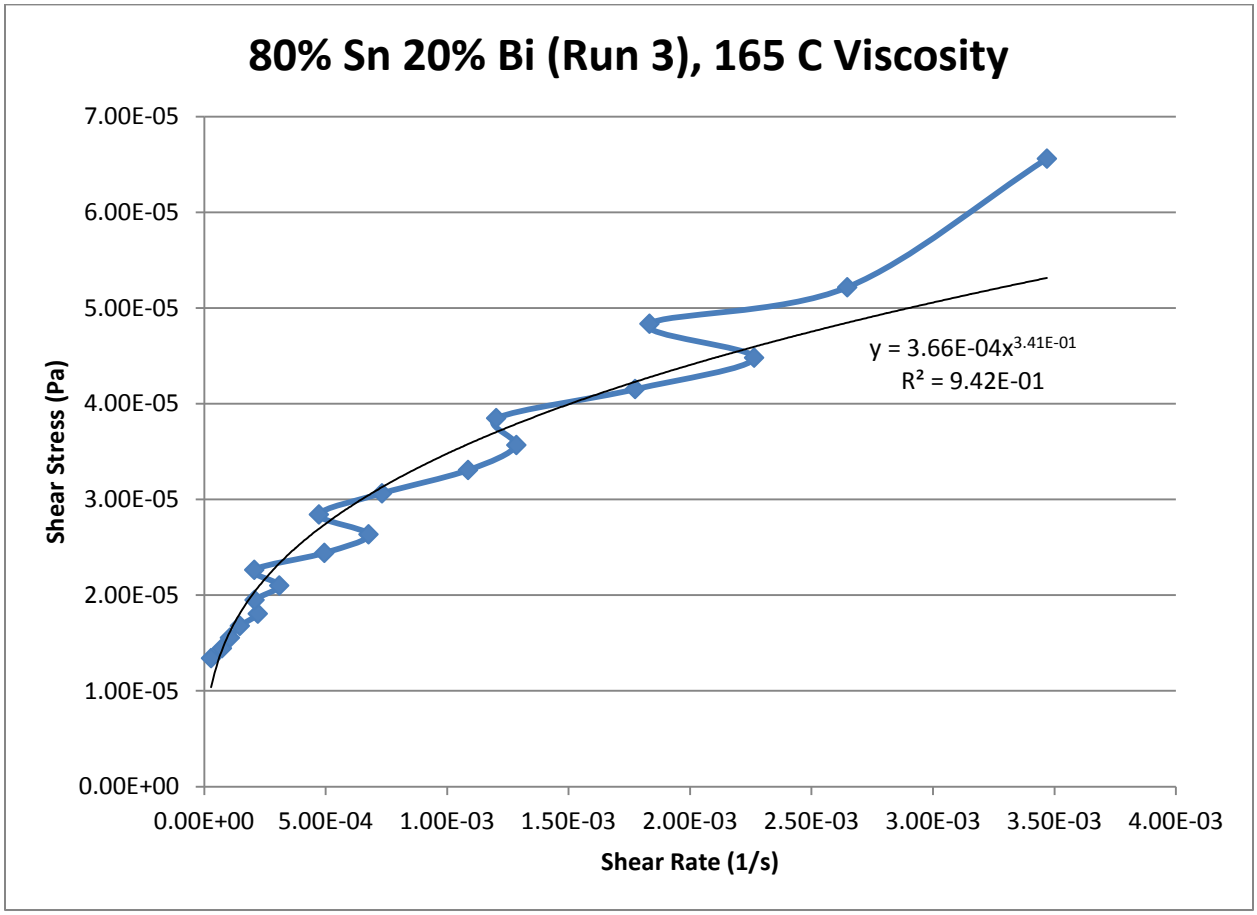

Figure 385- 80% Sn 20% Bi (Run 3), 165 C, Cone and Plate Viscosity

170 C

Fraction Solid	29.86 %
Power Law	$\tau = 1.76 * 10^{-4} * \dot{\gamma}^{0.2270}$
	$\mu = 4.00 * 10^{-5} * \dot{\gamma}^{-0.7730}$
R^2	84.03 %

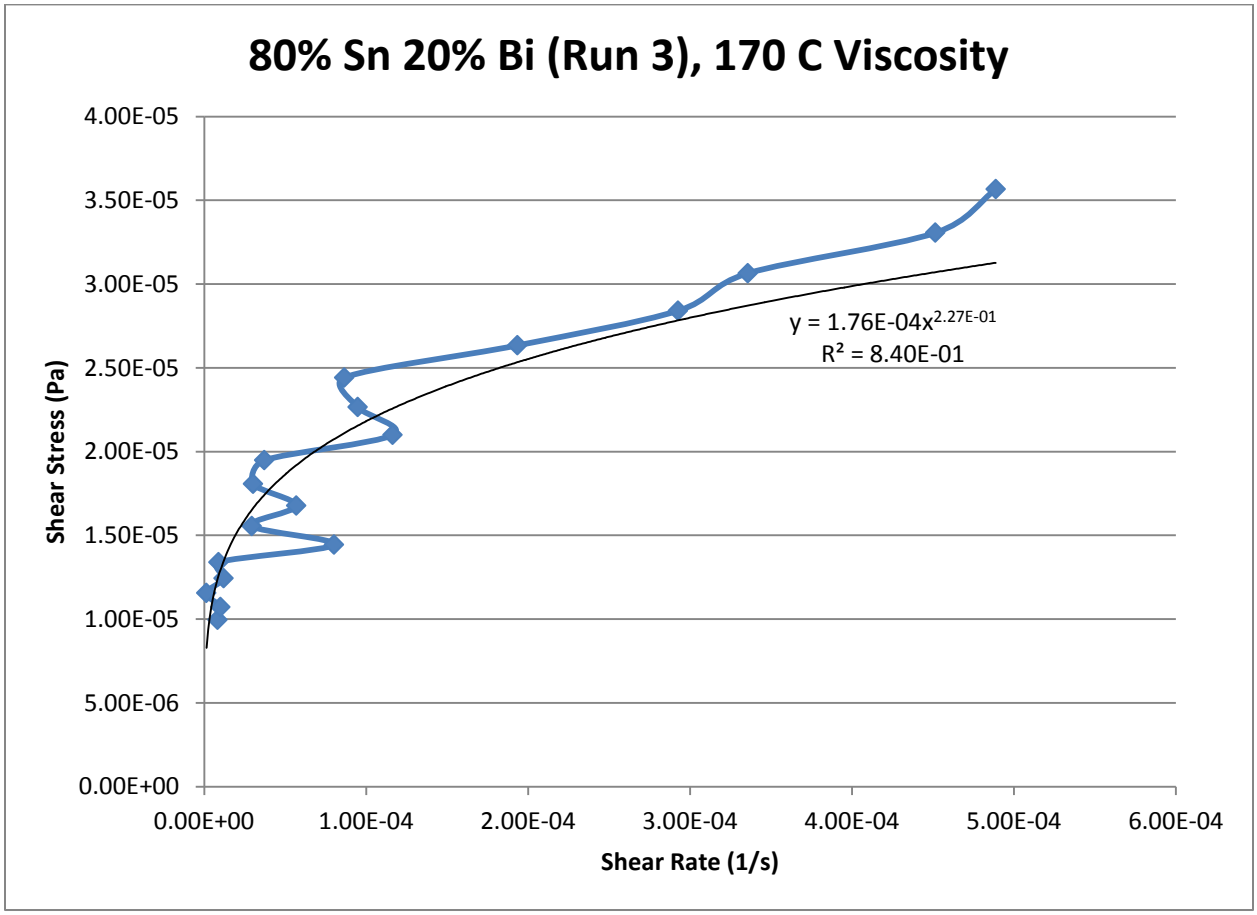

Figure 386- 80% Sn 20% Bi (Run 3), 170 C, Cone and Plate Viscosity

175 C

Fraction Solid	22.60 %
Power Law	$\tau = 1.04 * 10^{-4} * \dot{\gamma}^{0.1992}$
	$\mu = 2.07 * 10^{-5} * \dot{\gamma}^{-0.8008}$
R^2	84.08 %

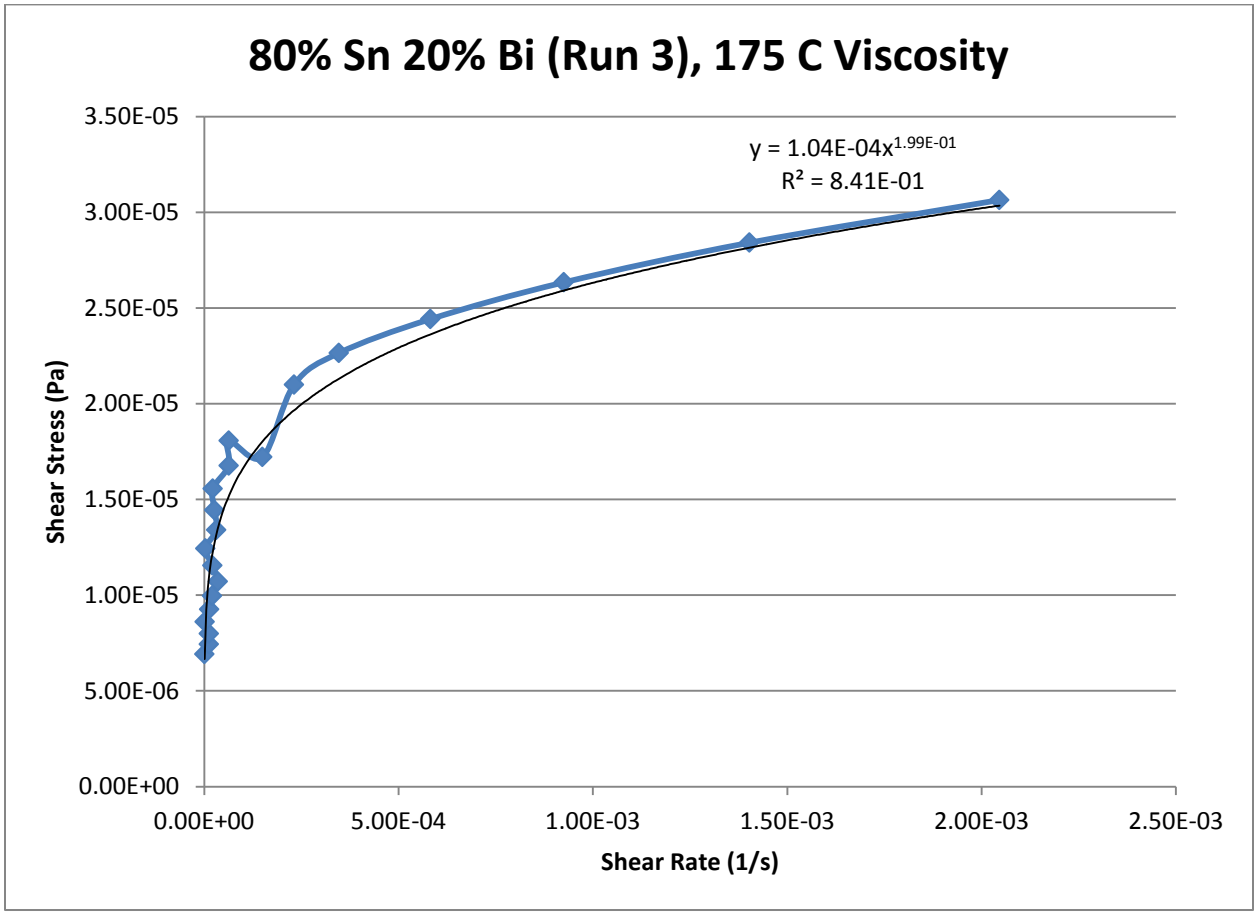

Figure 387- 80% Sn 20% Bi (Run 3), 175 C, Cone and Plate Viscosity

180 C

Fraction Solid	13.90 %
Power Law	$\tau = 6.19 * 10^{-5} * \dot{\gamma}^{0.1627}$
	$\mu = 1.01 * 10^{-5} * \dot{\gamma}^{-0.8373}$
R^2	89.51 %

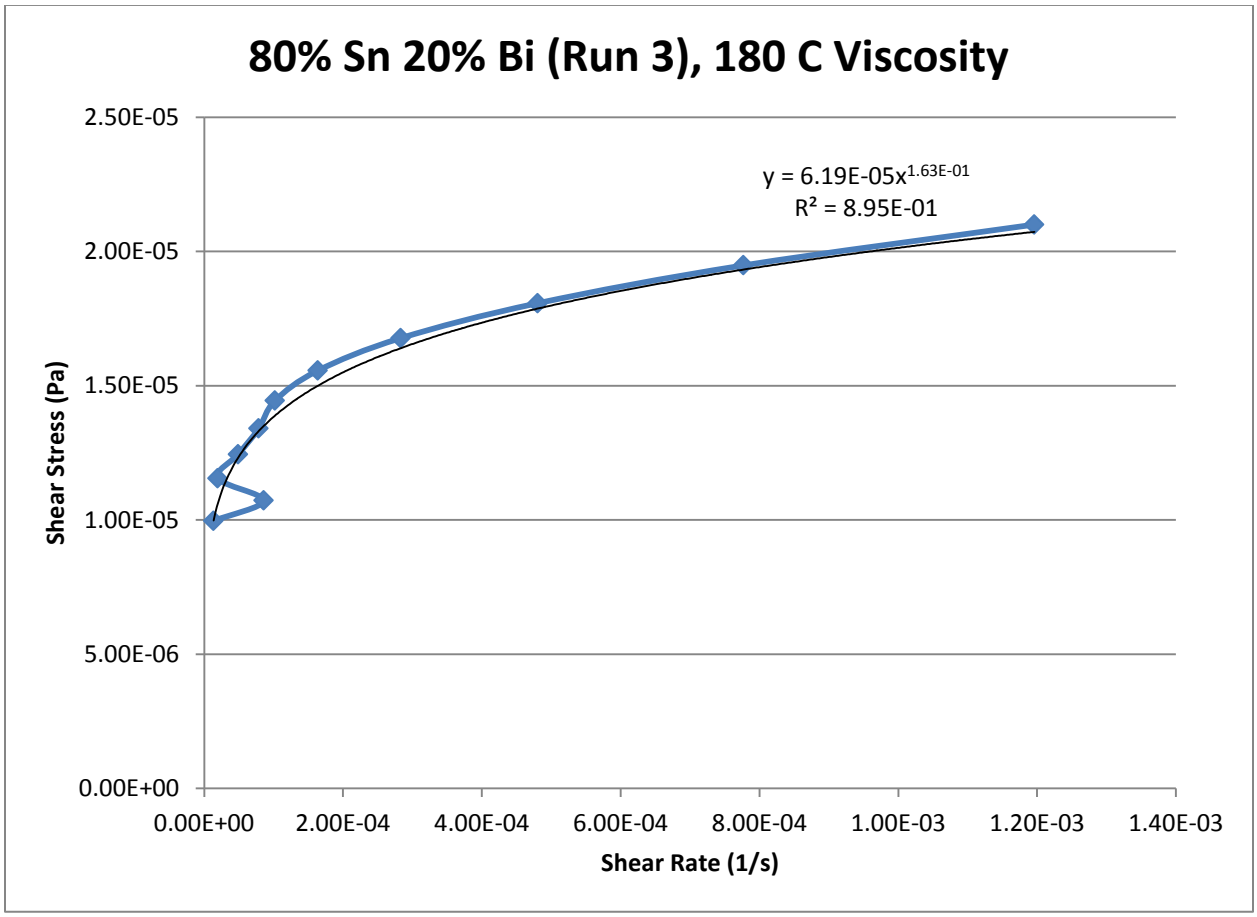

Figure 388- 80% Sn 20% Bi (Run 3), 180 C, Cone and Plate Viscosity

85% Tin 15% Bismuth (Run 1)

Predicted Composition: 87% Sn, 13% Bi

Theoretical Solidus Line: 139 C
Theoretical Liquidus Line: 203.9 C

Experimental Solidus Line: 140.3 C
Experimental Liquidus Line: 192.9 C

Set Up Notes

- The stage was heated to 185 C and the gap was zeroed. The temperature was then lowered in increments of 5 C for each stress sweep.

- The G'-G'' plots were very noisy and G' had too many negative values, which indicates that the temperature that the gap was zeroed at was too close to the liquidus line.

- At 175 C, G'' > G' before the crossover, which doesn't make sense since the semi-solid was not yet broken down into a liquid.

- At 170 C, the sample was extremely hard, lustrous, and chunky. It had a gray color. The material on the cone formed a thin, gray, solid film that required hard scraping to remove.

Plots

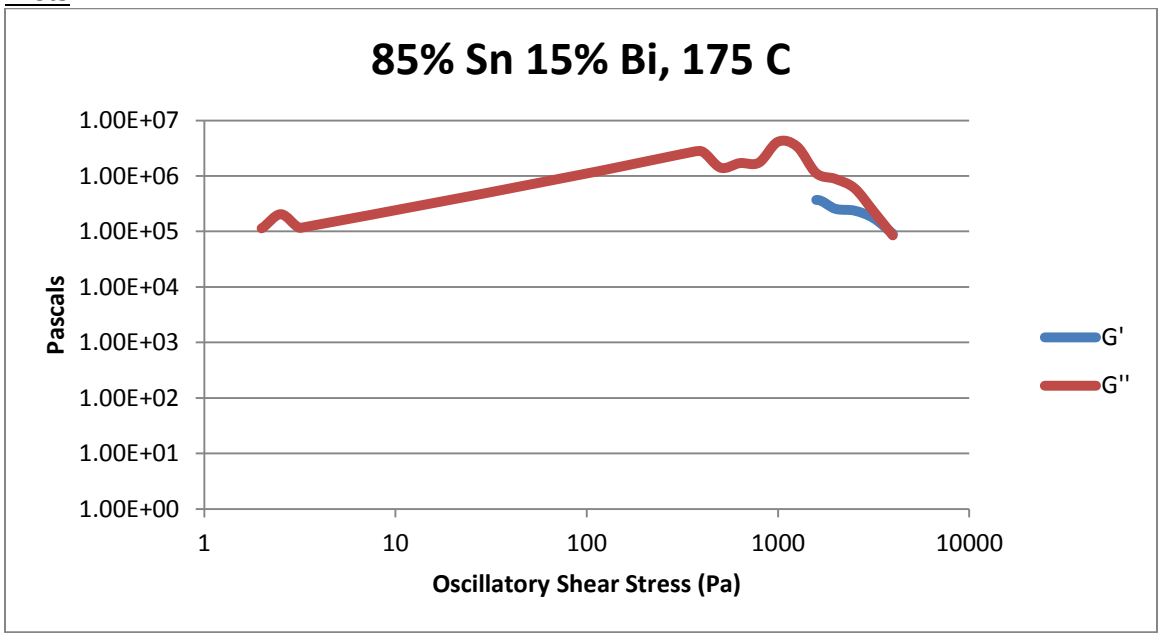

Figure 389- 85% Sn 15% Bi (Run 1), 175 C, Cone and Plate Stress Sweep

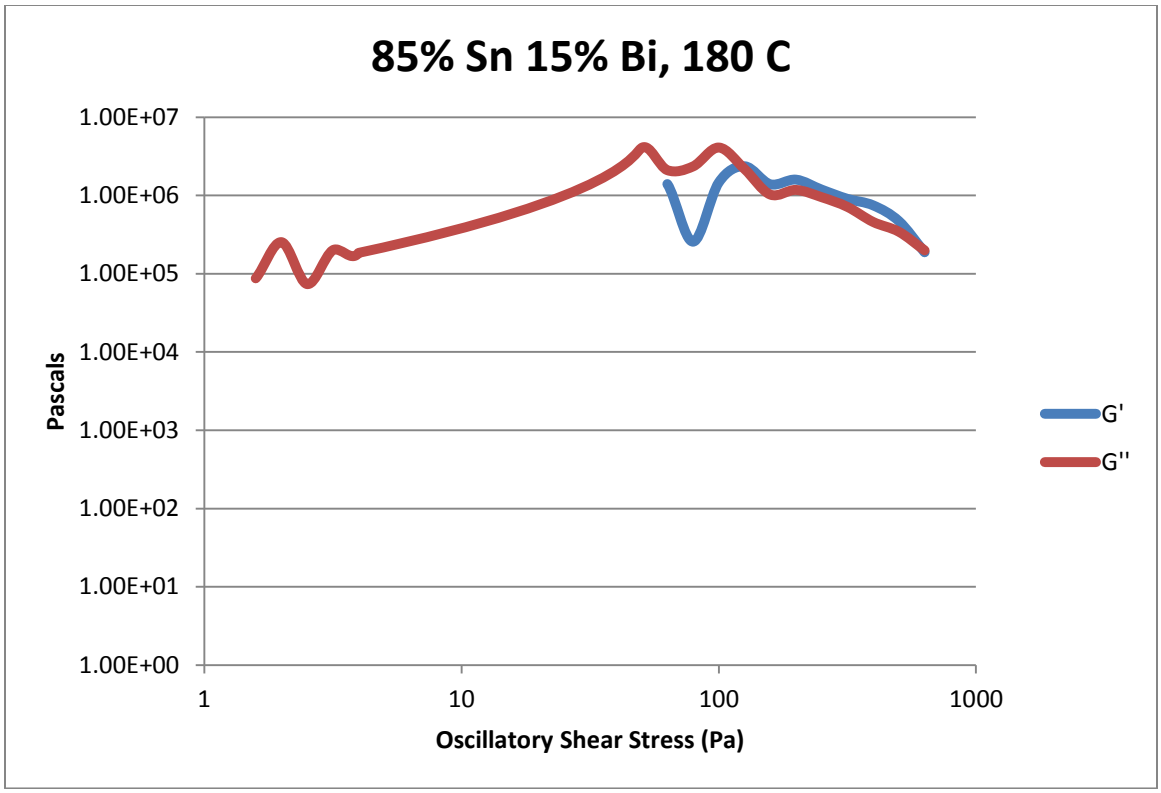

Figure 390- 85% Sn 15% Bi (Run 1), 180 C, Cone and Plate Stress Sweep

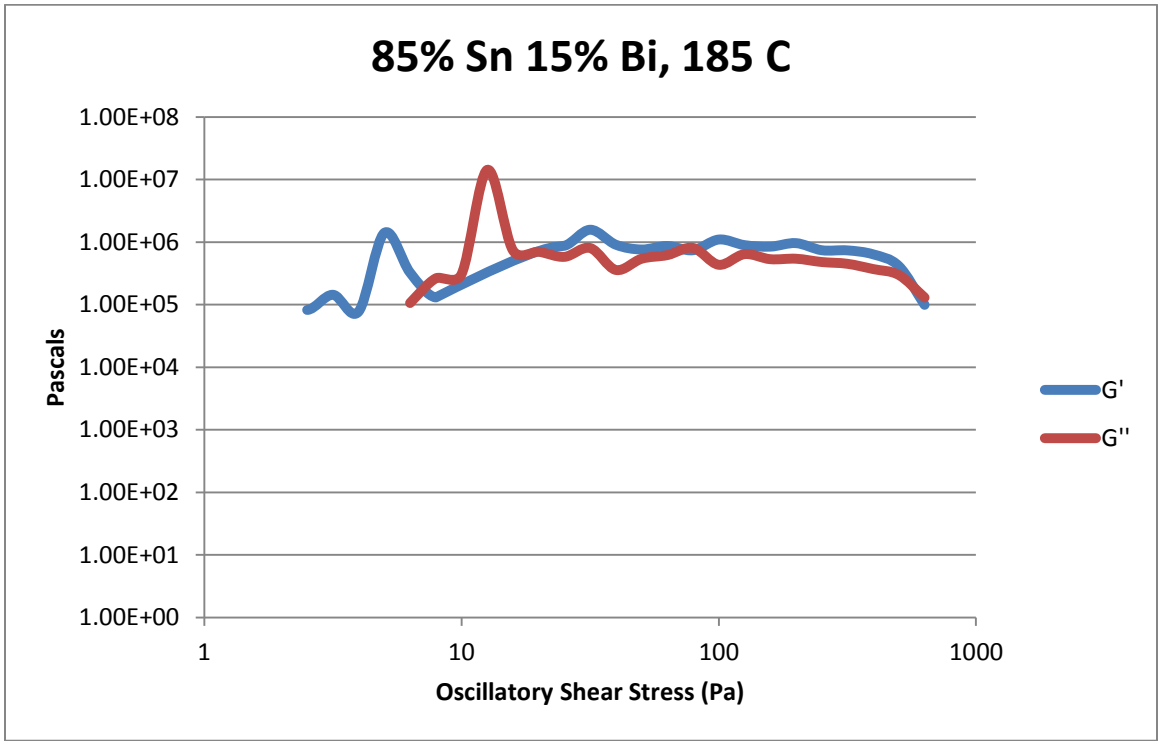

Figure 391- 85% Sn 15% Bi (Run 1), 185 C, Cone and Plate Stress Sweep

Temperature	Crossover Stress (Pa)	Crossover Stress (PSI)
175 C	$9.91 * 10^4$	14.4
180 C	$2.10 * 10^5$	30.5
185 C	$1.65 * 10^5$	23.9

Table 74- 85% Sn 15% Bi (Run 1), Cone and Plate Crossover Stresses

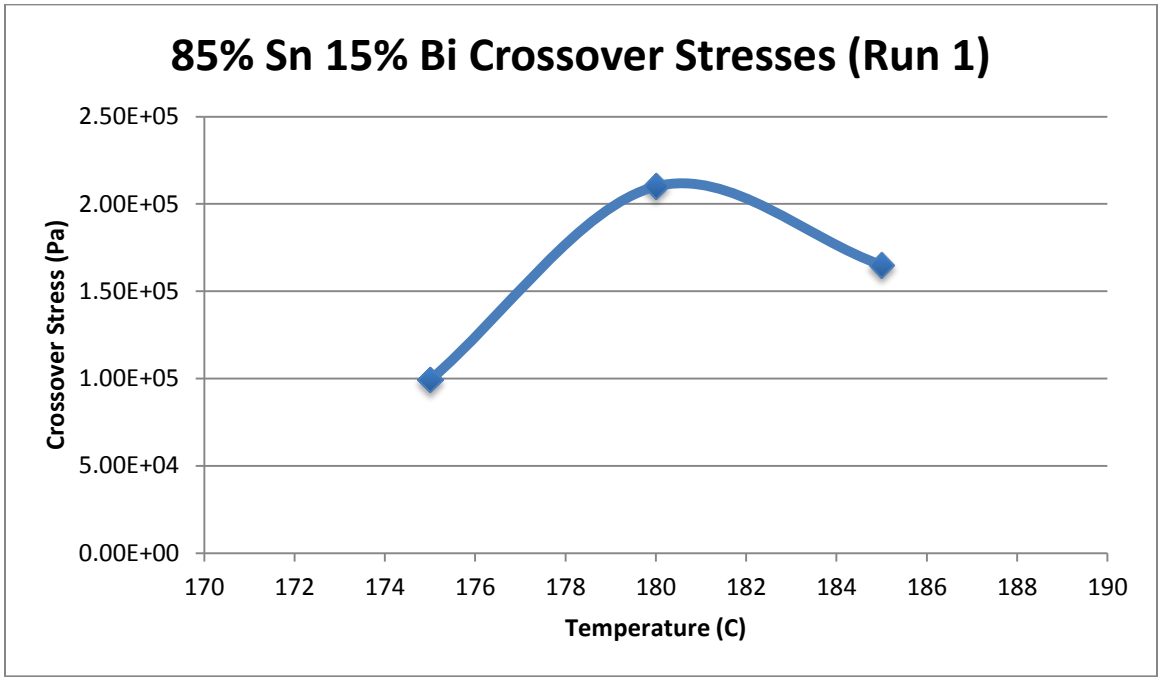

Temperature	Fraction Solid (At %)	G' Plateau (Pa)	G'' Plateau (Pa)
170 C	60.9	$7.70 * 10^6$	$5.93 * 10^5$
175 C	50.6	$5.72 * 10^6$	$1.71 * 10^6$
180 C	43.2	$1.40 * 10^6$	$1.05 * 10^6$
185 C	35.8	$8.49 * 10^5$	$5.88 * 10^5$

Table 75- 85% Sn 15% Bi (Run 1), Cone and Plate Plateau Stresses

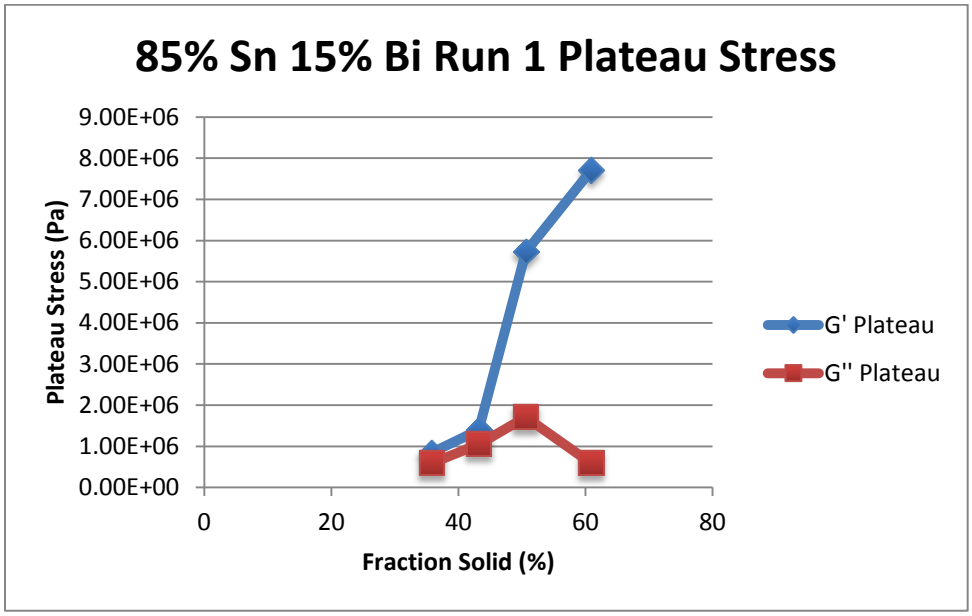

Figure 392- 85% Sn 15% Bi (Run 1), Cone and Plate Plateau Stresses vs. Fraction Solid

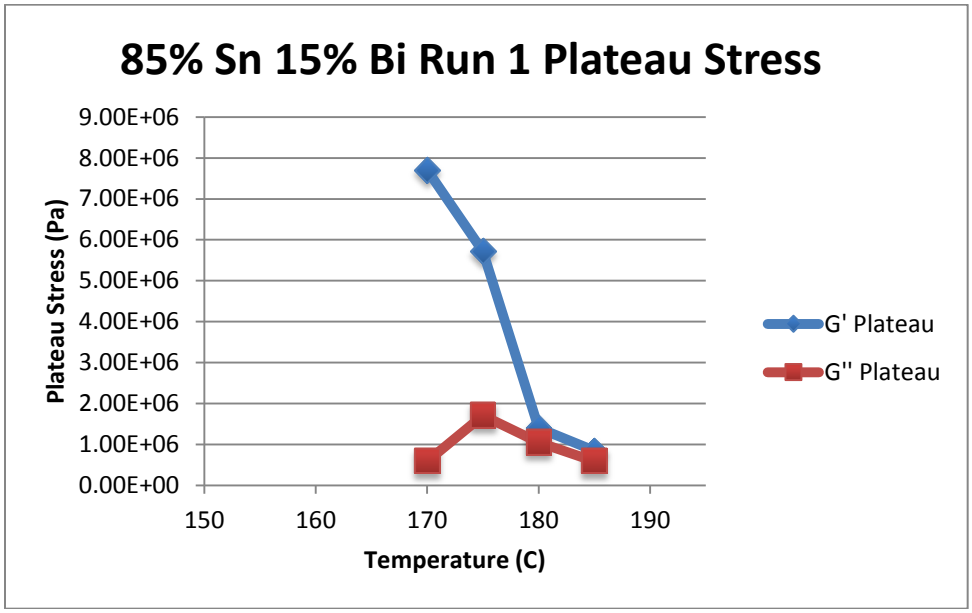

Figure 393- 85% Sn 15% Bi (Run 1), Cone and Plate Plateau Stresses vs. Temperature

85% Sn 15% Bi (Run 1) Viscosity					
Temperature	**Fraction Solid**	**Power Law**	**K**	**n**	**R^2**
170 C	60.9 %	$\tau = 2.53 * 10^{-4} * \dot{\gamma}^{0.0890}$ $\mu = 2.25 * 10^{-5} * \dot{\gamma}^{-0.9110}$	$2.53 * 10^{-4}$ Pa*s	0.0890	1.51 %
175 C	50.6 %	$\tau = 9.91 * 10^{-3} * \dot{\gamma}^{0.6349}$ $\mu = 6.29 * 10^{-3} * \dot{\gamma}^{-0.3651}$	$9.91 * 10^{-3}$ Pa*s	0.6349	36.65 %
180 C	43.2 %	$\tau = 4.65 * 10^{-5} * \dot{\gamma}^{0.0872}$ $\mu = 4.05 * 10^{-6} * \dot{\gamma}^{-0.9128}$	$4.65 * 10^{-5}$ Pa*s	0.0872	3.15 %
185 C	35.8 %	$\tau = 4.38 * 10^{-5} * \dot{\gamma}^{0.0907}$ $\mu = 3.97 * 10^{-6} * \dot{\gamma}^{-0.9093}$	$4.38 * 10^{-5}$ Pa*s	0.0907	1.41 %

Table 76- 85% Sn 15% Bi (Run 1), Cone and Plate Viscosity

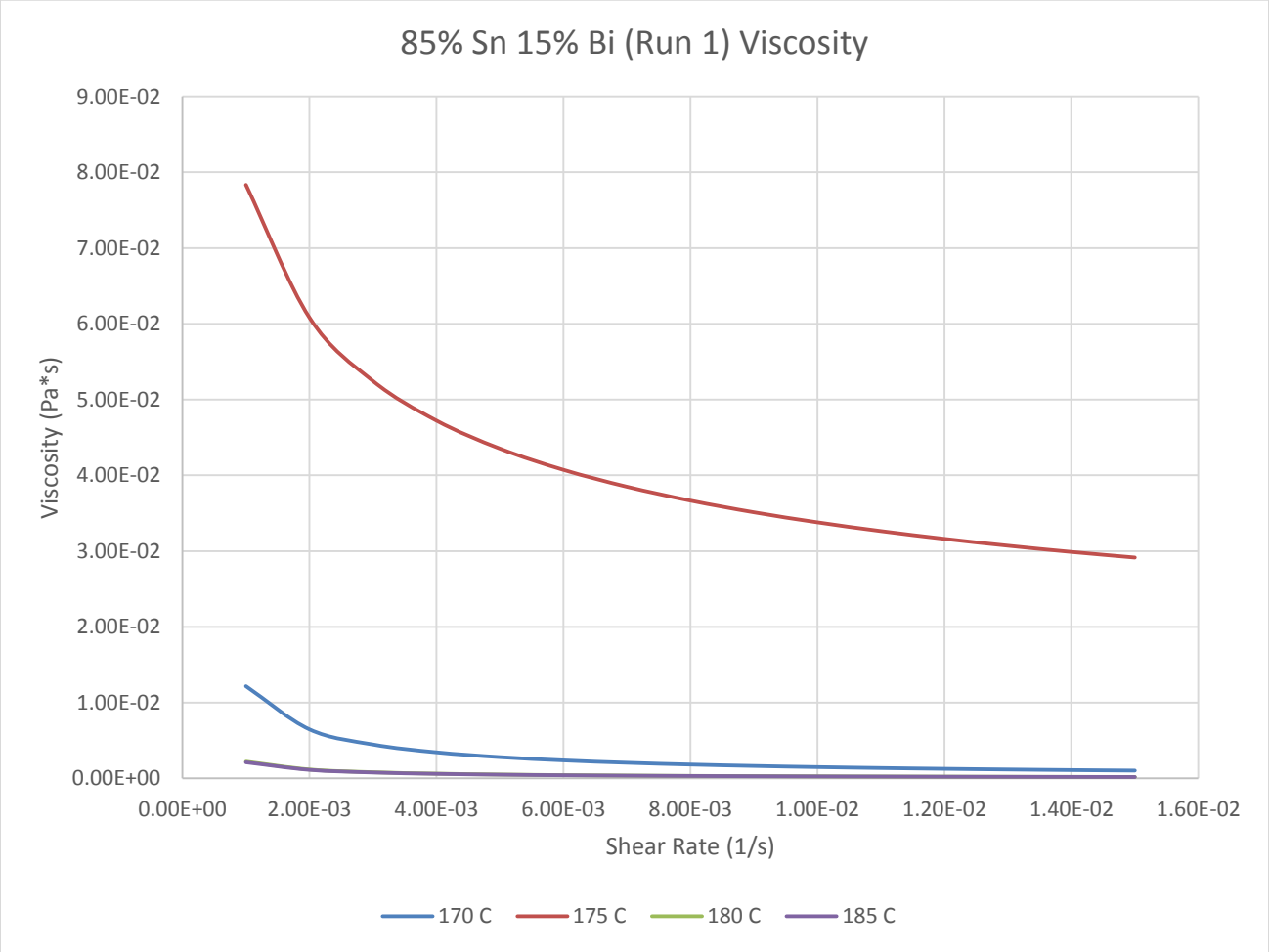

Figure 394- 85% Sn 15% Bi (Run 1), Cone and Plate Viscosity

170 C

Fraction Solid	60.9 %
Power Law	$\tau = 2.53 * 10^{-4} * \dot{\gamma}^{0.0890}$
	$\mu = 2.25 * 10^{-5} * \dot{\gamma}^{-0.9110}$
R^2	1.51 %

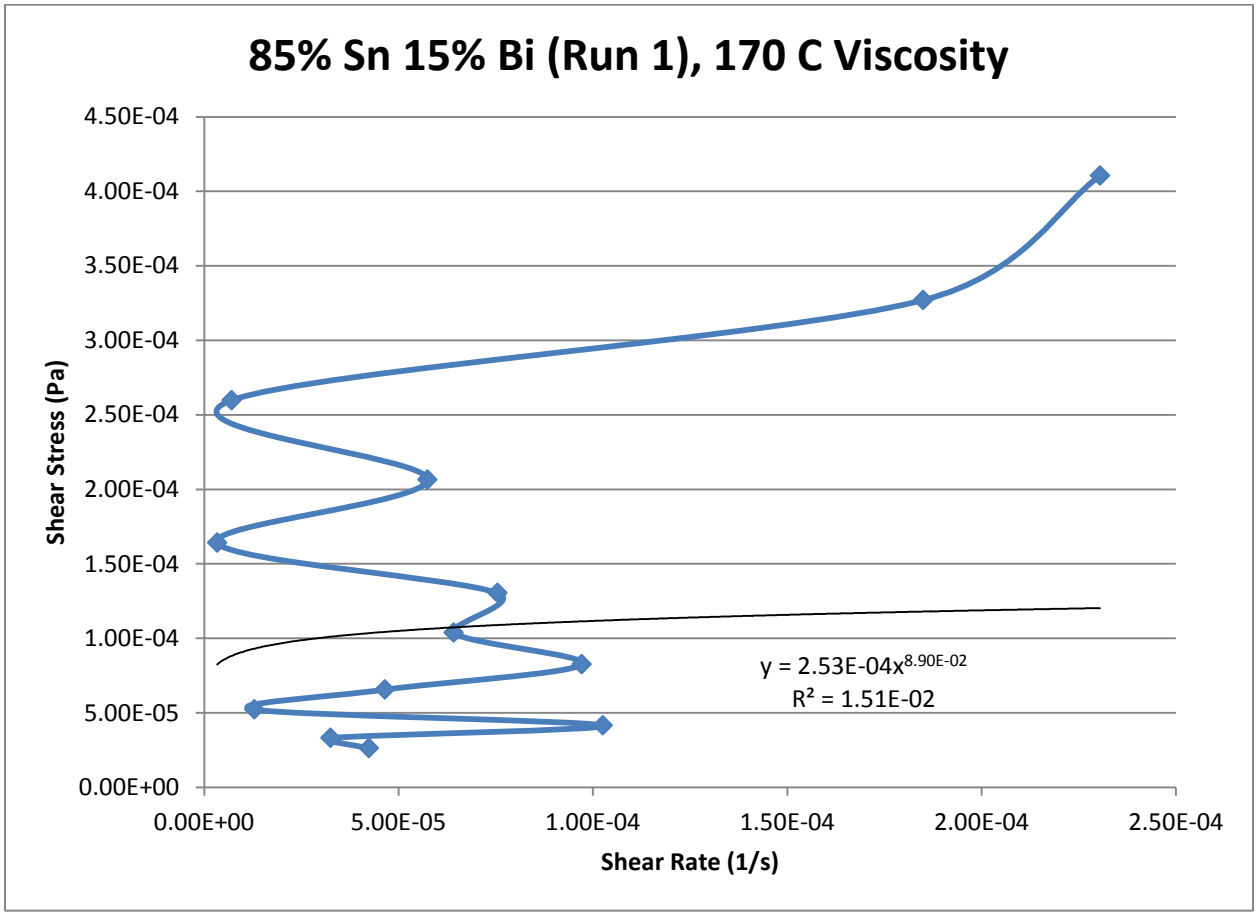

Figure 395- 85% Sn 15% Bi (Run 1), 170 C, Cone and Plate Viscosity

175 C

Fraction Solid	50.6 %
Power Law	$\tau = 9.91 * 10^{-3} * \dot{\gamma}^{0.6349}$
	$\mu = 6.29 * 10^{-3} * \dot{\gamma}^{-0.3651}$
R^2	36.65 %

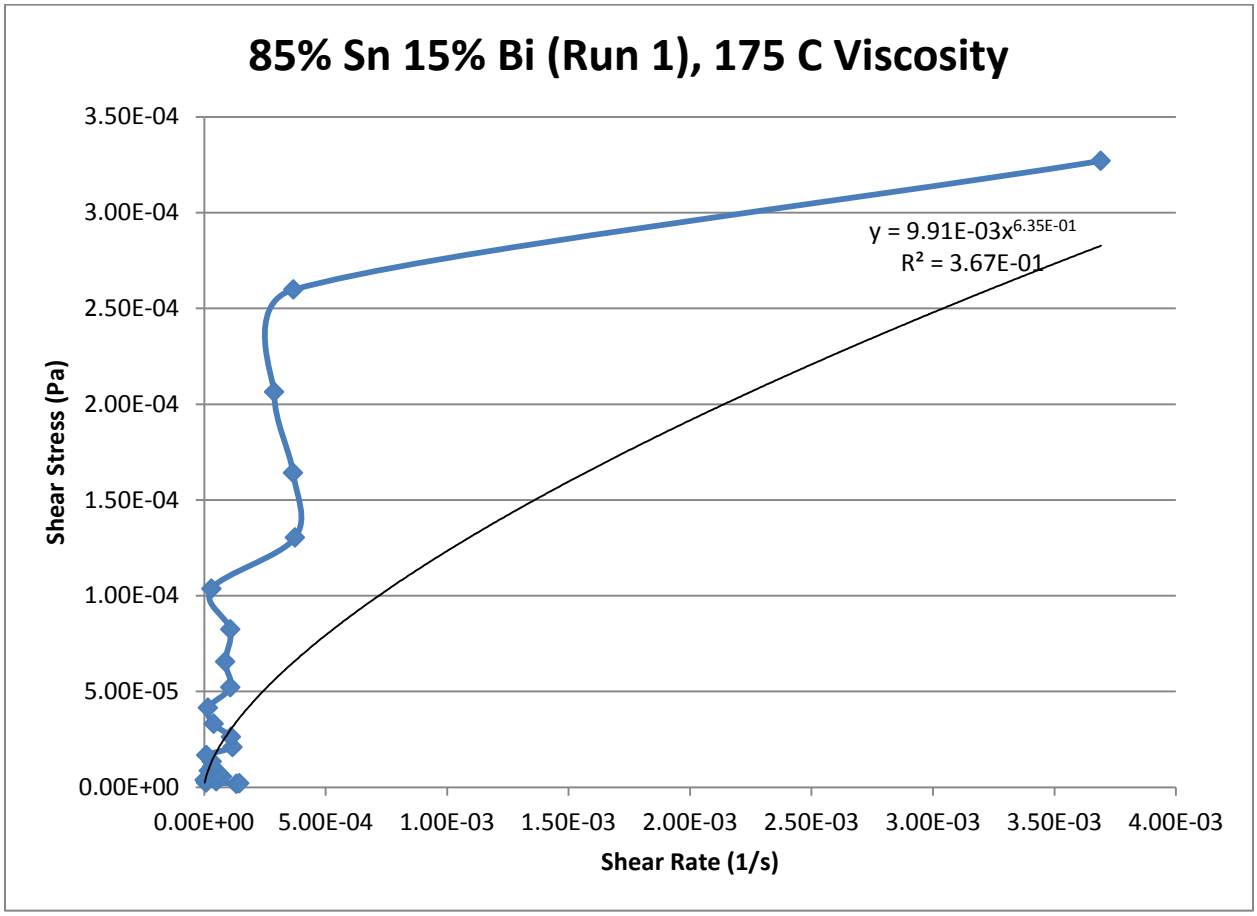

Figure 396- 85% Sn 15% Bi (Run 1), 175 C, Cone and Plate Viscosity

180 C

Fraction Solid	43.2 %
Power Law	$\tau = 4.65 * 10^{-5} * \dot{\gamma}^{0.0872}$
	$\mu = 4.05 * 10^{-6} * \dot{\gamma}^{-0.9128}$
R^2	3.15 %

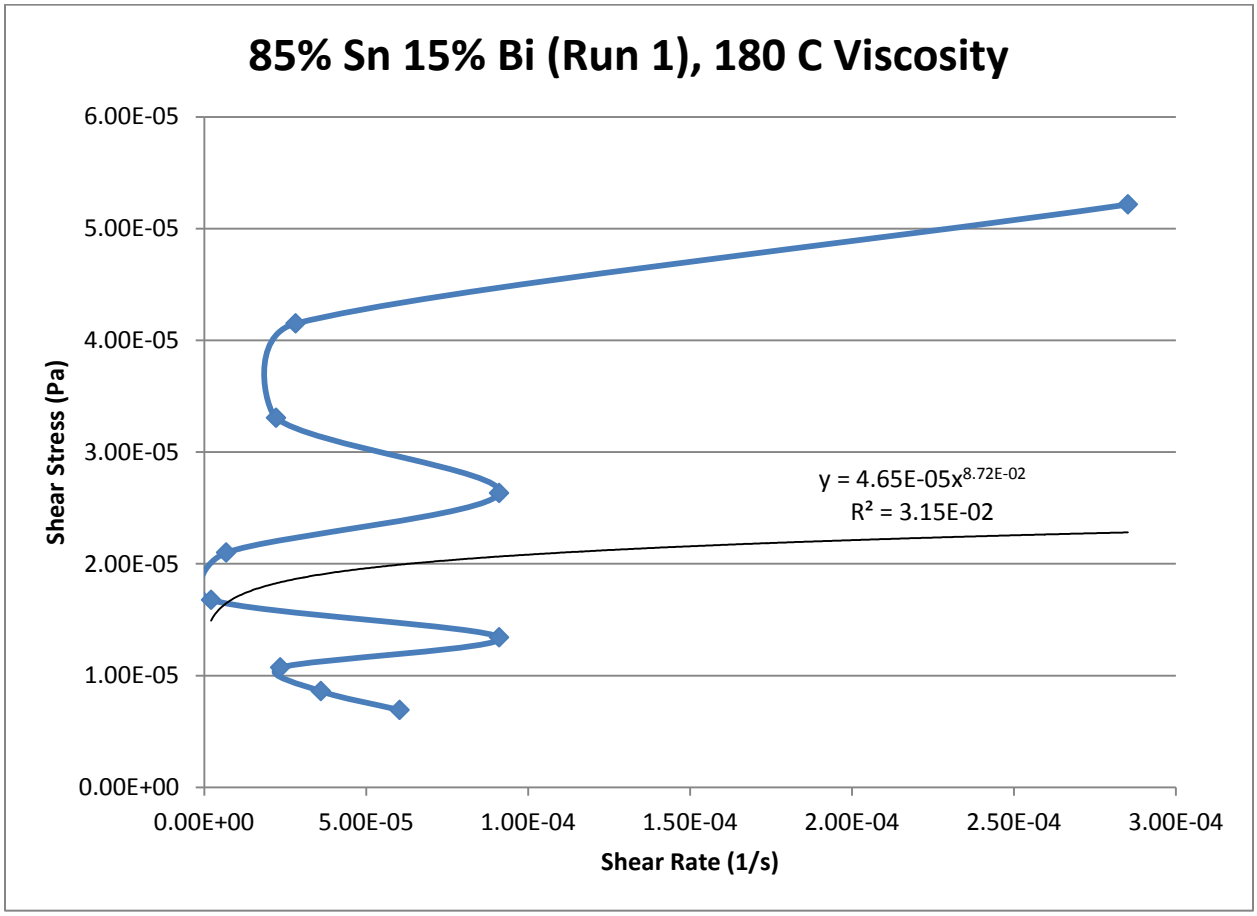

Figure 397- 85% Sn 15% Bi (Run 1), 180 C, Cone and Plate Viscosity

185 C

Fraction Solid	35.8 %
Power Law	$\tau = 4.38 * 10^{-5} * \dot{\gamma}^{0.0907}$
	$\mu = 3.97 * 10^{-6} * \dot{\gamma}^{-0.9093}$
R^2	1.41 %

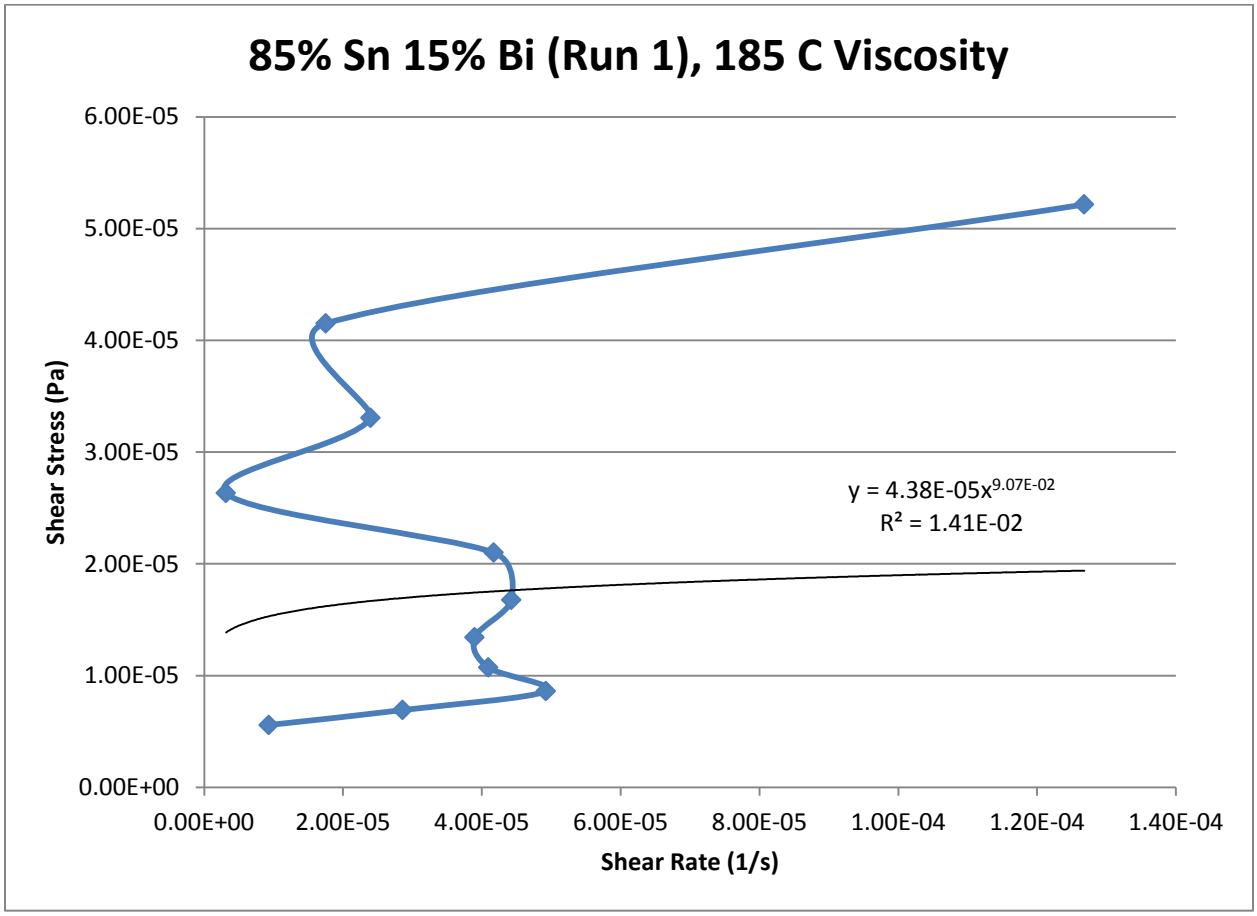

Figure 398- 85% Sn 15% Bi (Run 1), 185 C, Cone and Plate Viscosity

85% Tin 15% Bismuth (Run 2)

Predicted Composition: 87% Sn, 13% Bi

Theoretical Solidus Line: 139 C
Theoretical Liquidus Line: 203.9 C

Experimental Solidus Line: 140.3 C
Experimental Liquidus Line: 192.9 C

Set Up Notes

- The stage was heated to 195 C and the gap was zeroed. The temperature was then lowered in increments of 5 C for each stress sweep.

- The sample was very mushy and chunky in its liquid-dominant state rather than the traditional molten metal that flows.

- The experiment was stopped during the 170 C stress sweep since a thin film of the sample solidified on the cone. This was likely an oxide.

Plots

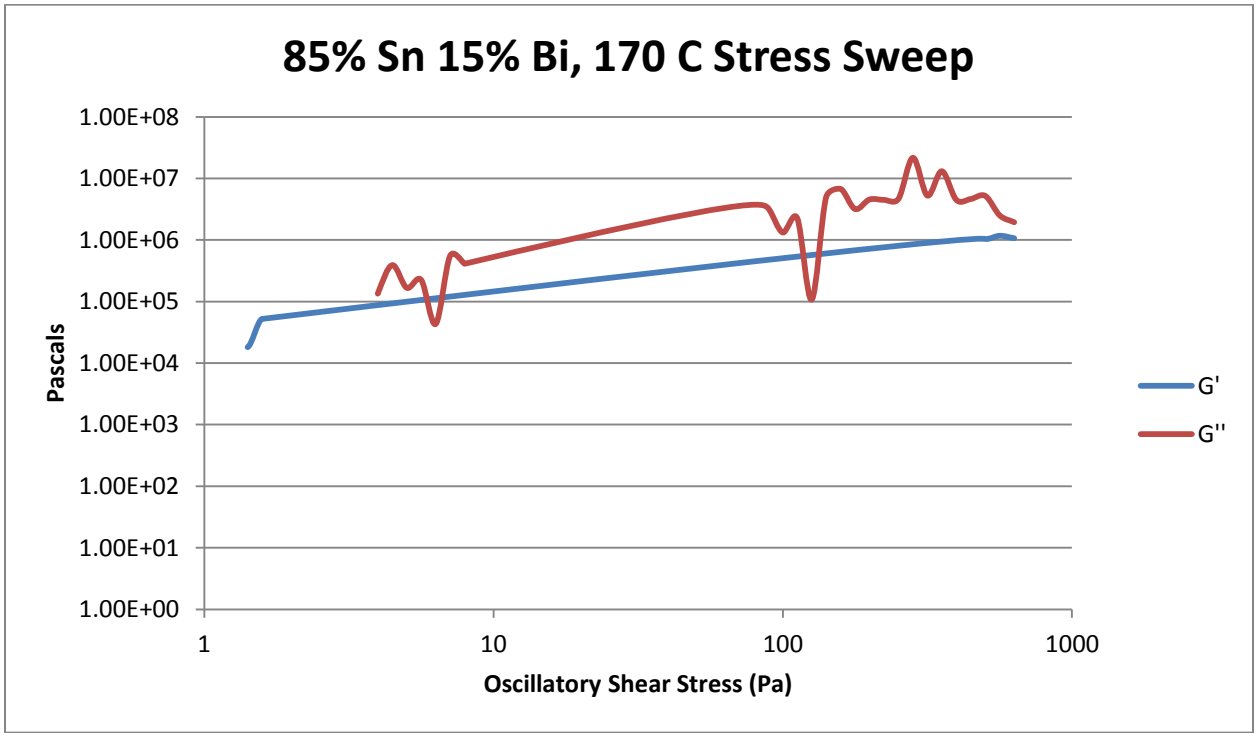

Figure 399- 85% Sn 15% Bi (Run 2), 170 C, Cone and Plate Stress Sweep

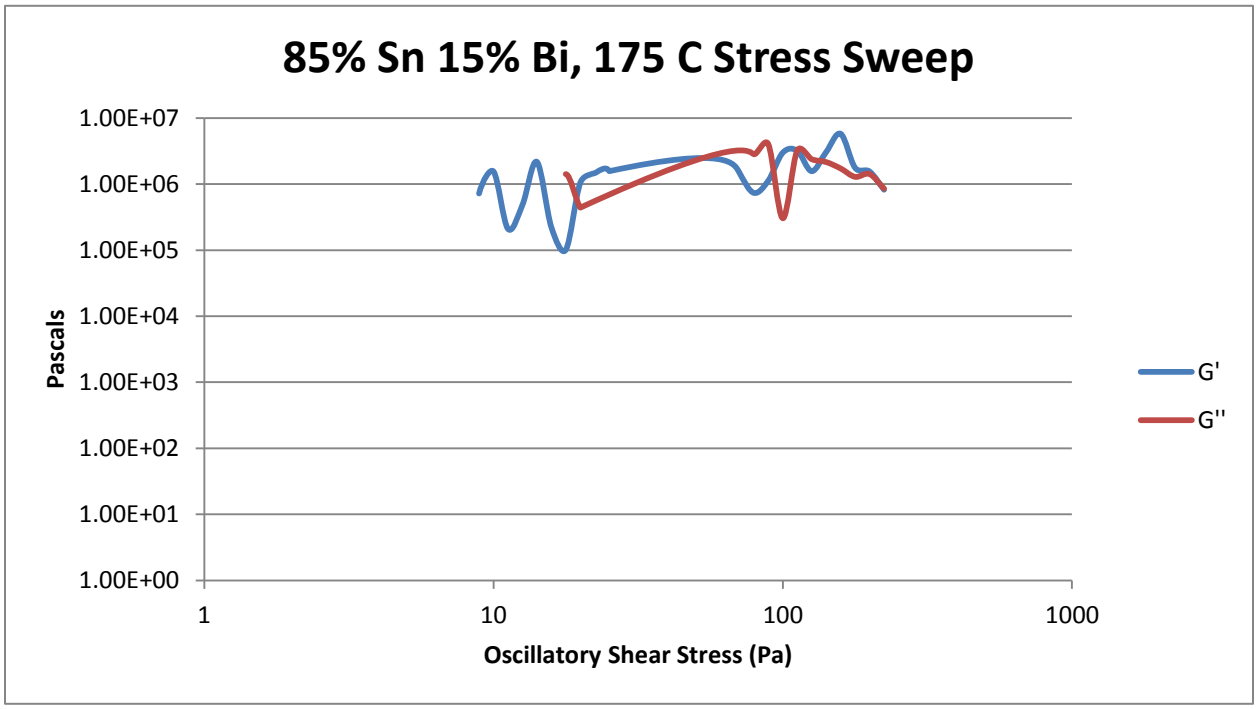

Figure 400- 85% Sn 15% Bi (Run 2), 175 C, Cone and Plate Stress Sweep

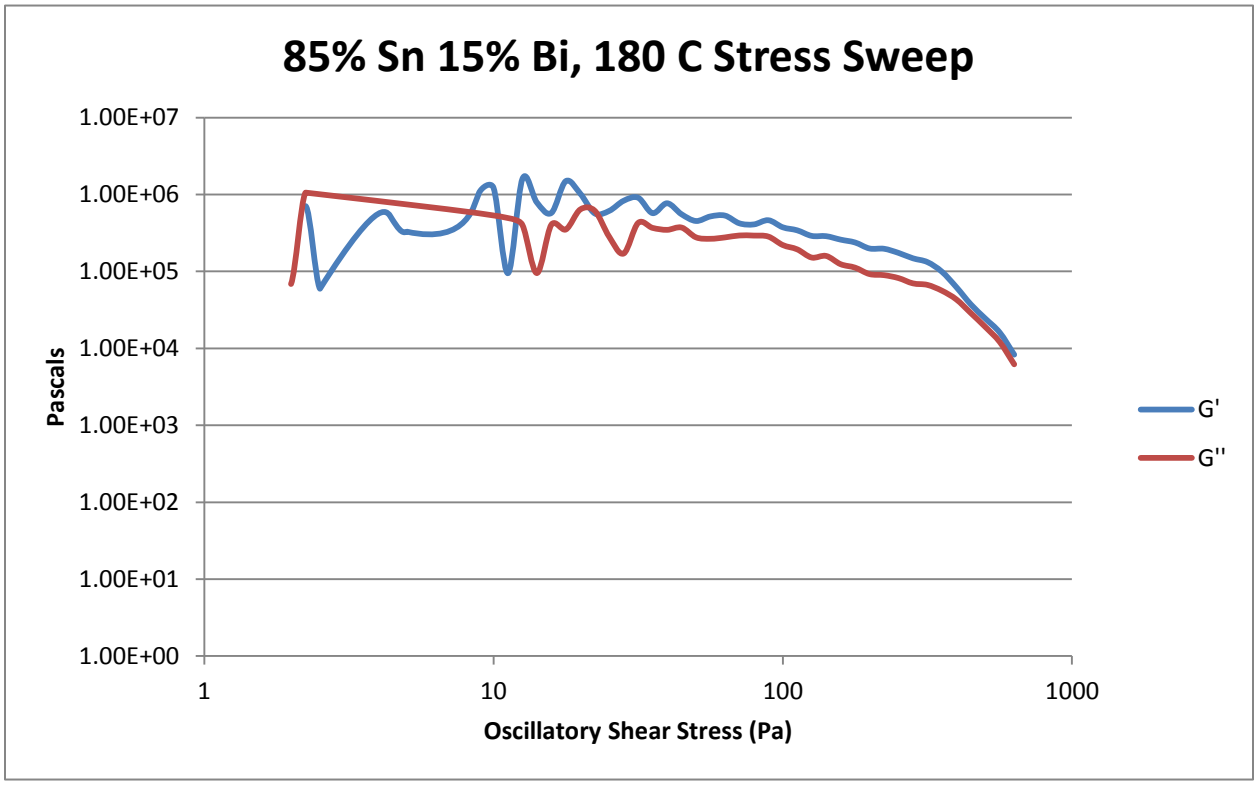

Figure 401- 85% Sn 15% Bi (Run 2), 180 C, Cone and Plate Stress Sweep

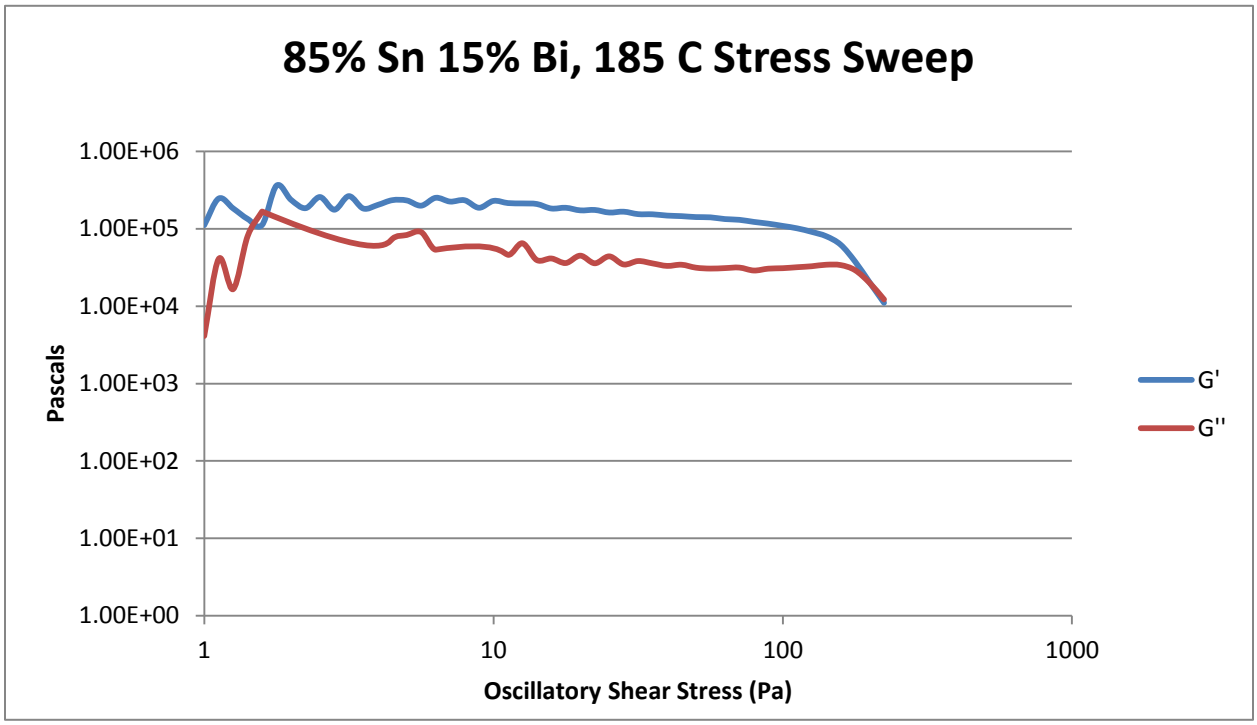

Figure 402- 85% Sn 15% Bi (Run 2), 185 C, Cone and Plate Stress Sweep

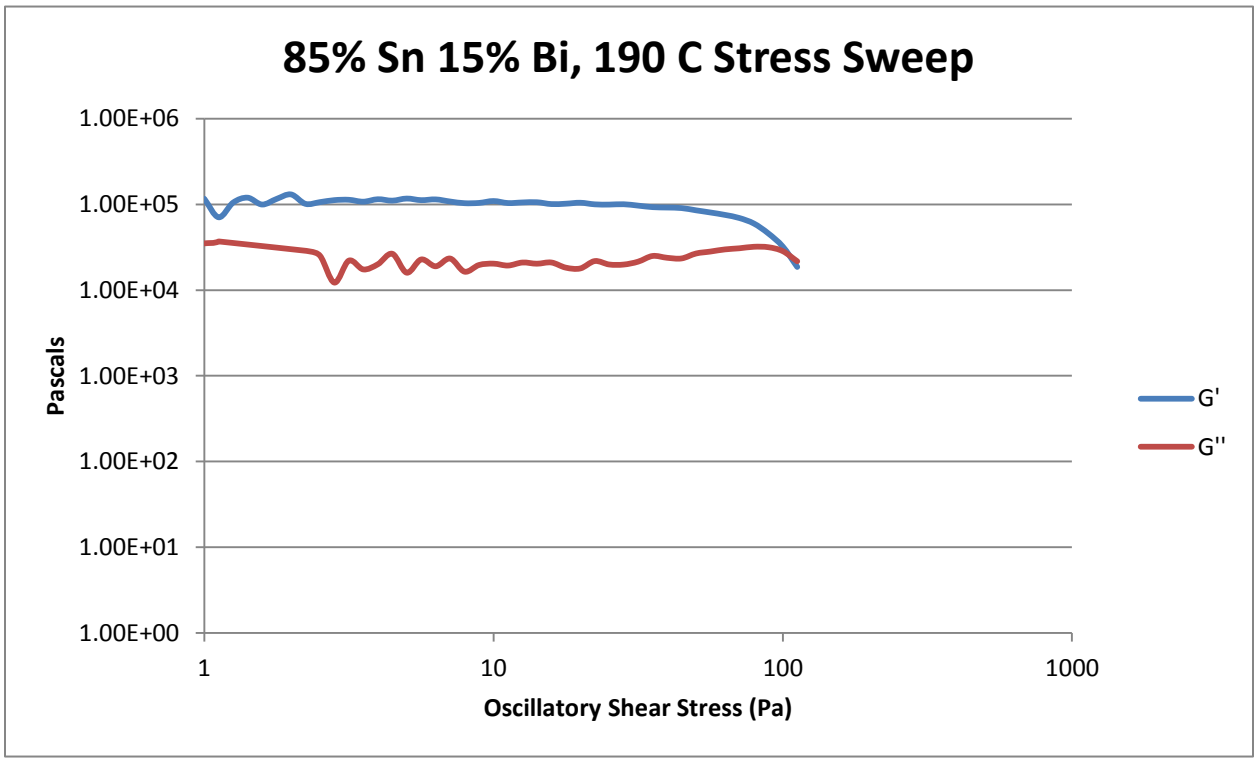

Figure 403- 85% Sn 15% Bi (Run 2), 190 C, Cone and Plate Stress Sweep

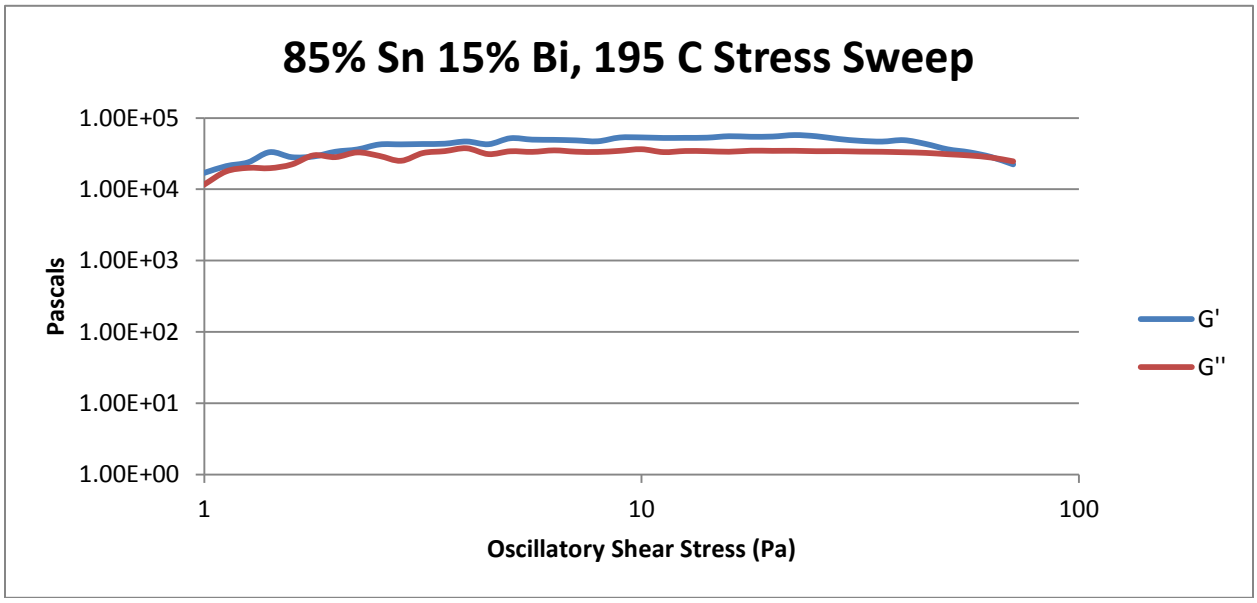

Figure 404- 85% Sn 15% Bi (Run 2), 190 C, Cone and Plate Stress Sweep

Temperature	Fraction Solid (At %)	Crossover Stress (Pa)	G' Plateau Stress (Pa)	G'' Plateau Stress (Pa)
170 C	60.9	N/A	$3.95 * 10^6$	$4.55 * 10^6$
175 C	50.6	$8.90 * 10^5$	$2.99 * 10^6$	$2.15 * 10^6$
180 C	43.2	N/A	$4.80 * 10^5$	$2.93 * 10^4$
185 C	35.8	$1.50 * 10^4$	$2.13 * 10^5$	$3.58 * 10^4$
190 C	27.5	$2.45 * 10^4$	$1.05 * 10^5$	$3.20 * 10^4$
195 C	21.4	$2.74 * 10^4$	$5.54 * 10^4$	$3.45 * 10^4$

Table 77- 85% Sn 15% Bi (Run 2), Cone and Plate Crossover and Plateau Stresses

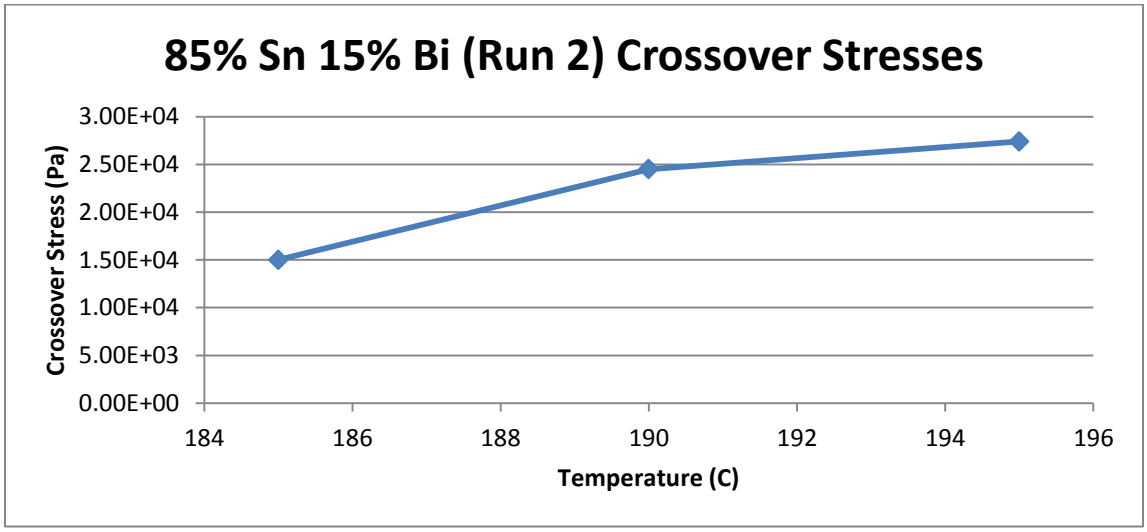

Figure 405- 85% Sn 15% Bi (Run 2), Cone and Plate Crossover Stresses

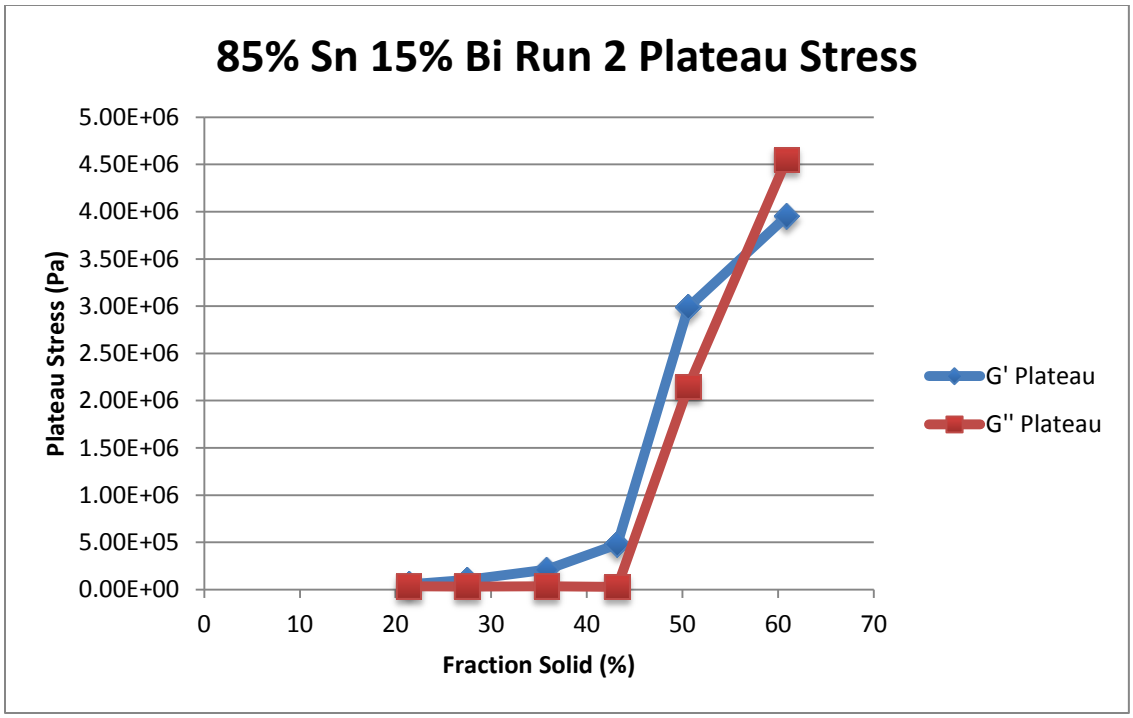

Figure 406- 85% Sn 15% Bi (Run 2), Cone and Plate Plateau Stresses vs. Fraction Solid

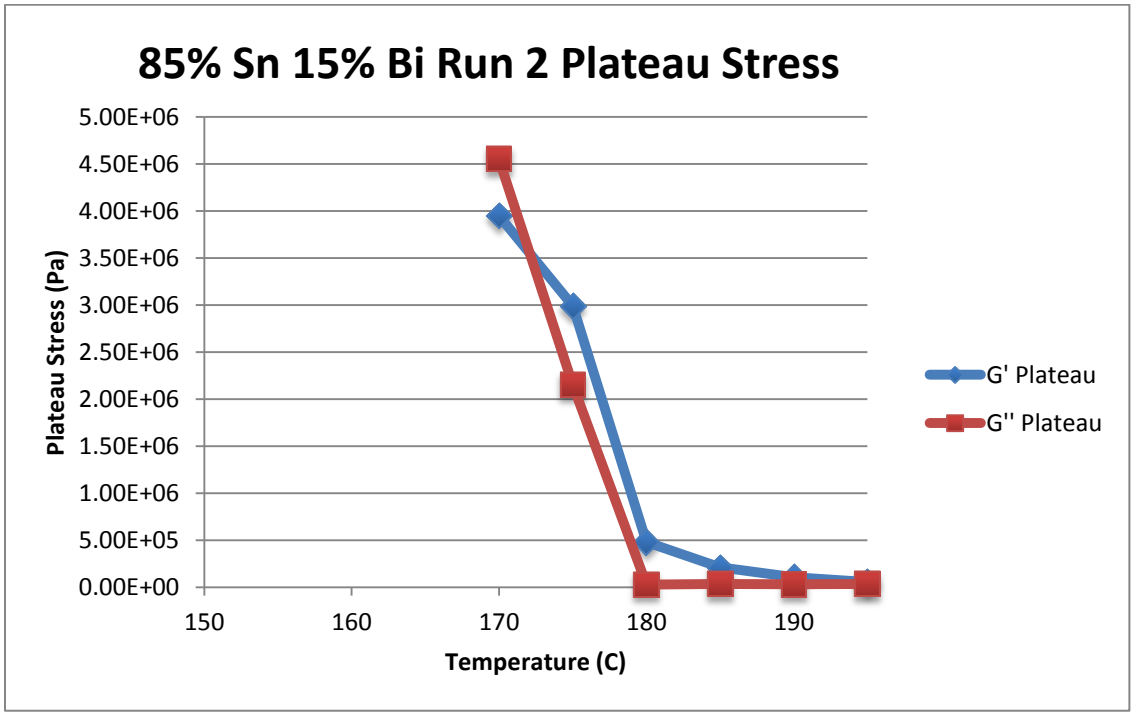

Figure 407- 85% Sn 15% Bi (Run 2), Cone and Plate Plateau Stresses vs. Temperature

85% Sn 15% Bi (Run 2) Viscosity					
Temperature	**Fraction Solid**	**Power Law**	**K**	**n**	**R^2**
170 C	60.9 %	$\tau = 1.11 * 10^{-4} * \dot{\gamma}^{0.1632}$ $\mu = 1.81 * 10^{-5} * \dot{\gamma}^{-0.8368}$	$1.11 * 10^{-4}$ Pa*s	0.1632	9.89 %
175 C	50.6 %	$\tau = 8.88 * 10^{-6} * \dot{\gamma}^{0.0073}$ $\mu = 6.48 * 10^{-8} * \dot{\gamma}^{-0.9927}$	$8.88 * 10^{-6}$ Pa*s	0.0073	0.05 %
180 C	43.2 %	$\tau = 2.01 * 10^{-4} * \dot{\gamma}^{0.2546}$ $\mu = 5.12 * 10^{-5} * \dot{\gamma}^{-0.7454}$	$2.01 * 10^{-4}$ Pa*s	0.2546	86.70 %
185 C	35.8 %	$\tau = 6.99 * 10^{-5} * \dot{\gamma}^{0.1772}$ $\mu = 1.24 * 10^{-5} * \dot{\gamma}^{-0.8228}$	$6.99 * 10^{-5}$ Pa*s	0.1772	24.61 %
190 C	28.6 %	$\tau = 1.22 * 10^{-5} * \dot{\gamma}^{0.1038}$ $\mu = 1.27 * 10^{-6} * \dot{\gamma}^{-0.8962}$	$1.22 * 10^{-5}$ Pa*s	0.1038	2.82 %
195 C	15.4 %	$\tau = 3.14 * 10^{-7} * \dot{\gamma}^{-0.204}$ Negative viscosity	$3.14 * 10^{-7}$ Pa*s	0.2040	14.77 %

Table 78- 85% Sn 15% Bi (Run 2), Cone and Plate Viscosity

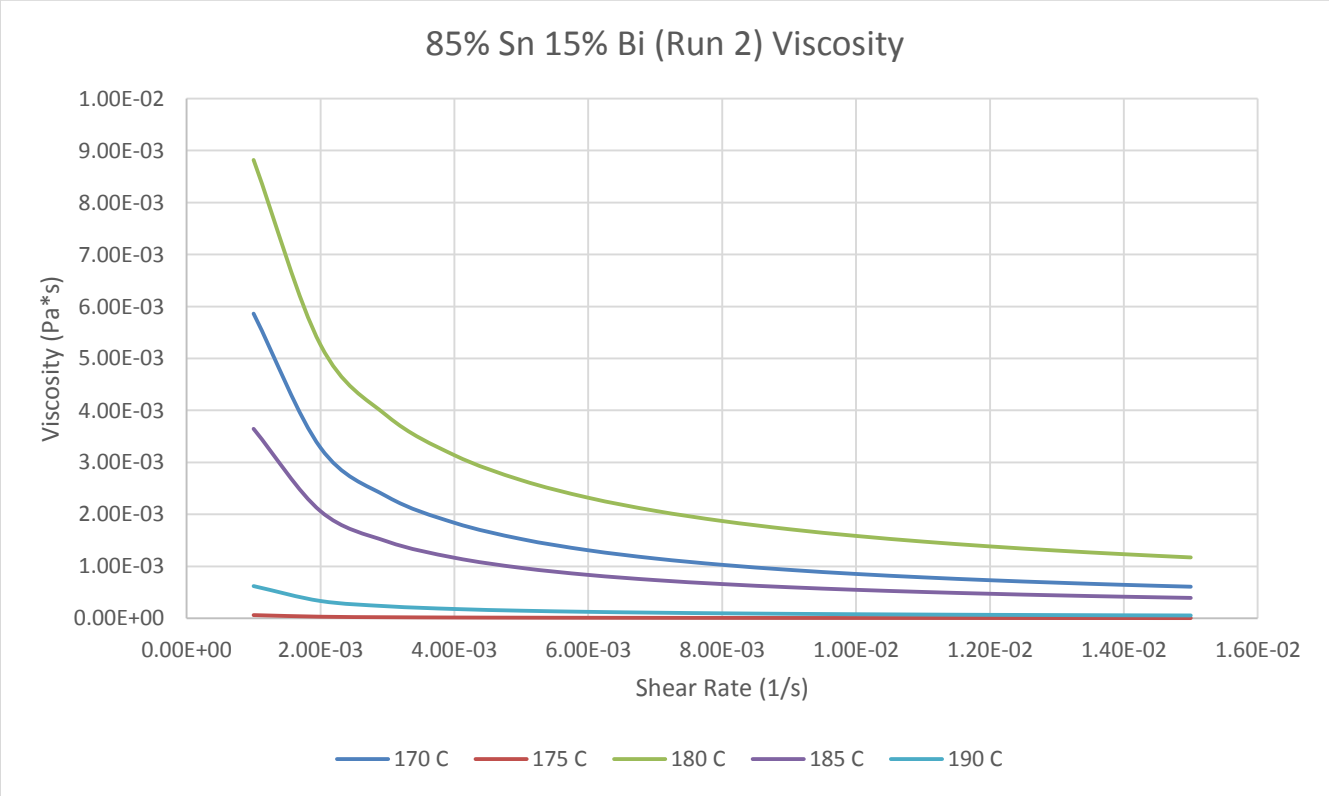

Figure 408- 85% Sn 15% Bi (Run 2), Cone and Plate Viscosity

170 C

Fraction Solid	60.9 %
Power Law	$\tau = 1.11 * 10^{-4} * \dot{\gamma}^{0.1632}$
	$\mu = 1.81 * 10^{-5} * \dot{\gamma}^{-0.8368}$
R^2	9.89 %

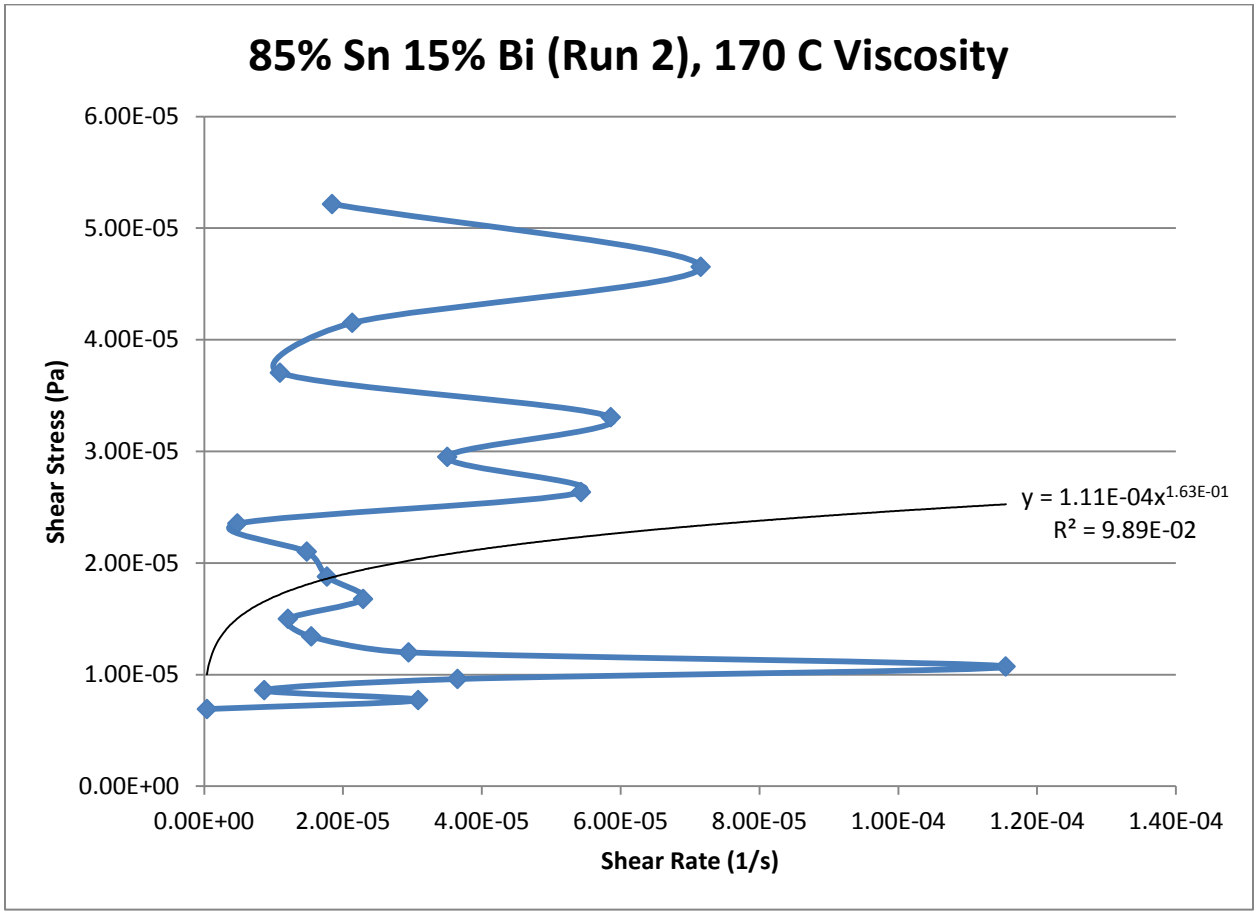

Figure 409- 85% Sn 15% Bi (Run 2), 170 C, Cone and Plate Viscosity

175 C

Fraction Solid	50.6 %
Power Law	$\tau = 8.88 * 10^{-6} * \dot{\gamma}^{0.0073}$
	$\mu = 6.48 * 10^{-8} * \dot{\gamma}^{-0.9927}$
R^2	0.05 %

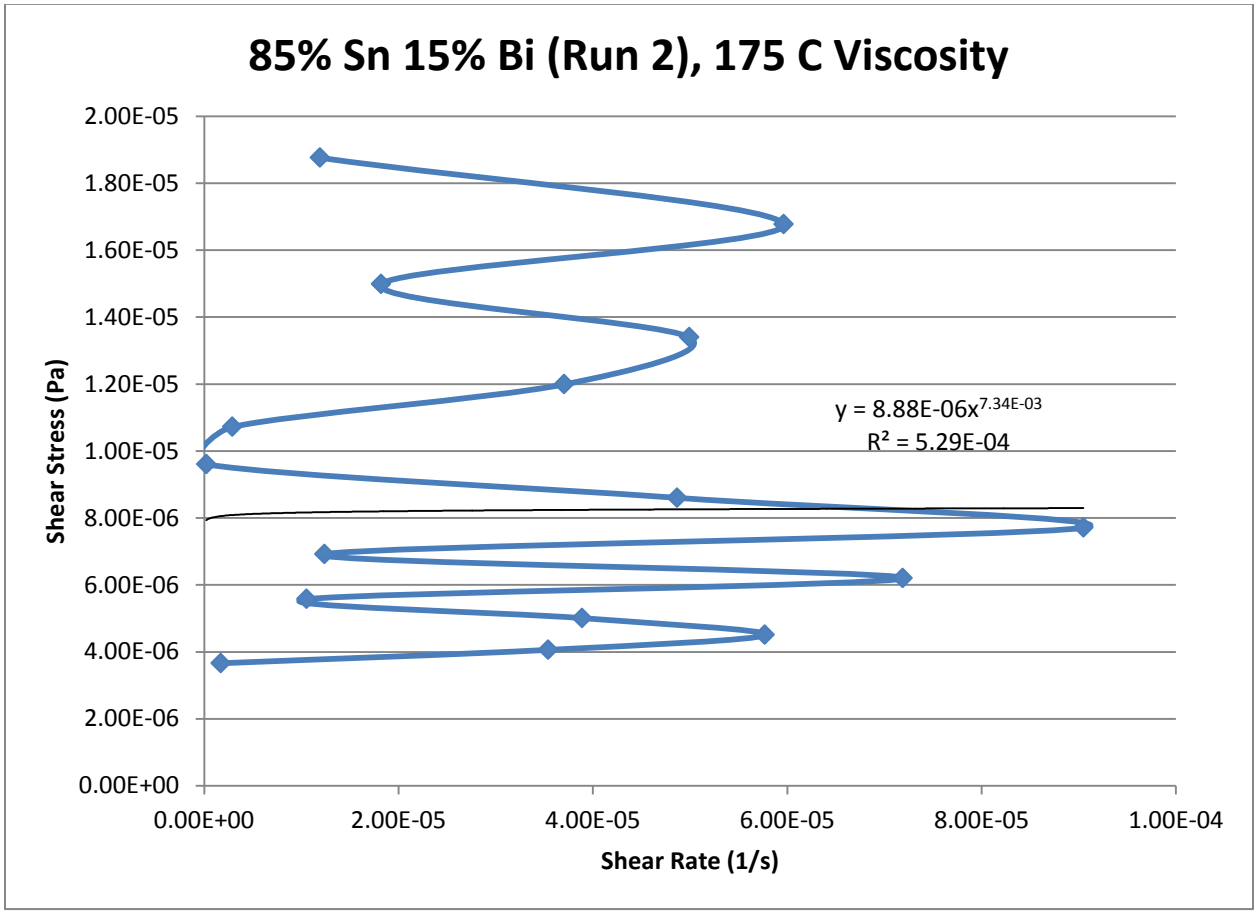

Figure 410- 85% Sn 15% Bi (Run 2), 175 C, Cone and Plate Viscosity

180 C

Fraction Solid	43.2 %
Power Law	$\tau = 2.01 * 10^{-4} * \dot{\gamma}^{0.2546}$
	$\mu = 5.12 * 10^{-5} * \dot{\gamma}^{-0.7454}$
R^2	86.70 %

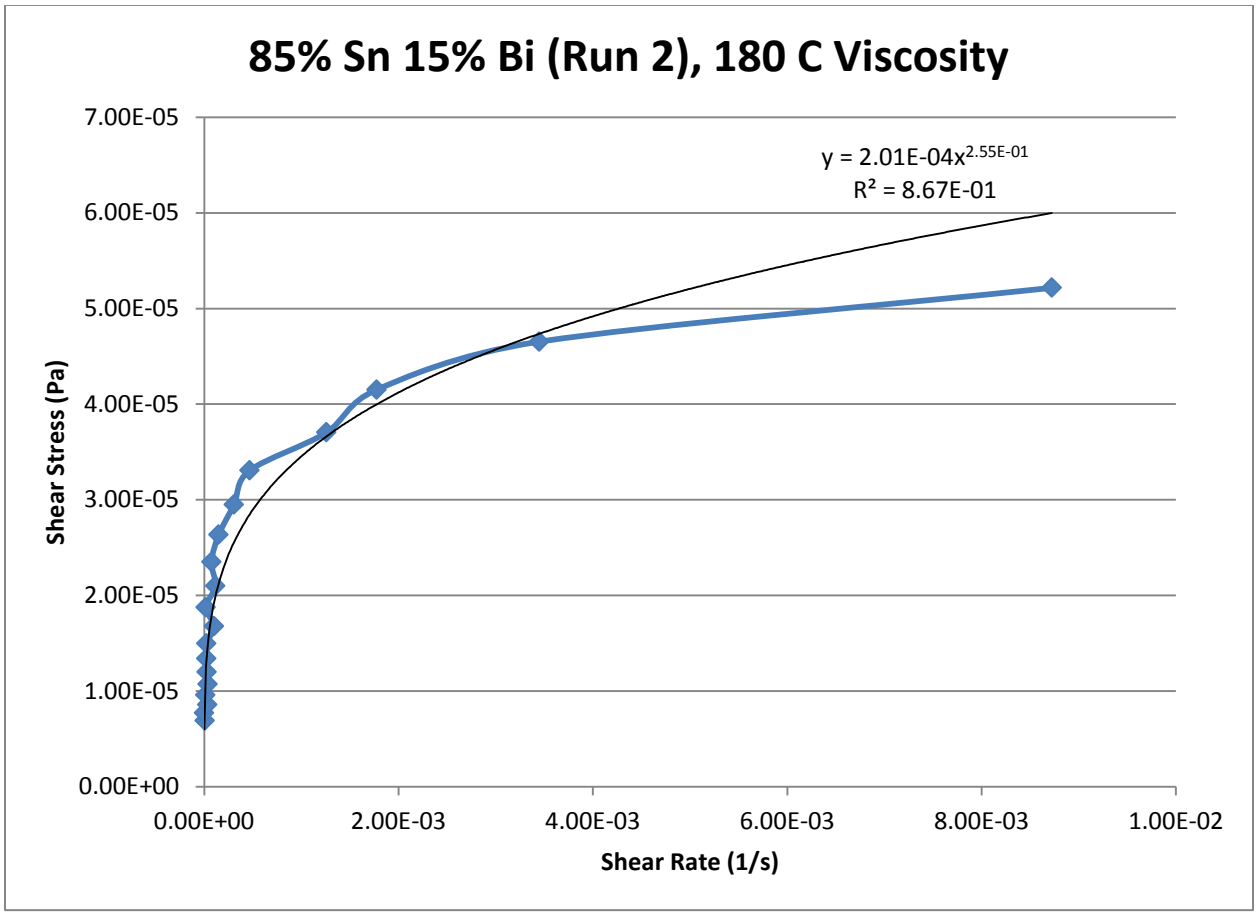

Figure 411- 85% Sn 15% Bi (Run 2), 180 C, Cone and Plate Viscosity

185 C

Fraction Solid	35.8 %
Power Law	$\tau = 6.99 * 10^{-5} * \dot{\gamma}^{0.1772}$
	$\mu = 1.24 * 10^{-5} * \dot{\gamma}^{-0.8228}$
R^2	24.61 %

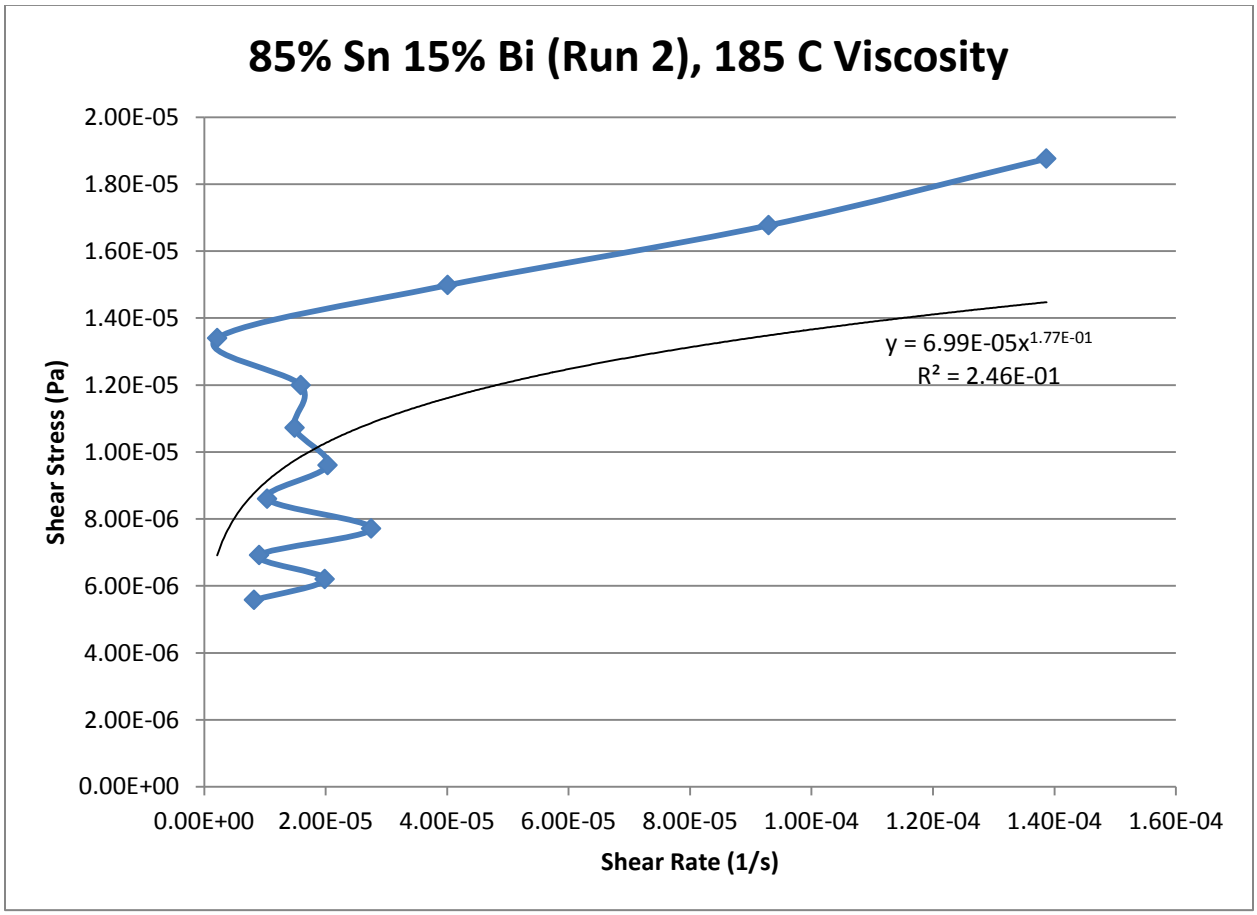

Figure 412- 85% Sn 15% Bi (Run 2), 185 C, Cone and Plate Viscosity

190 C

Fraction Solid	28.6 %
Power Law	$\tau = 1.22 * 10^{-5} * \dot{\gamma}^{0.1038}$
	$\mu = 1.27 * 10^{-6} * \dot{\gamma}^{-0.8962}$
R^2	2.82 %

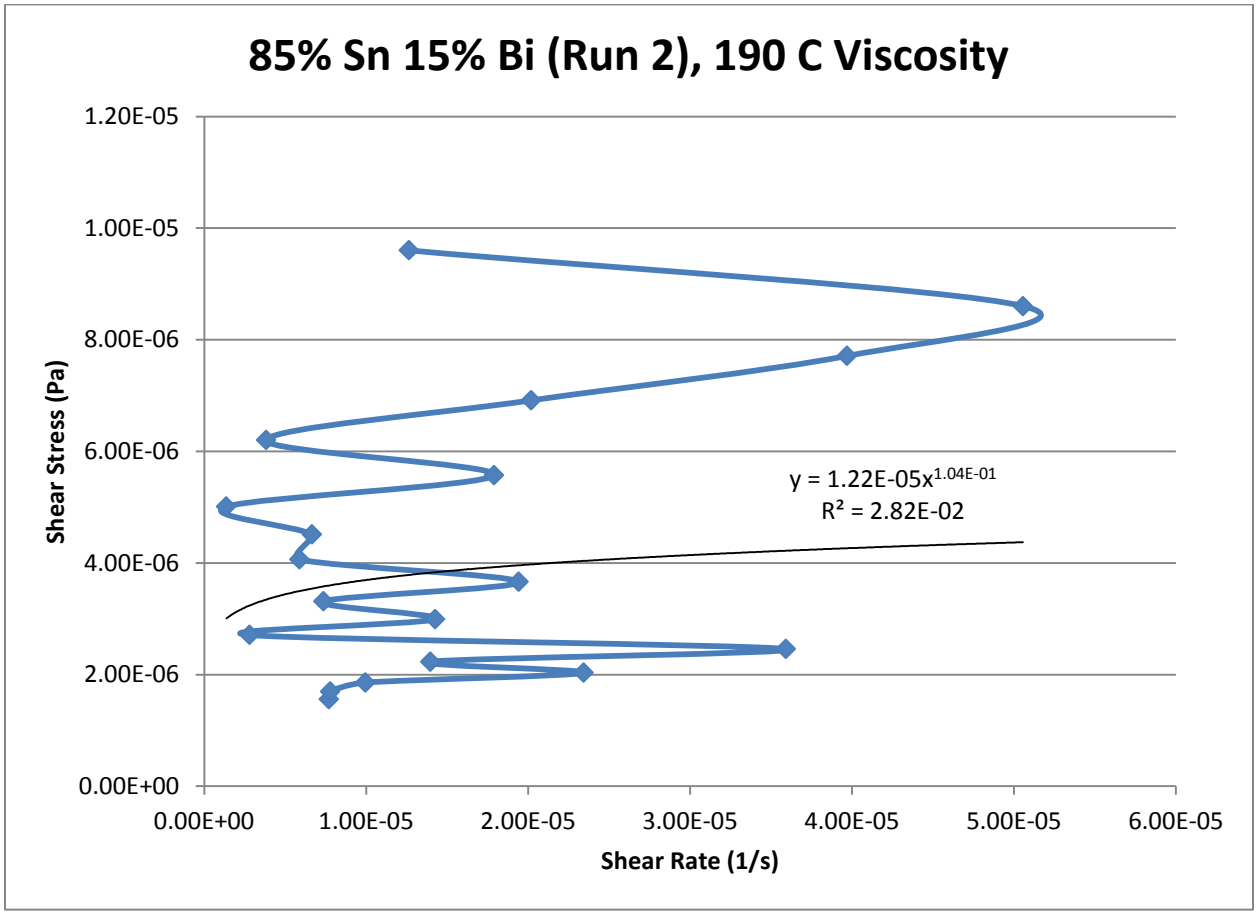

Figure 413- 85% Sn 15% Bi (Run 2), 190 C, Cone and Plate Viscosity

195 C

Fraction Solid	15.4 %
Power Law	$\tau = 3.14 * 10^{-7} * \dot{\gamma}^{-0.204}$
	$\mu = -6.41 * 10^{-8} * \dot{\gamma}^{-1.204}$
R^2	14.77 %

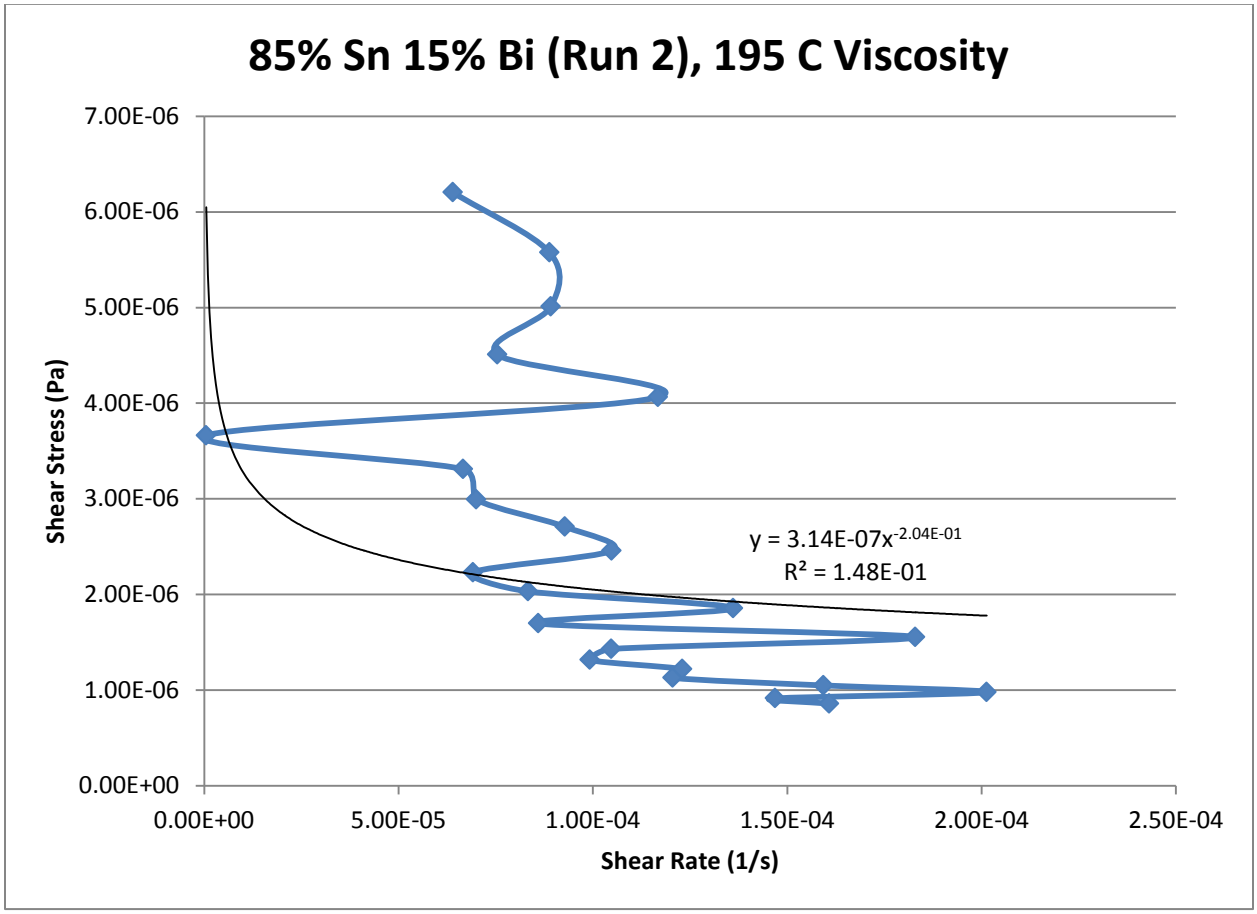

Figure 414- 85% Sn 15% Bi (Run 2), 195 C, Cone and Plate Viscosity

Appendix E- Oscillatory Shear Rheometer Data

10% Tin 90% Bismuth

Predicted Composition: 12% Sn 88% Bi

Theoretical Solidus Line: 139 C
Theoretical Liquidus Line: 243.6 C

Experimental Solidus Line: 138 C
Experimental Liquidus Line: 241.2 C

Pre-Shear: 15 RPM, 2 minutes
Angular Velocity: Constant, 10 rad/s
Strain Range: 0.01%-200%

10% Tin 90% Bismuth Oscillatory Shear Rheology								
Temperature (C)	**Fraction Solid (%)**	**Crossover Strain (%)**	**Crossover Stress (Pa)**	**Crossover Modulus (Pa)**	**Crossover Complex Viscosity (Pa*s)**	**Pre G' Plateau (Pa)**	**Pre G'' Plateau (Pa)**	**Final Complex Viscosity (Pa*s)**
250	0	2.78	0.091	2.78	0.33	15.0	2.96	0.021
249	2.62	1.29	0.159	8.70	1.22	37.8	12.4	0.026
248	5.43	2.11	0.285	9.59	1.36	62.8	21.3	0.053
247.5	8.25	5.33	0.592	7.91	1.13	133	21.5	0.095
247	11.1	5.72	0.640	7.45	1.07	134	10.0	0.113
246	13.9	4.59	0.823	12.7	1.80	250	18.0	0.143
245	16.7	10.2	7.70	53.5	7.78	558	65.0	0.397
240	28.6	31.0	257	583	82.1	1.54e5	2.78e4	42.6
235	39.3	167.5	1.39e3	577	81.9	1.20e5	1.33e4	52.1
230	45.9	> 200	> 1.73e3	< 606	< 86.1	1.38e5	1.71e4	86.1
225	51.2	138.7	1.83e3	936	133	1.82e5	1.96e4	102

Table 79- 10% Tin 90% Bismuth Oscillatory Shear Rheology

10% Tin 90% Bismuth Oscillatory Shear Complex Viscosity			
Temperature (C)	**Fraction Solid (%)**	**Power Law Equation**	**R^2 (%)**
250	0	$\eta^* = 0.6021\gamma^{-0.682}$	98.66
249	2.62	$\eta^* = 1.6836\gamma^{-0.822}$	98.48
248	5.43	$\eta^* = 2.4165\gamma^{-0.694}$	99.35
247.5	8.25	$\eta^* = 4.1402\gamma^{-0.793}$	98.48
247	11.1	$\eta^* = 4.247\gamma^{-0.694}$	99.57
246	13.9	$\eta^* = 5.6876\gamma^{-0.662}$	98.54
245	16.7	$\eta^* = 42.864\gamma^{-0.840}$	97.75
240	28.6	$\eta^* = 4485.6\gamma^{-1.018}$	94.30
235	39.3	$\eta^* = 2167.3\gamma^{-0.783}$	90.35
230	45.9	$\eta^* = 2188\gamma^{-0.736}$	88.97
225	51.2	$\eta^* = 2456.4\gamma^{-0.705}$	88.26

Table 80- 10% Tin 90% Bismuth Oscillatory Shear Complex Viscosity

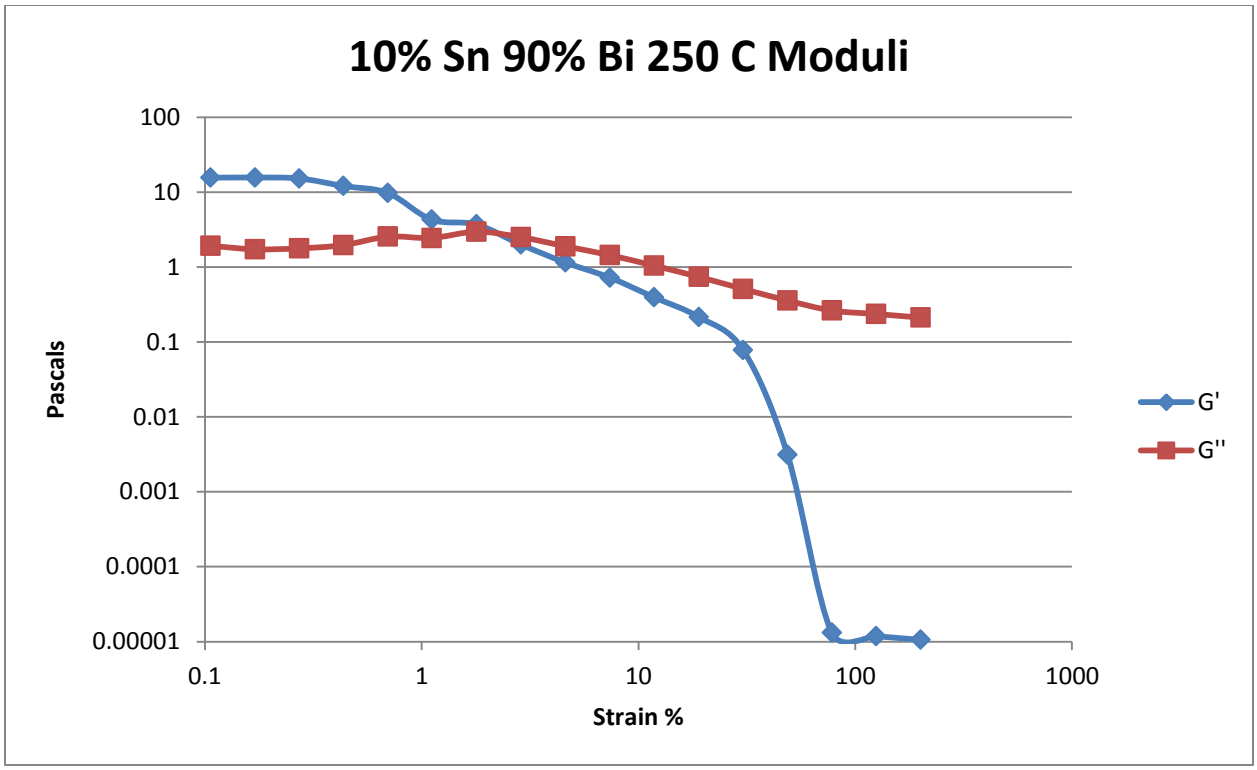

Figure 415- 10% Tin 90% Bismuth, 250 C, Oscillatory Shear Moduli

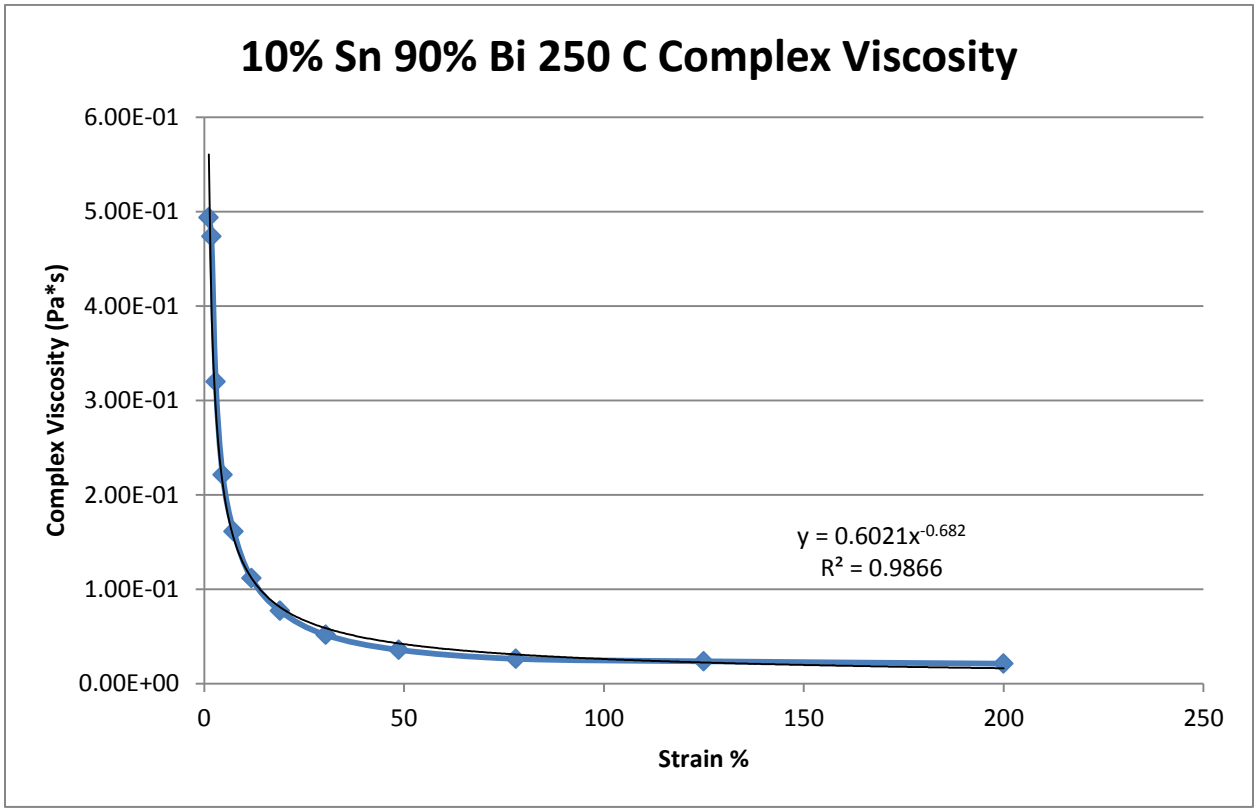

Figure 416- 10% Tin 90% Bismuth, 250 C, Oscillatory Shear Complex Viscosity

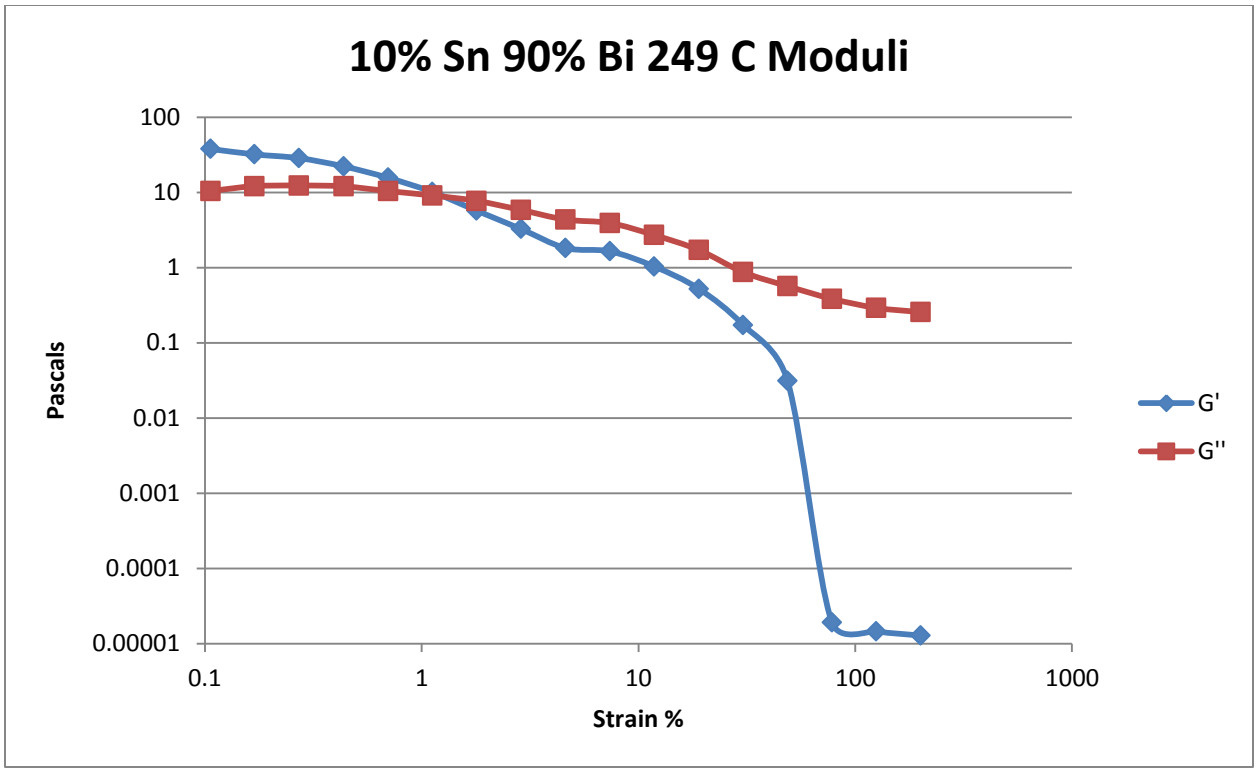

Figure 417- 10% Tin 90% Bismuth, 249 C, Oscillatory Shear Moduli

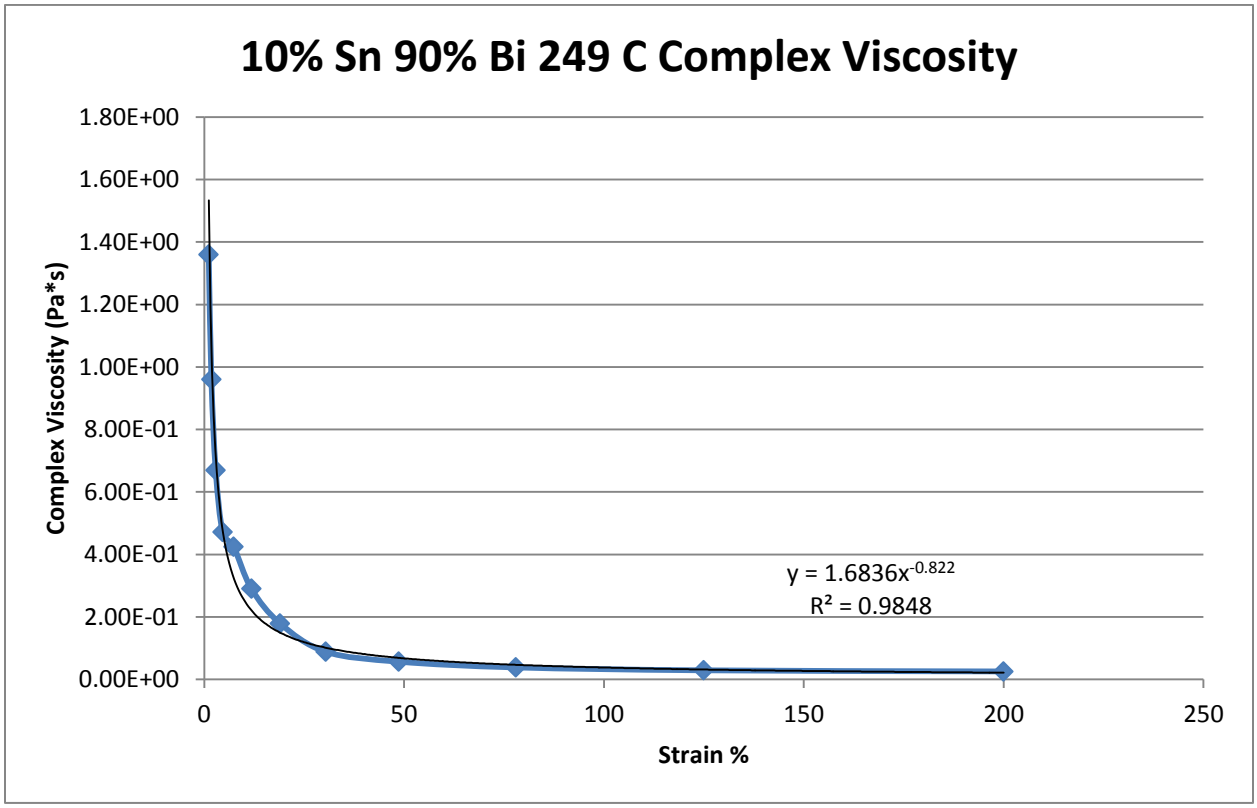

Figure 418- 10% Tin 90% Bismuth, 249 C, Complex Viscosity

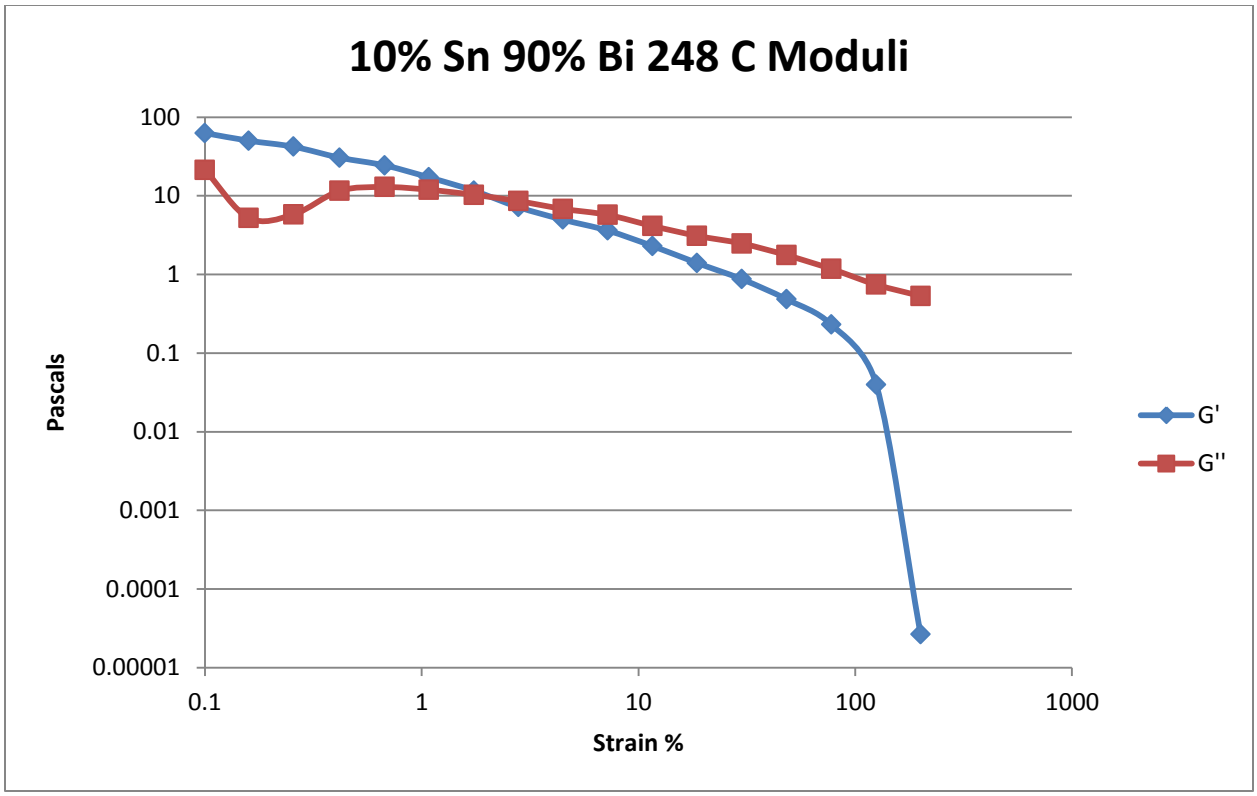

Figure 419- 10% Tin 90% Bismuth, 248 C, Oscillatory Shear Moduli

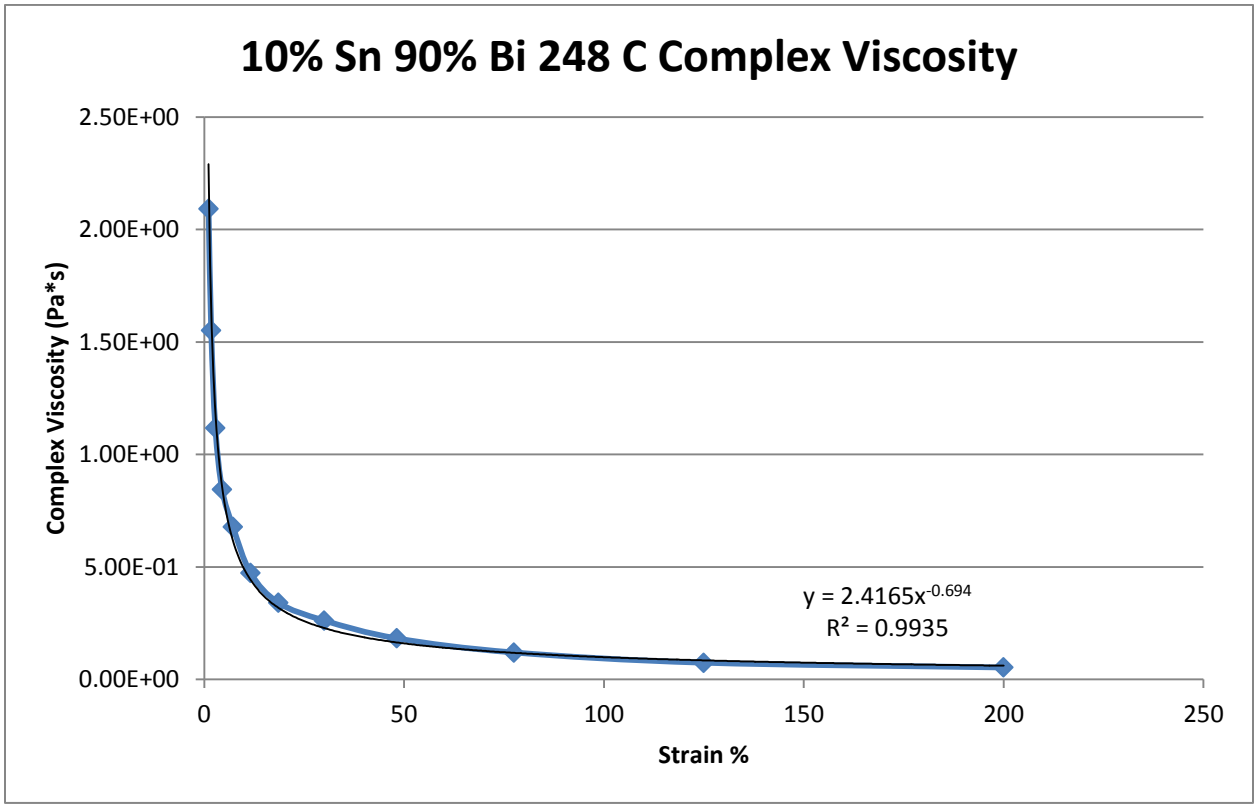

Figure 420- 10% Tin 90% Bismuth, 248 C, Oscillatory Shear Complex Viscosity

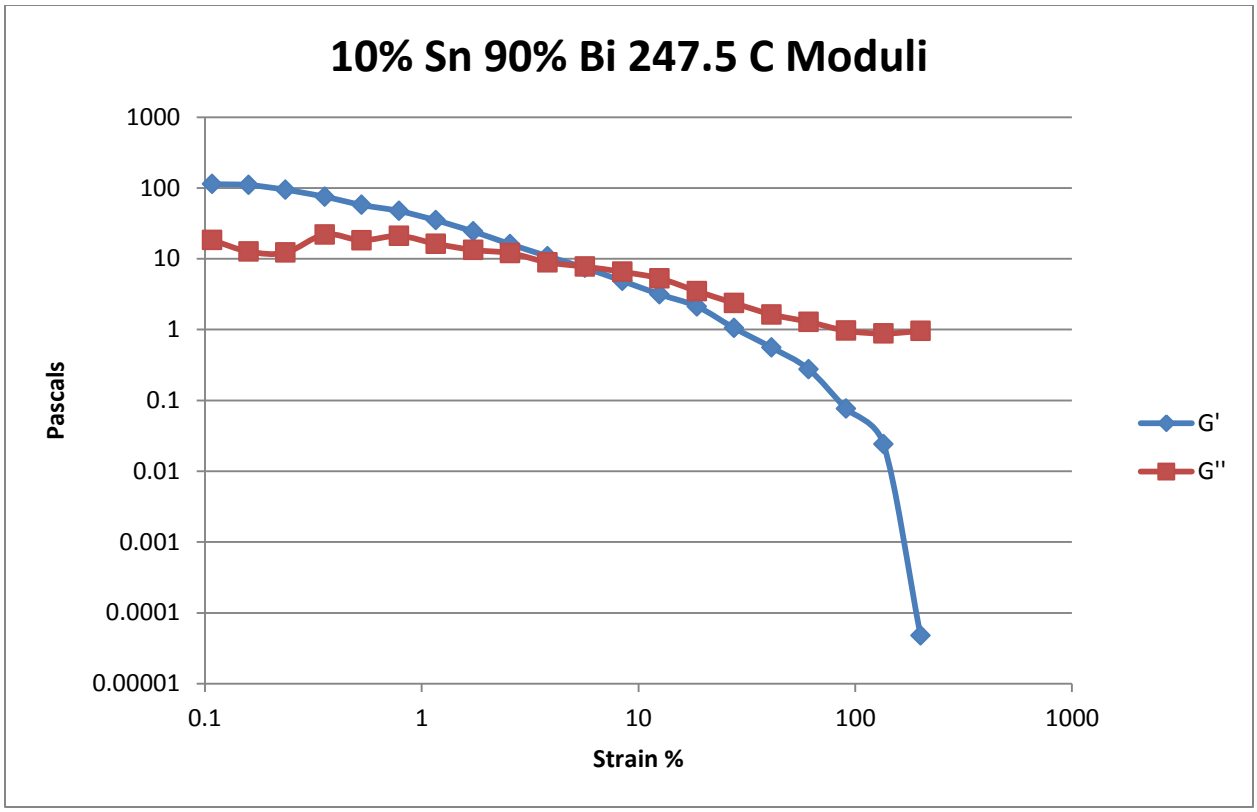

Figure 421- 10% Tin 90% Bismuth, 247.5 C, Oscillatory Shear Moduli

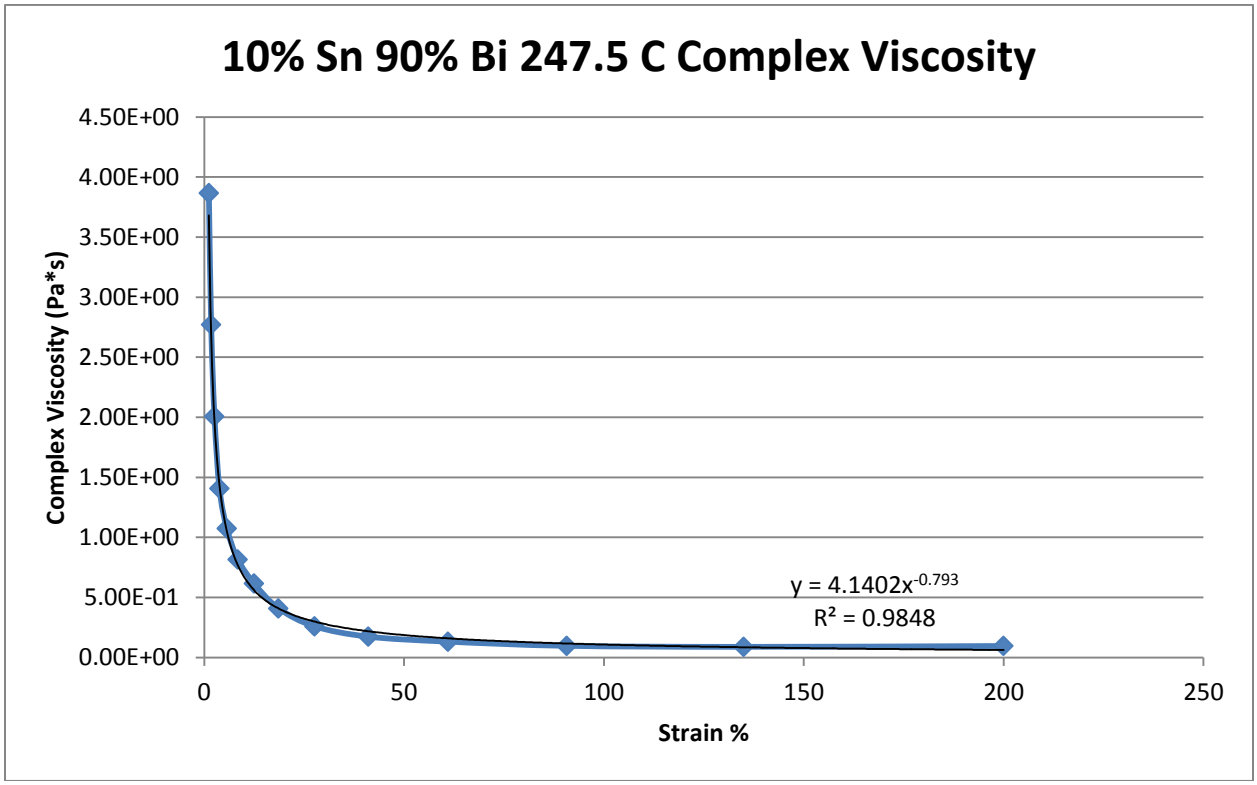

Figure 422- 10% Tin 90% Bismuth, 247.5 C, Oscillatory Shear Complex Viscosity

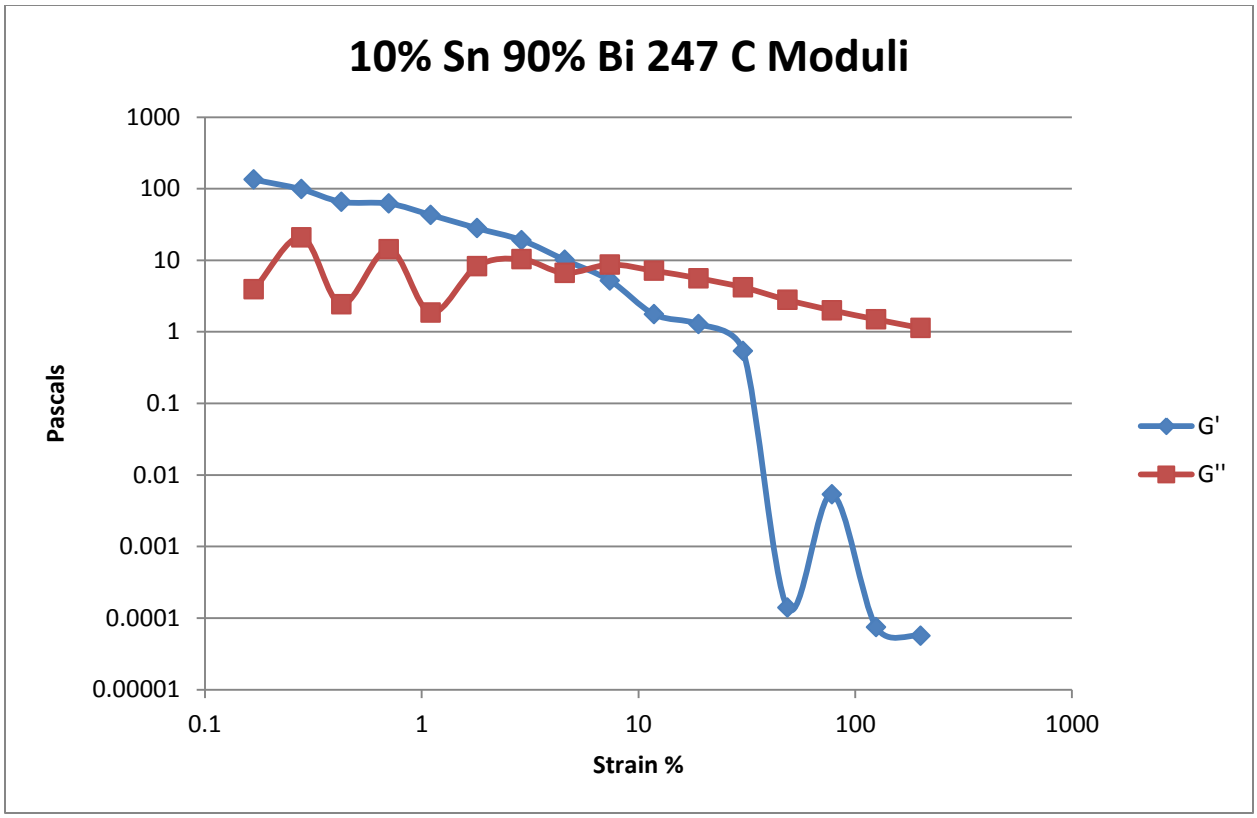

Figure 423- 10% Tin 90% Bismuth, 247 C, Oscillatory Shear Moduli

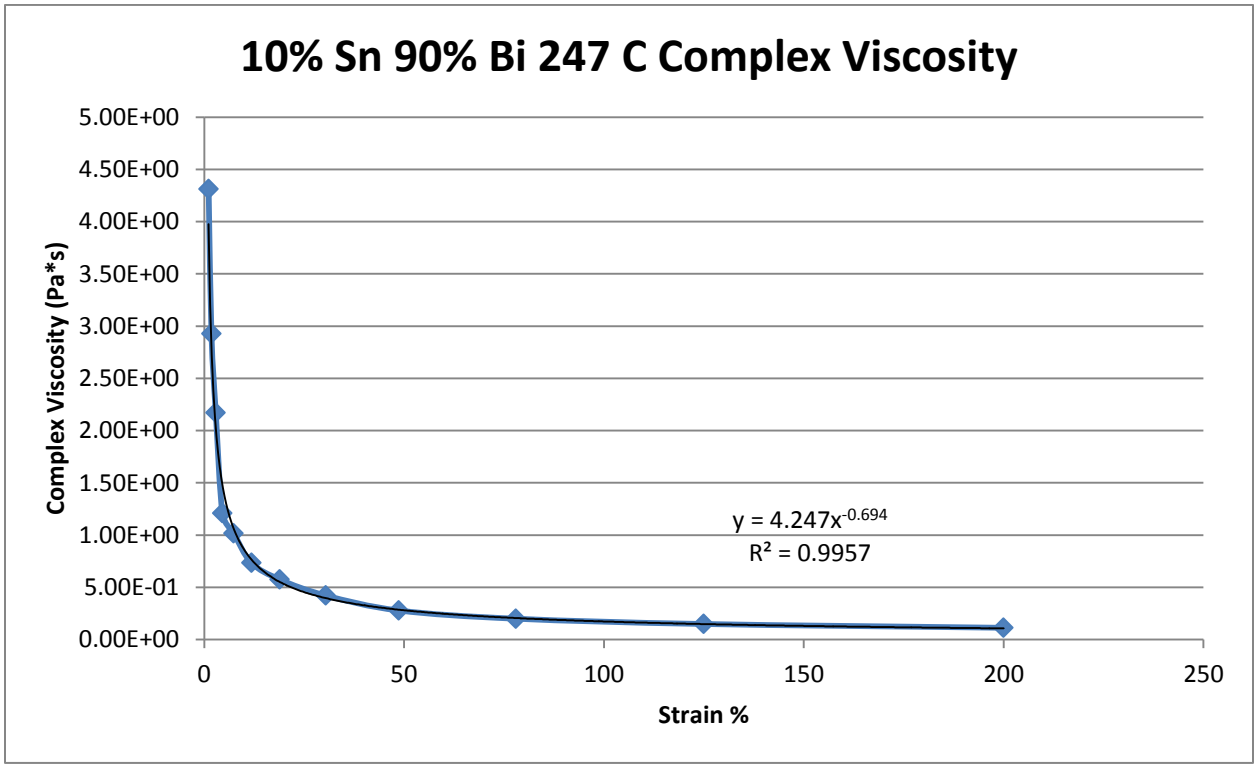

Figure 424- 10% Tin 90% Bismuth, 247 C, Oscillatory Shear Complex Viscosity

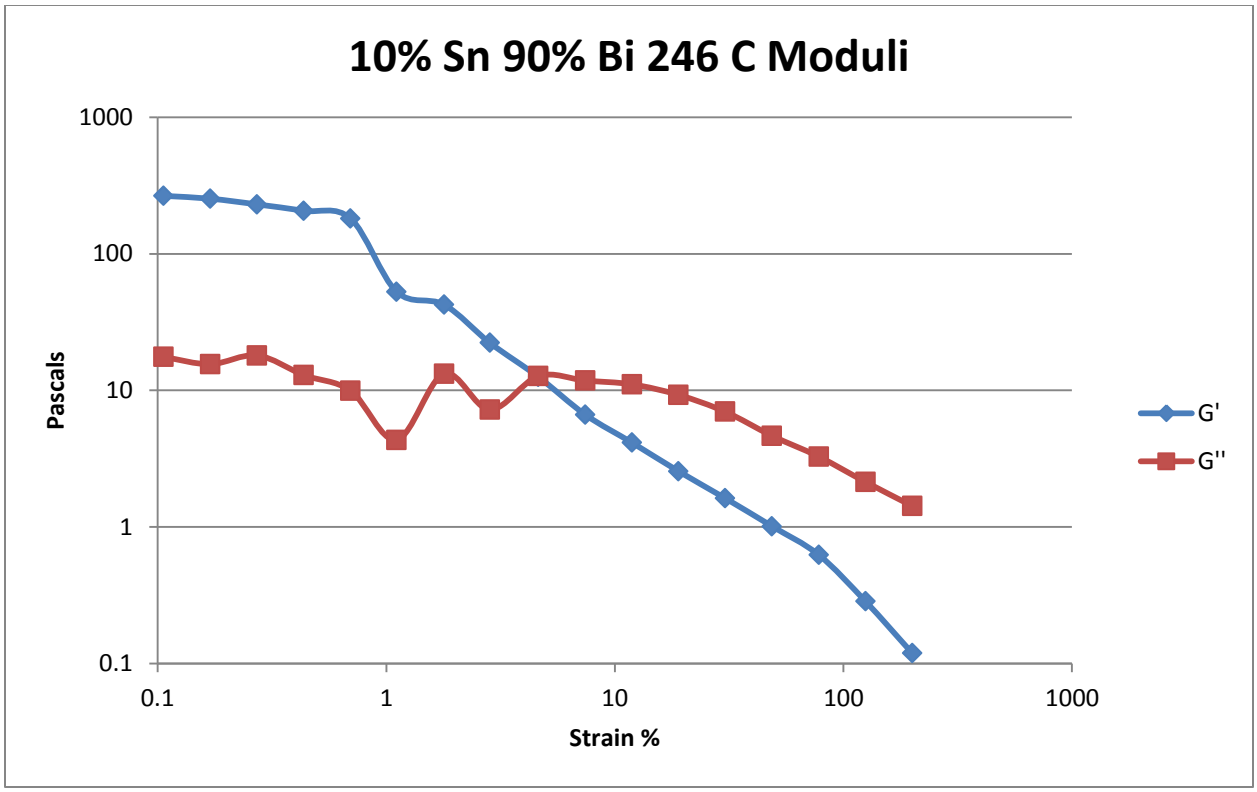

Figure 425- 10% Tin 90% Bismuth, 246 C, Oscillatory Shear Moduli

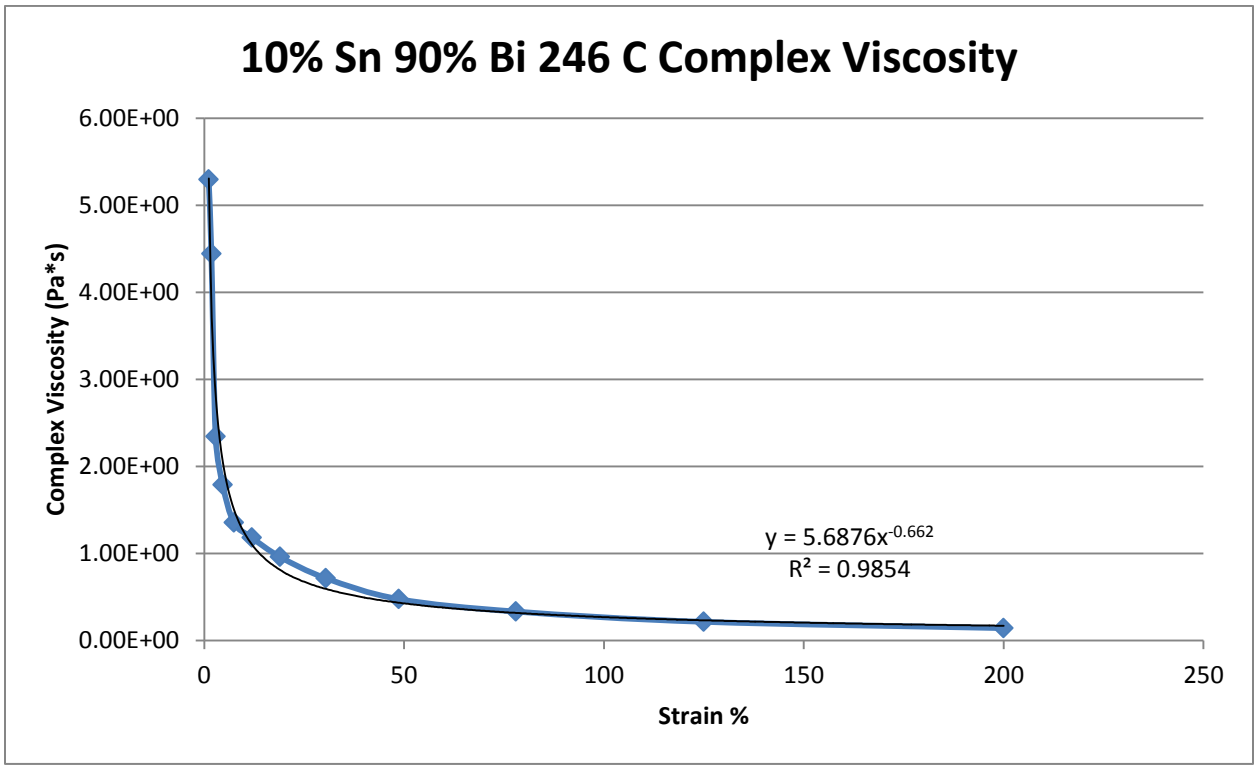

Figure 426- 10% Tin 90% Bismuth, 246 C, Oscillatory Shear Complex Viscosity

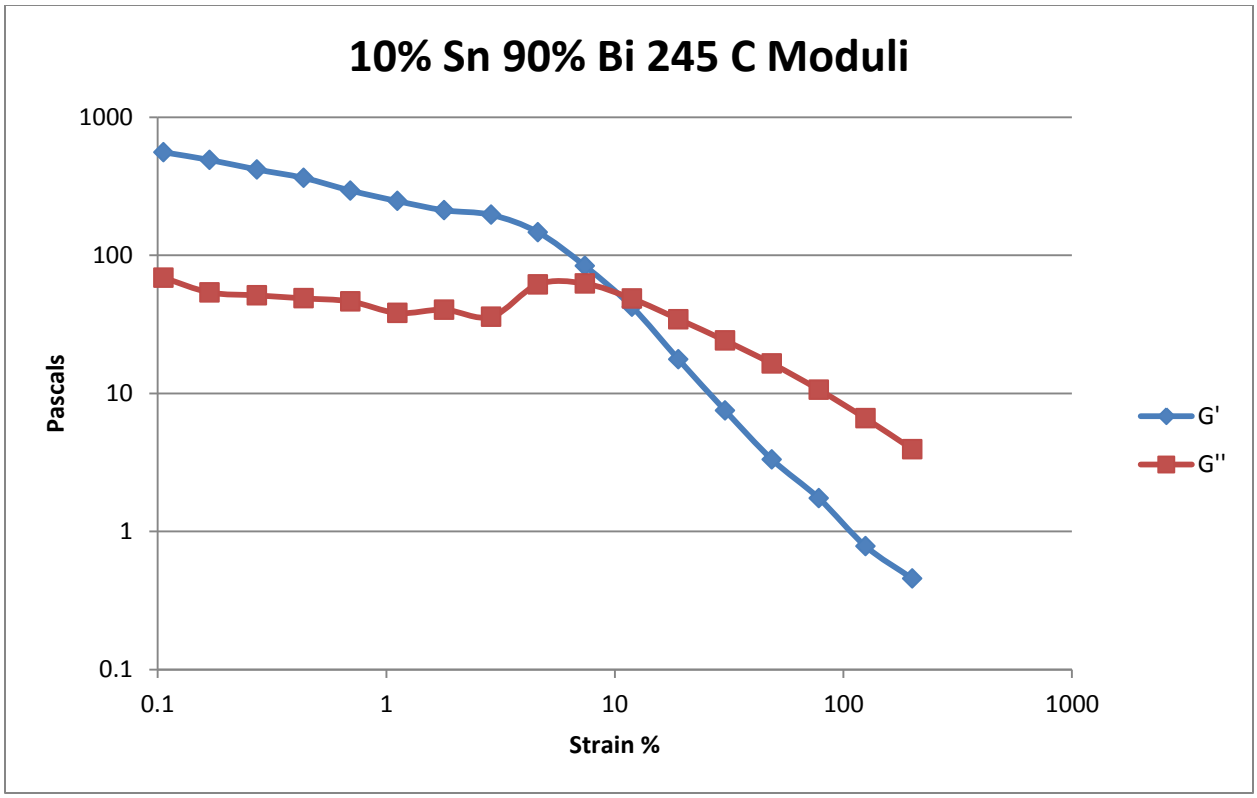

Figure 427- 10% Tin 90% Bismuth, 245 C, Oscillatory Shear Moduli

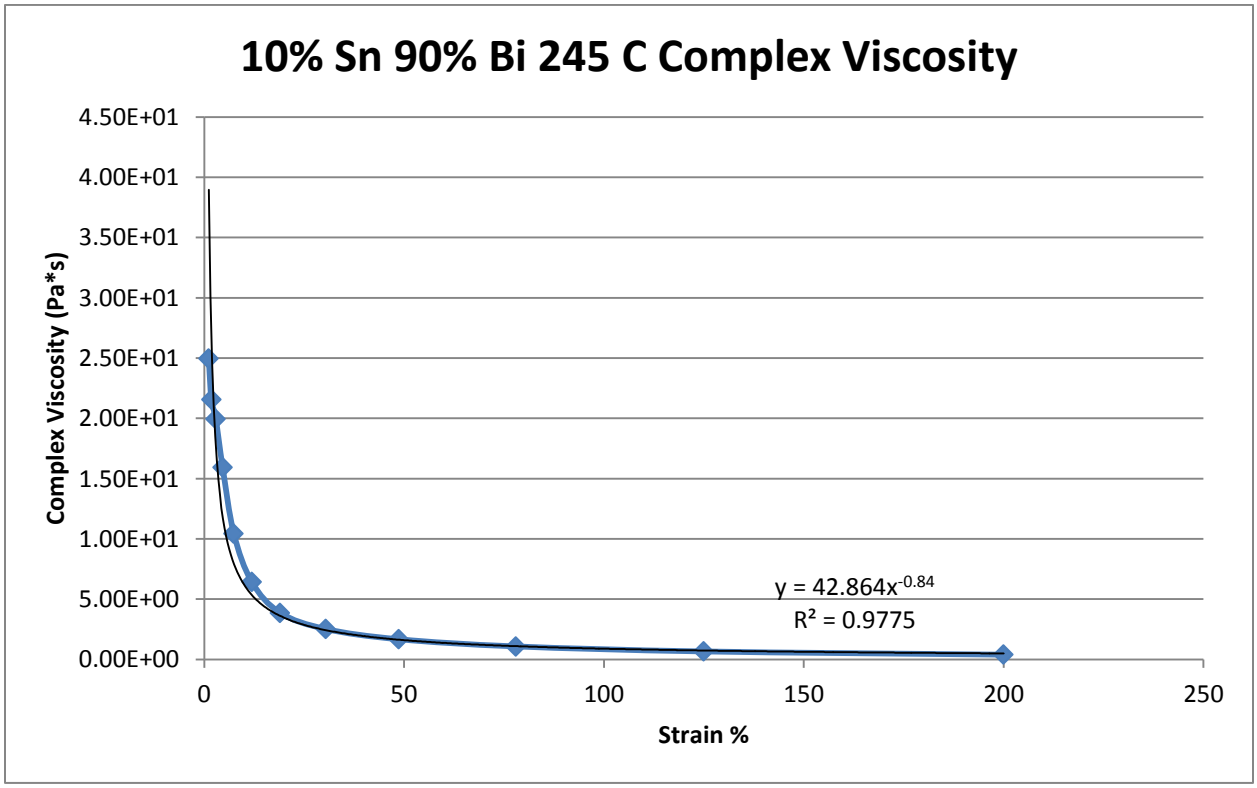

Figure 428- 10% Tin 90% Bismuth, 245 C, Oscillatory Shear Complex Viscosity

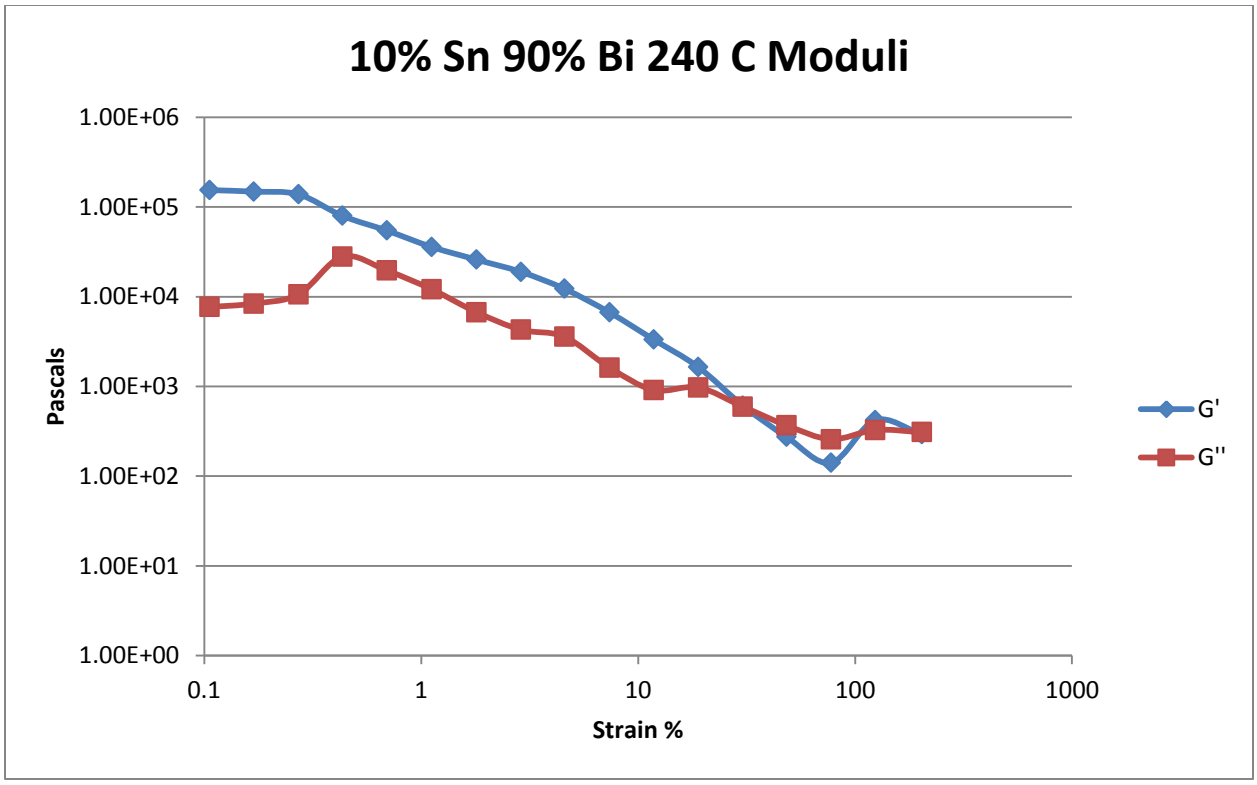

Figure 429- 10% Tin 90% Bismuth, 240 C, Oscillatory Shear Moduli

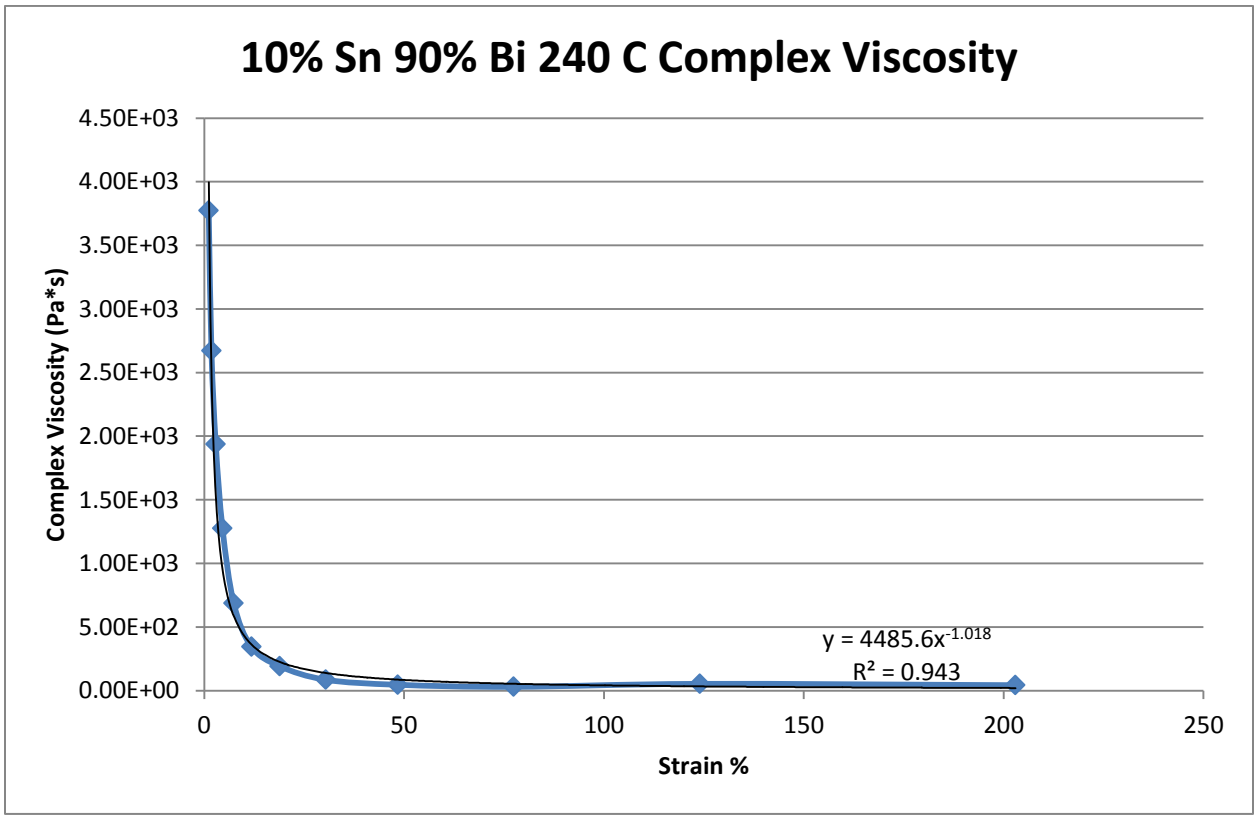

Figure 430- 10% Tin 90% Bismuth, 240 C, Oscillatory Shear Complex Viscosity

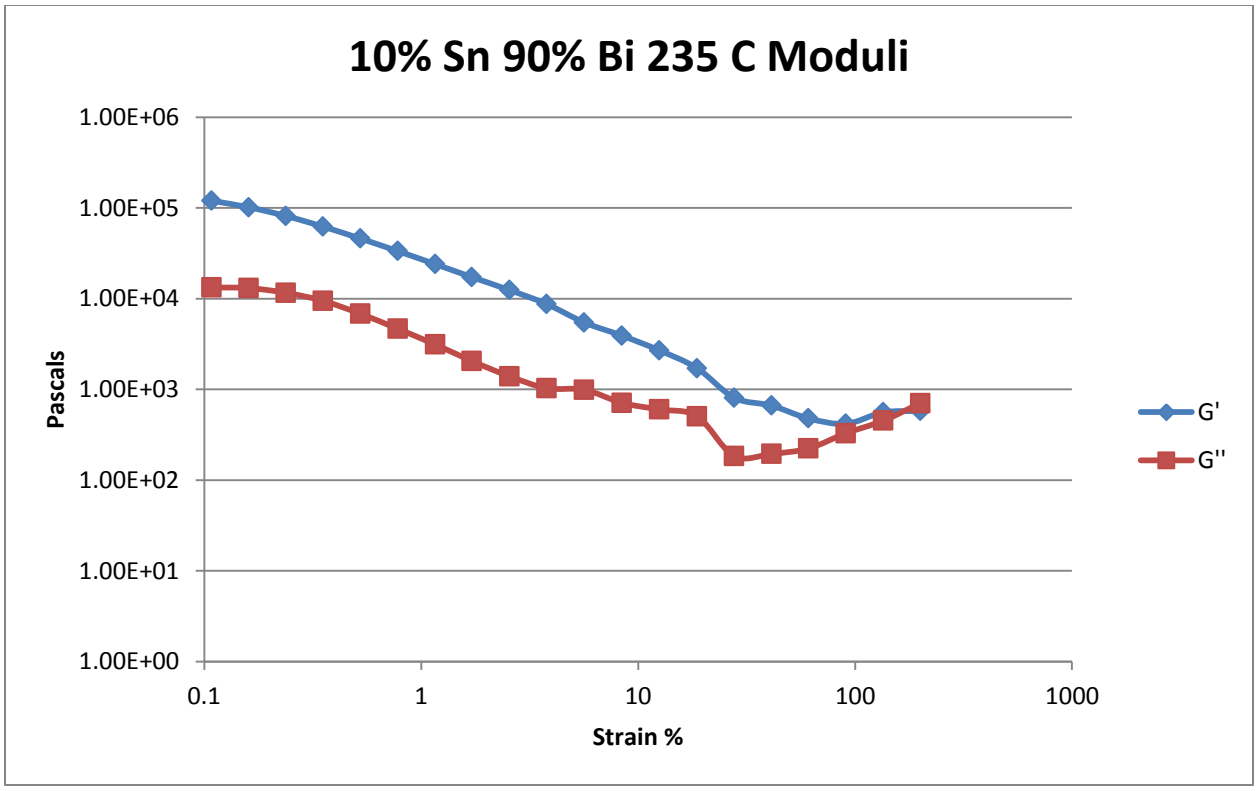

Figure 431- 10% Tin 90% Bismuth, 235 C, Oscillatory Shear Moduli

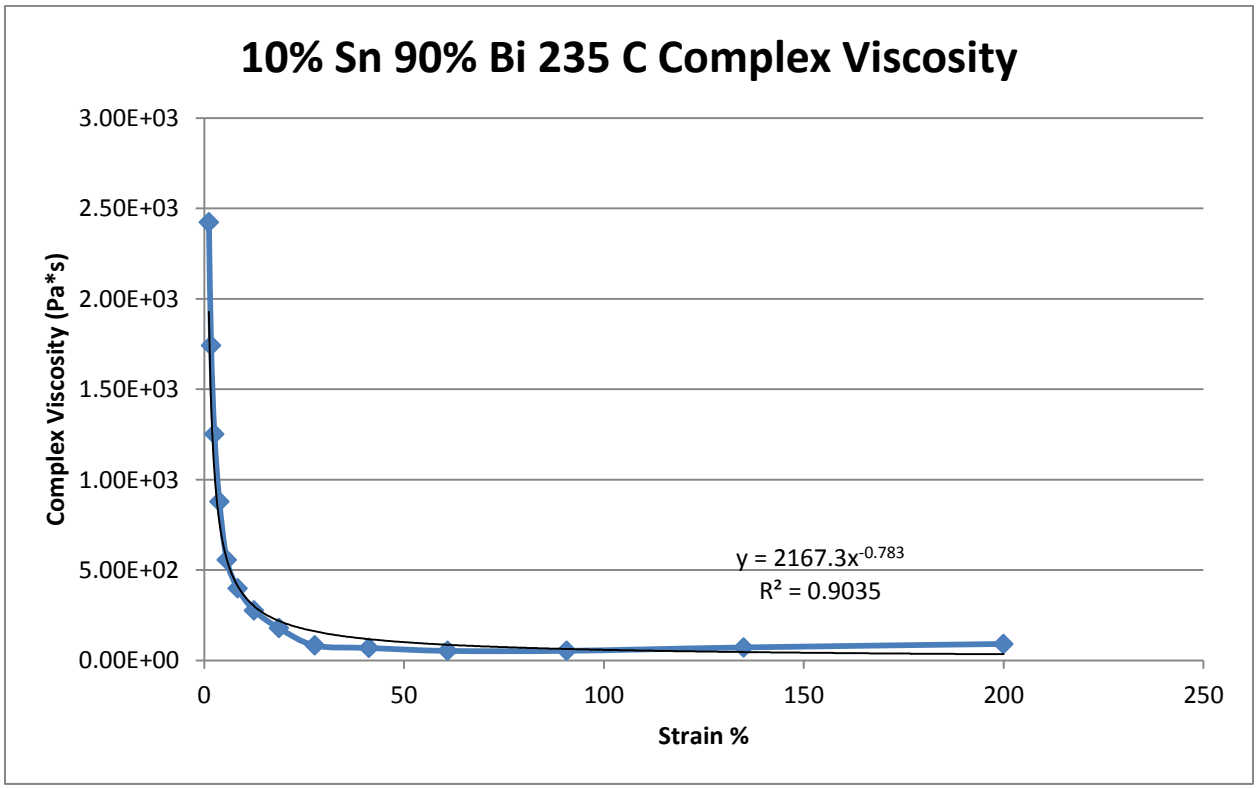

Figure 432- 10% Tin 90% Bismuth, 235 C, Oscillatory Shear Complex Viscosity

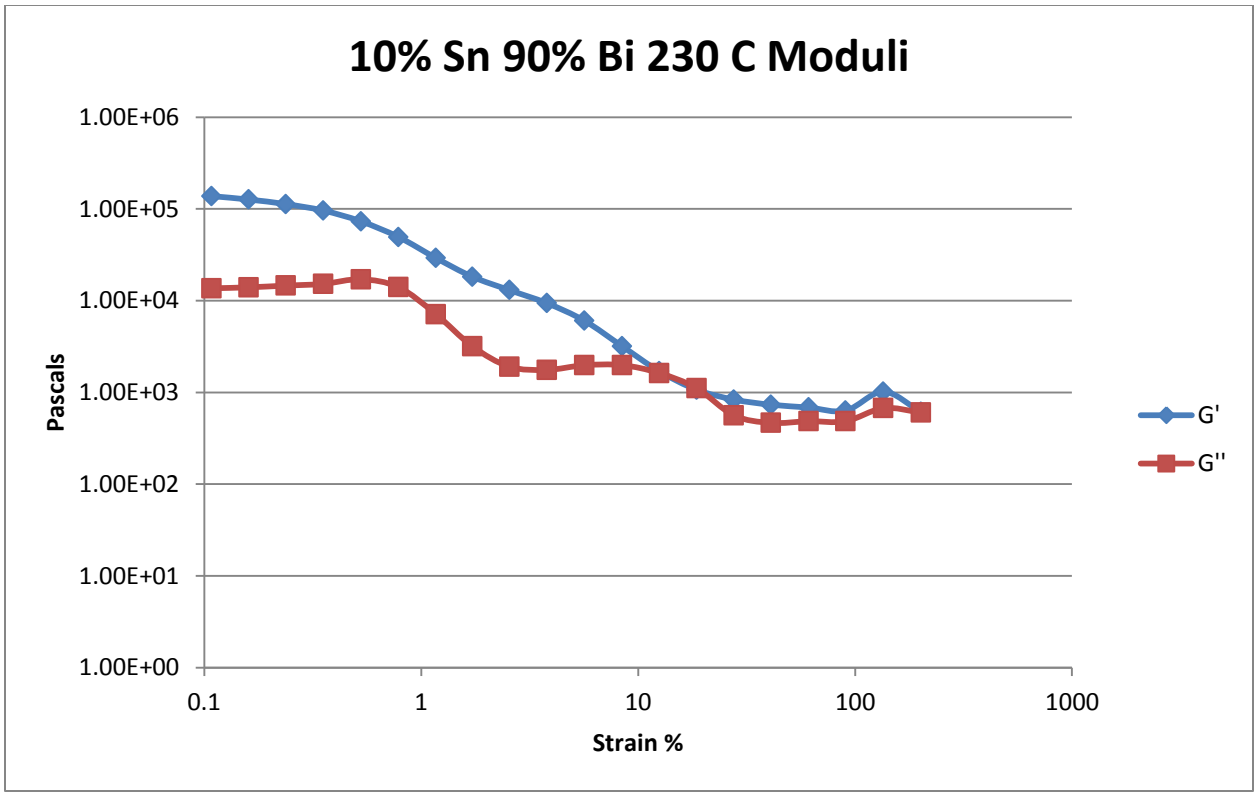

Figure 433- 10% Tin 90% Bismuth, 230 C, Oscillatory Shear Moduli

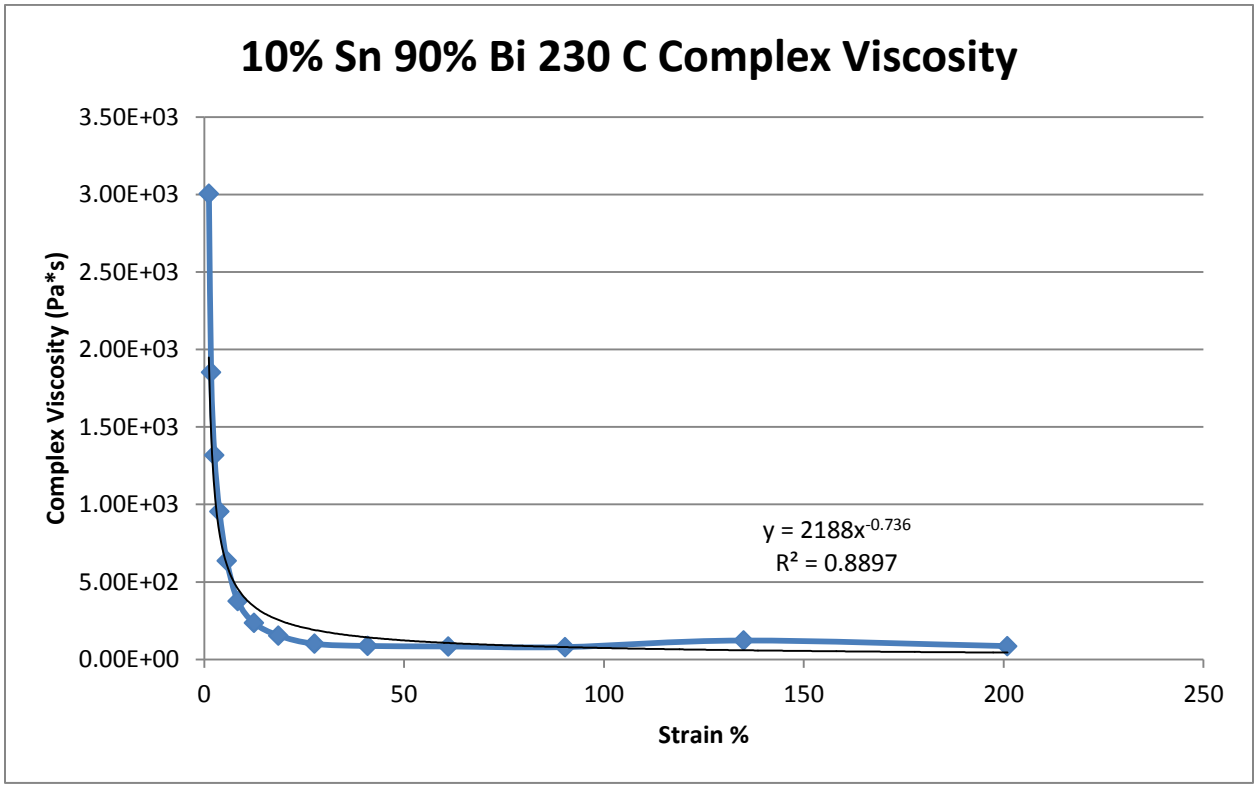

Figure 434- 10% Tin 90% Bismuth, 230 C, Oscillatory Shear Complex Viscosity

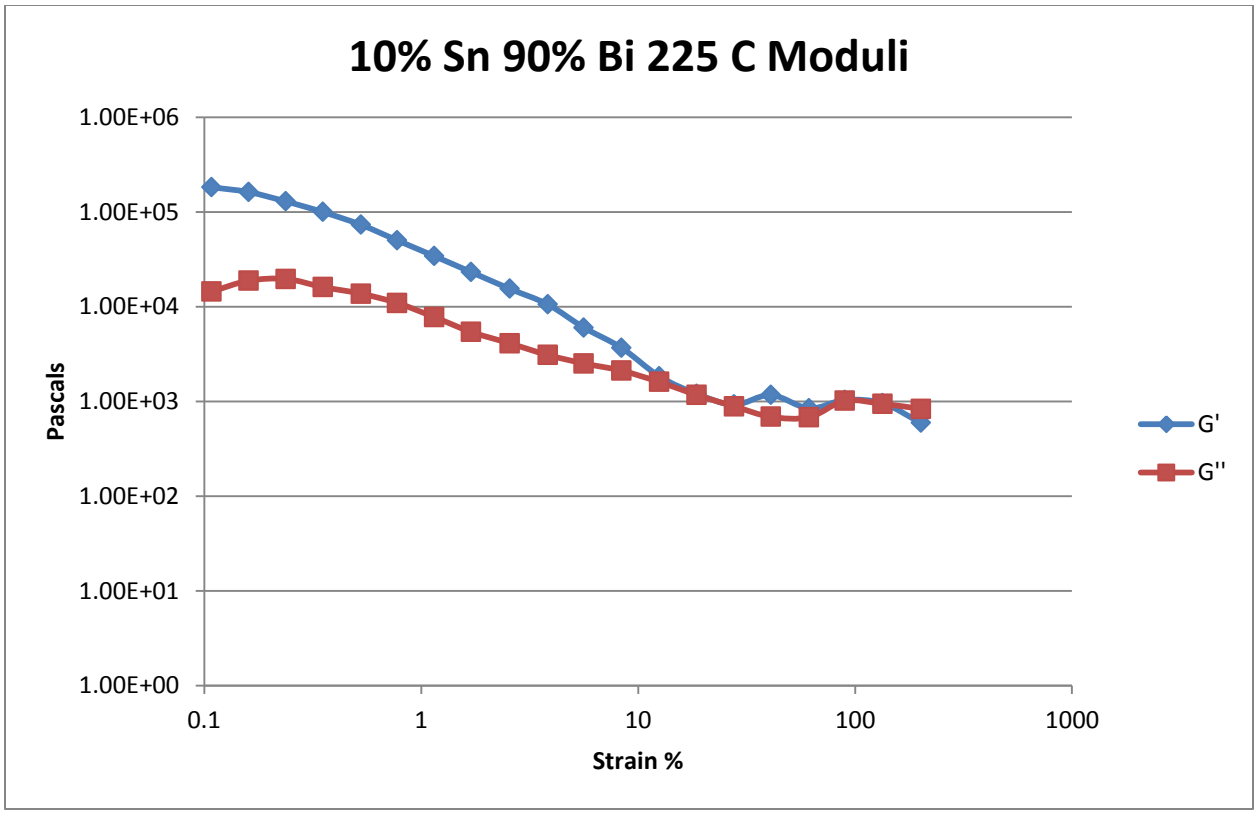

Figure 435- 10% Tin 90% Bismuth, 225 C, Oscillatory Shear Moduli

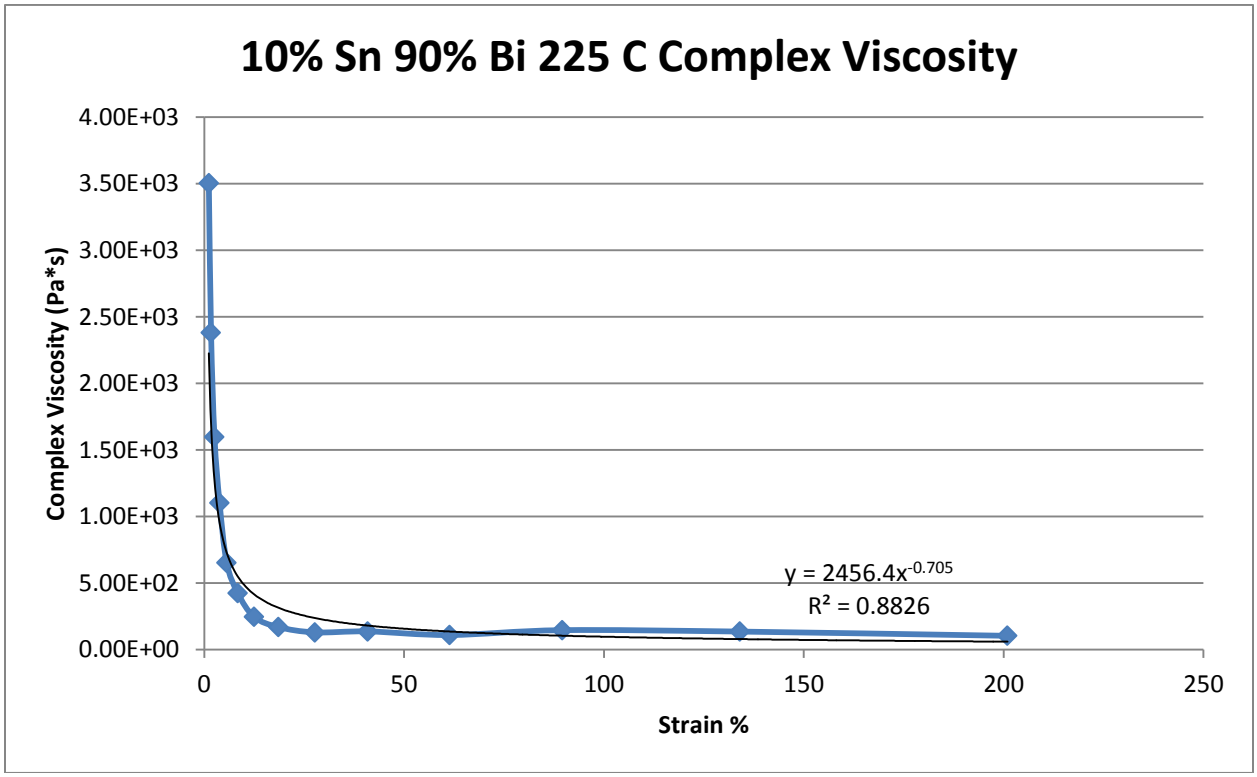

Figure 436- 10% Tin 90% Bismuth, 225 C, Oscillatory Shear Complex Viscosity

15% Tin 85% Bismuth

Predicted Composition: 17% Sn 83% Bi

Theoretical Solidus Line: 139 C
Theoretical Liquidus Line: 231.9 C

Experimental Solidus Line: 139.5 C
Experimental Liquidus Line: 234 C

Pre-Shear: 15 RPM, 2 minutes
Angular Velocity: Constant, 10 rad/s
Strain Range: 0.01%-200%

15% Tin 85% Bismuth Oscillatory Shear Rheology								
Temperature (C)	**Fraction Solid (%)**	**Crossover Strain (%)**	**Crossover Stress (Pa)**	**Crossover Modulus (Pa)**	**Crossover Complex Viscosity (Pa*s)**	**Pre G' Plateau (Pa)**	**Pre G'' Plateau (Pa)**	**Final Complex Viscosity (Pa*s)**
239	0	3.56	0.016	0.310	0.044	0.700	0.377	0.016
238	0	14.5	0.202	0.999	0.136	47.2	8.05	0.024
237	2.50	2.52	0.310	7.50	1.18	40.0	10.3	0.112
236	5.50	9.95	0.173	1.22	0.178	35.2	4.77	0.024
235	6.25	93.5	0.830	0.600	0.087	277	48.0	0.200
230	16.7	186	103	41.4	5.92	1.50e4	1.33e3	4.70
225	25.7	193	439	169	24.0	8.04e4	7.53e3	20.9

Table 81- 15% Tin 85% Bismuth Oscillatory Shear Rheology

15% Tin 85% Bismuth Oscillatory Shear Complex Viscosity			
Temperature (C)	**Fraction Solid (%)**	**Power Law Equation**	**R^2 (%)**
239	0	$\eta^* = 0.6037\gamma^{-0.317}$	82.83
238	0	$\eta^* = 1.5551\gamma^{-0.871}$	98.44
237	2.50	$\eta^* = 14.657\gamma^{-0.877}$	96.64
236	5.50	$\eta^* = 1.2812\gamma^{-0.826}$	98.36
235	6.25	$\eta^* = 338.22\gamma^{-1.463}$	79.75
230	16.7	$\eta^* = 574.73\gamma^{-0.969}$	91.53
225	25.7	$\eta^* = 3679.9\gamma^{-1.041}$	94.59

Table 82- 15% Tin 85% Bismuth Oscillatory Shear Complex Viscosity

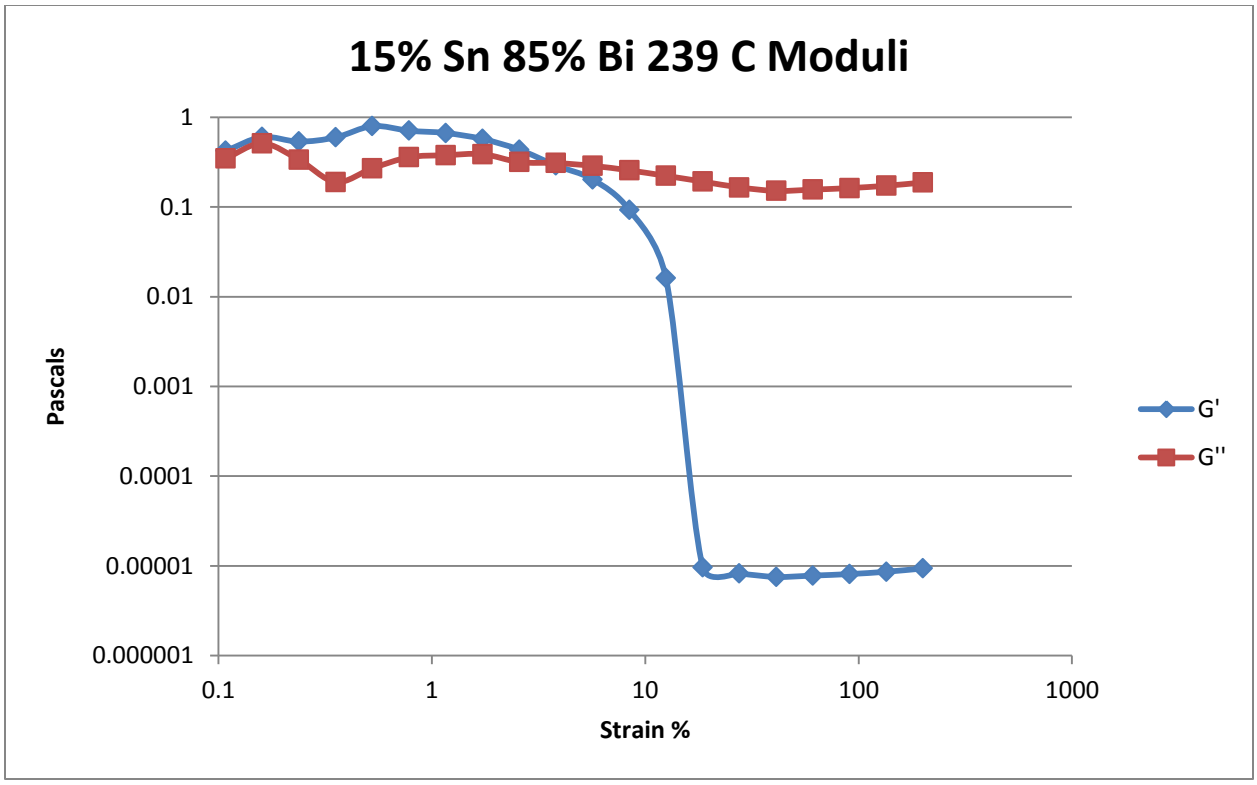

Figure 437- 15% Tin 85% Bismuth, 239 C, Oscillatory Shear Moduli

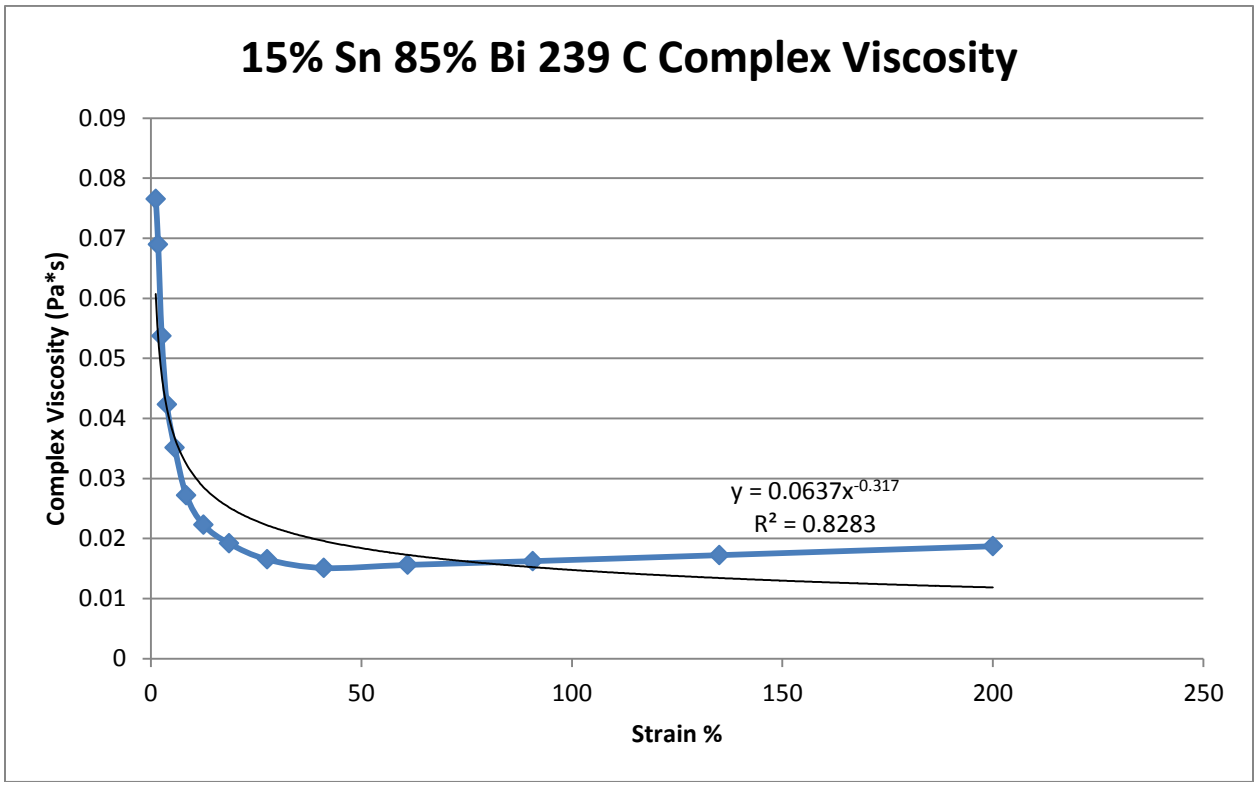

Figure 438- 15% Tin 85% Bismuth, 239 C, Oscillatory Shear Complex Viscosity

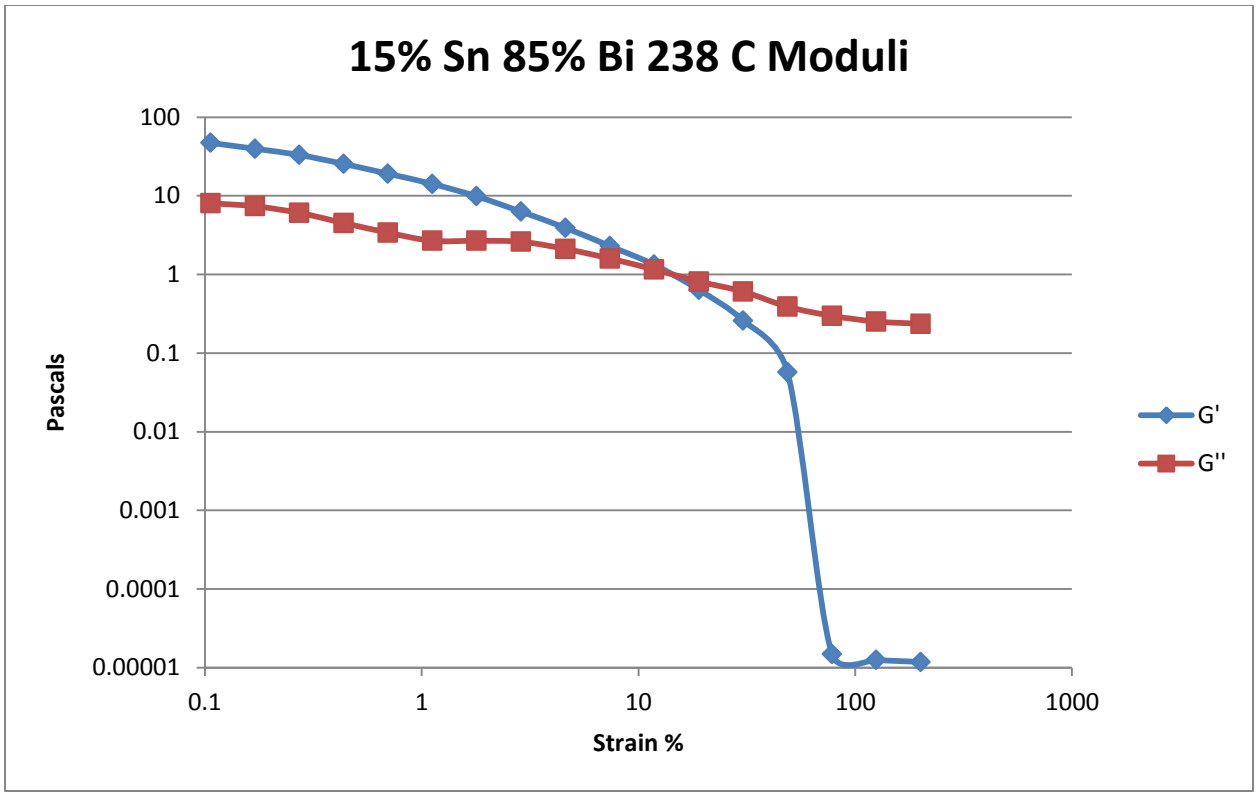

Figure 439- 15% Tin 85% Bismuth, 238 C, Oscillatory Shear Moduli

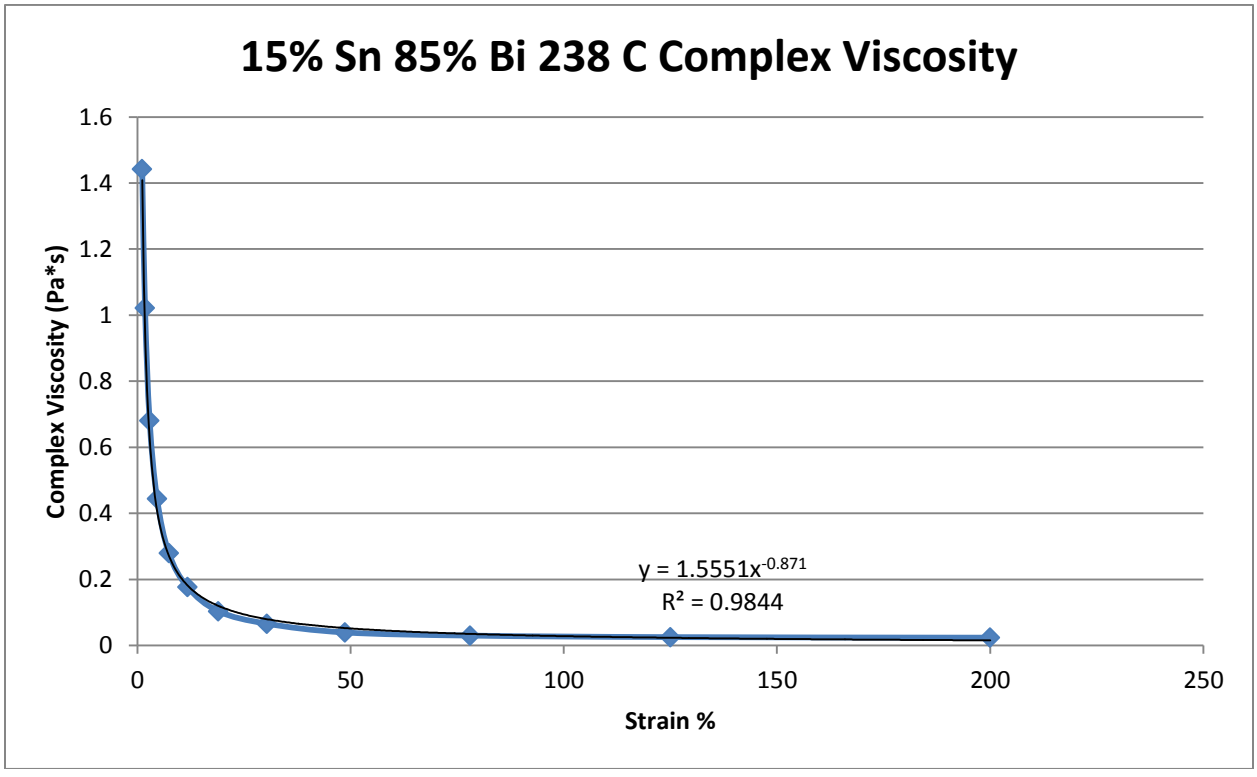

Figure 440- 15% Tin 85% Bismuth, 238 C, Oscillatory Shear Complex Viscosity

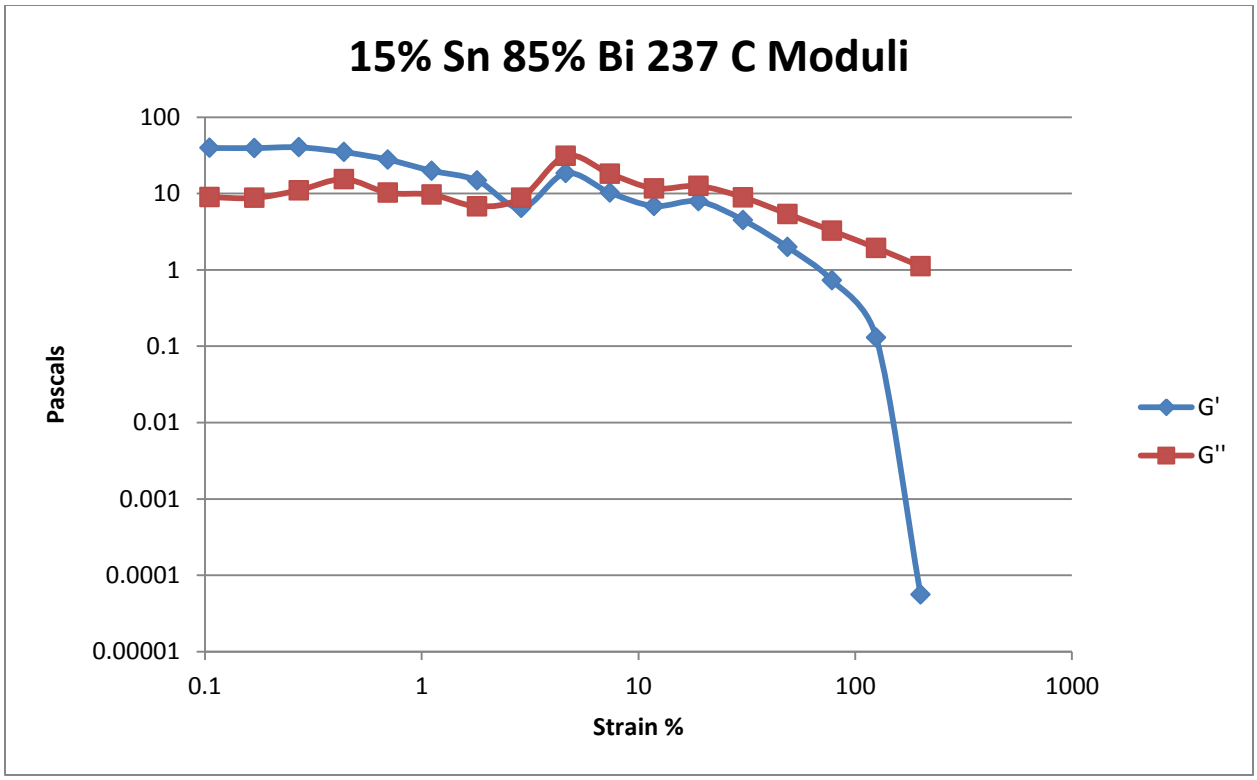

Figure 441- 15% Tin 85% Bismuth, 237 C, Oscillatory Shear Moduli

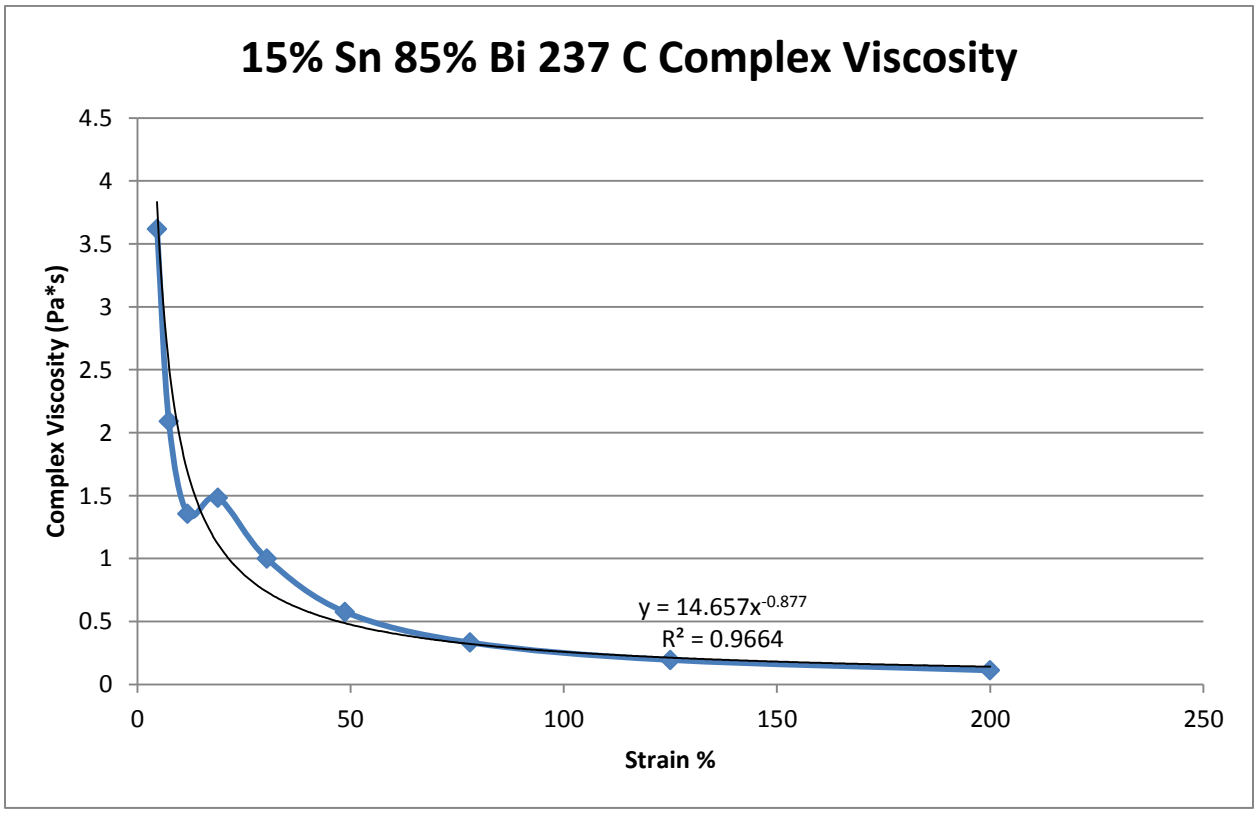

Figure 442- 15% Tin 85% Bismuth, 237 C, Oscillatory Shear Complex Viscosity

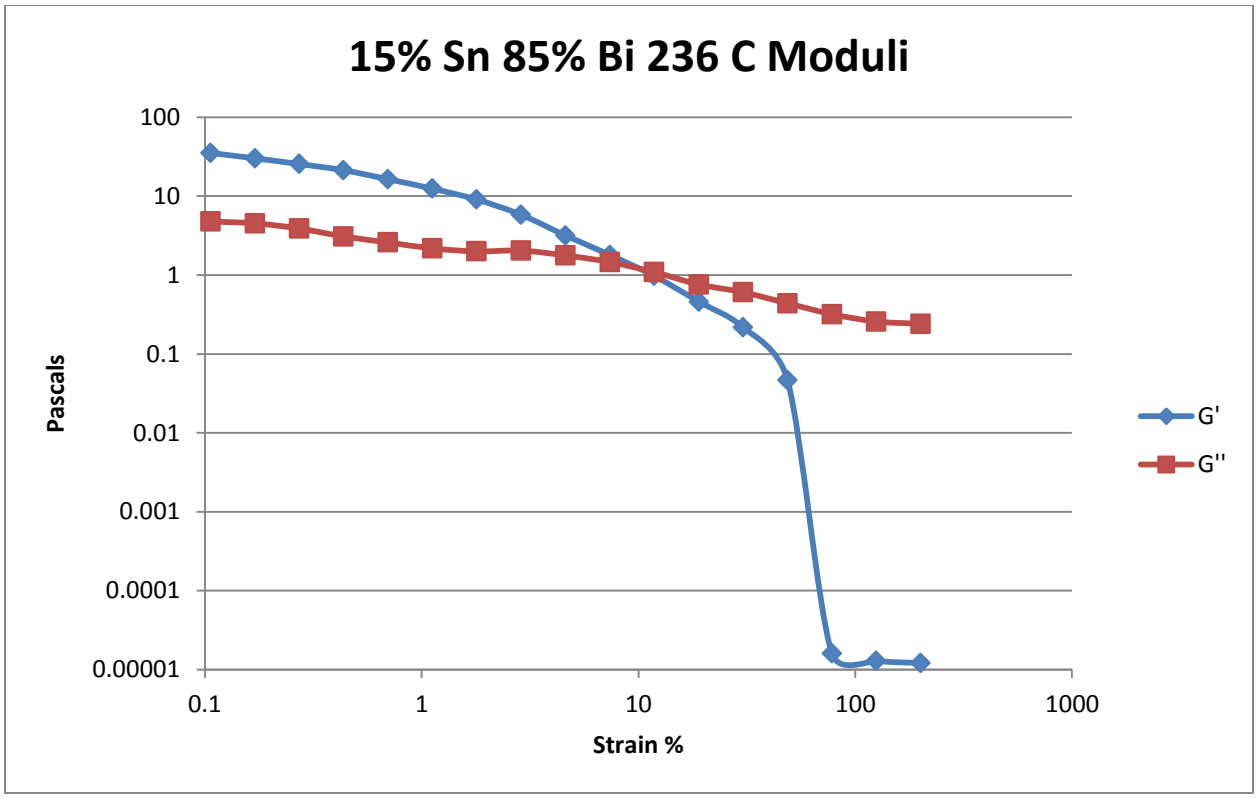

Figure 443- 15% Tin 85% Bismuth, 236 C, Oscillatory Shear Moduli

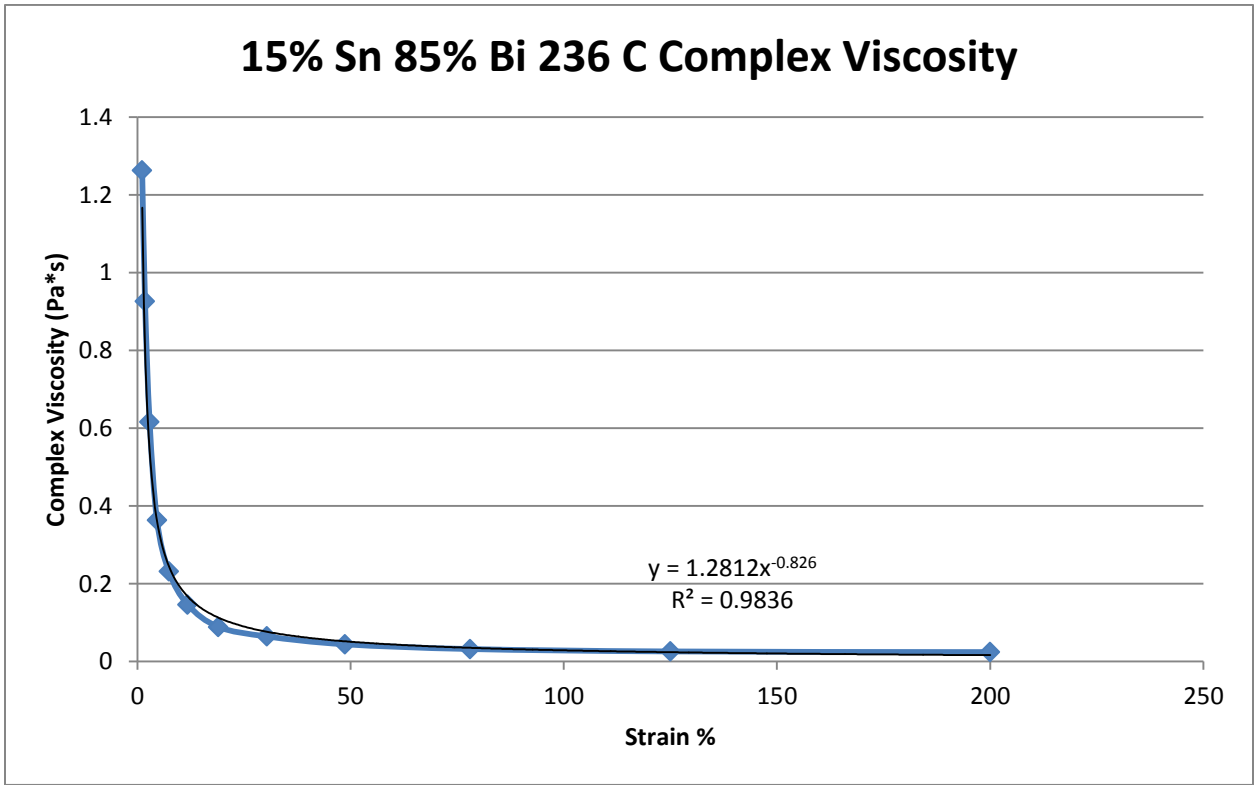

Figure 444- 15% Tin 85% Bismuth, 236 C, Oscillatory Shear Complex Viscosity

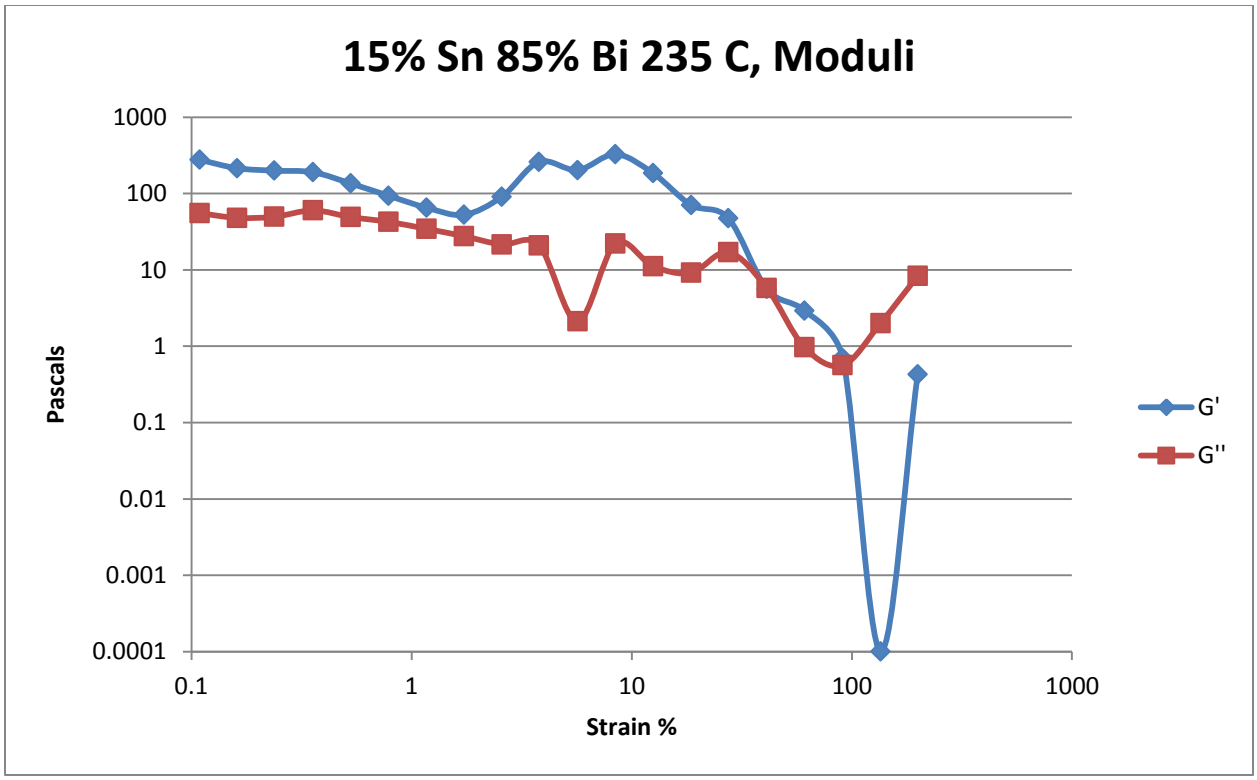

Figure 445- 15% Tin 85% Bismuth, 235 C, Oscillatory Shear Moduli

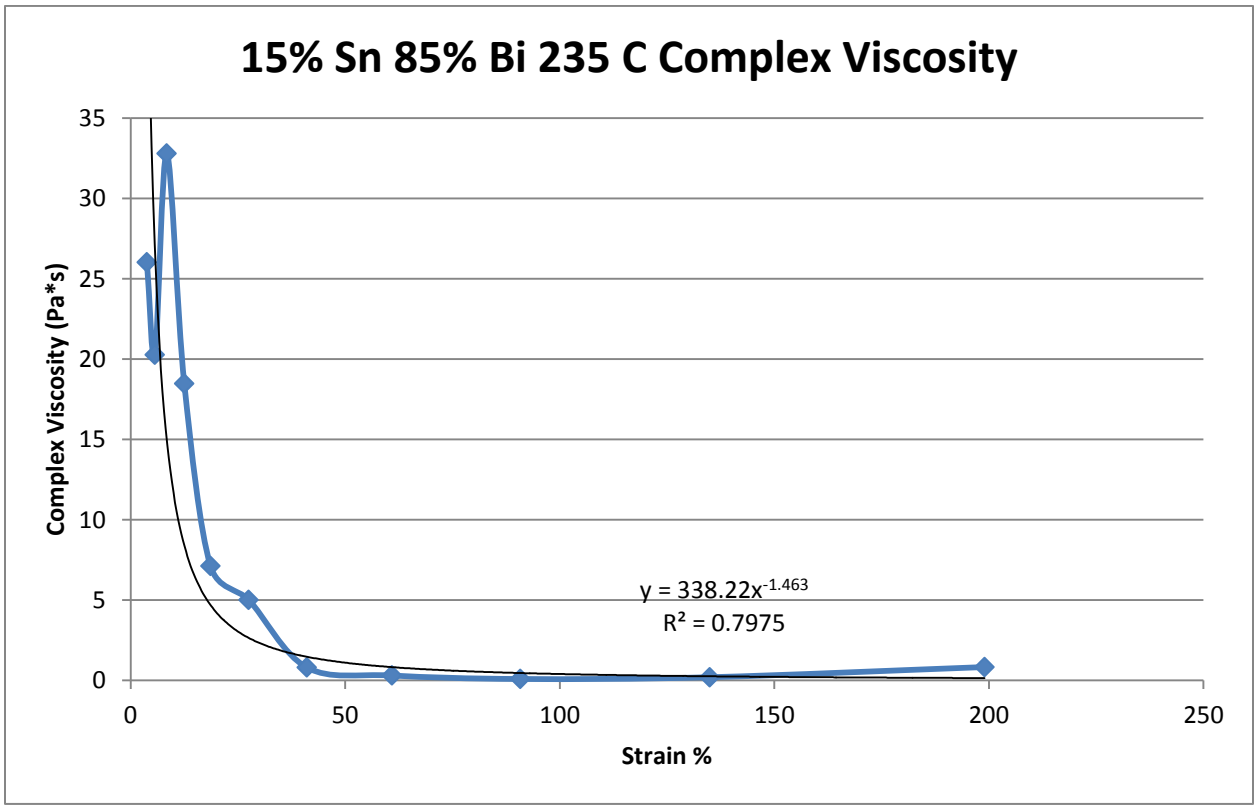

Figure 446- 15% Tin 85% Bismuth, 235 C, Oscillatory Shear Complex Viscosity

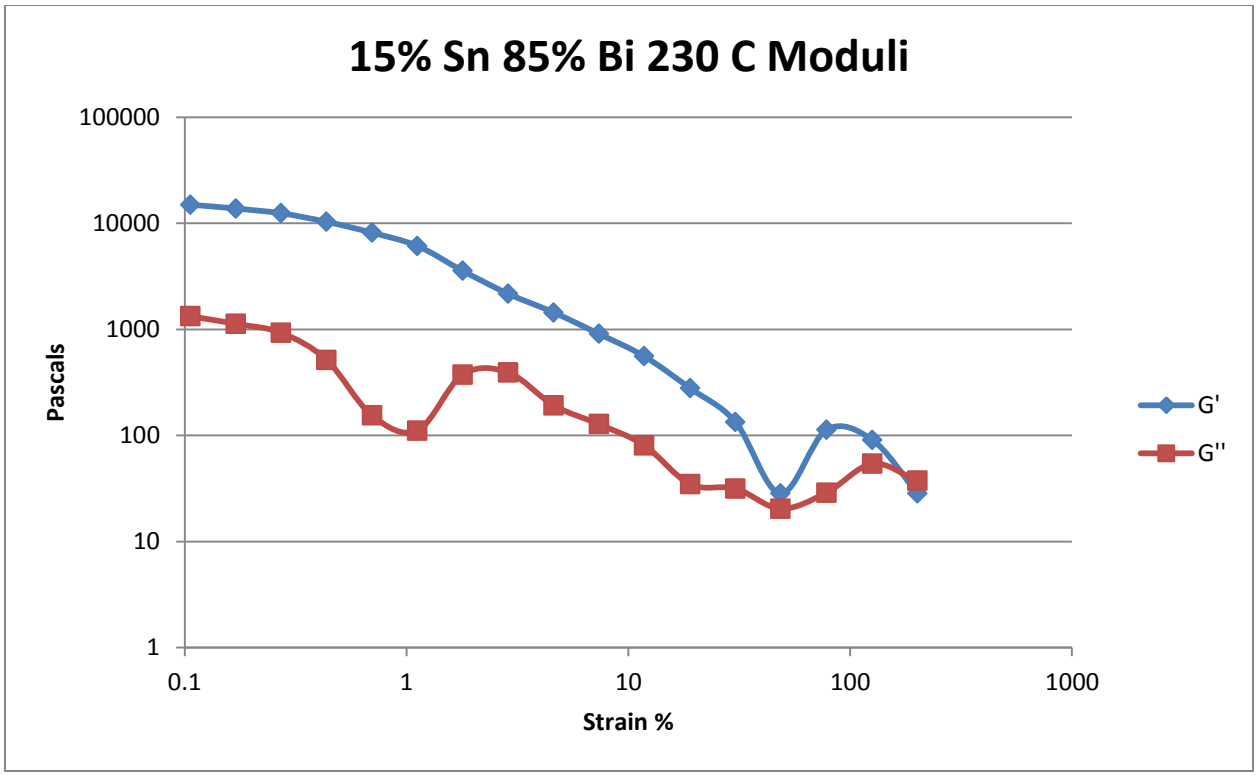

Figure 447- 15% Tin 85% Bismuth, 230 C, Oscillatory Shear Moduli

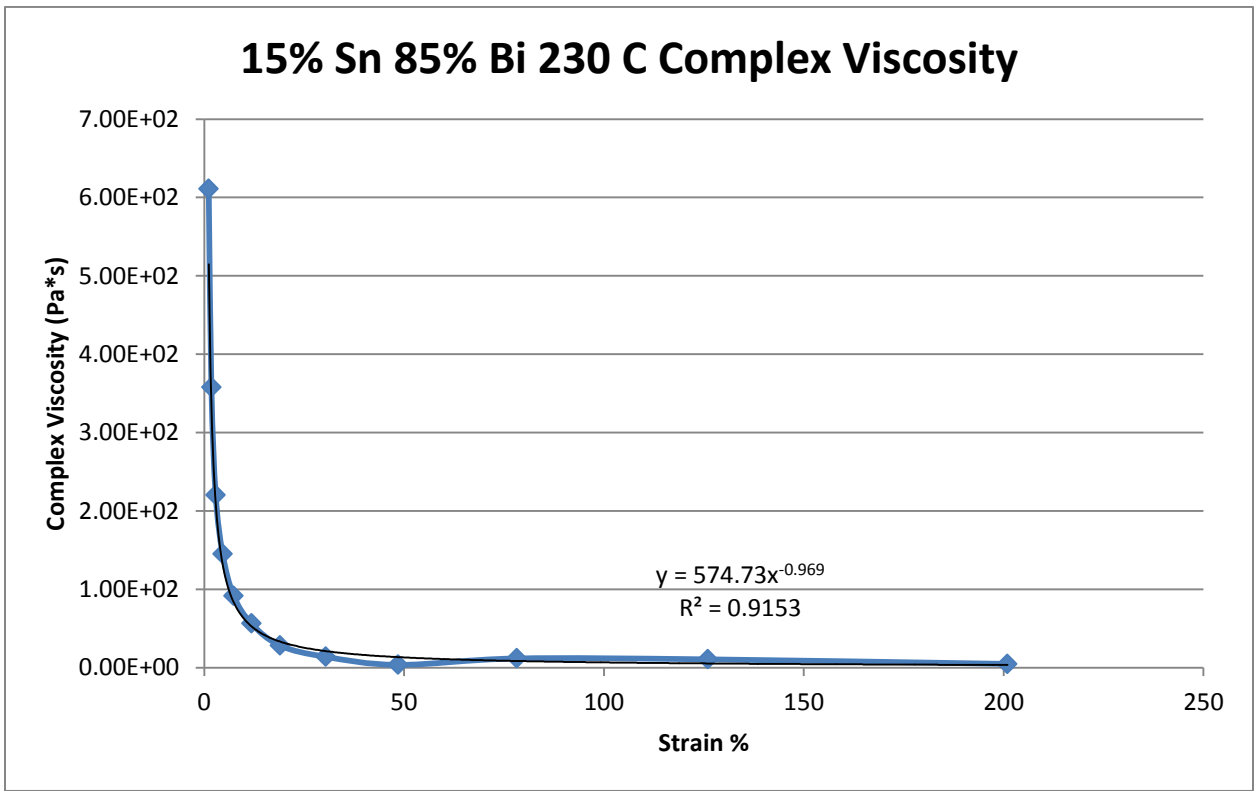

Figure 448- 15% Tin 85% Bismuth, 230 C, Oscillatory Shear Complex Viscosity

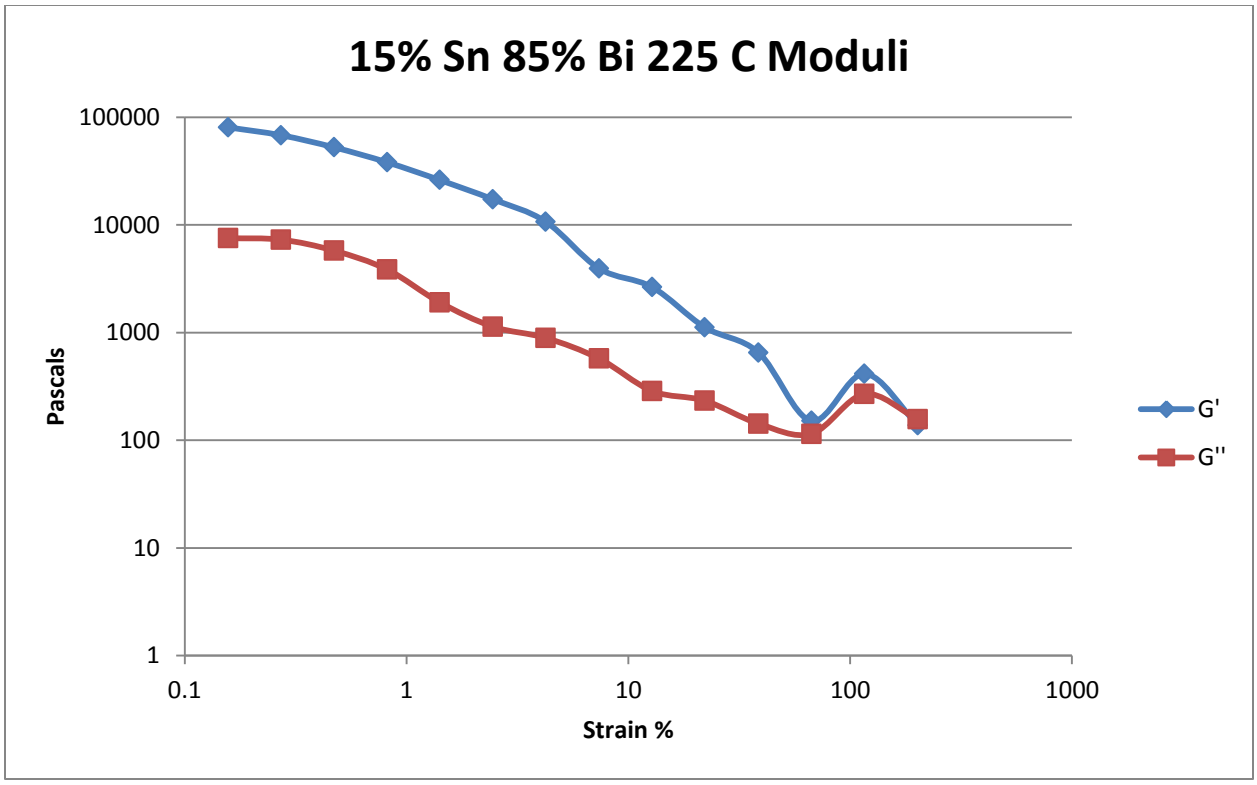

Figure 449- 15% Tin 85% Bismuth, 225 C, Oscillatory Shear Viscosity

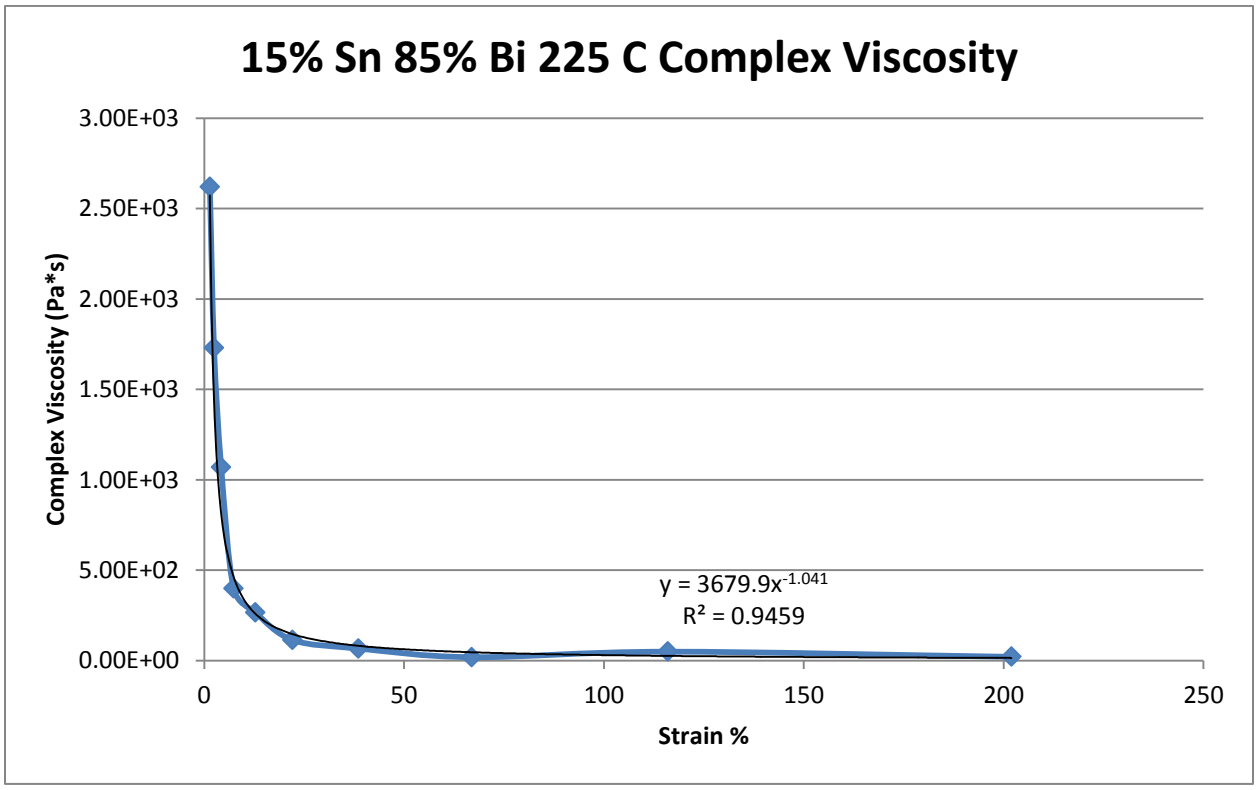

Figure 450- 15% Tin 85% Bismuth, 225 C, Oscillatory Shear Complex Viscosity

20% Tin 80% Bismuth

Predicted Composition: 22% Sn 78% Bi

Theoretical Solidus Line: 139 C
Theoretical Liquidus Line: 220.3 C

Experimental Solidus Line: 139.0 C
Experimental Liquidus Line: 217.5 C

Pre-Shear: 15 RPM, 2 minutes
Angular Velocity: Constant, 10 rad/s
Strain Range: 0.01%-200%

20% Tin 80% Bismuth Oscillatory Shear Rheology								
Temperature (C)	**Fraction Solid (%)**	**Crossover Strain (%)**	**Crossover Stress (Pa)**	**Crossover Modulus (Pa)**	**Crossover Complex Viscosity (Pa*s)**	**Pre G' Plateau (Pa)**	**Pre G'' Plateau (Pa)**	**Final Complex Viscosity (Pa*s)**
229	0	N/A	N/A	N/A	N/A	2.72e-5	0.747	0.025
225	0	35.2	0.117	0.232	0.031	0.387	0.327	0.021
220	0.63	14.1	0.044	0.216	0.038	0.987	0.511	0.029
215	9.46	1.56	0.188	8.60	1.21	104	22.3	0.020
210	16.86	6.40	22.0	242	35.3	3.60e3	899	1.04
205	23.14	29.3	163	396	61.7	1.83e4	5.33e3	9.97
200	28.55	17.5	212	864	132	1.86e4	4.98e3	12.1

Table 83- 20% Tin 80% Bismuth Oscillatory Shear Rheology

20% Tin 80% Bismuth Oscillatory Shear Complex Viscosity			
Temperature (C)	**Fraction Solid (%)**	**Power Law Equation**	**R^2 (%)**
229	0	$\eta^* = 0.0325\gamma^{-0.094}$	33.44
225	0	$\eta^* = 0.0474\gamma^{-0.199}$	33.93
220	0.63	$\eta^* = 0.0467\gamma^{-0.148}$	80.31
215	9.46	$\eta^* = 1.6132\gamma^{-0.870}$	99.48
210	16.86	$\eta^* = 175.53\gamma^{-0.955}$	99.58
205	23.14	$\eta^* = 597.13\gamma^{-0.744}$	97.97
200	28.55	$\eta^* = 839.28\gamma^{-0.758}$	97.17

Table 84- 20% Tin 80% Bismuth Oscillatory Shear Complex Viscosity

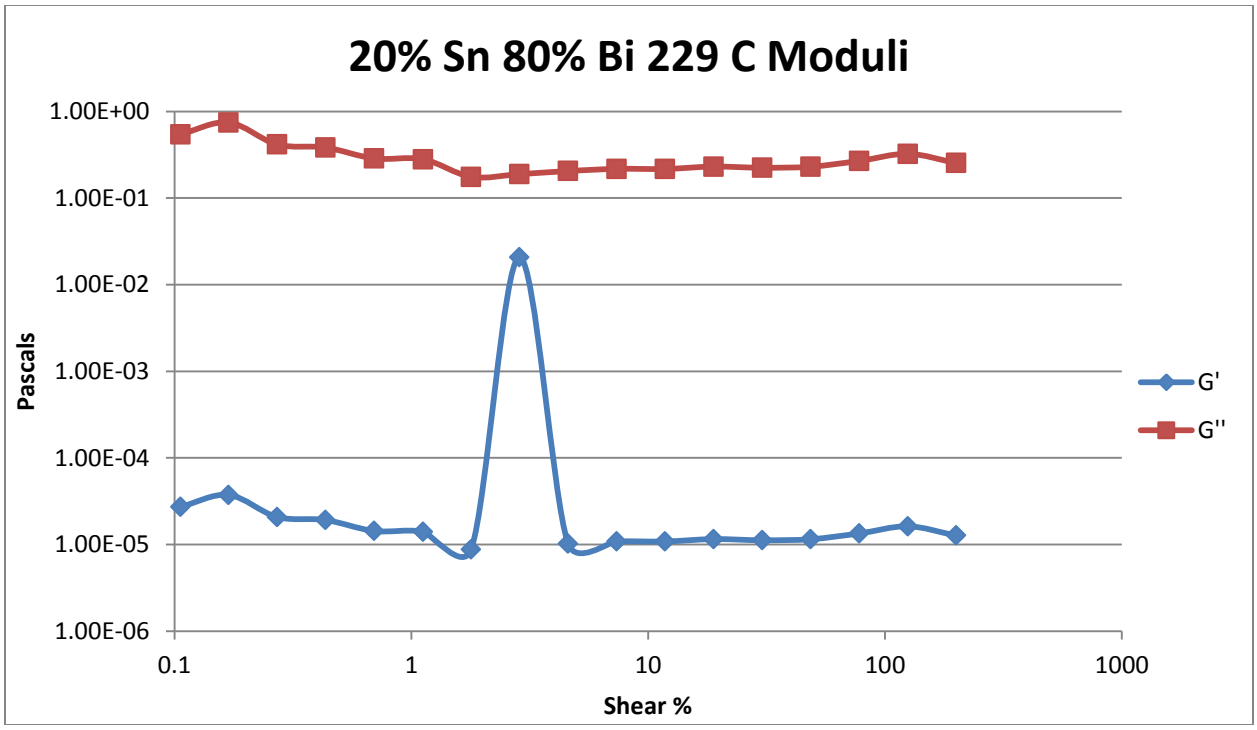

Figure 451- 20% Tin 80% Bismuth, 229 C, Oscillatory Shear Moduli

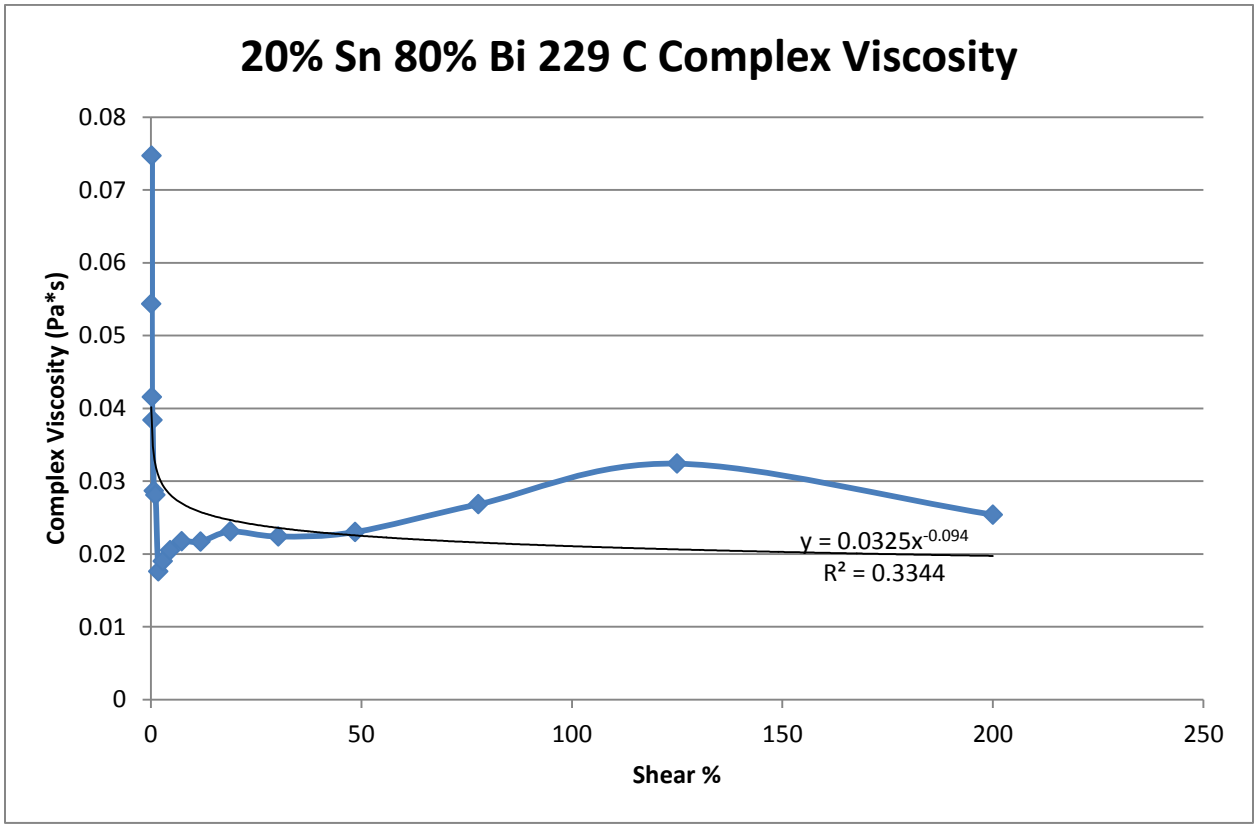

Figure 452- 20% Tin 80% Bismuth, 229 C, Oscillatory Shear Complex Viscosity

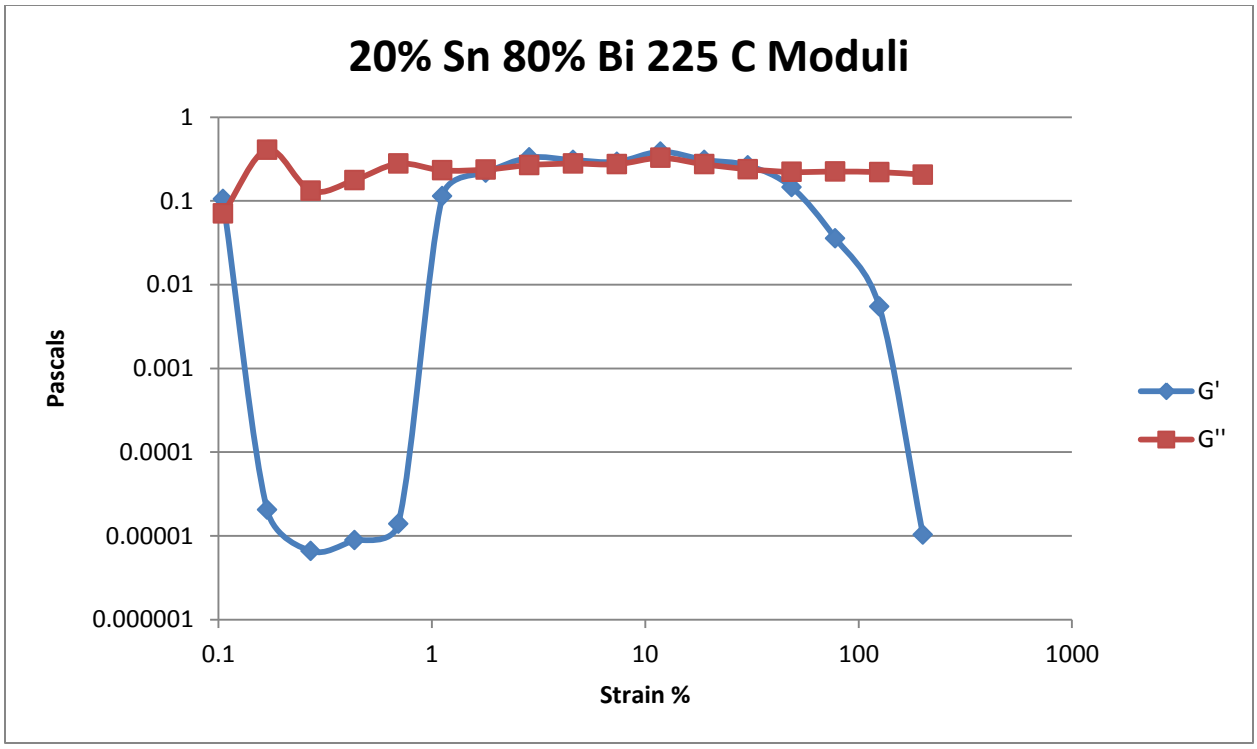

Figure 453- 20% Tin 80% Bismuth, 225 C, Oscillatory Shear Moduli

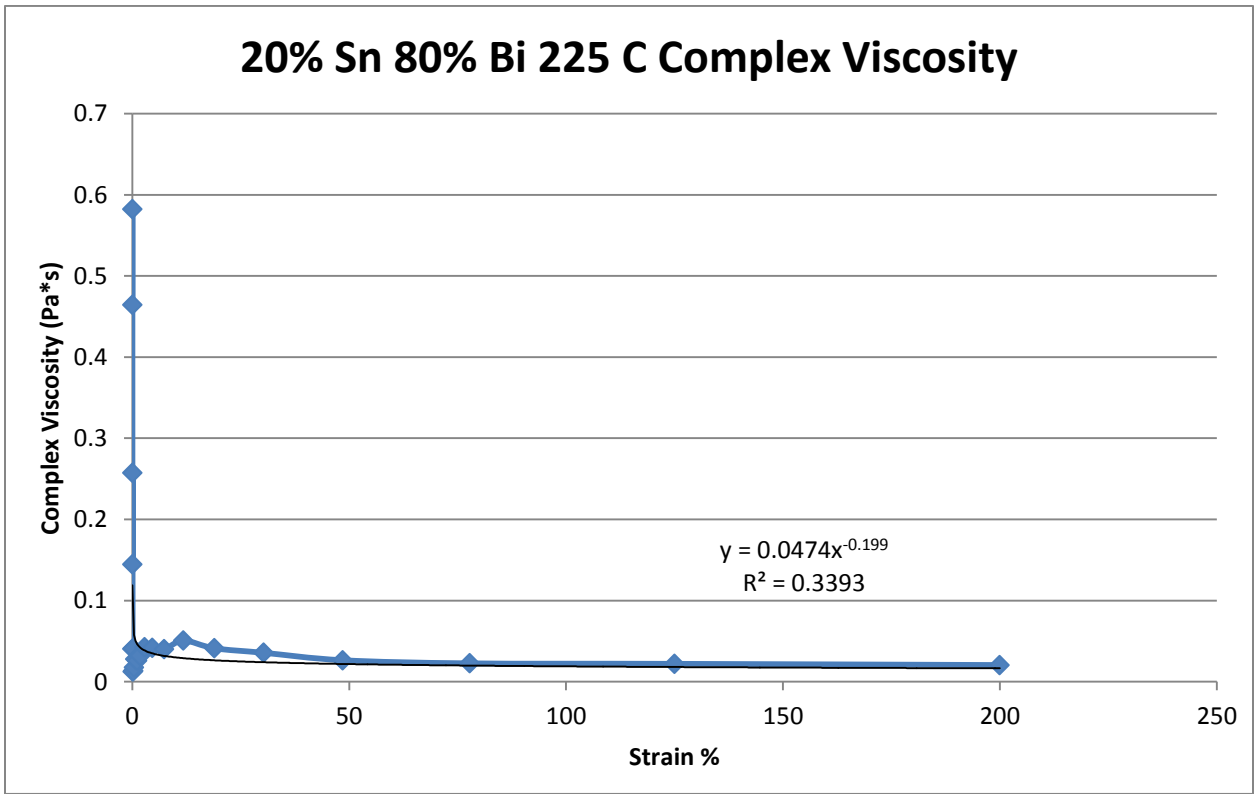

Figure 454- 20% Tin 80% Bismuth, 225 C, Oscillatory Shear Complex Viscosity

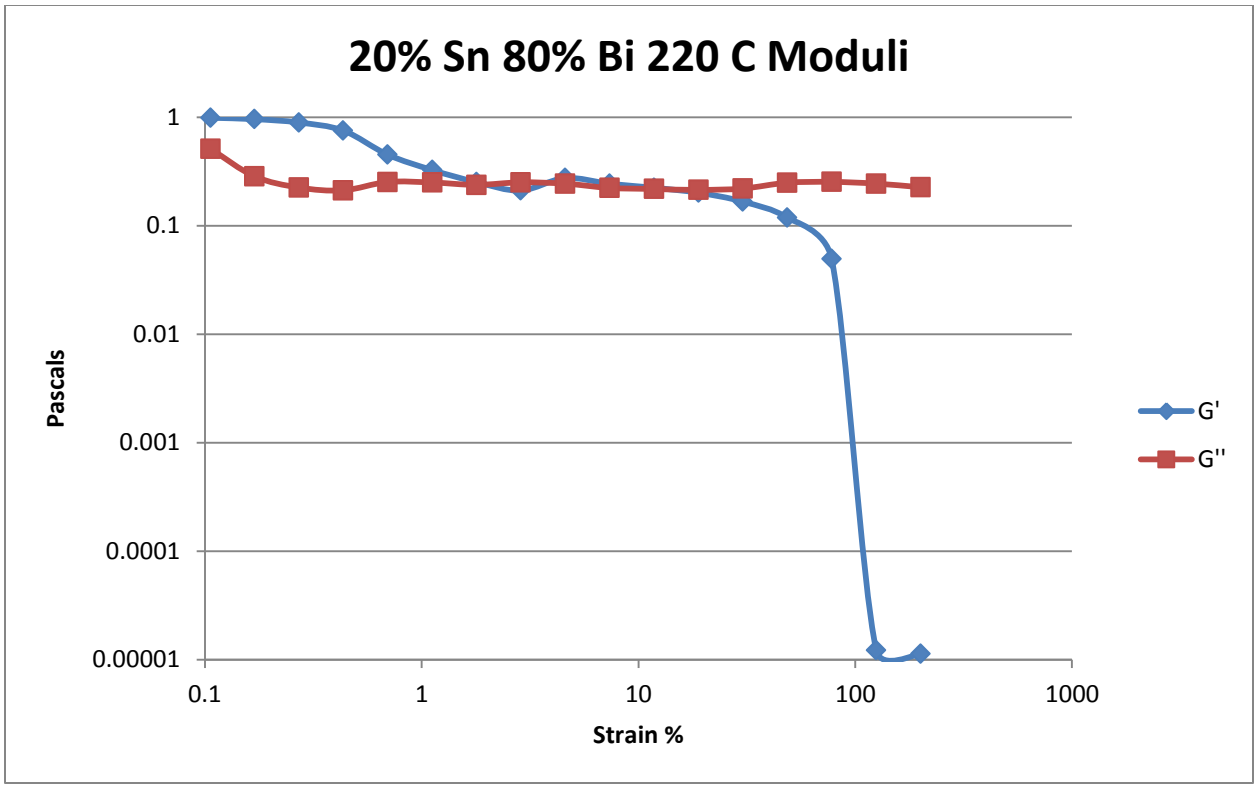

Figure 455- 20% Tin 80% Bismuth, 220 C, Oscillatory Shear Moduli

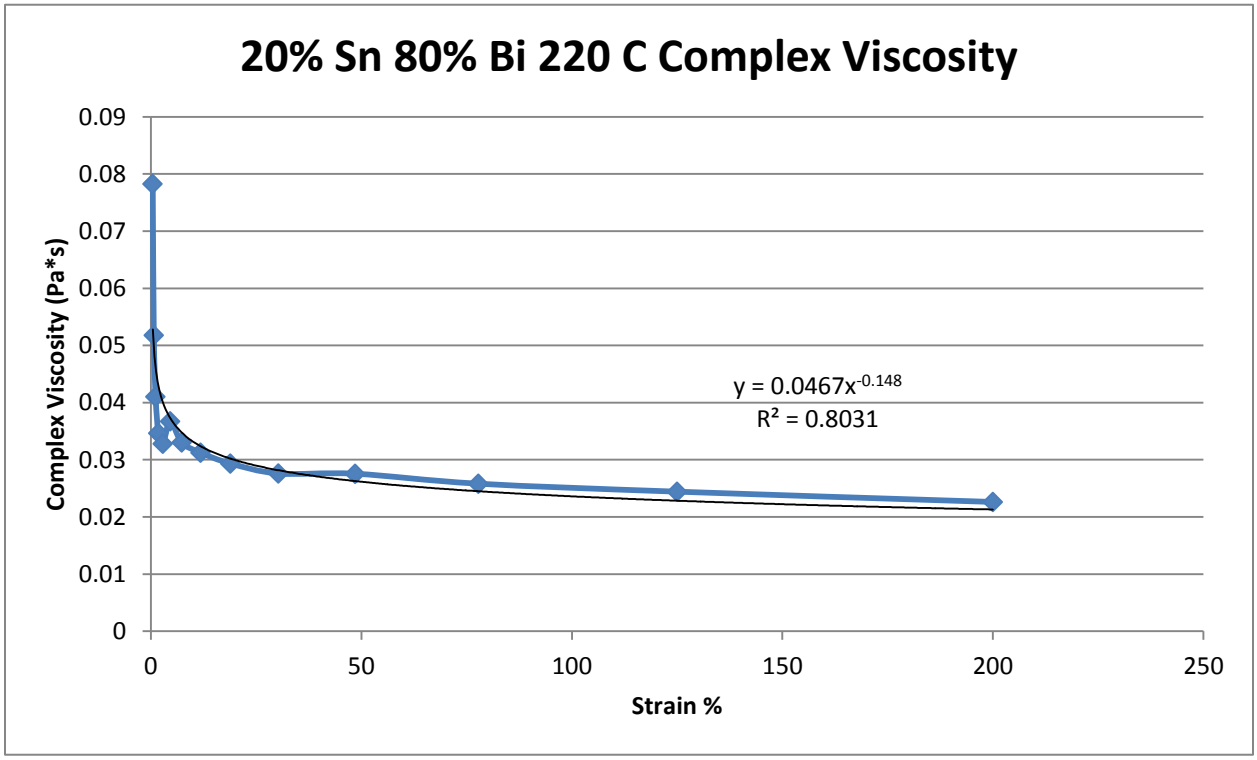

Figure 456- 20% Tin 80% Bismuth, 220 C, Oscillatory Shear Complex Viscosity

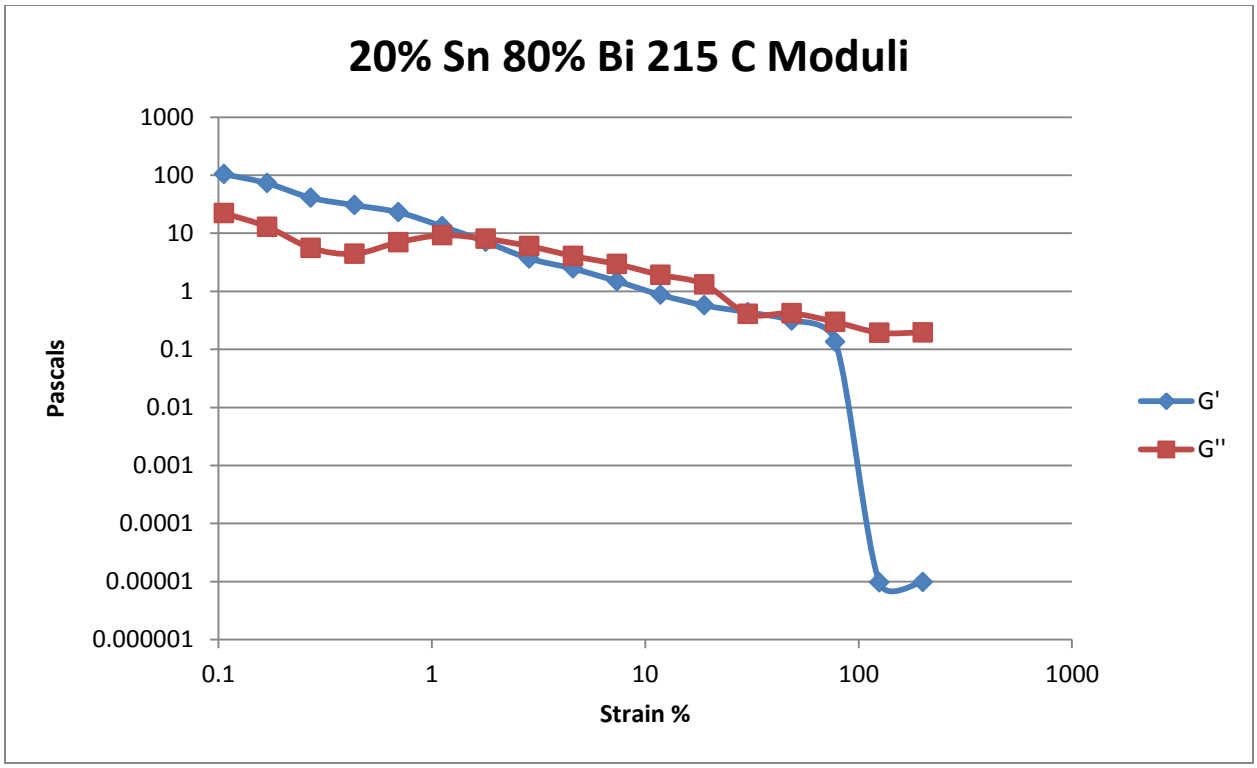

Figure 457- 20% Tin 80% Bismuth, 215 C, Oscillatory Shear Moduli

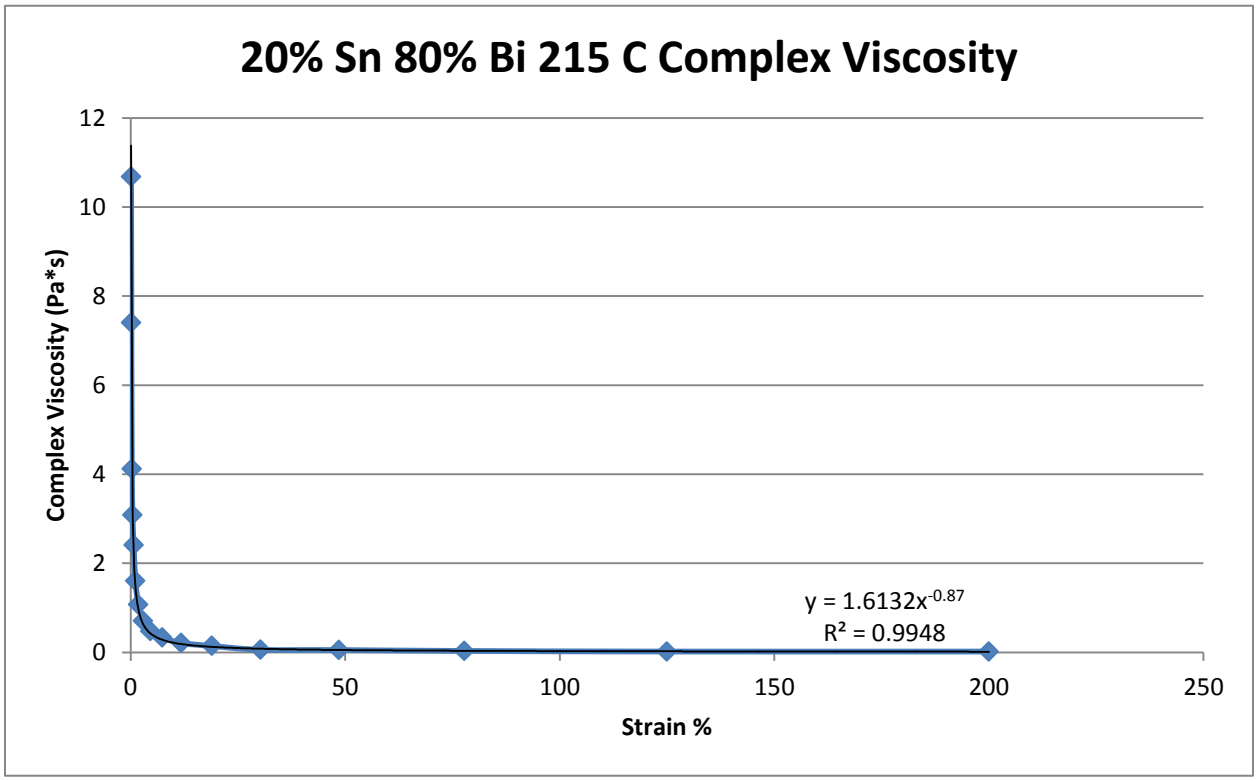

Figure 458- 20% Tin 80% Bismuth, 215 C, Oscillatory Shear Complex Viscosity

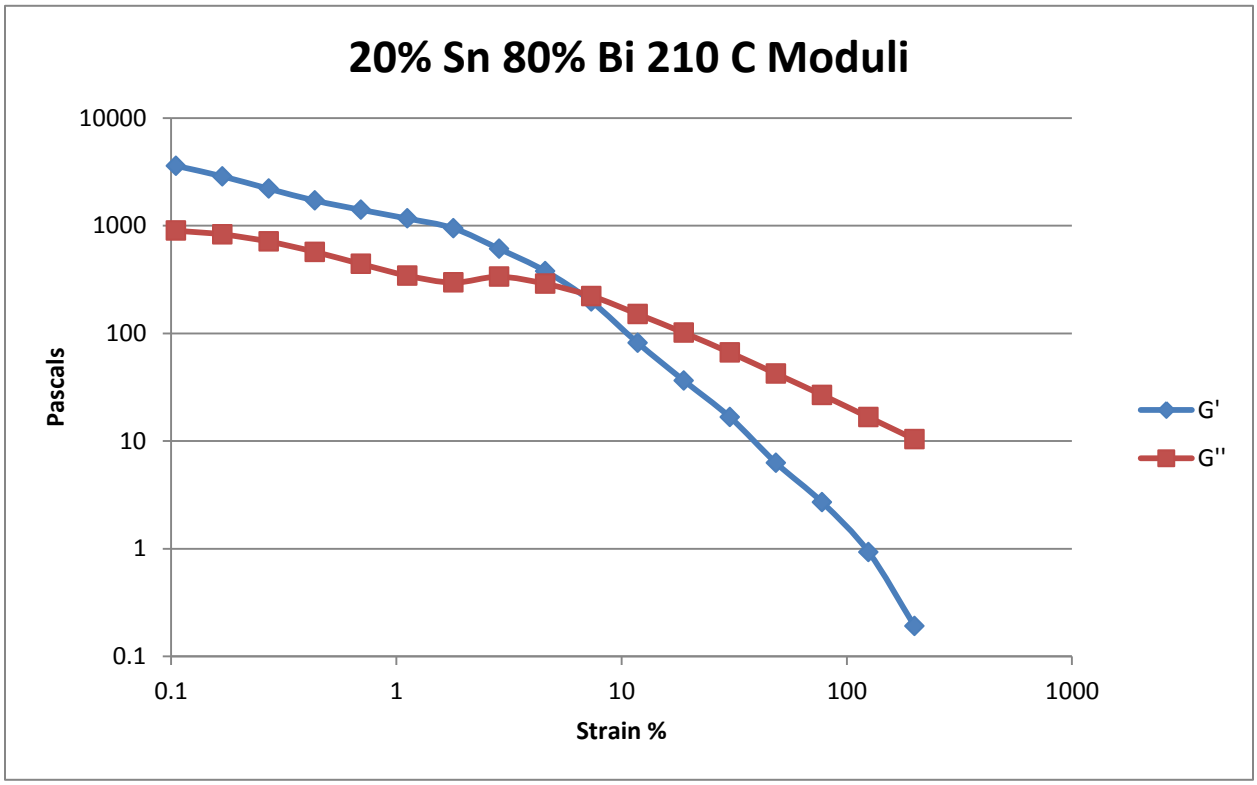

Figure 459- 20% Tin 80% Bismuth, 210 C, Oscillatory Shear Moduli

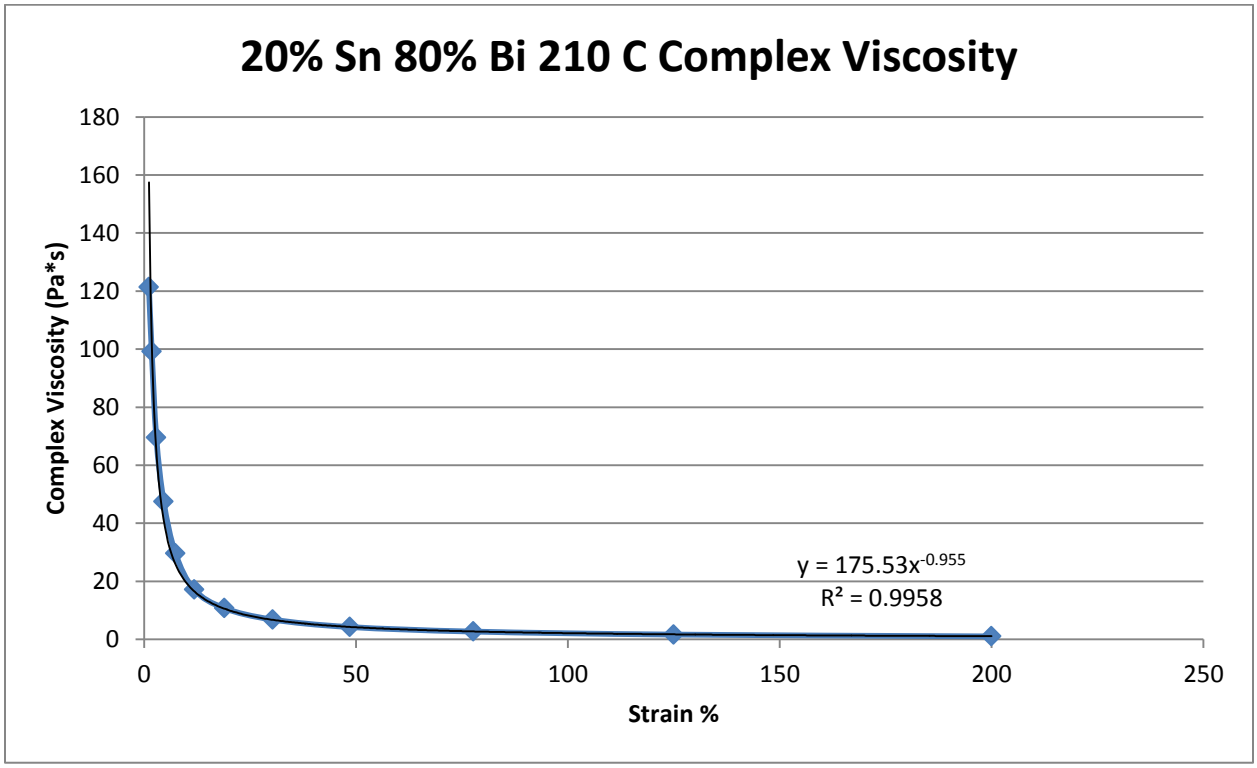

Figure 460- 20% Tin 80% Bismuth, 210 C, Oscillatory Shear Complex Viscosity

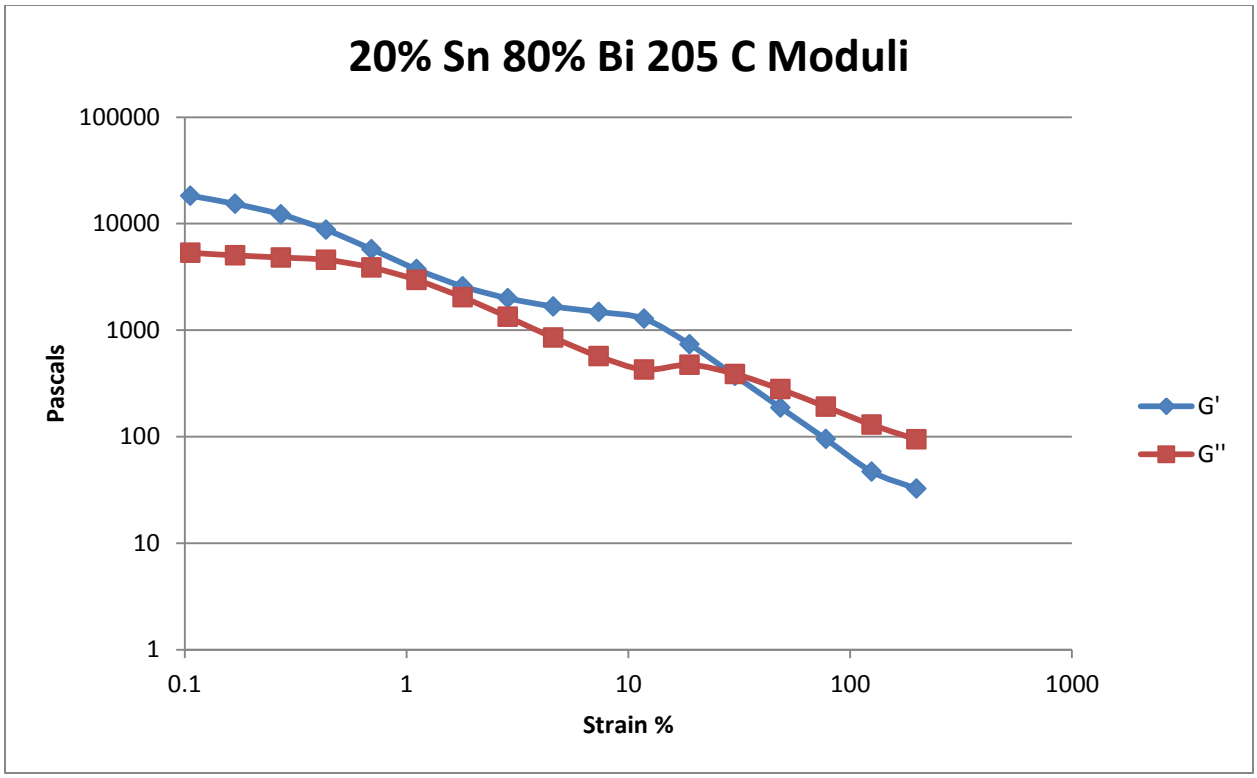

Figure 461- 20% Tin 80% Bismuth, 205 C, Oscillatory Shear Moduli

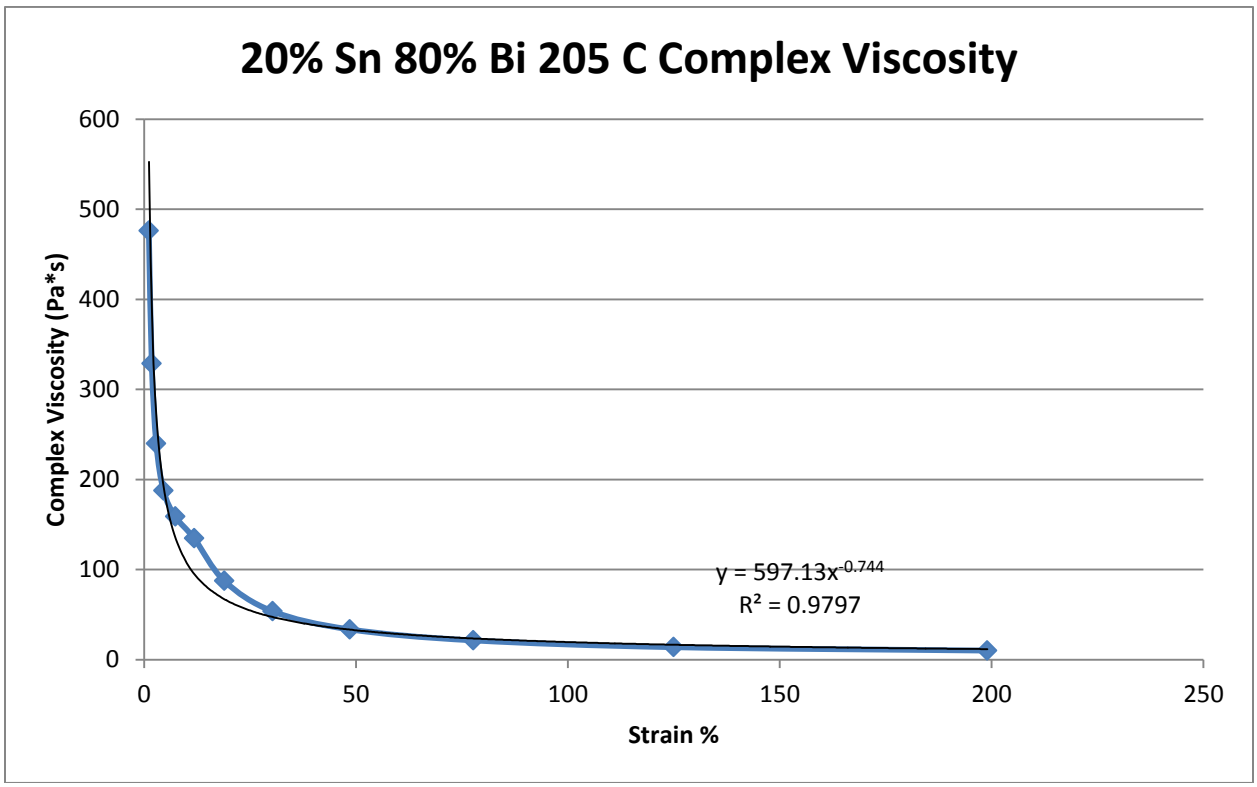

Figure 462- 20% Tin 80% Bismuth, 205 C, Oscillatory Shear Complex Viscosity

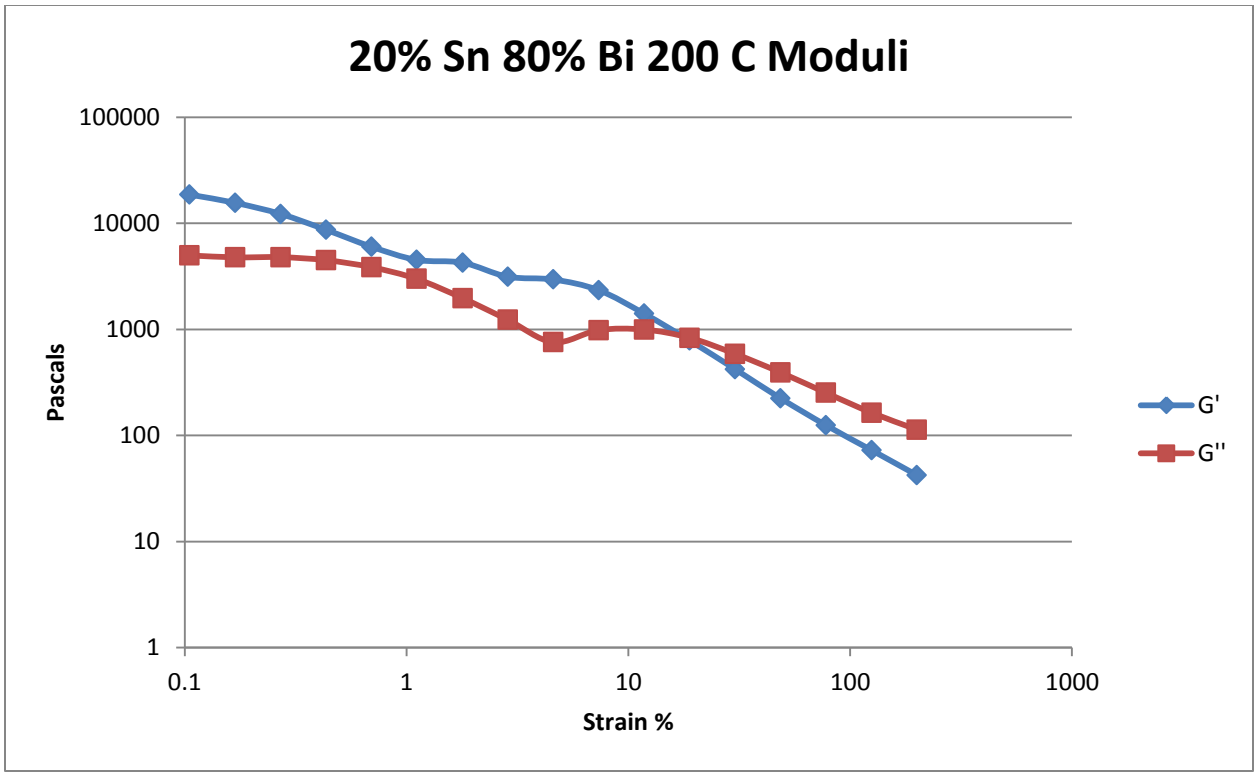

Figure 463- 20% Tin 80% Bismuth, 200 C, Oscillatory Shear Moduli

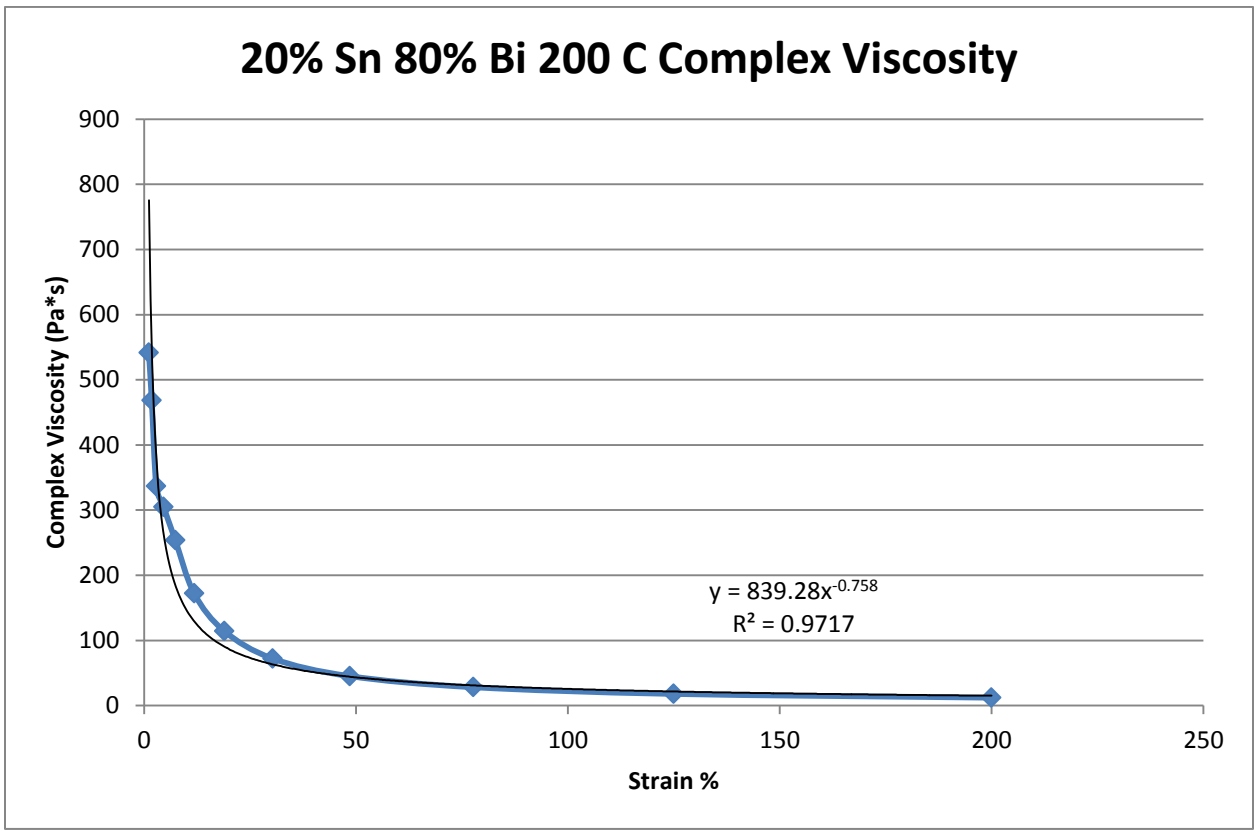

Figure 464- 20% Tin 80% Bismuth, 200 C, Oscillatory Shear Complex Viscosity

30% Tin 70% Bismuth

Predicted Composition: 22% Sn 78% Bi

Theoretical Solidus Line: 139 C
Theoretical Liquidus Line: 192.1 C

Experimental Solidus Line: N/A
Experimental Liquidus Line: N/A

Pre-Shear: 15 RPM, 2 minutes
Angular Velocity: Constant, 10 rad/s
Strain Range: 0.01%-200%

30% Tin 70% Bismuth Oscillatory Shear Rheology								
Temperature (C)	**Fraction Solid (%)**	**Crossover Strain (%)**	**Crossover Stress (Pa)**	**Crossover Modulus (Pa)**	**Crossover Complex Viscosity (Pa*s)**	**Pre G' Plateau (Pa)**	**Pre G'' Plateau (Pa)**	**Final Complex Viscosity (Pa*s)**
210	0	N/A	N/A	N/A	N/A	8.69e-6	0.170	0.017
205	0	3.01	0.021	0.498	0.016	1.08	0.617	0.016
200	0	2.22	0.021	0.670	0.096	1.47	0.844	0.018
195	2.74	30.4	81.1	68.5	273	9.88e3	722	25.0
190	8.73	39.4	94.9	176.3	22.8	8.23e4	7.56e4	7.77
185	14.0	3.57	131	2645	374	1.60e4	4.88e3	9.31
180	18.8	14.0	245	1267	170	6.29e4	1.04e4	27.3

Table 85- 30% Tin 70% Bismuth Oscillatory Shear Rheology

30% Tin 70% Bismuth Oscillatory Shear Complex Viscosity			
Temperature (C)	**Fraction Solid (%)**	**Power Law Equation**	**R^2 (%)**
210	0	$\eta^* = 0.1672\gamma^{-0.482}$	97.30
205	0	$\eta^* = 0.0952\gamma^{-0.393}$	94.41
200	0	$\eta^* = 0.1045\gamma^{-0.320}$	58.75
195	2.74	$\eta^* = 2237\gamma^{-0.764}$	84.98
190	8.73	$\eta^* = 1867.7\gamma^{-1.027}$	97.37
185	14.0	$\eta^* = 1074.3\gamma^{-0.935}$	96.57
180	18.8	$\eta^* = 2722\gamma^{-0.965}$	96.56

Table 86- 30% Tin 70% Bismuth Oscillatory Shear Complex Viscosity

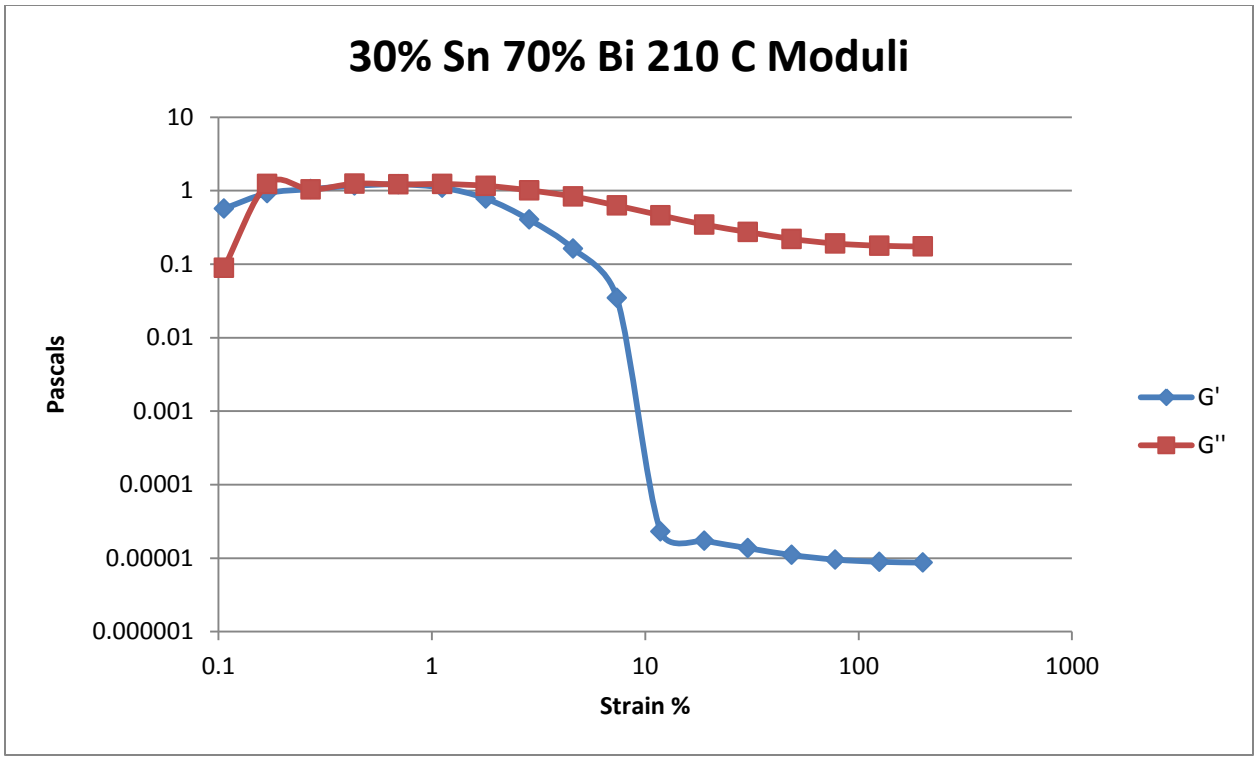

Figure 465- 30% Tin 70% Bismuth, 210 C, Oscillatory Shear Moduli

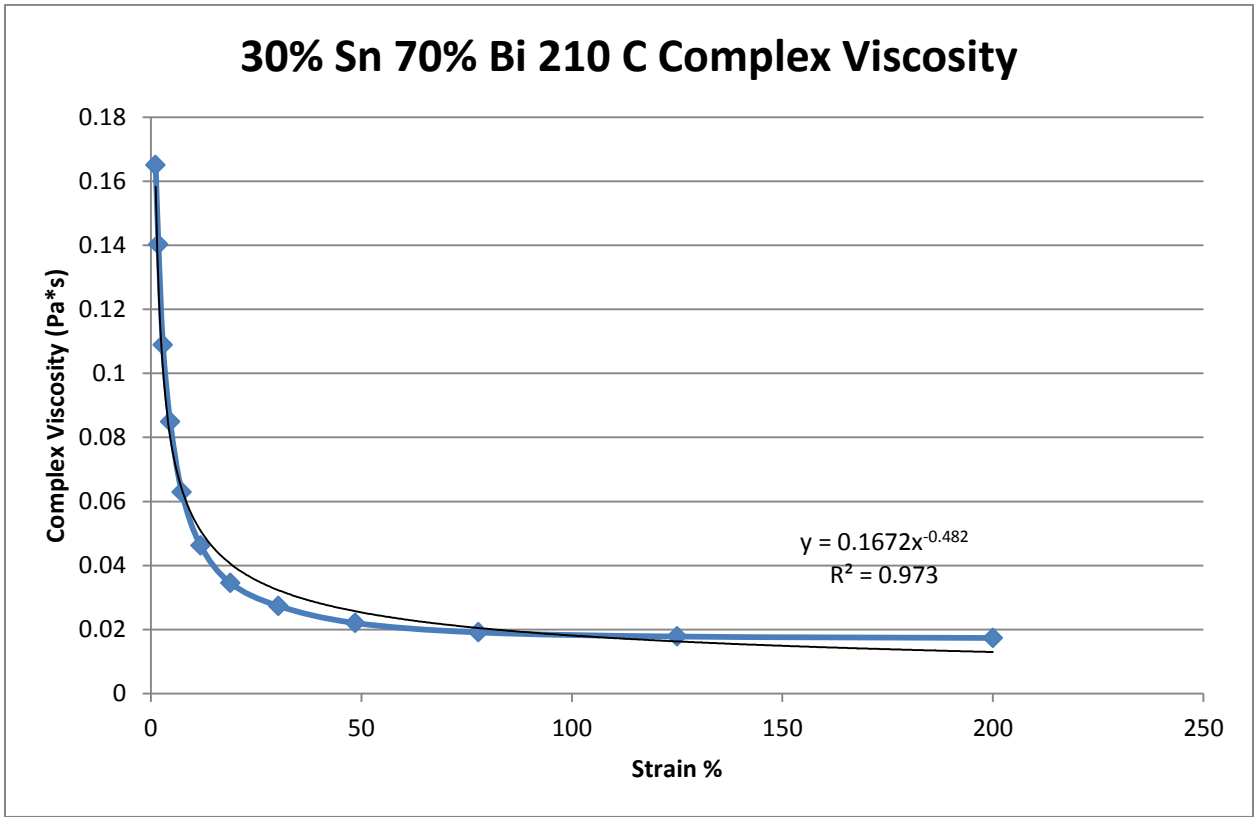

Figure 466- 30% Tin 70% Bismuth, 210 C, Oscillatory Shear Complex Viscosity

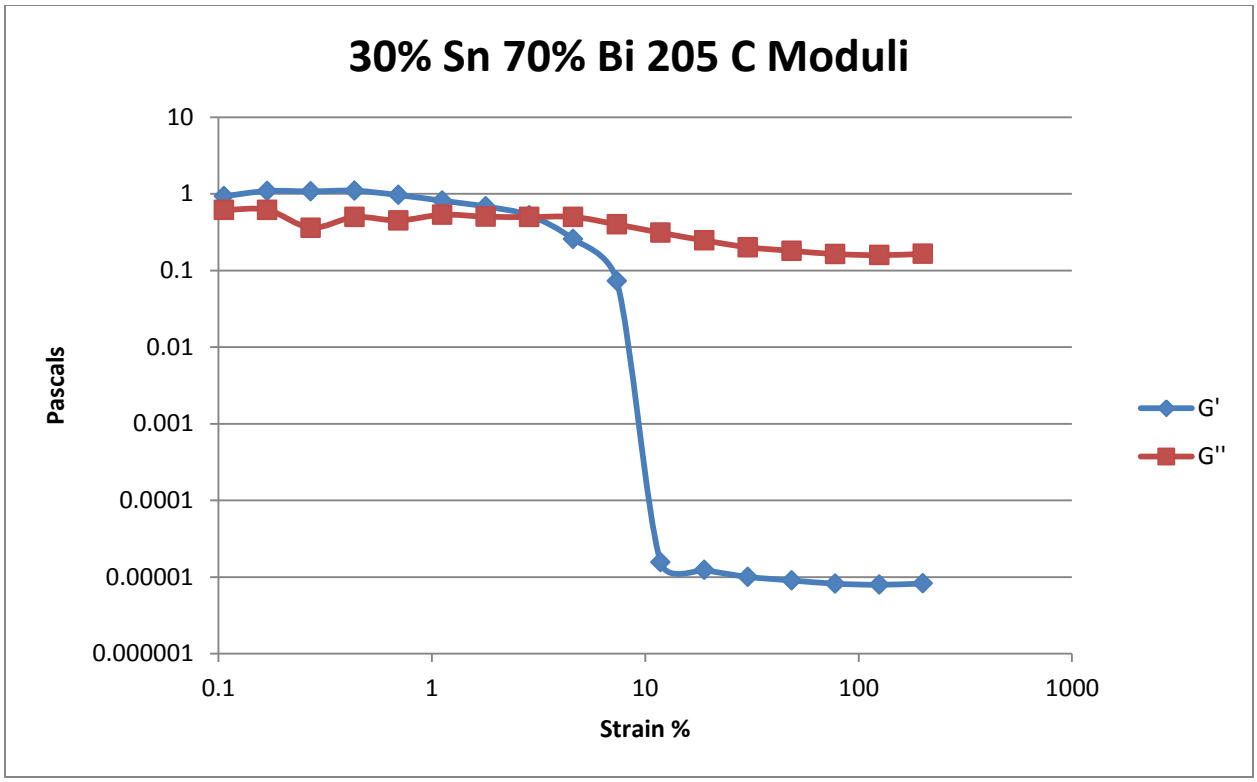

Figure 467- 30% Tin 70% Bismuth, 205 C, Oscillatory Shear Moduli

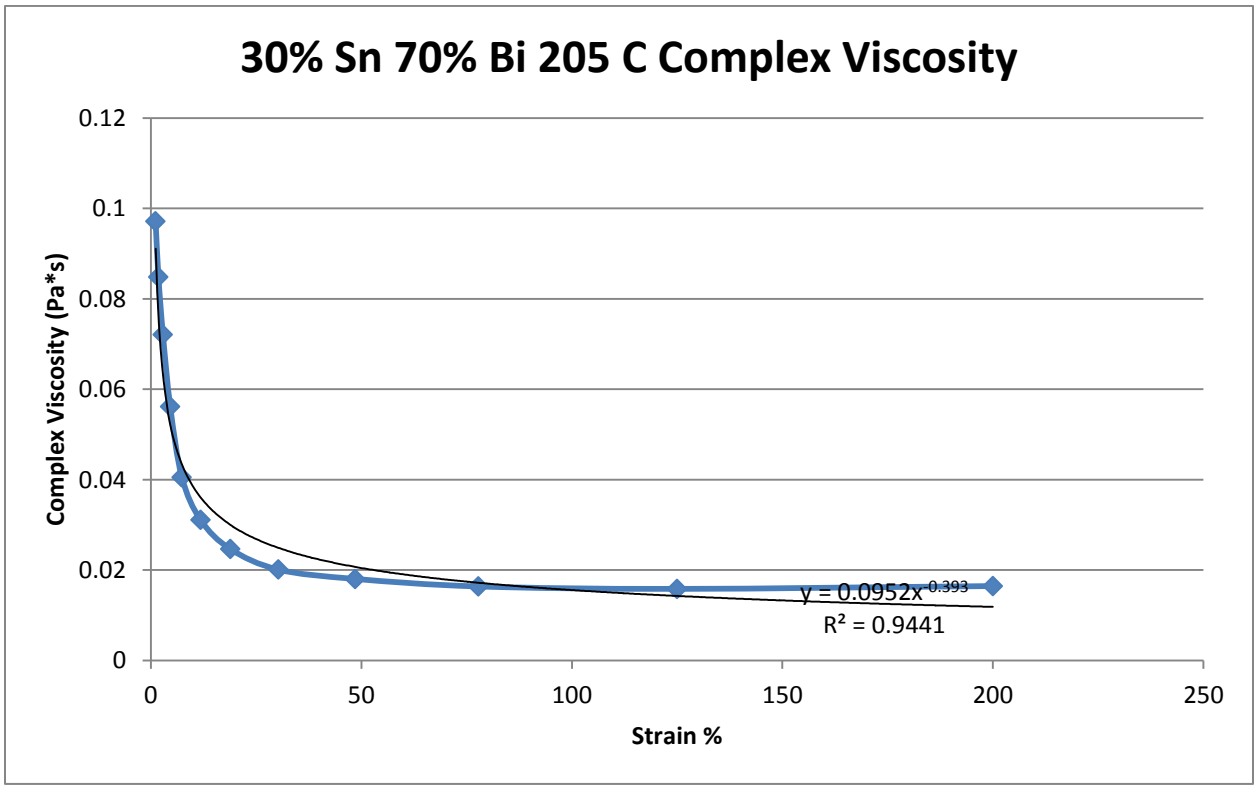

Figure 468- 30% Tin 70% Bismuth, 205 C, Oscillatory Shear Complex Viscosity

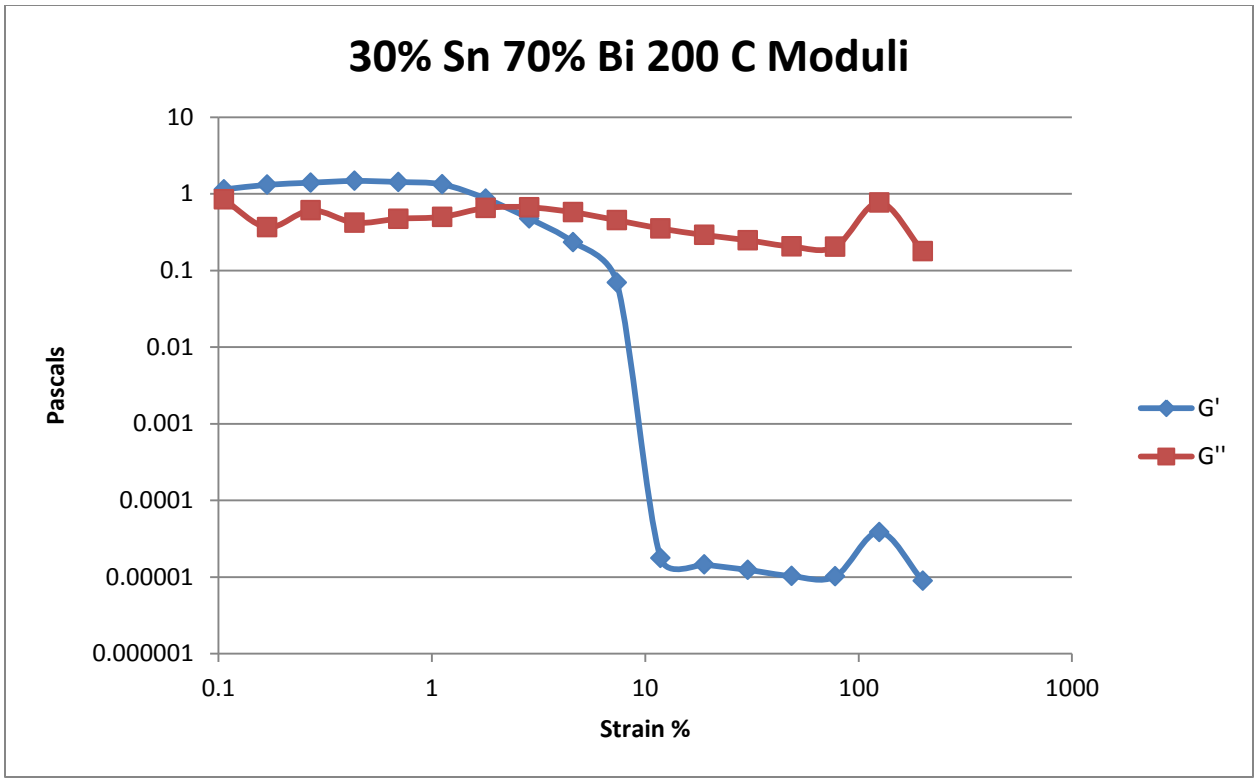

Figure 469- 30% Tin 70% Bismuth, 200 C, Oscillatory Shear Moduli

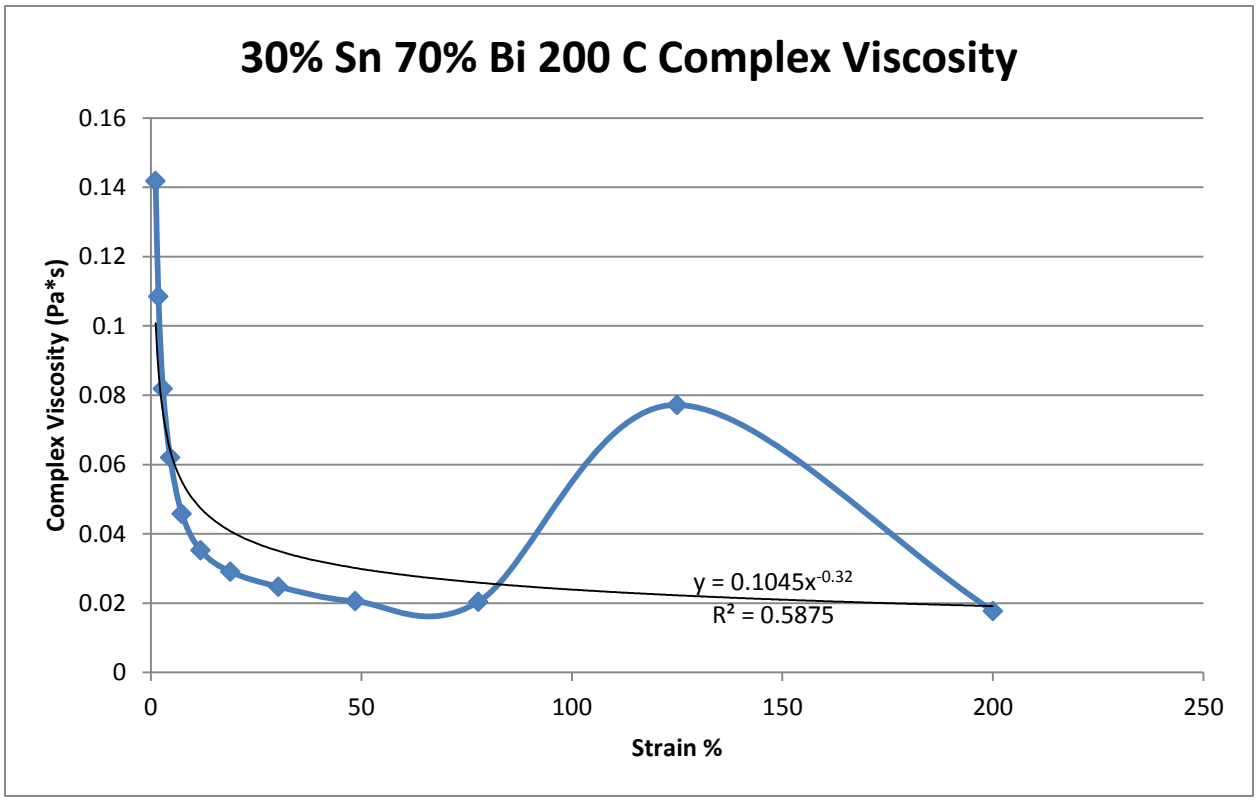

Figure 470- 30% Tin 70% Bismuth, 200 C, Oscillatory Shear Complex Viscosity

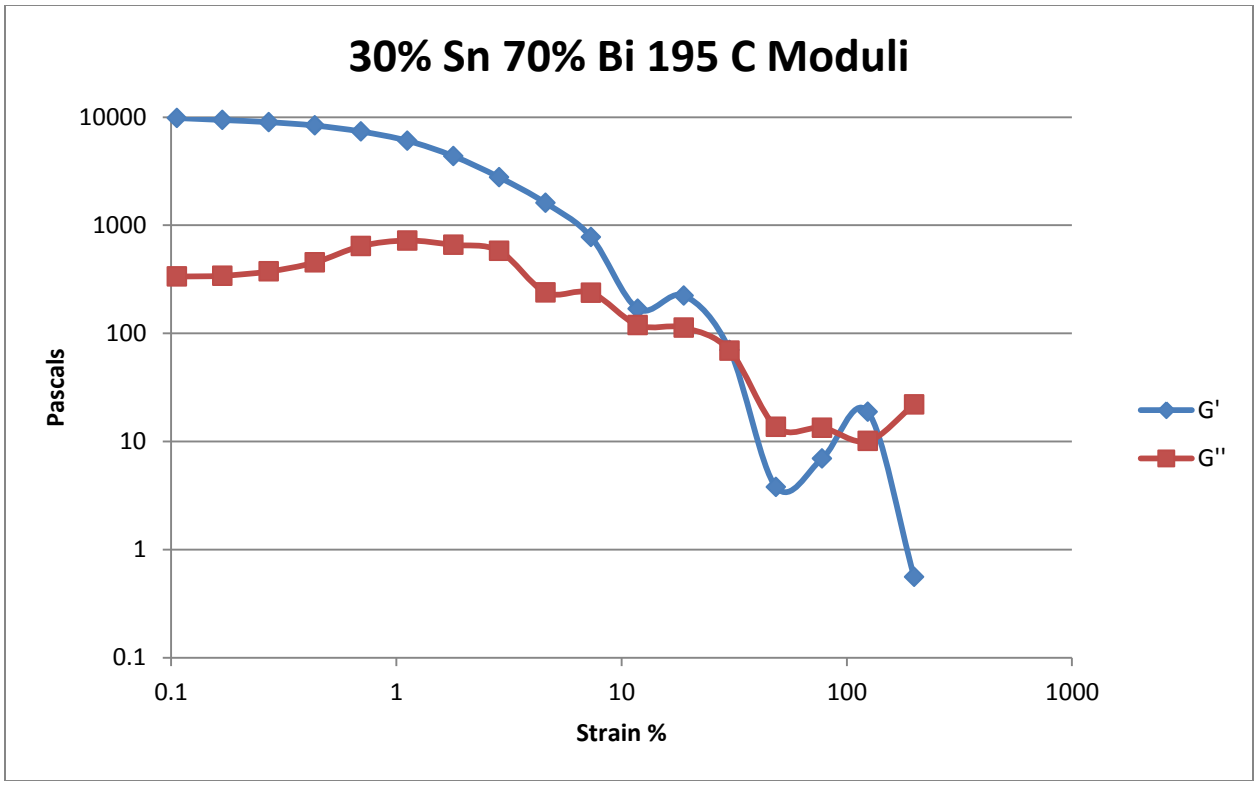

Figure 471- 30% Tin 70% Bismuth, 195 C, Oscillatory Shear Moduli

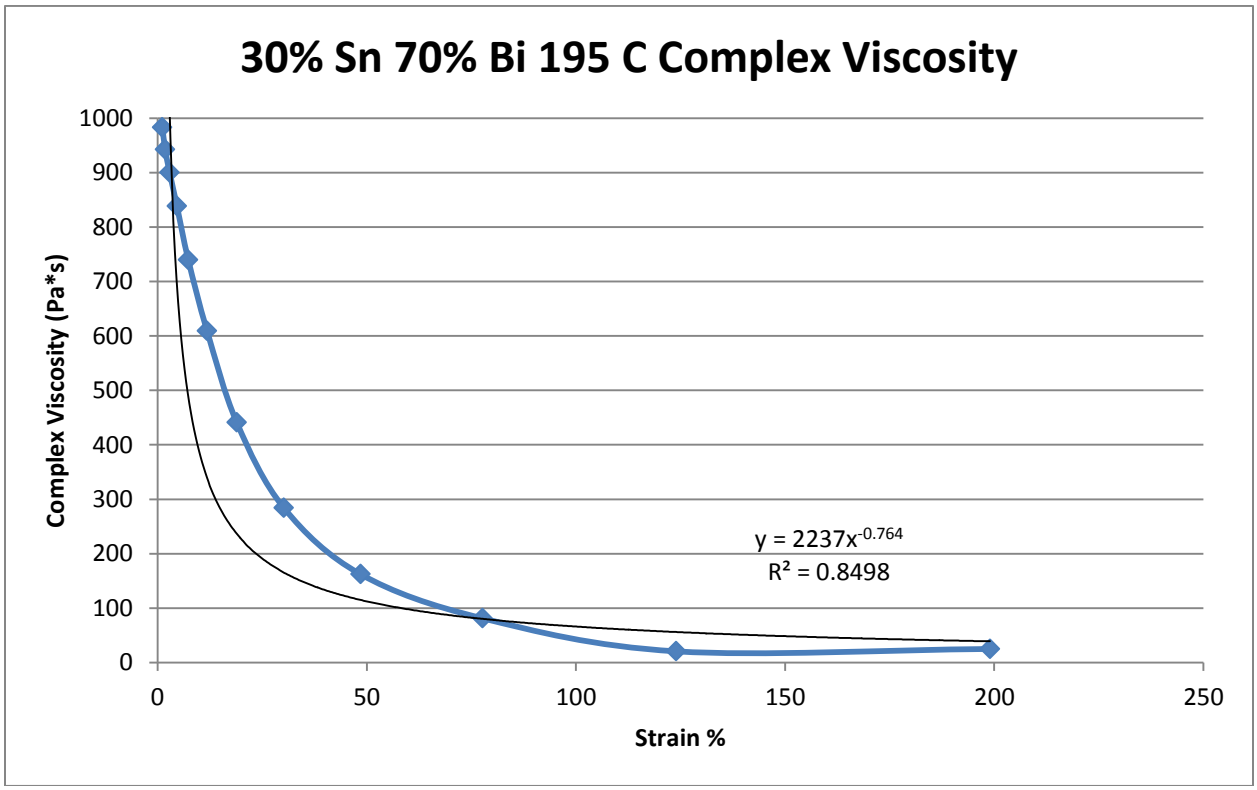

Figure 472- 30% Tin 70% Bismuth, 195 C, Oscillatory Shear Complex Viscosity

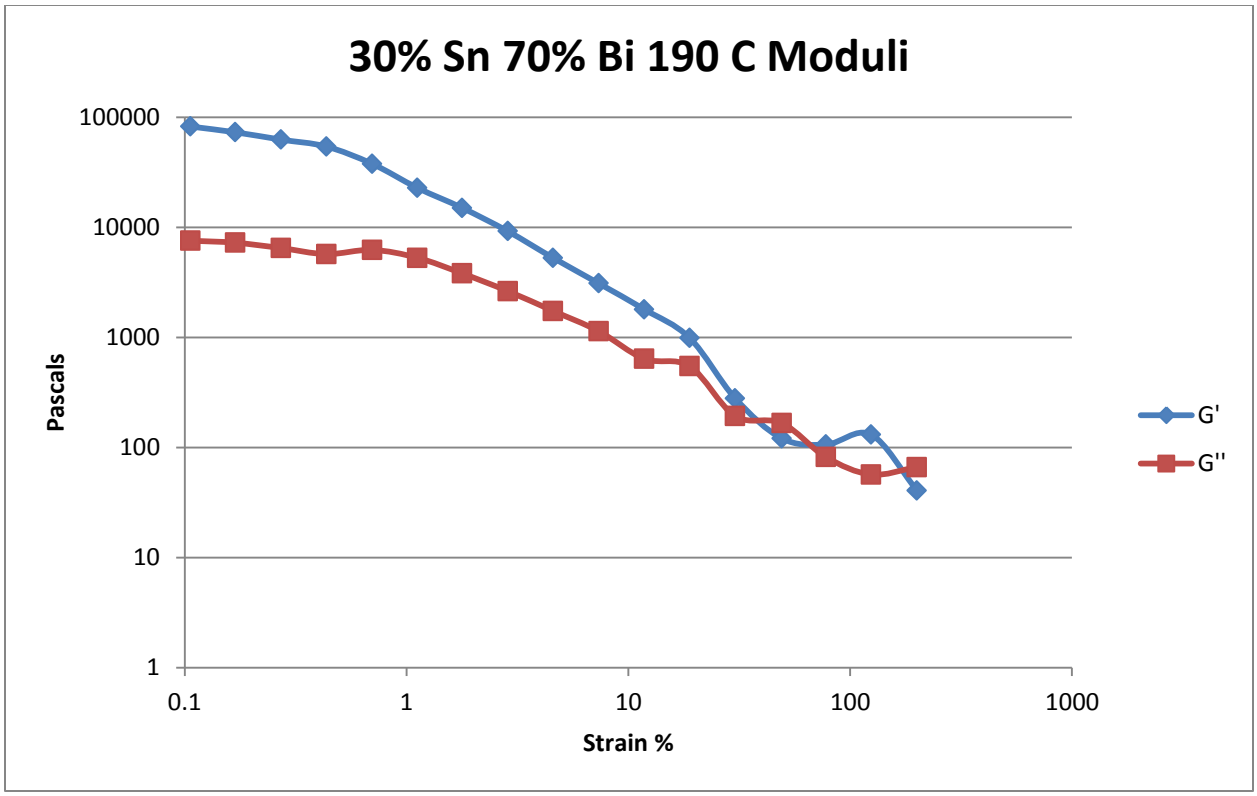

Figure 473- 30% Tin 70% Bismuth, 190 C, Oscillatory Shear Moduli

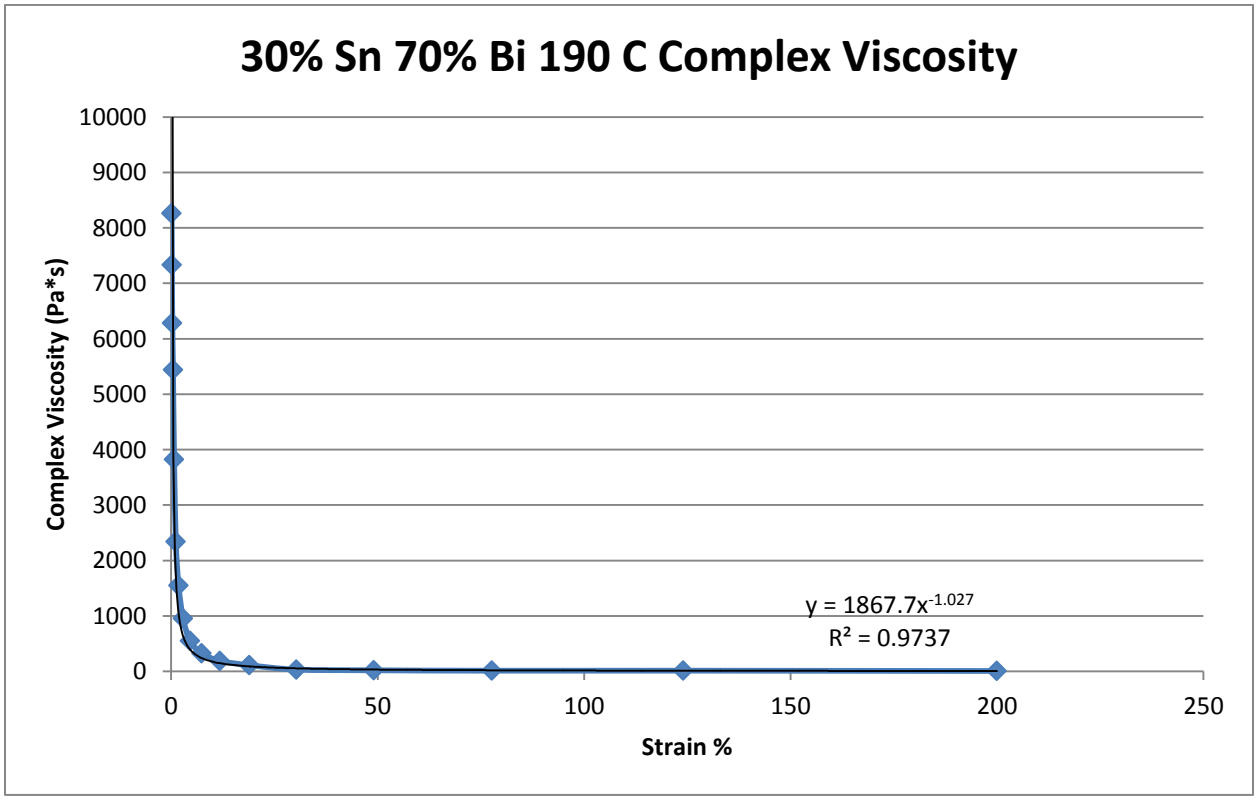

Figure 474- 30% Tin 70% Bismuth, 190 C, Oscillatory Shear Complex Viscosity

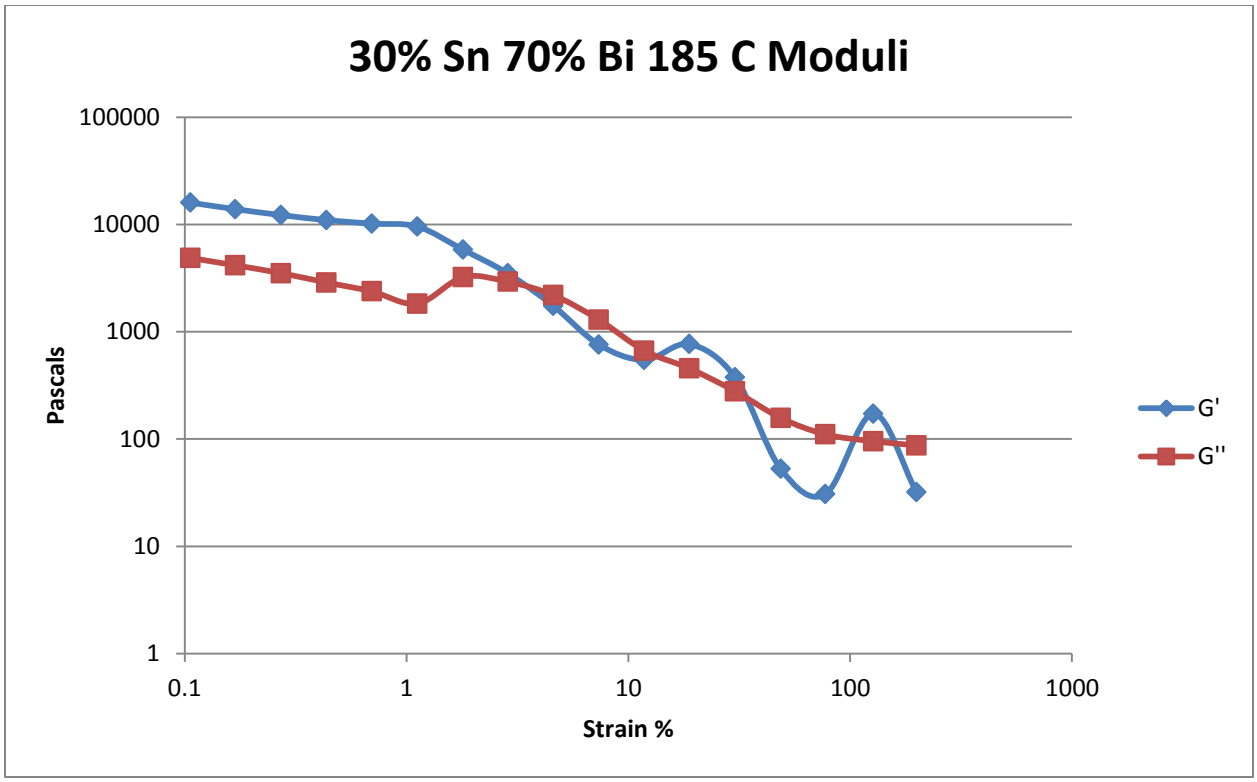

Figure 475- 30% Tin 70% Bismuth, 185 C, Oscillatory Shear Moduli

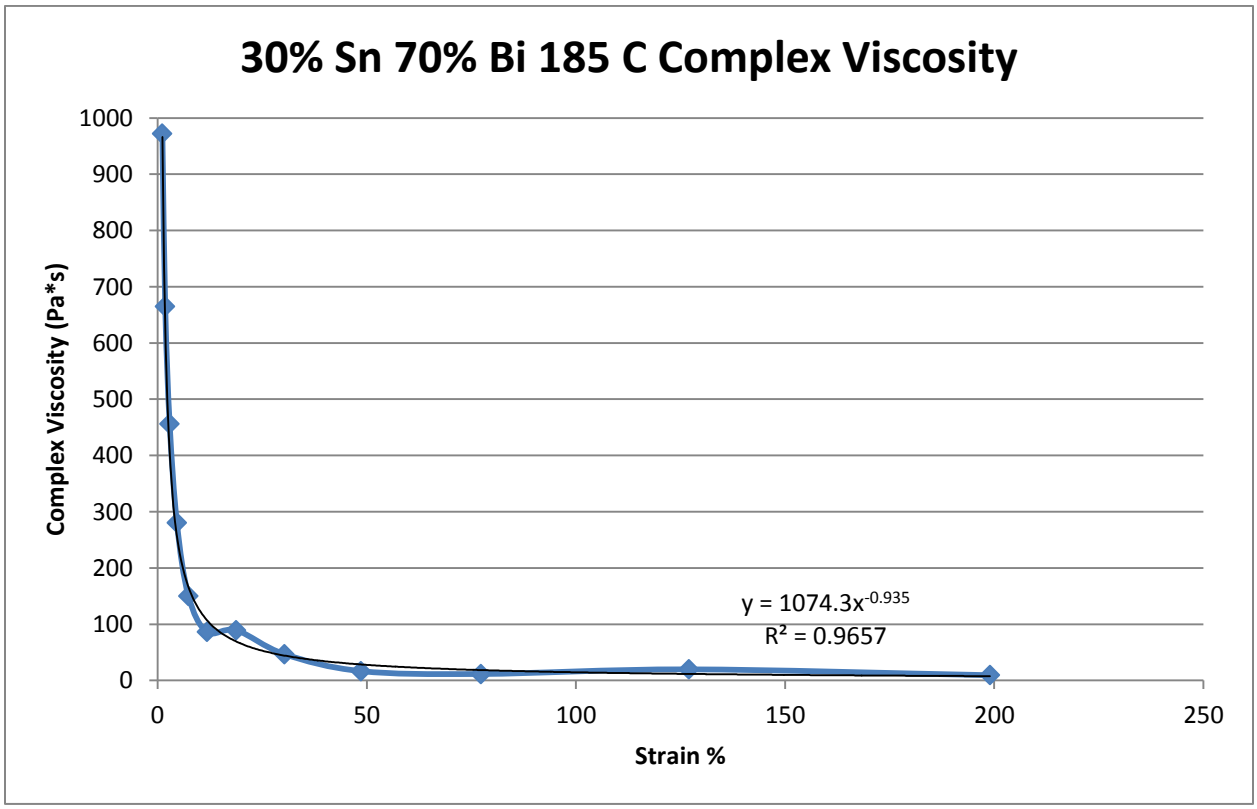

Figure 476- 30% Tin 70% Bismuth, 185 C, Oscillatory Shear Complex Viscosity

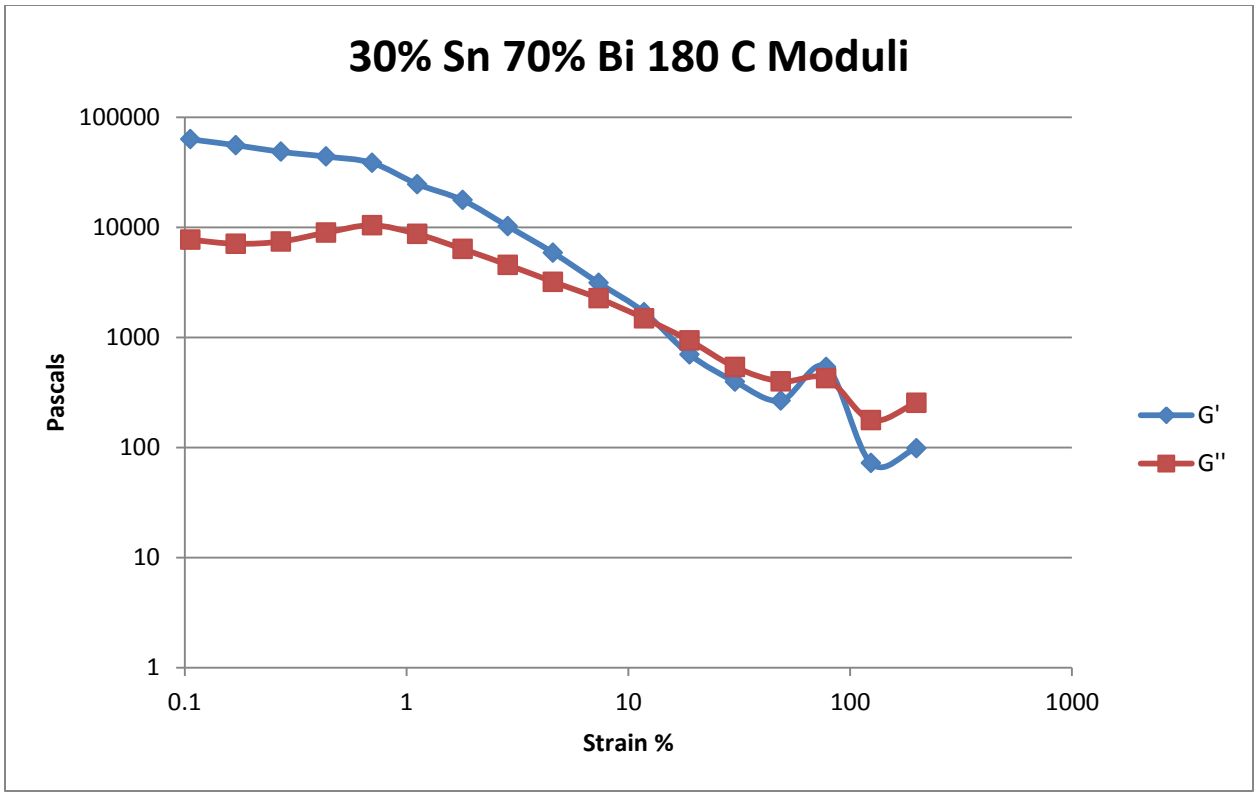

Figure 477- 30% Tin 70% Bismuth, 180 C, Oscillatory Shear Moduli

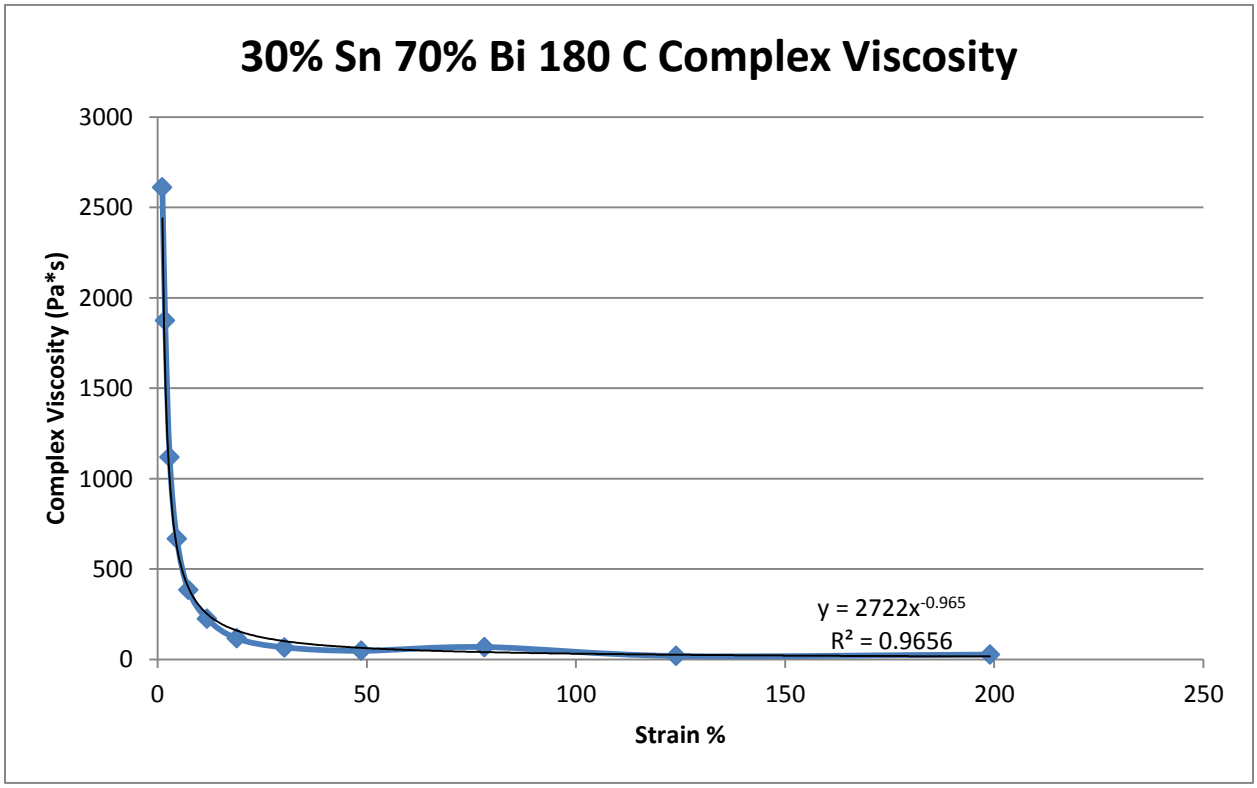

Figure 478- 30% Tin 70% Bismuth, 180 C, Oscillatory Shear Complex Viscosity

40% Tin 60% Bismuth

Predicted Composition: 42% Sn 58% Bi

Theoretical Solidus Line: 139 C
Theoretical Liquidus Line: 173.9 C

Experimental Solidus Line: 139.6 C
Experimental Liquidus Line: 177.3 C

Pre-Shear: 15 RPM, 2 minutes
Angular Velocity: Constant, 10 rad/s
Strain Range: 0.01%-200%

40% Tin 60% Bismuth Oscillatory Shear Rheology								
Temperature (C)	**Fraction Solid (%)**	**Crossover Strain (%)**	**Crossover Stress (Pa)**	**Crossover Modulus (Pa)**	**Crossover Complex Viscosity (Pa*s)**	**Pre G' Plateau (Pa)**	**Pre G'' Plateau (Pa)**	**Final Complex Viscosity (Pa*s)**
190	0	4.09	0.077	1.34	0.192	3.93	1.42	0.019
185	0	9.70	0.165	1.20	0.175	8.47	1.33	0.019
180	0	8.97	0.168	1.32	0.190	7.78	1.39	0.021
175	0	7.75	0.190	1.75	0.244	11.7	2.11	0.020
170	3.81	8.31	0.220	1.79	0.025	11.3	1.89	0.022
165	8.35	13.3	0.220	1.19	0.156	18.6	1.29	0.025

Table 87- 40% Tin 60% Bismuth Oscillatory Shear Rheology

40% Tin 60% Bismuth Oscillatory Shear Complex Viscosity			
Temperature (C)	**Fraction Solid (%)**	**Power Law Equation**	**R^2 (%)**
190	0	$\eta^* = 0.4347\gamma^{-0.666}$	97.68
185	0	$\eta^* = 1.0549\gamma^{-0.842}$	97.17
180	0	$\eta^* = 0.9077\gamma^{-0.788}$	95.87
175	0	$\eta^* = 1.4497\gamma^{-0.919}$	96.37
170	3.81	$\eta^* = 0.1868\gamma^{-0.899}$	96.82
165	8.35	$\eta^* = 1.9777\gamma^{-0.918}$	96.39

Table 88- 40% Tin 60% Bismuth Oscillatory Shear Complex Viscosity

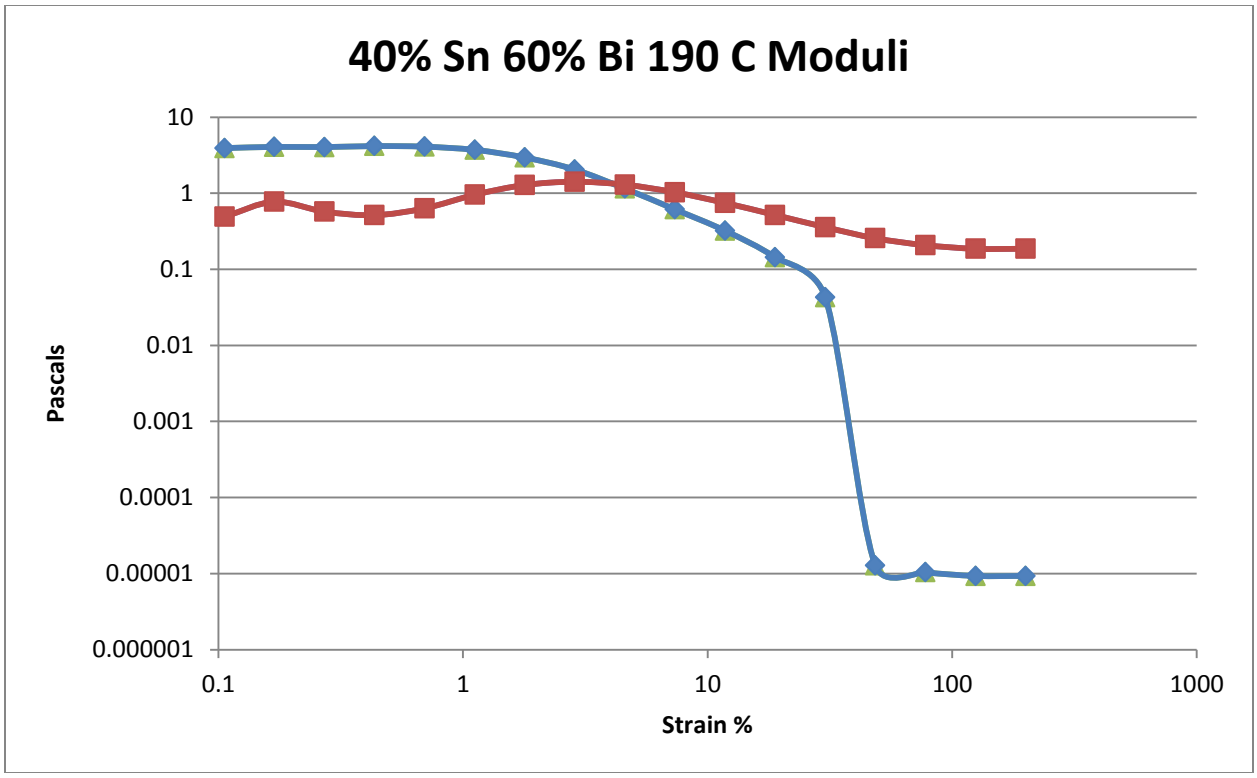

Figure 479- 40% Tin 60% Bismuth, 190 C, Oscillatory Shear Moduli

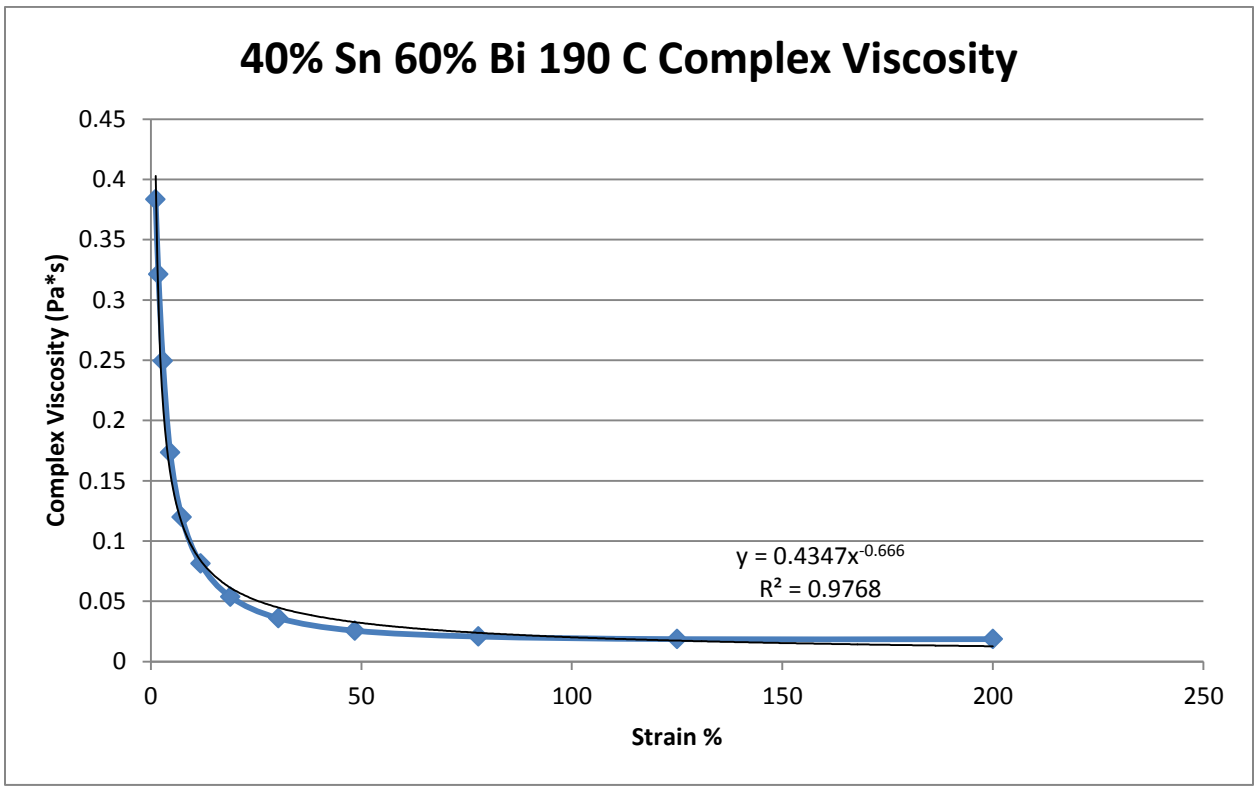

Figure 480- 40% Tin 60% Bismuth, 190 C, Oscillatory Shear Complex Viscosity

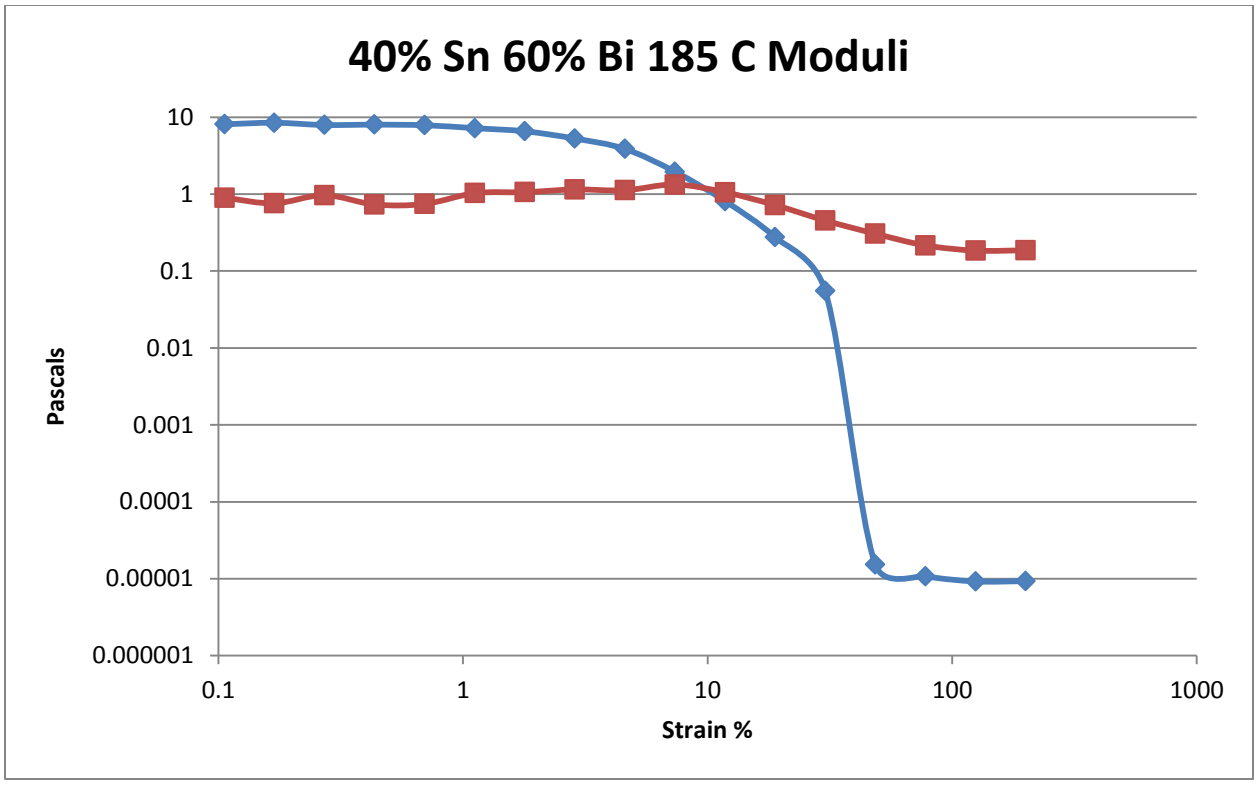

Figure 481- 40% Tin 60% Bismuth, 185 C, Oscillatory Shear Moduli

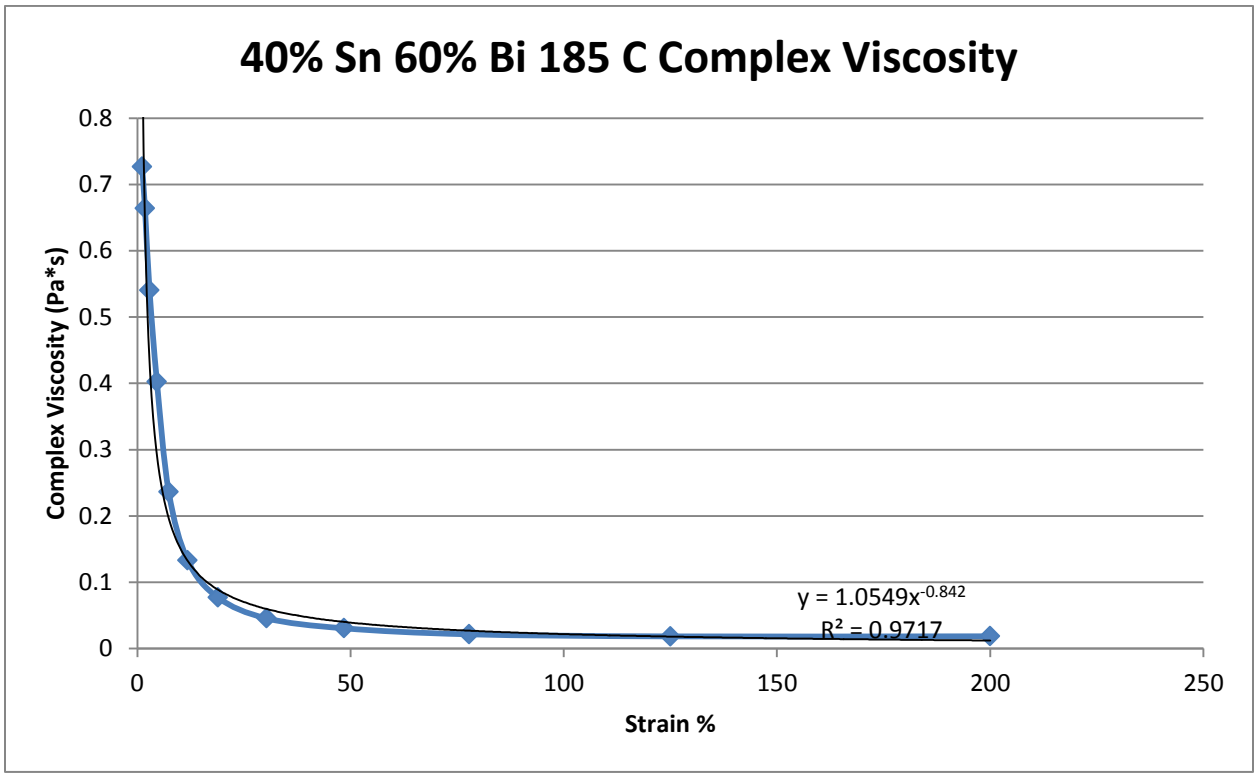

Figure 482- 40% Tin 60% Bismuth, 185 C, Oscillatory Shear Complex Viscosity

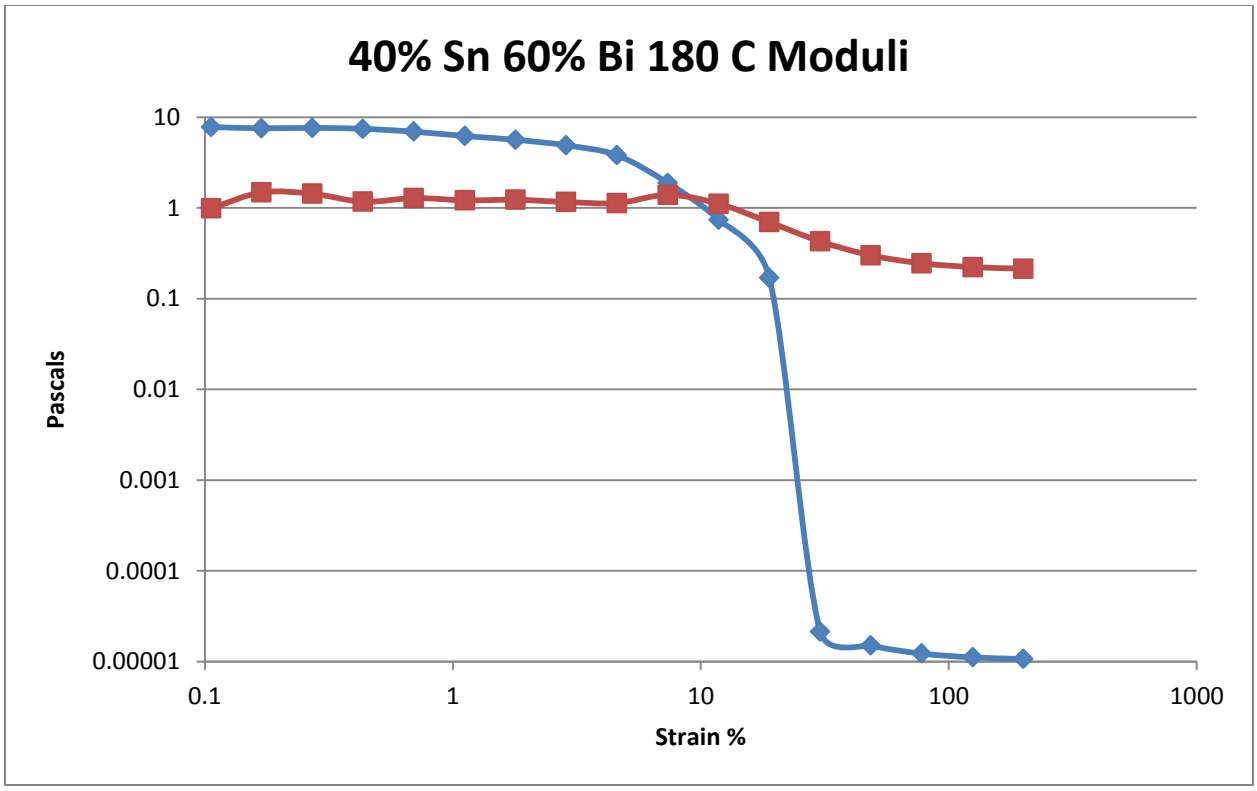

Figure 483- 40% Tin 60% Bismuth, 180 C, Oscillatory Shear Moduli

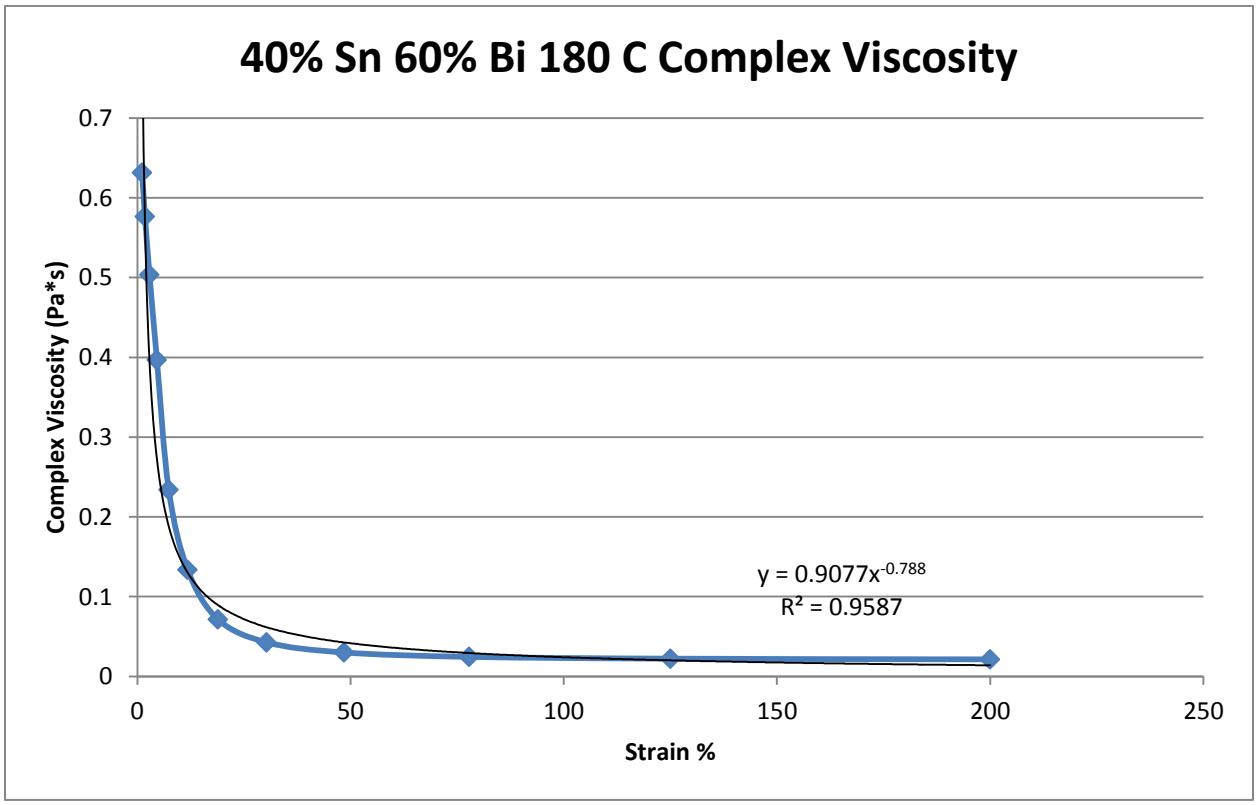

Figure 484- 40% Tin 60% Bismuth, 180 C, Oscillatory Shear Complex Viscosity

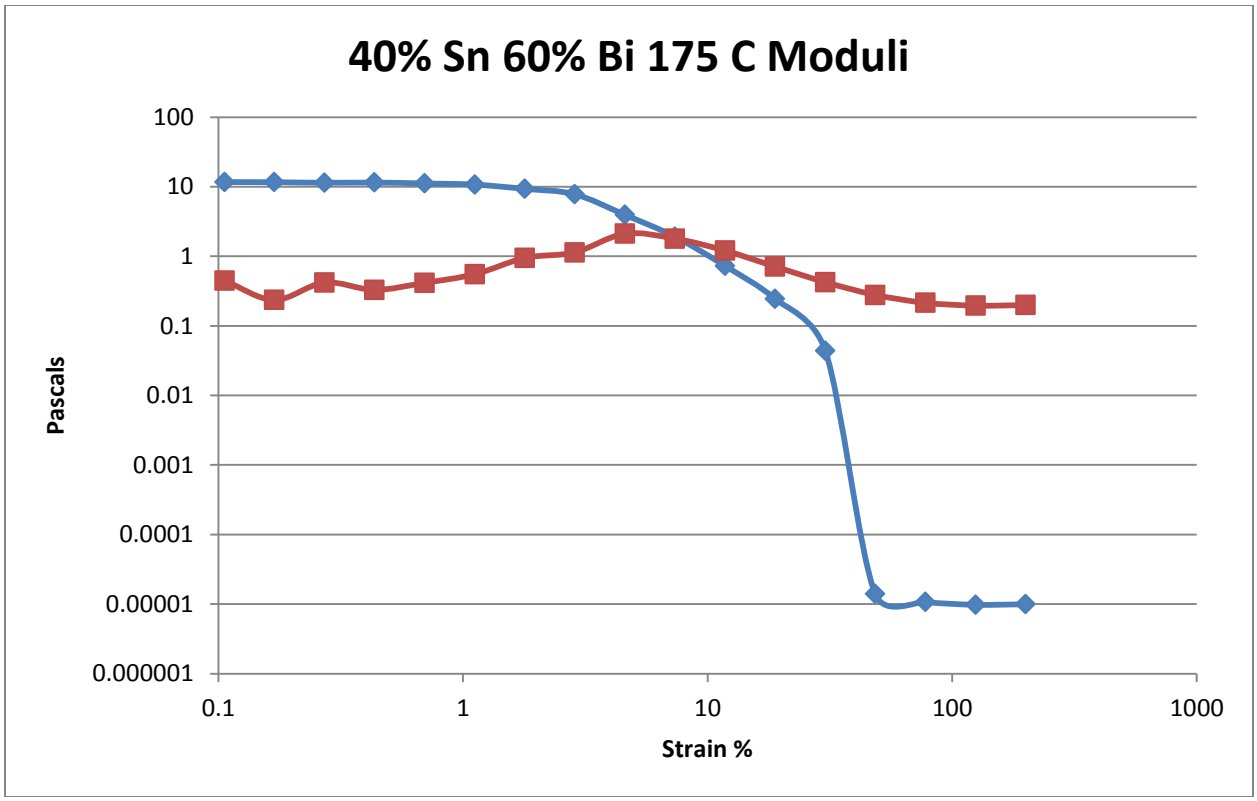

Figure 485- 40% Tin 60% Bismuth, 175 C, Oscillatory Shear Moduli

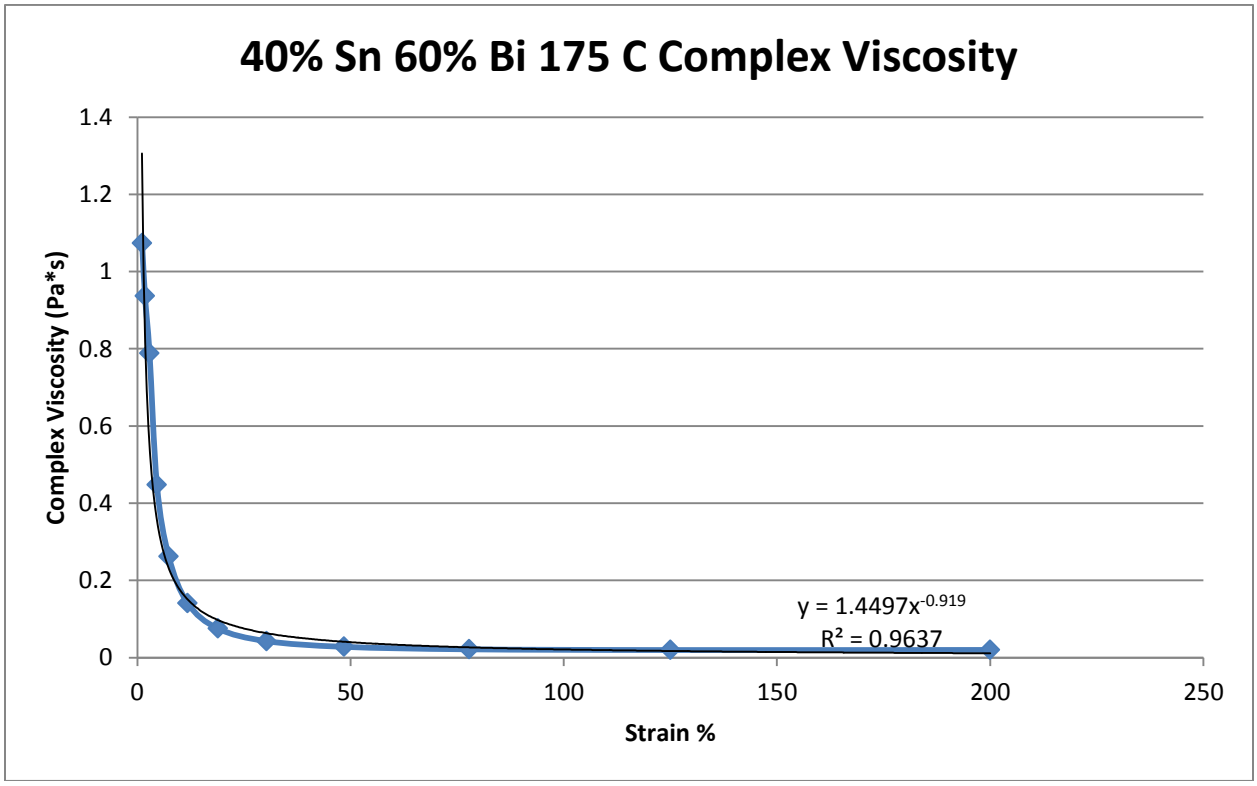

Figure 486- 40% Tin 60% Bismuth, 175 C, Oscillatory Shear Complex Viscosity

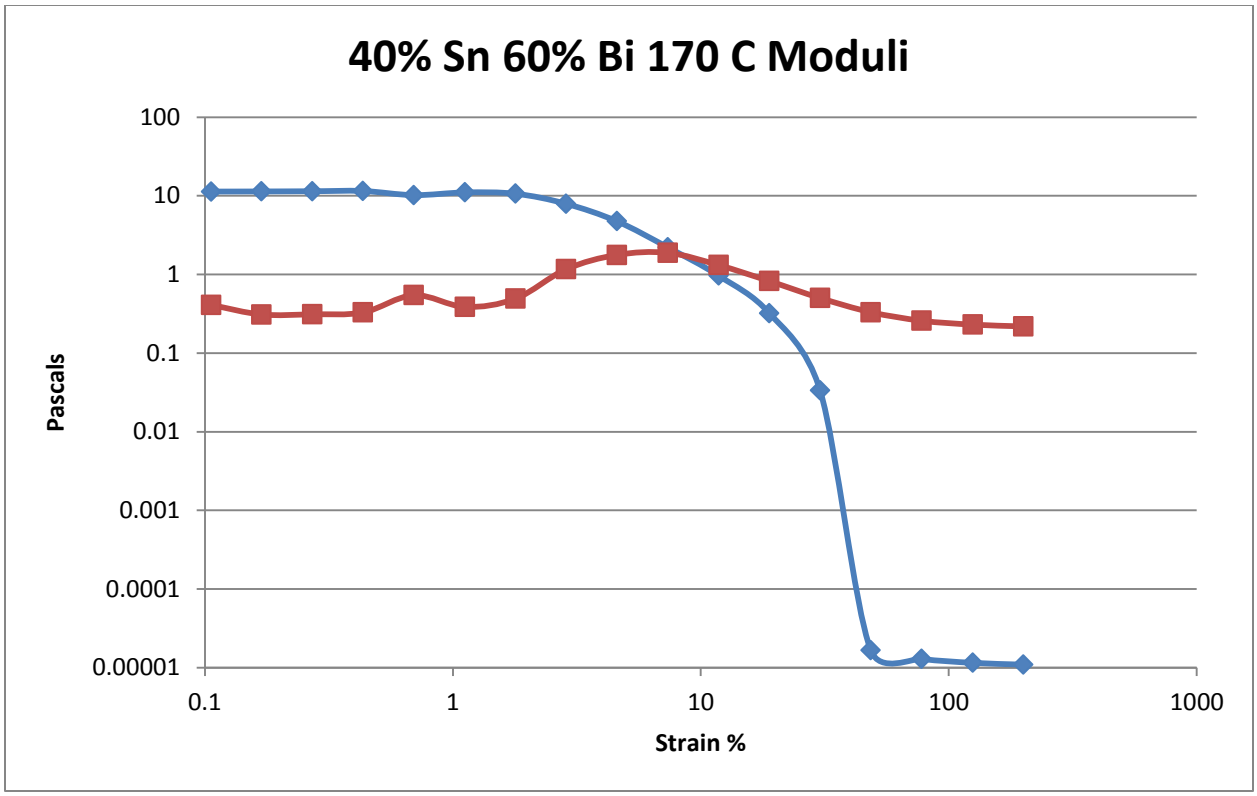

Figure 487- 40% Tin 60% Bismuth, 170 C, Oscillatory Shear Moduli

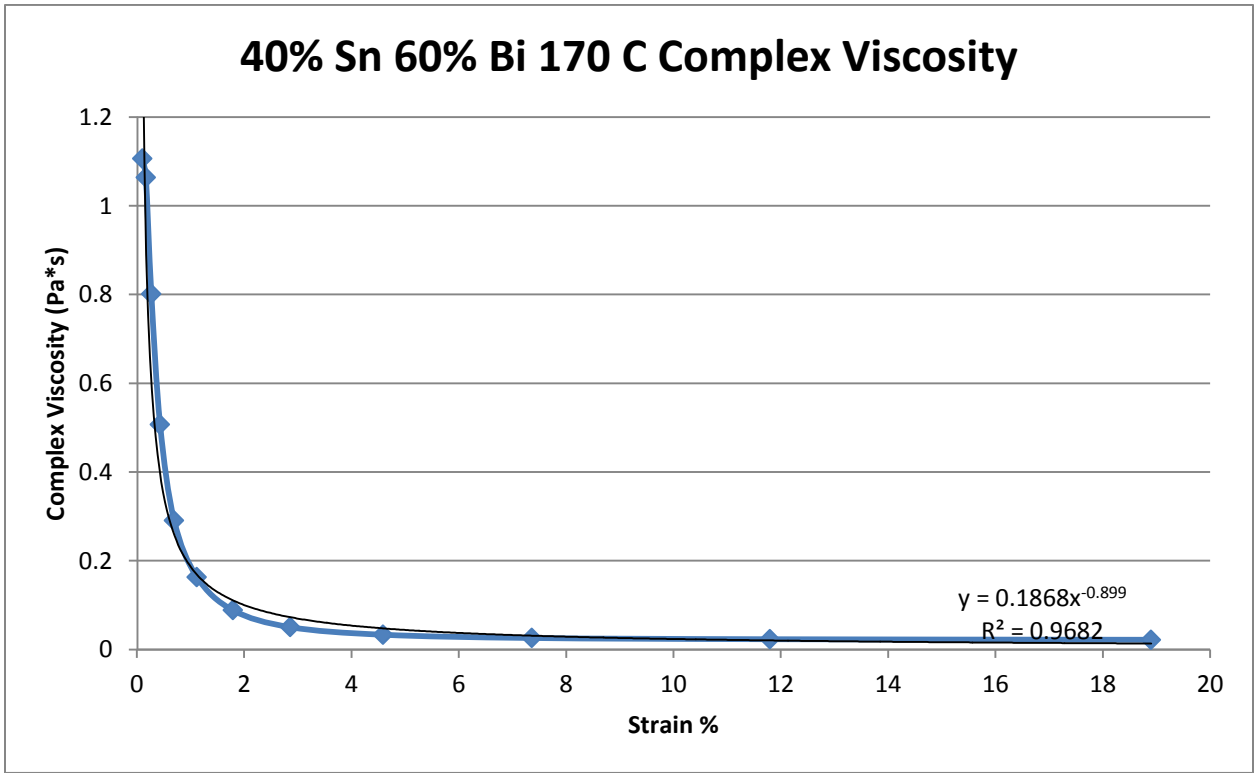

Figure 488- 40% Tin 60% Bismuth, 170 C, Oscillatory Shear Complex Viscosity

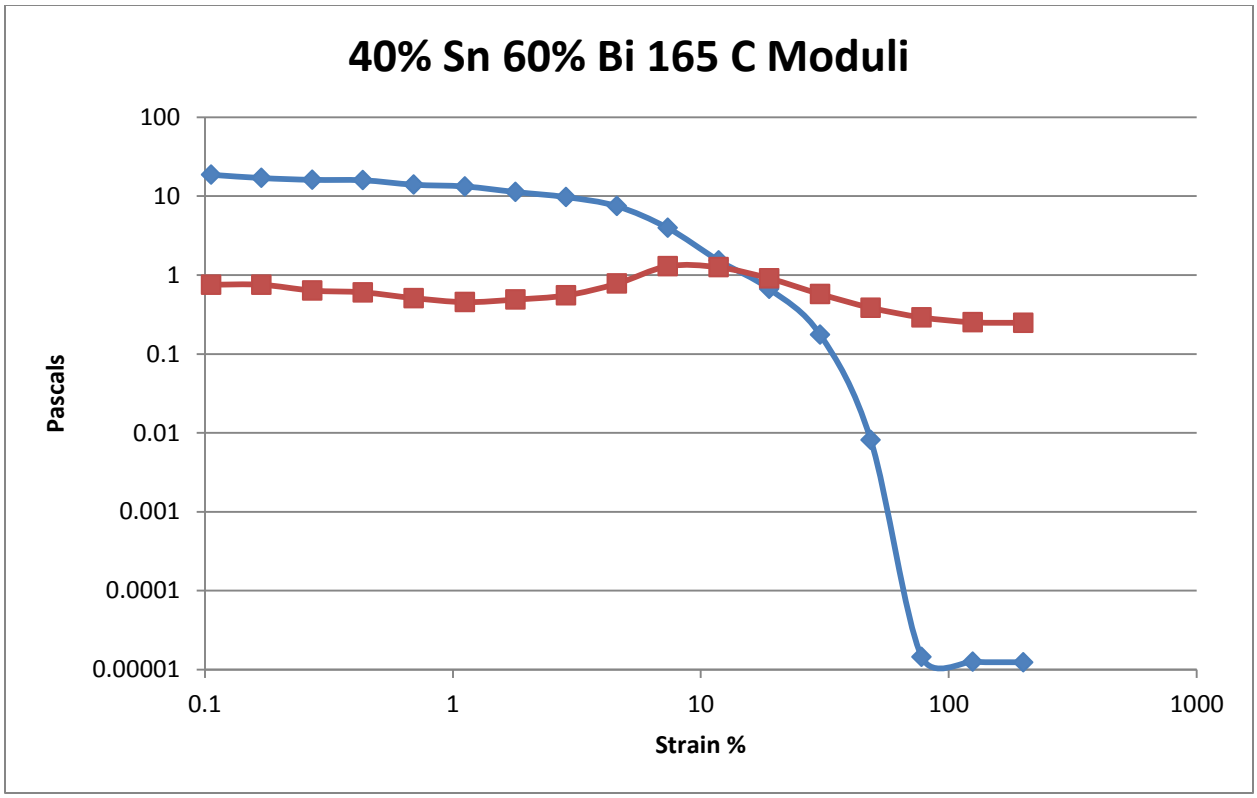

Figure 489- 40% Tin 60% Bismuth, 165 C, Oscillatory Shear Moduli

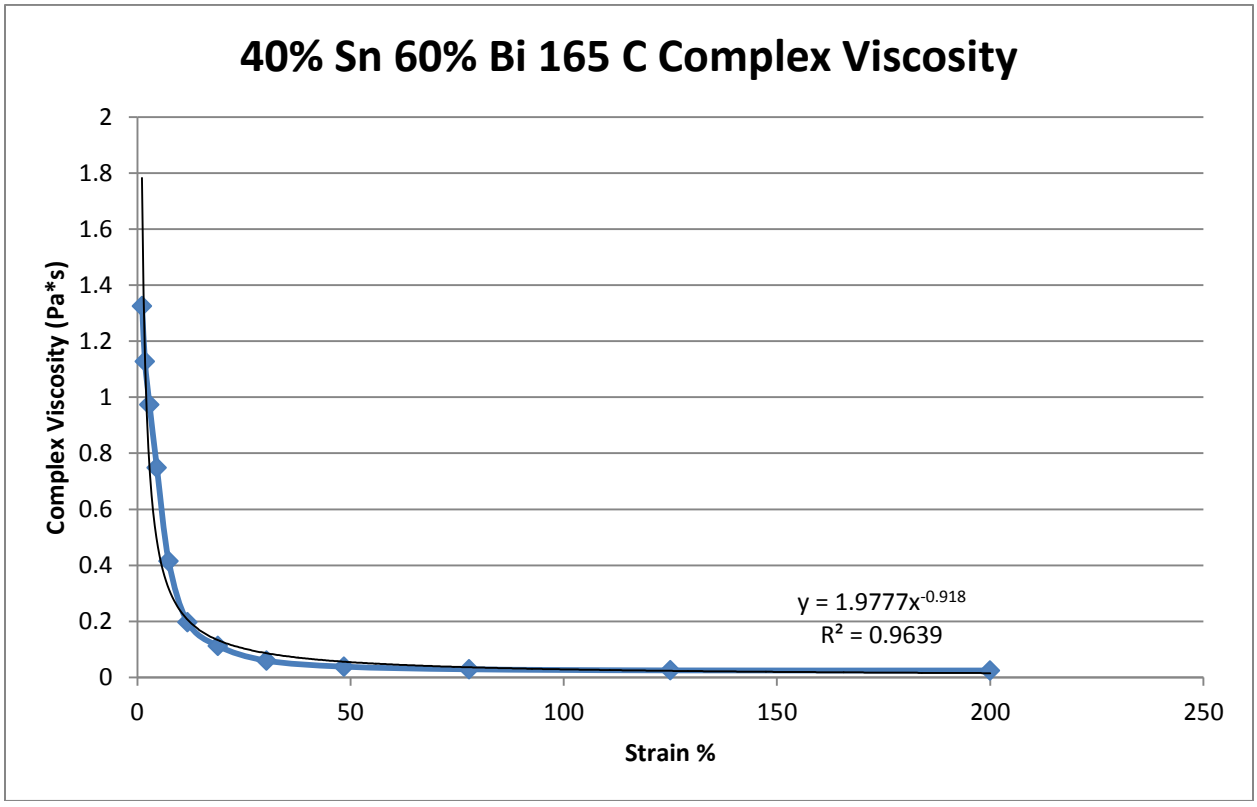

Figure 490- 40% Tin 60% Bismuth, 165 C, Oscillatory Shear Complex Viscosity

50% Tin 50% Bismuth

Actual Composition: 52.94% Sn, 47.06% Bi

Theoretical Solidus Line: 139 C
Theoretical Liquidus Line: 148.8 C

Experimental Solidus Line: 141.9 C
Experimental Liquidus Line: 151.5 C

Pre-Shear: None
Angular Velocity: Constant, 10 rad/s
Strain Range: 0.001%-10%

This test revealed a pre-shear is necessary before each sweep to eliminate dendrites. These tests were also only conducted up to 10% strain. Future tests were all carried to 200%.

50% Tin 50% Bismuth Oscillatory Shear Rheology								
Temperature (C)	**Fraction Solid (%)**	**Crossover Strain (%)**	**Crossover Stress (Pa)**	**Crossover Modulus (Pa)**	**Crossover Complex Viscosity (Pa*s)**	**Pre G' Plateau (Pa)**	**Pre G'' Plateau (Pa)**	**Final Complex Viscosity (Pa*s)**
170	0	0.142	0.182	0.96	225.5	12.5	1.82	24.2
165	0	0.113	0.158	0.99	242.0	9.56	1.38	26.8
160	0	0.165	0.188	0.82	115.0	10.4	1.41	24.3
155	1.00	0.145	0.181	0.90	125.6	8.93	1.32	26.4
150	4.81	0.172	0.195	0.82	115.6	11.6	1.26	27.2
145	8.33	0.140	0.195	0.99	140.5	13.6	1.55	30.4
144	9.42	0.140	0.242	1.22	172.2	14.4	1.40	32.1
142	10.5	0.840	0.600	0.48	262.8	20.9	6.77	31.5
140	11.6	1.76	1.70	0.75	102.3	7300	2654	41.3
138	100	N/A	N/A	N/A	N/A	2.69e4	2.02e4	6.35e5
136	100	N/A	N/A	N/A	N/A	1.22e4	8782	2.43e5

Table 89- 50% Tin 50% Bismuth Oscillatory Shear Rheology

10% Tin 90% Bismuth Oscillatory Shear Complex Viscosity			
Temperature (C)	**Fraction Solid (%)**	**Power Law Equation**	**R^2 (%)**
170	0	$\eta^* = 44.269\gamma^{-0.552}$	75.17
165	0	$\eta^* = 41.242\gamma^{-0.484}$	69.37
160	0	$\eta^* = 38.925\gamma^{-0.406}$	67.99
155	1.00	$\eta^* = 40.222\gamma^{-0.404}$	76.90
150	4.81	$\eta^* = 42.373\gamma^{-0.432}$	77.61
145	8.33	$\eta^* = 43.964\gamma^{-0.389}$	73.10
144	9.42	$\eta^* = 51.434\gamma^{-0.437}$	77.19
142	10.5	$\eta^* = 92.495\gamma^{-0.755}$	82.53
140	11.6	$\eta^* = 858.4\gamma^{-1.817}$	89.84
138	100	$\eta^* = 562965\gamma^{-0.856}$	98.43
136	100	$\eta^* = 353665\gamma^{-0.583}$	97.30

Table 90- 10% Tin 90% Bismuth Oscillatory Shear Complex Viscosity

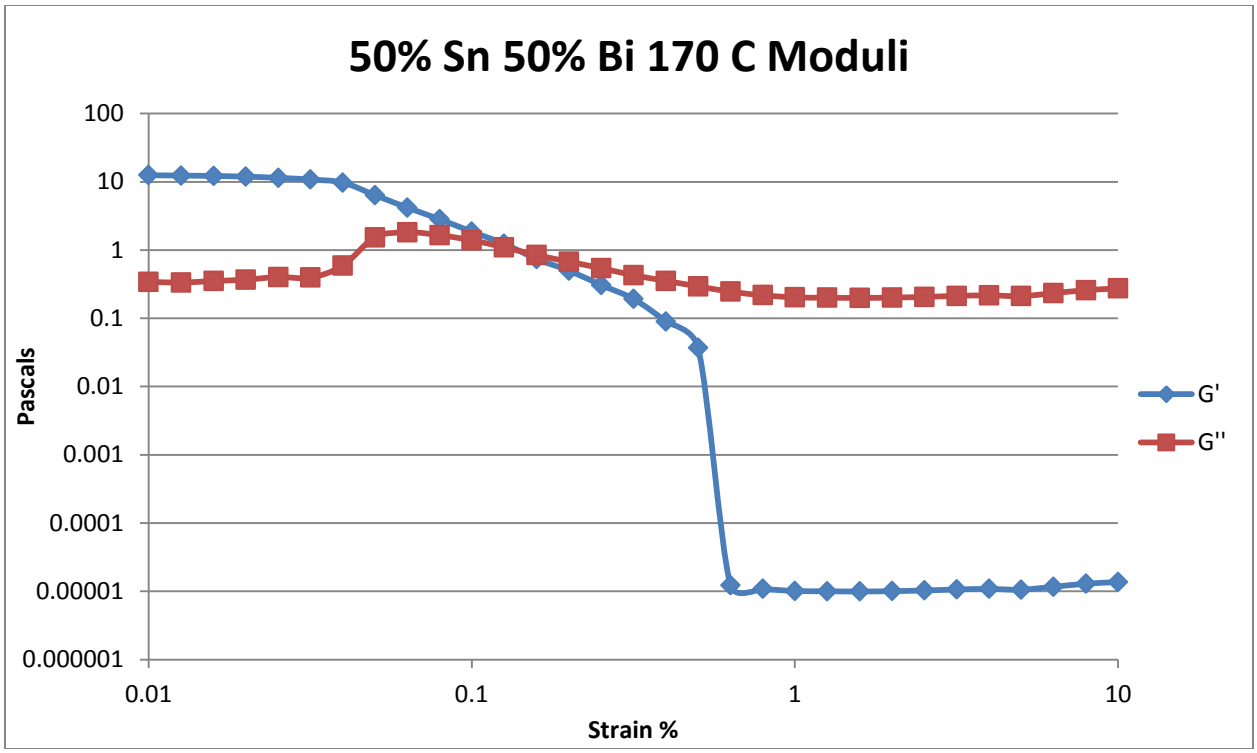

Figure 491- 50% Sn 50% Bi, 170 C, Oscillatory Shear Moduli

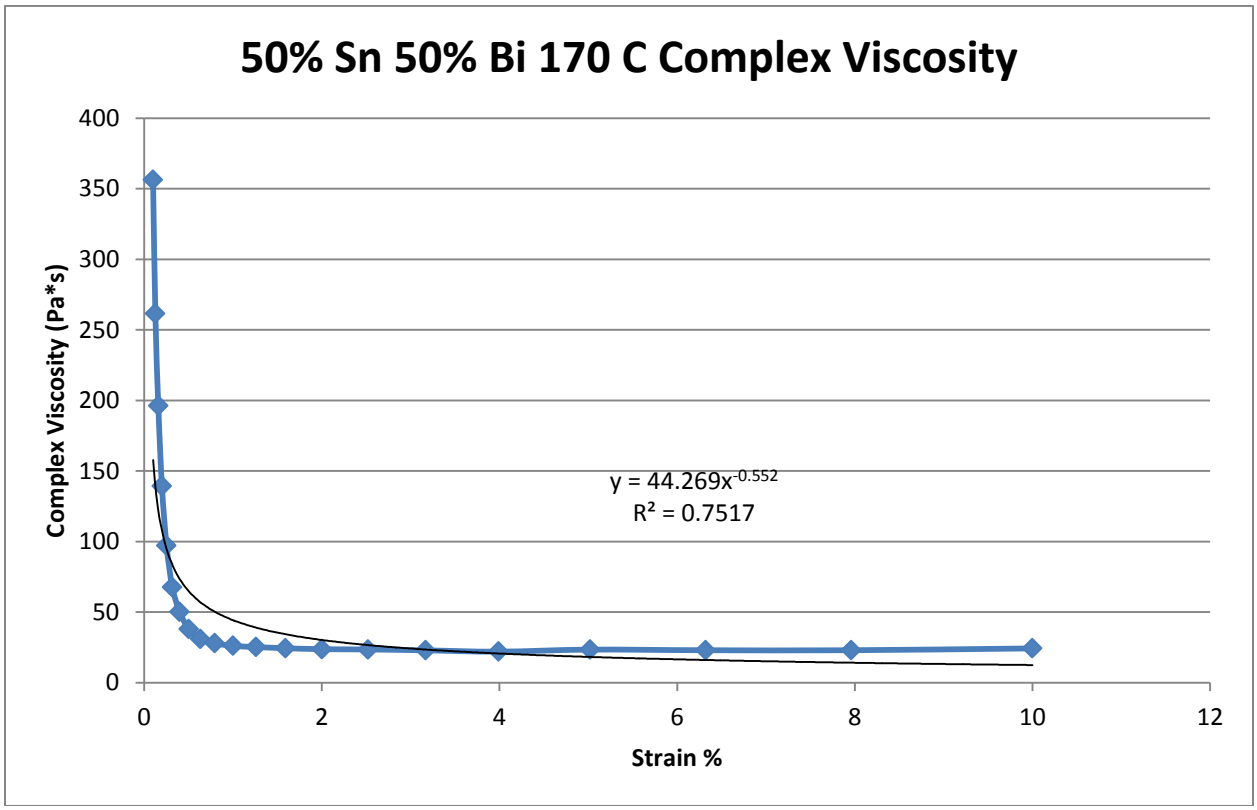

Figure 492- 50% Sn 50% Bi, 170 C, Oscillatory Shear Complex Viscosity

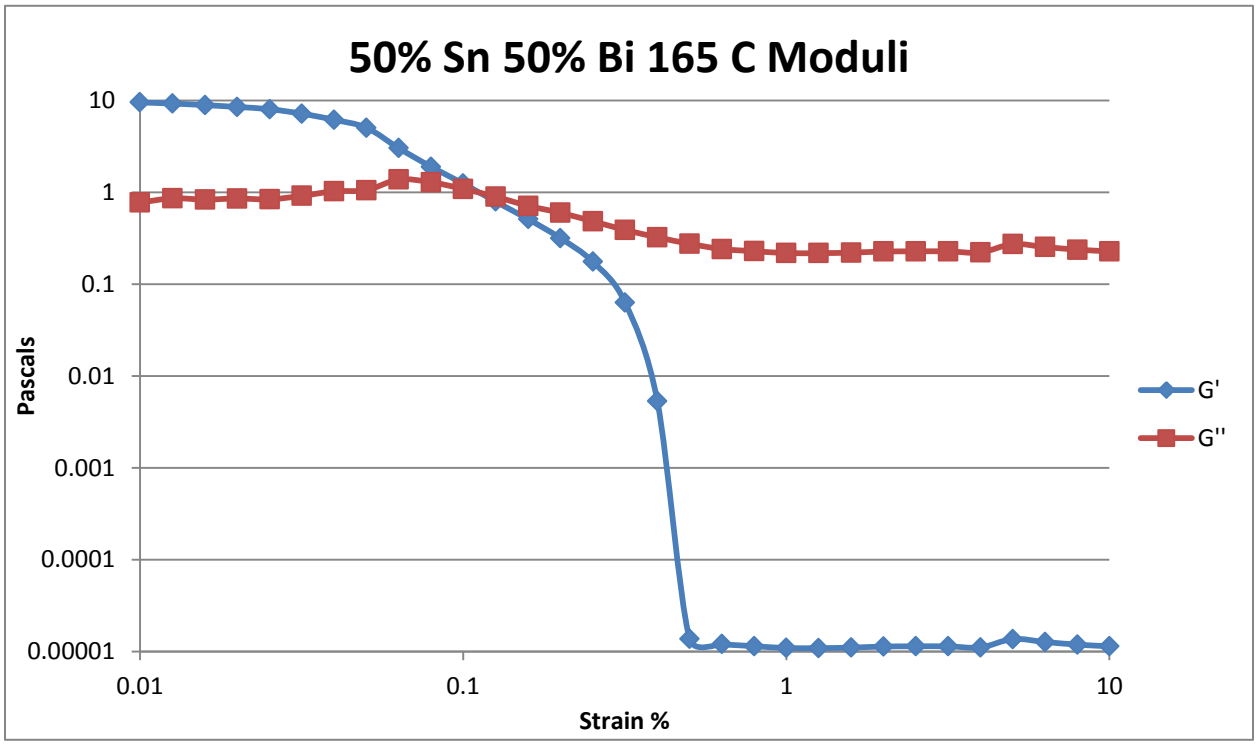

Figure 493- 50% Sn 50% Bi, 165 C, Oscillatory Shear Moduli

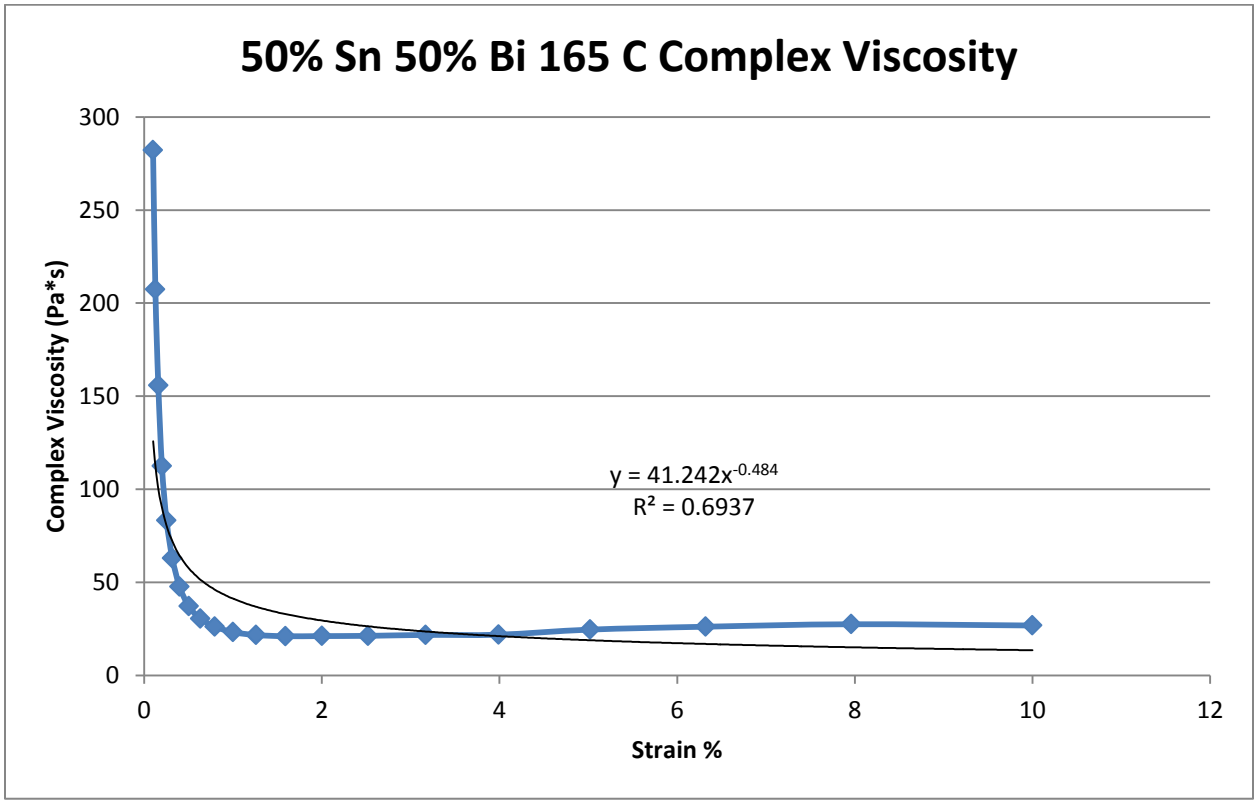

Figure 494- 50% Sn 50% Bi, 165 C, Oscillatory Shear Complex Viscosity

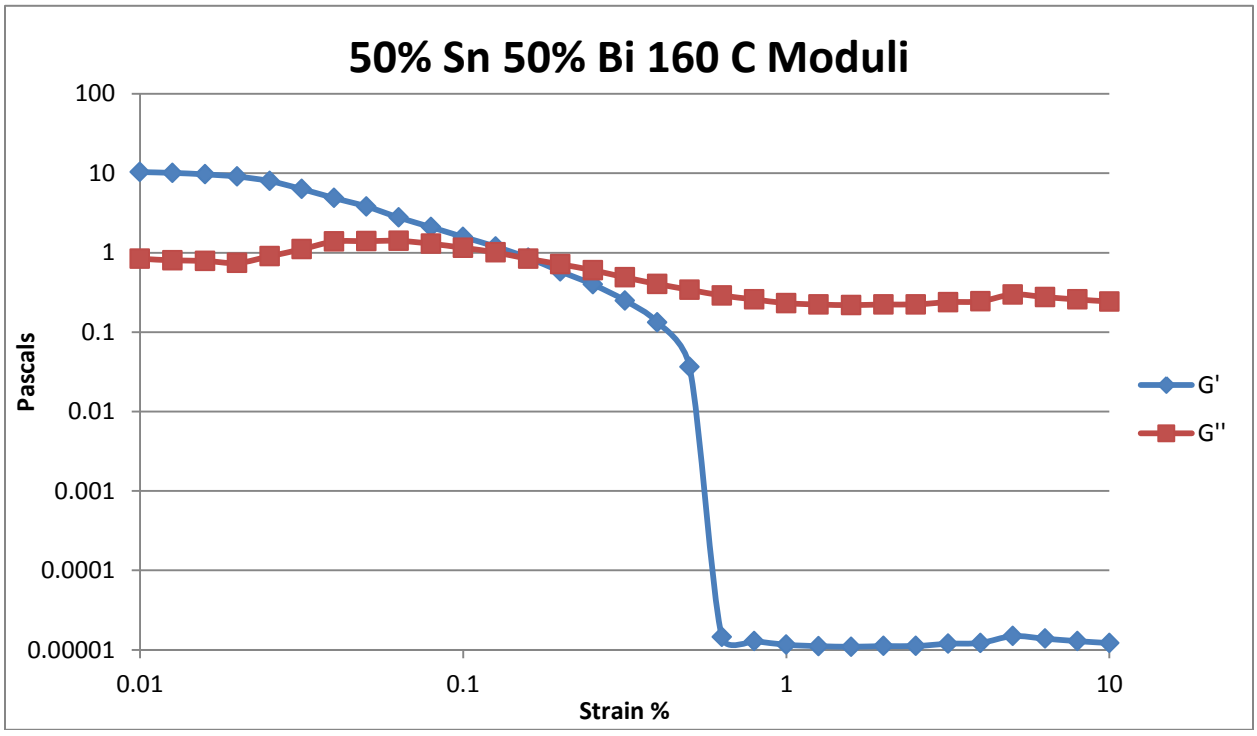

Figure 495- 50% Sn 50% Bi, 160 C, Oscillatory Shear Moduli

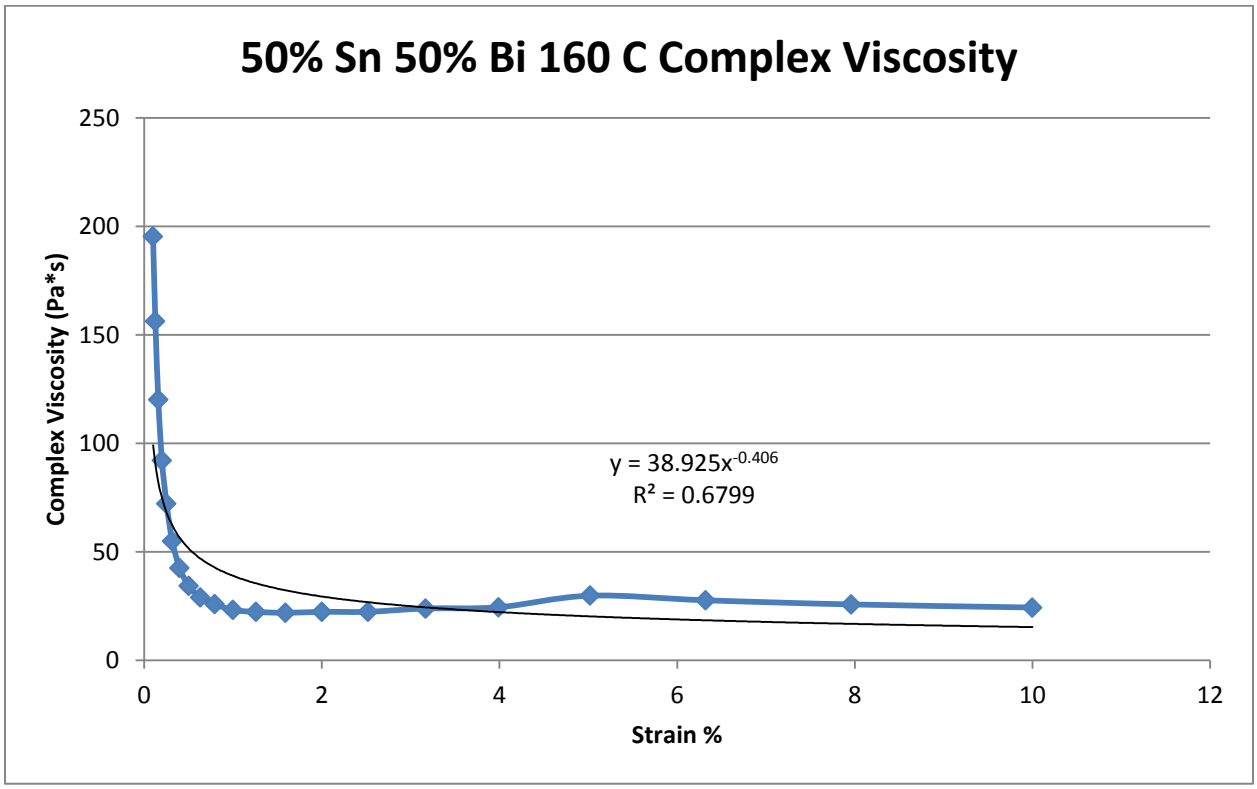

Figure 496- 50% Sn 50% Bi, 160 C, Oscillatory Shear Complex Viscosity

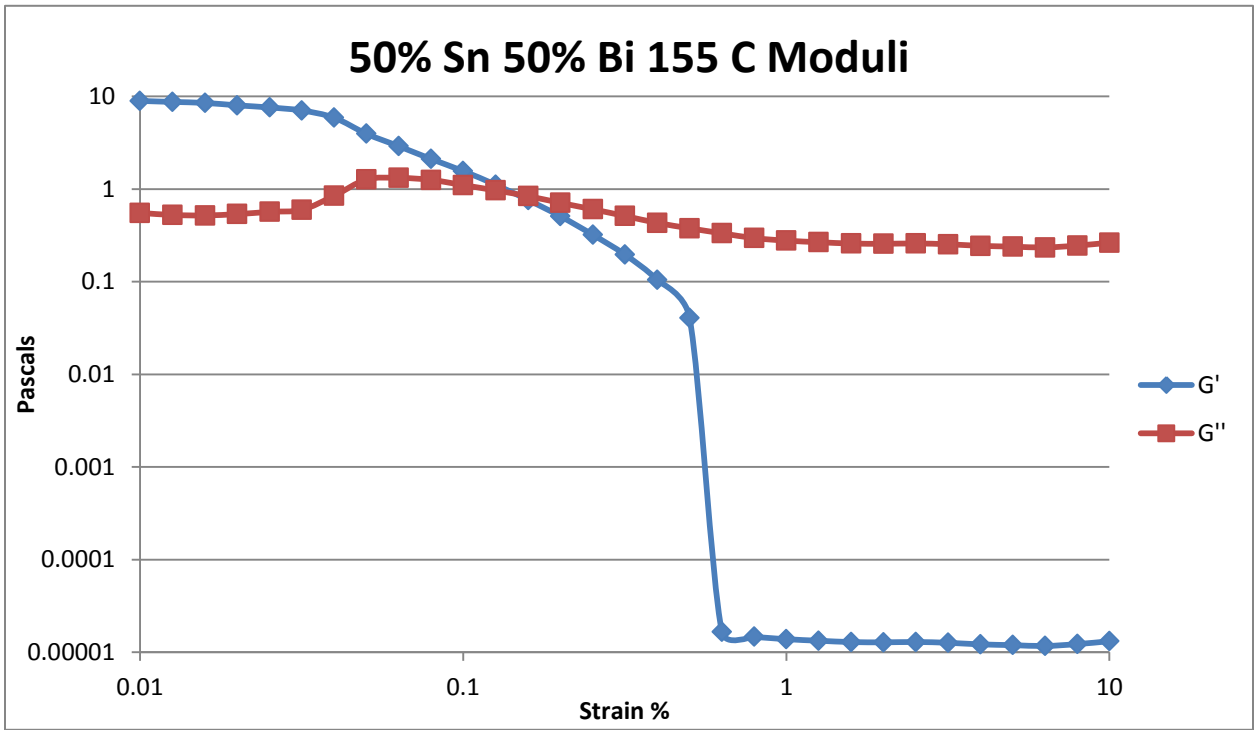

Figure 497- 50% Sn 50% Bi, 155 C, Oscillatory Shear Moduli

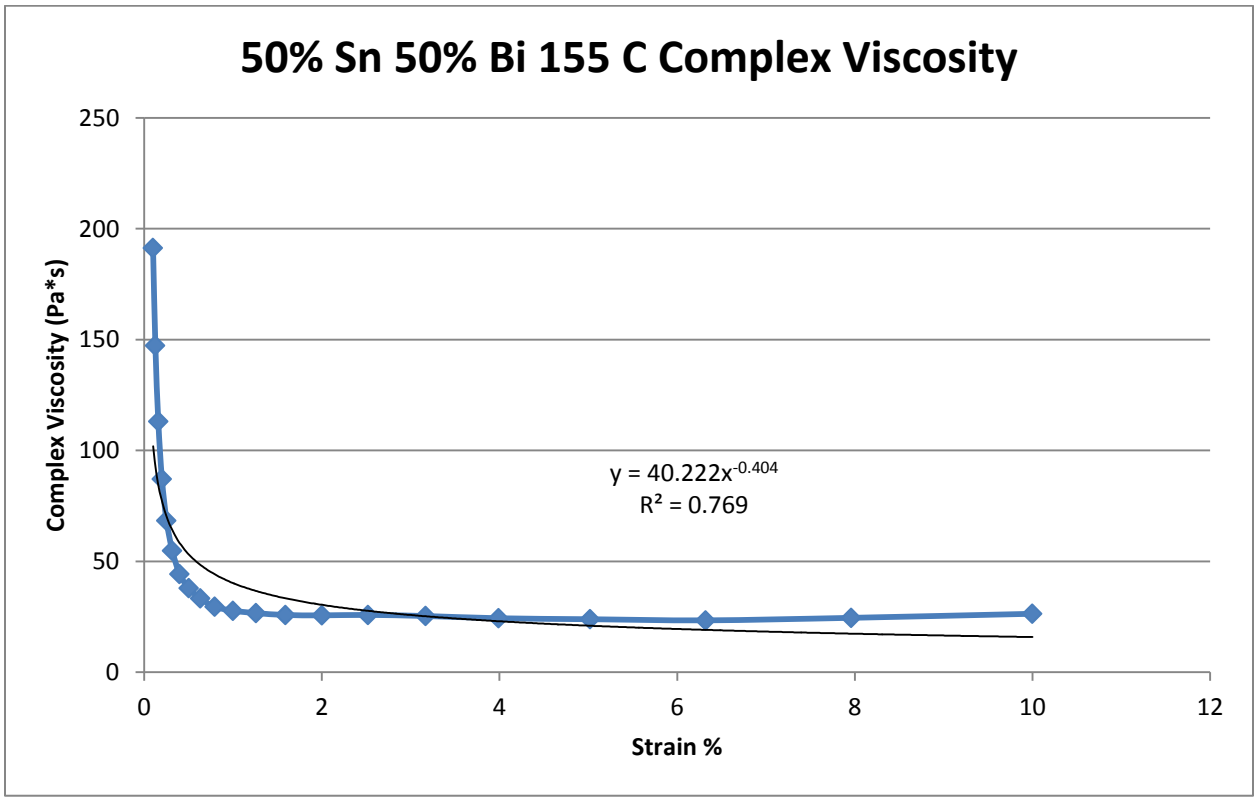

Figure 498- 50% Sn 50% Bi, 155 C, Oscillatory Shear Complex Viscosity

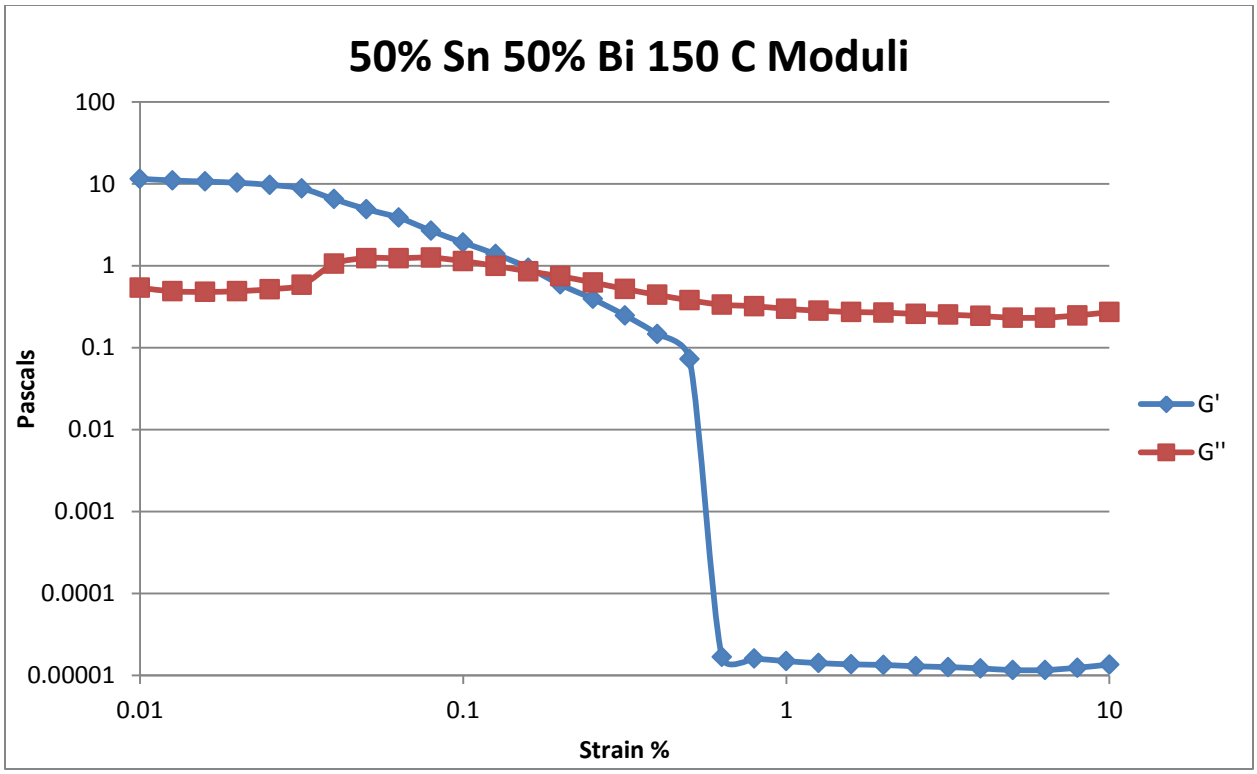

Figure 499- 50% Sn 50% Bi, 150 C, Oscillatory Shear Moduli

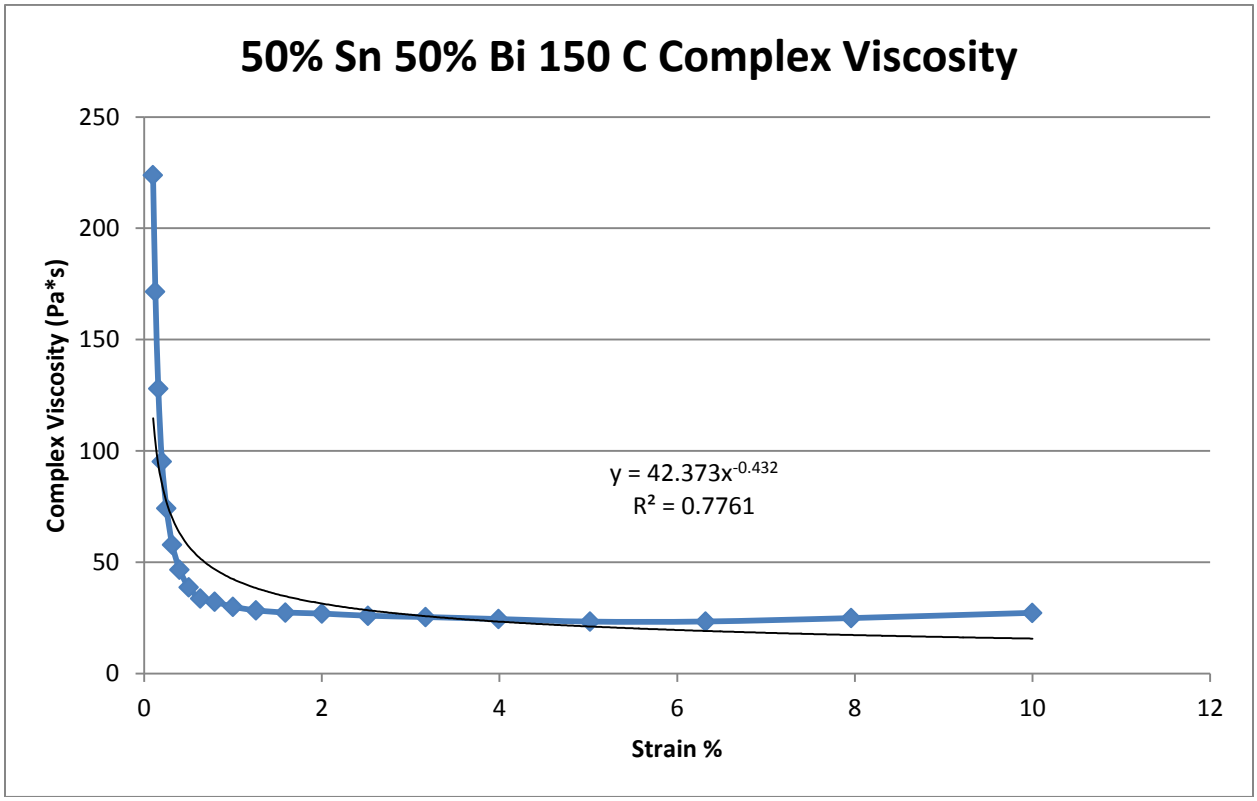

Figure 500- 50% Sn 50% Bi, 150 C, Oscillatory Shear Complex Viscosity

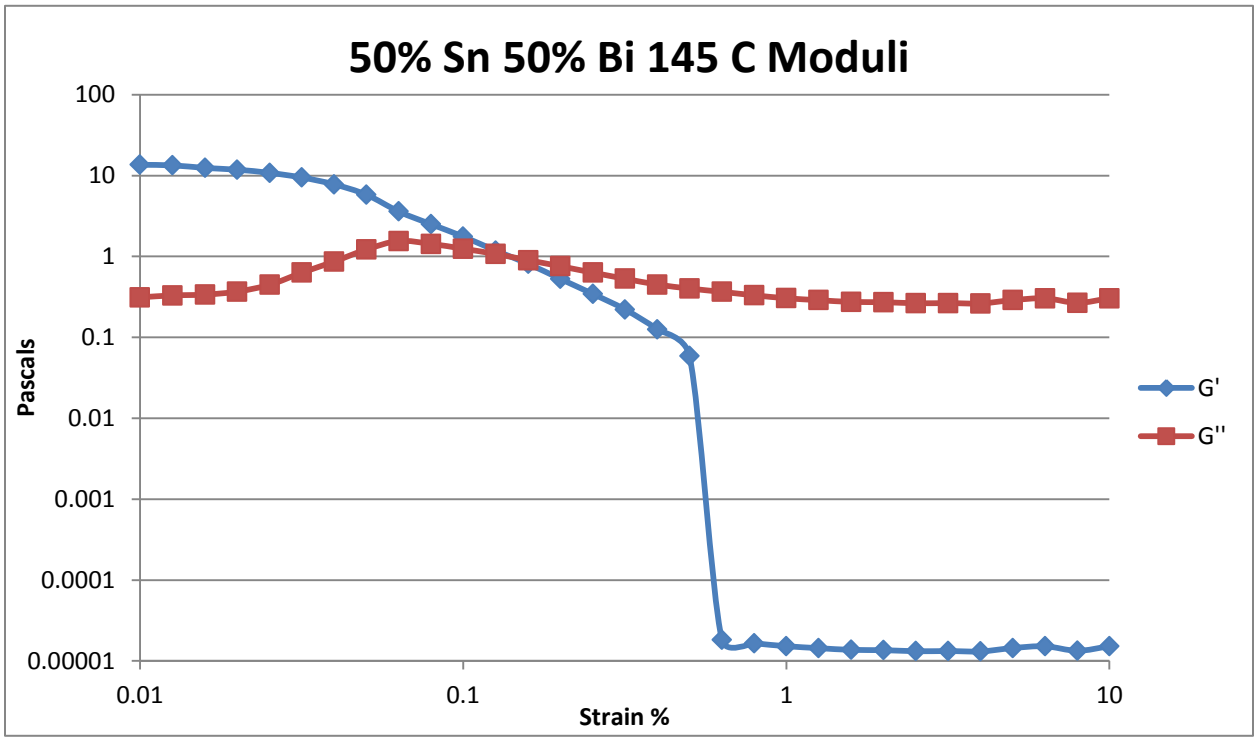

Figure 501- 50% Sn 50% Bi, 145 C, Oscillatory Shear Moduli

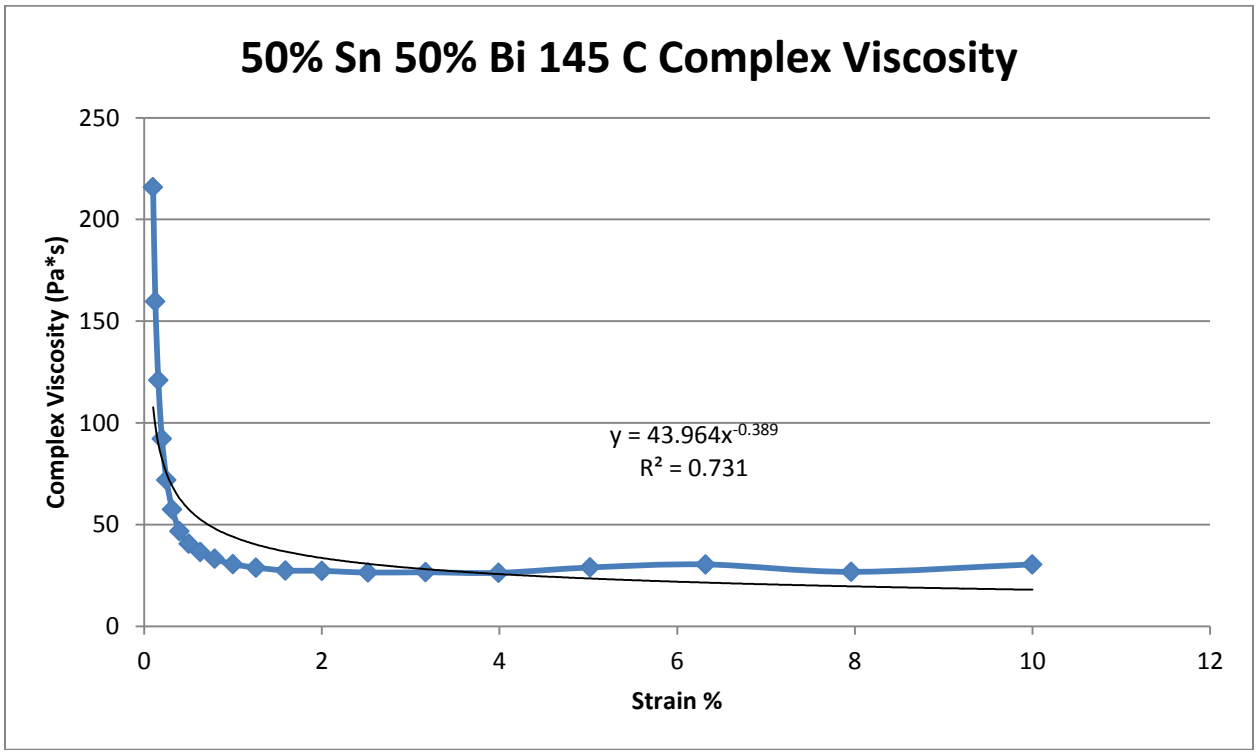

Figure 502- 50% Sn 50% Bi, 145 C, Oscillatory Shear Complex Viscosity

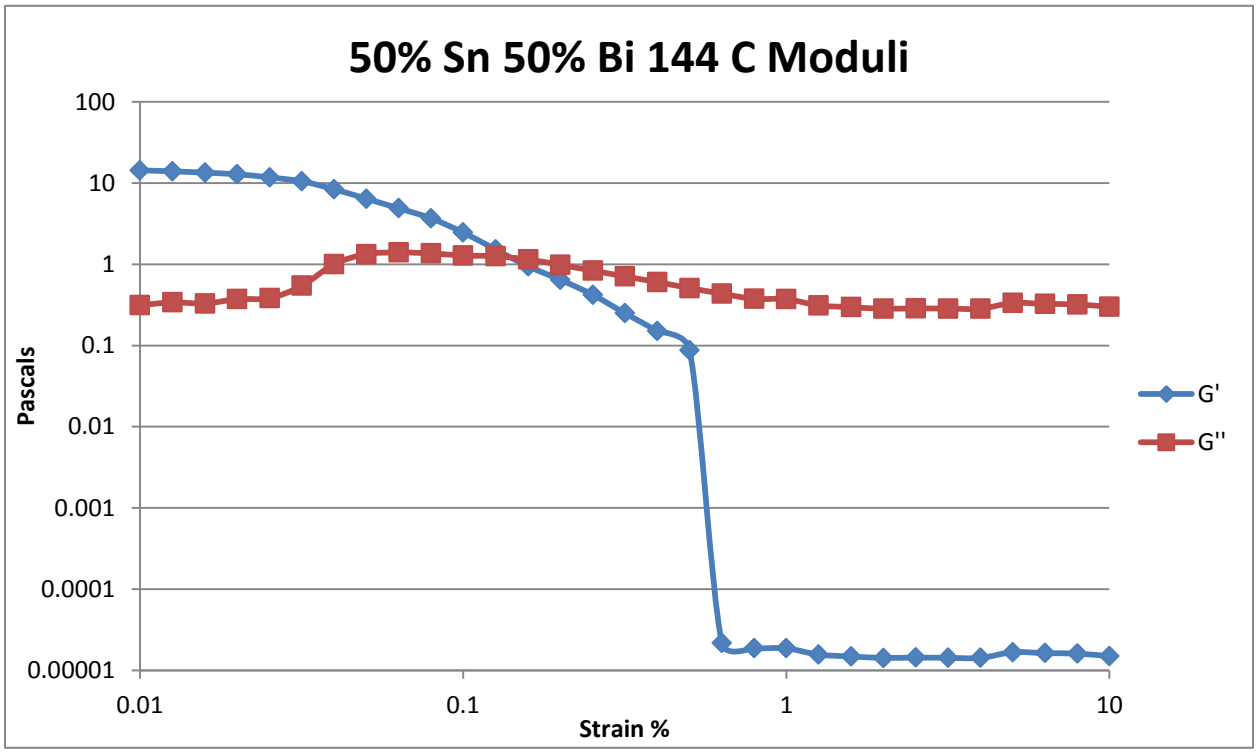

Figure 503- 50% Sn 50% Bi, 144 C, Oscillatory Shear Moduli

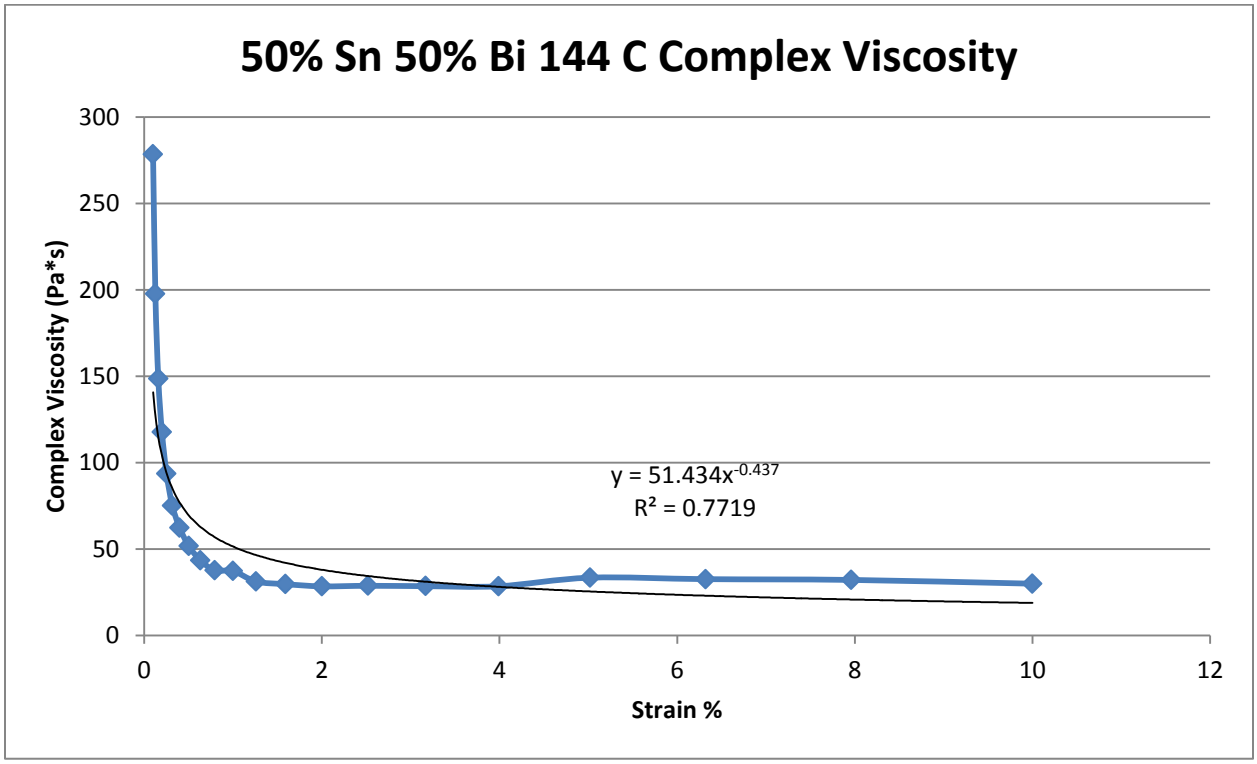

Figure 504- 50% Sn 50% Bi, 144 C, Oscillatory Shear Complex Viscosity

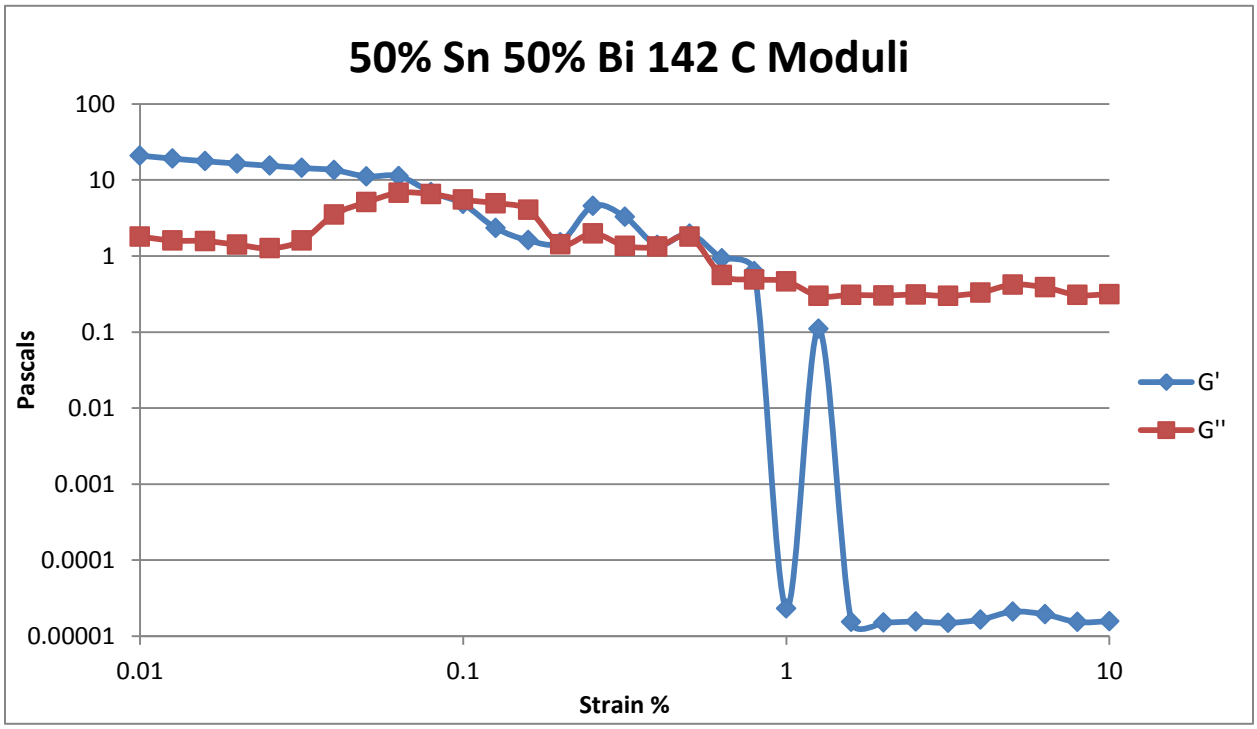

Figure 505- 50% Sn 50% Bi, 142 C, Oscillatory Shear Moduli

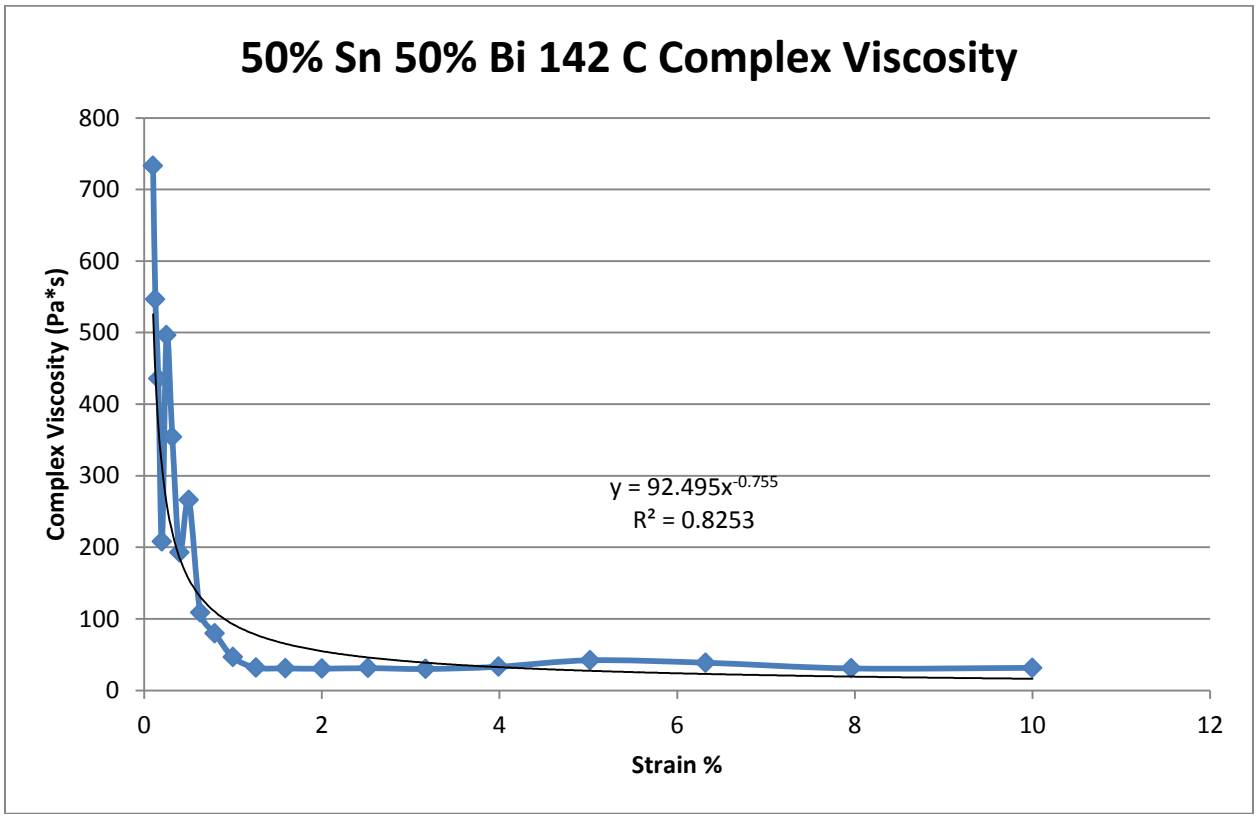

Figure 506- 50% Sn 50% Bi, 142 C, Oscillatory Shear Complex Viscosity

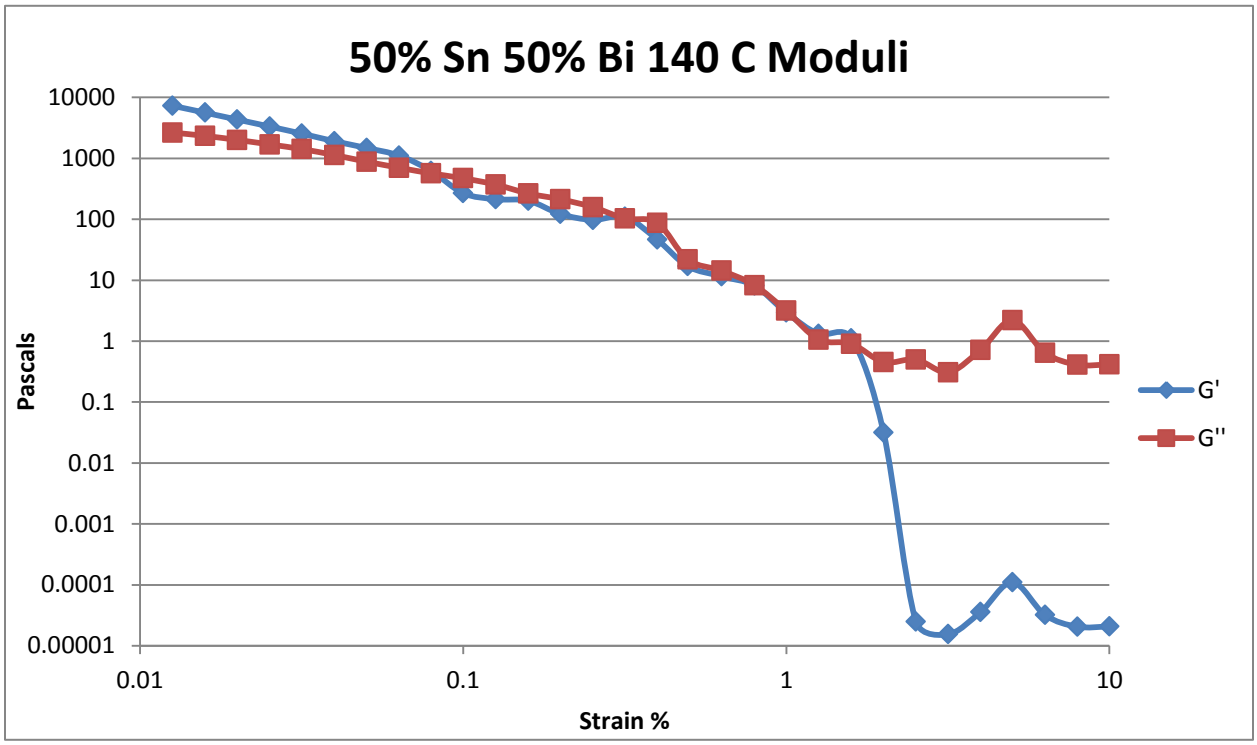

Figure 507- 50% Sn 50% Bi, 140 C, Oscillatory Shear Moduli

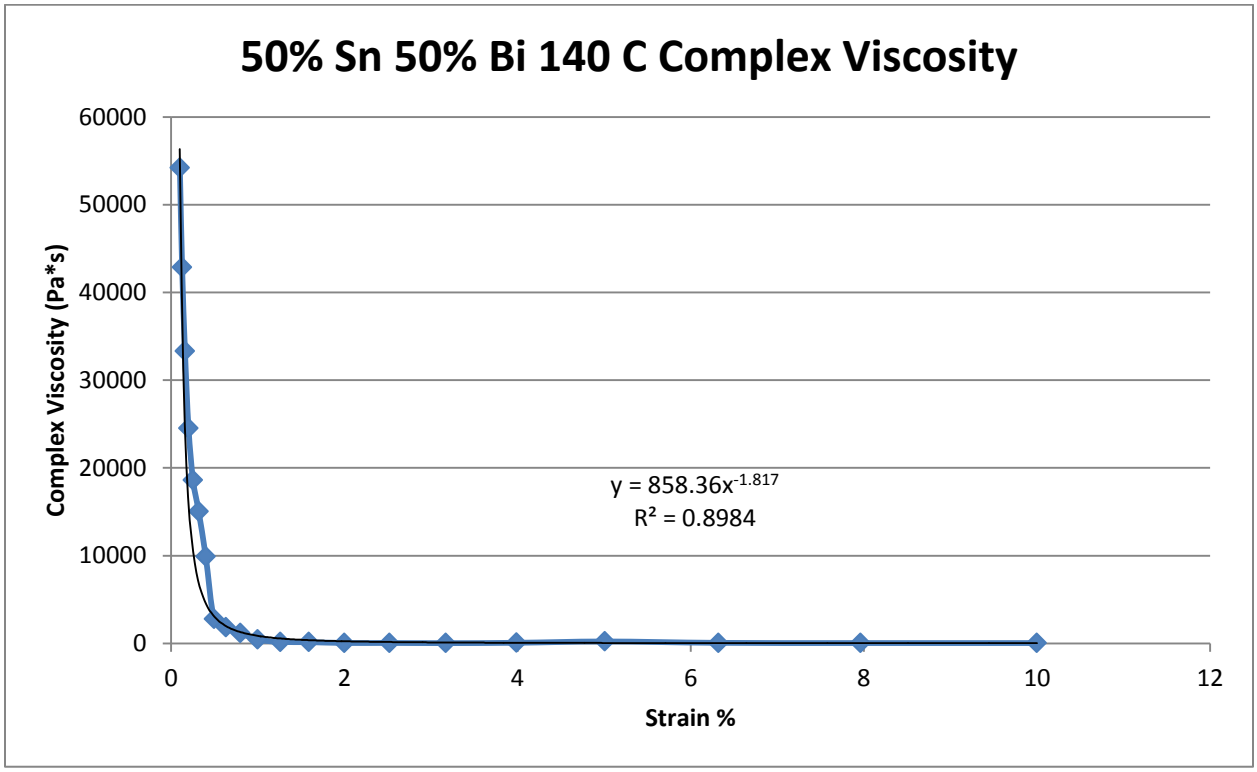

Figure 508- 50% Sn 50% Bi, 140 C, Oscillatory Shear Complex Viscosity

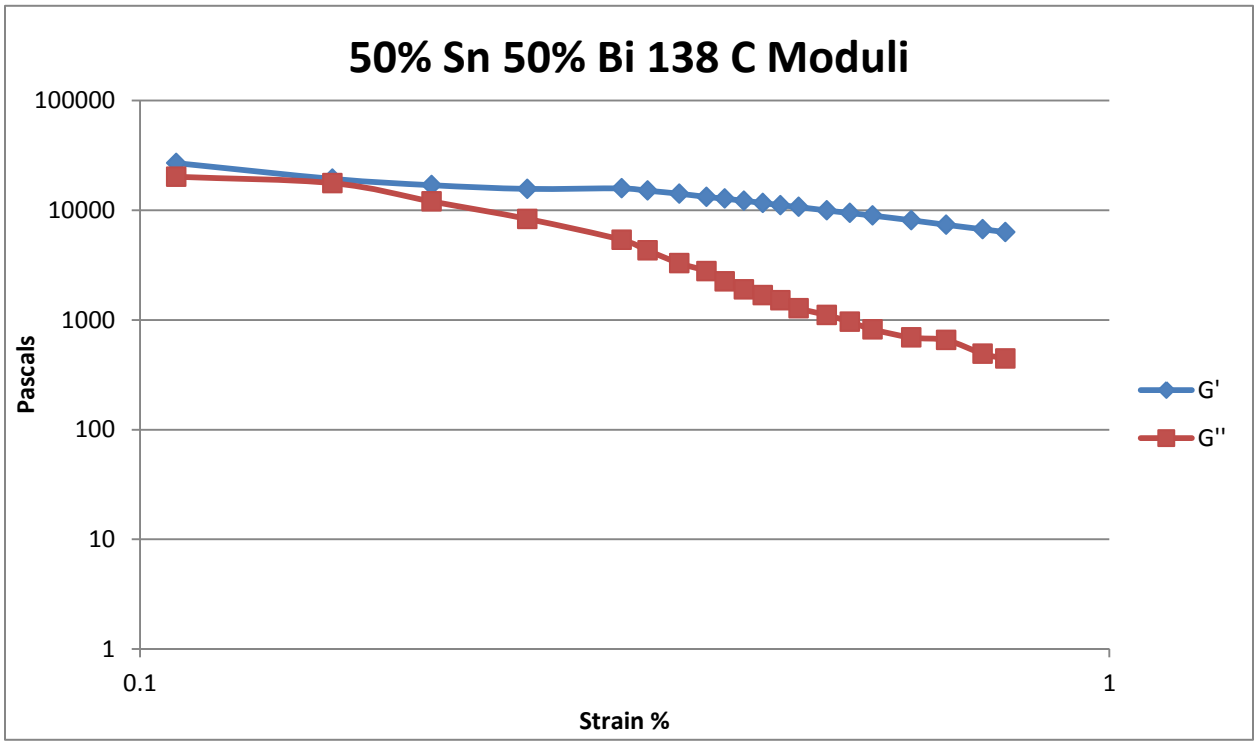

Figure 509- 50% Sn 50% Bi, 138 C, Oscillatory Shear Moduli

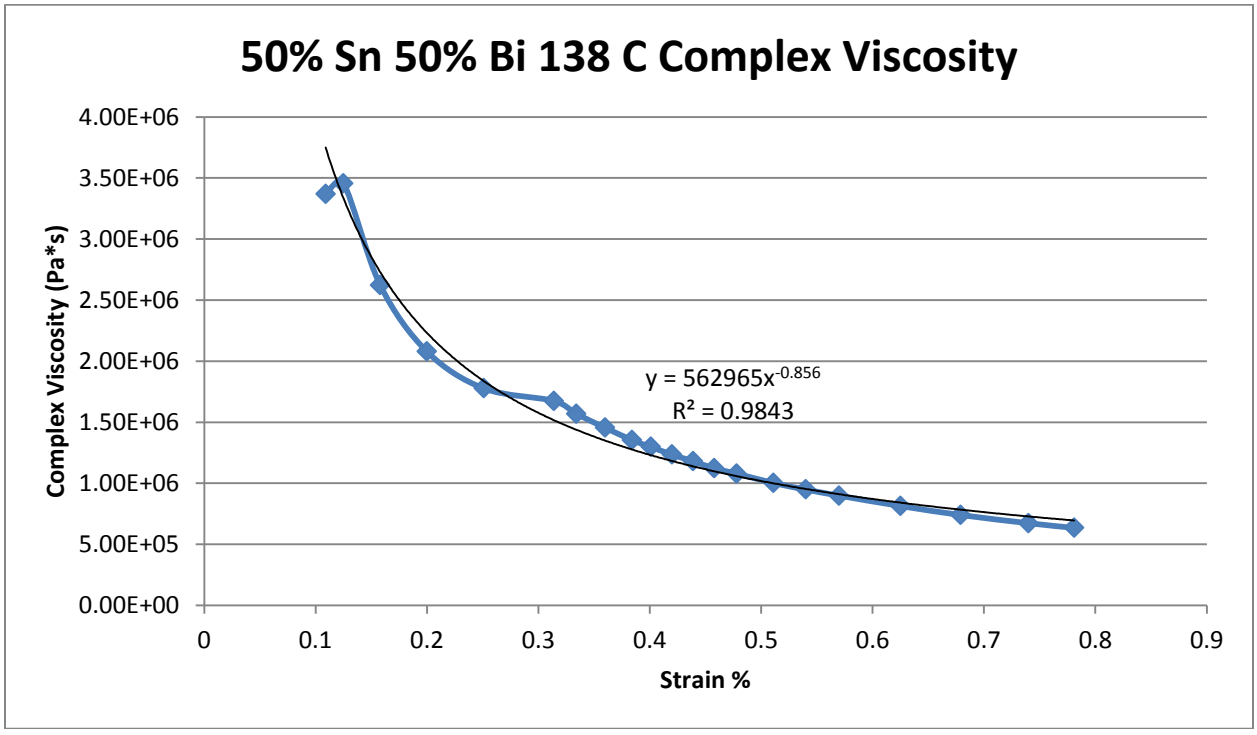

Figure 510- 50% Sn 50% Bi, 138 C, Oscillatory Shear Complex Viscosity

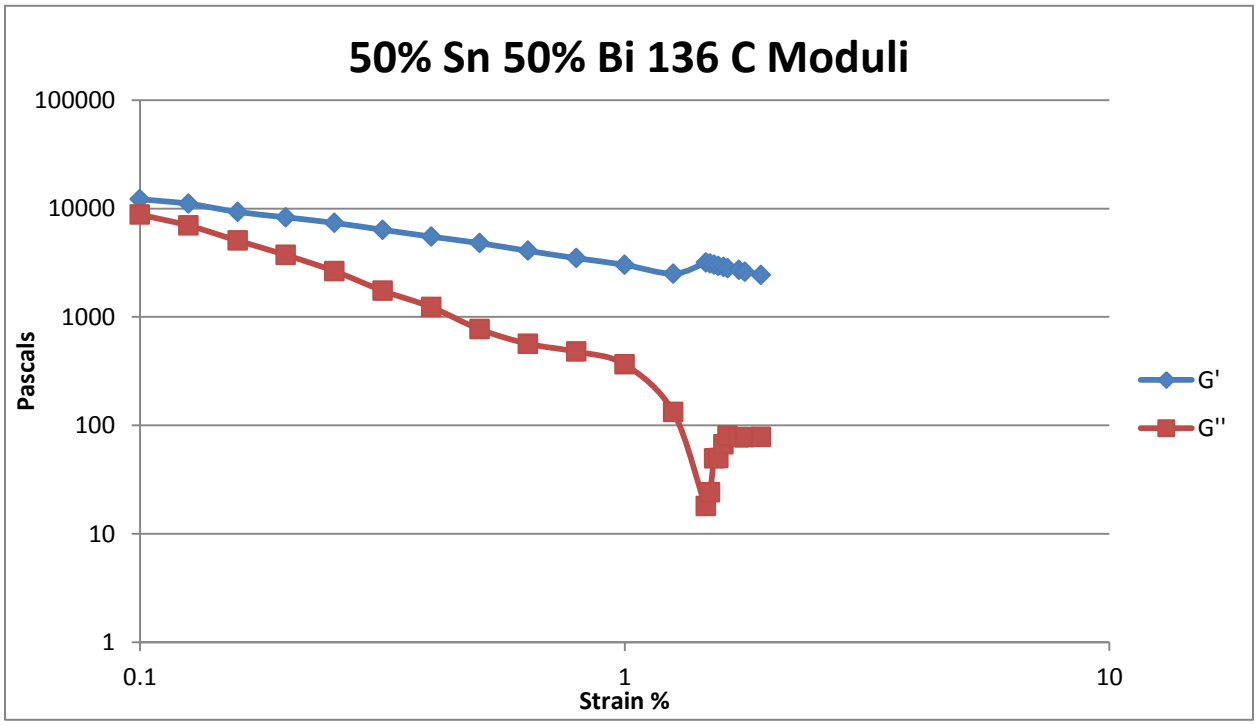

Figure 511- 50% Sn 50% Bi, 136 C, Oscillatory Shear Moduli

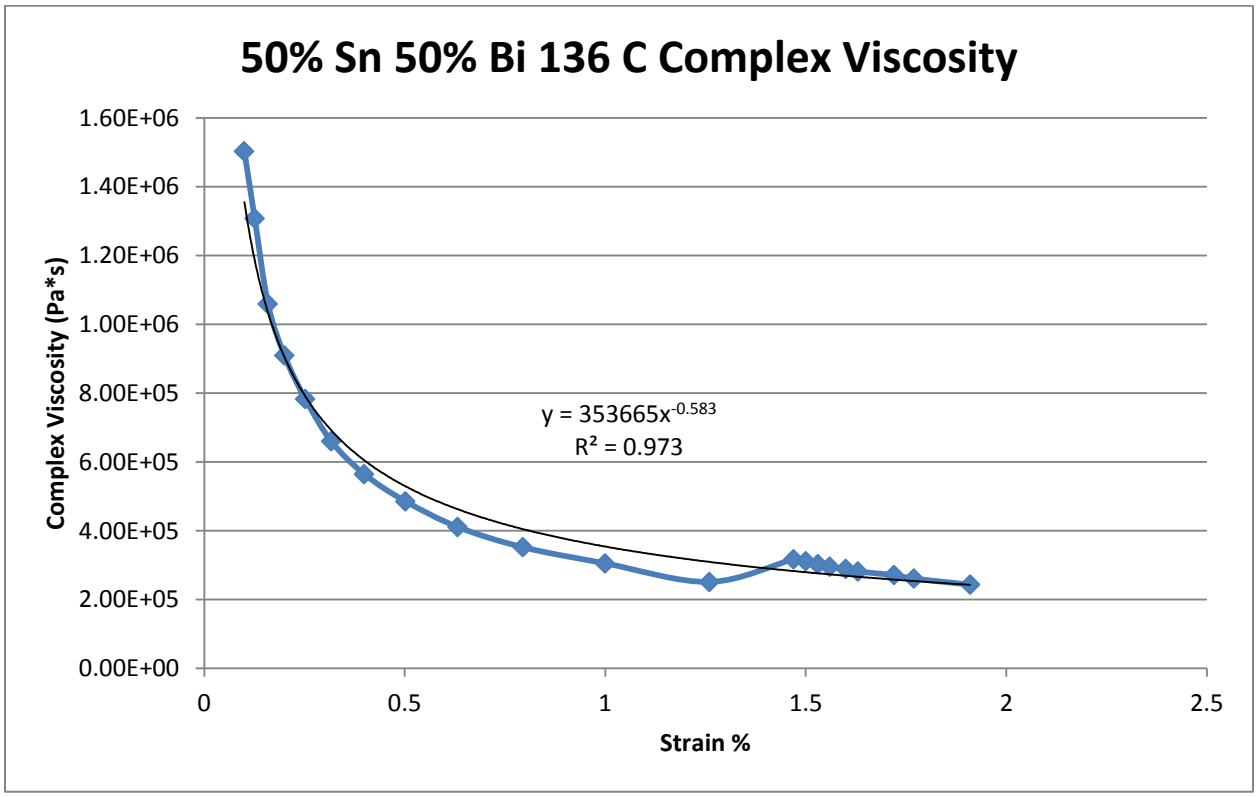

Figure 512- 50% Sn 50% Bi, 136 C, Oscillatory Shear Complex Viscosity

60% Tin 40% Bismuth

Expected Composition: 62.00% Sn, 38.00% Bi

Theoretical Solidus Line: 139 C
Theoretical Liquidus Line: 149.8 C

Experimental Solidus Line: 140.3 C
Experimental Liquidus Line: 147.0 C

Pre-Shear: 15 RPM, 2 minutes
Angular Velocity: Constant, 10 rad/s
Strain Range: 0.01%-200%

60% Tin 40% Bismuth Oscillatory Shear Rheology								
Temperature (C)	**Fraction Solid (%)**	**Crossover Strain (%)**	**Crossover Stress (Pa)**	**Crossover Modulus (Pa)**	**Crossover Complex Viscosity (Pa*s)**	**Pre G' Plateau (Pa)**	**Pre G'' Plateau (Pa)**	**Final Complex Viscosity (Pa*s)**
145	10.4	8.79	0.042	0.335	0.044	5.00	0.330	0.018
144	11.6	10.6	0.056	0.371	0.053	5.07	0.327	0.020
143	13.2	8.00	0.074	0.650	0.093	6.30	0.600	0.027
142	13.8	17.7	1.20	4.80	0.680	56.0	10.8	0.117
141	15.0	13.3	1.99	10.9	1.38	332	88.0	0.148
140	16.7	4.61	3.35	52.0	7.36	1.38e3	431	0.183

Table 91- 60% Tin 40% Bismuth Oscillatory Shear Rheology

60% Tin 40% Bismuth Oscillatory Shear Complex Viscosity			
Temperature (C)	**Fraction Solid (%)**	**Power Law Equation**	**R^2 (%)**
145	10.4	$\eta^* = 0.5671\gamma^{-0.962}$	94.62
144	11.6	$\eta^* = 0.7184\gamma^{-0.976}$	96.01
143	13.2	$\eta^* = 0.6425\gamma^{-0.784}$	95.78
142	13.8	$\eta^* = 2.7348\gamma^{-0.593}$	94.59
141	15.0	$\eta^* = 9.2501\gamma^{-0.803}$	97.21
140	16.7	$\eta^* = 28.699\gamma^{-0.994}$	99.32

Table 92- 60% Tin 40% Bismuth Oscillatory Shear Complex Viscosity

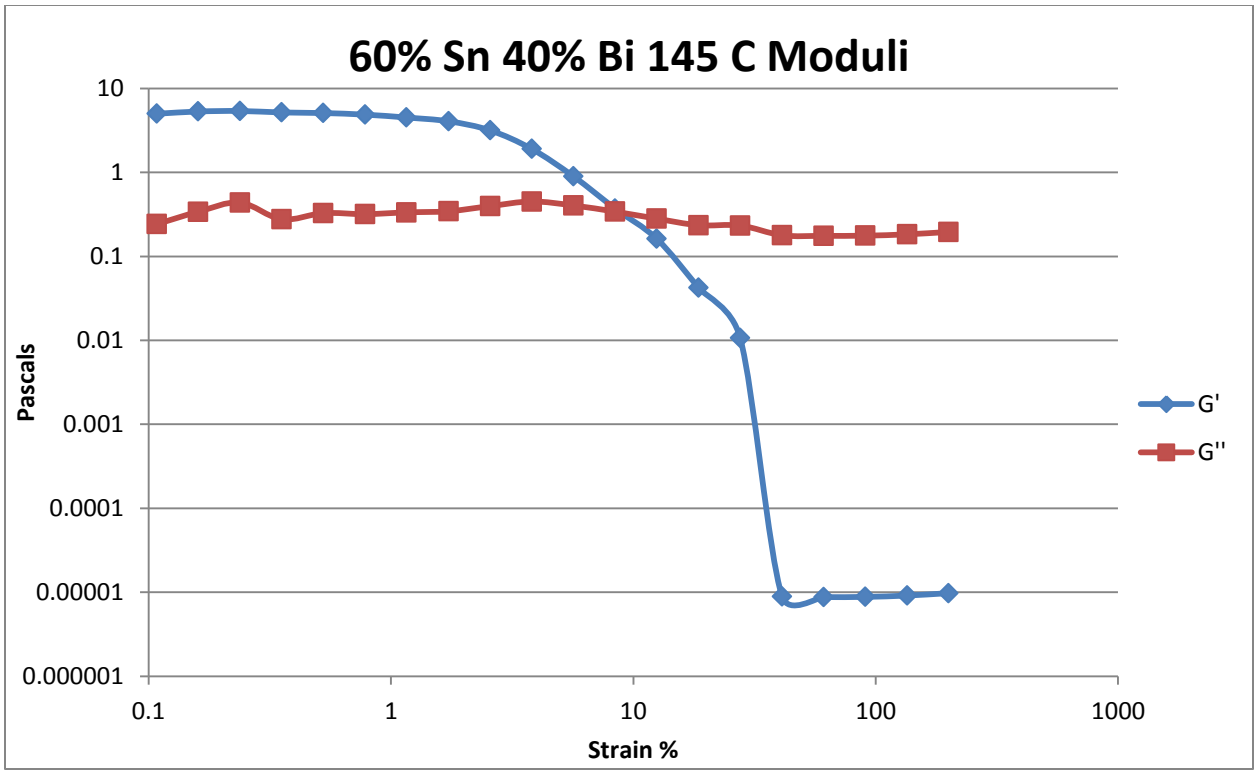

Figure 513- 60% Tin 40% Bismuth, 145 C, Oscillatory Shear Moduli

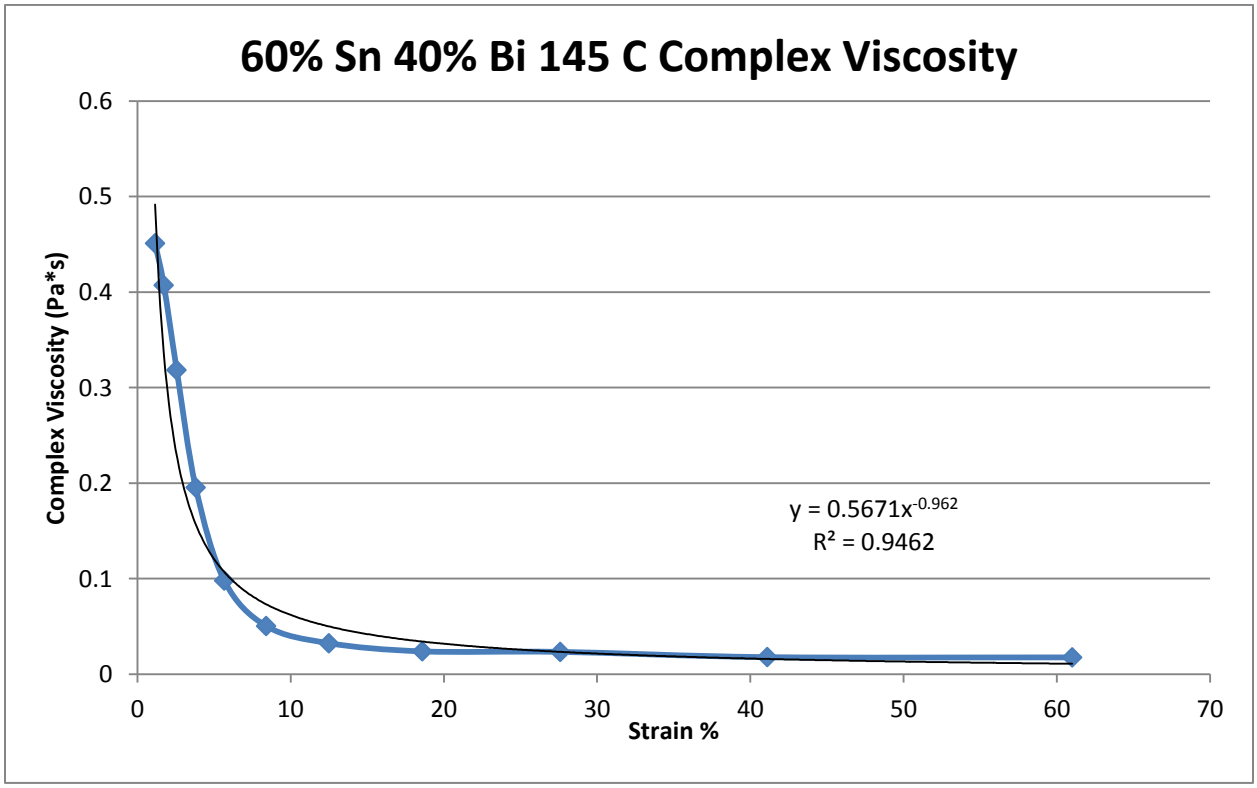

Figure 514- 60% Tin 40% Bismuth, 145 C, Oscillatory Shear Complex Viscosity

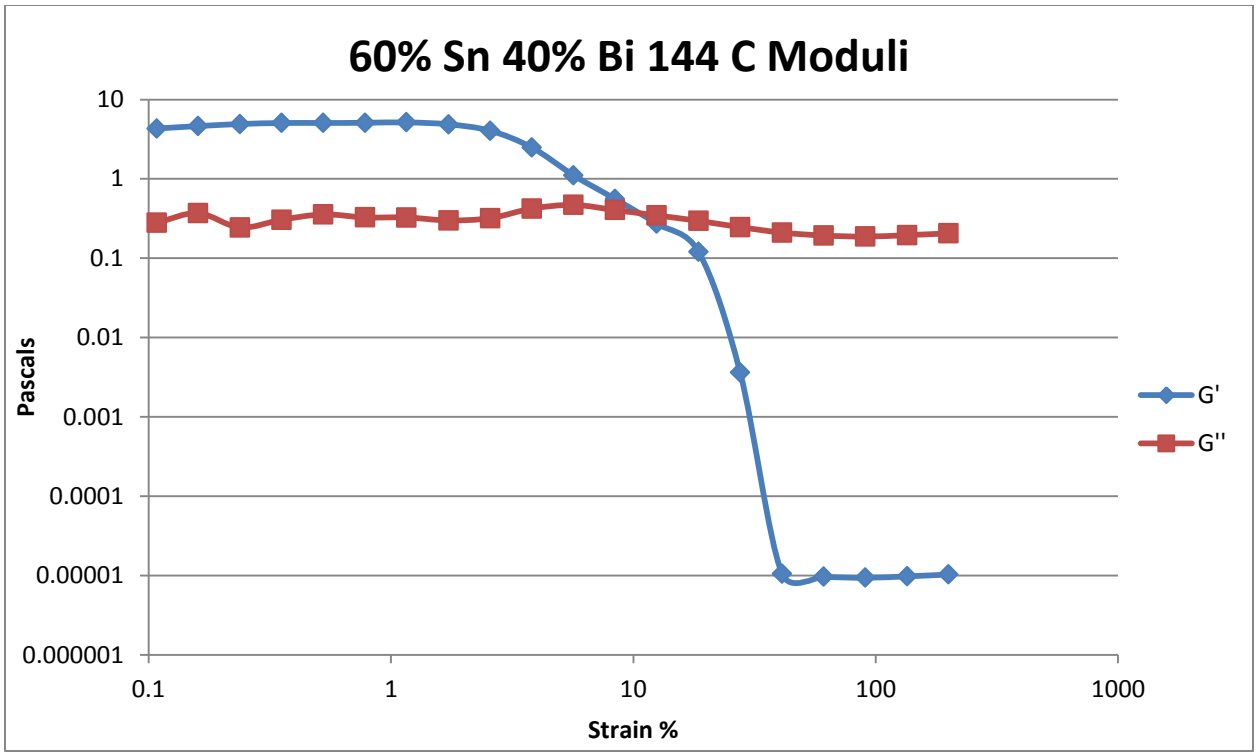

Figure 515- 60% Tin 40% Bismuth, 144 C, Oscillatory Shear Moduli

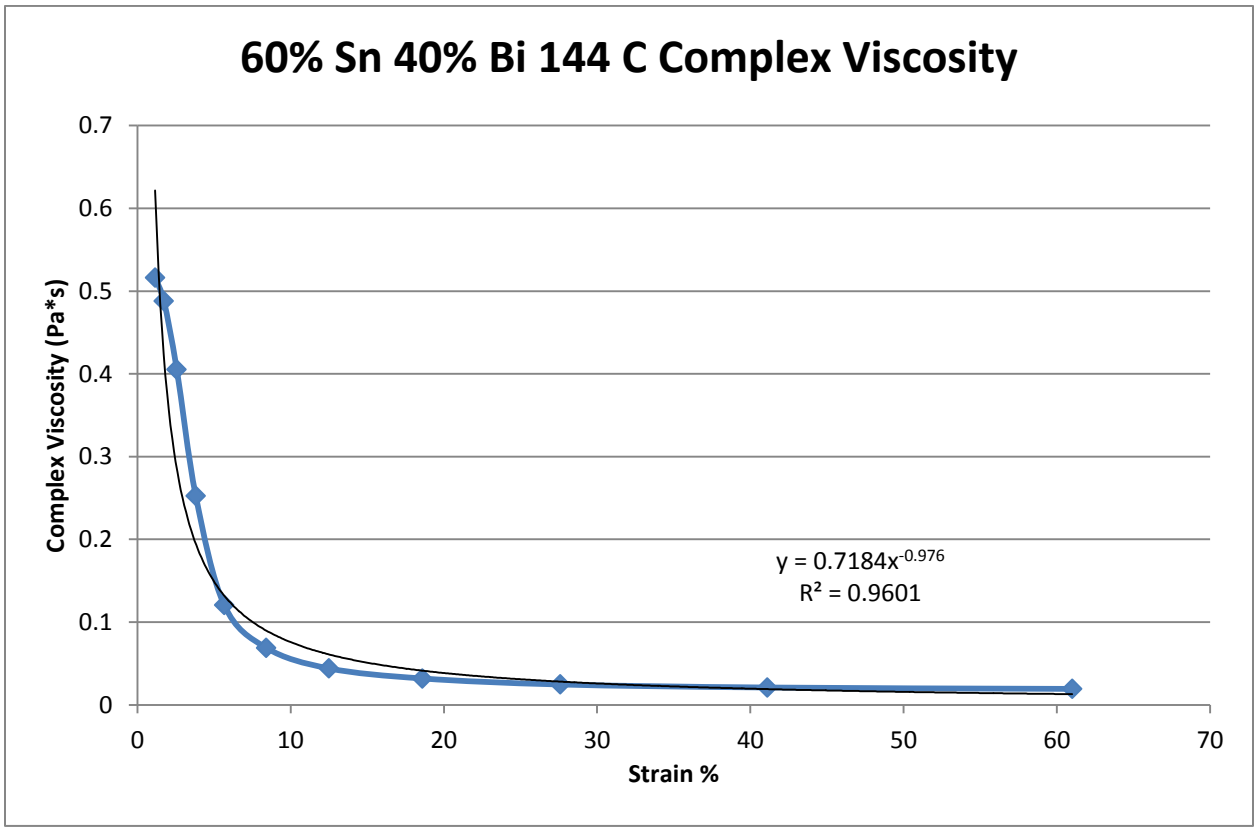

Figure 516- 60% Tin 40% Bismuth, 144 C, Oscillatory Shear Complex Viscosity

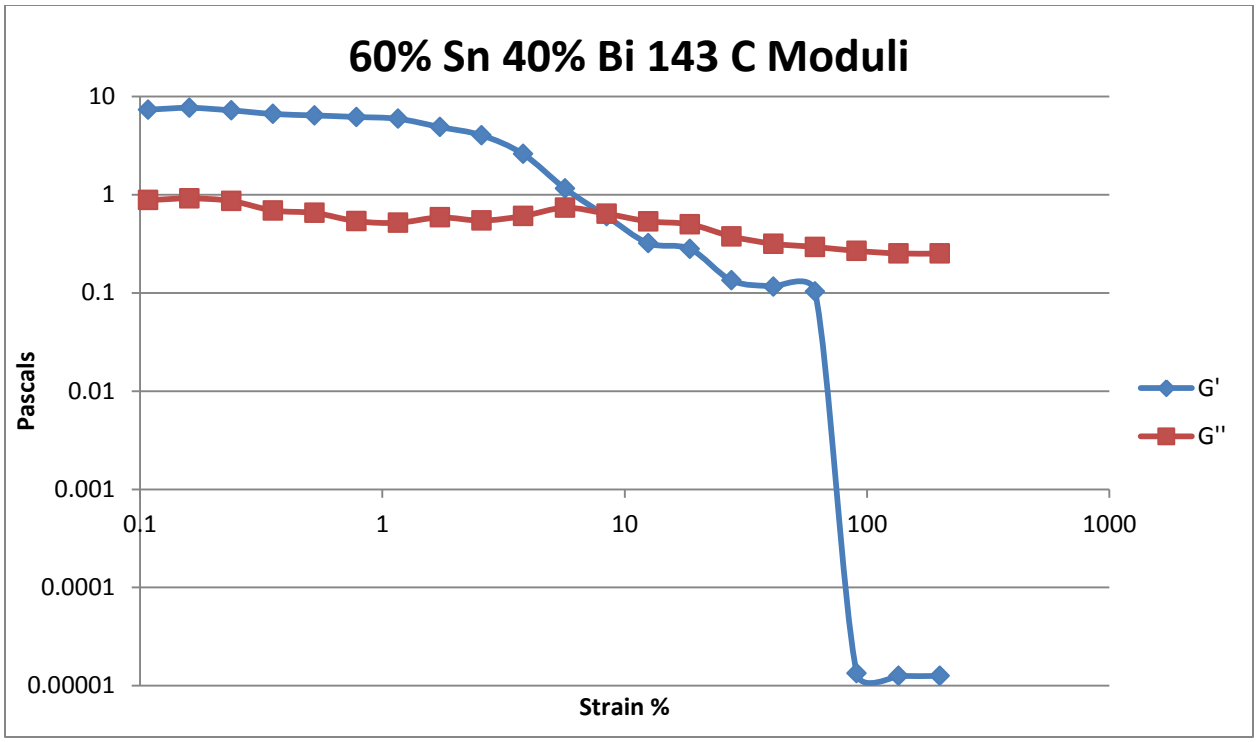

Figure 517- 60% Tin 40% Bismuth, 143 C, Oscillatory Shear Moduli

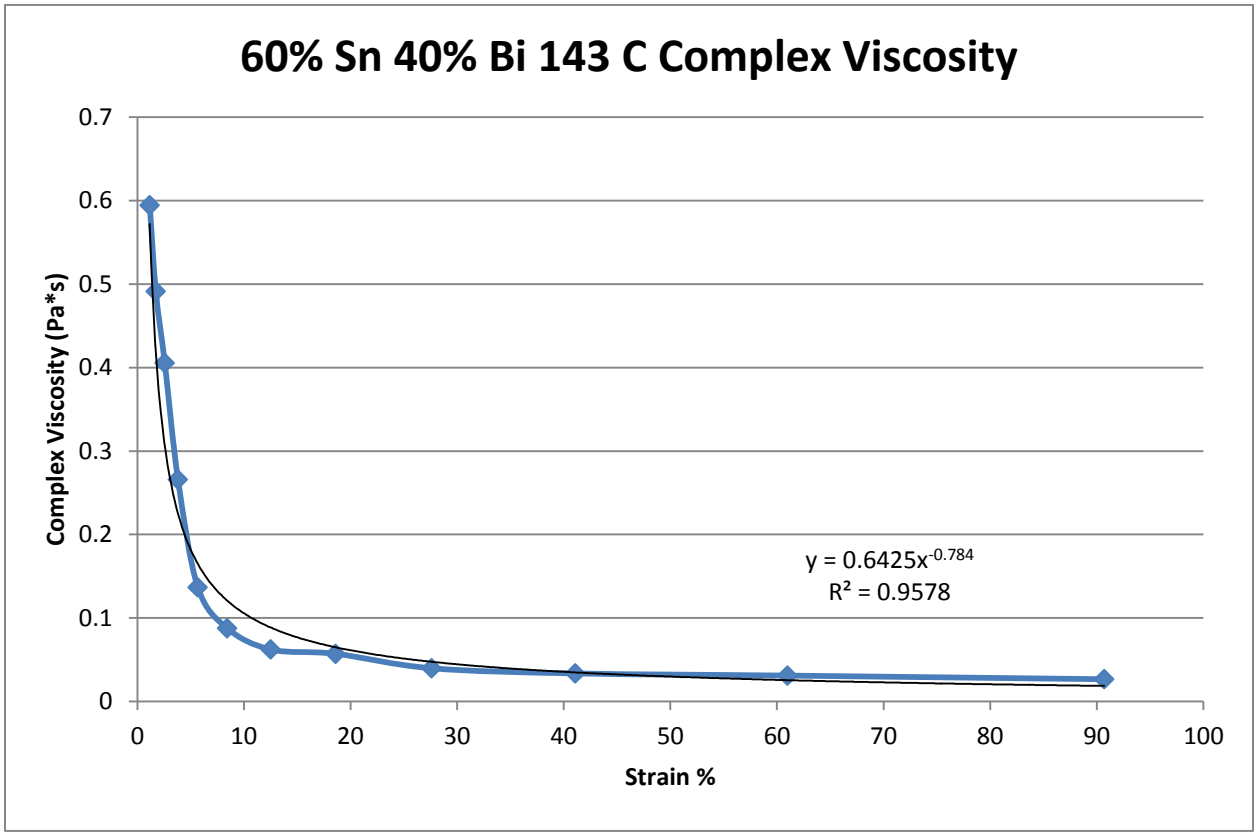

Figure 518- 60% Tin 40% Bismuth, 143, Oscillatory Shear Complex Viscosity

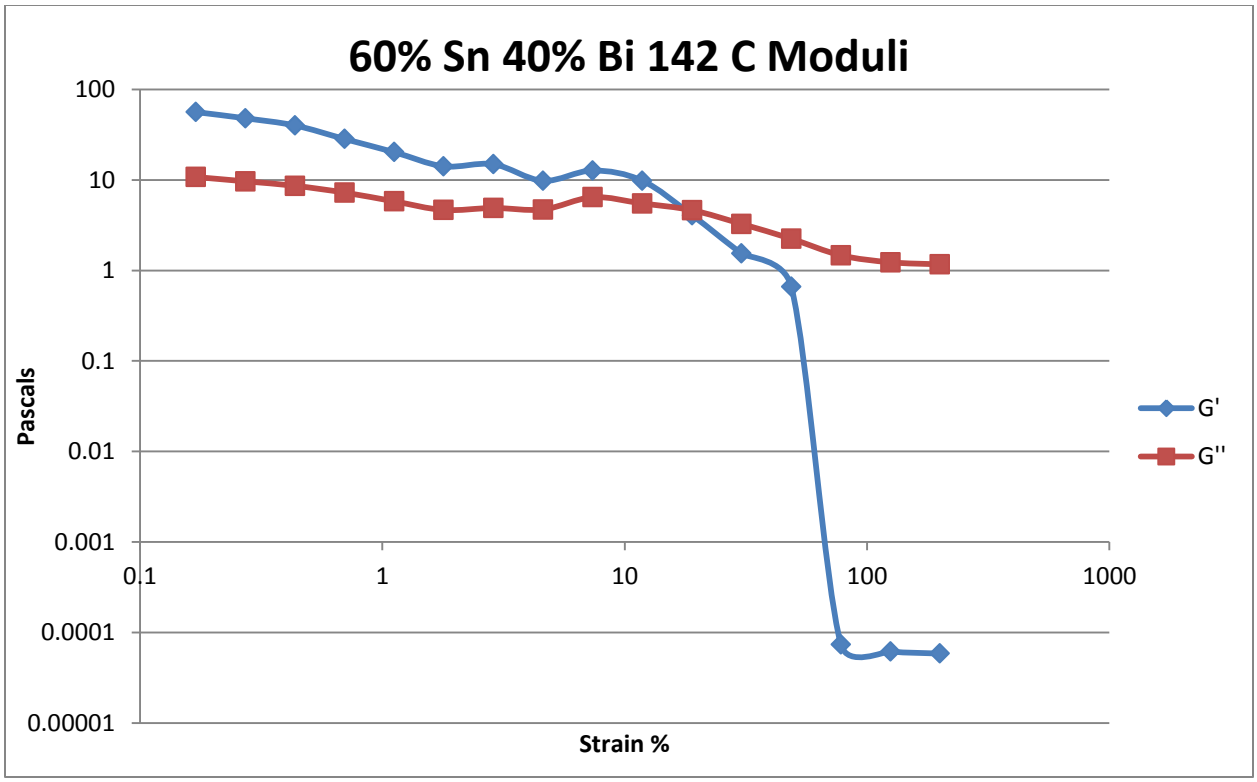

Figure 519- 60% Tin 40% Bismuth, 142 C, Oscillatory Shear Moduli

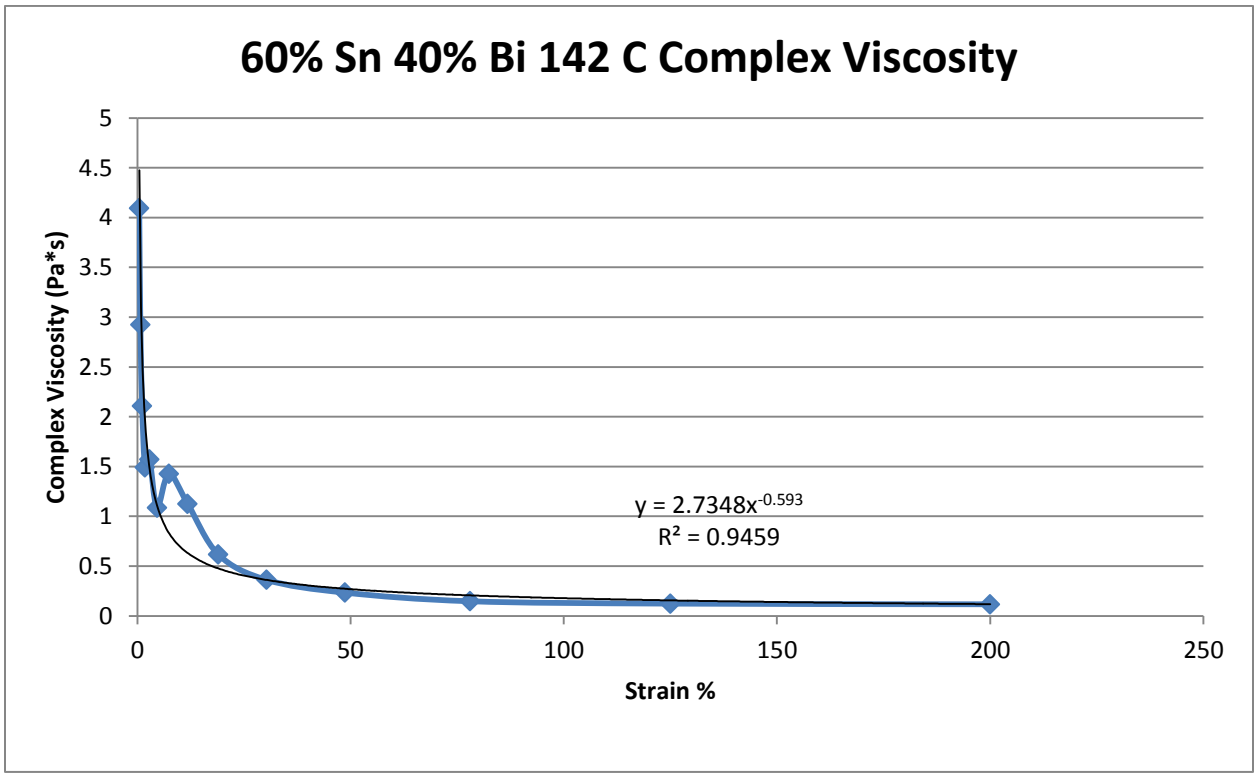

Figure 520- 60% Tin 40% Bismuth, 142 C, Oscillatory Shear Complex Viscosity

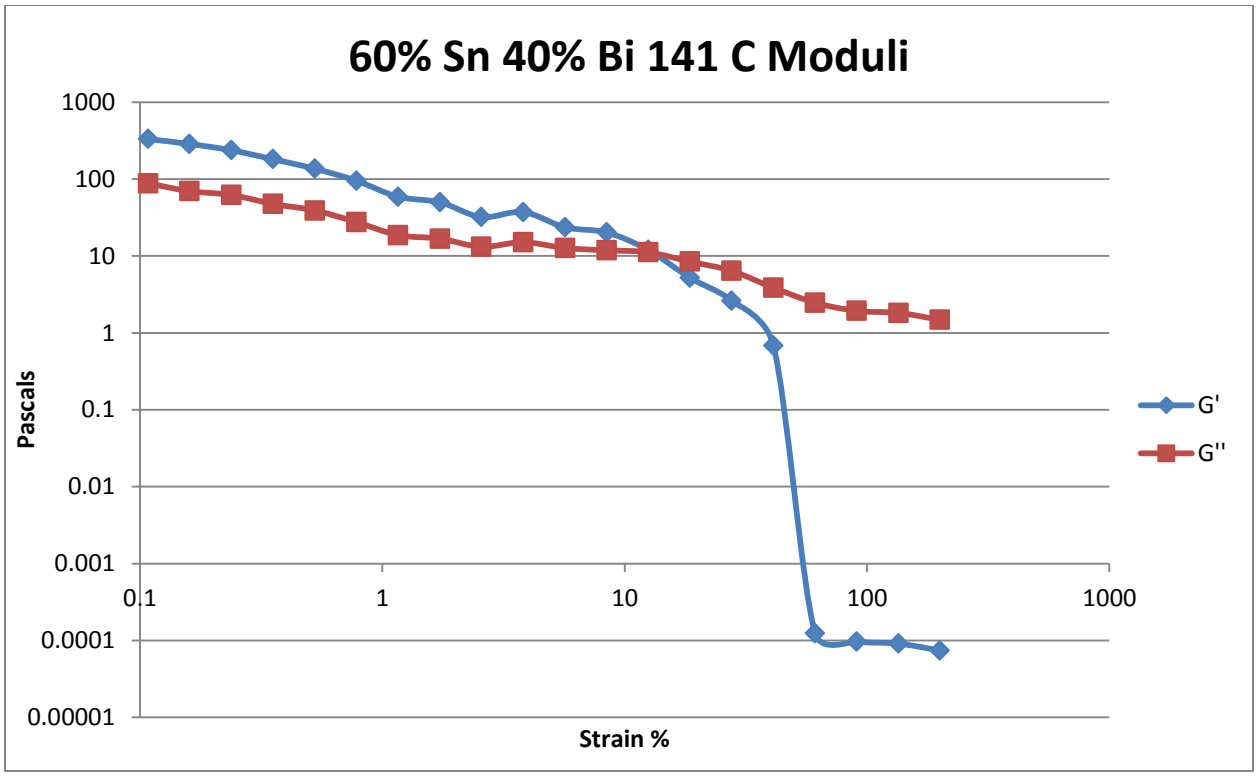

Figure 521- 60% Tin 40% Bismuth, 141 C, Oscillatory Shear Moduli

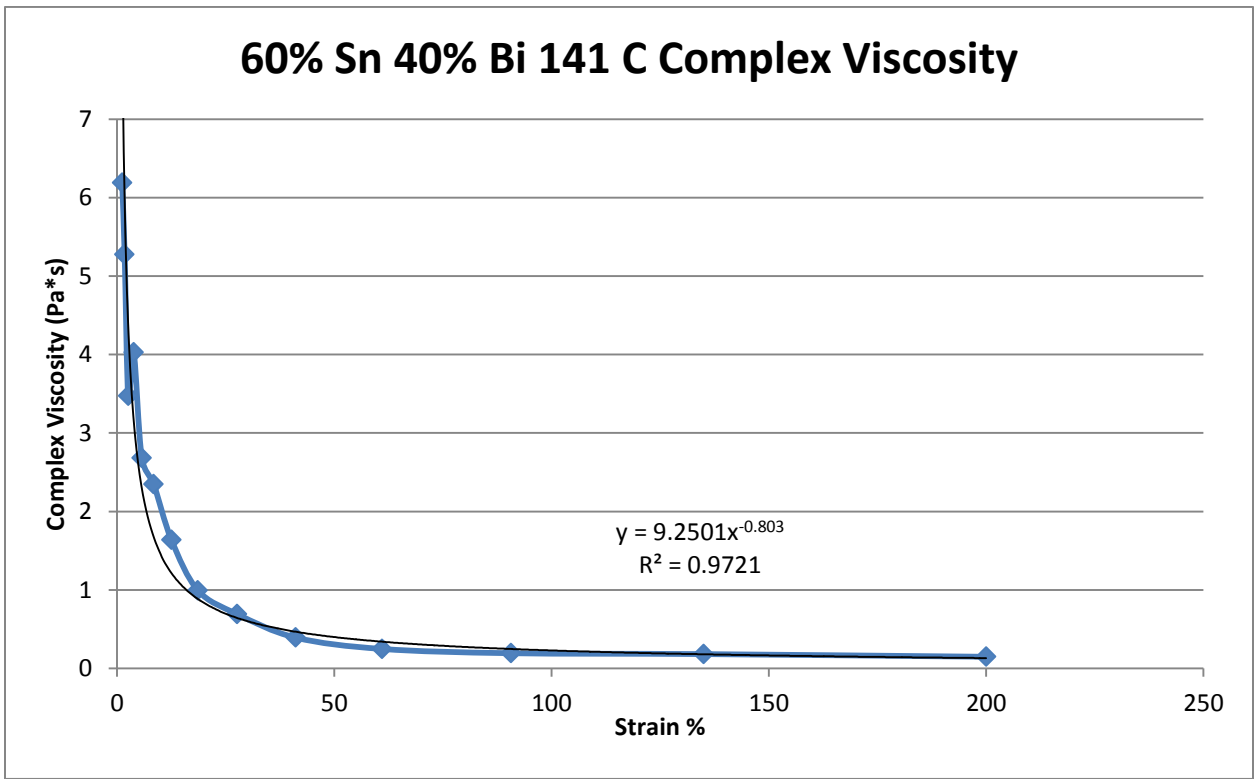

Figure 522- 60% Tin 40% Bismuth, 141 C, Oscillatory Shear Complex Viscosity

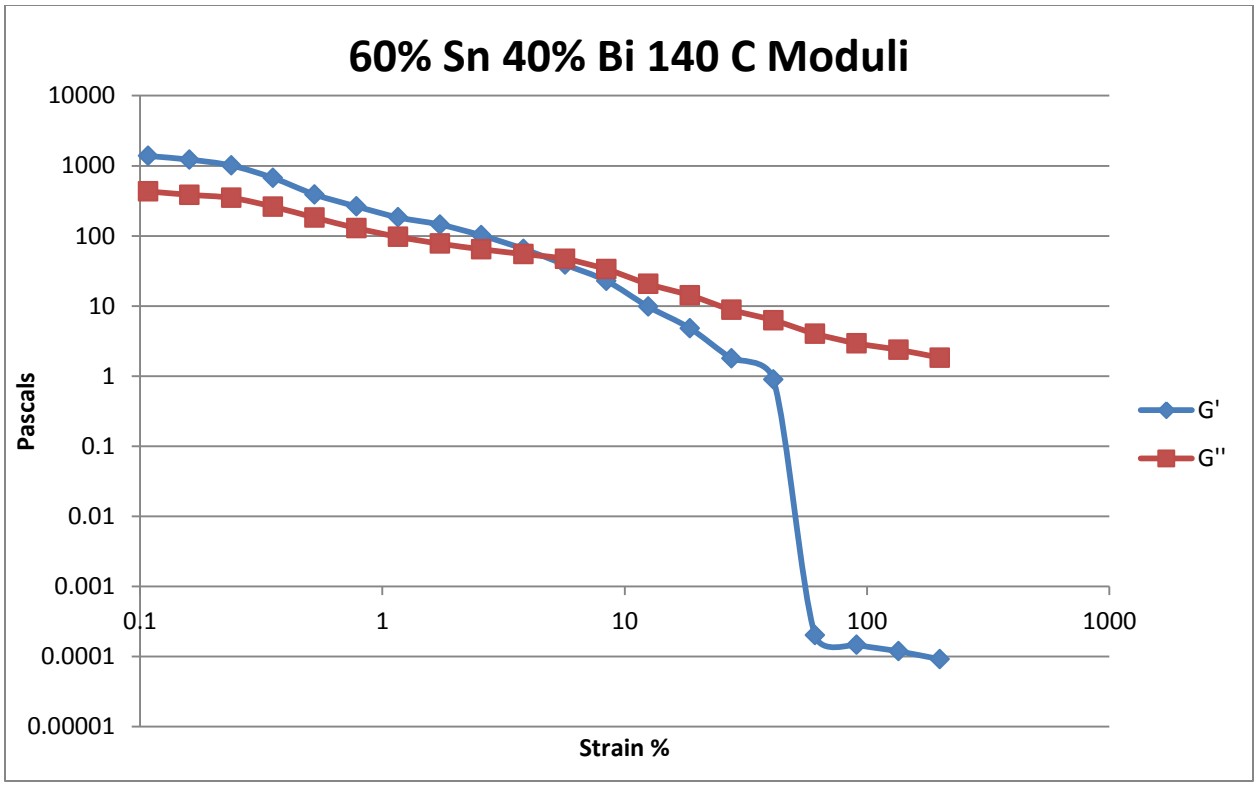

Figure 523- 60% Tin 40% Bismuth, 140 C, Oscillatory Shear Moduli

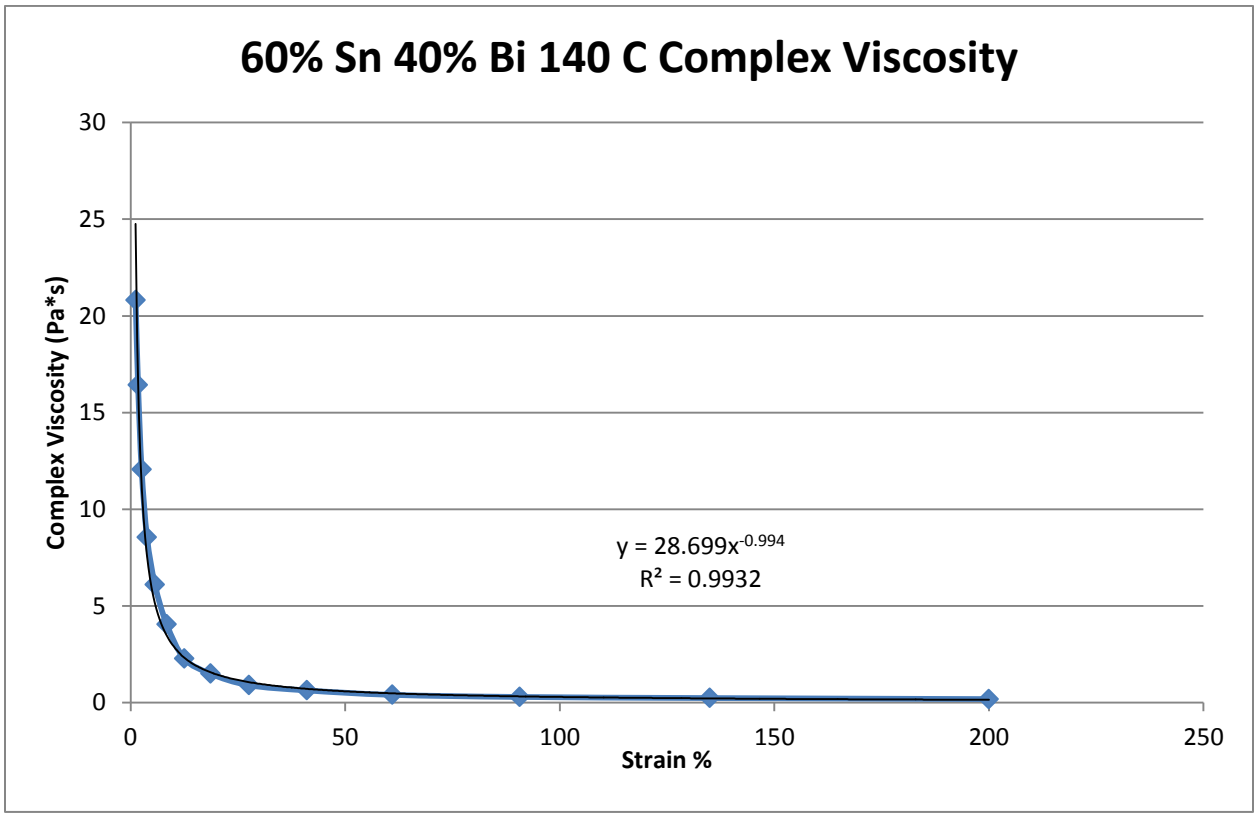

Figure 524- 60% Tin 40% Bismuth, 140 C, Oscillatory Shear Complex Viscosity

62.5% Tin 37.5% Bismuth

Expected Composition: 64.50% Sn, 35.50% Bi

Theoretical Solidus Line: 139 C
Theoretical Liquidus Line: 155.2 C

Experimental Solidus Line: 139.4 C
Experimental Liquidus Line: 156.5 C

Pre-Shear: 15 RPM, 2 minutes
Angular Velocity: Constant, 10 rad/s
Strain Range: 0.01%-200%

62.5% Tin 37.5% Bismuth Oscillatory Shear Rheology								
Temperature (C)	**Fraction Solid (%)**	**Crossover Strain (%)**	**Crossover Stress (Pa)**	**Crossover Modulus (Pa)**	**Crossover Complex Viscosity (Pa*s)**	**Pre G' Plateau (Pa)**	**Pre G'' Plateau (Pa)**	**Final Complex Viscosity (Pa*s)**
145	10.3	11.1	1.37	8.92	1.26	193	24.1	0.221
144	11.6	7.53	1.29	12.3	1.68	221	25.8	0.156
143	13.0	5.60	1.66	21.5	3.04	446	225	0.171
142	14.3	1.03	2.62	181	26.4	2226	954	0.221
141	15.6	0.84	4.39	365	55.2	6442	2468	0.234
140	17.0	1.22	3.45	202	29.0	3015	1266	0.254
139	100	0.76	2.10	195	28.2	1137	664	0.278
138.5	100	4.47	6.36	101	14.5	2263	1033	0.738

Table 93- 62.5% Tin 37.5% Bismuth Oscillatory Shear Rheology

62.5% Tin 37.5% Bismuth Oscillatory Shear Complex Viscosity			
Temperature (C)	**Fraction Solid (%)**	**Power Law Equation**	**R^2 (%)**
145	10.3	$\eta^* = 6.2245\gamma^{-0.771}$	96.00
144	11.6	$\eta^* = 6.6092\gamma^{-0.786}$	97.07
143	13.0	$\eta^* = 11.03\gamma^{-0.872}$	97.49
142	14.3	$\eta^* = 26.259\gamma^{-0.958}$	99.38
141	15.6	$\eta^* = 39.142\gamma^{-1.027}$	99.41
140	17.0	$\eta^* = 31.768\gamma^{-0.975}$	99.29
139	100	$\eta^* = 22.532\gamma^{-0.885}$	99.27
138.5	100	$\eta^* = 52.685\gamma^{-0.854}$	99.23

Table 94- 62.5% Tin 37.5% Bismuth Oscillatory Shear Complex Viscosity

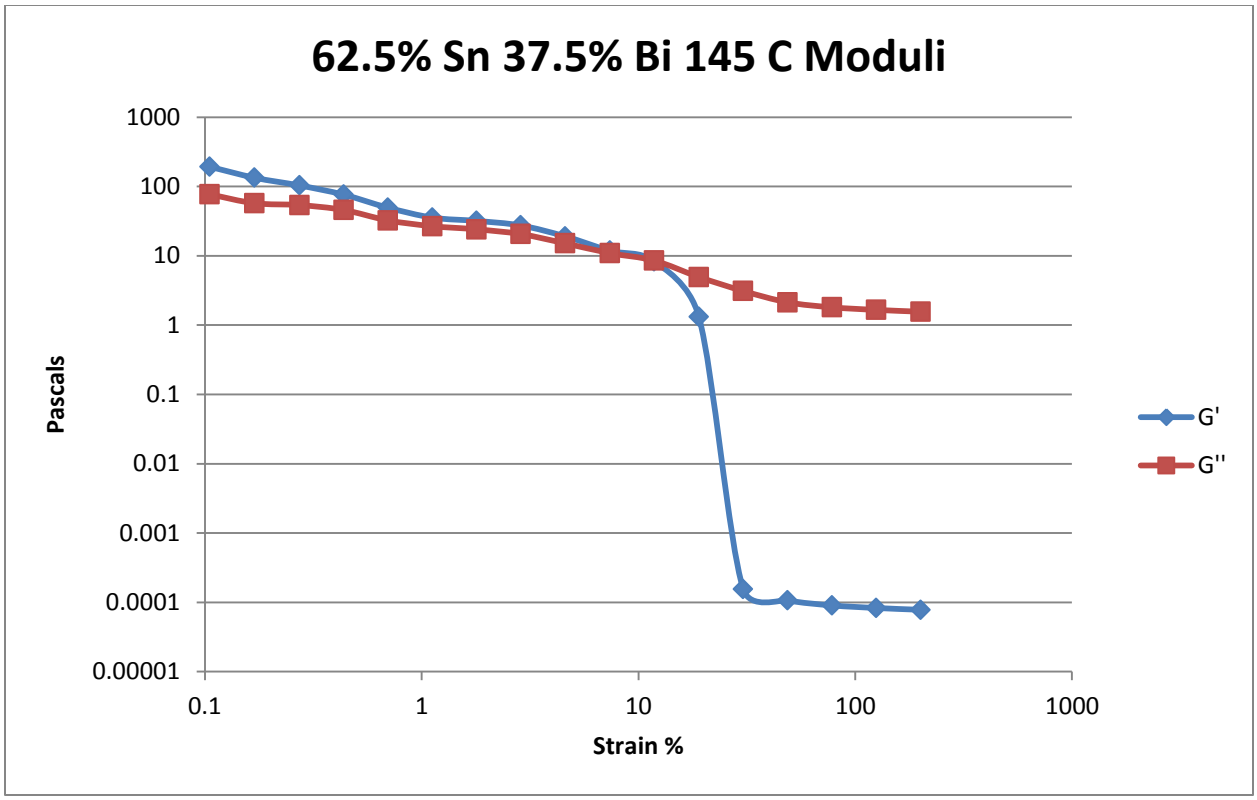

Figure 525- 62.5% Tin 37.5% Bismuth, 145 C, Oscillatory Shear Moduli

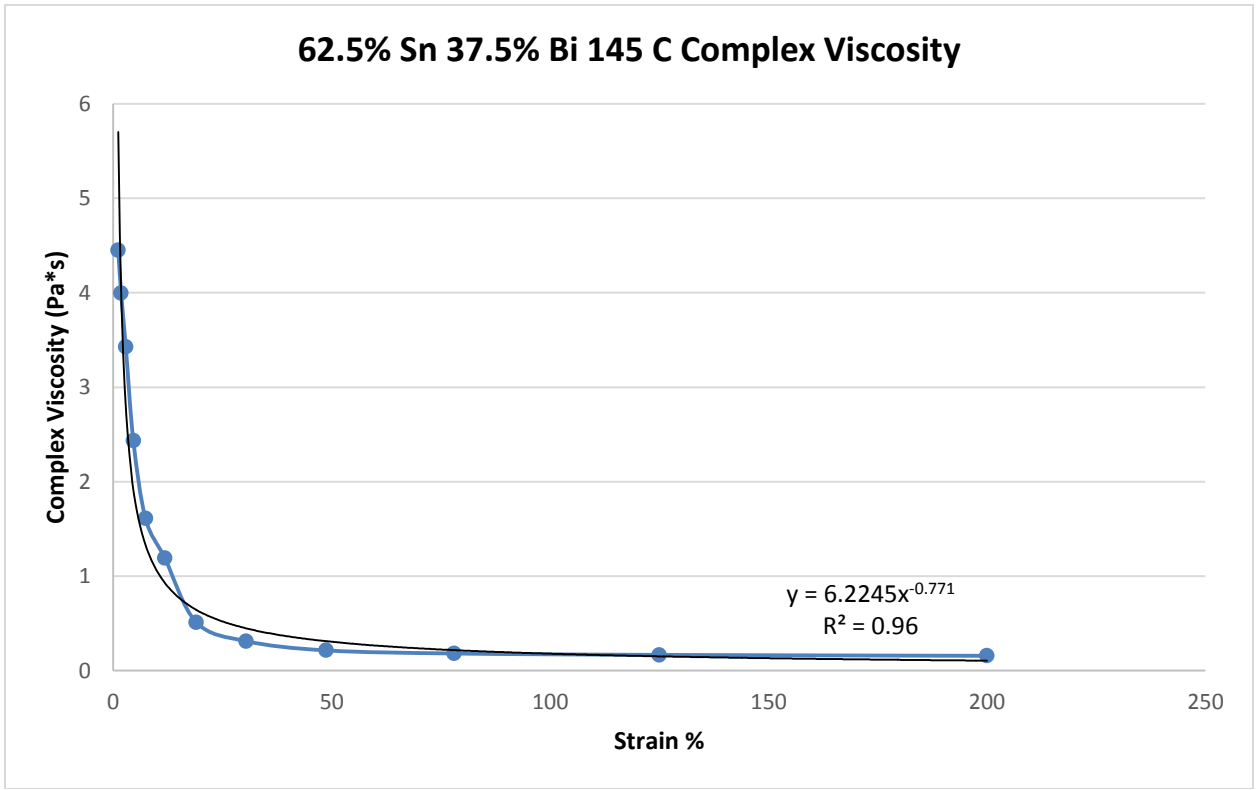

Figure 526- 62.5% Tin 37.5% Bismuth, 145 C, Oscillatory Shear Complex Viscosity

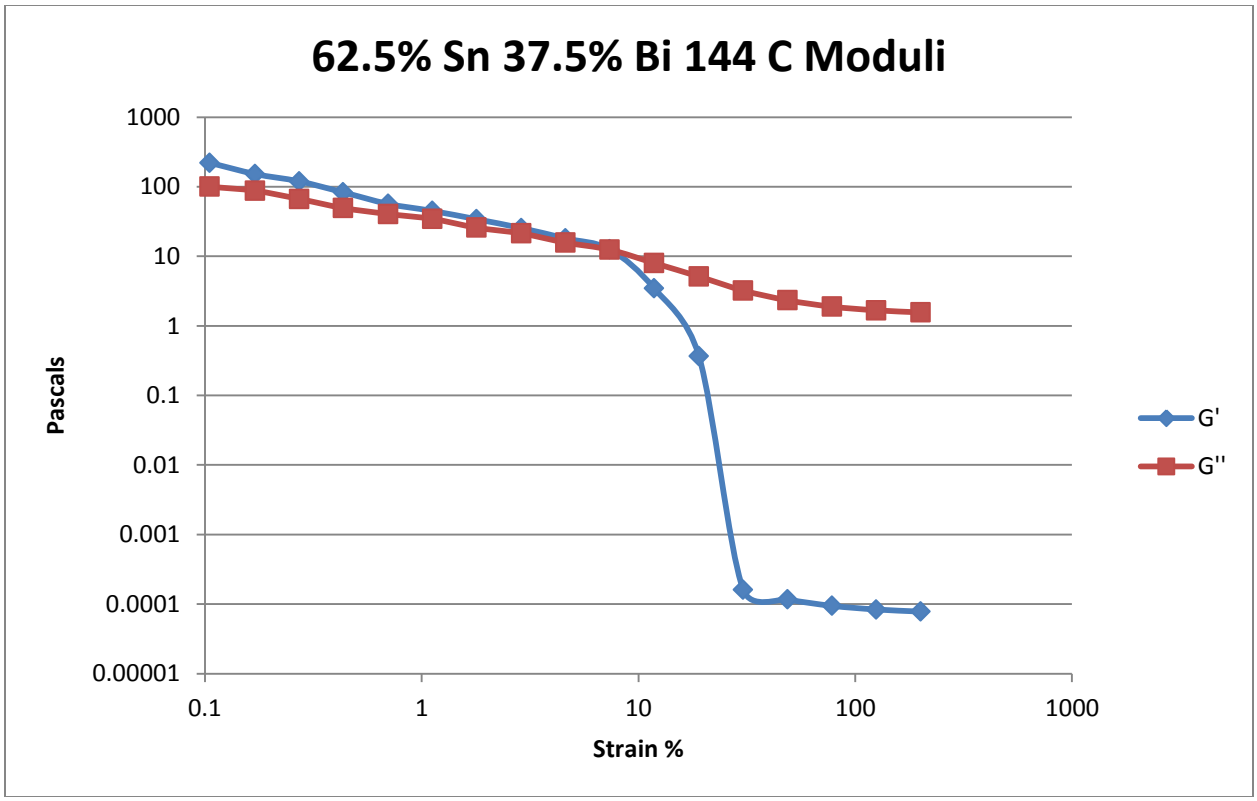

Figure 527- 62.5% Tin 37.5% Bismuth, 144 C, Oscillatory Shear Viscosity

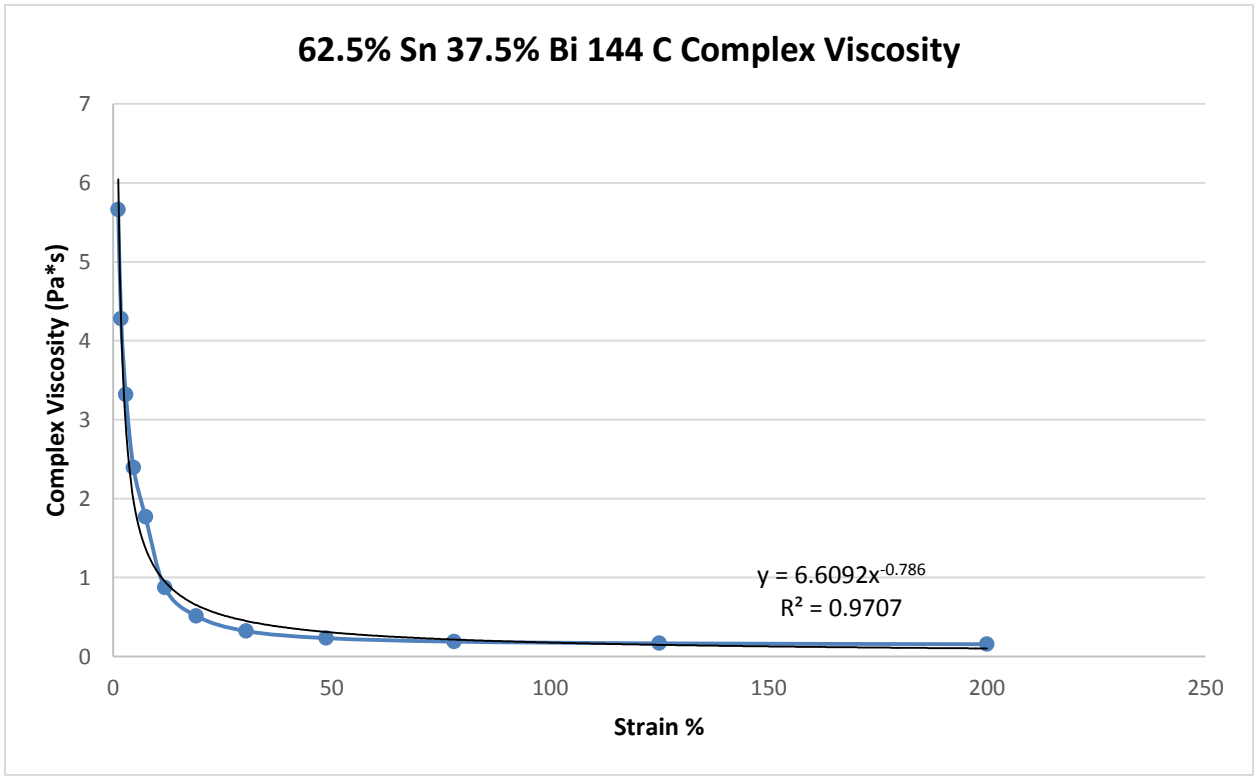

Figure 528- 62.5% Tin 37.5% Bismuth, 144 C, Oscillatory Shear Complex Viscosity

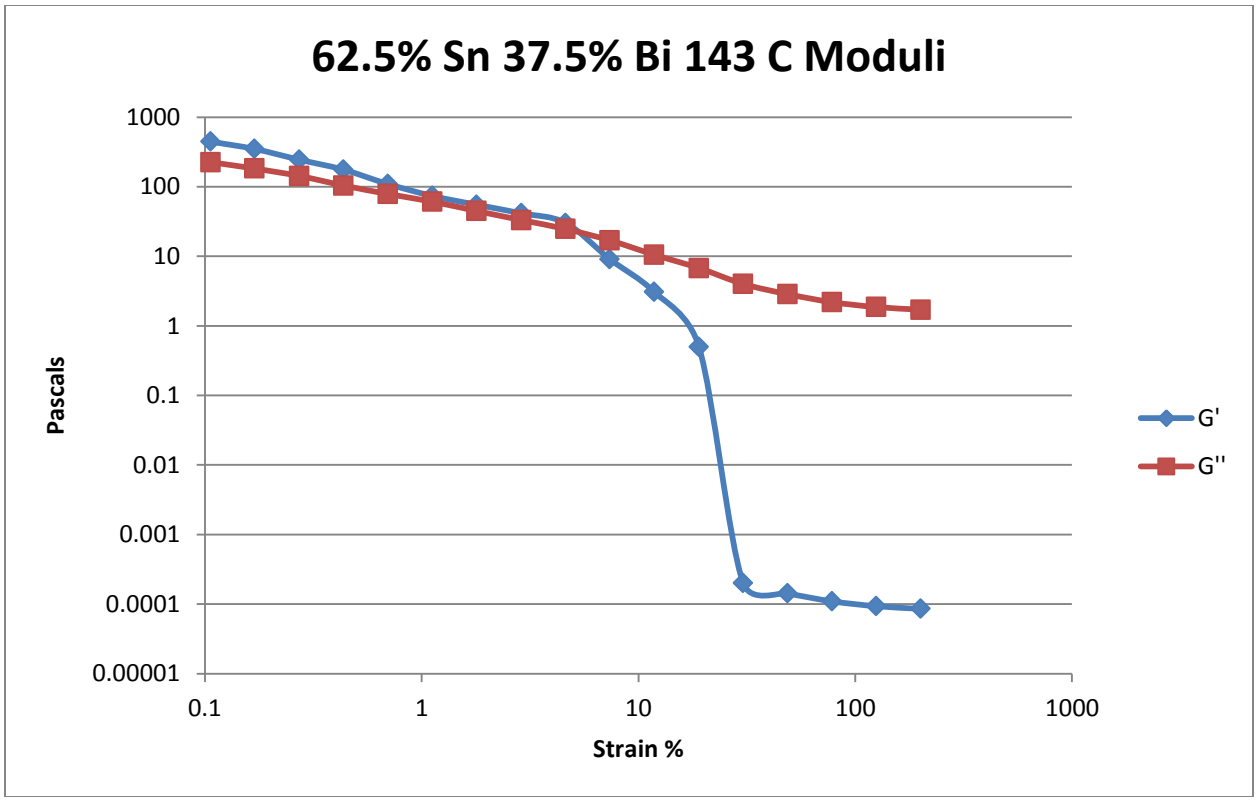

Figure 529- 62.5% Tin 37.5% Bismuth, 143 C, Oscillatory Shear Moduli

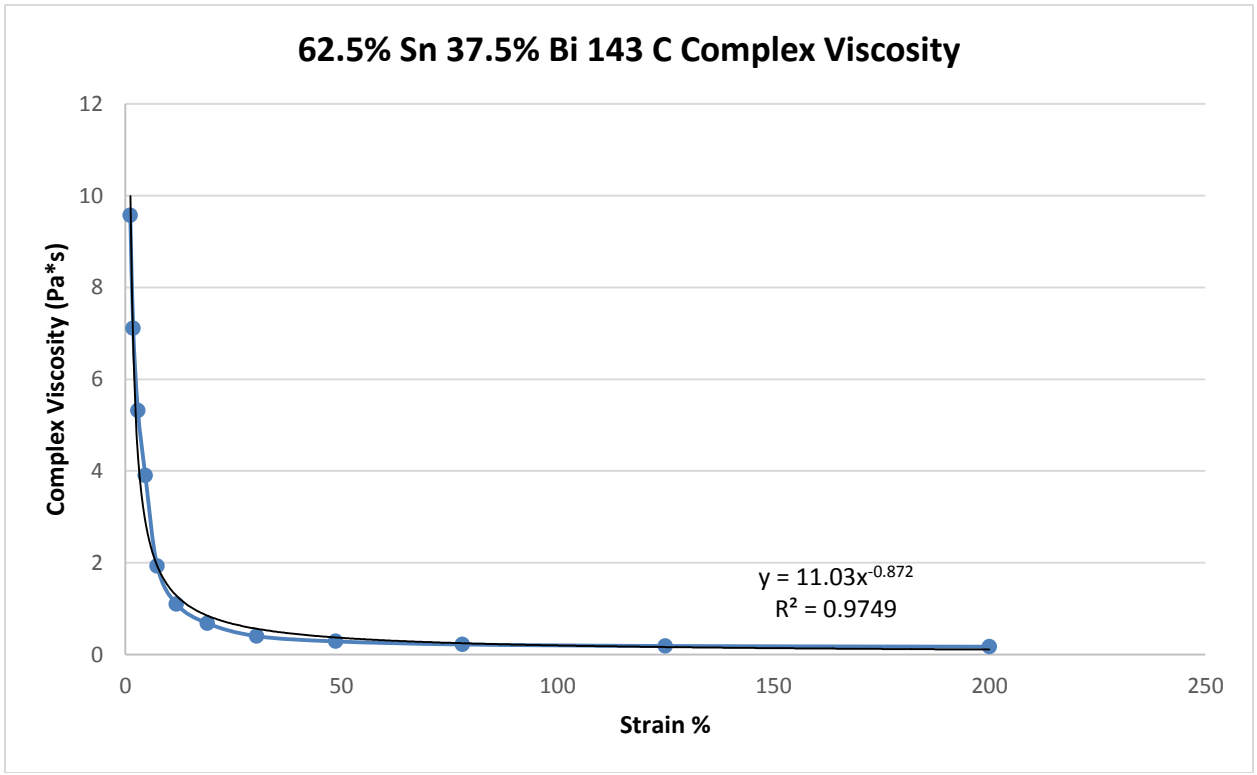

Figure 530- 62.5% Tin 37.5% Bismuth, 143 C, Oscillatory Shear Complex Viscosity

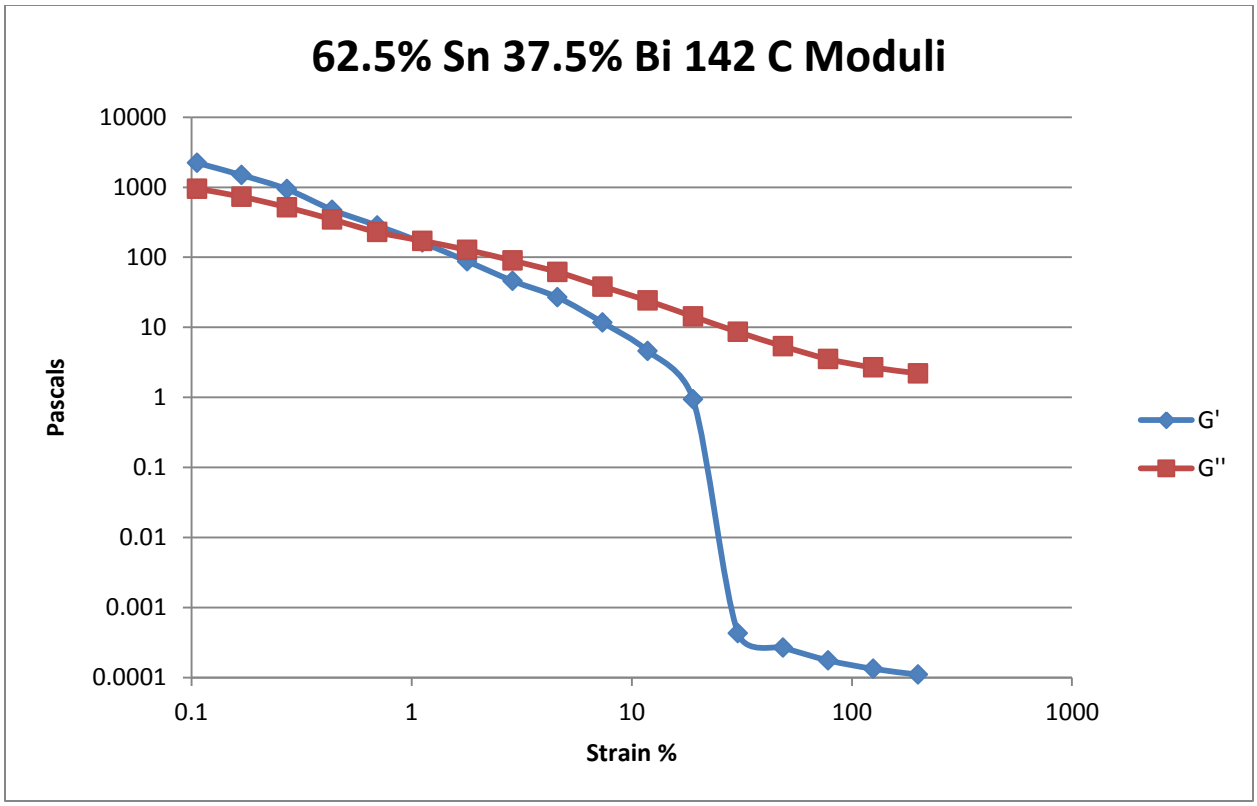

Figure 531- 62.5% Tin 37.5% Bismuth, 142 C, Oscillatory Shear Moduli

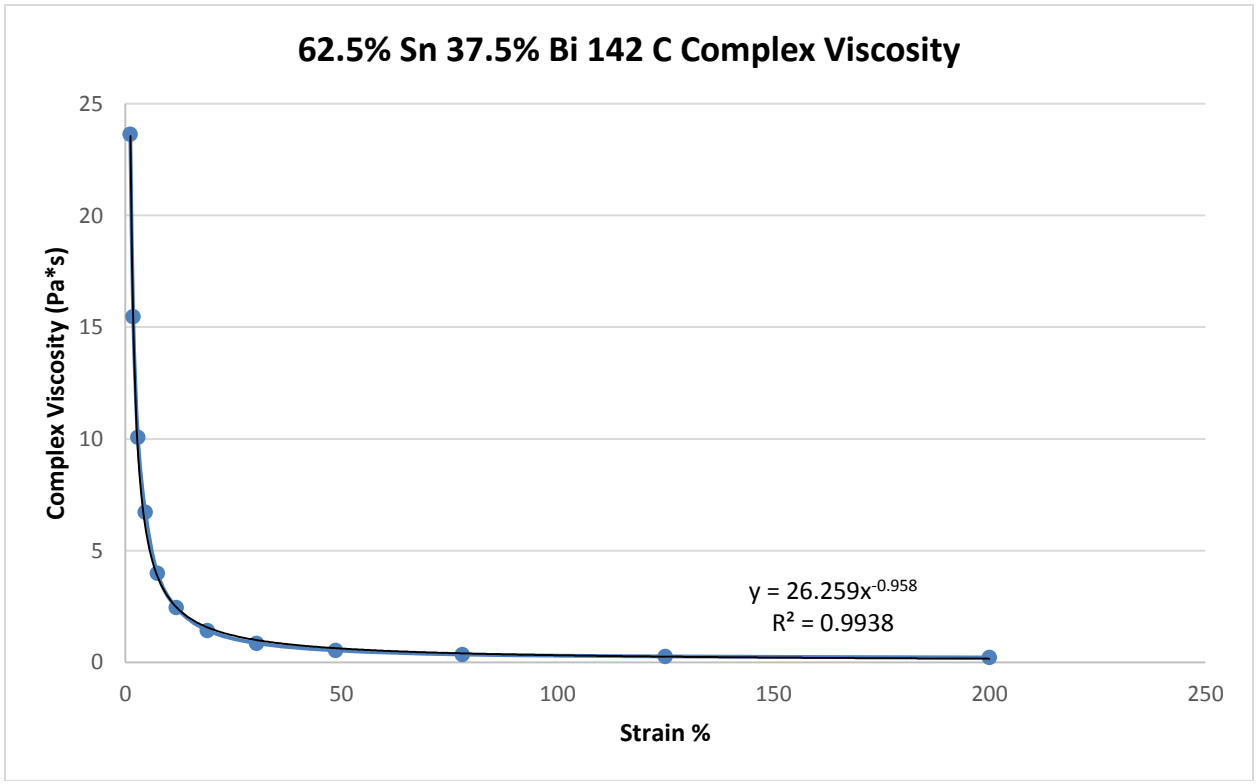

Figure 532- 62.5% Tin 37.5% Bismuth, 142 C, Oscillatory Shear Complex Viscosity

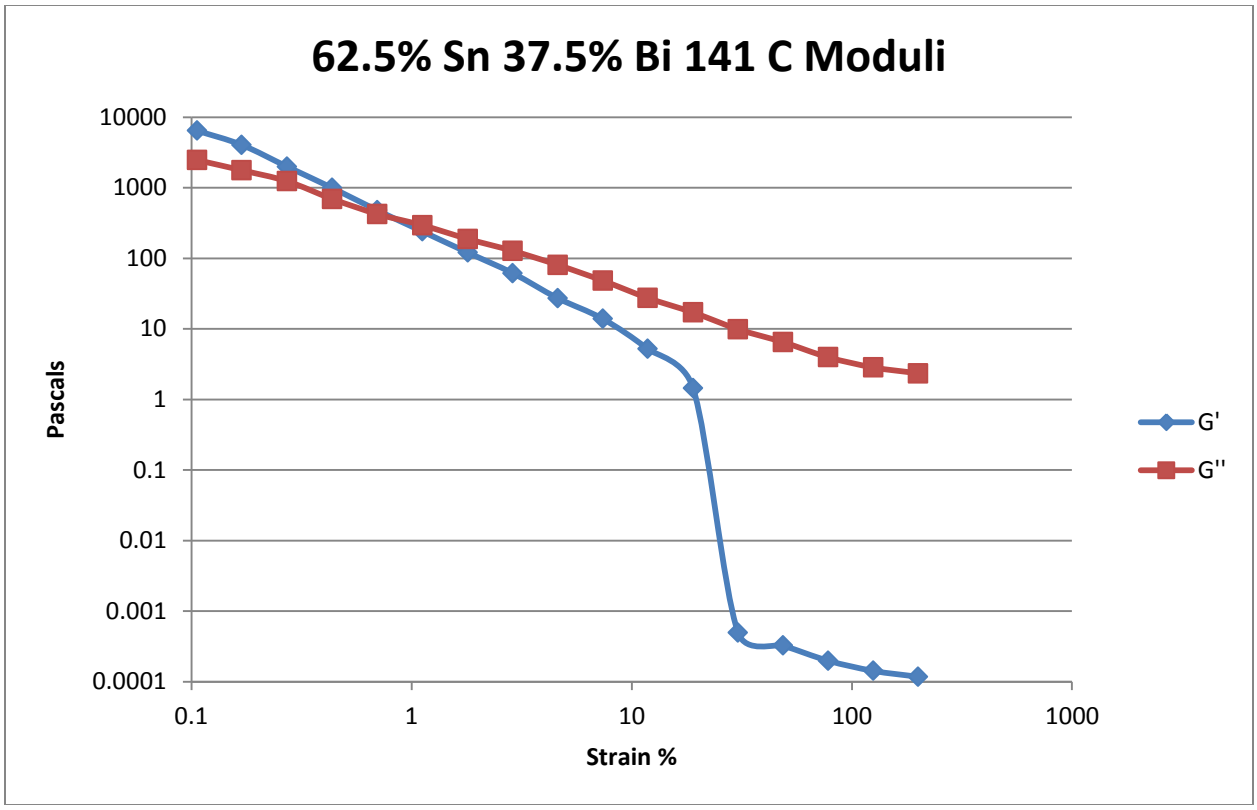

Figure 533- 62.5% Tin 37.5% Bismuth, 141 C, Oscillatory Shear Moduli

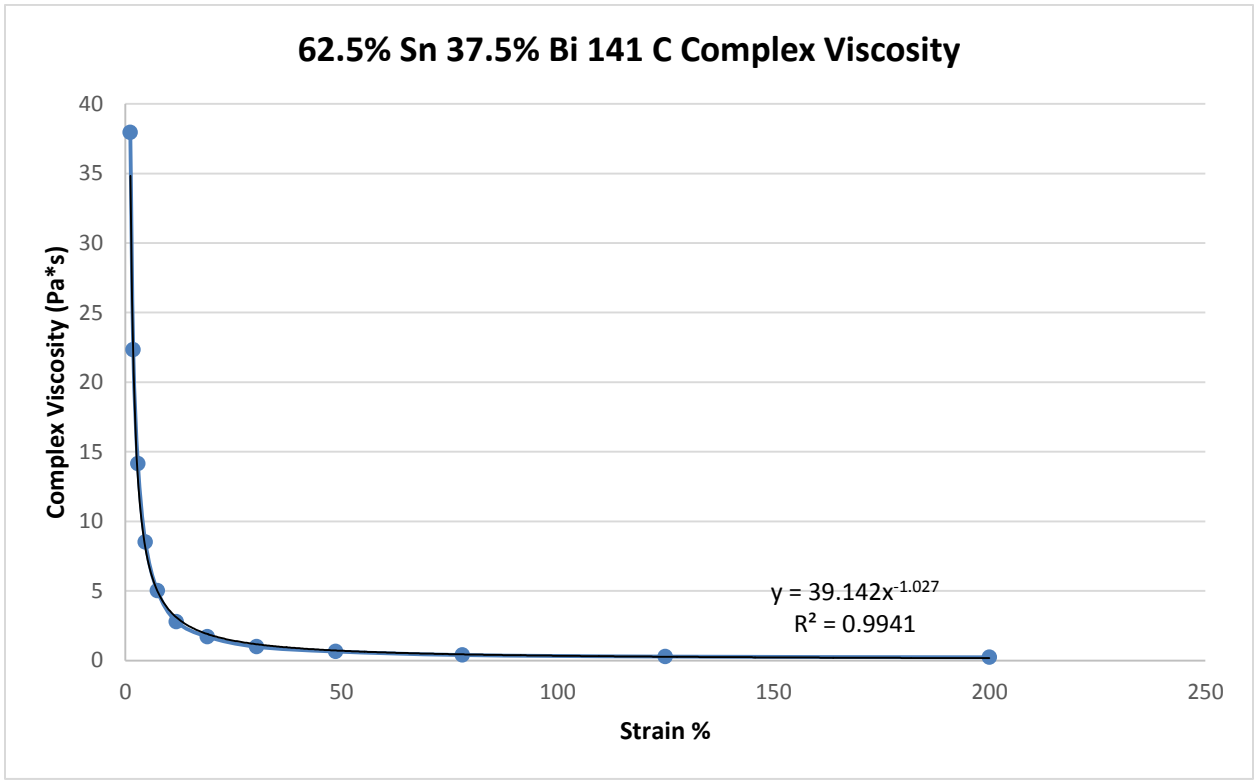

Figure 534- 62.5% Tin 37.5% Bismuth, 141 C, Oscillatory Shear Complex Viscosity

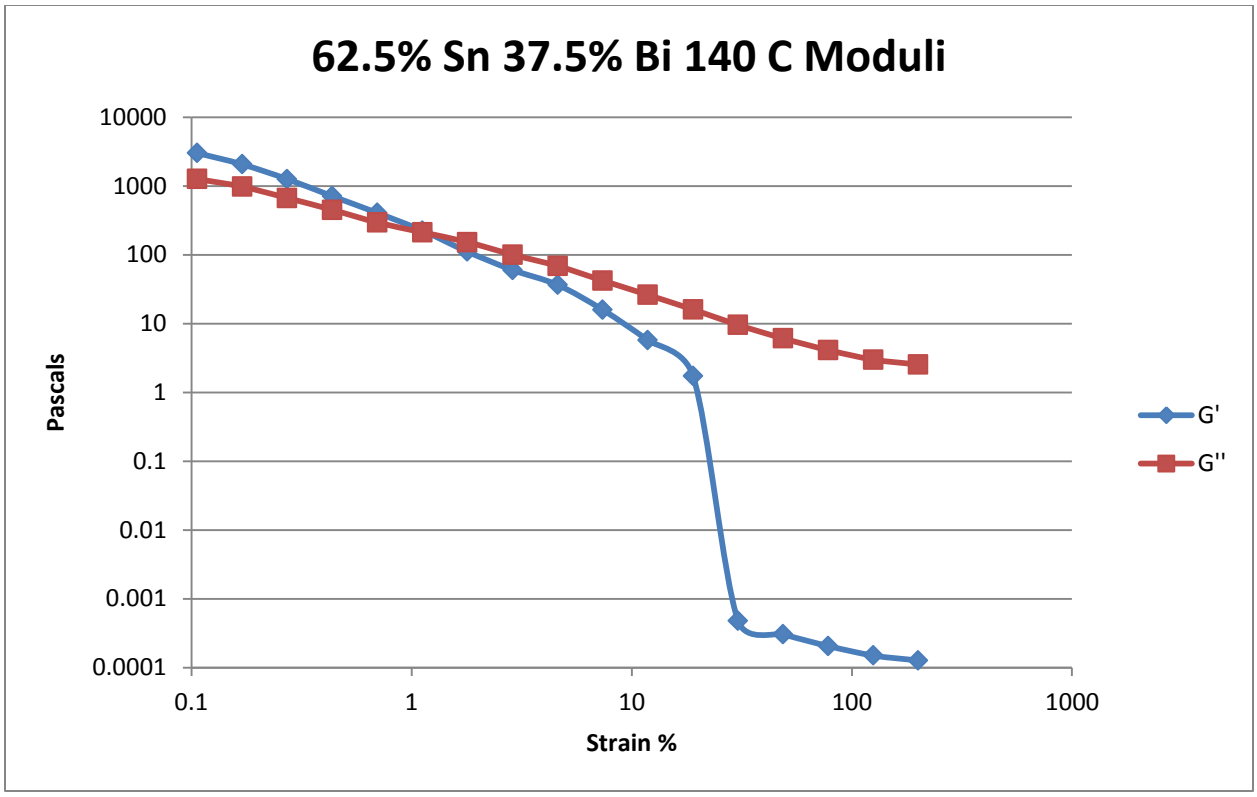

Figure 535- 62.5% Tin 37.5% Bismuth, 140 C, Oscillatory Shear Moduli

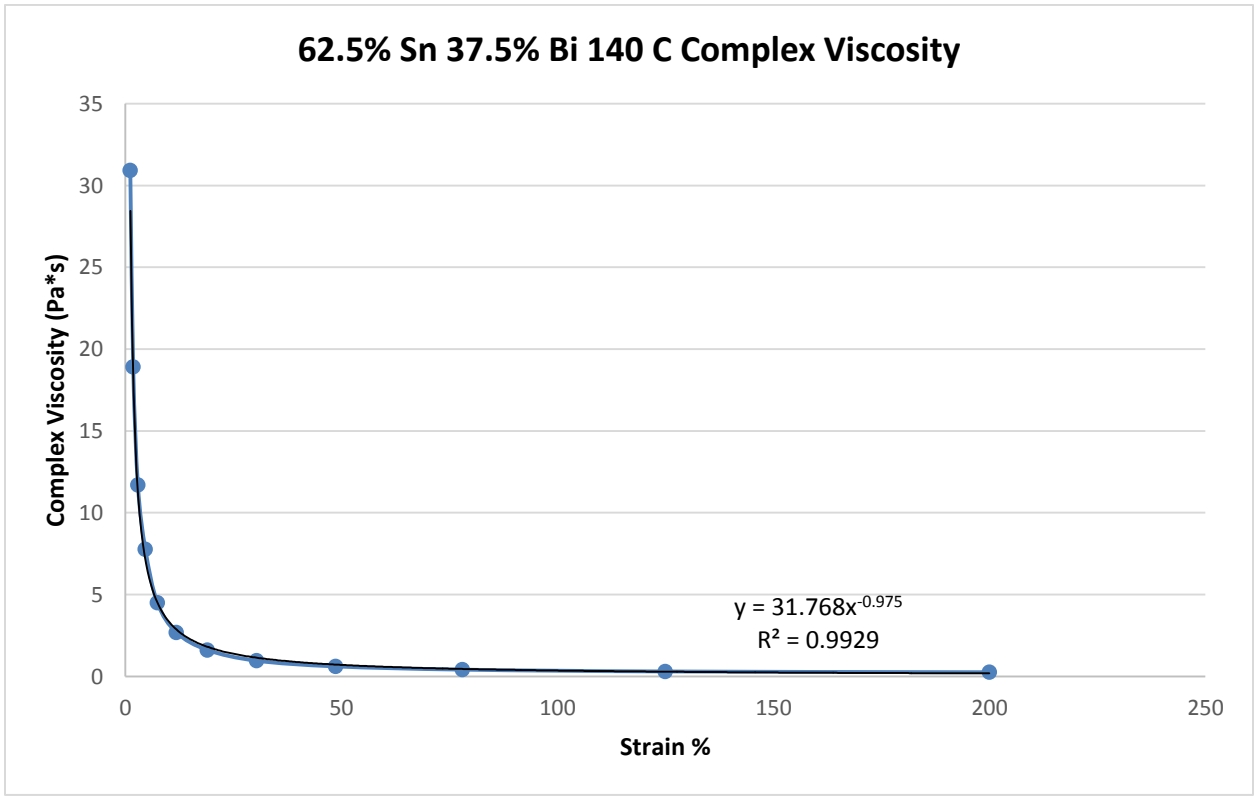

Figure 536- 62.5% Tin 37.5% Bismuth, 140 C, Oscillatory Shear Complex Viscosity

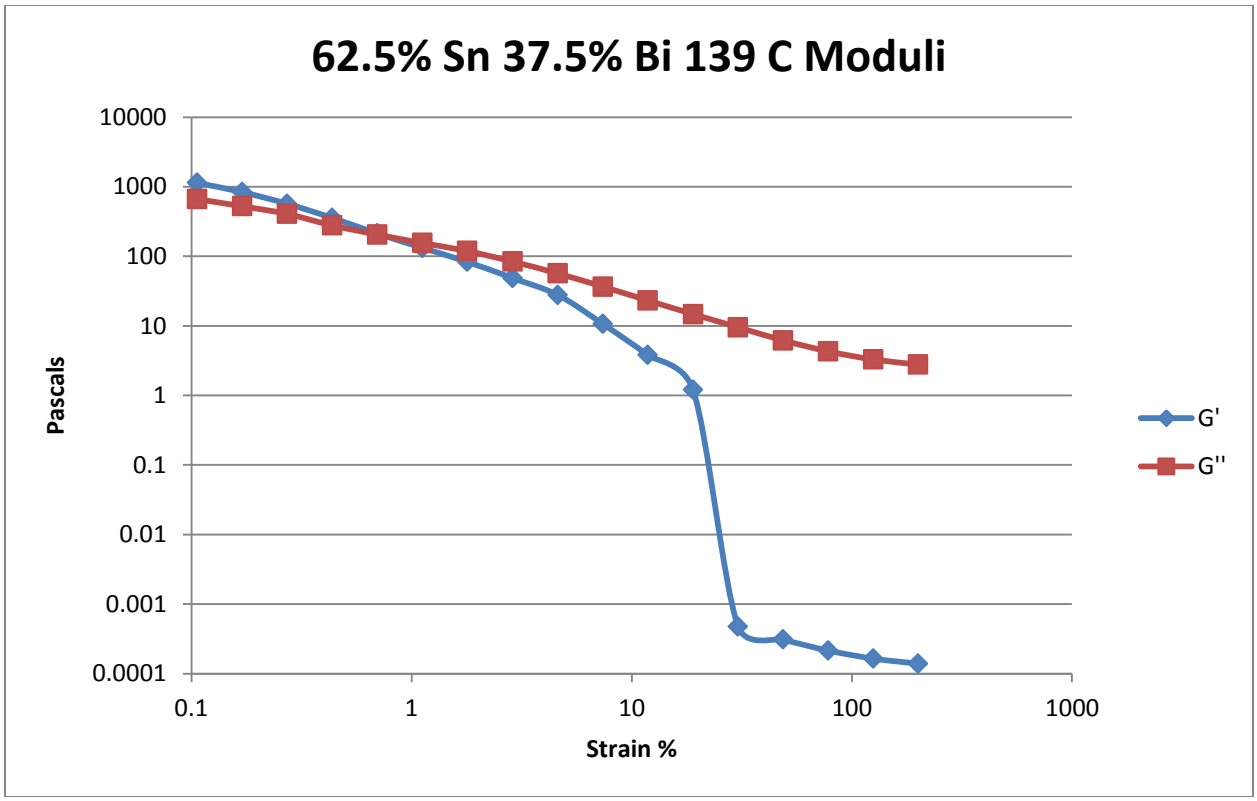

Figure 537- 62.5% Tin 37.5% Bismuth, 139 C, Oscillatory Shear Moduli

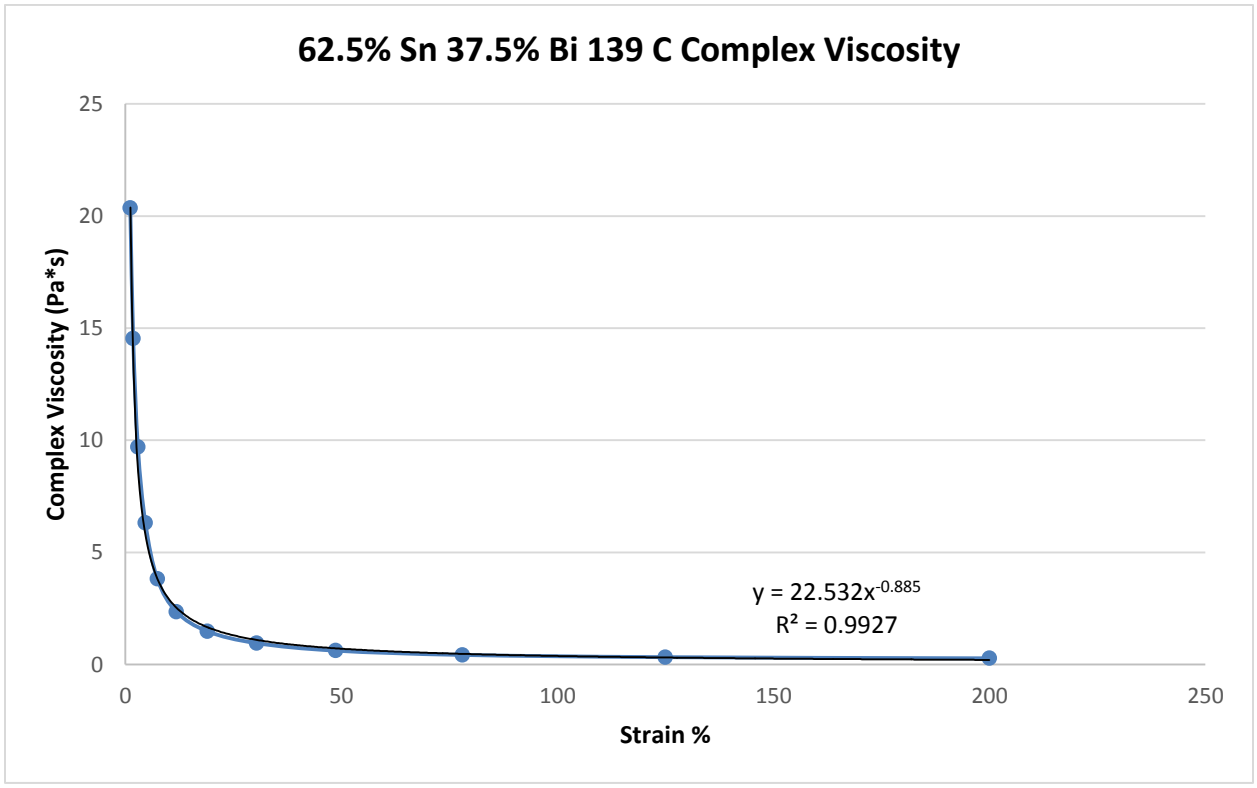

Figure 538- 62.5% Tin 37.5% Bismuth, 139 C, Oscillatory Shear Complex Viscosity

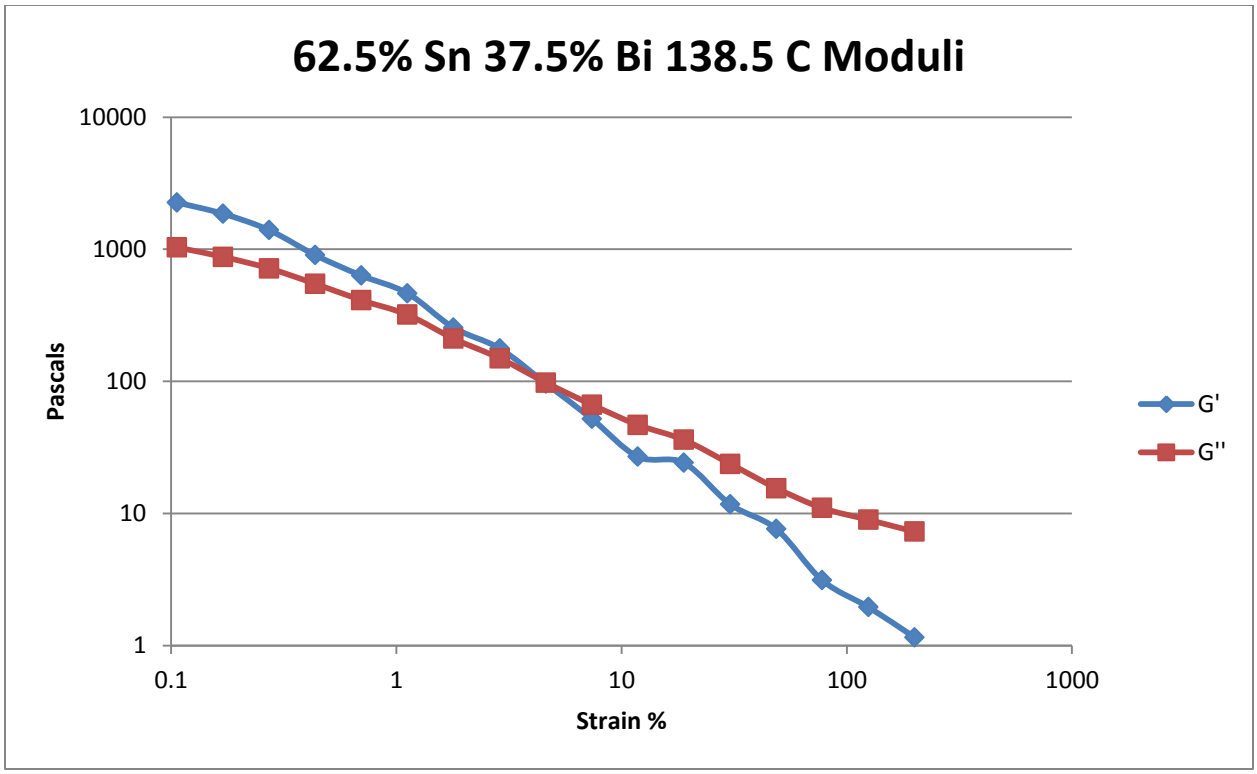

Figure 539- 62.5% Tin 37.5% Bismuth, 138.5 C, Oscillatory Shear Moduli

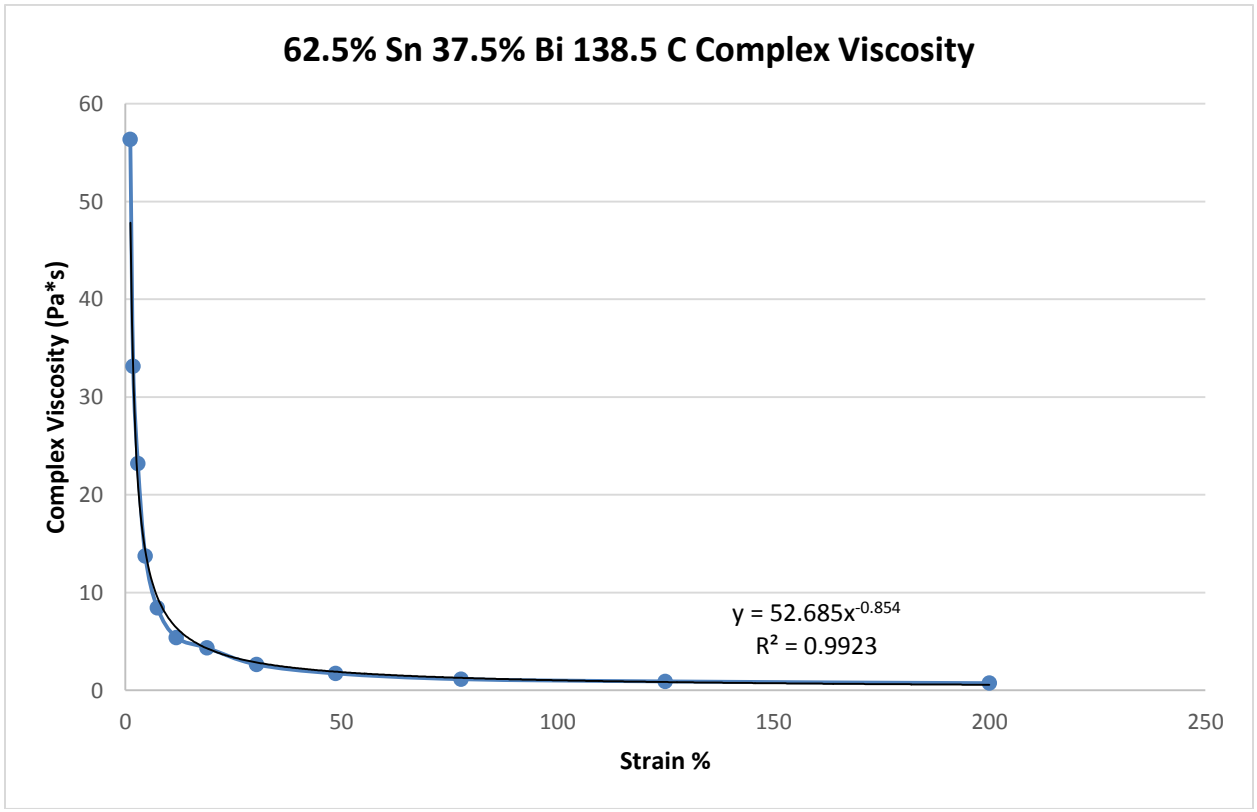

Figure 540- 62.5% Tin 37.5% Bismuth, 138.5 C, Oscillatory Shear Complex Viscosity

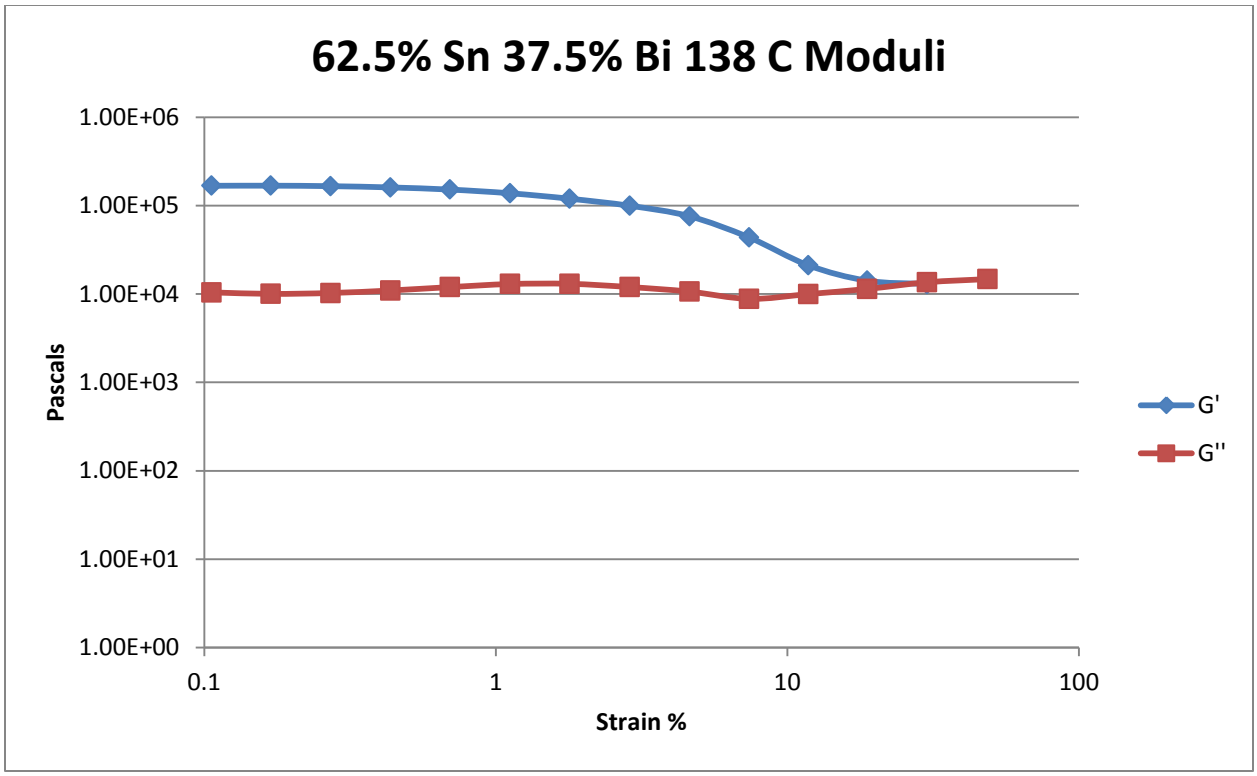

Figure 541- 62.5% Tin 37.5% Bismuth, 138 C, Oscillatory Shear Moduli

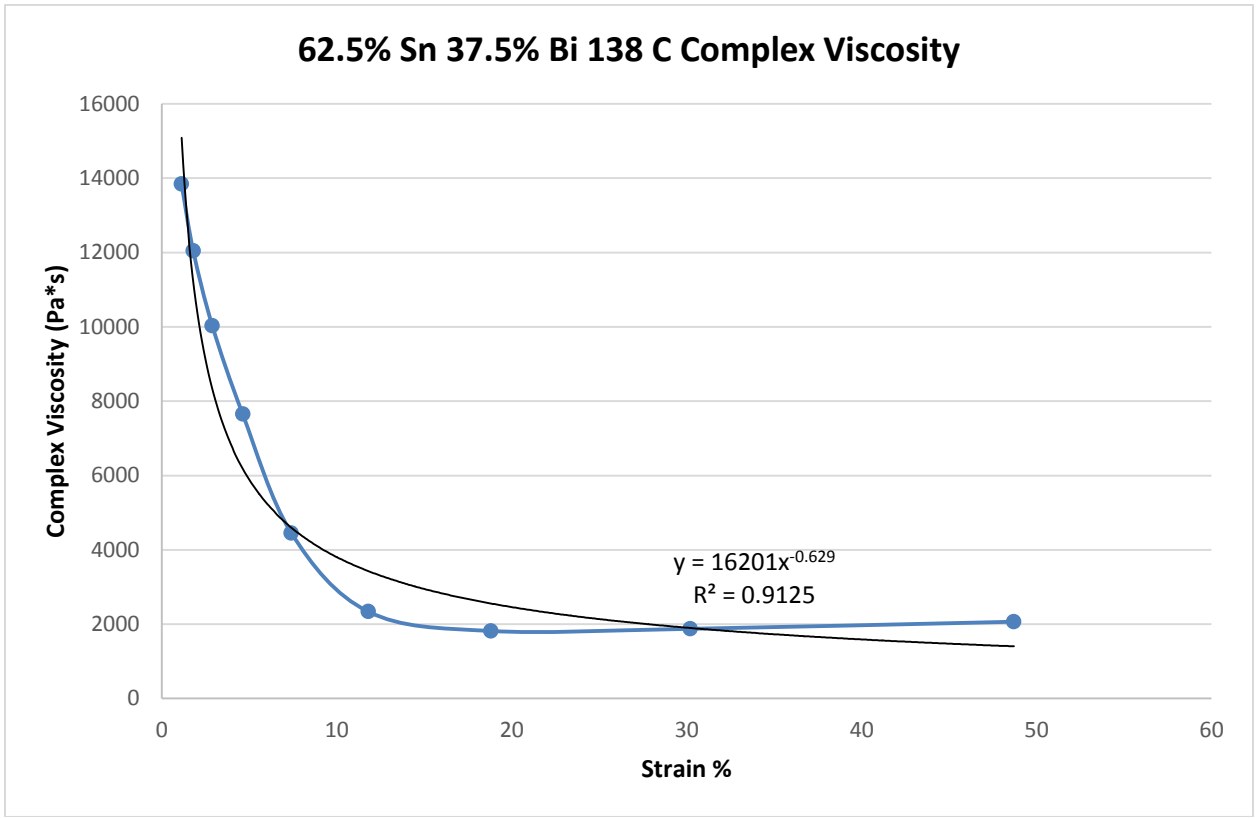

Figure 542- 62.5% Tin 37.5% Bismuth, 138 C, Oscillatory Shear Complex Viscosity

70% Tin 30% Bismuth

Actual Composition: 71.83% Sn, 28.17% Bi

Theoretical Solidus Line: 139 C
Theoretical Liquidus Line: 171.1 C

Experimental Solidus Line: 137.4 C
Experimental Liquidus Line: 169.9 C

Pre-Shear: 15 RPM, 2 minutes
Angular Velocity: Constant, 10 rad/s
Strain Range: 0.01%-200%

70% Tin 30% Bismuth Oscillatory Shear Rheology								
Temperature (C)	**Fraction Solid (%)**	**Crossover Strain (%)**	**Crossover Stress (Pa)**	**Crossover Modulus (Pa)**	**Crossover Complex Viscosity (Pa*s)**	**Pre G' Plateau (Pa)**	**Pre G'' Plateau (Pa)**	**Final Complex Viscosity (Pa*s)**
160	15.2	14.8	2.11	10.1	1.42	260	128	0.175
158	18.1	9.40	3.55	27.3	3.98	3.22e3	1.48e3	0.213
157	19.5	0.963	3.92	287	41.1	3.16e3	1.75e3	0.264
156	21.0	0.644	9.00	985	142	9.20e3	4.47e3	0.363
155	22.4	0.473	15.0	2.20e3	316	1.52e4	7.40e3	0.439
152	30.2	0.593	19.7	2.34e3	343	2.40e4	1.16e4	0.709
150	32.1	0.583	27.5	3.33e3	500	4.92e4	2.04e4	1.19

Table 95- 70% Tin 30% Bismuth Oscillatory Shear Rheology

70% Tin 30% Bismuth Oscillatory Shear Complex Viscosity			
Temperature (C)	**Fraction Solid (%)**	**Power Law Equation**	**R^2 (%)**
160	15.2	$\eta^* = 9.2148\gamma^{-0.782}$	95.32
158	18.1	$\eta^* = 33.309\gamma^{-1.033}$	98.43
157	19.5	$\eta^* = 36.954\gamma^{-1.008}$	98.90
156	21.0	$\eta^* = 73.45\gamma^{-1.059}$	99.43
155	22.4	$\eta^* = 107.61\gamma^{-1.095}$	99.49
152	30.2	$\eta^* = 158.25\gamma^{-1.061}$	99.78
150	32.1	$\eta^* = 250.62\gamma^{-1.026}$	99.94

Table 96- 70% Tin 30% Bismuth Oscillatory Shear Complex Viscosity

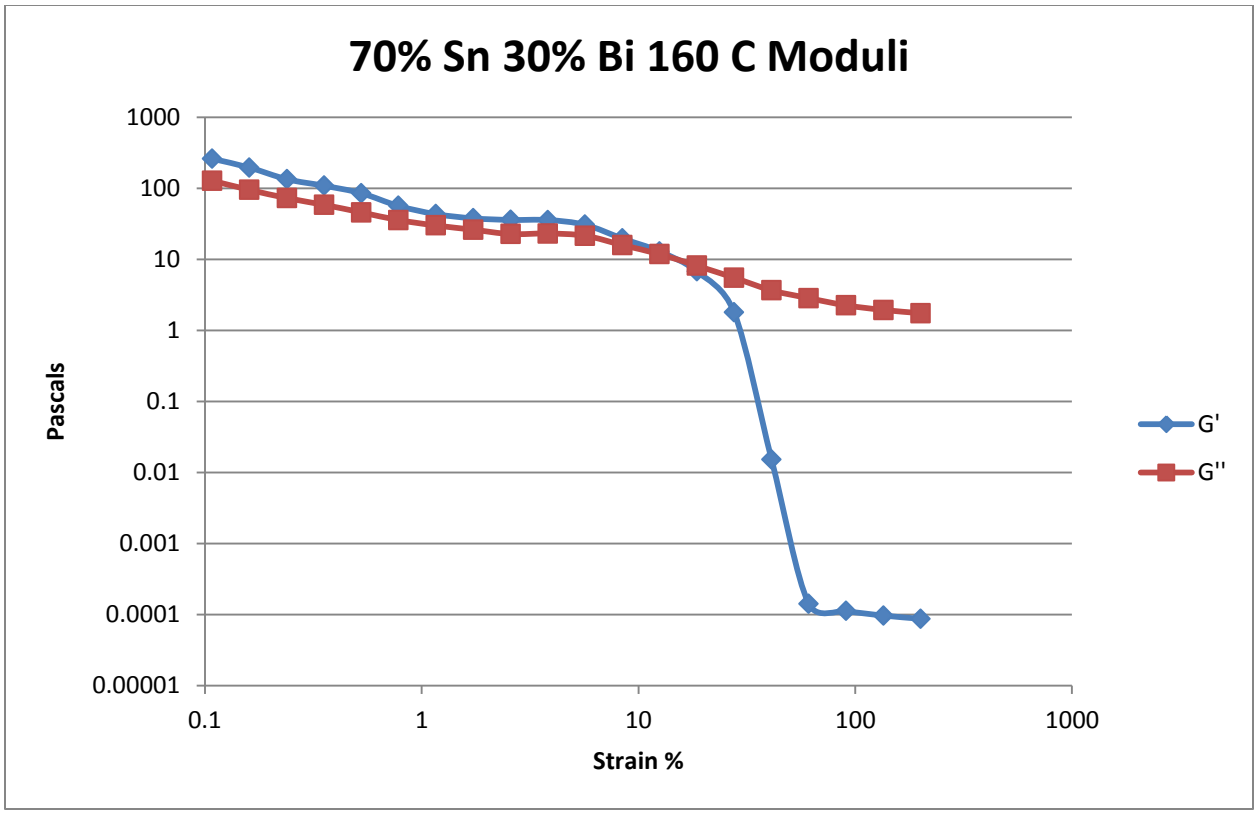

Figure 543- 70% Tin 30% Bismuth, 160 C, Oscillatory Shear Moduli

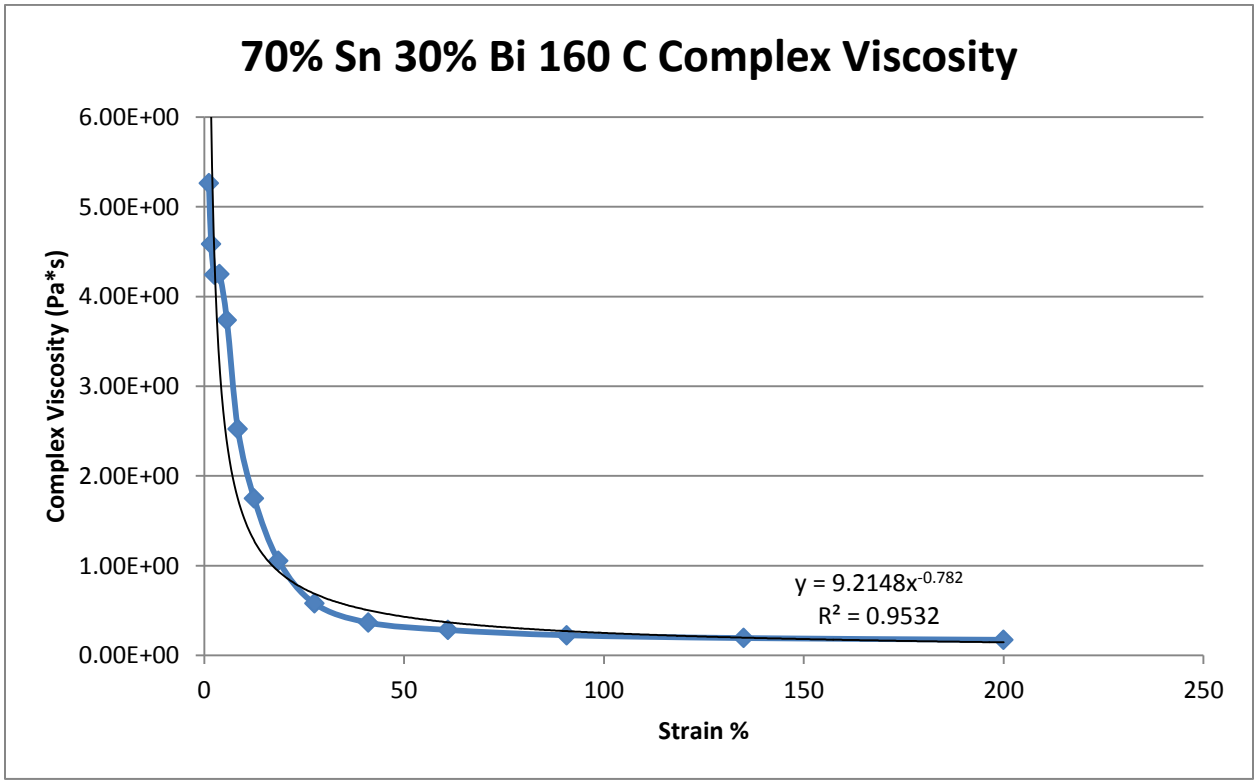

Figure 544- 70% Tin 30% Bismuth, 160 C, Oscillatory Shear Complex Viscosity

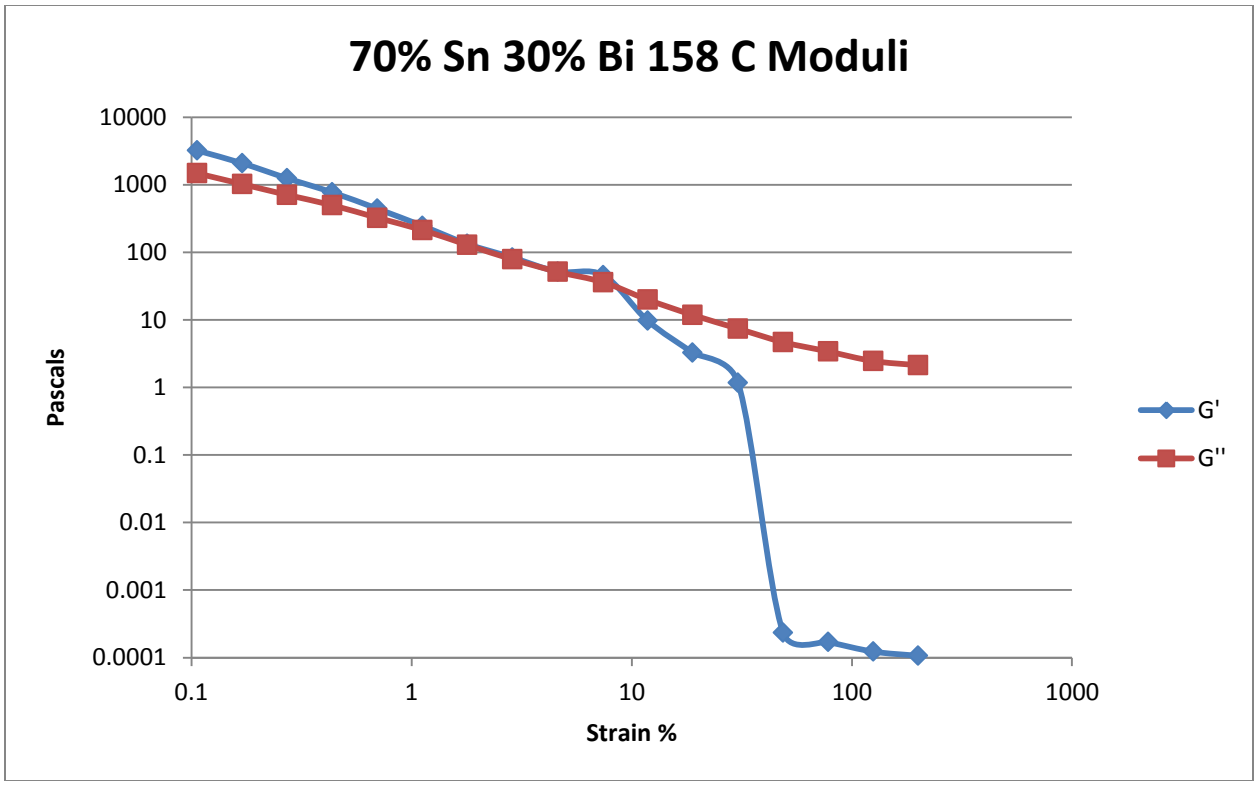

Figure 545- 70% Tin 30% Bismuth, 158 C, Oscillatory Shear Moduli

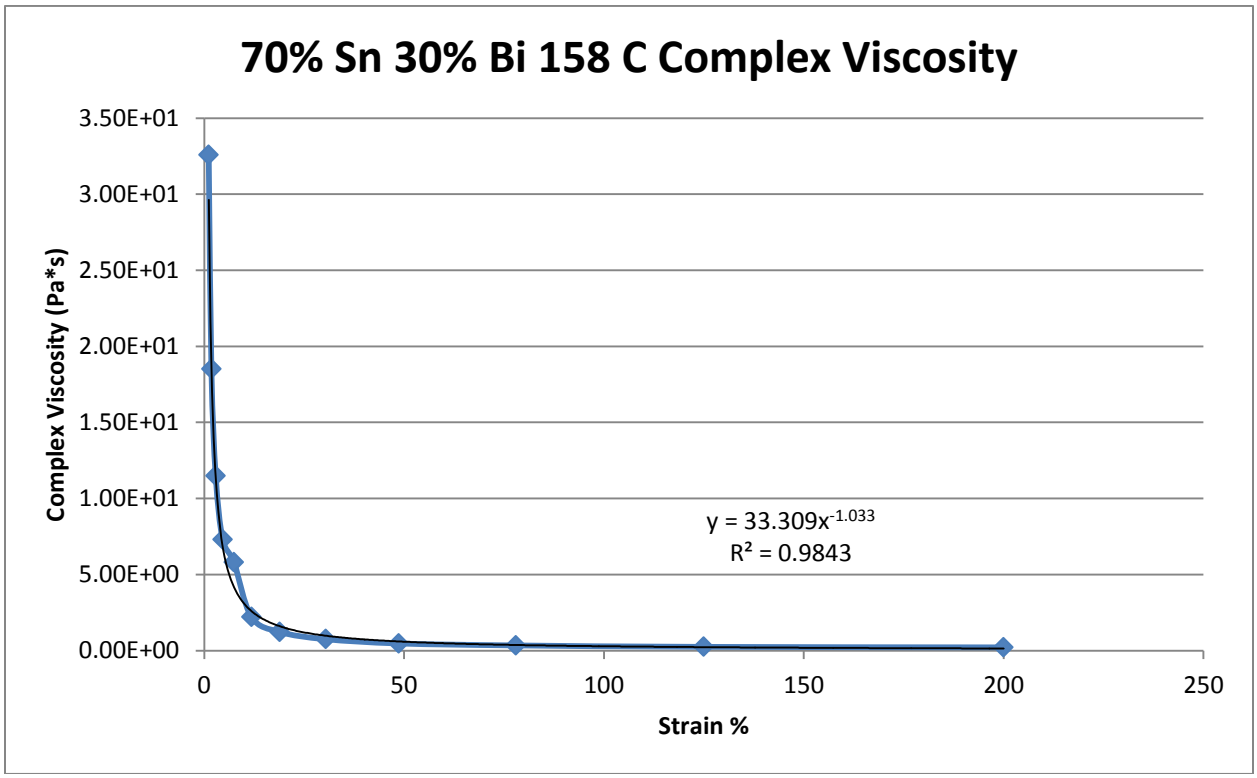

Figure 546- 70% Tin 30% Bismuth, 158 C, Oscillatory Shear Complex Viscosity

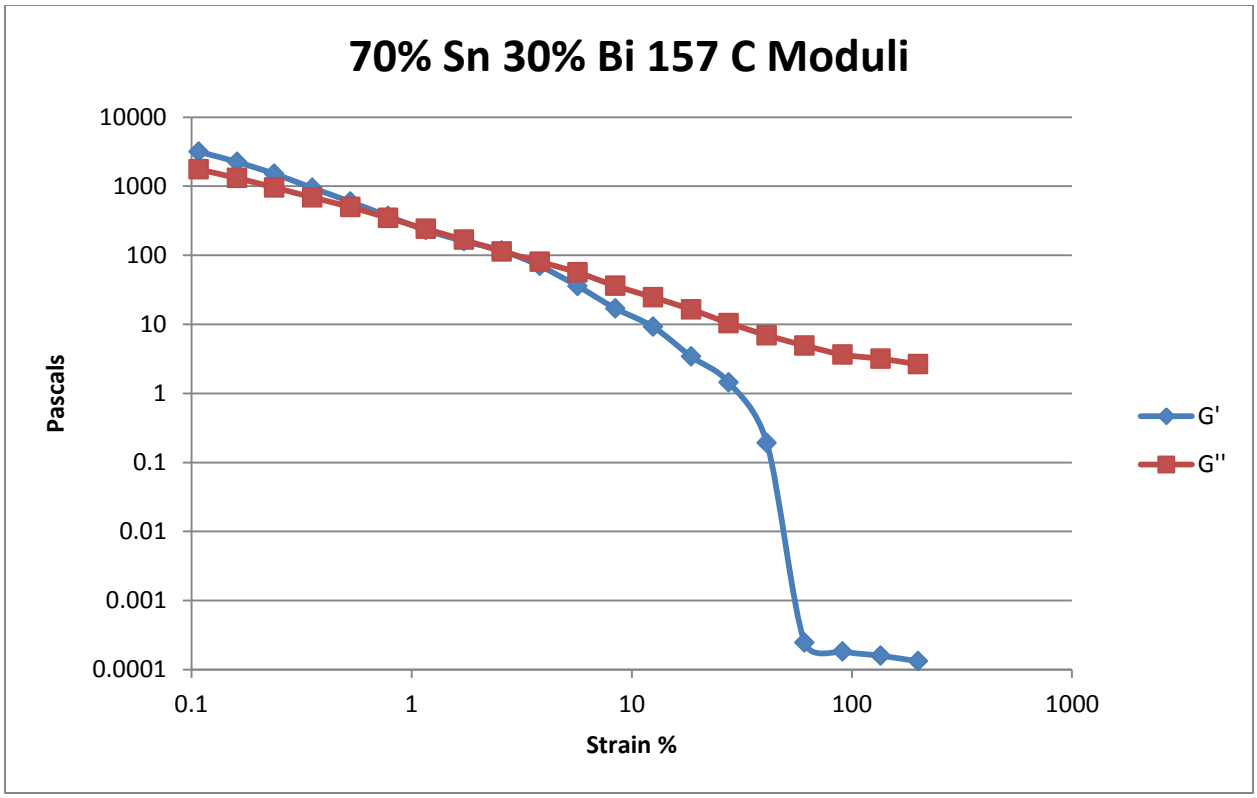

Figure 547- 70% Tin 30% Bismuth, 157 C, Oscillatory Shear Moduli

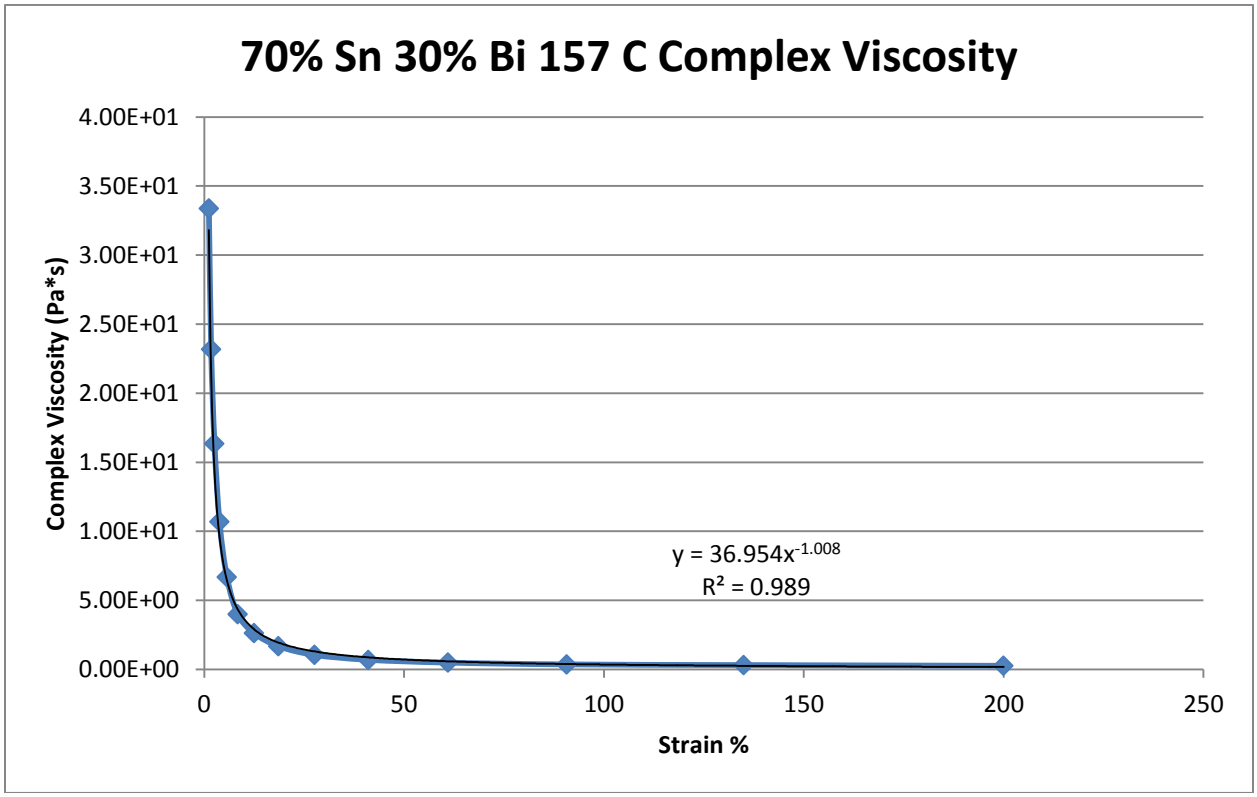

Figure 548- 70% Tin 30% Bismuth, 157 C, Oscillatory Shear Complex Viscosity

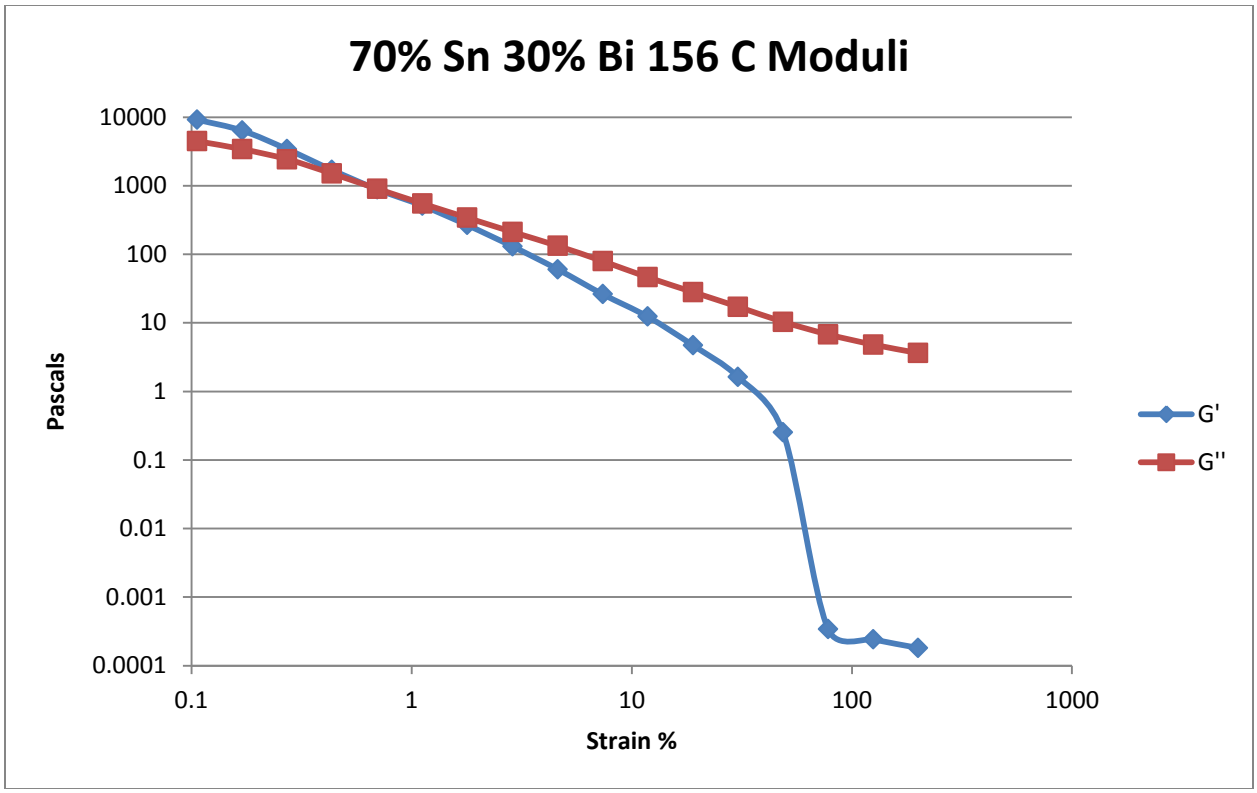

Figure 549- 70% Tin 30% Bismuth, 156 C, Oscillatory Shear Moduli

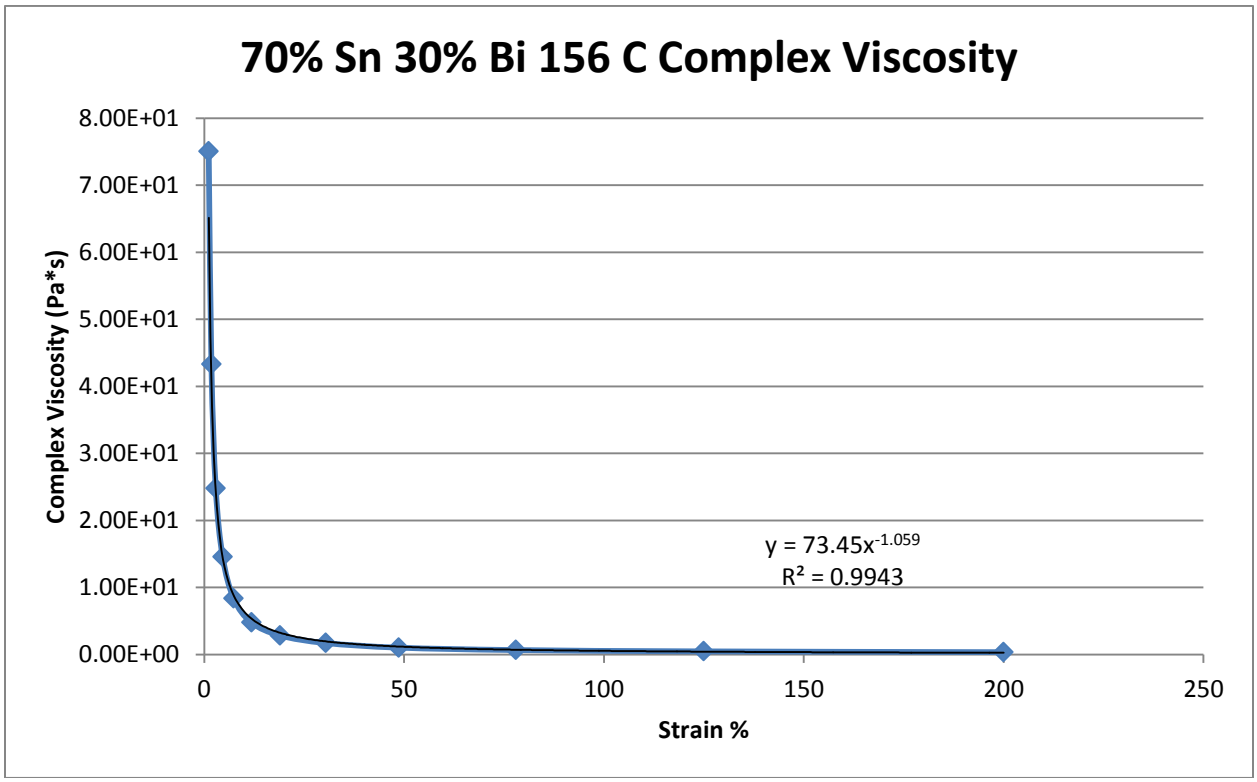

Figure 550- 70% Tin 30% Bismuth, 156 C, Oscillatory Shear Complex Viscosity

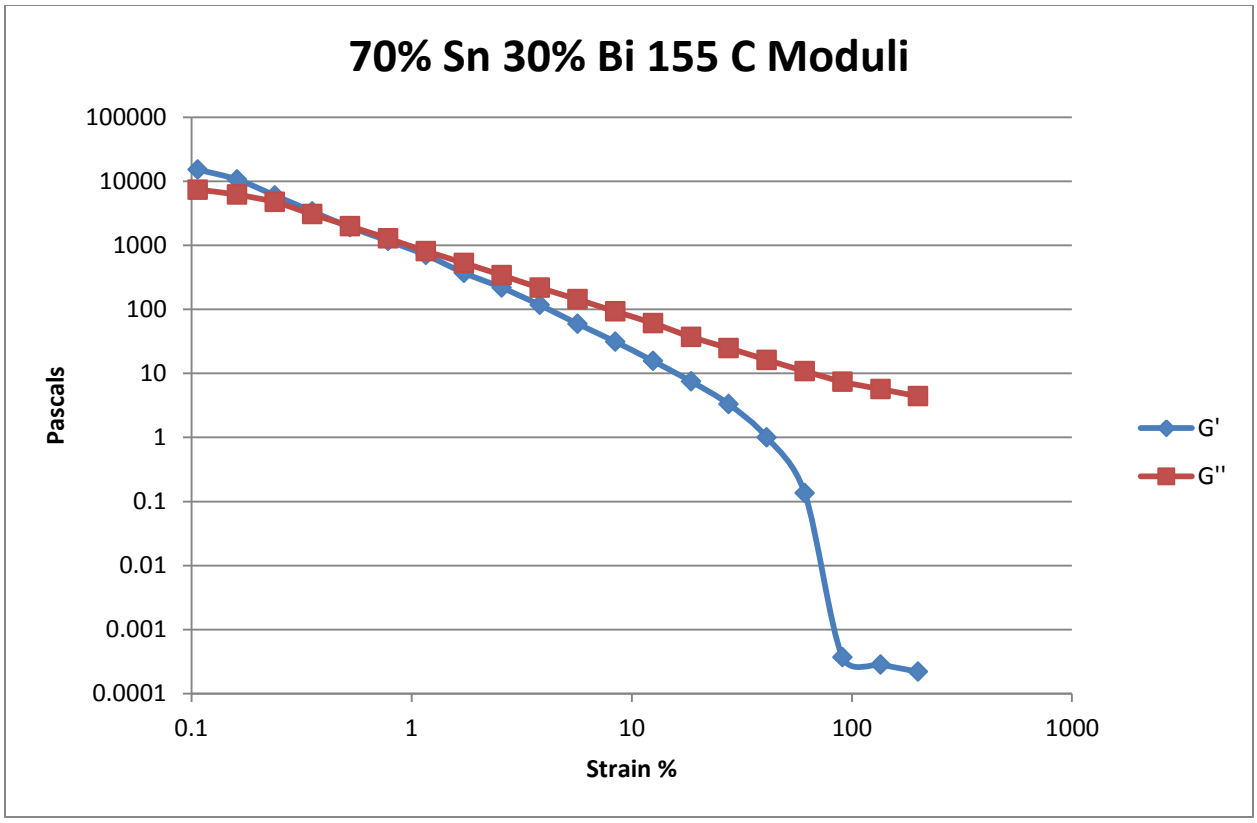

Figure 551- 70% Tin 30% Bismuth, 155 C, Oscillatory Shear Moduli

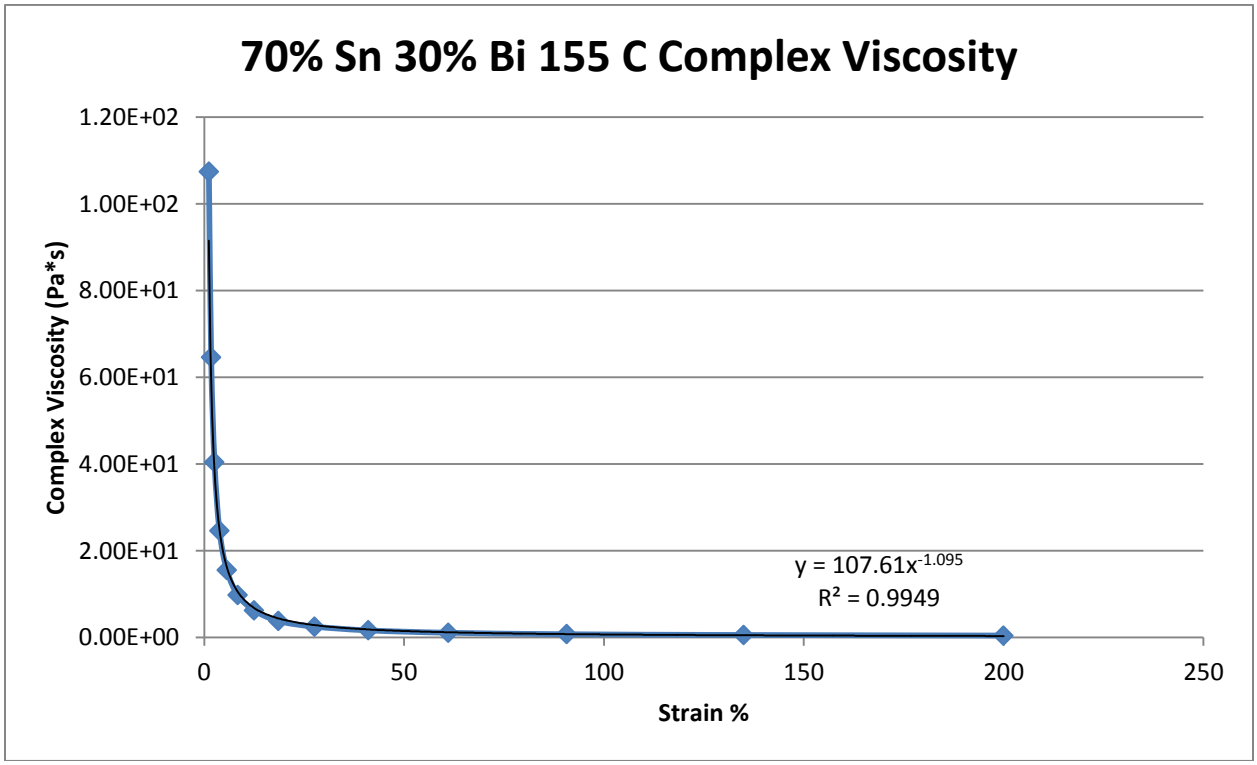

Figure 552- 70% Tin 30% Bismuth, 155 C, Oscillatory Shear Complex Viscosity

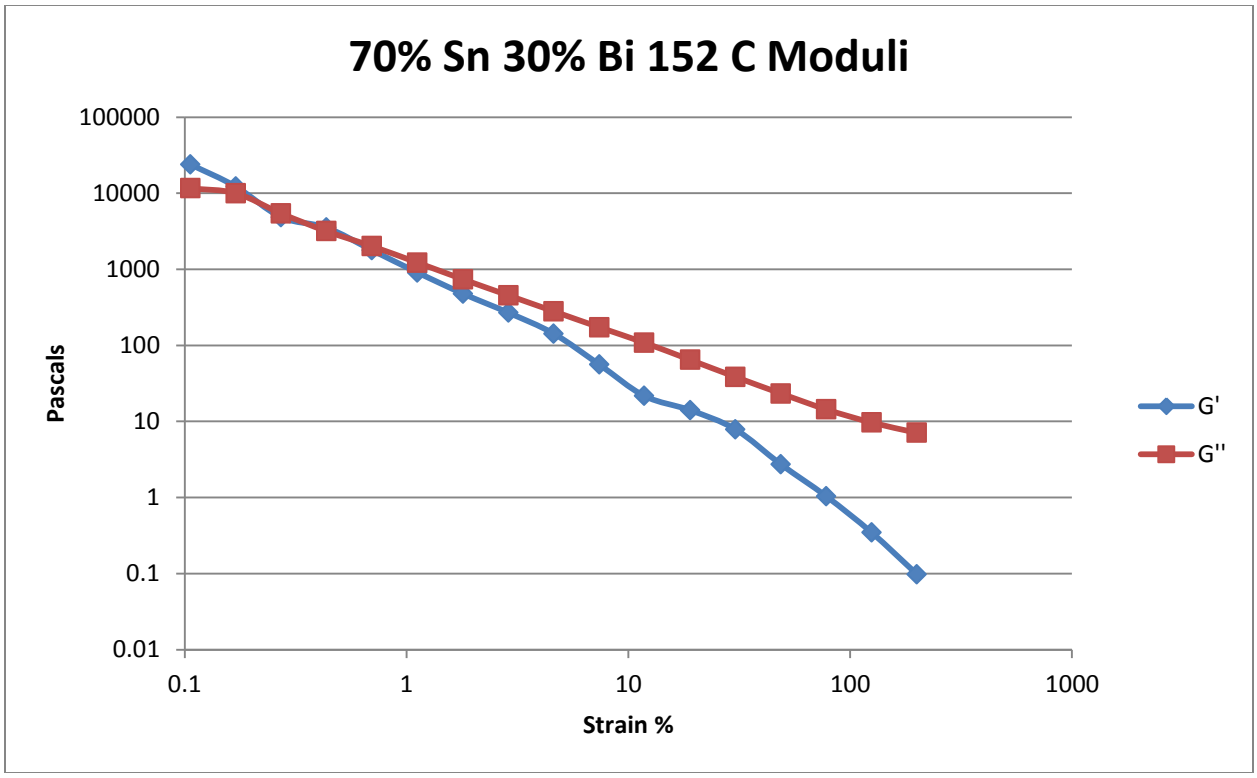

Figure 553- 70% Tin 30% Bismuth, 152 C, Oscillatory Shear Moduli

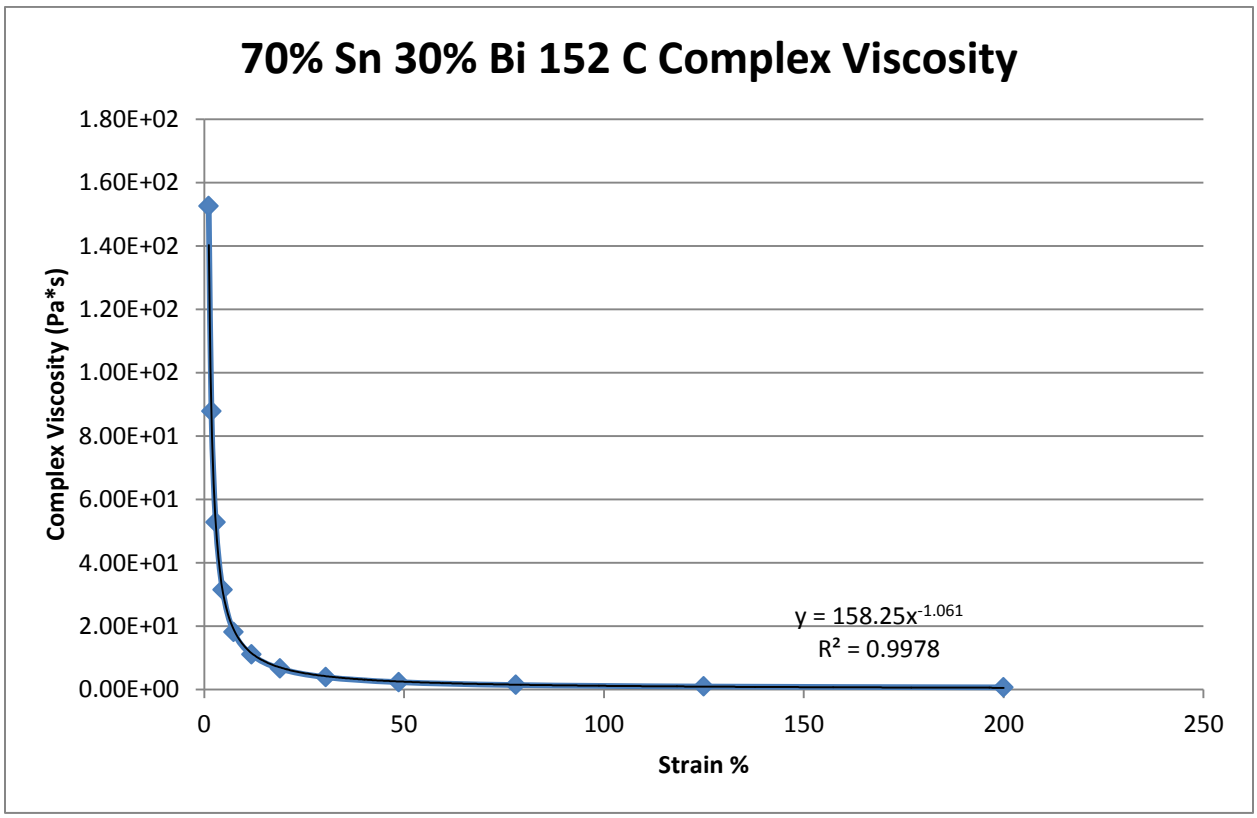

Figure 554- 70% Tin 30% Bismuth, 152 C, Oscillatory Shear Complex Viscosity

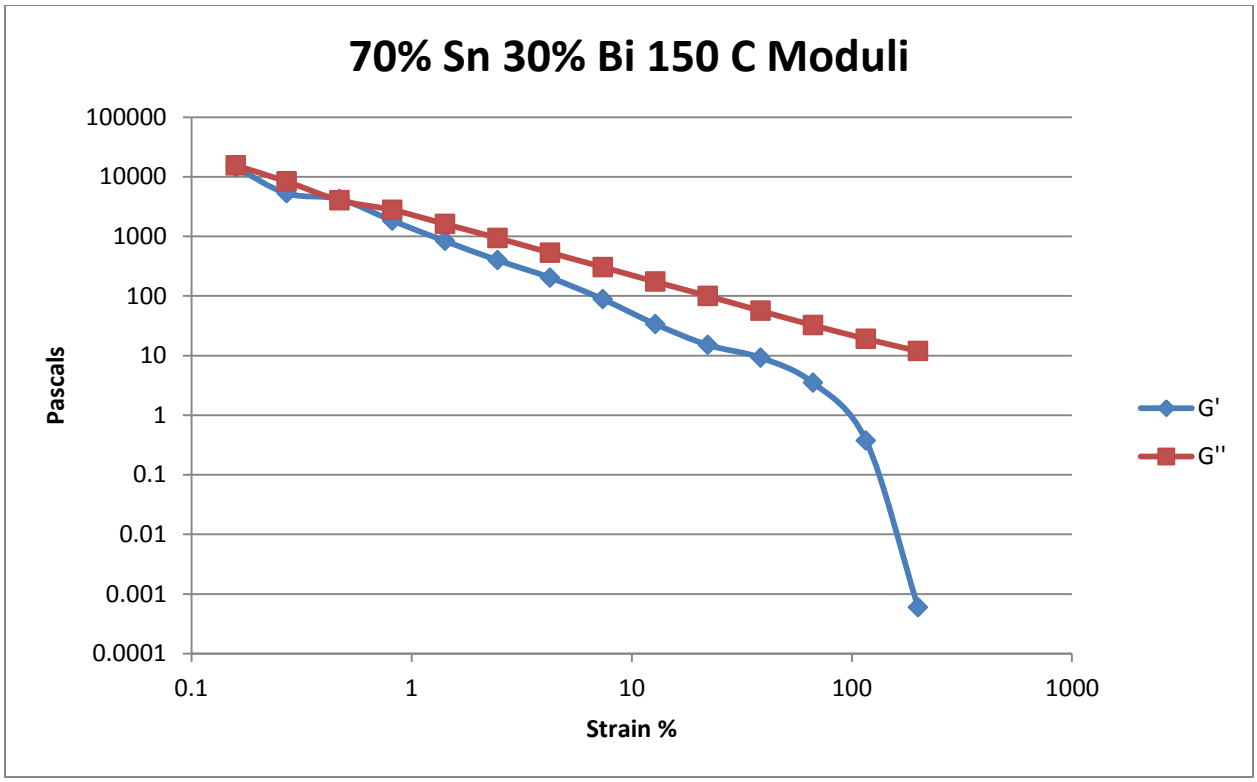

Figure 555- 70% Tin 30% Bismuth, 150 C, Oscillatory Shear Moduli

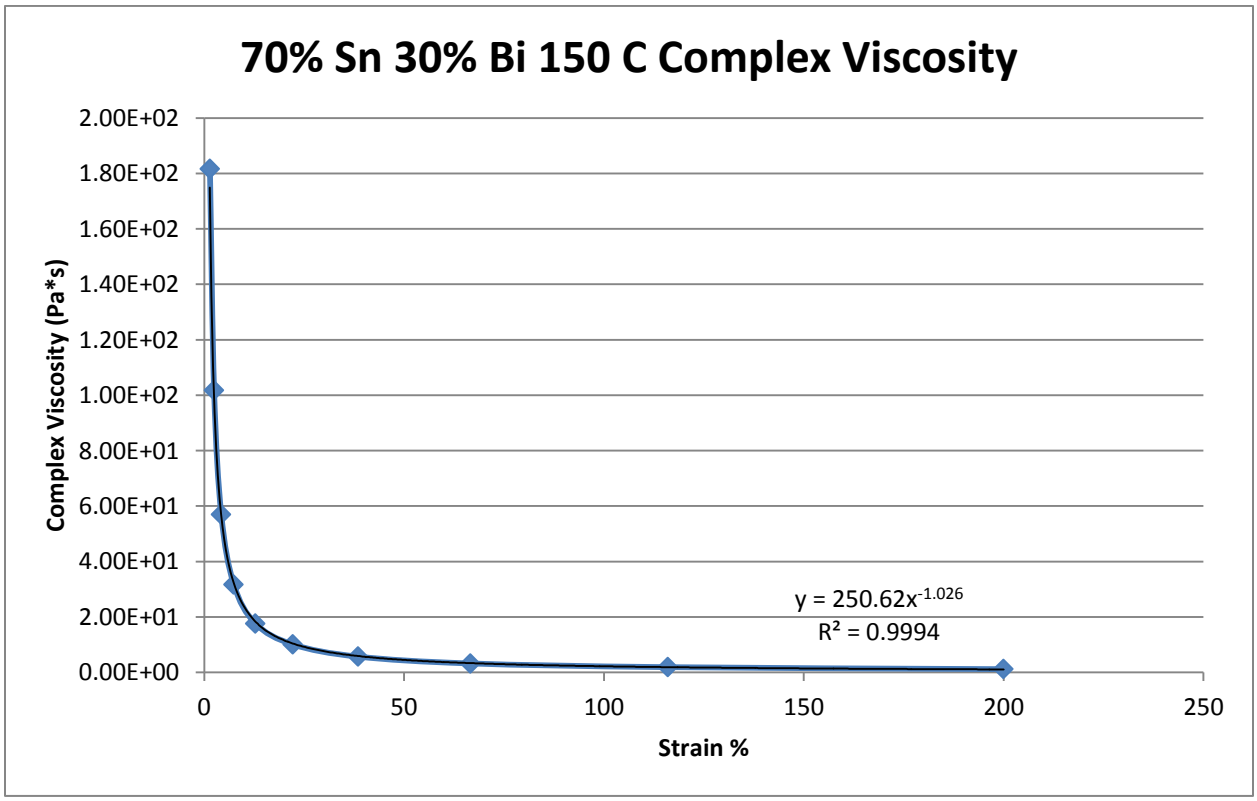

Figure 556- 70% Tin 30% Bismuth, 150 C, Oscillatory Shear Complex Viscosity

80% Tin 20% Bismuth

Actual Composition: 81.57% Sn, 18.43% Bi

Theoretical Solidus Line: 139 C
Theoretical Liquidus Line: 192.1 C

Experimental Solidus Line: 137.4 C
Experimental Liquidus Line: 185.9 C

Pre-Shear: 15 RPM, 2 minutes
Angular Velocity: Constant, 10 rad/s
Strain Range: 0.01%-200%

80% Tin 20% Bismuth Oscillatory Shear Rheology								
Temperature (C)	**Fraction Solid (%)**	**Crossover Strain (%)**	**Crossover Stress (Pa)**	**Crossover Modulus (Pa)**	**Crossover Complex Viscosity (Pa*s)**	**Pre G' Plateau (Pa)**	**Pre G'' Plateau (Pa)**	**Final Complex Viscosity (Pa*s)**
185	3.23	0.654	14.9	1606	1628	8.97e3	2.72e3	5.66
183	4.02	0.995	110	7810	1124	8.23e4	1.59e4	3.06
182	4.40	1.394	39.8	4446	281	5.31e4	1.09e4	2.73
181	4.78	0.776	49.9	4550	672	4.01e4	1.29e4	1.21
180	5.15	1.52	125	5790	843	1.01e5	2.42e4	4.28
175	6.99	0.485	29.5	4360	617	3.19e4	1.53e4	1.34
170	8.76	1.01	147	1.02e4	1521	1.43e5	3.37e4	6.97
165	10.5	1.72	622	2.65e4	3775	1.96e5	2.64e4	31.2
160	12.1	0.987	485	3.67e4	5395	1.97e5	3.73e4	30.5

Table 97- 80% Tin 20% Bismuth Oscillatory Shear Rheology

80% Tin 20% Bismuth Oscillatory Shear Complex Viscosity			
Temperature (C)	**Fraction Solid (%)**	**Power Law Equation**	**R^2 (%)**
185	3.23	$\eta^* = 780.90\gamma^{-0.891}$	98.14
183	4.02	$\eta^* = 969.40\gamma^{-1.098}$	99.95
182	4.40	$\eta^* = 819.89\gamma^{-1.092}$	99.85
181	4.78	$\eta^* = 411.90\gamma^{-1.122}$	99.84
180	5.15	$\eta^* = 1220.0\gamma^{-1.080}$	99.92
175	6.99	$\eta^* = 236.29\gamma^{-1.019}$	99.74
170	8.76	$\eta^* = 1539.7\gamma^{-1.022}$	99.95
165	10.5	$\eta^* = 5105.3\gamma^{-0.936}$	97.78
160	12.1	$\eta^* = 4386.5\gamma^{-0.944}$	99.80

Table 98- 80% Tin 20% Bismuth Oscillatory Shear Complex Viscosity

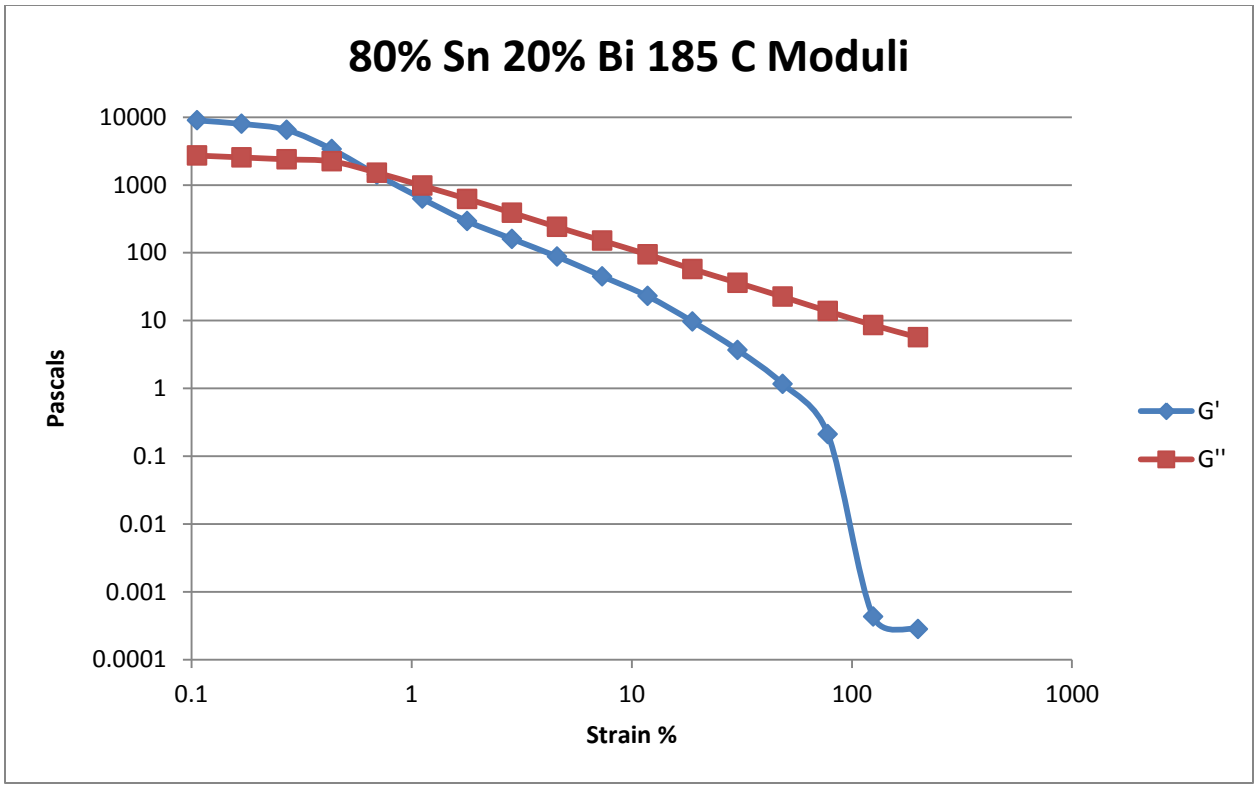

Figure 557- 80% Tin 20% Bismuth, 185 C, Oscillatory Shear Moduli

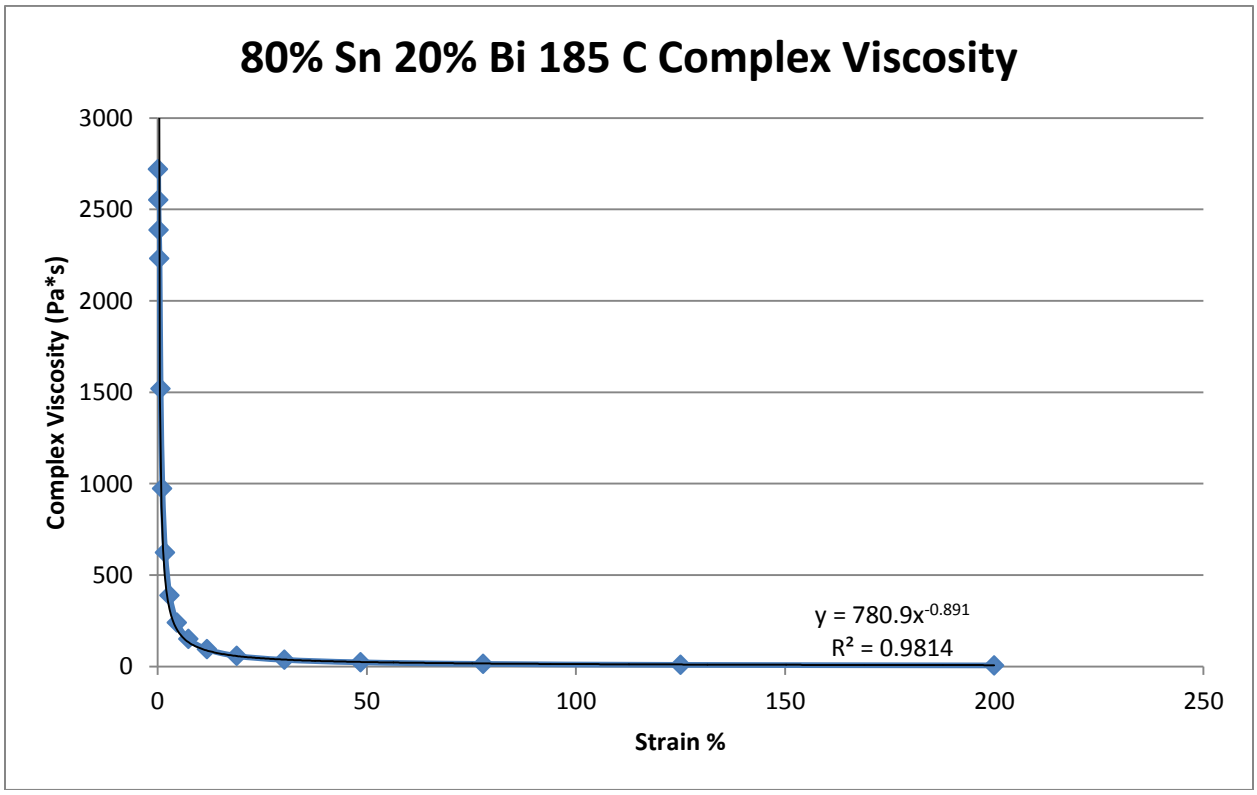

Figure 558- 80% Tin 20% Bismuth, 185 C, Oscillatory Shear Complex Viscosity

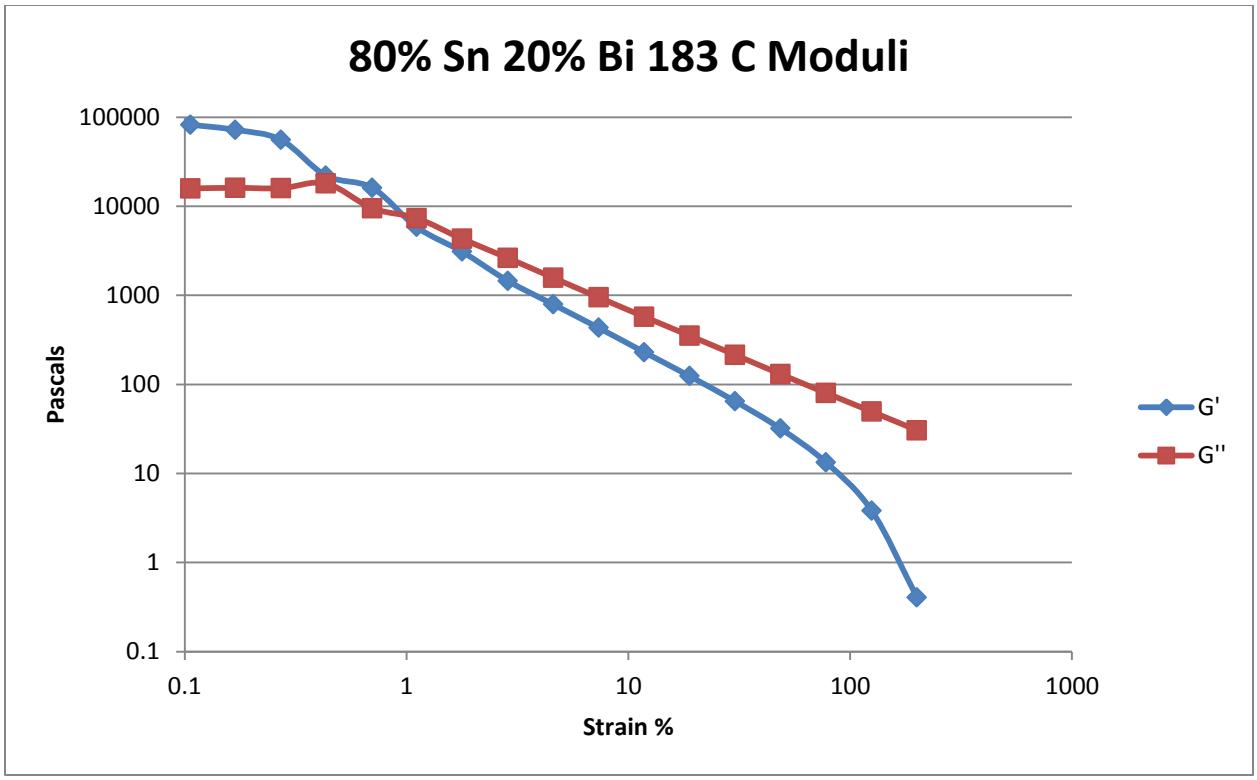

Figure 559- 80% Tin 20% Bismuth, 183 C, Oscillatory Shear Moduli

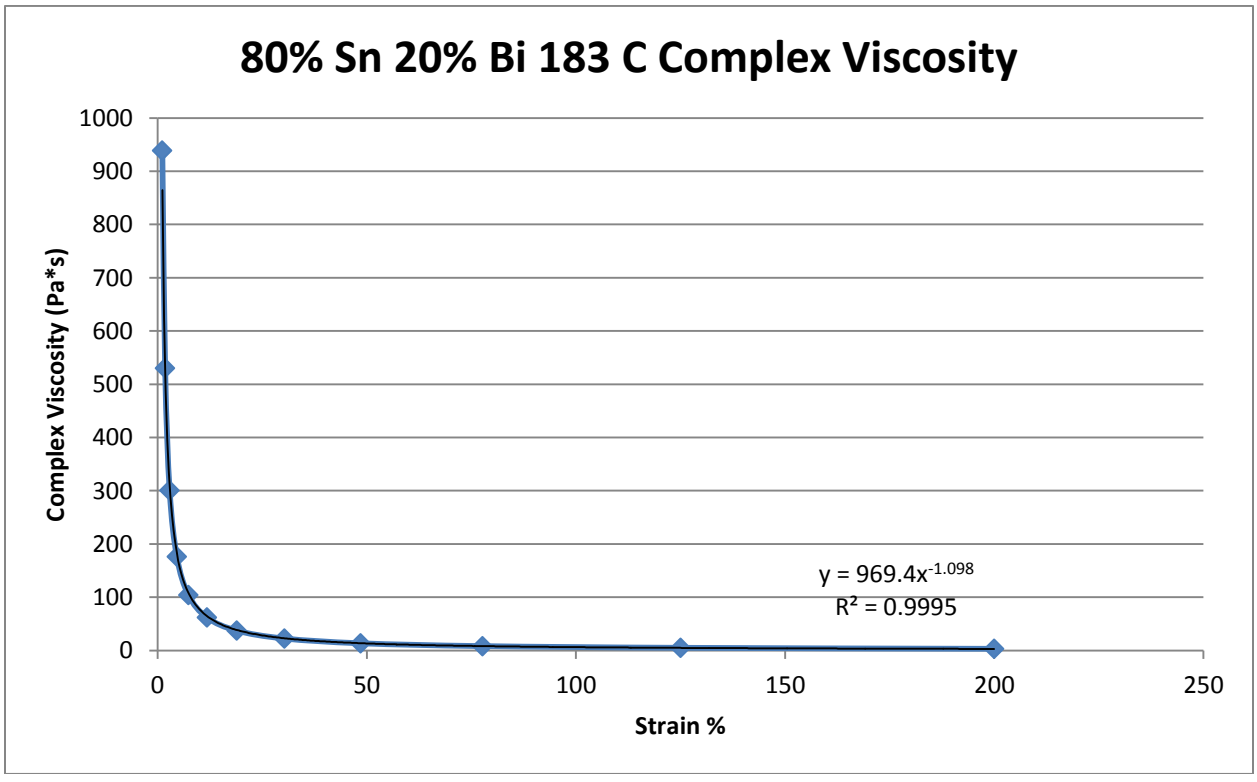

Figure 560- 80% Tin 20% Bismuth, 183 C, Oscillatory Shear Complex Viscosity

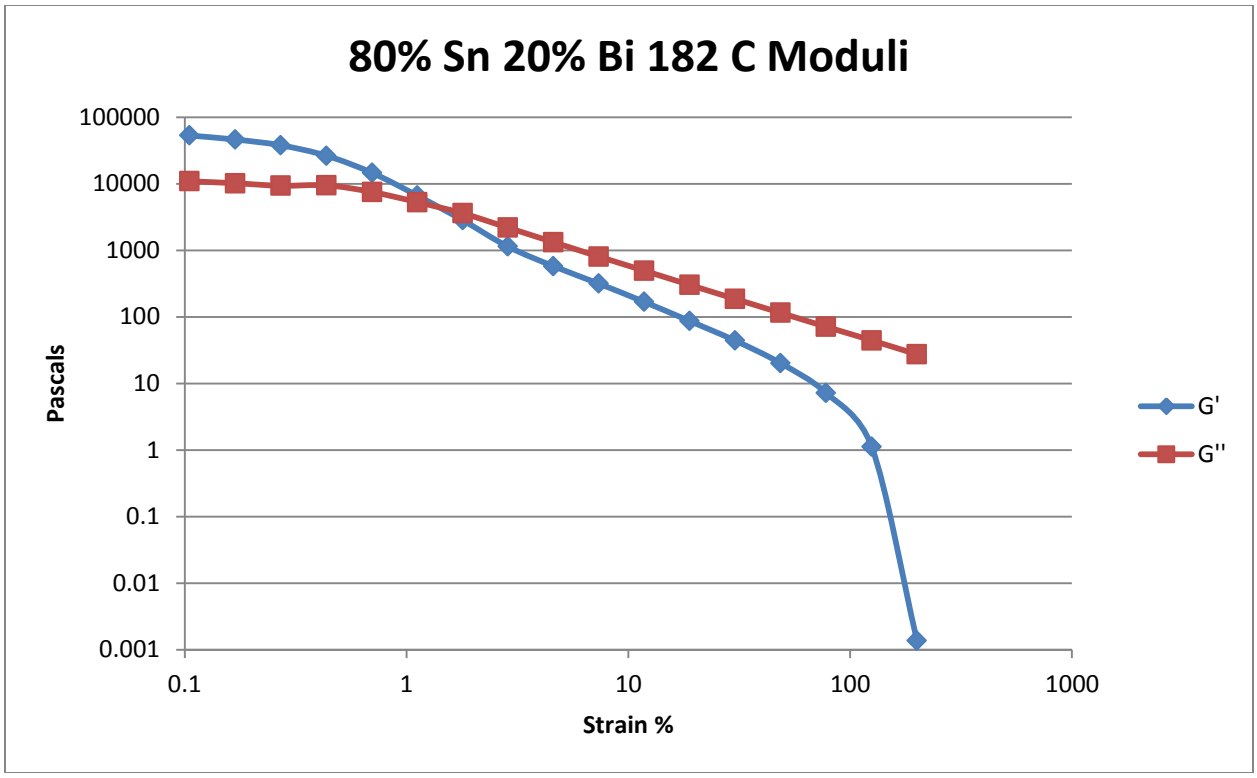

Figure 561- 80% Tin 20% Bismuth, 182 C, Oscillatory Shear Moduli

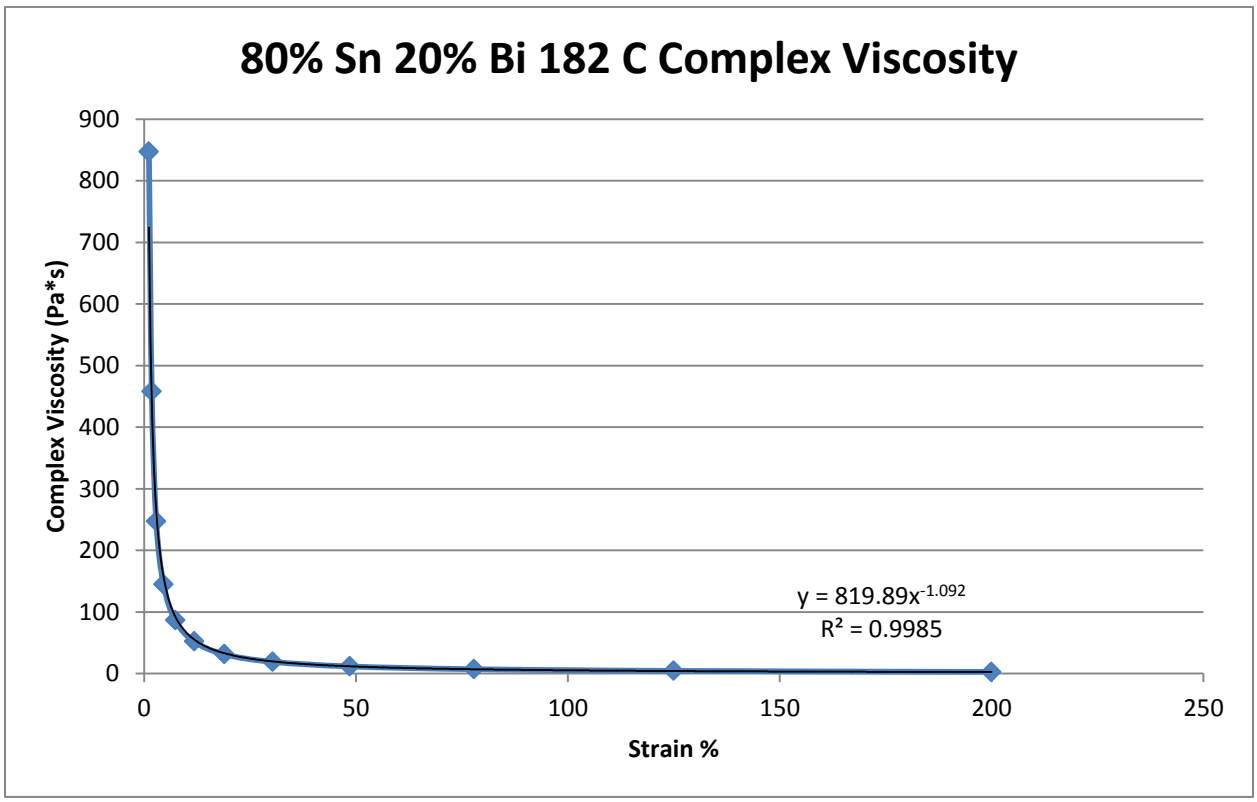

Figure 562- 80% Tin 20% Bismuth, 182 C, Oscillatory Shear Complex Viscosity

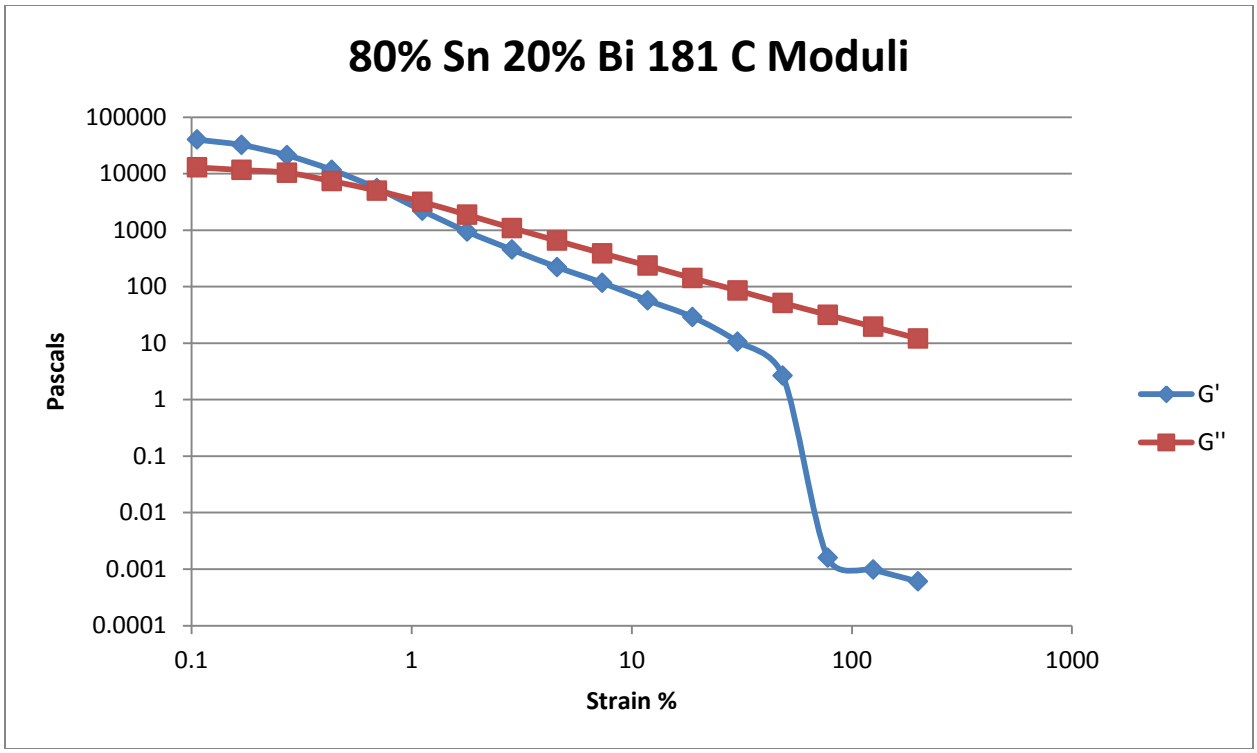

Figure 563- 80% Tin 20% Bismuth, 181 C, Oscillatory Shear Moduli

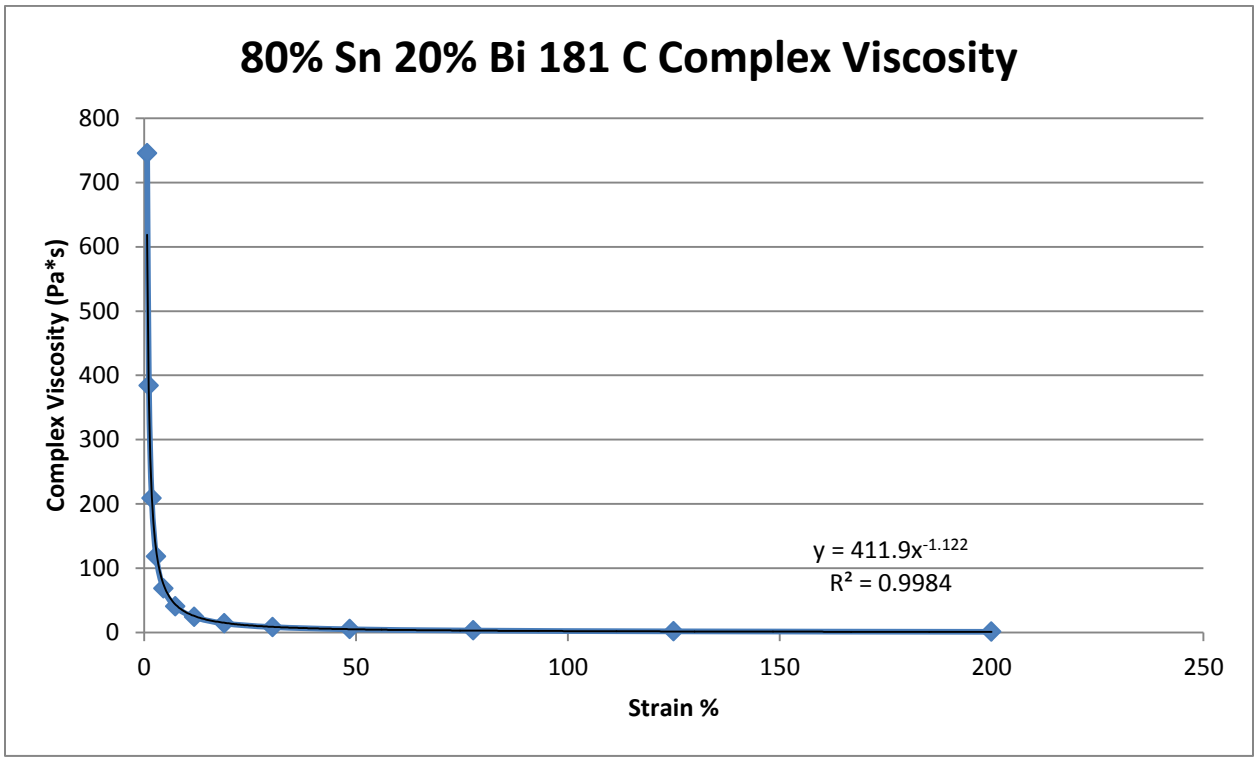

Figure 564- 80% Tin 20% Bismuth, 181 C, Oscillatory Shear Complex Viscosity

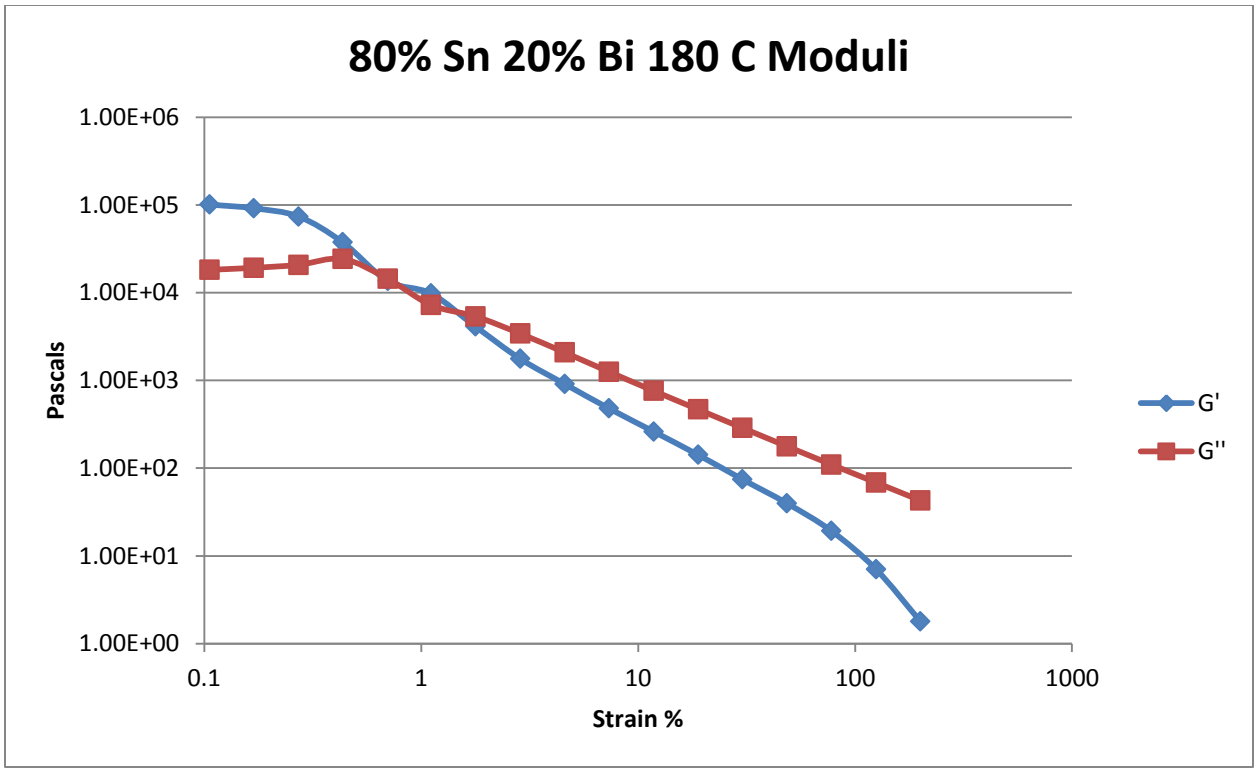

Figure 565- 80% Tin 20% Bismuth, 180 C, Oscillatory Shear Moduli

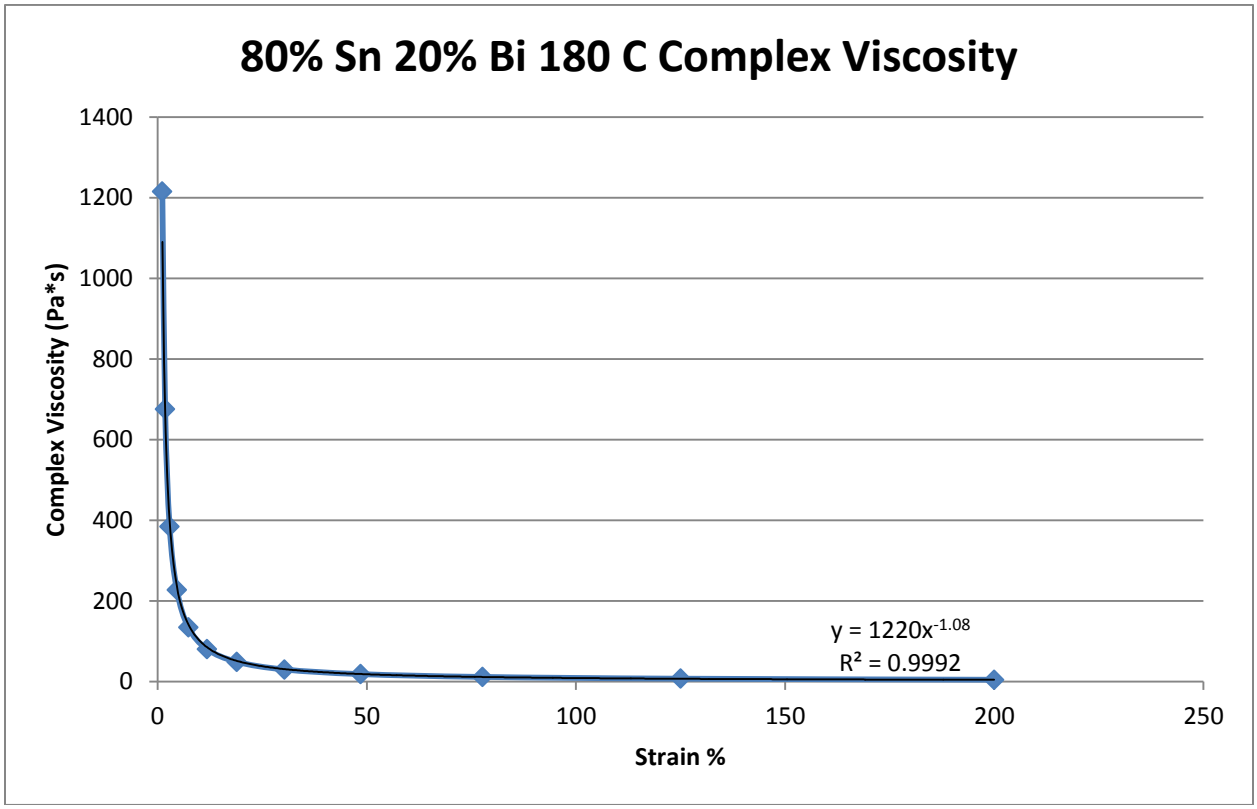

Figure 566- 80% Tin 20% Bismuth, 180 C, Oscillatory Shear Complex Viscosity

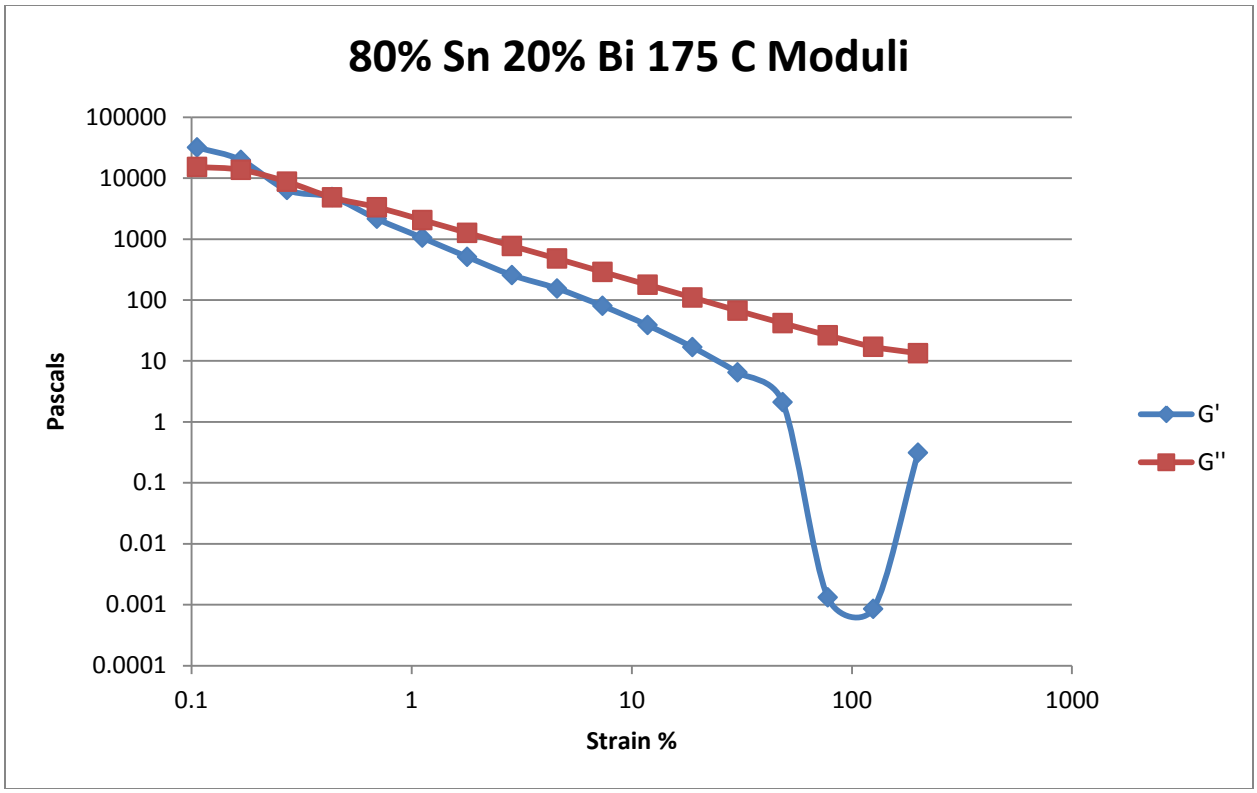

Figure 567- 80% Tin 20% Bismuth, 175 C, Oscillatory Shear Moduli

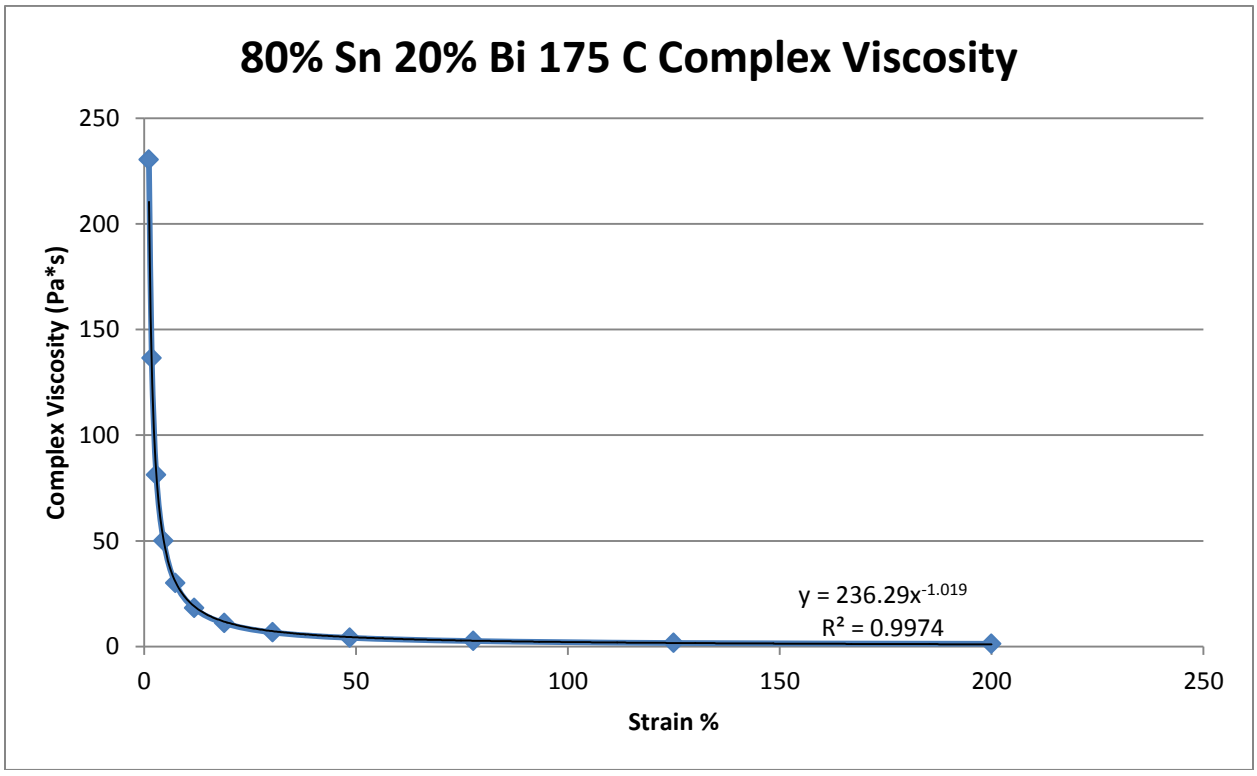

Figure 568- 80% Tin 20% Bismuth, 175 C, Oscillatory Shear Complex Viscosity

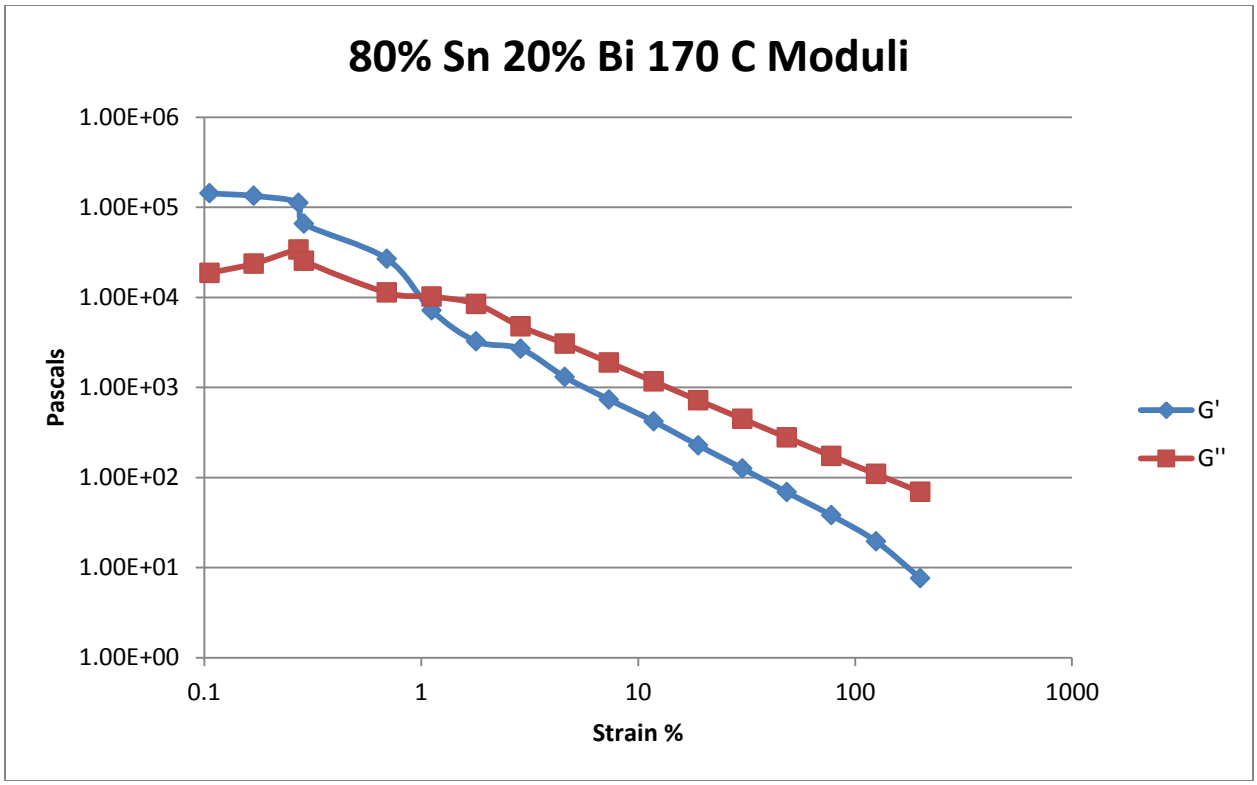

Figure 569- 80% Tin 20% Bismuth, 170 C, Oscillatory Shear Moduli

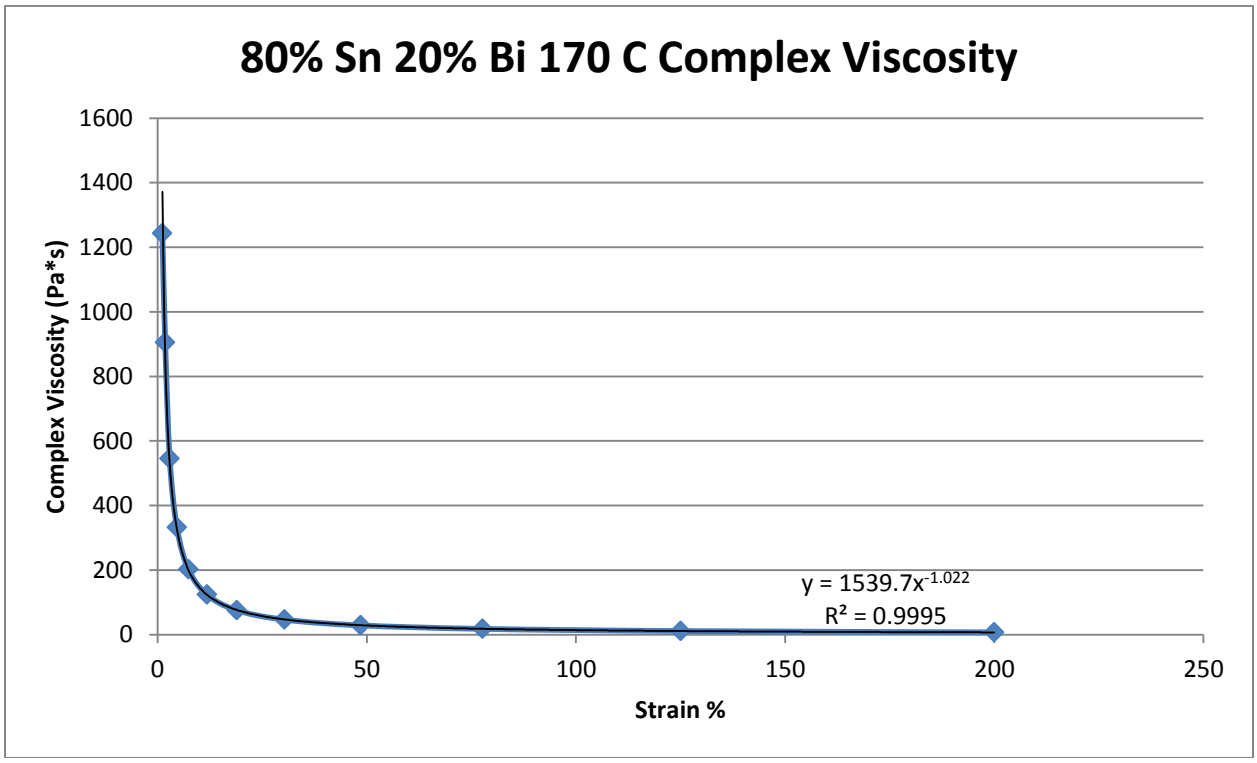

Figure 570- 80% Tin 20% Bismuth, 170 C, Oscillatory Shear Complex Viscosity

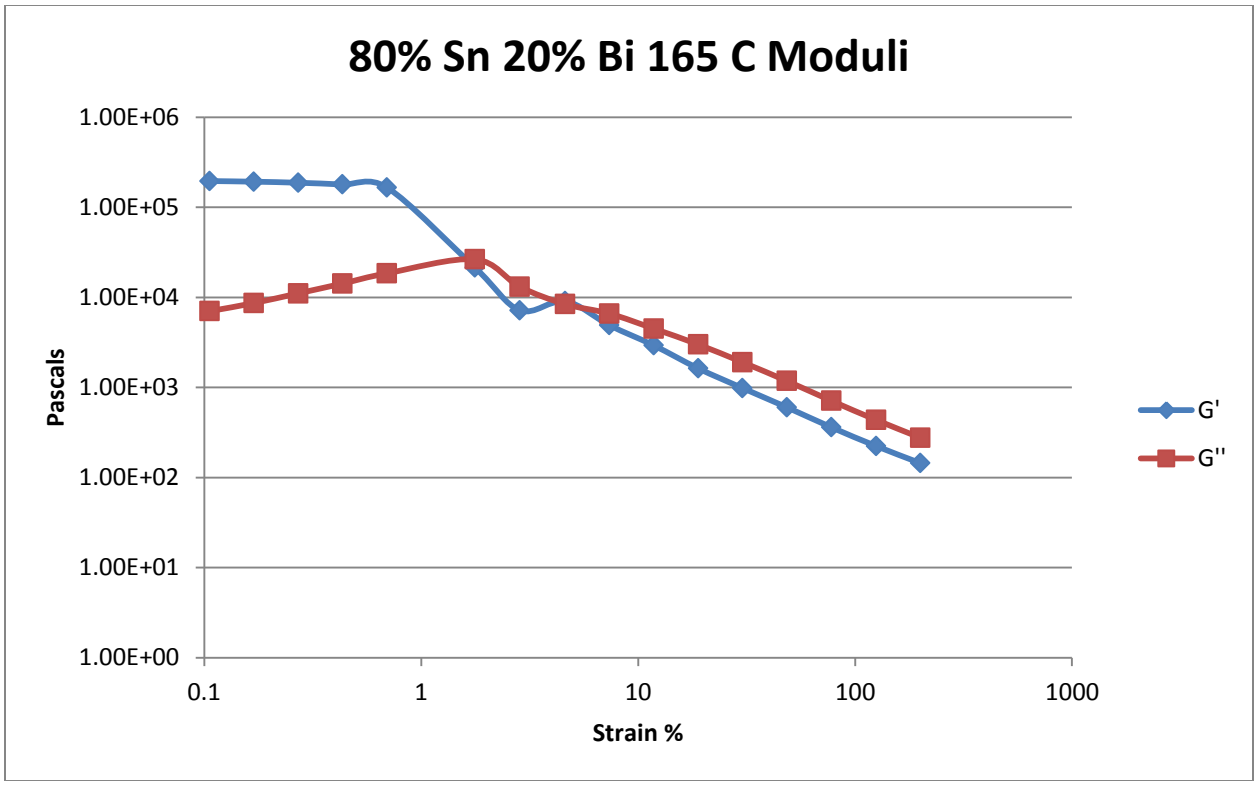

Figure 571- 80% Tin 20% Bismuth, 165 C, Oscillatory Shear Moduli

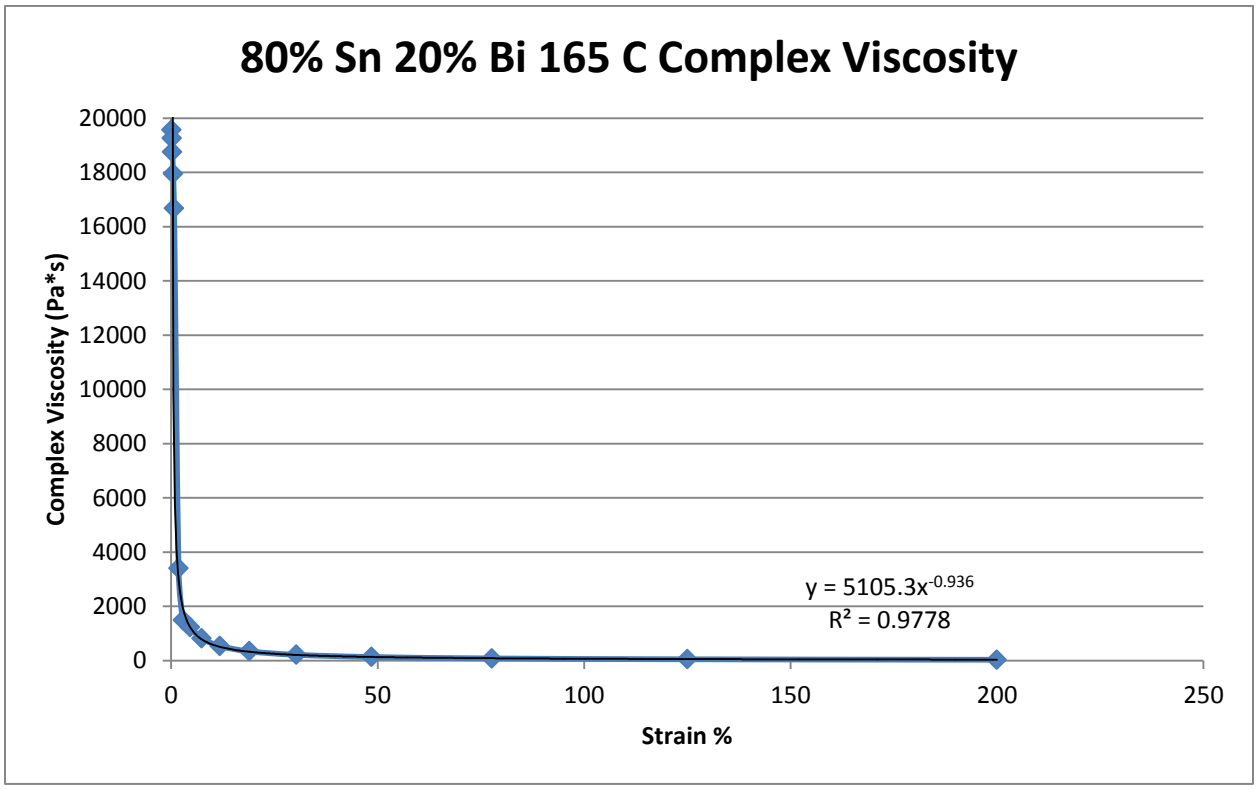

Figure 572- 80% Tin 20% Bismuth, 165 C, Oscillatory Shear Complex Viscosity

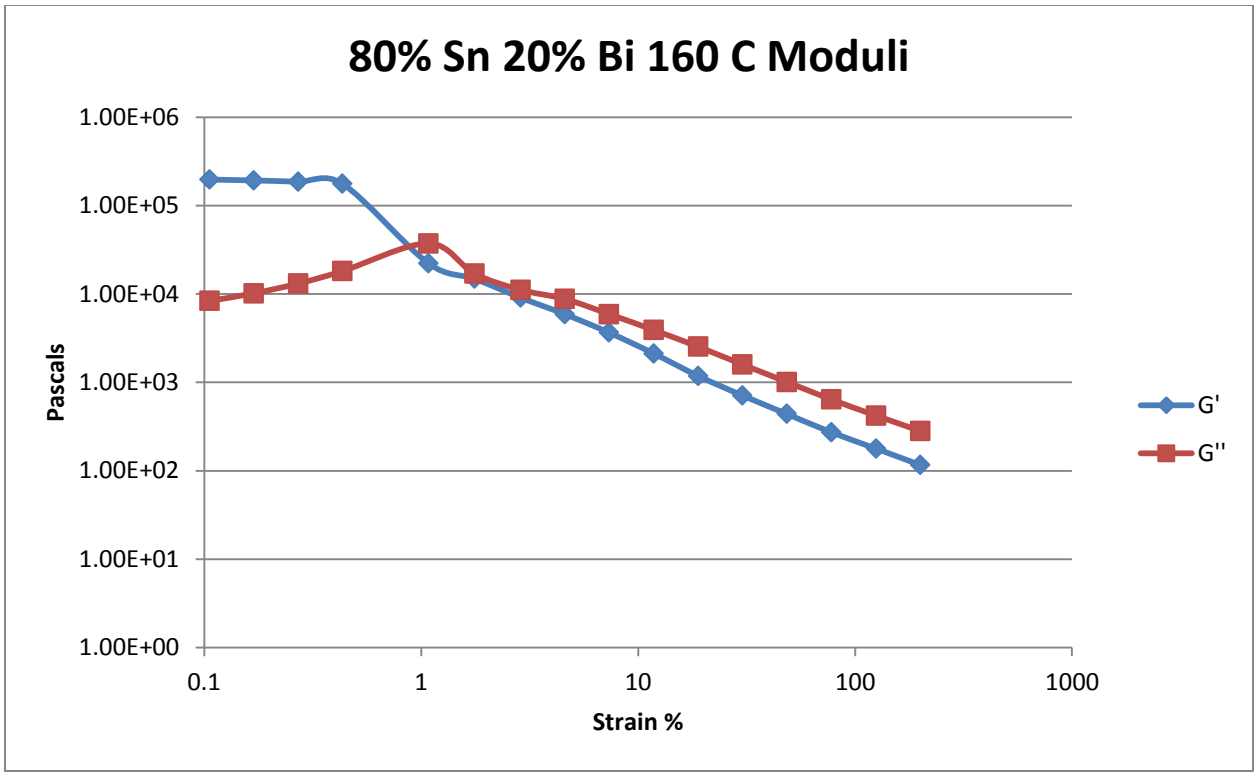

Figure 573- 80% Tin 20% Bismuth, 160 C, Oscillatory Shear Moduli

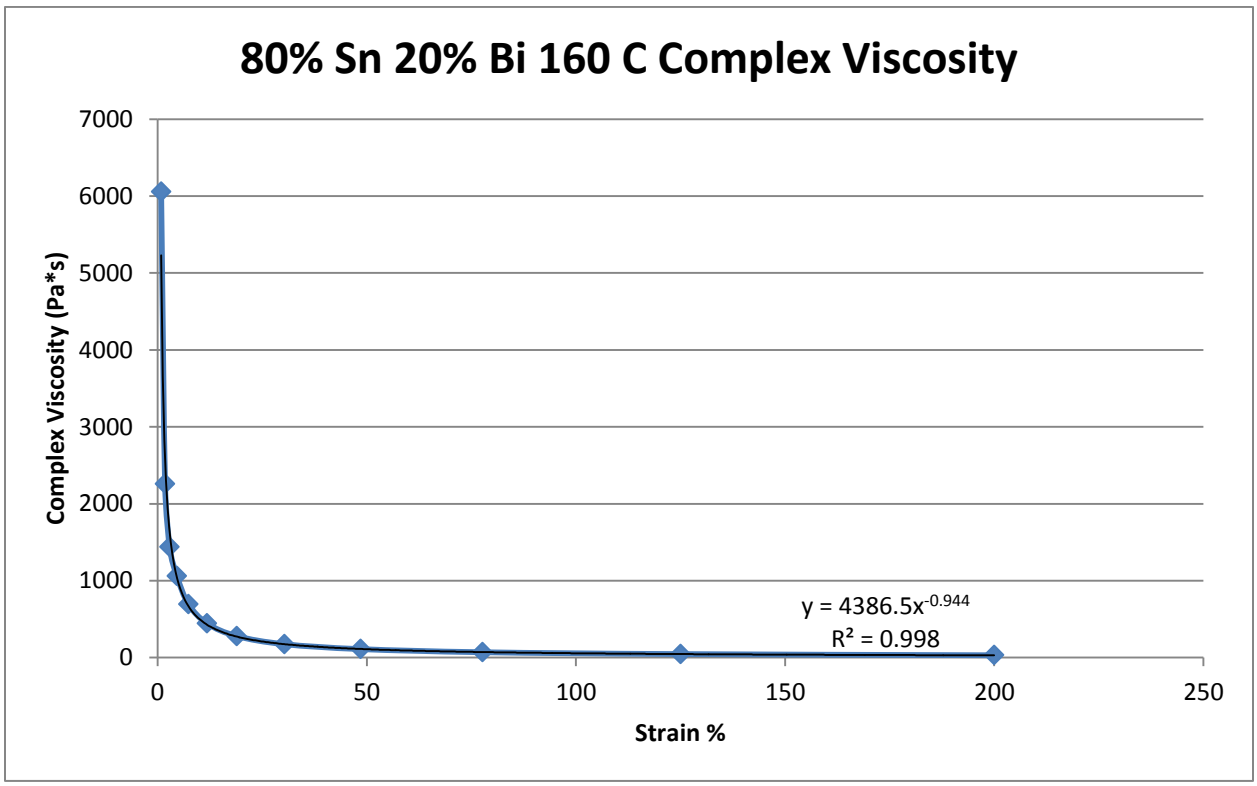

Figure 574- 80% Tin 20% Bismuth, 160 C, Oscillatory Shear Complex Viscosity

Appendix F- Rotational True Viscosity

20% Tin 80% Bismuth

Predicted Composition: 22% Sn 78% Bi

Theoretical Solidus Line: 139 C
Theoretical Liquidus Line: 220.3 C

Experimental Solidus Line: 139.0 C
Experimental Liquidus Line: 217.5 C

Pre-Shear: 15 RPM, 2 minutes
Shear Rate: 1%-10%

20% Tin 80% Bismuth True Viscosity				
Composition	**Fraction Solid (%)**	**Temperature (C)**	**Viscosity Equation (Pa·s)**	**True Viscosity (Pa·s)**
20% Sn 80% Bi	0	229	$\eta = 0.1491\dot{\gamma}^{-0.890}$	0.019
20% Sn 80% Bi	0	225	$\eta = 0.1223\dot{\gamma}^{-0.698}$	0.025
20% Sn 80% Bi	0.63	220	$\eta = 0.1863\dot{\gamma}^{-0.919}$	0.022
20% Sn 80% Bi	9.46	215	$\eta = 0.9877\dot{\gamma}^{-0.844}$	0.141
20% Sn 80% Bi	16.9	210	$\eta = 58.051\dot{\gamma}^{-1.298}$	2.92
20% Sn 80% Bi	23.1	205	$\eta = 91.501\dot{\gamma}^{-0.901}$	11.5
20% Sn 80% Bi	28.6	200	$\eta = 228.29\dot{\gamma}^{-1.102}$	18.1

Table 99- 20% Tin 80% Bismuth True Viscosity

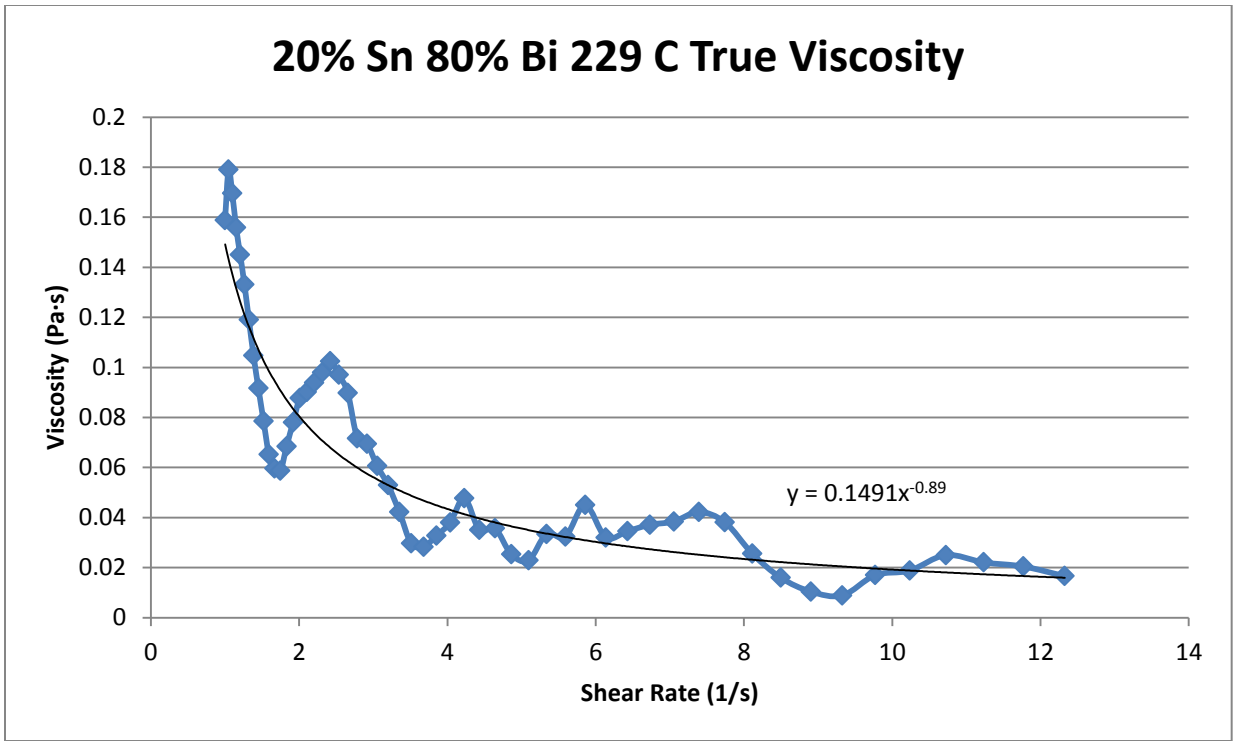

Figure 575- 20% Tin 80% Bismuth, 229 C, Rotational True Viscosity

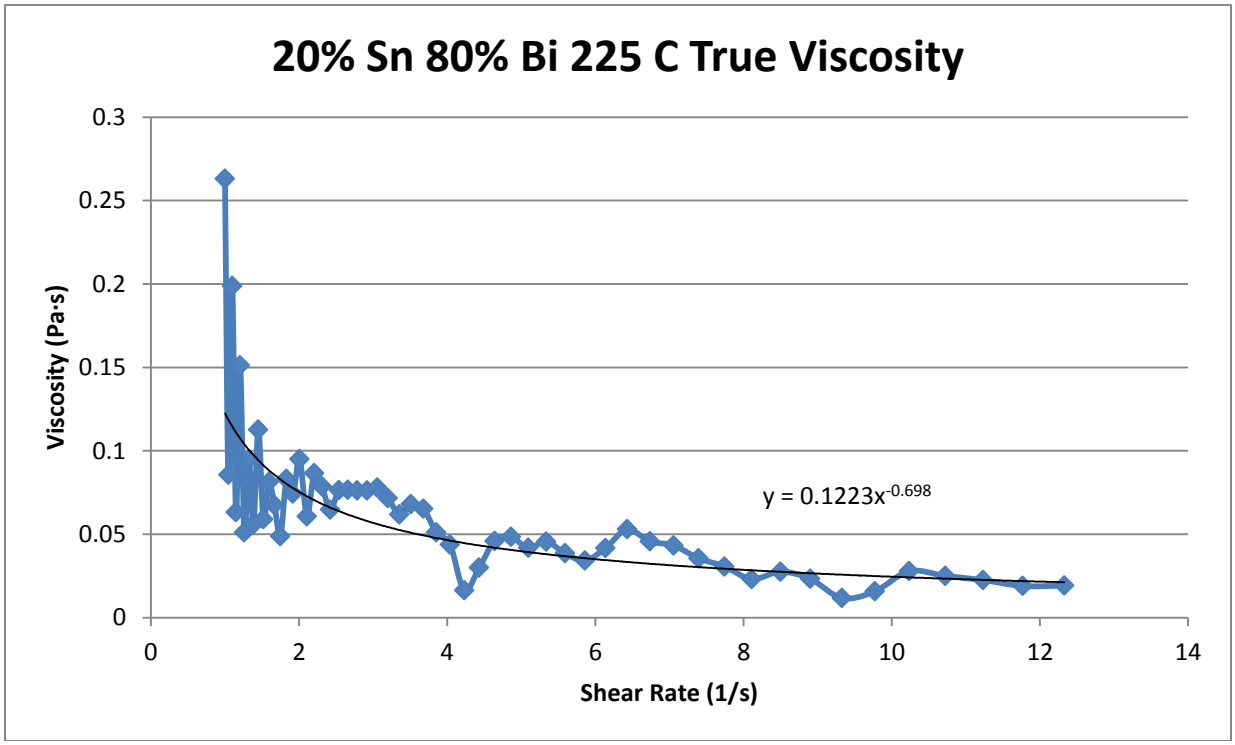

Figure 576- 20% Tin 80% Bismuth, 225 C, Rotational True Viscosity

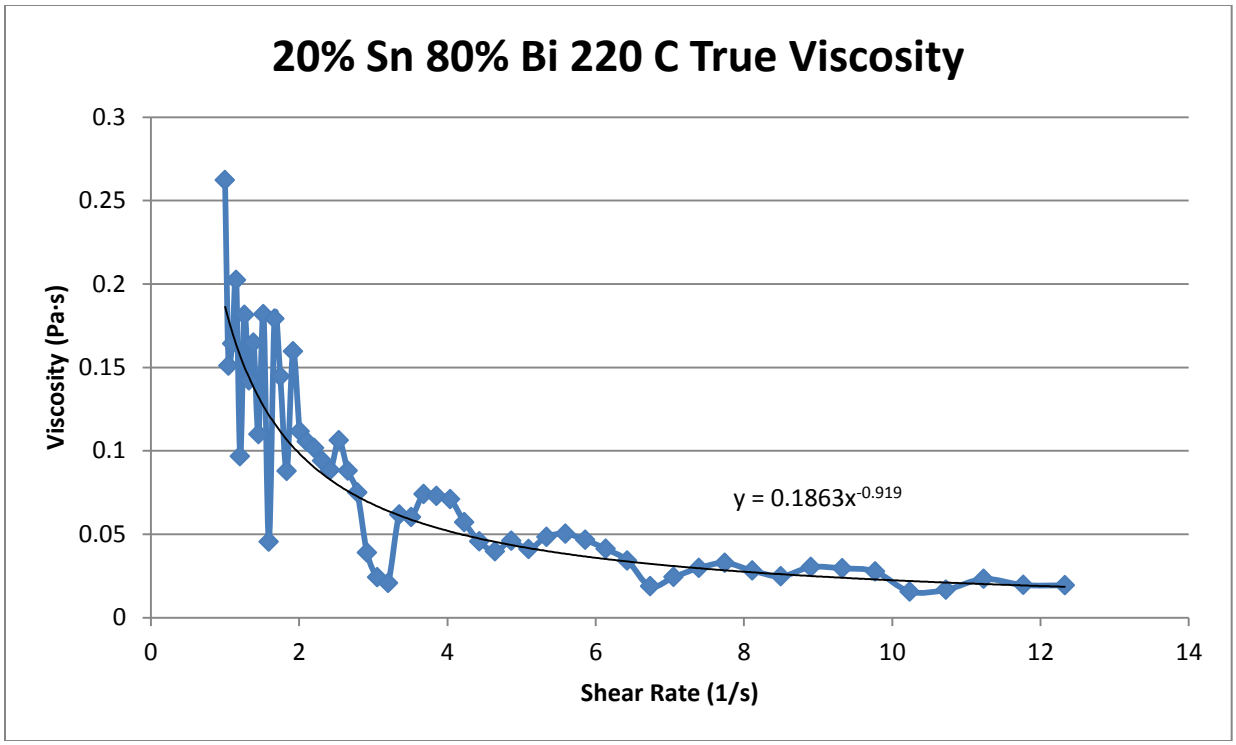

Figure 577- 20% Tin 80% Bismuth, 220 C, Rotational True Viscosity

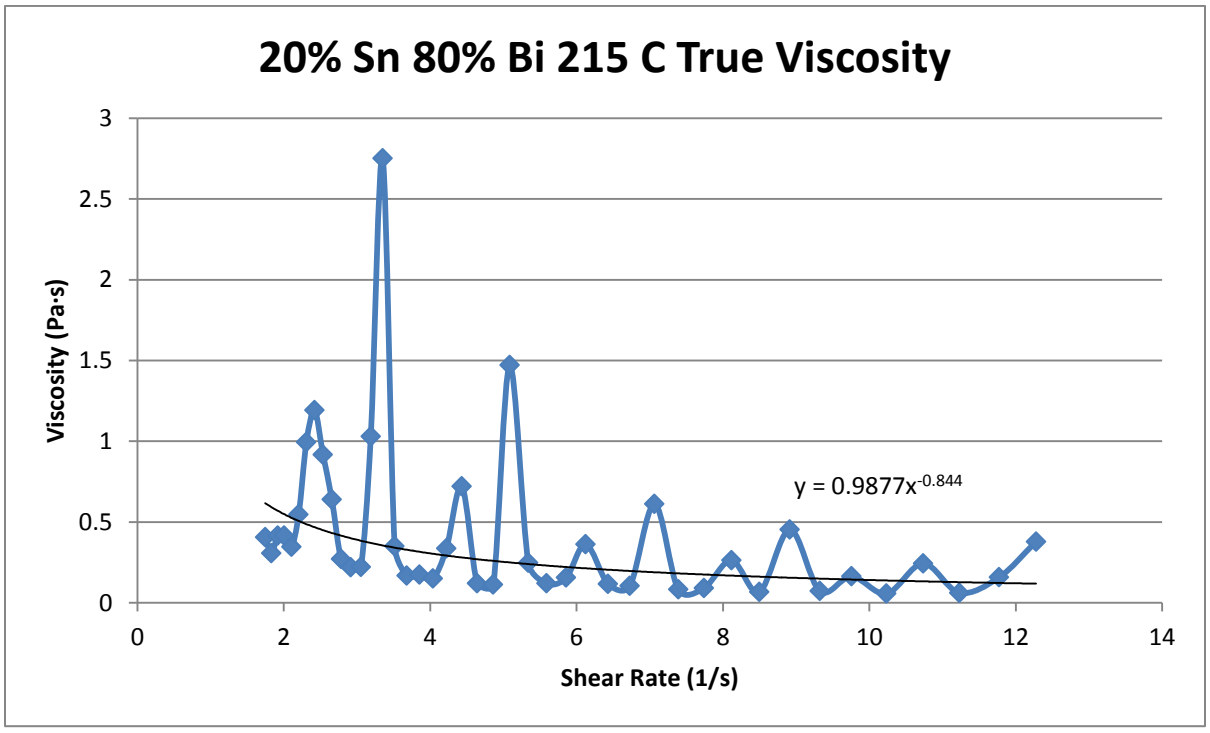

Figure 578- 20% Tin 80% Bismuth, 215 C, Rotational True Viscosity

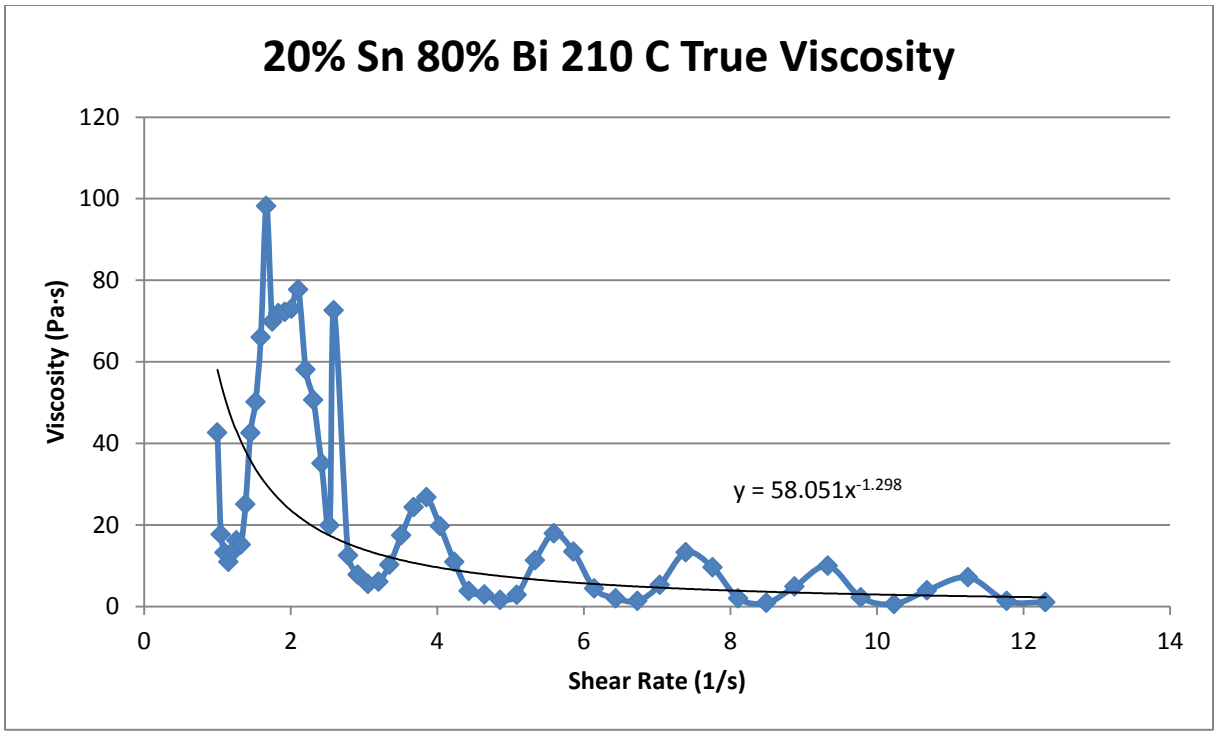

Figure 579- 20% Tin 80% Bismuth, 210 C, Rotational True Viscosity

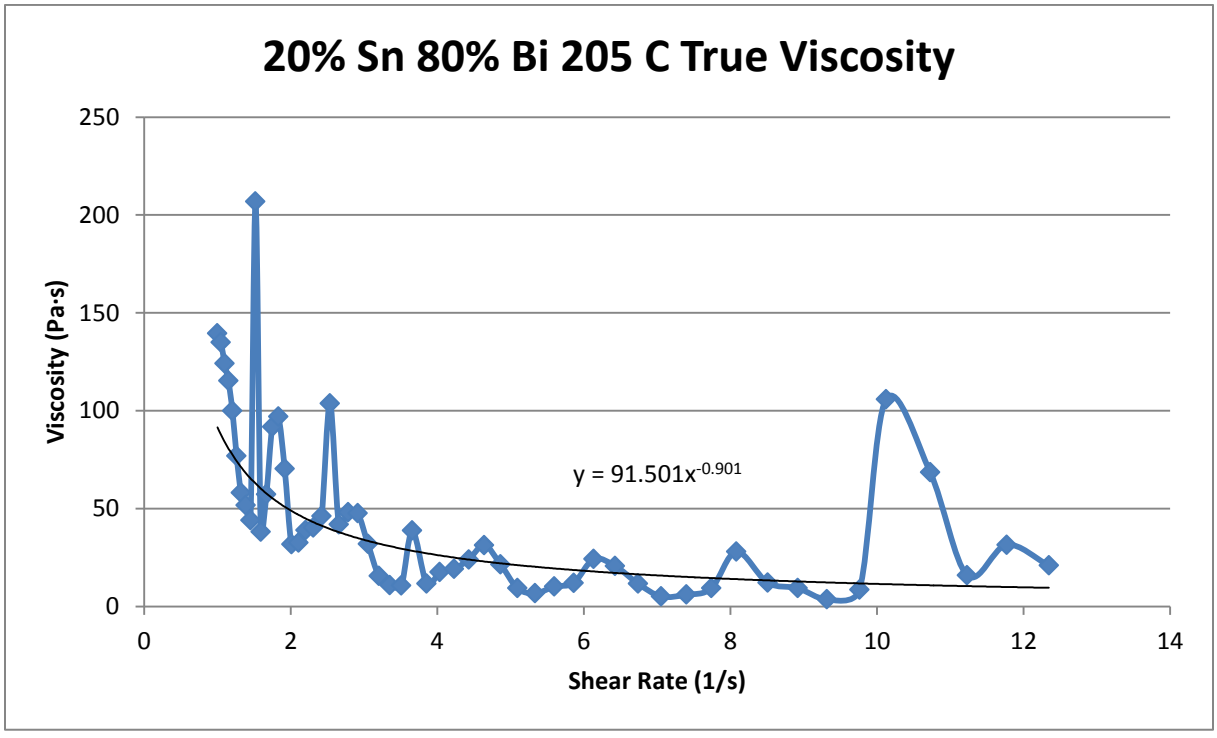

Figure 580- 20% Tin 80% Bismuth, 205 C, Rotational True Viscosity

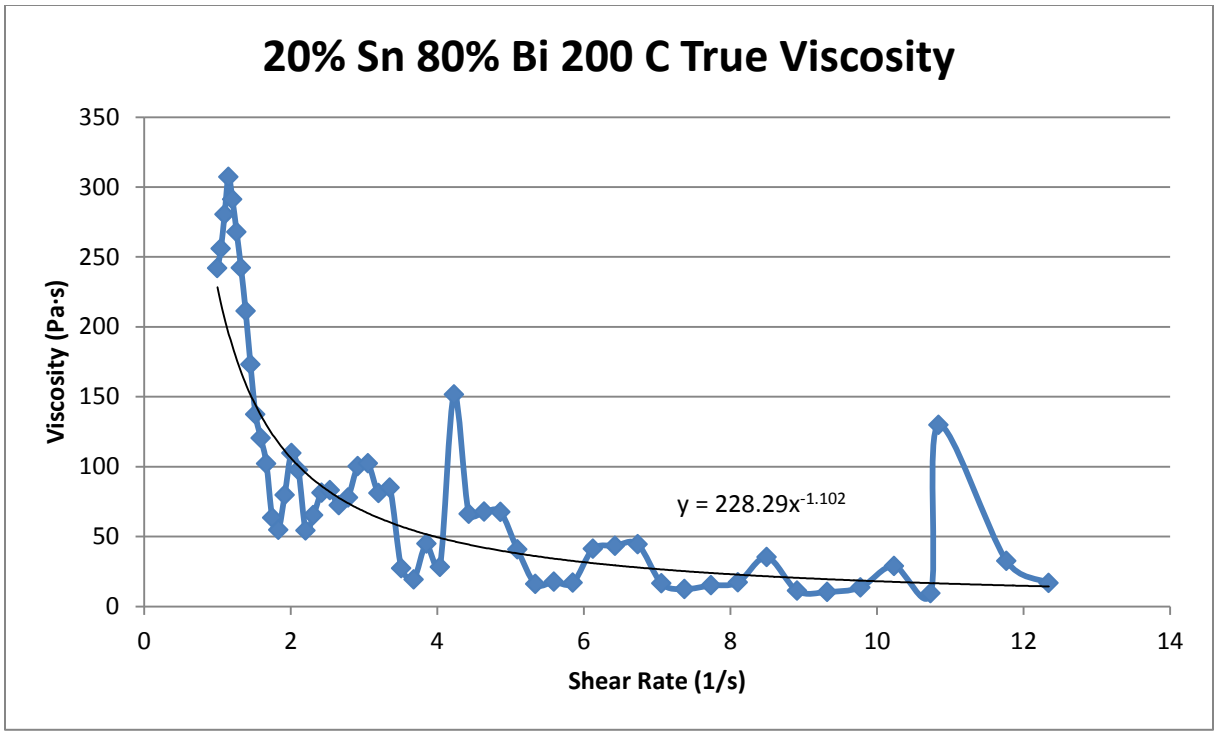

Figure 581- 20% Tin 80% Bismuth, 200 C, Rotational True Viscosity

30% Tin 70% Bismuth

Predicted Composition: 22% Sn 78% Bi

Theoretical Solidus Line: 139 C
Theoretical Liquidus Line: 192.1 C

Experimental Solidus Line: N/A
Experimental Liquidus Line: N/A

Pre-Shear: 15 RPM, 2 minutes
Shear Rate: 1%-10%

30% Tin 70% Bismuth True Viscosity				
Composition	**Fraction Solid (%)**	**Temperature (C)**	**Viscosity Equation (Pa·s)**	**True Viscosity (Pa·s)**
30% Sn 70% Bi	0	210		0.002
30% Sn 70% Bi	0	205		0.002
30% Sn 70% Bi	0	200		0.436

Table 100- 30% Tin 70% Bismuth True Viscosity

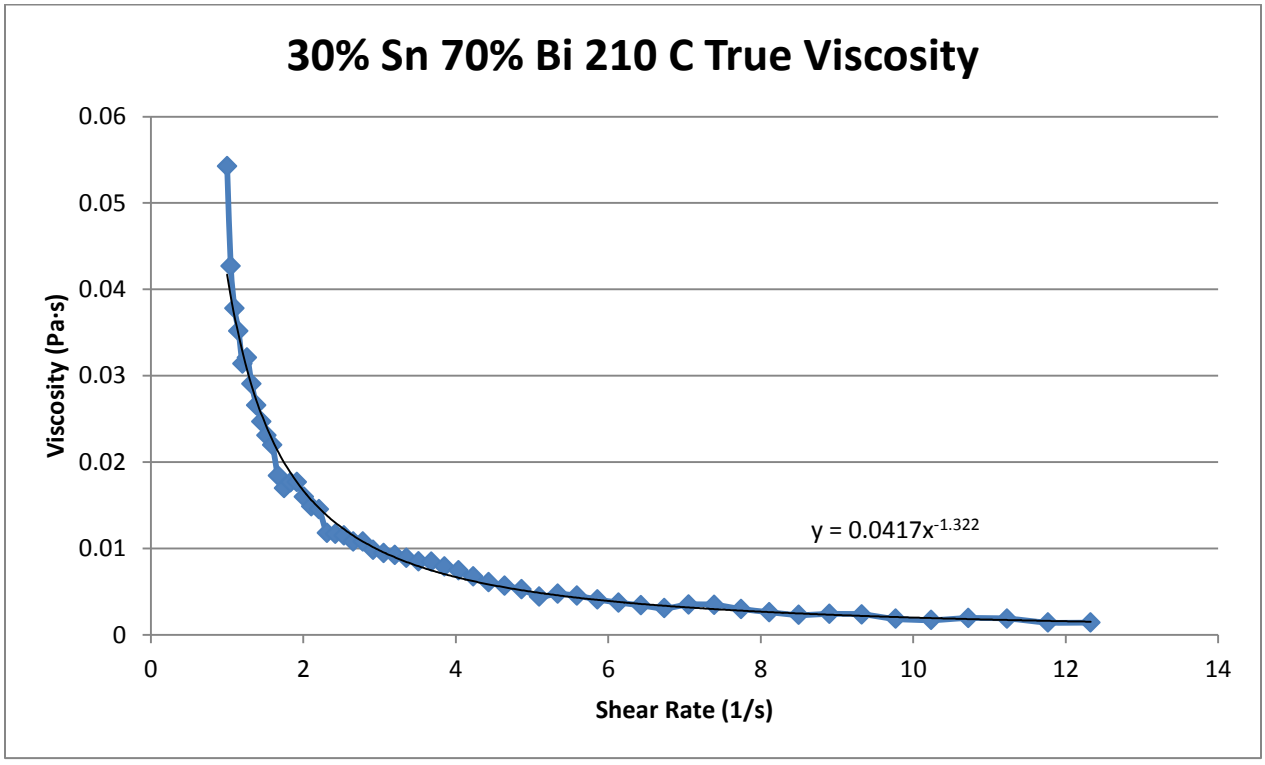

Figure 582- 30% Tin 70% Bismuth, 210 C, Rotational True Viscosity

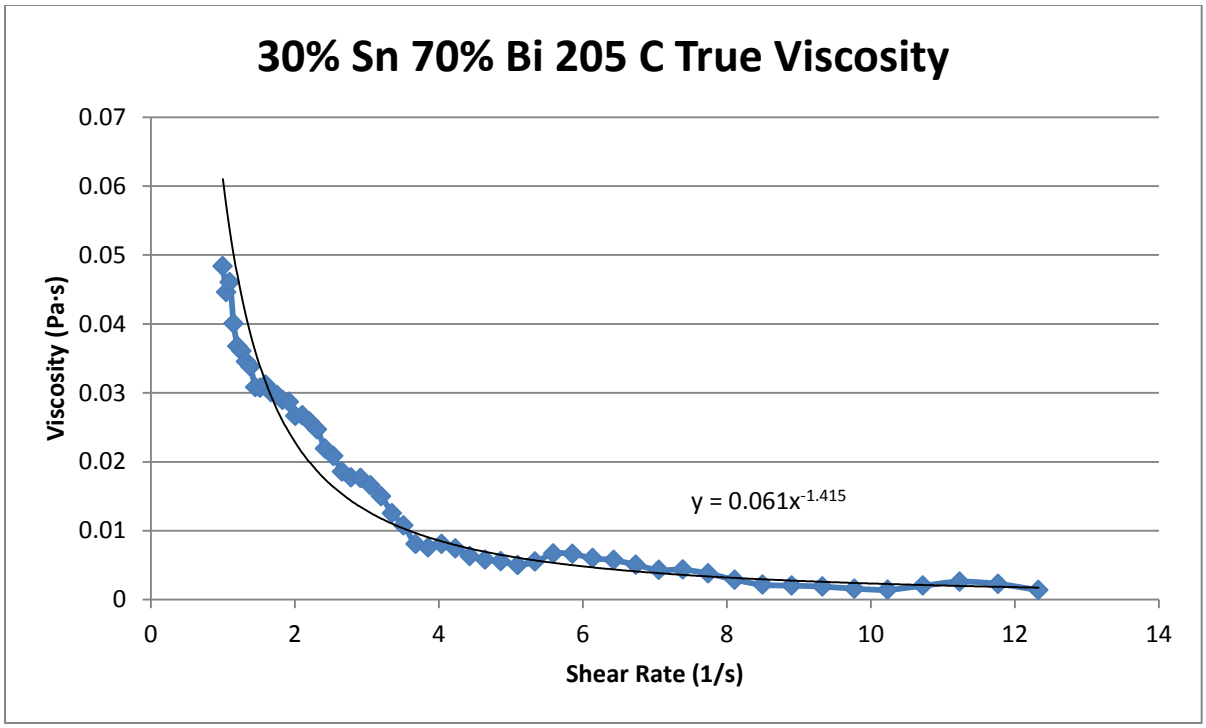

Figure 583- 30% Tin 70% Bismuth, 205 C, Rotational True Viscosity

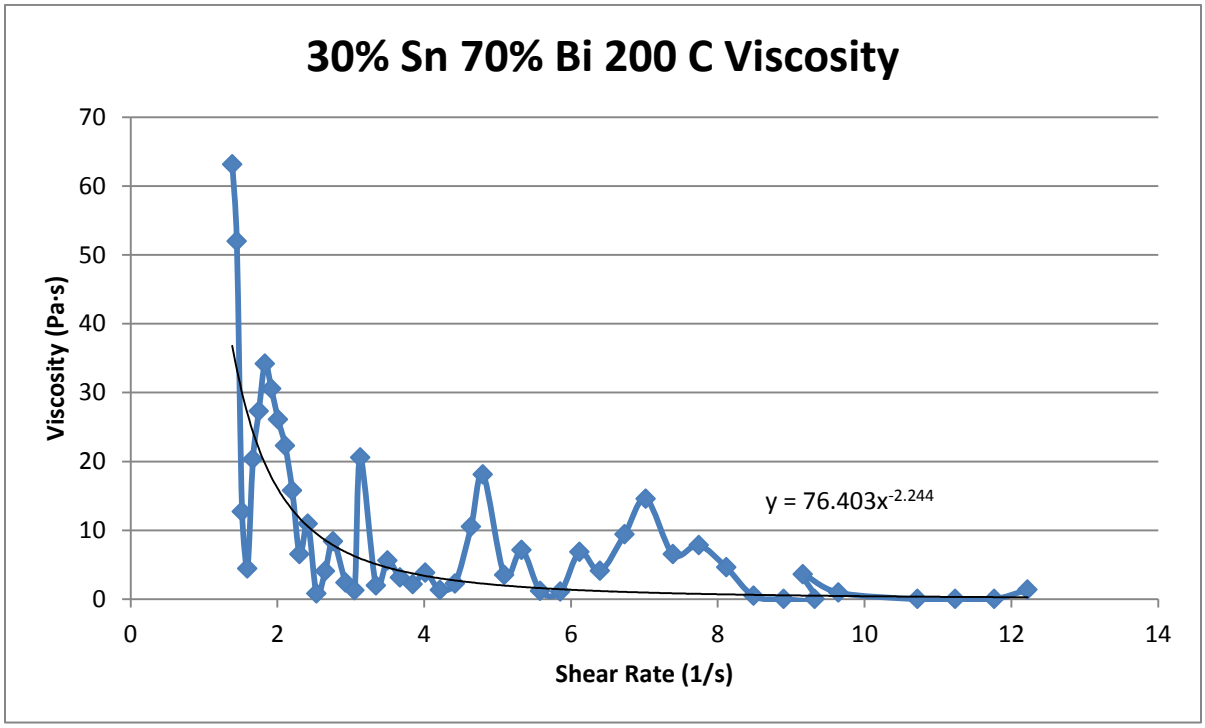

Figure 584- 30% Tin 70% Bismuth, 200 C, Rotational True Viscosity

40% Tin 60% Bismuth

Predicted Composition: 42% Sn 58% Bi

Theoretical Solidus Line: 139 C
Theoretical Liquidus Line: 173.9 C

Experimental Solidus Line: 139.6 C
Experimental Liquidus Line: 177.3 C

Pre-Shear: 15 RPM, 2 minutes
Shear Rate: 1%-10%

40% Tin 60% Bismuth True Viscosity				
Composition	**Fraction Solid (%)**	**Temperature (C)**	**Viscosity Equation (Pa▪s)**	**True Viscosity (Pa▪s)**
40% Sn 60% Bi	0	190	$\eta = 0.0944\dot{\gamma}^{-1.32}$	0.005
40% Sn 60% Bi	0	185	$\eta = 0.1389\dot{\gamma}^{-1.061}$	0.012
40% Sn 60% Bi	0	180	$\eta = 0.1320\dot{\gamma}^{-0.991}$	0.013
40% Sn 60% Bi	0	175	$\eta = 0.1324\dot{\gamma}^{-0.968}$	0.014
40% Sn 60% Bi	3.81	170	$\eta = 0.1527\dot{\gamma}^{-0.987}$	0.016
40% Sn 60% Bi	8.35	165	$\eta = 0.5448\dot{\gamma}^{-1.596}$	0.014

Table 101- 40% Tin 60% Bismuth True Viscosity

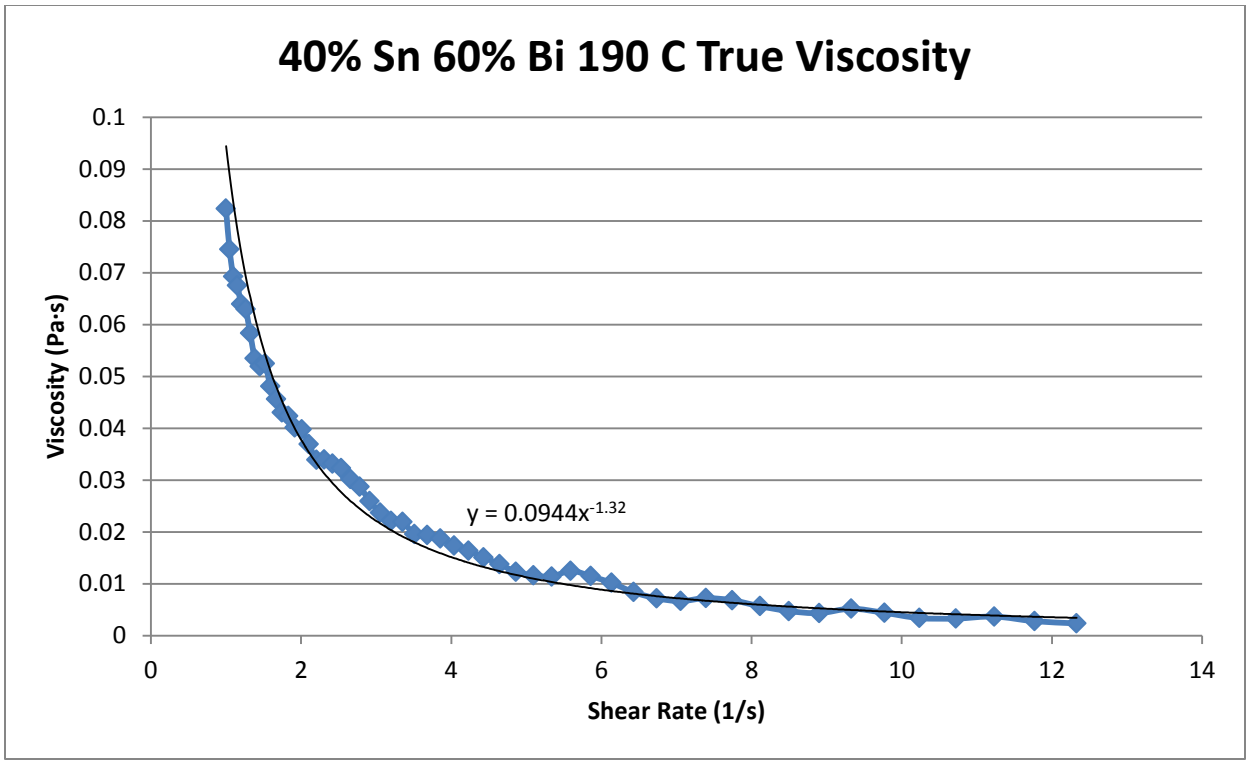

Figure 585- 40% Tin 60% Bismuth, 190 C, Rotational True Viscosity

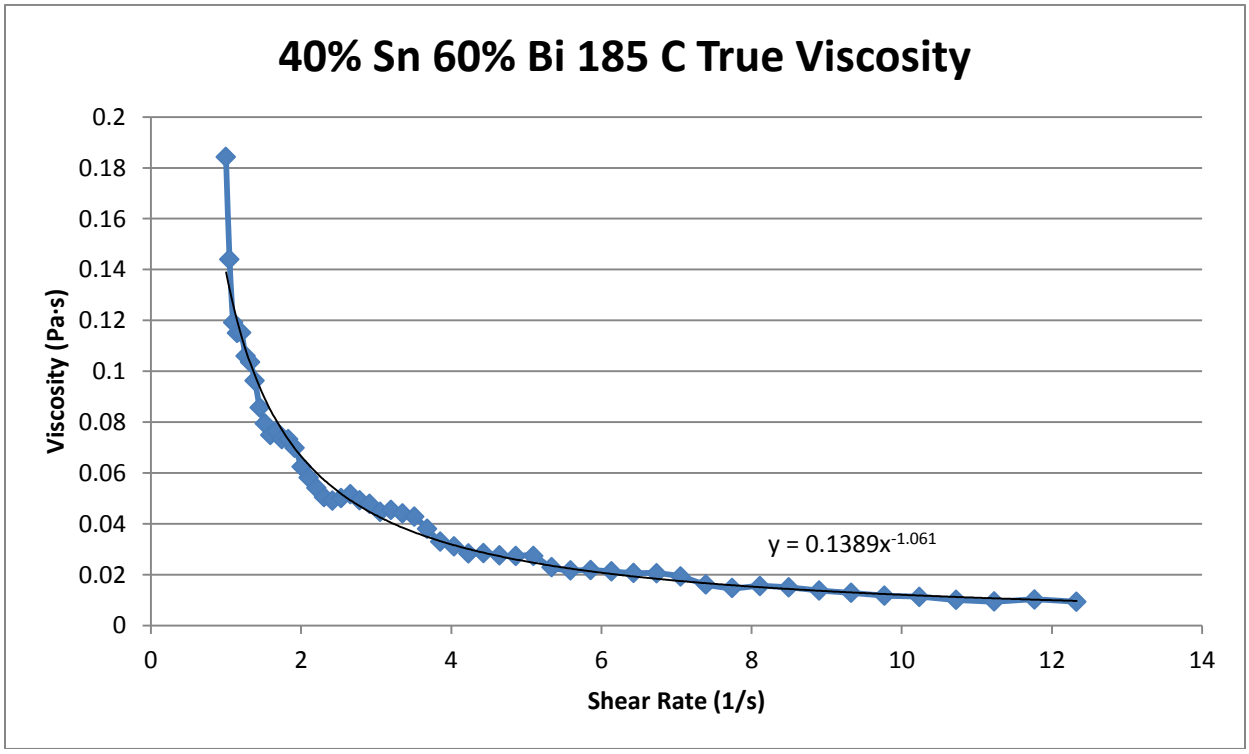

Figure 586- 40% Tin 60% Bismuth, 185 C, Rotational True Viscosity

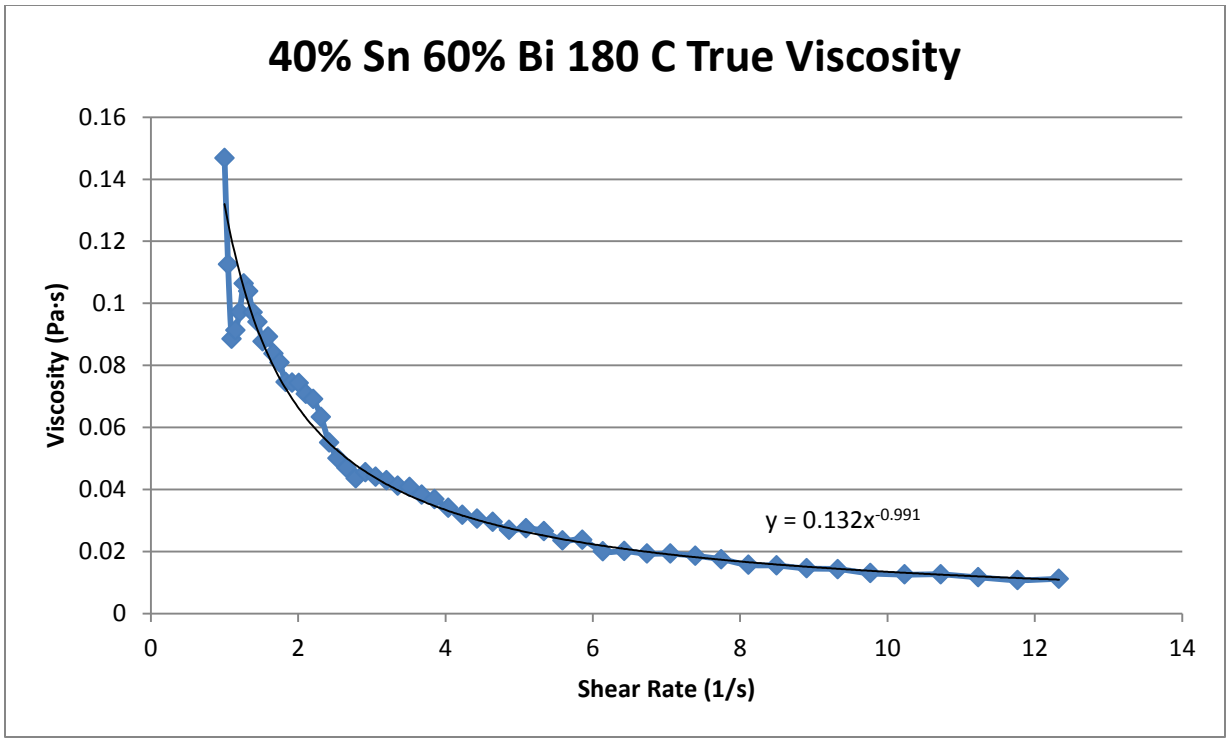

Figure 587- 40% Tin 60% Bismuth, 180 C, Rotational True Viscosity

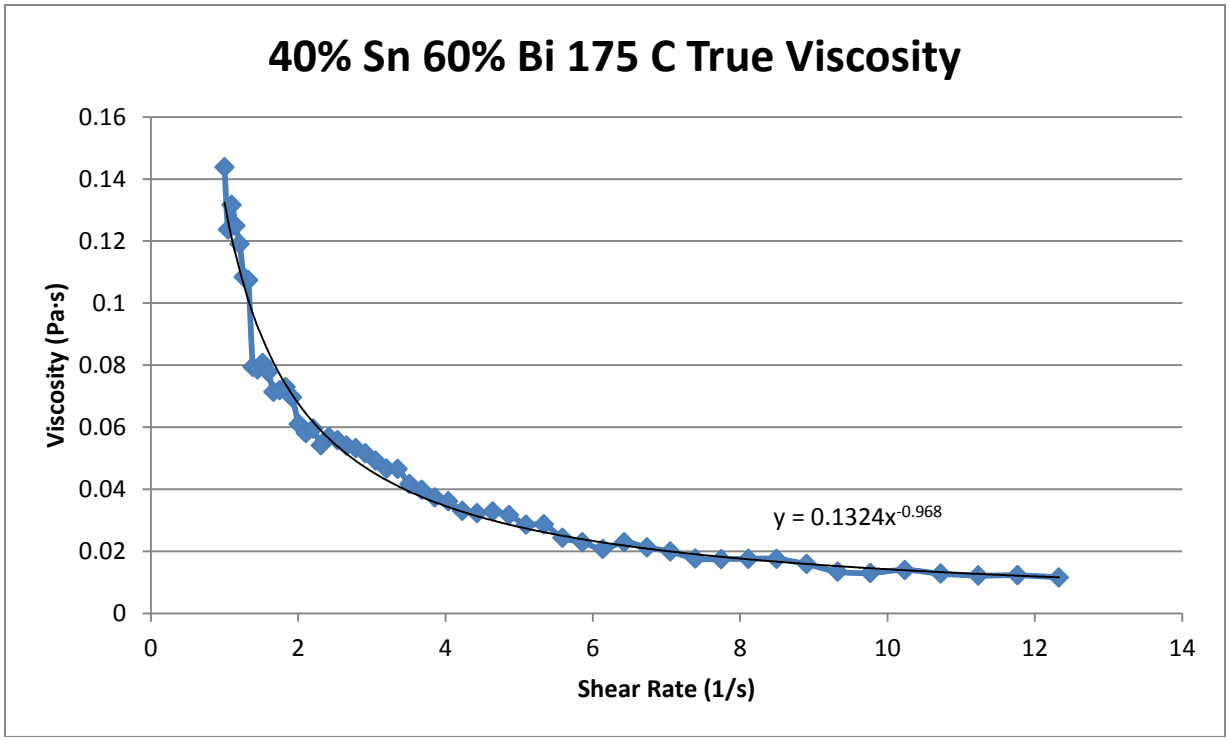

Figure 588- 40% Tin 60% Bismuth, 175 C, Rotational True Viscosity

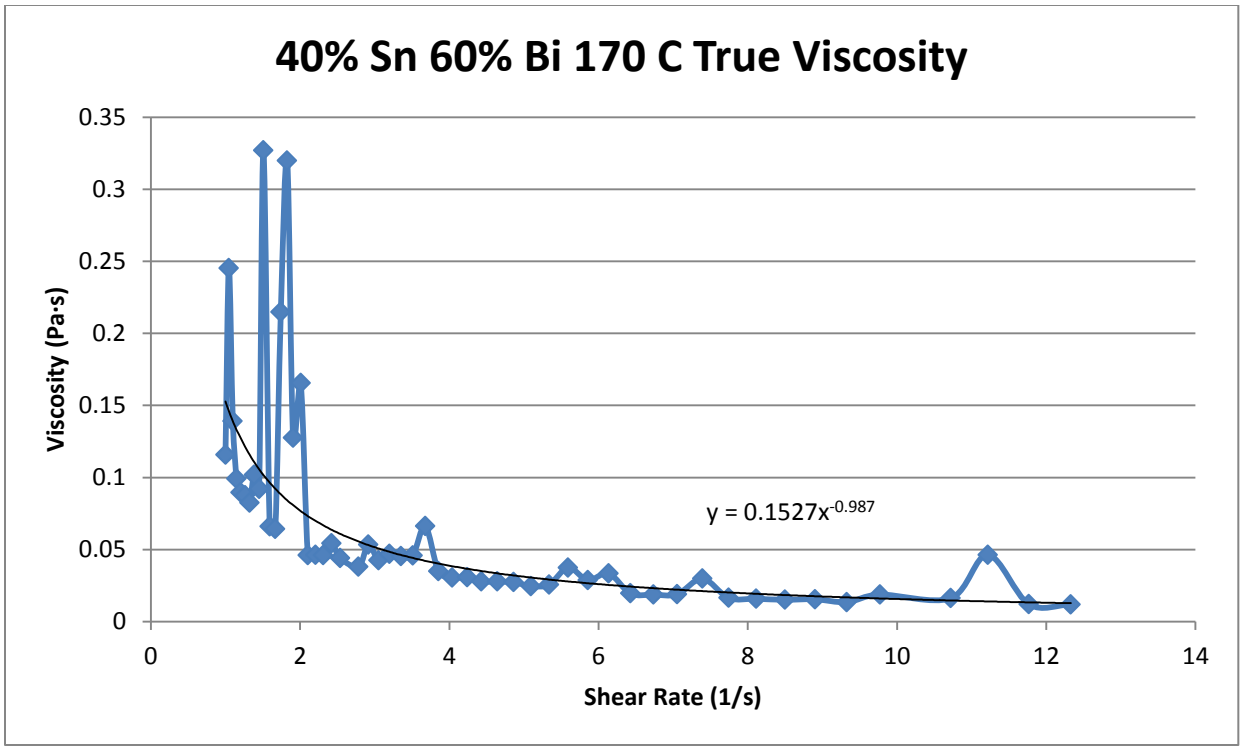

Figure 589- 40% Tin 60% Bismuth, 170 C, Rotational True Viscosity

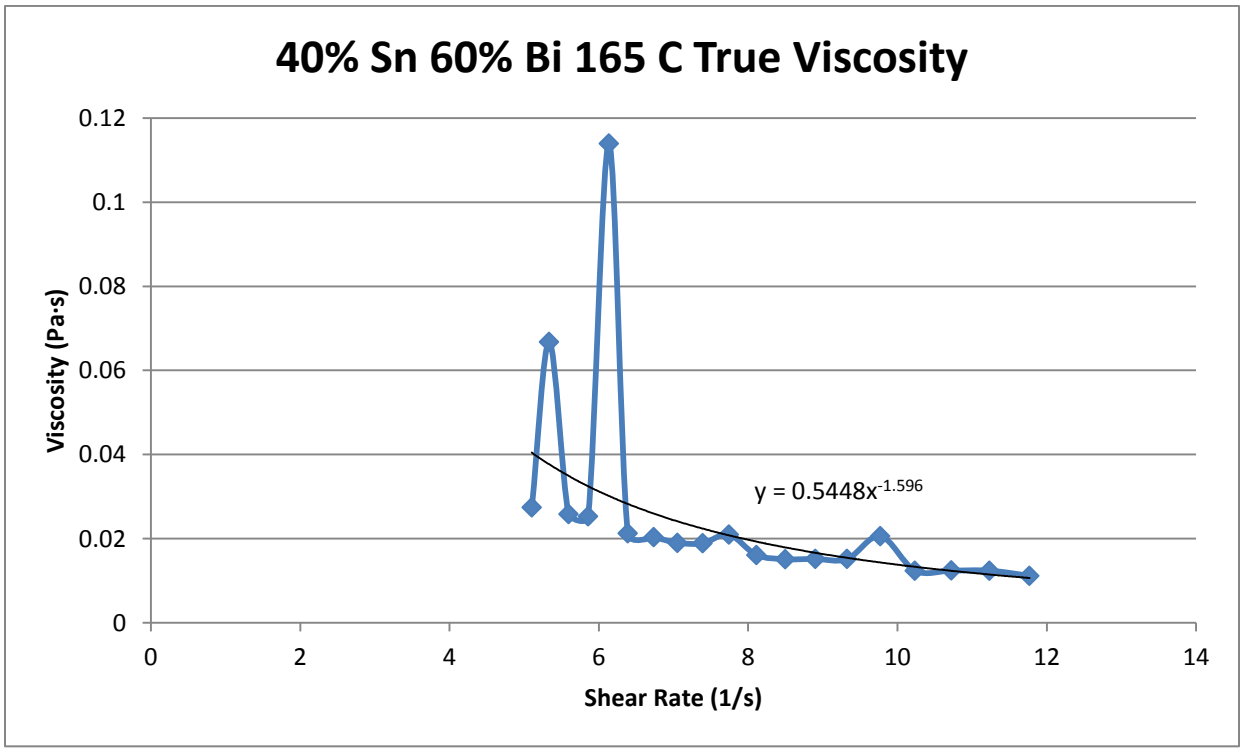

Figure 590- 40% Tin 60% Bismuth, 165 C, Rotational True Viscosity

80% Tin 20% Bismuth

Actual Composition: 81.57% Sn, 18.43% Bi

Theoretical Solidus Line: 139 C
Theoretical Liquidus Line: 192.1 C

Experimental Solidus Line: 137.4 C
Experimental Liquidus Line: 185.9 C

Pre-Shear: 15 RPM, 2 minutes
Shear Rate: 1%-10%

80% Tin 20% Bismuth True Viscosity				
Composition	**Fraction Solid (%)**	**Temperature (C)**	**Viscosity Equation (Pa·s)**	**True Viscosity (Pa·s)**
80% Sn 20% Bi	3.23	185	$\eta = 118.36\dot{\gamma}^{-1.263}$	6.46
80% Sn 20% Bi	4.02	183	$\eta = 58.615\dot{\gamma}^{-0.980}$	6.14
80% Sn 20% Bi	4.40	182	$\eta = 79.098\dot{\gamma}^{-0.996}$	7.98
80% Sn 20% Bi	4.78	181	$\eta = 73.263\dot{\gamma}^{-0.884}$	9.57
80% Sn 20% Bi	5.15	180	$\eta = 82.478\dot{\gamma}^{-0.872}$	11.07
80% Sn 20% Bi	6.99	175	$\eta = 213.93\dot{\gamma}^{-1.114}$	16.45
80% Sn 20% Bi	8.76	170	$\eta = 253.31\dot{\gamma}^{-1.265}$	13.76
80% Sn 20% Bi	10.5	165	$\eta = 2061.4\dot{\gamma}^{-1.471}$	69.69
80% Sn 20% Bi	12.1	160	$\eta = 1965.3\dot{\gamma}^{-1.287}$	101.5

Table 102- 80% Tin 20% Bismuth True Viscosity

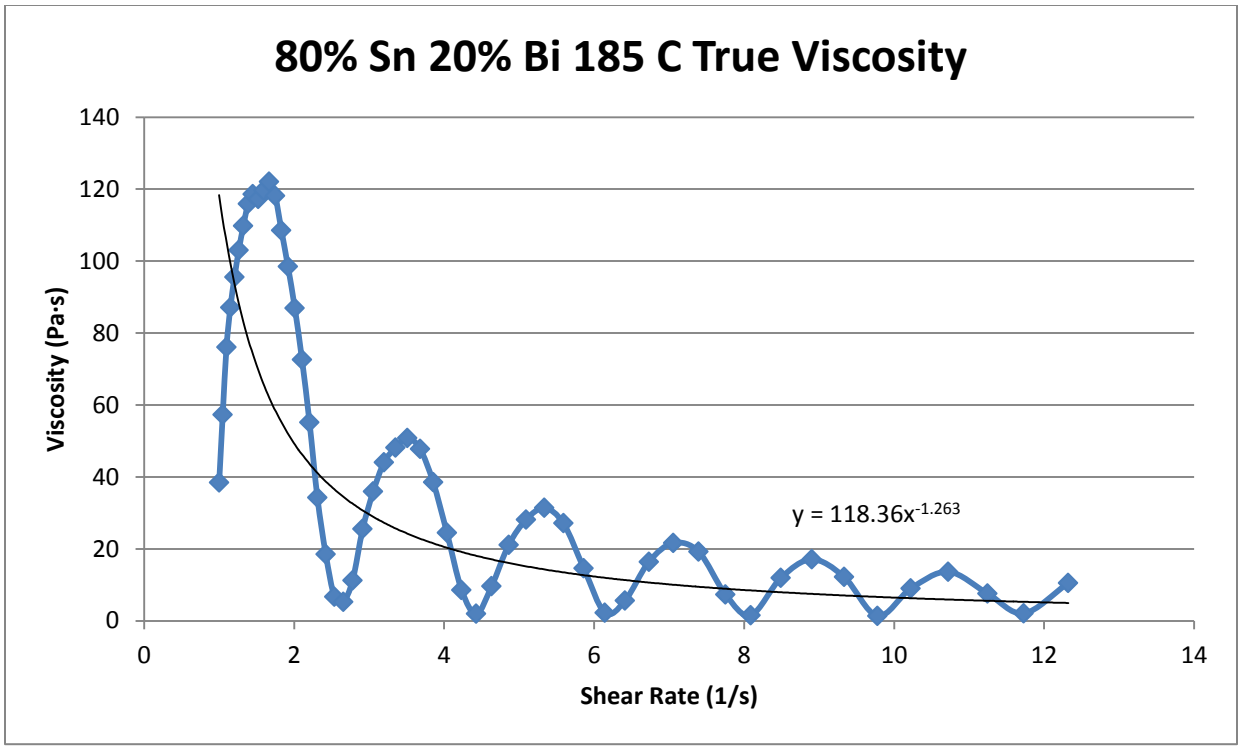

Figure 591- 80% Tin 20% Bismuth, 185 C, Rotational True Viscosity

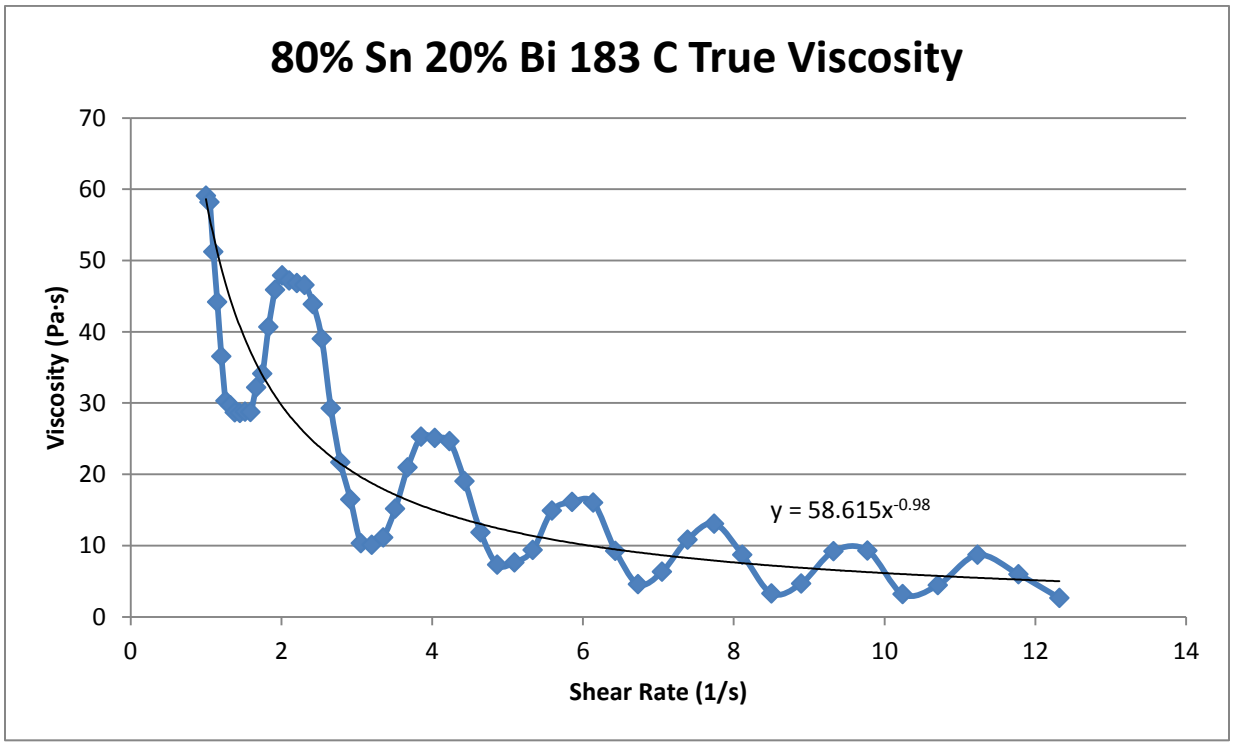

Figure 592- 80% Tin 20% Bismuth, 183 C, Rotational True Viscosity

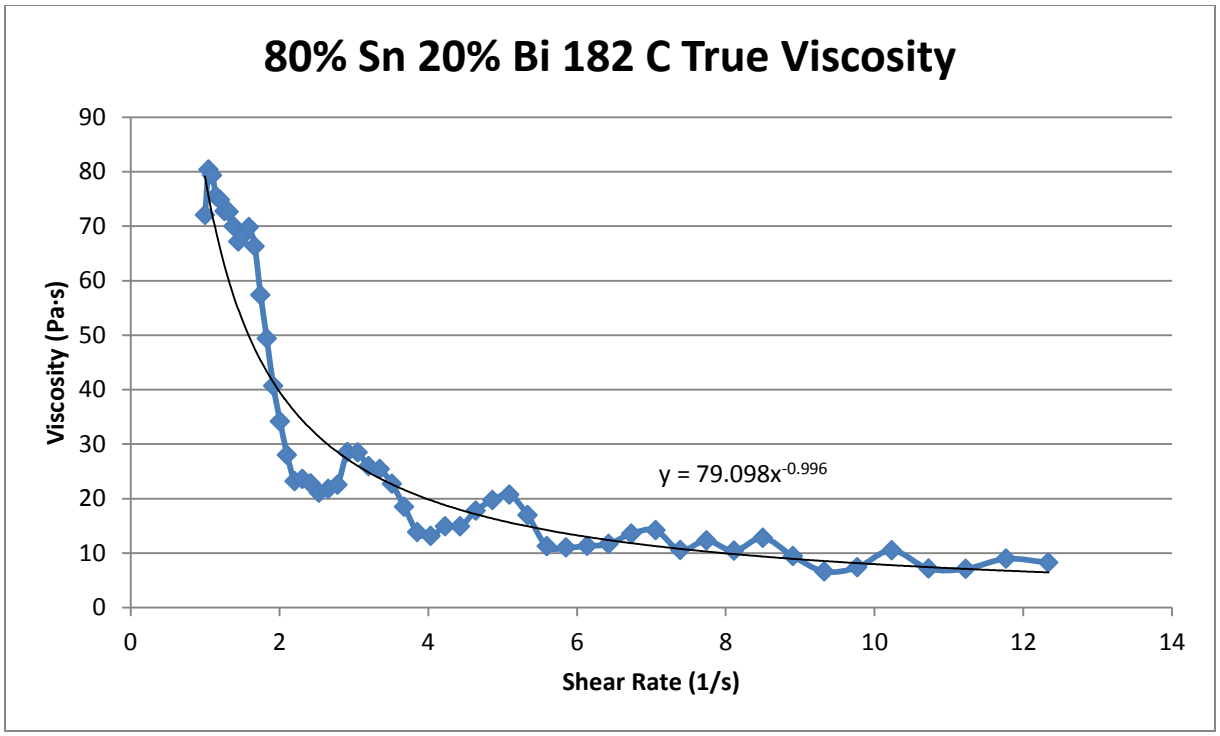

Figure 593- 80% Tin 20% Bismuth, 182 C, Rotational True Viscosity

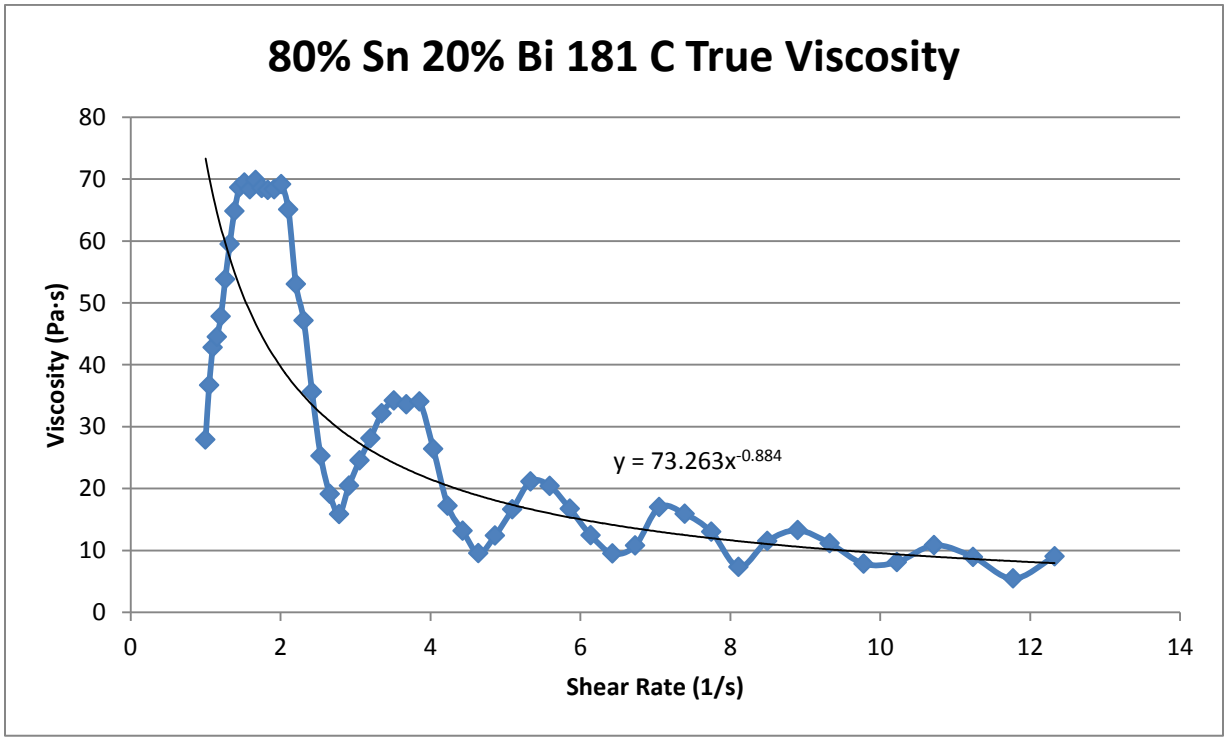

Figure 594- 80% Tin 20% Bismuth, 181 C, Rotational True Viscosity

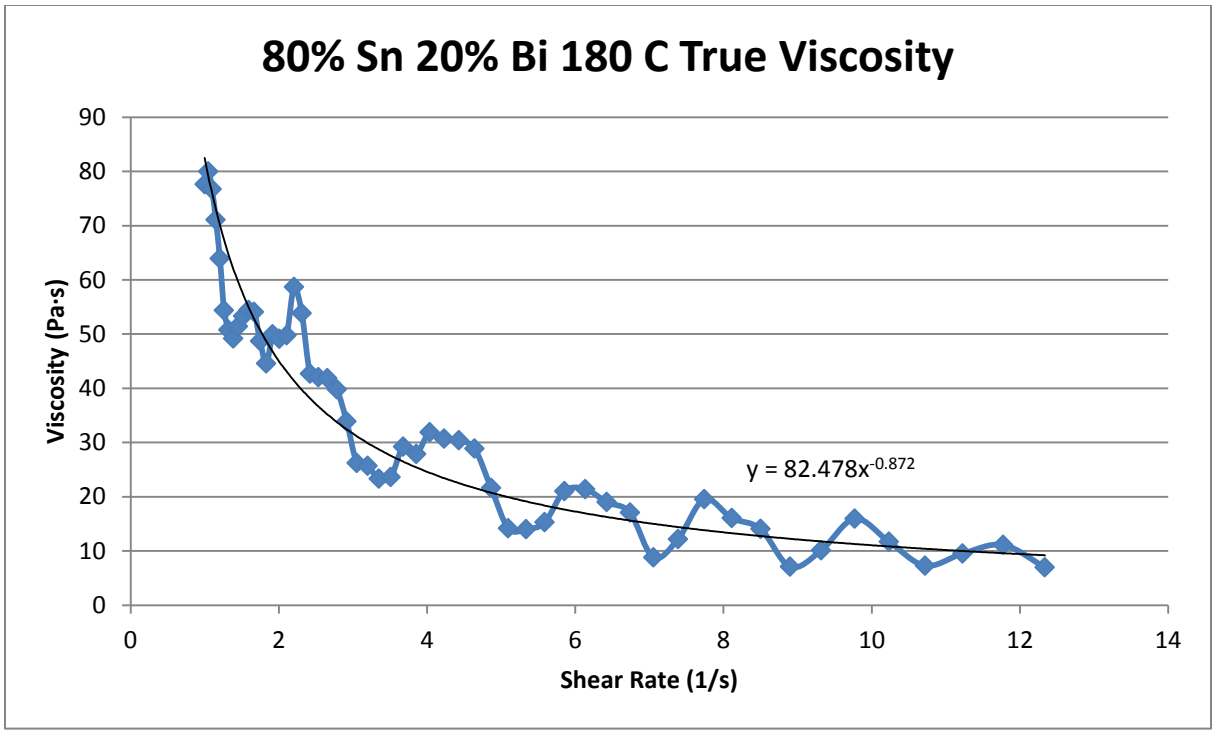

Figure 595- 80% Tin 20% Bismuth, 180 C, Rotational True Viscosity

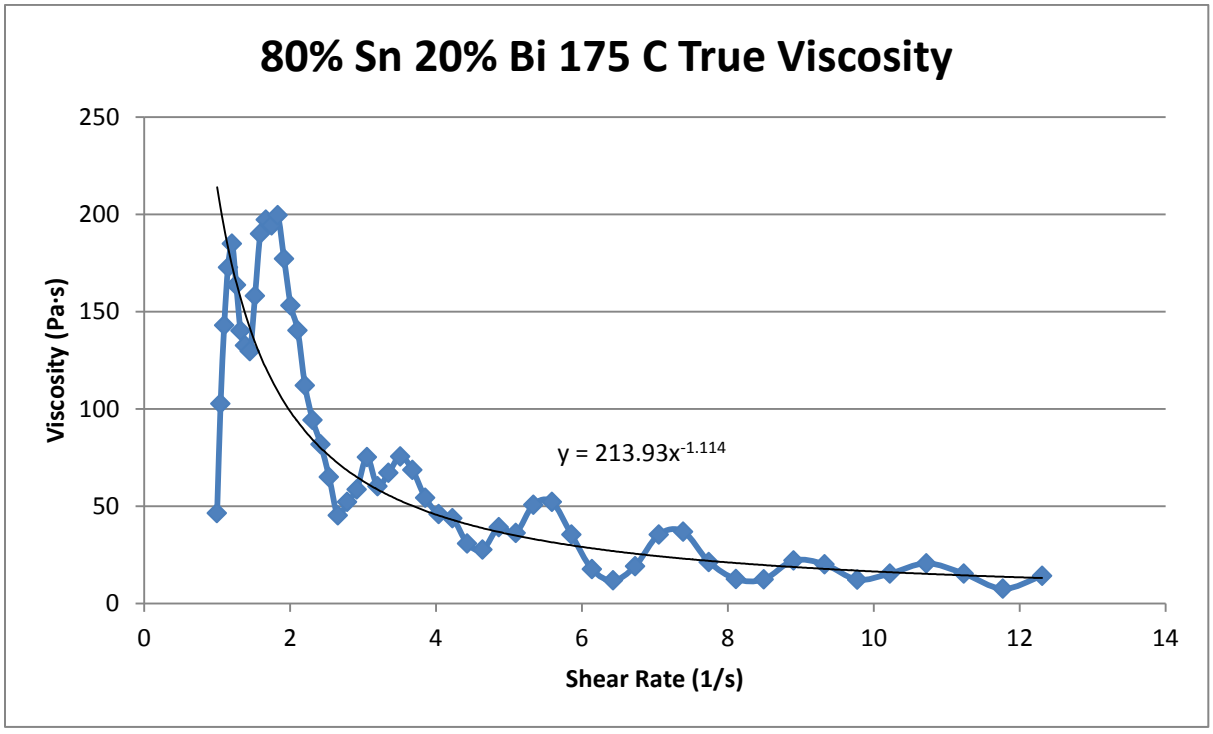

Figure 596- 80% Tin 20% Bismuth, 175 C, Rotational True Viscosity

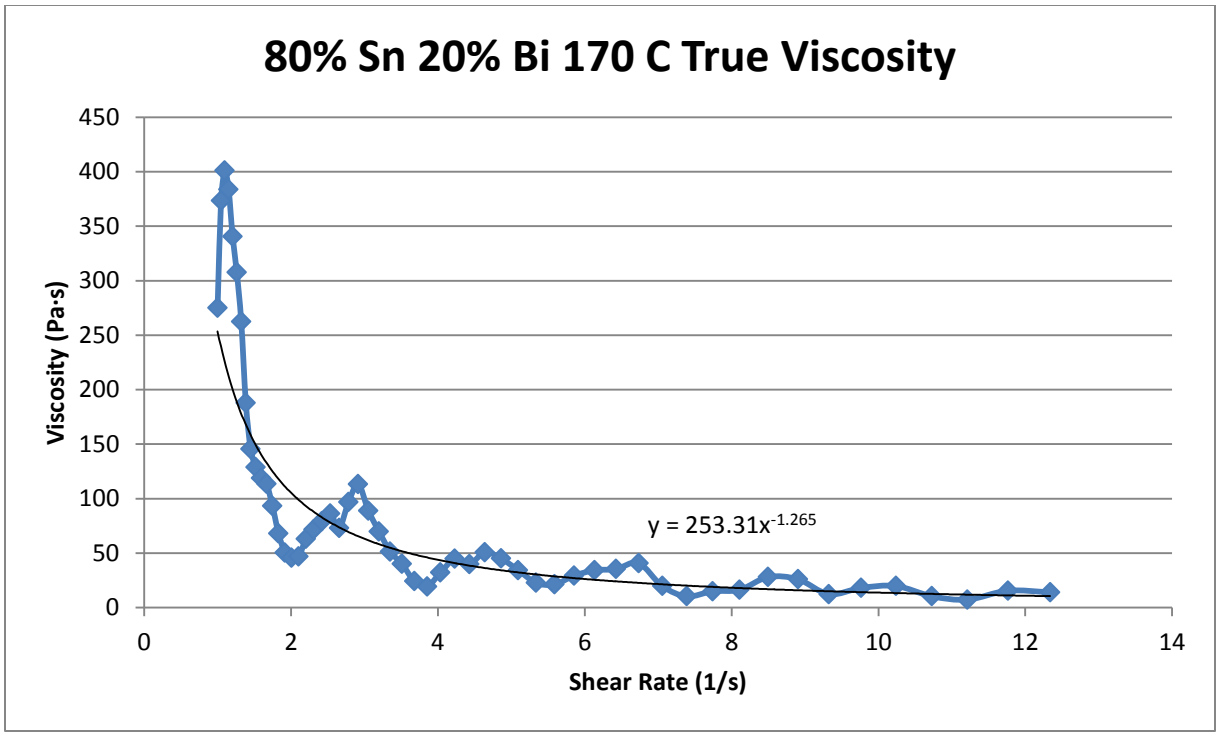

Figure 597- 80% Tin 20% Bismuth, 170 C, Rotational True Viscosity

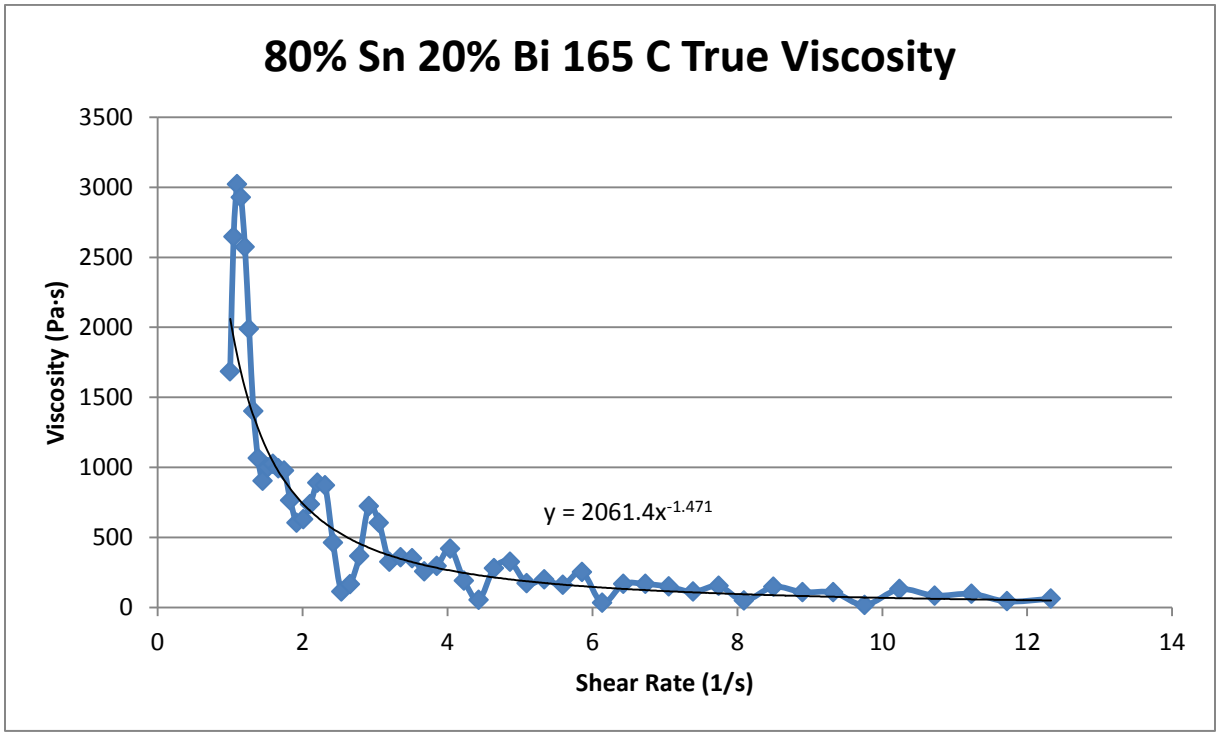

Figure 598- 80% Tin 20% Bismuth, 165 C, Rotational True Viscosity

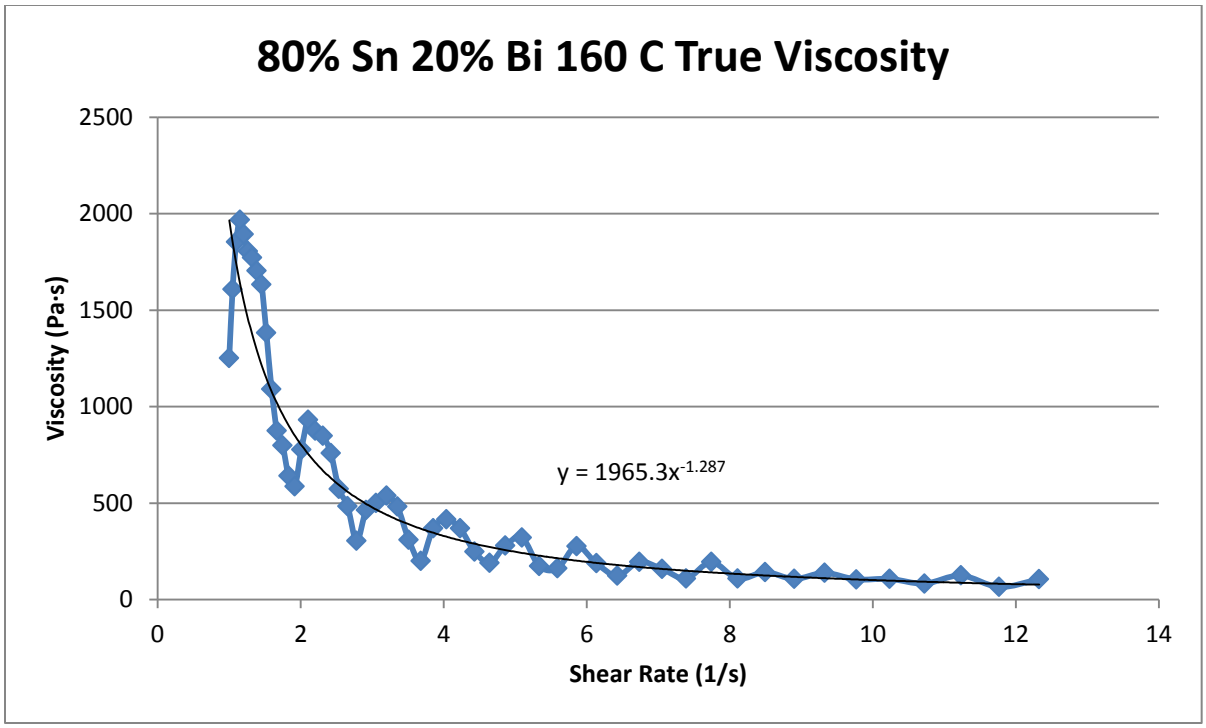

Figure 599- 80% Tin 20% Bismuth, 160 C, Rotational True Viscosity

Appendix G- Nozzle Simulations

Simulation 1- 500 Microns

Parameters

Geometry	
Inlet Diameter	10 mm
Outlet Diameter	0.5 mm (500 microns)
Nozzle Height	15 mm
Nozzle Angle	72.429°
Tank Diameter	10 mm
Tank Height	5 mm

Mesh Parameters	
Accuracy (Refinement Factor)	5
Minimum Wall Thickness	0.5 mm
Minimum Element Size	0.1 mm
Smoothing	2
Ratio	2
Coarsening Loops	1
Minimal Accuracy After Coarsening	5

Mesh Properties	
Control Volumes (X Direction)	154
Control Volumes (Y Direction)	144
Control Volumes (Z Direction)	150
Composed Part Cells	143,060
Total Part Cells	39,189
Blocked Cells	0

Process Definitions	
Material Temperature	596 C
Fraction Solid	44%
Close Mold Time	0 s
Fill Time	0.25 s
Hold Time After Filling	1 s

Table 103- Simulation 1 (500 Microns), Parameters

Notes

- First run with a far smaller tank (tank consisted of only the inlet)
    - This should result in more data during the actual flow through the nozzle.
- Significantly higher velocity in center (2-3 times higher near outlet, greater near inlet)
- Viscosity on walls is almost half that in middle towards outlet
- Pressure triples just as SSM approaches the outlet

Mesh

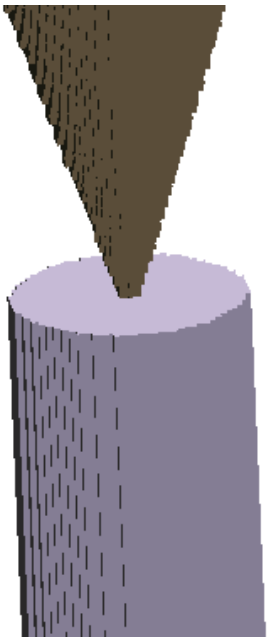

Figure 600- Simulation 1 (500 Microns), Mesh

Velocity

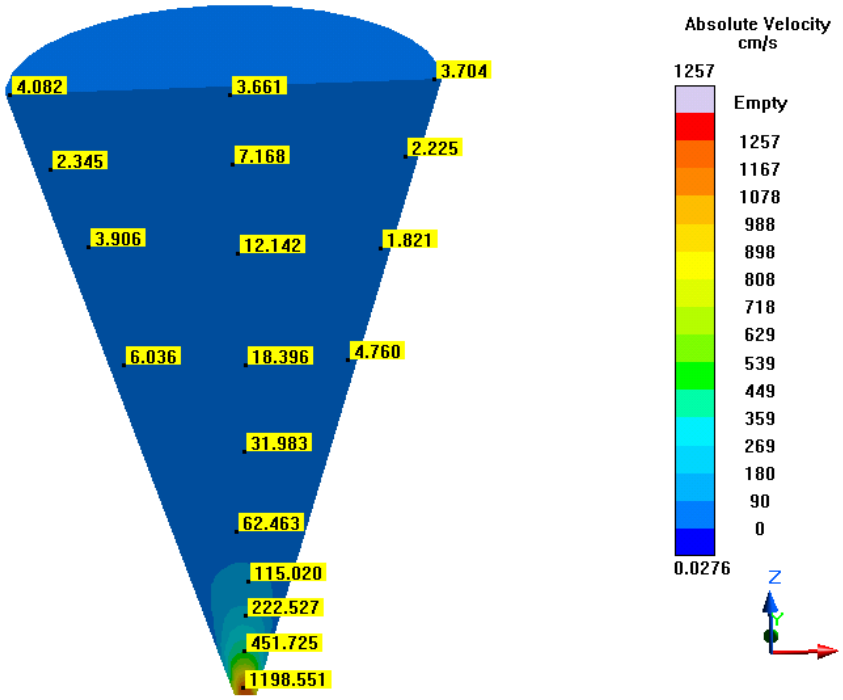

Figure 601- Simulation 1 (500 Microns), Velocity

Viscosity

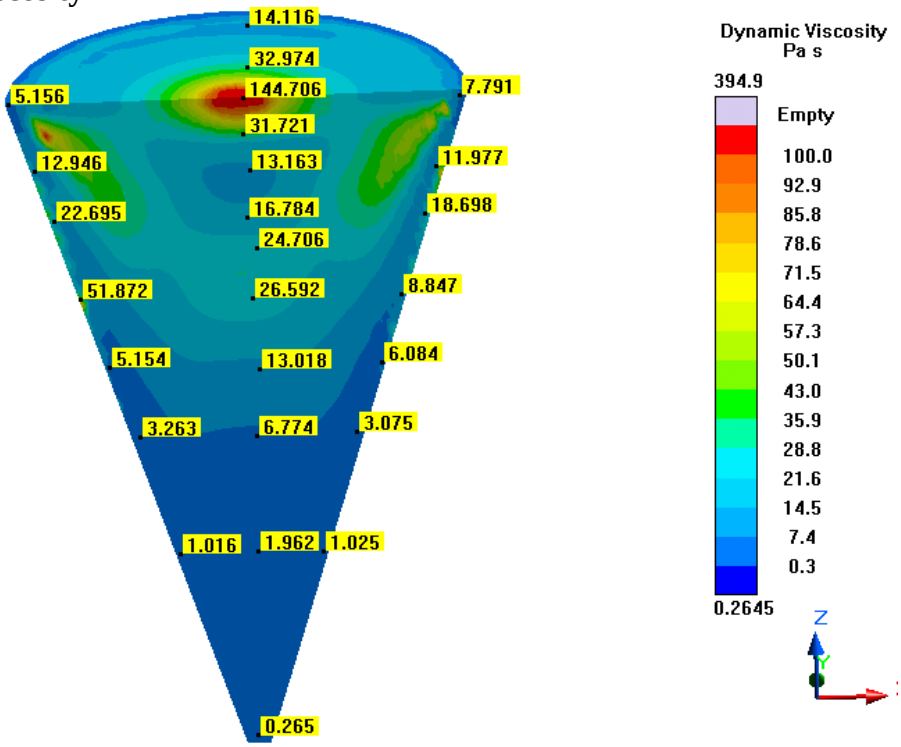

Figure 602- Simulation 1 (500 Microns), Viscosity

Cooling Rate

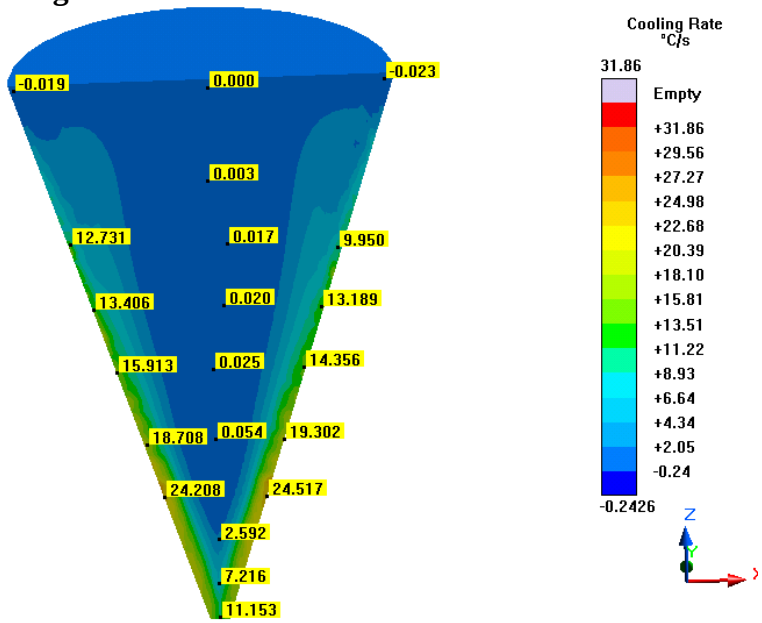

Figure 603- Simulation 1 (500 Microns), Cooling Rate

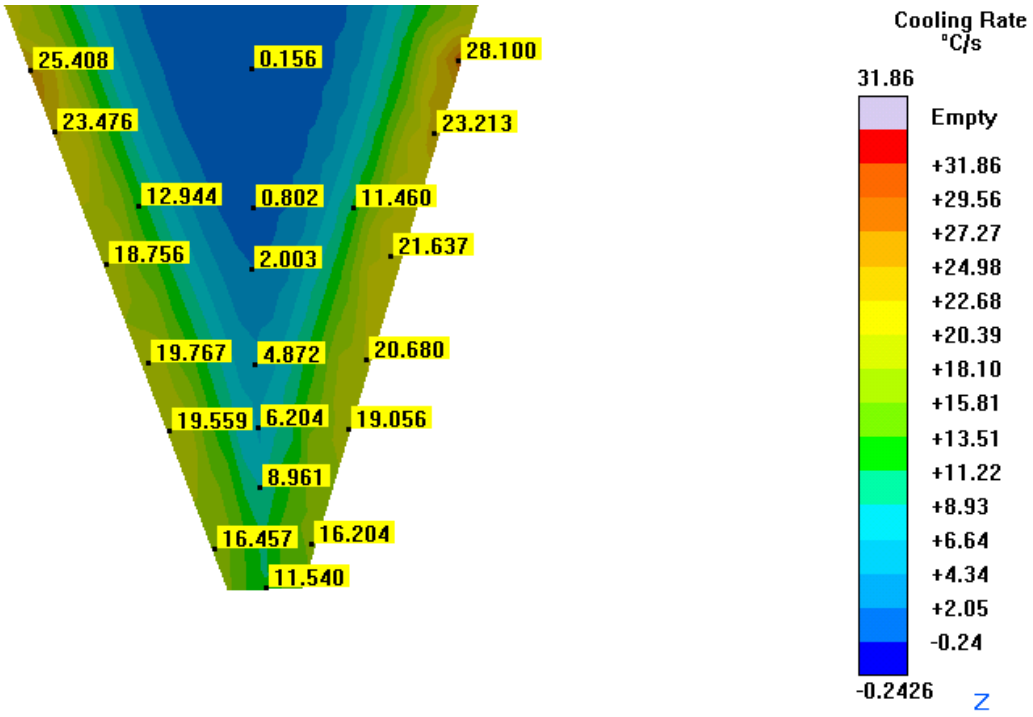

Figure 604- Simulation 1 (500 Microns), Cooling Rate at Nozzle

Pressure

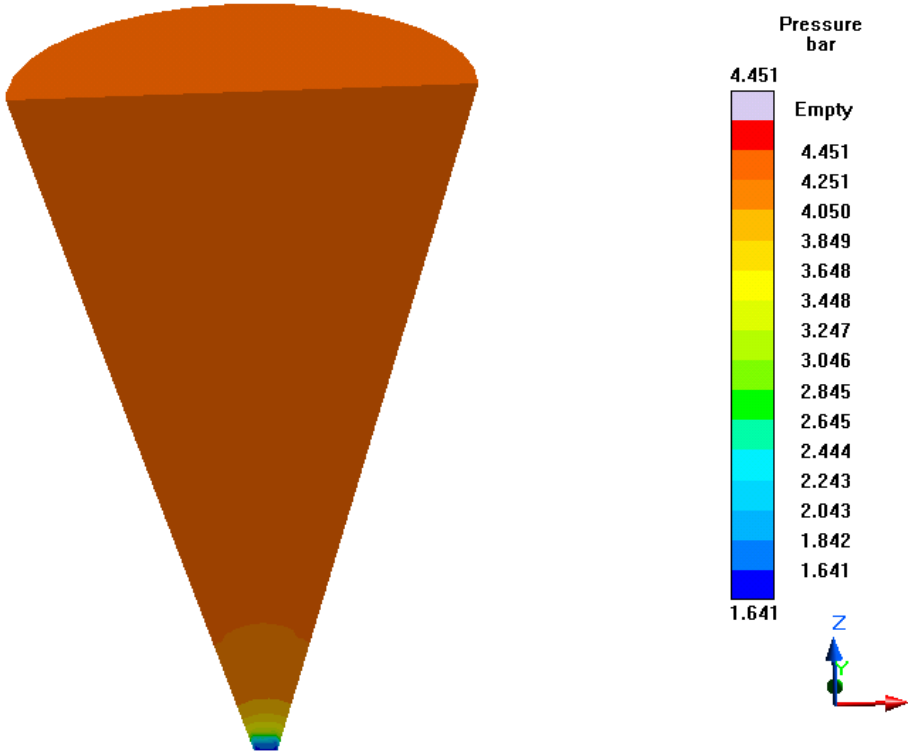

Figure 605- Simulation 1 (500 Microns), Pressure

Shear Heating

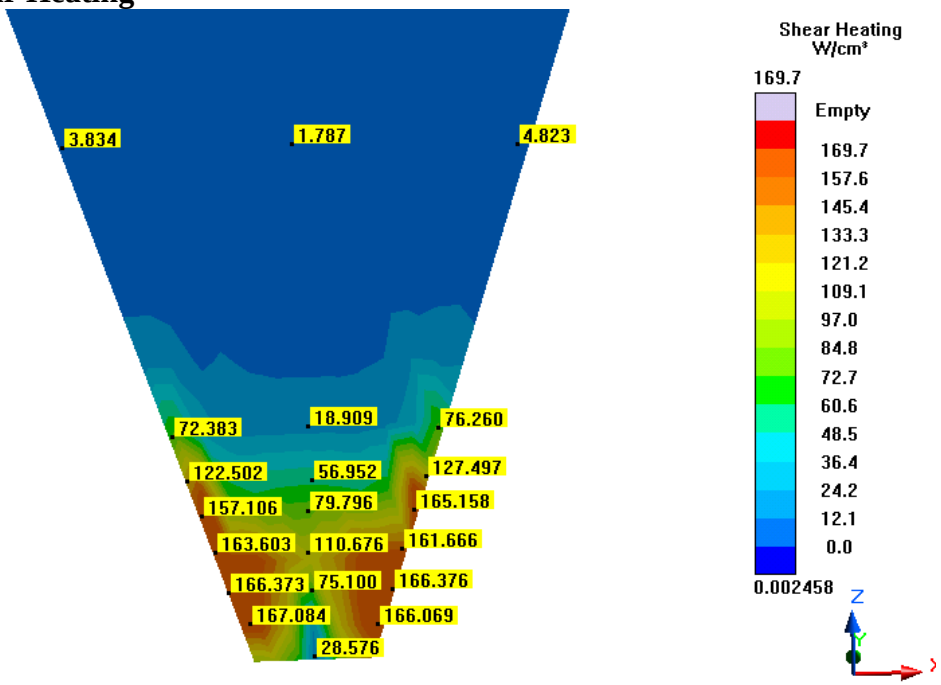

Figure 606- Simulation 1 (500 Microns), Shear Heating

Shear Rate

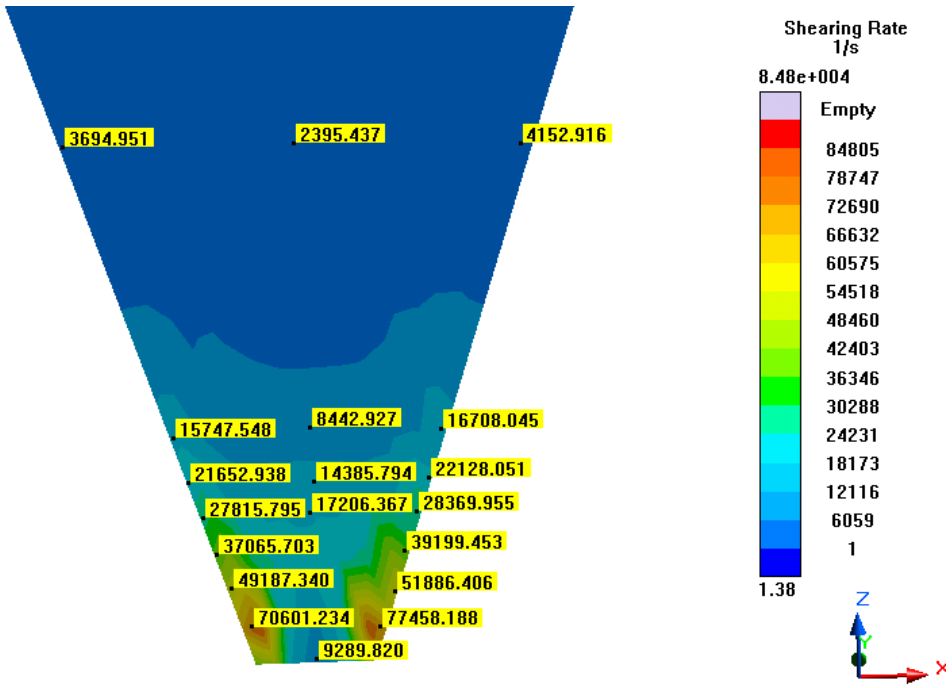

Figure 607- Simulation 1 (500 Microns), Shear Rate

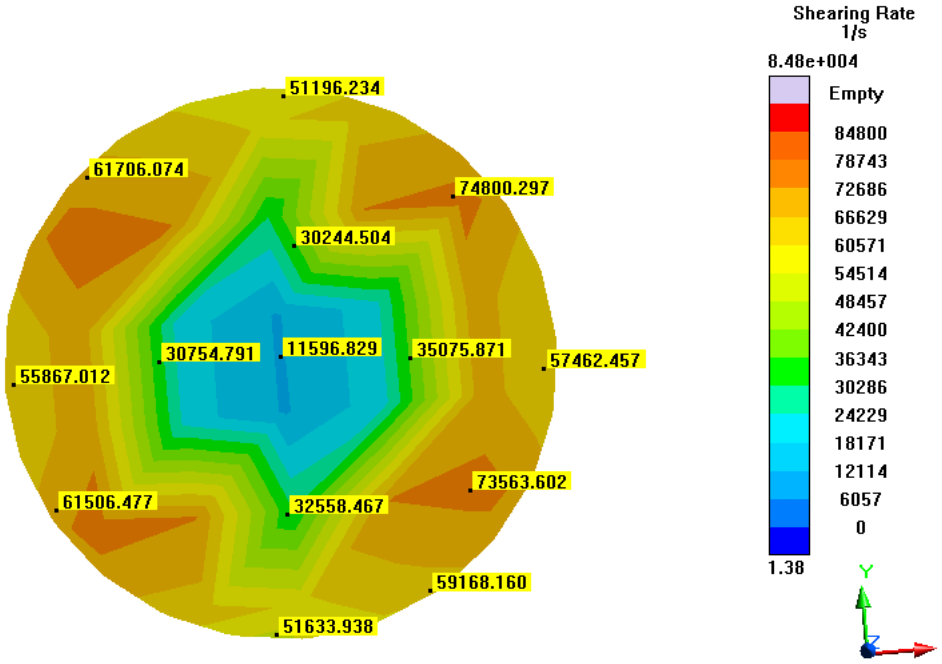

Figure 608- Simulation 1 (500 Microns), Tip Shear Rate

Shear Stress

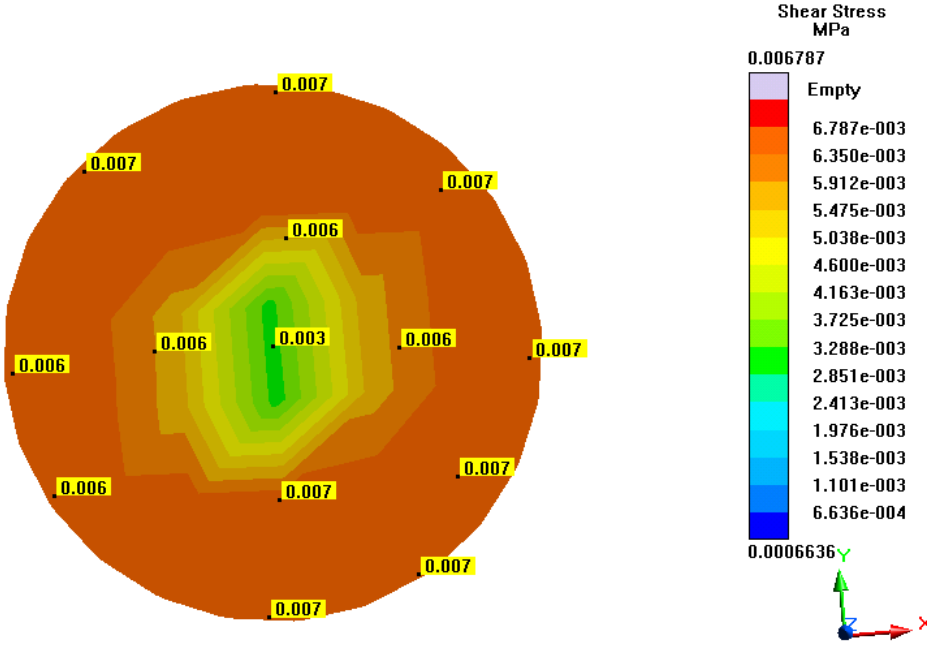

Figure 609- Simulation 1 (500 Microns), Tip Shear Stress

Temperature

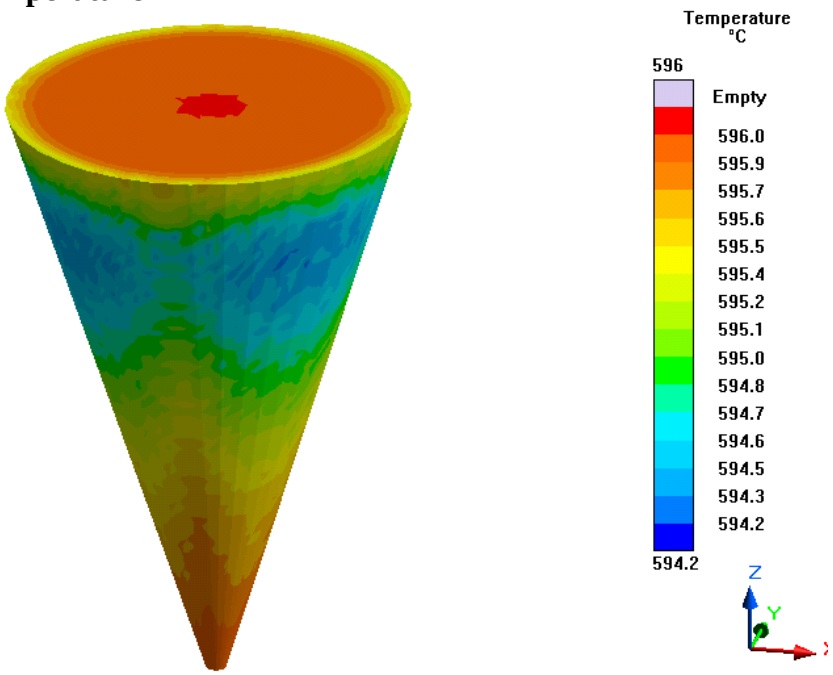

Figure 610- Simulation 1 (500 Microns), Temperature

Simulation 2- 500 Microns (Slower)

Parameters

Geometry	
Inlet Diameter	10 mm
Outlet Diameter	0.5 mm (500 microns)
Nozzle Height	15 mm
Nozzle Angle	72.429°
Tank Diameter	10 mm
Tank Height	5 mm

Mesh Parameters	
Accuracy (Refinement Factor)	5
Minimum Wall Thickness	0.5 mm
Minimum Element Size	0.1 mm
Smoothing	2
Ratio	2
Coarsening Loops	1
Minimal Accuracy After Coarsening	5

Mesh Properties	
Control Volumes (X Direction)	154
Control Volumes (Y Direction)	144
Control Volumes (Z Direction)	150
Composed Part Cells	143,060
Total Part Cells	39,189
Blocked Cells	0

Process Definitions	
Material Temperature	596 C
Fraction Solid	44%
Close Mold Time	0 s
Fill Time	0.3125 s
Hold Time After Filling	1 s

Table 104- Simulation 2 (500 Microns, Slower), Parameters

Notes

- Fill time increased by 25%
- Lower velocity, pressure, shear rate, & cooling rate by almost 25%
- Higher viscosity, but outlet was the same

Velocity

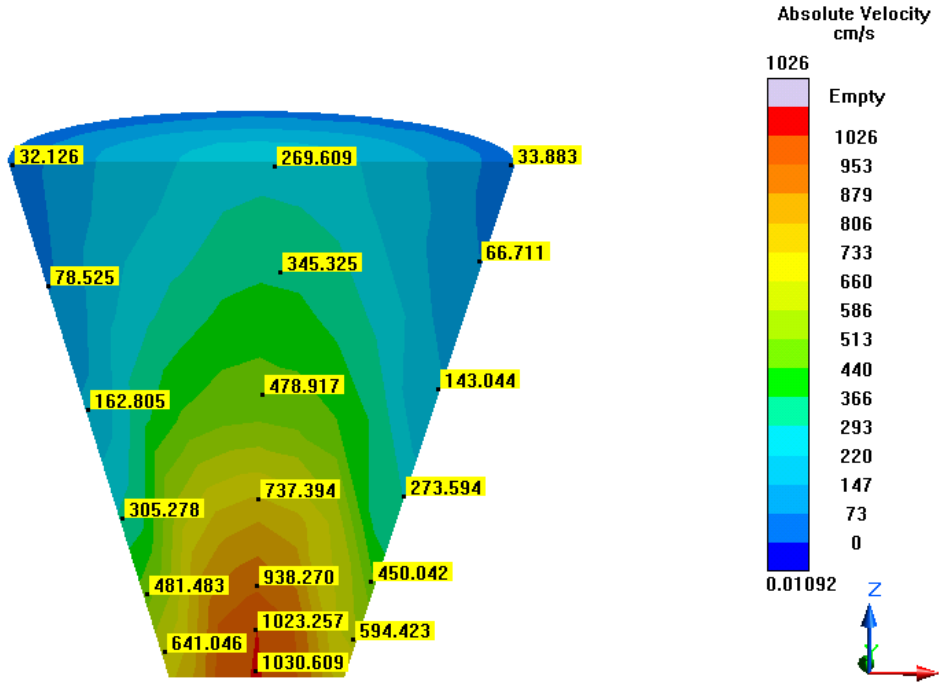

Figure 611- Simulation 2 (500 Microns, Slower), Velocity

Viscosity

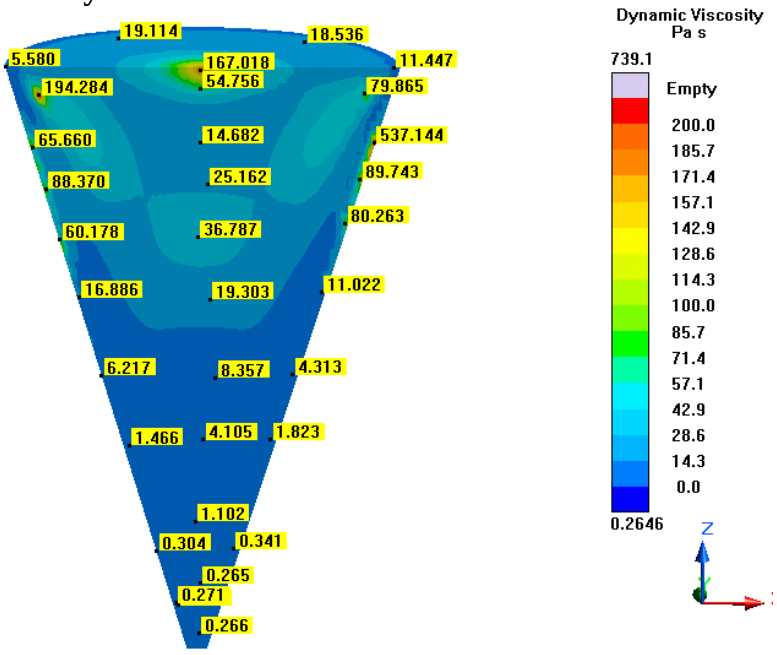

Figure 612- Simulation 2 (500 Microns, Slower), Viscosity

Cooling Rate

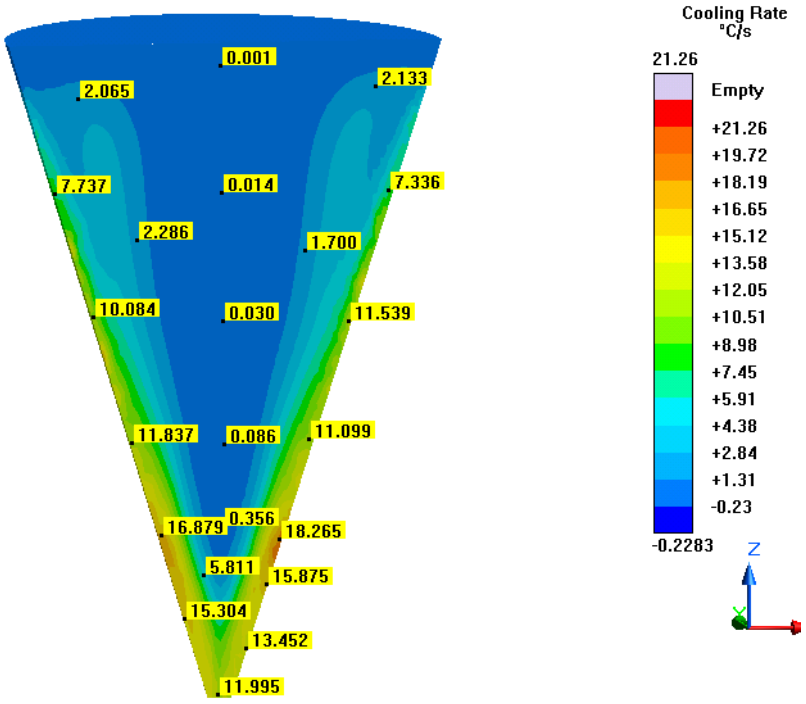

Figure 613- Simulation 2 (500 Microns, Slower), Cooling Rate

Pressure

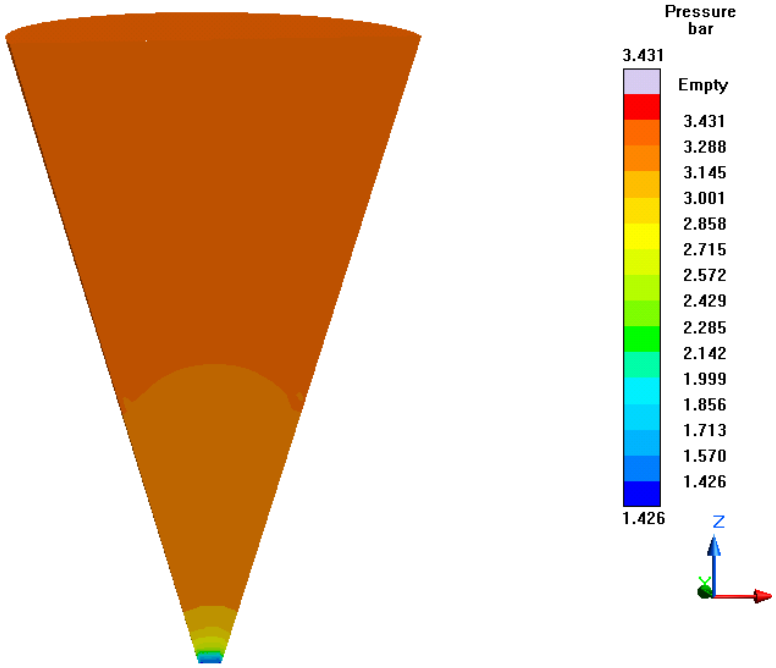

Figure 614- Simulation 2 (500 Microns, Slower), Pressure

Shear Heating

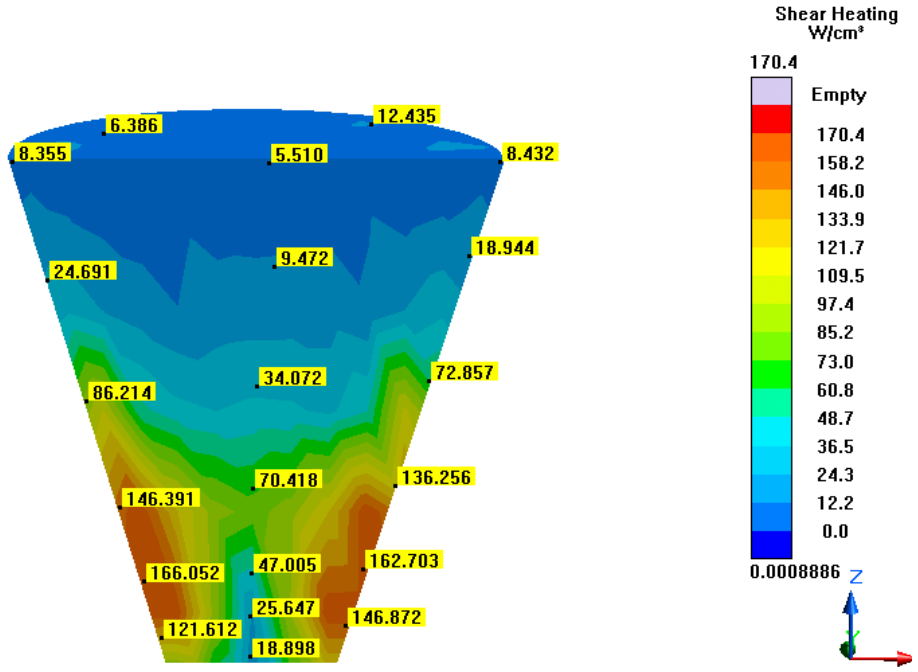

Figure 615- Simulation 2 (500 Microns, Slower), Shear Heating

Shear Rate

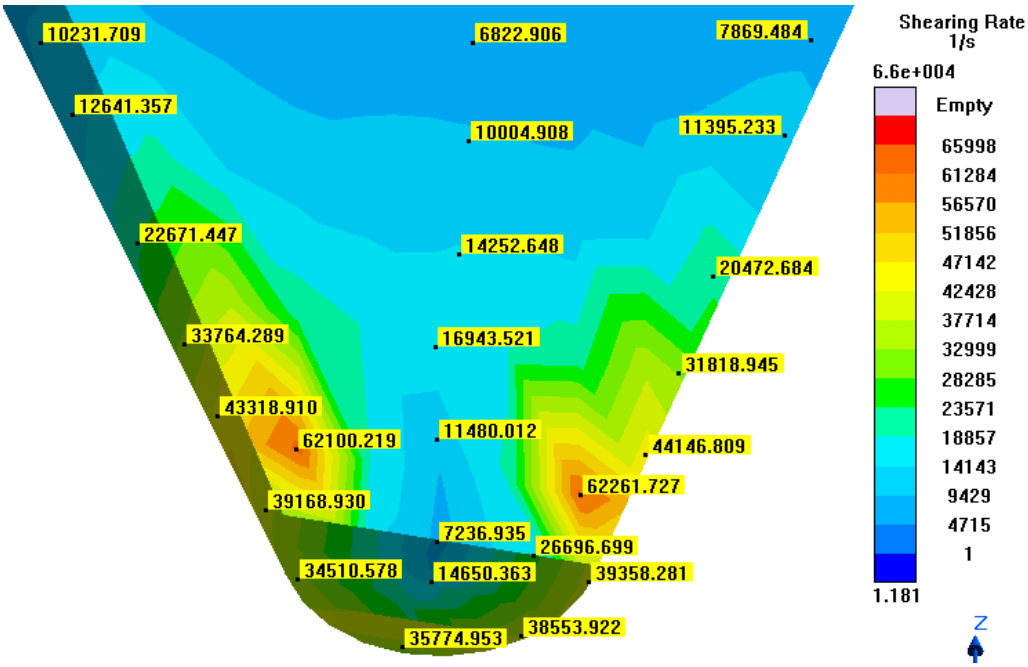

Figure 616- Simulation 2 (500 Microns, Slower), Shear Rate

Shear Stress

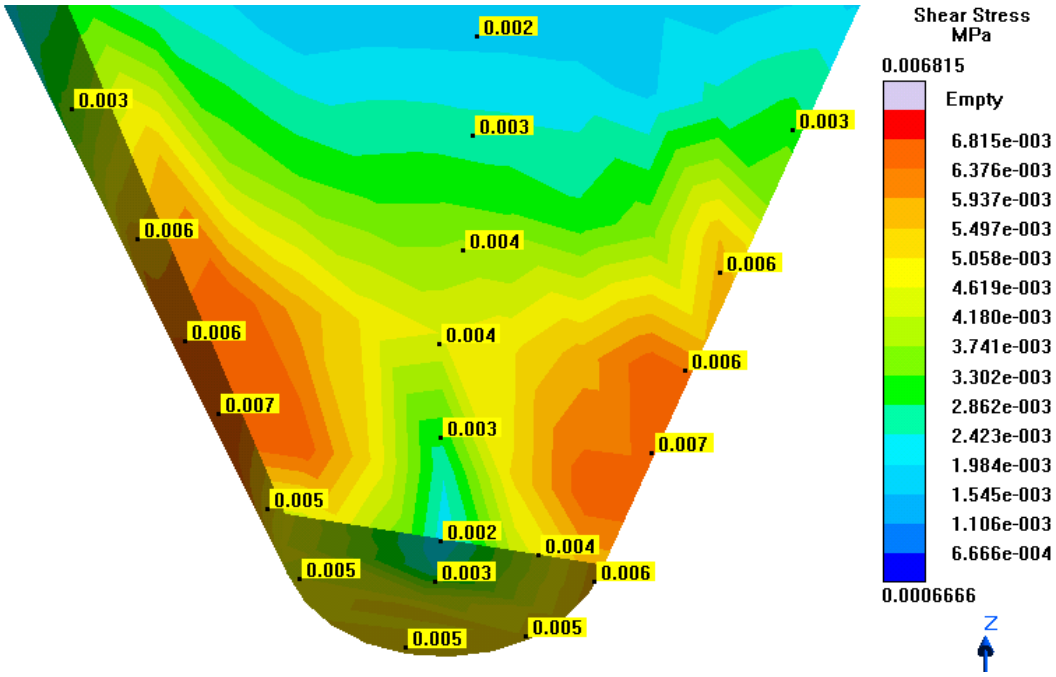

Figure 617- Simulation 2 (500 Microns, Slower), Shear Stress

Temperature

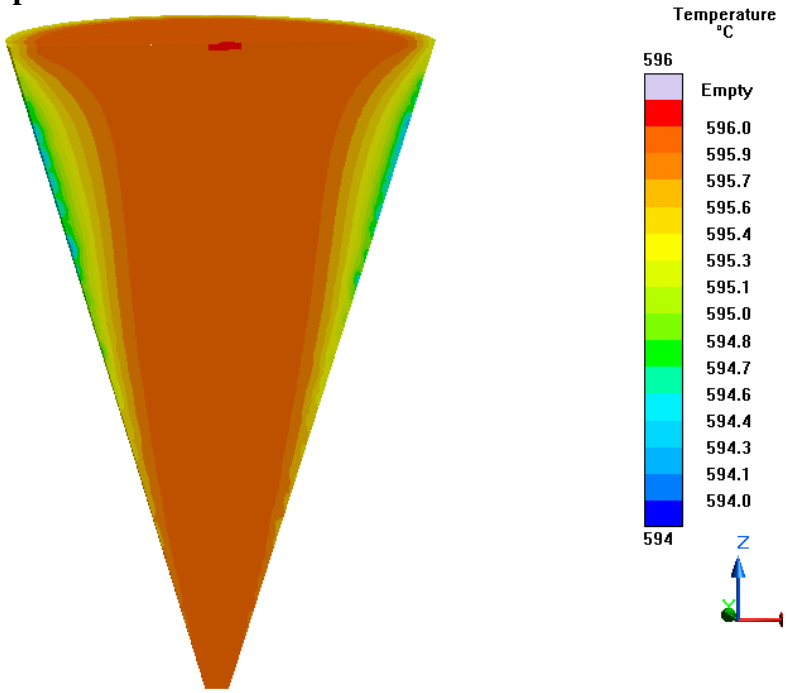

Figure 618- Simulation 2 (500 Microns, Slower), Temperature

Simulation 3- 500 Microns (Faster)

Parameters

Geometry	
Inlet Diameter	10 mm
Outlet Diameter	0.5 mm (500 microns)
Nozzle Height	15 mm
Nozzle Angle	72.429°
Tank Diameter	10 mm
Tank Height	5 mm

Mesh Parameters	
Accuracy (Refinement Factor)	5
Minimum Wall Thickness	0.5 mm
Minimum Element Size	0.1 mm
Smoothing	2
Ratio	2
Coarsening Loops	1
Minimal Accuracy After Coarsening	5

Mesh Properties	
Control Volumes (X Direction)	154
Control Volumes (Y Direction)	144
Control Volumes (Z Direction)	150
Composed Part Cells	143,060
Total Part Cells	39,189
Blocked Cells	0

Process Definitions	
Material Temperature	596 C
Fraction Solid	44%
Close Mold Time	0 s
Fill Time	0.1875 s
Hold Time After Filling	1 s

Table 105- Simulation 3 (500 Microns, Faster), Parameters

Velocity

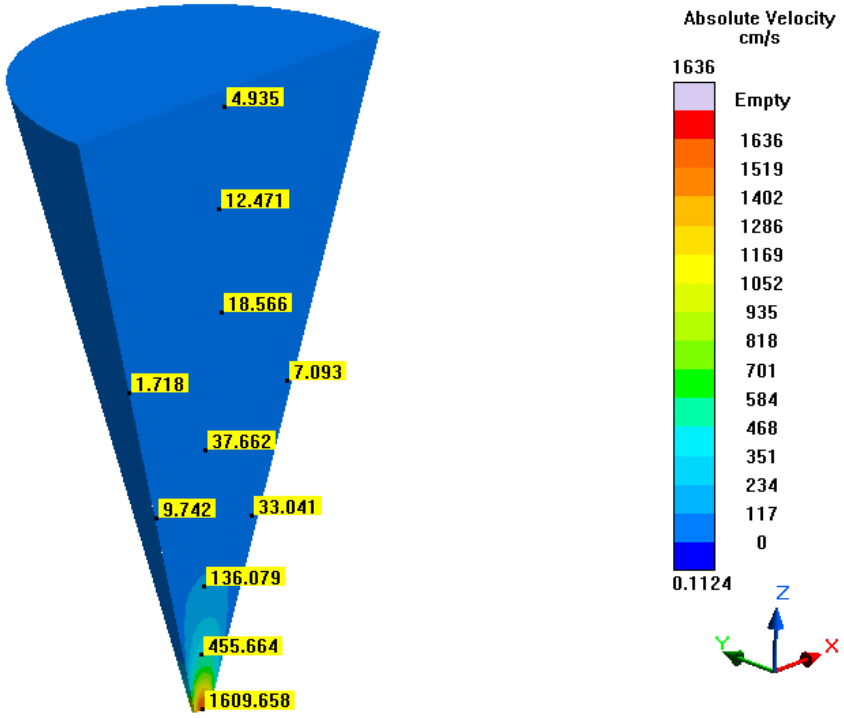

Figure 619- Simulation 3 (500 Microns, Faster), Velocity

Viscosity

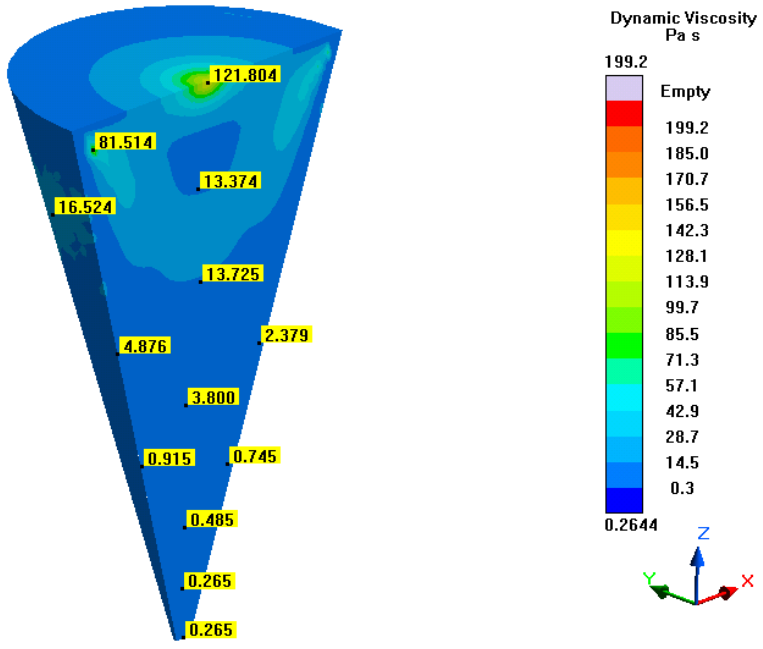

Figure 620- Simulation 3 (500 Microns, Faster), Viscosity

Cooling Rate

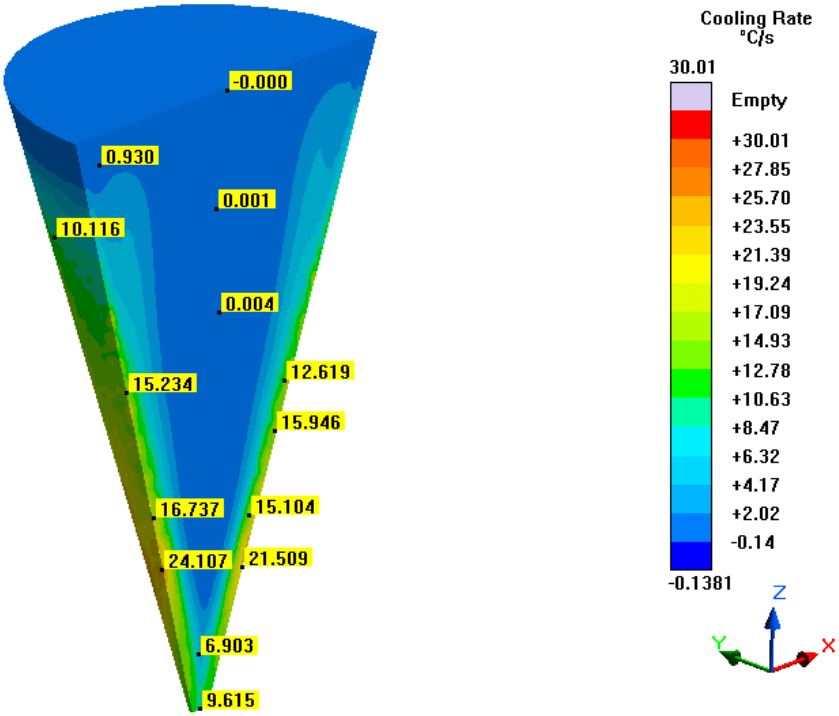

Figure 621- Simulation 3 (500 Microns, Faster), Cooling Rate

Pressure

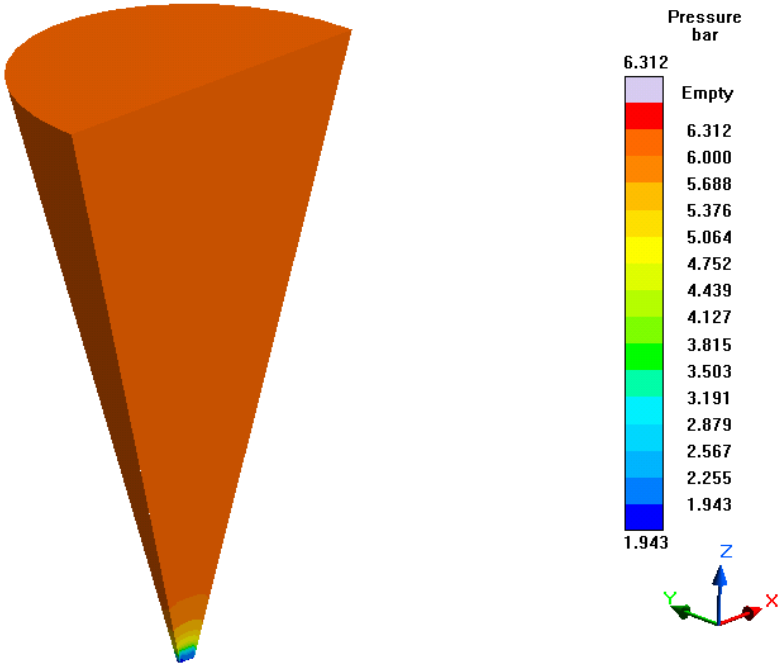

Figure 622- Simulation 3 (500 Microns, Faster), Pressure

Shear Heating

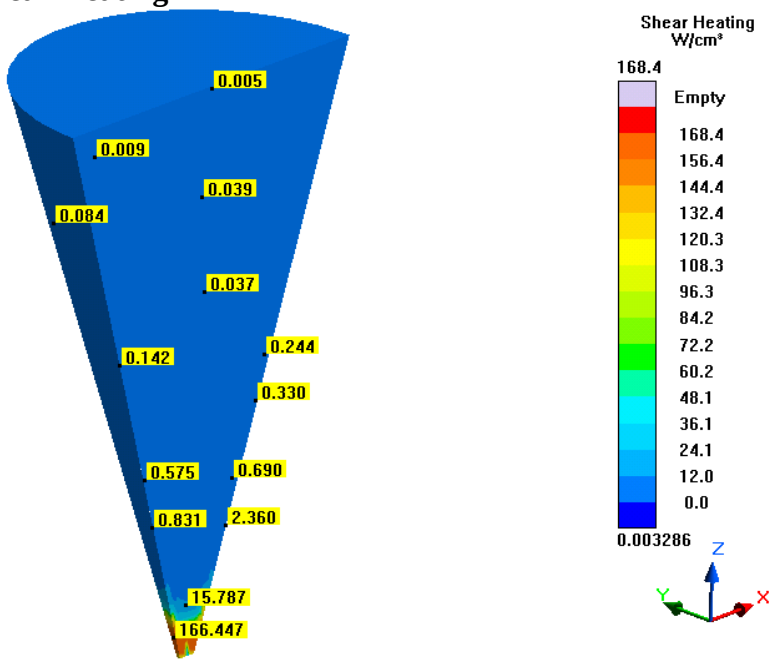

Figure 623- Simulation 3 (500 Microns, Faster), Shear Heating

Shear Rate

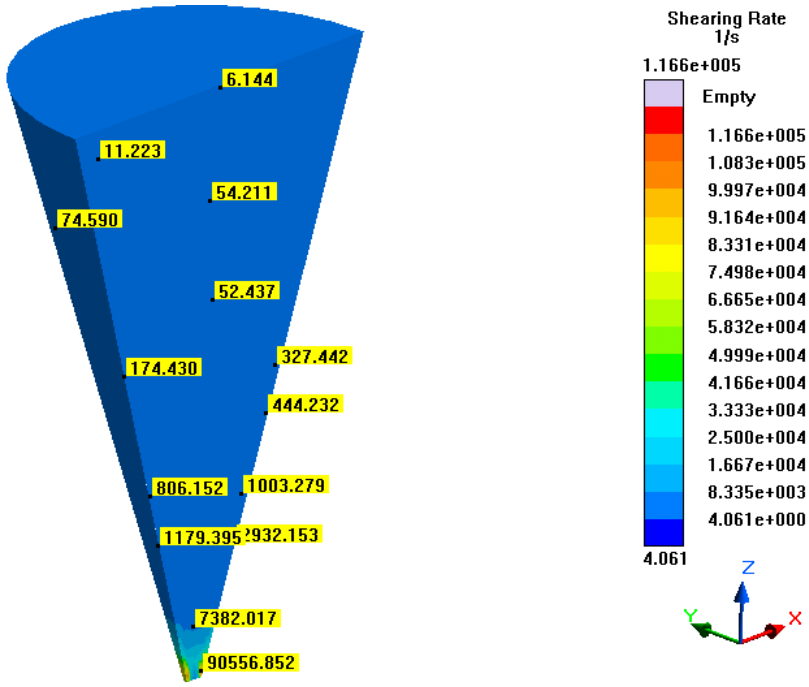

Figure 624- Simulation 3 (500 Microns, Faster), Shear Rate

Shear Stress

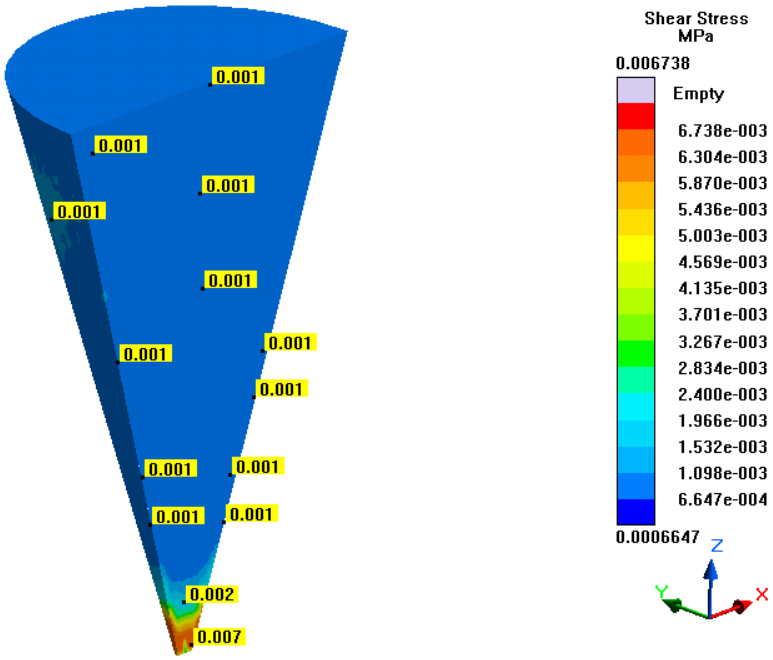

Figure 625- Simulation 3 (500 Microns, Faster), Shear Stress

Temperature

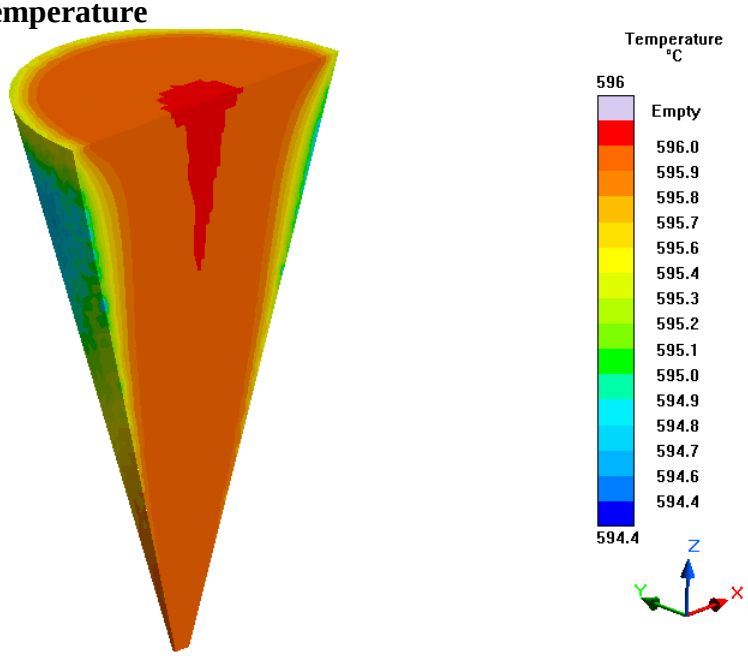

Figure 626- Simulation 3 (500 Microns, Faster), Temperature

Simulation 4- 375 Microns

Parameters

Geometry	
Inlet Diameter	10 mm
Outlet Diameter	0.375 mm (375 microns)
Nozzle Height	15 mm
Nozzle Angle	72.212°
Tank Diameter	10 mm
Tank Height	5 mm

Mesh Parameters	
Accuracy (Refinement Factor)	5
Minimum Wall Thickness	0.375 mm
Minimum Element Size	0.075 mm
Smoothing	2
Ratio	2
Coarsening Loops	1
Minimal Accuracy After Coarsening	5

Mesh Properties	
Control Volumes (X Direction)	202
Control Volumes (Y Direction)	206
Control Volumes (Z Direction)	198
Composed Part Cells	65,776
Total Part Cells	286,497
Blocked Cells	0

Process Definitions	
Material Temperature	596 C
Fraction Solid	44%
Close Mold Time	0 s
Fill Time	0.25 s
Hold Time After Filling	1 s

Table 106- Simulation 4 (375 Microns)

Velocity

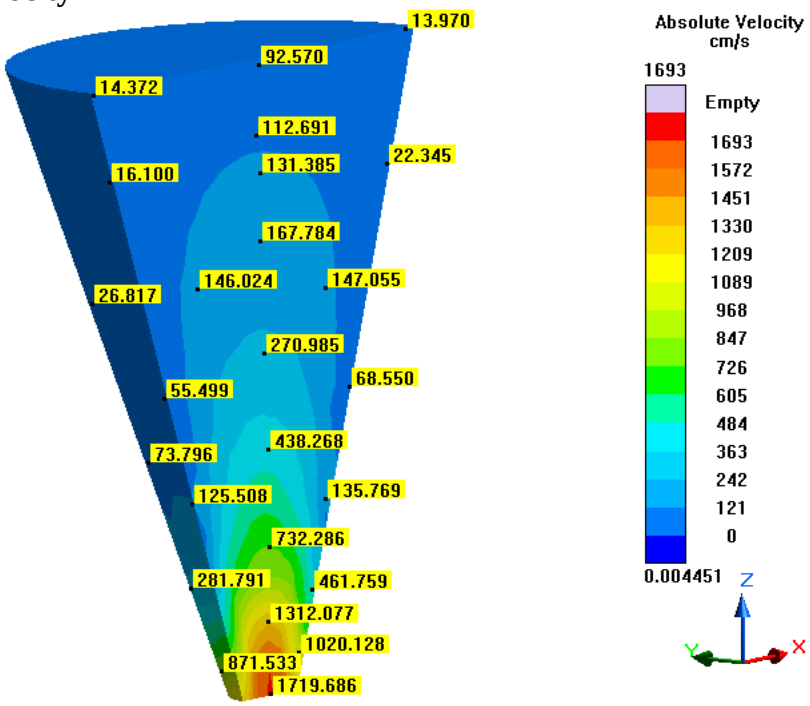

Figure 627- Simulation 4 (375 Microns)

Viscosity

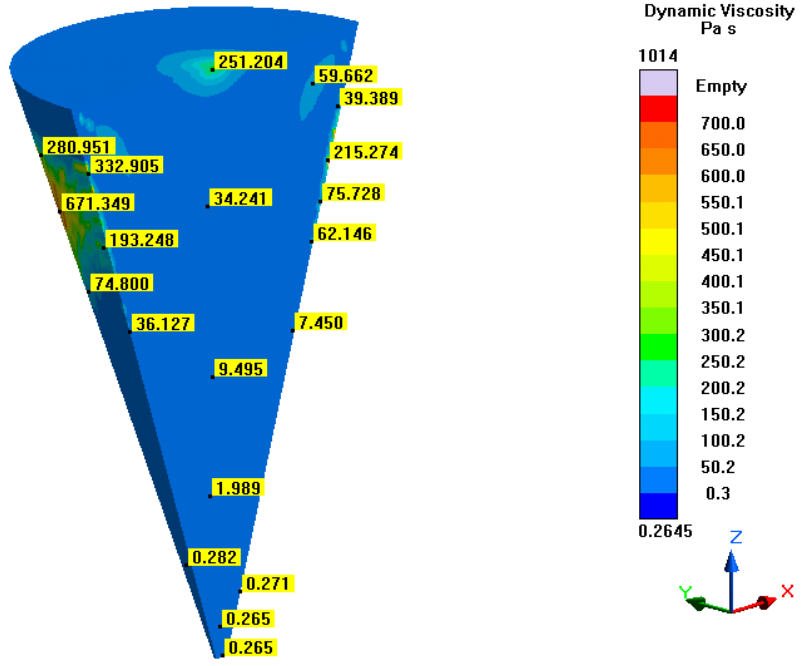

Figure 628- Simulation 4 (375 Microns), Viscosity

Cooling Rate

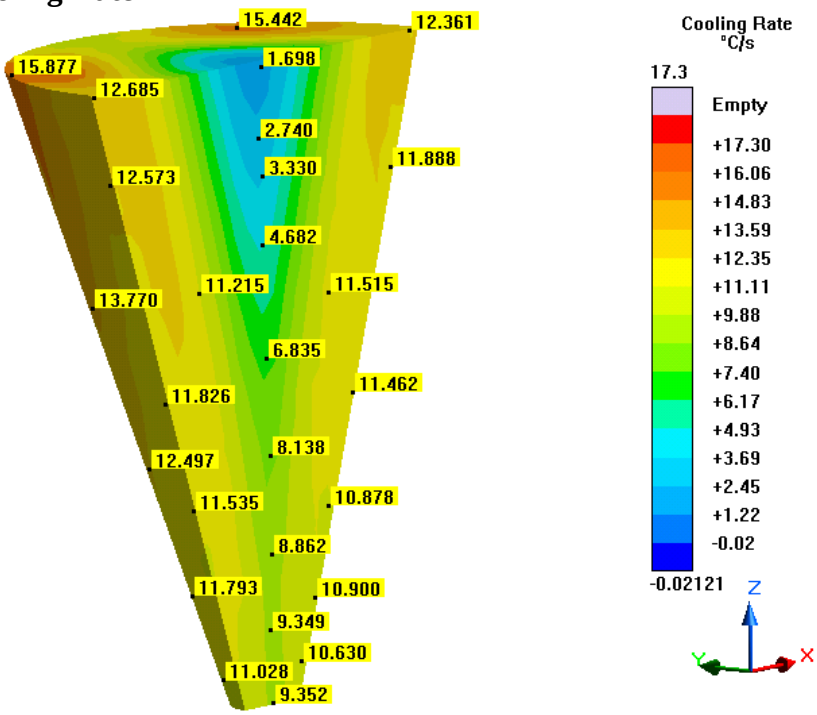

Figure 629- Simulation 4 (375 Microns), Cooling Rate

Pressure

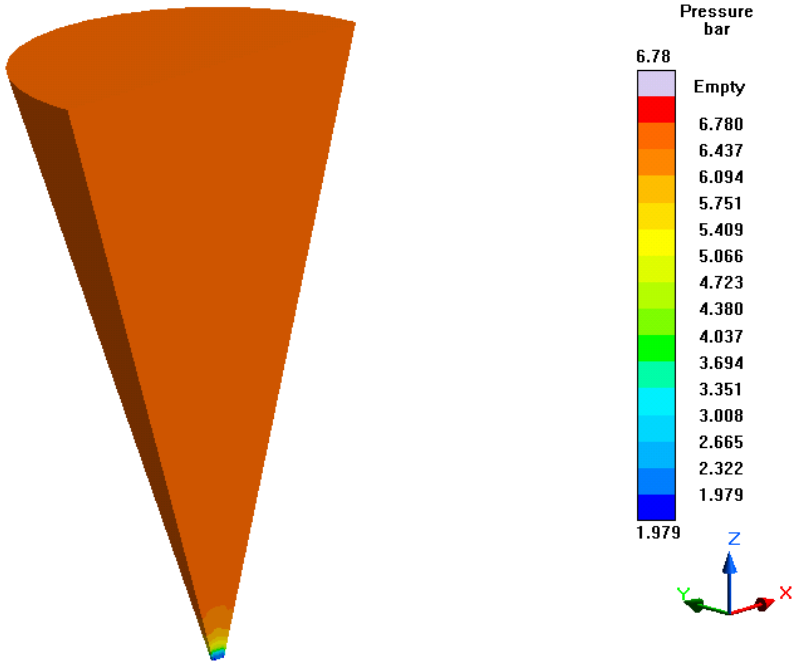

Figure 630- Simulation 4 (375 Microns), Pressure

Shear Heating

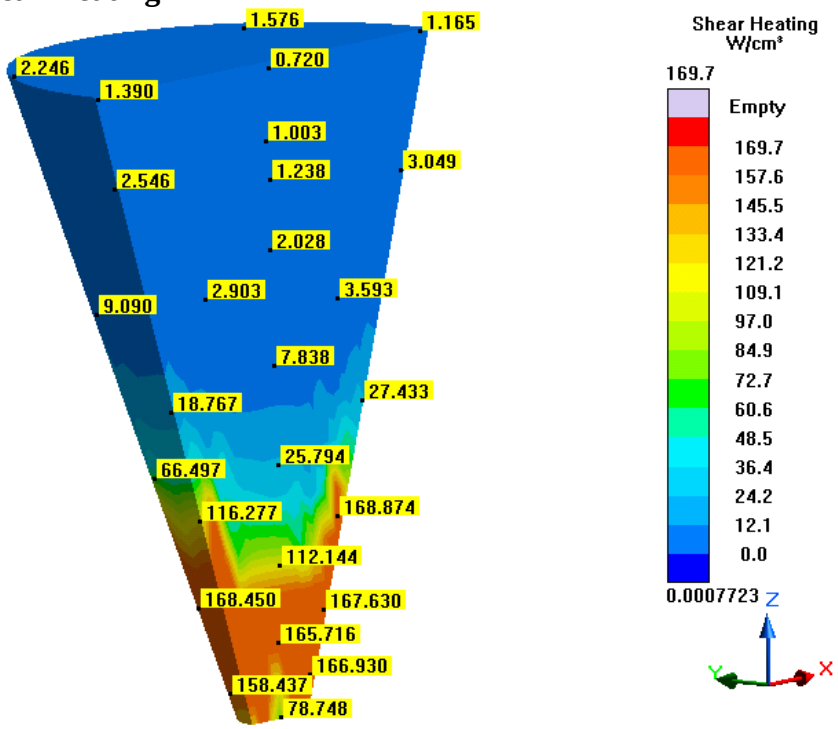

Figure 631- Simulation 4 (375 Microns), Shear Heating

Shear Rate

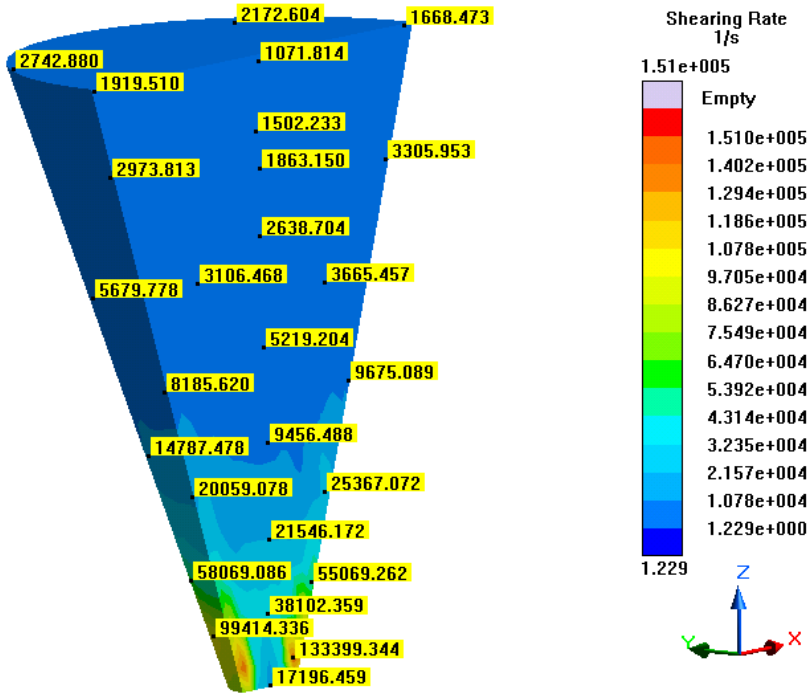

Figure 632- Simulation 4 (375 Microns), Shear Rate

Shear Stress

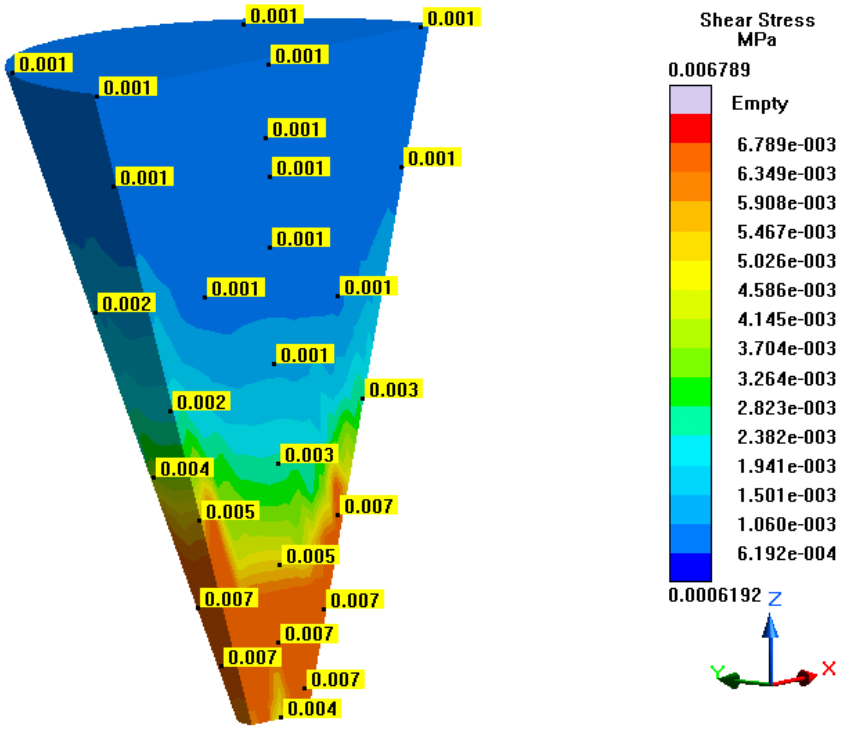

Figure 633- Simulation 4 (375 Microns), Shear Stress

Temperature

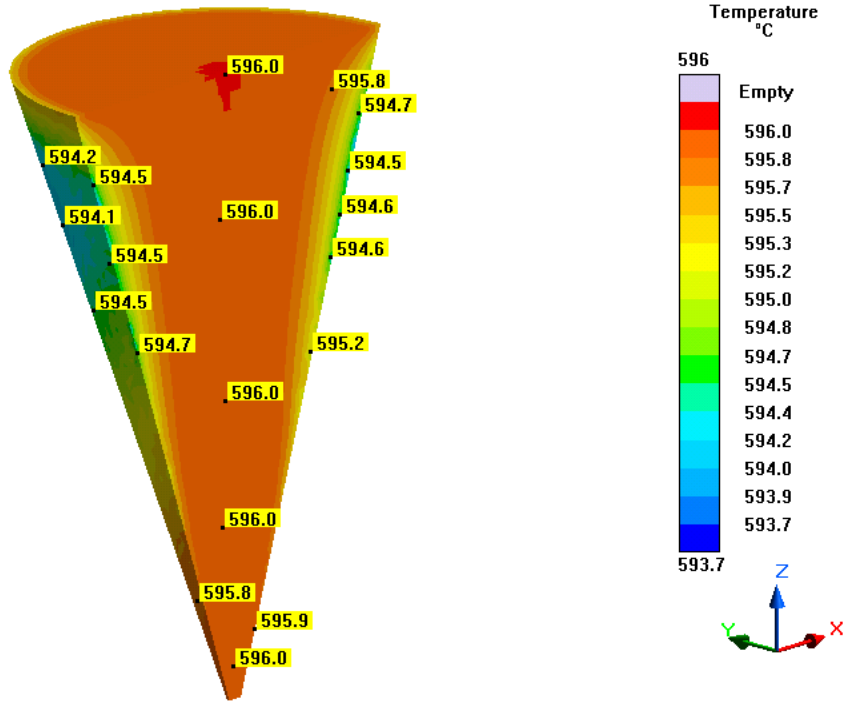

Figure 634- Simulation 4 (375 Microns), Temperature

Simulation 5- 500 Microns (Longer)

Parameters

Geometry	
Inlet Diameter	10 mm
Outlet Diameter	0.5 mm (500 microns)
Nozzle Height	18.75 mm
Nozzle Angle	75.784°
Tank Diameter	10 mm
Tank Height	5 mm

Mesh Parameters	
Accuracy (Refinement Factor)	5
Minimum Wall Thickness	0.5 mm
Minimum Element Size	0.1 mm
Smoothing	2
Ratio	2
Coarsening Loops	1
Minimal Accuracy After Coarsening	5

Mesh Properties	
Control Volumes (X Direction)	238
Control Volumes (Y Direction)	224
Control Volumes (Z Direction)	238
Composed Part Cells	44,219
Total Part Cells	175,245
Blocked Cells	0

Process Definitions	
Material Temperature	596 C
Fraction Solid	44%
Close Mold Time	0 s
Fill Time	0.25 s
Hold Time After Filling	1 s

Table 107- Simulation 5 (500 Microns, Longer), Parameters

Velocity

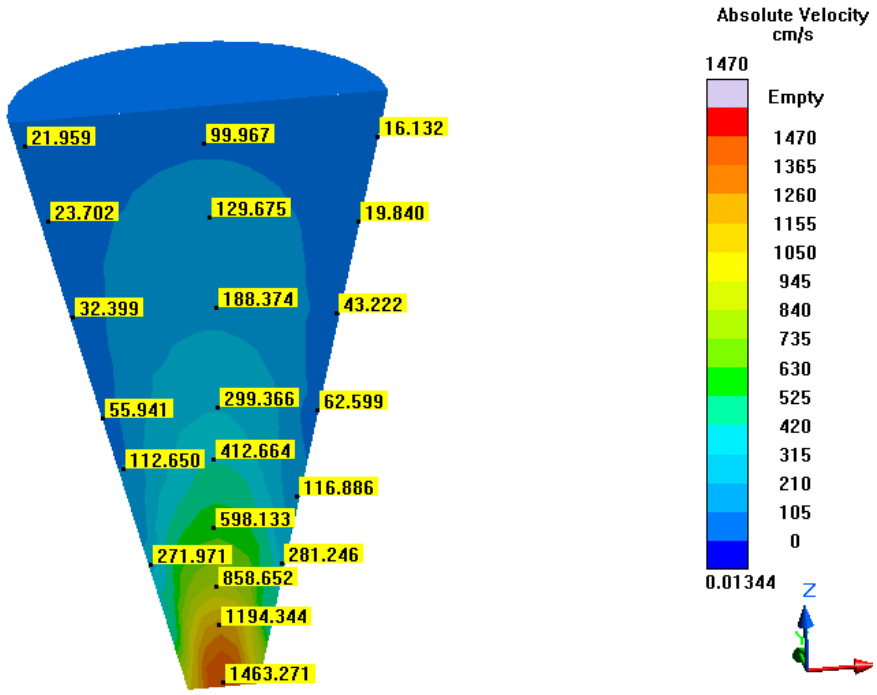

Figure 635- Simulation 5 (500 Microns, Longer), Velocity

Viscosity

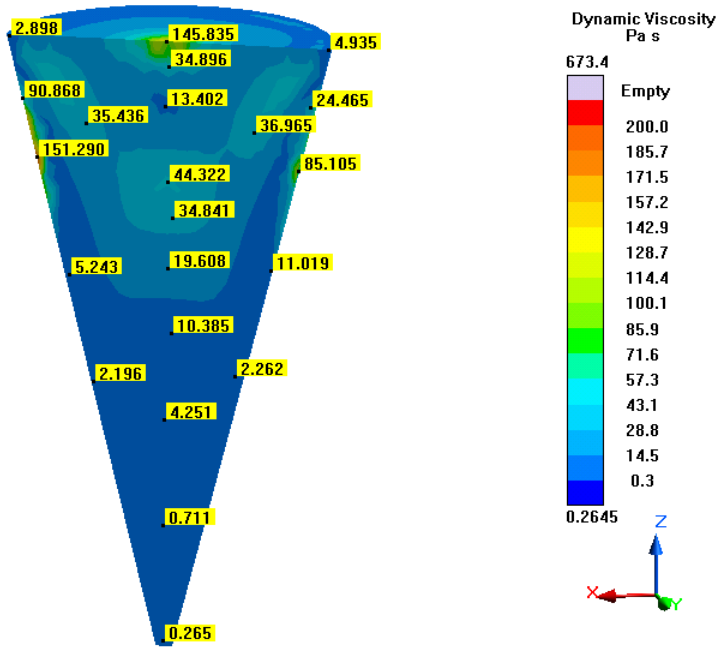

Figure 636- Simulation 5 (500 Microns, Longer), Viscosity

Cooling Rate

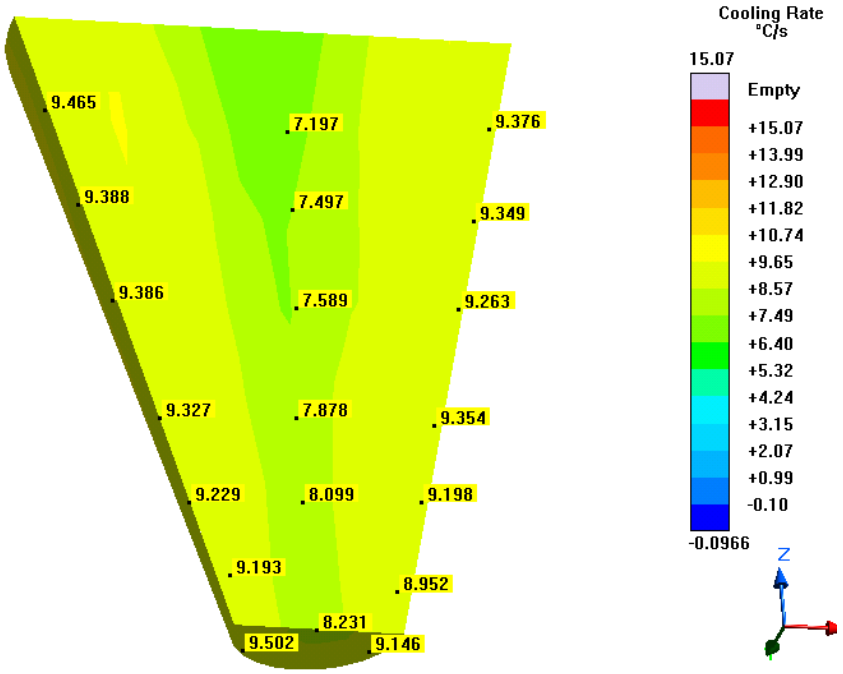

Figure 637- Simulation 5 (500 Microns, Longer), Cooling Rate

Pressure

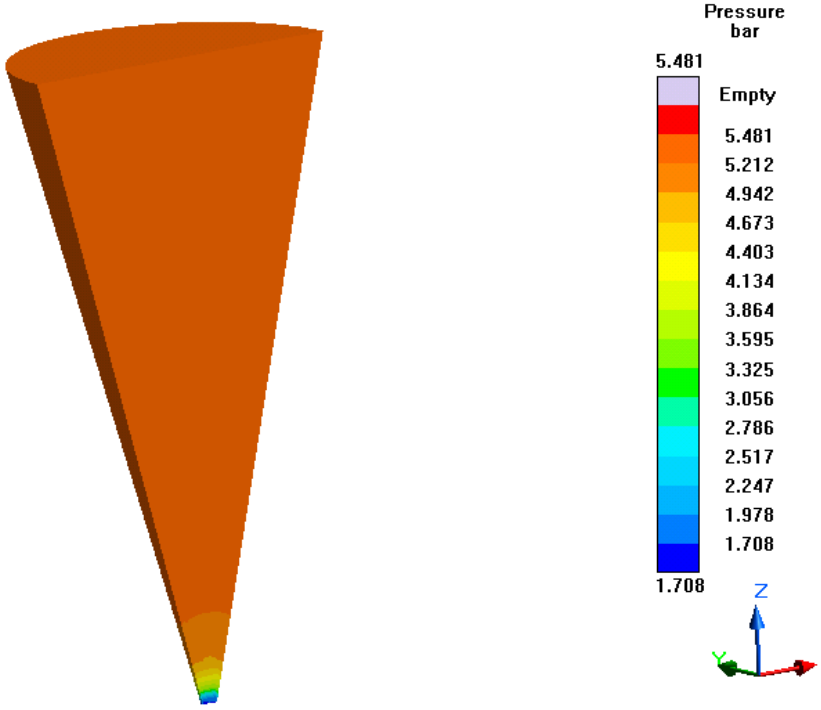

Figure 638- Simulation 5 (500 Microns, Longer), Pressure

Shear Heating

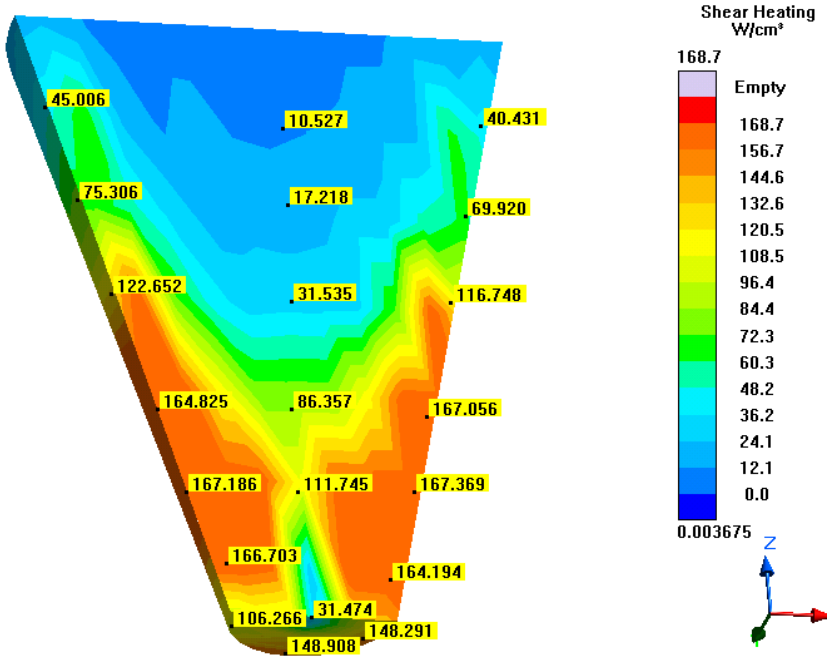

Figure 639- Simulation 5 (500 Microns, Longer), Shear Heating

Shear Rate

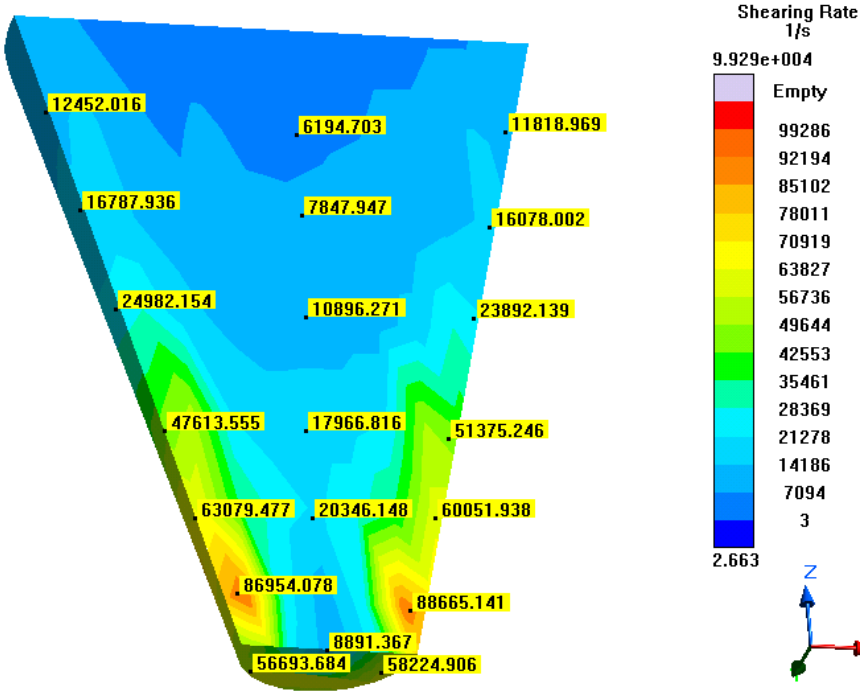

Figure 640- Simulation 5 (500 Microns, Longer), Shear Rate

Shear Stress

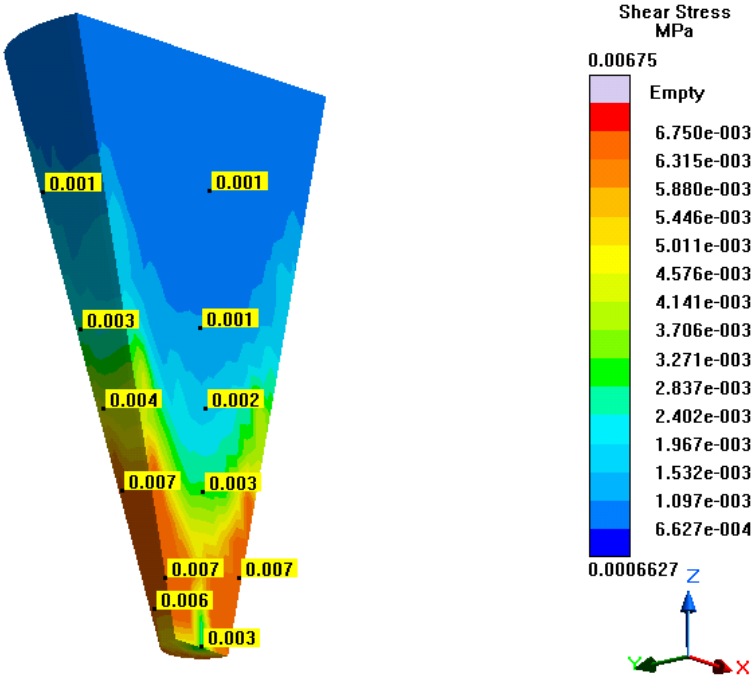

Figure 641- Simulation 5 (500 Microns, Longer), Shear Stress

Temperature

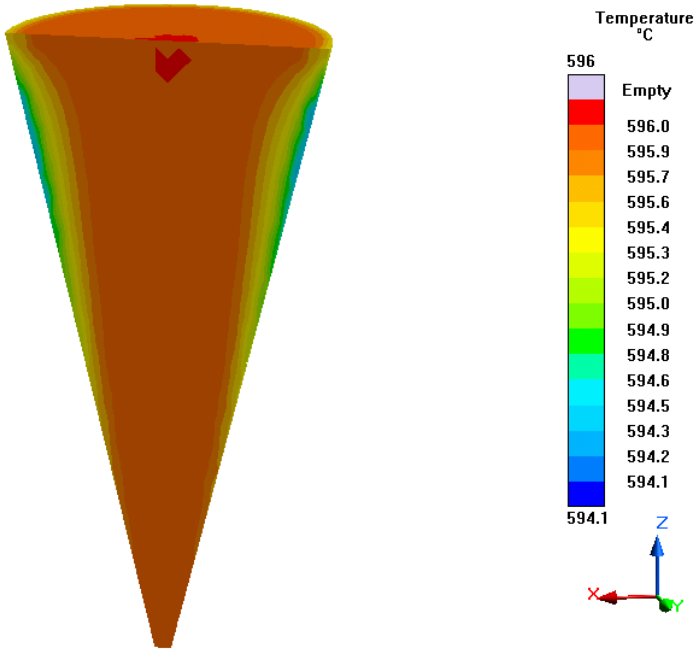

Figure 642- Simulation 5 (500 Microns, Longer), Temperature

Simulation 6- 500 Microns (Shorter)

Parameters

Geometry	
Inlet Diameter	10 mm
Outlet Diameter	0.500 mm (500 microns)
Nozzle Height	11.25 mm
Nozzle Angle	67.109°
Tank Diameter	10 mm
Tank Height	5 mm

Mesh Parameters	
Accuracy (Refinement Factor)	5
Minimum Wall Thickness	0.5 mm
Minimum Element Size	0.1 mm
Smoothing	2
Ratio	2
Coarsening Loops	1
Minimal Accuracy After Coarsening	5

Mesh Properties	
Control Volumes (X Direction)	182
Control Volumes (Y Direction)	182
Control Volumes (Z Direction)	192
Composed Part Cells	37,866
Total Part Cells	158,821
Blocked Cells	0

Process Definitions	
Material Temperature	596 C
Fraction Solid	44%
Close Mold Time	0 s
Fill Time	0.25 s
Hold Time After Filling	1 s

Table 108- Simulation 6 (500 Microns, Shorter), Parameters

Velocity

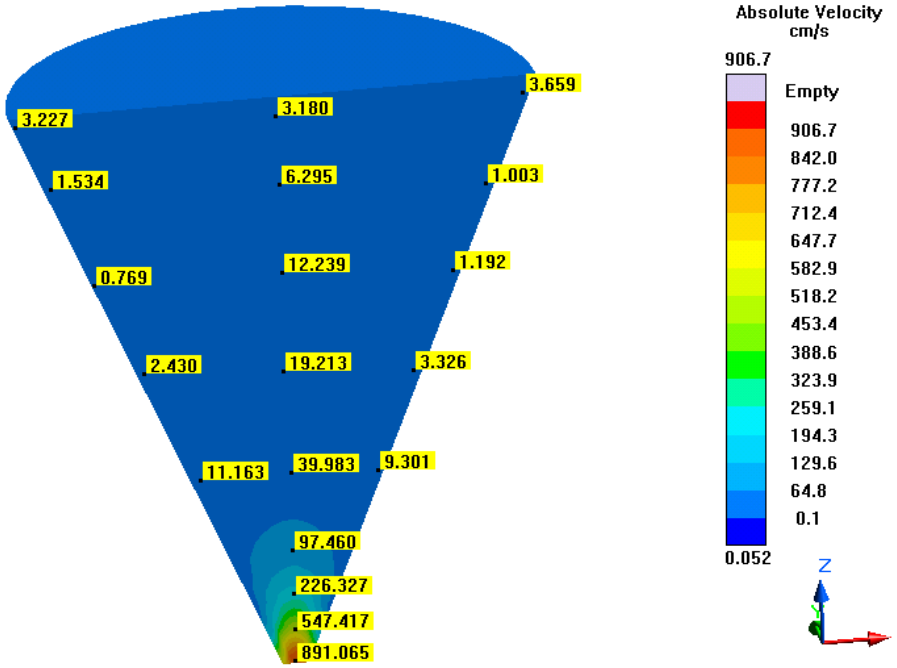

Figure 643- Simulation 6 (500 Microns, Shorter), Velocity

Viscosity

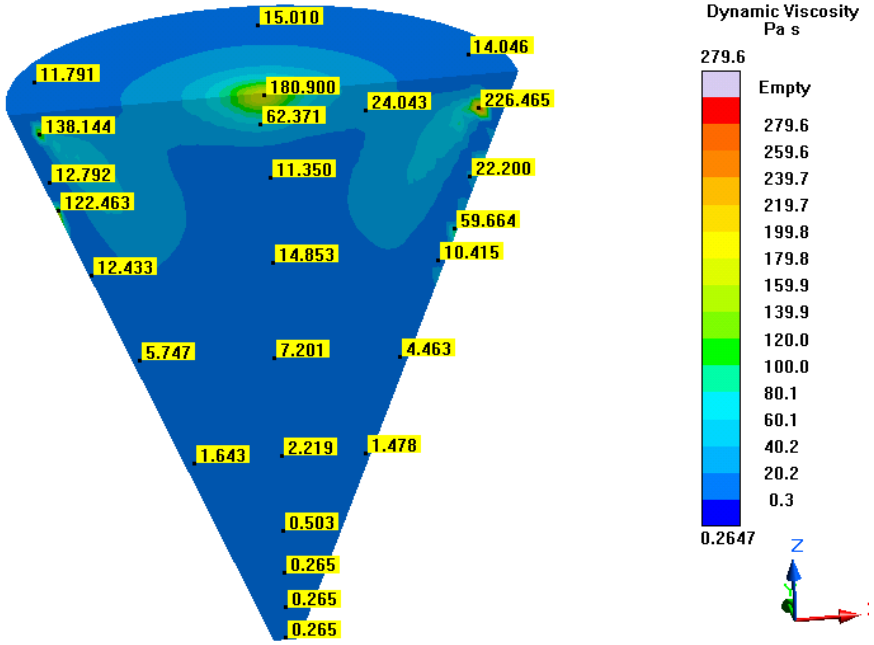

Figure 644- Simulation 6 (500 Microns, Shorter), Viscosity

Cooling Rate

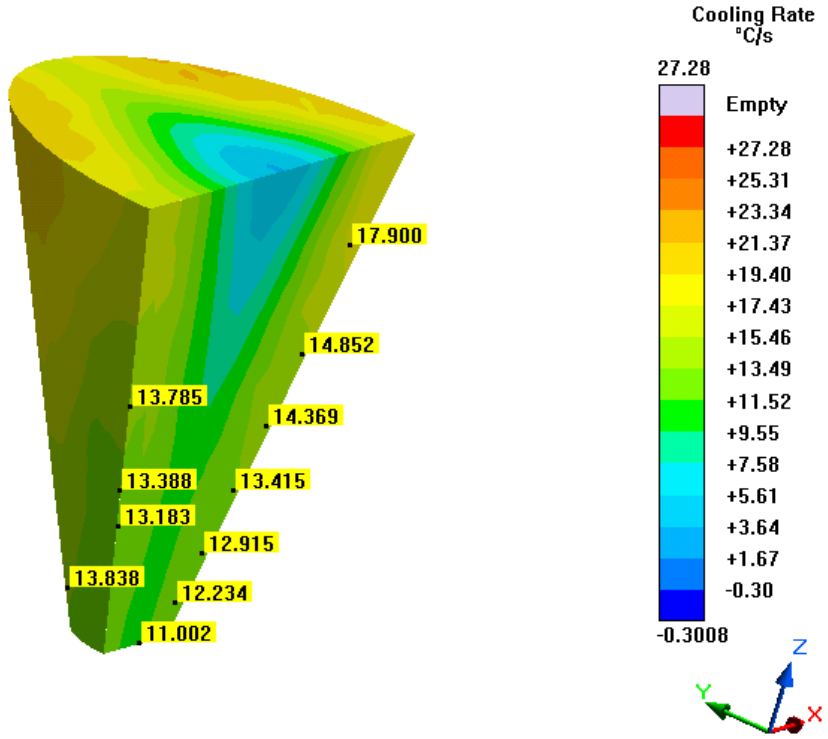

Figure 645- Simulation 6 (500 Microns, Shorter), Cooling Rate

Pressure

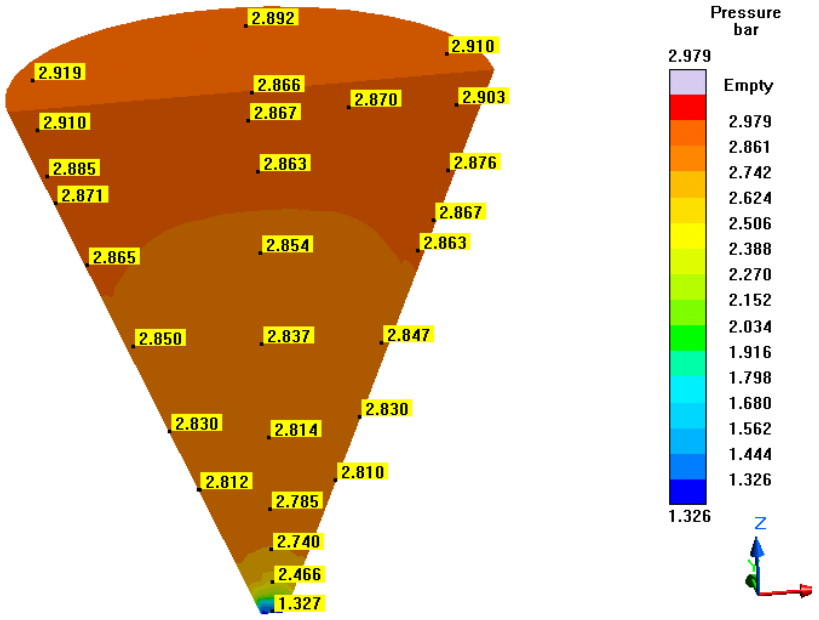

Figure 646- Simulation 6 (500 Microns, Shorter), Pressure

Shear Heating

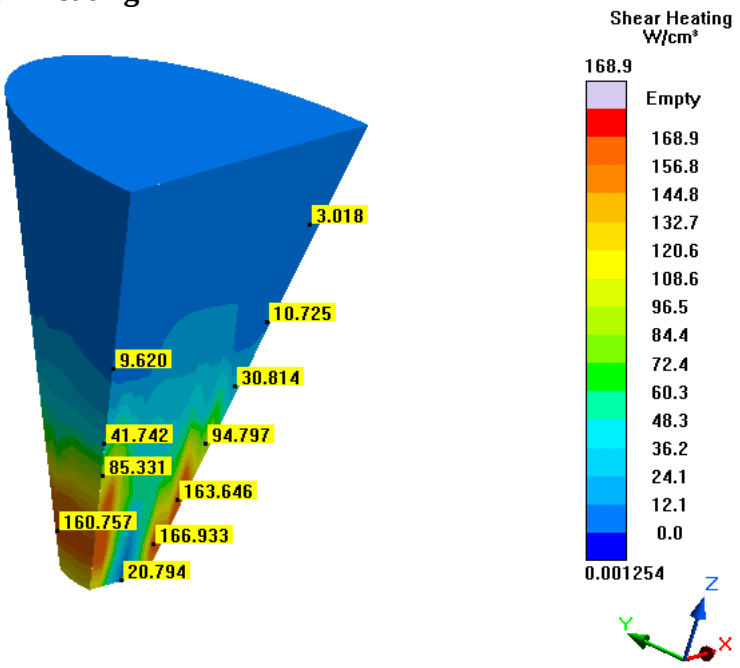

Figure 647- Simulation 6 (500 Microns, Shorter), Shear Heating

Shear Rate

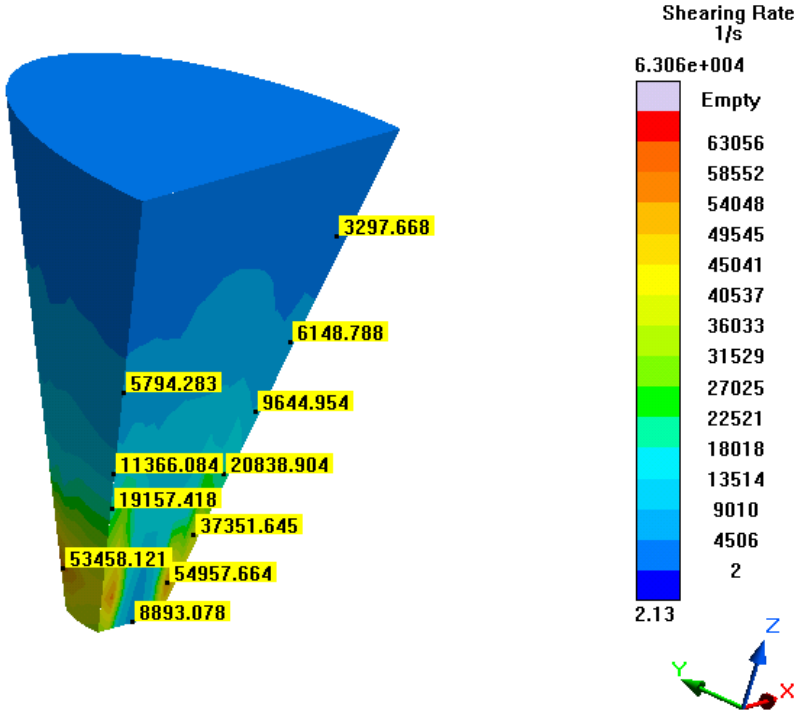

Figure 648- Simulation 6 (500 Microns, Shorter), Shear Rate

Shear Stress

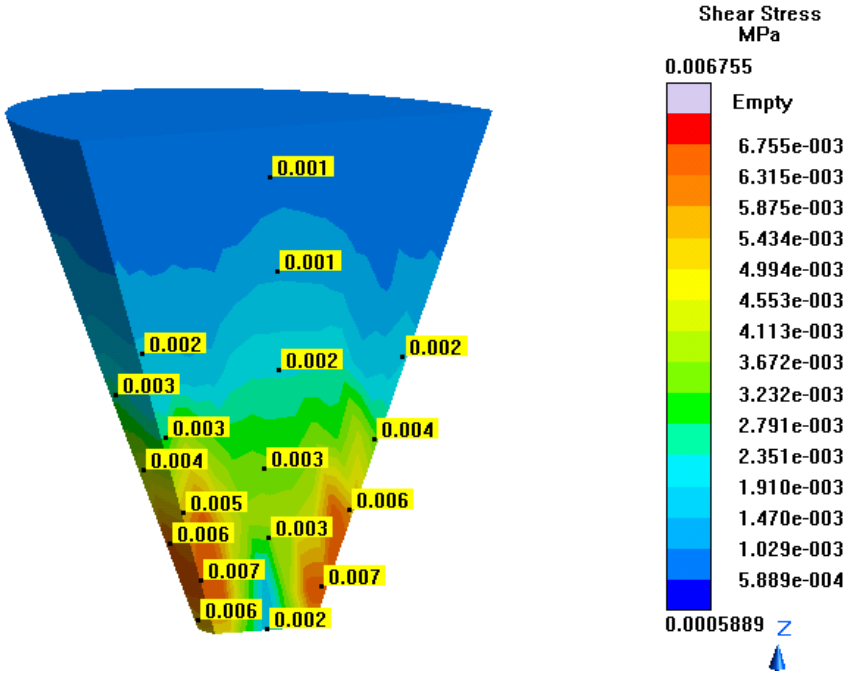

Figure 649- Simulation 6 (500 Microns, Shorter), Shear Stress

Temperature

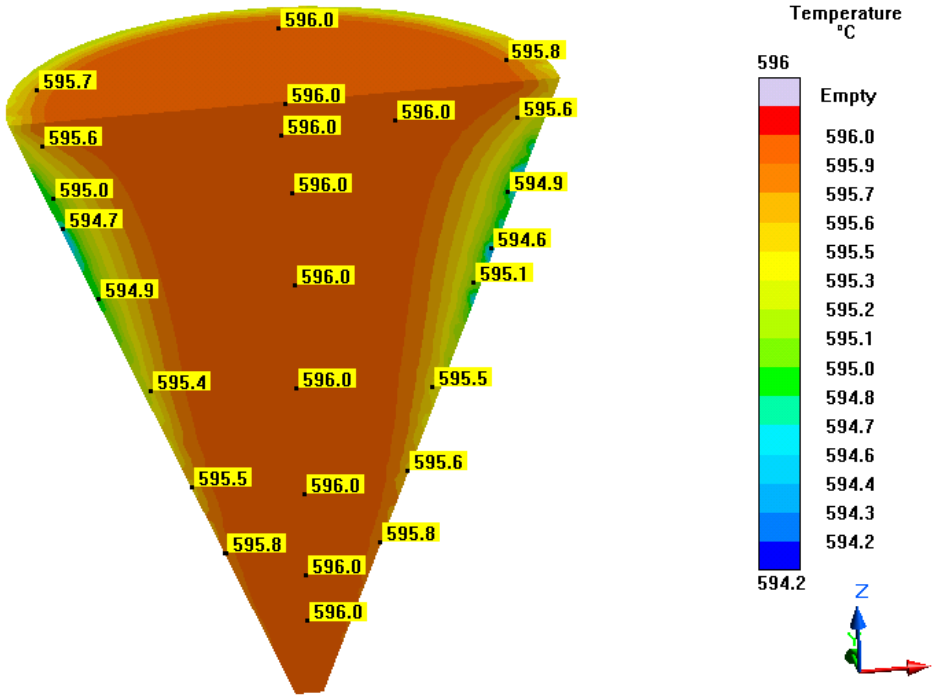

Figure 650- Simulation 6 (500 Microns, Shorter), Temperature

Simulation 7- 500 Microns (Smaller Inlet)

Parameters

Geometry	
Inlet Diameter	7.5 mm
Outlet Diameter	0.500 mm (500 microns)
Nozzle Height	15 mm
Nozzle Angle	76.866°
Tank Diameter	7.5 mm
Tank Height	5 mm

Mesh Parameters	
Accuracy (Refinement Factor)	5
Minimum Wall Thickness	0.5 mm
Minimum Element Size	0.1 mm
Smoothing	2
Ratio	2
Coarsening Loops	1
Minimal Accuracy After Coarsening	5

Mesh Properties	
Control Volumes (X Direction)	174
Control Volumes (Y Direction)	176
Control Volumes (Z Direction)	190
Composed Part Cells	27,835
Total Part Cells	102,413
Blocked Cells	0

Process Definitions	
Material Temperature	596 C
Fraction Solid	44%
Close Mold Time	0 s
Fill Time	0.25 s
Hold Time After Filling	1 s

Table 109- Simulation 7 (500 Microns, Smaller Inlet), Parameters

Velocity

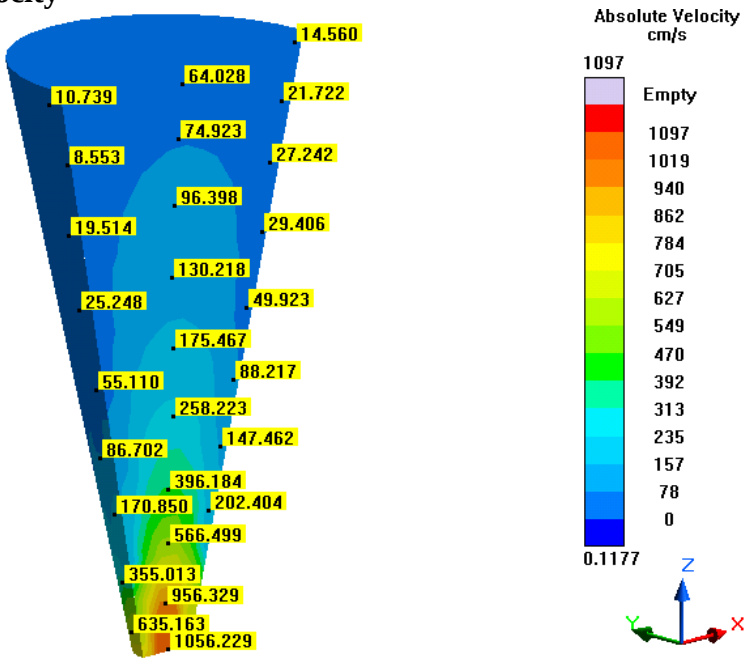

Figure 651- Simulation 7 (500 Microns, Smaller Inlet), Velocity

Viscosity

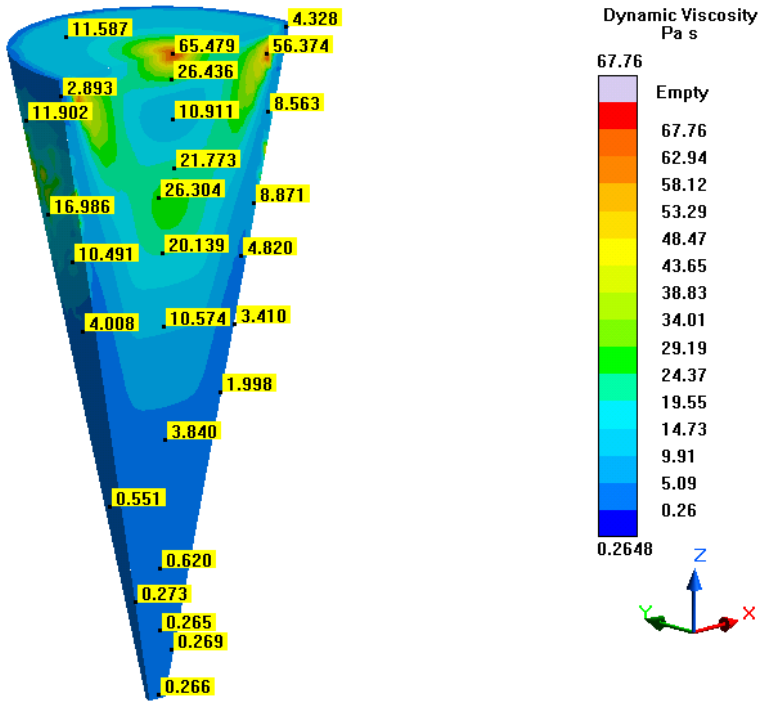

Figure 652- Simulation 7 (500 Microns, Smaller Inlet), Viscosity

Cooling Rate

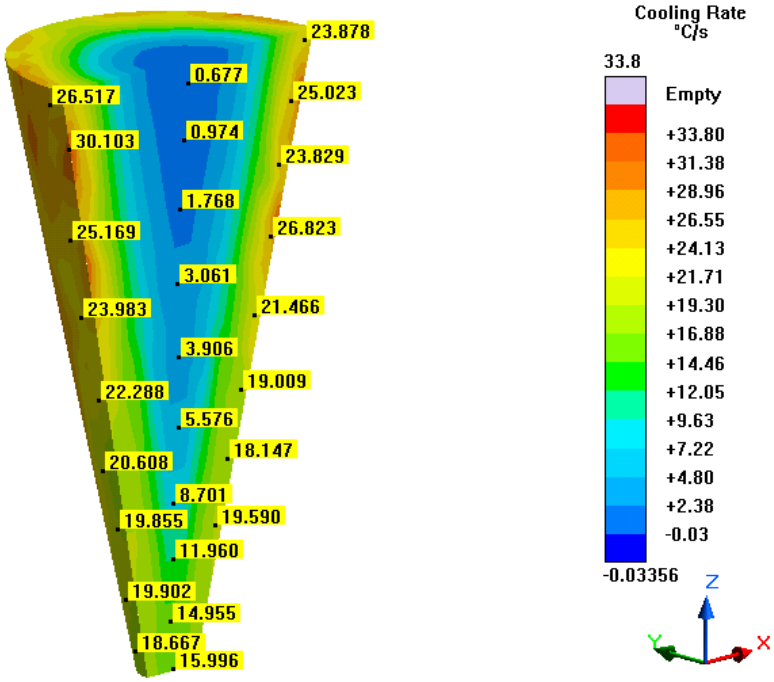

Figure 653- Simulation 7 (500 Microns, Smaller Inlet), Cooling Rate

Pressure

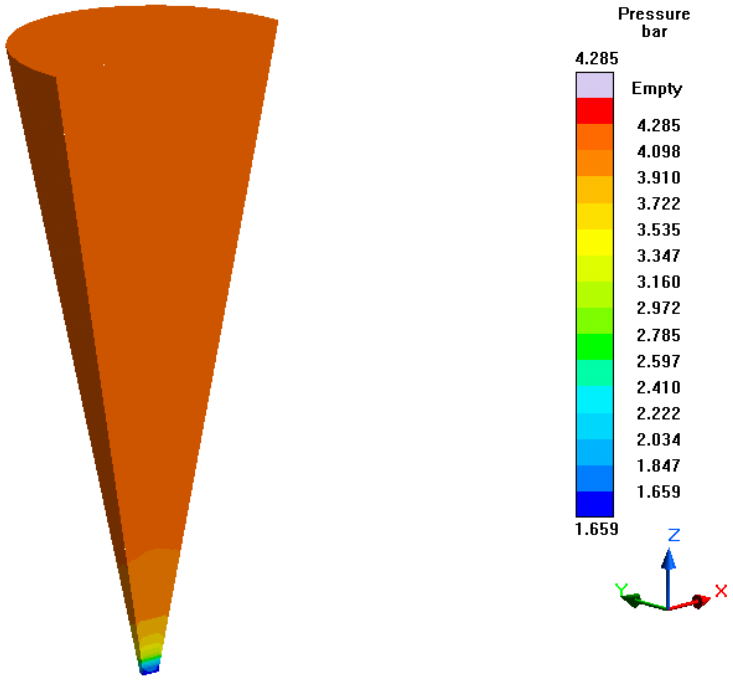

Figure 654- Simulation 7 (500 Microns, Smaller Inlet), Pressure

Shear Heating

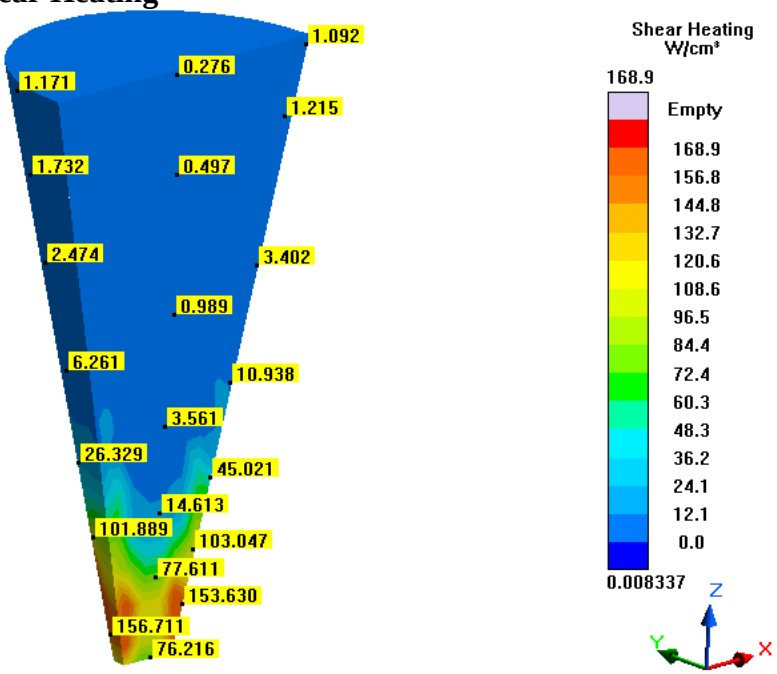

Figure 655- Simulation 7 (500 Microns, Smaller Inlet), Shear Heating

Shear Rate

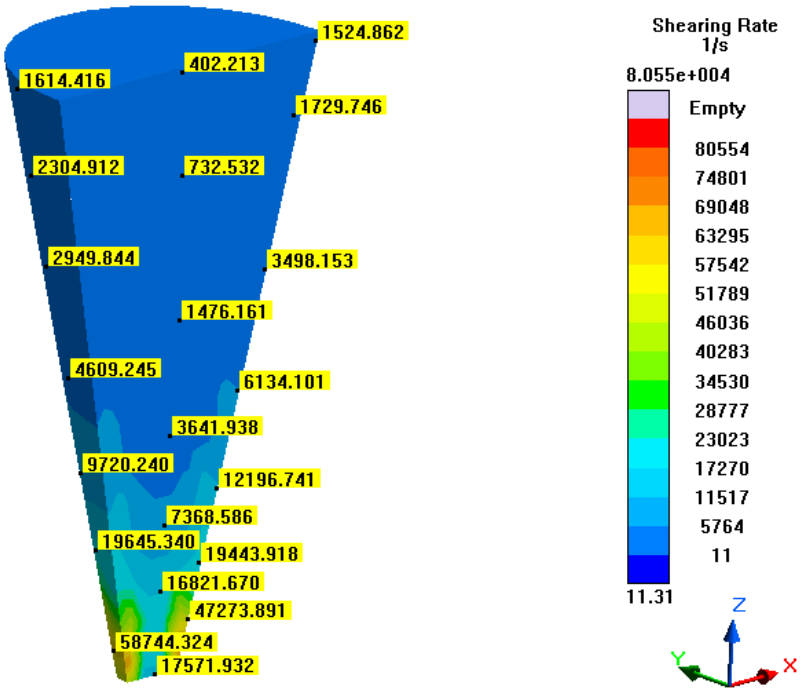

Figure 656- Simulation 7 (500 Microns, Smaller Inlet), Shear Rate

Shear Stress

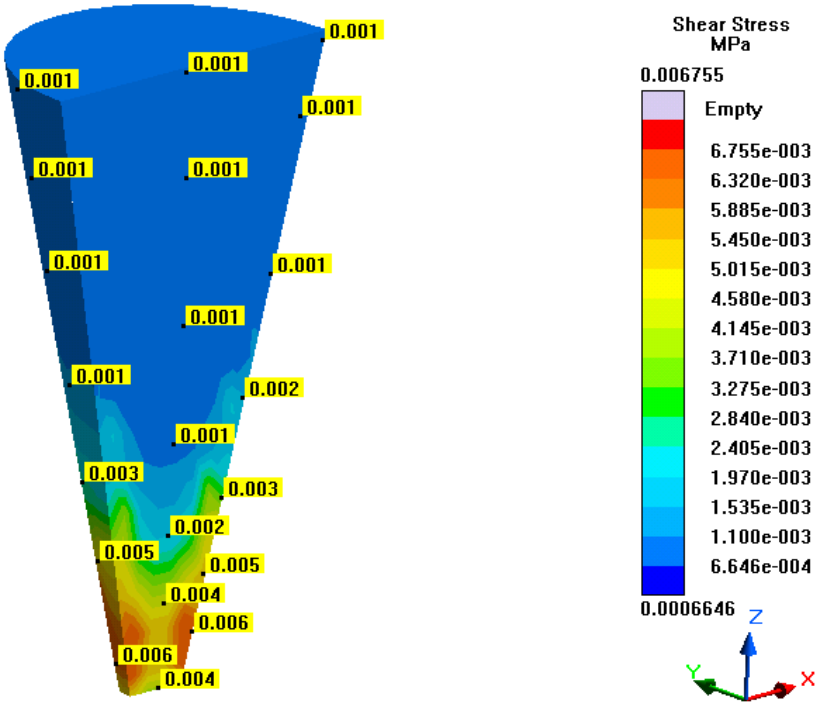

Figure 657- Simulation 7 (500 Microns, Smaller Inlet), Shear Stress

Temperature

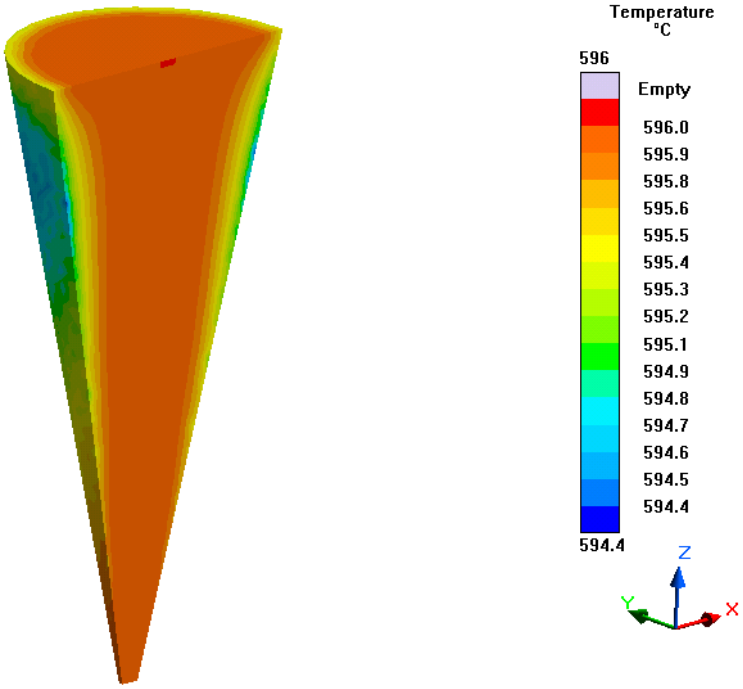

Figure 658- Simulation 7 (500 Microns, Smaller Inlet), Temperature

Simulation 8- 625 Microns

Parameters

Geometry	
Inlet Diameter	10 mm
Outlet Diameter	0.625 mm (625 microns)
Nozzle Height	15 mm
Nozzle Angle	77.957°
Tank Diameter	10 mm
Tank Height	5 mm

Mesh Parameters	
Accuracy (Refinement Factor)	5
Minimum Wall Thickness	0.625 mm
Minimum Element Size	0.125 mm
Smoothing	2
Ratio	2
Coarsening Loops	1
Minimal Accuracy After Coarsening	5

Mesh Properties	
Control Volumes (X Direction)	136
Control Volumes (Y Direction)	150
Control Volumes (Z Direction)	154
Composed Part Cells	18,863
Total Part Cells	72,651
Blocked Cells	0

Process Definitions	
Material Temperature	596 C
Fraction Solid	44%
Close Mold Time	0 s
Fill Time	0.25 s
Hold Time After Filling	1 s

Table 110- Simulation 8 (625 Microns), Parameters

Velocity

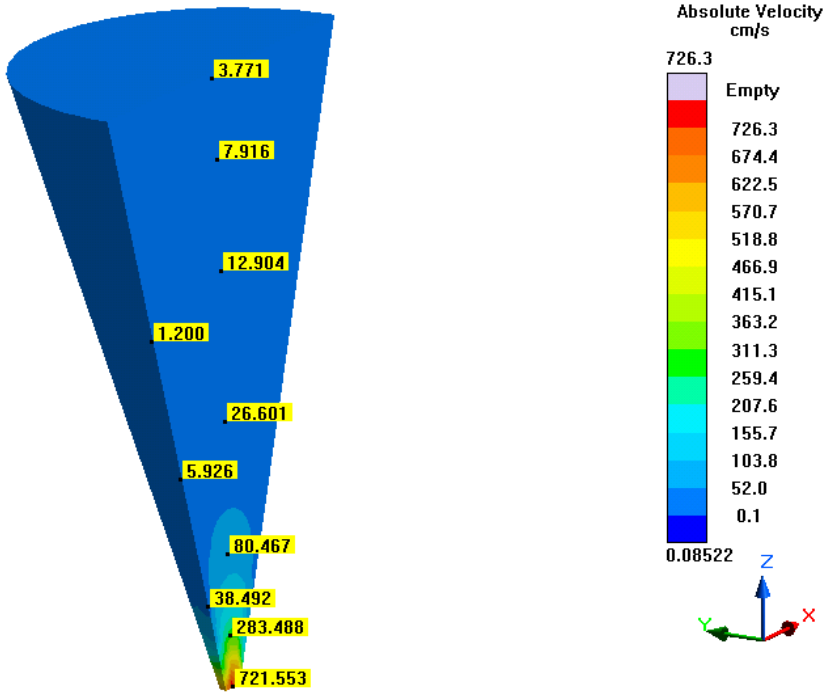

Figure 659- Simulation 8 (625 Microns), Velocity

Viscosity

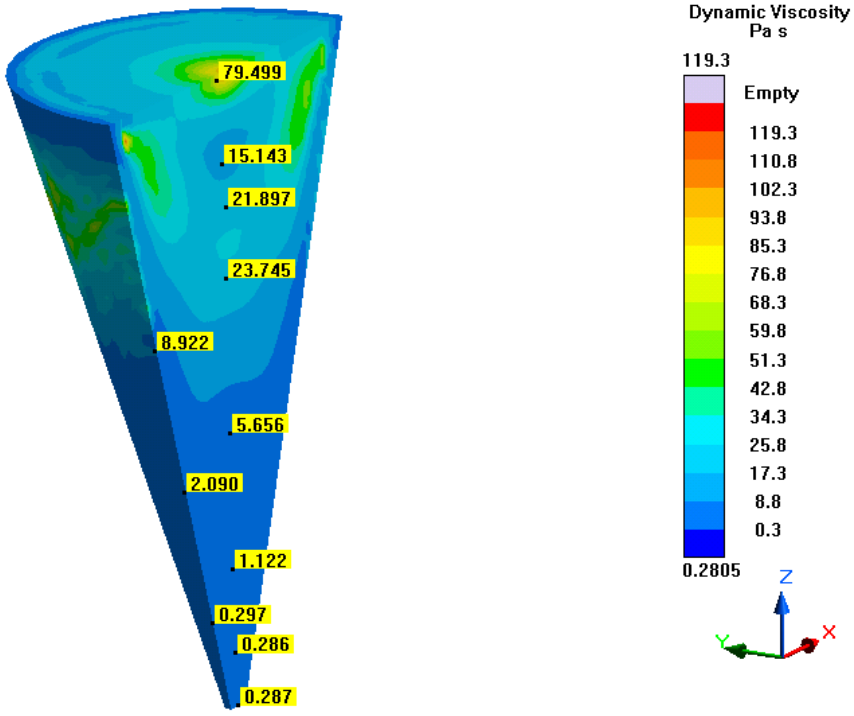

Figure 660- Simulation 8 (625 Microns), Viscosity

Cooling Rate

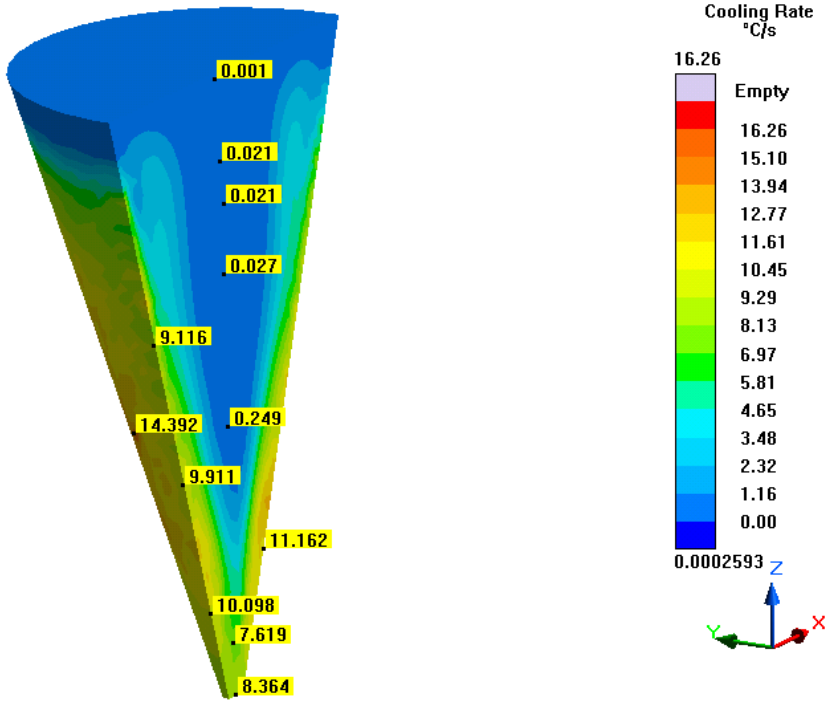

Figure 661- Simulation 8 (625 Microns), Cooling Rate

Pressure

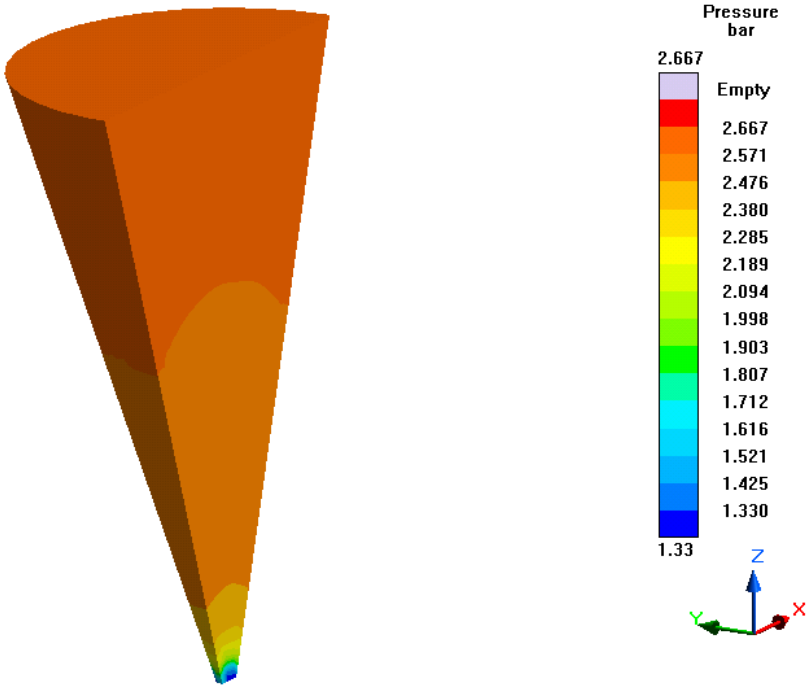

Figure 662- Simulation 8 (625 Microns), Pressure

Shear Heating

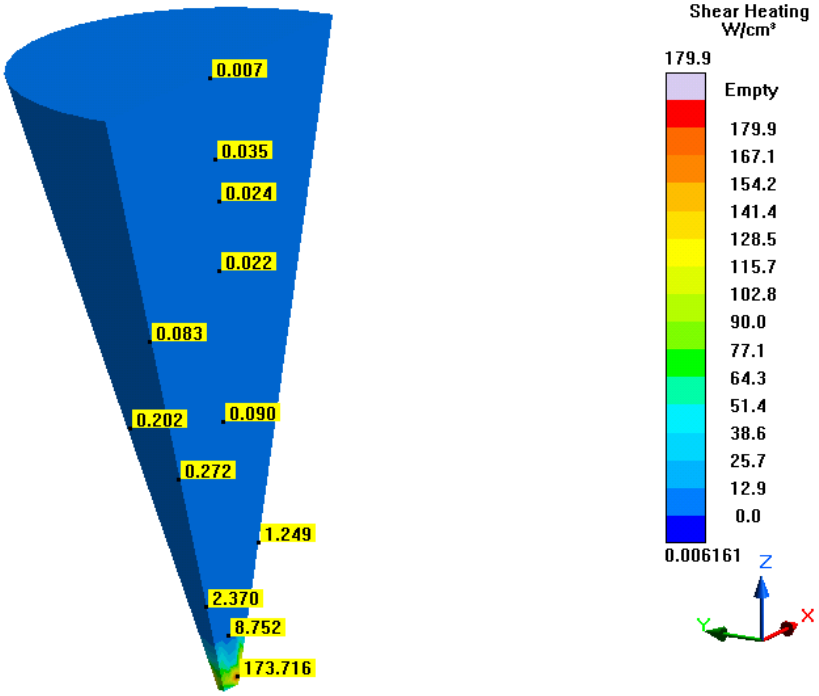

Figure 663- Simulation 8 (625 Microns), Shear Heating

Shear Rate

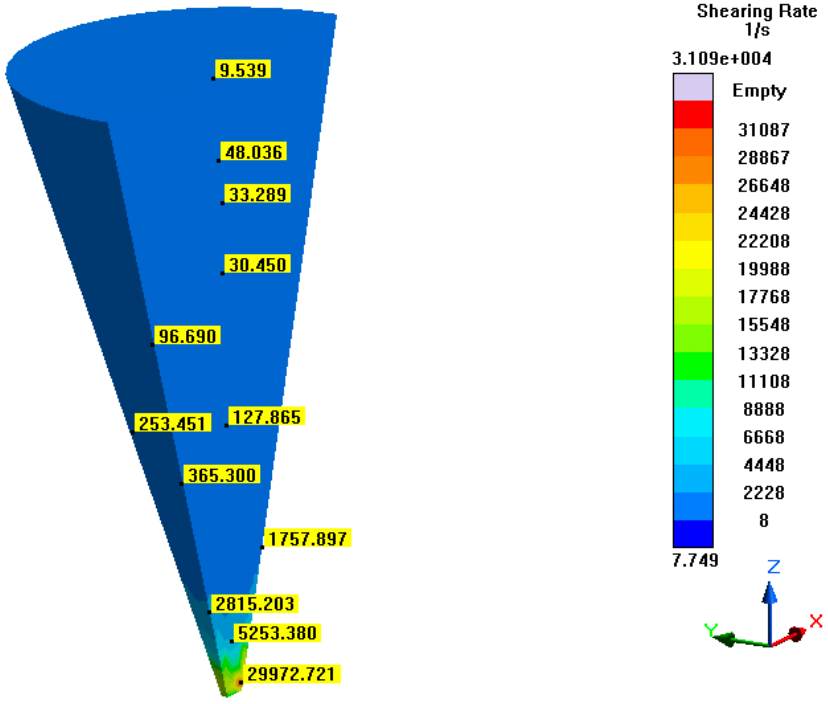

Figure 664- Simulation 8 (625 Microns), Shear Rate

Shear Stress

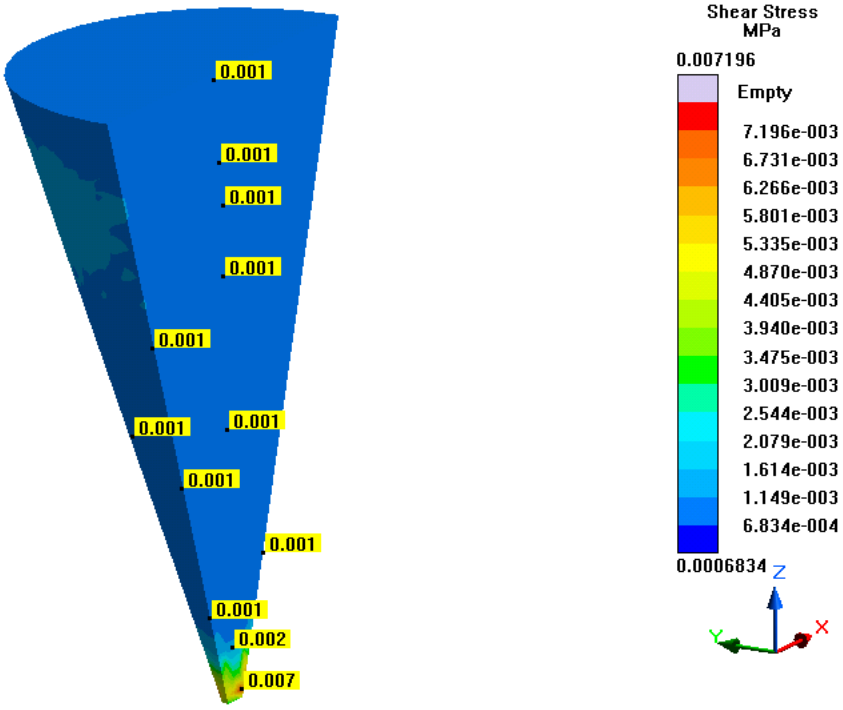

Figure 665- Simulation 8 (625 Microns), Shear Stress

Temperature

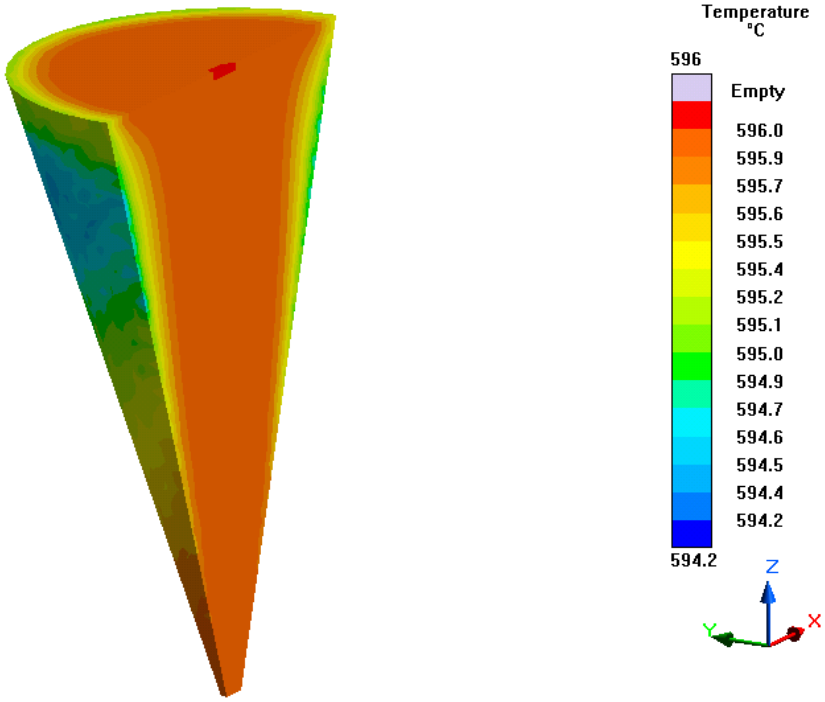

Figure 666- Simulation 8 (625 Microns), Temperature

Simulation 9- 500 Microns (Larger Inlet)

Parameters

Geometry	
Inlet Diameter	15 mm
Outlet Diameter	0.500 mm (500 microns)
Nozzle Height	15 mm
Nozzle Angle	64.204°
Tank Diameter	10 mm
Tank Height	5 mm

Mesh Parameters	
Accuracy (Refinement Factor)	5
Minimum Wall Thickness	0.500 mm
Minimum Element Size	0.100 mm
Smoothing	2
Ratio	2
Coarsening Loops	1
Minimal Accuracy After Coarsening	5

Mesh Properties	
Control Volumes (X Direction)	238
Control Volumes (Y Direction)	224
Control Volumes (Z Direction)	238
Composed Part Cells	44,219
Total Part Cells	175,245
Blocked Cells	0

Process Definitions	
Material Temperature	596 C
Fraction Solid	44%
Close Mold Time	0 s
Fill Time	0.25 s
Hold Time After Filling	1 s

Table 111- Simulation 9 (500 Microns, Larger Inlet), Parameters

Velocity

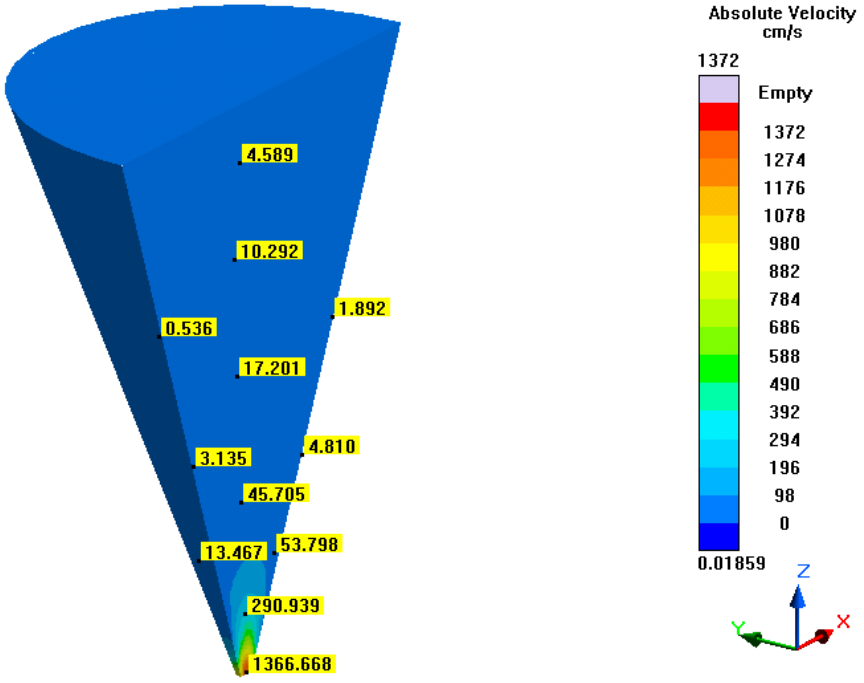

Figure 667- Simulation 9 (500 Microns, Larger Inlet), Velocity

Viscosity

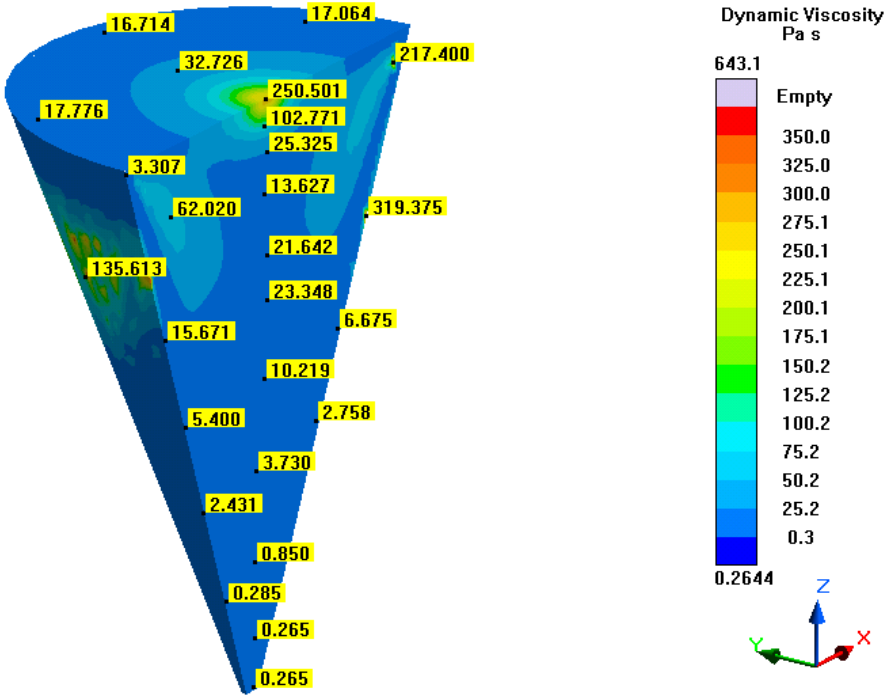

Figure 668- Simulation 9 (500 Microns, Larger Inlet), Viscosity

Cooling Rate

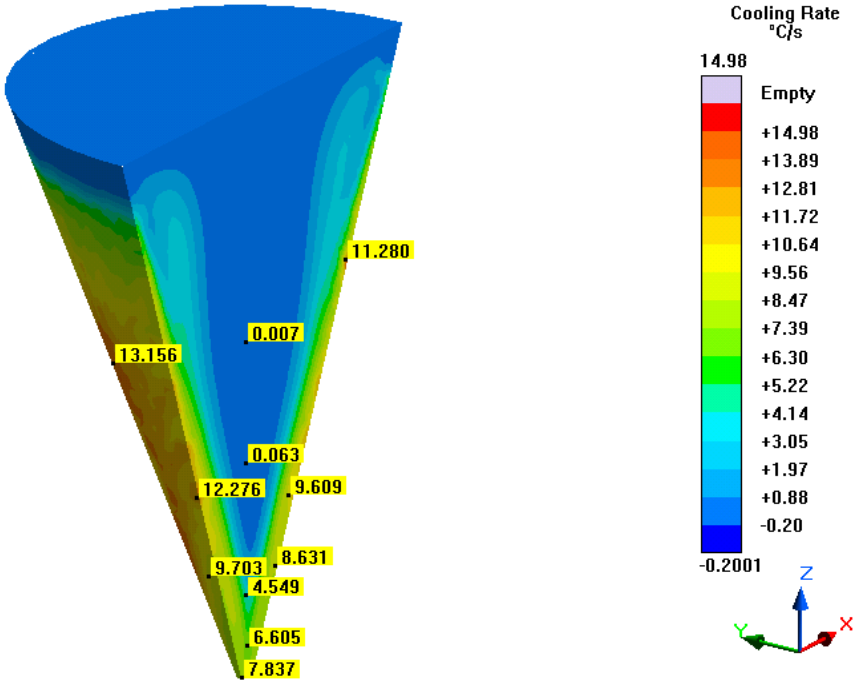

Figure 669- Simulation 9 (500 Microns, Larger Inlet), Cooling Rate

Pressure

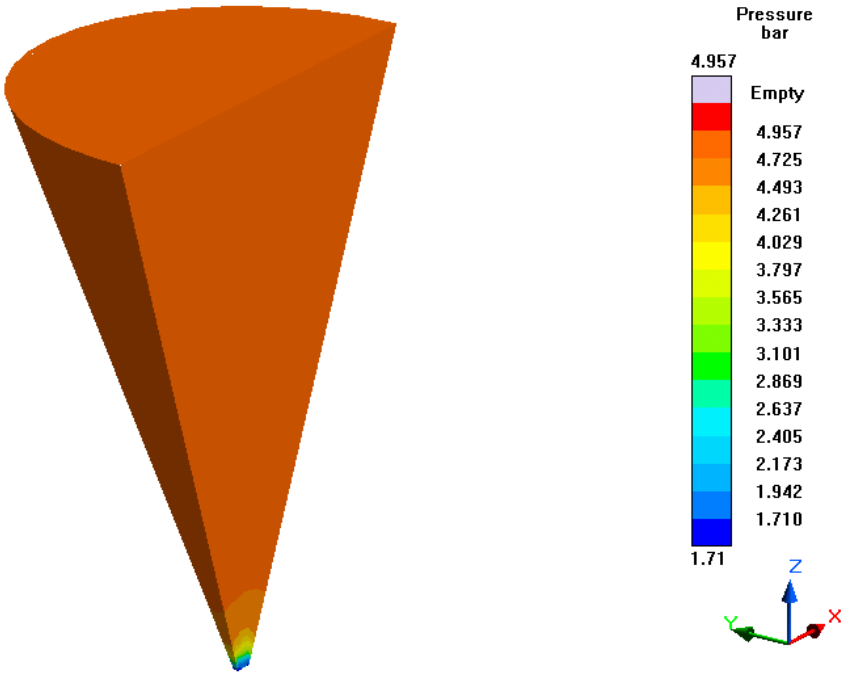

Figure 670- Simulation 9 (500 Microns, Larger Inlet), Pressure

Shear Heating

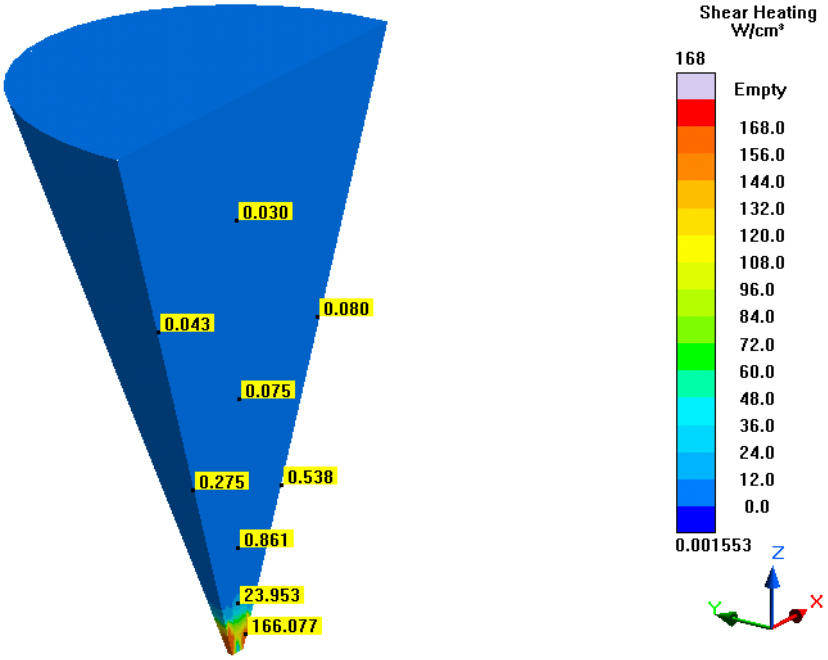

Figure 671- Simulation 9 (500 Microns, Larger Inlet), Shear Heating

Shear Rate

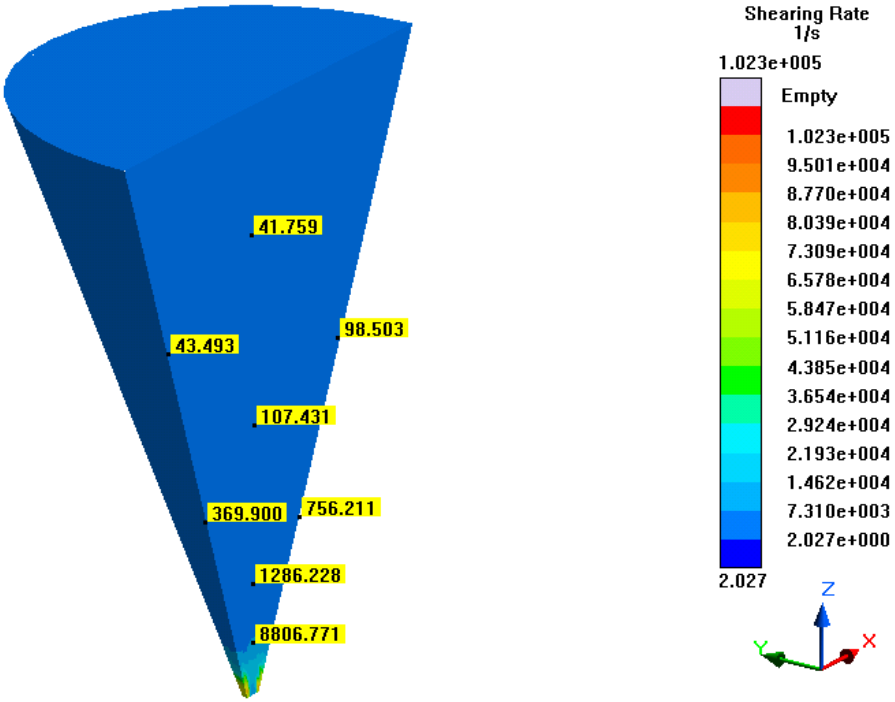

Figure 672- Simulation 9 (500 Microns, Larger Inlet), Shear Rate

Shear Stress

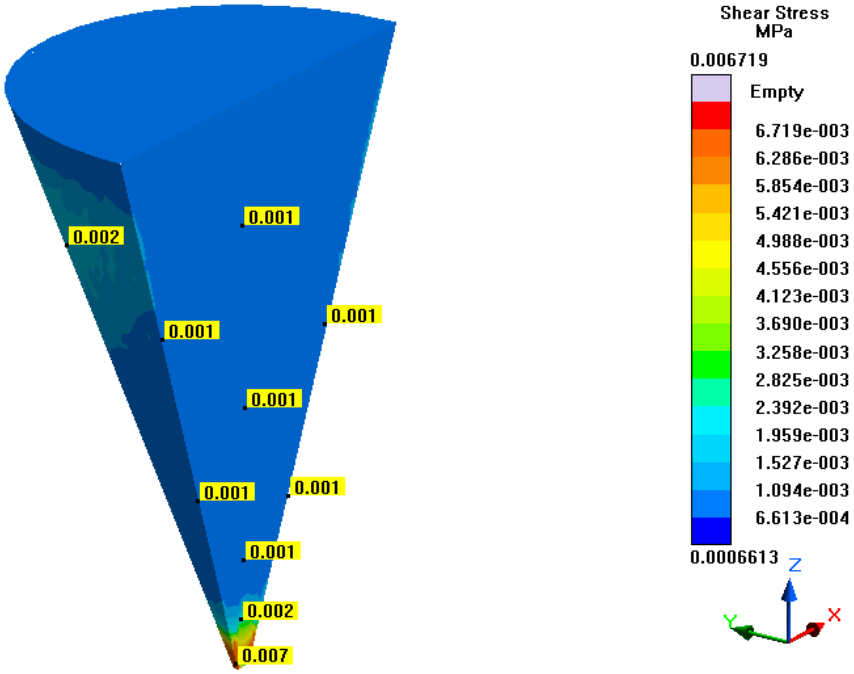

Figure 673- Simulation 9 (500 Microns, Larger Inlet), Shear Stress

Temperature

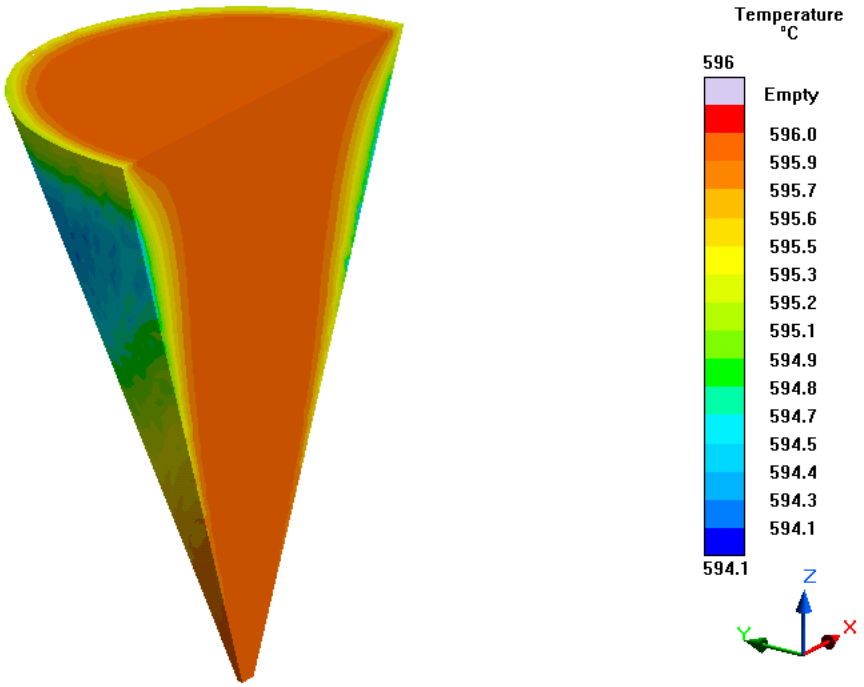

Figure 674- Simulation 9 (500 Microns, Larger Inlet), Temperature

Simulation 10- Cylindrical Nozzle

Parameters

Geometry	
Inlet Diameter	0.5 mm (500 microns)
Outlet Diameter	0.5 mm (500 microns)
Nozzle Height	7.5 mm
Nozzle Angle	90°
Conic Runner Inlet	0.5 mm (500 microns)
Conic Runner Outlet	10 mm
Conic Runner Height	15 mm
Tank Diameter	10 mm
Tank Height	5 mm

Mesh Parameters	
Accuracy (Refinement Factor)	5
Minimum Wall Thickness	0.5 mm
Minimum Element Size	0.1 mm
Smoothing	2
Ratio	2
Coarsening Loops	1
Minimal Accuracy After Coarsening	5

Mesh Properties	
Control Volumes (X Direction)	192
Control Volumes (Y Direction)	192
Control Volumes (Z Direction)	206
Composed Part Cells	39,562
Total Part Cells	155,137
Blocked Cells	0

Process Definitions	
Material Temperature	596 C
Fraction Solid	44%
Close Mold Time	0 s
Fill Time	0.25 s
Hold Time After Filling	1 s

Table 112- Simulation 10 (Cylindrical Nozzle), Parameters

Velocity

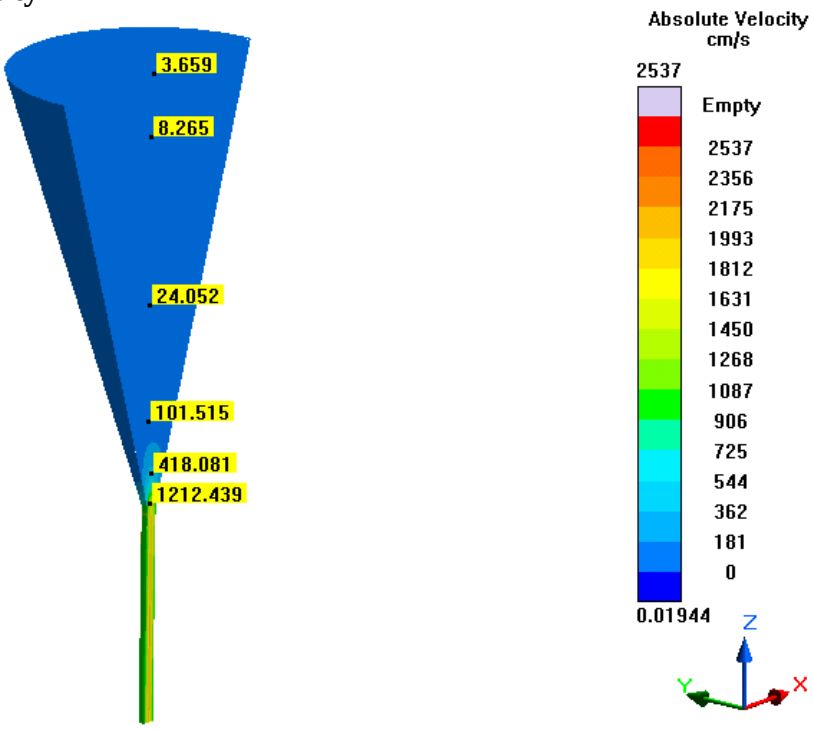

Figure 675- Simulation 10 (Cylindrical Nozzle), Velocity

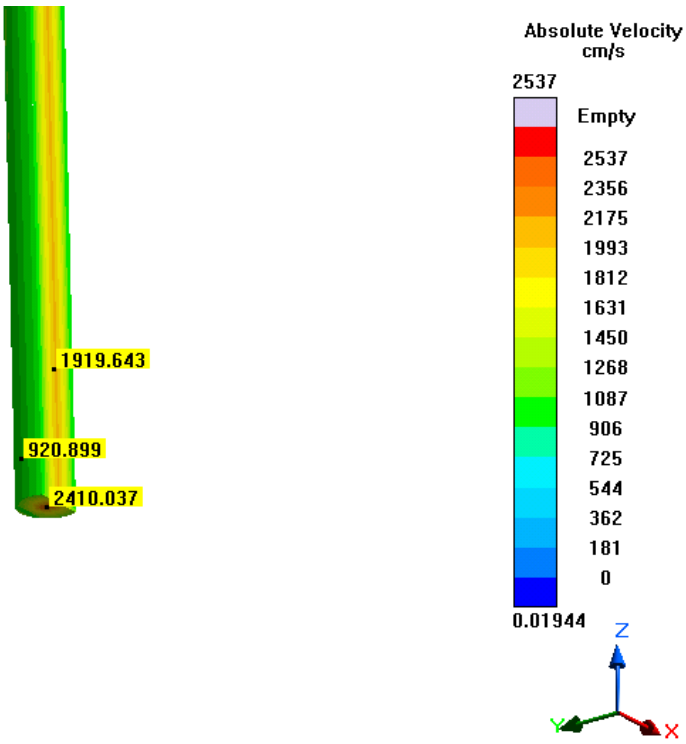

Figure 676- Simulation 10 (Cylindrical Nozzle), Tip Velocity

Viscosity

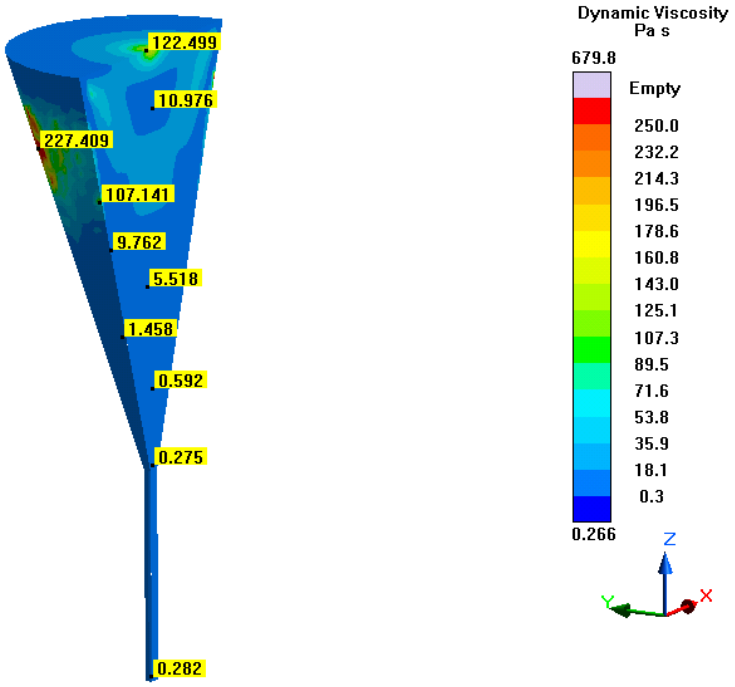

Figure 677- Simulation 10 (Cylindrical Nozzle), Viscosity

Cooling Rate

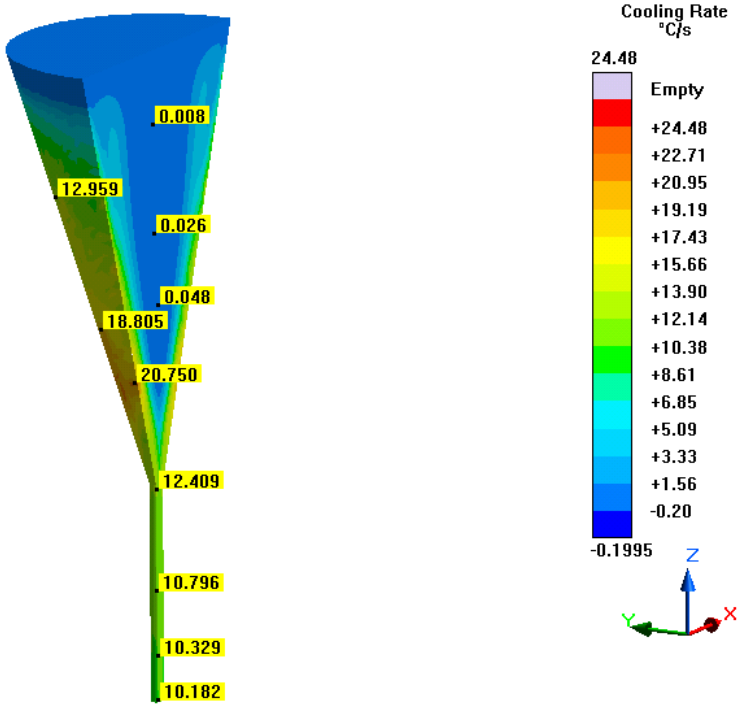

Figure 678- Simulation 10 (Cylindrical Nozzle), Cooling Rate

Pressure

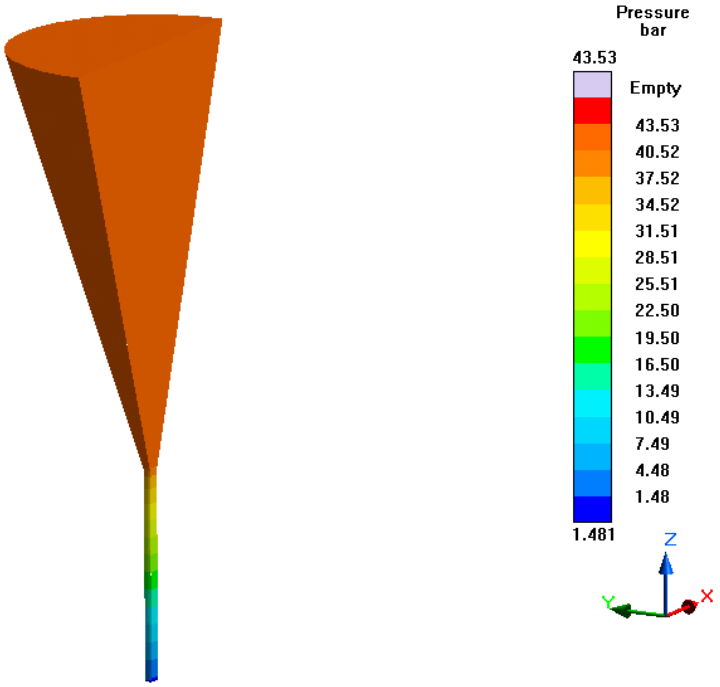

Figure 679- Simulation 10 (Cylindrical Nozzle), Pressure

Shear Heating

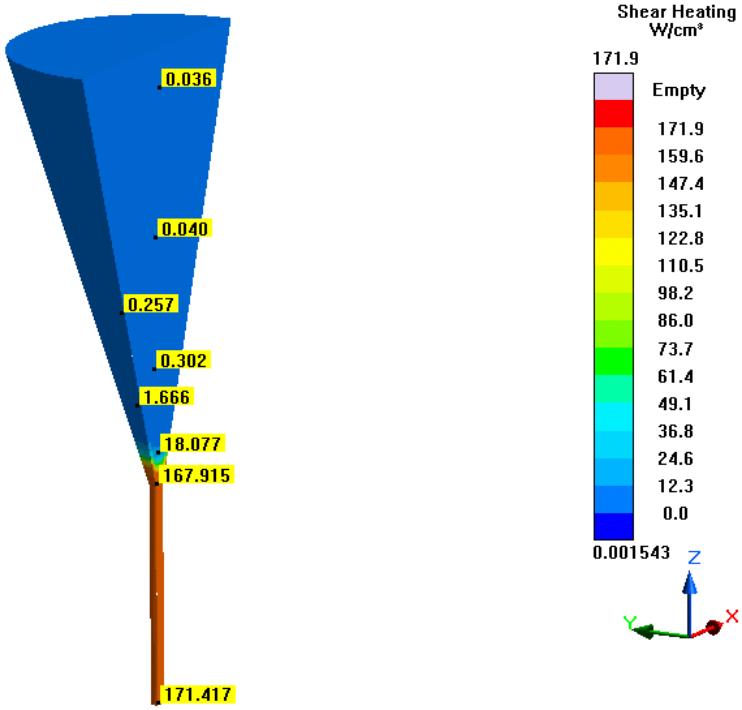

Figure 680- Simulation 10 (Cylindrical Nozzle), Shear Heating

Shear Rate

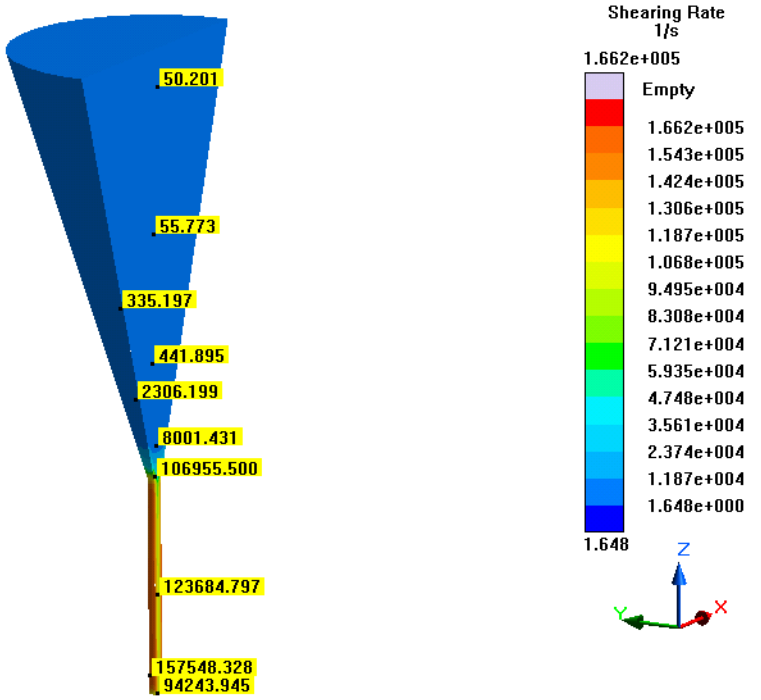

Figure 681- Simulation 10 (Cylindrical Nozzle), Shear Rate

Shear Stress

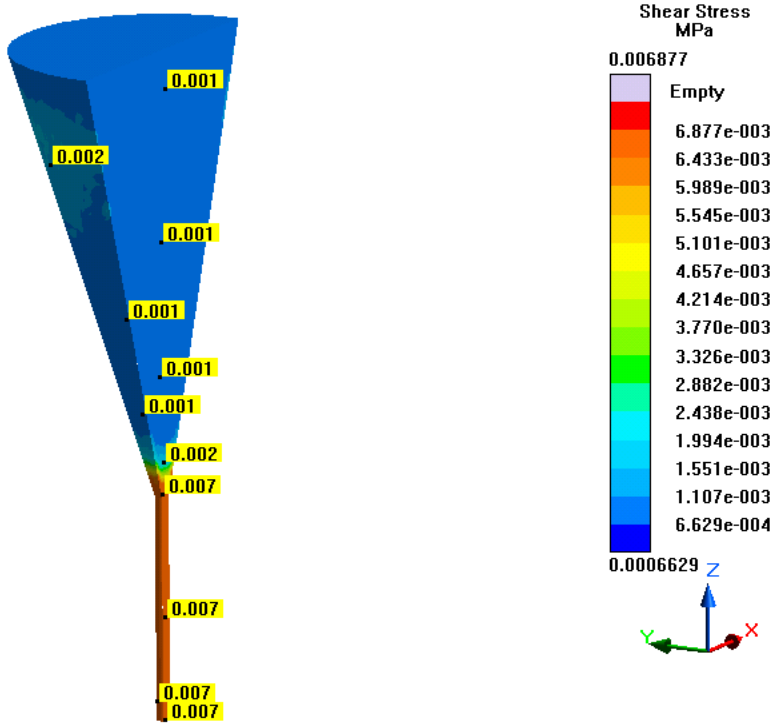

Figure 682- Simulation 10 (Cylindrical Nozzle), Shear Stress

Temperature

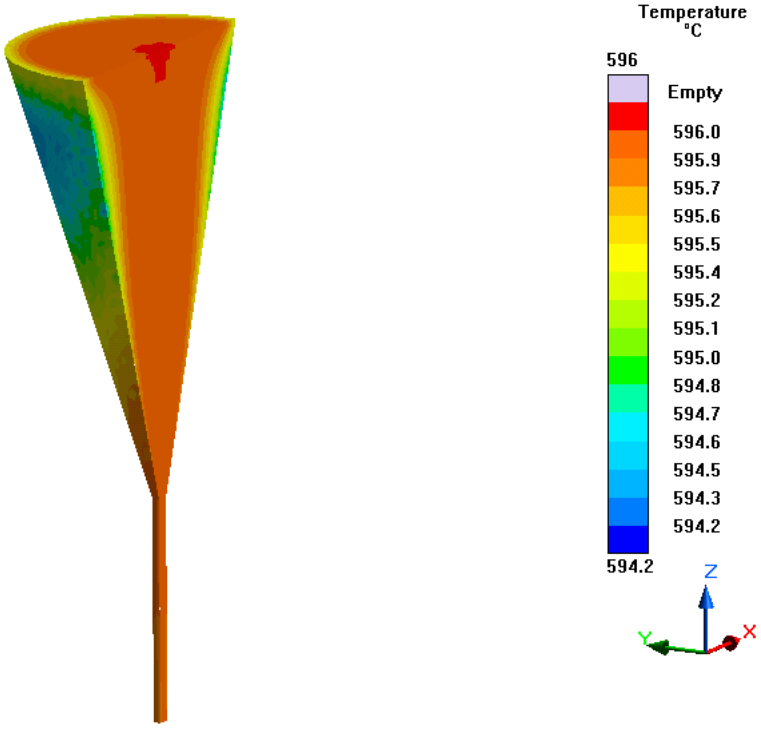

Figure 683- Simulation 10 (Cylindrical Nozzle), Temperature

Simulation 11- Cylindrical Nozzle (Faster)

Parameters

Geometry	
Inlet Diameter	0.5 mm (500 microns)
Outlet Diameter	0.5 mm (500 microns)
Nozzle Height	7.5 mm
Nozzle Angle	90°
Conic Runner Inlet	0.5 mm (500 microns)
Conic Runner Outlet	10 mm
Conic Runner Height	15 mm
Tank Diameter	10 mm
Tank Height	5 mm

Mesh Parameters	
Accuracy (Refinement Factor)	5
Minimum Wall Thickness	0.5 mm
Minimum Element Size	0.1 mm
Smoothing	2
Ratio	2
Coarsening Loops	1
Minimal Accuracy After Coarsening	5

Mesh Properties	
Control Volumes (X Direction)	192
Control Volumes (Y Direction)	192
Control Volumes (Z Direction)	206
Composed Part Cells	39,562
Total Part Cells	155,137
Blocked Cells	0

Process Definitions	
Material Temperature	596 C
Fraction Solid	44%
Close Mold Time	0 s
Fill Time	0.188 s
Hold Time After Filling	1 s

Table 113- Simulation 11 (Cylindrical Nozzle, Faster), Parameters

Velocity

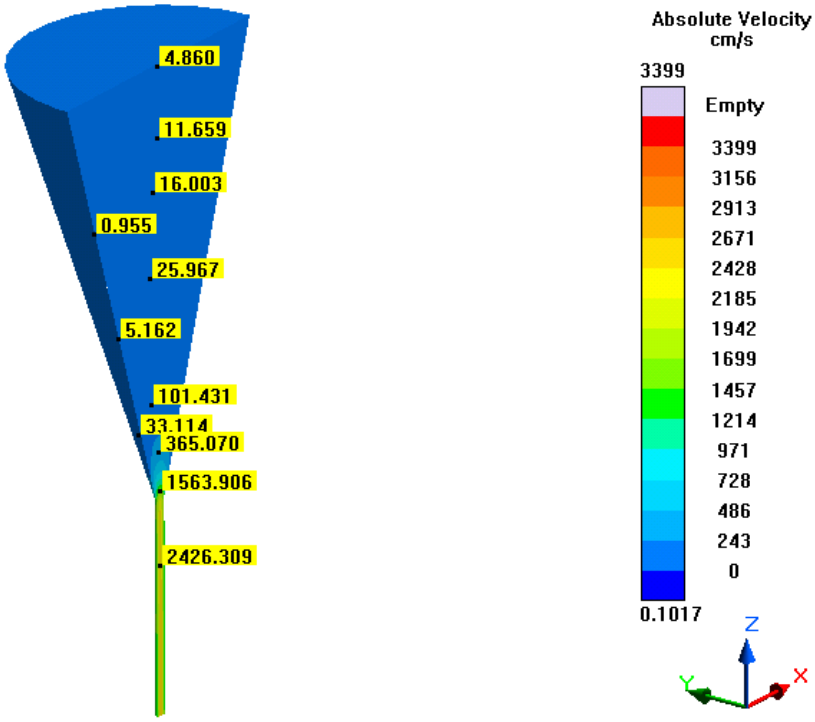

Figure 684- Simulation 11 (Cylindrical Nozzle, Faster), Velocity

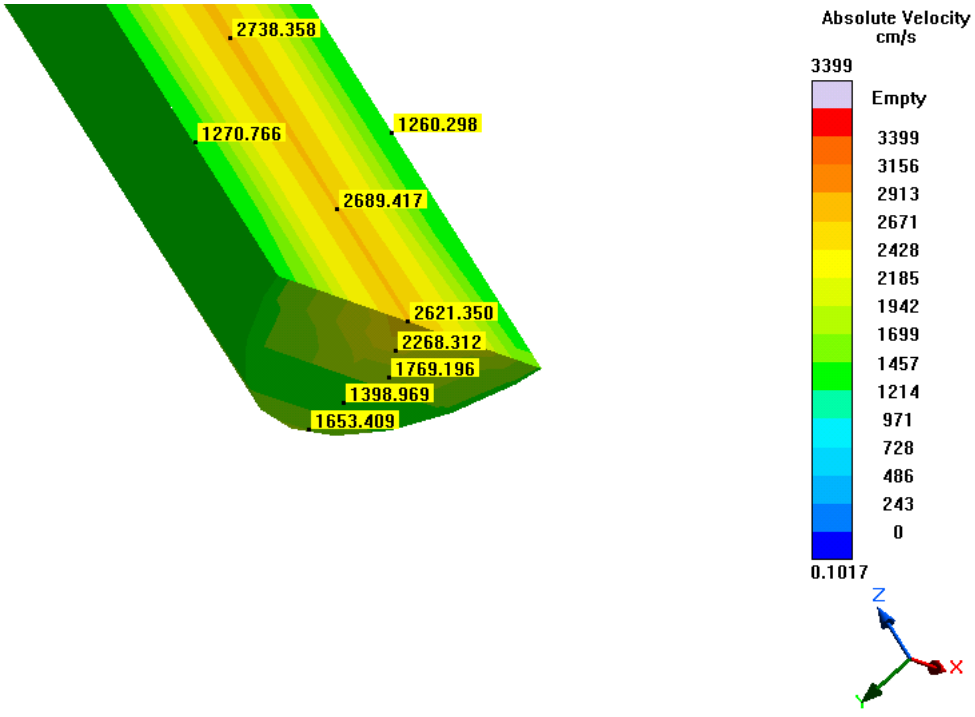

Figure 685- Simulation 11 (Cylindrical Nozzle, Faster), Tip Velocity

Viscosity

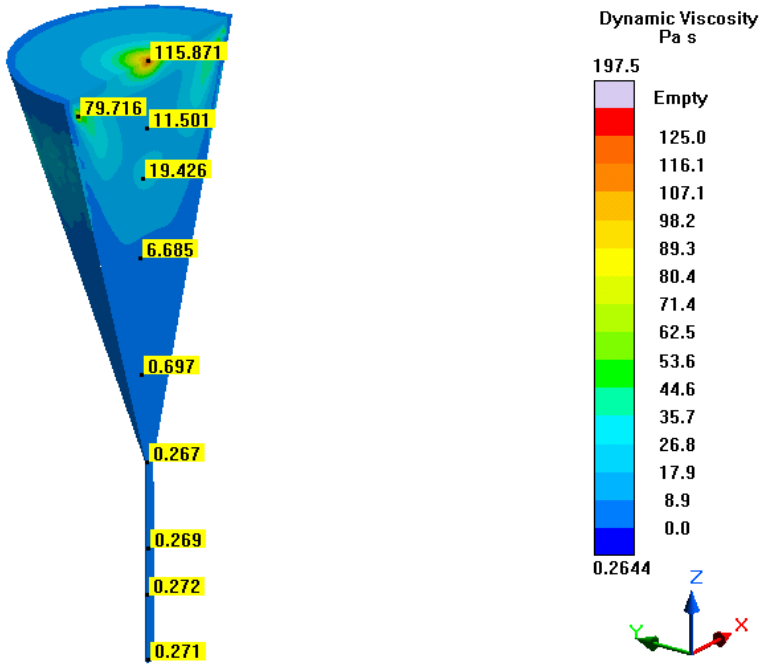

Figure 686- Simulation 11 (Cylindrical Nozzle, Faster), Viscosity

Cooling Rate

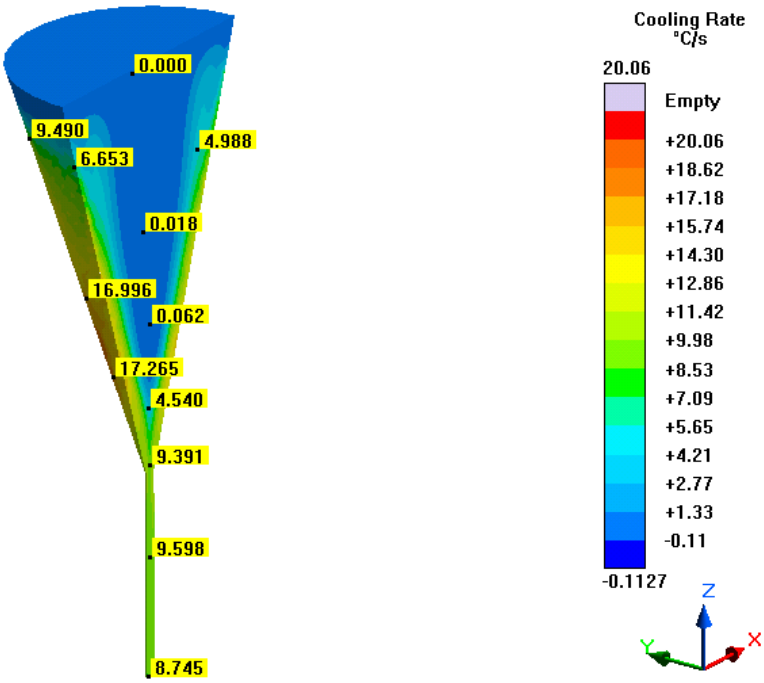

Figure 687- Simulation 11 (Cylindrical Nozzle, Faster), Cooling Rate

Pressure

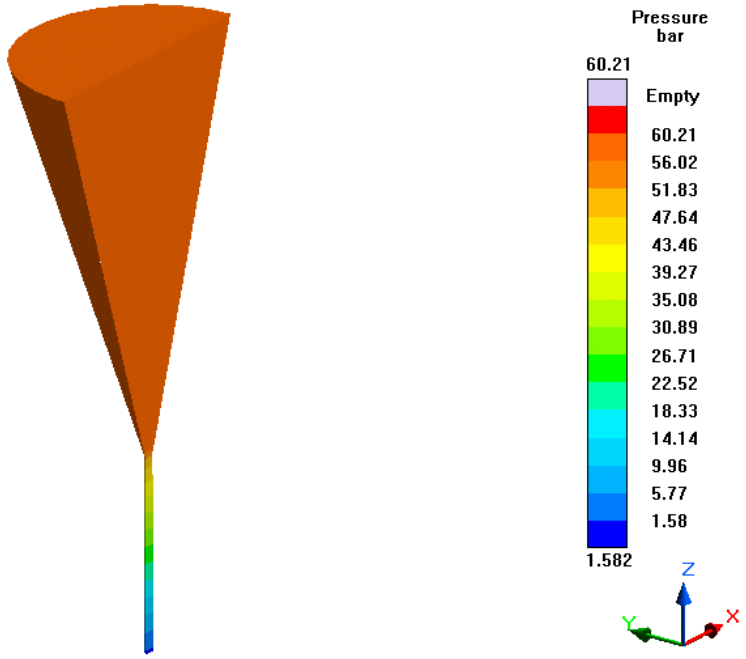

Figure 688- Simulation 11 (Cylindrical Nozzle, Faster), Pressure

Shear Heating

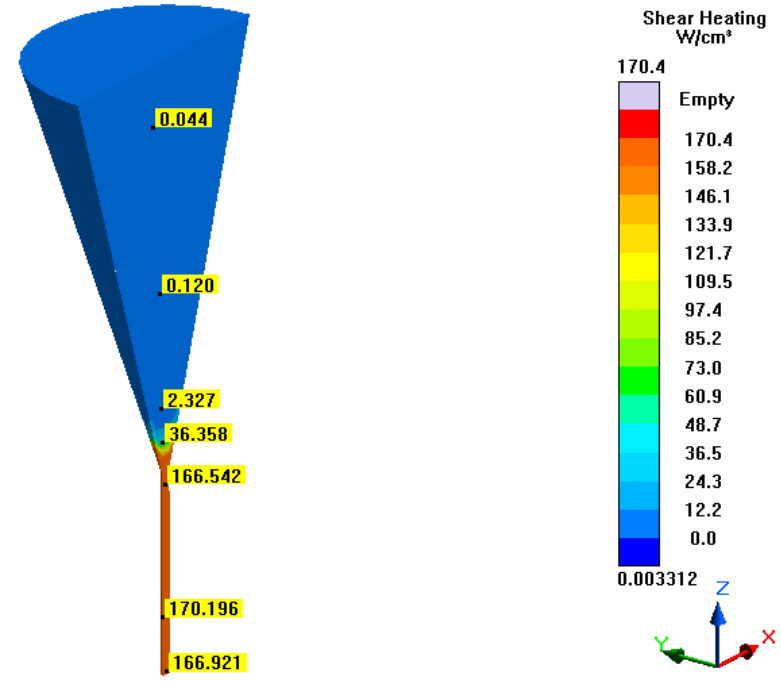

Figure 689- Simulation 11 (Cylindrical Nozzle, Faster), Shear Heating

Shear Rate

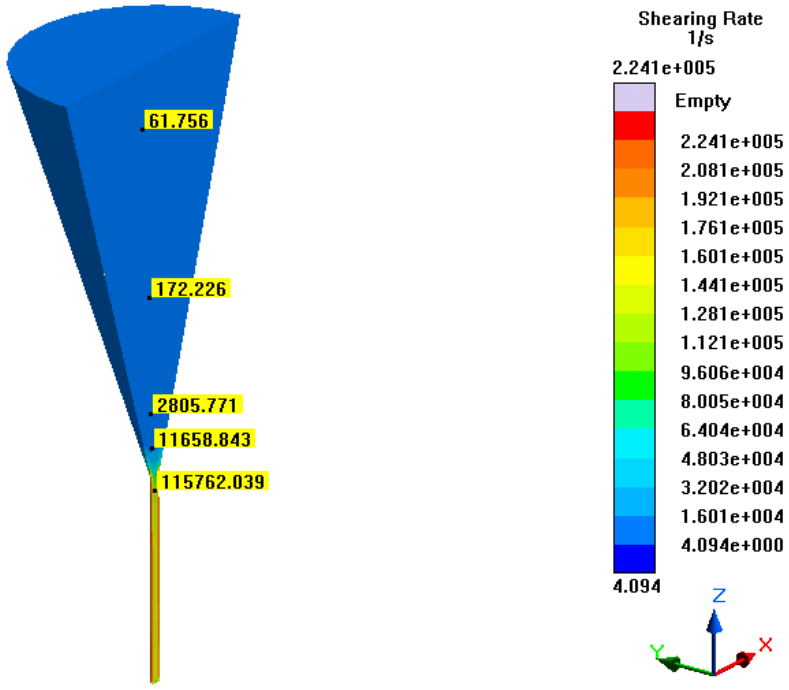

Figure 690- Simulation 11 (Cylindrical Nozzle, Faster), Shear Rate

Shear Stress

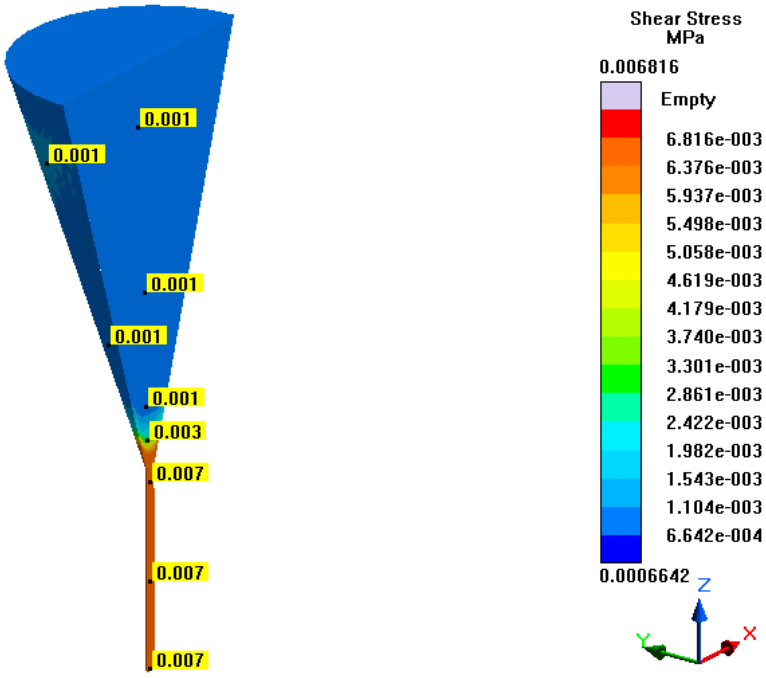

Figure 691- Simulation 11 (Cylindrical Nozzle, Faster), Shear Stress

Temperature

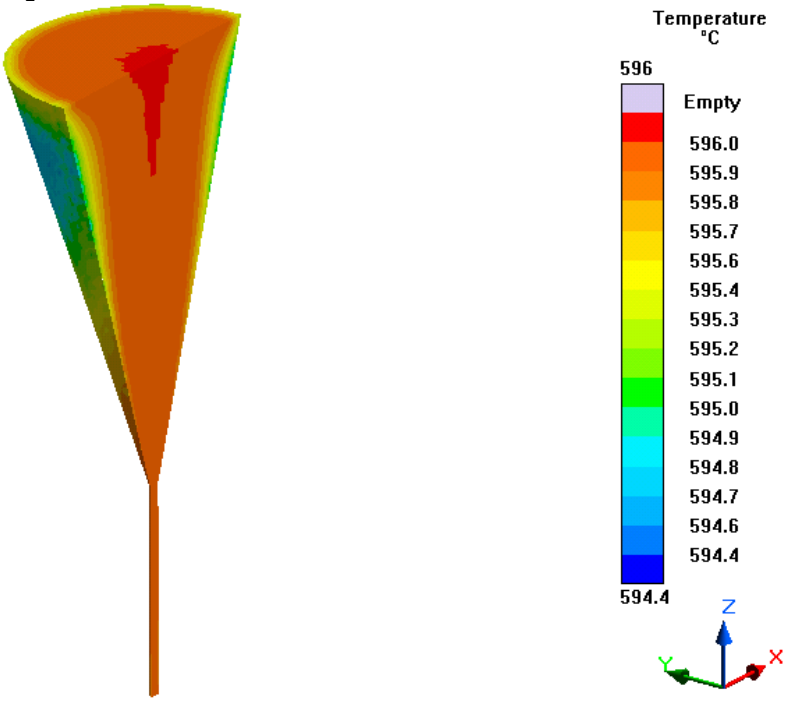

Figure 692- Simulation 11 (Cylindrical Nozzle, Faster), Temperature

Simulation 12- Dual Cylindrical Nozzle

Parameters

Geometry	
Inlet Diameter	0.5 mm (500 microns)
Outlet Diameter	0.5 mm (500 microns)
Nozzle Height	7.5 mm
Nozzle Angle	90°
Cylindrical Runner Inlet	10 mm
Cylindrical Runner Outlet	10 mm
Cylindrical Runner Height	15 mm
Tank Diameter	10 mm
Tank Height	5 mm

Mesh Parameters	
Accuracy (Refinement Factor)	5
Minimum Wall Thickness	0.5 mm
Minimum Element Size	0.1 mm
Smoothing	2
Ratio	2
Coarsening Loops	1
Minimal Accuracy After Coarsening	5

Mesh Properties	
Control Volumes (X Direction)	232
Control Volumes (Y Direction)	226
Control Volumes (Z Direction)	282
Composed Part Cells	53,082
Total Part Cells	189,826
Blocked Cells	0

Process Definitions	
Material Temperature	596 C
Fraction Solid	44%
Close Mold Time	0 s
Fill Time	0.188 s
Hold Time After Filling	1 s

Table 114- Simulation 12 (Dual Cylindrical Nozzle), Parameters

Velocity

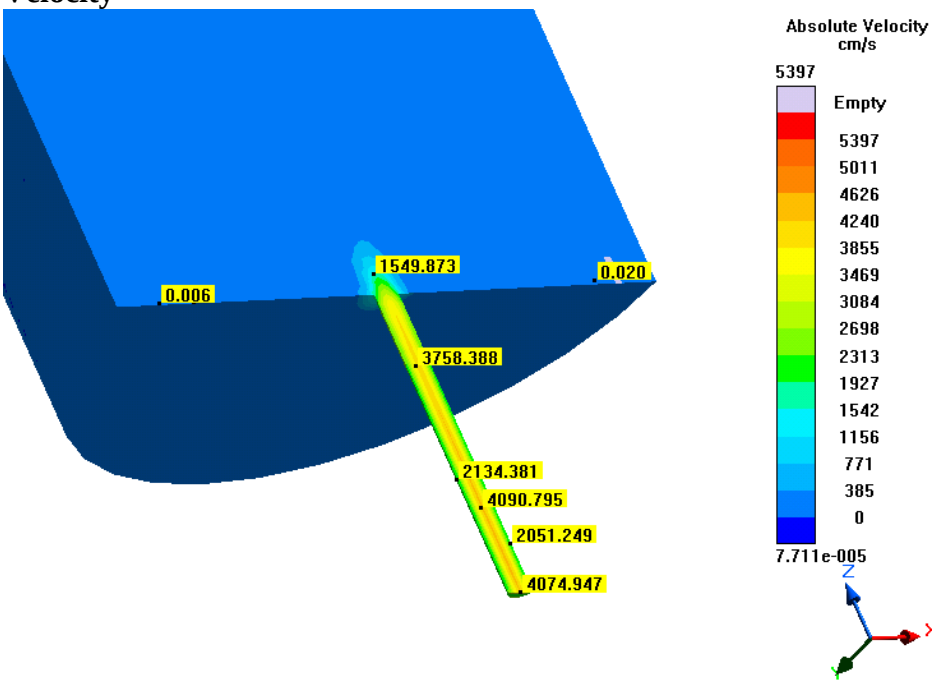

Figure 693- Simulation 12 (Dual Cylindrical Nozzle), Velocity

Viscosity

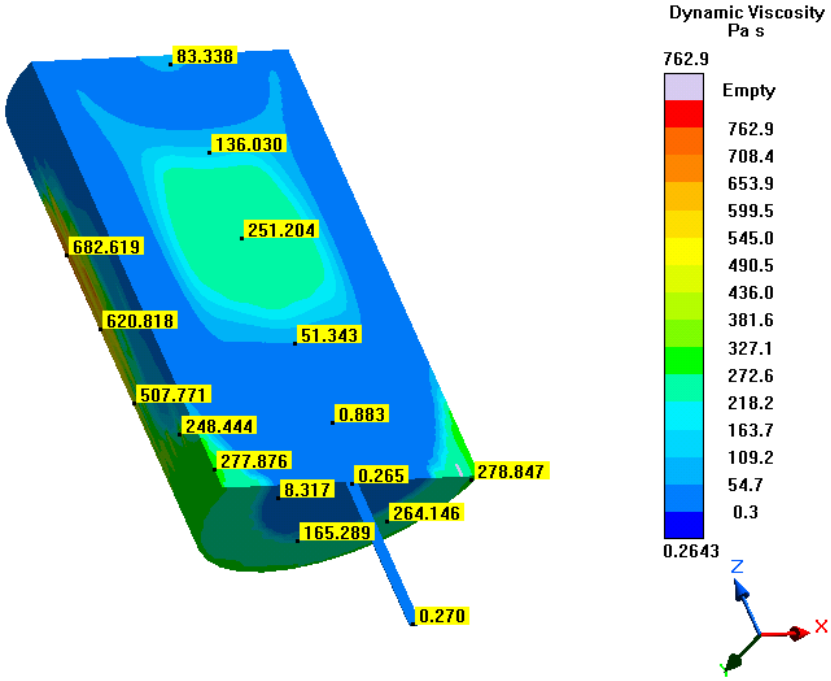

Figure 694- Simulation 12 (Dual Cylindrical Nozzle), Viscosity

Fraction Solid

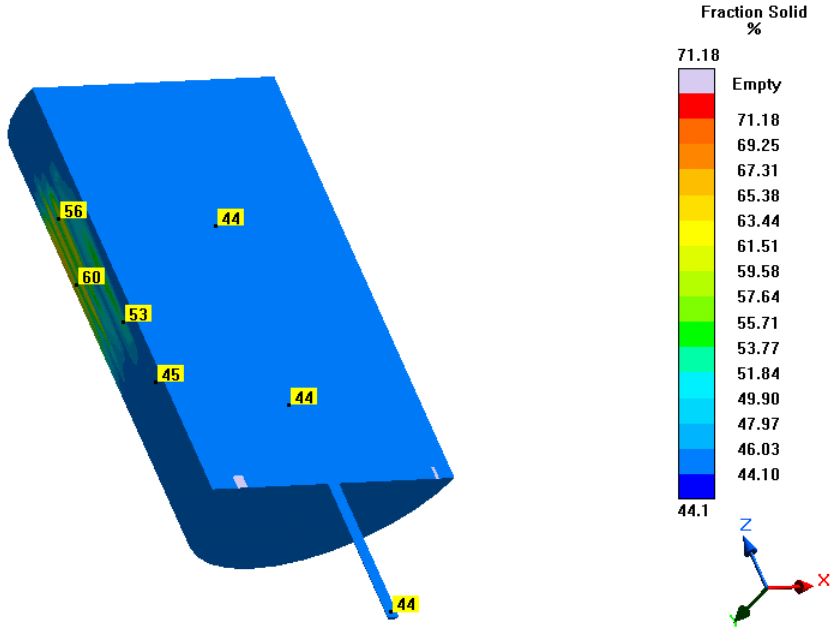

Figure 695- Simulation 12 (Dual Cylindrical Nozzle), Fraction Solid

Cooling Rate

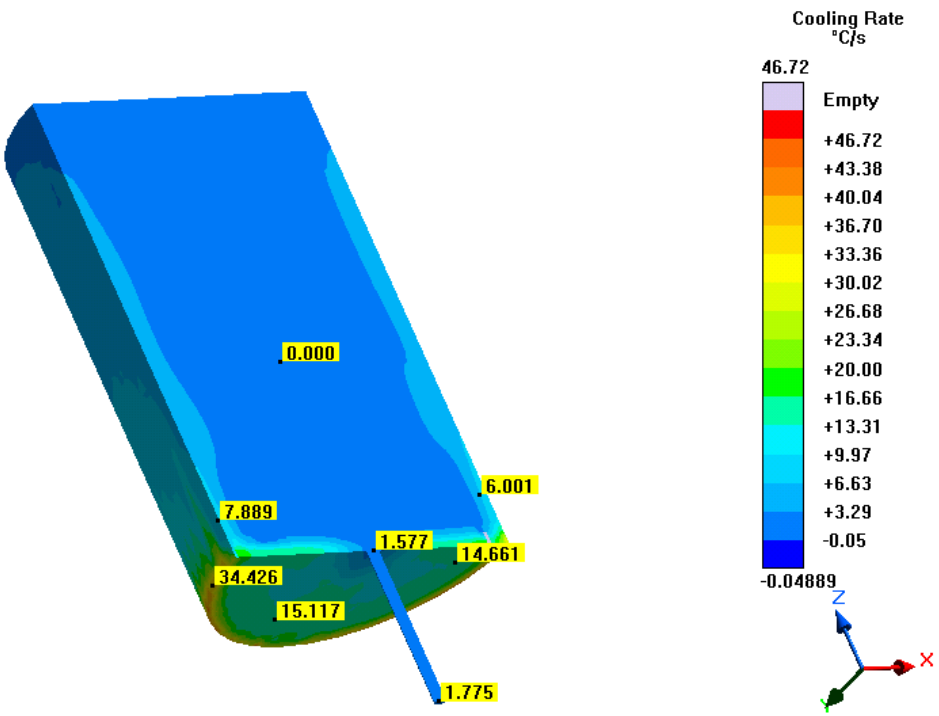

Figure 696- Simulation 12 (Dual Cylindrical Nozzle), Cooling Rate

Pressure

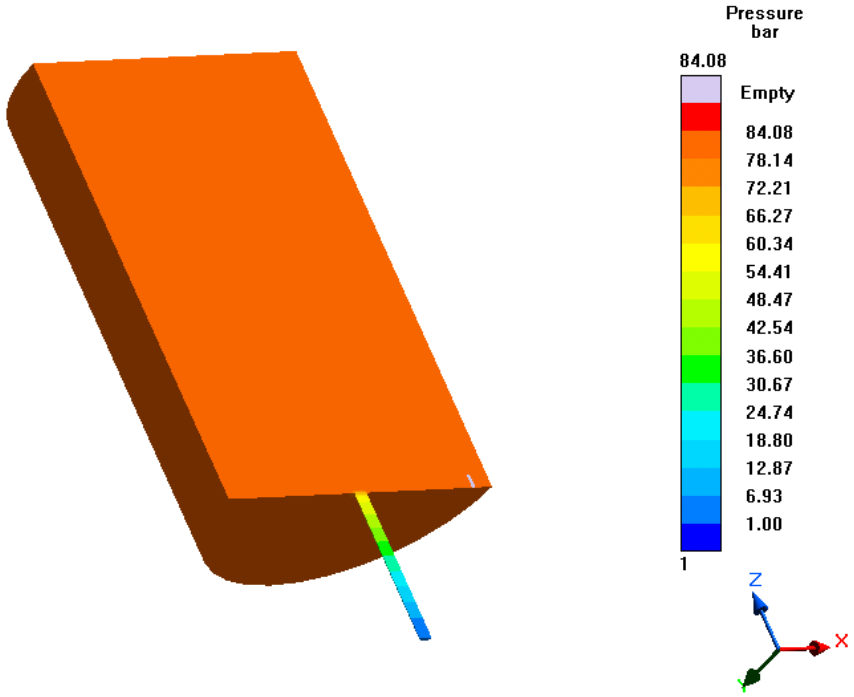

Figure 697- Simulation 12 (Dual Cylindrical Nozzle), Pressure

Shear Heating

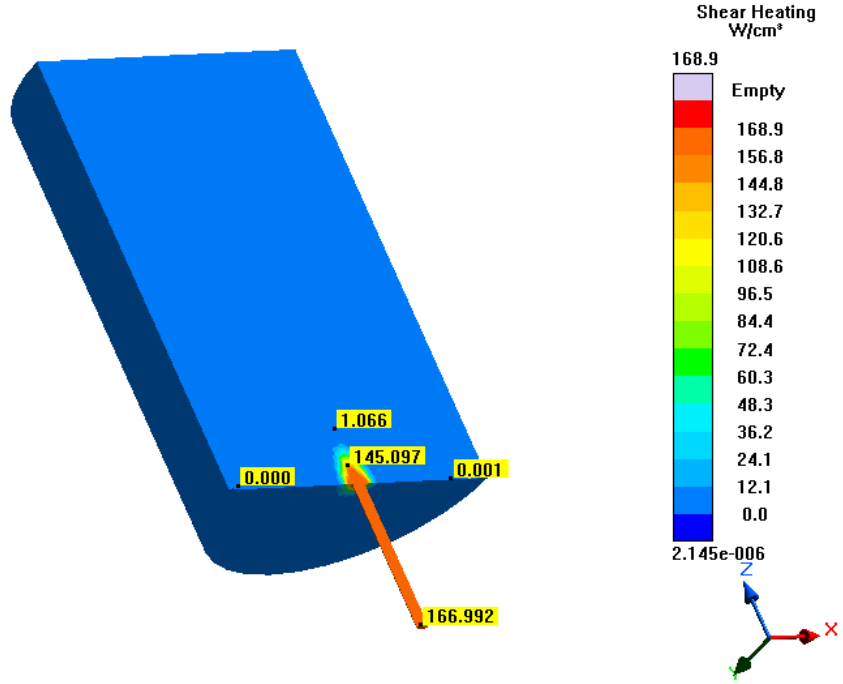

Figure 698- Simulation 12 (Dual Cylindrical Nozzle), Shear Heating

Shear Rate

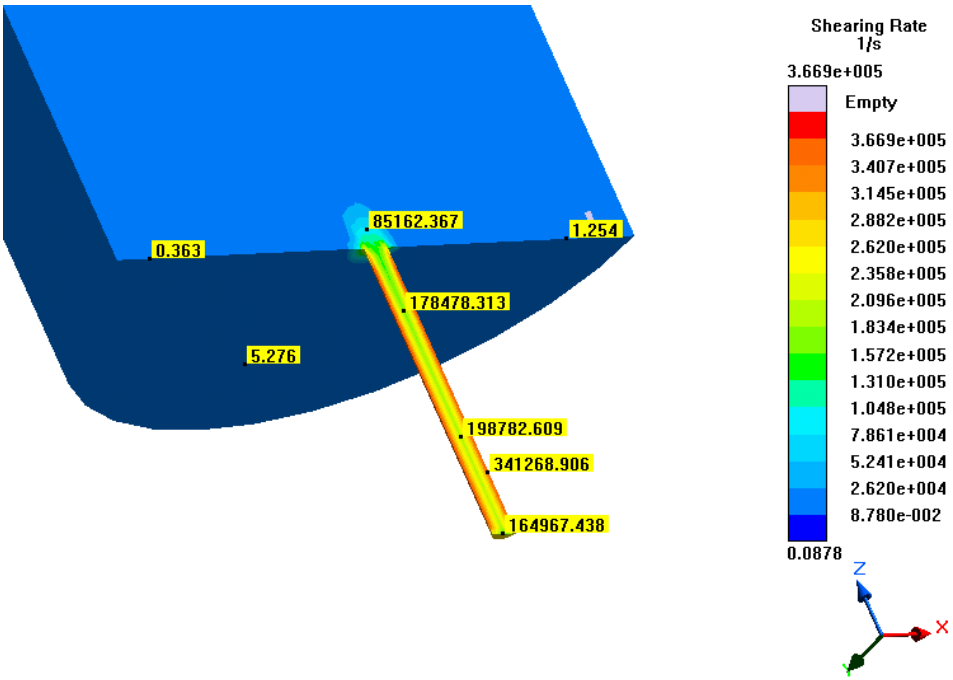

Figure 699- Simulation 12 (Dual Cylindrical Nozzle), Shear Rate

Shear Stress

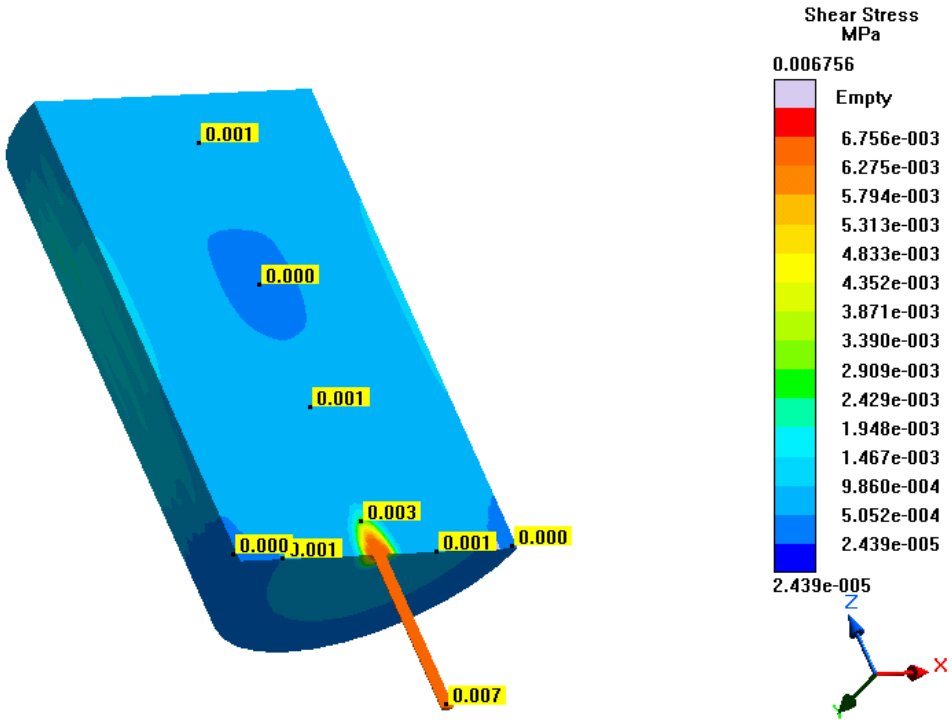

Figure 700- Simulation 12 (Dual Cylindrical Nozzle), Shear Stress

Temperature

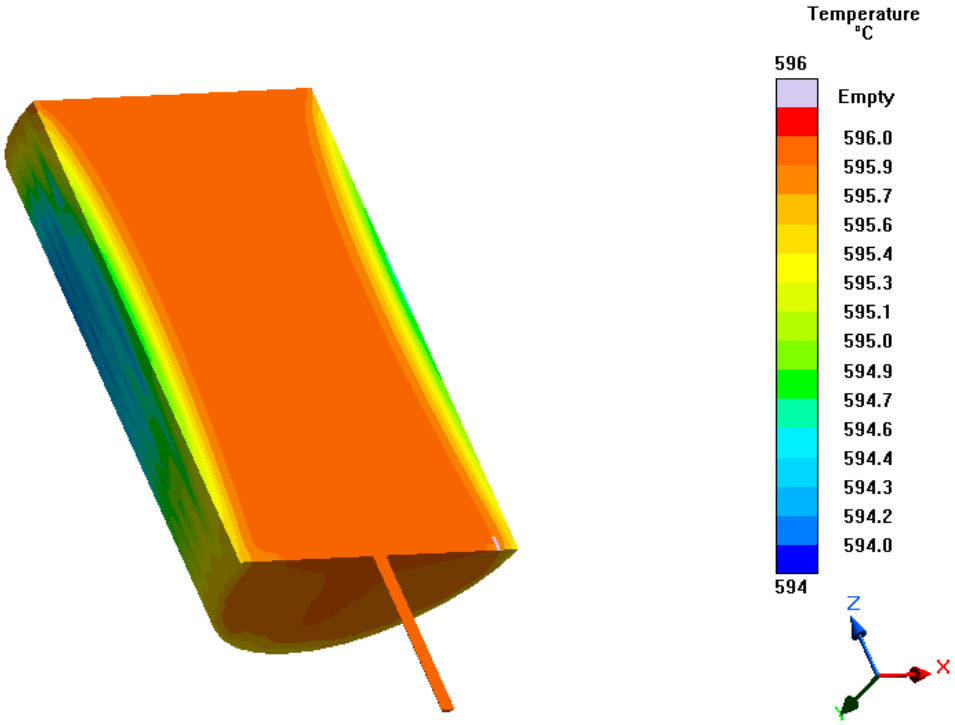

Figure 701- Simulation 12 (Dual Cylindrical Nozzle), Temperature

Simulation 13- LLNL 30 Micron

Parameters

Geometry	
Inlet Diameter	0.03 mm (30 microns)
Outlet Diameter	0.03 mm (30 microns)
Nozzle Height	0.3 mm
Nozzle Angle	90°
Tank Height	6.5 mm

Mesh Parameters	
Accuracy (Refinement Factor)	3
Minimum Wall Thickness	0.03 mm
Minimum Element Size	0.01 mm
Smoothing	2
Ratio	2
Coarsening Loops	1
Minimal Accuracy After Coarsening	5

Mesh Properties	
Control Volumes (X Direction)	534
Control Volumes (Y Direction)	562
Control Volumes (Z Direction)	578
Composed Part Cells	393,055
Total Part Cells	1,174,110
Blocked Cells	0

Process Definitions	
Material Temperature	594 C
Fraction Solid	72.46-85.52 %
Close Mold Time	0 s
Fill Time	0.1 s
Hold Time After Filling	1 s

Table 115- Simulation 13 (LLNL 30 Micron), Parameters

Notes

- Very difficult to generate a nozzle tip at the 30 micron level. Meshes were massive and tip could only have 1 element across.
- Attempted to run with a far shorter top to prevent the program from exceeding the available RAM on the computer.

Velocity

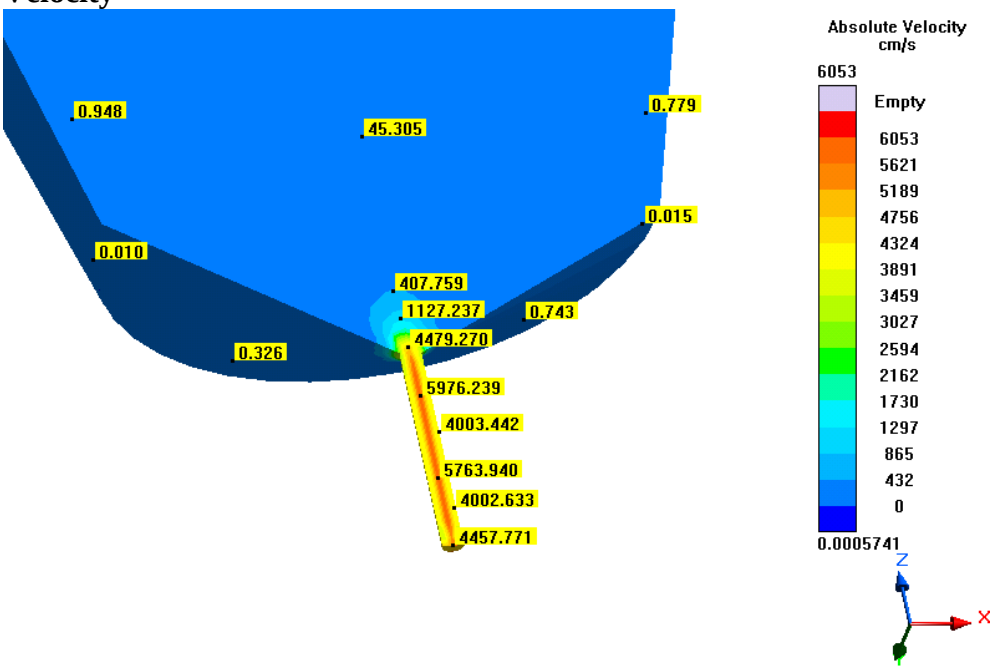

Figure 702- Simulation 13 (LLNL 30 Micron), Velocity

Viscosity

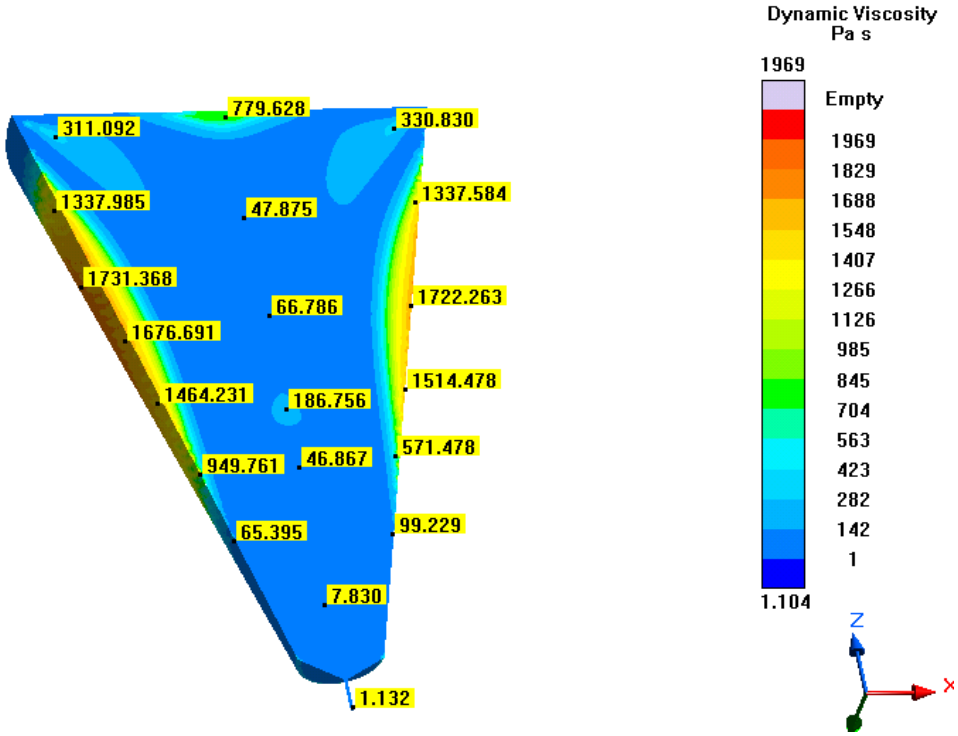

Figure 703- Simulation 13 (LLNL 30 Micron), Viscosity

Pressure

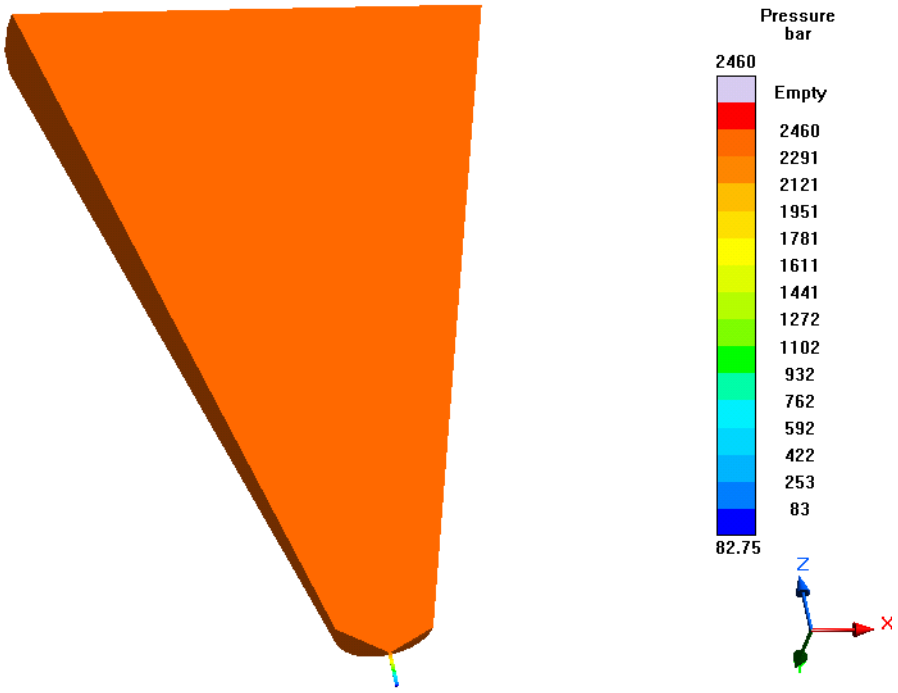

Figure 704- Simulation 13 (LLNL 30 Micron), Pressure

Cooling Rate

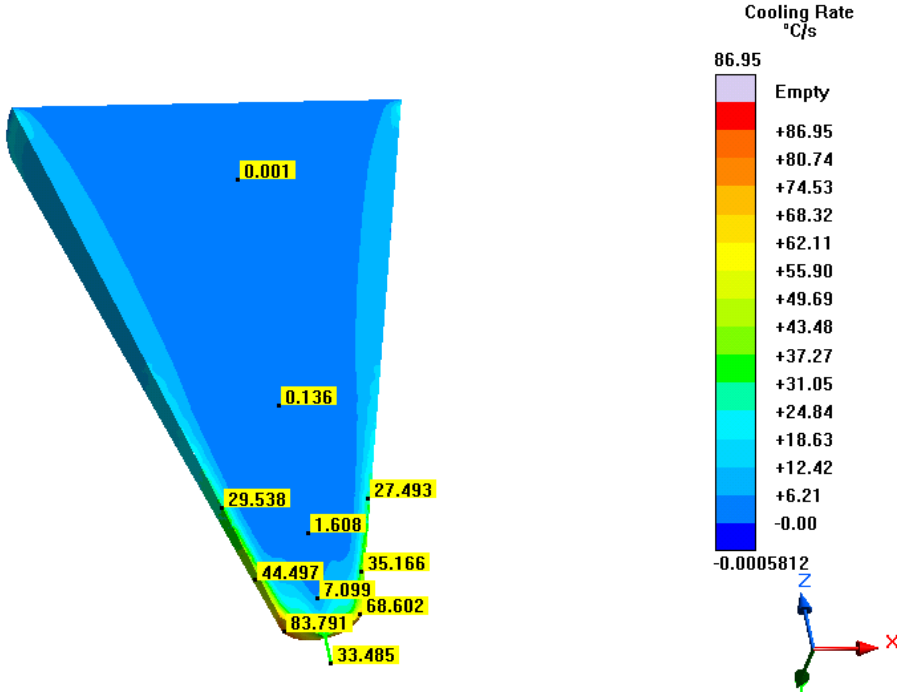

Figure 705- Simulation 13 (LLNL 30 Micron), Cooling Rate

Fraction Solid

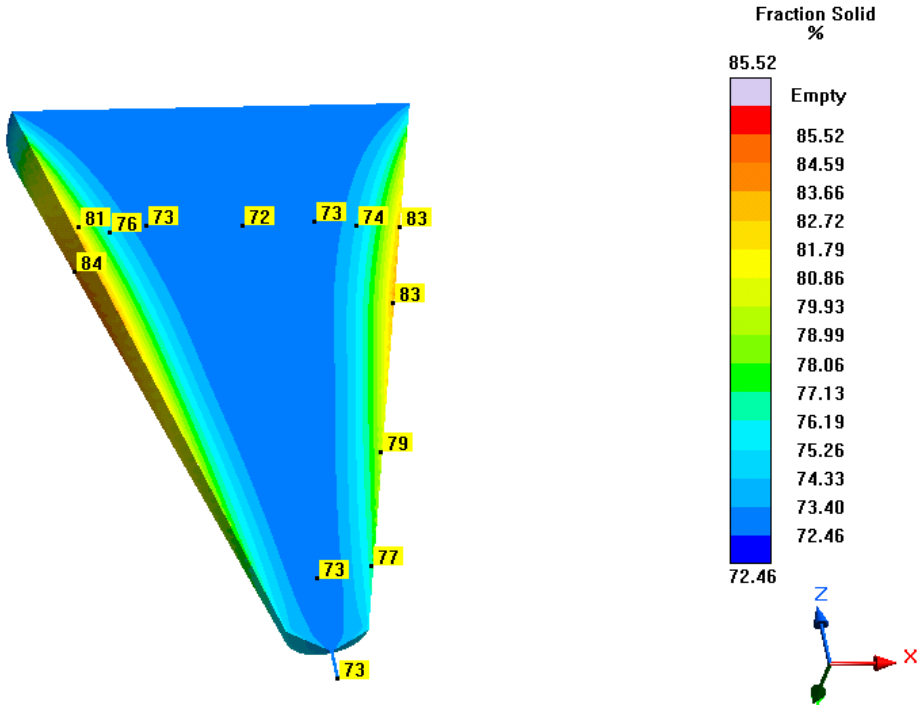

Figure 706- Simulation 13 (LLNL 30 Micron), Fraction Solid

Shear Heating

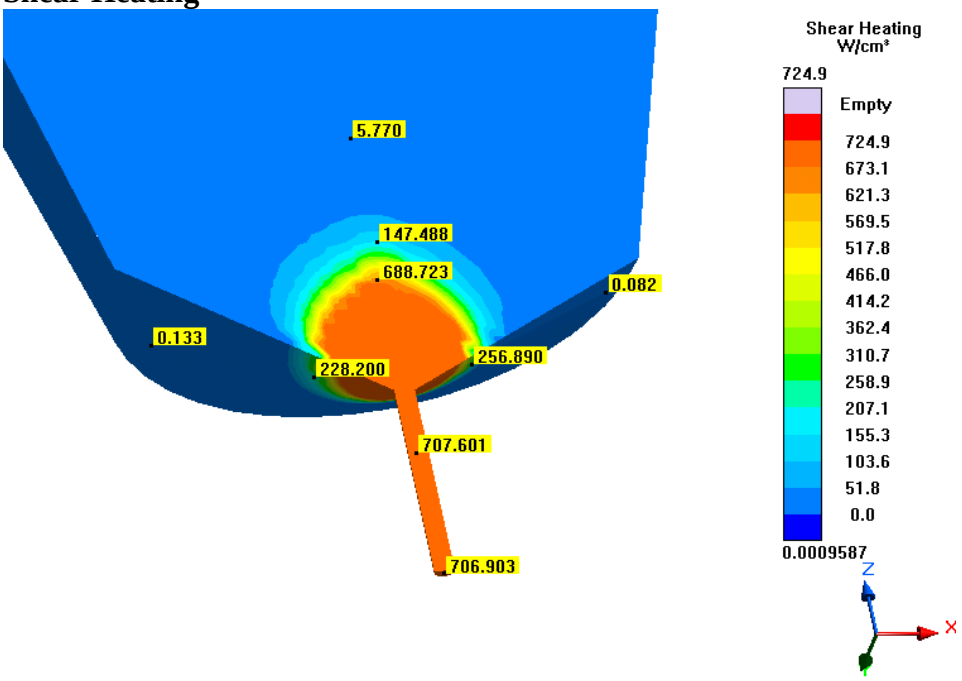

Figure 707- Simulation 13 (LLNL 30 Micron), Shear Heating

Shear Rate

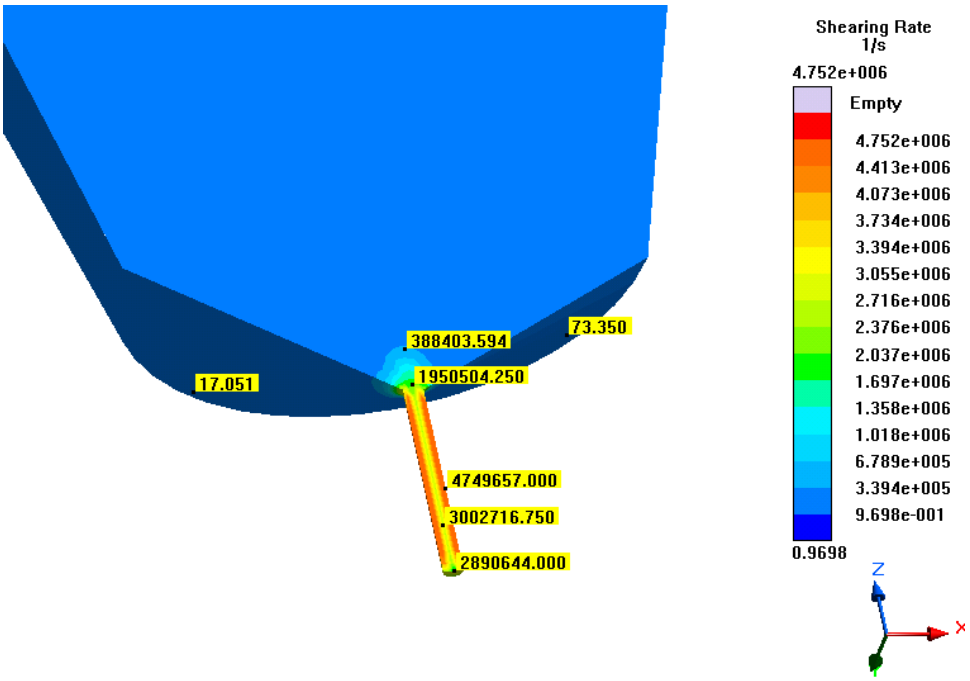

Figure 708- Simulation 13 (LLNL 30 Micron), Shear Rate

Shear Stress

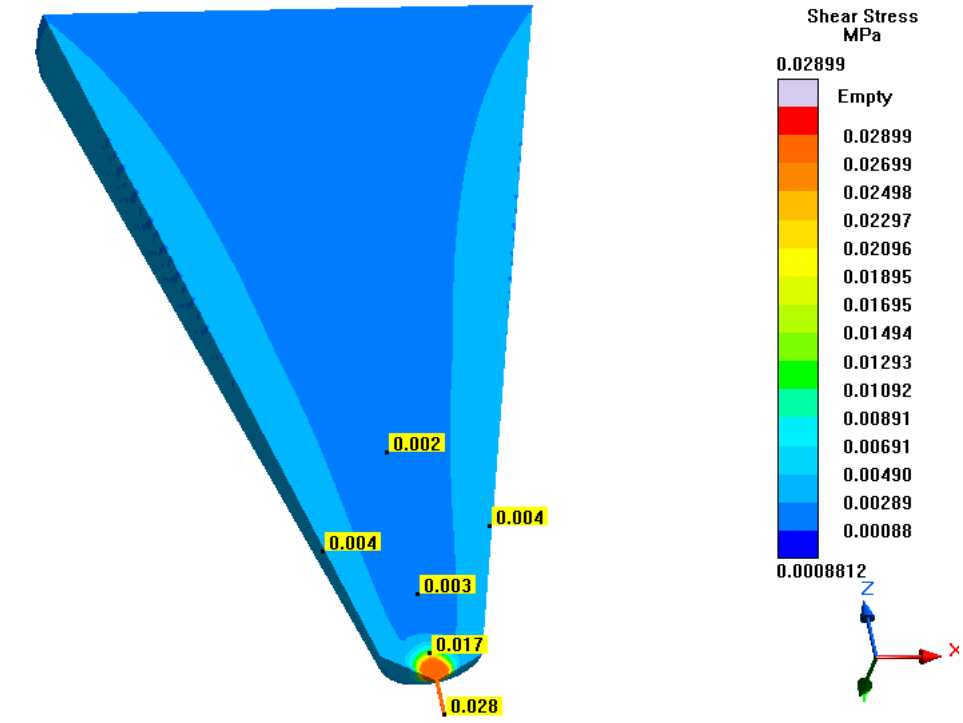

Figure 709- Simulation 13 (LLNL 30 Micron), Shear Stress

Temperature

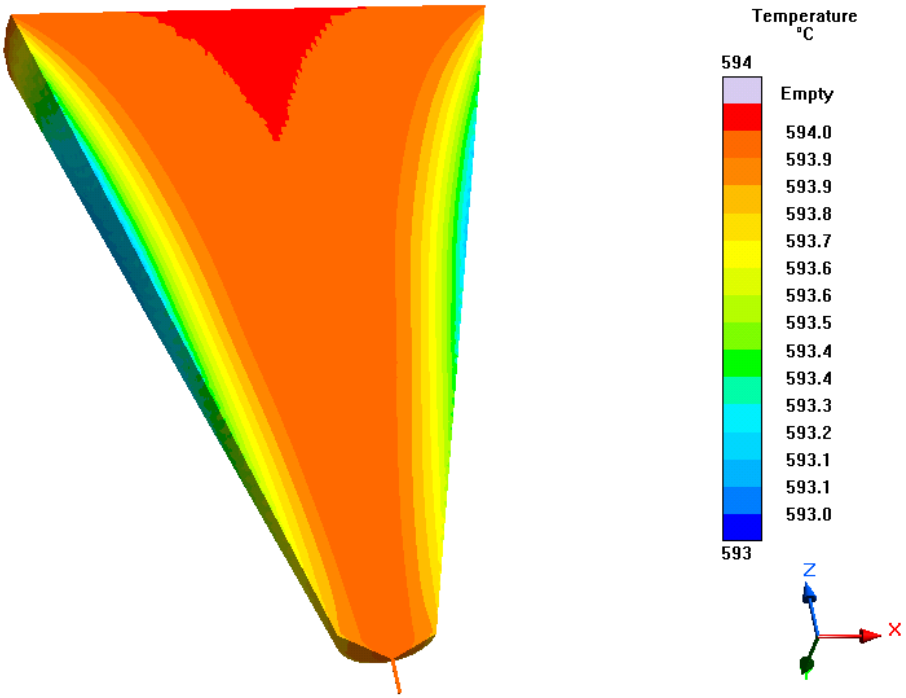

Figure 710- Simulation 13 (LLNL 30 Micron), Temperature

Simulation 14- LLNL 500 Micron

Parameters

Geometry	
Inlet Diameter	0.50 mm (500 microns)
Outlet Diameter	0.50 mm (500 microns)
Nozzle Height	1 mm
Nozzle Angle	90°
Tank Height	18.25 mm

Mesh Parameters	
Accuracy (Refinement Factor)	3
Minimum Wall Thickness (Nozzle)	0.21 mm
Minimum Element Size (Nozzle)	0.07 mm
Minimum Wall Thickness (Part)	0.48 mm
Minimum Element Size (Part)	0.16 mm
Smoothing	2
Ratio	2
Coarsening Loops	1
Minimal Accuracy After Coarsening	5

Mesh Properties	
Control Volumes (X Direction)	282
Control Volumes (Y Direction)	282
Control Volumes (Z Direction)	326
Composed Part Cells	34,714
Total Part Cells	108,766
Blocked Cells	0

Process Definitions	
Material Temperature	594 C
Fraction Solid	44-76.6 %
Close Mold Time	0 s
Fill Time	0.25 s
Hold Time After Filling	1 s

Table 116- Simulation 14 (LLNL 500 Micron), Parameters

Notes

- SIGMASOFT fills the solid areas of an imported CAD model, not the empty regions

Velocity

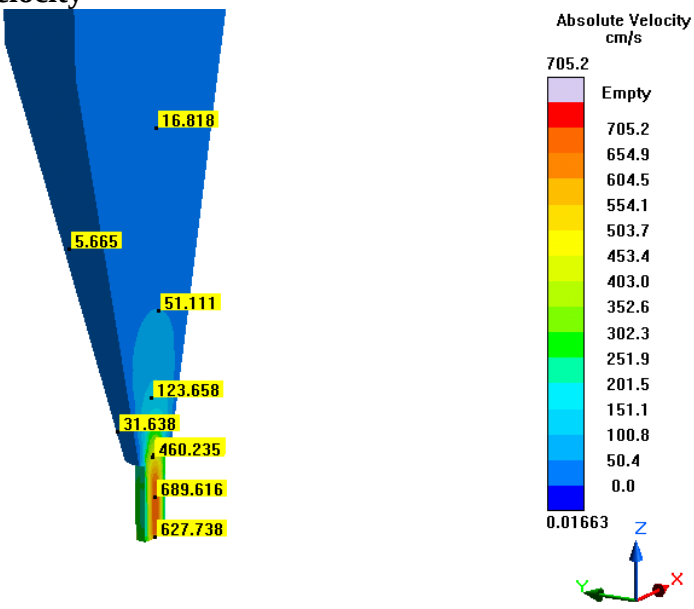

Figure 711- Simulation 14 (LLNL 500 Micron), Velocity

Viscosity

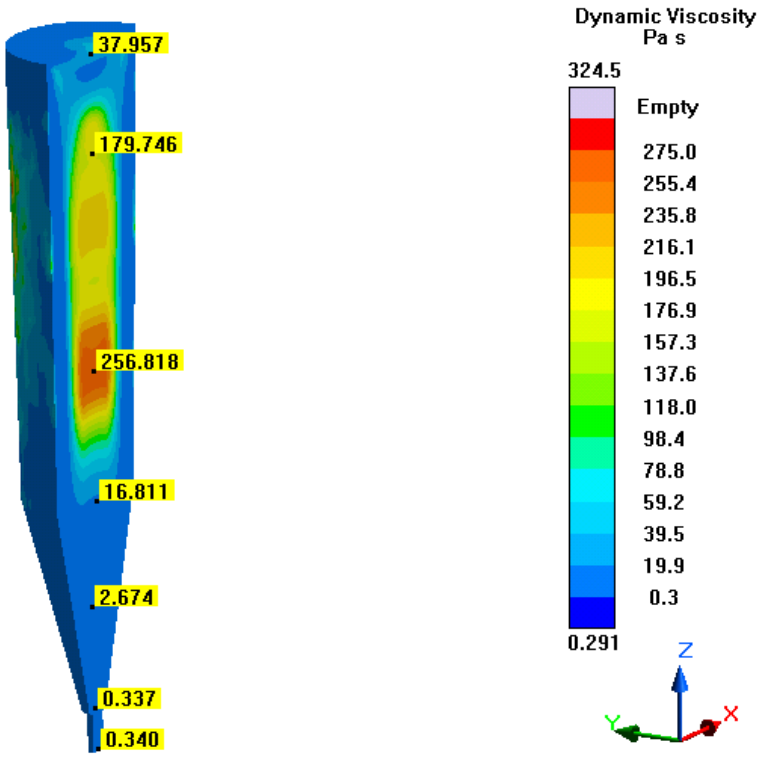

Figure 712- Simulation 14 (LLNL 500 Micron), Viscosity

Pressure

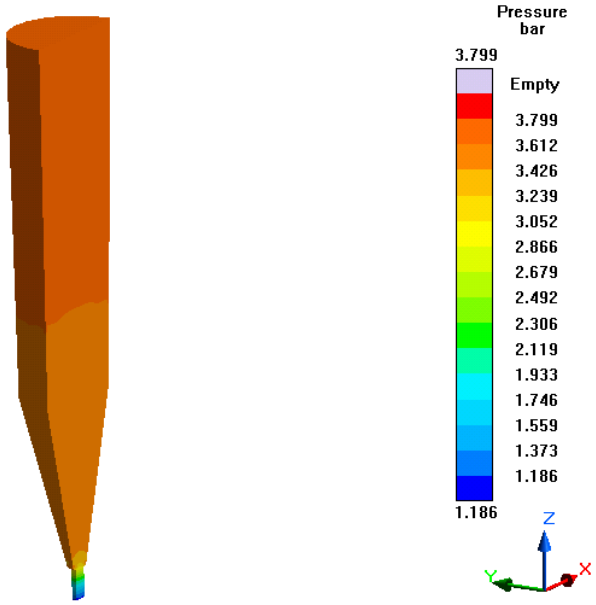

Figure 713- Simulation 14 (LLNL 500 Micron), Pressure

Fraction Solid

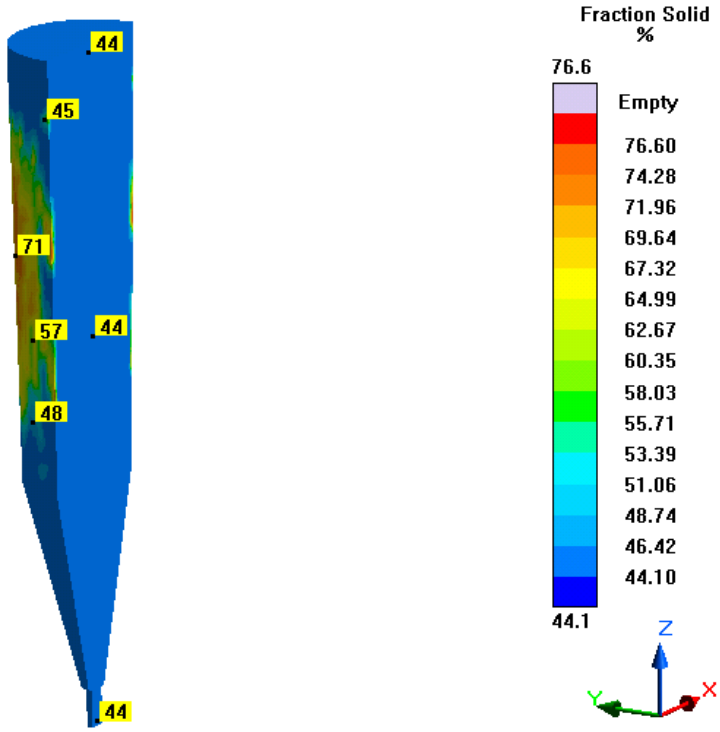

Figure 714- Simulation 14 (LLNL 500 Micron), Fraction Solid

Cooling Rate

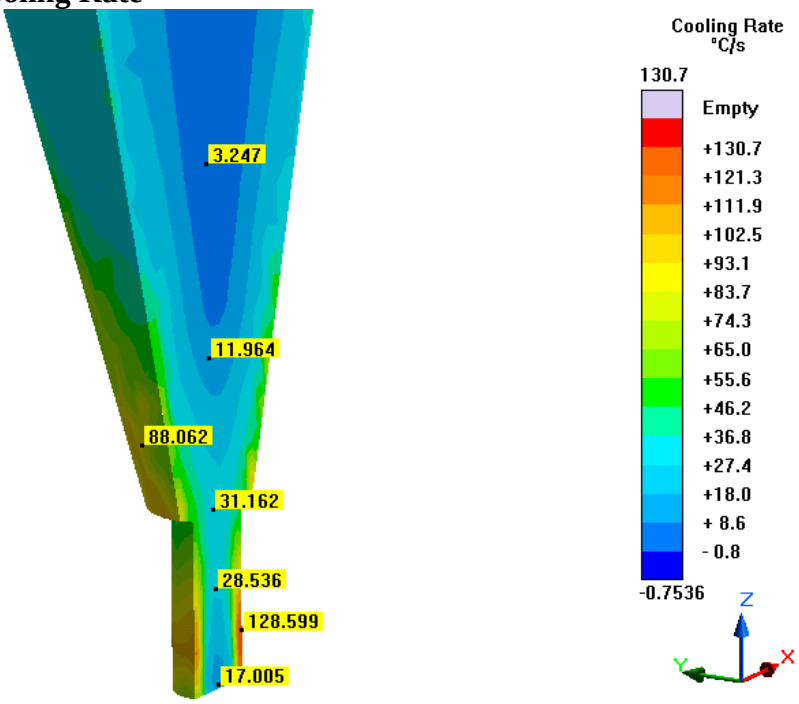

Figure 715- Simulation 14 (LLNL 500 Micron), Cooling Rate

Shear Heating

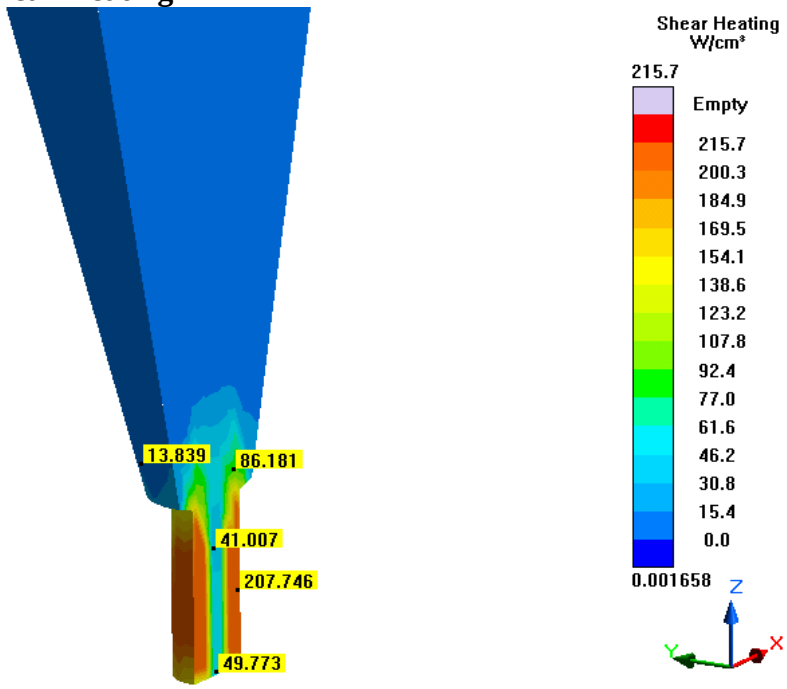

Figure 716- Simulation 14 (LLNL 500 Micron), Shear Heating

Shear Rate

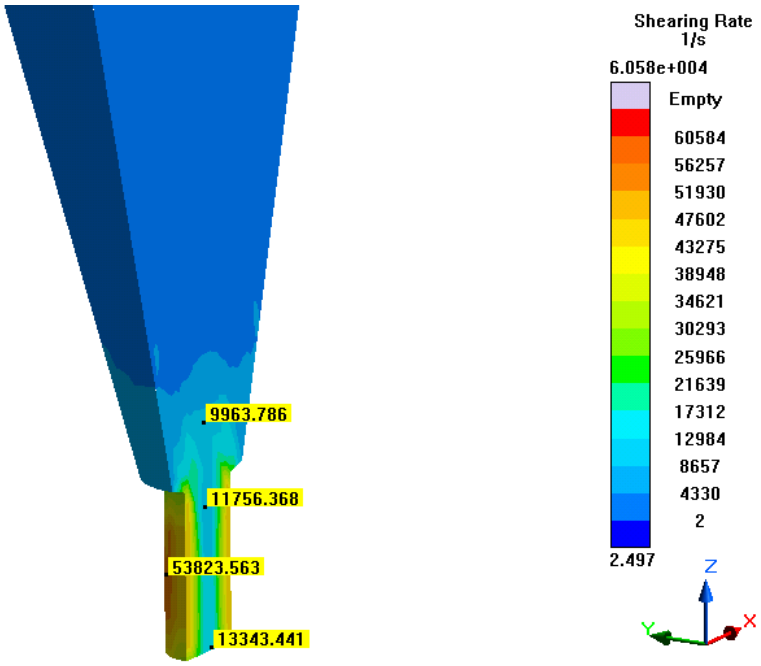

Figure 717- Simulation 14 (LLNL 500 Micron), Shear Rate

Shear Stress

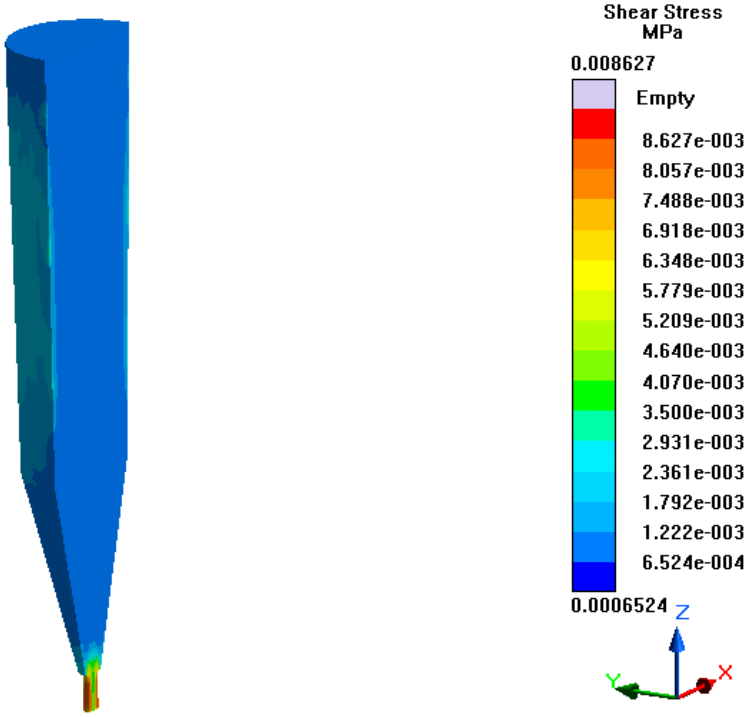

Figure 718- Simulation 14 (LLNL 500 Micron), Shear Stress

Temperature

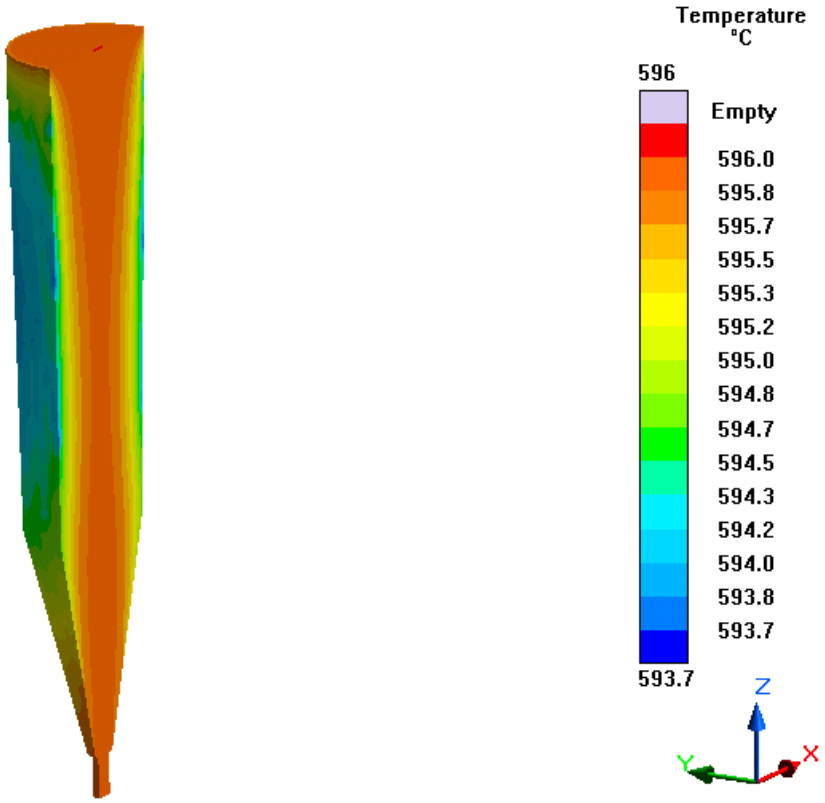

Figure 719- Simulation 14 (LLNL 500 Micron), Temperature

Simulation 15- LLNL 400 Micron

Parameters

Geometry	
Inlet Diameter	0.40 mm (400 microns)
Outlet Diameter	0.40 mm (400 microns)
Nozzle Height	1 mm
Nozzle Angle	90°
Tank Height	18.25 mm

Mesh Parameters	
Accuracy (Refinement Factor)	3
Minimum Wall Thickness (Nozzle)	0.21 mm
Minimum Element Size (Nozzle)	0.07 mm
Minimum Wall Thickness (Part)	0.24 mm
Minimum Element Size (Part)	0.08 mm
Smoothing	2
Ratio	2
Coarsening Loops	1
Minimal Accuracy After Coarsening	5

Mesh Properties	
Control Volumes (X Direction)	282
Control Volumes (Y Direction)	282
Control Volumes (Z Direction)	328
Composed Part Cells	33,963
Total Part Cells	109,620
Blocked Cells	0

Process Definitions	
Material Temperature	594 C
Fraction Solid	44-76.6 %
Close Mold Time	0 s
Fill Time	0.25 s
Hold Time After Filling	1 s

Table 117- Simulation 15 (LLNL 400 Micron), Parameters

Velocity

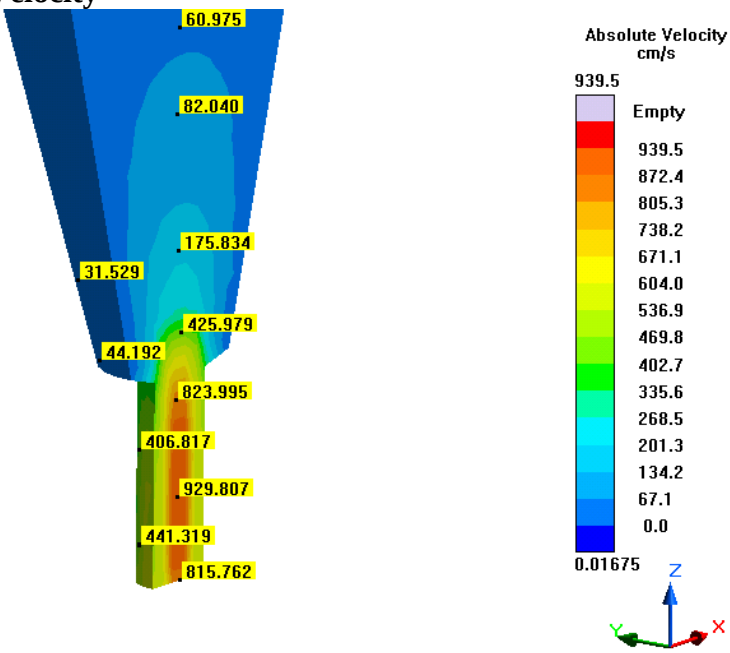

Figure 720- Simulation 15 (LLNL 400 Micron), Velocity

Viscosity

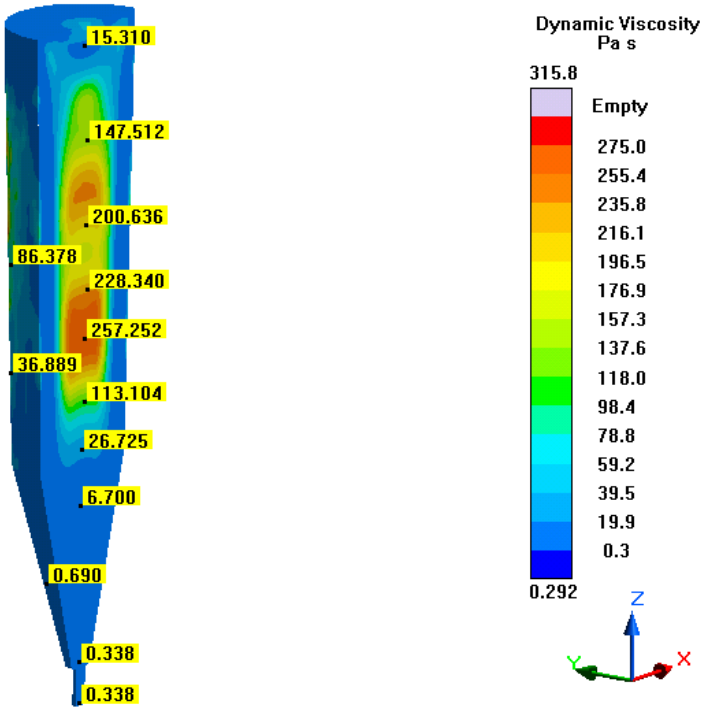

Figure 721- Simulation 15 (LLNL 400 Micron), Viscosity

Pressure

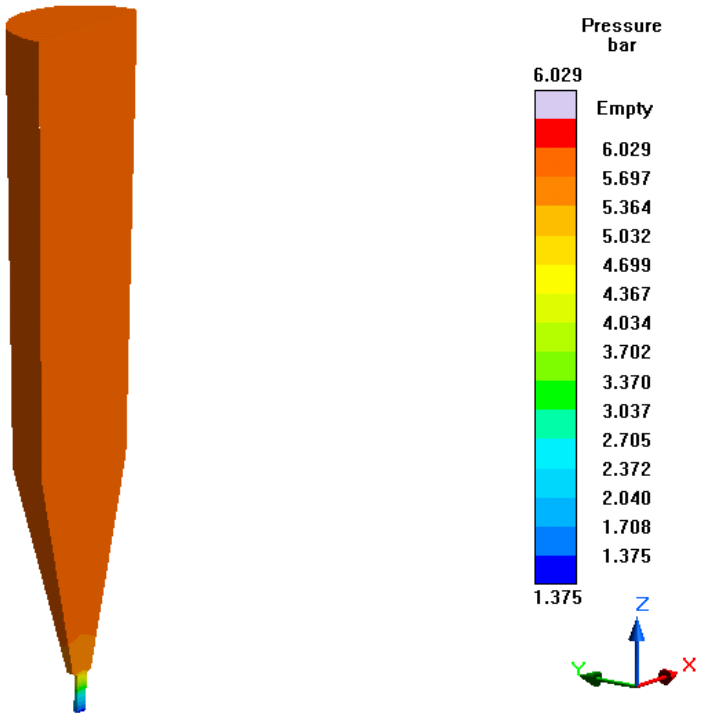

Figure 722- Simulation 15 (LLNL 400 Micron), Pressure

Fraction Solid

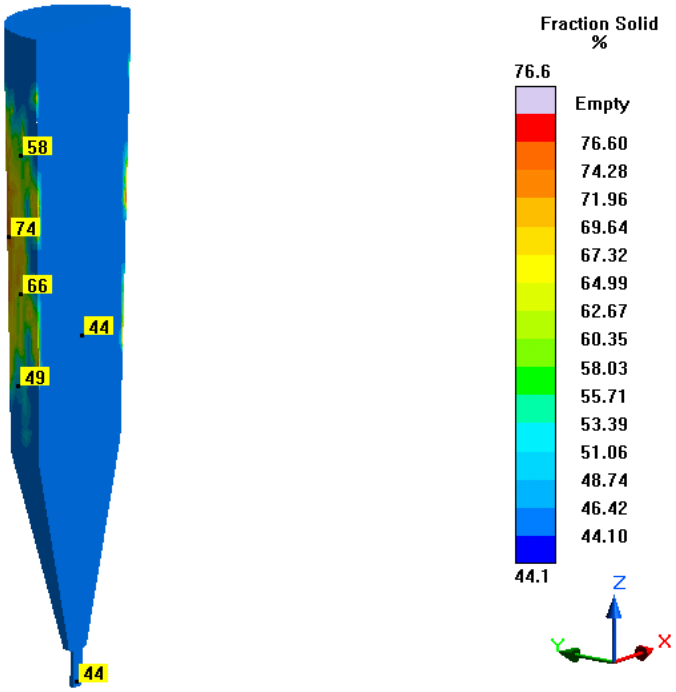

Figure 723- Simulation 15 (LLNL 400 Micron), Fraction Solid

Cooling Rate

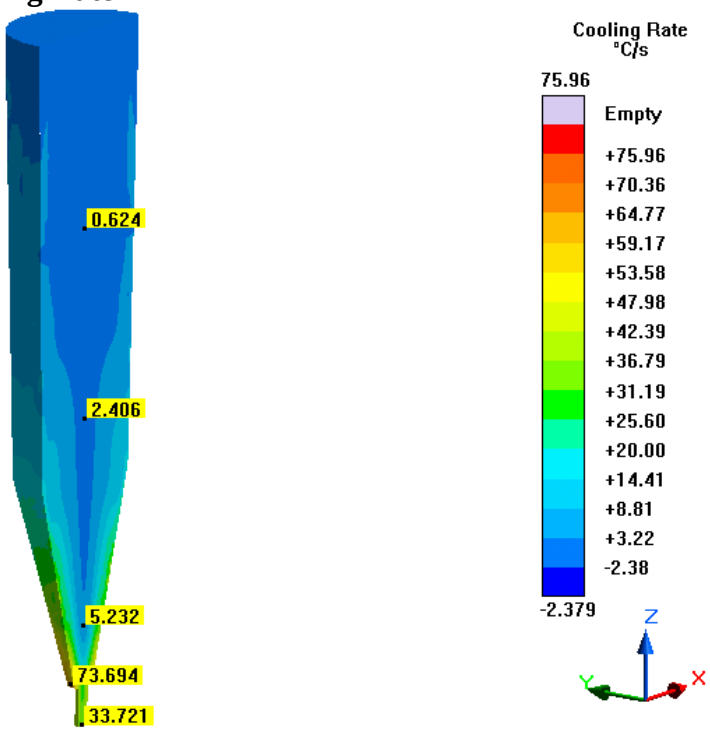

Figure 724- Simulation 15 (LLNL 400 Micron), Cooling Rate

Shear Heating

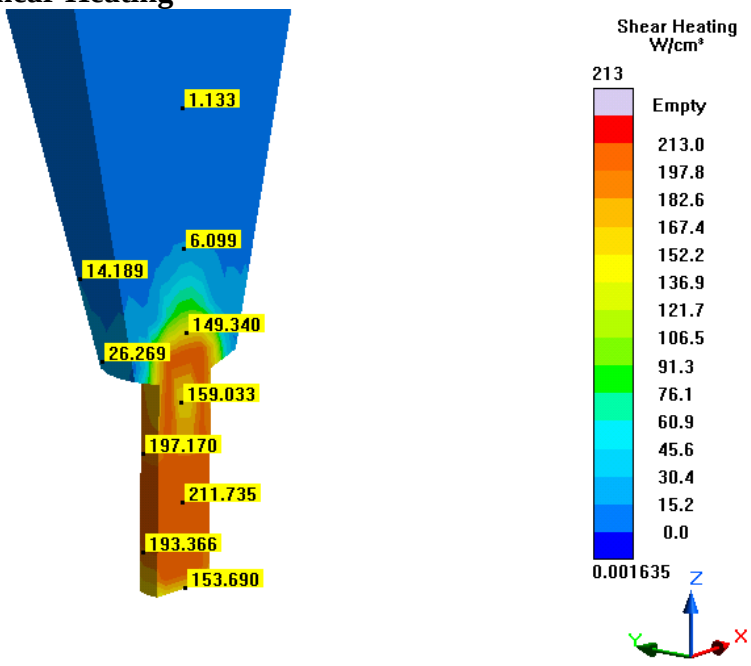

Figure 725- Simulation 15 (LLNL 400 Micron), Shear Heating

Shear Rate

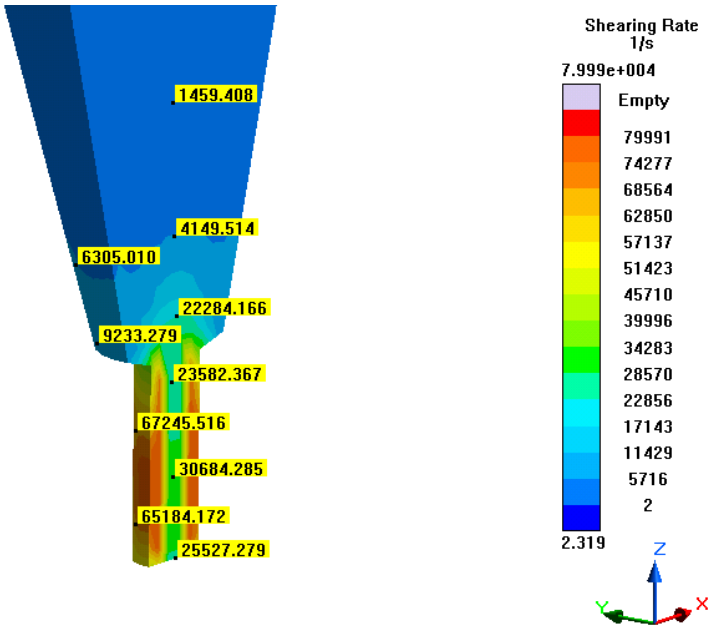

Figure 726- Simulation 15 (LLNL 400 Micron), Shear Rate

Shear Stress

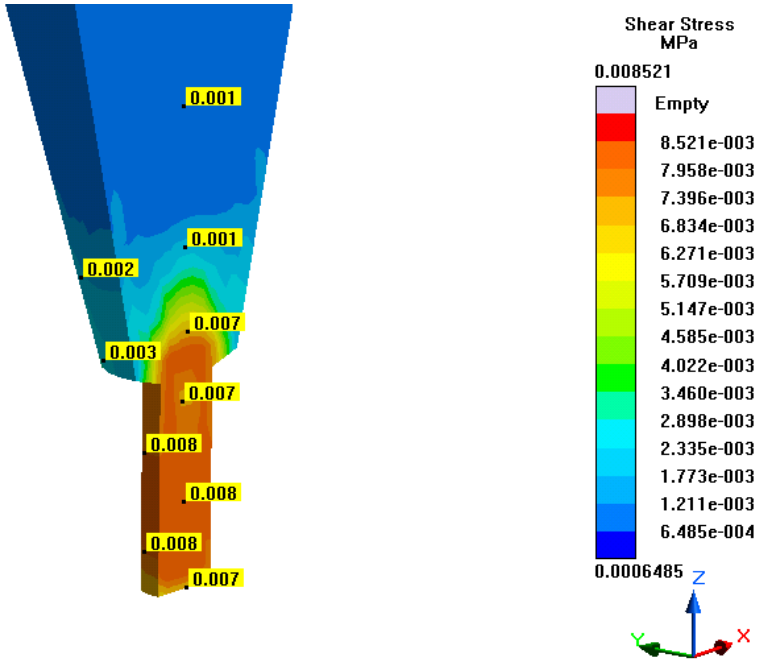

Figure 727- Simulation 15 (LLNL 400 Micron), Shear Stress

Temperature

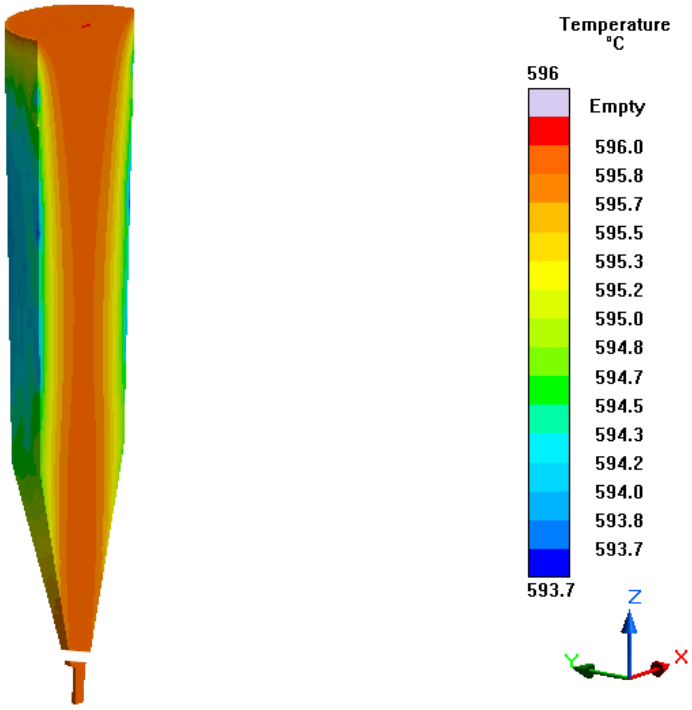

Figure 728- Simulation 15 (LLNL 400 Micron), Temperature

Simulation 16- LLNL 300 Micron

Parameters

Geometry	
Inlet Diameter	0.30 mm (300 microns)
Outlet Diameter	0.30 mm (300 microns)
Nozzle Height	1 mm
Nozzle Angle	90°
Tank Height	18.25 mm

Mesh Parameters	
Accuracy (Refinement Factor)	3
Minimum Wall Thickness (Nozzle)	0.21 mm
Minimum Element Size (Nozzle)	0.07 mm
Minimum Wall Thickness (Part)	0.24 mm
Minimum Element Size (Part)	0.08 mm
Smoothing	2
Ratio	2
Coarsening Loops	1
Minimal Accuracy After Coarsening	5

Mesh Properties	
Control Volumes (X Direction)	282
Control Volumes (Y Direction)	282
Control Volumes (Z Direction)	328
Composed Part Cells	33,967
Total Part Cells	109,648
Blocked Cells	0

Process Definitions	
Material Temperature	594 C
Fraction Solid	44.1-76.6 %
Close Mold Time	0 s
Fill Time	0.25 s
Hold Time After Filling	1 s

Table 118- Simulation 16 (LLNL 300 Micron), Parameters

Velocity

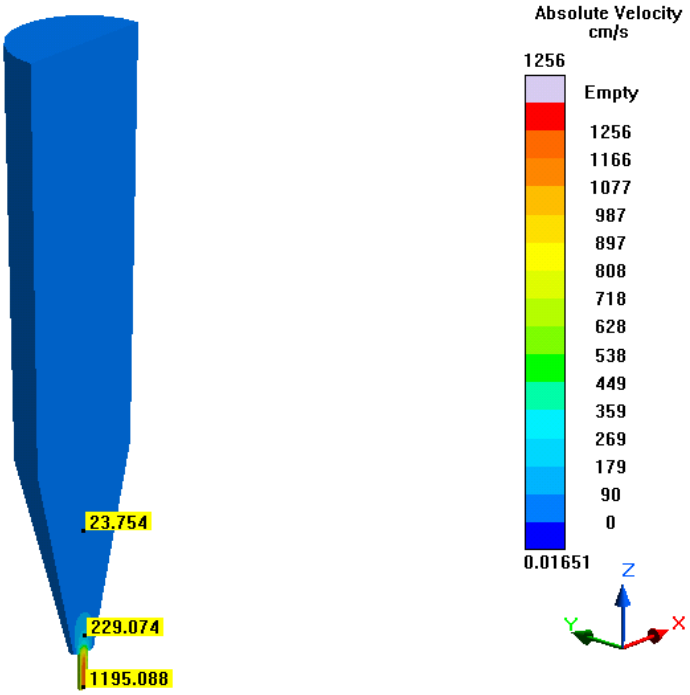

Figure 729- Simulation 16 (LLNL 300 Micron), Velocity

Viscosity

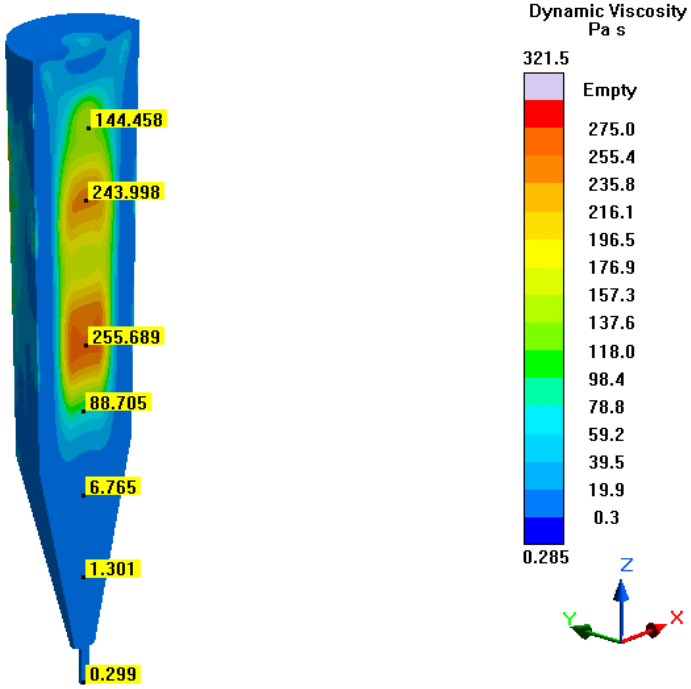

Figure 730- Simulation 16 (LLNL 300 Micron), Viscosity

Pressure

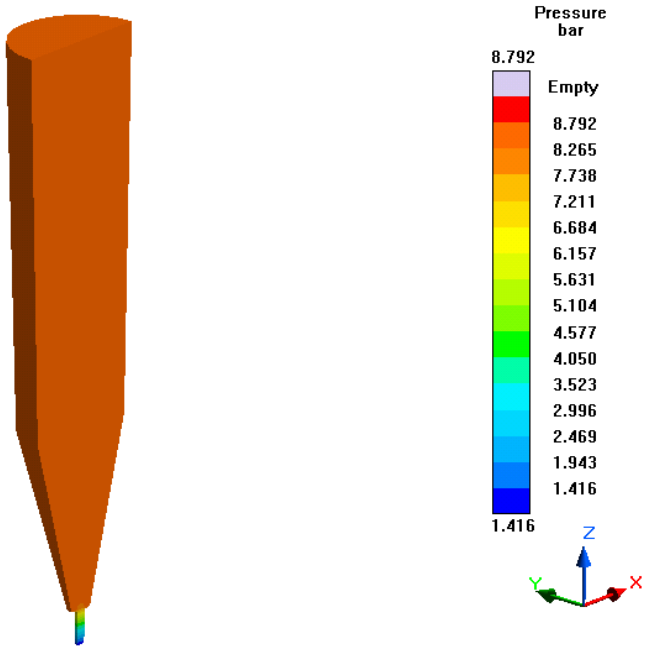

Figure 731- Simulation 16 (LLNL 300 Micron), Pressure

Fraction Solid

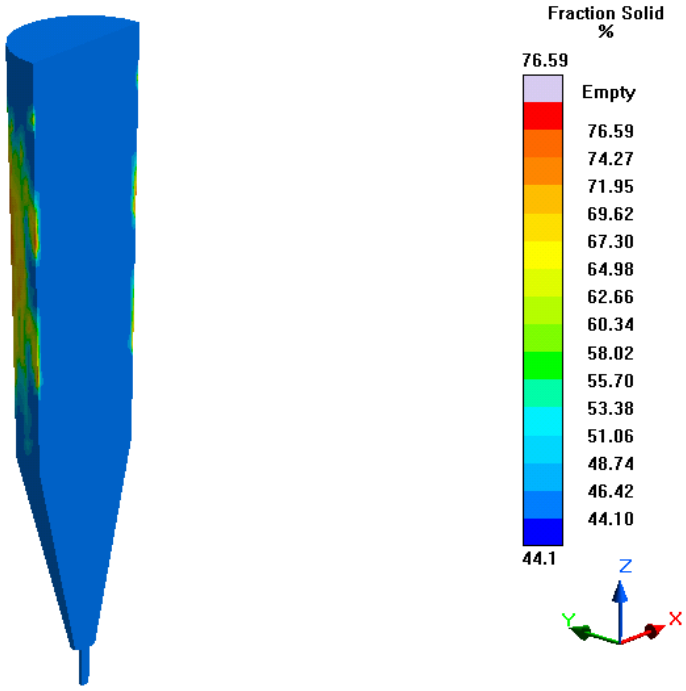

Figure 732- Simulation 16 (LLNL 300 Micron), Fraction Solid

Cooling Rate

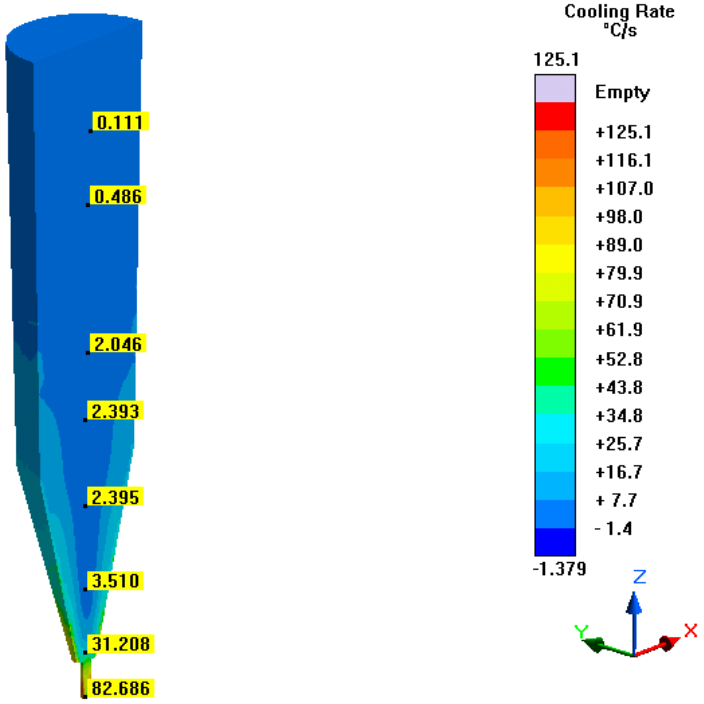

Figure 733- Simulation 16 (LLNL 300 Micron), Cooling Rate

Shear Heating

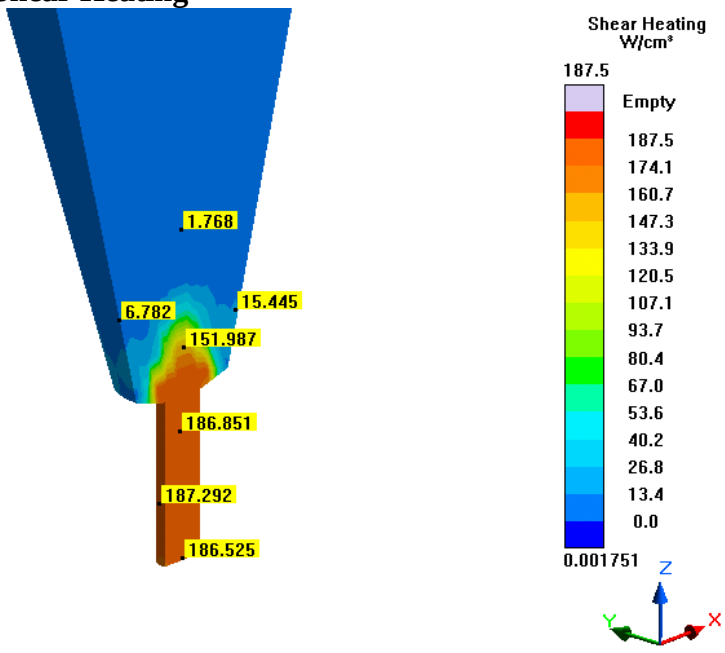

Figure 734- Simulation 16 (LLNL 300 Micron), Shear Heating

Shear Rate

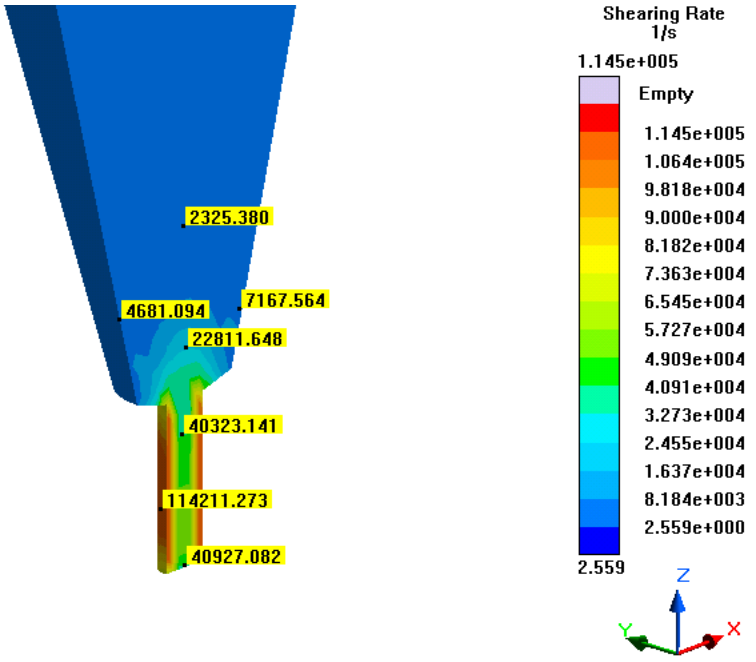

Figure 735- Simulation 16 (LLNL 300 Micron), Shear Rate

Shear Stress

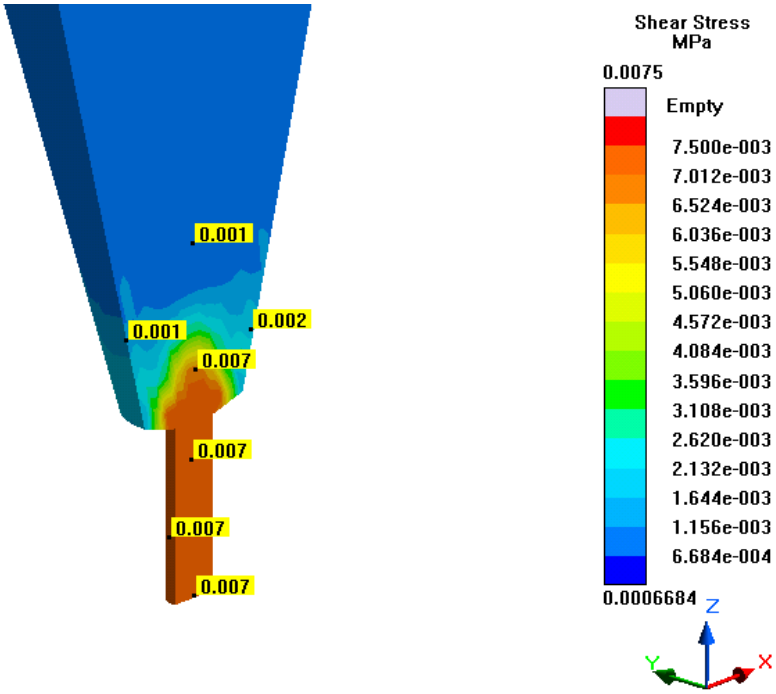

Figure 736- Simulation 16 (LLNL 300 Micron), Shear Stress

Temperature

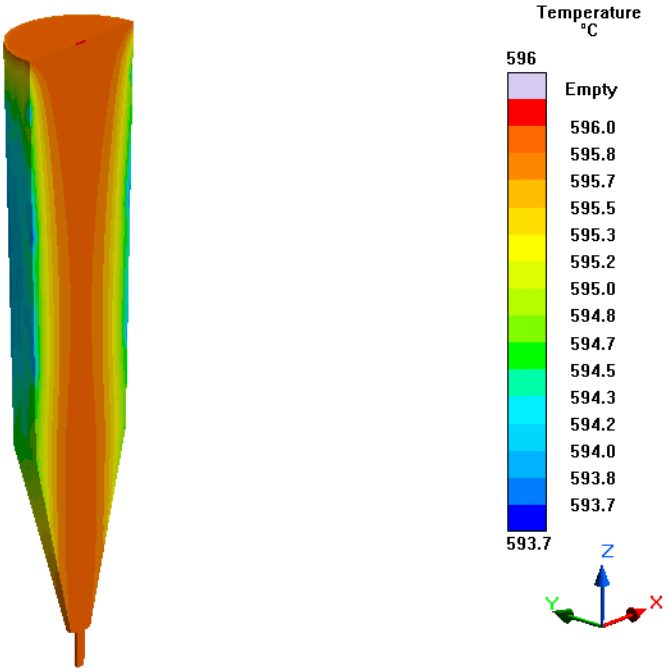

Figure 737- Simulation 16 (LLNL 300 Micron), Temperature

Simulation 17- LLNL 200 Micron (0.25 s)

Parameters

Geometry	
Inlet Diameter	0.20 mm (200 microns)
Outlet Diameter	0.20 mm (200 microns)
Nozzle Height	1 mm
Nozzle Angle	90°
Tank Height	18.25 mm

Mesh Parameters	
Accuracy (Refinement Factor)	3
Minimum Wall Thickness (Nozzle)	0.09 mm
Minimum Element Size (Nozzle)	0.03 mm
Minimum Wall Thickness (Part)	0.24 mm
Minimum Element Size (Part)	0.08 mm
Smoothing	2
Ratio	2
Coarsening Loops	1
Minimal Accuracy After Coarsening	5

Mesh Properties	
Control Volumes (X Direction)	578
Control Volumes (Y Direction)	578
Control Volumes (Z Direction)	694
Composed Part Cells	156,001
Total Part Cells	693,572
Blocked Cells	0

Process Definitions	
Material Temperature	594 C
Fraction Solid	44.1-82.09 %
Close Mold Time	0 s
Fill Time	0.25 s
Hold Time After Filling	1 s

Table 119- Simulation 17 (LLNL 200 Micron, 0.25 s), Parameters

Velocity

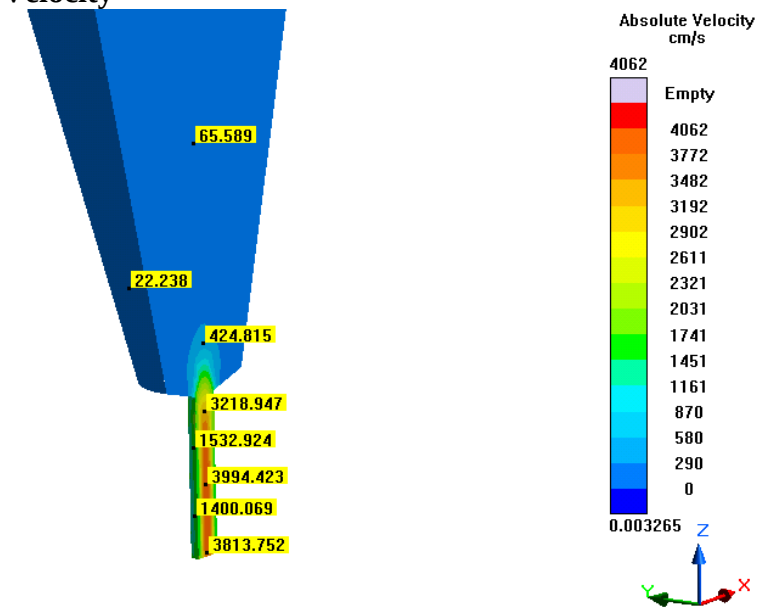

Figure 738- Simulation 17 (LLNL 200 Micron, 0.25 s), Velocity

Viscosity

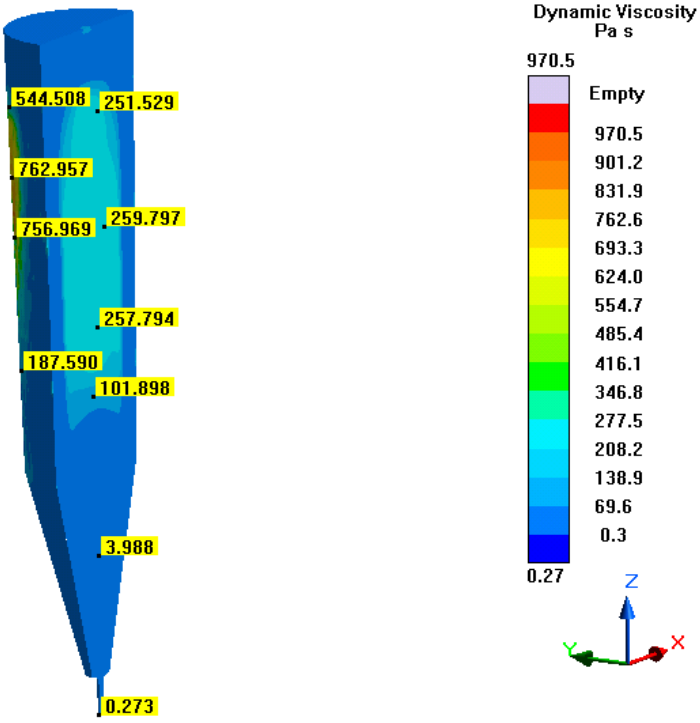

Figure 739- Simulation 17 (LLNL 200 Micron, 0.25 s), Viscosity

Pressure

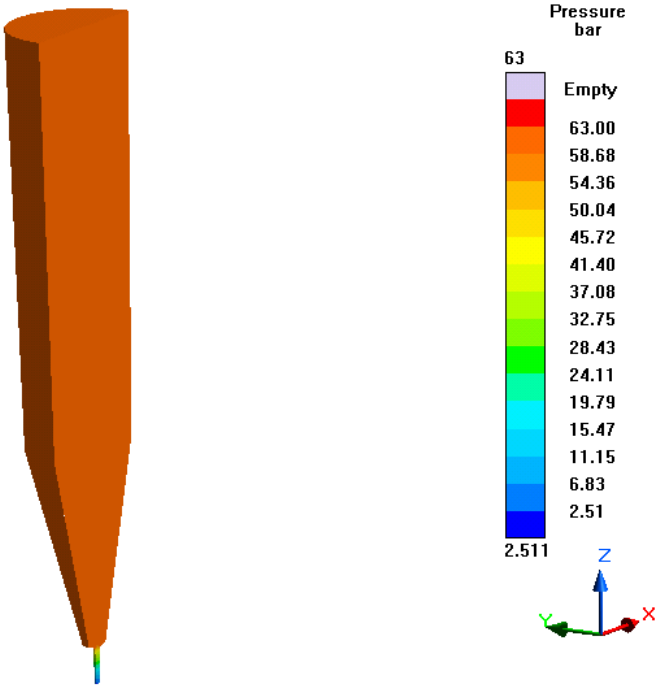

Figure 740- Simulation 17 (LLNL 200 Micron, 0.25 s), Pressure

Fraction Solid

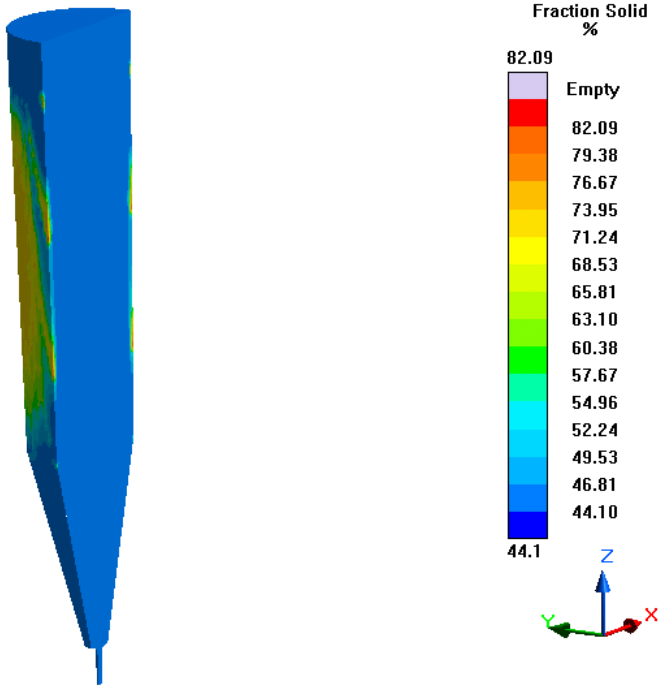

Figure 741- Simulation 17 (LLNL 200 Micron, 0.25 s), Fraction Solid

Cooling Rate

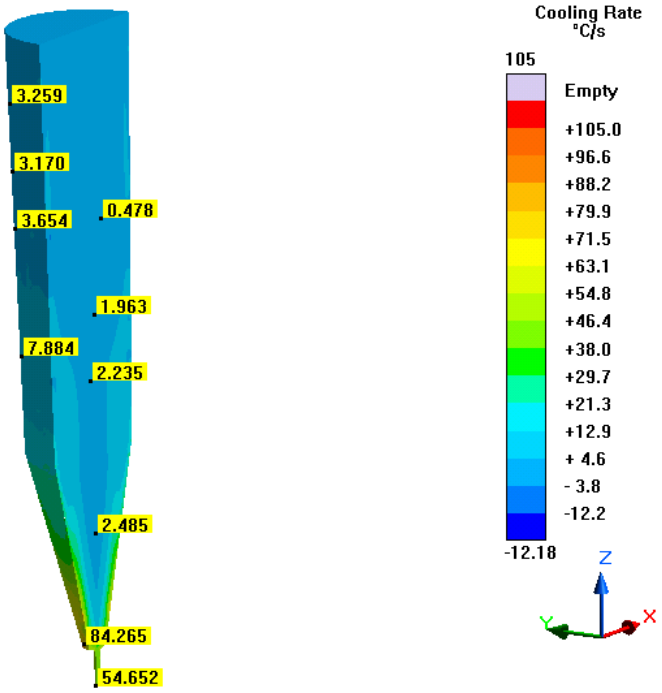

Figure 742- Simulation 17 (LLNL 200 Micron, 0.25 s), Cooling Rate

Shear Heating

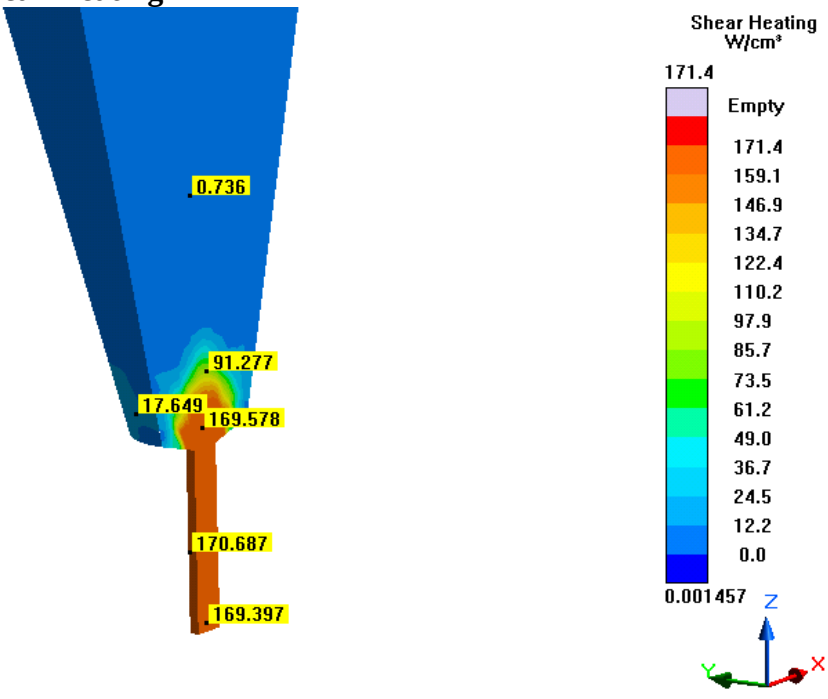

Figure 743- Simulation 17 (LLNL 200 Micron, 0.25 s), Shear Heating

Shear Rate

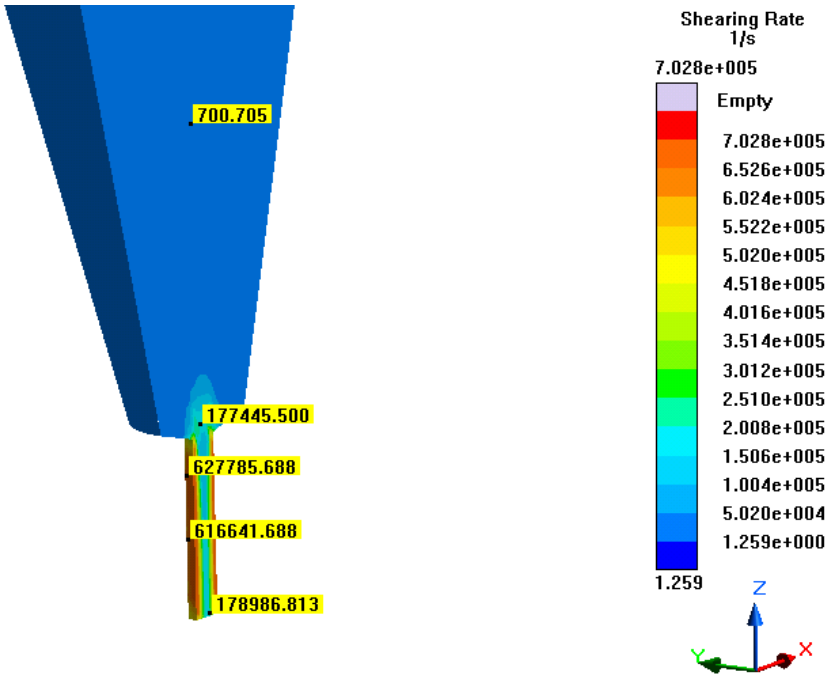

Figure 744- Simulation 17 (LLNL 200 Micron, 0.25 s), Shear Rate

Shear Stress

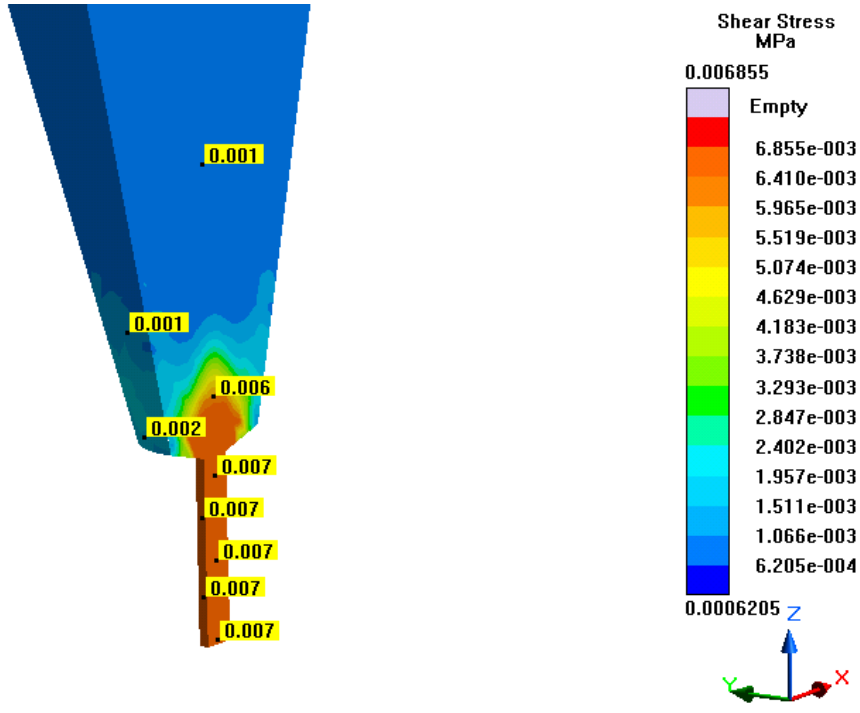

Figure 745- Simulation 17 (LLNL 200 Micron, 0.25 s), Shear Stress

Temperature

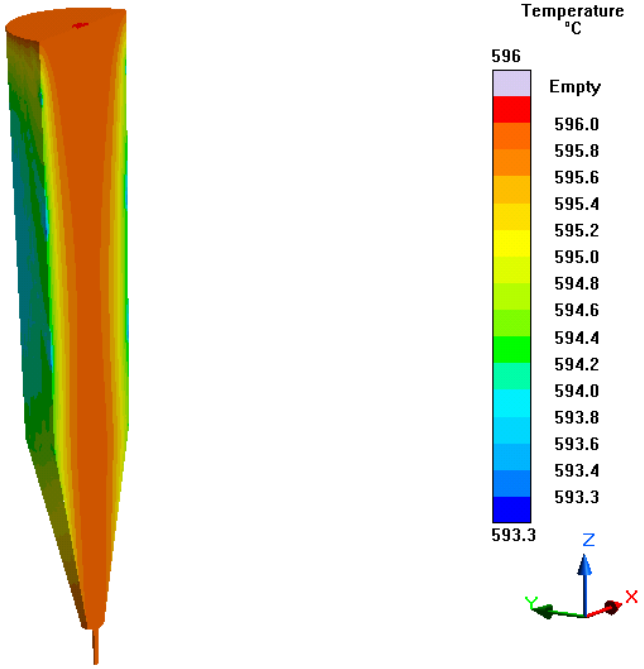

Figure 746- Simulation 17 (LLNL 200 Micron, 0.25 s), Temperature

Simulation 18- LLNL 100 Micron

Parameters

Geometry	
Inlet Diameter	0.10 mm (100 microns)
Outlet Diameter	0.10 mm (100 microns)
Nozzle Height	1 mm
Nozzle Angle	90°
Tank Height	18.25 mm

Mesh Parameters	
Accuracy (Refinement Factor)	3
Minimum Wall Thickness (Nozzle)	0.06 mm
Minimum Element Size (Nozzle)	0.02 mm
Minimum Wall Thickness (Part)	0.18 mm
Minimum Element Size (Part)	0.06 mm
Smoothing	2
Ratio	2
Coarsening Loops	1
Minimal Accuracy After Coarsening	5

Mesh Properties	
Control Volumes (X Direction)	848
Control Volumes (Y Direction)	848
Control Volumes (Z Direction)	1086
Composed Part Cells	387,677
Total Part Cells	2,119,197
Blocked Cells	0

Process Definitions	
Material Temperature	594 C
Fraction Solid	44.1-76.62 %
Close Mold Time	0 s
Fill Time	0.25 s
Hold Time After Filling	1 s

Table 120- Simulation 18 (LLNL 100 Micron), Parameters

Velocity

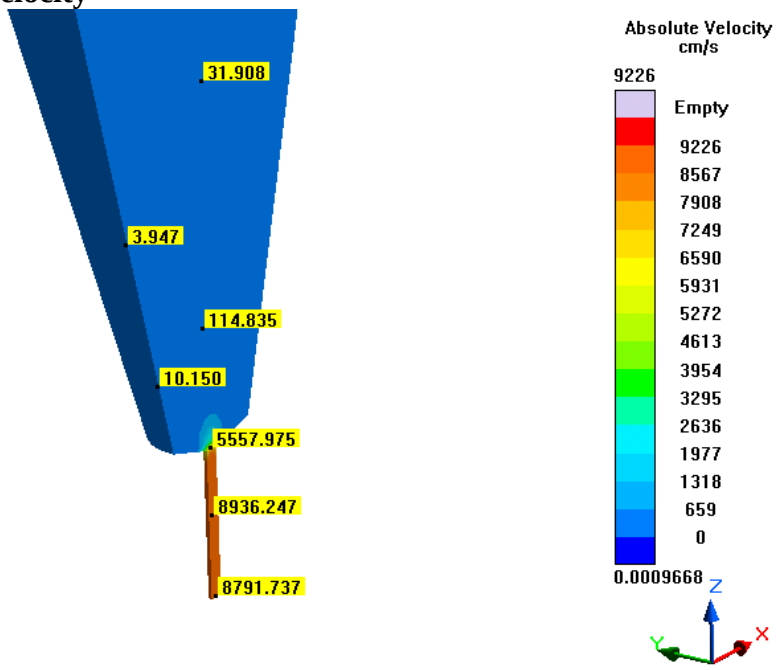

Figure 747- Simulation 18 (LLNL 100 Micron), Velocity

Viscosity

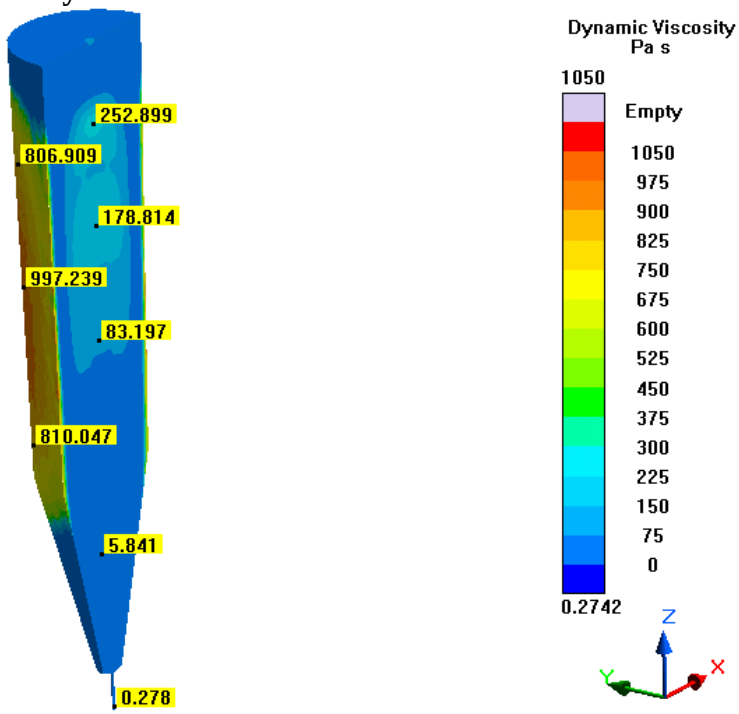

Figure 748- Simulation 18 (LLNL 100 Micron), Viscosity

Pressure

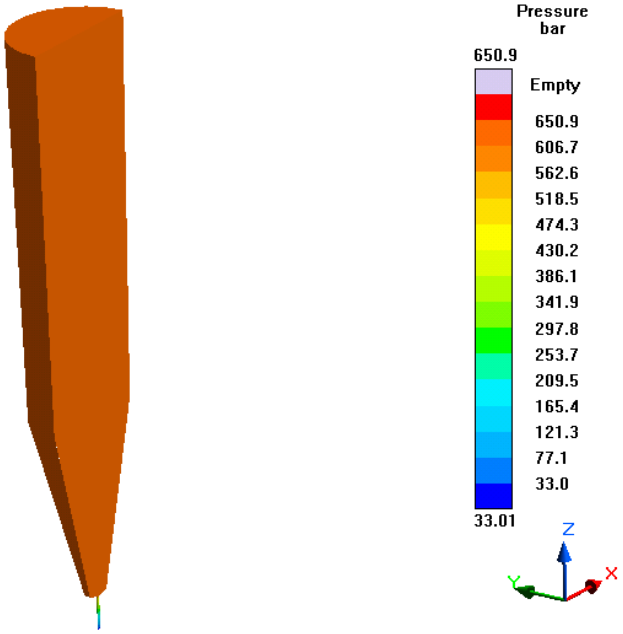

Figure 749- Simulation 18 (LLNL 100 Micron), Pressure

Fraction Solid

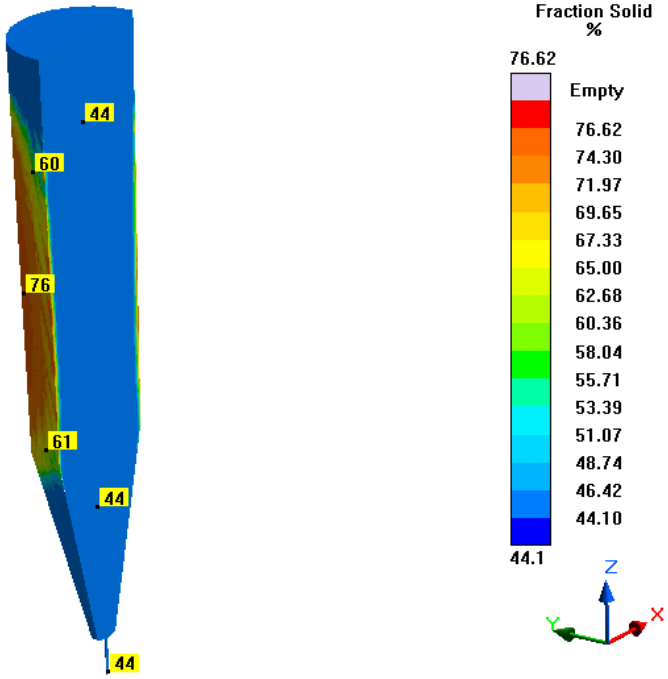

Figure 750- Simulation 18 (LLNL 100 Micron), Fraction Solid

Cooling Rate

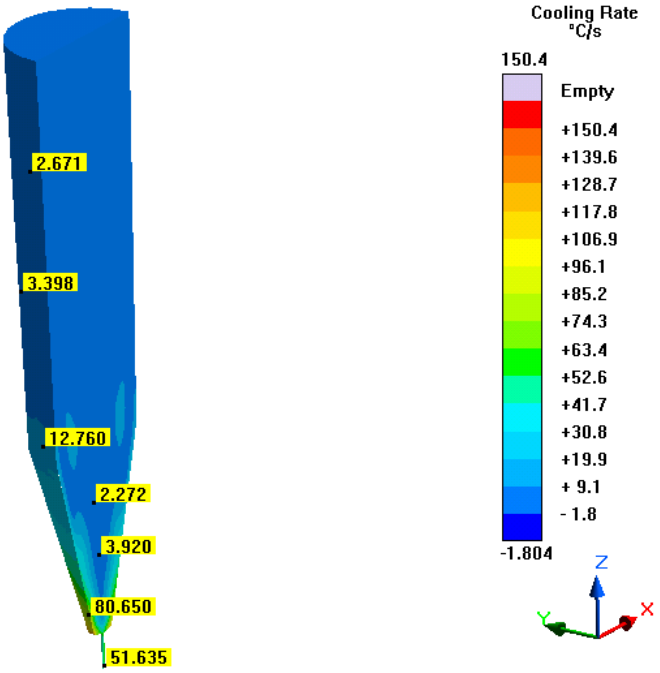

Figure 751- Simulation 18 (LLNL 100 Micron), Cooling Rate

Shear Heating

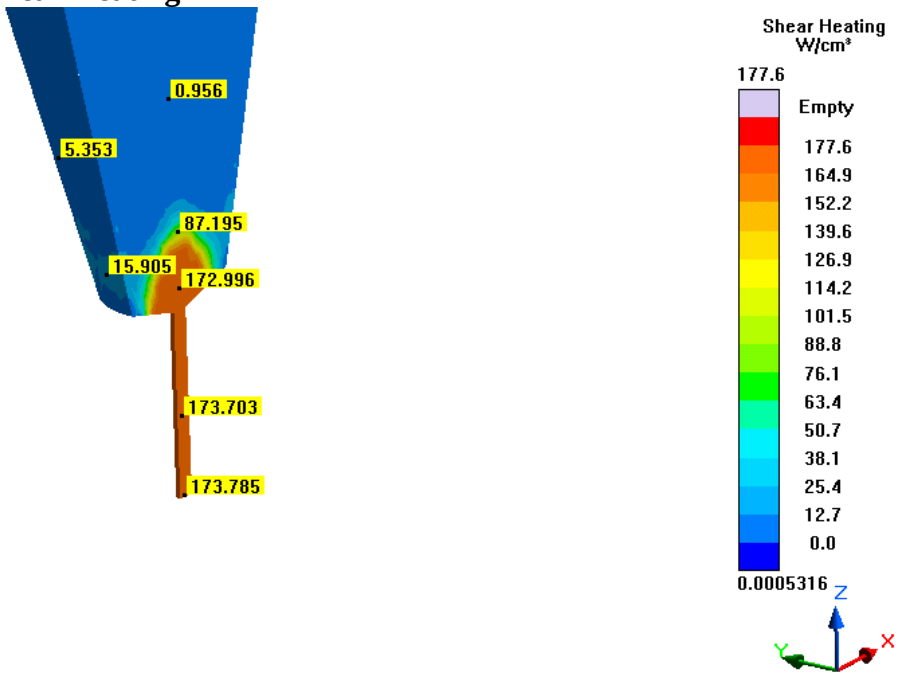

Figure 752- Simulation 18 (LLNL 100 Micron), Shear Heating

Shear Rate

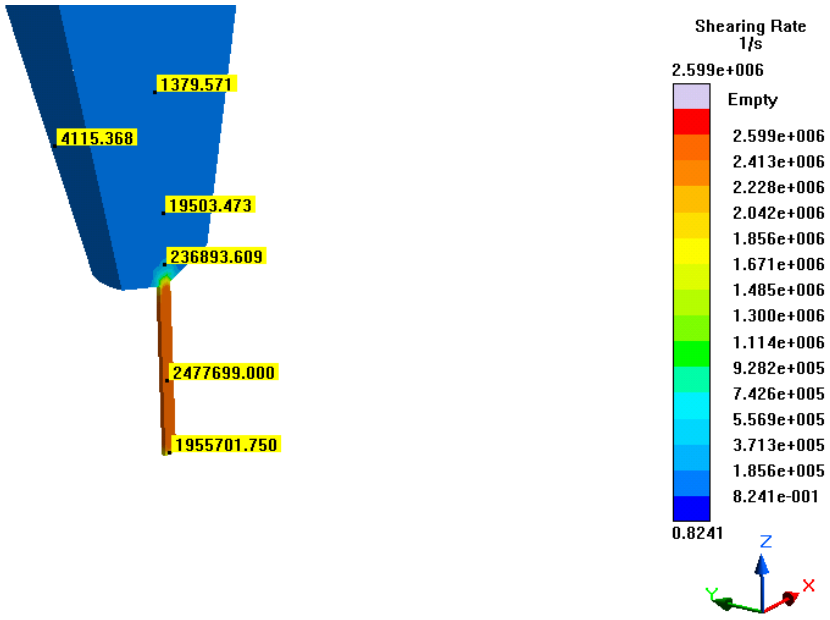

Figure 753- Simulation 18 (LLNL 100 Micron), Shear Rate

Shear Stress

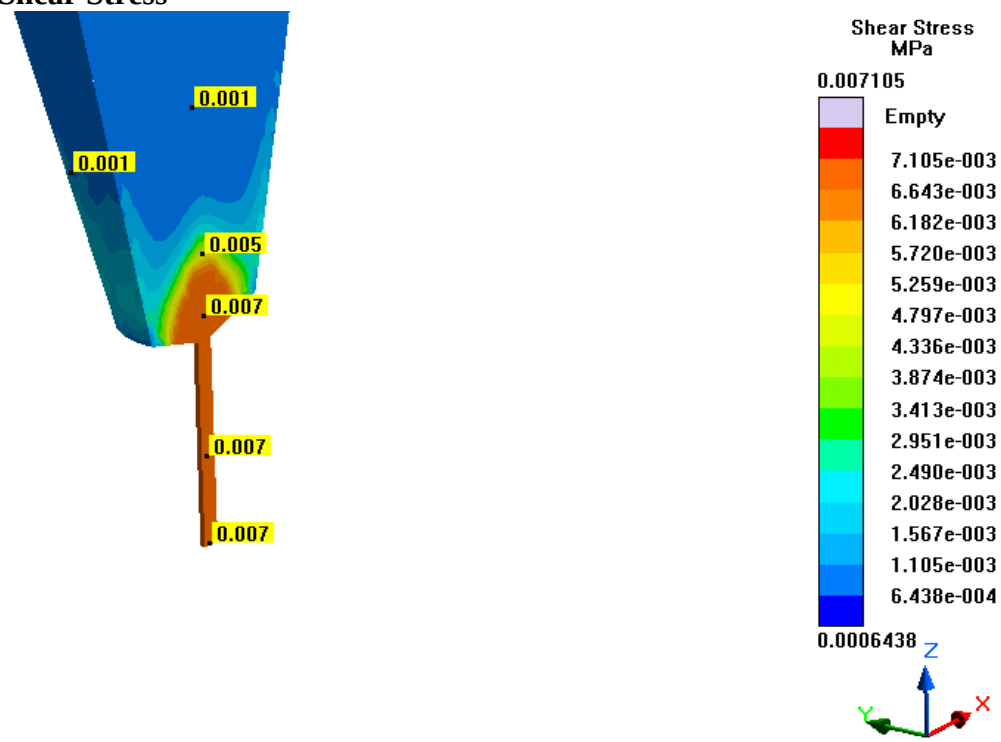

Figure 754- Simulation 18 (LLNL 100 Micron), Shear Stress

Temperature

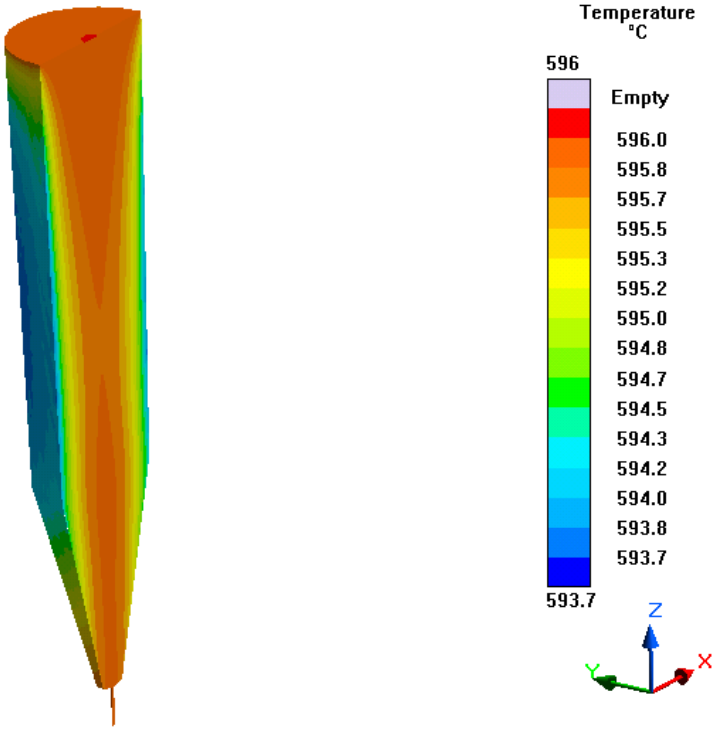

Figure 755- Simulation 18 (LLNL 100 Micron), Temperature

Simulation 19- LLNL 50 Micron (0.25 s)

Parameters

Geometry	
Inlet Diameter	0.05 mm (50 microns)
Outlet Diameter	0.05 mm (50 microns)
Nozzle Height	0.30 mm
Nozzle Angle	90°
Tank Height	18.25 mm

Mesh Parameters	
Accuracy (Refinement Factor)	3
Minimum Wall Thickness (Nozzle)	0.06 mm
Minimum Element Size (Nozzle)	0.02 mm
Minimum Wall Thickness (Part)	0.42 mm
Minimum Element Size (Part)	0.14 mm
Smoothing	2
Ratio	2
Coarsening Loops	1
Minimal Accuracy After Coarsening	5

Mesh Properties	
Control Volumes (X Direction)	942
Control Volumes (Y Direction)	950
Control Volumes (Z Direction)	1136
Composed Part Cells	526,591
Total Part Cells	2,806,167
Blocked Cells	0

Process Definitions	
Material Temperature	594 C
Fraction Solid	44.1-77.1 %
Close Mold Time	0 s
Fill Time	0.25 s
Hold Time After Filling	1 s

Table 121- Simulation 19 (LLNL 50 Micron, 0.25 s), Parameters

Notes

- Appears behavior at the tip wasn't included in the simulation (extremely low pressure drop and no cooling rate)
- Presence of 32 two-layer elements may have caused the stress and strain calculations to be inaccurate

Velocity

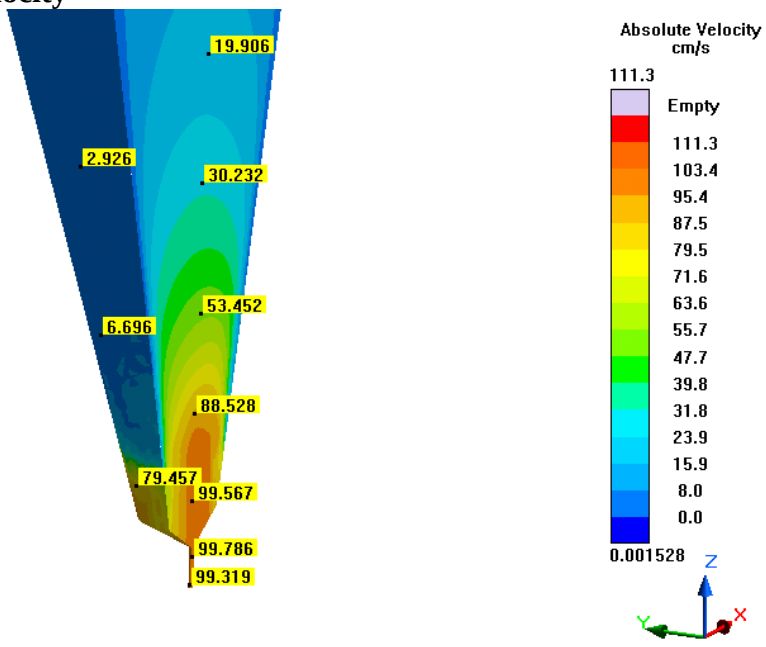

Figure 756- Simulation 19 (LLNL 50 Micron, 0.25 s), Velocity

Viscosity

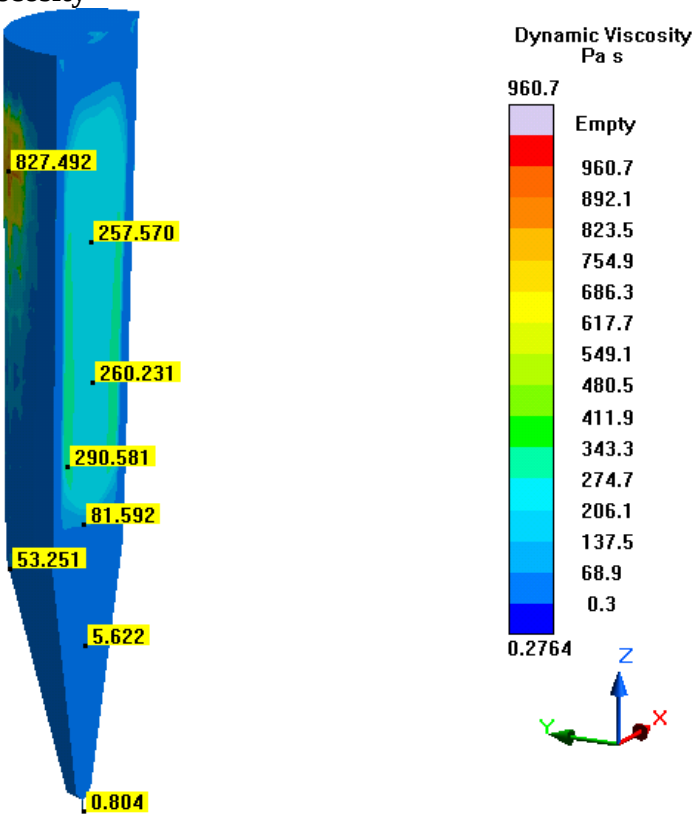

Figure 757- Simulation 19 (LLNL 50 Micron, 0.25 s), Viscosity

Pressure

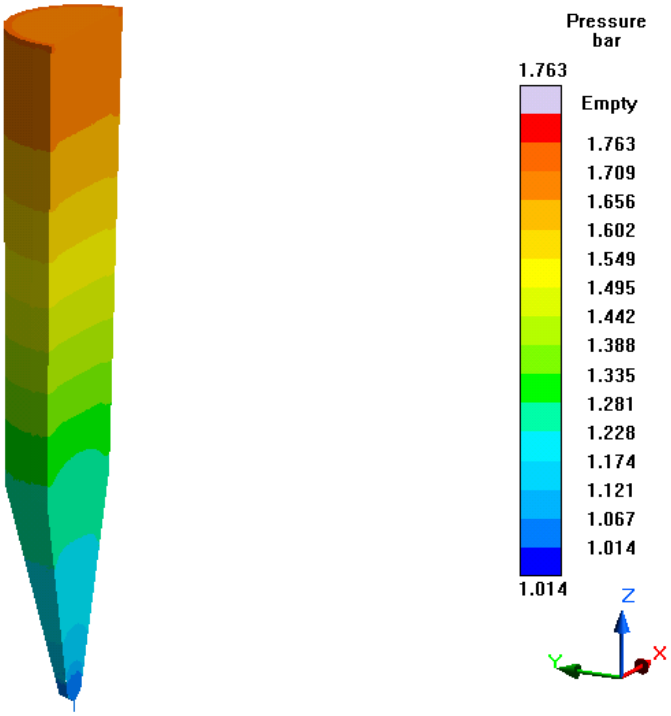

Figure 758- Simulation 19 (LLNL 50 Micron, 0.25 s), Pressure

Fraction Solid

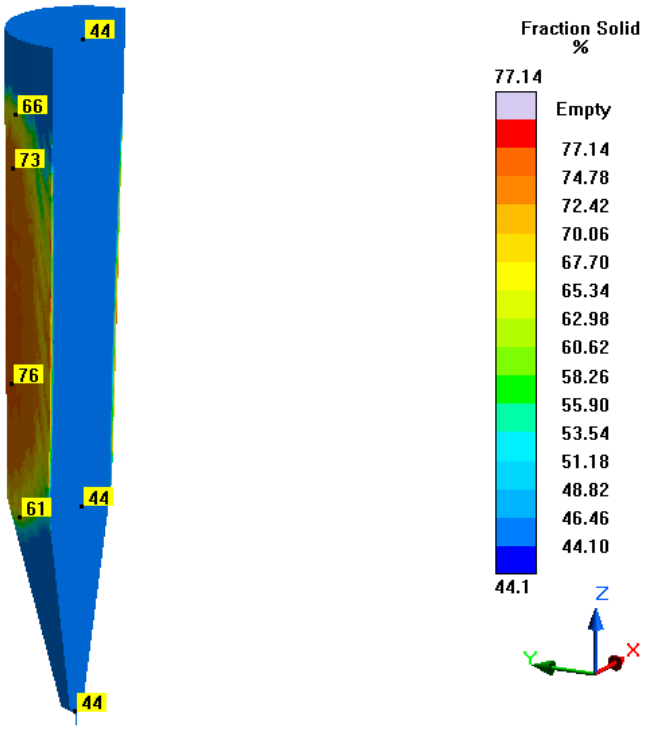

Figure 759- Simulation 19 (LLNL 50 Micron, 0.25 s), Cooling Rate

Cooling Rate

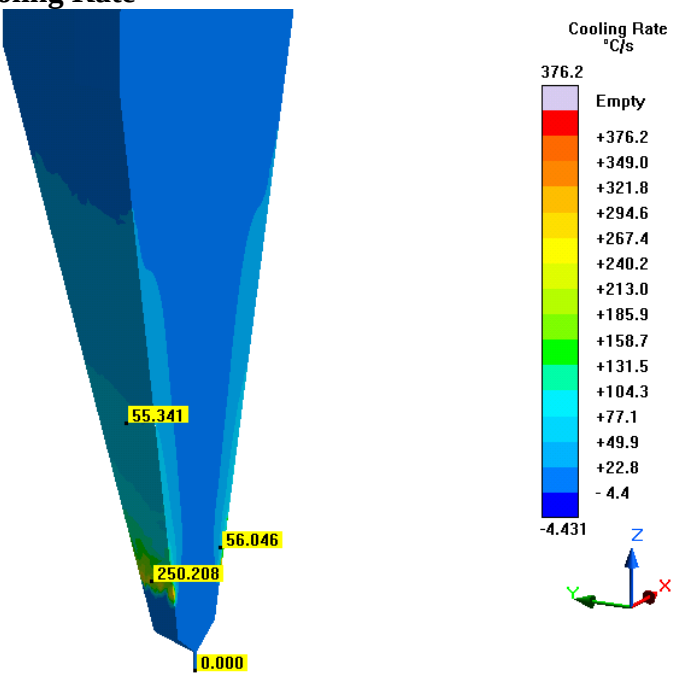

Figure 760- Simulation 19 (LLNL 50 Micron, 0.25 s), Cooling Rate

Temperature

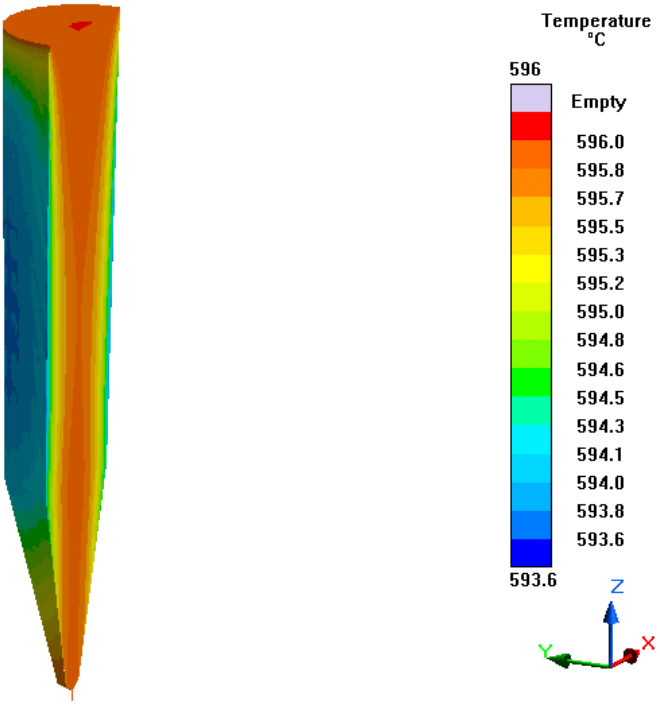

Figure 761- Simulation 19 (LLNL 50 Micron, 0.25 s), Temperature

Simulation 20- LLNL 50 Micron (0.3125 s)

Parameters

Geometry	
Inlet Diameter	0.05 mm (50 microns)
Outlet Diameter	0.05 mm (50 microns)
Nozzle Height	0.30 mm
Nozzle Angle	90°
Tank Height	18.25 mm

Mesh Parameters	
Accuracy (Refinement Factor)	3
Minimum Wall Thickness (Nozzle)	0.06 mm
Minimum Element Size (Nozzle)	0.02 mm
Minimum Wall Thickness (Part)	0.42 mm
Minimum Element Size (Part)	0.14 mm
Smoothing	2
Ratio	2
Coarsening Loops	1
Minimal Accuracy After Coarsening	5

Mesh Properties	
Control Volumes (X Direction)	942
Control Volumes (Y Direction)	950
Control Volumes (Z Direction)	1136
Composed Part Cells	526,591
Total Part Cells	2,806,167
Blocked Cells	0

Process Definitions	
Material Temperature	594 C
Fraction Solid	44.1-79.27 %
Close Mold Time	0 s
Fill Time	0.3125 s
Hold Time After Filling	0.3125 s

Table 122- Simulation 20 (LLNL 50 Micron, 0.3125 s), Parameters

Notes

- Appears behavior at the tip wasn't included in the simulation (extremely low pressure drop and no cooling rate)
- Presence of 32 two-layer elements may have caused the stress and strain calculations to be inaccurate

Velocity

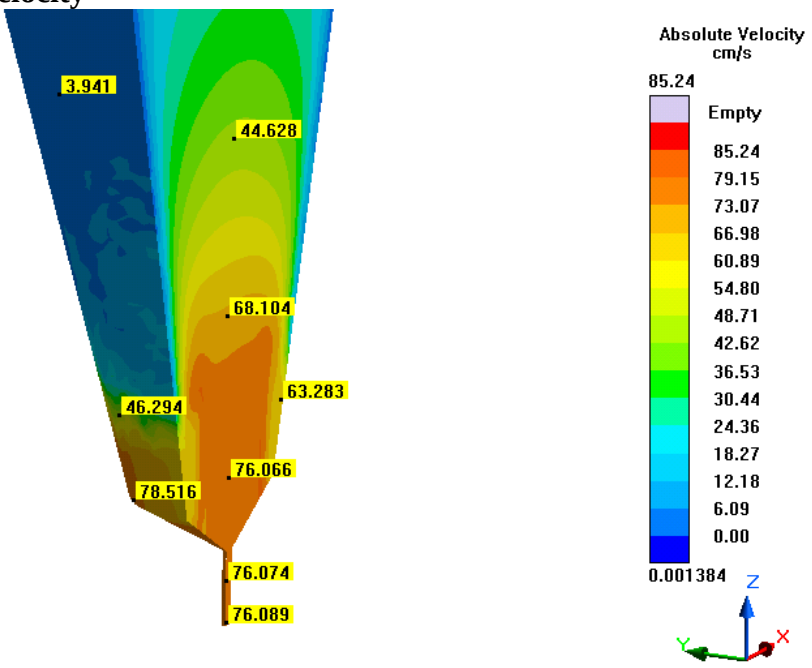

Figure 762- Simulation 20 (LLNL 50 Micron, 0.3125 s), Velocity

Viscosity

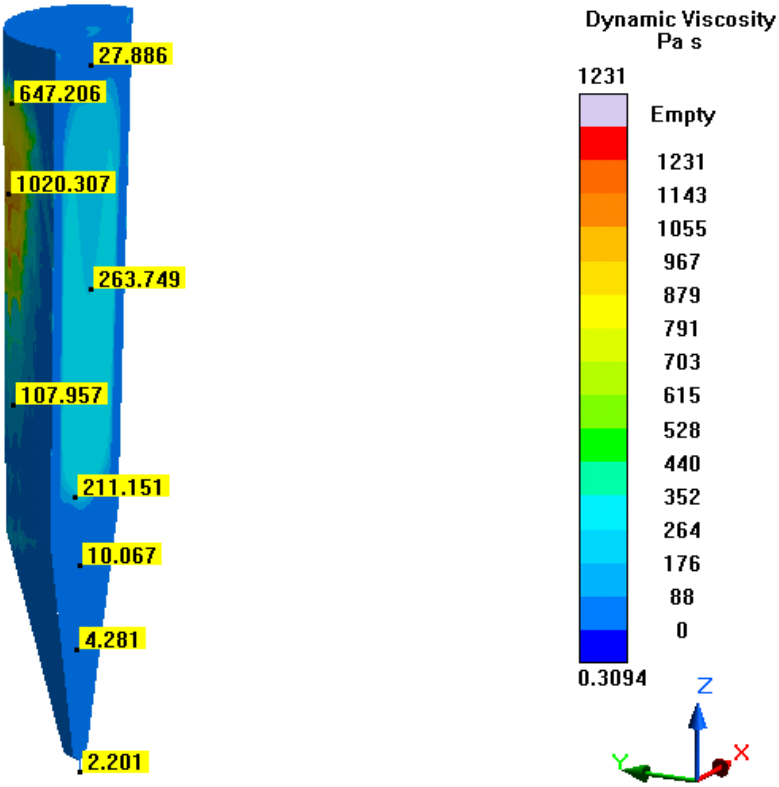

Figure 763- Simulation 20 (LLNL 50 Micron, 0.3125 s), Viscosity

Pressure

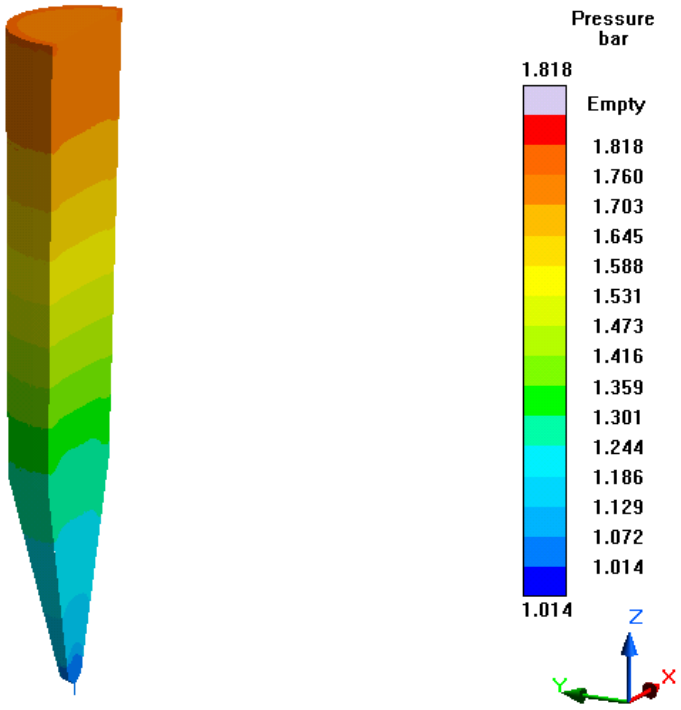

Figure 764- Simulation 20 (LLNL 50 Micron, 0.3125 s), Pressure

Fraction Solid

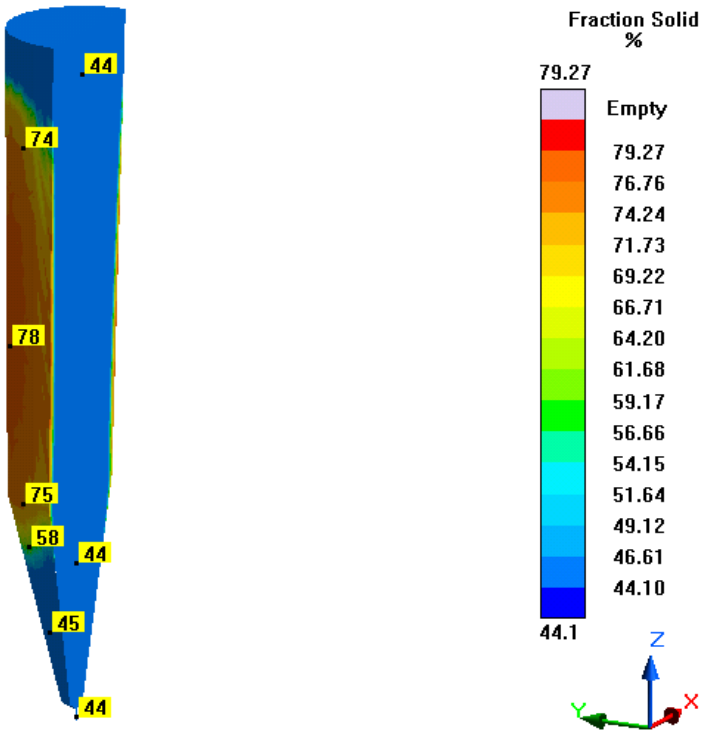

Figure 765- Simulation 20 (LLNL 50 Micron, 0.3125 s), Fraction Solid

Temperature

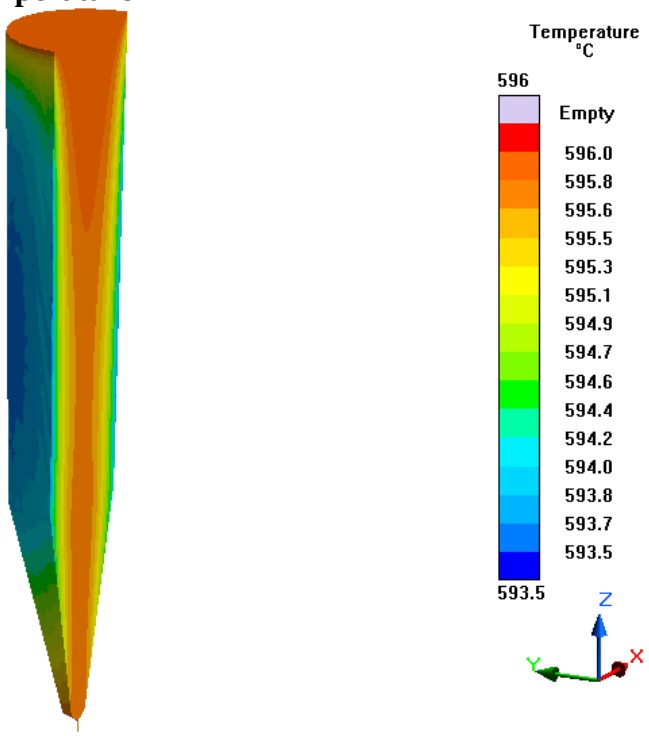

Figure 766- Simulation 20 (LLNL 50 Micron, 0.3125 s), Temperature

Simulation 21- LLNL 50 Micron (1 s)

Parameters

Geometry	
Inlet Diameter	0.05 mm (50 microns)
Outlet Diameter	0.05 mm (50 microns)
Nozzle Height	0.30 mm
Nozzle Angle	90°
Tank Height	18.25 mm

Mesh Parameters	
Accuracy (Refinement Factor)	3
Minimum Wall Thickness (Nozzle)	0.06 mm
Minimum Element Size (Nozzle)	0.02 mm
Minimum Wall Thickness (Part)	0.42 mm
Minimum Element Size (Part)	0.14 mm
Smoothing	2
Ratio	2
Coarsening Loops	1
Minimal Accuracy After Coarsening	5

Mesh Properties	
Control Volumes (X Direction)	942
Control Volumes (Y Direction)	950
Control Volumes (Z Direction)	1136
Composed Part Cells	526,591
Total Part Cells	2,806,167
Blocked Cells	0

Process Definitions	
Material Temperature	594 C
Fraction Solid	44.1-79.27 %
Close Mold Time	0 s
Fill Time	1 s
Hold Time After Filling	1 s

Table 123- Simulation 21 (LLNL 50 Micron, 1 s), Parameters

Notes

- Appears behavior at the tip wasn't included in the simulation (extremely low pressure drop and no cooling rate)
- Presence of 32 two-layer elements may have caused the stress and strain calculations to be inaccurate

Velocity

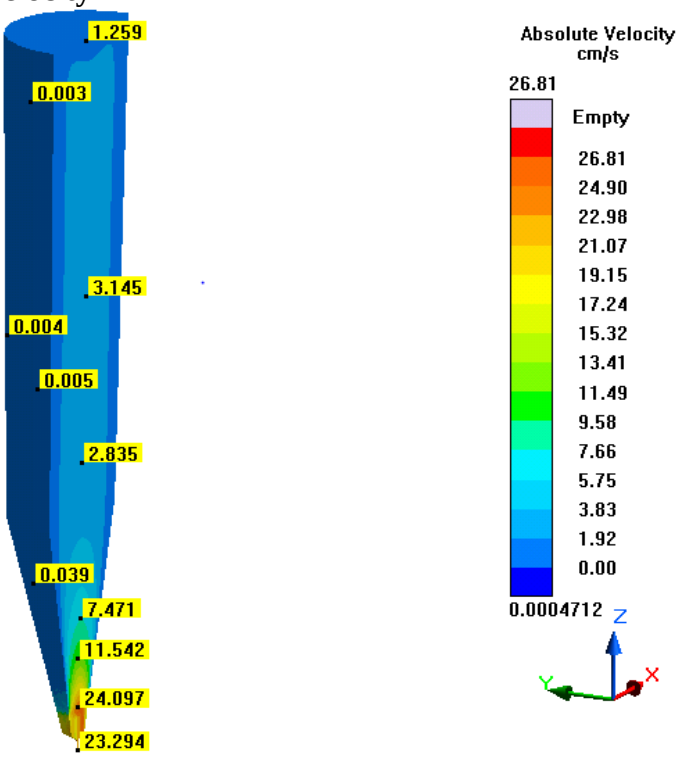

Figure 767- Simulation 21 (LLNL 50 Micron, 1 s), Velocity

Viscosity

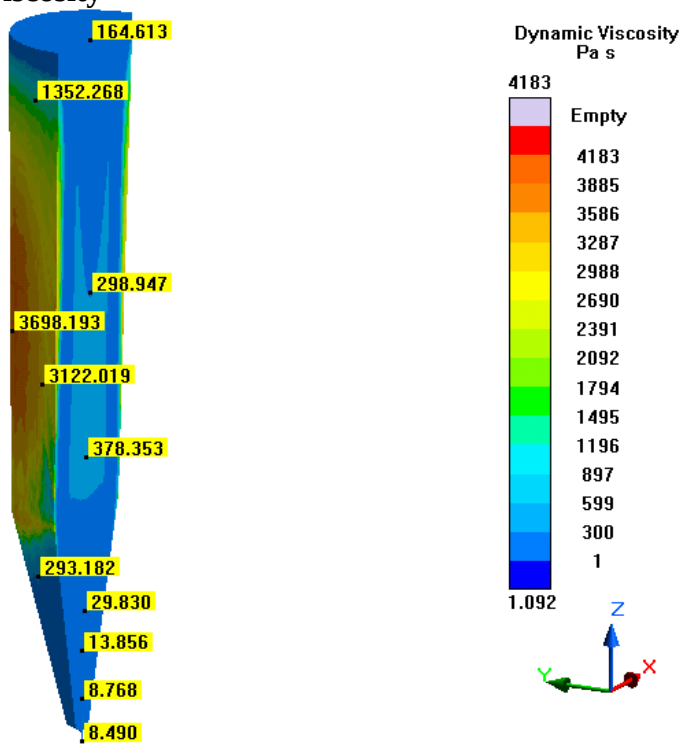

Figure 768- Simulation 21 (LLNL 50 Micron, 1 s), Viscosity

Pressure

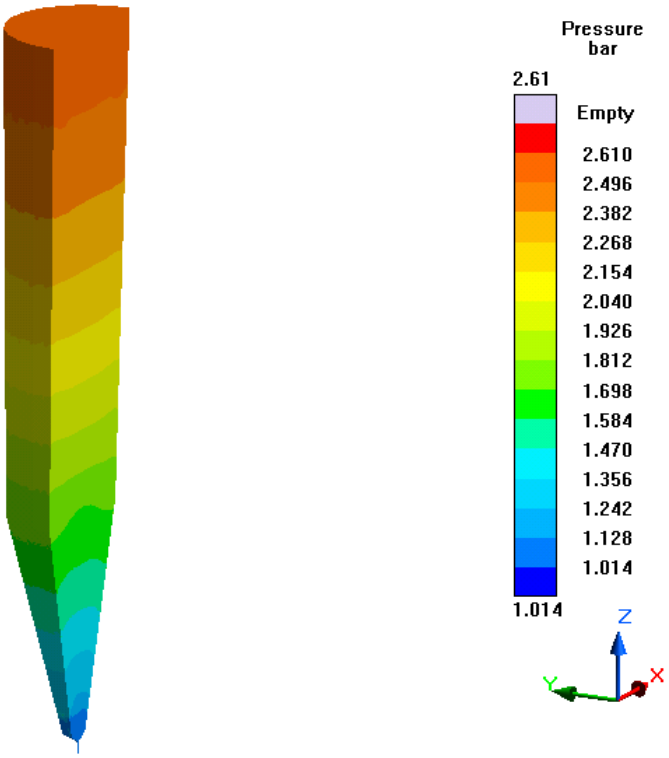

Figure 769- Simulation 21 (LLNL 50 Micron, 1 s), Pressure

Fraction Solid

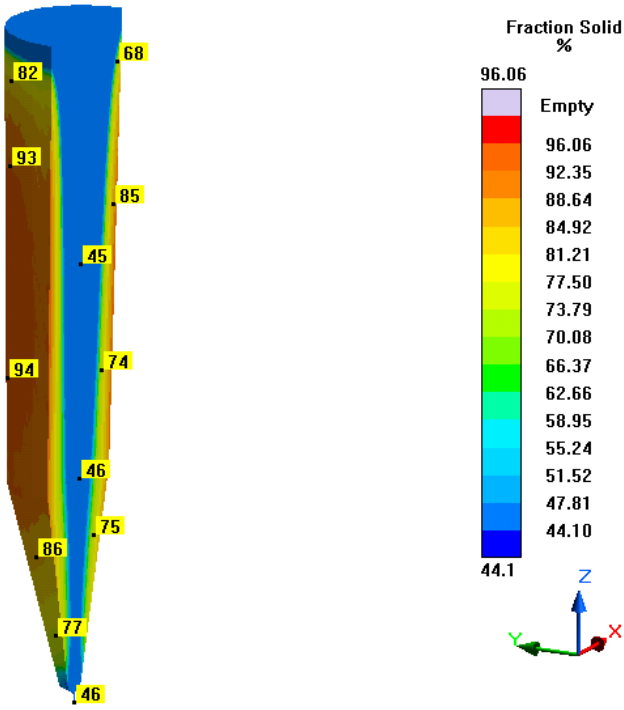

Figure 770- Simulation 21 (LLNL 50 Micron, 1 s), Fraction Solid

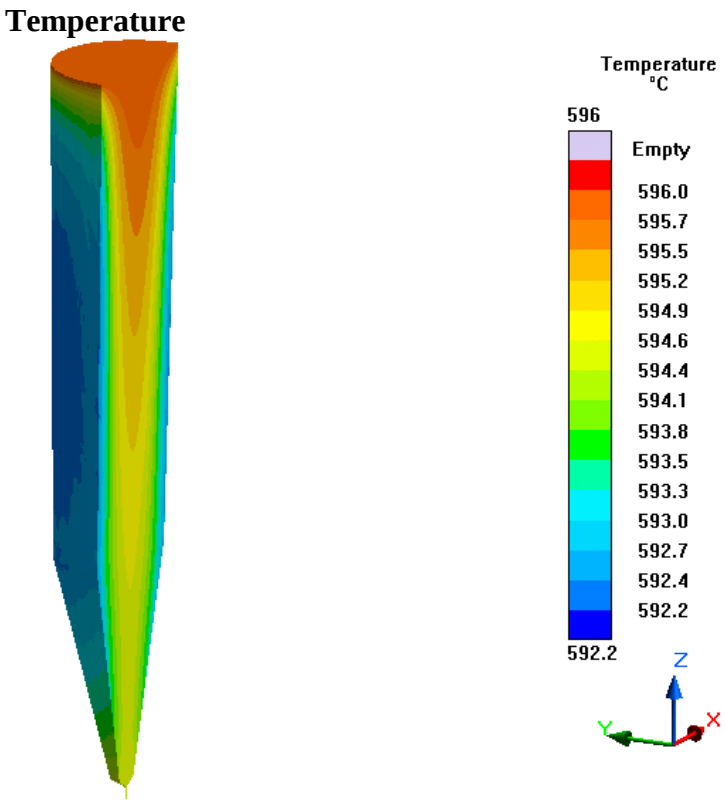

Figure 771- Simulation 21 (LLNL 50 Micron, 1 s), Temperature

Simulation 22- LLNL 200 Micron (1 s)

Parameters

Geometry	
Inlet Diameter	0.20 mm (200 microns)
Outlet Diameter	0.20 mm (200 microns)
Nozzle Height	1 mm
Nozzle Angle	90°
Tank Height	18.25 mm

Mesh Parameters	
Accuracy (Refinement Factor)	3
Minimum Wall Thickness (Nozzle)	0.09 mm
Minimum Element Size (Nozzle)	0.03 mm
Minimum Wall Thickness (Part)	0.24 mm
Minimum Element Size (Part)	0.08 mm
Smoothing	2
Ratio	2
Coarsening Loops	1
Minimal Accuracy After Coarsening	5

Mesh Properties	
Control Volumes (X Direction)	578
Control Volumes (Y Direction)	578
Control Volumes (Z Direction)	694
Composed Part Cells	156,001
Total Part Cells	693,572
Blocked Cells	0

Process Definitions	
Material Temperature	594 C
Fraction Solid	44.1-98.08 %
Close Mold Time	0 s
Fill Time	1 s
Hold Time After Filling	2 s

Table 124- Simulation 22 (LLNL 200 Micron, 1 s), Parameters

Velocity

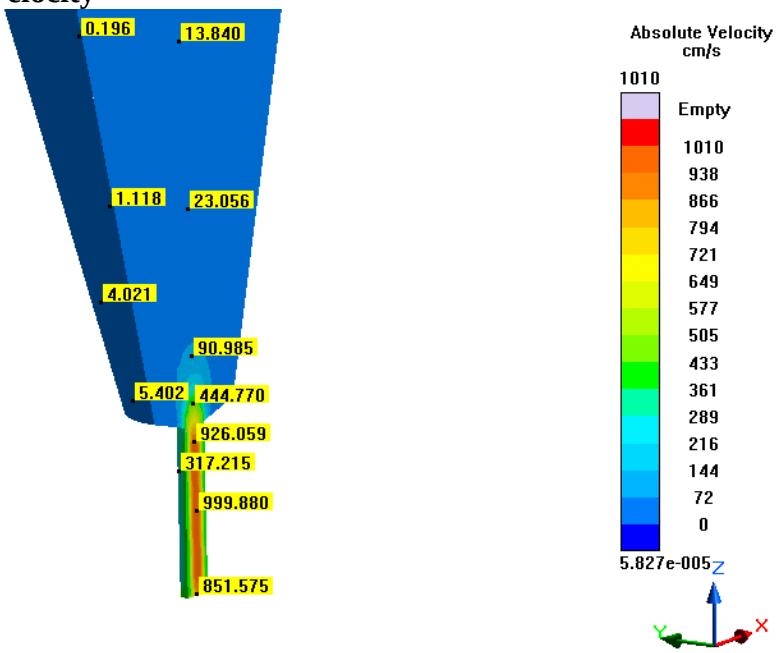

Figure 772- Simulation 22 (LLNL 200 Micron, 1 s), Velocity

Viscosity

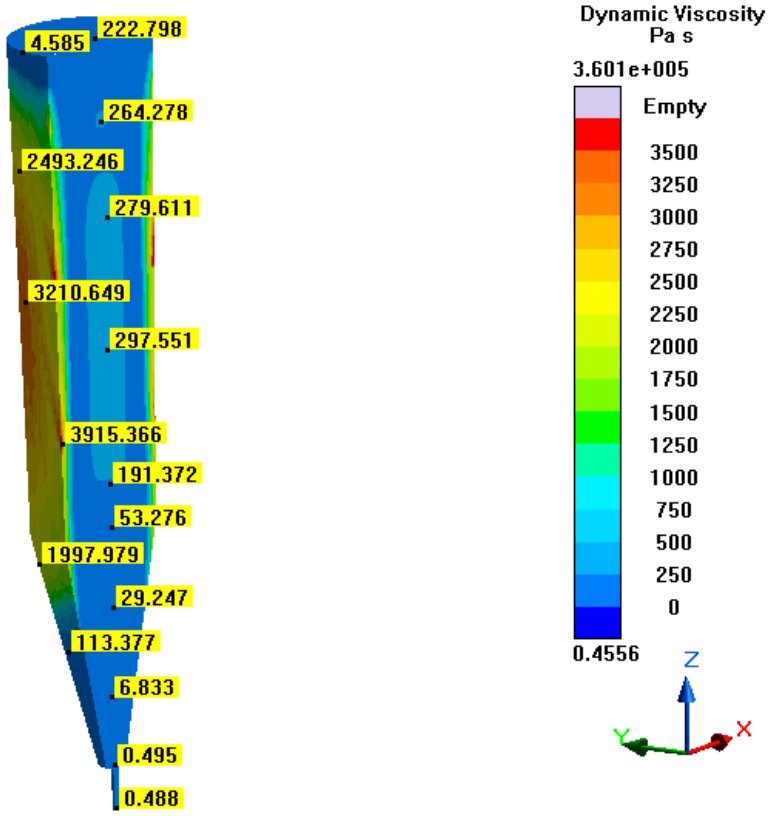

Figure 773- Simulation 22 (LLNL 200 Micron, 1 s), Viscosity

Pressure

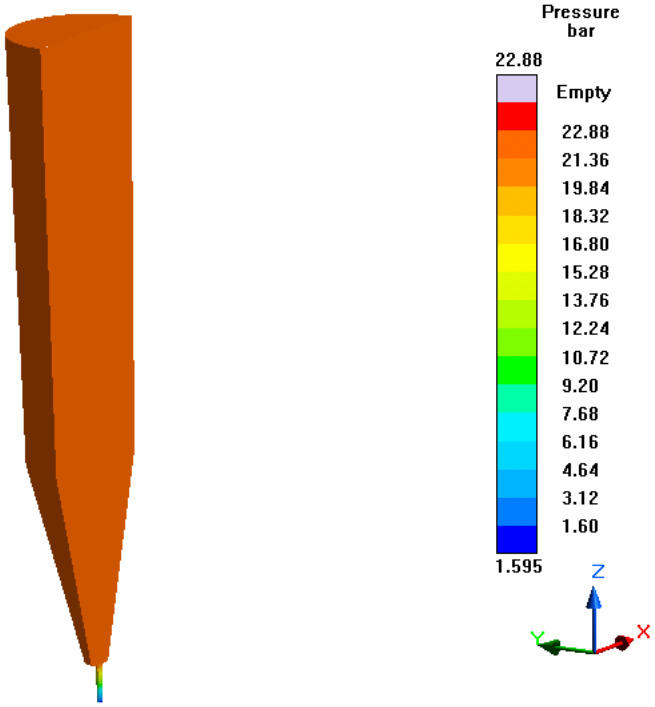

Figure 774- Simulation 22 (LLNL 200 Micron, 1 s), Pressure

Fraction Solid

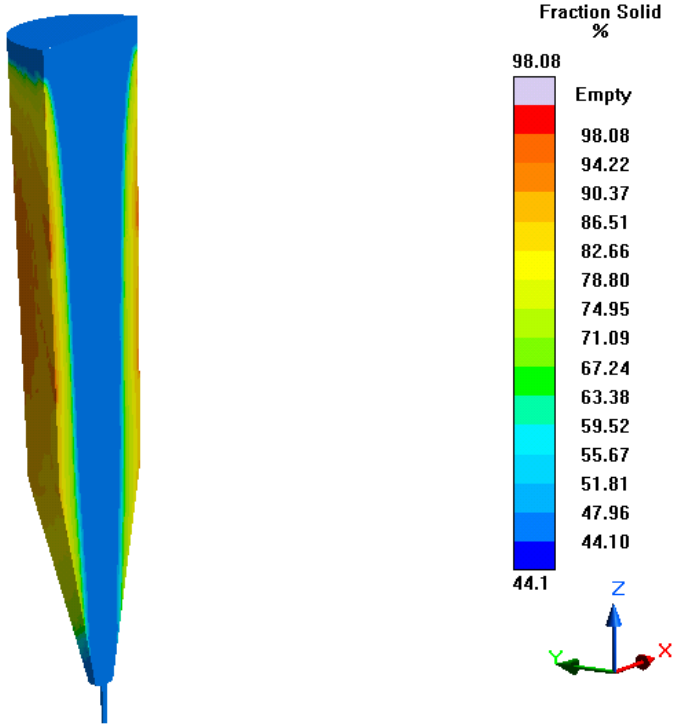

Figure 775- Simulation 22 (LLNL 200 Micron, 1 s), Fraction Solid

Cooling Rate

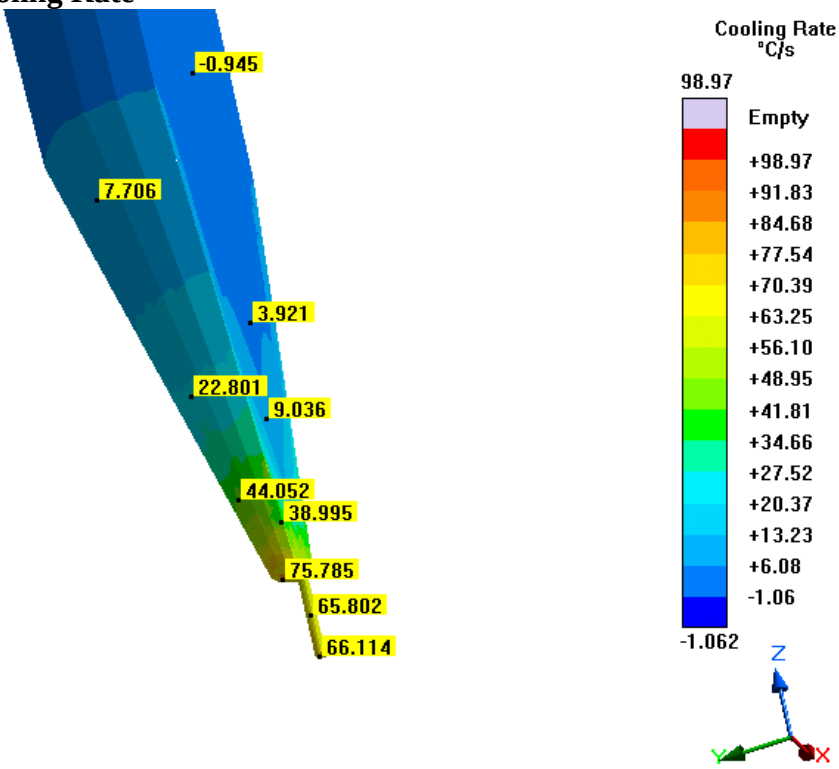

Figure 776- Simulation 22 (LLNL 200 Micron, 1 s), Cooling Rate

Shear Heating

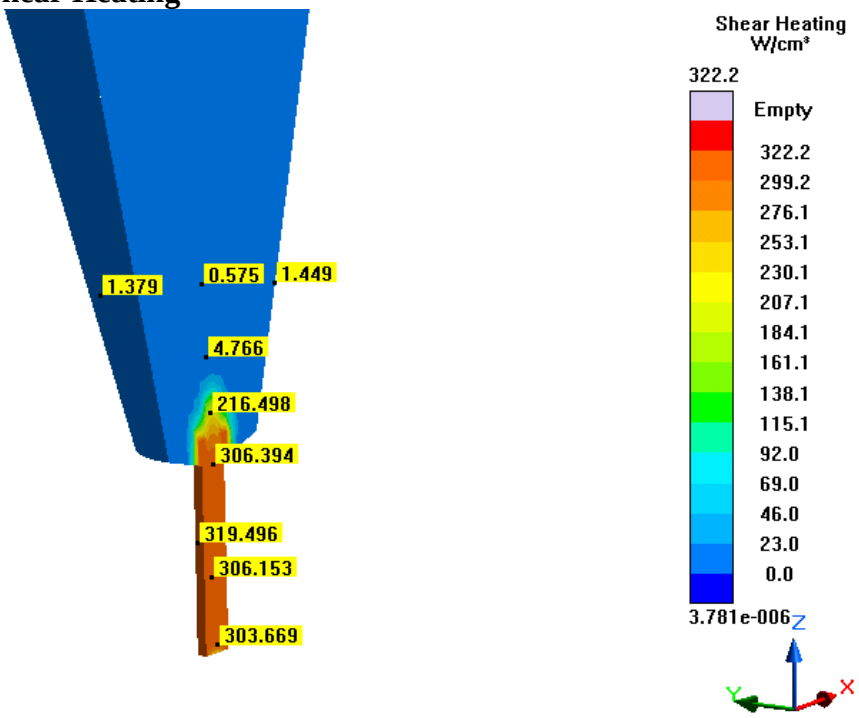

Figure 777- Simulation 22 (LLNL 200 Micron, 1 s), Shear Heating

Shear Rate

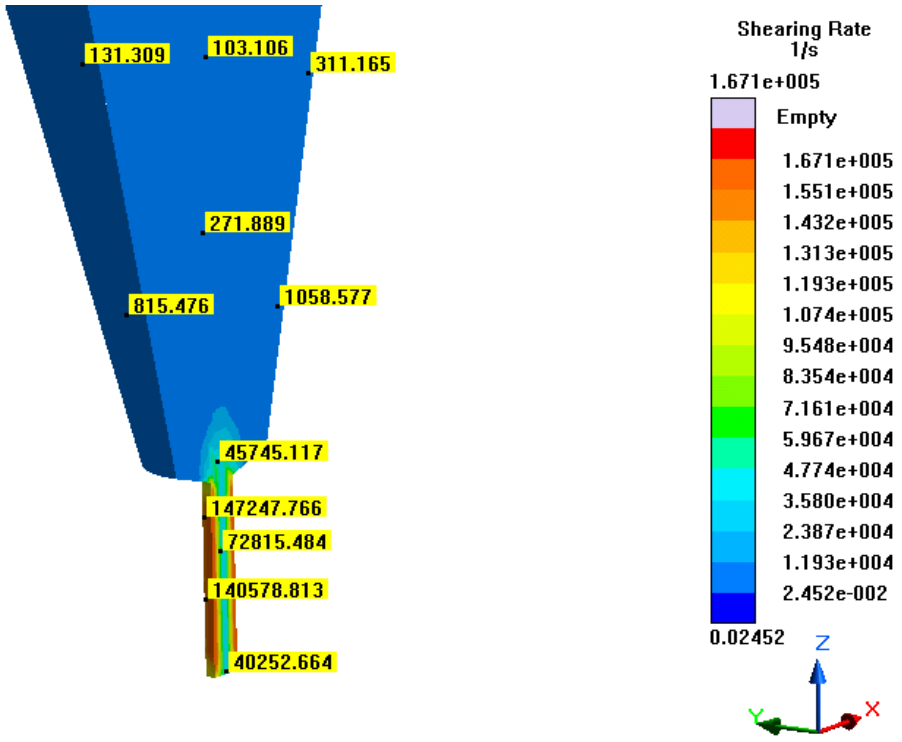

Figure 778- Simulation 22 (LLNL 200 Micron, 1 s), Shear Rate

Shear Stress

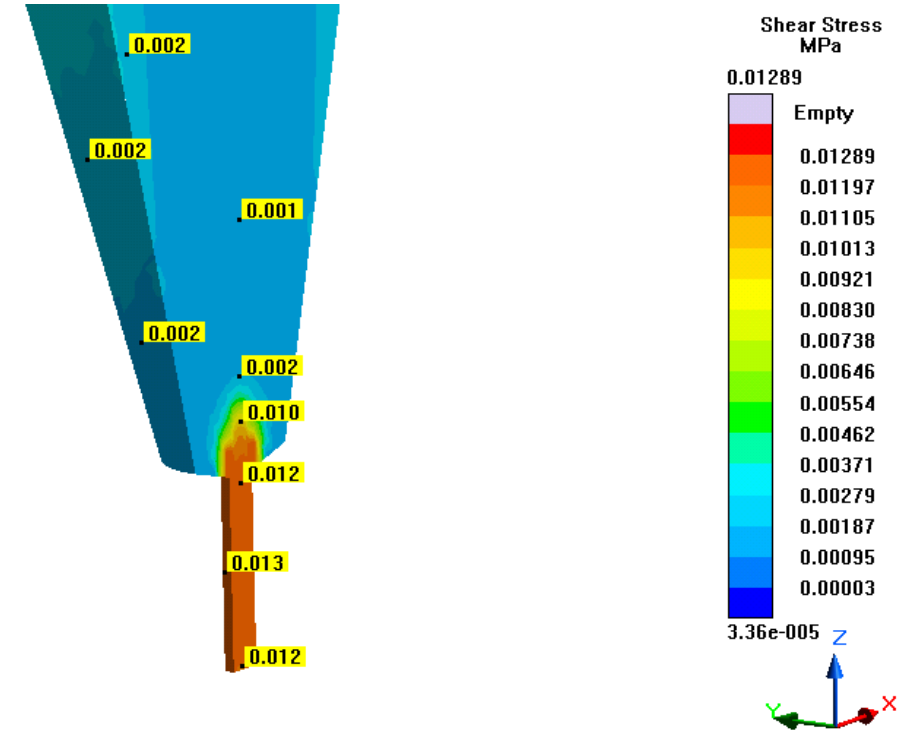

Figure 779- Simulation 22 (LLNL 200 Micron, 1 s), Shear Stress

Temperature

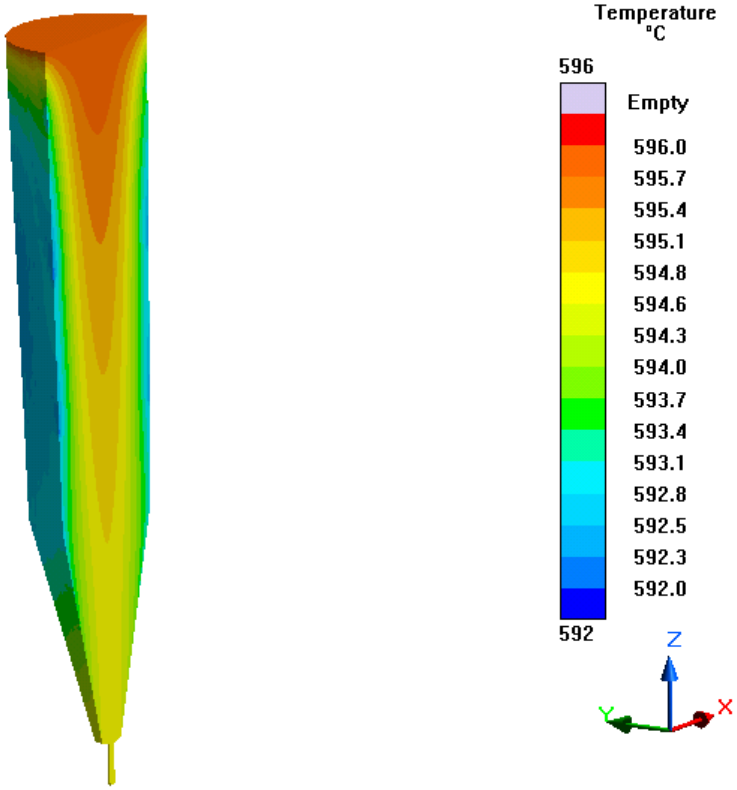

Figure 780- Simulation 22 (LLNL 200 Micron, 1 s), Temperature

Simulation 23- LLNL 200 Micron (1.5 s)

Parameters

Geometry	
Inlet Diameter	0.20 mm (200 microns)
Outlet Diameter	0.20 mm (200 microns)
Nozzle Height	1 mm
Nozzle Angle	90°
Tank Height	18.25 mm

Mesh Parameters	
Accuracy (Refinement Factor)	3
Minimum Wall Thickness (Nozzle)	0.09 mm
Minimum Element Size (Nozzle)	0.03 mm
Minimum Wall Thickness (Part)	0.24 mm
Minimum Element Size (Part)	0.08 mm
Smoothing	2
Ratio	2
Coarsening Loops	1
Minimal Accuracy After Coarsening	5

Mesh Properties	
Control Volumes (X Direction)	578
Control Volumes (Y Direction)	578
Control Volumes (Z Direction)	694
Composed Part Cells	156,001
Total Part Cells	693,572
Blocked Cells	0

Process Definitions	
Material Temperature	594 C
Fraction Solid	44.1-98.46 %
Close Mold Time	0 s
Fill Time	1.5 s
Hold Time After Filling	2 s

Table 125- Simulation 23 (LLNL 200 Micron, 1.5 s), Parameters

Notes

- The longer fill time was designed to reduce the pressure drop and exit velocity, but the cooling rate became an issue, especially near the nozzle
- Improved heating must be added around the heater, especially near the nozzle tip

Velocity

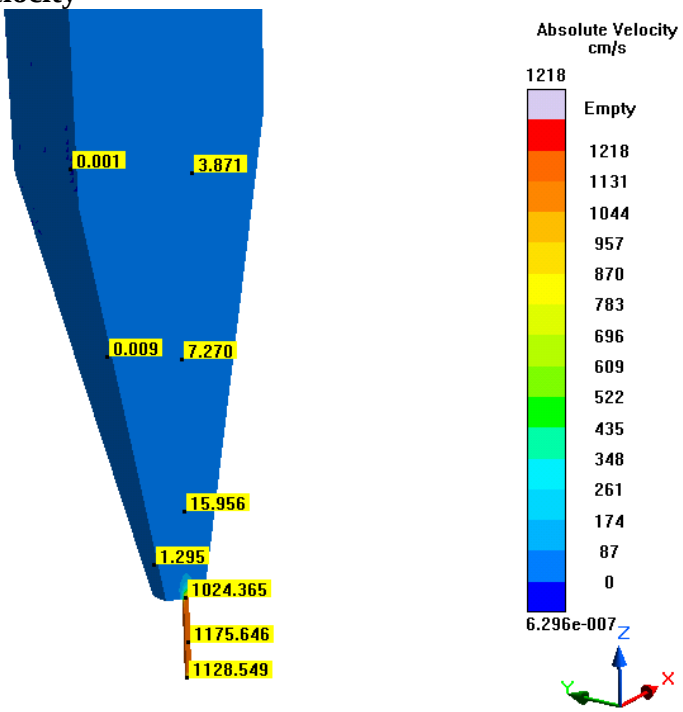

Figure 781- Simulation 23 (LLNL 200 Micron, 1.5 s), Velocity

Viscosity

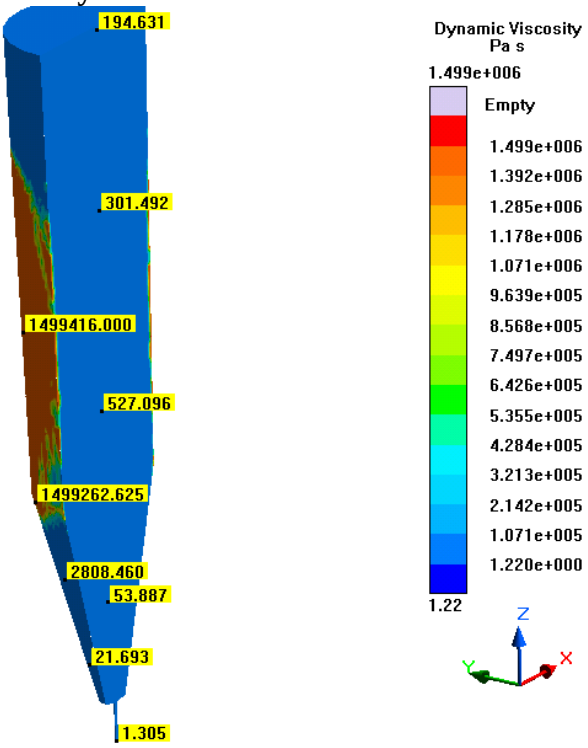

Figure 782- Simulation 23 (LLNL 200 Micron, 1.5 s), Viscosity

Pressure

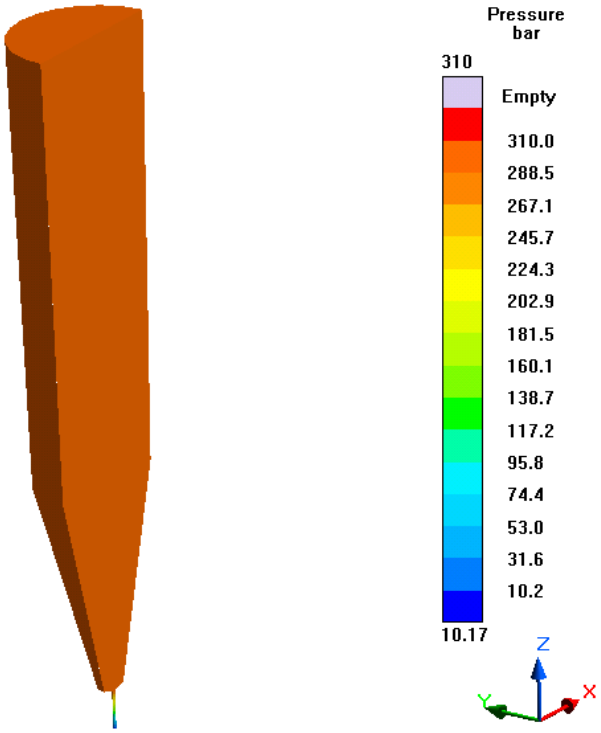

Figure 783- Simulation 23 (LLNL 200 Micron, 1.5 s), Pressure

Fraction Solid

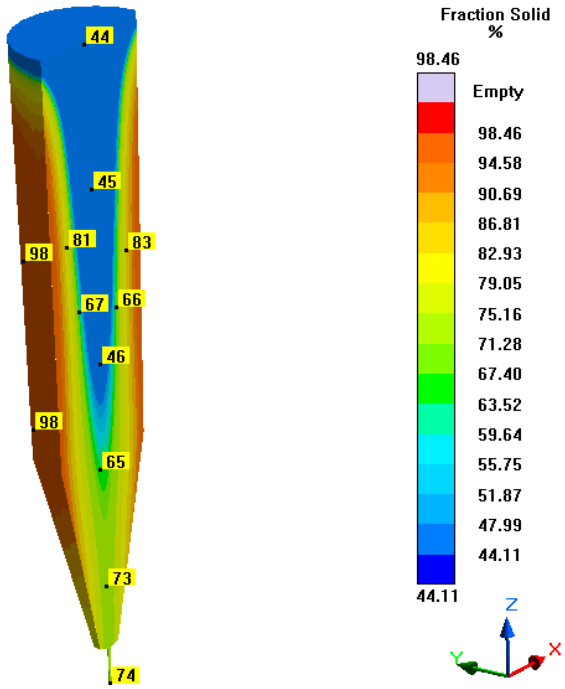

Figure 784- Simulation 23 (LLNL 200 Micron, 1.5 s), Fraction Solid

Cooling Rate

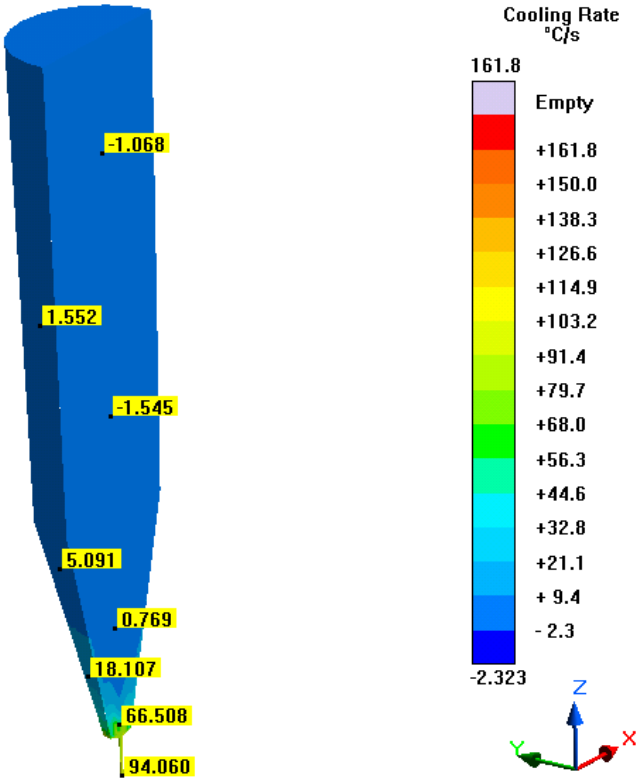

Figure 785- Simulation 23 (LLNL 200 Micron, 1.5 s), Cooling Rate

Shear Heating

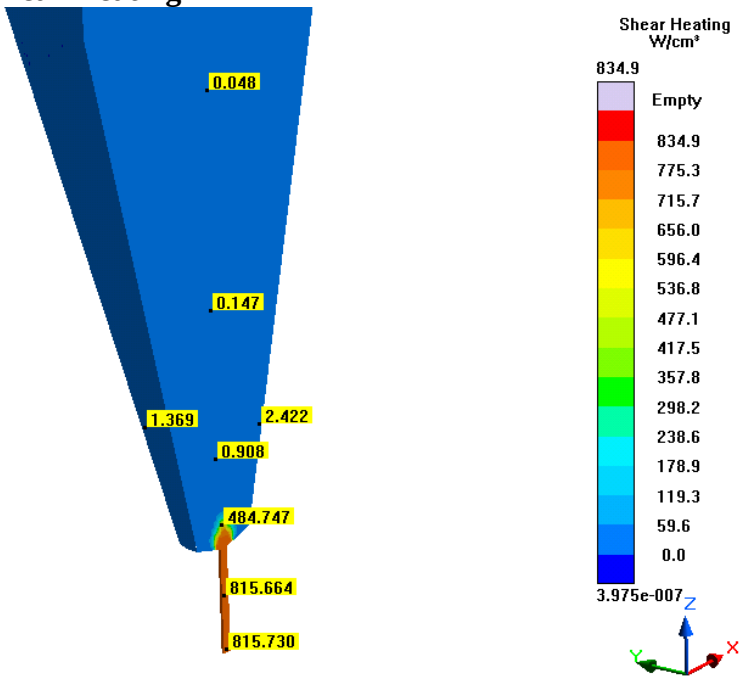

Figure 786- Simulation 23 (LLNL 200 Micron, 1.5 s), Shear Heating

Shear Rate

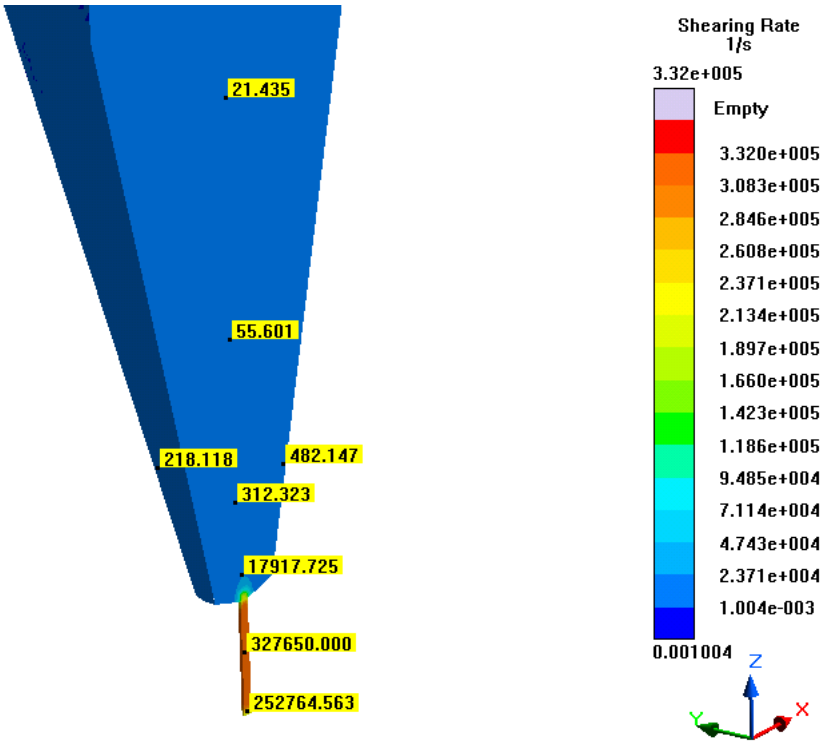

Figure 787- Simulation 23 (LLNL 200 Micron, 1.5 s), Shear Rate

Shear Stress

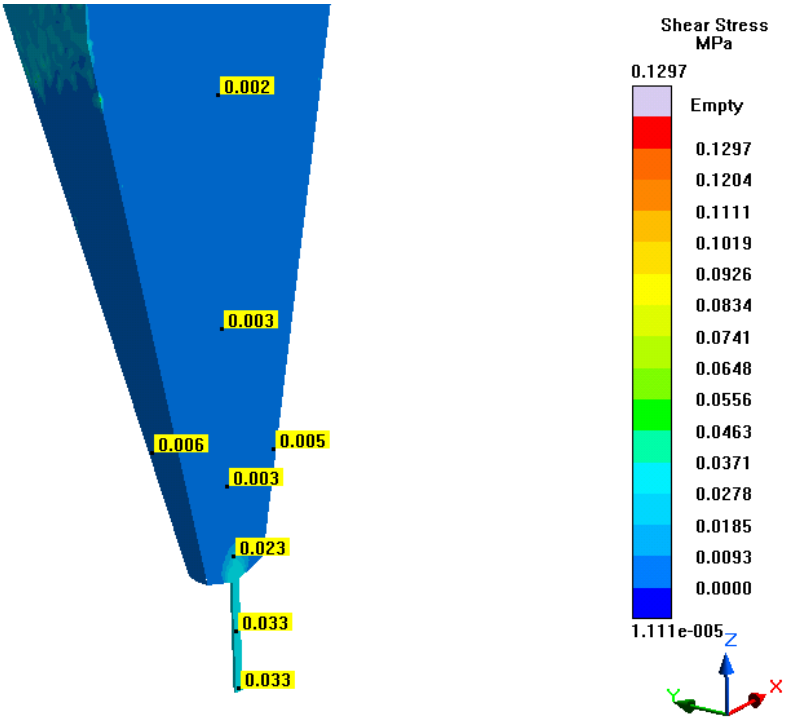

Figure 788- Simulation 23 (LLNL 200 Micron, 1.5 s), Shear Stress

Temperature

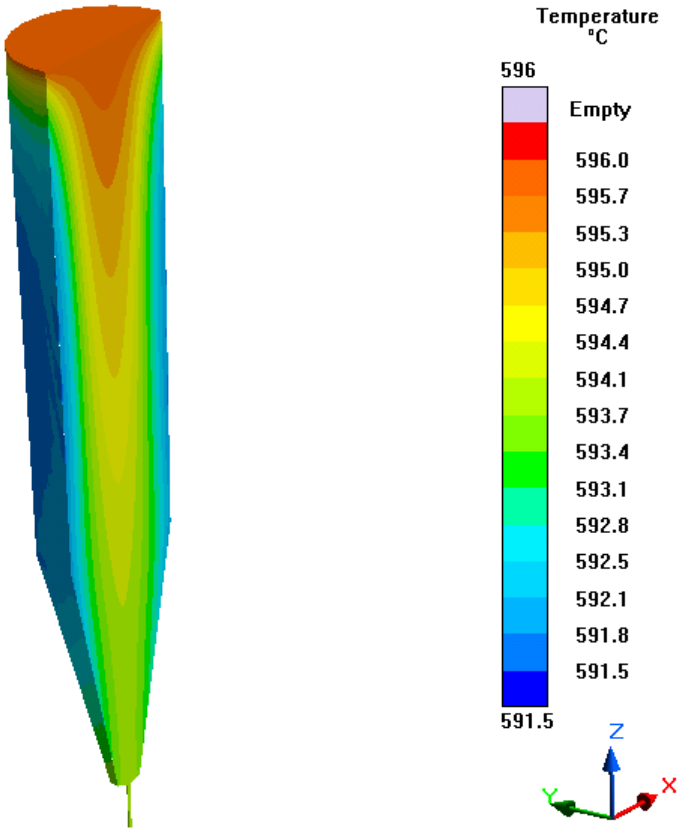

Figure 789- Simulation 23 (LLNL 200 Micron, 1.5 s), Temperature

Simulation 24- LLNL 300 Micron (TC, 3 s)

Parameters

Geometry	
Inlet Diameter	0.30 mm (300 microns)
Outlet Diameter	0.30 mm (300 microns)
Nozzle Height	1 mm
Nozzle Angle	90°
Tank Height	18.25 mm

Mesh Parameters	
Accuracy (Refinement Factor)	3
Minimum Wall Thickness (Nozzle)	0.21 mm
Minimum Element Size (Nozzle)	0.07 mm
Minimum Wall Thickness (Part)	0.24 mm
Minimum Element Size (Part)	0.08 mm
Smoothing	2
Ratio	2
Coarsening Loops	1
Minimal Accuracy After Coarsening	5

Mesh Properties	
Control Volumes (X Direction)	282
Control Volumes (Y Direction)	282
Control Volumes (Z Direction)	328
Composed Part Cells	33,967
Total Part Cells	109,648
Blocked Cells	0

Process Definitions	
Material Temperature	596 C
Fraction Solid	44.1-44.1 %
Close Mold Time	0 s
Fill Time	3 s

Table 126- Simulation 24 (LLNL 300 Micron, TC, 3 s), Parameters

Notes

- First simulation with TC runner definitions throughout
- TC Runners simulate heaters positioned throughout the nozzle
- If perfect heating is obtained, the metal flows far more easily and is more uniform, especially with regards to fraction solid

Velocity

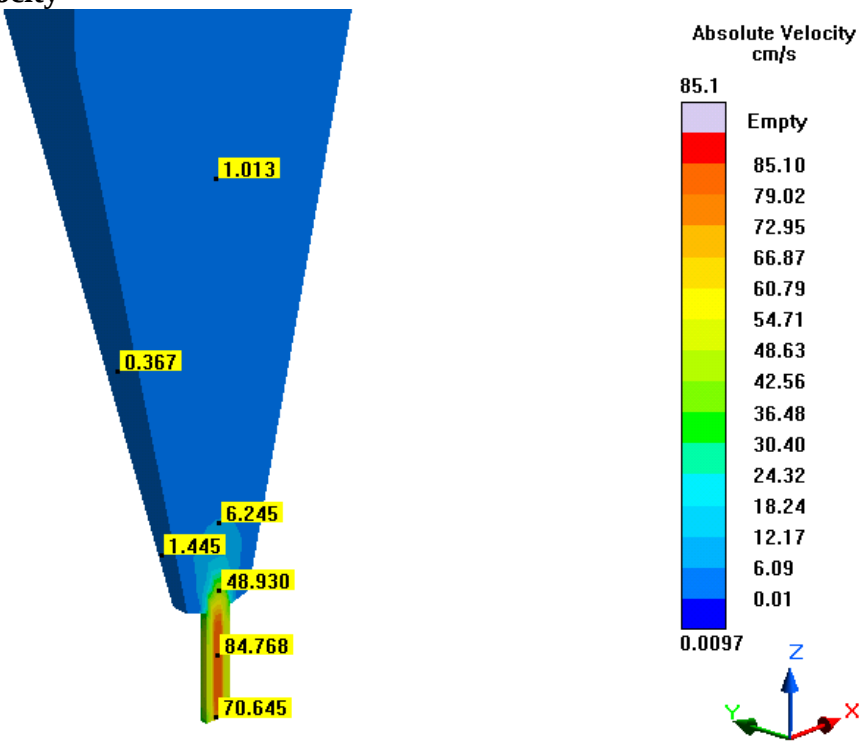

Figure 790- Simulation 24 (LLNL 300 Micron, TC, 3 s), Velocity

Viscosity

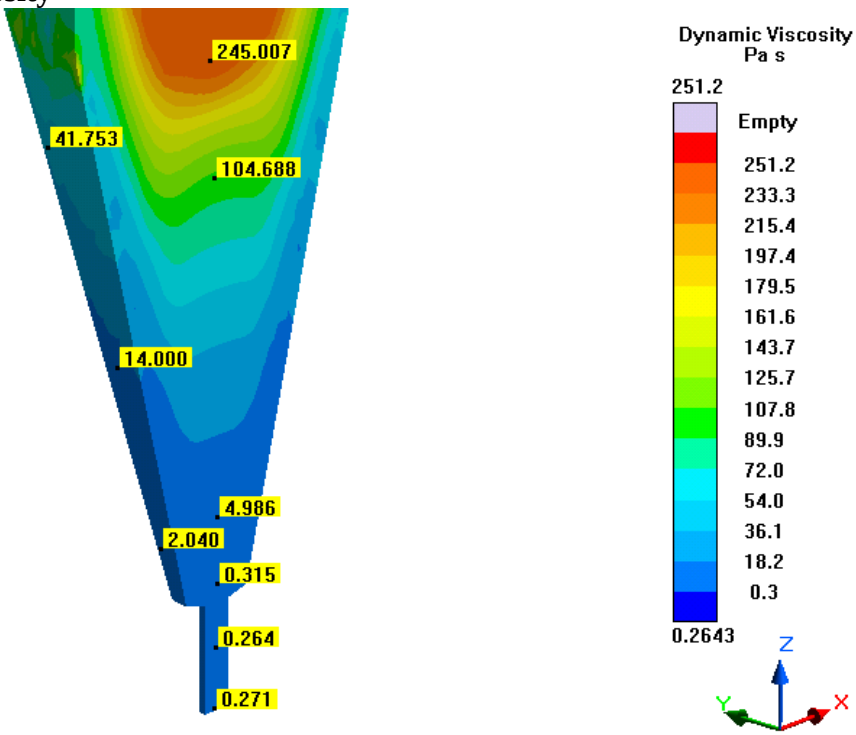

Figure 791- Simulation 24 (LLNL 300 Micron, TC, 3 s), Viscosity

Pressure

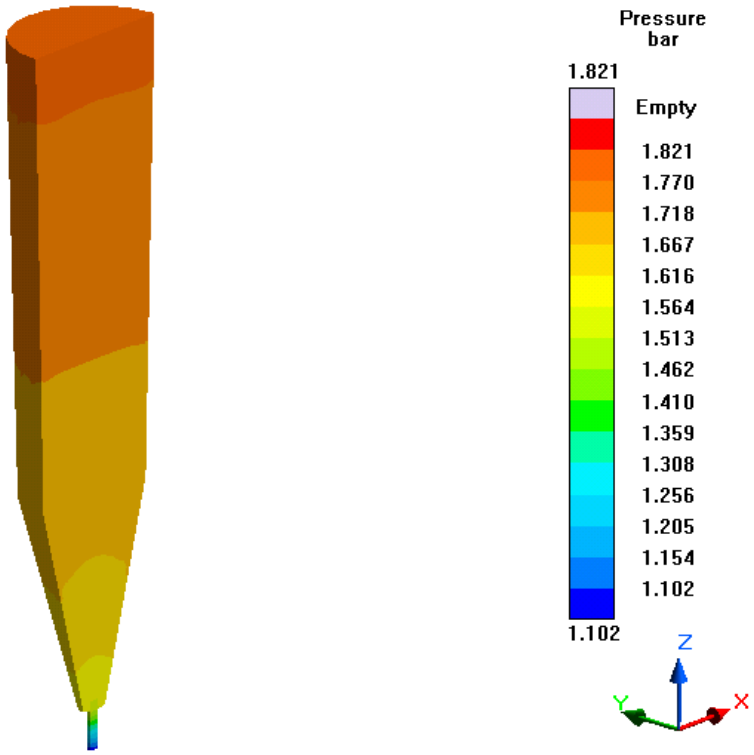

Figure 792- Simulation 24 (LLNL 300 Micron, TC, 3 s), Pressure

Fraction Solid

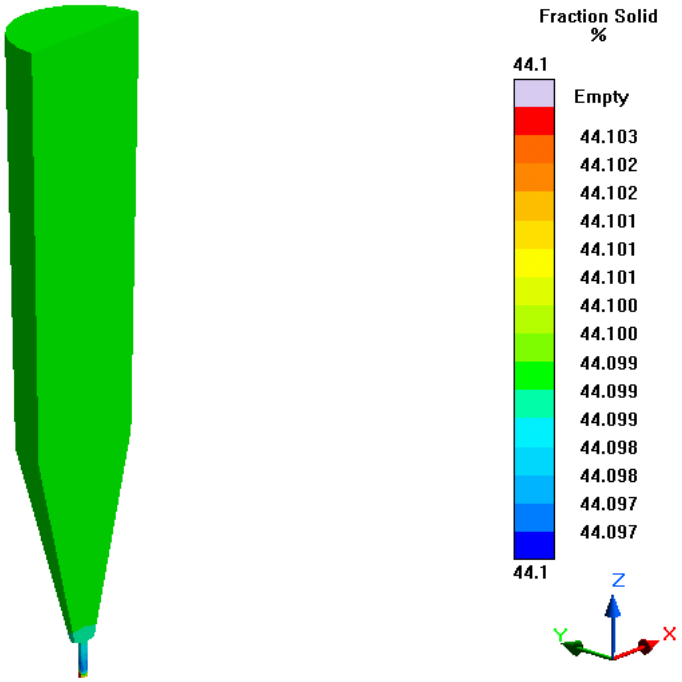

Figure 793- Simulation 24 (LLNL 300 Micron, TC, 3 s), Fraction Solid

Cooling Rate

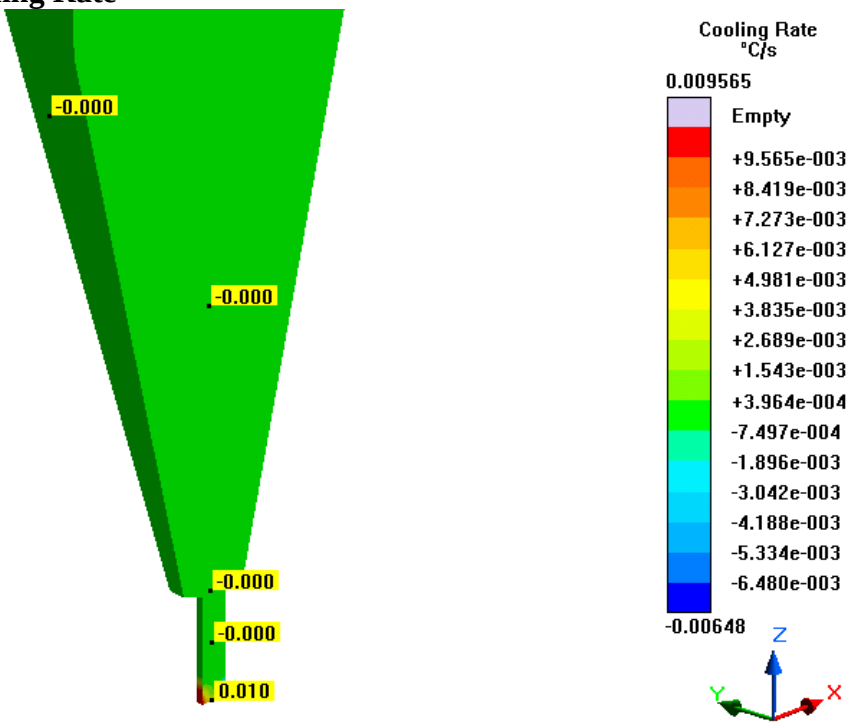

Figure 794- Simulation 24 (LLNL 300 Micron, TC, 3 s), Cooling Rate

Shear Heating

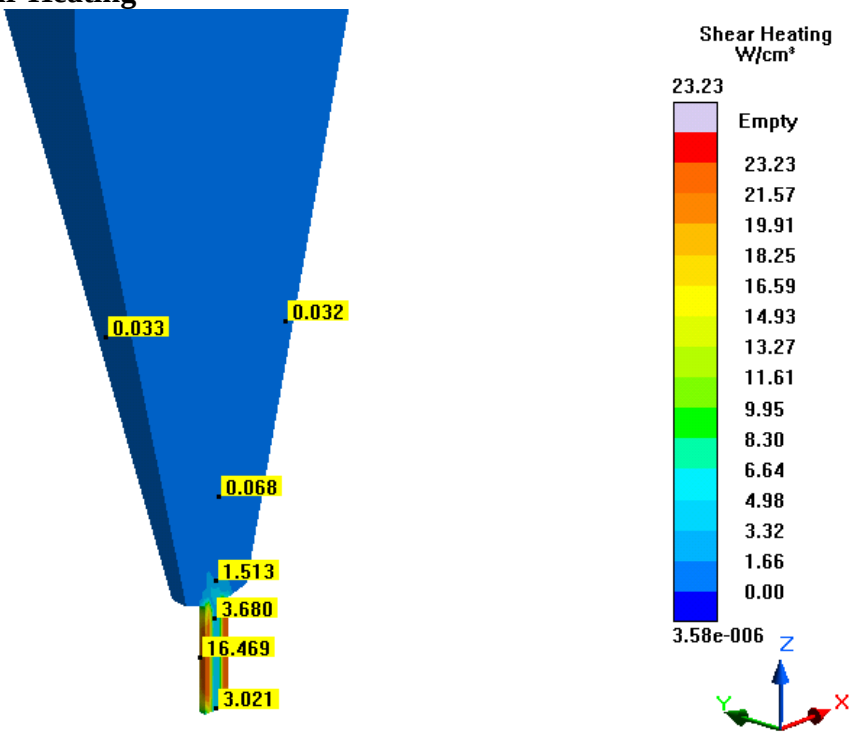

Figure 795- Simulation 24 (LLNL 300 Micron, TC, 3 s), Shear Heating

Shear Rate

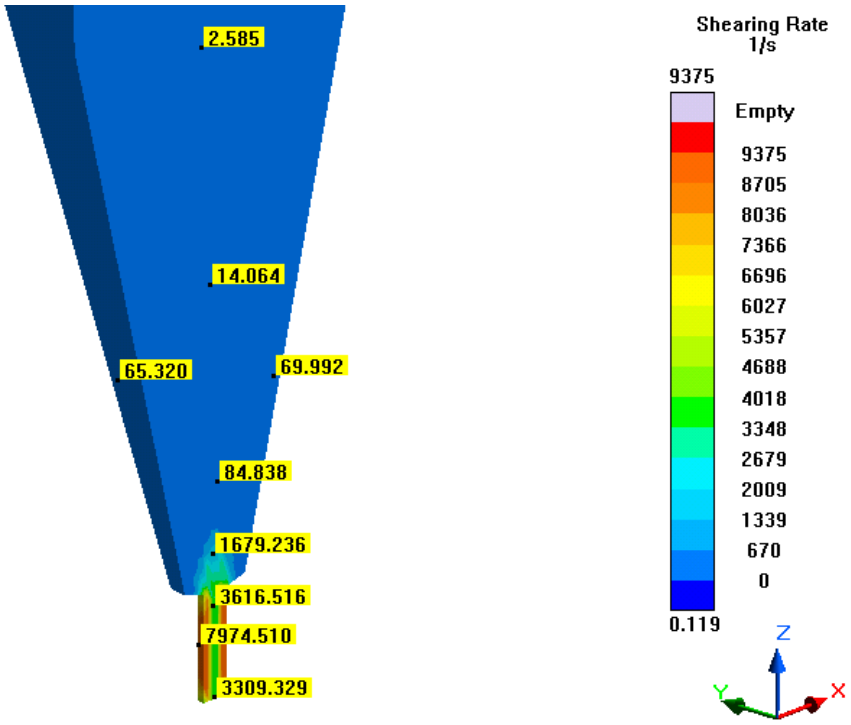

Figure 796- Simulation 24 (LLNL 300 Micron, TC, 3 s), Shear Rate

Shear Stress

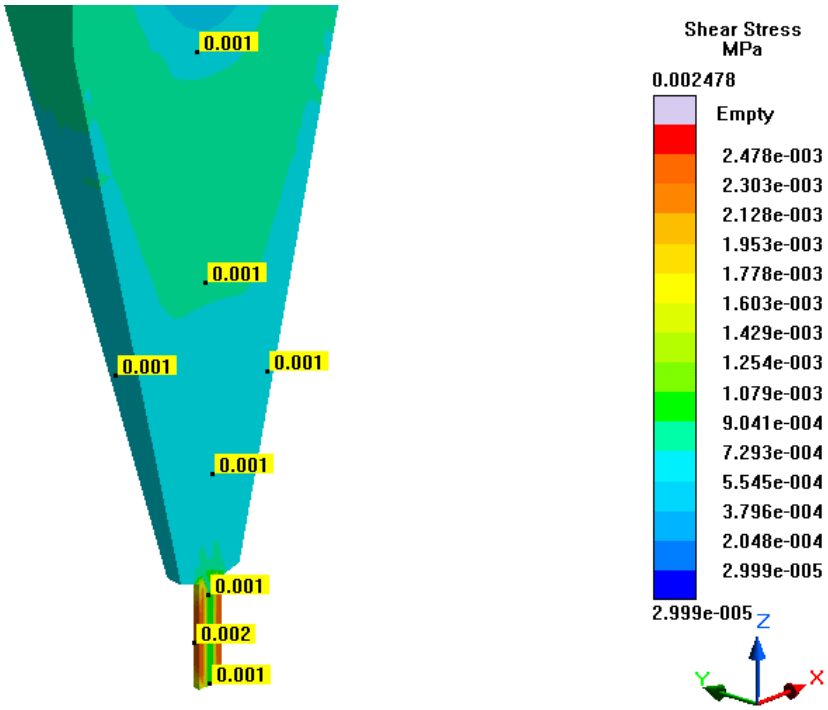

Figure 797- Simulation 24 (LLNL 300 Micron, TC, 3 s), Shear Stress

Temperature

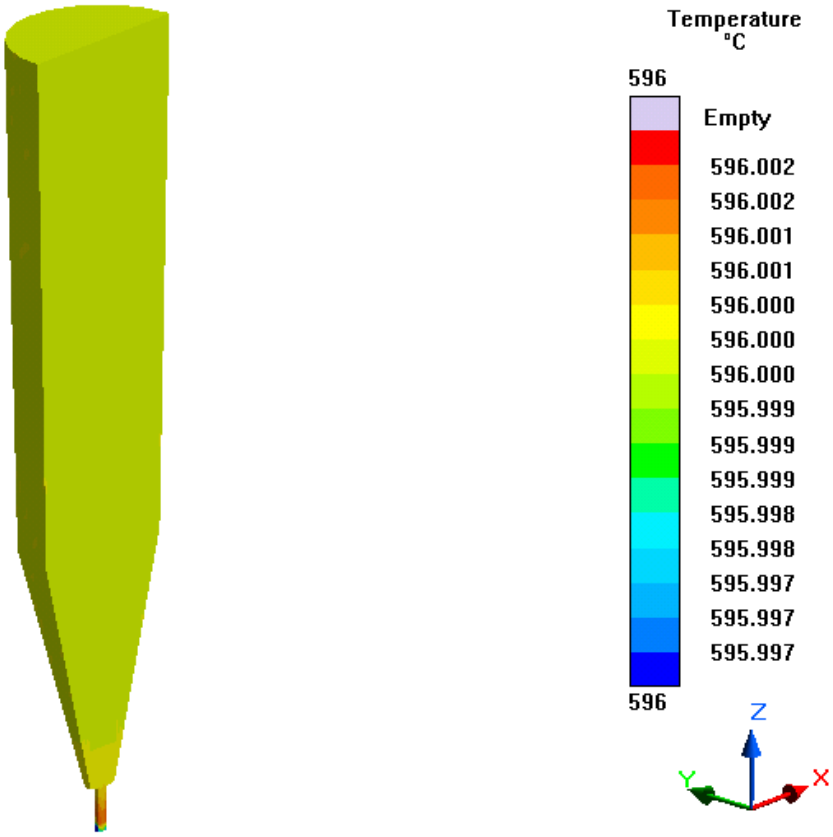

Figure 798- Simulation 24 (LLNL 300 Micron, TC, 3 s), Temperature

Simulation 25- LLNL 300 Micron (TC, 2.5 s)

Parameters

Geometry	
Inlet Diameter	0.30 mm (300 microns)
Outlet Diameter	0.30 mm (300 microns)
Nozzle Height	1 mm
Nozzle Angle	90°
Tank Height	18.25 mm

Mesh Parameters	
Accuracy (Refinement Factor)	3
Minimum Wall Thickness (Nozzle)	0.21 mm
Minimum Element Size (Nozzle)	0.07 mm
Minimum Wall Thickness (Part)	0.24 mm
Minimum Element Size (Part)	0.08 mm
Smoothing	2
Ratio	2
Coarsening Loops	1
Minimal Accuracy After Coarsening	5

Mesh Properties	
Control Volumes (X Direction)	282
Control Volumes (Y Direction)	282
Control Volumes (Z Direction)	328
Composed Part Cells	33,967
Total Part Cells	109,648
Blocked Cells	0

Process Definitions	
Material Temperature	596 C
Fraction Solid	44.1-44.1 %
Close Mold Time	0 s
Fill Time	2.5 s

Table 127- Simulation 25 (LLNL 300 Micron, TC, 2.5 s), Parameters

Velocity

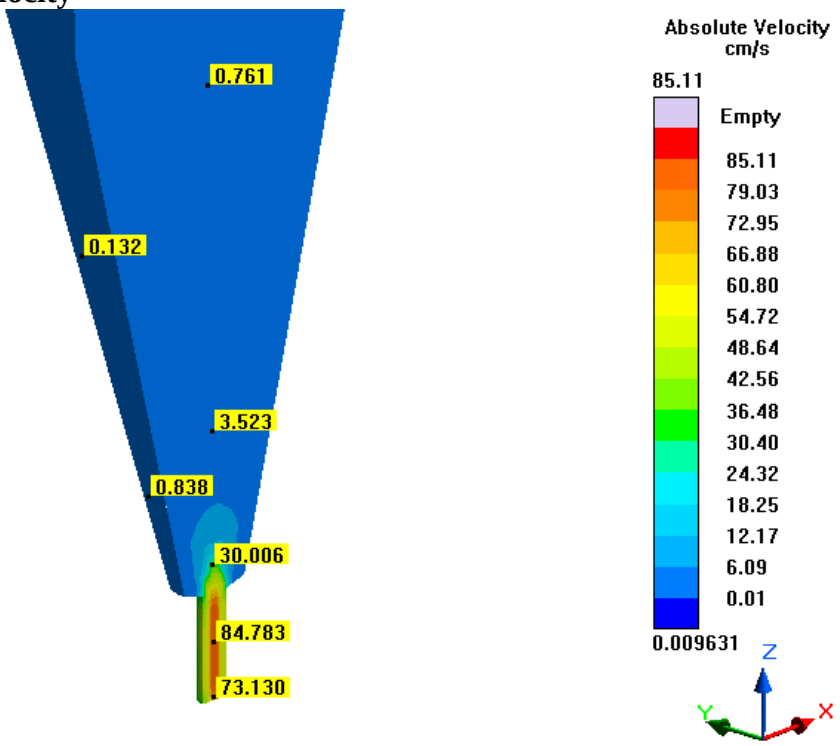

Figure 799- Simulation 25 (LLNL 300 Micron, TC, 2.5 s), Velocity

Viscosity

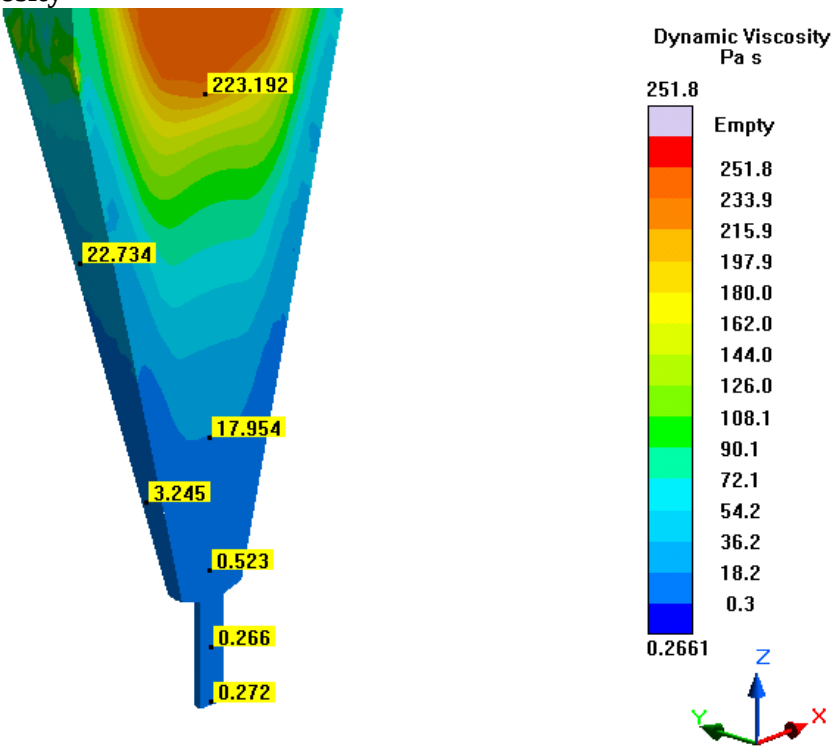

Figure 800- Simulation 25 (LLNL 300 Micron, TC, 2.5 s), Viscosity

Pressure

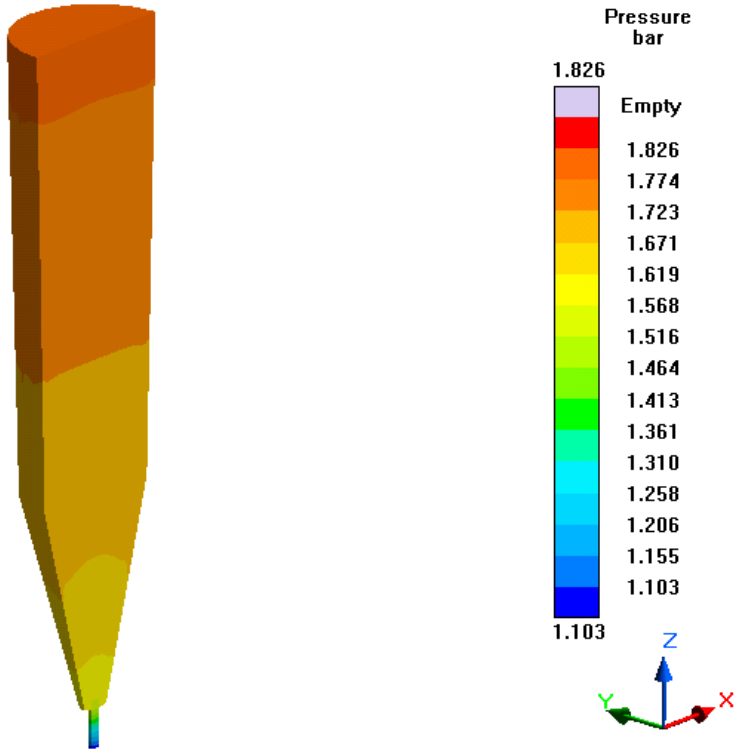

Figure 801- Simulation 25 (LLNL 300 Micron, TC, 2.5 s), Pressure

Fraction Solid

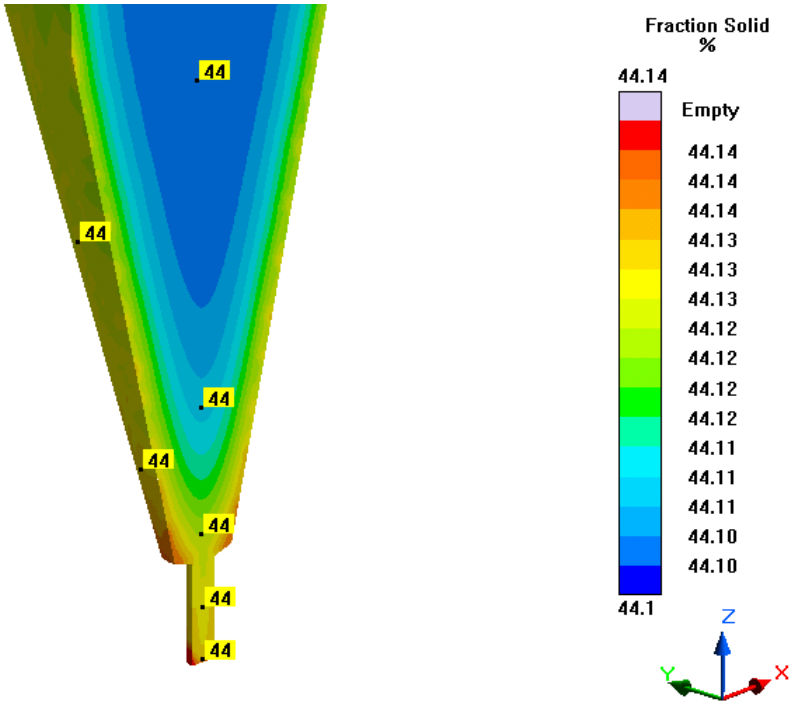

Figure 802- Simulation 25 (LLNL 300 Micron, TC, 2.5 s), Fraction Solid

Cooling Rate

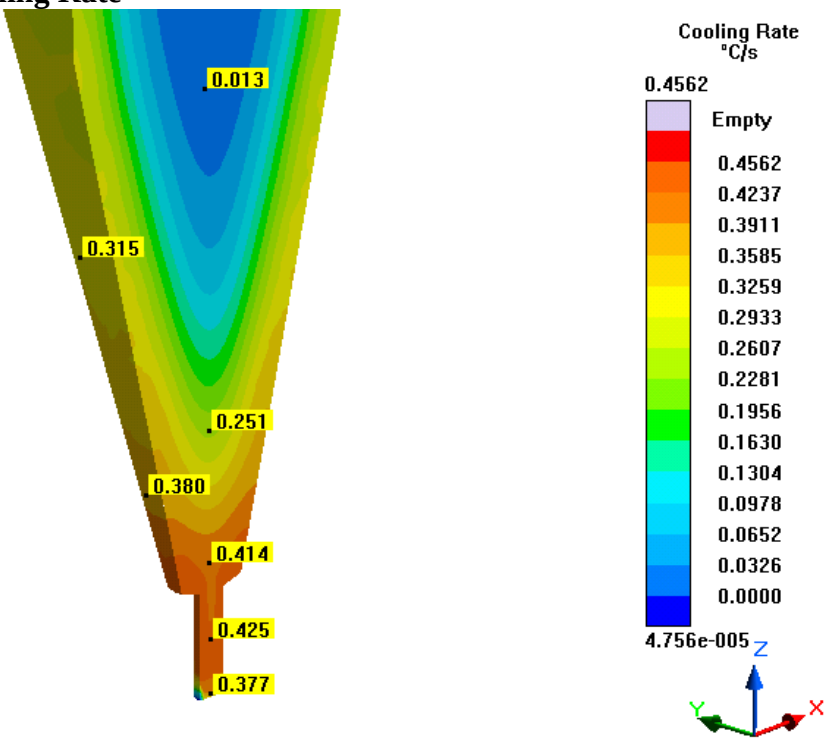

Figure 803- Simulation 25 (LLNL 300 Micron, TC, 2.5 s), Cooling Rate

Shear Heating

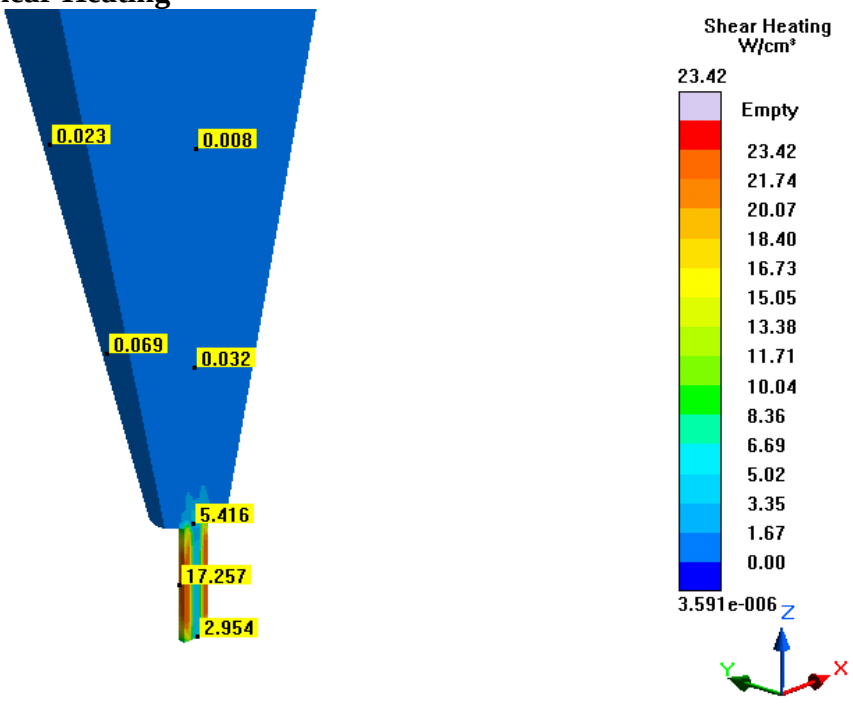

Figure 804- Simulation 25 (LLNL 300 Micron, TC, 2.5 s), Shear Heating

Shear Rate

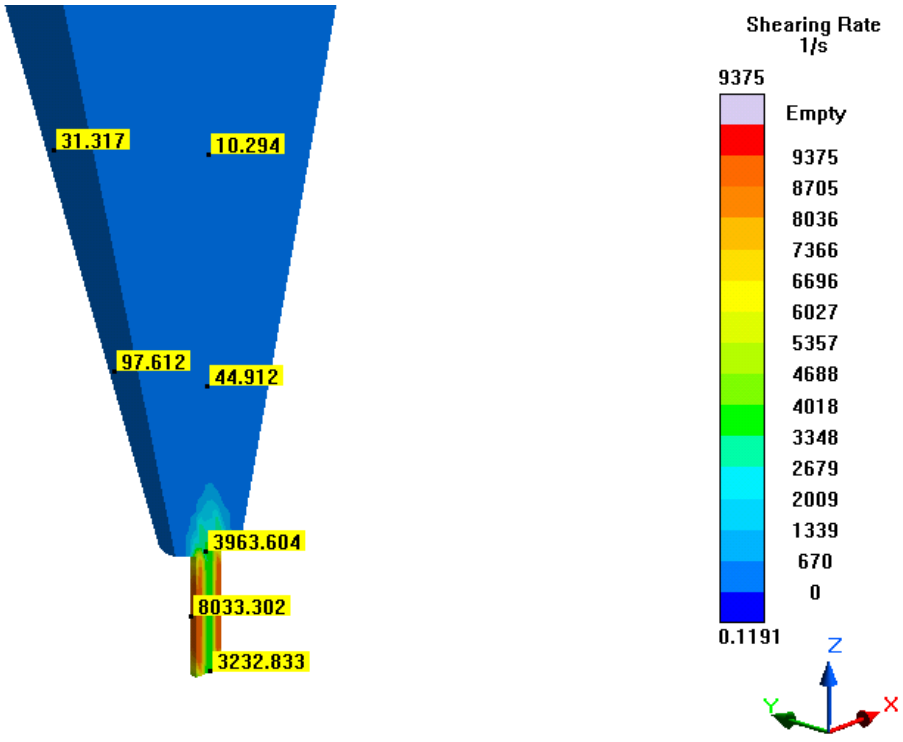

Figure 805- Simulation 25 (LLNL 300 Micron, TC, 2.5 s), Shear Rate

Shear Stress

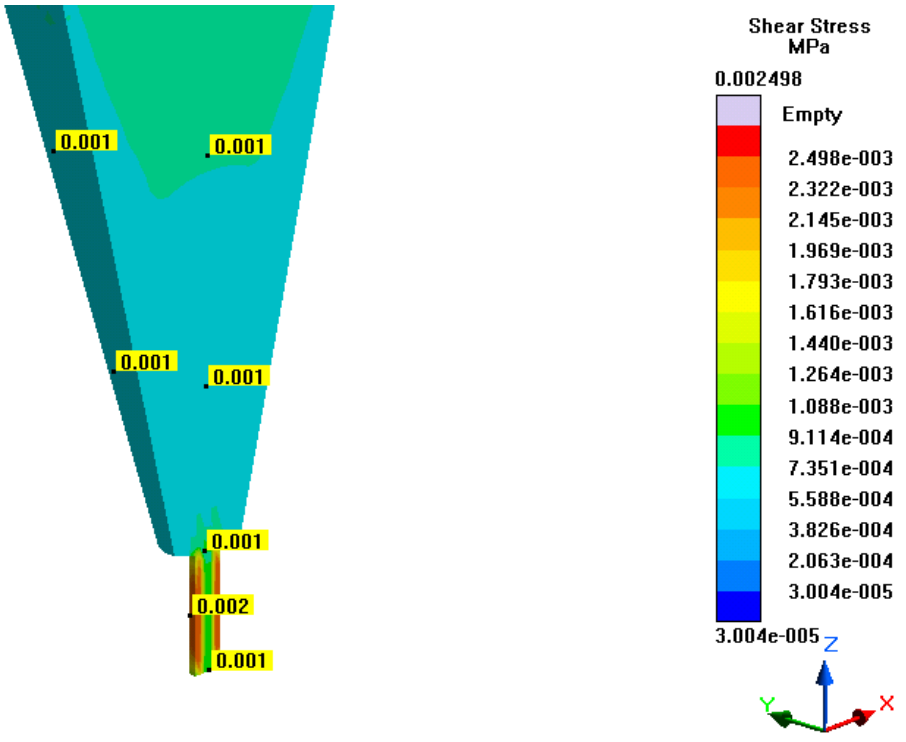

Figure 806- Simulation 25 (LLNL 300 Micron, TC, 2.5 s), Shear Stress

Temperature

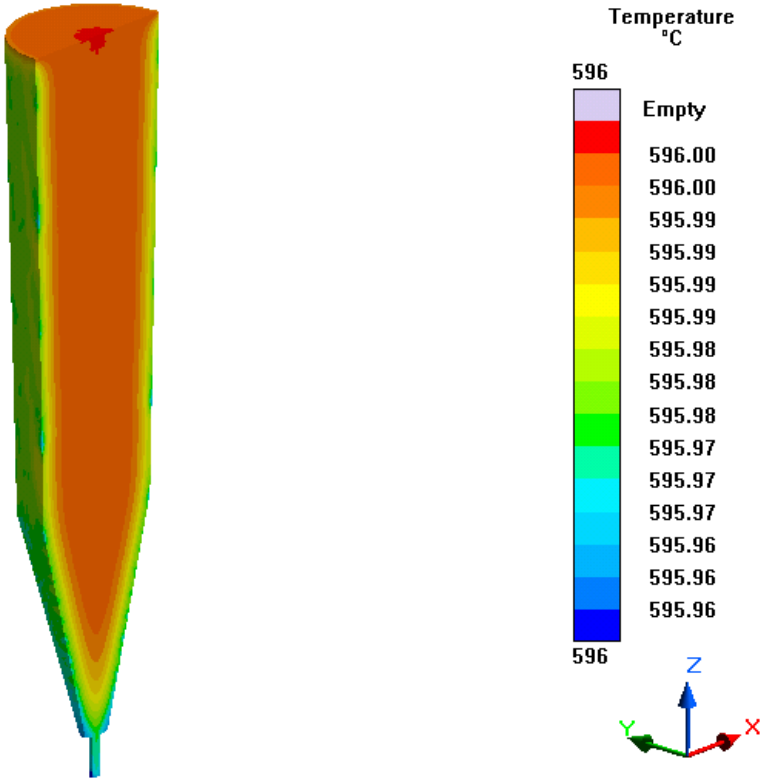

Figure 807- Simulation 25 (LLNL 300 Micron, TC, 2.5 s), Temperature

Simulation 26- LLNL 300 Micron (2 s)

Parameters

Geometry	
Inlet Diameter	0.30 mm (300 microns)
Outlet Diameter	0.30 mm (300 microns)
Nozzle Height	1 mm
Nozzle Angle	90°
Tank Height	18.25 mm

Mesh Parameters	
Accuracy (Refinement Factor)	3
Minimum Wall Thickness (Nozzle)	0.21 mm
Minimum Element Size (Nozzle)	0.07 mm
Minimum Wall Thickness (Part)	0.24 mm
Minimum Element Size (Part)	0.08 mm
Smoothing	2
Ratio	2
Coarsening Loops	1
Minimal Accuracy After Coarsening	5

Mesh Properties	
Control Volumes (X Direction)	282
Control Volumes (Y Direction)	282
Control Volumes (Z Direction)	328
Composed Part Cells	33,967
Total Part Cells	109,648
Blocked Cells	0

Process Definitions	
Material Temperature	596 C
Fraction Solid	44.1-100 %
Close Mold Time	0 s
Fill Time	2 s

Table 128- Simulation 26 (LLNL 300 Micron, 2 s), Parameters

Notes

- Simulation reached 100% fraction solid and stopped
- Demonstrates the importance of the heaters unless very high shear is applied

Velocity

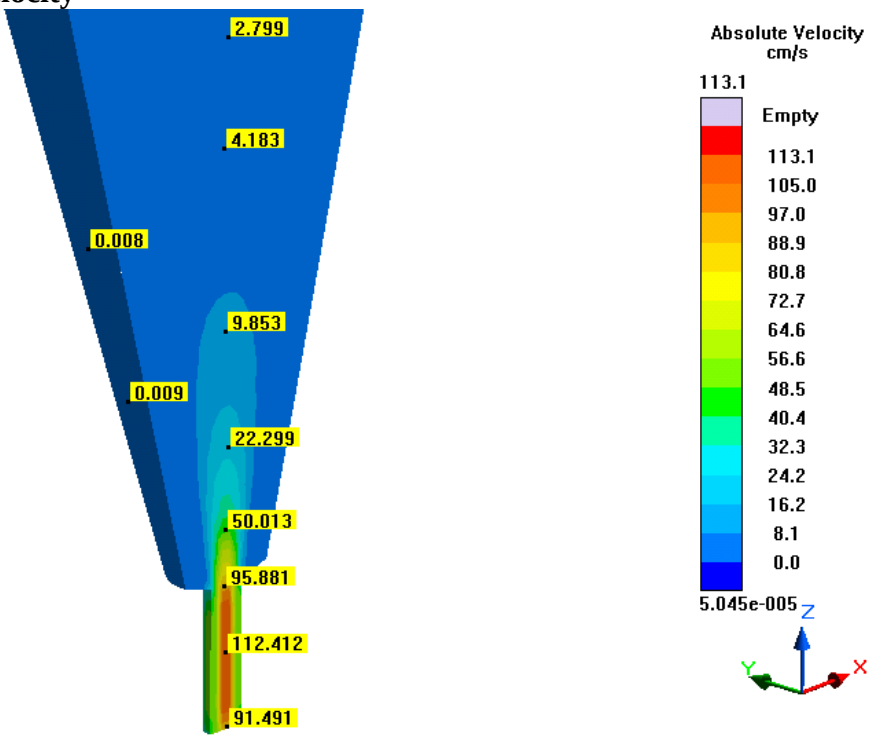

Figure 808- Simulation 26 (LLNL 300 Micron, 2 s), Velocity

Viscosity

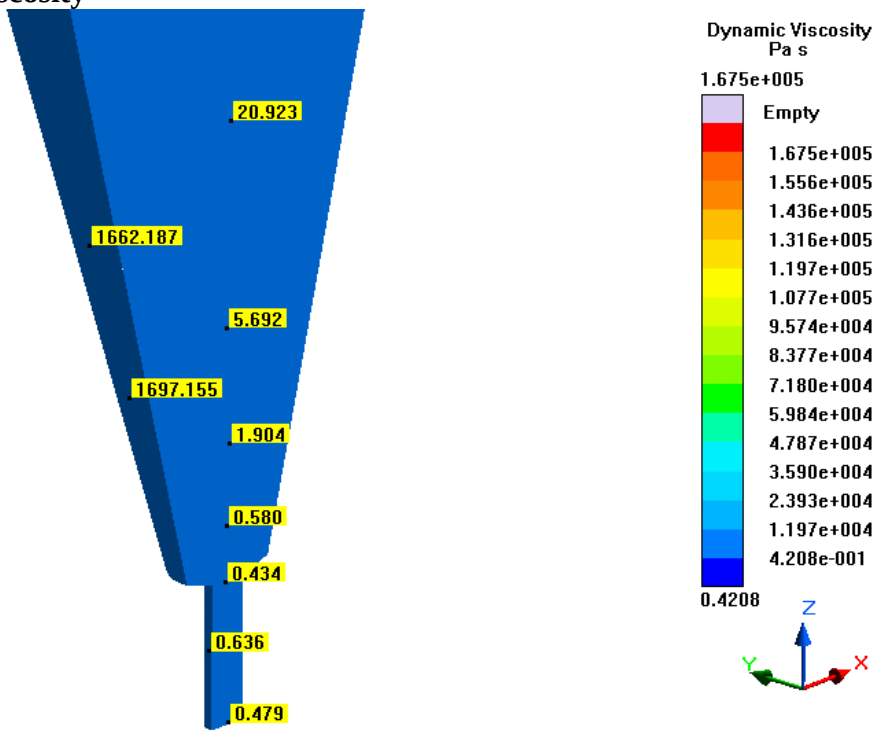

Figure 809- Simulation 26 (LLNL 300 Micron, 2 s), Viscosity

Pressure

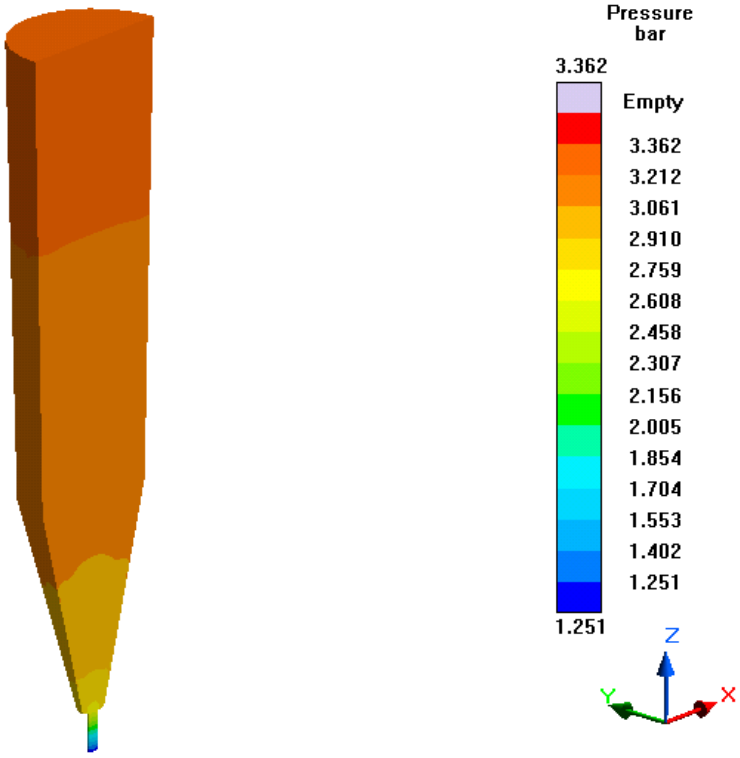

Figure 810- Simulation 26 (LLNL 300 Micron, 2 s), Pressure

Fraction Solid

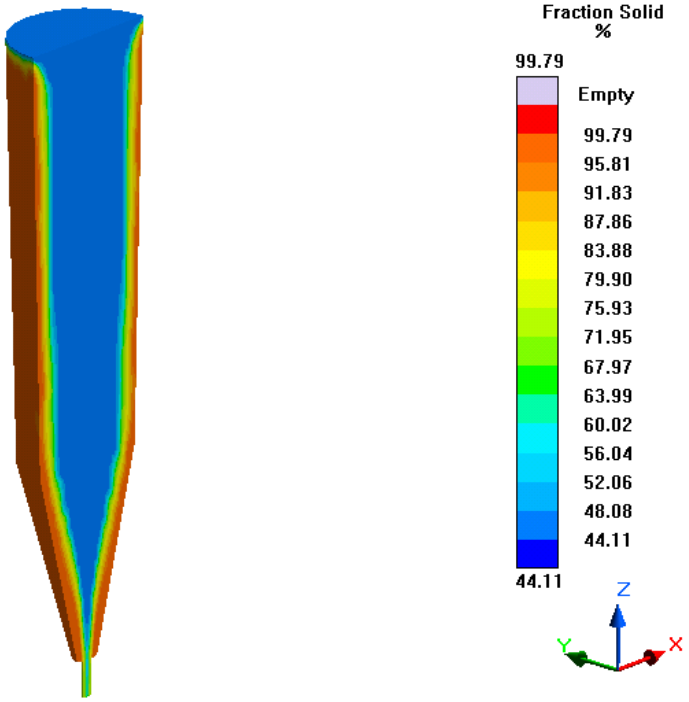

Figure 811- Simulation 26 (LLNL 300 Micron, 2 s), Fraction Solid

Shear Rate

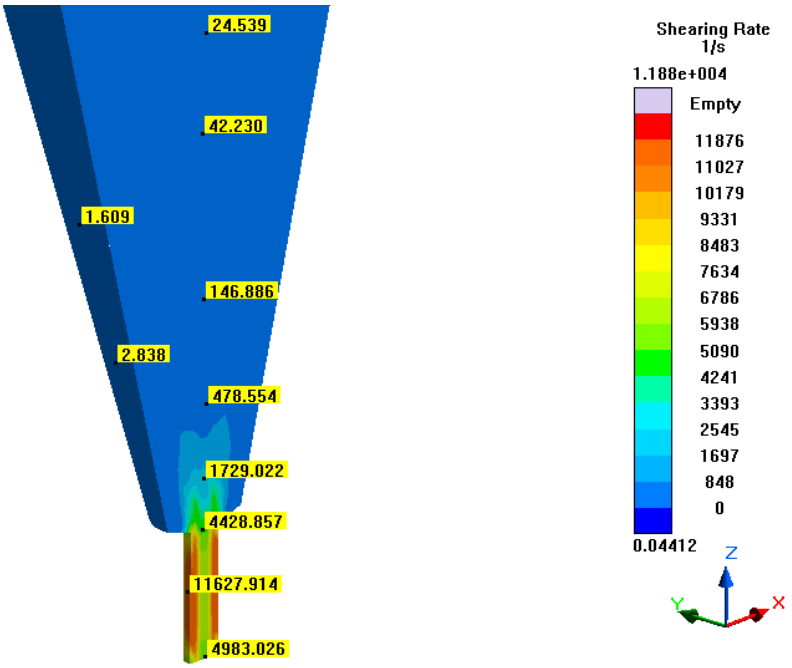

Figure 812- Simulation 26 (LLNL 300 Micron, 2 s), Shear Stress

Temperature

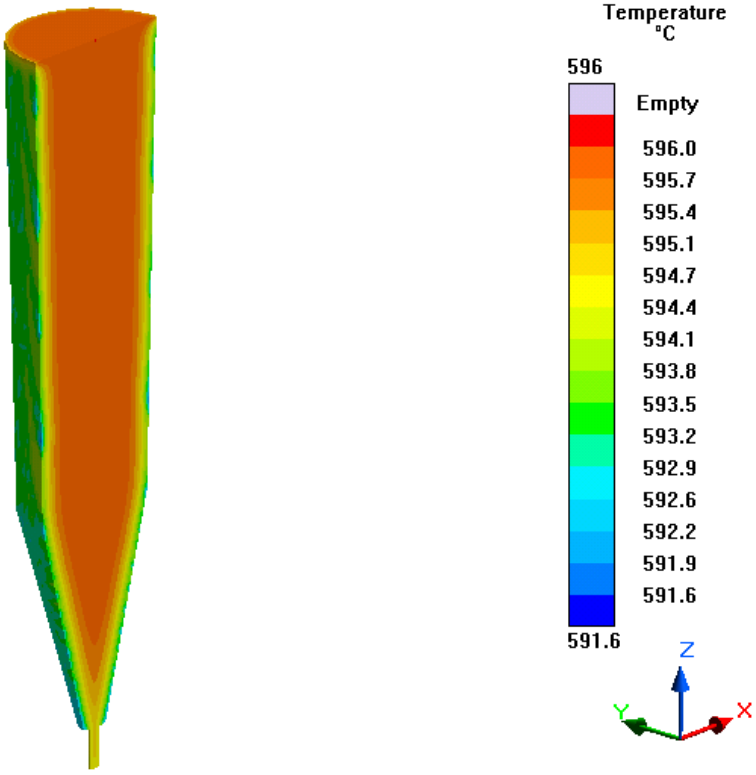

Figure 813- Simulation 26 (LLNL 300 Micron, 2 s), Temperature

Simulation 27- LLNL 300 Micron (TC, 2 s)

Parameters

Geometry	
Inlet Diameter	0.30 mm (300 microns)
Outlet Diameter	0.30 mm (300 microns)
Nozzle Height	1 mm
Nozzle Angle	90°
Tank Height	18.25 mm

Mesh Parameters	
Accuracy (Refinement Factor)	3
Minimum Wall Thickness (Nozzle)	0.21 mm
Minimum Element Size (Nozzle)	0.07 mm
Minimum Wall Thickness (Part)	0.24 mm
Minimum Element Size (Part)	0.08 mm
Smoothing	2
Ratio	2
Coarsening Loops	1
Minimal Accuracy After Coarsening	5

Mesh Properties	
Control Volumes (X Direction)	282
Control Volumes (Y Direction)	282
Control Volumes (Z Direction)	328
Composed Part Cells	33,967
Total Part Cells	109,648
Blocked Cells	0

Process Definitions	
Material Temperature	596 C
Fraction Solid	44.1-44.13 %
Close Mold Time	0 s
Fill Time	2 s

Table 129- Simulation 27 (LLNL 300 Micron, TC, 2 s), Parameters

Velocity

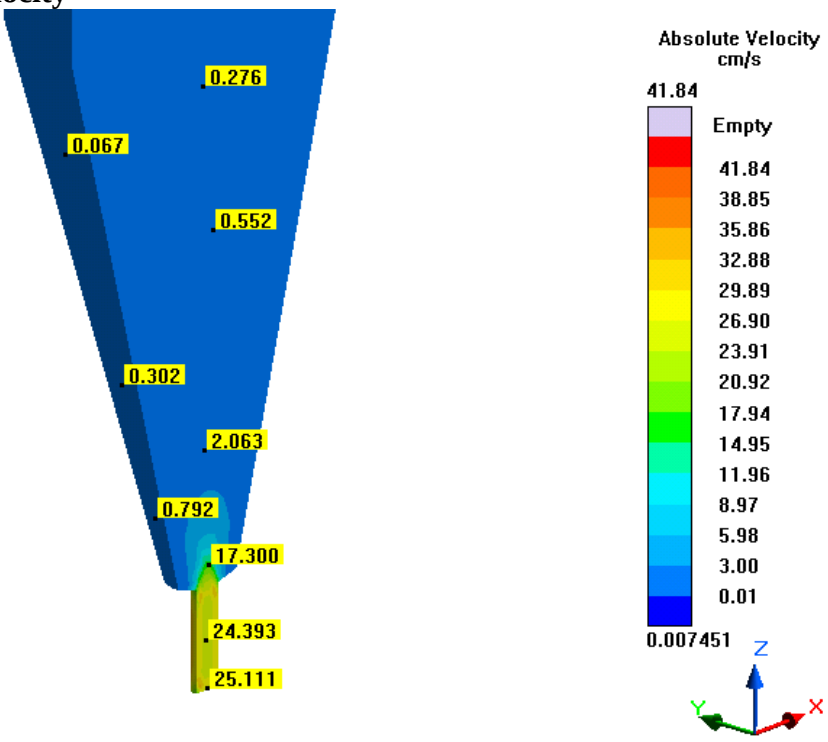

Figure 814- Simulation 27 (LLNL 300 Micron, TC, 2 s), Velocity

Viscosity

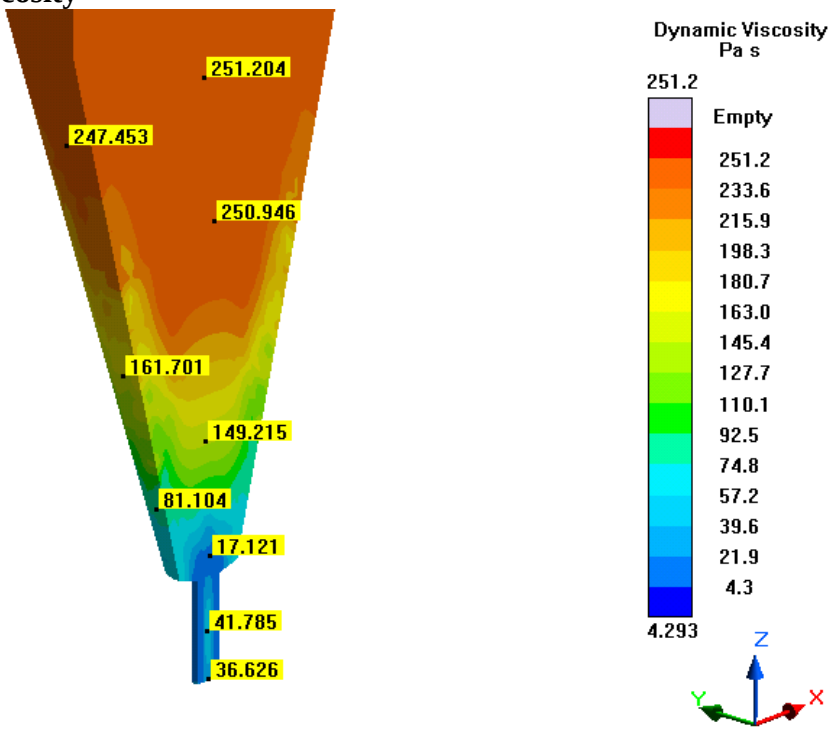

Figure 815- Simulation 27 (LLNL 300 Micron, TC, 2 s), Viscosity

Pressure

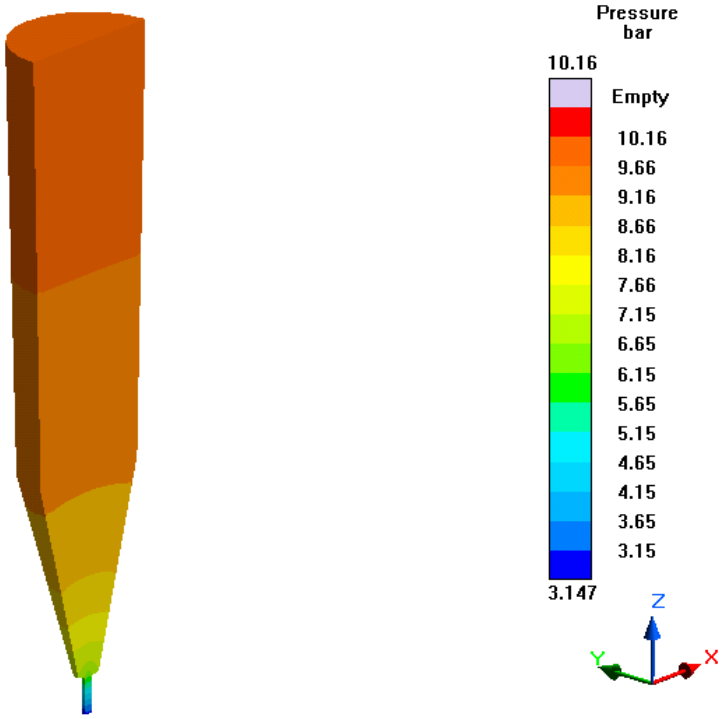

Figure 816- Simulation 27 (LLNL 300 Micron, TC, 2 s), Pressure

Fraction Solid

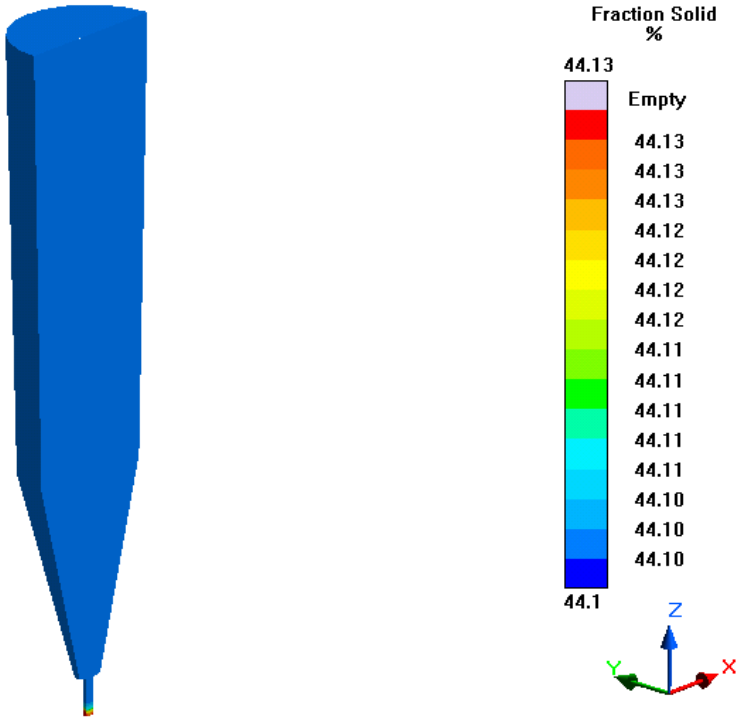

Figure 817- Simulation 27 (LLNL 300 Micron, TC, 2 s), Fraction Solid

Cooling Rate

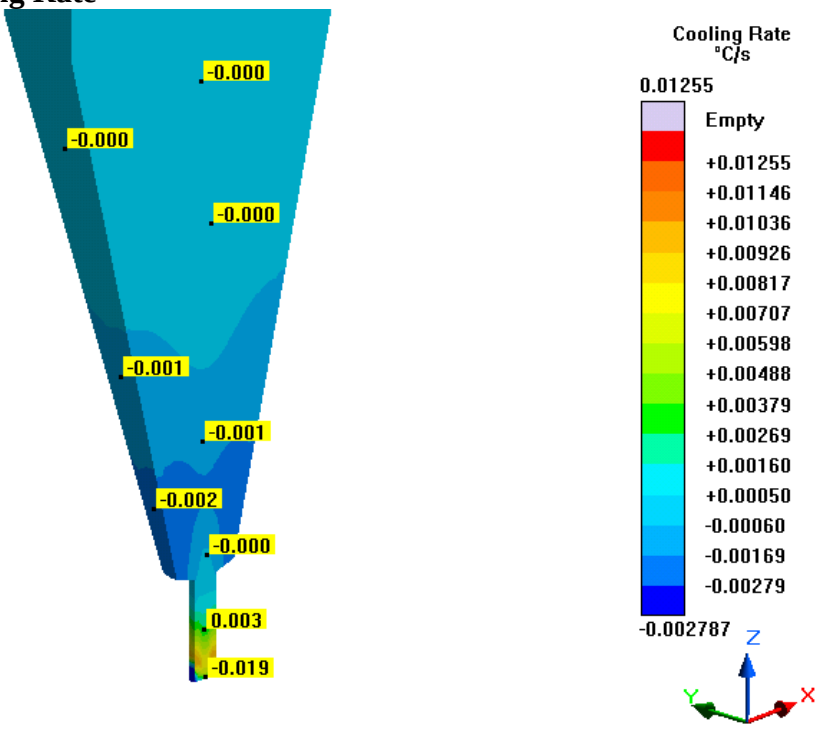

Figure 818- Simulation 27 (LLNL 300 Micron, TC, 2 s), Cooling Rate

Shear Heating

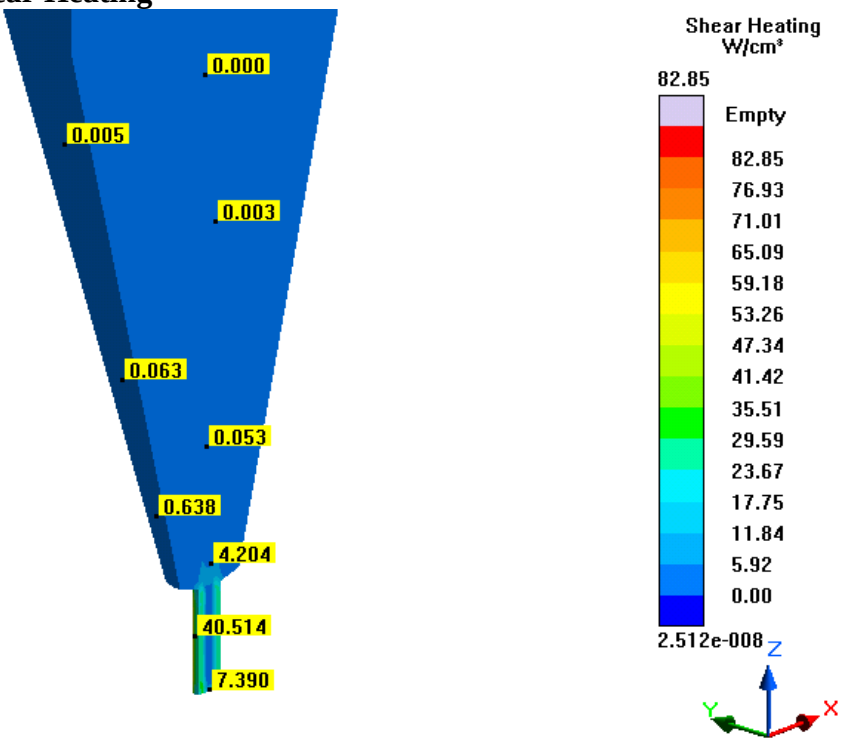

Figure 819- Simulation 27 (LLNL 300 Micron, TC, 2 s), Shear Heating

Shear Rate

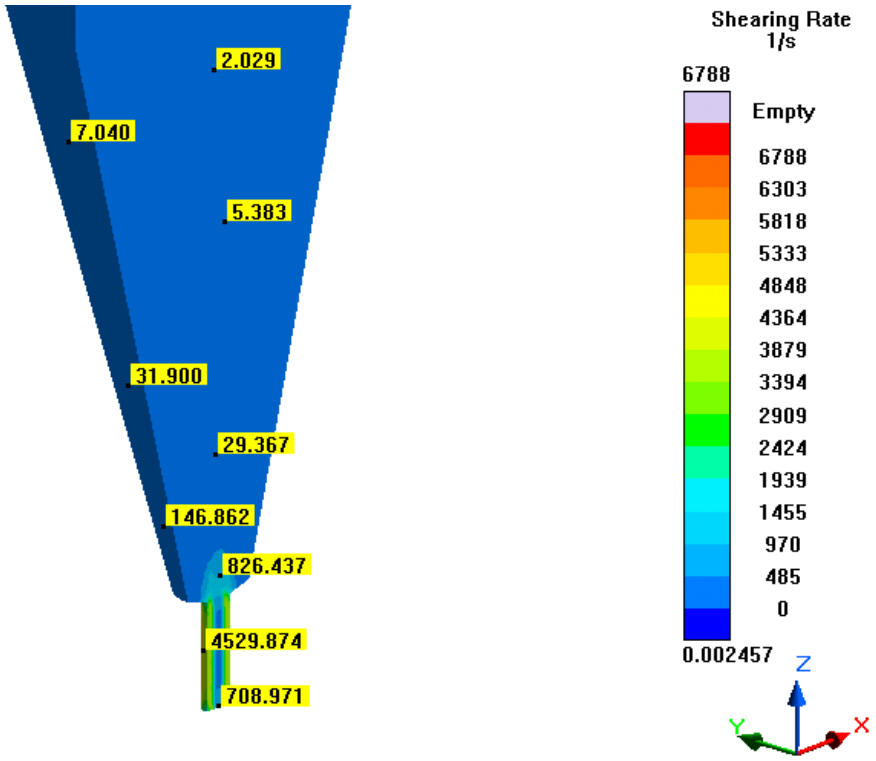

Figure 820- Simulation 27 (LLNL 300 Micron, TC, 2 s), Shear Rate

Shear Stress

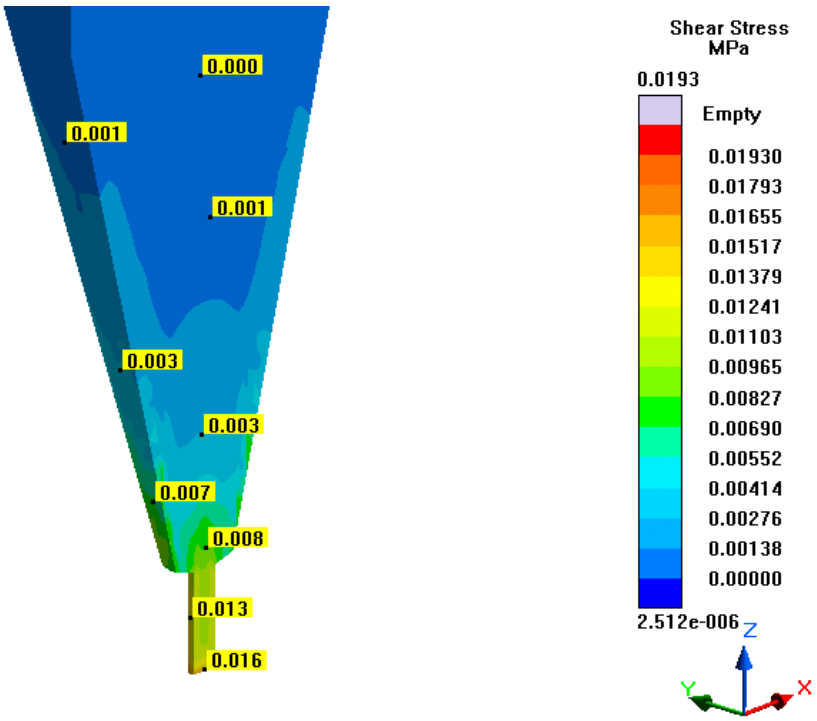

Figure 821- Simulation 27 (LLNL 300 Micron, TC, 2 s), Shear Stress

Temperature

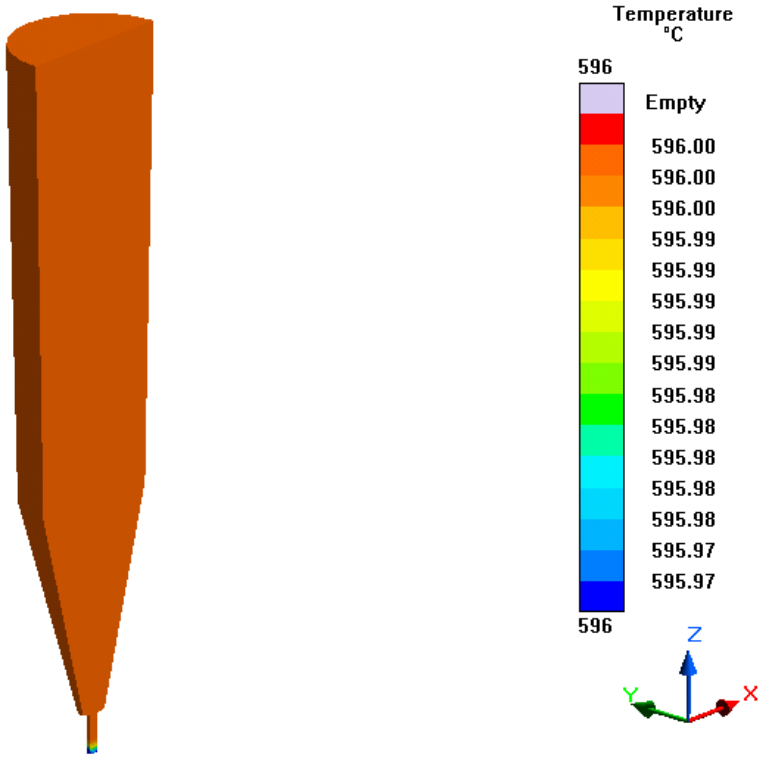

Figure 822- Simulation 27 (LLNL 300 Micron, TC, 2 s), Temperature